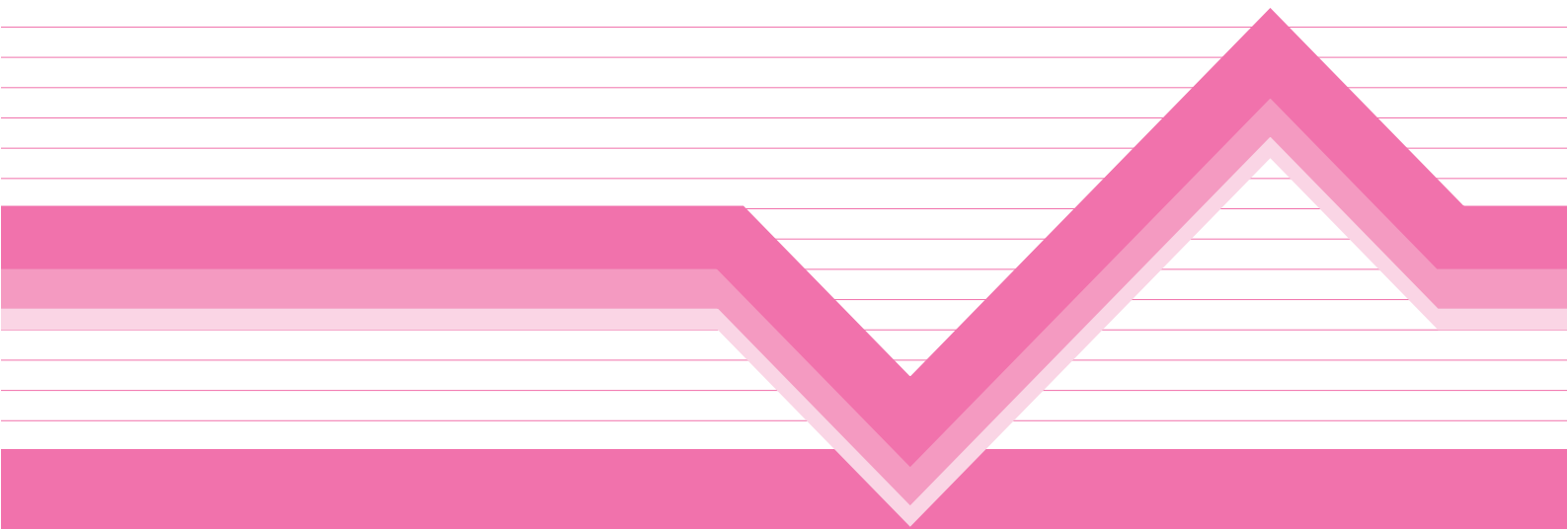


21st Century COE Program
Evolution of Urban Earthquake Engineering

Third International Conference on Urban Earthquake Engineering



*Center for Urban Earthquake Engineering
Tokyo Institute of Technology*

Tokyo Tech
CUEE

21st Century COE Program
Evolution of Urban Earthquake Engineering

Third International Conference on Urban Earthquake Engineering

*Center for Urban Earthquake Engineering
Tokyo Institute of Technology*

Tokyo Tech
CUEE

PREFACE

On behalf of the Center for Urban Earthquake Engineering (CUEE), Tokyo Institute of Technology, I am very delighted to have this 3rd International Conference, inviting many distinguished guests, and experts from inside and outside Japan. Our center was established two and a half years ago to carry out the COE (Center of Excellence) program entitled “Evolution of Urban Earthquake Engineering”. It is a five-year program sponsored by the Ministry of Education, Culture, Sports, Science and Technology (MEXT). This COE program aims not only to promote research for overall earthquake risk reduction technology but also to strengthen the graduate education program as well as to launch international collaboration in research and education.

In my belief, this kind of effort is urgently needed, not only in Japan, but also in other earthquake prone countries around the world. As an example, consider the tragedy caused by the Sumatra Island earthquake and tsunami of December 26, 2004. The catastrophic disasters and the subsequent widespread disaster chain reinforced the pressing need for enhancing our activities, especially the collaboration with foreign institutions. In view of this global-scale tragedy and our above-mentioned mission, we have launched a Distance-Learning graduate program between Tokyo Tech and Chulalongkorn University, Thailand, this year. I would like to take this opportunity to express my deep gratitude and appreciation for the great help and coordination in successfully executing the program. In addition, we have organized a special tsunamis session for this conference, inviting experts from the tsunami-affected countries such as Indonesia, Sri Lanka and Thailand. In contrast to our 1st and 2nd conferences, our 3rd conference will however also be featuring a range of contributions from our young researchers and graduate students who are strongly encouraged to make presentations followed by active discussions with international participants. Thus, we would appreciate your kind cooperation along this line.

Currently we are at the end of the 3rd year of the COE program, and ten months ago, in the middle of last May, we had an interim evaluation. To our satisfaction, we had a best evaluation result, thanks to all our members working for CUEE. In our quest for the real success of the COE program, we would appreciate your support.

Tatsuo Ohmachi

Director and Professor, Center for Urban Earthquake Engineering and

Leader of the 21st Century COE Program: Evolution of Urban Earthquake Engineering.

TABLE OF CONTENTS

Papers Presented in the Oral Sessions

Keynote Presentation

(Engineering Seismology and Seismic Hazard Mitigation Planning)

Earthquake engineering research and practice in Mexico after the Michoacan earthquake of 1985: a 2006 review	1
Esteva, L	

Keynote Presentation

(Earthquake Response Analysis and Experiment)

Recent advances in hybrid testing for earthquake performance evaluation	17
Shing, P. B.	

Engineering Seismology

Differences in earthquake source and ground motion characteristics between surface and buried earthquakes	25
Somerville, P. and Pitarka, A.	
Identification of nonlinear site response using the H/V spectral ratio method	33
Wen, K. L., Chang, T. M., Lin, C. M. and Chiang, H. J.	
Development of earthquake motion simulator with high resolution and its application	41
Ichimura, T., Hori, M. and Samo, T.	
Long period ground motion characteristics in a mega-city Osaka during expected huge subduction earthquake	47
Kamae, K. and Kawabe, K.	
Monitoring and interpretation of creep behavior in Chihshang active fault zone	55
Chen, M. H., Wu, R. S., Wang, C. Y., Lin, C. P., Lee, C. J., Chou, H. T. and Dong, J. J.	
How to evaluate spatial distribution of earthquake ground motion in the northern Japan	63
Takai, N., Maeda, T. and Sasatani, T.	
A study on waveform inversion for characterized source models using genetic algorithms	69
Motoki, K., Yamanaka, H. and Seo, K.	

Geotechnical Earthquake Engineering

Assessing the potential for strength loss and deformations in low plasticity silts and clays during earthquakes.....	77
Boulanger, R. W. and Idriss, I. M.	
Pushover analysis for lateral piles subjected to liquefaction-induced flow pressure	85
Hwang, J. H. and Chung, M. C.	
Behaviour of piled bridge abutment on liquefiable soils.....	95
Takahashi, A, Sugita, H. and Tanimoto, S.	
Observed pile-soil interaction during buckling instability	103
Bhattacharya, S. and Tokimatsu, K.	
Dynamic behavior of embankments resting on liquefiable sandy deposit	113
Tobita, T., Iai, S. and Ueda, K.	
Effect of saturation on liquefaction resistance of sandy soil	121
Okamura, M. and Soga, Y.	
Nonlinear behavior of Taipei silty clay under irregular strain loading.....	129
Lee, C. J. and Sheu, S. F.	
Strength and deformation characteristics of soft rocks from the Guadalupe tuff formation in Metro Manila when subjected to large cyclic loading	137
Peckley Jr, D. and Uchimura, T.	
Developing time varying wave transmitting boundaries using joint time-frequency representation method	145
Farahani, A. and Konagai, K.	

Keynote Presentation

(Engineering Seismology and Seismic Hazard Mitigation Planning)

Development of simple, economic and efficient retrofitting method for masonry buildings considering local availability and acceptability in earthquake prone regions	153
Meguro, K.	

Seismic Hazard Mitigation Planning and Human Response

Vehicle routing for rescue operation in earthquakes.....	161
Hsueh, C. F. and Chen, H. K.	
Learning disaster preparedness and response through gaming simulation	169
Kikkawa, T. and Yamori, K.	
Risk assessment for Taiwan residential earthquake insurance pool-modeling and application.....	175
Hsu, W. K., Chiang, W. L., Hung, D. M., Tseng, C. P. and Tsai, C. H.	
A proposal on a method to determine risk-based seismic design level	183
Nakajima, M., Morikawa, H. and Hirata, K.	
Changes of building use and structure in Tokyo 23-ku	191
Meshitsuka, Y.	

Development of an effective tool for virtual experience of environmental hazard -a survey of disaster education facilities in Japan-.....	197
Ryu, J., Soeda, M. and Ohno, R.	

Keynote Presentation (Tsunami)

Global disaster due to the 2004 Indian ocean tsunami	205
Imamura, F., Koshimura, S., Goto, K., Yanagisawa, H. and Iwabuchi, Y.	

Tsunami

Environmental restoration of tsunami impacted inland water bodies in Sri Lanka	211
Gunaratna, P. P.	
Report of two field visits to assess tsunami damage in Sri Lanka due to the Sumatra-Andaman earthquake of December 26, 2004	219
Wijeyewickrema, A. C., Inoue, S., Matsumoto, H., Miura, H., Gunaratna, P., Madurapperuma, M. and Sekiguchi, T.	
Tsunami arrival time in Sri Lanka due to the 2004 Sumatra earthquake.....	231
Inoue, S., Wijeyewickrema, A. C., Matsumoto, H., Miura, H., Gunaratna, P., Madurapperuma, M. and Sekiguchi, T.	
Extraction of tsunami inundation area in the eastern part of Sri Lanka due to the 2004 Sumatra earthquake using high-resolution satellite images.....	237
Miura, H. and Midorikawa, S.	
Effect of wave frequency dispersion in the Indian ocean tsunami	245
Shigihara, Y. and Fujima, K.	
What can we do for minimizing tsunami disaster?.....	251
Iwasaki, S.	
Accounts and modeling of the old and modern Sumatra tsunamis for mitigation in the future.....	259
Latief, H., Natwidjaya, D.H., Sunendar, H., Gusman, A.R. and Tanioka, Y.	
Performance and database of buildings damaged in Thailand in the 2004 Indian ocean tsunami	267
Ruangrassamee, A. and Foytong, P.	
Problem and Improvement of the Tsunami Warning System	275
Takahashi, T.	
Early tsunami forecasting using real-time offshore observatories.....	281
Matsumoto, H. and Mikada, H.	
Numerical simulation of tsunami inundation in urban area.....	287
Hiraishi, T.	

Development of high performance simulator for tsunami based on shallow water equations	293
Akoh, R., Ii, S. and Xiao, F.	
Study on the oil spread caused by 1964 Niigata earthquake tsunami	301
Iwabuchi, Y., Koshimura, S. and Imamura, F.	

Concrete Structures

Damage control system using prestressed concrete members with graded composite strands	309
Kono, S., Ichioka, Y., Watanabe, F., Nishiyama, M. and Arakane, S.	
Testing on 2-story and 2-bay reinforced concrete frames with substandard reinforcing details	317
Wang, Y. C., Huang, J. S. and Chen, B. C.	
Mechanical characteristics of reinforced concrete members strengthened by carbon fiber flexible reinforcement	323
Sato, Y. and Kobayashi, A.	
Crack tracing process for smeared-crack-based nonlinear fem	331
Sato, Y. and Naganuma, K.	
Shear behavior of connecting bars on precast joint under axial tensile force and shear force from seismic load	339
Katori, K., Hayashi, S. and Takagi, H.	
Development of RC flat beam and column joint system	345
Nishimura, K., Takiguchi, K., Hotta, H., Tsuneki, Y., Koitabashi, Y. and Nakanishi, N.	
Performance assessment for reinforced concrete buildings with soft first stories	353
Nagae, T.	
Nonlinear analysis of reinforced concrete viaducts by 3D lattice model	361
Miki, T. and Niwa, J.	

Steel Structures

Collaborative structural analysis system by linking sophisticated programs through internet	369
Tada, M.	
Seismic behavior of concrete encased steel columns subjected to axial load and bi-axial bending	377
Hsu, H. L. and Jan, F. J.	
Continuous column effects on seismic response of steel moment frames in perspective of instantaneous stability	385
Tagawa, H., MacRae, G. and Lowes, L.	
Development of link-to-column connections for steel eccentrically braced frames	393
Okazaki, T., Engelhardt, M. D.	

Dynamic tests of steel frames with column uplift for seismic response reduction	401
Ishihara, T., Midorikawa, M. Azuhata, T. and Waka, A.	
Seismic behavior of beam-column connections based on damage-controlled-design	407
Kishiki, S., Yamada, S., Takeuchi, T. and Waka, A.	
Study on fracture and ultimate performance of steel beam-to-column connections	415
Matsumoto, Y.	

Bridge Structures

Proposal of a remote bridge monitoring system for damage detection	423
Sasaki, E., Miki, C., Tohmori, M., Ishikawa, Y. and Miyazaki, S.	
Shake table tests of reinforced concrete bridge columns that mitigate residual displacements following earthquakes.....	431
Sakai, J. and Mahin, S. A.	
Nonlinear seismic response control of isolated bridges using MR dampers	439
Lee, T. Y. and Kawashima, K.	
Cyclic elasto-plastic behavior of buckling-restrained brace members	447
Kasai, A., Usami, T. and Kato, M.	
Ductility of welded joints with weaker welding material.....	455
Tanabe, A. and Kato, M.	
Effect of near-field ground motions on the inelastic force and displacement demand of bridge structures.....	463
Watanabe, G. and Kawashima, K.	
Seismic resistance evaluation of beam-to-circular column connections of steel bridge frame piers with circular column.....	471
Kinoshita, K. and Tanabe, A.	
Response analysis of bridges supported by C-bent columns.....	479
Nagata, S. and Kawashima, K.	

Passive Control and Base Isolation

MATLAB-based health monitoring system for buildings and its data management system	487
Mita, A., Inamura, T. and Yoshikawa, S.	
Seismic retrofit of existing building with hysteretic dampers	495
Takeuchi, T., Yasuda, K., Yuasa, K. and Iwata, M.	
Prediction for cumulative plastic deformation of damper in elasto-plastically damped structure.....	503
Ito, H. and Kasai, K.	
Seismic isolation Structures in Japan.....	511
Ohmiya, M. and Teramoto, T.	

Fundamental study on effect of damping on distribution of story shear coefficient.....	519
Ooki, Y., Kasai, K., Igusa, T. and Shimoda, T.	
Evaluation on aseismic performance of hybrid type of base-isolation system with powered-mass couplers damper.....	527
Mukai, Y	
Performance-based seismic provisions for seismically isolated buildings in Japan	535
Midorikawa, M, Iiba, M., Koshika, N. and Kani, N.	

Earthquake Response Analysis and Experiment

Residual seismic capacity of concrete block infilled RC frames: crack development mechanism of concrete block wall	543
Nakano, Y. and Choi, H.	
Seismic responses of structures subjected to artificial ground motions generated using 1D, 2D and 3D ground models	551
Chen, H. T., Wang, Y. C. and Juang, D. S.	
Equivalent single-story model for multi-story unsymmetric frame buildings with elasto-plastic seismic control devices	559
Fujii, K.	
Spectrum-based prediction rule for peak structural responses of SDOF system pounding against rigid structures	567
Tran, B. T. and Kasai, K.	
Seismic shutoff characteristics of intelligent gas meter deployed for individual customers	575
Maruyama, Y., Yamazaki, F., Nabana, K. and Yamauchi, A.	
A shaking table test of 2-story R/C frames with partial walls independent from columns.....	583
Hotta, H. and Nakajima, T.	
Earthquake response monitoring of traditional Japanese timber pagoda	591
Fujita, K., Hanazato, T. and Sakamoto, I.	

Papers Presented in the Poster Sessions

Engineering Seismology

Lessons learned from recent earthquake disasters - for mega-cities on huge sedimentary basins -	599
Seo, K., Motoki, K. and Eto, K.	
Joint inversion of receiver function and Rayleigh-wave phase velocity for estimation of S-wave velocity of sedimentary layer in Niigata, Japan.....	607
Yamanaka, H. and Kurose, T.	

A method for estimation of 2-D subsurface structure using gravity and microtremor data simultaneously.....	615
Sakai, K. and Morikawa, H.	
Estimation of S-wave velocity model in the western coastal plain of Taiwan.....	623
Lin, C. M., Wen, K. L. and Chang, T. M.	

Geotechnical Earthquake Engineering

Effects of lateral response of embedded footing on piles.....	629
Tamura, S. and Tokimatsu, K.	
Detection of subsurface V_s recovery process using microtremor and weak ground motion records in Ojiya, Japan	637
Arai, H.	
Active type shear box and its application on a stability of shallow tunnel in a centrifuge.....	645
Takemura, J., Izawa, J., Shibayama, S. and Kusakabe, O.	
Estimation of seismic behavior of pile group in non-liquefied and liquefied ground through centrifuge model tests	653
Suzuki, H., Tokimatsu, K. and Ozawa, G.	
Analytical study for damage to cast-in-place concrete pile in laterally spreading ground during the 1995 Hyogoken-Nambu earthquake	659
Koyamada, K., Tokimatsu, K. and Miyamoto, Y.	
The construction of beam-on-spring model considered liquefaction between the piles.....	667
Yoshida, H., Imamura, A. and Yagishita, F.	
1-G shaking table tests on the lateral resistance of in-line double piles subjected to lateral spreading.....	673
Dungca, J. R., Kuwano, J. and Nishio, S.	
Evaluation of nonlinear soil amplification at Ojiya K-net and JMA stations during the 2004 mid Niigata prefecture earthquake	681
Tokimatsu, K., Sekiguchi, T. and Yamataka, M.	
Micro-tremor measurements at a fill dam damaged by the 2004 Niigata-Chuetsu earthquake	687
Ohmachi, T., and Inoue, S.	

Seismic Hazard Mitigation Planning and Human Response

Consideration about influence of floor characteristics on furniture behavior during earthquake -fundamental study on establishment of evaluation method for seismic resistance of floor finishing system part 2-	695
Yokoyama, Y., Yokoi, T. and Iida, R.	
Trust security, and peace of mind	703
Fujii, S., Kikkawa, T. and Takemura, K.	

Use of digital city for seismic hazard representation.....	709
Midorikawa, S., Miura, H. and Inoue, S.	

Concrete Structures

Research on weight reduction of composite PC beams using prestressed UFC truss	713
Murata, H., Niwa, J., Chigira, E. and Miki, T.	
Applicability of design code and simplified truss model for shear carrying capacity of externally prestressed concrete beams	719
Sivaleepunth, C., Niwa, J. and Miki, T.	

Bridge Structures

Proposed torsional hysteretic model for RC columns under combined cyclic bending and torsion	727
Tirasit, P. and Kawashima, K.	
Carbon fiber sheet retrofit of reinforced concrete bridge columns under cyclic loading	735
Gallardo, R. M. and Kawashima, K.	

Passive Control and Base Isolation

Progress in E-defense shaking table experiments of full-scale 5-story building with dampers.....	743
Kasai, K., Ooki, Y., Motoyui, S. and Tekeuchi, T.	

Earthquake Response Analysis and Experiment

Evaluation of earthquake resistance of steel building structure based on deformation capacity of members	753
Yamada, S.	

EARTHQUAKE ENGINEERING RESEARCH AND PRACTICE IN MEXICO AFTER THE MICHOACAN EARTHQUAKE OF 1985: A 2006 REVIEW

Luis Esteva

Professor Emeritus, Institute of Engineering, National University of Mexico; Mexico City, MEXICO
lestevam@ii.unam.mx

Abstract: A brief review is presented of the main engineering lessons learned from the performance of urban constructions during the Michoacan (Mexico) earthquake of 1985, which produced significant damage in Mexico City. Specially important among those lessons were those related to concepts such as the unexpectedly high values of local intensities at soft soil sites, the limitations of conventional methods for the estimation of the nonlinear dynamic response of irregular systems, and the need for more strict quality control procedures during construction, including special attention to the details oriented to ensure local ductile behavior of structural members. Research efforts during the twenty years elapsed since the earthquake have been primarily oriented to responding to those lessons, through the improvement of our estimates of seismic hazard and risk for different local soil conditions, as well as of our capacity to produce adequate predictions of peak nonlinear dynamic response of complex systems, including the influence of soil-structure interaction. Seismic design regulations for Mexico City have been updated several times during this interval (1987, 1993, 2004), in addition to the emergency norms issued a few weeks after the event. The paper ends with a review of some of the most relevant concepts in the 2004 version.

1. INTRODUCTION

Detailed reports about the engineering lessons derived from the performance of structural systems during the Michoacan earthquake of 19 September 1985, and about the research and implementation activities following it, have been presented in many publications. A summary about the consequences, lessons, and impact on research and practice has been presented by the author (Esteva, 1987, 1988); the latter is an article that serves as an introduction for a series of three special issues of Earthquake Spectra (Vol. 3, Nos. 3, 4; Vol. 5, No. 1), describing an important part of the work developed in Mexico and abroad during the first two and a half years after the earthquake. Trying to avoid unnecessary repetitions, this information is taken here as a starting point; however, a very brief summary of it is presented in the following, trying to provide a background for the actions that have led to our current state of knowledge and practice, as well as about the technical challenges we are still facing. This is followed by a bird's eye view of the research programs during the last years, as well as of the most relevant aspects of the revision of the seismic design codes in Mexico City. Attention is concentrated on research related to the prediction of the nonlinear dynamic response of complex systems and to the development of reliability-and-performance-based design criteria.

2. SEISMIC HISTORY OF MEXICO CITY BEFORE 1985

The city was founded by the Aztecs in 1325, on an island in the middle of a shallow lake in the Valley of Mexico. The soil at the surface of the island and under the bottom of the lake was constituted by very soft clay formations, with extremely high void ratios, created by the deposit of

ashes generated by eruptions of a large number of volcanoes around the valley. In 1521, the city was conquered by the Spaniards, who transformed it into a very important hub of Spanish power in the American continent during the colonial times. Traditional Aztec temples and houses were gradually replaced by a new type of constructions, inspired on those typical of Spain in those times, including large churches and palaces that have remained until now as jewels of the national architectural heritage. All of them were characterized by short natural vibration periods.

In the course of the centuries, a drainage system had to be built in order to send the water out of the valley and permit the spreading of the city beyond the edges of the original island. Thus, the urban area that includes the original city evolved into one of the largest in the world. Unfortunately, it is also one with the most difficult foundation conditions: soft clay sediments under the urban area can extend to depths as large as 70m, with shear wave velocities as low as 90m/s at some sites, and dominant ground periods as high as 4.5 in the Eastern side of the city or 2.0-2.5s in the downtown area. (See Figures 1 and 2.)

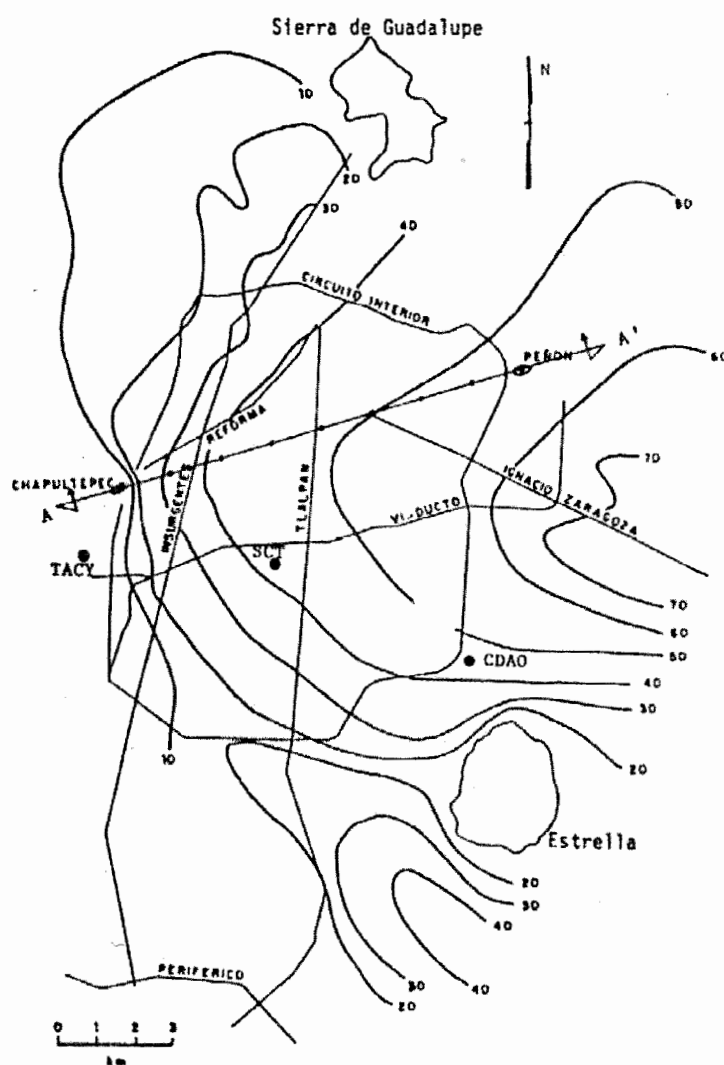


Figure 1 Depth of soft clay formation in the Valley of Mexico
(From Sánchez-Sesma *et al*, 1988)

Seismic hazard in the urban area largely results from the activity of the subduction zone at the contact between the American and the Cocos plates, along the Southern coast of the country, at a

distance greater than 250km. Because of this, high intensities are not likely at firm ground sites in the city, even for large earthquake magnitudes. This was the case for the Michoacan event, which had a magnitude $M_S = 8.1$ and an epicentral distance of 360 km from the city. The high intensities observed at soft soil sites were the result of extremely high ground motion amplification, in particular for wave frequencies in the vicinity of the dominant ground period at each site. An aftershock, with a magnitude of 7.5, occurred 36 hours later.

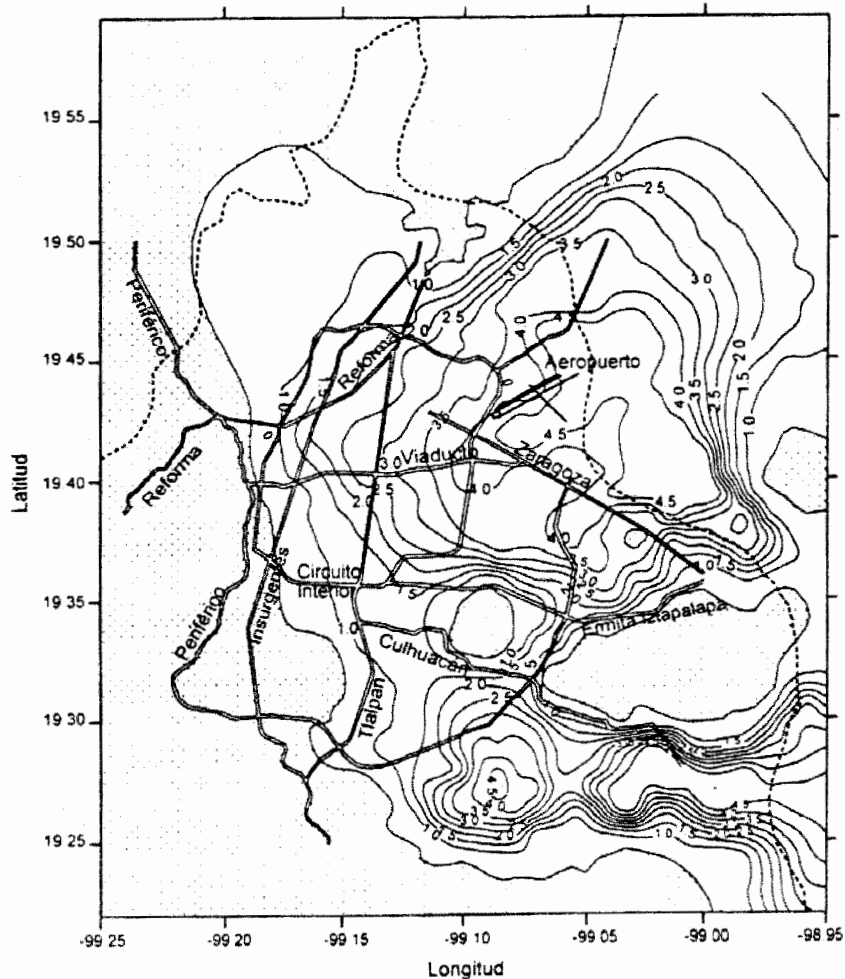


Figure 2 Dominant ground periods in Mexico City Metropolitan Area

In spite of its long history and its unfavorable local soil conditions, the city had never experienced an earthquake as damaging as that of 1985. This can be easily explained in terms of the types of constructions that were exposed to earthquakes during the last six centuries, before the advent of modern high-rise constructions, in the middle of the twentieth century. As mentioned above, they were short-period constructions, not sensitive to the narrow-band ground motions with energy inputs concentrated in dominant frequencies corresponding to the dominant ground periods. Prior to 1985, the highest damage ratio ever recorded throughout the urban area was that produced by the earthquake of July 28, 1957, with a magnitude $M_S = 7.6$ and an epicentral distance of 256km, which resulted in the collapse of a few buildings and the loss of about 100 lives. The evolution of seismic design regulations in the city during the interval 1957-1985 was strongly influenced by the observations about structural performance during the 1957 event and during a number of moderate

intensity shocks occurring every five years in the average. The highest acceleration occurred on soft soil during this interval was estimated as 0.06g; that is, about one third of that recorded in 1985 near the SCT building, within the area of the city with the highest damage level.

3. 1985: LESSONS LEARNED AND QUESTIONS RAISED

When the 1985 earthquake occurred, seismic design codes were essentially based on the experience derived from the 1957 earthquake. The urban area was divided into three micro-zones: I Firm ground, II Transition zone (soft sediments with a depth lower than 20m) and III Soft soil (soft sediments deeper than 20m). Linear response spectra (5 percent damping) specified for design had maximum ordinates of 0.16, 0.20 and 0.24 for these zones, respectively. Reduction factors to account for nonlinear behavior ranged from 1 to 6, depending on the type of structural arrangement and ductility-oriented details (García-Ranz and Gómez, 1988). These values were widely exceeded by those depicted in Figure 3 (taken from Seed *et al*, 1988), which shows mean values of the horizontal pseudo-acceleration response spectra in two orthogonal directions, recorded at different sites in Mexico City. These discrepancies are evident in Figure 4 (Castro *et al*, 1988), which shows a comparison of the Fourier amplitude spectrum of the EW component of the ground acceleration at the SCT site with the ordinates predicted by means of the attenuation functions derived on the basis of previous seismic events, which had greatly influenced decisions about codified seismic design requirements. Given the overwhelming differences between observed intensities and design capacities, it must be concluded that the stability of constructions rested mainly on the reserves associated with the strength of elements not accounted for in design, as well as with the energy dissipating capacity of those elements and those that were recognized as structural members. Therefore, for the purpose of improving the technical basis for earthquake engineering, understanding the survival of so many structures during this earthquake (and during many others, for this matter) is at least as important as identifying causes for the failures observed.

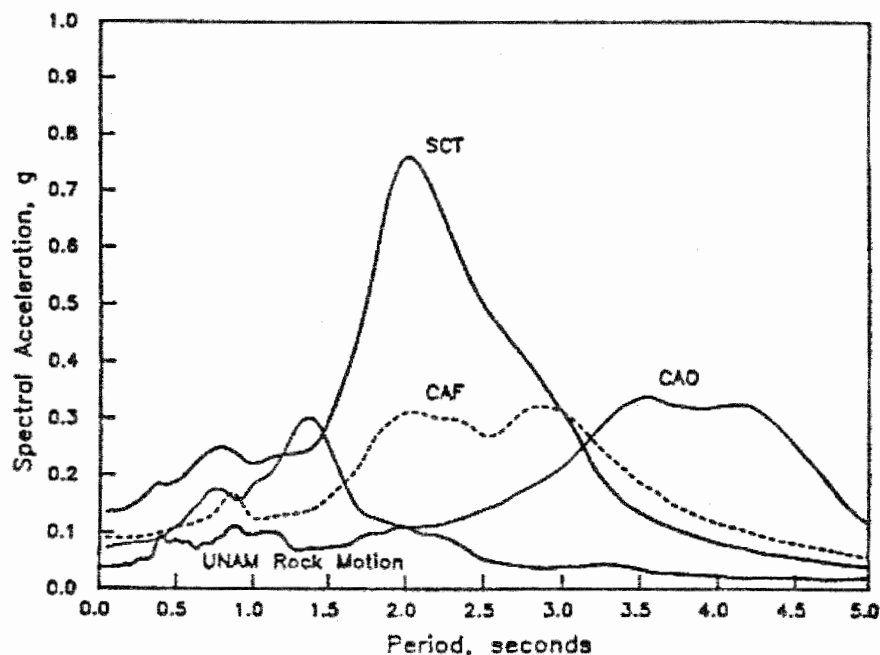


Figure 3 Mean values of pseudo-acceleration response spectra at different sites
(From Seed *et al*, 1988)

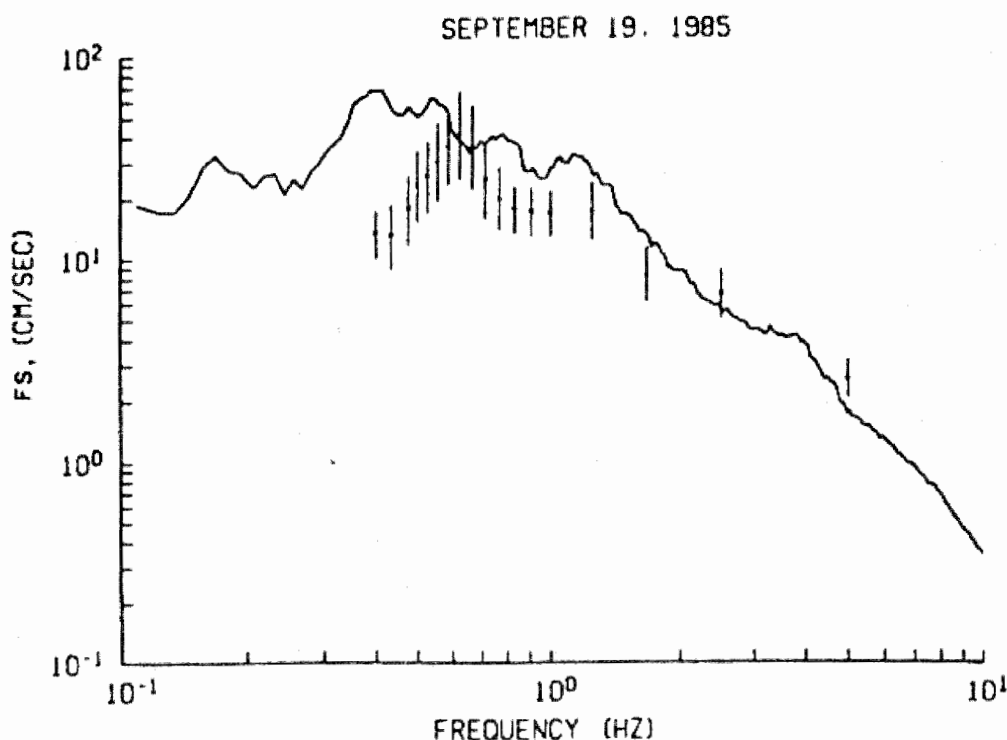


Figure 4 Comparison of observed and predicted values of the Fourier amplitude spectrum of the EW-SCT-850919 ground motion acceleration record (From Castro *et al*, 1988)

Table 1. Causes and types of failure and damage

Causes and types	Percentage of the population of damaged structures
Corner buildings (pronounced asymmetry in stiffness)	42
Other cases of pronounced asymmetry in stiffness	15
Weak first story (large ductility demands)	8
Short columns (brittle failure)	3
Excessive mass (overload)	9
Previous differential settlement	2
Inadequate foundation performance	13
Impact between adjacent constructions	15
Previous seismic damage	5
Shear failure in connections of flat-slabs to columns	4
Collapse of top stories	38
Collapse of intermediate stories	40

Meli and Rosenblueth (1986) made a review of the main causes of failure and damage; they summarized their observations in Table 1, which indicates the percentage of the population of damaged systems where each type of performance was observed. The paragraphs that follow contain a summary of the comments presented by Esteva (1987, 1988) about the main causes of damage associated with the limitations of structural analysis and design criteria, as well as with the deficiencies in the practice of quality control.

Moderate-height buildings located at block-corners usually possess flexible frames along their

facades and rigid masonry diaphragms at the opposite sides, along the limits with the adjacent plots of land. Often, this gives place to very large in-plan eccentricities (both in strength and stiffness) and, therefore, to very high torsional-response demands. A large number of the systems in this case did not possess the capacity to resist those demands, either because they were much larger than estimated on the basis of the specified design requirements or because the application of the latter had been overlooked. This explains the large number of cases of collapse of systems of this type.

A large portion of the structures that failed showed significant irregularities in the variation of the lateral stiffness and/or strength along the building height. These irregularities in some cases gave place to large concentrations of ductility demands at the weakest segments of the structural system, thus leading to values of those demands much in excess of those that are estimated on the basis of the simplified rules (such as the "equal-displacement" rule) ordinarily used to transform the results of linear response analysis into those corresponding to the nonlinear response of multi-degree-of-freedom systems. $P-\Delta$ effects, propitiated by stiffness degradation, may have played a significant role in many cases of collapse, as evidenced by the many cases of large story drift and tilting that could be appreciated after the earthquake.

Deficient performance of foundations was an important source for high damage levels, including many cases of collapse. This was a consequence of the especially difficult foundation conditions prevailing in the soft soil area in the city, and led to many cases of excessive residual differential settlements or to failure produced by insufficient bearing capacity of the foundation. In other cases, conditions of structural tilting prior to the earthquake led to the development of non-symmetric force-displacement functions for lateral shear, which in turn led to excessively high ductility demands. Insufficient bond strength in friction piles was in some cases the cause for generalized foundation failure.

About 40 percent of the cases of partial collapse involved failure of one or more stories in the upper third of the height of the structure. In many of those cases, pounding between adjacent structures was determinant; others were ascribed to a number of potential causes including, for instance, the influence of higher modes of vibration, the lack of capacity of small-width columns to provide sufficient bond development-lengths to permit the stresses on the longitudinal reinforcement of concurring beams to change from yield stress in tension to yield stress in compression from one face of the column to the other, and the rapid increase in response amplitude owing to base-rocking caused by soil-structure interaction. The latter assumption was later dismissed as a result of some theoretical studies (Esteva, 1989).

Deficiencies in quality control and inadequate compliance with codified rules, or with generally accepted principles for earthquake-resistant construction, are often cited as having a significant role in the generation of seismic damage in urban constructions around the world. Mexico City was no exception in this regard, as witnessed by the high observed number of the following types of damage:

- a) Noncompliance with seismic design requirements for soft-ground-floor systems, which established lower reduction factors for base-shear ratios (or for design response spectra) for systems with sharp discontinuities in story strength or stiffness along their height. This problem was mentioned above.
- b) Brittle failure in columns, associated with poor concrete aggregates, inadequate confining capacity of typical reinforcement details, excessively high bond stresses and poor restriction to buckling of longitudinal reinforcement.
- c) Punching failure in the vicinity of the joints between waffle-slabs and columns, due to insufficient shear capacity of the former elements.
- d) Pounding between adjacent buildings, resulting from noncompliance with the requirements for minimum allowable separations. Risk related to this type of damage was enhanced by the contribution of foundation rocking to the displacements in the upper portions of buildings.
- e) Excessively high live loads, resulting from using a building for a type of occupancy differing

from that assumed in design.

More details about the observed performance of constructions have been presented in a number of publications issued shortly after the earthquake; for practical reasons, only a few of them are included in the list of references (Meli and Rosenblueth, 1986; Meli and Avila, 1989; Rodríguez and Díaz, 1989; Osteraas and Krawinkler, 1989; Ruiz and Diederich, 1989; Miranda and Bertero, 1989; Goodno *et al*, 1989).

4. IMMEDIATE ACTIONS

Immediately after the earthquake, an ad-hoc Advisory Committee on Structural Safety was formed with the responsibilities of recommending immediate actions and updating Mexico City Building Code. This committee undertook also the job of coordinating research work relevant to code revision. It also formulated a two-step strategy for the required code updating: a nearly immediate emergency code and a long term (about one year) thorough revision. The former was issued five weeks after the earthquake; its main concepts were supported by the immediate conclusions derived from damage surveys.

On the basis of the large amount of damage observed, but also of the many cases of satisfactory performance, specified base-shear coefficients were raised in 67 percent for the soft-soil zone and 33 for the transition zone (both specified in the 1976 version of the building code, which was in force during the earthquake). Strength reduction factors (to be applied to nominal values of ultimate capacities) were decreased in 18 to 33 percent for brittle failure modes of reinforced concrete and steel structures; more drastic reductions were applied to bond between soil and friction piles. Structures that had experienced significant damage should be repaired in compliance with the emergency code. Design values of live loads in office buildings were raised and the obligation to place a sign in each story of a building showing the maximum allowable live load was stressed.

Structures showing at any story torsional eccentricities in excess of 20 percent of the width of that story in the direction of the eccentricity were banned.

The influence of damage due to previous differential settlements above allowable values set by the code should be explicitly taken into account, and the calculated value of the lateral capacity of the structure should be reduced accordingly.

The code calls for the participation of a supervisor, responsible of structural safety, independent from the contractor, for all permanent constructions (both ordinary and special) taller than 15m or with a built area larger than 3000m². Finally, any change of occupancy of a construction requires the approval, by the city authorities, of a detailed study made by a registered engineer, showing that safety conditions will not be lower than those corresponding to the type of occupancy considered in the structural design.

In 1988 the National Center for Disaster Prevention (CENAPRED) was constituted, as a joint enterprise of the National University of Mexico and the Government of the country. During the first years of its operation, the Center counted with the technical advice and the economic support of the Japan International Cooperation Agency (JICA).

5. AN OVERVIEW OF POST-1985 RESEARCH

Having in mind the need for research programs aimed at providing the basis for future actions of updating and improvement of seismic design codes, the Advisory Committee on Structural Safety obtained funds from the Government of the City, which have permitted that group to provide sponsorship for research projects along the following general lines:

- a) Seismology, seismicity, ground motion and seismic hazard.
- b) Experimental research on the behavior of materials, structural and non structural elements.
- c) Seismic response of buildings and other structural systems.

- d) Passive control of seismic structural response.
- e) Special and very important structures.
- f) Instrumentation and identification of structural systems.
- g) Damage assessment, repair and retrofit methods.
- h) Soils and soil structures, foundations and soil-structure interaction.
- i) System vulnerability, reliability and seismic risk analysis.
- j) Earthquake-resistant design methods and regulations.

The results of these projects are contained in special reports to the Advisory Committee; they have also found their way to more general national and international audiences, through articles in specialized journals and papers in national and international conferences. Due to the wide variety and extension of the studies undertaken, in this paper it is only feasible to give some details about some of the results that had more impact on the ensuing building code revisions. This approach was adopted in the following.

5.1 Network of strong-motion recording instruments

Only eight accelerographs recorded the ground motion in Mexico City during the 1985 earthquakes. Three of them were located at sites on the former lakebed deposits where the highest damage levels were experienced. Three years later, eighty more accelerographs had been installed, out of which seventy were placed on the ground surface and ten at underground stations. The number has gradually grown during the last few years, now exceeding one hundred. The records they have provided have contributed to make substantial improvements in our understanding of the patterns of local ground motion amplification; they have been reflected in later revisions to the micro-zonation of the city, including that presented in the Technical Norms for Earthquake Resistant Design, Complementary to the 2004 issue of Mexico City Building Code.

5.2 Intensity attenuation functions for firm ground sites on top of volcanic rock around Mexico City

Using the information derived from strong-motion instruments placed on firm ground at sites lying between Mexico City and the southern coast of the country, Ordaz and Singh (1992) obtained attenuation equations for ordinates of the Fourier amplitude spectra of the ground acceleration. They show evidences suggesting the occurrence of significant amplification of those ordinates on firm ground sites in the vicinity of Mexico City, with respect to those estimated by means of the attenuation equations established on the basis of records obtained at the other sites. An example of this is shown in Figure 5 for a frequency equal to 0.5hz. A careful analysis of this information led to the conclusion that even sites known as "firm ground" in the Valley of Mexico are subjected to significant local amplifications of ground motion, due to the low values of S waves that characterize the volcanic rocks that underlie the valley. This is an important concept to have in mind for the purpose of seismic hazard assessment.

5.3 Estimating response spectra in the lake-bed zone of the Valley of Mexico

Some records obtained by the network of instruments mentioned in Section 5.1 were used by Ordaz *et al* (1988) to obtain transfer functions for Fourier amplitude spectra of the ground acceleration at a large number of sites in the city. These functions were later used in conjunction with the Fourier amplitude spectrum of ground acceleration at a firm ground site (CU) during the 1985 earthquake, in order to estimate the corresponding Fourier amplitude spectra at all the sites under study. The latter spectra were in turn transformed into pseudo-acceleration response spectra for 0.05 damping, with the aid of the theory of random vibrations. These spectra were later applied to the formulation of codified expressions to estimate site-specific response spectra for seismic design.

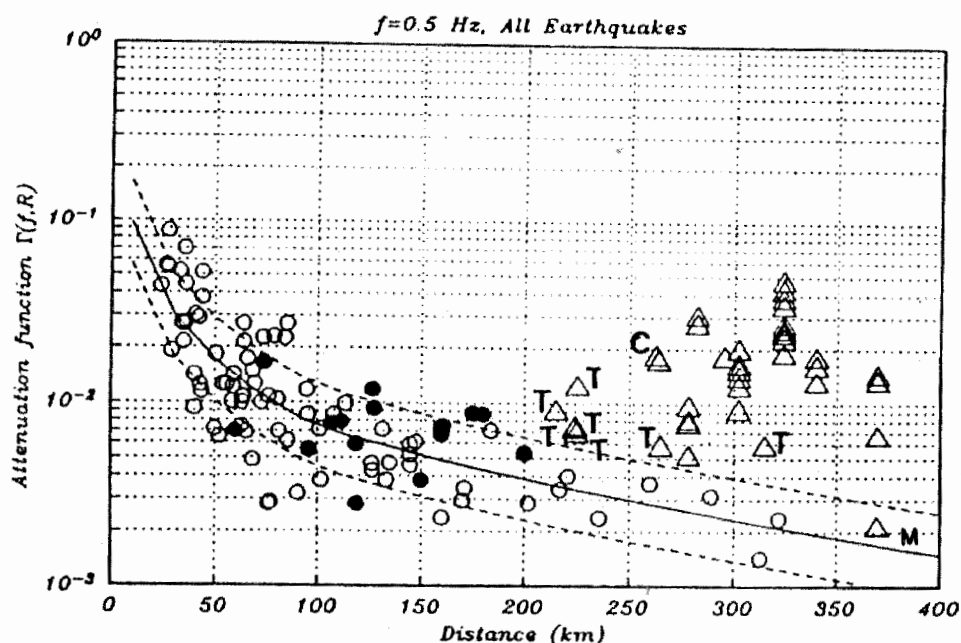


Figure 5 Evidence of amplification of earthquake spectra on the surface of volcanic rock formations (From Ordaz and Singh, 1992)

Rosenblueth *et al* (1989) used an intensity attenuation function of the form proposed by Boore (1983) to estimate Fourier amplitude spectra of earthquake accelerations at a firm-ground site in Mexico City. This information was used in conjunction with the transfer functions mentioned in the preceding paragraph in order to obtain linear response spectra for several soft-soil sites in Mexico City, with natural periods equal to 0.87s, 2.08s and 3.97s, respectively. Several characteristic events were considered for this purpose, corresponding to the most unfavorable combinations of magnitude and distance associated with different seismic sources: a) an inverse-fault earthquake generated at the subduction zone along the southern coast of Mexico, b) an intermediate-depth, normal-fault earthquake, at the lower end of the subducting plate, c) a local earthquake, generated at the Trans Mexican Volcanic Belt, and d) a shallow continental-plate earthquake. The resulting response spectra, including that corresponding to firm ground conditions, were normalized with respect to the maximum ordinate of the design response spectrum for the soft-soil region, as specified in the 1987 revision to the Building Code (Figure 6). The latter spectrum was shown to provide an upper bound to the corresponding constant-hazard spectrum for an annual exceedance rate equal to 0.007 (i.e., a return interval of about 143 years). Response spectra corresponding to this exceedance rate were then obtained for the other three sites. An envelope was then fitted to the maximum ordinates of these functions, including both the constant-hazard and the prescribed-source cases, and was later used to specify the variation of the maximum ordinates of the design spectra in terms of the local value of the dominant ground period.

5.4 Soil-structure interaction

Avilés and Pérez-Rocha (1995) conducted a research program oriented to obtaining approximate expressions for the natural period and damping ratio of an equivalent “replacement oscillator”, founded on a rigid base. Their model is intended to provide reasonably accurate estimations of the peak relative displacements of a system on a soft foundation, including the influence of soil-structure interaction. It adopts a form previously accepted in the literature, according to which the square of the natural period of the replacement system is taken equal to the sum of the squares of the natural periods corresponding to a rigid-foundation model of the system

and two models that incorporate respectively the rotational and the horizontal translational flexibilities of the foundation, considering the superstructure as rigid. Two viscous dampers are added in the interface between the ground and the foundation, in order to represent radiation damping: one to account for rotational displacements and the other to account for horizontal translation. The mentioned authors made parametric studies to analyze the influence of variables such as the depth of embedment and the depth of the soft soil layer above the underlying firm-rock formation. They compared the properties of the equivalent systems obtained according to their model with those derived from rigorous solutions and previously available simplified models. They show that their model produces sufficiently accurate results, provided the ratio of the height of the system to the depth of the soft-soil layer is not too small, relative to the foundation depth or to the height of the system above the ground surface.

The mentioned authors also study the reduction in the allowable value of the effective ductile capacity of a nonlinear system that results as a consequence of the contribution of foundation rotation to the total displacement at the roof, and provide an equation to determine a reduction coefficient. They also present the results of nonlinear dynamic response analysis using rigorous and equivalent models of several soil-structure systems. For high values of the aspect ratio (height/width) of the system, the ductility demands on the replacement oscillator are very similar to those resulting from applying the reduction coefficient mentioned above to the ductility demands calculated for the corresponding rigid-base systems; however, for low aspect ratios the former may be significantly higher than the latter, in particular for high values of the ratio $T_s H_0 / T_0 H_s$, where T_s and H_s are respectively the dominant period and the depth of the soil; T_0 and H_0 are the natural period (ignoring the influence of soil-structure interaction) and the height of the structural system.

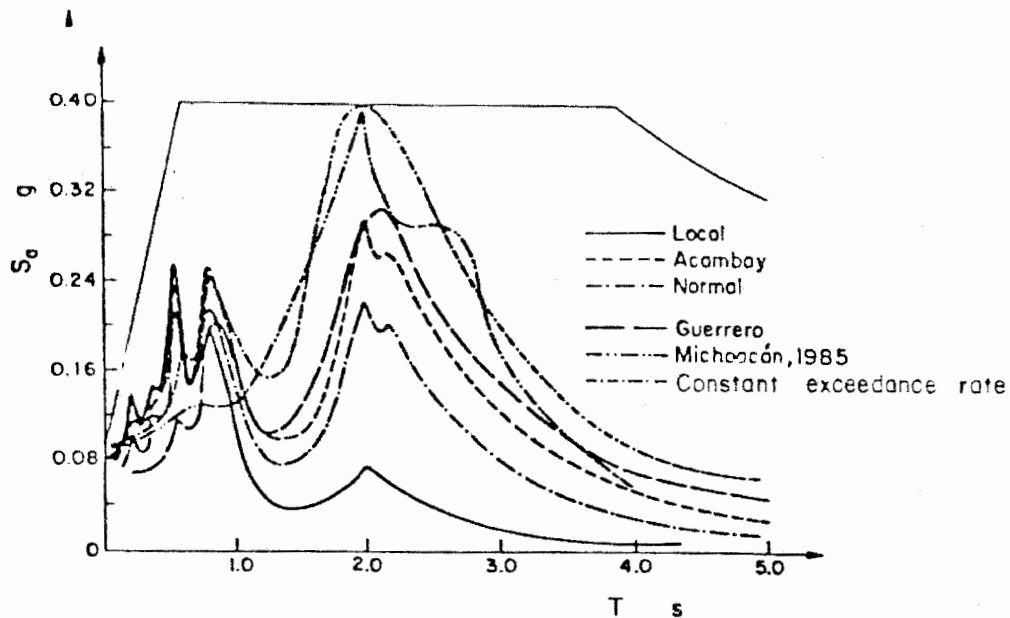


Figure 6 Pseudo-acceleration response spectra at site SCT, normalized with respect to design spectrum specified in 1987 revision of the building code
(From Rosenblueth *et al*, 1989)

5.5 Quantitative evaluation of the performance of individual structures

Significant research efforts were devoted to understand the behavior of individual structural systems and to evaluate the adequacy of available mathematical models and computational tools to estimate the response and performance of complex nonlinear systems. Unfortunately, the lack of response records for real systems did not permit detailed quantitative comparisons. Therefore, the

efforts were addressed to qualitative descriptions of performance. For instance, Meli and Avila (1989) studied six buildings, varying in height between seven and twelve stories. They were all located in the lake-bed area and were representative of the type of construction that suffered the highest damage levels, and were typical in terms of shape, size, height, construction materials and quality control. All buildings had cast-in-place reinforced concrete structures; five had waffle-slab floor systems and the remaining one had reinforced concrete rigid frames with solid-slab floor system. Only two of them had concrete shear walls, but all possessed masonry infills. They were all supported on a deep foundation box with friction piles.

For the cases studied, it was concluded that the observed performance could be at least qualitatively predicted by generally accepted methods of nonlinear response analysis. The level of damage depended both on their lateral strength and on the detailing of the reinforcement. The large number of low-frequency, high-amplitude cycles that are associated with high-intensity narrow-band ground motion imposes severe requirements related to regularity conditions and type of structural details in order to ensure adequate performance. This must be carefully considered when writing design recommendations that permit base-shear reductions based on the possibility of energy dissipation resulting from hysteretic response cycles.

Similar conclusions about the capability of mathematical models to produce reliable qualitative predictions of damage were reached by Rodríguez and Díaz (1989), after studying a fifteen-story waffle-slab building that was severely damaged during the earthquake. In particular, they found a good agreement between the distribution of computed values of maximum rotational ductility demands on the slabs with the damage observed in those elements.

In their study about the performance of steel structures, Osteraas and Krawinkler (1989) emphasize the importance of using the real (expected) values of the mechanical properties of structural systems (rather than the nominal values used for design) when carrying out studies about nonlinear response and performance. This was of particular relevance to compare the predicted responses and the observed performance of several tall buildings, ranging on height from fourteen to twenty one stories. Other important lessons derived from the earthquake are the need to avoid column overloading, even under ultimate conditions, and the benefits of redundancy to prevent collapse.

5.6 Nonlinear response of soft-first-story buildings (SFSB)

An important number of the buildings that suffered collapse during the September 1985 earthquake belonged to the category of soft-first-story systems: they were characterized by possessing a significantly lower number of wall panels (either considered as structural or non-structural elements in design) in one or both of two orthogonal directions in the first story, as compared to that at the upper stories. It had been previously recognized (Esteva, 1980) that the resulting sharp variation of lateral strength along the building height may lead to significant concentrations of ductility demands at the weakest story and, as a consequence, to an increased probability of collapse. The evidence brought by the observations about the performance of systems of this type pointed at the need to understand a) to what extent the behavior of SFSB may be more unfavorable than that of buildings with uniform or slowly varying distribution of lateral stiffness along the building height, designed for the same seismic coefficient or response spectrum, and b) how the design criteria that apply to the former should be adjusted in order to obtain safety levels consistent with those that would result for the latter.

Ruiz and Diederich (1989) and Esteva (1987, 1992) carried out step-by-step analyses of the dynamic response of a number of soft-first-story models. In all cases, the seismic excitation consisted in an ensemble of artificial earthquakes with statistical properties similar to those of the EW component of the 19 September 1985 earthquake at the SCT site (SCT-EW-850919; dominant ground period = 2.08s). A series of preliminary studies considered a set of two-story shear beams, with base shear capacities equal to 1.0 and 1.4 the values specified in the 1987 revision of the

Complementary Technical Norms for Seismic Design of Mexico City Building Code. A parametric study was developed, considering two sets of independent variables: the fundamental period of the system, T (ranging from 0.7 to 2.0s), and the ratio r_{21} of the safety factor for lateral shear in the second story to the value of the same factor for the first story (1.0 to 8.0). The results show similar patterns of variation of the ductility demand on the first story, with values as high as 4 or 5 times those obtained for systems with uniform safety factors along their height; they are greater for small than for large values of T and reach their peak for values of r_{21} around 2.0. Qualitatively similar results were obtained for shear-beam models of multistory buildings with values of the number of stories ranging from 7 to 20 and of the fundamental period ranging from 0.4 to 2.0. Both bilinear-hysteretic and stiffness-degrading systems were considered. The sensitivity of the results to P-delta effects was evaluated. For this case, the results are presented in terms of the minimum value of the safety factor needed to maintain the ductility demand under a specified threshold value. The results are very sensitive to the ratio of post-yield to initial tangent stiffness and to the consideration of constitutive functions that account for stiffness-degrading effects.

5.7 Nonlinear response of systems with asymmetrical force-deflection curves

Asymmetry in force-deflection functions for lateral shear in two opposite directions may be due to the characteristics of the structural arrangement or to the presence of initial tilting due to differential settlements of the foundation. The latter condition often occurs in buildings located in Mexico City soft-soil area. Its influence on the nonlinear response of those systems may be highly relevant for purposes related to the evaluation of the safety of existing structures, as well as for the repair or retrofitting of systems damaged by earthquakes. It has long been known that these conditions may trigger a process of accumulation of ductility demands on the weaker direction, thus leading to values much higher than those shown by structures with symmetrical force-deflection functions, with a strength value equal to that of the weak direction of the asymmetric system.

Ruiz *et al* (1989) evaluated the responses of single-story systems to a set of artificial earthquakes with statistical properties similar to those of the SCT-EW-850919 record. They considered several natural periods, ranging from 0.87 to 3.5s, and five values of the level of asymmetry (defined as one half of the ratio of the difference in the lateral capacities in both directions to their average value), ranging from 0.0 to 0.02. Two alternative approximations were proposed to estimate the amplification functions for ductility demands that result from the asymmetry in the force-deflection curves. The parameters of these functions are practically independent of the natural period, but are highly sensitive to the level of asymmetry and to the average value of the lateral capacity. Additional studies with different values of the effective ground motion duration showed that the amplification of the ductility demand is a rapidly increasing function of this variable.

5.8 Other research lines related to the estimation of seismic response and performance

Other research lines related to the estimation of seismic response and performance have received significant attention after the 1985 earthquake. The writer would like to mention two more, highly relevant, currently in progress. Esteva and Ruiz (1989) presented and applied the basic concepts for the life-cycle reliability analysis of multistory systems, using the concept of ductile-deformation capacity. García-Ramírez (2004) is working on the development of simplified models for the reliability-based design of multistory systems with in-plan eccentricities.

6 EVOLUTION OF SEISMIC DESIGN CODES

Three revisions (1987, 1993, 2004) of the Technical Norms for Seismic Design, Complementary to Mexico City Building Code, have followed the Emergency Regulations of 1985. The following paragraphs refer to the 2004 Edition; some information about the 1976 version, in force at the time

of the earthquake, are provided for comparison.

As mentioned in Section 3, the urban area was divided into three micro-zones: I Firm ground, II Transition zone (soft sediments with a depth lower than 20m) and III Soft soil (soft sediments deeper than 20m). Linear response spectra (5 percent damping) specified for design had the shape shown in Figure 7, with maximum ordinates of 0.16, 0.20 and 0.24 for the mentioned zones, respectively. Reduction factors to account for over-strength and nonlinear behavior ranged from 1 to 6, depending on the type of structural arrangement and ductility-oriented details. The plateaus determined by T_a and T_b are intended to account for uncertainties associated with the frequency content of the ground motion. They were taken as (0.3s-0.8s), (0.5s-2.0s) and (0.8s-3.3s), respectively.

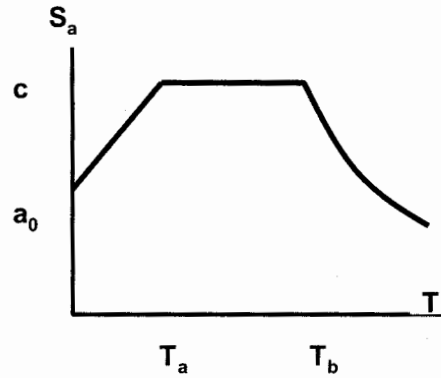


Figure 7 Shape of design spectra, depending on local conditions.

$$\begin{aligned}
 S_a &= a_0 + (c - a_0)T/T_a, \text{ for } T < T_a \\
 &= c, \text{ for } T_a < T < T_b \\
 &= c(T_b/T)^r, \text{ for } T > T_b
 \end{aligned}$$

The 2004 revision of the building code offers two options to the designers: a) a conventional approach, presented in the main body (designated in the following as basic criterion) and b) an improved criterion (designated as advanced), presented in Appendix A. The basic criterion includes a substantially more refined micro-zonation map than those previously adopted; it specifies six micro-zones, the boundaries of which depend on the values of the dominant ground periods shown in Figure 2, which includes information derived from high-intensity ground-motion records, as well as from artificial micro-tremor studies. The advanced criterion includes specifications to determine site-specific response spectra, which depend on the value of the dominant ground period at the site. They both define new values of the ductility factors Q , used to determine the response reduction factors Q' . The values of Q are now made to depend on more strict requirements for structural details intended to attain adequate ductile deformation capacities. They also include special requirements related to regularity conditions in the structural arrangement, to maximum allowable values of torsional eccentricities and to asymmetrical load deflection curves, including the assessment of the safety of structures affected by previous tilting for the purpose of retrofitting.

The functions describing the design response spectra corresponding to the basic criterion are similar to those shown at the foot of Figure 7. The values of their parameters are summarized in Table 1.

Table 1. Design spectra according to basic criterion in 2004 building code

Zone	c	a_0	T_a	T_b	r
I	0.16	0.04	0.20	1.35	1.0
II	0.32	0.08	0.20	1.35	1.33
IIIa	0.40	0.11	0.53	1.80	2.0
IIIb	0.45	0.11	0.85	3.00	2.0
IIIc	0.40	0.10	1.25	4.20	2.0
IIId	0.30	0.10	0.85	4.20	2.0

The advanced criterion is expressed in a format that explicitly recognizes two performance conditions for two different design intensities. Design spectra for the ultimate-failure performance condition are represented by the following equations, which are slightly different from those shown at the foot of Figure 7.

$$S_a = a_0 + (\beta c - a_0)T/T_a, \text{ for } T < T_a \quad (1a)$$

$$= \beta c \quad T_a < T < T_b \quad (1b)$$

$$= \beta c p (T_b/T)^2 \quad T > T_b \quad (1c)$$

where β is intended to account for soil-structure interaction, $p = k + (1-k)(T_b/T)^2$, and k is chosen so as to lead to an spectral displacement equal to the peak ground displacement for $\beta = 1.0$ (no influence of soil-structure interaction), when T tends to infinity. The code provides rules to determine β in terms of the effective values of the natural period and damping ratio of the system, taking into account the influence of soil-structure interaction. The values of a_0 , c , T_a , T_b and k are presented as functions of the dominant ground period, T_s . They were obtained by fitting conservative functions for the parameters appearing in Equations 1a-c used to represent the uniform-hazard linear response spectra, for damping = 0.05 and a return interval of 125 years, that were obtained at 1600 points forming a rectangular grid covering most of the populated area in Mexico City. Details about the information used and the derivation of these functions were presented by Ordaz and Meli (2004). Some of the resulting spectra are shown in Figure 8, for illustration.

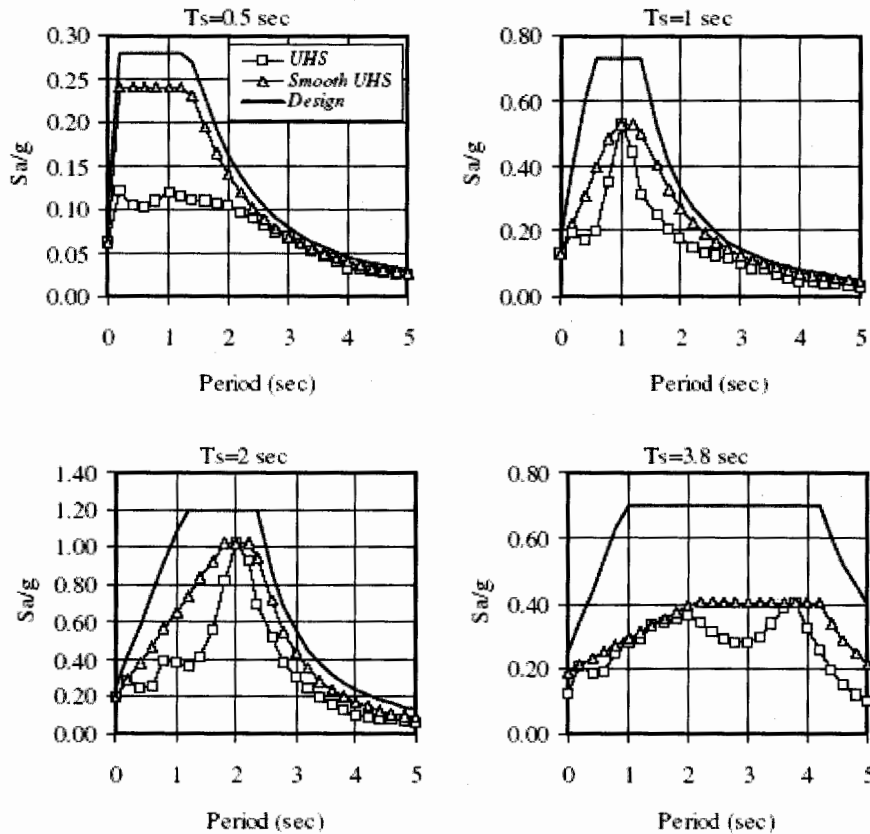


Figure 8 Original and smoothed uniform hazard spectra at different sites, compared with those calculated by means of Equations 1a-c (From Ordaz and Meli, 2004)

It can be observed that the specified spectra lie always on the conservative side. In some cases the safety margins may reach very high values, as a consequence of the large dispersions in the ordinates of the uniform-hazard spectra used to obtain the equations for the parameters of Equations 1a-c. It can also be observed that the ordinates of the response spectra can be much higher than those specified in accordance with the basic design criterion. This (apparent) discrepancy arises because the values of c shown in Table 1 include a reduction to account for the over-strength ratio (as mentioned above), while this reduction is openly introduced according to the advanced design criterion, which proposes that the site response spectra derived from Equations 1a-c be divided by a factor equal to the product $Q'R$, where Q' (function of Q) accounts for the ductile deformation capacity and R is an over-strength factor that depends on the fundamental period of the system.

According to this criterion, it is also necessary to verify acceptance conditions related to maximum lateral distortions for the limit states associated with both the collapse-prevention and the serviceability performance levels.

7 CONCLUDING REMARKS

A bird's eye view has been presented in the foregoing pages about the research and implementation efforts to improve the practice of seismic design in Mexico City. It is easily realized that the targets and trends of our research largely coincide with those that are followed in the other regions in the world with high seismic hazard conditions. However, due to the exceptional features of the seismic events that may affect sites with the type of soft soil formations that support a large part of the structures in the city, the characteristics of ground motion and, therefore, of structural response, are also exceptional and often call for the use of models and tools that differ significantly from those applied at firm-ground sites, where seismic risk is essentially determined from the contribution of near-source earthquakes. Accordingly, significant efforts are devoted to the development of methods to estimate seismic reliability functions of complex structural systems, as well as to the transformation of the results in to practically applicable methods and tools for reliability- and performance-based earthquake-resistant design that account for the special features of narrow-band earthquake ground motion excitations (Esteva *et al*, 2002; Esteva and Ismael, 2003; Ismael *et al*, 2004).

Significant efforts are also invested on the development and/or updating of models for the constitutive functions of reinforced concrete, masonry and steel structures, using both internationally available information and the results of experimental research in Mexico. This has not been included in this paper.

Finally, the 1985 earthquake had also an impact on the arising of awareness and consciousness about seismic hazard in other regions in the country. This led to the updating of seismic zonation and seismic design criteria throughout the country. The most demanding challenges, however, coincide with those typical of many areas in the world: preserving that consciousness in engineering design and quality control decisions long enough after the occurrence of damaging events.

8. References:

- Avilés, J., and Pérez-Rocha, L. E. (1995), "Efectos de Sitio e Interacción Suelo-Estructura para Fines de Reglamentación Sísmica" (Site Effects and Soil-Structure Interaction for Seismic Codes), *Proc. IV National Symposium on Earthquake Engineering, Mexican Society for Earthquake Engineering*, Oaxaca, Mexico.
- Boore, D. M. (1983), "Stochastic simulation of high-frequency ground motions based on seismological models of the radiated spectra", *Bull. Seism. Soc. Am.*, **73**, 1865-1894.
- Castro, R., Singh, S.K. and Mena, E. (1988), "An Empirical Model to Predict Fourier Amplitude Spectra of Horizontal Ground Motion", *Earthquake Spectra*, **4**(4) 675-685.

- Esteva, L. (1980), "Design: General", Chapter 3 of the book "Design of Earthquake Resistant Structures", edited by E. Rosenblueth, Pentech Press, London.
- Esteva, L. (1987), "Earthquake Engineering Research and Practice in Mexico after the 1985 Earthquakes", *Bulletin of the New Zealand National Society for Earthquake Engineering*, **20**(3).
- Esteva, L. (1988), "The Mexico Earthquake of September 19, 1985: Consequences, Lessons, and Impact on Research and Practice", *Earthquake Spectra*, **4**(3) 413-426.
- Esteva, L. (1989), "Research and Practice of Earthquake Engineering after the 1985 Mexico Earthquake", *ASCE Specialty Conference – Seventh Annual Structures and Pacific Rim Engineering Congress*, San Francisco, CA.
- Esteva, L. and Ruiz, S. E. (1989), "Seismic failure rates of multistory frames", *ASCE Journ. Str. Engng.*, **115** (2) 268-284.
- Esteva, L. (1992), "Nonlinear seismic response of soft-first-story buildings subjected to narrow-band accelerograms", *Earthquake Spectra*, **5**(3).
- Esteva, L., Diaz-López, O., García-Pérez, J., Sierra, G. and Ismael, E. (2002), "Life-cycle optimization in the establishment of performance-acceptance parameters for seismic design", *Structural Safety*, **24**, 187-204.
- Esteva, L. and Ismael, E. (2003), "A maximum likelihood approach to system reliability to respect to seismic collapse", *IFIP WG7.5 Working Conference*, Banff, Canada.
- García-Ramírez, F. (2004), "Respuesta sísmica torsional de sistemas no-lineales para fines de diseño por desempeño" (Seismic torsional response of nonlinear systems for performance-based design).
- García-Ranz, F. and Gómez, R. (1988), "The Mexico Earthquake of September 19, 1985 – Seismic Design Regulations of the 1976 Mexico Building Code", *Earthquake Spectra*, **4**(3) 427-439.
- Gómez, A., Ortega, O., Guerrero, J. J., González, E., Paniagua, J.P. and Iglesias, J. (1989), "Response and Design Spectra Obtained from Earthquake-Damaged Buildings", *Earthquake Spectra*, **5**(1) 113-120.
- Goodno, B. J., Craig, J. I. and Zeevaert-Wolf, A. E. (1989), "Behavior of Heavy Cladding Components", *Earthquake Spectra*, **5**(1) 195-222.
- Ismael-Hernández, E., Diaz-López, E. and Esteva, L. (2004), "Seismic vulnerability análisis for ptimum designo f multistory reinforced concrete buildings", *Proc. 13WCEE*, Vancouver, Canada.
- Meli, R. and Rosenblueth, E. (1986), "The earthquake of 19 September 1985. Effects in Mexico City", *Concrete International*, **8**(4) 23-34.
- Meli, R. and Avila, J. (1989), "Analysis of Building response", *Earthquake Spectra*, **5**(1) 1-17.
- Miranda, E. and Bertero, V. V. (1989), "Performance of Low-Rise Buildings in Mexico City", *Earthquake Spectra*, **5**(1) 121-143.
- Noreña, F., Castañeda, C. and Iglesias, J. (1989) "Evaluation of the Seismic Capacity of Buildings in Mexico City", *Earthquake Spectra*, **5**(1) 19-24.
- Ordaz, M., Singh, S.K., Reinoso, E., Lermo, J., Espinosa, M. and Domínguez, T. (1988), "Estimation of Response Spectra in the Lake Bed Zone of the Valley of Mexico", *Earthquake Spectra*, **4**(4) 815-834.
- Ordaz, M. and Singh, S. K. (1992), "Source spectra and spectral attenuation of seismic waves from Mexican earthquakes, and evidence of amplification in the hill zone of Mexico City", *Bull. Seism. Soc. Am.*, **82**, 24-43.
- Ordaz, M. and Meli, R. (2004), "Seismic design and codes in Mexico", *Proc. 13WCEE*, Vancouver, paper 4000.
- Osteraas J. and Krawinkler, H. (1989), "Behavior of Steel Buildings", *Earthquake Spectra*, **5**(1) 51-88.
- Rodríguez, M. and Díaz, C. (1989), "Analysis of the Seismic Performance of a Medium Rise, Waffle Flat Plate Building", *Earthquake Spectra*, **5**(1) 25-40.
- Rosenblueth, E., Ordaz, M., Sánchez-Sesma, F. J. and Singh, S. K. (1989), "Design spectra for Mexico's Federal District", *Earthquake Spectra*, **5**(1) 273-291.
- Ruiz, S. E. and Diederich, R. (1989), "The Seismic Performance of Buildings with Weak First Story", *Earthquake Spectra*, **5**(1) 89-102.
- Ruiz, S. E., Rosenblueth, E. and Diederich, R. (1989), "Seismic Response of Asymmetrically Yielding Structures", *Earthquake Spectra*, **5**(1) 103-111.
- Seed, H. B., Romo, M. P., Sun, J. I., Jaime, A. and Lysmer, J. (1988), "Relationship between Soil Conditions and Earthquake Ground Motions", *Earthquake Spectra*, **4**(4), 687-730.

RECENT ADVANCES IN HYBRID TESTING FOR EARTHQUAKE PERFORMANCE EVALUATION

P. B. Shing

*Professor, Dept. of Structural Engineering, University of California at San Diego, La Jolla, CA, USA
pshing@ucsd.edu*

Abstract: A number of real-time hybrid test methods have been developed in recent years to study the performance of structures and soil-structure systems under earthquake and other dynamic loads. This paper discusses some of these developments and presents a fast hybrid test system that is based on an unconditionally stable implicit time integration scheme. The system has adopted a general structural analysis framework as its computational platform for substructure test applications. The performance of the system has been demonstrated. The system can achieve a rate of load that approaches real-time earthquake response. However, the speed of a test can be limited by the computation time needed to handle the nonlinearity in the analytical substructure and to record the simulation data.

1. INTRODUCTION

In recent years, a number of real-time hybrid test methods have been developed to study the performance of structures and soil-structure systems under earthquake and other dynamic loads. Most of these methods are, in essence, based on the on-line computer controlled test concept first proposed by Hakuno et al. (1969) and later extended by Takanashi et al. (1974). The technique is often called the pseudodynamic test method because such a test can be conducted at a very slow rate and the dynamic effect is simulated with a computer model. With the extension of these methods to high loading rates, the term “hybrid test methods” have been used to reflect the fact that they combine numerical simulation with physical testing to achieve the best of the two worlds. Such tests normally use servo-hydraulic actuators and sometimes a shake table to exert static or dynamic loads on a test article. They are intended to provide an efficient alternative or enhancement to the shake table test method. This paper summarizes some of these recent developments and the related work carried out by the author and his co-workers.

Since its development by Takanashi et al., the pseudodynamic test method has been used and advanced by researchers worldwide for earthquake performance testing. The essence of the method is the use of a numerical time integration technique to solve the temporally and spatially discretized equations of motion for the structural system being investigated based on the actual load-displacement characteristics of the structure that are measured experimentally using actuators and sensors. When compared to a shake table test, its main advantage is that it can be applied to large-scale structural systems and components using reaction-wall facilities, which are generally less costly. In such a test, loads are often applied at a very slow rate, which can be more than 100 times slower than the real-time earthquake response of a structure. This is sometimes considered an advantage in that it allows a close observation of the damage evolution in the structure during a test. Nevertheless, it also raises questions with regard to the rate-of-loading effect on the strength and damage behavior of a structure. In

particular, a slow test cannot be applied to a structure that has highly rate sensitive components such as visco-elastic dampers and certain active or semi-active structural control devices.

The success of the pseudodynamic test method can be attributed, to a large extent, to a better understanding of the influence of experimental errors on the test results and the development of effective methods to mitigate the effect of these errors (Shing and Mahin 1983, Nakashima and Kato 1987, Shing et al. 1991). Furthermore, two lines of major development have occurred to extend its applications. One is the substructure test method, in which only the most critical subassemblage of a structure is tested while the rest of it is modeled in a computer. This technique was first successfully developed by Dermitzakis and Mahin (1985) and later improved by a number of researchers (Nakashima et al. 1990, Shing et al. 1994, Pinto et al. 2004). The other is the real-time pseudodynamic testing, first successfully conducted by Nakashima et al. (1992), to circumvent the rate-of-loading problem mentioned above.

Recently, a fast hybrid test system has been developed (Shing et al. 2004) as part of the George E. Brown, Jr. Network for Earthquake Engineering Simulation (NEES) Program sponsored by the US National Science Foundation. This system further advances the current state-of-the-art in real-time substructure tests with several unique features. It has a flexible system architecture that incorporates a general structural analysis framework for simulating the nonlinear behavior of the analytical substructure. It also uses an unconditionally stable implicit time integration scheme to provide a robust computational environment. This system and its performance will be discussed in this paper.

2. REAL-TIME HYBRID TESTING

Nakashima et al. (1992) successfully developed one of the early real-time hybrid test systems, in which actuators were kept in continuous motion with the use of a staggered solution approach to solve the equations of motion. Horiuchi et al. (1996) have developed a delay compensation technique for hybrid testing and used it to evaluate the dynamic response of a secondary system with the primary structure modeled in a computer. This method has been further extended by Nakashima et al. (1999) to arrive at a real-time test method in which both extrapolation and interpolation are used to generate displacement commands to move actuators continuously at high speed. Real-time test systems have also been developed by other researchers such as Darby et al. (1999). Most of these systems are, however, based on the central difference method, which is conditionally stable, for time integration. This imposes a severe limitation on substructure tests where high-frequency modes are common and may even exist in an experimental substructure. Magonette et al. (1998) have developed a high-speed continuous substructure test method using a staggered implicit-explicit integration technique, in which the equations of motion for the experimental substructure are solved with an explicit scheme, while those for the analytical substructure with an implicit method. However, this has only partially addressed the stability issue.

Bayer et al. (2000) have implemented an implicit integration scheme for hybrid testing. Similar to the work of Horiuchi et al., they used a shake table to evaluate the dynamic response of a secondary system, while the primary structure was simulated in a computer. During the test, the force developed by the secondary system was measured and used to compute the response of the primary structure. However, the primary structure was assumed to be linearly elastic and only the physical specimen exhibited a nonlinear behavior. This permits the use of a simple sub-stepping technique to handle the nonlinearity and the iterative correction required for an implicit scheme.

Reinhorn et al. (2004) have proposed a hybrid test technique that combines shake table excitation with dynamic actuators for advanced applications such as soil-structure interaction tests. Nevertheless, the implementation of such a method is challenging and it is still under development.

3. NEES FAST HYBRID TEST SYSTEM

The Fast Hybrid Test (FHT) system developed by the author and his co-workers is presented here. While the system framework is general enough to incorporate any implicit integration scheme, the unconditionally stable α -method of Hilber *et al.* (Hughes 1983) has been selected. For a nonlinear structure, the α -method requires a Newton-type iterative procedure to solve the equations of motion. Since it is generally difficult to acquire the tangent stiffness of a structure accurately during a test, a modified Newton approach using the initial structural stiffness has to be used. Furthermore, in a real-time hybrid test using a digital servo-controller, servo-hydraulic actuators controlling the structural displacements have to move continuously with a smooth velocity, and the displacement commands to the actuators have to be sent at the update frequency of the controller, which is 1024 Hz for the system used here. To meet these requirements, a special iterative procedure that adopts a fixed number of iterations in each time step has been developed. The details of the computational procedure can be found in Jung and Shing (2006).

To model an analytical substructure in a hybrid test, an open-source, object-oriented structural analysis framework, OpenSEES, developed by McKenna and Fenves (2000), has been adapted to serve as the computational platform. The numerical integration scheme mentioned above has been implemented in this software, and an interface has been developed to interact with the experimental substructure through a digital control and data-acquisition system. To have a full and deterministic control over all of the control and computational resources during a high-speed test, OpenSEES is executed in an embedded real-time operating system. A pair of host-target computers is used for this purpose. The host computer is for program development and the construction of the structural model for testing. A compiled program is downloaded from the host to the target for execution in a real-time environment.

Figure 1 shows the configuration of the FHT system, which is also designed for teleparticipation and teleobservation by remote users through the NEES Point of Presence (NEESpop) and NEES Telepresence Server. There are two pairs of host-target computers. Target computer 1 is for running OpenSEES, which solves the equations of motion in an iterative manner, while the second target computer is responsible for the generation of displacement commands using

Simulink when more than 1/1024 sec. is needed by OpenSEES to perform one iteration. Furthermore, the second target computer is equipped to run Simulink models of the servo-hydraulic system and test structure for pre-test simulations, which are often desirable. These functions use Mathworks' xPC-Target as the real-time kernel.

The performance of the system has been evaluated in detail, with the consideration of the numerical integration scheme, system dynamics, and PID control, through numerical simulations and system transfer functions. If both the servo-hydraulic system and the test structure are assumed to be linear, a complete hybrid test system can be represented by the block diagram shown in Fig. 2. With

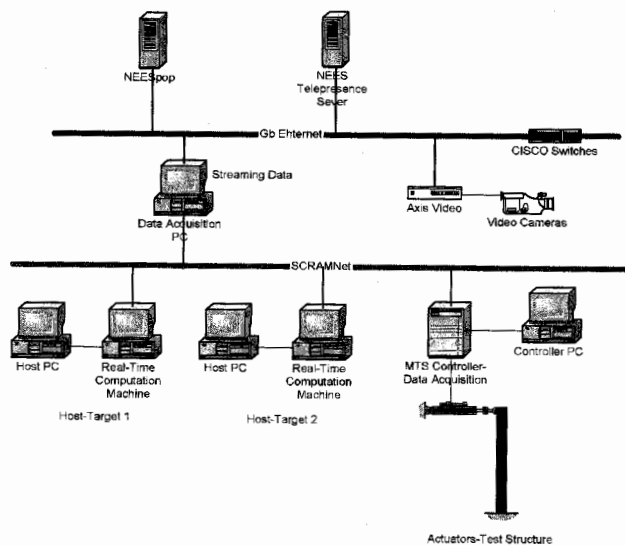


Figure 1 Configuration of the Fast Hybrid Test System

this the system transfer function can be expressed as

$$RTPD(s) = \frac{d''(s)}{f(s)} = \frac{EF(s) \cdot EC(s) \cdot P(s)}{e^{2s\delta\tau} - IC(s) \cdot EC(s) \cdot P(s) - EP(s) \cdot EC(s) \cdot P(s)} \quad (1)$$

in which $EF(s)$, $EP(s)$, and $IC(s)$ are transfer functions representing the external force, explicit prediction, and implicit correction components of the numerical integration scheme, and $P(s)$ is the transfer function of the physical system, including the servo-hydraulic system and test structure. The detailed derivation of the above expression and the corresponding transfer functions can be found in Jung and Shing (2006).

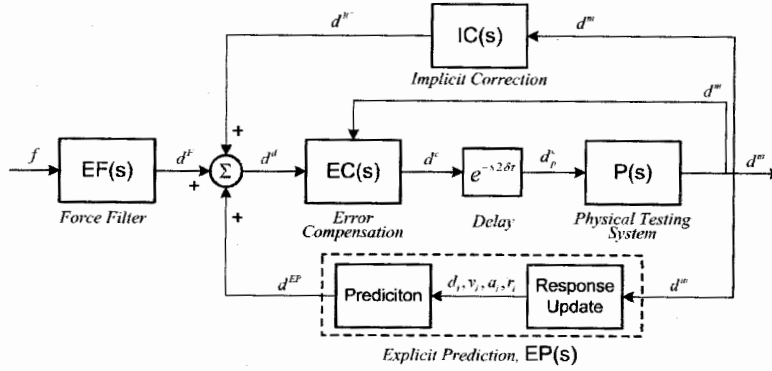


Figure 2 System Transfer Function

The transfer function in Eq. (1) can be used to examine the interaction of the system dynamics with numerical computation in a real-time or high-speed test. All servo-hydraulic systems have an inevitable delay in response, which can have an important impact on the numerical computation. With PID control, the degree of this delay depends on the proportional gain k_p . Figure 3 compares the dynamic amplifications and phase angles obtained with the transfer function in Eq. (1) using different proportional gains with the exact analytical solution that reflects the dynamics of the structural model alone. The test structure considered here has a natural frequency of 9.20 Hz, and the structural model is assumed to have a mass that is 36.8 times of that of the specimen, resulting in a natural frequency of 1.24 Hz. From the top graph, it can be observed that a low proportional gain leads to a low dynamic amplification due to the damping effect introduced by the phase-lag error. The second plot in Fig. 3 shows that increasing k_p also increases the oil column resonance amplitude, which could potentially destabilize a system. However, as shown, this can be effectively suppressed by the ΔP feedback.

It is also noticed that the resonance frequency obtained from the system transfer function in Eq. (1) is slightly lower than that of the analytical solution irrespective of the proportional gain. This discrepancy has been found to be caused by the inertia force of the test structure, which is undesirably introduced into the response calculation through the force feedback. This inertia effect is indicated in the following equation of motion, which is actually solved in a hybrid test.

$$Ma + [r + M_t \lambda_t^2 a] = f \quad (2)$$

in which M is the mass of the structural model, M_t is the actual mass of the test structure, a is the acceleration response to be computed, r is force related to the structural deformation, f is excitation force, and λ_t is the time scale factor with which a test is conducted. The bracketed term represents the total force actually measured during a test and used in the numerical computation.

However, since the dynamic response is simulated numerically, we often have $M_t \ll M$ to simplify the experimental setup. Furthermore, in a slow test, it is not unusual that $\lambda_t \ll 1$. Under these conditions, the second term within the brackets can be neglected as in the case of a traditional pseudodynamic test. On the other hand, in a real-time test, $\lambda_t = 1$ and the inertia effect can be significant especially when the excitation frequency is close to the resonance frequency of the structural model. To overcome this problem, one may instead solve the following equation.

$$[M - M_t \lambda_t^2]a + [r + M_t \lambda_t^2 \dot{a}] = f \quad (3)$$

However, the above remedy is possible only if the time scaling is uniform throughout a test. If the time scaling is not uniform, then Eq. (3) cannot be used and the actual acceleration during a test has to be measured and the inertia force be calculated and subtracted from the total measured force. This has been proven to be a feasible approach (Jung and Shing 2006).

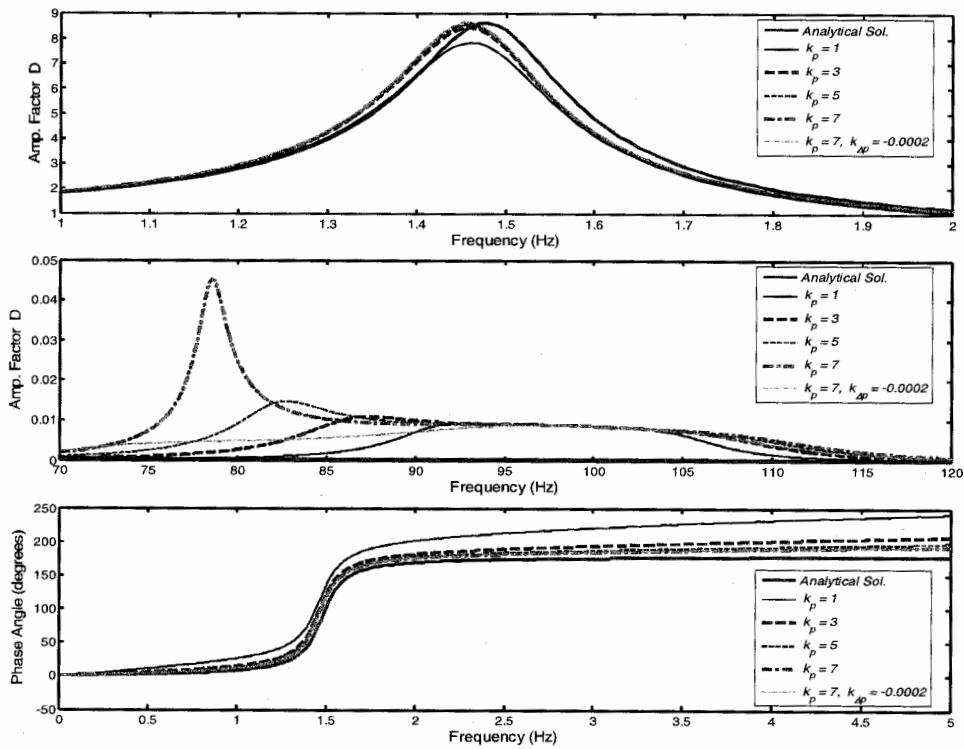


Figure 3 Influence of Proportional Gain

4. TEST EXAMPLES

4.1 Two-Degree-of-Freedom

A two-degree-of-freedom test was conducted to evaluate the performance of the FHT system. In this test, the computation was carried out by a Simulink program executed in a real-time xPC-Target environment. The structure was a scaled model of a two-story steel frame with simple beam-to-column connections as shown in Fig. 4. To take advantage of the structural symmetry, only a single column was tested with two actuators as shown in the figure. The integration time step was 0.01 sec and ten iterations were used per time step. To compensate for the various delays in the control system and

actuator response, a feed-forward control was used to supplement the PID control.

The column remained elastic in the test. Figure 5 compares the first-story displacement response

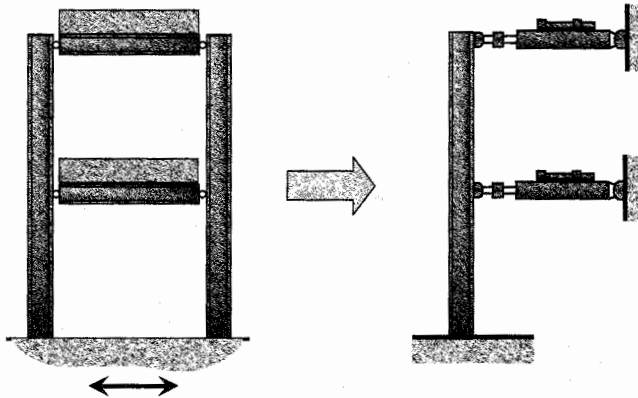


Figure 4 Two-Story Steel Frame

obtained from the test to the exact numerical solution and the result of a real-time simulation. The real-time simulation was conducted with the same equipment but with the test specimen and hydraulic actuators modeled by a Simulink program. In the real-time test and simulation, damping in the structural model was assumed to be 4% of the critical for each mode. However, in the exact numerical solution, damping in each mode was assumed to be 6% of the critical. The difference in damping is to account for the additional damping effect introduced by the test

specimen. It can be seen from Fig. 5 that the results obtained from the three cases are all very close to each other, while the real-time simulation shows a little more damping. This is probably due to fact that the damping assumed for the specimen model in the real-time simulation was a little too high.

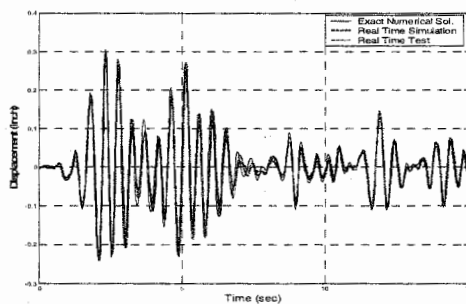


Figure 5 Displacement Response at 1st Story
(1 in. = 25.4 mm)

4.2 Substructure Tests on a Zipper Frame

A 1/3-scale model of a three-story suspended zipper frame, as shown in Fig. 6, was tested using a substructuring method and the OpenSEES program. The prototype frame and the scale model were designed by Yang et al. (2006). For the hybrid tests, the partition of the frame model into an analytical part and an experimental part is illustrated in Fig. 6. The experimental part consists of only the bottom-story braces connected with the same type of gusset plates as those in the zipper frame model. The first-story columns and beam

and the entire second and third stories were modeled analytically. The braces in the second-story were expected to buckle during the tests. This presents a severe assessment of the test method.

For the tests presented here, the specimen was subjected to a sequence of three ground motions. The ground motion records corresponded to LA22 of the SAC steel research program. The first two records had accelerations scaled to 30 and 80% of the original, and the last had the peak acceleration scaled to 200%, which was equivalent to the full-strength ground motion for the prototype frame. The time integration interval used for these tests was 0.0035 sec. Because of the severe nonlinearity in the analytical substructure and the time needed for data recording, the tests had to be carried out at a speed that was 86 times slower than a real-time test. For the 30% level earthquake, an almost perfect match of the test and simulation results was obtained. Figure 7 shows the displacement time histories for the 80 and 200% level ground motions. The structure experienced mild inelastic deformation and brace buckling at the 80% level. At the 200% level, one brace fractured suddenly in tension right outside the gusset plate during the first cycle of strong motion. This was most likely caused by a defect introduced by the welding of the slotted end of the brace to the gusset plate. Until

the brace fractured, the experimental and simulation results show a close correlation.

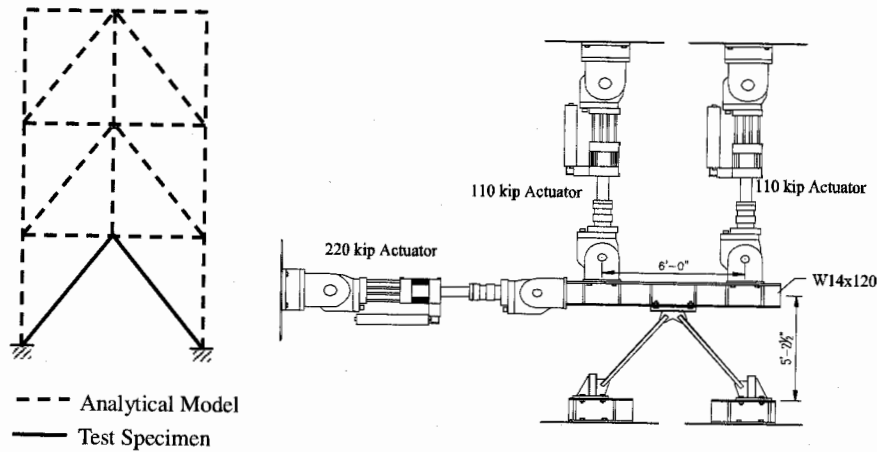


Figure 6 Zipper Frame Tests (1 kip = 4.45 kN)

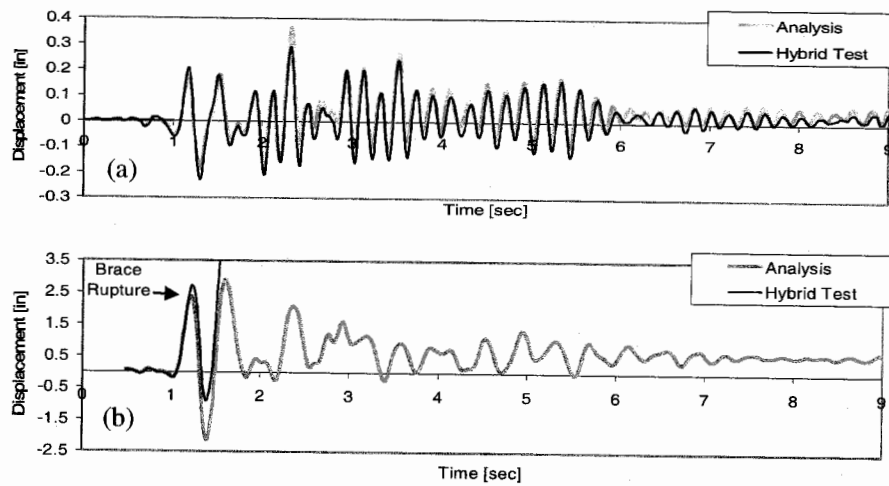


Figure 7 Displacement Time Histories at First Story: (a) 80% and (b) 200% Ground Motion (1 in. = 25.4 mm)

5. CONCLUSIONS

This paper summarizes some of the recent developments in real-time hybrid testing and the related work carried out by the author and his co-workers. A fast hybrid test system utilizing an unconditionally stable implicit time integration scheme is described, and its performance is discussed and illustrated with two test examples. The reliability of the system has been demonstrated. The system can achieve a rate of load that approaches the real-time response of a structure to an earthquake ground motion. However, the speed of a test can be limited by the computation time needed to handle the nonlinearity in the analytical substructure and to record the simulation data, which can be a significant overhead.

Acknowledgements:

This study was sponsored by the US National Science Foundation under Award Nos. CMS 0086592 and CMS 0324468. However, opinions expressed in this paper are those of the author and do not necessarily represent those of the sponsor. The Fast Hybrid Test system was developed at the University of Colorado as part of NEES. The author would also like to thank his current and former students, Andreas Stavridis, Dr. Rae-Young Jung, and Dr. Zhong Wei, and the research staff, Dr. Eric Stauffer and Robert Wallen, at the University of Colorado for their contributions to the work reported here.

References:

- Bayer, V., Dorka, U.E., and Fullekrug, U. (2000), "A New Algorithm for Real-Time Sub-Structure Pseudodynamic Tests," *Proc. of 12th World Conference on Earthquake Engineering*, Auckland, New Zealand.
- Darby, A.P., Blakeborough, A., and Williams, M.S. (1999), "Real-Time Substructure Tests using Hydraulic Actuators," *Journal of Engineering Mechanics*, American Society of Civil Engineers, **125**, 1133-1139.
- Dermitzakis, S.N. and Mahin, S.A. (1985), "Development of Substructuring Techniques for On-Line Computer Controlled Testing," *UBC/EERC-85/04*, Earthquake Engineering Research Center, University of California, Berkeley, CA.
- Hakuno, M., Shidawara, M., and Hara, T. (1969), "Dynamic Destructive Test of a Cantilever Beam Controlled by an Analog Computer," *Trans. Japanese Society of Civil Engineers*, **171**, 1-9.
- Horiuchi, T., Nakagawa, M., Sugano, M., and Konno, T. (1996), "Development of a Real-Time Hybrid Experimental System with Actuator Delay Compensation," *Proc. of 11th World Conference on Earthquake Engineering*, Paper No. 660, Acapulco, Mexico.
- Hughes, T.J.R. (1983), "Analysis for Transient Algorithms with Particular Reference to Stability Behavior," Belyschko T, Hughes T.J.R., Editors. *Computational Methods for Transient Analysis*. Amsterdam, North-Holland.
- Jung, R. and Shing, P.B. (2006), "Performance Evaluation of a Real-time Pseudodynamic Test System," *Earthquake Engineering and Structural Dynamics* (in press).
- Magonette, G., Pegon, P., Molina, F.J., and Buchet, P. (1998), "Development of Fast Continuous Pseudodynamic Substructuring Tests," *Proc. of 2nd World Conference on Structural Control*, Kyoto, Japan.
- McKenna, F. and Fenves, G.L. (2000), "An Object-Oriented Software Design for Parallel Structural Analysis," *Proc. of the SEI/ASCE Structures Congress*, Philadelphia, PA.
- Nakashima, M. and Kato, H. (1987), "Experimental Error Growth Behavior and Error Growth Control in On-Line Computer Control Test Method," *BRI Research Paper No. 123*, Building Research Institute, Ministry of Construction, Japan.
- Nakashima, M., et al. (1990), "Integration Techniques for Substructure Pseudodynamic Test," *Proc. of 4th U.S. National Conference on Earthquake Engineering*, **II**, Palm Springs, CA, 515-524.
- Nakashima, M., Kato, H., and Takaoka, E. (1992), "Development of Real-Time Pseudo Dynamic Testing," *Earthquake Engineering and Structural Dynamics*, **21**, 79-92.
- Nakashima, M. and Masaoka, N. (1999), "Real-Time On-Line Test for MDOF Systems," *Earthquake Engineering and Structural Dynamics*, **28**, 393-420.
- Pinto, A.V., Pegon, P., Magonette, G., and Tsionis, G. (2004), "Pseudo-Dynamic Testing of Bridges using Non-Linear Substructuring," *Earthquake Engineering and Structural Dynamics*, **33**, 1125-1146.
- Reinhorn, A.M., Sivaselvan, M.V., Weinreber, S., and Shao, X. (2004), "Real-Time Dynamic Hybrid Testing of Structural Systems," *Proc. of 3rd European Conference on Structural Control*, Vienna, Austria.
- Shing P.B. and Mahin, S.A. (1983), "Experimental Error Propagation in Pseudodynamic Testing," *UCB/EERC-83/12*, Earthquake Engineering Research Center, University of California, Berkeley, CA.
- Shing, P.B., Vannan, M.T., and Carter, E. (1991), "Implicit Time Integration for Pseudodynamic Tests," *Earthquake Engineering and Structural Dynamics*, **20**, 551-576.
- Shing, P.B., Bursi, O.S., and Vannan, M.T. (1994), "Pseudodynamic Tests of a Concentrically Braced Frame using Substructuring Techniques," *Journal of Constructional Steel Research*, **29**, 121-148.
- Shing, P.B., Wei, Z., Jung, R., and Stauffer, E. (2004), "NEES Fast Hybrid Test System at the University of Colorado," *Proc. of 13th World Conference in Earthquake Engineering*, Vancouver, Canada.
- Takanashi, K., et al. (1974), "Seismic Failure Analysis of Structures by Computer-Pulsator On-Line System," *Journal of Institute of Industrial Science*, **26**(11), University of Tokyo, Tokyo, 13-25.
- Yang, C.-S., Leon, R.T., and DesRoches, R. (2006), "On the Development of Zipper Frames by Pushover Testing," *Proc. of 5th Conference on the Behavior of Steel Structures in Seismic Areas*, Yokohama, Japan.

DIFFERENCES IN EARTHQUAKE SOURCE AND GROUND MOTION CHARACTERISTICS BETWEEN SURFACE AND BURIED EARTHQUAKES

P. Somerville¹⁾ and A. Pitarka¹⁾

*1)URS Corporation, Pasadena, CA 91101, USA
paul_somerville@urscorp.com, arben_pitarka@urscorp.com*

Abstract: In previous work, we have shown that the ground motions from earthquakes that break the ground surface are weaker than the ground motions from buried faulting earthquakes. In this paper, we describe differences in kinematic and dynamic source parameters that may give rise to these differences in ground motion levels. From kinematic rupture models, we show that the slip velocity of surface faulting earthquakes is less than the slip velocity of buried faulting earthquakes. From dynamic rupture models, we infer that rupture in the shallow part of fault (upper few km) is controlled by velocity strengthening, with larger slip weakening distance D_c , larger fracture energy, larger energy absorption from the crack tip, lower rupture velocity, and lower slip velocity than at greater depths on the fault. Dynamic rupture modeling using these properties results in lower ground motions for surface faulting than for buried faulting events, consistent with the observations.

1. OBSERVED DIFFERENCES IN GROUND MOTIONS

At short and intermediate periods (0.3-3.0s) the recorded ground motions from earthquakes that produce large surface rupture are systematically weaker than the ground motions from earthquakes whose rupture is confined to the subsurface (Somerville, 2003; Kagawa et al., 2004). The large differences in ground motion levels between surface and buried faulting events are evident in Figure 1, which shows the response spectra of near-fault recordings of recent large earthquakes. The left panel shows recordings from four surface faulting earthquakes in the M_w range of 7.4 to 7.9, and the right panel shows recordings from two buried faulting earthquakes of magnitude M_w 6.7 and 7.0. The response spectra of the deep earthquakes are much stronger than those of the larger shallow earthquakes for periods less than 1.5 sec. Figure 2 shows the event terms for larger sets of surface rupture earthquakes at the top, and subsurface rupture earthquakes at the bottom. The unit line represents the Abrahamson and Silva (1977) model, and lines above this line indicate that the event's ground motions on average exceed the model (Abrahamson et al., 1990). The ground motions of the subsurface rupture earthquakes are systematically stronger than average, and those of the surface rupture earthquakes are weaker than average, over a broad period range centered at one second, which dominates peak velocity. This phenomenon is not region dependent, since the data used in the analyses are from crustal earthquakes in different tectonically active regions around the world (Kagawa et al., 2004).

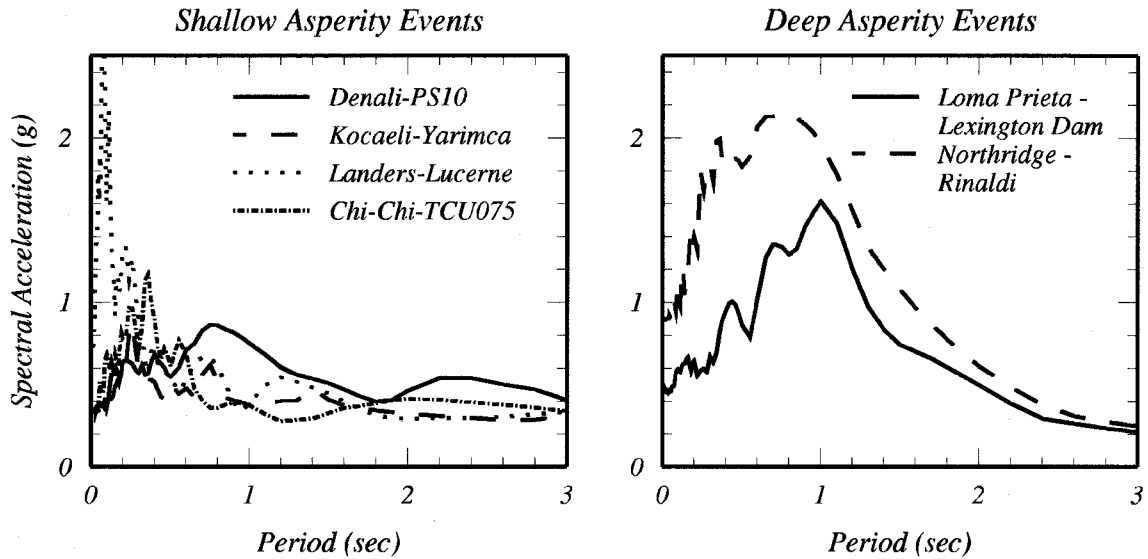


Figure 1 Near-fault response spectra of recent large earthquakes. Left: Four earthquakes, M_w 7.2 to 7.9, with shallow asperities and large surface faulting. Right: Two earthquakes, M_w 6.7 and 7.0, with deep asperities and no surface faulting.

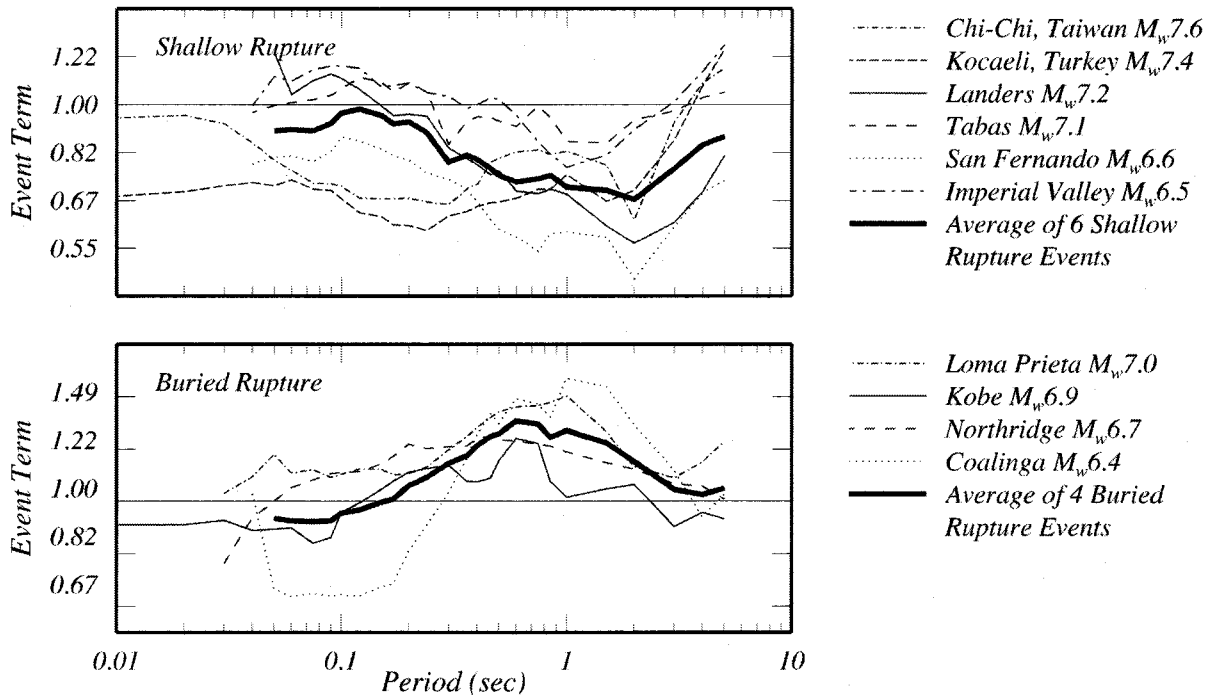


Figure 2 Comparison of response spectral amplitude of individual earthquakes having surface rupture (top) and buried rupture (bottom), averaged over recording sites, with the amplitude of the average earthquake as represented by the model of Abrahamson and Silva (1997), represented by the unit line, which accounts for magnitude, closest distance and recording site category. The event terms (residuals) are shown as the ratio of the event to the model. Source: Somerville (2003).

2. OBSERVED DIFFERENCES IN KINEMATIC SOURCE CHARACTERISTICS

Somerville (2003) and Kagawa et al. (2004) have shown that earthquakes with surface rupture have asperities (regions of large slip, as defined by Somerville et al., 1999) at depths shallower than 5 km (and possibly others that are deeper), while earthquakes with subsurface rupture have

asperities that are all deeper than 5 km. The observation of weaker ground motions for surface than for buried faulting earthquakes seems paradoxical, because the shallow events have much larger near-surface displacements. This can be seen by comparing the distribution of slip with depth, averaged along strike, for surface faulting earthquakes, shown at the top of Figure 3, with that for buried faulting earthquakes, shown at the bottom of Figure 3.

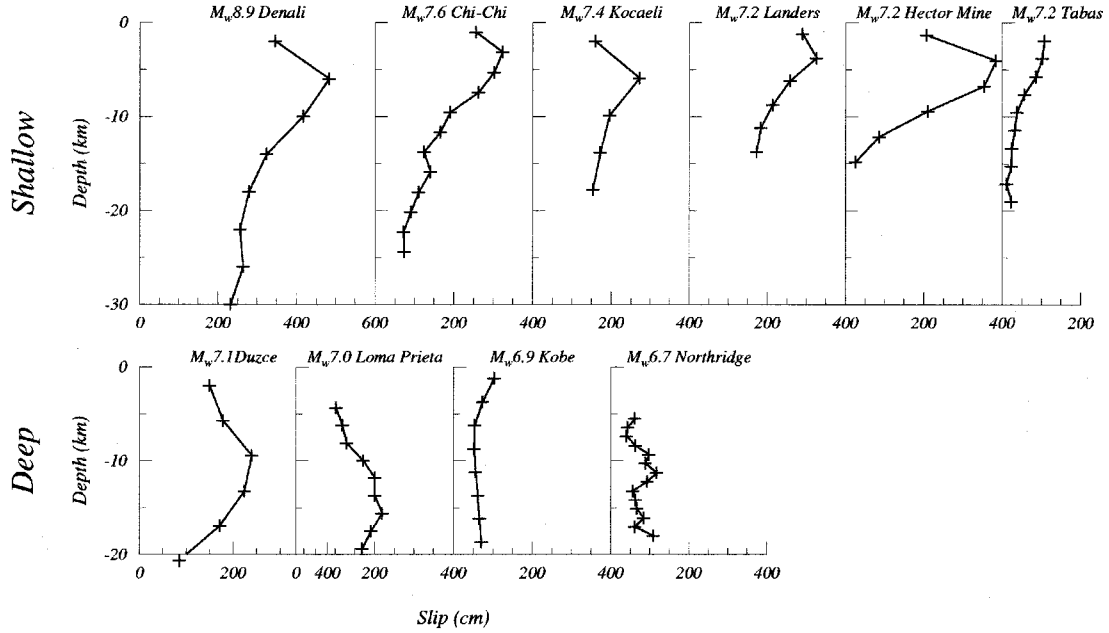


Figure 3 Distribution of slip for shallow (top) and deep (bottom) earthquakes.

However, slip velocity is a much more important determinant of strong motion levels than fault slip (Dan and Sato, 1999). The effective slip velocity is defined by Ishii et al. (2000) as the slip velocity averaged over the time in which the slip grows from 10% to 70% of its final value, and represents the dynamic stress drop. As shown in Figure 4, the distribution of effective slip velocity with depth for shallow events is quite different from the distribution of slip with depth. The shallow events have large near-surface displacements, but they do not have correspondingly large slip velocities. The slip velocities of the deep events, as high as 2 m/sec, are larger than those of the shallow events, causing larger ground motion levels because slip velocity strongly controls strong motion levels. Averaged over 9 shallow events and 8 deep events, the slip velocity of shallow events is about 70% that of deep events. This is true both for the fault as a whole and for the asperities on the fault. We consider that this difference in slip velocity between shallow and deep events is an important aspect of earthquake source characterization for the simulation of strong ground motion.

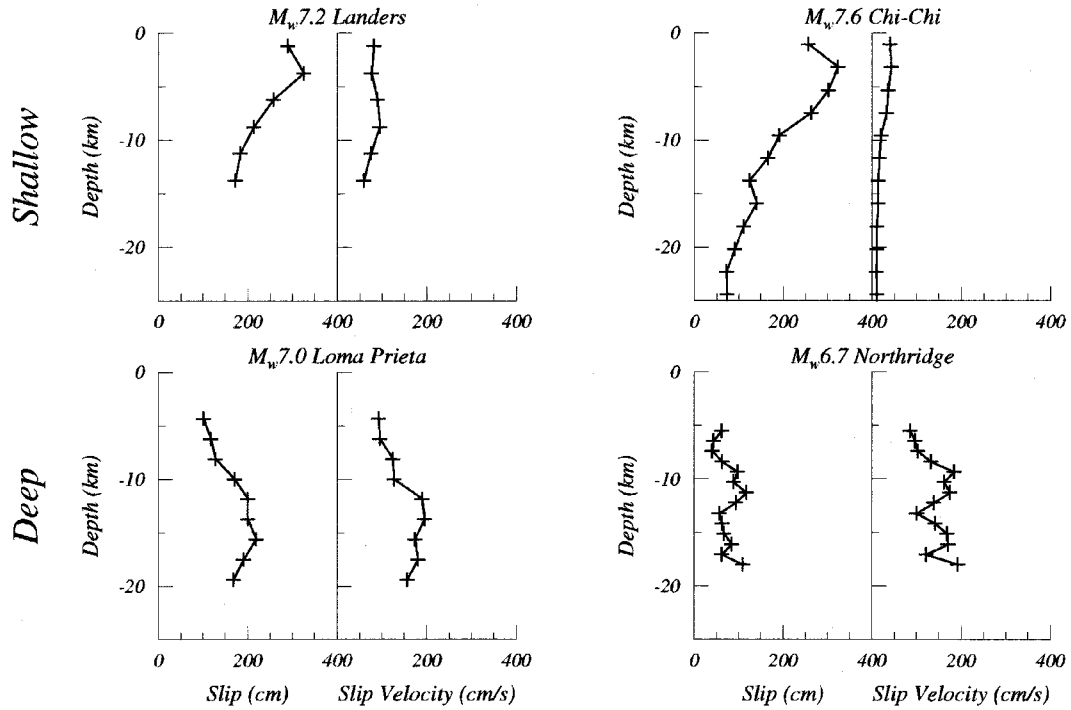


Figure 4 Distribution of slip (left panel) and slip velocity (right panel) for shallow (top) and deep (bottom) earthquakes. The left hand side compares two strike slip earthquakes and the right hand side compares two thrust earthquakes.

3. OBSERVED DIFFERENCES IN DYNAMIC SOURCE CHARACTERISTICS

In a systematic analysis of dynamic rupture models of crustal earthquakes, Mai et al. (2005) found that the fracture energy is large for surface faulting events, and small for subsurface faults, as shown in Figure 5, in which the events on the left side are for surface faulting, and the events on the right side are for buried faulting. The large fracture energy of shallow events reduces the amount of energy available for seismic radiation, causing such events to produce mainly long period seismic radiation. This is consistent with surface faulting events producing weak high frequency ground motions as described in Figures 1 and 2. Abercrombie and Rice (2005) and Tinti et al. (2005) both show that fracture energy increases with seismic moment. This would cause a corresponding decrease in radiated energy, inhibiting the growth of strong motion amplitudes with

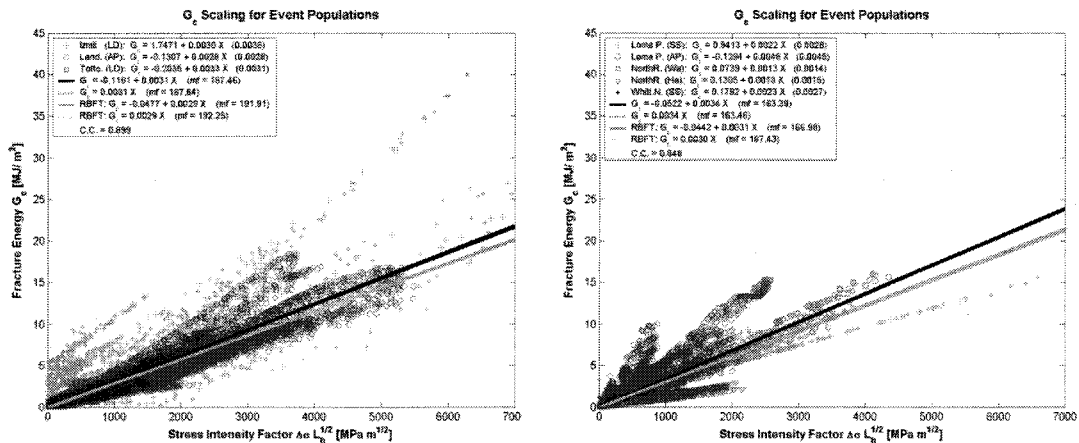


Figure 5 Distribution of fracture energy (vertical axis) and stress intensity factor (horizontal axis) for surface rupture (left) and buried rupture (right) events. Source: Mai et al. (2005).

increasing seismic moment for earthquakes that are large enough to break the surface, and thus tending to limit the growth of ground motion amplitudes with magnitude.

Both numerical models (Day and Ely, 2002) and laboratory models (Brune and Anooshehpour, 1988) of the weak zone have revealed its significant effects on rupture dynamics and near-fault particle motion. In the weak zone, the friction increases with sliding velocity (velocity strengthening), and the dynamic friction is quite low compared with that in the deeper part of the fault. Velocity strengthening causes negative or small positive stress drop, and reduces the radiated seismic energy. Consequently, the contribution to the ground motion from shallow asperities is low. Rock mechanics experiments have shown that the presence of a thick gouge layer produces similar effects (e.g. Marone and Scholz, 1988; Shimamoto and Logan, 1981). We expect that the effect of velocity strengthening is significant for shallow slip on existing faults and in soft sedimentary rocks.

Estimates of the slip weakening distance D_c from dynamic rupture models have been summarized by Mai et al. (2005). It is notable that the 1994 Northridge earthquake had an unusually short slip weakening distance, between 0.1 and 0.15 meters, as estimated by three separate studies (Nielsen and Olsen, 2000; Oglesby and Day, 2002; and Hartzell et al., 2005), in contrast with values of 0.4 to 0.9m, 0.4 – 1.5m, and 0.8 – 3.5 m for the Tottori, Kobe and Landers earthquakes respectively. Among the four events analyzed, the Northridge earthquake is the only thrust event, and the only event having no surface rupture. These measurements of fracture energy and slip weakening distance are consistent with rupture in the shallow part of the fault (upper 5 km) being controlled by velocity strengthening, with larger slip weakening distance D_c , larger fracture energy, larger energy absorption from the crack tip, lower rupture velocity, and lower slip velocity than at greater depths on the fault, resulting in lower ground motions for surface faulting than for buried faulting events.

Fluctuations in rupture velocity may affect the frequency content of the seismic energy generated during the rupture. The slowdown in rupture velocity due to velocity hardening and increase of D_c in the shallow part of the fault could cause the suppression of high frequency energy and enhancement of long period ground motion energy. The overall rupture behavior, and consequently the frequency content of near-fault ground motion, may be different depending on whether the hypocenter is shallow or deep.

4. MODELING OF DIFFERENCES USING RUPTURE DYNAMICS

We have used rupture dynamic modeling (Pitarka and Dalguer, 2003) to shed light on the physics of why surface faulting earthquakes have weaker ground motions than those of buried faulting (Pitarka et al., 2005). The top panel of Figure 6 is a buried rupture, and the panels below it are for increasingly weak shallow zones (represented by decreasing values of stress drop) in the upper 5 km of the crust. With increasing weakness, the shallow zone is increasingly effective at arresting the upward propagation of rupture to the surface, reducing the slip velocity on the fault, and reducing the strength of the ground motion. The ratio of buried to surface spectral acceleration is shown as a function of period in the third column of Figure 6. For increasingly low values of strength of the shallow zone, the ground motion values become increasingly weak. Figure 7 compares buried rupture with the third surface rupture case (shallow stress drop = 1Mpa) from Figure 6, showing much larger slip velocities on the fault for the buried rupture case than for the surface faulting case. This demonstrates that we can find realistic rheological models of the shallow part of the fault that are consistent with the observation of weaker ground motions from surface faulting than from buried faulting earthquakes.

Effect of Stress Drop in the Weak Zone

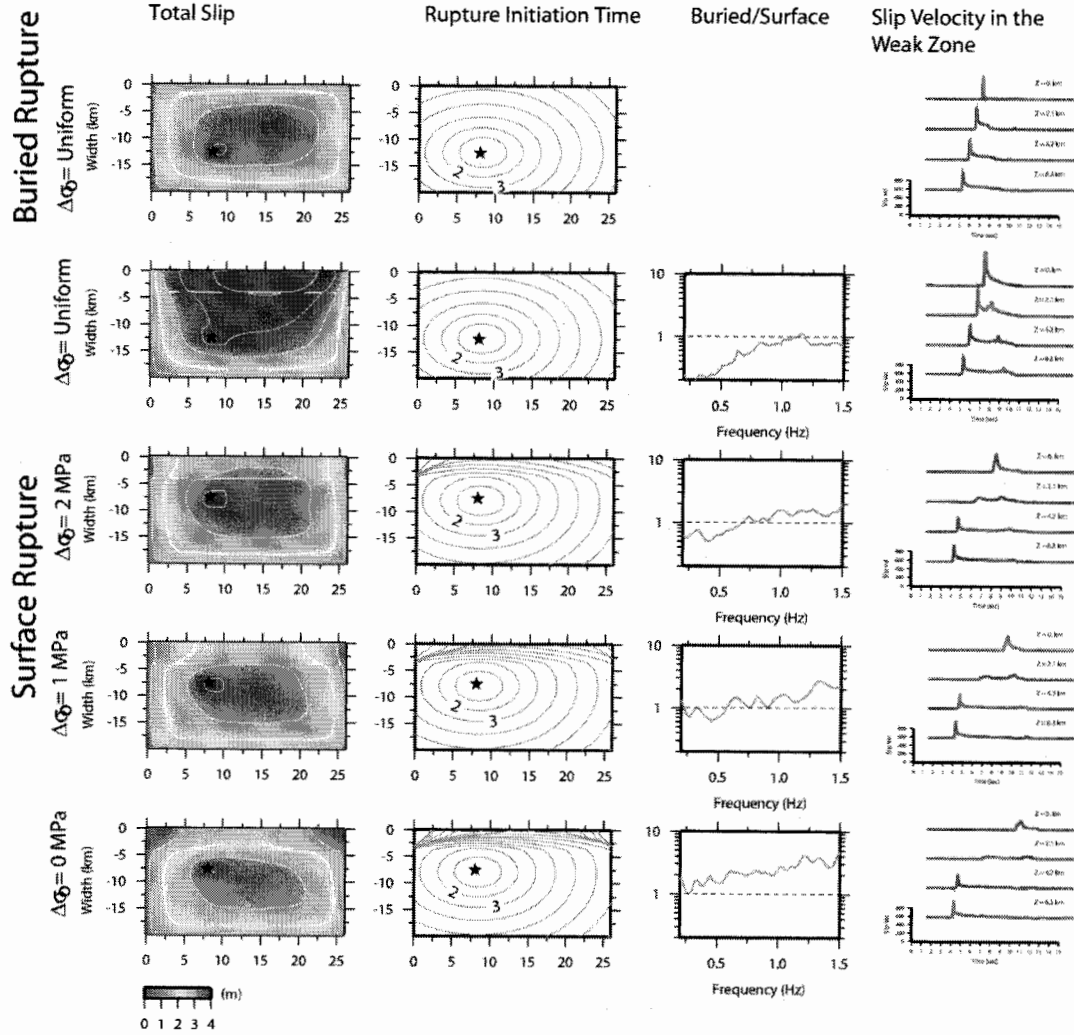


Figure 6 Dynamic simulation of buried and surface rupture earthquakes. The top panel is a buried rupture, and the panels below it are for increasingly weak shallow zones in the upper 5 km of the crust. The shallow zone is increasingly effective at arresting the upward propagation of rupture to the surface, reducing the slip velocity on the fault, and reducing the strength of the ground motion.

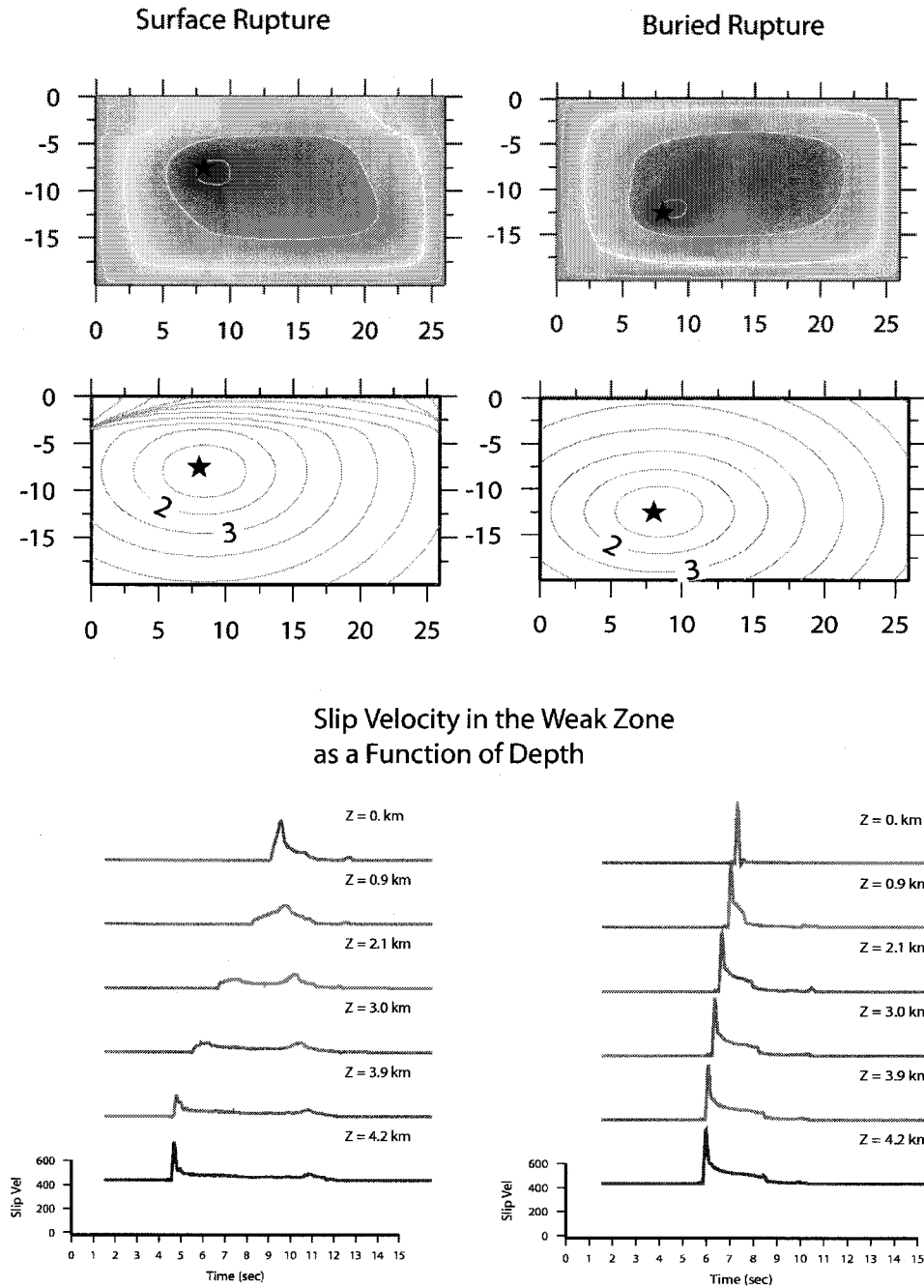


Figure 7 Detail from Figure 6 comparing buried rupture with third surface rupture case (shallow stress drop = 1Mpa), showing much larger slip velocities on the fault for the buried rupture case.

5. CONCLUSIONS

The ground motions from earthquakes that break the ground surface are weaker than the ground motions from buried faulting earthquakes. From kinematic rupture models, we show that the slip velocity of surface faulting earthquakes is less than the slip velocity of buried faulting earthquakes. From dynamic rupture models, we infer that rupture in the shallow part of fault (upper few km) is controlled by velocity strengthening, with larger slip weakening distance D_c , larger fracture energy, larger energy absorption from the crack tip, lower rupture velocity, and lower slip velocity than at

greater depths on the fault. Dynamic rupture modeling using these properties results in lower ground motions for surface faulting than for buried faulting events, consistent with the observations.

Acknowledgments

The work on rupture dynamic models by Mai et al. (2005) was sponsored in part by a grant from METI under the direction of Professor Irikura, and done in collaboration with Ohsaki Research Institute.

References:

- Abercrombie, R.E. and J.R. Rice, "Can observations of earthquake scaling constrain slip-weakening?," *Geophys. J. Int.*, (in press), 2005.
- Abrahamson, N.A., P.G. Somerville, and C. Allin Cornell (1990), "Uncertainty in numerical strong motion predictions," *Proc. 4th U.S. National Conference on Earthquake Engineering*, 1, 407- 416.
- Abrahamson, N.A. and W.J. Silva (1997), "Empirical response spectral attenuation relations for shallow crustal earthquakes," *Seism. Res. Lett.* 68, 94-127.
- Brune, J.N. and R. Anooshehpour (1988), "A physical model of the effect of a shallow weak layer on strong ground motion for strike-slip ruptures," *Bull. Seism. Soc. Am.* 88, 1070-1078.
- Dan, K. and T. Sato (1999), "A semi-empirical method for simulating strong ground motions based on variable-slip rupture models of large earthquakes," *Bull. Seism. Soc. Am.* 89, 36-53.
- Day, S.M. and G.P. Ely (2002), "Effect of a shallow weak zone on fault rupture: numerical simulation of scale-model experiments," *Bull. Seism. Soc. Am.* 92, 3022-3041.
- Hartzell, S.H., M. Guatteri, P.M. Mai, P.-C. Liu, and M.Fisk (2005), "Calculation of broadband time histories of ground motion, Part II: Kinematic and dynamic modeling using theoretical Green's functions and comparison with the 1994 Northridge earthquake," Unpublished manuscript.
- Ishii, T., T. Sato and Paul G. Somerville (2000), "Identification of main rupture areas of heterogeneous fault models for strong motion estimation," *J. Struct. Constr. Eng., AIJ*, No. 527, 61-70.
- Kagawa, T., K. Irikura and P. Somerville (2004), "Differences in ground motion and fault rupture process between surface and buried rupture earthquakes," *Earth, Planets and Space* 56, 3-14.
- Mai, P.M., P. Somerville, A. Pitarka, L. Dalguer, H. Miyake, S. Song, G. Beroza, and K. Irikura (2005), "On the scaling of dynamic source parameters and their relation to near-source ground motion prediction," *Seismological Research Letters* 76, p.261.
- Marone, C. and C. Scholtz (1988), "The depth of seismic faulting and the upper transition from stable to unstable slip regimes," *Geophys. Res. Lett.* 15, 621-624.
- Neilsen, S. and K.B. Olsen (2000), "Constraints on stress and friction from dynamic rupture models of the 1994 Northridge, California earthquake," *Pure App. Geophys.* 157, 2029-2046.
- Oglesby, D.D. and S.M. Day (2002), "Stochastic faults: Implications for fault dynamics and ground motion," *Bull. Seism. Soc. Am.* 92, 3006-3021.
- Pitarka, A. and L. Dalguer (2003), "Estimation of dynamic stress parameters of the 1992 Landers earthquake," Abstracts, 2003 AGU Fall Meeting, San Francisco, California.
- Pitarka, A., S. Day, and L. Dalguer (2005), "Investigation of shallow crustal weak zone effects on rupture dynamics of surface and subsurface faulting," Proceedings and Abstracts Vol. XV, 2005 SCEC Annual Meeting, Palm Springs, California, 168.
- Shimamoto, T., and J.M. Logan (1981), "Effects of simulated clay gouges on the sliding behavior of Tennessee sandstone," *Tectonophysics*, 75, 243-255.
- Somerville, P.G. (2003), "Magnitude scaling of the near fault rupture directivity pulse," *Phys. Earth. Planetary. Int.*, 137, 201-212.
- Somerville, P.G., K. Irikura, R. Graves, S. Sawada, D. Wald, N. Abrahamson, Y. Iwasaki, T. Kagawa, N. Smith and A. Kowada (1999), "Characterizing earthquake slip models for the prediction of strong ground motion," *Seismological Research Letters*, 70, 59-80.
- Tinti, E., P. Spudich, and M. Cocco, "Earthquake fracture energy inferred from kinematic rupture models on extended faults," *submitted to J. Geophys. Res.*, 2005.

IDENTIFICATION OF NONLINEAR SITE RESPONSE USING THE H/V SPECTRAL RATIO METHOD

K. L. Wen¹⁾, T. M. Chang²⁾, C. M. Lin³⁾ and H. J. Chiang³⁾

1) Professor, Institute of Geophysics, National Central University, Taiwan

2) Associate Research Fellow, National Center for Research on Earthquake Engineering, Taiwan

3) PhD Candidate, Institute of Geophysics, National Central University, Taiwan

wenkl@earth.ncu.edu.tw, tmchang@ncree.org.tw, cheminlin@gmail.com, s1642006@cc.ncu.edu.tw

Abstract: The horizontal-to-vertical spectral ratio has become popular in studies of the site effect and the determination of the predominant period of a site. In this study, this method is extended to identify nonlinear soil responses. To establish this fact, borehole array records that have already shown nonlinear site responses previously using the spectral ratios between surface and borehole station pairs are analyzed. However in this study, the horizontal-to-vertical spectral ratio method is used for weak and strong motion records from the same datasets. The results show that nonlinear site responses can be evaluated using horizontal-to-vertical spectral ratios of surface recordings at a single station.

1. INTRODUCTION

Nonlinear site effects, such as an increase in damping and reduction in shear wave velocity as input strength increases, are commonly recognized in the dynamic loading of soils from geotechnical models. Findings of recent years indicate that nonlinear site effects are more common than previously recognized in strong-motion seismology (Beresnev and Wen, 1996). Direct seismological evidence of nonlinear site effects has been reported using spectral ratio techniques for a two-station pair including soil-to-rock or surface-to-borehole station pairs (Wen, 1994; Wen *et al.*, 1994).

In recent years, several large earthquakes have been recorded by modern digital surface and vertical arrays. Borehole data ensure a reliable evaluation of the soil transfer function. Observations in different parts of the world already provide established direct evidence of the significance of nonlinear site effects. Wen *et al.* (1995) used the spectral ratio method to show that the strong motion records of the LSST array in Taiwan (Wen *et al.*, 1986) presented with nonlinear site response; however, the SMART2 array in Taiwan (Chiu *et al.*, 1994) did not. Aguirre and Irikura (1997) compared the spectral ratios between surface- and borehole-station records in Port Island, Japan and showed that the nonlinearity effect occurred during the 1995 Hyogo-ken Nanbu earthquake.

On the basis of two-station pair spectral ratio analysis, results can be used to study nonlinearity in a local area. When a destructive earthquake occurs, there is usually a high level of ground motion or liquefaction ground failure over a large region. In most instances, however, the borehole array is non-existent making the two-station pair spectral ratio method unavailable. In this study, the horizontal-to-vertical (H/V) spectral ratio for a single surface station is introduced to identify

nonlinear site response. In order to show the applicability of the technique, borehole-array data previously used to show nonlinear site response is utilized.

2. H/V SPECTRAL RATIO METHOD

Kagami *et al.* (1982; 1986) proposed that the ratio of the horizontal components of the velocity spectra at the sediment site to those at the rock site can be used as a measure of microseism ground motion amplification. This proposition assumes a common source and similar paths for sediment and bedrock sites. Nakamura (1989) proposed a hypothesis that microtremor site effects can be determined by simply evaluating the spectral ratio of horizontal versus vertical components of motion observed at the same site. Field and Jacob (1993) and Theodulidis *et al.* (1996) showed that this H/V spectral ratio can also be used for earthquake records to study site response. Site response estimations analyzed from the H/V spectral ratio and other methods have been compared by Field and Jacob (1995), Bonilla *et al.* (1997), Riepl *et al.* (1998), and Huang and Teng (1999).

In this study, data used by Wen *et al.* (1995) and Aguirre and Irikura (1997) to show the nonlinear soil response by two-station (surface and borehole) spectral ratio analysis are utilized. The horizontal-to-vertical spectral ratios are calculated for the same earthquake data; then the spectral ratios between strong and weak motion events are compared with the purpose of identifying nonlinear site response during an earthquake.

3. IDENTIFICATION OF NONLINEAR SITE RESPONSE

3.1 Borehole Arrays in Taiwan

As mentioned above Wen *et al.*'s (1995) dataset was selected for this study. Table 1 gives the LSST array data, including 11 weak motion events with peak ground acceleration (PGA) less than 60 gal and 3 strong motion events that PGA are greater than 150 gal; whilst, Table 2 presents data for the SMART2 array. Here, 8 weak motion events with PGA less than 20 gal and 3 strong motion events with PGA greater than 100 gal are selected. Wen *et al.* (1995) showed that these three strong motion events recorded by the LSST array had nonlinear soil response, whereas the SMART2 array did not, due to the firm soil site conditions.

Figure 1a shows the spectral ratio of surface to 11-m depth borehole station for the LSST array. This is the same as that obtained by Wen *et al.* (1995). A 10-sec S-wave portion is selected and the spectral ratio calculated between surface and borehole stations. Each ratio was then smoothed 5 times using the 3-point average method with weightings of 1/4, 1/2, and 1/4. Three strong motion events show nonlinear soil response after comparison of the spectral ratios between the surface and borehole stations and that of the weak motion events. The results are in agreement with Wen *et al.* (1995). For the same events, the H/V spectral ratios of the surface station are shown in Figure 1b. In Figure 1b, we can also find the dominant frequency shift to lower frequency and de-amplification between strong motion events and weak motion events in a frequency range from ~2 Hz to 10 Hz as shown in Figure 1a.

The same comparison for a main- and after-shock pair from the May 20, 1986 earthquake sequence and for the foreshock-mainshock-aftershock sequence on July 30, 1986 are shown in Figures 2 and 3 respectively. Again, the H/V spectral ratios show dominant frequency shift and de-amplification phenomena for mainshock's ratios (Figures 2b and 3b). Which can compare to the spectral ratio results of surface to an 11-m depth (Figures 2a and 3a).

The surface to 200-m borehole depth spectral ratio for the SMART2 array was calculated by the same procedure. This array is located in the Hualien gravel layer area and the results show that the strong motion events did not have nonlinear effects in this firm soil site (Figure 4a). Figure 4b

shows the same characteristics from the H/V spectral ratio for the same dataset.

These comparisons indicate that nonlinear soil responses occurring in the LSST array can be identified using the H/V spectral ratio method. For the SMART2 array, both methods show linear response.

Table 1. Selected LSST events (same data as Wen *et al.*, 1995)

Event	Date	Depth (km)	M_L	Δ (km)	PGA* (gal)
Weak motion					
3	07/11/85	74	5.5	17	27.3
5	29/03/86	10	4.7	8	41.4
6	08/04/86	11	5.4	31	35.4
8	20/05/86	22	6.2	69	35.0
14	30/07/86	2	4.9	5	57.5
20	10/12/86	98	5.8	42	23.8
21	06/01/87	28	6.2	77	31.8
22	04/02/87	70	5.8	16	43.4
23	24/06/87	31	5.7	52	31.7
24	27/06/87	1	5.3	40	23.7
27	18/09/88	63	5.6	68	22.3
Strong motion					
7	20/05/86	16	6.5	66	223.6
12	30/07/86	2	6.2	5	186.7
16	14/11/86	7	7.0	78	167.2
Foreshock to event 12					
9	11/07/86	1	4.5	5	72.8
10	16/07/86	1	4.5	6	70.0

Note: PGA* is peak ground acceleration recorded at the free surface.

Δ is the epicenter distance.

Table 2. Selected SMART2 events (same data as Wen *et al.*, 1995)

Event	Date	Depth (km)	M_L	R (km)	PGA* (gal)
Weak motion					
176	21/05/92	16.7	4.5	38.4	15.4
185	30/06/92	28.6	4.5	33.9	17.5
189	23/07/92	12.8	4.5	31.1	15.3
198	09/10/92	15.9	4.1	24.1	16.5
222	04/05/93	1.0	4.0	5.8	17.5
231	24/06/93	65.0	5.2	87.4	12.0
234	25/06/93	4.6	3.9	12.2	17.5
235	26/06/93	6.7	3.6	11.6	17.0
Strong motion					
183	25/06/92	22.7	4.5	24.2	160.2
192	14/08/92	15.7	4.5	26.3	135.9
202	28/12/92	16.2	4.9	32.4	154.4

Note: PGA* is peak ground acceleration recorded at the free surface.

R is the hypocenter distance.

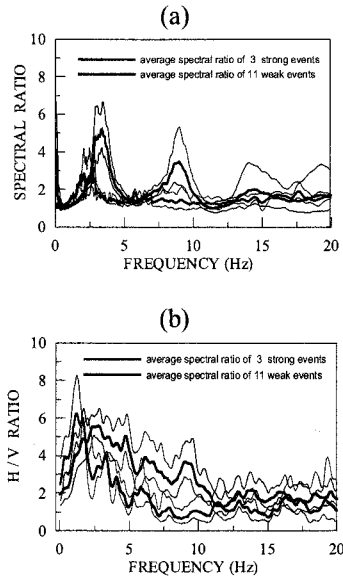


Figure 1. (a) Strong and weak motion spectral ratios of surface to 11-m deep borehole station for the LSST array. (b) H/V spectral ratio for strong events (red line) and weak events (black line) for the same data used in (a). Thick line is the mean value and thin lines show the one standard deviation range. Red lines for strong motion events and blue lines for weak motion events.

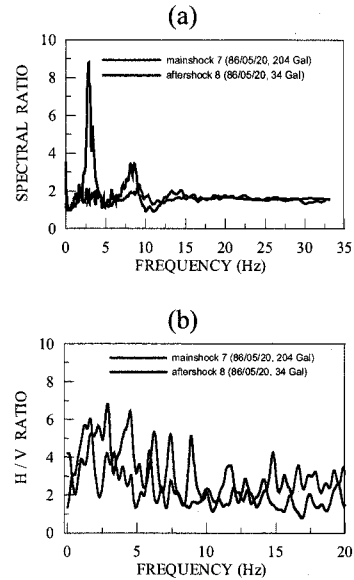


Figure 2. (a) Spectral ratios of surface to 11-m deep borehole station for a mainshock and aftershock pair of May 20, 1986 earthquake recorded by the LSST array. (b) H/V spectral ratios for mainshock and aftershock (black line) for the same events in Fig. 2a. Red and blue lines are the ratios of the mainshock and aftershock, respectively.

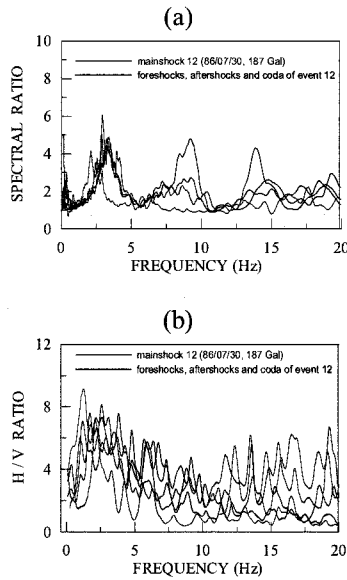


Figure 3. Spectral ratios for foreshock, mainshock, aftershock sequence of July 30, 1986 earthquake recorded by the LSST array. Mainshock shows in red line and weak motions in blue lines. (a) Spectral ratios of surface to 11 m deep borehole station; (b) H/V spectral ratios of the surface station.

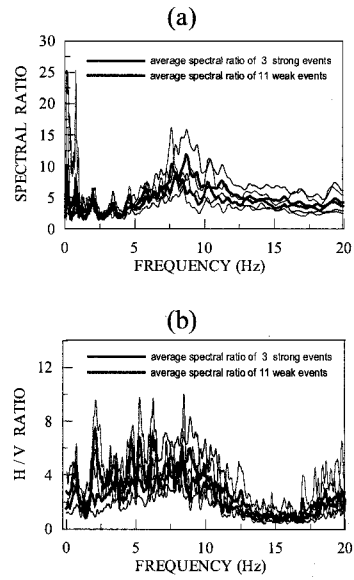


Figure 4. (a) Strong and weak motion spectral ratios of surface to 200-m deep borehole station for the SMART2 array. Shaded areas show one standard deviation range. (b) H/V spectral ratio for strong events (red line) and weak events (blue line) for the same data used in (a). Thick line is the mean value and thin lines show the one standard deviation range.

3.2 Port Island Array in Japan

During the 1995 Hyogo-ken Nanbu earthquake, a large area of Port Island was subject to liquefaction damage. Aguirre and Irikura (1997) compared the spectral ratios between the records at surface and borehole stations in Port Island and showed that a large variation in the spectral ratios during strong ground motions and during the liquefied state. Nonlinearity effect occurred during the 1995 Hyogo-ken Nanbu earthquake. In this section, the horizontal-to-vertical spectral ratio method is applied to the records of the surface station of the borehole array in Port Island to identify nonlinear site response.

Table 3 lists part of the data used by Aguirre and Irikura (1997). The waveform of the ground motion recorded at the free surface during the 1995 Hyogo-ken Nanbu earthquake is shown in Figure 5. The time windows (MpI, MpII, A – H) used by Aguirre and Irikura (1997) are also plotted in Figure 5. A time window of 10.24 sec (except windows MpI, B, and F are 5.12 sec) is selected to calculate the spectral ratio and with the same smoothing method. The spectral ratio between the surface (PR4) and a 16-m depth (PR3) for the 5 small events before the mainshock is calculated as the referent weak motion ratio. The results show strong nonlinear soil responses occurred in the strong ground motion window (MPI) and liquefied state windows (after MPII windows) (Figure 6a). The 0858 aftershock shows not-so-strong nonlinear effect compared to the results of the mainshock. The same characteristic was shown by Aguirre and Irikura (1997). The H/V ratios for the time windows in Figure 5 are calculated and compared with the average H/V ratio of the weak motions. Figure 6b plots the H/V ratios of the mainshock record in different time windows (red line) and compares this with the average H/V ratio from the weak motions of the 5 small events (black line). The area in yellow shows a one standard deviation range of the weak motion ratios. The H/V ratios in different time windows are clearly lower than that of the referent weak motion ratio in the larger frequency band. Nonlinear soil response occurred in the mainshock record of the 1995 Hyogo-ken Nanbu earthquake during the strong ground motions and the liquefied state. The H/V ratio of the 0858 aftershock shows similar results as the spectral ratio of surface to borehole station pair in Figure 6a. The results in Figure 6b can be compared with the results from the spectral ratios between the surface and borehole records of Figure 6a and those of Aguirre and Irikura (1997). Although the peak ground acceleration of the 0858 aftershock is less than 50 gal (Table 3), the spectral ratio of the 0858 aftershock ~24 hrs later still shows as being nonlinear and still not back to around the same as that of the reference motions. This is due to liquefaction in the Port Island area. Site conditions had already changed as explained by Aguirre and Irikura (1997).

This analysis shows that the H/V ratio method can be successfully applied to the records of the Port Island borehole array to study nonlinear soil response during the 1995 Hyogo-ken Nanbu earthquake. The results are comparable with spectral ratio analysis using the surface-borehole station pair (Aguirre and Irikura, 1997).

Table 3 Selected events recorded by the downhole array in Port Island, Japan.

Date	Time	Depth (km)	M_L	Δ (km)	PGA* (gal)
28/06/94	13:08:53.02	16.0	4.6	65.4	5.66
28/07/94	10:01:52.04	11.5	4.1	40.3	7.92
24/10/94	11:51:10.72	15.1	4.3	45.6	11.56
09/11/94	20:26:56.41	10.4	4.1	32.6	5.58
10/11/94	00:38:17.72	11.1	3.9	32.1	6.98
17/01/95	05:46:46.74	16.0	6.9	17.7	555.00
17/01/95	08:58:16.14	18.8	4.7	15.1	43.75

Note: PGA* is peak ground acceleration recorded at the free surface.

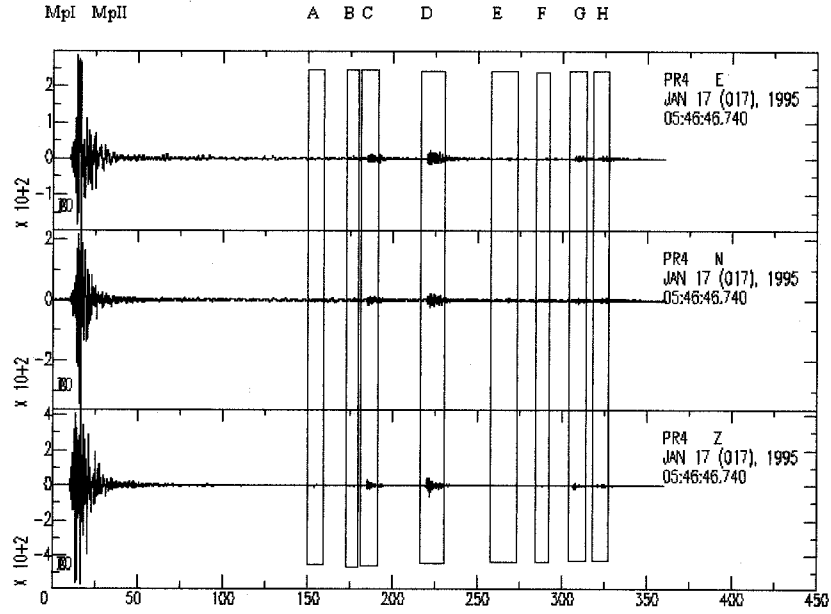


Figure 5. The waveform recorded at free surface in Port Island, Japan during the 1995 Hyogo-ken Nanbu earthquake. Windows Mpl, MplI, and A to H are the same as those used by Aguirre and Irikura (1997).

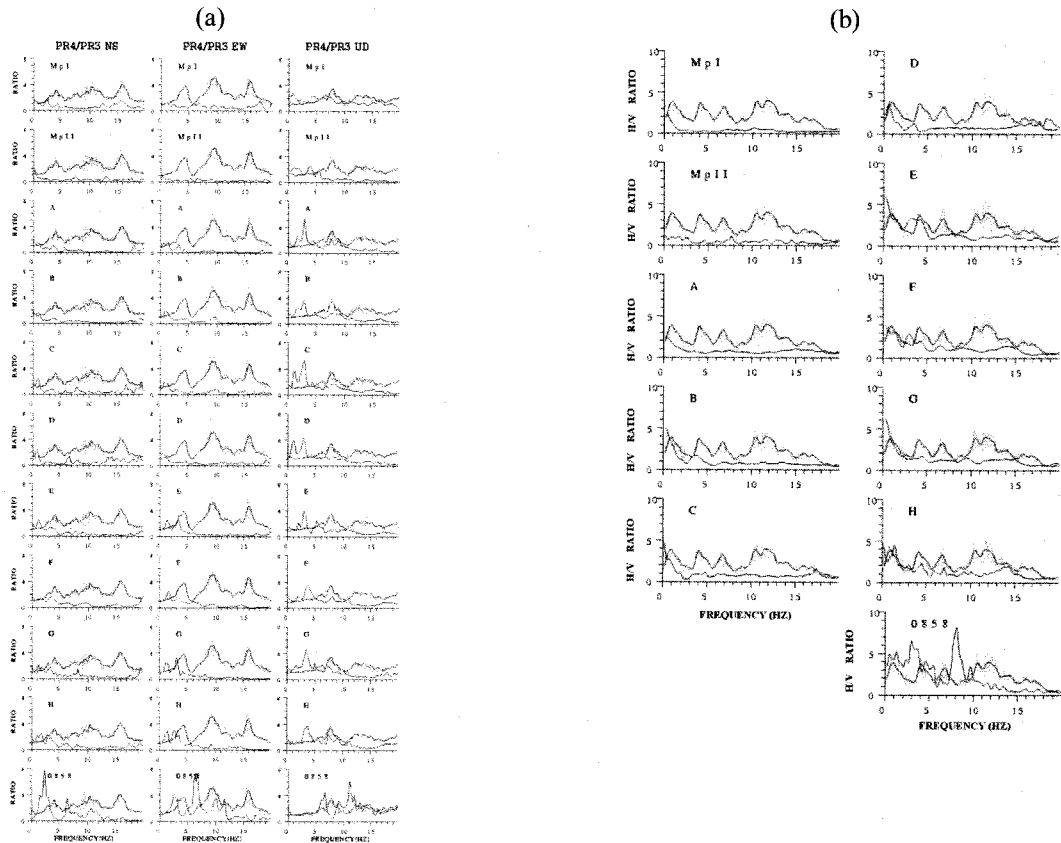


Figure 6. Spectral ratios in the different time windows calculated from the mainshock and one aftershock of the 1995 Hyogo-ken Nanbu earthquake (red line). Time windows are the same as those in Fig. 5. Black line is the mean ratio of the weak motions before the Kobe mainshock and yellow area shows the one standard deviation area; (a) The results of surface to a 16-m deep borehole station pair are given and are the same as those of Aguirre and Irikura (1997). (b) The results of H/V ratios from the surface station.

4. CONCLUSIONS AND DISCUSSIONS

Findings of recent years indicate that nonlinear site effects are more common than previously recognized in strong-motion seismology. Direct seismological evidence of nonlinear site effects were reported using spectral ratio techniques. In recent years, several large earthquakes have been recorded by modern digital surface and vertical arrays. Borehole data ensure a reliable evaluation of soil transfer function. Observations in different parts of the world already provide established direct evidence of the significance of nonlinear site effects. But the borehole array is not common in most areas and the results analyzed from borehole array data are only applicable to site response in that local area. In this study, the horizontal-to-vertical spectral ratio (H/V spectral ratio) method was introduced to identify the nonlinear site response. The data at LSST and Port Island's borehole arrays, which had already shown nonlinear site responses from previous spectral ratio analyses between surface and borehole station pairs, are used to show the applicability of H/V technique for nonlinear site response identification.

Many studies already shown the shear-wave nonlinearity calculated from the horizontal records of surface to downhole seismometers, between weak and strong motions (Beresnev and Wen, 1996). Beresnev *et al.* (2002) analyzed the data from the KiK-net borehole arrays in Japan and found that the nonlinearity in P waves is observed at the acceleration levels roughly exceeding 0.1 g. It is similar to that observed in S waves. The spectral ratios of the vertical component in Figure 6a also indicated nonlinearity occurred in the vertical motions as that observed by Beresnev *et al.* (2002).

As most data shown the peak ground acceleration in vertical component usually is less than horizontal component. So, we can expect that nonlinear soil response in horizontal component is stronger than that in vertical component. The PGA data recorded during the 1995 Hyogo-ken Nanbu earthquake in the Port Island's borehole array shows that the horizontal PGA in the depth of 16 m and ground surface were less than that recorded at vertical component. It implies that H/V spectral ratio method is possible to identify the nonlinear soil response.

This study shows that the H/V technique can be used to identify nonlinearity of site response after a strong event. For most areas that do not have borehole arrays to check spectral ratios between surface-borehole station pairs, the horizontal-to-vertical technique can be used to study site response characteristics during strong earthquakes.

Acknowledgements:

This paper have submitted to Terrestrial, Atmospheric and Oceanic Sciences Journal. Thanks to Prof. K. Irikura of the Kyoto University, Japan for providing some small event and aftershock data of the 1995 Hyogo-ken Nanbu earthquake recorded by the borehole array in Port Island, Japan. This study was supported by the National Science Council under the grant numbers NSC89-2625-Z-002-041 and NSC93-2625-Z-008-004.

References:

- Aguirre, J., and Irikura, K. (1997), "Nonlinearity, Liquefaction, and Velocity Variation of Soft Soil Layers in Port Island, Kobe, During the Hyogo-ken Nanbu Earthquake," *Bull. Seism. Soc. Am.*, **87**(5), 1244-1258.
- Beresnev, I.A., and Wen, K.L. (1996), "Nonlinear Ground Response - A Reality? (A Review)," *Bull. Seis. Soc. Am.*, **86**(6), 1964-1978.
- Beresnev, I.A., Nightengale, A.M., and Silva, W.J. (2002), "Properties of Vertical Ground Motions," *Bull. Seism. Soc. Am.*, **92**(8), 3152-3164.
- Bonilla, L.F., Steidl, J.H., Lindley, G.T., Tumarkin, A.G., and Archuleta, R.J. (1997), "Site Amplification in the San Fernando Valley, California: Variability of Site-Effect Estimation Using the S-Wave, Coda and H/V Methods," *Bull. Seis. Soc. Am.*, **87**, 710-730.
- Chiu, H.C., Yeh, Y.T., Ni, S.D., Lee, L., Liu, W.H., Wen, G.F., and Liu, C.C. (1994), "A New Strong-Motion Array in Taiwan: SMART-2," *Ter. Atm. Oce.*, **5**, 463-475.

- Field, E.H., and Jacob, K.H. (1993), "The Theoretical Response of Sedimentary Layers to Ambient Seismic Noise," *Geophysical Research Letters*, **20**, 2925-2928.
- Field, E.H., and Jacob, K.H. (1995), "A Comparison and Test of Various Site-Response Estimation Techniques Including Three That Are Not Reference-Site Dependent," *Geophys. Res. Lett.*, **20**, 2925-2928.
- Huang, H.C., and Teng, T.L. (1999), "An Evaluation on H/V Ratio vs Spectral Ratio for Site-Response Estimation Using the 1994 Northridge Earthquake Sequence," *PAGEOPH*, **156**, 631-649.
- Kagami, H., Duke, C.M., Liang, G.C., and Ohta, Y. (1982), "Observation of 1- to 5-second Microtremors and Their Application to Earthquake Engineering. Part II. Evaluation of Site Effect Upon Seismic Wave Amplification Due to Extremely Deep Soil Deposits," *Bull. Seism. Soc. Am.*, **72**(3), 987-998.
- Kagami, H., Okada, S., Shiono, K., Oner, M., Dravinski, M., and Mal, A.K. (1986), "Observation of 1- to 5-second Microtremors and Their Application to Earthquake Engineering. Part III. A Two Dimensional Study of Site Effects in the San Fernando Valley," *Bull. Seism. Soc. Am.*, **76**(6), 1801-1812.
- Nakamura, Y. (1989), "A Method for Dynamic Characteristics Estimation of Subsurface Using Microtremor on the Ground Surface," *QR of RTR1*, **30**(1), February.
- Riepl, J., Bard, P.Y., Hatzfeld, D., Papaioannou, C., and Nechtschein, S. (1998), "Detailed Evaluation of Site-response Estimation Methods Across and Along the Sedimentary Valley of Volvi (Euro-Seistest)," *Bull. Seism. Soc. Am.*, **88**, 445-502.
- Theodulidis, N., Bard, P.Y., Archuleta, R.J., and Bouchon, M. (1996), "Horizontal to Vertical Spectral Ratio and Geological Conditions: The Case of Garner Valley Downhole Array in Southern California," *Bull. Seism. Soc. Am.*, **86**, 306-319.
- Wen, K.L. (1994), "Non-linear Soil Response in Ground Motions," *Earthq. Eng. Struct. Dyn.*, **23**(6), 599-608.
- Wen, K.L., Yeh, Y.T., and Liu, C.C. (1986), "The Observation System and Data Processing of the LSST Array (in Chinese)," Institute of Earth Sciences, Academia Sinica, ASIES-CR8602.
- Wen, K.L., Beresnev, I.A., and Yeh, Y.T. (1994), "Non-linear Soil Amplification Inferred From Downhole Strong Seismic Motion Data," *Geophys. Res. Lett.*, **21**(24), 2625-2628.
- Wen, K.L., Beresnev, I.A., and Yeh, Y.T. (1995), "Investigation of Nonlinear Site Amplification at Two Downhole Strong Ground Motion Arrays in Taiwan," *Earthq. Eng. Struct. Dyn.*, **24**(3), 313-324.

DEVELOPMENT OF EARTHQUAKE MOTION SIMULATOR WITH HIGH RESOLUTION AND ITS APPLICATION

T. Ichimura¹⁾, M. Hori²⁾ and T. Samo³⁾

1) Associate Professor, Department of Civil Engineering, Tokyo Institute of Technology, Japan

2) Professor, Earthquake Research Institute, Univ. of Tokyo, Japan

3) Department of Civil Engineering, Tokyo Institute of Technology, Japan

ichimura@cv.titech.ac.jp, hori@eri.u-tokyo.ac.jp, samo@e-society.cv.titech.ac.jp

Abstract: Realistic simulation of a possible earthquake is crucial for producing a pertinent counter plan against earthquake disasters. Such simulation is realized herein through the development of Integrated Earthquake Simulator (IES), which is an assemblage of a computer-based high-resolution strong ground motion (SGM) simulator and a Virtual Reality city constructed from GIS/CAD data. In this paper, schematic view of such SGM simulator, the methodology to construct a virtual reality (VR) city and the prototype of the IES are briefly presented. Earthquake disaster simulation in a VR city is conducted to demonstrate IES performance.

1. INTRODUCTION

Realistic earthquake disaster simulation of possible earthquake is important for making pertinent counter plan. This paper presents such a simulation method, Integrated Earthquake Simulator (IES) using strong ground motion (SGM) information with high resolution and Virtual Reality (VR) city constructed from GIS/CAD data.

2. Earthquake Motion Simulator with High Resolution

There are works for SGM simulation along full 3-D numerical simulation (for example; see Bao et al. (1996), Faccioli, et al. (1997), Komatitsch et al (1998), Furumura et al. (1998), Pitarka (1999), Fujiwara (2000), Aoi and Fujiwara (1999)). Though full 3-D numerical simulation is one of effective approaches for providing SGM information with high resolution, there could be two major difficulties: 1) huge amount of computation; 2) uncertainty of soil-crust information. For resolving these difficulties, new analysis method, macro-micro analysis method (MMAM) has been proposed. In this section, brief summary and flowchart of MMAM is presented (for detail and application example; see Ichimura and Hori).

MMAM takes advantage of the multi-scale analysis and the bounding medium theory for efficient and accurate numerical computation. The multi-scale analysis can reduce computation amount required at one time, and the bounding media theory can resolve the uncertainty of soil-crust structure information. Wave propagation processes from fault to ground surface can be computed with sufficiently high spatial and temporal resolution.

The multi-scale analysis of the MMAM, which is based on singular perturbation expansion, uses spatial coordinates of two length scales. The macro-analysis and the micro-analysis are set for computing the wave propagation in the geological scale with low resolution and in each town or ward

in engineering scale with high resolution, respectively.

The uncertainty of geological and ground structures is resolved by considering a stochastic model, which prescribe stochastic distribution of structure configuration and mechanical properties, such as the mean and the variance. The bounding medium theory is used to make fictitious but deterministic models for the stochastic model such that the mean responses of the stochastic model can be bounded by the responses of these deterministic models.

MMAM is constructed employing multi-scale analysis based on the singular perturbation and the bounding medium theory. The procedures of MMAM is summarized as follows:

- a) Construct a stochastic model for crust and ground structures of a metropolis, by prescribing the mean and variance for the configuration (such as the location of the interface between neighboring layers) and the material properties (such as the elasticity and the density) for each layer.
- b) Applying the bounding media theory, determine two fictitious but deterministic models that provide optimistic and pessimistic estimates of the mean behavior of the stochastic model.
- c) Applying the singular perturbation expansion, make multi-scale analysis to calculate a distribution of SGM in the target metropolis; the multi-scale analysis consists of the macro-analysis with low spatial resolution and the micro-analysis with high spatial resolution, i.e., in macro-analysis, compute SGM for whole ground structure under the metropolis at the spatial resolution of 100[m]. In micro-analysis, compute SGM for each small region of ground structure under the metropolis at the spatial resolution of 1[m].

Figure 1 presents a schematic view of the above procedures of the MMAM.

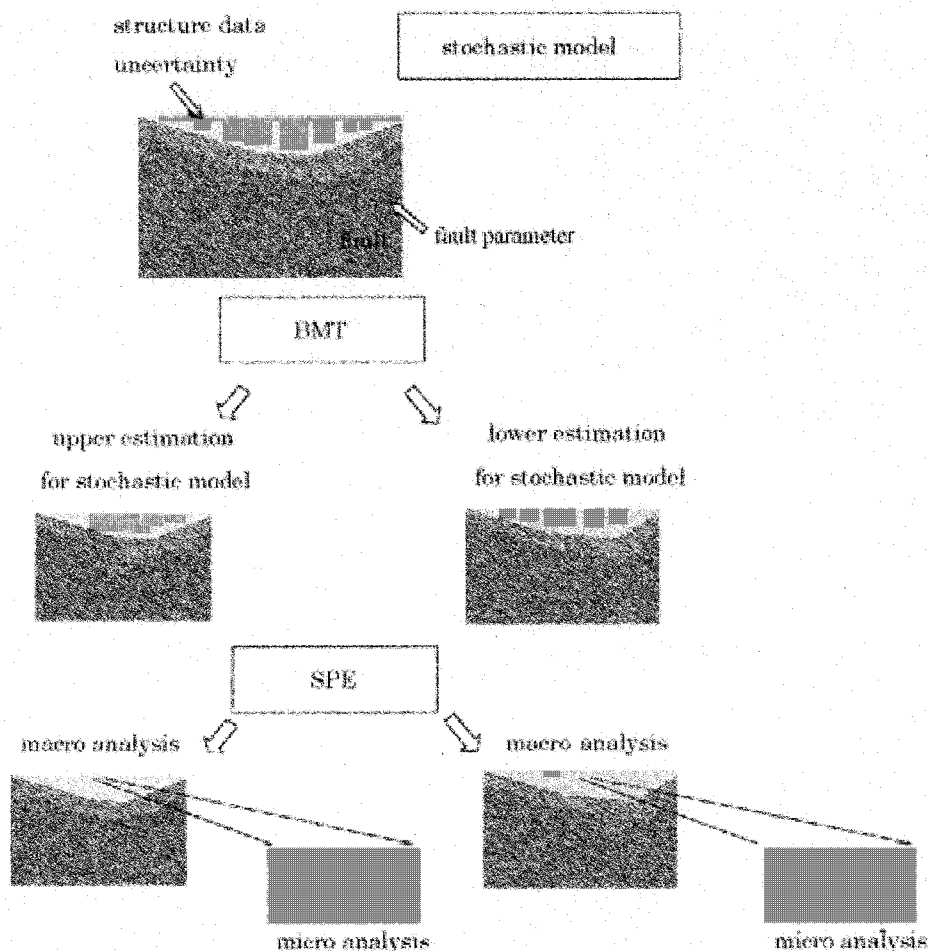


Fig. 1 Flowchart of macro-micro analysis method

The prototype of SGM simulator is able to compute the SGM distribution with high spatial and temporal resolution, say, 1 or 2 meter and 10 Hz. Such resolution is needed for the dynamic analysis of structures whose natural frequency goes up to a few Hz. Also, in this resolution, the wave amplification near the ground surfaces that consist of soft layers is computed accurately, and some 3 D topographical effects on the amplification can be computed.

3. Application Example of Integrated Earthquake Simulator Prototype

One of effective application of SGM information with high resolution could be earthquake disaster estimation with high resolution. We have proposed the IES, which is computer-based earthquake disaster estimation (Ichimura et al. (2005)). In this section, an example of VR city and application example of the IES prototype are briefly presented (for detail; see Ichimura et al. (2005)). Earthquake disaster simulation in a VR city is conducted to demonstrate IES performance.

3.1 Schematic view of Integrated Earthquake Simulator

The IES can serve to support construction of earthquake disaster countermeasures based on common recognition because it offers: 1) a VR city that is reconstructed on a computer from measured digital data (GIS/CAD); 2) simulators for soil, steel, reinforced concrete structures, etc.; 3) a SGM simulator with high resolution; and 4) simulators for human evacuation, network damage, etc. (Fig. 2 depicts the IES system). An SGM simulator shakes a VR city on the computer with a realistic setting. Consequently, we can realistically visualize and analyze an earthquake disaster. Estimation of an earthquake disaster in a whole city in such an integrated manner enables us to evaluate not only structural damage, but also the effects of network damage, and other damage.

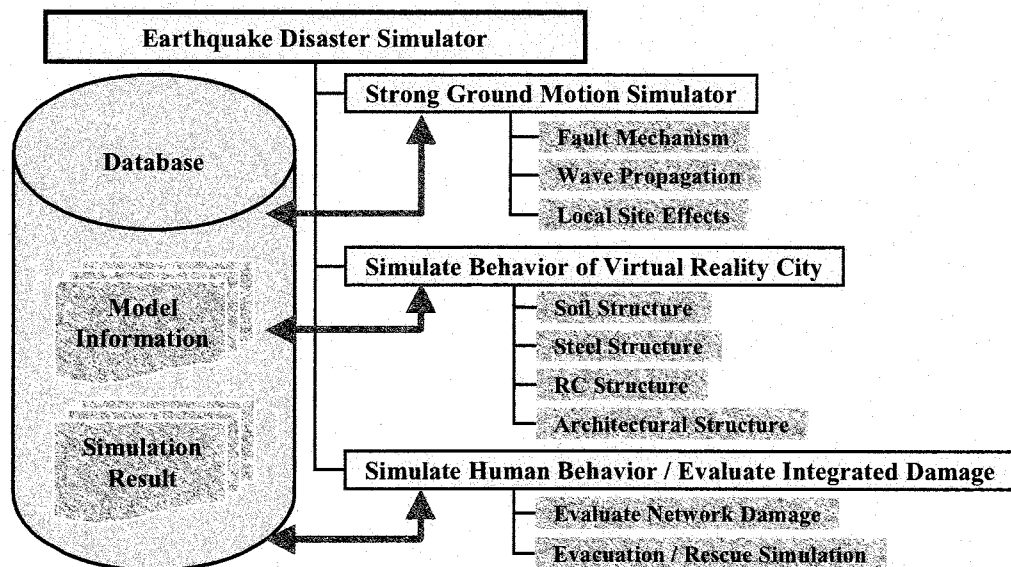


Fig. 2 Schematic view of Integrated Earthquake Simulator

3.2 Construction of a VR Kobe City

The VR Kobe city prototype, including the three-dimensional (3-D) soil structure, buildings and a bridge, is constructed using borehole data, surface elevation data (50 m grid), two-dimensional (2-D) CAD data for buildings, classification data of buildings, a bridge blueprint, and other information. Though VR Kobe city is constructed in all Kobe area, for explanation, a small domain was selected as the target area for this application illustration, but an application example of the entire domain was

also conducted. Figure 3 shows the VR city of the target domain including the 3-D soil structure, buildings, and bridges.

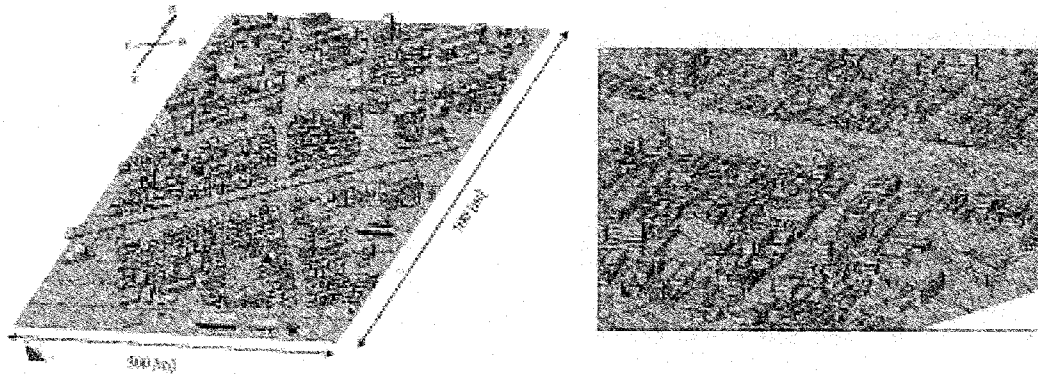


Figure 3: A Part of the VR City

The 3-D soil structure was estimated using an approach similar to that of precedent studies with borehole data and surface elevation data (50 m grid). The surface topography is almost horizontal, but the interface between the soft layer and engineering basin is inclined in the east-west direction. The VR city bridge is constructed using 3-D CAD data that were digitized from a blueprint of the actual bridge. This bridge has a data structure that readily allows us to model each bridge member using an ID and transform data resolution. The 3-D building model is constructed using 2-D CAD data for buildings along with building classification data. The target domain includes 1261 buildings. Each building has an ID and an associated data file that includes data for location, 3-D geometry, classification, and other data. Each structure in this VR city has a data structure and ID that make the voluminous data tractable. When we specify the ID, the structural data are extracted automatically. Furthermore, data transformation can be handled easily.

3.3 Earthquake disaster simulated by IES prototype

Earthquake disaster simulation is conducted using the VR Kobe city constructed in the above section and IES prototype. This IES prototype comprises an SGM simulator with high resolution (3-D dynamic FEM, see Ichimura and Hori), a bridge simulator (3-D dynamic FEM analysis tool for large-scale structure, see Yamada et al. (2005)), and a building simulator (approximated modal analysis). These numerical simulation tools are selected to correspond to the data model quality because only limited data are available for construction of the VR city.

The dynamic behavior of the VR Kobe city is estimated for three scenarios according to a primary study. RickerWavelet (center frequency 1 Hz, center time 1 s) is input from the bottom surface of the 3-D soil structure in the north-south and east-west directions. Maximum amplification is modified as fit to earthquake motion observed at Takatori Station during the Hanshin Great Earthquake. The following three scenarios are considered.

scenario 1: the wave input is from underneath and perpendicular.

scenario 2: the wave input is from underneath and perpendicular. The soil structure is approximated to horizontally layer media.

scenario 3: the wave input is inclined by 5° .

Estimation of dynamic behavior of the VR Kobe city is summarized briefly. Figures 4(a) and 4(b) show maximum velocity distributions on the surface and the maximum drift angle (DA) of each building. The SGM distribution is uniform and DAs of similar buildings are the same in scenario 2 because the soil structure is approximated to horizontally layered media. On the other hand, the SGM and DA distributions are not uniform and localized in scenarios 1 and 3. Figure 4(c) shows estimations

of building damage; they were conducted based on the maximum DA and criteria for each building type. The damage distribution indicates that building damage is affected strongly by local effects of SGM and the buildings' characteristics. These estimations and discussions reveal that different scenarios engender remarkable differences of resulting earthquake disasters in complicated cities.

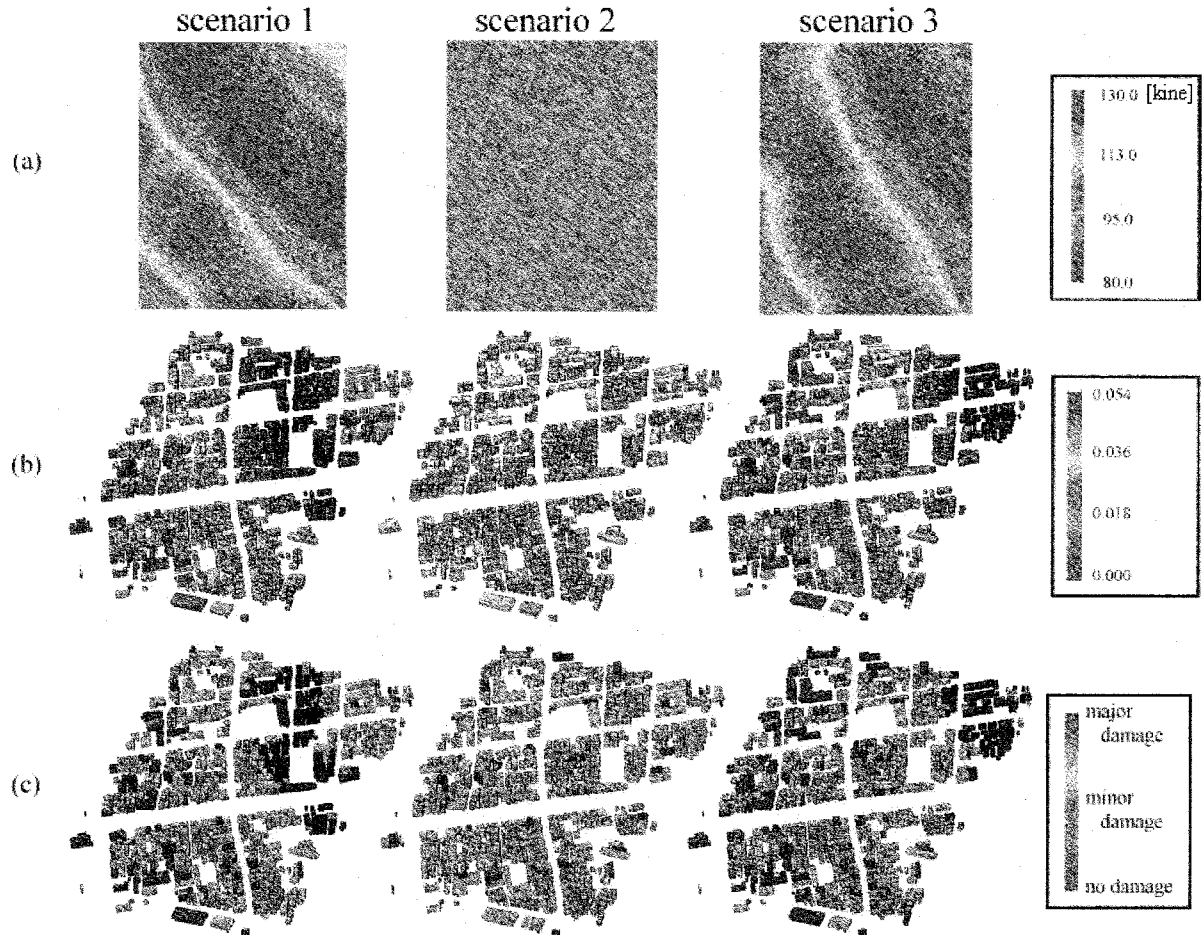


Figure 4: (a) maximum velocity distribution (kine), (b) maximum drift degree distribution and (c) damage distribution

4. CONCLUSIONS

This paper described schematic view of SGM simulator with high resolution and an IES prototype as application of SGM information with high resolution. Some application examples were presented to illustrate the need for integrated simulation and integrated estimation on earthquake disasters, and the utility of the IES.

In the near future, more simulators for various structures will be incorporated into the IES. A data transfer protocol to provide links among various simulators will be examined. Sensitivity analyses against data will be made from the viewpoint of required data for reasonable earthquake disaster simulation. Following the explorations mentioned above, earthquake disaster simulation in a more realistic setting would be attempted using the IES.

Acknowledgements:

For this study, we have used the computer systems of Earthquake Information Center of Earthquake Research Institute, University of Tokyo.

References:

- Bao, H., J. Bielak, O. Ghattas, L. F. Kallivokas, D. R. O'Hallaron, J. R. Shewchuk and J. Xu. (1996), "Earthquake ground motion modeling on parallel computers", *In Proceedings of Supercomputing '96*.
- Faccioli, E, F. Maggio, R. Paolucci and A. Quarteroni (1997), "2D and 3D elastic wave propagation by a pseudo-spectral domain decomposition method", *Journal of Seismology*, 1:237-251.
- Komatitsch, D. and Vilotte J. (1998), "The spectral element method: an efficient tool to simulate the seismic response of 2D and 3D geological structures", *Bull. Seism. Soc. Am.*, 88:368-392.
- Furumura, T. and K. Koketsu (1998), "Specific distribution of ground motion during the 1995 Kobe earthquake and its generation mechanism", *Geophys. Res. Lett.*, 25:785-788.
- Pitarka, A. (1999), "3D elastic finite-difference modeling of seismic motion using staggered grids with non-uniform spacing", *Bull. Seism. Soc. Am.*, 89:54-68.
- Fujiwara, H. (2000), "The fast multi-pole method for solving integral equations of three-dimensional topography and basin problems", *Geophys. J. Int.*, 140:198-210.
- Aoi, S., and H. Fujiwara (2000), "3D finite-difference method using discontinuous grids", *Bull. Seism. Soc. Am.* 1999; 89:918-930.
- T. Ichimura and M. Hori (in press), "Macro-Micro Analysis Method for Wave Propagation in Stochastic Media", *Earthquake Engineering & Structural Dynamics*.
- T. Ichimura and M. Hori (in press), "Strong Ground Motion Prediction using Macro-Micro Analysis Method", *Earthquake Engineering & Structural Dynamics*.
- T. Ichimura, M. Hori, K. Terada, T. Yamakawa (2005), "On Integrated Earthquake Simulator Prototype: Combination of Numerical Simulation and Geographical Information System", *Structural Eng./Earthquake Eng.*, JSCE, Vol.22, No.2, pp. 233s-243s.
- T. Ichimura, H. Itami, T. Samo, M. Hori and N. Yamaguchi (2005), "Construction of Digital City Kobe & A Basic Discussion on Application of IES approach to Earthquake Disaster Simulation", *Journal of Structural Engineering*, JSCE, Vol. 51, pp.513-520.
- T. Yamada, T. Ichimura, N. Ohbo, T. Samo, M. Hori and K. Ikeda (2005), "Seismic Response Behavior of Ramp Structure in the Tunnel and Consideration of its Countermeasure", *Journal of Structural Engineering*, JSCE, Vol. 51, pp.561-568.

LONG PERIOD GROUND MOTION CHARACTERISTICS IN A MEGA-CITY OSAKA DURING EXPECTED HUGE SUBDUCTION EARTHQUAKE

K. Kamae¹⁾ and K. Kawabe²⁾

1) Professor, Research Reactor Institute, Kyoto University, Japan

*2) Research Associate, Research Reactor Institute, Kyoto University, Japan
kamae@kuca.rrri.kyoto-u.ac.jp, kawabe@rrri.kyoto-u.ac.jp*

Abstract: There is high possibility of the occurrence of the Tonankai and Nankai earthquakes which are capable of causing immense damage to mega-city Osaka which located inside the Osaka basin. The Central Disaster Prevention Council in Japan has opened the seismic intensity map due to the expected huge subduction earthquake linked by Nankai and Tonankai earthquakes. In this study, we tried to predict broad-band strong ground motions of engineering interest during such subduction earthquakes using the empirical Green's function method. Furthermore, to understand the effects of the 3-dimensional deep underground structure of the Osaka basin to the long period ground motions, we carried out the 3-D finite difference simulation. In a mega-city Osaka located inside basin, the long period ground motions (4 ~ 6 seconds) with very long duration have been predicted for both huge earthquakes. The amplitude of the predicted response spectrum is over the design spectrum around period of five second. These results suggest that we need to investigate the seismic safety of high-rise buildings and base-isolated buildings and so on..

1. INTRODUCTION

In Japan, long-term probabilities of several huge subduction earthquakes have been evaluated by the Headquarters for Earthquake Research Promotion (HERP). The huge subduction earthquakes along the Nankai trough have a high potential for the next occurrences. On the other hand, the Central Disaster Prevention Council in Japan has recently opened the seismic intensity map due to the expected huge subduction earthquake linked by Nankai and Tonankai earthquakes occurred along the Nankai trough. In order to mitigate the disaster caused by such earthquakes, it is very important to predict not only the seismic intensity but also the broad-band strong ground motions of engineering interest before events. A methodology to predict strong ground motions from scenario earthquakes (inland earthquakes as well as subduction earthquakes) has been proposed by Irikura et al.(2003). They call it the recipe for strong ground motion prediction. In this study, we try to predict broad-band strong ground motions from the expected Nankai (M8.4) as well as the Tonankai (M8.1) earthquakes based on the recipe. In particular, we concentrate the prediction of strong ground motions inside the Osaka basin with very complicated underground structure. Broad-band strong ground motions have been predicted by the empirical Green's function method. Furthermore, the characteristics of long period ground motions have preliminarily been investigated by the 3-D finite difference computation considering 3-D underground structure of the Osaka basin.

2. SOURCE MODEL FOR EXPECTED NANKAI AND TONANKAI EARTHQUAKES

We basically use the characterized source models proposed by the HERP. Such models are based on the recipe for strong ground motion prediction by Irikura et al.(2003). Figure 1 shows the source

model composed of three asperities on the fault for the Nankai and the Tonankai earthquakes. The area of the largest asperity and the area of the combined asperities for each source model are basically determined from the self-similar scaling relations of asperities with respect to seismic moments derived statistically from the source inversion results for actual earthquakes. The main source parameters for each earthquake are summarized in Table 1. In case of estimating individual occurrence of the Nankai and the Tonankai earthquakes, the rupture starting points for both earthquakes were put at symbol ★1 and ★2, respectively. We assumed the rupture propagates radially.

3. SYNTHETICS BY THE EMPIRICAL GREEN'S FUNCTION METHOD

Firstly, we predicted broad-band strong ground motions at several sites by the empirical Green's function method by Irikura (1986). The locations of sites are shown in Figure 1, together with the epicenter of the earthquakes (EGF-1 and EGF-2) used as the empirical Green's functions. The symbols ○ and ● showing site locations depict the sediment sites inside basin, rock outcropping sites or hard sediment sites, respectively. Table 2 shows the information of the earthquakes as the empirical Green's functions and its source parameters estimated roughly from the displacement source spectra computed as vectorial summation of two horizontal components of the recordings at hard sediment sites. Figure 2 shows the empirical Green's functions at 5 sites (OSA, WOS, WKY, MUR and SHI) for the Nankai earthquake. You can easily see that the waveforms represent the characteristics due to each site condition. Figure 3 shows the synthesized ground motions at 5 sites from the Nankai earthquake. When we concentrate the synthetics at OSA and WOS inside basin, we can point out the long duration affected by the long path as well as the effect due to 3-dimensional underground structure of the basin. Furthermore, as you can see in Figure 4 depicting pseudo velocity response spectra, the synthetics are predominant in long period

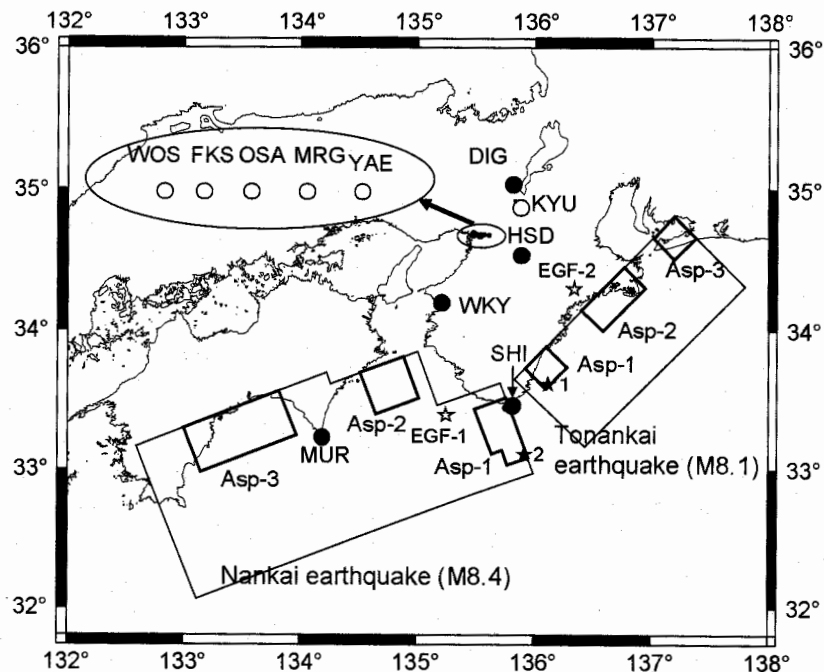


Figure 1 Map showing the source model composed of three asperities on the fault for the Nankai and the Tonankai earthquakes and site locations. EGF-1 and EGF-2 are the epicenters of earthquakes used as the empirical Green's functions for the Nankai and the Tonankai earthquakes, respectively.

Table 1 Source parameters for the Nankai and the Tonankai earthquakes

	Nankai earthquake			Tonankai earthquake		
Magnitude	8.4			8.1		
Fault Area (Km ²)	35800			14500		
Seismic Moment (N · m)	8.34E+21			2.15E+21		
Averaged Stress Drop (Mpa)	3			3		
Rupture Velocity (km/sec)	2.7			2.7		
	Asperity			Asperity		
	1	2	3	1	2	3
Area (km ²)	2672	1336	1336	1082	541	541
Averaged slip (cm)	1141	954	954	850	601	601
Seismic Moment (N · m)	1.46E+21	5.16E+20	5.16E+20	3.76E+20	1.33E+20	1.33E+20
Stress Drop (MPa)	20.1	20.1	20.1	20.1	20.1	20.1
	Back Ground			Back Ground		
Area (km ²)	30457			12336		
Averaged slip (cm)	470			299		
Seismic Moment (N · m)	5.85E+21			1.51E+21		
Stress Drop (MPa)	2.7			2.7		

Table 2 Source parameters for the earthquakes used as the empirical Green's functions

	EGF-1	EGF-2
Date	1991/10/20	2000/10/31
Latitude (deg)	33.395	34.2
Longitude (deg)	135.248	136.4
Depth (km)	37	40
Magnitude (JMA)	5.1	5.7
Seismic Moment (N · m)	3.00E+16	1.70E+17
Fault Area (km ²)	1.5	4
Stress Drop (MPa)	40	50

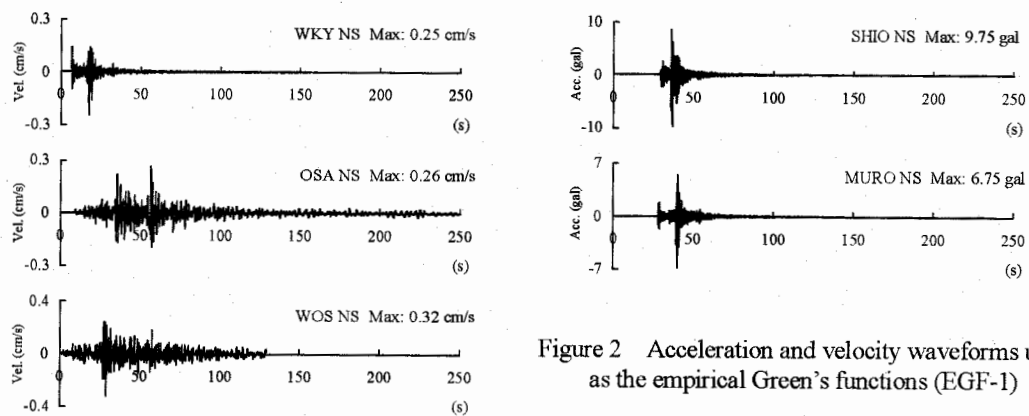


Figure 2 Acceleration and velocity waveforms used as the empirical Green's functions (EGF-1)

range (4 ~ 6 seconds). These amplitudes are over the safety regulation of the standard design spectra in Japan. This result suggests the strong effect to high-rise buildings and base-isolated buildings with long natural period. Figure 5 and Figure 6 show the synthesized ground motions and these pseudo velocity response spectra at 6 sites (FKS, MRG, YAE, DIG, HSD and KYU) for the Tonankai earthquake. The peak horizontal accelerations and velocities as well as the predominant periods of the synthetic motions inside basin are almost the same as those predicted for the Nankai earthquake, although the site locations for both earthquakes are slightly different each other. In above predictions, we used only one earthquake data as empirical Green's function for each subduction earthquake. To increase the accuracy of the predicted ground motions, we need to use the plural earthquake data reproducing the propagation path effects. Furthermore, we can emphasize the necessity of the more advanced prediction of long period ground motions in a mega-city Osaka located inside the Osaka basin.

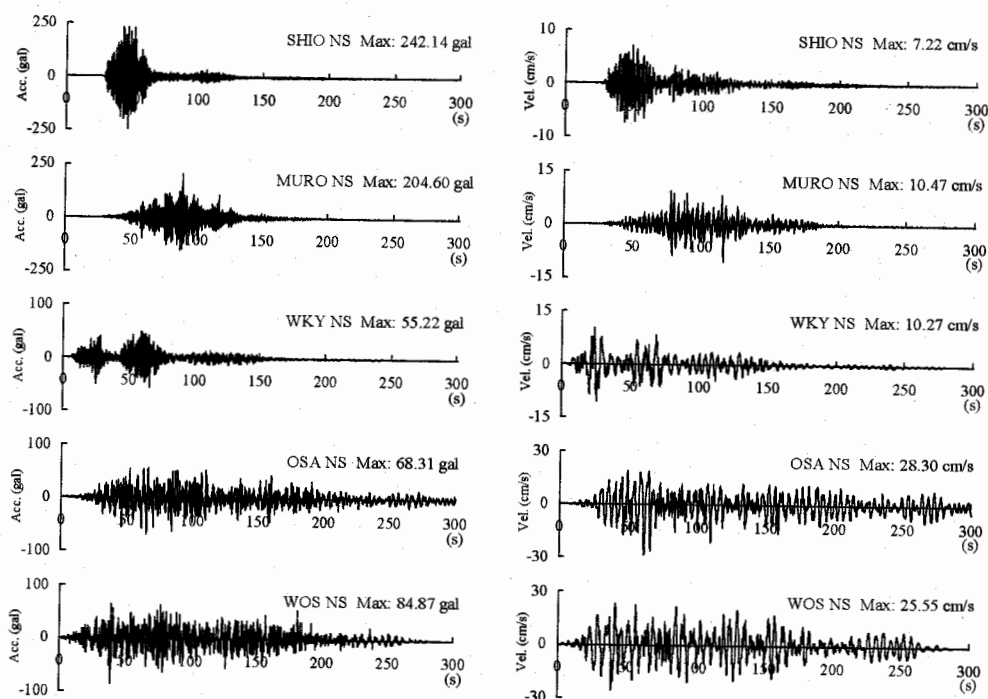


Figure 3 Predicted acceleration and velocity motions at 5 sites for the Nankai earthquake.

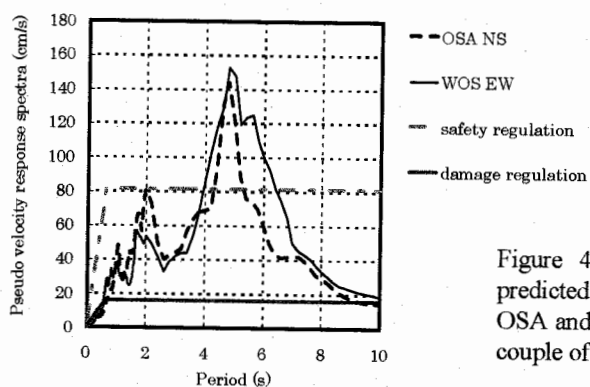


Figure 4 Pseudo velocity response spectra of the predicted ground motions for the Nankai earthquake at OSA and WOS sites located inside the Osaka basin. A couple of the design spectra are depicted in this figure.

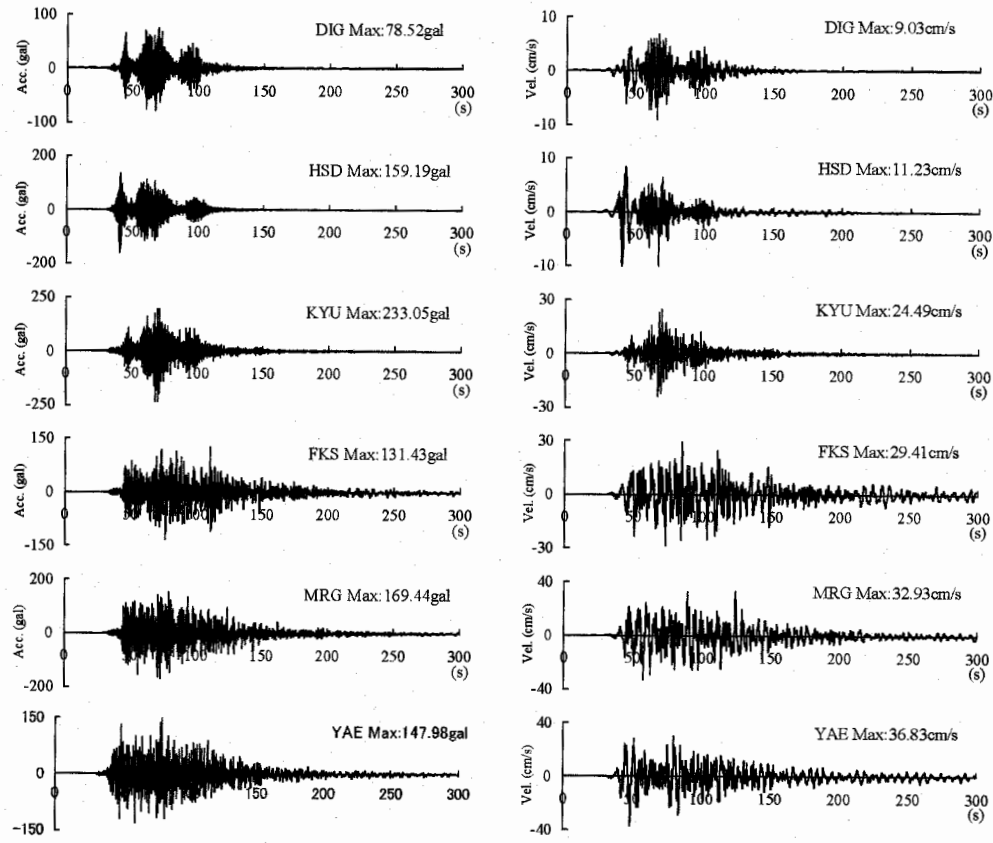


Figure 5 Predicted acceleration and velocity motions at 6 sites for the Tonankai earthquake.

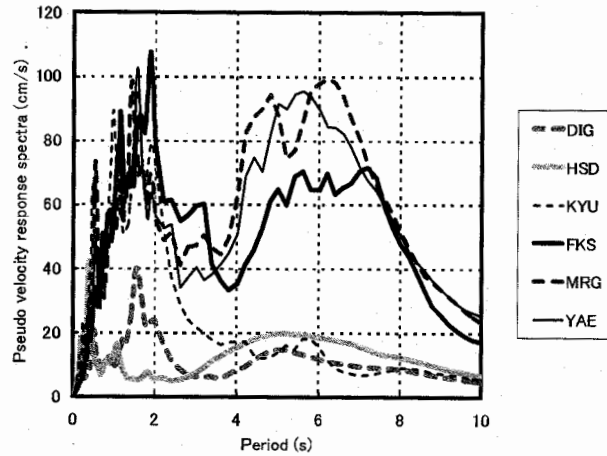


Figure 6 Pseudo velocity response spectra of the predicted ground motions for the Tonankai earthquake at 6 sites located inside (FKS,MRG,YAE) and outside (DIG,KYU,HSD) the Osaka basin.

In next section, we introduce a preliminary theoretical calculation for long period ground motions during the Nankai and the Tonankai earthquakes to investigate the effects of the 3-dimensional basin structure and to verify the seismic safety of high-rise and base-isolated buildings existing in Osaka area.

4. PRELIMINARY LONG PERIOD GROUND MOTION PREDICTION USING THE 3-D FINITE DIFFERENCE METHOD

We try to predict long period ground motions using the 3-D finite difference method (Graves,1996, Pitarka, 1998). The 3-dimensional underground structure models for the Osaka basin have been proposed by some researchers (e.g., Miyakoshi et al.,1999, Horikawa et al.,2002). Here, we constructed a rough three-dimensional velocity model with three sediment layers on bedrock referring to Horikawa et al.,2002. The depth of each sedimentary layer is depicted in Figure 7, and the parameters of the sediment layers and bedrock are shown in Table 3. We calculated velocity seismograms inside the basin for both expected subduction earthquakes. All the synthetics are bandpass filtered in the frequency range 0.05 to 0.4 Hz to exclude the numerical errors in higher frequencies. Figure 8 shows synthetic peak velocity distributions for the expected Nankai earthquake. You can see that the fault normal component (NS component) is predominant and peak velocity changes inside the basin depending on the complicated deep underground structure. Figure 9 and 10 show the synthetic velocity ground motions at three sites (WOS, FKS and YAE in Figure 1) for the expected Nankai and Tonankai earthquakes.

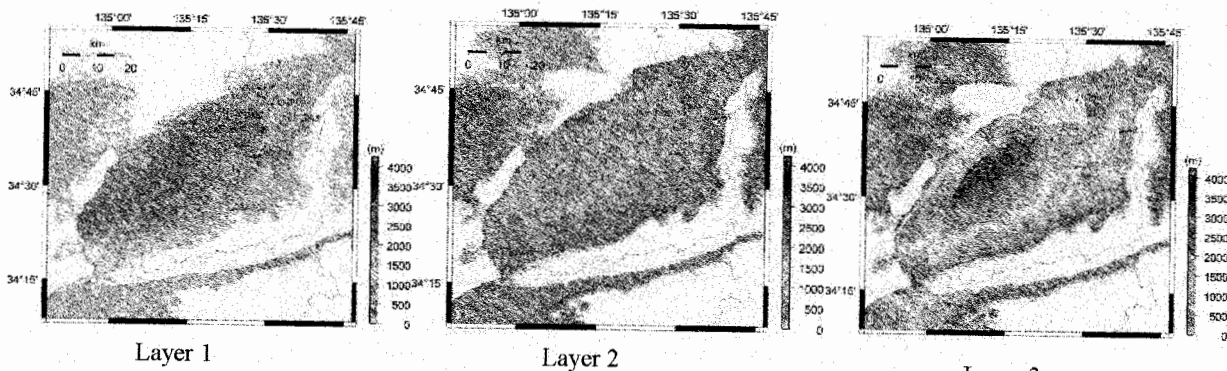


Figure 7 Depth of each sedimentary layer

Table 3 Parameters for each sedimentary layer (Layer 1,2,3) and base rocks (from Layer 4 to 9)

Layer Number	Layer 1	Layer 2	Layer 3	Layer 4	Layer 5	Layer 6	Layer 7	Layer 8	Layer 9
Vs (km/s)	0.4	0.55	1.0	3.2	3.87	4.33	2.5	3.9	4.5
Vp (km/s)	1.6	1.8	2.5	5.4	6.6	7.2	4.8	6.8	7.8
ρ (g/cm ³)	1.7	1.8	2.1	2.7	2.8	3.0	2.6	2.9	3.1
Qs (1Hz)	200	275	500	1600	1935	2000	2000	2000	2000

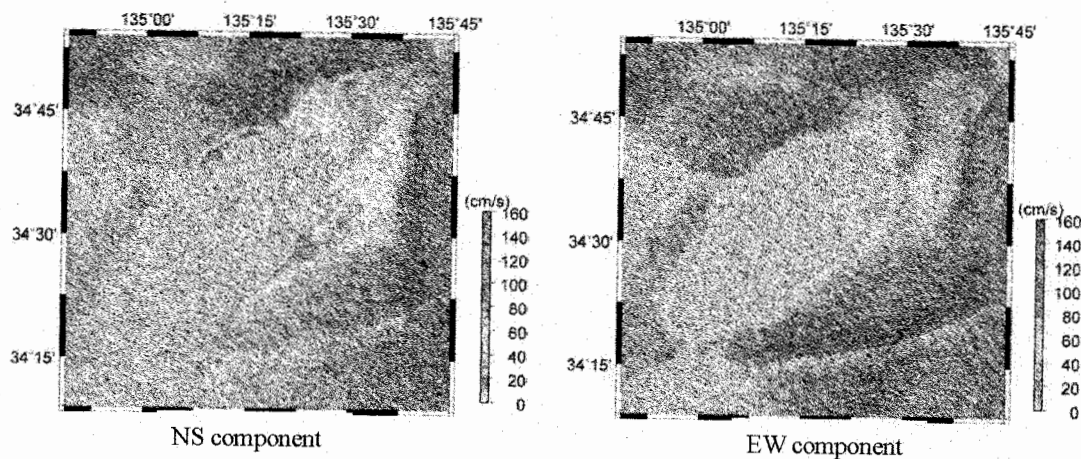


Figure 8 Peak velocity distributions inside the Osaka basin during the expected Nankai earthquake

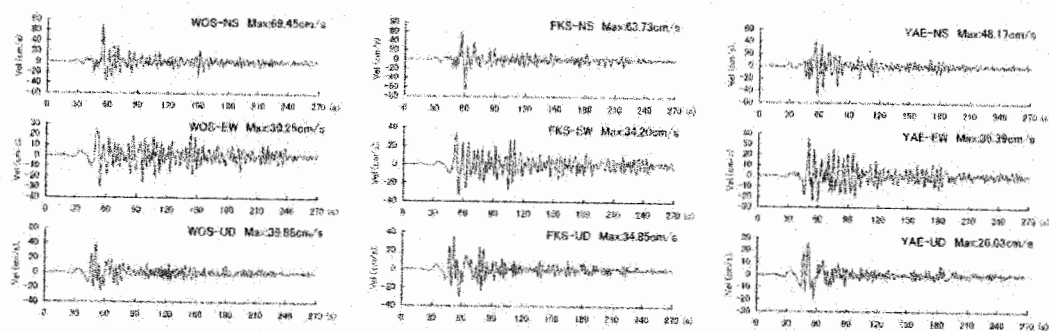


Figure 9 Synthetic velocity ground motions at three sites inside the Osaka basin for the expected Nankai earthquake (Filter: 0.05 to 0.4 Hz)

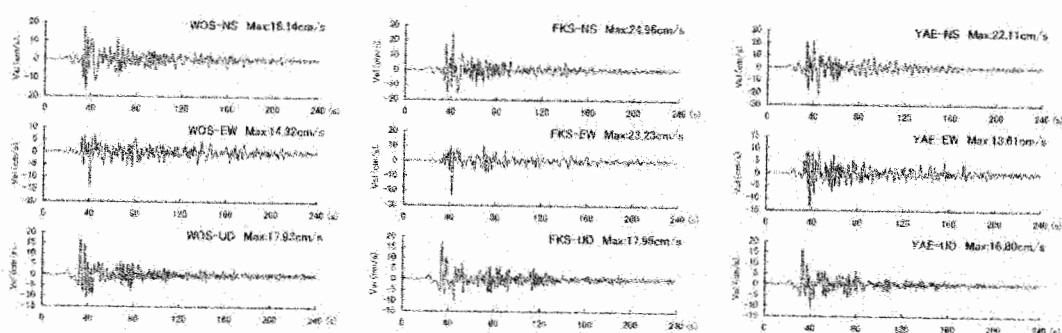


Figure 10 Synthetic velocity ground motions at three sites inside the Osaka basin for the expected Tonankai earthquake (Filter: 0.05 to 0.4 Hz)

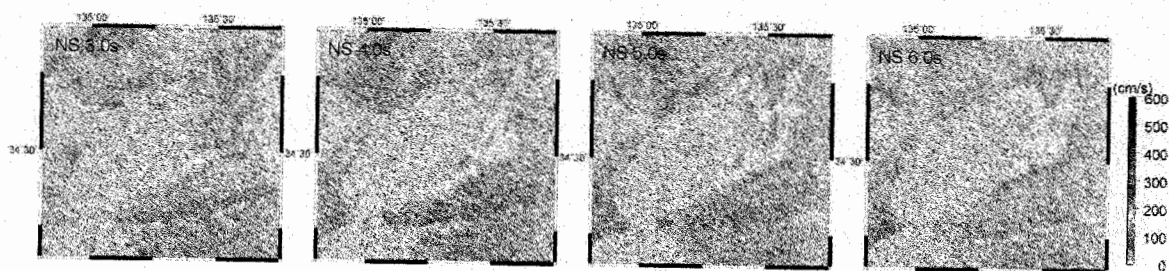


Figure 11 Distributions of pseudo velocity response spectral amplitudes in periods of 3.0, 4.0, 5.0 and 6.0 sec of the predicted ground motions (NS component) for the expected Nankai earthquake

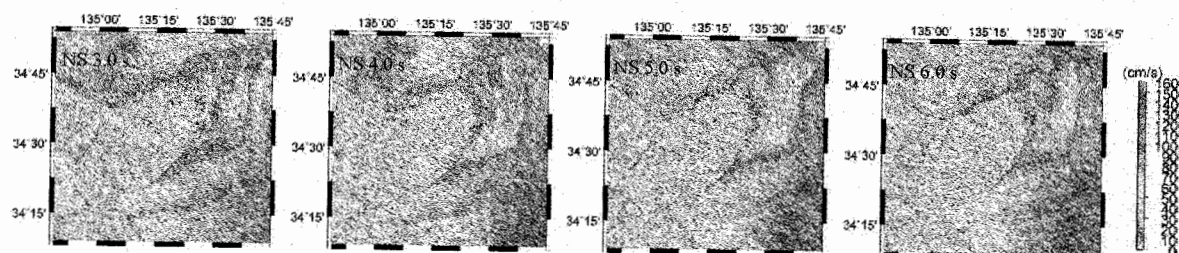


Figure 12 Distributions of pseudo velocity response spectral amplitudes in periods of 3.0, 4.0, 5.0 and 6.0 sec of the predicted ground motions (NS component) for the expected Tonankai earthquake

Figure 11 and 12 show the distributions of pseudo velocity response spectral amplitudes with

damping factor of 0.05 for the predicted long period ground motions during the expected Nankai and Tonankai earthquakes, respectively. You can see the variation of the amplitudes depending on the periods in both earthquakes. The predominant periods of the long period ground motions change depending on the complicated deep underground structure inside the Osaka basin. These results suggest us the importance of the advanced 3-D underground structure model to increase the accuracy of the predicted ground motions.

3. CONCLUSIONS

We attempted to predict strong ground motions from the expected huge subduction earthquakes (Nankai and Tonankai earthquakes) using the empirical Green's function method and 3-D finite difference method. In a mega-city Osaka located inside basin, the long period ground motions (4 ~ 6 seconds) with very long duration have been predicted for both huge earthquakes. The amplitude of the predicted response spectrum is over the design spectrum around period of 5 sec. These results suggest that we need to investigate the seismic safety of high-rise buildings and base-isolated buildings and so on. Furthermore, we need to increase the accuracies of the predicted strong ground motions, in special, long period ground motions inside the Osaka basin.

Acknowledgements:

This work is partially supported by the Special Project for Earthquake Disaster Mitigation in Urban Areas by the Ministry of Education, Culture, Sports, Science and Technology, Japan. We used strong motion records observed by the Committee of Earthquake Observation and Research in Kansai Area (CEORKA). The authors would like to thank these organizations.

References:

- Irikura, K., H. Miyake, T. Iwata, K. Kamae, H. Kawabe, and L. A. Dalgner (2003). Recipe for predicting strong ground motion from future large earthquake, *Annals of Disaster Prevention Research Institute, Kyoto University*, No.46B, pp.105-120, (in Japanese with English abstract).
- Irikura, K. (1986). Prediction of strong acceleration motion using empirical Green's function, *Proc. 7th Japan Earthquake Symp.*, pp.151-156.
- Graves, R. W. (1996). Simulating seismic wave propagation in 3D elastic media using staggered-grid finite differences, *Bull. Seism. Soc. Am.* 86, 1091-1106.
- Pitarka, A., K. Irikura, T. Iwata, and H. Sekiguchi (1998). Three-dimensional simulation of the near-fault ground motion for the 1995 Hyogo-ken Nanbu (Kobe), Japan, earthquake, *Bull. Seism. Soc. Am.*, 88, 428-440.
- Miyakoshi, K., T. Kagawa, B. ZHAO, T. Tokubayashi and S. Sawada (1999). Modeling of deep sedimentary structure of the Osaka Basin (3), *Proc. 25th JSCE Earthq. Eng. Symp.*, 185-188 (in Japanese with English abstract).
- Horikawa, H., K. Mizuno, K. Satake, H. Sekiguchi, Y. Kase, Y. Sugiyama, H. Yokota, M. Suehiro and A. Pitarka (2002). Three-dimensional subsurface structure model beneath the Osaka Plain, *Annual Report on Active Fault and Paleoequake Researches, Geological Survey of Japan/AIST*, No. 2 (in Japanese with English abstract).

MONITORING AND INTERPRETATION OF CREEP BEHAVIOR IN CHIHSHANG ACTIVE FAULT ZONE

M. H. Chen¹⁾, R. S. Wu²⁾, C. Y. Wang³⁾, C. P. Lin⁴⁾, C. J. Lee³⁾, H. T. Chou³⁾ and J. J. Dong⁵⁾

1) Research Associate, Center for Bridge Engineering Research, National Central University, Chungli, Taiwan 32054, ROC

2) Professor and Chair, Department of Civil Engineering, National Central University, Chungli, Taiwan 32054, ROC

3) Professor, Department of Civil Engineering, National Central University, Chungli, Taiwan 32054, ROC

4) Professor, Department of Civil Engineering, National Chiao-Tung University, Hsinchu, Taiwan 300, ROC

5) Professor, Institute of Applied Geology, National Central University, Chungli, Taiwan 32054, ROC

mhchen@cc.ncu.edu.tw; raywu@ncu.edu.tw; cywang@cc.ncu.edu.tw; cplin@mail.nctu.edu.tw; cjleeciv@cc.ncu.edu.tw;

htchou@cc.ncu.edu.tw; jjdong@app.geo.ncu.edu.tw;

Abstract: The objective of the research is to develop techniques for monitoring and interpretation of the active Chihshang fault. The newly high accuracy fiber optical tilting meters (FOTM) are embedded into the subsurface to measure the ground movements above and below the sliding plane. Time domain reflectometry (TDR) is another adopted instrument to sense the actual depth of fault plane. Infrasonic monitoring system (IMS) is set to build up the infrasonic signal database for fault activities. Small-scale centrifuge test was used to model the phenomena on faulting. After a long term monitoring period, the ability for prediction and evaluating the earthquake hazard from creep of active fault can be improved.

1. INTRODUCTION

Earthquake is one of the major geological hazards for engineering environment. The abilities for the prevention, assessment, and mitigation of earthquake hazards are very important in the field of engineering environment. Some relationships do exist between fault movement and earthquakes. Therefore, monitoring the movement of an active fault is very important. Relatively, the techniques for monitoring surface movement of faults have been better established. However, the techniques for subsurface monitoring still have room for further improvement. Furthermore, the techniques for properly interpreting the movement of active fault need to be developed.

The Longitudinal Valley in eastern Taiwan is the present-day suture zone between the Philippine Sea plate and the Eurasian plate (Fig. 1). Based on GPS studies (Yu et al., 1997), the oblique convergence of these two plates occurs in the NW-SE direction across the Taiwan mountain belt at a shortening rate of 85 mm/year. Results of the analysis of the geodetic trilateration network (Yu et al., 1990) and geological site investigation (Angelier et al., 1997) indicated that the Longitudinal Valley Fault (LVF) absorbed about one fourth (20-25 mm/year) of the total plate convergence (Fig. 2). Some rod-type creepmeters, each composed of two invar alloy rods attached to the firmly anchored piers on each end, straddling the surface rupture of active fault were set to monitor the movement of the active fault since 1998 (Fig. 3). Very detail surface rupture movements had been recorded by these rod-types creepmeters, but the recorded movements show the creep behavior of active fault is complex and irregular. The possible factors may include the thermal effect of the concrete basement, earth tidal effect, water table in the nearby rice field, rainfall, etc.

An important reason to undertake this study lies on the relationships between changes in creep velocity and variations in the earthquake hazard. Although these relationships are still under study, an anomalous low creep rate of the active fault would be a possible indication of the lock of the fault

movement. This research is to develop techniques for monitoring and interpretation of an active fault. Chihshang active fault, as an example to demonstrate the techniques developed provides a good opportunity to look inside the relationships between fault movement and earthquakes. Of major interest are the variations of slip rates with time, because they may have strong influence in terms of earthquake hazard. Extensively researches had been reported to study the creep of Chihshang active fault according to the measured surface movement and geological in-field investigation (Yu and Liu, 1989; Angelier et al., 2000; Lee et al., 2000; Lee et al., 2001). Some interesting phenomena do reveal the mystery of active fault and earthquakes (Lee et al., 2003). A comprehensive model is worthy to develop for interpreting the monitored data. Besides, to simulate the behavior of fault movement, subsurface information is essential. It is pity for the subsurface movement of active fault is not available in the Chihshang active fault zone. Development of proper sensors to monitor the subsurface displacement of active fault is necessary. It is anticipated that the results from the proposed study will largely enhance or improve the ability for interpreting the phenomenon of active fault movement.

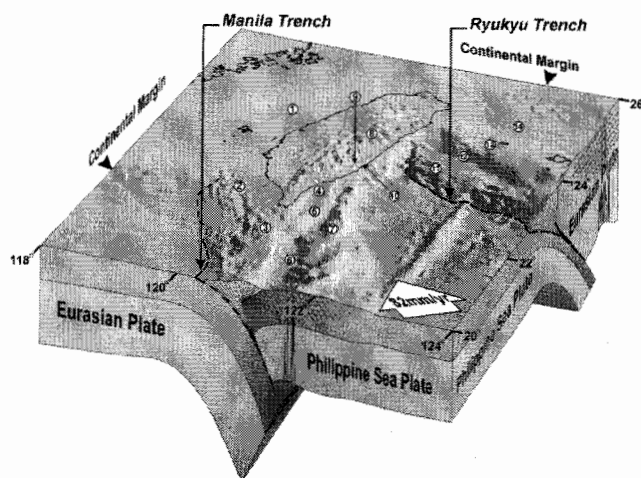


Figure 1. Schematic view of Philippine Sea Plate and Eurasian Plate

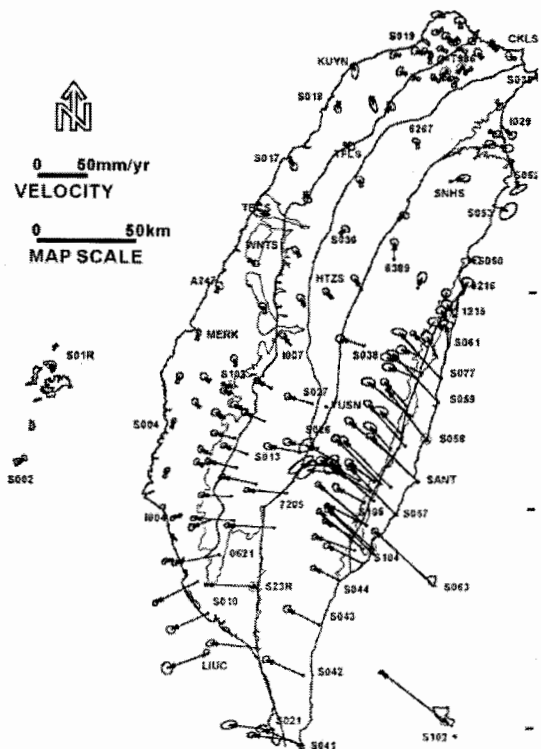
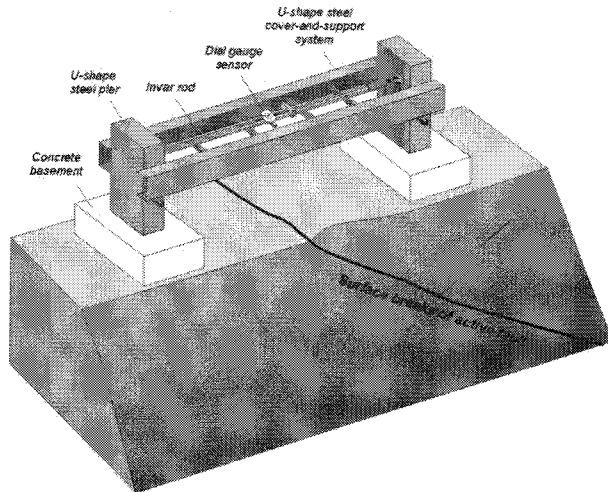
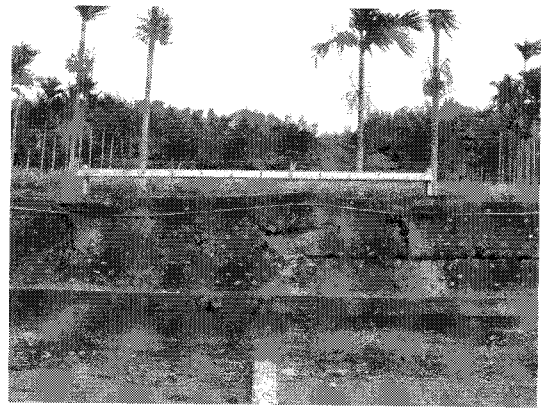


Figure 2. Map of the velocities of GPS stations in and around Taiwan. (Yu et al. 1997)



(a)



(b)

Figure 3. (a)schematic representation of the rod-type creepmeter across an active fault, (b)a front view photograph of the creepmeter on an embankment

2. THE MONITORING SYSTEM AND CENTRIFUGE MODEL

An integrated modeling system was used to assess the activity of fault using the data acquired from various sensors. A proper site which is located on the foot of Costal Range (Fig. 4) was selected to install suitable sensors that can provide essential data of fault movement. Subsurface deformation monitoring of active fault is conducted by placing different sensors into three boreholes (30m, 30m and 60m in depth). The sensors should continuously and stably acquire physical data under severe environmental conditions (temperature, moisture, corrosion and large deformation). Following sensing technologies are selected. The integrated monitoring system specifically addresses basic research and developments in the following key areas:



Figure 4. The monitoring site is located on the foot of the Costal Range

Time Domain Reflectometry (TDR):

TDR is based on transmitting an electromagnetic pulse through a coaxial cable and watching for reflections of this transmission due to impedance mismatches along the cable. The characteristic impedance of the cable is determined solely by its cross-sectional geometry if the insulating material between conductors remains unchanged. Reflections of the electromagnetic pulse are recorded if the coaxial cable is subjected to shear force and "crimped", as shown in Fig. 5. When a coaxial cable is

embedded in a rock mass, it can be used to monitor the shear deformation of the rock mass. Previous studies of the Chihshang fault utilized only the measurements from the creepmeter or GPS stations. These monitoring techniques measure the ground surface motion in an attempt to determine what is occurring at depth with the rock/soil. In most cases, however, motion will initiate at depth along a plane. This motion may, or may not, be seen quickly at surface as the geologic mass distributes such motion. In addition, rotational and surface components come into play, rendering it difficult at times to determine exactly what is occurring at depth. TDR will be used as a 'distributed' sensor to monitor localized shear deformations due to fault movements. TDR monitoring cable will be installed in two boreholes (30 m and 60 m, respectively) to delineate the slip surface of the fault. TDR is characterized by its distributed feature and capability to monitor large deformation. The relationship between the magnitude of the reflected pulse and the slip displacement will be further studied and quantified in the laboratory.

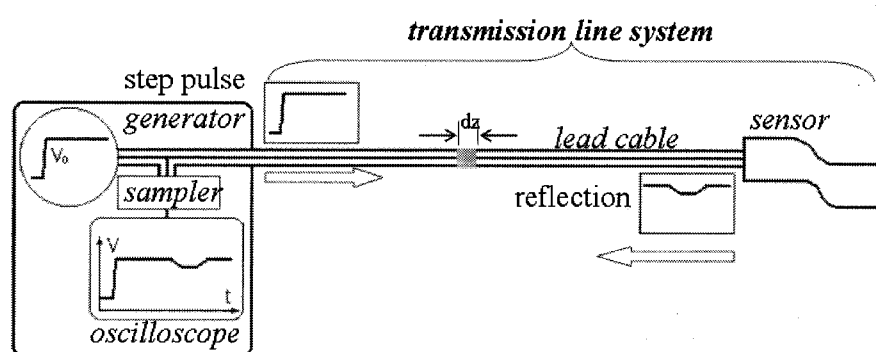


Figure 5. Principle of time domain reflectometry

Fiber Optical Tilting Meter (FOTM):

The advantage of fiber optical sensors include light weight, small size, immunity to electromagnetic interference (EMI), large bandwidth, environmental ruggedness, electrical and optical multiplexing. Thus, fiber optical sensors are suitable to be the ideal sensors for the applications of monitoring of structural performance. In recent years, the technology of fiber optical sensors has been applied in the field of civil infrastructures like buildings, bridges, transportation system and specialized industrialized sectors. An optical-fiber-type tilting meter for geotechnical engineering has been developed by an optical fiber corporation in Taiwan (Fig. 6). Through the temperature compensated strains measured by FBG sensors, the resolution of the tilting angle is $4/10,000$ degree. This measurement system can detect the deformation curve of a borehole due to the movement of ground. The research group has developed a data acquisition and deformation analysis algorithm for this type of sensing method. It is believed that this newly developed sensing technology is very accurate, reliable and durable for the monitoring of the performance of active fault.

Infrasonic Monitoring System (IMS):

Naturally occurring infrasound is produced by earthquakes, volcano eruptions, landslides and debris flows. Infrasound covers the inaudible acoustic spectrum below 20 Hz, which results from the compressibility of the air. Infrasound propagates to large distance in the atmosphere at the speed of sound for the low adsorption in the air and the high reflectivity of the ground. The infrasonic signals induced by fault movement are related to the magnitude of the failure zone. In order to establish the monitoring system for the active fault, this proposed study will explore the infrasonic signals for the active fault by experiments and field study. The monitoring system includes the sensitive infrasonic transducers, data logger and signal processors.

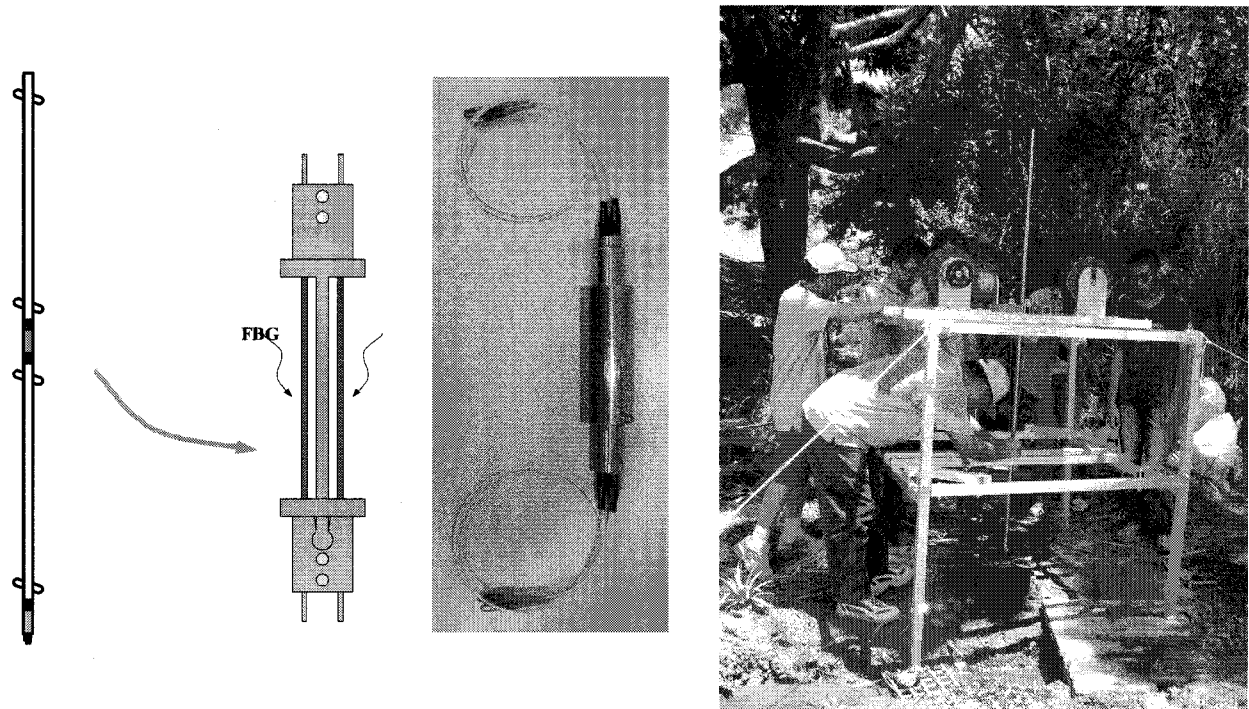


Figure 6. schematic representation of fiber optical tilting meter and field installation

Centrifuge Model:

To achieve a proper model simulation of geotectonics in eastern Taiwan, a series of centrifuge model tests simulating the collision of Eurasia and the Philippine Sea Plate will be conducted. Sand box experiments tested in an accelerated gravity field have been a useful means for simulating the geotectonic activity. In the study, a sand box (64.5×40×35cm) is manufacturing. One of the sidewalls is made of transparent acrylic to permit viewing of the subsurface events during the test. A sand layer in the sand box may be stretched or compressed with a pushing plate driven with a motor in the different directions.

3. RESULTS

According to the preliminary monitoring result, many subsurface movements at different depths caused by fault activities have been observed by TDR method (Fig. 7). Comparing to the FOTM measuring result, it is shown that two sliding planes were found at the depth of 10m and 23m (Fig. 8). Similar outputs were achieved by these two methods since these two boreholes are at a distance of 2m on surface. It is the first time to measure the subsurface ground movement.

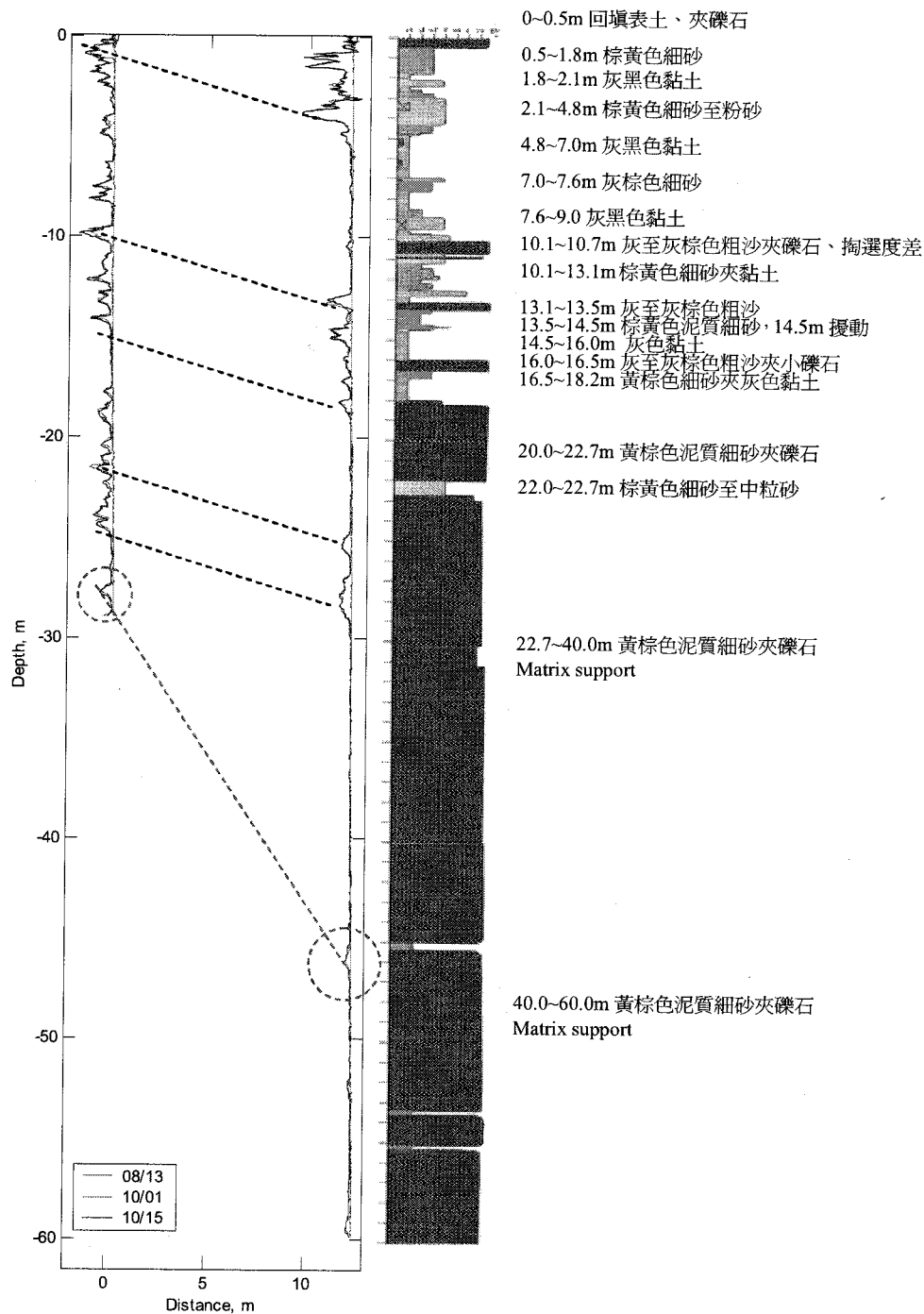


Figure 7. Measuring data of TDR comparing to geological profile

In the centrifuge model test, a sand box was tested under a field of 20g to simulate the plate convergence behaviors (Fig. 9). These tests were divided into three situations: the sea plate strength is larger, equal to, or less than the continental plate. These tests were modeled by changing the strength of clay and keep the conditions of sand. Thus, three failure mechanisms can be derived as following:

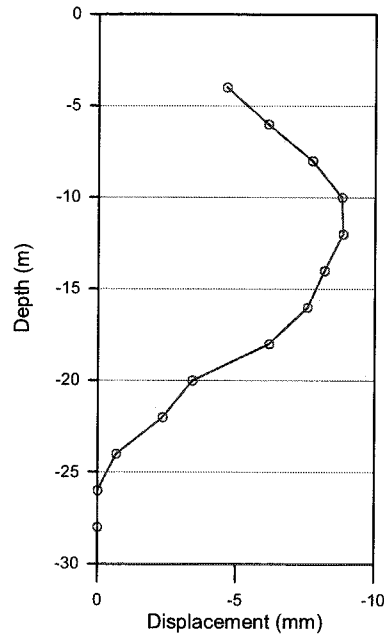


Figure 8. Measuring result of FOTM for 30m

$$\frac{1}{2}\gamma_c H^2 (K_p)_c \times 1 + 2c \times H \times 1 > \frac{1}{2}\gamma_s \times (K_p)_s \times H^2 \times 1 \quad (1)$$

$$\frac{1}{2}\gamma_c H^2 (K_p)_c \times 1 + 2c \times H \times 1 = \frac{1}{2}\gamma_s \times (K_p)_s \times H^2 \times 1 \quad (2)$$

$$\frac{1}{2}\gamma_c H^2 (K_p)_c \times 1 + 2c \times H \times 1 < \frac{1}{2}\gamma_s \times (K_p)_s \times H^2 \times 1 \quad (3)$$

where c is the undrained shear strength, γ_c is the unit weight of clay, γ_s is the unit weight of sand, H is the layer thickness, $(K_p)_c$ is the coefficient of passive earth pressure equals to 1, $(K_p)_s$ is the coefficient of passive earth pressure equals to 5.31. The results show that the larger shear strength of clay plate leads to sand plate contains most horizontal compressive deformation (Fig. 10), both the clay and sand plates heave when the shear strength are identical (Fig. 11), and the less shear strength of clay plate induce only the clay plate deforms (Fig. 12).

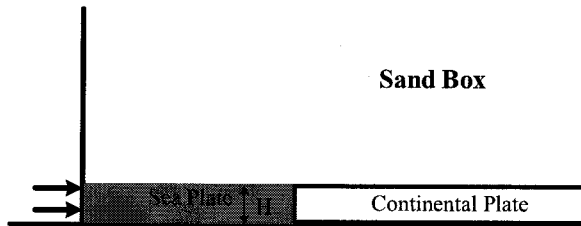


Figure 9. Layout of the centrifuge test model

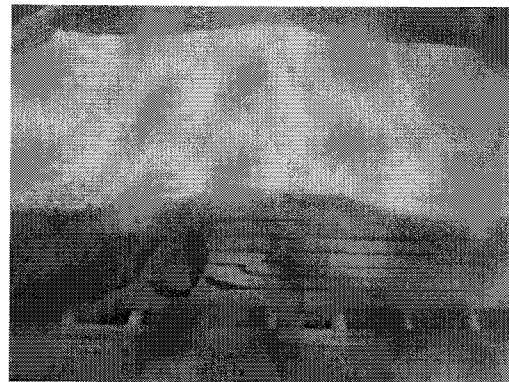


Figure 10. Larger shear strength of clay plate

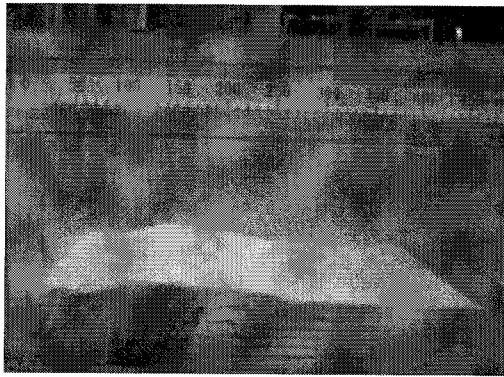


Figure 10. The shear strength of clay plate is equal to sand plate

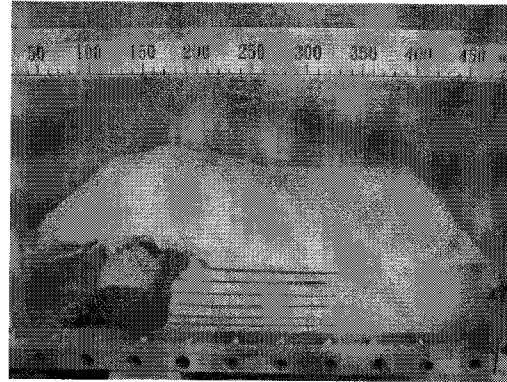


Figure 10. Less shear strength of clay plate

4. CONCLUSIONS

The subsurface movements of the active Chihshang fault were studied in this research. Newly sensing technologies including time domain reflectometry and fiber optical tilting meter were adopted to measure the sliding depth and displacements. In the centrifuge model test, the convergence of two tectonic Plates is simulated by means of pushing one end of the boundary toward another, and it reveals that the strength of Sea Plate and Continental Plate at Chihshang fault is likely to be comparable. The study results provide an opportunity to enhance or improve the ability for interpreting the phenomenon of active fault movement.

Acknowledgements:

The authors acknowledge support from University System of Taiwan formed by National Central University, National Chiao Tung University, National Tsing Hua University, and National Yang-Ming University.

References:

- Yu, S.B., and C.C. Liu (1989) Fault creep on the central segment of the Longitudinal Valley fault, eastern Taiwan: *Proc. Geol. Soc. China*, 32, 3, 209-231.
- Yu, S.B., D.D. Jackson, G.K. Yu and C.C. Liu (1990) Dislocation model for crustal deformation in the Longitudinal Valley area, eastern Taiwan: *Tectonophysics*, 183, 97-109.
- Yu, S.B., H.Y. Chen, and L.C. Kuo (1997) Velocity field of GPS stations in the Taiwan area : *Tectonophysics*, 274, 41-59.
- Angelier, J., Chu, H.T., and Lee, J.C., (1997) Shear concentration in a collision zone: kinematics of the active Chihshang Fault, Longitudinal Valley, eastern Taiwan: *Tectonophysics*, 274, 117-144.
- Angelier, J., Chu, H.T., Lee, J.C., and Hu, J.C. (2000) Active faulting and earthquake risk: the Chihshang Fault case, Taiwan: *Jour. Geodynamics*, 29, 151-185.
- Lee, J.C., Jeng, F.S., Chu, H.T., Angelier, J. and Hu, J.C. (2000) A rod-type creepmeter for measurement of displacement in active fault zone: *Earth, Planets, and Space*, 52, 5, 321-328.
- Lee, J.C., Angelier, J., Chu, H.T., Hu, J.C., and Jeng, F.S. (2001) Continuous monitoring of an active fault in a plate suture zone: a creepmeter study of the Chihshang active fault, eastern Taiwan, *Tectonophysics*, 333, 219-240.
- Lee, J.C., Angelier, J., Chu, H.T., Hu, J.C., Jeng, F.S. and Rau, R.J. (2003) Active Fault Creep Variations at Chihshang, Taiwan, Revealed by Creepmeter Monitoring, 1998-2001. *Journal of Geophysical Research*, 108, B11, 2528, doi:10.10129/2003JB002394.
- Lin, C.-P. and Tang, S.-H. (2005), "Development and calibration of a TDR extensometer for geotechnical monitoring," *Geotechnical Testing Journal*, Vol. 28, No. 5, Paper ID: GTJ12188.

HOW TO EVALUATE SPATIAL DISTRIBUTION OF EARTHQUAKE GROUND MOTION IN THE NORTHERN JAPAN

N. Takai¹⁾, T. Maeda²⁾ and T. Sasatani³⁾

1) Associate Professor, Faculty of Engineering, Hokkaido University, Japan

2) Researcher, Institute of Seismology and Volcanology, Hokkaido University, Japan

3) Associate Professor, Faculty of Science, Hokkaido University, Japan

tki@eng.hokudai.ac.jp, tmaeda@ares.sci.hokudai.ac.jp, sasatani@ares.sci.hokudai.ac.jp

Abstract: The attenuation relation of earthquake strong ground motion, which is predictable in wide area, is important. In this study, we show how to evaluate spatial distribution of ground motion in the northern Japan. It is tried that the attenuation formula based on positional relation of volcanic front (VF), hypocenter and observation site is made. The attenuation formula which respects the effect of irregular deep underground structure will be obtained, by requiring the regression formula by the division of hypocentral distance in the volcanic front, in the northern Japan. Further, spatial distribution features of strong ground motion during 2003 Tokachi-oki earthquake are discussed using this method.

1. INTRODUCTION

Many experimental attenuation formulas for the estimation of ground motions severity have been developed by means of regression analysis [1, 2]. These formulas are useful to predict strong ground motion and to compare the observed data. These formulas are based on the homogenous structure of underground, hence the predicted value are distributed as concentric circle. However, the region of anomalous seismic intensity caused by irregular deep underground structure is found to exist in northern Japan, accordingly it is difficult to apply these formulas in the region widely. In this region, we must consider the complex Q-value structure within subduction zones. On the other hand, it has been indicated that the distribution of earthquake motions greatly differs in the region divided in the volcanic front (V.F.: shown in Figure 1) in the effect of the Q-value structure. Especially, large earthquakes occurred around Pacific plate boundary in Hokkaido frequently, and they became a cause of the damage in the wide area. Figure 2 shows the relation between epicentral distance and JMA instrumental intensity during earthquake that occurred in Hokkaido. In two regions classified by the volcanic front, the tendency of the attenuation by the distance is greatly different, as it is clear from the figure. The objective of this study is to develop an attenuation formula based on the positional relation of V.F., hypocenters and the observation points.

2. CONCEPT

The volcanic front located in northern Japan is shown in Figure 1. The distance from the epicenter to V.F. ($\Delta 1$) and the distance from V.F. to the observation points ($\Delta 2$) is derived by dividing the hypocentral distances by V.F.. Next, the hypocentral distance is divided at the ratio of $\Delta 2$ and $\Delta 1$, and

$R1 (=R*\Delta1/\Delta)$ and $R2 (=R*\Delta2/\Delta)$ for the regression analysis are required. Figure 3 shows the relation between epicenter, hypocenter, observation site, $R1$, $R2$, $\Delta1$, $\Delta2$ and volcanic front. JMA instrumental seismic intensity data from K-NET[3] is used for the analysis. A regression analysis is performed for each earthquake, using seismic intensity as the response variable and the distances as the explanatory variables. The values derived from the analysis and the magnitudes are used for performing further regression analysis.

3. DATA

Kyoshin Net (K-NET) is the system that provides strong-motion data on the internet web. The data are obtained at 1,000 observatories deployed all over Japan (Figure 1). The average station-to-station distance is about 25km[3]. In this study, the analysis is carried out using the data of K-NET, and the target area is fixed in Tohoku and Hokkaido region (the northern part of Japan). Under the condition that the magnitude is over 5.0 and the strong motion records are obtained at over 50 observatories, we select appropriate earthquakes as data used in this study from the earthquakes that occurred in and around the target area. Figure 1 shows epicenters of selected earthquakes. They consist of 3 type of earthquake, as shallow crustal, intra-plate and inter-plate earthquakes. Through the examination of all data, the intra-plate type was clear that the accuracy was more improved [4]. Therefore, we tried to make attenuation formula for intra-plate earthquake. Earthquakes used to construct formula are reported in Table 1.

4. CONSTRUCTION ATTENUATION FORMULA FOR INTENSITY

4.1 Regression Analysis

Possibility in which prediction accuracy is greatly improved by this technique became clear for the intra-plate earthquake [4], therefore the prediction expression in the intra-plate earthquake is constructed. 2 kinds of intensity attenuation models for the orthodox and this method were prepared. These are given by

$$I = C + aM_{JMA} + hD - 2\log R - bR \quad (1)$$

$$I = C + aM_{JMA} + hD - 2\log R - b_1R1 - b_2R2 \quad (2)$$

where I is seismic intensity, aM_{JMA} is seismic source term, hD is focal depth term, $\log R$ represents geometric spreading, bR represents anelastic attenuation and C is regression coefficient.

About Equation (2), anelastic attenuation term is divided, since difference of attenuation characteristics. The coefficient of $\log R$ is 1.0 for the equation of peak ground acceleration, because it is mainly affected by the body wave. The coefficients of conversion expression which converts from peak ground acceleration to seismic intensity are almost due to be 2.0 [5], thus the coefficient of $\log R$ in these equations are constrained in 2.0. The two stages regression analysis [1,2,5] is used to obtain the coefficients in equations (1) and (2). At the first step b is determined, and then C , h and a are determined.

Determined equations by regression analysis are (3) and (4).

$$I = -0.46 + 1.41M_{JMA} + 0.0018D - 2\log R - 0.0069R \quad (3)$$

$$I = -0.64 + 1.35M_{JMA} + 0.0038D - 2\log R - 0.0024R1 - 0.011R2 \quad (4)$$

4.2 Discussions on the Result of Regressions : Application to Prediction

The attenuation expressions of instrumental intensity were obtained by the regression analysis of the above. The $R2$ coefficient is larger than the $R1$ coefficient, and it can be well understood that attenuation of earthquake motion differs in both sides of volcanic front. That is to say, fore-arc side's Qs values are larger than back-arc side's. This result is accordant with features of anomalous seismic intensity.

The equation (2) by this method becomes not prediction curve for the 2 variables but curved surface, and, for example, M8 case is shown in Figure 4. The comparison with the observation record is difficult, when it is given in the prediction curved surface. Therefore, ratio of $R1$ and $R2$ length is introduced. By utilizing this ratio, gradients of curves of attenuation are decided, and curves in two dimensions for hypocentral distance can be expressed. Curves of attenuation for the 2003 Miyagi-oki earthquake (No. 7 in Table 1) are shown in Figure 5. Like this, the prediction expression with multiple gradients for one earthquake is able to be constructed. These ratios are completely different from the correction factor of the site amplification conditions. They are defined only from the relationships of hypocenter, V. F. and observation point, thus they absolutely change by the earthquake location. The predicted intensity by this study is compared with observed seismic intensity (Figure 5). The 2003 Miyagi-oki earthquake ($M_{JMA}=7.1$) was intra-plate earthquake, and much damage was generated in Tohoku Region. Seismic intensity distribution maps are shown in Figure 8. In Figure 8, (a) is predicted with equation (3), (b) is calculated with equation (4) and (c) is observed distribution. The map (a) which is predicted with orthodox method has a concentric circular isoseismal, thus it is different from observed map (c). On the other hand, the map (b) which is predicted with this method is similar to observed map (c).

5. TRIAL APPLICATION TO THE 2003 TOKACHI-OKI EARTHQUAKE

It was mentioned earlier, this concept is effective for intra-plate earthquakes. It seems to be that seismic intensity filter characteristics and high frequency excitation of the intra-plate earthquakes are concern to cause of this effectiveness. However, how will it change if we think according to period range of strong ground motion?

The 2003 Tokachi-oki earthquake, a large ($M_{JMA}=8.0$) inter-plate earthquake, occurred on 26 September, 2003. This is the first earthquake with a magnitude of 8 after the K-NET was installed. We calculate velocity response spectra (damping factor $h=0.05$) based on about 300(K-NET) data in the northern Japan and make the spatial distribution maps and attenuation relationships for 0.1, 1.0 and 10.0sec velocity responses (Figure 8, 9).

The spatial distribution maps (Figure 8) show different features depending on the period. The 0.1sec map (Figure 8(a)) shows strong attenuation of the response at back-arc side of the volcanic front; this can be explained by the S-wave attenuation structure beneath the northern Japan. This tendency is able to be predicted by this concept. The attenuation relationships also show different features depending on the period. In Figure 9, color code means ratio of $R1/R$ for each observation site. The 0.1 sec relationship (Figure 9(a)) shows different attenuation between the fore-arc and back-arc side of the volcanic front at distances less than about 200 km. For the fore-arc side data, the decay rate changes at about 300 km; the decay rate decreases at distances greater than about 300 km. This is explained by very large Qs values of the lower slab.

Long period attenuation maps (Figure 8(b), (c)) and relationships (Figure 9(b)(c)) are different from short period. This feature is explained by the following factors. The attenuation relationship less than 300 km is due to direct S-waves; however the relationship greater than 300 km is due to surface waves. The large scatter around 300 km is due to radiation pattern of Rayleigh waves. Therefore amplification factor of the site on period range will have to be also grasped in future.

6. CONCLUSION

An attenuation formula that reflects the effect of a large-scale attenuation structure was obtained through deriving a regression formula dividing hypocentral distance by V.F.. It became clear that the longer the distance from the hypocenter to V.F., the smaller the attenuation for seismic intensity at an observation point. The intensity distribution maps predicted by this formula is similar to observed anomalous intensity distribution. Moreover with some revision with ground condition, this formula would become a further accurate prediction method. Through case study on the 2003 Tokachi-oki earthquake, it was shown that we could apply this concept to other earthquake type on period range. Hereafter, we will develop the prediction method of spatial distribution of strong ground motion, for a large earthquake such as the 2003 Tokachi-oki earthquake.

Acknowledgements:

We used K-NET strong ground motion data.

References:

- 1 Boore D.M, and Joyner W.B, "The empirical prediction of ground motion." Bull. Seism. Soc. Am 1982; 72:S43-S60.
- 2 Fukushima Y, and Tanaka T. "A new attenuation relation for peak horizontal acceleration of strong earthquake ground motion in Japan", Bull. Seism. Soc. Am 1991; 80: 757-783.
- 3 K-NET http://www.k-net.bosai.go.jp/k-net/index_en.shtml
- 4 Takai N., and Shimizu G. and Okada S. "New attenuation formula of earthquake ground motions passing through the volcanic front" Proc. of the 13th World Conference on Earthquake Engineering 2004; No.731.
- 5 Japan Meteorological Agency "Note on the JMA seismic intensity." Gyosei, 1996:(in Japanese).
- 6 Shabestari, K.T, Yamazaki F. "Attenuation Relationship of JMA Seismic Intensity Using Recent JMA Records." Proc. of the 10th Japan Earthquake Engineering Symposium 1998; 10: 529-534.

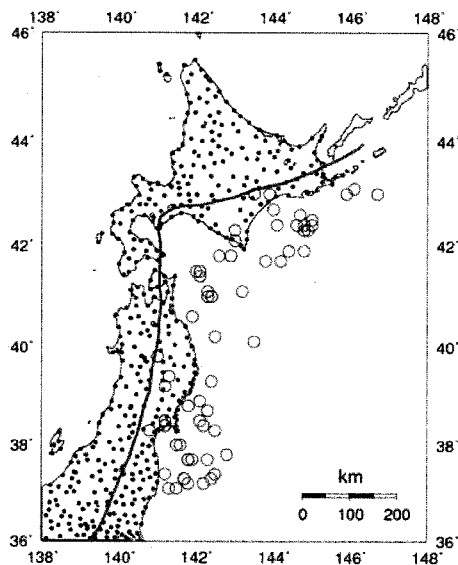


Figure 1. Target area and epicenters of selected earthquakes. A red solid line shows the volcanic front, solid dots are K-NET site.

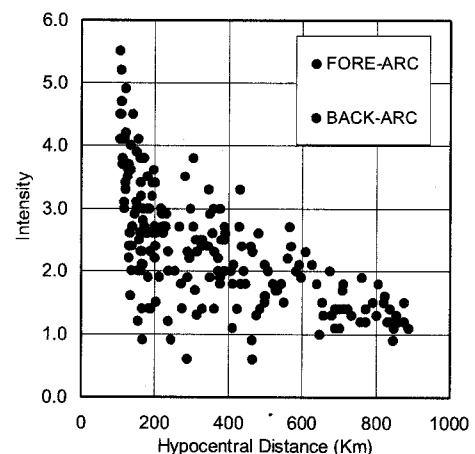


Figure 2. Relation between hypocentral distance and JMA intensity at 1999 Kushiro region earthquake (No.1 in Table 1).

Table 1. Table of earthquakes used in this study

No.	DATE	TIME(JST)	LONGT(E)	LAT(N)	Depth(km)	(M _{JMA})	Region
1	1999/05/13	02:59	143.9	43.0	106	6.3	KUSHIRO_REGION
2	2000/01/28	23:21	146.7	43.0	59	7.0	OFF_NEMURO_PENINSULA
3	2000/12/22	19:13	147.4	44.5	141	6.5	ETOROHU ISLAND
4	2001/04/27	02:49	145.9	43.0	80	5.9	OFF_NEMURO_PENINSULA
5	2001/12/02	22:02	141.3	39.4	122	6.4	SOUTHERN_IWATE_PREF
6	2002/12/01	18:57	144.0	42.7	103	5.5	SE_OFF_TOKACHI
7	2003/05/26	18:24	141.8	38.8	72	7.1	KINKAZAN_REGION

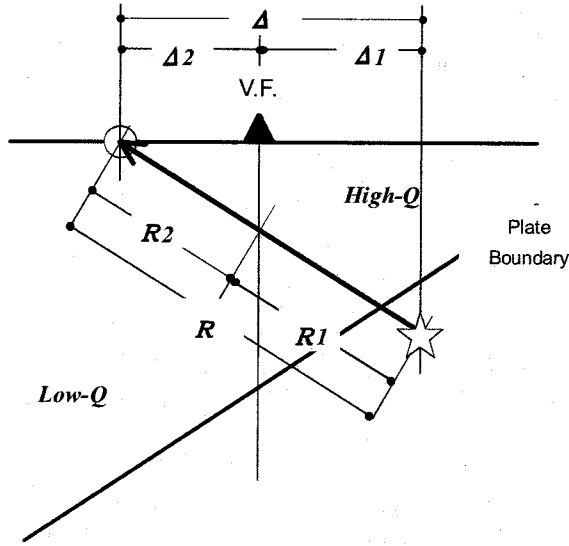


Figure 3. Relation between hypocentral distance, epicentral distance and $R1, R2$.

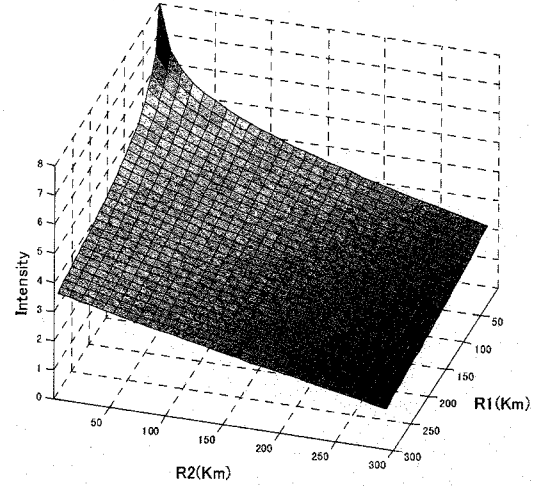


Figure 4. Attenuation curved surface for M8 earthquake.

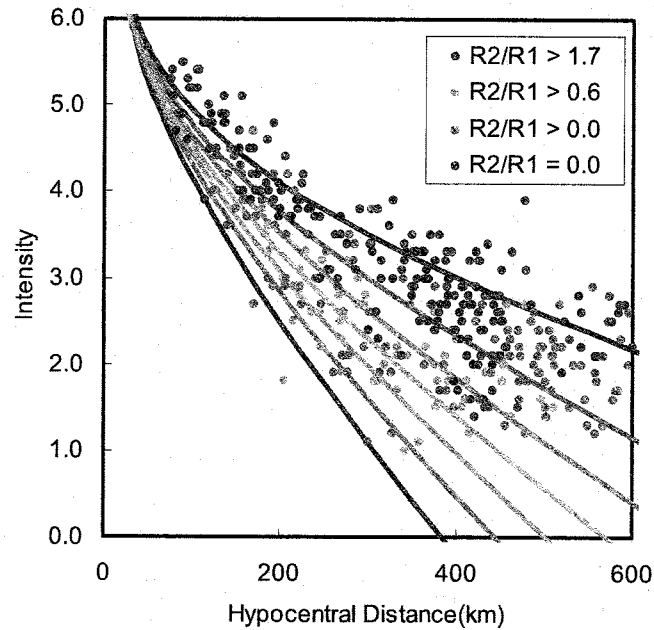


Figure 5. Intensity attenuation by hypocentral distance of the 2003 Miyagi-oki earthquake (No.7 in Table 1). Solid lines are calculated with equation (3) for each ratio.

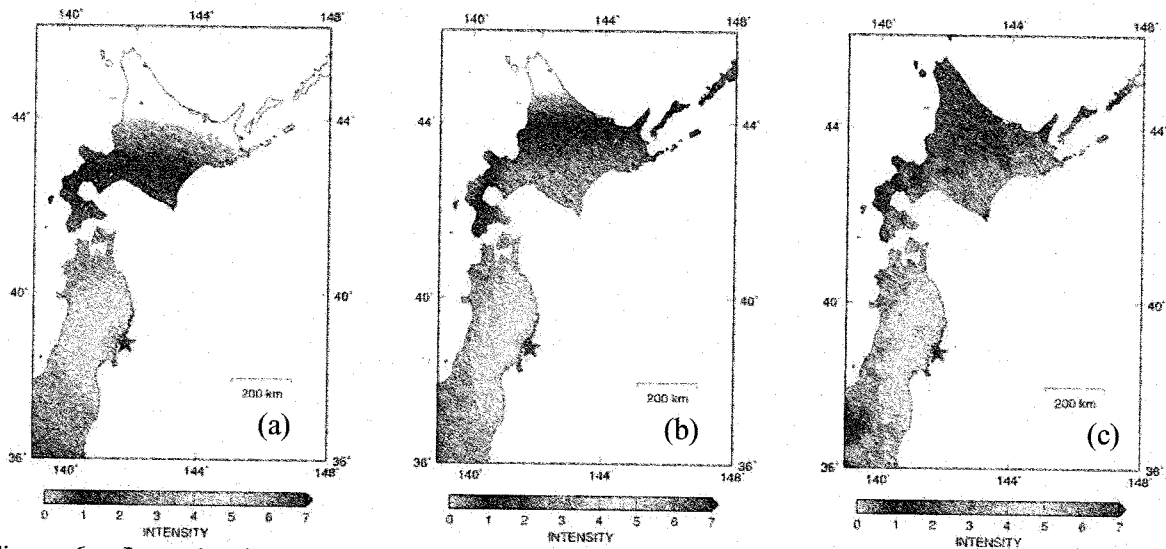


Figure 6. Intensity distribution maps of (a) predicted intensity with equation (4), (b) predicted with equation (3) by this method, (c) observed, during the 2003 Miyagi-oki Earthquake (Eq. No.7).

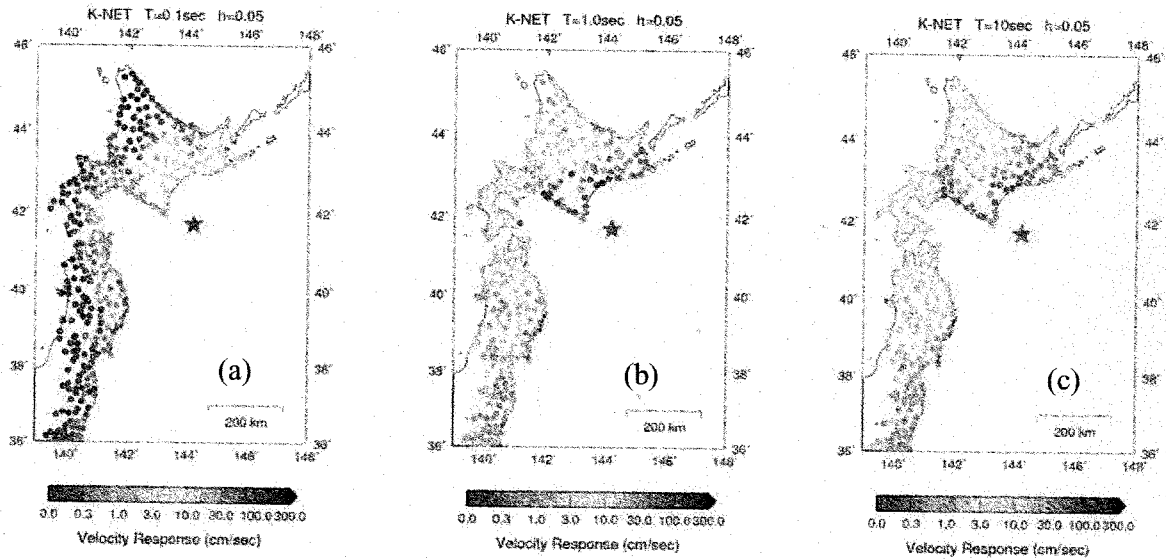


Figure 7. Spatial distribution maps of velocity response during the 2003 Tokachi-oki Eq. for a dumping factor of 5% and natural periods of (a) 0.1, (b) 1.0 and (c) 10sec.

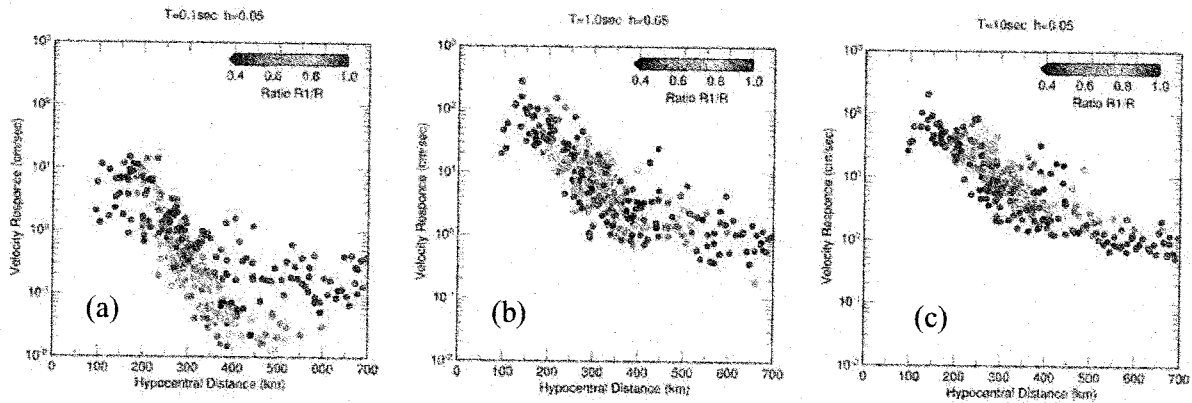


Figure 8. Attenuation relationships of velocity response during the 2003 Tokachi-oki Eq. for a dumping factor of 5% and natural periods of (a) 0.1, (b) 1.0 and (c) 10sec.

A STUDY ON WAVEFORM INVERSION FOR CHARACTERIZED SOURCE MODELS USING GENETIC ALGORITHMS

K. Motoki¹⁾, H. Yamanaka²⁾, and K. Seo³⁾

1) Research Associate, Dept. of Built Environment, Tokyo Institute of Technology, Japan

2) Associate Professor, Dept. of Environmental Science and Technology, Tokyo Institute of Technology, Japan

3) Professor, Dept. of Built Environment, Tokyo Institute of Technology, Japan

kmoto@enveng.titech.ac.jp, yamanaka@depe.titech.ac.jp, seo@enveng.titech.ac.jp.

Abstract: Strong motions near source regions highly depend on the heterogeneity of the source, and an appropriate procedure to distribute asperities is necessary. A number of source models have been already evaluated in recent a couple of decades since Hartzell and Heaton (1983). But their source models are too complicated to directly apply a model for an estimation of future earthquakes. The information compiled by Somerville et. al. (1999) are referred to make a source model as inner source parameters. But the criteria are not based on physical manner and not always to produce an optimal solution. The purpose of this study is to evaluate directly a characterized source model, which is composed of asperities and background region and useful for a prediction of earthquake motions, with observed waveforms using genetic algorithms.

This method produces simple models and the number of unknown parameters of this method is less than the conventional method, but this model cannot solve as a linear problem. Each unknown parameter is transformed to binary and allocated to a variable gene. Before applying observed data, we conducted a numerical test. This method is useful only less for 3 asperities, because the calculation for more than 4 asperities costs enormous time. We applied in the case of the 1995 Kobe earthquake. The solved source model successfully reproduces the observed ground motions, and it is similar to the models evaluated in previous researches.

1. INTRODUCTION

The heterogeneity of source process is very effective for an estimation of strong motions near the source regions or large earthquakes. In order to obtain the heterogeneity, a number of studies have been made on detailed source processes for the past few decades since Hartzell and Heaton(1983) and Olson and Apsel(1982) developed waveform inversion techniques. The resultant source processes are regarded as one of the most appropriate models. For Kobe earthquake, Several model were published (e.g. Sekiguchi(2000), Yoshida *et. al.* (1996)) and Takemura(1998) discussed the differences and the commons among them. We can say reasonable that these models approximate to each other by and large, and lots of differences can be found in detail due to the differences of observed data sets, the models of subsurface structure and modelizations to optimise. The differences results from the procedures; the source time functions for every subfault divided whole of the fault model equally are calculated. According to Yoshida (1995), such kind of inversion come to ill-condition model and reduce stability caused from a large number of unknown parameters against the number of observation data. To suppress instability, constraints need to be added. On most of studies, smoothing operation were imposed as the constraint for time and spatial domain. Therefore, the consequent resolution come down from given a grid size against time and space.

The source models calculated for past earthquakes are used as basic materials to estimate for future earthquakes. The characterization suggested by Somerville et. al. (1999) were performed to simplify the already calculated source models, because of difficulty to convert them as it is. The criteria are not based on physically aspects and cannot always produce an optimal solution. In this study, we propose a waveform inversion technique to evaluate characterized source model directly to make an basic material for future earthquakes using genetic algorithms. We tried our developing method for Kobe earthquake, because the earthquake is the most devastating for recent 50 years, and it is to be desirable to analyze the causes as simple as possible.

2. METHOD

The source behavior in the inversion problem is parameterized to the moment rate tensor as a function of time and space. In general, the fault surface is divided into subfaults, and the source time functions for each subfault along 2 slip direction are allocated as unknown parameter. In addition to space, the heterogeneity of time domain can be represented by history with multi time window. For example, associated with M7 earthquakes, the number of subfault may reach to 100, and if the number of time window is set to 5, the number of parameters to solve amounts to 1000. A lot of parameter can be solved using least square method with some constraints which are smoothing or non-negative operator as mentioned above. However, we have some difficulties in practical applications of linearized least square inversions. They are mainly on numerical instability in calculating inverse matrix and on preparation of an appropriate initial model. In order to solve these difficulties, we adopt genetic algorithms (GA) as a heuristic method. The algorithms were developed to study artificial intelligence by Holland (1975). The differences of this method from conventional method are shown in TABLE 1. Yamanaka and Ishida (1996) successfully calculated the model underground velocity structure using GAs with phase velocity based on microtremor array exploration. The misfit function, $E(m)$ for the model, m , is calculated from

$$E(m) = \frac{1}{N} \sum \frac{|F_c - F_o|^2}{\sigma^2} \quad \sigma = \begin{cases} \sigma_c & (\sigma_c \leq \sigma_o) \\ \sigma_o & (\sigma_o < \sigma_c) \end{cases}$$

where F_c and f_o are a synthetic velocity and an observed velocity, and σ and N are standard deviation and the number of observed data, respectively. the schematic image of the modelization in this study is shown in Fig 1. Before an inversion with GA, the Greens function need to be calculated to decrease calculation costs. We calculated synthetics with an interval of 1km, that is, dx and dy is set to 1km. The asperity model moving already set position. The unknown parameters of this model are seismic moments, locations, sizes, shapes, rake angles, locations of the trigger points, rise times, rupture velocities inside of asperities and rupture velocities outside of asperities. These unknown parameters is allocated to each asperities, and these parameters are uniform in each asperity. The asperities start to rupture at Li/Vr out, and the ruptures propagate with the Vr in. The

TABLE 1 Comparison between conventional method and this study

	conventional method	this study
# of parameters	about 1000 or more	20 or 30
algorithm	linear square method	genetic algorithm
constraint	smoothing and/or non-negative	finite search area
solution	detail	simple

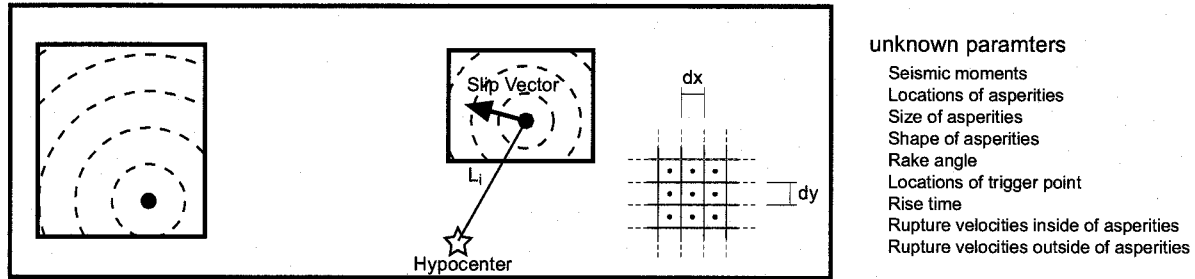


Figure 1 Schematic Image of characterized source model adopt in this study. The sources can move only on release point on which Green's function were calculated in advance.

shape of source time function is adopted to Herrman type and single time window with various rise time to represent as simple as possible. We did not perform smoothing mentioned above at all. These parameters cannot be linear problem like a conventional method and calculation costs come down. However, this method can take arbitrary parameters, and choose only important parameters.

3. DATA

We used strong ground motion records observed by Committee of Earthquake Observation and Research in the Kansai Area (CEORKA) and Japan Meteorological Agency (JMA) for analysis and the locations of the stations are shown in Fig. 2. The distribution of stations covers evenly all direction from the source and the epicentral distances are less than 150km. The seismograms recorded by accelerographs shown in TABLE 2 were numerically integrated to obtain the velocity waveforms. The resultant velocities are band-pass filtered between 0.1 and 0.4 Hz and sampled with an interval of 0.5s. In calculation of the Green's functions, frequency range are used same to the observed data. We adopt the stratified velocity structure model shown in TABLE 3, which was based on refraction experiments (Aoki and Muramatsu(1974)). We use the reflectivity method extended by Kohketsu (1985) as Green's function. The fault surface is set to same to the model of Yoshida et. al. (1996)

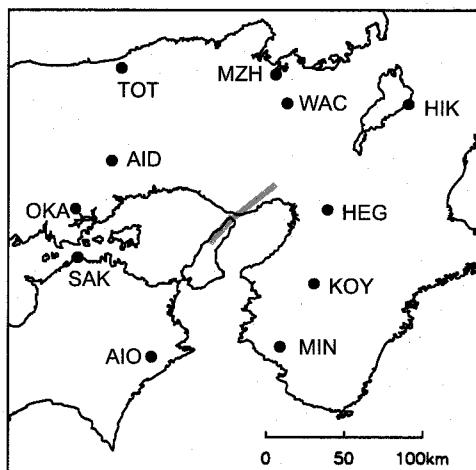


Figure 2 Distribution of observation stations. The distribution can covers evenly every direction.

TABLE 2 Strong motion records list used in this study

Name	Latitude	Longitude	Seismograph	Using Component
AID	34.940	134.168	Acc	EW UD
AIO	33.792	134.452	Acc	EW UD
HEG	34.653	135.685	Acc	EW UD
HIK	35.273	136.247	Acc	EW NS UD
KOY	34.218	135.593	Acc	EW UD
MIN	33.850	135.353	Acc	EW UD
MZH	35.449	135.321	Acc	EW NS UD
OKA	34.659	133.919	Acc	EW NS UD
SAK	34.373	133.932	Acc	EW UD
TOT	35.486	134.240	Acc	EW NS UD
WAC	35.283	135.402	Acc	EW UD

TABLE 3 Velocity Structure

H(km)	Vp(km/s)	Vs(km/s)	ρ (g/cm ³)	Qp	Qs
2.0	5.5	3.2	2.6	300	150
20.0	6.0	3.46	2.7	500	250
10.0	6.6	3.81	3.0	800	400
∞	7.8	4.5	3.2	1000	500

4. RESULTS AND DISCUSSIONS

To examine the validity of this method, we applied it to the ground motion synthesized from an artificial models. We prepared 2 different models of 2 asperities and 3 asperities. In numerical test, to confirm the sensitivities of this method, we calculated with the different calculation models shown in TABLE 4 and all of models include the identical solution. The total bits counts to 42 to 60 for the 2 asperity models and to 63 to 90 for the 3 asperity models. The main operations of GA are crossover, mutation and selection. We set that the probability of crossover is fixed to 0.9 and the probability of mutation is set to 0.3 at first generation and gradually decreasing towards 0.05. Because random search is desirable in early generation, and convergence is desirable in later generation. The manner of selection is set to roulette selection with the inverses of the misfits. The individuals which has small misfit will be survive and be inherited. We always remain the best individual in each generation. The population is set to 500 and the final generation is set to 500. Therefore, the total number of calculation counts to 250000. Figure 3 shows the transition of the average of misfits resulted from 10 times calculations for each model shown in TABLE 4. In early generation, the difference are not appeared among them, but the misfits of model 1 and model 2 are decreasing higher than other models from about 300th generation. Although models 3 to 6 have no significant difference in the transition of the misfits, the difference may appear in more than 500 generation like in the decreasing models 1 and 2 from about 300th generation.

The search areas given are in fault plane for the location and between 1.0 and 16.0×10^{18} Nm for seismic moment. We chose 2 asperity model and 3 asperity model and each asperity has 21 bits for unknown parameters. We didn't perform 4 asperity model, because the total bits becomes high.

TABLE 4 Calculation models for numerical test

Model	1	4	2	5	3	6
# of asperities	2	3	2	3	2	3
rake angle	2		4		4	
location x	5		5		5	
location y	3		3		3	
asperity size	2		2		2	
shape type	0		0		1	
trigger point x	2		3		3	
trigger point y	2		2		2	
rise time	1		1		2	
M0	4		4		5	
vr out	0		1		2	
vr in	0		1		1	
total bit	42	63	52	78	60	90

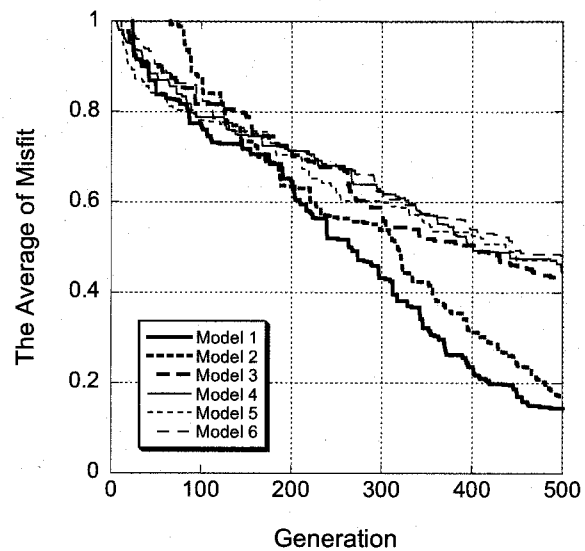


Figure 3 The average of misfits resulted 10 times calculation for each models

We calculated 48 times for 3 asperity model and 84 times for 2 asperity model. The solutions for 3 asperity model has less misfit than those for 2 asperity model. It can be considered that this result comes from not the total binary but the complexity to release waves. A comparison of waveforms between observed and synthetic of an example solution for 3 asperity model is shown in Fig. 4. By and large, the synthetic waveforms successfully reproduce the main phases of observed ones. But the amplitudes are quite different. This differences are caused by the misfit function which set to be near observed and synthetic standard deviation as mentioned above. But synthetic waveforms have only a couple of phases and observed ones are complex and have many phases. It is cannot said that the complex phases in observed waveforms are result from the complexity of the source or the Green's function. This method did not adopt the appropriate Green's function to represent later phase due to site effects. If the solution of this method reproduce later phases, the source models have to be complex. We hesitated to fit all waveforms including later phases only with sources, because this study aims to producing simple source models and the Green's function is not always appropriate.

The total seismic moments are evaluated to $1.74 \times 10^{19} \text{Nm}$ (Mw6.73) or $1.56 \times 10^{19} \text{Nm}$ (Mw6.75) at the average with 3 asperity model and 2 asperity model, respectively. The results are rather small than the results in previous researches. It can be considered that these source models are simple and cannot reproduce complex waveforms. The import of the background area has possiblity to improve this matter. Figure 5 shows the location of the selected 41 solutions by the minimum misfit at the final generation. The color of each asperity is light gray and the area overlaying asperities becomes dense. The more dence the color of area is, the more the solutions are on the area. Namely, the density shows the probability of the existence of an asperity. From Fig. 5, Awaji area has large and

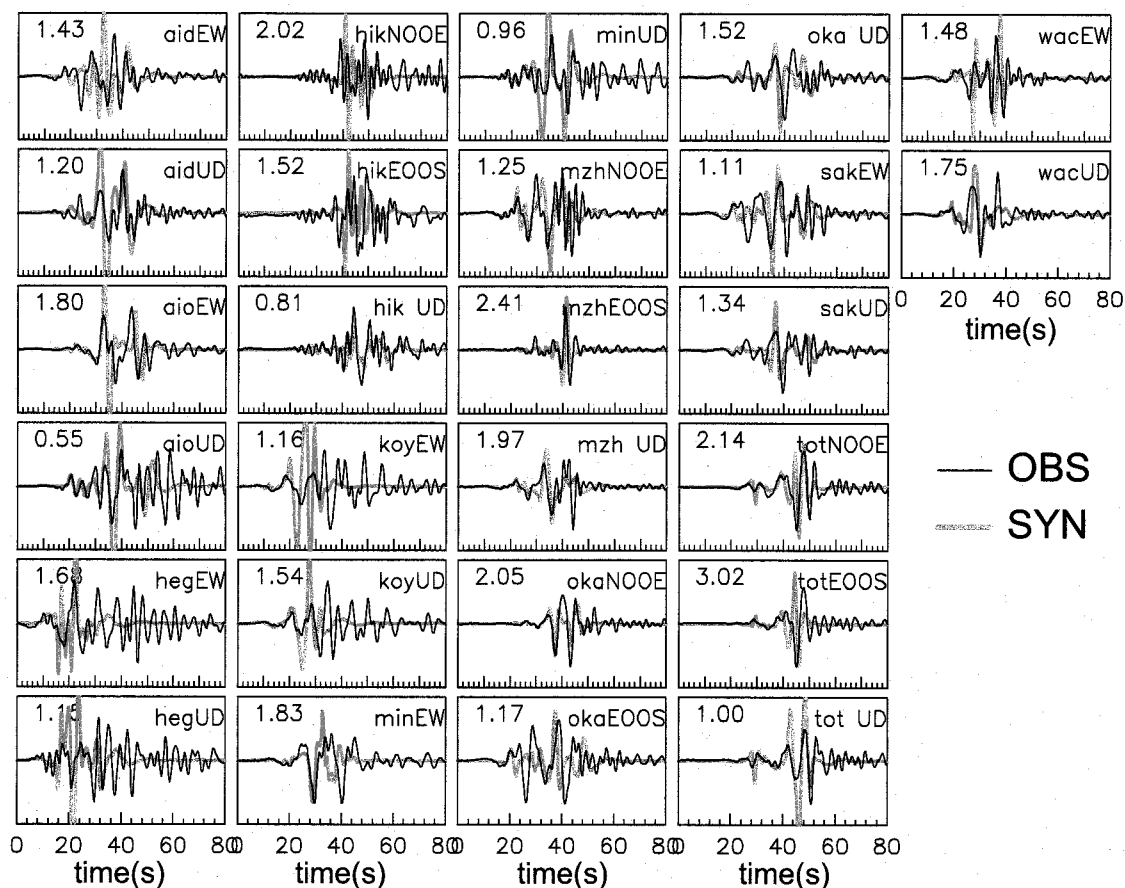


Figure 4 Comparison of observed and synthetic waveforms as an example of 3 asperity modell.

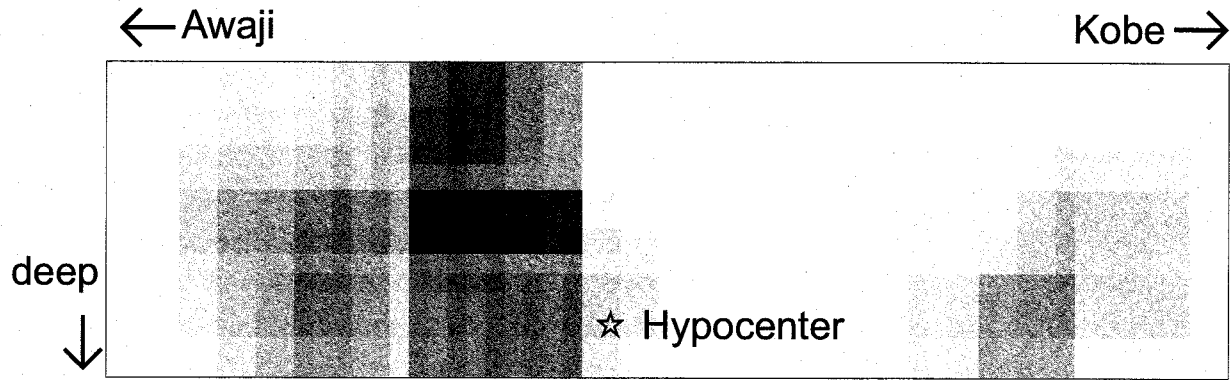


Figure 5 The location of asperities of solutions. The pixels with dense colors has overlaid many solutions. The density shows the probability of the existence of an asperity.

dense area and Kobe area has the light gray area. Therefore, the possibilities of the existence of asperities are high in Awaji area corresponding to below the Nojima fault, and Kobe area correspond to just below the Kobe city. This result is consistent with the previous researches. Although we adopt 3 asperity model, the main possible area are almost 2. This result is caused by the simplified source time function, because we had cases that 1 solution has all 3 asperities in Awaji area. Awaji area must release higher seismic moment than other area, and the solution is lead to large amplitude area in the inversion technique. An improvement of the technique is necessary keeping the simple source model.

5. CONCLUSIONS

We developed the new waveform inversion method using genetic algorithms. This inversion result can get good fitting and Source model is consistent with the previous researches. But asperities of the solution are not always appropriately distributed. Improvements are required to solve this problem and to optimize near source region together, which has higher frequency range than this case.

Acknowledgements:

We thank the Committee of Earthquake Observation and Research in the Kansai Area and the Japan Meteorological Agency for providing the strong motion data. The Research was partially supported by the Ministry of Education, Science, Sports and Culture-in-Aid for Young Scientists (B), 15760423, 2003-2005.

Reference:

- Aoki H. and I. Muramatsu, Crustal structure in the profile across Kinki and Shikoku, Japan, as derived from the Miboro and the Toyama explosions, *Zishin*, 27, 104-109, 1974 (in Japanese)
- Hartzell, S. H. and T. H. Heaton, Inversion of strong ground motion and teleseismic waveform data for the fault rupture history of the 1979 Imperial Valley, California, earthquake, *Bull. Seism. Soc. Am.*, 73 1553-1585, 1983.
- Holland, J. H., *Adaptation in natural and artificial systems*, University of Michigan press, Ann. Arbor, MI. 1975
- Koketsu K., The extended reflectivity method for synthetic near-field seismograms, *J. Phys. Earth*, 33, 121-131, 1985
- Olson, A. H. and R. J. Apsel, Finite faults and inverse theory with applications to the 1979 Imperial Valley earthquake, *Bull. Seism. Soc. Am.*, 72, 1969-2001, 1982
- Sekiguchi, H., K. Irikura and T. Iwata, Fault geometry at the rupture termination of the 1995 Hyogo-ken nanbu earthquake, *Bull. Seism. Soc. Am.*, 90, 117-133, 2000
- Somerville, P., K. Irikura, R. Graves, S. Sawada, D. Wald, N. Abrahamson, Y. Iwasaki, T. Kagawa, N. Smith and A. Kowada, Characterizing crustal earthquake slip models for the prediction of strong ground motion, *Seism. Res. Lett.*, 70, No.1, 59-80, 1999
- Takemura M., Review of source process studies for the 1995 Hyogo-ken-nanbu earthquake part. 1 results from

- waveform inversion, Programme and Abstracts The Seismological Society of Japan, A49, 1996 No.2, (in Japanese)
- Yamanaka H. and H. Ishida, Application of genetic algorithms to an inversion of surface-wave dispersion data, Bull. Seism. Soc. Am., 86, 436-444, 1996
- Yoshida S., Waveform inversion methods for the earthquake source, J. Phys. Earth, 43, 183-209, 1995
- Yoshida, Shingo, Kazuki Kohketsu, Bunichiro Shibasaki, Takeshi Sagiya, Teruyuki Kato, Yasuhiro Yoshida, Joint Inversion of Near- and Far-Field Waveforms and Geodetic Data for the Rupture Process of the 1995 Kobe Earthquake, J. Phys. Earth, Vol. 44, 437-454, 1996

ASSESSING THE POTENTIAL FOR STRENGTH LOSS AND DEFORMATIONS IN LOW PLASTICITY SILTS AND CLAYS DURING EARTHQUAKES

R. W. Boulanger¹⁾ and I. M. Idriss²⁾

1) Professor, Dept. of Civil and Environmental Engineering, University of California, Davis, California, USA

2) Professor Emeritus, Dept. of Civil and Environmental Engineering, University of California, Davis, California, USA
rwboulanger@ucdavis.edu, imidriss@aol.com

Abstract: Criteria are presented for selecting the engineering procedures that are used for predicting potential strains and strength loss in saturated silts and clays during seismic loading. The new criteria are based on monotonic and cyclic undrained loading test data showing that fine-grained soils transition, over a fairly narrow range of plasticity indices (PI), from soils that behave more fundamentally like sands (sand-like or cohesionless behavior) to soils that behave more fundamentally like clays (clay-like or cohesive behavior), with the distinction having a direct correspondence to the type of engineering procedures that are best suited to evaluating their seismic behavior. References to case history studies are provided.

1. INTRODUCTION

Field experiences have shown that earthquake loading can trigger the onset of significant strains and strength loss in a broad range of saturated soils, including sands, silts, and clays. Evaluating the potential for the associated ground deformations requires the selection of appropriate site characterization and engineering analysis methods.

This paper discusses criteria for selecting the engineering procedures that are best suited for predicting potential strains and strength loss in saturated low-plasticity silts and clays during seismic loading. The procedures that are best used for sands and for clays are discussed first, with attention to the soil mechanics behaviors that have guided the development of these procedures. The behavior of low-plasticity silts and clays is then discussed, with their monotonic and cyclic undrained loading behavior being found to transition, over a fairly narrow range of plasticity indices (PI), from soils that behave more fundamentally like sands (sand-like or cohesionless behavior) to soils that behave more fundamentally like clays (clay-like or cohesive behavior). Index criteria for describing this transition, and their comparison to existing liquefaction susceptibility criteria, are discussed. The recommended criteria and engineering analysis procedures have been applied to case histories involving ground failure in low-plasticity silts and clays, and shown to provide improved distinctions between areas of good and poor performance compared to other liquefaction susceptibility criteria (Boulanger and Idriss 2004, 2005a).

2. PROCEDURES FOR ESTIMATING CYCLIC STRENGTHS

2.1 Procedures for Sand-like or Cohesionless Soils

The engineering analysis procedures that are commonly used to estimate the cyclic strength of saturated sand (or cohesionless soils) have evolved in response to key features of the monotonic and

cyclic undrained behavior of sands and some practical limitations of site characterization methods (e.g., NRC 1985). The monotonic and cyclic undrained resistance of saturated sand is strongly dependent on the sand's relative density (D_R), effective consolidation stress, and several other factors such as age, cementation, fabric, and stress and strain history. The consequences of triggering an excess pore water pressure ratio (r_u) of 100% during undrained cyclic loading of saturated sand (often used as one possible definition of "liquefaction") are also very dependent on D_R among other factors, with the consequences being most significant for loose sands and least for dense sands. The in situ D_R of sand is dependent on its depositional environment and loading history, and has no unique relation to its confining stress history alone. Sands are highly susceptible to disturbance using conventional tube sampling techniques, and hence the in situ cyclic resistance ratio (CRR) of sand is most commonly evaluated using SPT- and CPT-based liquefaction correlations. These correlations are based on case histories where the occurrence or non-occurrence of liquefaction is judged primarily on the basis of observations of sand boils and ground deformations, such that the development of $r_u=100\%$ in situ is an inferred condition.

SPT- and CPT-based liquefaction correlations have been developed for soils that range from clean sand to sandy silts, as illustrated in Figure 1(a) showing case history data points for silty sands and sandy silts having fines contents (FC) greater than 35%. Alternatively, the penetration resistances can be converted to equivalent clean sand values, as illustrated in Figure 1(b) showing case history data points for liquefied sites having FC ranging from less than 5% to greater than 35%. These types of SPT- and CPT-based correlations are considered appropriate for nonplastic fines, which exhibit monotonic and cyclic undrained laboratory behaviors that are similar to those for clean sands and which are similarly difficult to sample and test.

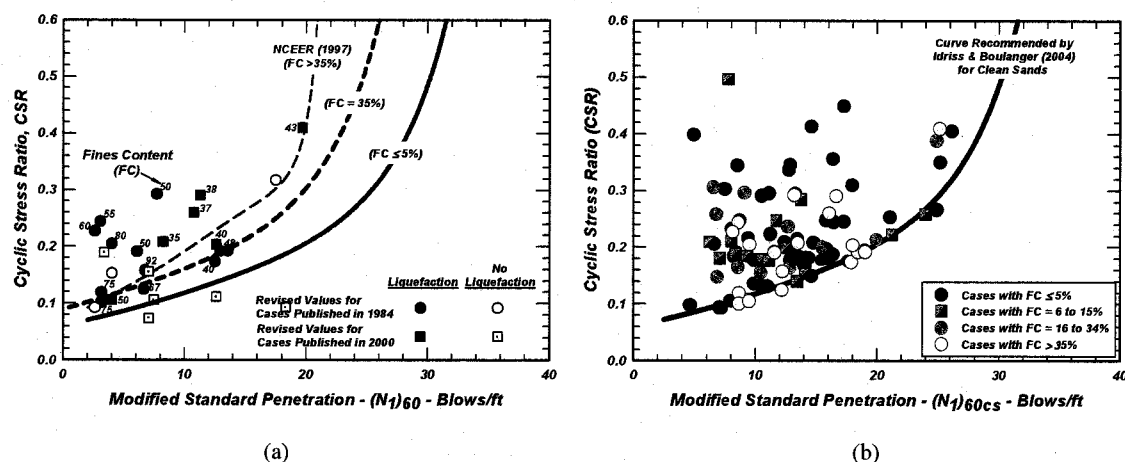


Figure 1. SPT-based liquefaction correlations and case histories of cohesionless soils for $M=7.5$ and $\sigma'_{vc} = 1$ atm: (a) Showing case histories with FC greater than 35%, (b) Showing liquefied cases histories in terms of equivalent clean sand SPT $(N_1)_{60cs}$ values for all FC ranges (Idriss and Boulanger 2004).

2.2 Procedures for Clay-like or Cohesive Soils

The engineering analysis procedures for clays (sometimes informally referred to as cohesive soils) similarly have evolved in response to some fundamental aspects of their monotonic and cyclic undrained behaviors and some practical issues of site characterization methods. The monotonic undrained stress-strain and shear strength (s_u) behavior can often be closely expressed as a function of consolidation stress history, as illustrated in Figure 2. These results by Ladd and Foott (1974) show that normalizing shear stresses by the effective vertical consolidation stress (σ'_{vc}) can result in

relatively unique normalized stress-strain behavior for the same overconsolidation ratio (OCR). These data also illustrate how the undrained strength of clay can be expressed in the form:

$$\frac{s_u}{\sigma'_{vc}} = S \cdot OCR^m \quad (2)$$

where S is the value of s_u/σ'_{vc} when the $OCR=1$ and m is the slope of the s_u/σ'_{vc} versus OCR relation on a log-log plot. Ladd (1991) provided detailed recommendations regarding appropriate values for S (often about 0.22 for simple shear) and m (often about 0.8) to be used in analyses of staged embankment construction, and further noted that a careful assessment of a clay deposit's stress history (i.e., OCR) is generally the most important factor for defining s_u .

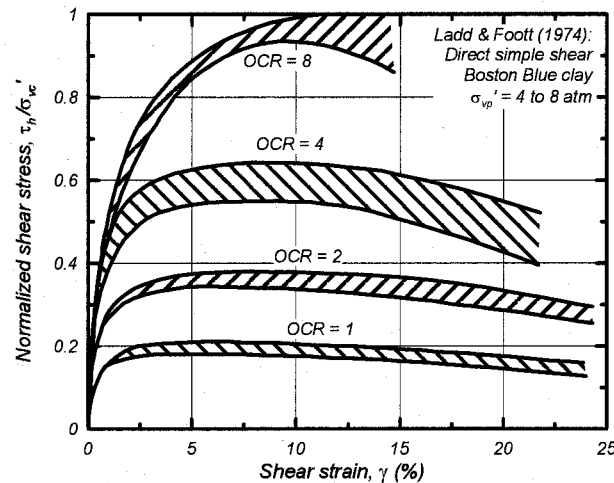


Figure 2. Normalized shear stress versus shear strain response of Boston Blue clay in undrained direct simple shear tests with preconsolidation stresses of 400 to 800 kPa and OCR of 1, 2, 4, and 8 (after Ladd and Foott 1974)

Undrained cyclic loading of clays can produce significant shear strains and stress-strain loops that have some similarities to those observed for saturated sands, as illustrated in Figure 3. The stress-strain loops for the clay (Figure 3b) dissipate more energy than the stress-strain loops for the sand (Figure 3a), but both soils are capable of developing large shear strains if the cyclic loading is sufficiently strong. Furthermore, the stress-strain loops for the clay did not develop the very flat middle portions (where the shear stiffness is nearly zero) that was observed for the sand because the peak r_u in the clay was limited to about 80% whereas the peak r_u in the sand was 100%.

The cyclic strength of saturated clay normalizes well by its undrained monotonic shear strength, as illustrated by the data in Figure 4 for two different fine-grained soils at a range of consolidation stresses and OCR values in both simple shear and triaxial loading. The cyclic stress required to generate shear strains of 3% during 15 uniform cycles of undrained loading at 1 Hz in both triaxial and direct simple shear devices was about 0.88 to 1.01 (average 0.92 for DSS tests) times the respective undrained monotonic shear strength for natural clays and slightly lower for younger tailings slimes (Boulanger and Idriss 2004). The τ_{cyc}/s_u exceeds unity for failure in one loading cycle because the reference value of s_u is for conventional monotonic loading rates that are much slower than the cyclic loading rate.

In situ undrained shear strengths (s_u) for clay can be assessed using in situ tests (e.g., vane shear and CPT tests), empirical correlations based on stress-history normalized properties, or laboratory testing of field samples obtained using conventional thin-walled tube sampling techniques since clays

are less susceptible to disturbance than sands. In all cases, the interpretation and proper execution of in situ and laboratory tests requires a careful accounting of the effective consolidation stress and stress history conditions in the field.

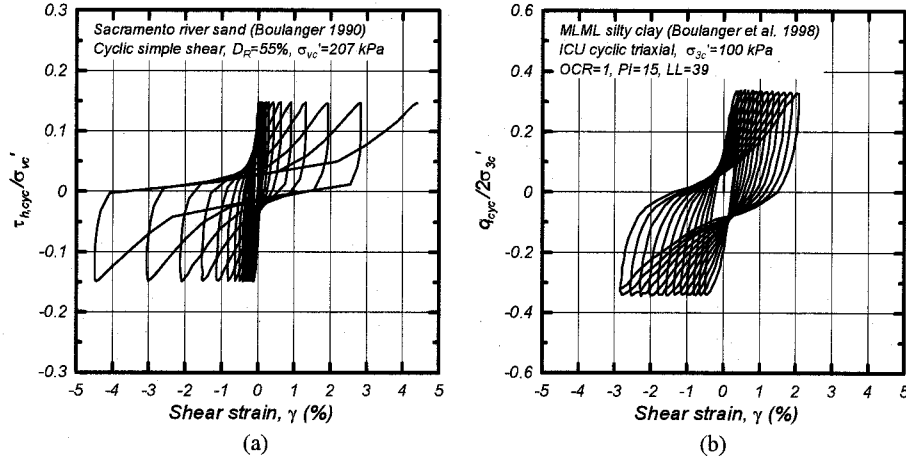


Figure 3. Stress-strain response during undrained cyclic loading tests on: (a) clean sand, and (b) low-plasticity clay.

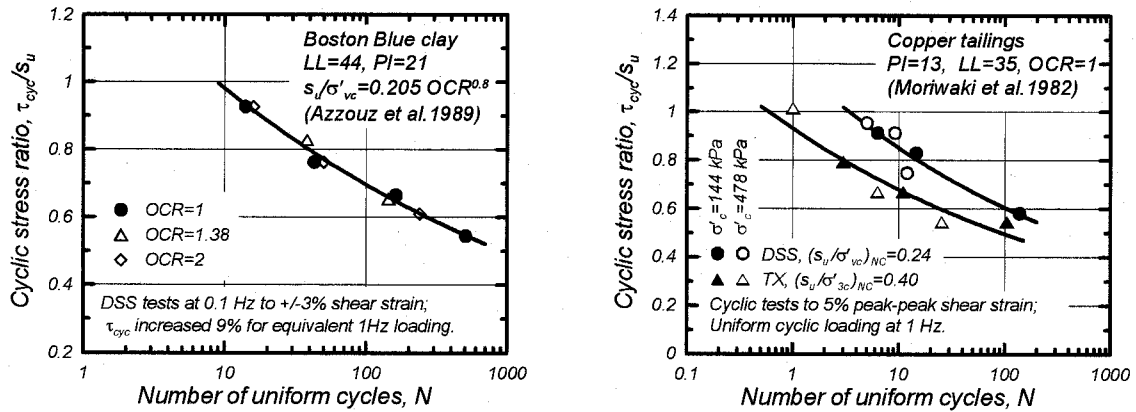


Figure 4. Cyclic strength ratios for undrained uniform cyclic loading of two fine-grained soils.

The consequences of cyclic failure (e.g., triggering of 3% shear strain) in saturated clays depend on the potential for strength loss, which is related to the soil's sensitivity (i.e., S_t = ratio of peak to remolded undrained shear strengths). The sensitivity of a fine-grained soil is dependent on numerous factors, but can be approximately related to the liquidity index [$LI = (w_c - PL)/(LL - PL)$] and effective consolidation stress, as illustrated in Figure 5 (Mitchell and Soga 2005). The consequences of cyclic failure can range from severe strength loss in highly sensitive or quick clays, to relatively insignificant strength loss in well-compacted or highly overconsolidated clays.

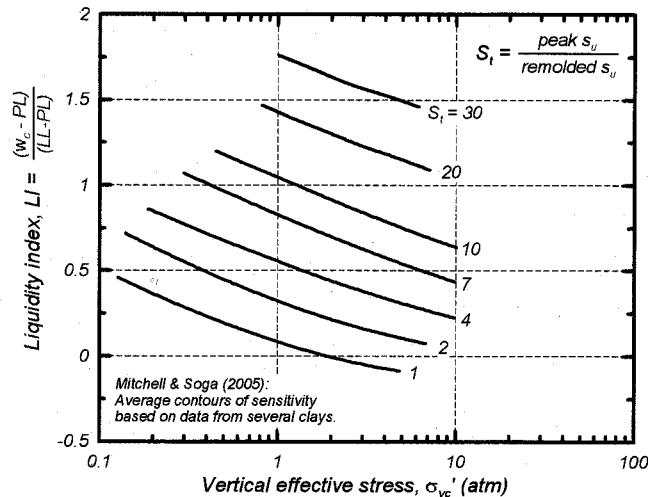


Figure 5. Relation between sensitivity, liquidity index, and effective consolidation stress (after Mitchell and Soga 2005)

3. CRITERIA FOR SELECTING THE ANALYSIS PROCEDURE

3.1 Existing Liquefaction Susceptibility Criteria

It is common in practice to assume that soils that classify as "liquefiable" by liquefaction susceptibility criteria should be evaluated using procedures developed primarily for sands (e.g., SPT- and CPT-based liquefaction correlations), even though current liquefaction susceptibility criteria were not necessarily developed for that purpose.

The Chinese Criteria have been widely used since the early 1980's as a means for evaluating the liquefaction susceptibility of silts and clays. These criteria were based on observations of "liquefaction" in fine-grained soils (includes CL, CL-ML, and ML soil classifications) at sites in China during strong earthquakes (Wang 1979). No details were provided regarding how the field data were collected or interpreted. Seed and Idriss (1982) summarized Wang's findings as follows: clayey soils having less than 15% finer than 5 μm , a liquid limit (LL) less than 35, and water content (w_c) greater than 0.9LL may be vulnerable to severe strength loss as a result of earthquake shaking.

More recently, Andrews and Martin (2000) reviewed empirical observations from a few case histories, discussed the relevance of various indices, and concluded that: (1) soils are susceptible to liquefaction if they have <10% finer than 2 μm and $LL < 32$, (2) soils are not susceptible to liquefaction if they have $\geq 10\%$ finer than 2 μm and $LL \geq 32$, and (3) further study is required for soils that meet one, but not both, of these criteria.

Bray et al. (2004) proposed new liquefaction susceptibility criteria for soils with significant fines contents based primarily on observations of ground failure in fine-grained soils during the 1999 Kocaeli earthquake and results of cyclic laboratory tests on field samples from some of the sites studied. The criteria by Bray et al. (2004) are that fine-grained soils with $PI \leq 12$ and $w_c > 0.85LL$ are susceptible to liquefaction, while soils with $12 < PI < 20$ and $w_c > 0.8LL$ are "systematically more resistant to liquefaction but still susceptible to cyclic mobility." The $PI \leq 12$ criterion provides a close enveloping of the field data. Seed et al. (2003) proposed liquefaction susceptibility criteria that are similar to those by Bray et al. (2004), except that they include slightly different w_c/LL limits and include constraints on LL. Seed et al.'s (2003) criteria are described by three zones on the Atterberg Limits Chart, which aside from slightly rounded corners, are bounded by the following PI and LL

values: Zone A soils have $PI \leq 12$ and $LL \leq 37$ and are considered potentially susceptible to "classic cyclically induced liquefaction" if the water content is greater than 80% of the LL; Zone B soils have $PI \leq 20$ and $LL \leq 47$ and are considered potentially liquefiable with detailed laboratory testing recommended if the water content is greater than 85% of the LL; and Zone C soils with $PI > 20$ or $LL > 47$ are considered generally not susceptible to classic cyclic liquefaction, although they should be checked for potential sensitivity.

These and other liquefaction susceptibility criteria (e.g., Pollito 1999) appear to have been developed by implicitly or explicitly trying to answer the question, "what types of silts and clays are susceptible to liquefaction?" Development of liquefaction susceptibility guidelines for silts and clays are complicated by difficulties in defining the meaning of liquefaction and by the fact that observations from the ground surface at damaged sites provide little insight into the soil mechanics behavior of the problem soils, other than the fact that they have developed significant strains and excess pore water pressures. Consider, for example, the cyclic test results shown previously in Figure 3 for clean sand and low-plasticity clay specimens. The clay sample reached an excess pore pressure ratio (r_u) of only about 80% and dissipated more hysteretic energy than the sand, but it still developed large shear strains, which could certainly be manifested as ground deformations in the field during strong earthquake shaking.

3.2 Recommended Criteria

An alternative approach to developing liquefaction susceptibility criteria is to ask the question: "what is the best way to estimate the potential for strength loss and large strains in different types of fine-grained soils?" For most practice, this corresponds to asking, "what types of fine-grained soils are best evaluated using procedures adapted from those for sands versus procedures adapted from those for clays?"

To answer this question, experimental data for fine-grained soils was compiled from the literature and categorized in soils that exhibited sand-like, clay-like, or intermediate behaviors. Clay-like soils were those that exhibited stress-history normalized shear strength and related behaviors best described using procedures commonly associated with clays. The results are summarized on the Atterberg limits chart in Figure 6, showing that fine-grained soils transition between sand-like and clay-like behaviors over a fairly narrow range of PI. For practical purposes, fine-grained soils can confidently be expected to exhibit clay-like behavior if they have $PI \geq 7$. If a soil plots as CL-ML, the PI criterion may be reduced to $PI \geq 5$ and still be consistent with the available data. Fine-grained soils that do not meet the above criteria should be considered as likely exhibiting sand-like behavior (i.e., liquefiable), unless shown otherwise through detailed in situ and laboratory testing. Fine-grained soils with PI values of 3 to 6 may exhibit intermediate behavior, such that detailed in situ and laboratory testing may still provide benefits relative to reliance on SPT- and CPT-based liquefaction correlations alone. Thus, the proposed criteria provide a reasonable screening guide, after which the potential benefits of more detailed in situ and laboratory testing programs can be assessed relative to the site heterogeneity, level of seismic hazard, and other project specific conditions.

The w_c and gradation (minus 2 or 5 μm fraction) are not considered to be useful indicators of whether a fine-grained soil should be analyzed using procedures adapted from those for sands versus those for clays. The w_c of a saturated sand is related to its D_R and the w_c of a saturated clay is related to its LI, and therefore the w_c is related to the potential consequences (strength loss) of earthquake-induced shear strains rather than being a reliable indicator of fundamental soil behavior. The percentage of clay-sized minerals is also not a reliable index for distinguishing between clay-like and sand-like behavior in a fine-grained soil. Clay-size fraction has not proven a useful index for describing monotonic shear strengths of fine-grained soils, and so it is a poor choice as an empirical parameter for describing cyclic behavior.

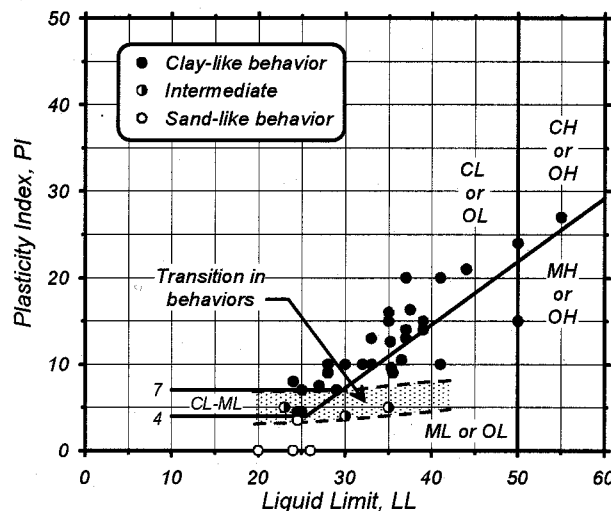


Figure 6. Atterberg limits chart showing representative values for soils that exhibited clay-like, sand-like, or intermediate behaviors in undrained loading.

4. CONCLUDING REMARKS

The first step in evaluating the potential for ground failure in silts and clays during earthquakes is to determine the appropriate framework and engineering procedures to be used. For fine-grained soils that behave more fundamentally like clays, the cyclic and monotonic undrained shear strengths are closely related and show relatively unique stress-history normalized behaviors. Cyclic strengths can then be evaluated based on information from in situ testing, laboratory testing, and empirical correlations that are similar to, or build upon, established procedures for evaluating the monotonic undrained shear strengths of such deposits. For fine-grained soils that behave more fundamentally like sands, the cyclic strengths may be more appropriately estimated within the framework of existing SPT- and CPT-based liquefaction correlations.

For practical purposes, fine-grained soils can confidently be expected to exhibit clay-like behavior if they have $PI \geq 7$. Fine-grained soils with PI values of 3 to 6 may exhibit intermediate behavior, such that detailed in situ and laboratory testing may still provide benefits relative to reliance on SPT- and CPT-based liquefaction correlations alone. Thus, the proposed criteria provide a reasonable screening guide, after which the potential benefits of more detailed in situ and laboratory testing programs can be assessed relative to the site heterogeneity, level of seismic hazard, and other project specific conditions.

Procedures for evaluating the potential for cyclic failure of clay-like fine-grained soils are presented in Boulanger and Idriss (2004, 2005a), along with an evaluation of those procedures against case histories involving areas of failure and non-failure in fine-grained soils. The recommended liquefaction susceptibility criteria and the cyclic failure analysis procedures were shown to provide an improved means for distinguishing between the conditions that did and did not lead to ground deformations at these sites. It is hoped that the recommended liquefaction susceptibility criteria and cyclic failure analysis procedures will provide a framework for future developments and refinements in this area, as additional case histories and experimental data are compiled and analyzed.

Acknowledgements:

The authors acknowledge support from the Japan Ministry of Education, Culture, Sport, Science, and Technology (MEXT) for establishing the Center for Urban Earthquake Engineering (CUEE) in Tokyo Institute of Technology and thereby making this international conference and exchange possible.

References:

- Andrews, D. C. A., and Martin, G. R. (2000). "Criteria for liquefaction of silty soils." Proc. 12th World Conference on Earthquake Engineering, Auckland, New Zealand.
- Azzouz, A. S., Malek, A. M., and Baligh, M. M. (1989). "Cyclic behavior of clays in undrained simple shear, J. Geotechnical Engineering Div., ASCE, 115(5): 637-657.
- Boulanger, R. W., and Idriss, I. M. (2005a). "Evaluating cyclic failure in silts and clays." Proceedings, Geotechnical Earthquake Engineering Satellite Conference on Performance Based Design in Earthquake Geotechnical Engineering: Concepts and Research. Prepared by TC4 Committee of ICSMGE, Japanese Geotechnical Society, Tokyo, 78-86.
- Boulanger, R. W., and Idriss, I. M. (2005b). "New criteria for distinguishing between silts and clays that are susceptible to liquefaction versus cyclic failure." Proceedings, Technologies to Enhance Dam Safety and the Environment, 25th Annual United States Society on Dams Conference, USSD, Denver, CO, 357-366.
- Boulanger, R. W., and Idriss, I. M. (2004). "Evaluating the potential for liquefaction or cyclic failure of silts and clays." Report No. UCD/CGM-04/01, Center for Geotechnical Modeling, Dept. of Civil & Envir. Engrg., Univ. of California, Davis, 129 pp., http://cee.engr.ucdavis.edu/faculty/boulanger/PDFs/2004/Boulanger_Idriss_CGM04-01_2004.pdf.
- Boulanger, R. W., Meyers, M. W., Mejia, L. H., and Idriss, I. M. (1998). "Behavior of a fine-grained soil during Loma Prieta earthquake." Canadian Geotechnical J., 35: 146-158.
- Bray, J. D., Sancio, R. B., Riemer, M. F., and Durgunoglu, T. (2004). "Liquefaction susceptibility of fine-grained soils." 11th Int. Conf. on Soil Dynamics and Earthquake Engineering and 3rd Int. Conf. on Earthquake Geotechnical Engineering, D. Doolin et al., eds., Stallion Press, pp 655-662.
- Idriss, I. M., and Boulanger, R. W. (2004). "Semi-empirical procedures for evaluating liquefaction potential during earthquakes." Proc., 11th Int. Conference on Soil Dynamics and Earthquake Engineering, and 3rd Int. Conference on Earthquake Geotechnical Engineering, D. Doolin et al., eds., Stallion Press, Vol. 1, 32-56.
- Ladd, C. C. (1991). "Stability evaluation during staged construction," Journal of Geotechnical Engineering, ASCE, 117(4), 540-546.
- Ladd, C. C., and Foott, R. (1974). "New design procedure for stability of soft clays." Journal of the Geotechnical Engineering Div., ASCE, 100(7), 763-786.
- Mitchell, J. K., and Soga, K. (2005). Fundamentals of Soil Behavior, 3rd Edition, John Wiley and Sons, Inc.
- Moriwaki, Y., Akky, M. R., Ebeling, R., Idriss, I. M., and Ladd, R. S. (1982). "Cyclic strength and properties of tailing slimes." Specialty Conference on Dynamic Stability of Tailings Dams, Preprint 82-539, ASCE.
- National Research Council (1985). Liquefaction of soils during earthquakes. National Academy Press, Washington, D.C., 240 pp.
- Pollito, C. P. (1999). The effects of non-plastic and plastic fines on the liquefaction resistance of sandy soils. Ph.D. thesis, Virginia Polytechnic Institute and State University, Dec.
- Seed, H. B., and Idriss, I. M. (1982). Ground motions and soil liquefaction during earthquakes, Earthquake Engineering Research Institute, Berkeley, CA, 134 pp.
- Seed, R. B., Cetin, K. O., Moss, R. E. S., Kammerer, A., Wu, J., Pestana, J., Riemer, M., Sancio, R. B., Bray, J. D., Kayen, R. E., and Faris, A. (2003). "Recent advances in soil liquefaction engineering: A unified and consistent framework." Keynote presentation, 26th Annual ASCE Los Angeles Geotechnical Spring Seminar, Long Beach, CA.
- Wang, W. S. (1979). "Some findings in soil liquefaction." Water Conservancy and Hydroelectric Power Scientific Research Institute, Beijing, China.

PUSHOVER ANALYSIS FOR PILES SUBJECTED TO LIQUEFACTION-INDUCED FLOW PRESSURE

J. H. Hwang¹⁾ and M. C. Chung²⁾

1) Professor, Dept. of Civil Engineering, National Central University, Chung-li, Taiwan 32054 R.O.C.

*2) Ph.D. Candidate, Dept. of Civil Engineering, National Central University, Chung-li, Taiwan 32054 R.O.C.
Hwangjin@cc.ncu.edu.tw, s0322028@cc.ncu.edu.tw*

Abstract: This paper presents a pushover analysis approach for piles exerted by liquefaction-induced flow pressure. The flow pressure is estimated from seismic design specification of Japanese Road Association, and the non-linear behavior of the pile is modeled by a tri-linear moment-curvature relationship. The push over analysis was conducted by the software SAP 2000. The capacity curve of the lateral pile was expressed in terms of the total flow force imposing on the pile and the pile head displacement. Then, the seismic performances of the pile can be clearly identified on the curve when subjected to different design earthquakes which cause varying flow pressures. The proposed approach is simple and clear, so it can be easily applied to perform the seismic performance-based design of pile foundation.

1. INTRODUCTION

Performance-based design has been the future trend of the seismic design codes (CEN/TC250/SC8 2000, JRA 1996, SEAOC 1995, GBJ11-89 1989) in the world. In the recently developed seismic performance-based design (SPBD) approach, nonlinear analysis procedure plays a key role in identifying the damage patterns and levels for understanding the inelastic behavior and the failure mechanism of the structure during severe seismic events. Pushover analysis is a simplified, nonlinear, static, step-by step procedure where a predefined pattern of earthquake loads is applied incrementally to framework structures until a plastic collapse mechanism is reached. By this procedure, structure capacity is represented by a capacity curve. The most convenient way to plot the capacity curve is by tracking the base shear and the roof displacement of the structure during the pushover process. This curve can help engineers better understand how structures will behave when subjected to major earthquakes.

Numerous studies on SPBD of structures have been published in the past two decades. These research results have formed the bases of current SPBD codes in the world. Up to now, although there have been more and more SPBD-related studies focusing structural and foundation engineering area, few have been devoted to liquefaction engineering area. To introduce the concept of SPBD to the problem of lateral pile response when subjected to liquefaction-induced flow pressure, this paper proposes a simple pushover analysis approach for the problem. The major idea of the approach is based that the capacity of the lateral pile can be obtained by tracking the total flow force exerting on the pile and the pile head displacement during the pushover process.

2. PUSHOVER APPROACH

The main procedures of this approach include: (1) liquefaction analysis and flow pressure estimation, (2) set up nonlinear pile analysis model, (3) pushover analysis by software SAP2000 (SAP2000 V9 manuals 1995), and (4) plot the capacity curve of the lateral pile.

The procedures of (1) and (2) will be described in this section, and the procedures of (3) and (4) will be described in next section through a case analysis.

2.1 Liquefaction analysis and flow pressure estimation

The liquefaction analysis and flow potential of a site can be assessed by the method suggested in the seismic specification of Japanese Road Association (JRA) in 1996. If a pile foundation site is identified to have high potential of lateral ground spreading, the JRA (1996) specification has proposed that the action of liquefaction-induced lateral spreading on the piles can be represented by the flow earth pressure, as shown in Figure 1, where q_{NL} and q_L are the linearly distributed earth pressures exerted on the piles by the non-liquefying and liquefying soil layers in the flow area. The earth pressures can be computed by Eqs. (1) and (2) as

$$q_{NL}(x) = C_s C_{NL} K_p \gamma_{NL} x, \quad 0 \leq x \leq H_{NL}, \quad (1)$$

$$q_L(x) = C_s C_L \{ \gamma_{NL} H_{NL} + \gamma_L (x - H_{NL}) \}, \quad H_{NL} \leq x \leq H_{NL} + H_L, \quad (2)$$

where:

$q_{NL}(x)$: Flow earth pressure (kN/m^2) of a non-liquefying layer acting on a pile at a depth of x ;

$q_L(x)$: Flow earth pressure (kN/m^2) of a liquefying layer acting on a pile at a depth of x ;

C_s : Modification factor based on the distance from the waterfront, as shown in Table 1;

C_{NL} : Modification factor for the ground flow force in a non-liquefying layer. The value according to liquefaction potential index P_L (m^2), which is defined by $P_L = \int_0^{20} (1 - F_L)(1 - 0.5x) dx$, is shown in Table 2 where F_L is the safety factor to resist liquefaction; when $F_L > 1$, set $F_L = 1$;

C_L : Modification factor for the force of the ground flow in a liquefying layer (the suggested value is 0.3);

K_p : Passive earth pressure coefficient using Coulomb's $K_p = (1 + \sin\phi)/(1 - \sin\phi)$;

γ_{NL} : Average unit weight (kN/m^3) of a non-liquefying layer;

γ_L : Average unit weight (kN/m^3) of a liquefying layer;

x : Depth below the ground surface (m);

H_{NL} : Non-liquefying layer thickness (m);

H_L : Liquefying layer thickness (m).

Table 1 Modification factor C_s based on the distance from the waterfront (JRA 1996)

Distance from waterfront, s (m)	Modification factor, C_s
$s \leq 50$	1.0
$50 < s \leq 100$	0.5
$100 < s$	0

Table 2 Modification factor C_{NL} for the ground flow force in a non-liquefying soil layer (JRA 1996)

Liquefaction potential index, P_L (m^2)	Modification factor, C_{NL}
$P_L \leq 5$	0
$5 < P_L \leq 20$	$(0.2P_L - 1)/3$
$20 < P_L$	1.0

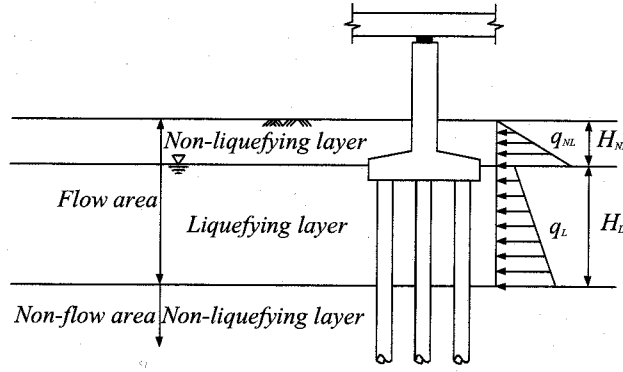


Figure 1 Analysis model of a pile group subjected to the flow earth pressures (JRA 1996)

To convert a pile group problem to a single pile one, some simplifying assumptions must be made. The assumptions include:

- (1) The geometrical dimensions and material properties of all the piles are the same.
- (2) The pile cap is perfectly rigid, so that the horizontal displacements of all the piles are the same.
- (3) The flow earth pressure on every pile is the same.

Given the above assumptions, the analysis of a pile group can be simplified as the model of a single pile, as shown in Figure 2. Multiplying the flow earth pressures from Eqs. (1) and (2) by the effective foundation width B , we can obtain the flow forces per unit depth for the pile group. For a pile foundation, the foundation width B is defined as the distance between the external edges of the two outermost piles. The foundation width of the pier and the pile cap is the width of the pier and the cap. These definitions are shown in Figure 3. By dividing the total flow force per unit depth with the number of piles, one can obtain the flow force per depth of one pile. Thus, the flow forces per unit depth q_{n1} , q_{n2} (kN/m) at the top and the bottom of non-liquefying layer for each pile can be expressed as

$$q_{n1} = \frac{B \times (C_s C_{NL} K_p \gamma_{NL} D_f)}{N_{total}}, \quad (3a)$$

$$q_{n2} = \frac{B \times [C_s C_{NL} K_p \gamma_{NL} (D_f + h_{nl})]}{N_{total}}. \quad (3b)$$

The flow force per unit depth q_{l1} , q_{l2} (kN/m) at the top and the bottom of liquefying layer for each pile can be expressed as

$$q_{l1} = \frac{B \times \{C_s C_L [\gamma_{NL} (D_f + h_{nl})]\}}{N_{total}}, \quad (4a)$$

$$q_{l2} = \frac{B \times \{C_s C_L [\gamma_{NL} (D_f + h_{nl}) + \gamma_L h_l]\}}{N_{total}}, \quad (4b)$$

where:

B : Effective width (m) for computing the flow force;

D_f : Embedded depth (m) of the pile cap;

h_{nl} : Thickness of the non-liquefying layer (m) for a single pile;

h_l : Thickness of the liquefying layer (m) for a single pile;

N_{total} : Number of piles.

The flow forces per unit depth at any depth in the non-liquefying and liquefying layers can be linearly interpolated by Eqs. (5) and (6).

$$q_1(x) = q_{n1} + (q_{n2} - q_{n1}) \frac{x}{h_{nl}}, \quad 0 \leq x \leq h_{nl}, \quad (5)$$

$$q_2(x) = q_{l1} + (q_{l2} - q_{l1}) \frac{x - h_{nl}}{h_l}, \quad h_{nl} \leq x \leq h_{nl} + h_l, \quad (6)$$

where:

$q_1(x)$: Flow force per unit depth (kN/m) at a depth of x in a non-liquefying layer;

$q_2(x)$: Flow force per unit depth (kN/m) at a depth of x in a liquefying layer;

x : Depth (m) from the pile head.

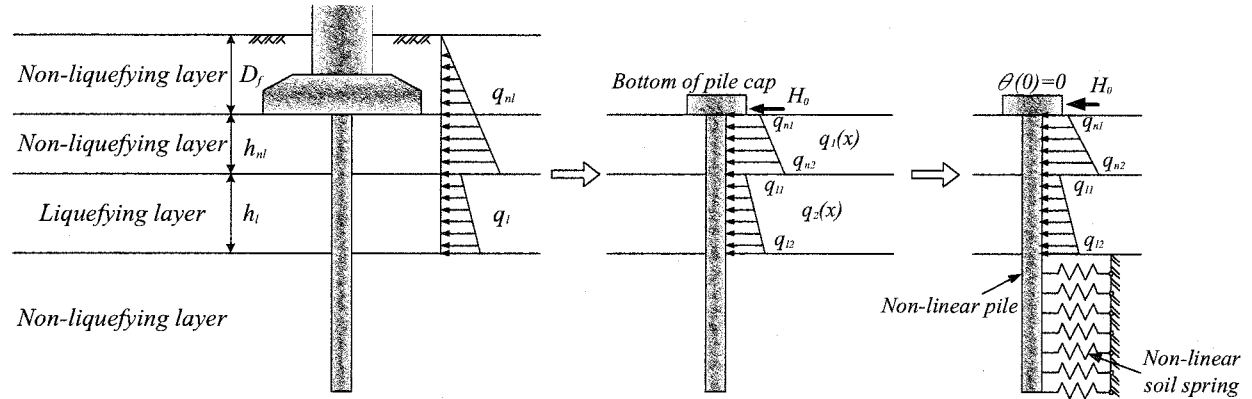
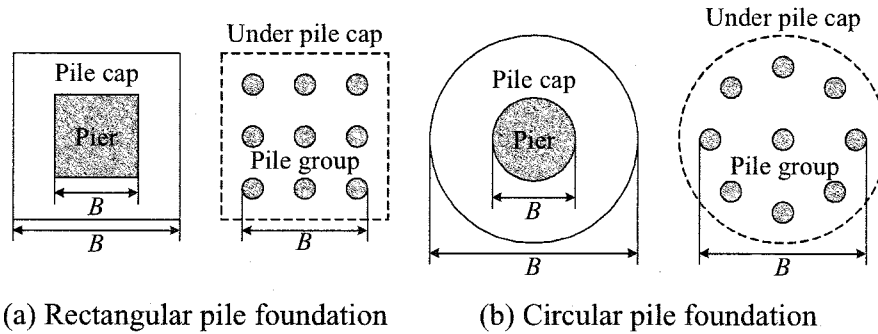


Figure 2 Analysis model of a single pile subjected to flow earth pressure



(a) Rectangular pile foundation

(b) Circular pile foundation

Figure 3 Effective width for computing flow earth pressures

2.2 Set up nonlinear pile analysis model

The modeling of a single pile subject to the action of lateral flow pressure can be simplified as a free standing pile with the lower part embedded in the underlying non-liquefying deposit and the upper part acted by the flow pressures, as shown in Figure 2. A pile embedded in an underlying non-liquefying soil layer in a non-flow area can be simulated by a nonlinear pile laterally supported by a series nonlinear soil springs, while the pile in the flow area can be simulated as a nonlinear beam model exerted by the flow pressures with a zero rotation restraint at the top of the pile.

The nonlinear behavior of the pile is modeled by a tri-linear moment curvature relation and the nonlinear behavior of the underlying non-liquefying soil is modeled by an elastic-perfectly plastic soil spring. Any commercial programs having nonlinear beam-column and spring elements can be used to analyze this nonlinear soil-pile interaction problem.

3. CASE ANALYSIS

To demonstrate how to conduct pushover procedure using the above analysis model, one pile damage case that occurred during the 1995 Kobe earthquake was chosen as an analysis example. This case had been reported in detail by Ishihara and Cubrinovski (2004). In this case, the 69 pre-stressed high-strength precast concrete piles, supporting an oil-storage tank with a storage

capacity of 2450 *kl* , were seriously damaged due to a lateral ground displacement estimated to be about 35- 55 *cm*. The piles are 23 *m* long and 45 *cm* in diameter. The moment-curvature relationship of the pile is shown in Figure 4, where D_0 is the diameter of the pile and N is the axial force on the pile. It can be seen in the figure, that the cracking moment capacity M_c , yielding moment capacity M_y and ultimate moment capacity M_u are approximately 105, 200, and 234 *kN-m*, respectively. The geological profile and the cross section of tank TA72 and its foundation are shown in Figure 5. Sand compaction piles have been installed around the perimeter of the tank foundation to strengthen the foundation soils. The depth of the improvement is approximately 15 *m*. A detailed field investigation using a bore-hole camera and inclinometer was conducted to inspect for damage to the No.2 and No.9 piles of the tank. The outcome is shown in Figure 6. The figures show that the piles developed multiple cracks and that the greatest damage occurred at a depth of approximately 8 to 14 *m*, which is about the depth of the interfacial zone between the liquefying deposits and the underlying non-liquefying silty layer. There was significant shear-induced damage at a depth of 14 to 15 *m* on the No.2 pile. The joint of the No. 9 pile seems to have broken and slipped at a depth of 10.5 *m* due to the large shear force.

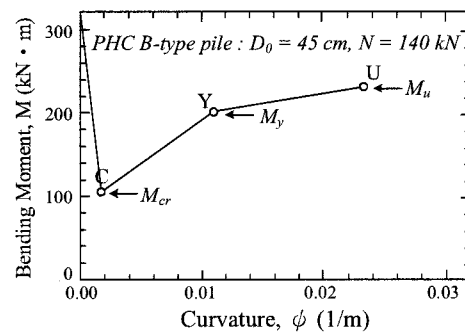


Figure 4 Tri-linear M - ϕ relationship of the pile (Ishihara and Cubrinovski 2004)

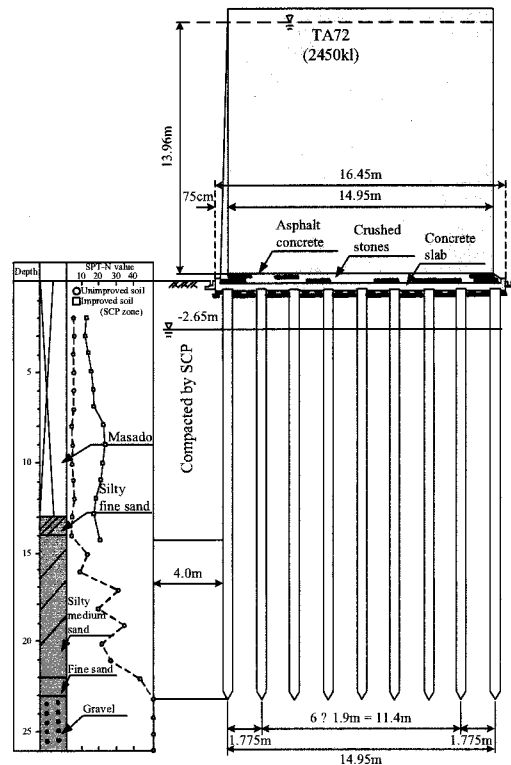


Figure 5 Cross sectional view of tank TA72 and its foundations (Ishihara and Cubrinovski 2004)

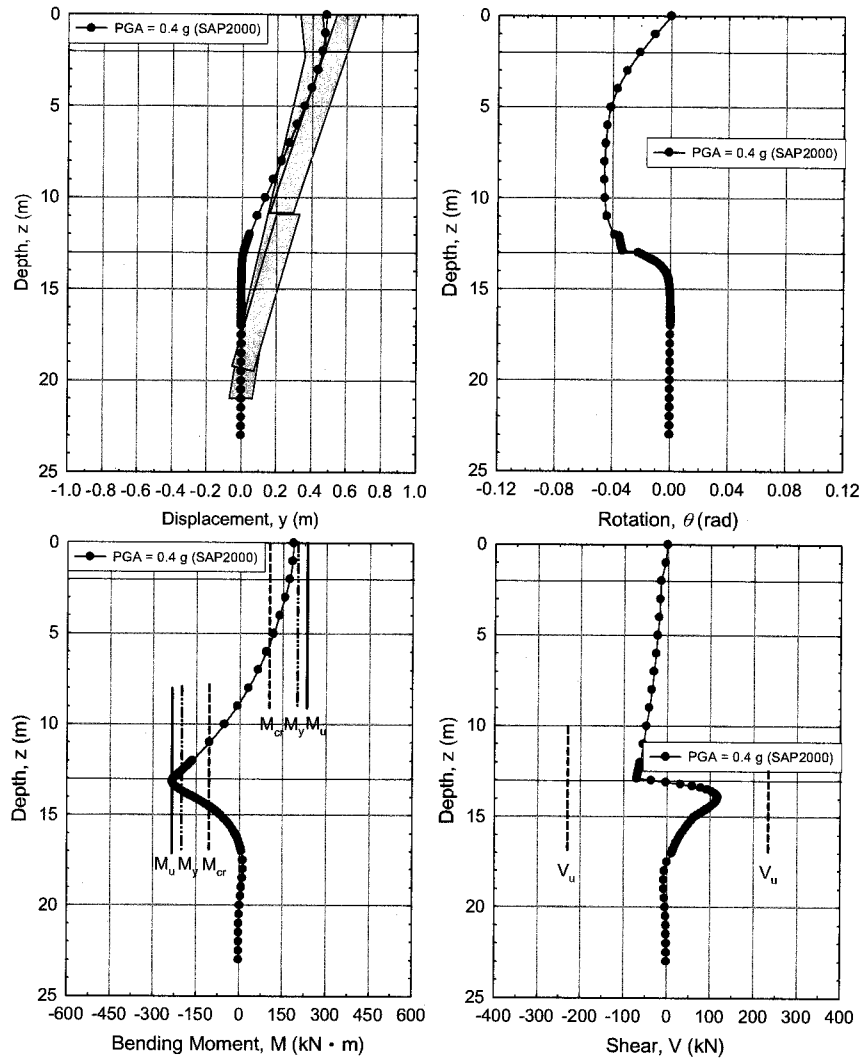


Figure 6 Analyzed deformations and internal forces along the pile

3.1 Liquefaction evaluation and flow pressure

The results of liquefaction analysis are shown in Table 3. It can be seen that the soil deposits from the surface to a depth of 13.5 m are in the flow area. The non-liquefying deposits go from the surface to a depth of 2.5 m and the liquefying deposits run from a depth of 2.5 m to a depth of 13.5 m. The soil deposits below 13.5 m are in the non-flow area. An average value of three seismic records with a PGA of 0.4 g, is used in the analysis. We use the liquefaction assessment method proposed by the JRA (1996). The computed liquefaction potential index P_L for the flow area is 16.54. In this case, the horizontal force acting on the pile head comes from the flow force at the top of the non-liquefying layer 0.5 m below the ground surface. The horizontal force is about 1.19 kN per pile. The flow forces per unit depth of the non-liquefying and liquefying layers in the flow area can be calculated by Eqs. 3 and 4. The unit flow forces at the top and bottom of the non-liquefying layer are 4.47 kN/m and 23.48 kN/m, respectively. The unit flow forces at the top and bottom of the liquefying layer are 3.01 kN/m and 16.27 kN/m, respectively.

3.2 Pushover analysis by SAP2000

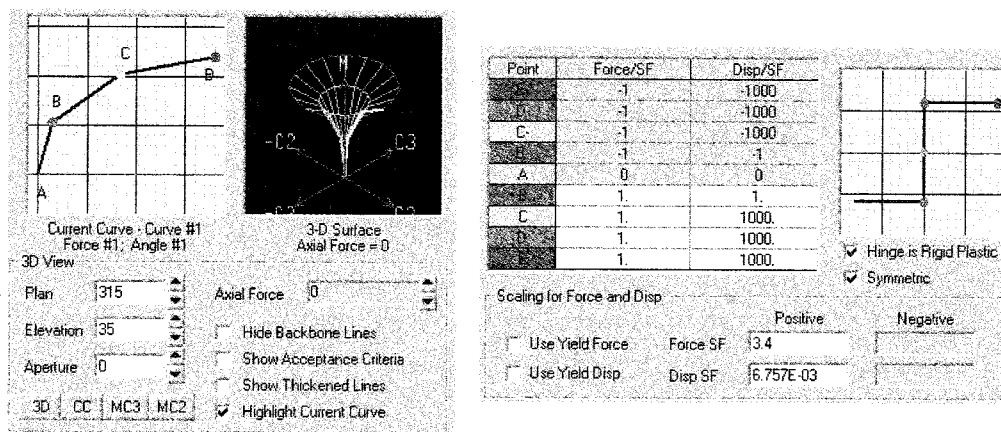
We use the software SAP2000 to perform the pushover analysis. The software provides the nonlinear static analysis function which can incrementally apply loads in multi-stages and the

function of defining hinge properties assigned to frame elements to model their nonlinear behaviors. The user-defined hinge properties assigned to the pile and the soil spring are shown in Figure 7. Figure 8 shows the whole structure model established by SAP2000. To accurately monitor the evolution of the plastic hinge, A great number of pile elements and soil springs are installed near the interface of the flow and non-flow areas, where dramatic changes of the internal forces of the pile are expected. Figure 9 shows the capacity curve of the pile in terms of the total flow force and the pile head displacement. Thus, different stressed states, including cracking, yielding, and the ultimate state can be identified on the capacity curve.

Table 3 Soil profile and the results of liquefaction analysis

Depth (m)	Soil type	SPT-N value	Unit weight (kN/m ³)	Friction angle (degree)	F_L	Liquefy or Non-liquefy	P_L
0.0~0.5	Masado Soil	7	18	29.1	-	Non-liquefy	-
0.5~2.5	Masado Soil	12	18	30.6	-	Non-liquefy	-
2.5~10.0	Masado Soil	17	18	30.4	0.68	Liquefy	11.85
10.0~13.5	Masado Soil	17	18	30.4	0.59	Liquefy	4.69
13.5~14.0	Silty Sand	25	18	34.5	1.29	Non-liquefy	0.00
14.0~17.0	Silty Sand	30	18	36.0	1.57	Non-liquefy	0.00
17.0~20.0	Silty Sand	30	18	39.0	3.26	Non-liquefy	0.00
20.0~23.5	Fine Sand	40	20	39.0	1.88	Non-liquefy	0.00

Incidentally, the development of the plastic hinges at the pile and variations in pile deformation during the different stressed stages can be clearly seen shown in Table 4. It can be seen that the pile will reach the ultimate state when pile head displacement is 0.48m. The distributions of the pile deformations and internal forces under the action of $PGA=0.4g$ are shown in Figure 6. It can be seen that the displacement and rotation of the non-linear pile are very close to those of the field case, and the maximum bending moment and the shear force of the pile were constrained by the ultimate moment M_u . There are two plastic hinges that occur on the pile under the action of the flow pressure. The first one occurs at the interface between the liquefying layer and the non-liquefying layer. The second one occurs at the top of the pile due to the restraint of the pile cap. At these two locations, the rotation angles of the pile change abruptly due to the formations of the plastic hinge angles.



(a) pile plastic hinge

(b) soil spring plastic hinge

Figure 7 Hinge properties of the pile and soil spring

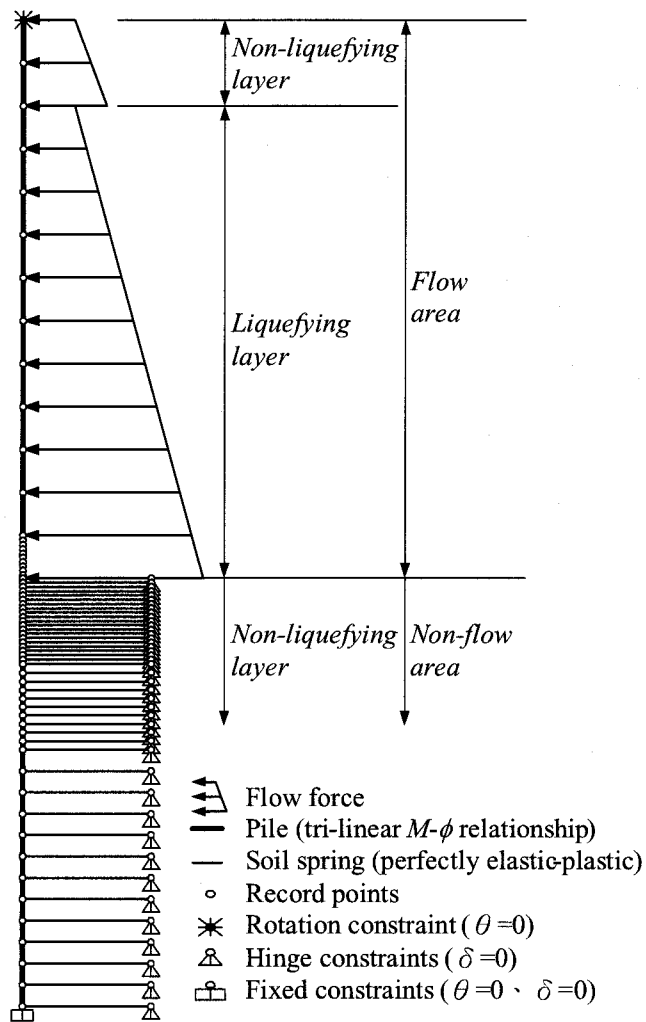


Figure 8 Pushover model of the lateral pile

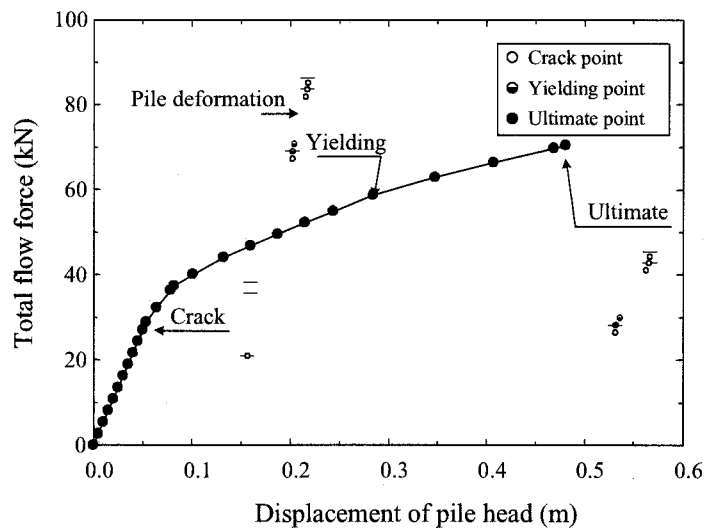
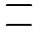
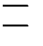

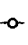




Figure 9 Capacity curve of the pile under tank TA72 using SAP2000

Table 4 Development of the plastic hinges and deformation

Status	Crack	Yielding	Ultimate
Displacement of pile head (m)	0.0536	0.2843	0.4807
Deformation			
Plastic hinge ○ Crack point ● Yielding point ● Ultimate point			

3.3 Correlation of *PGA* with pile damage state

The proposed flow pressure assumption and the non-linear pile analysis model can tentatively provide a practical and valuable methodology, which can be applied to improve seismic performance-based design of the pile when subjected to different liquefaction-induced flow pressures. By the above analysis, we can correlate peak ground accelerations with different damage states of the pile. As we all know, the larger the peak ground acceleration, the more severe the ground liquefaction, and the larger the induced flow pressure. Based on the JRA method, the variations of the total flow force and the liquefaction potential index with the *PGA* for the case site is show in Figure 10. The total flow force increases from zero to a maximum value about 150 kN while the *PGA* varies from 0.295 g to 0.448 g. Since the original pile size is too small to resist the actual flow force caused by 0.4 g, the bending failure occurred at the pile section near the interface of the flow and non-flow areas. To completely show the whole pushover process to the ultimate state, Another B-type PHC pile with a larger diameter of 0.6m is used in the analysis. The pushover analysis is re-carried out and Figure 11 shows the capacity curve of the new pile. The cracking yielding and ultimate states of the pile are marked on the curve with open circles and the *PGAs* inducing different flow forces are marked with solid circles. Based on this figure, the non-linear lateral responses of the pile can be clearly traced when subjected to flow pressures caused by different seismic intensities. Besides, we can understand where and when the plastic hinge will occur and capture the damage mechanism of the pile. We can also easily check if the pile behavior satisfies the seismic demand under the action of the design *PGA* or not. In this case analysis, the maximum moment of the pile is in the ranges between the cracking and the yielding moment when the *PGA* varies from 0.295g to 0.382g. The maximum moment exceeds the yielding moment when the *PGA*=0.4g, and reaches the ultimate moment when the *PGA*=0.448g. As compared with the original pile, the maximum moment of the new pile only exceeds the yielding moment a little and doesn't reach the ultimate state under the action of real *PGA*=0.4g in Kobe earthquake. The top displacement of the new pile is about 0.2m, which is significantly smaller than that of the original pile. This shows that the seismic capacity of the new pile is better than that of the original pile.

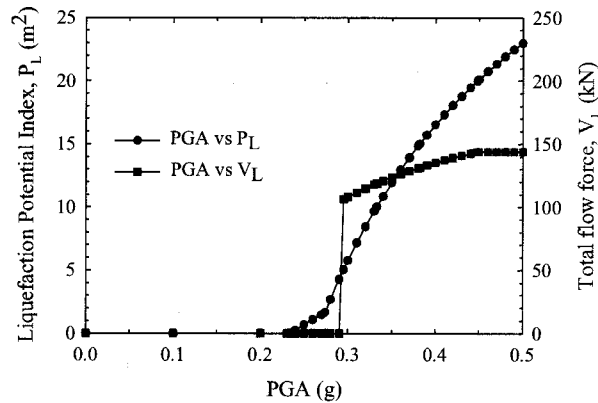


Figure 10 Variations of total flow force and P_L with PGA

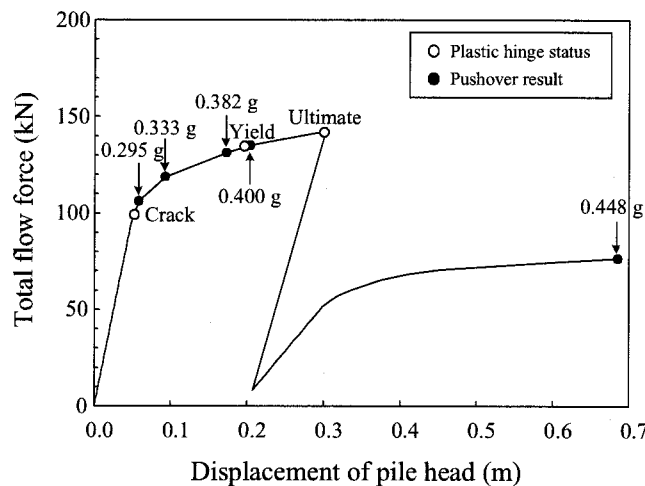


Figure 11 Capacity curve of the new pile ($D=0.60m$)

4. CONCLUSION

This paper presents a simple pushover analysis for the piles subjected to liquefaction induced flow pressure. The analysis is a non-linear static one. It models pile as a tri-linear beam-column member and soil-pile interaction as an elastic-rigid plastic spring. The analysis converts a grouped pile problem to a single pile one, and thus greatly simplifies the problem. The analysis can produce the seismic capacity curve of the lateral pile and provide a close link to the design peak ground acceleration. Based on the curve, engineers can easily perform the seismic performance design.

References:

- CEN/TC250/SC8 (2000), *Eurocode8: Design of structures for Earthquake Resistance - Part1: General Rules Seismic Actions Rules for Buildings*, DRAFT No. 1.
- Computers and Structures, Inc. (1995), *SAP2000 V9 Manuals*, Berkeley, California, USA.
- Ishihara, K. and Cubrinovski, M. (2004) "Case Studies on Pile Foundations Undergoing Lateral Spreading in Liquefied Deposits," *Proceedings of 5th International Conference on Case Histories in Geotechnical Engineering*, New York, CD Rom, Paper SOAP 5.
- Japan Road Association, JRA (1996), *Specifications for Highway Bridges – Part V: Seismic Design*, Tokyo, Japan (in Japanese).
- Structural Engineers Association of California, SEAOC, Vision 2000 Committee (1995), *Performance Based Seismic Engineering of Buildings*, Structural Engineers Association of California, Sacramento, California, USA.
- Chinese Building Industry Publishing House (1989), *Building Code of Earthquake Resistance Design – GBJ11-89*, Beijing, China (in Chinese).

BEHAVIOUR OF PILED BRIDGE ABUTMENT ON LIQUEFIABLE SOILS

A. Takahashi¹⁾, H. Sugita²⁾, and S. Tanimoto³⁾

1) Senior Researcher, Earthquake Disaster Prevention Research Group, Public Works Research Institute, Japan

2) Team Leader, Earthquake Disaster Prevention Research Group, Public Works Research Institute, Japan

3) Researcher, Earthquake Disaster Prevention Research Group, Public Works Research Institute, Japan

aki-taka@pwri.go.jp, sugita@pwri.go.jp, s-tanimoto@pwri.go.jp

Abstract: Seismic response of a bridge abutment located near a river dyke is the consequence of complex interactions among bridge(s), abutment, foundation ground, embankment, river dyke, and associated lateral spreading of liquefied soils. This paper reports result of preliminary dynamic 3D FE analyses on a bridge abutment constructed adjacent to a river dyke, considering liquefaction of foundation soils, and demonstrates importance of consideration of kinematic loading induced by surrounding soils on assessment of seismic response of bridge abutment on liquefiable soils.

1. INTRODUCTION

When seismic performance of a piled road bridge abutment on liquefiable soils is assessed in accordance with the ductility design method adopted in the 2002 Japanese Specifications for Highway Bridges (JRA 2002), as in the other bridge design specifications, we calculate response of the piled abutment subjected to (1) inertia forces of a superstructure and the abutment, and (2) seismic active earth pressure of backfill. In the calculation, liquefaction of foundation soils only contributes to reduce lateral soil resistances in the adjacent soils for simplicity, and no kinematic load induced by interaction between surrounding soils and structure is considered. As a result, the current ductility design method could underestimate horizontal displacement of abutment and pile foundation deformation when (1) a height of the abutment is relatively smaller than a thickness of liquefiable soil layer, and/or (2) liquefied ground adjacent to the abutment laterally spreads (Shirato *et al.*, 2005).

We encounter these kinds of situation when a bridge (1) is built on a floodplain or reclaimed area, i.e., liquefiable ground, and (2) crosses river or channel, and especially (3) its abutment is located adjacent to river dyke or revetment, since the river dyke and revetment easily move waterward during an earthquake and cause lateral spreading of soils when their foundation soils are liquefied. The abutment meets these conditions was damaged at Takenouchi, Tottori in the 2000 Western Tottori Earthquake (Sasaki *et al.*, 2001). Moreover, a road embankment connected to the bridge could be another cause of soil lateral spreading and could make amount of the spreading induced by the river dyke (or revetment) movement larger. As seismic response of bridge abutment on liquefiable soils is the consequence of complex interactions among these, identification of relevant factors that dominate the bridge abutment response for design situation is crucial.

This paper reports result of preliminary dynamic three-dimensional finite element analyses on a bridge abutment constructed adjacent to a river dyke, considering liquefaction of foundation soils, and demonstrates importance of consideration of kinematic loading induced by surrounding soils on assessment of seismic response of bridge abutment on liquefiable soils.

2. NUMERICAL ANALYSIS CONDITIONS

Target road bridge abutment is a piled abutment constructed in a river dyke. Plan view and cross section of the target abutment are illustrated in Fig. 1. The target bridge crosses a river and distance of two opposed abutments was 70m. The abutment foundation consisted of six 2m-cast-in-place concrete piles whose length=20m. The piles were arranged in 2x3 grids having 5m spacing. Width of the bridge was 15m and slope of road embankment connected to the 10m-height piled abutment and river dyke was 1:2. Water level was set 7.5m below the river dyke crest. The ground level was at a height of 5m above riverbed. Thickness of liquefiable layer (loose sand deposit) below water table was 12.5m and materials of the river dyke and road embankment were assumed the same as that of surface layer above water table. The piles were installed in two layers; a bottom non-liquefiable layer (dense sand deposit) and the liquefiable layer.

In the numerical analysis, only half width of the road bridge in y -direction was modelled taking the advantage of symmetry. Width of the analytical domain in y -direction was 100m, length in x -direction was 240m and depth in z -direction from the riverbed was 20m. Soils, wall and base slab of the abutment were modelled by solid elements and piles were modelled by elastic beam elements whose flexural rigidity was set to that at main reinforcement yielding. The extended subloading surface model proposed by Hashiguchi & Chen (1998) was adopted for the soil layers. Details of material parameters used and boundary conditions in the analyses are summarised in Takahashi *et al.* (2005) and details of the numerical analysis code is described in Takahashi (2002). Liquefaction resistance of the non-liquefiable and liquefiable layers is summarised as the cyclic shear stress ratio plotted against the number of loading cycles to cause liquefaction in triaxial tests as shown in Fig. 2. Figure 3 shows the applied earthquake motion whose maximum acceleration is 525gal. This was applied in x -direction. In order to obtain the numerical solution, the differential equations were integrated along time. The integration scheme used was Newmark's β method, and the time step for the integration was $\Delta t=0.005$ sec. System damping was represented by Rayleigh damping and the

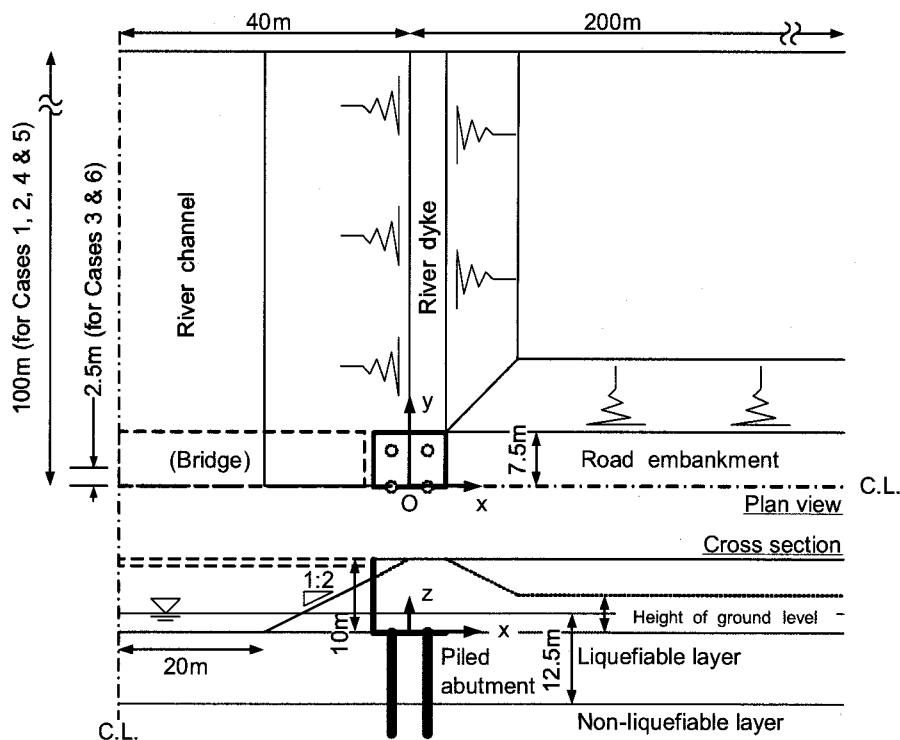


Figure 1 Plan view and cross section of target abutment

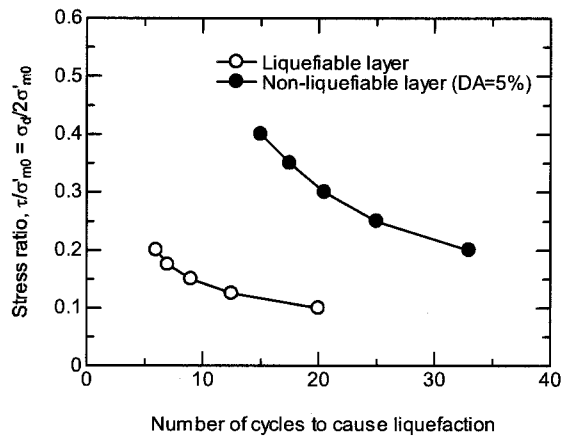


Figure 2 Relationship between cyclic stress ratio and number of cycles to cause liquefaction

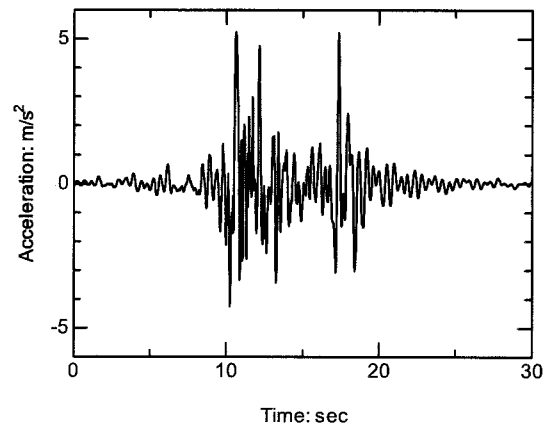


Figure 3 Time history of input motion

Table 1 Analysis conditions

Case	Abutment	River dyke	Ground level	
1	w/ piles	O	5m	
2	w/ piles	O	10m	
3	w/ piles	X	–	Quasi-2D analysis
4	w/o piles	O	5m	
5	w/o piles	O	10m	
6	w/o piles	X	–	2D analysis

damping ratio of 2.5 % in a first mode of free vibration of the system was used.

Addition to the calculation under the conditions mentioned above (Case 1), five calculations were conducted as listed in Table 1. In Case 2, the ground level is set at a height of 10m above riverbed (at the same level of the river dyke crest) in order to demonstrate contribution of waterward deformation of the river dyke on the permanent displacement of the abutment in the comparison between Cases 1 & 2. To gain further insight into the effects of interactions among river dyke, foundation ground and road embankment on the permanent deformation of the abutment, responses of the abutments isolated from the river dyke response and the downslope response of the road embankment were calculated in Case 3. To create such conditions in Case 3, the abutment was modelled as a wall whose length is infinite in y -direction. However still three-dimensional interaction between the piles and soils has to be modelled properly, the three-dimensional FE modelling was employed considering pile spacing (width of the analytical domain in y -direction was set 2.5m as shown in Fig. 1). For easy distinction of Case 3 from Cases 1 & 2, the term 'quasi-2D' will be used to describe the analytical model for Case 3 in the subsequent text. The stabilising effect of the piles on the horizontal movement of abutment will be addressed in Cases 4-6 using a model without piles.

Limitations of the analysis are that (1) bridge(s) and associated bridge pier(s) are not modelled and (2) the abutment top could freely moves without restriction. Interaction between bridge(s) and the abutment was ignored, since our main concern is the interactions among the abutment, foundation ground, road embankment and river dyke. As a result of the limitations mentioned above, calculated

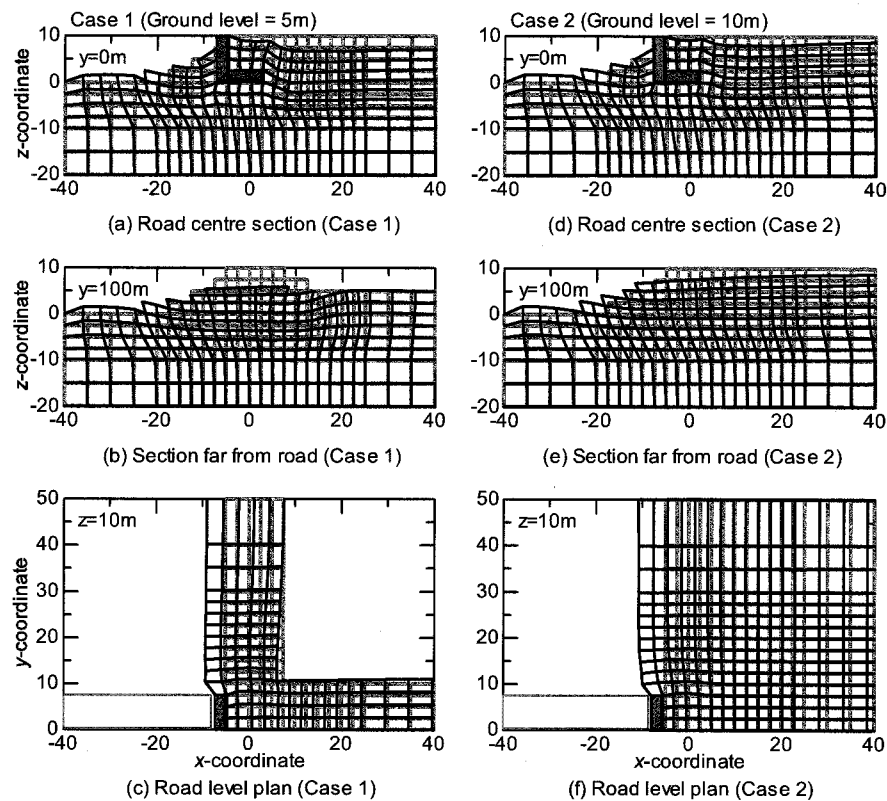


Figure 4 Ground deformations around piled abutment, where displacement scale is magnified by a factor of ten (Cases 1 & 2 at $t=30\text{sec}$)

deformation and/or vibration modes of the abutment could differ from those expected in a realistic bridge-foundation system.

3. ANALYSIS RESULTS AND DISCUSSION

3.1 Responses of Abutment and Surrounding Ground

Ground deformations around the piled abutment (Cases 1 & 2) at $t=30\text{sec}$ (when ground shaking almost ceases) are drawn in Fig. 4. Large shear deformation of the loose sand deposit under the abutment and the connected road embankment was observed in both cases, which probably made the horizontal displacement of the abutment larger. In the case of the ground level is lower than the height of the river dyke crest (Case 1), the road embankment showed relatively large settlement and marked settlement occurred just above the heel of the abutment base: This was due to the downslope displacement of the road embankment and resulted in larger horizontal displacement of the river dyke adjacent to the abutment compared to that far from the road embankment (see ground deformation at the river dyke crest level, the lower graphs in Fig. 4). Although the plots for the abutment without piles (Cases 4 & 5) are not shown here, they are more or less the same as those for the piled abutment, except the abutment tilting (remarkable tilting of the abutment were seen in Cases 4 & 5) and relative horizontal displacement between the river dyke and abutment (the relative displacement was not so large).

Despite the fact that the above-mentioned permanent deformations of the abutment and surrounding soils were caused by generation of the excess pore water pressure at the loose sand deposit, it doesn't necessarily mean that the full liquefaction took place all over the area: the loose sand deposit just under the river dyke and road embankment was not fully liquefied while full

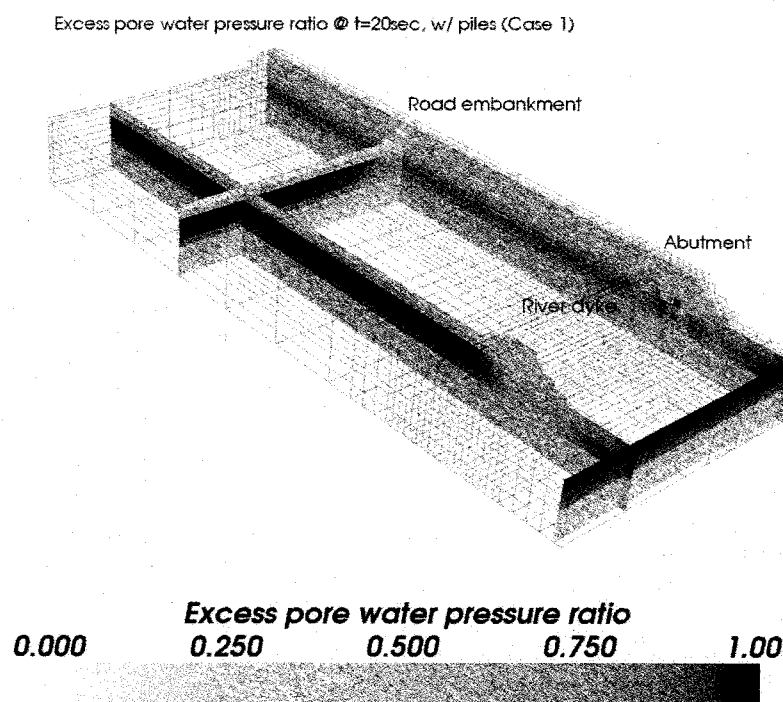


Figure 5 Excess pore water pressure ratio contours at $t=20\text{sec}$ (Case 1)

liquefaction took place in the other area as shown in Fig. 5.

Figure 6 plots time histories of the horizontal displacement of the abutment top for all the cases. In general the horizontal displacement of the abutment increased with shaking and two large fluctuations in the horizontal displacement time histories coincided with the two large shocks in the input motion (see Fig. 3). As expected the permanent displacements of the piled abutment (Cases 1-3) were smaller than those of the abutment without piles (Cases 4-6). And importantly, the permanent abutment displacement was larger than the displacement at the first large shock for all the cases.

Figure 7 shows time histories of the coefficient of the earth pressure acting on the abutment back face ($x=5\text{m}$). Before the arrival of the first shock, the earth pressure acting on the abutment back face was kept more or less constant. At the first shock arrival the earth pressure time histories showed sharp spikes and then the pressure decreased to certain levels in all the cases. For the cases without piles (Cases 4-6) and the case with the lower ground level (Case 1), the earth pressure coefficient after the main shock kept smaller values (very close to the active earth pressure coefficient) while that was relatively large for the piled abutment cases with the higher ground level (Case 2) and the quasi-2D case (Case 3).

When seismic performance of a piled road bridge abutment is assessed in accordance with the ductility design method adopted in the current specifications, the event at the first main shock arrival is thought to be critical for the abutment. However, in all the cases, the horizontal displacements of the abutment when the maximum earth pressure acts on the abutment are not the maximum displacements throughout shaking. This evidence supports that the situation considered in the current specifications is not necessarily critical for the abutment and importance of consideration of the permanent deformation of surrounding soils for the abutment performance assessment. Comparisons and discussion on the abutment responses for the cases with and without consideration of abutment-river dyke interaction will be made later.

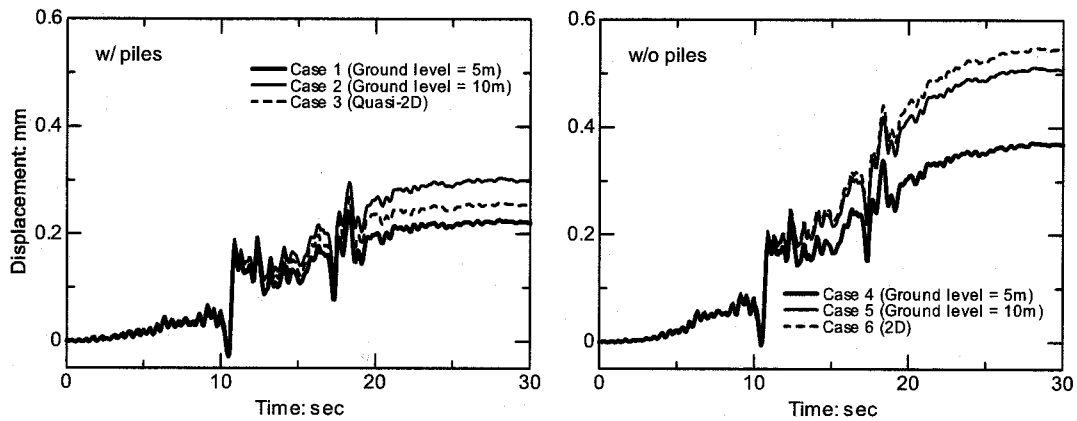


Figure 6 Time histories of horizontal displacement of abutment top

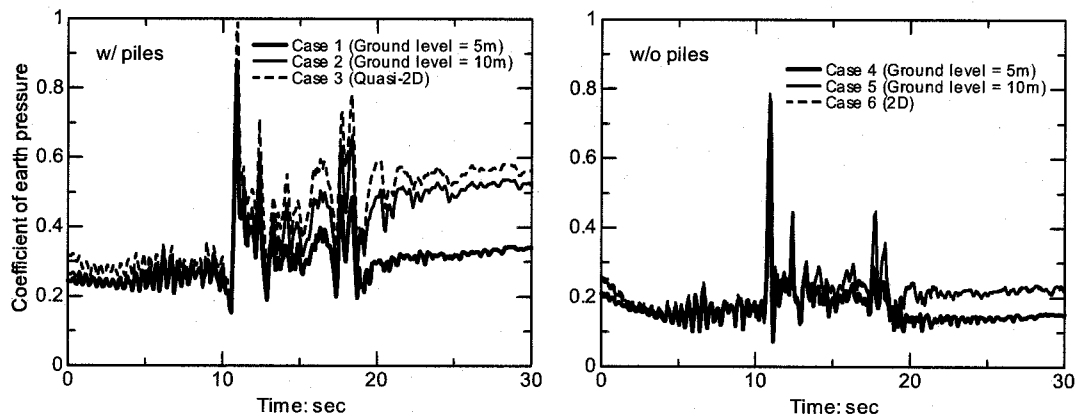


Figure 7 Time histories of coefficient of earth pressure acting on abutment back face

3.2 Pile Foundation Responses

Distributions of pile bending moment at $t=10.88\text{sec}$ (when the earth pressure acting on the abutment was maximum) are plotted in Fig. 8 for Cases 1-3 together with the maximum and minimum bending moment distributions throughout shaking (plotted in dashed lines). Since all the bending moment distributions of the piles were almost the same irrespective to the pile position, average values for all the piles are plotted in this figure. Surprisingly, at the pile head ($z=0\text{m}$) and at the interface between the liquefiable and non-liquefiable layers ($z=10\text{m}$) where the large bending moments were observed, the bending moments at $t=10.88\text{sec}$ coincide with (or are very close to) the maximum bending moments throughout shaking.

Figure 9 plots time histories of the pile bending moment at $z=0$ and 10m for Cases 1 & 2. Although continuous changing trends of the bending moment were observed, the bending moments at the first large shock were maximums in the analyses (except at $z=10\text{m}$ in Case 2). This fact implies that at a large shock arrival piles are in critical situation against bending when an inland direct strike type earthquake motion like Fig. 3 is considered, while it may be not necessarily true against an earthquake having long duration like a plate boundary type earthquake.

3.3 Three-dimensional Effects on Permanent Abutment Displacement

Table 2 tabulates the horizontal abutment top displacements and the maximum backfill settlement

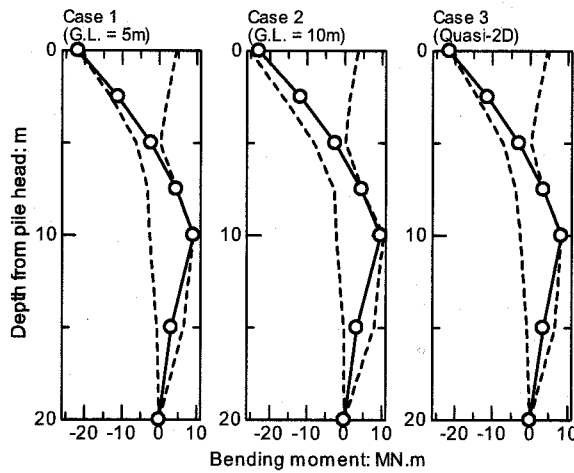


Figure 8 Distributions of pile bending moment at $t=10.88\text{sec}$ together with maximum and minimum values throughout shaking

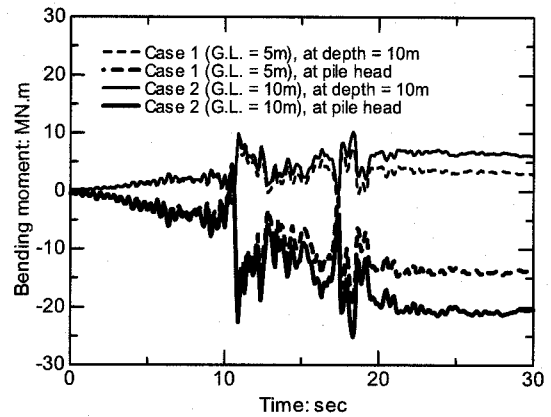


Figure 9 Time histories of pile bending moment at $z=0$ and 10m (Cases 1 & 2)

Table 2 Summary of permanent deformation of abutment ($t=30\text{sec}$, unit: mm)

Case	Maximum backfill settlement	Abutment horizontal displacement
1	330	220
2	200	300
3	210	250
4	370	370
5	230	510
6	220	550

at $t=30$ (at the end of shaking) for all the cases. When comparisons of the horizontal abutment displacements for the different ground level are made, it can be noticed that the horizontal displacements of the abutment for the cases with the higher ground level (Cases 2 & 5) are closer to those for the quasi-2D cases (Cases 3 & 6), while those for the lower ground level cases (Cases 1 & 4) are much smaller than those for the quasi-2D. This fact is naturally acceptable since the downslope (normal to the bridge axis) movement of the road embankment may reduce amount of lateral spreading of soils toward river channel induced by backfill. The fact also suggests that the quasi-2D analysis gives us conservative results for the horizontal displacement assessment as a whole, while this is not true when Cases 2 & 3 are compared (reasons for this will be explained later). On the other hand, regarding the backfill settlement, the settlement for the lower ground level cases (Cases 1 & 4) is much larger than that for the other cases. These facts indicate that seismic performance assessment of an abutment made by the quasi-2D analysis is conservative for the horizontal displacement, but not for the backfill settlement. However, as recovery of the backfill settlement is normally much easier than restoration of the horizontally displaced abutment, the (quasi-) 2D analysis is probably enough for the assessment for the life-safety objective under a rare earthquake (Level 2 earthquake) in the design procedure.

The horizontal displacement of the non-piled abutment in the 2D analysis (Case 6) is larger than that in 3D analysis (Case 5), while the contrary result is obtained for the piled abutment (Cases 2 & 3)

as mentioned above. This is probably due to the interaction between abutment and river dyke and difference in amount of relative horizontal displacement between them may have played an important role for this: For the non-piled abutment cases, as the abutment displacement was large, the relative horizontal displacement between abutment and river dyke was small, resulting in the smaller waterward frictional force acting on the abutment side wall (the force was less than 10% of the horizontal force caused by the earth pressure acting on the abutment back face). On the contrary, the relative displacement was large and the waterward frictional force acting on the abutment side wall was more than 80% of the force acting on the abutment back face for the piled abutment case. The ignorance of this frictional force in the quasi-2D analysis (Case 3) made the horizontal displacement of the abutment smaller than that for the 3D analysis (Case 2). Although this effect depends on many factors, e.g., type of revetment, abutment embedment condition, and the other configurations, designers should take thought for it when the performance assessment is made by (quasi-) 2D analysis.

4. CONCLUSIONS

Preliminary dynamic three-dimensional finite element analyses on a bridge abutment constructed adjacent to a river dyke were performed to demonstrate importance of consideration of kinematic loading induced by surrounding soils on assessment of seismic response of bridge abutment on liquefiable soils. Key findings obtained are as follows:

1. Permanent abutment displacement obtained is larger than the displacement at the large shock in an earthquake motion, although the event at the main shock arrival is thought to be critical in the current design specifications. This evidence demonstrates importance of consideration of the permanent deformation of surrounding soils for the abutment performance assessment.
2. Calculated bending moment of piles reveals that at a large shock arrival piles are in critical situation against bending when an inland direct strike type earthquake motion is considered, while it may be not necessarily true against an earthquake having long duration like a plate boundary type earthquake.
3. Seismic performance assessment of an abutment made by the quasi-2D analysis is conservative for the horizontal displacement, but not for the backfill settlement. However, as recovery of the backfill settlement is normally much easier than restoration of the horizontally displaced abutment, (quasi-) 2D analysis is probably enough for the assessment for the life-safety objective under a rare earthquake in the design procedure.

References:

- Hashiguchi, K. & Chen, Z.P. 1998. Elastoplastic constitutive equation of soils with the subloading surface and the rotational hardening. *International Journal for Numerical and Analytical Methods in Geomechanics*, Vol.22, 197-277.
- Japan Road Association. 2002. Specifications for road bridges, Part V, Seismic Design, 333pp.
- Sasaki, T., Matsuo, O., Kobayashi, H., Watanabe, T. & Maeda, T. 2001. Abutment damage induced by lateral spreading in the 2000 Western Tottori Earthquake, *Proceedings of 56th Annual Conference of JSCE*, 3-A, 230-231 (in Japanese).
- Shirato, M., Fukui, J. & Koseki, J. 2005. Current status of ductility design of abutment foundations against large earthquakes, *Soils and Foundations*, (submitted).
- Takahashi, A. 2002. Soilpile interaction in liquefaction-induced lateral spreading of soils, DEng. Dissertation, Tokyo Institute of Technology.
- Takahashi, A., Sugita, H. & Tanimoto, S. 2005. Permanent deformation of bridge abutment on liquefiable soils, *Proceedings of 21st US-Japan Bridge Workshop*.

OBSERVED PILE-SOIL INTERACTION DURING BUCKLING INSTABILITY

S. Bhattacharya¹⁾ and K. Tokimatsu²⁾

1) Departmental Lecturer in Engineering Science, University of Oxford, (United Kingdom), previously Centre for Urban Earthquake Engineering (CUEE), Tokyo Institute of Technology (Japan)

*2) Professor, Dept. of Architecture and Building Engineering, Tokyo University of Technology, (Japan)
subhamoy.bhattacharya@eng.ox.ac.jp, kohji@o.cc.titech.ac.jp*

Abstract: Collapse of structures resting on piled foundations is still observed in liquefiable soils after strong earthquakes. Buckling of piles due to the loss of lateral support owing to liquefaction has been identified as one of the failure mechanisms. Essentially, if piles are too slender, they require lateral support from the surrounding soil if they are to avoid buckling instability. This lateral support can fall to near zero due to seismic liquefaction and a slender pile may buckle. This paper postulates a hypothesis of pile-soil interaction during buckling instability. Centrifuge test results are presented to verify the hypothesis.

1. INTRODUCTION

Pile-supported structures founded on or passing through liquefiable soils still collapse during earthquakes, for example 1995 Kobe earthquake, 1999 Turkey earthquake or the 2001 Bhuj earthquake. As earthquakes are very rapid events and as much of the damage to piles occurs beneath the ground, it is hard to ascertain the failure mechanism unless deep excavations are carried out. Excavations were carried out at various sites in Japan, (see for example NHK building site in Niigata) which showed the piles beneath the foundation suffered structural failure by formation of plastic hinges. Similar observations of plastic hinge formations in piles were reported by Tokimatsu et al (1997) in a 3-storied building after the 1995 Kobe earthquake and by Fukuoka (1966) in the well known Showa Bridge failure.

During earthquakes, the predominant loads acting on a pile are: (a): Axial load (P) that acts at all times on a pile. The axial load may increase due to inertial effect of the superstructure and kinematic effects due to soil movement. (b): Inertia loads due to the superstructure which is oscillating in nature. (c): Loads due to ground movement commonly known as kinematic effects. This load can be of two types, such as transient (during shaking due to the dynamic effects) and residual (after the shaking ceased due to lateral spreading).

As mentioned earlier, excavations of the piles showed the formation of plastic hinges. This implies that there were structural failures in the pile. The fundamental failure mechanisms for a structural concrete or steel section are: (a) Shear failure in the pile due to the lateral loads such as inertia or kinematic loads or a combination of the above. This is particularly damaging to hollow circular concrete piles (non-ductile) with a low shear capacity. (b): Bending failure due to the combined effect of lateral and axial loads i.e. formation of a collapse mechanism. (c): Buckling failure in slender piles due to the effect of axial load and the loss of surrounding confining pressure provided by the soil owing to liquefaction, see Bhattacharya (2003). Buckling is sensitive to imperfections such lateral loads, out-of-line straightness. This would imply that in presence of lateral loads, a pile would buckle at a load much lower than the Euler's Critical Load.

The aim of the paper is two folds: (a) to discuss the different phases of loading experienced by a pile during seismic liquefaction. Emphasis is given to the buckling mode of failure. Centrifuge tests were carried out to verify the failure mechanism by buckling instability. (b) To postulate a hypothesis of post-buckling pile-soil interaction.

2. DIFFERENT PHASES OF LOADING IN A PILE DURING SEISMIC LIQUFACTION AND BUCKLING INSTABILITY

During earthquakes, soil layers overlying the bedrock are subjected to seismic excitation consisting of numerous incident waves, namely shear (S) waves, dilatational or pressure (P) waves, and surface (Rayleigh and Love) waves which result in ground motion. The ground motion at a site will depend on the stiffness characteristics of the layers of soil overlying the bedrock. This motion will also affect a piled structure. As the seismic waves arrive in the soil surrounding the pile, the soil layers will tend to deform. This seismically deforming soil will try to move the piles and the embedded pile-cap with it. Subsequently, depending upon the rigidity of the superstructure and the pile-cap, the superstructure may also move with the foundation. The pile may thus experience two distinct phases of initial soil-structure interaction:

Before the superstructure starts oscillating, the piles may be forced to follow the soil motion, depending on the flexural rigidity (EI) of the pile. Here the soil and pile may take part in kinematic interplay and the motion of the pile may differ substantially from the free field motion. This may induce bending moments in the pile.

As the superstructure starts to oscillate, inertial forces are generated. These inertia forces are transferred as lateral forces and overturning moments to the pile via the pile-cap. The pile-cap transfers the moments as varying axial loads and bending moments in the piles. Thus the piles may experience additional axial and lateral loads, which cause additional bending moments in the pile.

These two effects occur with only a small time lag. If the section of the pile is inadequate, bending failure may occur in the pile. The behaviour of the pile at this stage may be approximately described as a beam on an elastic foundation, where the soil provides sufficient lateral restraint. The available confining pressure around the pile is not expected to decrease substantially in these initial phases. The response to changes in axial load in the pile would not be severe either, as shaft resistance continues to act. This is shown in Figure 1 (Stage II).

In loose saturated sandy soil, as the shaking continues, pore pressure will build up and the soil will start to liquefy. With the onset of liquefaction, an end-bearing pile passing through liquefiable soil will experience distinct changes in its stress state.

The pile will start to lose its shaft resistance in the liquefied layer and shed axial loads downwards to mobilise additional base resistance. If the base capacity is exceeded, settlement failure will occur.

The liquefied soil will begin to lose its stiffness so that the pile acts as an unsupported column as shown in Figure 1 (Stage III). Piles that have a high slenderness ratio will then be prone to axial instability, and buckling failure will occur in the pile, enhanced by the actions of lateral disturbing forces and also by the deterioration of bending stiffness due to the onset of plastic yielding. Dynamic centrifuge tests, Bhattacharya, (2003), study of case histories, Bhattacharya et al (2004) numerical work and analytical work carried out has conclusively shown the above failure mechanism. Figure 2 shows some photographs of buckling failures of piles. This particular mechanism is not explicitly mentioned in most codes of practice.

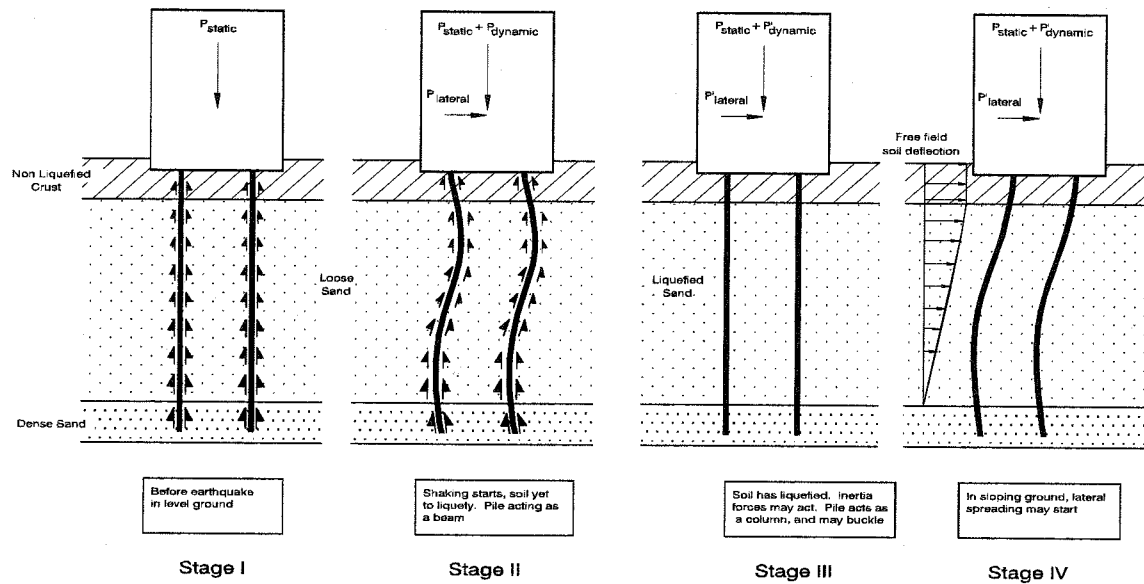


Figure 1: Different phases of loading in a pile

In sloping ground, even if the pile survives the above load conditions, it may experience additional drag load due to the lateral spreading of soil. Under these conditions, the pile may behave as a beam-column (column with lateral loads); see Figure 1 (Stage IV). This bending mechanism is currently considered most critical for pile design and is incorporated in JRA (1996).

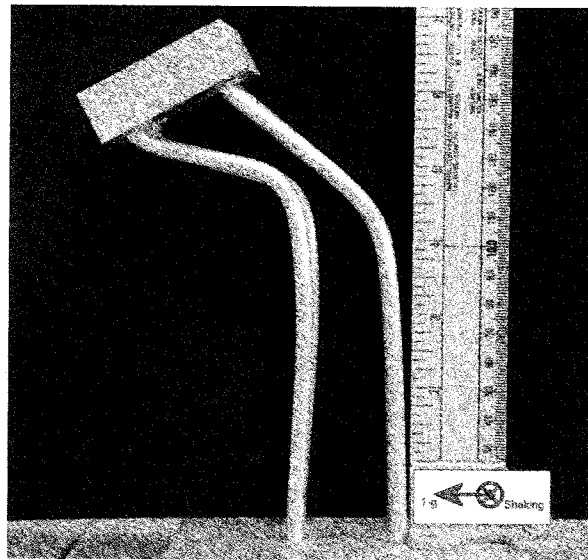
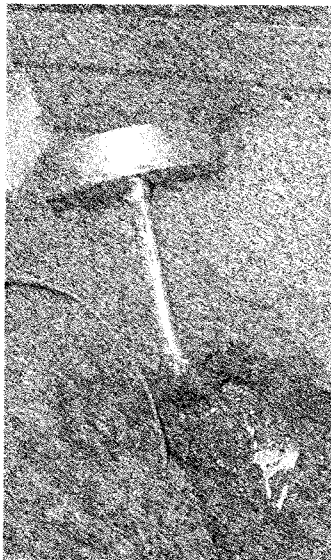


Fig 2(a): Buckling of single pile as observed in a 50-g centrifuge test, see Bhattacharya (2003). Figure 2(b): Buckling of a group of piles in a centrifuge test, Knappett and Madabhushi (2005)

3. OBSERVED PILE-SOIL INTERACTION DURING BUCKLING INSTABILITY

Sufficient information has been obtained from the centrifuge models to propose a hypothesis of pile-soil interaction during a buckling event. The pile begins to buckle when the front of zero effective stress reaches a critical depth H_C . This buckling instability will cause the pile to shear the soil adjacent to it,

which will start offering. Figure 3 schematically shows the pile-soil interaction during the post-buckling period.

The soil element in front of the buckling pile, marked A in Figure 3, will be subjected to monotonic shearing in addition to the cyclic shearing due to the earthquake. The “ V/k ” ratio (i.e. the ratio of velocity of the pile to the permeability of the soil) which was of the order of 100’s, suggests that the event is best looked upon as undrained. The resistance to the buckling pile is due to this “undrained strength of the soil”, which is the strength when sheared at constant volume. It should be obvious from the definition that the stress path must follow the Critical State line, defined by Schofield and Wroth (1968).

In the q - p' plot shown in Figure 4, a soil element during the pre-buckling period, will start from some point in the q - p' plot, shown by X, and generate positive pore pressure due to the earthquake shaking. The stress path will progress towards the origin until it hits the “Phase Transformation” line.

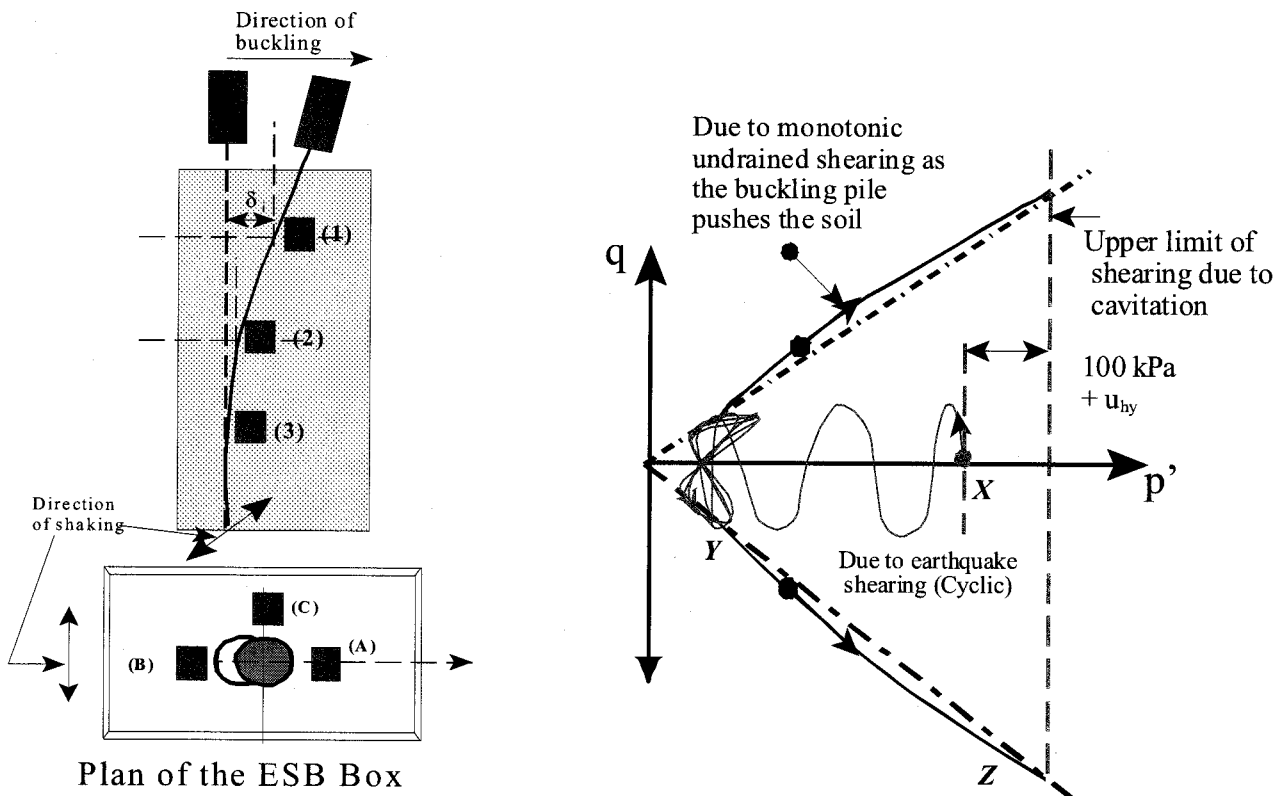


Figure 3: Schematic diagram of pile-soil interaction during buckling. Figure 4: Stress path of a soil element close to the pile, where u_{hy} = hydrostatic pressure

The stress path will run up and down like a butterfly wing passing through or near the origin. At the same time, the pile length will progressively be unsupported by the soil grains, in top down fashion, until the critical depth is reached. As the critical depth is reached the pile starts to buckle. The behaviour of a soil element in front of the pile (marked A in Figure 3) can be described as similar to “Triaxial Extension” while the soil behind the pile (marked B in Figure 3) can be described as similar to “Triaxial Compression”. Due to the mode shape of the pile, the top-soil in the near field (marked 1 in Figure 3) will be sheared more than the bottom soil in the near field (marked 3 in Figure 3).

The imposition of undrained monotonic shear strains (pile pushing the soil) in loose to medium dense sand at low effective stresses will lead to an attempt to dilate. The event being at constant volume will suppress this potential dilatancy by a negative increment of pore pressure in the locally sheared soil. This negative increment of pore pressure creates an increase in effective stress, which temporarily provides support to the buckling pile.

The pore fluid pressure in the sheared zone can drop to a maximum of -100kPa, which would correspond to the greatest possible effective stress increment during shearing. Beyond this value, vapour bubbles tends to nucleate. On the stress path the soil element in front of the pile moves from Y to Z, Figure 4. This local reduction of pore pressure would induce a transient flow into the sheared soil from the neighbouring “liquefied but not monotonically sheared soil” shown schematically in Figure 5. The lateral resistance of the liquefied soil would then decrease.

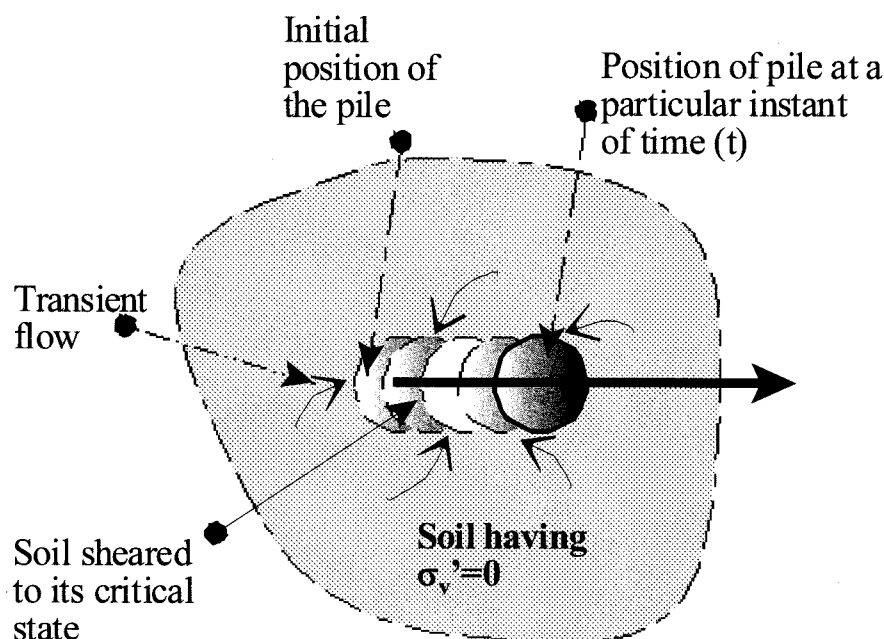


Figure 5: Transient flow

It is the upper part of a liquefiable sand layer that remains longest in a state of zero effective stress due to upward hydraulic gradients. It is also the upper part of the pile which displaces most, and which can fully soften to zero shear strength the supporting soil adjacent to it. Ultimately, therefore, the upper part of the soil can be properly described as liquefied, in the true sense of the word in science or common language, according to the necessary conditions laid down by Schofield (1981). For the lower part of the pile, the resistance will increase as the pile shears the “initially liquefied soil” but not for a sufficient duration. This is due to the development of negative pore pressure in the sheared soil which will induce transient flow from the neighbouring “liquefied but not monotonically sheared” soil. The buckling pile will also suffer increasing loss of bending stiffness due to plastic yielding, so the restraint necessary to hold it in equilibrium will also increase.

This imbalance between increasing bending moment created by displacement of pile cap, deteriorating bending stiffness of the pile and the reducing differential soil support along its length, creates a shallow plastic hinge which then leads to the dynamic collapse of the structure.

3.1 A typical PPT result from a centrifuge test

To verify the hypothesis of pile-soil interaction, measurements were taken in a centrifuge test. In the test, the pile had an axial load of 872N and the outside diameter is 9.3mm. Pore Pressure Transducers (PPT) were placed in the front and at the back of a pile in the direction of buckling. The buckling of the pile was guided in the direction of the pore pressure by restraining the pile in the orthogonal direction. Figure 6 compares the PPT traces at 2.6m depth (equivalent prototype depth). PPT 6260 measures pore pressure in the front of the pile, i.e. in the direction of eventual buckling i.e. pore pressure at the soil element A in

Figure 3. PPT 6793 records the pore pressure behind the pile (i.e. pore pressure at the soil element B in Figure 3). PPT J13 records the far field pore pressure.

At first, up to 0.4 s, the three PPTs record the same pressures rising to the state of zero effective stress. Then, until 1.0 s the PPT in front of the pile (PPT 6260) shows a circa 10 kPa reduction of pore pressure with additional sharper downward spikes at each earthquake cycle. The PPT behind the pile (PPT 6793) shows positive spikes which are at first out of phase with those in front and which then come in phase. The cyclic component of the PPT data behaviour is clearly related to the shaking, and therefore to motions orthogonal to the eventual direction of buckling. But the steady component of pore pressure reduction in front of the pile must be due to suppressed dilation as the pile begins to push the previously “liquefied” soil aside. Evidently the soil in that zone is liquefied no longer, but enjoys a vertical effective stress of between 10 and 20 kPa – enough for the pile to receive significant support – again, temporarily.

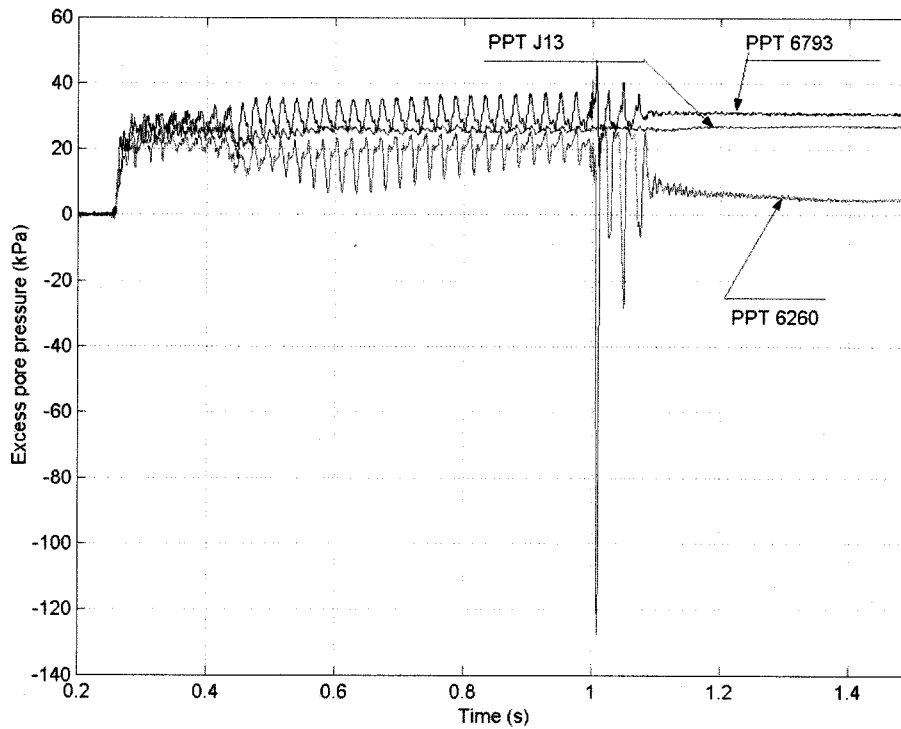


Figure 6: Near field (PPT 6260 & PPT 6793) and far field (PPT J13) pore pressure measurements.

4. ANALYTICAL SOLUTIONS FOR POST-BUCKLING PILE SOIL INTERACTION

This section makes an attempt to model analytically the pile-soil interaction after the pile has buckled and during shearing of the soil next to it. Prediction of some of the results of the centrifuge tests is also attempted. This section attempts to predict the pore pressure generation. Figure 7 shows the free body diagram of a buckling pile in liquefied soil. It will be assumed that the undrained resistance of the liquefied soil holds the pile in quasi-static equilibrium until the transient flow feeds the dilation of the shearing soil and reduces the resistance. The pile then moves to a new equilibrium position. In this analysis, dynamic effects are not taken into consideration. The mobilisable undrained resistance of the soil (w) is assumed to be constant with depth and is the difference in pressure between front and back of the pile in the direction of buckling.

From the moment equilibrium at any depth z , the differential equation 1 obtained

$$EI \frac{d^2 y}{dz^2} = - \left(P \cdot y - w \cdot \frac{z^2}{2} \right)$$

Equation 1

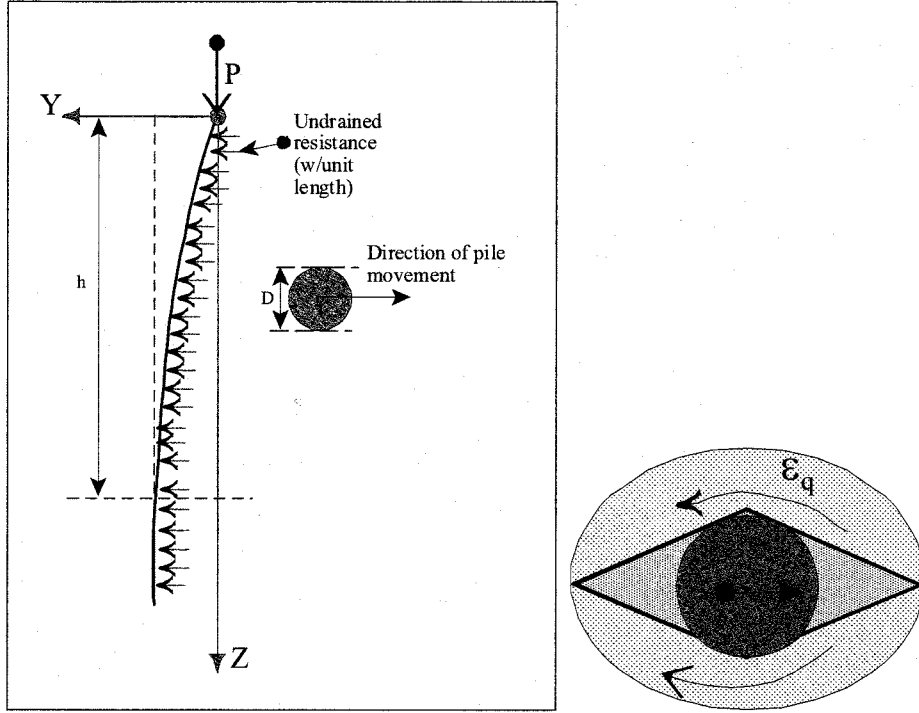


Figure 7: (a): Free body diagram of a buckling pile; (b): Undrained mechanism around a moving pile

Rearranging equation 1 gives the equation 2

$$\frac{d^2 y}{dz^2} + \left(\frac{P}{EI} \right) \cdot y - \frac{w}{2EI} z^2 = 0$$

Equation 2

The general solution of Equation 2 is given by Equation 3

$$y = A \cdot \sin(\lambda z) + B \cdot \cos(\lambda z) + \left(\frac{w}{2P} \right) \cdot z^2 - \left(\frac{wEI}{P^2} \right)$$

Equation 3, where

$$\lambda = \sqrt{\frac{P}{EI}}$$

Applying the following boundary conditions

- At $z = 0$; the relative pile head displacement is zero i.e. $y = 0$.

- At $z = h$; the slope is zero i.e. $\left(\frac{dy}{dz} \right) = 0$,

The general expression for deflection is obtained as equation 4.

$$y = \frac{w}{P \cdot \lambda^2} \left[\left(\tan(\lambda h) - \frac{\lambda h}{\cos(\lambda h)} \right) \sin(\lambda z) + \cos(\lambda z) + \frac{(\lambda z)^2}{2} - 1 \right]$$

Equation 4

The above equation is only stable for $\lambda h < (\pi/2)$ i.e. P less than P_{cr} (Critical load).

Making an engineering assumption that curvature is zero at $z = h$, provides an estimate of the depth h . Imposing the condition, at $z = h$, the second derivative of y is zero, the following condition, equation 5 is obtained.

$$\tan\left(\frac{\lambda h}{2}\right) = \lambda h$$

Equation 5

The first root that satisfies equation 5, is $(\lambda h) = 2.325$ which will give the expression for h.

$$h = 2.325 \sqrt{\frac{EI}{P}}$$

The general equations for displacements and moments are given by Equations 6 and 7 respectively.

Deflection

$$y = \frac{w}{P.\lambda^2} \left[2.33 \sin(\lambda z) + \cos(\lambda z) + \frac{(\lambda z)^2}{2} - 1 \right]$$

Equation 6

Moment

$$M_z = \frac{w}{\lambda^2} [2.33 \sin(\lambda z) + \cos(\lambda z) - 1]$$

Equation 7

Using the above set of equation, the pile head deflection will be estimated:

Pile head deflection (δ)

Substituting $z = h$, the deflection (y) will reveal the pile head deflection (δ) given by Equation 8;

$$\delta = \frac{2.72w}{P.\lambda^2}$$

Equation 8, which

gives

$$w = \frac{0.36P^2\delta}{EI}$$

Equation 9

From the above expression it must be concluded that as the pile deflects, more resistance has to be generated by the soil to keep the pile in quasi-equilibrium. This is in agreement with the pore pressure data of the centrifuge tests, Figure 6, where additional sharper downward spikes were noticed at the end of each earthquake cycle, representing the generation of negative pore pressure compared to its surrounding soil. The undrained resistance of the soil is represented by w (Figure 7) and is the difference in soil reaction due to the horizontal motion of the pile in the liquefied soil. It is assumed that the soil maintains the pile in quasi-static equilibrium and thereby reaches a limiting condition. The stress path of the shearing soil element moves along the critical state line.

At each position of the pile, there is a unique value of q in the q - p' plot (Figure 4) and it may be reasonable to assign a single deviatoric strain (ϵ_q) in the soil in the zone of plastic deformation. The soil in front of the pile will form an “undrained mechanism”, see Figure 7(b). If the shear stress induced in the soil is denoted by τ_p , the ultimate resistance of the soil (w) can be approximated by equation 10, following Randolph and Houlsby (1984).

$$w = 10.\tau_p.D$$

Equation 10

Combining equations 6.20 and 6.22 gives an expression for the limiting shear stress τ_p acting on the pile.

$$\tau_p = \frac{P.\lambda^2}{27.2D} \delta$$

Equation 11

The effective stress or the negative excess pore pressure generated can be estimated using equation 12.

$$p' = \frac{\tau_p}{\sin \phi_{PTL}}$$

Equation 12

where ϕ_{PTL} is the angle of “Phase Transformation”.

For the model pile in the centrifuge test (Figure 6), $P = 872\text{N}$, $D = 9.3\text{mm}$, $EI = 7.77 \times 10^{-6}\text{N.mm}^2$, $\phi_{PTL} = 32^\circ$. For 20mm movement, it is expected to have a mean effective stress increase of 10 kPa. This should also be the amount of negative excess pore pressure to be generated in the locally sheared soil relative to the liquefied far field. PPT records show that the suction generated was of the order of 10 to 15 kPa.

4. CONCLUSIONS

The failure of pile-supported structures during earthquakes in liquefiable level ground may be decomposed into three phases: (a) Soil and pile response to earthquakes, (b) Pile response to soil stiffness degradation; (c) Soil response to pile buckling behaviour. The first phase is the generation of excess pore pressure in the soil whereby the effective stress comes to oscillate near zero. The piled structure also vibrates. In the second phase, the piled structure may become unstable, depending on the axial load and the pile material. In other words, the response would dictate whether the pile would buckle and push the soil monotonically. In the third phase, if the pile buckles, it would shear the initially liquefied soil; there would be local reduction of pore fluid pressure inducing a transient flow.

Seismic pile-soil interaction in liquefiable soil is a very complex phenomenon involving different mechanisms and physical processes. All the processes are highly non-linear. For example, buckling is itself non-linear and earthquake perturbations makes it even more non-linear. The pre-buckling behaviour of pile is governed by the “Euler’s elastic critical load” and the post-buckling behaviour is controlled by “Critical State” soil mechanics. The pile-soil interaction in level ground can be described as a combination of two critical phenomena and transient flow.

Acknowledgements:

The authors acknowledge the support from Japan Ministry of Education, Culture, Sport, Science, and Technology (MEXT) for establishing the Center for Urban Earthquake Engineering (CUEE) in Tokyo Institute of Technology.

References:

- Bhattacharya, S (2003): Pile Instability during earthquake liquefaction, PhD thesis, University of Cambridge (U.K).
- Bhattacharya, S., Madabhushi, S.P.G., and Bolton, M.D. (2004): “An alternative mechanism of pile failure in liquefiable deposits during earthquakes”, *Geotechnique* 54, April issue, No.3.
- Fukuoka, M (1966): “Damage to Civil Engineering Structures”, Soils and Foundations, Tokyo, Japan, Volume-6, No-2, March 1966, pp 45-52
- J.R.A (1996): Japanese Road Association Code, Highway bridge specification, Part 5.
- Knappett, J.A and Madabhushi, S.P.G (2005): “Instability of slender pile groups during earthquake-induced liquefaction”, Proceedings SECED Young Engineers Conference, University of Bath (U.K), 21-22 March, 2005.
- Knappett, J.A and Madabhushi, S.P.G (2005): “Instability of slender pile groups observed in dynamic centrifuge tests”, Workshop on piled foundations, University of California (Davis), ASCE Special Publications.
- Randolph, M.F and Houslby, G.T (1984): “The limiting pressure on a circular pile loaded laterally in cohesive soil”, *Geotechnique* 34, No 4, pp 613-623
- Schofield, A. N. and Wroth, C.P (1968): “Critical State Soil Mechanics”. Mc Graw-Hill, London.
- Schofield, A. N. (1981): “Dynamic and Earthquake Geotechnical Centrifuge Modelling”, Proceedings of the International Conference Recent Advances in Geotechnical Earthquake Engineering and Soil Dynamics, Vol. 3, 1081-1100.
- Tokimatsu, K., Oh-oka Hiroshi, Satake, K., Shamoto Y. and Asaka, Y (1997): “Failure and deformation modes of piles due to liquefaction-induced lateral spreading in the 1995 Hyogoken-Nambu earthquake”, *Journal Struct. Eng. AIJ (Japan)*, No-495, pp 95-100.

DYNAMIC BEHAVIOR OF EMBANKMENTS RESTING ON LIQUEFIABLE SANDY DEPOSIT

T. Tobita¹⁾, S. Iai²⁾, and K. Ueda³⁾

1) Assistant Professor, Disaster Prevention Research Institute, Kyoto University, Japan

2) Professor, Disaster Prevention Research Institute, Kyoto University, Japan

3) Graduate student, Department of Civil and Earth Resource Engineering, Kyoto University, Japan
tobita@geotech.dpri.kyoto-u.ac.jp, iai@geotech.dpri.kyoto-u.ac.jp, ueda@geotech.dpri.kyoto-u.ac.jp

Abstract: Dynamic behavior of an embankment (3 m height) made of dry sand underlain by saturated sand deposit with 5 m depth were studied. Firstly, centrifuge experiments under 50 G were conducted. The relative density of saturated sand deposit was approximately either 30 % or 70 %. Sinusoidal input motions with various levels of peak acceleration amplitude were employed. Test results show that the maximum settlement was 1.4 m and 0.09 m, respectively, for loose and dense deposit. The amount of settlements for dense deposit were found to be proportional to the peak amplitude of input acceleration, while it may have a plateau for the case of loose deposit with increase of input acceleration amplitude. Following the centrifuge experiments, an effective stress analysis was carried out with the same prototype dimension of the experiments. The numerical analysis simulated well deformations and transient motions of the experimental counterparts. It was found that, in the analysis for loose deposit, when input acceleration increased, non-liquefied area underneath the embankment became large, causing larger non-liquefied wedge pushing liquefied soils aside.

1. INTRODUCTION

Liquefaction have caused tremendous damage to earth structures, such as, earth dams, embankments and river dikes (Bardet and Davis 1996, Seed et al. 1975, Seed et al. 1990). After the 1995 Hyogo-ken Nanbu, Japan, earthquake, for example, river dikes along the Yodo river with total length of about 9.3 km were severely damaged due to liquefaction (Matsuo 1996). After the 2003 Tokachi-oki, Japan, earthquake, river dikes were damaged at 66 locations with total length of about 27 km (Nishimoto 2003). Not only the failure of structures themselves, but also second disaster, such as inundation or flooding, may occur after their collapses [e.g., the 1948 Fukui, Japan, earthquake (GHQ-Report 1948)]. Triggered by those devastating damage after large earthquakes, dynamic behavior of an embankment have been studied experimentally and numerically by many researchers. Extensive literature review can be found in Adalier et al. (1998).

Experimental studies have been conducted using the shaking table in 1G field, [e.g. Koga and Matsuo (1990)] or centrifuge field [e.g., Adalier et al. (1998); Adalier and Sharp (2004); Fiegel and Kutter (1994); Koseki et al. (1994)] Takeuchi et al. (1991) conducted shaking table tests on dikes founded on saturated sand deposit and investigated the effectiveness of compaction as a countermeasure against flow-type of deformation. In a series of tests they conducted, when the area of compaction is in the free field near the toe, compacted area did not move but the dike deformed excessively, while the area of compaction is beneath the dike, the compacted area acted effectively and the deformations were very small.

Kazama et al. (1996) conducted centrifuge testing for an embankment made of sands with two different centrifugal accelerations and verified the applicability of similitude law. They also carried out stability analysis with the Swedish method by taking account of the effects of acceleration and pore water pressure buildup and suggested possibility of the static analysis to the stability of embankments

resting on liquefiable sand deposit.

Major difficulty associated with computation of flow-liquefaction arises when the dynamic behavior of embankments on saturated sand deposit is considered. Yasuda et al. (1999) proposed a static FE method to evaluate the amount of liquefaction-induced flow by using bilinear stress-strain relationship calibrated against data obtained from the combination of cyclic and static loading tests. Their model utilizes the stress-strain curve constituted of low rigidity region and rigidity recovering region as strain being large, and simulates well deformations of structures associated liquefaction-induced flow.

When earth structures were designed or remediation measures are practiced based on displacement criteria which is much cost effective than those based on the factor of safety approach [Finn (2000); ISO23469 (2005)], it is required to specify and verify the criteria for serviceability and safety. Those criteria for embankments may be given by the amount of crest settlements against intensity of input motion. Therefore, the development of methodology to check if a designed structure behaves within those criteria is of prime importance. Thus, one of the main objective of the present study is to verify the applicability of the effective stress analysis proposed by Iai et al. (1992) by comparing results with experimental counterparts. In what follows, units are in prototype, if not otherwise specified.

2. CENTRIFUGE EXPERIMENTS

Experiments were carried out in a rigid wall container mounted on the 2.5 m radius geotechnical centrifuge at the Disaster Prevention Research Institute, Kyoto University (DPRI-KU). Overall dimension of the rigid container is 450 x 150 x 300 mm in length, width, and height, respectively (Fig. 1). Dynamic excitation was given in longitudinal direction. The applied centrifugal acceleration was 50 G. A shake table unidirectionally driven by a servo hydraulic actuator is mounted on a platform and it is controlled through a laptop computer on the centrifuge arm. All the equipment necessary for shake table control is put together on the arm. The laptop PC is accessible during flight from a PC in the control room through wireless LAN and "Remote Desktop Environment" of WindowsXP (Microsoft 2003).

A model configuration shown in Fig. 1 is a cross section of an embankment resting on a saturated sand deposit. The crest height is 3.0 m, and lateral length at the top and bottom are, respectively, 4.0 m and

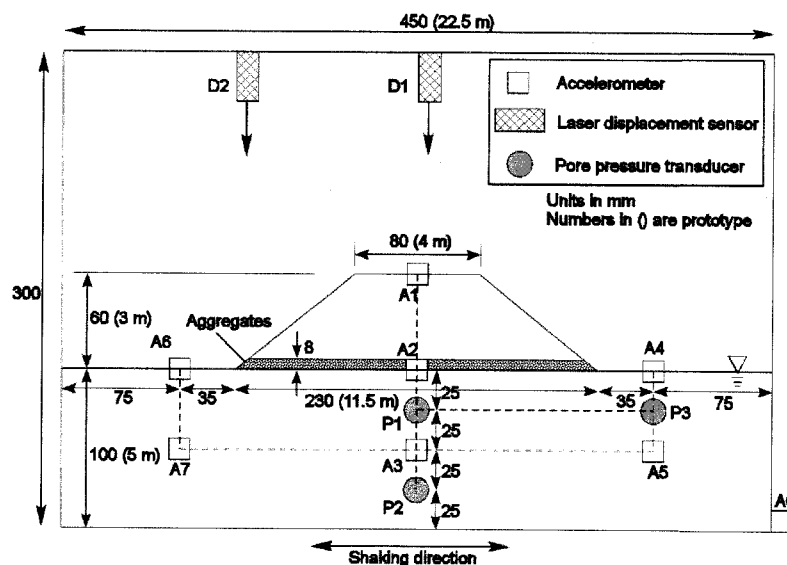


Figure 1. Model configuration in rigid container.

Table 1. Summary of test cases

Case	Soil type	Dr (%)	Max. input acceleration	Settlements (m)
1	Loose	27	81	0.01
2		30	179	1.00
3		30	313	1.40
4	Dense	69	79	0.00
5		71	169	0.01
6		67	574	0.09

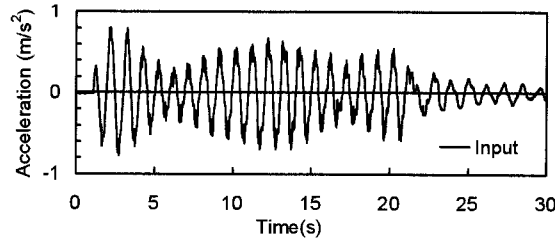


Figure 2. Input acceleration for Case 1.

11.5 m. and side slope of 1:1.25. The model was instrumented with 8 accelerometers (SSK, A6H-50), 2 laser displacement transducers (Keyence, LB-080) and 3 pore water pressure transducers (SSK, P306A-5) (Fig. 1). All the electric data was recorded by digital data recorders (TML, DC-104R) mounted on the centrifuge arm. Sampling frequency was 5 kHz.

Silica sand ("Soma" sand No. 5) ($e_{\max}=1.11$, $e_{\min}=0.69$, $D_{50}=0.38$ mm) were used for both the deposit and embankment. Only the sand deposit was saturated with viscous fluid (Metolose, SM-25 Shin-Etsu Chemical Co.) whose viscosity was adjusted to 50 times of water (50 cSt).

Total six tests were employed as shown in Table 1. Two types of sand deposit were prepared by water-pluviating sand to relative densities of approximately 30 % and 70 % for, respectively, loose and dense deposit in about 100 mm lifts (model scale). Before filling sands, rehydratable noodles, which served as inclinometers for saturated sand deposit, were attached to the inner side of Plexiglas-like wall installed in the soil container. The embankment was made by dry sand with the relative density approximately 70 %. Aggregates were placed at the bottom of the embankment aiming at preventing the embankment from soaking up pore water by suction.

Input motion was intended to be sinusoidal with 1 Hz and 20 waves. However, as shown in Fig. 2, for example, the amplitude was not constant. This might be due to the effect of mechanical resonance with the centrifuge arm during shaking. In a series of the experiments, the peak amplitude of input acceleration was varied (Table 1) to see their effects on deformation characteristics of an embankment.

3. NUMERICAL ANALYSIS WITH FLIP

To see the applicability of the effective stress analysis by FLIP (Iai et al. 1992), results of the numerical analysis are compared with the experimental counterparts. The numerical model dimension was set as the prototype scale. The analysis constituted of four steps of self-weight analysis under drained condition as indicated by STEP1 to STEP4 in Fig. 3, and a dynamic analysis under undrained condition. The recorded input motion was specified along the base. For solid phase, to mimic boundary conditions of the rigid container, displacement degrees of freedom at the base were fixed both horizontally and vertically, and at two lateral boundaries, only lateral displacements were fixed. For liquid phase, zero pressure was prescribed at the surface of the deposit and at the bottom of the embankment (water table is precisely at the surface of the deposit), and at the base and two lateral boundaries were impervious.

Pore water pressure model in FLIP uses the concept of liquefaction front, in which the state variable S (conceptually equivalent to a mean effective stress) is defined by the combination of liquefaction front parameter, S_0 , which is a function of the shear work, and shear stress ratio, r (Fig. 4). Then modulus is adjusted by a function of mean effective stress ratio. Details on modeling can be found in Iai et al. (1992).

Modeling parameters are defined in Table 2 and 3. They were determined by the standard procedure used in FLIP, i.e., assuming corrected SPT blow count, N_{65} , to be 1 for loose deposit, and 40 for dense deposit. These values of N_{65} for the deposit of 30 % and 70 % of relative density were determined by engineering judgments and they are confirmed to be within a range of the existing correlations [e.g. Skempton (1986)].

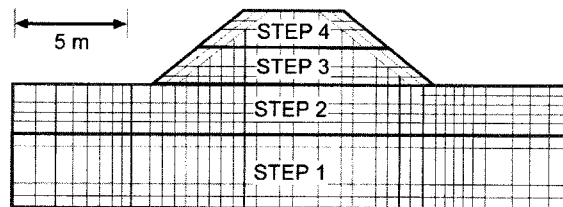


Figure 3. Finite element mesh for numerical analysis. The areas indicated by STEPs are order of self-weight analysis.

Table 2. Model parameters for deformation properties.

Soil Type	Corrected SPT Blow count, N	Density	Porosity	Parameter for deformation characteristic							Max. damping ratio
				Elastic tangent shear modulus at p_r	Elastic tangent bulk modulus at p_r	Reference mean effective stress	Poisson ratio	Exponent of a power function for modulus	Internal friction angle	Cohesion	
				G_r (kPa)	K_r (kPa)	p_r (kPa)	ν	m	ϕ_r (°)	c (kPa)	
	(N_{65})	(kg/m^3)	n								h_{max}
Loose	1	1.34×10^3	0.498	1.987×10^4	5.182×10^4				37.50		
Dense	40	1.45×10^3	0.451	1.885×10^5	4.916×10^5	98.0	0.33	0.50	43.27	0.0	0.24
Levee	40	1.45×10^3	0.450	1.885×10^5	4.916×10^5				43.27		

Table 3. Model parameters for liquefaction properties.

Soil Type	Corrected SPT blow count, (N_{65})	Parameter for liquefaction characteristic					
		Phase trans. Ang.	Parameters for dilatancy				
		Φ_p (°)	w_1	p_1	p_2	c_1	S_1
Loose	5	28.0	4.634	0.50	1.037	1.548	0.005
Dense	40	28.0	21.40	0.50	0.407	13.26	0.005

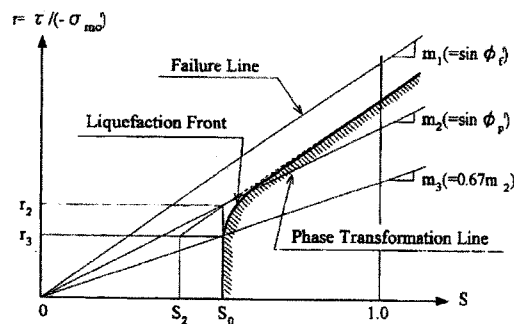


Figure 4 Schematic view of the pore pressure model implemented in FLIP (Iai et al. 1992)

4. MEASURED AND COMPUTED DEFORMATION OF THE EMBANKMENT

Measured and computed deformation of the embankment for four cases (Case 2, 3, 5, and 6) are depicted in Fig. 5. Deformation of Case 1 and 4 were small and not presented. In Fig. 5, upper 50 mm of cross sections of experiments were delineated from photographs taken after shaking. Lower 50 mm were hidden behind the wall of container. Time histories of (a) crest acceleration (A1), (b) crest settlement (D1), and (c) pore water pressure (P2), for Case 3 and 6 are shown in Fig. 6.

At the peak amplitude of input motion 179 Gal for Case 2 in Fig. 5(a), the embankment settled but kept its shape in both measured and computed. Soils near toes are laterally pushed in the direction opposite to the embankment and slightly uplifted, while soils under the embankment were compressed vertically and sheared. The measured amount of crest settlement was 1 m, while it was 0.89 m in the analysis.

At the peak amplitude of 313 Gal for Case 3 in Fig. 5(b), the embankment was laterally expanded and compared to that of Case 2 its shoulders became rounded in the experiment. The large deformation also occurred in the simulation and the deformed shape of the embankment was similar to the experimental counterpart. As shown in Fig. 6(b), LDT reading was saturated due to large settlements, therefore the amount of residual crest settlement was alternatively obtained from the direct measurement of the height of the embankment before and after shaking. Measured and computed residual crest settlements were coincidentally or precisely 1.4 m (47 % of its original height). Although first few cycles of computed crest acceleration shown in Fig. 6(a) are over estimated, the amplitude after five seconds agrees well. Time histories of computed settlements (up to 8 seconds) and pore water pressure buildup shown in Fig. 6(b) and (c) are also consistent with measured ones.

At the peak amplitude of 169 Gal for Case 5 in Fig. 5(c), residual crest settlement was as small as 4.8 mm (0.16 % of its original height) in the experiment and that was 1.3 mm (0.04 %) in the analysis. As shown in Fig. 5(c), shoulders of the embankment were slightly deformed in the analysis, while they are not clearly seen in the measured one. In the experiment, the height of the crown is drawn above the initial level in Fig. 5(c). This might be attributed to primarily model construction error. The photograph taken "before" shaking revealed somehow rounded shape of shoulders, and compared to the photograph after shaking, settlements were hardly detected by the naked eye.

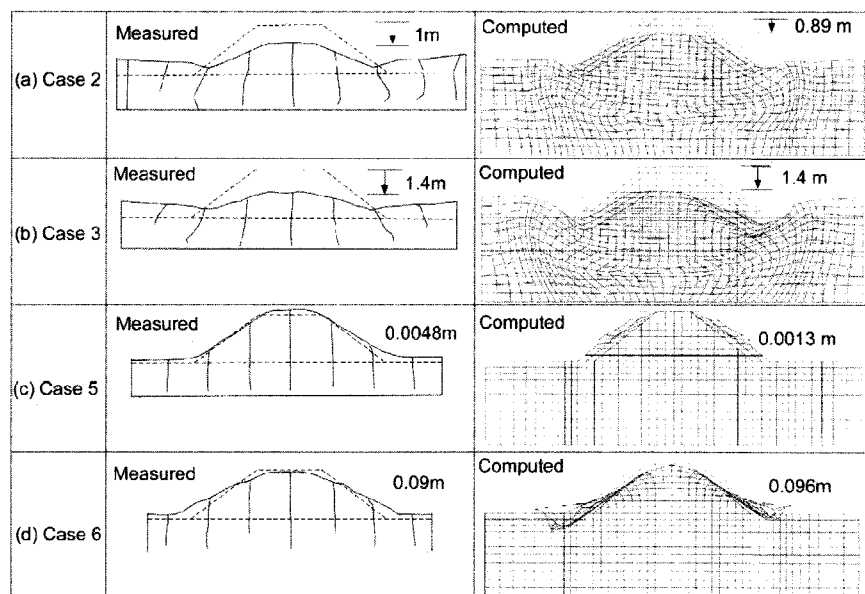


Figure 5. Measured and computed deformation of the levee: (a) Case 2, (b) Case 3, (c) Case5, and (d) Case 6. Amount of crest settlements are indicated.

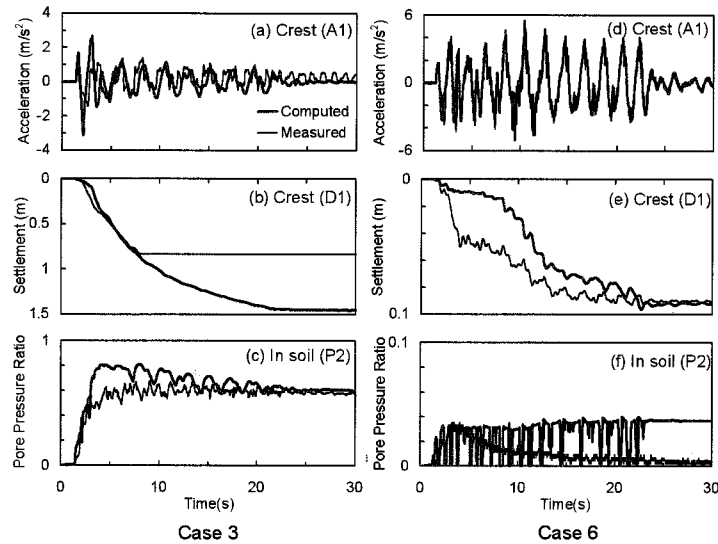


Figure 6. Time histories of (a) acceleration at the crest (A1), (b) settlement at the crest (D1), (c) pore water pressure buildup (P2) for Case 3, (d) acceleration at the crest (A1), (e) settlement at the crest (D1), and (f) pore water pressure buildup (P2) for Case 6.

At the peak amplitude of 574 Gal for Case 6 in Fig. 5(d), no deformation was observed in the saturated sand deposit in both computed and measured. Shoulders were rounded in the experiment and some sands were fallen off. Because there was no reduction of input acceleration due to liquefaction, large acceleration was input and shear stress was concentrated at the shoulders in the body of embankment. This may be simulated, however, as shown in Fig. 5(d), mesh is overlapped at the bottom of the embankment. This is because the numerical method used here is based on the assumption of infinitesimal strains, and does not properly simulate large deformations, such as falling off sands.

5. AMOUNTS OF SETTLEMENTS AND THE INTENSITY OF SHAKING

As it is expected, the amount of crest settlements shown in Fig. 7 is proportional to the peak input acceleration in both loose and dense deposit. In Fig. 7(a), three computational results, i.e., model parameters corresponding to N_{65} of 1, 3 and 5, are shown for comparison purposes together with measured ones. Among these computations, settlements for the case of $N_{65} = 1$ are in reasonable agreement with experimental counterpart.

Crest settlements on loose deposit were resulted from the deformation of an embankment associated with the settlement of the underneath deposit, while on the dense deposit they were resulted from the deformation of the embankment's body itself (see Fig. 5).

In the analysis for loose deposit, when the input acceleration increased (Case 2 and 3 in Fig. 7), non-liquefied area under the embankment becomes large, leading larger non-liquefied wedge penetrating in a liquefied deposit, i.e., a wedge is pushing more liquefied soils aside. The mechanism can be explained as follows; it is obvious that the mean effective stress just under an embankment is high due to the overburden pressure. However, rocking-like motion of an embankment induced by cyclic input motions may further increase the mean effective stress in the deposit near an embankment, or, equivalently, the area of low pore pressure ratio may be increased by shaking as shown in Fig. 8(b). Although the area shifts left and right with shaking, pore pressure ratio near the center of an embankment is always low, and this arcuate area may become large with the intensity of input motion.

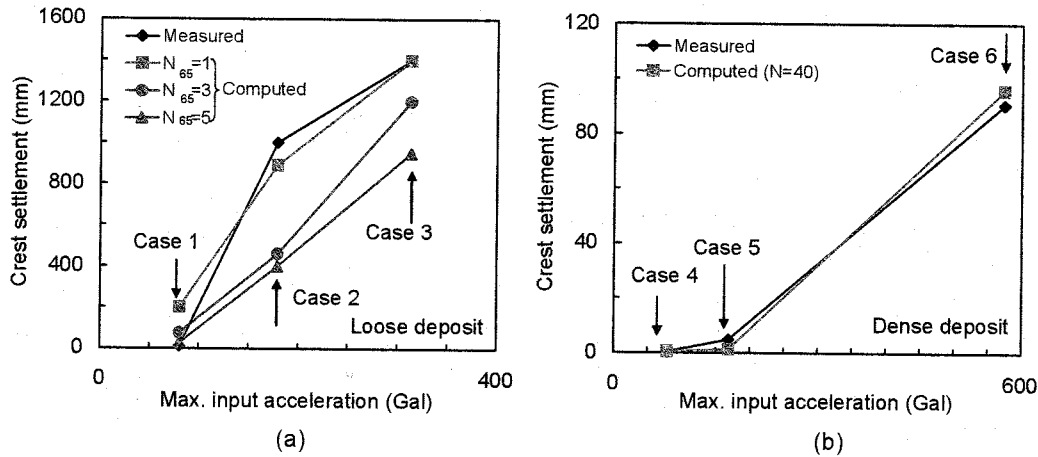


Figure 7. Variation of settlements versus maximum input acceleration.

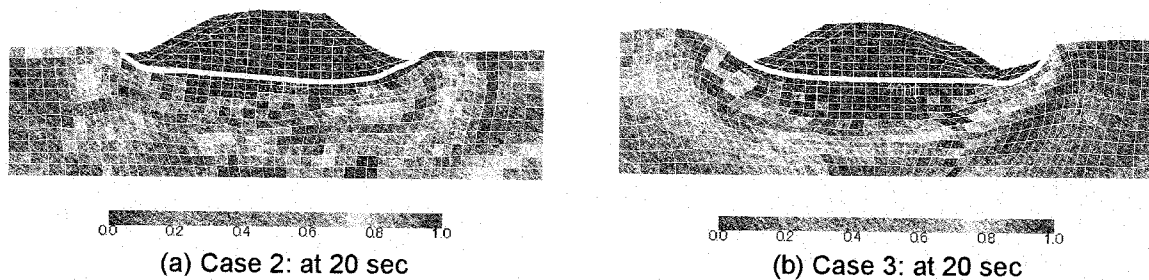


Figure 8. Comparison of deformation and pore pressure ratio at 20 sec: (a) Case 2, (b) Case 3. Areas of non-liquefied zone below the levee is larger in Case 3.

6. CONCLUSIONS

Centrifuge experiments under 50 G were conducted to study dynamic behavior of a embankment (3 m height) made of dry sand underlain by saturated sand deposit with 5 m depth. The relative density of saturated sand deposit was approximately either 30 % or 70 %. Based on the results presented, the following conclusions are reached in this paper:

1. It was observed in the centrifuge experiments that the crest settlements and the peak input acceleration was correlated. The numerical method simulated well not only the above-mentioned relation, but also the transient motions, i.e., deformation, acceleration, and pore water pressure buildup, of an embankment on saturated sand deposit during strong shaking, and, therefore, its applicability was confirmed.
2. It was found that, in the analysis for loose deposit, when the input acceleration increased, non-liquefied area underneath the embankment became large, leading larger non-liquefied wedge penetrating in a liquefied deposit i.e., a wedge is pushing more liquefied soils aside. This mechanism may explain why the compacted area underneath an embankment is an effective measure for deformation due to liquefaction. Further experimental studies are needed to verify the wedge formation and to explain mechanism of settlements related to the peak input acceleration.

The relation between the crest settlements and the peak input acceleration obtained from the centrifuge experiments were used only for comparison purposes in the present paper.

Acknowledgements:

This study was financially supported by the Ports and Airports Department, Kinki Regional Development Bureau, Ministry of Land, Infrastructure and Transport, Japan, and partially supported by the Ministry of Education, Science, Sports and Culture, Grant-in-Aid for young scientists (B), "Research on the seismic resistance on raised bed river (16710131)", 2004-2005. Authors would like to thank for the members of the FLIP consortium (Secretariat: Coastal Development Institute of Technology), Mr. T. Nakahara (Penta Ocean Co.) for their advice and assistance to carry out this study.

References:

- Adalier, K., Elgamal, A.-W., and Martin, G. M. (1998), "Foundation liquefaction countermeasures for earth embankments," *Journal of Geotechnical and Environmental Engineering*, ASCE, **124**(6), 500-517.
- Adalier, K., and Sharp, M. K. (2004), "Embankment dam on liquefiable foundation - dynamic behavior and densification remediation," *Journal of Geotechnical and Environmental Engineering*, **130**(11), 1214-1224.
- Bardet, J. P., and Davis, C. A. (1996), "Performance of San Fernando dams during the 1994 Northridge Earthquake," *Journal of Geotechnical Engineering*, ASCE, **122**(7), 554-564.
- Fiegel, G. L., and Kutter, B. L. (1994), "Liquefaction-induced lateral spreading of mildly sloping ground," *Journal of Geotechnical Engineering*, ASCE, **120**(8), 2236-2243.
- Finn, W. D. L. (2000), "State-of-the-art of geotechnical earthquake engineering practice," *Soil Dynamics and Earthquake Engineering*, **20**(1), 1-15.
- GHQ-Report. (1948), "The Fukui Earthquake, Hokuriku Region, Japan 28 June 1948," General Headquarters, Far East Command, *Gendai Shiryo Shuppan*, 1998, Tokyo.
- Iai, S., Matsunaga, Y., and Kameoka, T. (1992), "Strain space plasticity model for cyclic mobility," *Soils and Foundations*, *Japanese Society of Soil Mechanics and Foundation Engineering*, **32**(2), 1- 15.
- ISO23469. (2005), "Bases for design of structures - Seismic actions for designing geotechnical works," *International Organization of Standardization*.
- Kazama, M., Inatomi, T., Iizuka, E., and Nagayoshi, T. (1996), "Stability of embankment on liquefiable sand layers in centrifuge shaking table tests," *Journal of Geotechnical Engineering*, JSCE, 547/III-36, 107-106 (in Japanese).
- Koga, Y., and Matsuo, O. (1990), "Shaking table tests of embankments resting on liquefiable sandy ground," *Soils and Foundations*, **30**(4), 162-174.
- Koseki, J., Koga, Y., and Takahashi, A. (1994), "Liquefaction of sandy ground and settlement of embankments," *Proc. of Centrifuge 94*, 215-220.
- Matsuo, O. (1996), "Damage to river dikes," *Special Issue of Soils and Foundations*, *Japanese Geotechnical Society*, 235-240.
- Microsoft. (2003), "Windows XP Professional," Microsoft Co., One Microsoft Way, Redmond, WA 98052-6399, USA.
- Nishimoto, S. (2003), "Damage on levees," *Reconnaissance report on the 2003 Tokachi-oki, Japan, Earthquake*, JSCE (in Japanese), <http://www.jsce.or.jp/>.
- Seed, H. B., Lee, K. L., Idriss, I. M., and Makdisi, F. I. (1975), "The slides in the San Fernando Dams during the earthquake of February 9, 1971," *Journal of Geotechnical Engineering*, ASCE, **101**(7), 651-688.
- Seed, R. B., Dickenson, S. E., Riemer, M. F., Bray, J. D., Sitar, N., Mitchell, J. K., Idriss, I. M., Kayen, R. E., Kropp, A., Hander, L. F. J., and Power, M. S. (1990), "Preliminary Report on the Principal Geotechnical Aspects of the October 17, 1989, Loma Prieta Earthquake," *Report No. UCB/EERC-90/05*, *Earthquake Engineering Research Center, University of California Berkeley*.
- Skempton, A. W. (1986), "Standard penetration test procedures and the effects in sands of overburden pressure, relative density, particle size, ageing and overconsolidation," *Geotechnique*, **36**(3), 425-447.
- Takeuchi, M., Yanagihara, S., and Ishihara, K. (1991), "Shaking table tests on model dikes founded on sand deposits with compacted zone," *Proceedings of International Conference on Geotechnical Engineering for Coastal Development (GEO-COAST'91)*, Yokohama, Japan, 2 Vols., 1, 509-514.
- Yasuda, S., Yoshida, N., Adachi, K., Kiku, H., and Gose, S. (1999), "A simplified analysis of liquefaction-induced residual deformation," *Proceedings of the 2nd International Conference on Earthquake Geotechnical Engineering*, 555-560.

EFFECT OF SATURATION ON LIQUEFACTION RESISTANCE OF SANDY SOIL

M. Okamura¹⁾, and Y. Soga²⁾

1) Associate Professor, Department of Civil and Environmental Engineering, Ehime University, Japan

2) Graduate student, Kyoto University (Formerly Ehime University)

okamura@dpc.ehime-u.ac.jp

Abstract: Desaturation of soils could be an effective way to enhance the soil resistance to liquefaction with very low costs in the field. In this study, influential factors of the liquefaction resistance of partially saturated sand are derived from theoretical consideration and effects of the factors are examined through a series of triaxial test. It was confirmed that the liquefaction resistance depends not only on the degree of saturation but on the initial confining pressure and the initial pore pressure as well; the higher the confining pressure and the lower the initial pore pressure, the higher the liquefaction resistance of partially saturated soil is. A unique relationship between liquefaction resistance ratios and the hypothetical volumetric strain was found, which enable to estimate the liquefaction resistance of partially saturated sand with the effects of the three factors taken into account.

1. INTRODUCTION

Natural soil deposits below the ground water table are usually fully or nearly saturated with water (Taukamoto et al., 2002). Recent investigations revealed, however, that injection of air in a soil could lower the degree of saturation of the soil substantially (Tokimatsu et al., 1990; Okamura et al., 2003) and the unsaturated condition of the desaturated soil has lasted for a long time, typically more than tens of years as shown in **Fig.1** (Okamura et al., 2006). This fact suggests that desaturation of soils could be an effective way to enhance the soil resistance to liquefaction with very low costs in the field.

The effect of degree of saturation on the liquefaction resistance has been studied through laboratory tests. In the early research works, degree of saturation of tested specimens was mostly in the range close to 100%, because the primary objective in those studies was to establish the standard for the laboratory cyclic shear test to avoid undesirable unsaturated condition which resulted in overestimation of the liquefaction resistance (e.g. Martin et al., 1978). Thereafter, partially saturated sands with degree of saturation down to 70% were tested by several researchers. **Figure 2** depicts some recent test results in the literature summarized in the form of the relationship between degree of saturation and liquefaction resistance of the partially saturated sand normalized with respect to that of the fully saturated sand (Huang et al., 1999; Yoshimi et al., 1989; Yasuda et al., 1999; Ishihara et al., 2001; Goto and Shamoto, 2002). Liquefaction resistances reported by any

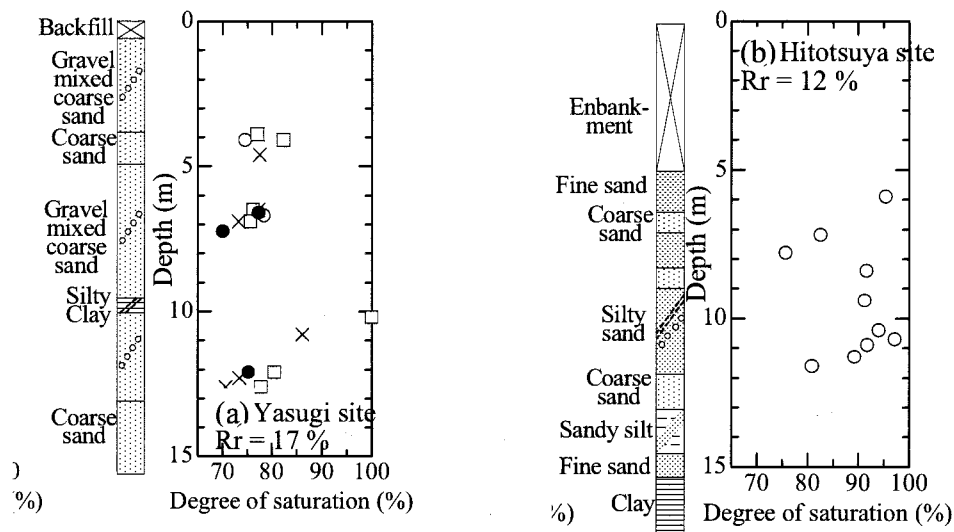


Figure 1 Degree of saturation observed in situ: (a) several days after air injection, and (b) 7 years after air injection

researchers consistently increased with decreasing the degree of saturation. However, the liquefaction resistance ratios were considerably different for different sands tested at different conditions, indicating that the degree of saturation may not be the only factor dominating liquefaction resistances of partially saturated sands.

As can be seen in Fig.2, existence of air in a soil significantly enhances the liquefaction resistance. Researchers have paid great attention to saturate specimens completely for laboratory tests and model grounds for shaking table tests to avoid overrating soil resistances to liquefaction. Replacement of

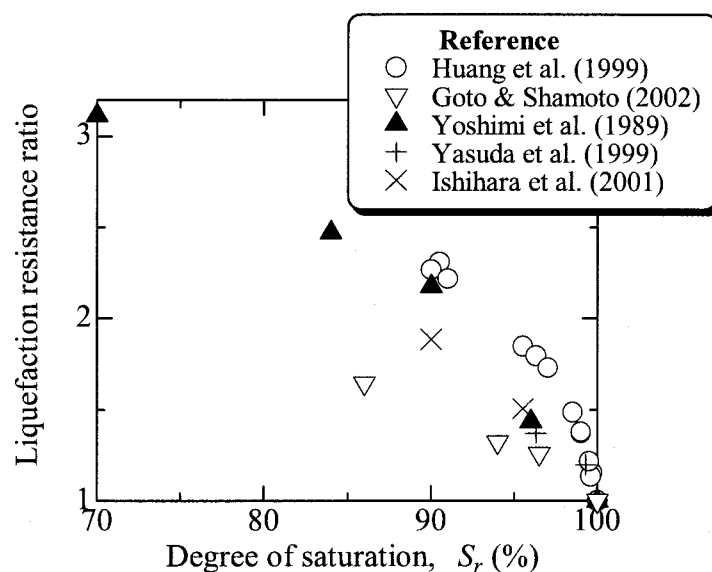


Figure 2 Results of tests on the effect of degree of saturation on liquefaction resistance: liquefaction

air in the void of soils by carbon dioxide before introducing deaired water and applying a vacuum pressure are the typical techniques that have been developed. We, however, often observed contradictory phenomenon that a sand deposit in a small container or a bottle, being almost filled with water but contains visible air bubbles in the deposit, can be easily liquefied by shaking the container gently. This also alludes existence of influential factors of the liquefaction resistance of a partially saturated sand other than the degree of saturation.

In this study, influential factors of the liquefaction resistance of the partially saturated sand are derived from theoretical consideration and effects of the factors are examined through a series of triaxial test. Results are summarized in the form which can be easily applied to evaluate liquefaction resistances of partially saturated sands in situ.

2. FACTORS AFFECTING LIQUEFACTION RESISTANCE OF UNSATURATED SAND

Existence of air in the pore of soil is considered to enhance the liquefaction resistance of the soil in such a way that air in the pore plays a role of absorbing generated excess pore pressures by reducing its volume. The Bulk modulus of the pore fluid changes significantly by the presence of air bubbles. The bulk modulus and change in volume of the pore fluid, that is air water mixture, may be the factors dominating this mechanism.

Consider a soil mass with the pore filled with air and water. For a small change in the pore pressure, Δp , the volumetric strains of the air and the water can be written by equations

$$\Delta p = \varepsilon_a B_a \quad (1)$$

$$\Delta p = \varepsilon_w B_w \quad (2)$$

and volumetric strain of the fluid (water and air mixture) is

$$\varepsilon_{vf} = \frac{\Delta p}{B_f} = [(1 - S_r)\varepsilon_a + S_r\varepsilon_w] = \Delta p \left(\frac{1 - S_r}{B_a} + \frac{S_r}{B_w} \right) \quad (3)$$

where S_r is degree of saturation of the soil mass and B_a , B_w and B_f are bulk moduli of the air, the water and the fluid, respectively. Since B_w is much higher than B_a , the second term in equation (3), S_r/B_w , is negligible. Introducing Boyle's law and assuming soil grains to be incompressible, we obtain the volumetric strain of the soil mass as

$$\varepsilon_v = \frac{\Delta p}{B_a} (1 - S_r) \frac{e}{1 + e} = \frac{\Delta p}{p_0 + \Delta p} (1 - S_r) \frac{e}{1 + e} \leq \frac{\sigma_c'}{p_0 + \sigma_c'} (1 - S_r) \frac{e}{1 + e} \equiv \varepsilon_v^* \quad (4)$$

where p_0 and e denote the absolute pressure of the fluid and the void ratio of the soil mass, respectively. The highest value of the volumetric strain for a soil is achieved when the Δp attains its possible maximum value which is equal to the effective confining stress, σ_c' . The highest value of the volumetric strain is hereafter in this paper termed as hypothetical volumetric strain, ε_v^* .

3. TRIAXIAL TEST

In this study, effects of the factors derived in the preceding section were investigated through a series of triaxial tests. Three testing parameters including the initial effective confining pressure, σ'_c , the back pressure, p_0 , and the degree of saturation, S_r , were varied between tests while the void ratio of the specimens was kept constant throughout the test series.

3.1 Preparation of specimen

Toyoura sand was used in tests conducted in this study. The specific gravity of the sand is 2.64 and the minimum and the maximum void ratios are $e_{\min} = 0.609$ and $e_{\max} = 0.973$, respectively. Triaxial specimens were either saturated or partially saturated sand. Test specimens were prepared as follows. Wet sand with a water content of 5% was tamped to a relative density $D_r = 40\%$ in a mold with internal dimensions of 50 mm in diameter and 100 mm in high. The sand was set in the triaxial cell and deaired water was introduced from the pedestal for a while. Then the water flow was once suspended and the back pressure of 98 kPa was applied. Volume of air in the specimen was estimated from Boyle's law with the measured volume of the water pushed into the specimen due to the back pressure increase. The procedure of introducing deaired water and the air volume estimation was repeated until the specimen contained predetermined volume of air. It should be noted that the adsorption path and the desorption path of the soil-water characteristic curves are generally different. However, the volume of the water pushed in and expelled from the specimen during increasing and decreasing the back pressure was essentially the same. This is probably because that the matric suction of this particular sand is very low in the range of degree of saturation tested in this study.

For the saturated specimen, deaired water was introduced until the Skempton's B value became 0.95 or higher. The effective confining pressure was kept constant to 10 kPa throughout the course of the preparation. On completion of preparation, the initial effective stress and the back pressure were applied and the specimens were subjected to the cyclic shear stress with a frequency of 0.01 Hz under undrained condition.

3.2 Testing parameters

In this study, undrained cyclic triaxial tests were conducted on saturated and partially saturated specimens. Three testing parameters derived in the previous section were varied between tests as shown in **Table 1**. It should be noted that the back pressure, p_0 , used throughout this paper is the absolute pressure instead of the ordinary used gauge pressure. The ranges of the parameters tested was wide enough so that the range of ε_v^* covers that of possible field situation which might be encountered in practice; the initial effective confining pressure was varied between 19.8 kPa and 196 kPa and the range of S_r was similar to that of the in-situ soils desaturated by the sand compaction pile installation (Okamura et al., 2003, 2006). The values of the hypothetical volumetric strain, ε_v^* , are also given in **Table 1**.

Table 1 Triaxial test conditions

Relative density, D_r	Degree of saturation*, S_r (%)	Effective confining pressure, σ'_c (kPa)	Absolute back pressure, p_0 (kPa)	Hypothetical volumetric strain, ε_v^*
39-43%	100	49, 98	199	0
	98 (97.0-98.5)	19.6	199	0.00084
		49		0.00184
		98		0.00305
	96 (95.5-96.0)	19.6	199	0.00165
		49		0.00362
		98		0.00601
	90 (89.0-92.0)	98	199	0.0151
			297	0.0113
	80 (78.5-83.0)	98	199	0.0300
			297	0.0225
	70 (70.0-72.0)	98	199	0.0451
			297	0.0338

*: Degree of saturation in the parentheses was estimated from the measured volume of water pushed into the specimen by increasing the back pressure.

4. RESULTS AND DISCUSSIONS

4.1 Effect of the factors

This section discusses effects of the three factors, that is the degree of saturation, the confining pressure and the back pressure on the liquefaction resistance. **Figure 3** depicts the relationship between cyclic stress ratios and the number of cycles, N , to cause double amplitude axial strain, DA , of 5% for cases with $\sigma'_c = 98$ kPa and $p_0 = 199$ kPa. As the degree of saturation decreases, the cyclic stress ratio increased irrespective of number of cycles. The cyclic stress ratio almost doubled

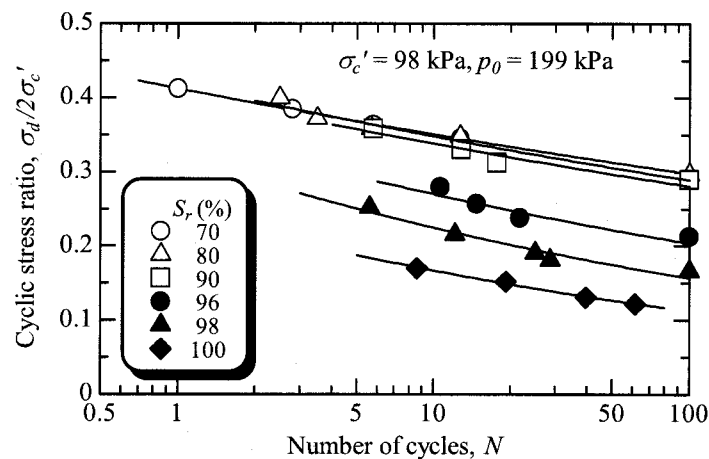


Figure 3 Effect of degree of saturation on the relationship between cyclic stress ratio and number of cycles

as the degree of saturation decreased from 100% to 90%, while in the range of the degree of saturation lower than 90% it increased at a lower rate with decreasing the degree of saturation. Hereafter, in this paper, the cyclic stress ratio to cause $DA = 5\%$ in 20 cycles is termed as the liquefaction resistance.

Liquefaction resistances are plotted against initial confining pressures in **Fig.4**. Unlikely to a reconstituted fully saturated sand, the cyclic stress ratio of the partially saturated sand is apparently dependent on the initial confining pressure. The liquefaction resistances of the partially saturated sand increase with the initial confining pressures, with the liquefaction resistances being higher for lower S_r . The liquefaction resistance of the partially saturated sand approaches to that of fully saturated sand as the confining pressure decreases to zero. In other words, degree of saturation has little effect on the liquefaction resistance of sand under a very low confining pressure. This is what happens in the small scale shaking table test at 1g environment that a model can easily liquefy even if the model ground contains considerable amount of air bubbles. **Figure 5** indicates effects of the back pressure on the cyclic stress ratio. Unlikely to fully saturated sand, the liquefaction resistance apparently depends on the back pressure. In opposition to the effect of the confining pressure, the liquefaction resistance decreases as the pressure increases.

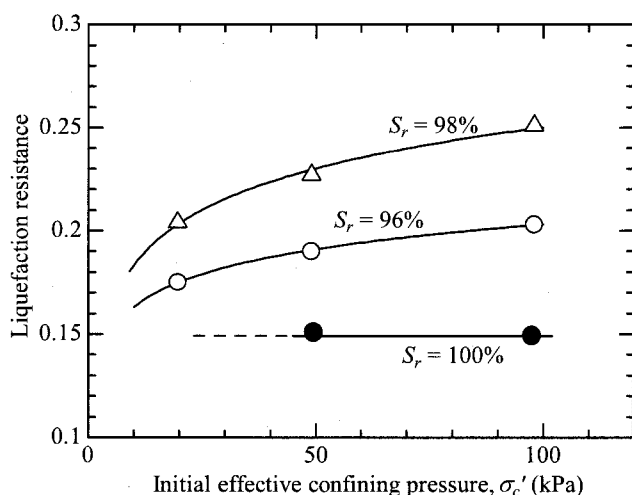


Figure 4 Revolution of liquefaction resistance with initial effective confining pressure

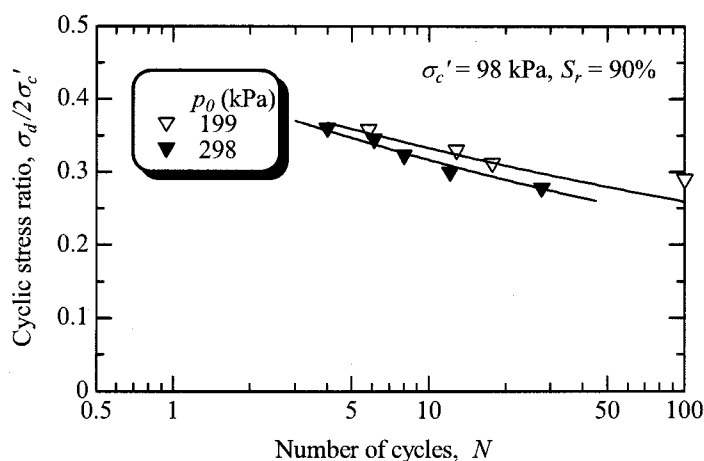


Figure 5 Effect of initial pore pressure on the relationship between cyclic stress ratio and number of cycles

4.2 Liquefaction resistance of desaturated sand

Finally, the effect of the hypothetical volumetric strain, ε_v^* , given by equation (4) on the liquefaction resistance is discussed in this section. All the effects of three influential factors on the liquefaction resistance discussed above qualitatively support the idea of the first mechanism. Thus,

the liquefaction resistance ratio, which is the liquefaction resistance of a partially saturated sand normalized with respect to that of the fully saturated sand, is plotted against the hypothetical volumetric strain in **Fig.6(a)**. All the data lies along a unique curve, confirming that the hypothetical volumetric strain is the determining factor of the effect of degree of saturation on this specific sand at relative density of 40%. Data retrieved from the literature is also shown in **Fig.6(b)** in the same manner. The data plotted in this figure was obtained from tests on specimens prepared using different sand at different relative density and at different pressures as summarized in the figure. Despite these different conditions, all the data lies along the same curve as that in **Fig.6(a)**. This confirms that the effect of the degree of saturation on liquefaction resistance, which is arisen from the first mechanism, can be estimated using this curve.

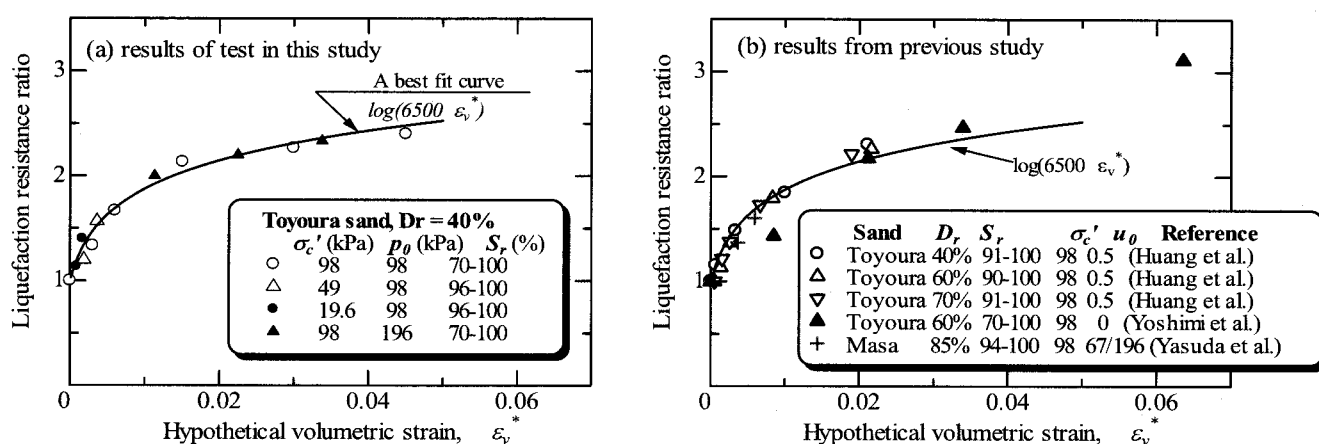


Figure 6 Relationship between hypothetical volumetric strain and liquefaction resistance of partially saturated sand normalized with that of fully saturated sand.

5. CONCLUDING REMARKS

Resistance to liquefaction of partially saturated sand was investigated through a series of triaxial tests in this study. Three parameters obtained from theoretical consideration, that is the degree of saturation, the initial confining pressure and the initial fluid pressure, were selected as testing parameters in the tests.

It is confirmed that the degree of saturation has significant effect on the liquefaction resistance of sand. The liquefaction resistance also strongly depends on the initial confining pressure and the initial pore pressure. The effect of the existence of air on the liquefaction resistance is more significant for soil under the higher confining pressure and the lower initial pore pressure. This fact implies that the

effect of the degree of saturation of soil in a model ground is not that significant for small scale models at 1g but for larger models and centrifuge models. In field conditions, if liquefiable foundation soil is desaturated in some way with an intention to enhance liquefaction resistance, a significant effect can be expected except for soils near ground surface.

It was found that there is a unique relationship between the normalized liquefaction resistance and the hypothetical volumetric strain. The liquefaction resistance of partially saturated sand can be reasonably estimated from that of fully saturated sand in conjunction with the hypothetical volumetric strain using the relationship obtained in this study.

References:

- Bishop, A.W. and Blight, G.E. (1963): Some aspects of effective stress in saturated and partly saturated soils, *Geotechnique*, 13, 177-197.
- Goto, S. and Shamoto, Y. (2002): Estimation method for the liquefaction strength of unsaturated sandy soil (part 2), *Proc. 37th Jpn. Nat. Conf. Geotech. Engrg.*, 1987-1988
- Huang, Y., Tsuchiya, H. and Ishihara, K. (1999): Estimation of partial saturation effect on liquefaction resistance of sand using P-wave velocity, *Proc. JGS Symposium* 113, 431-434.
- Ishihara, K., Tsuchiya, H., Huang, Y. and Kamada, K. (2001): Recent studies on liquefaction resistance of sand – effect of saturation, *Proc. 4th Int. Conf. Recent Advance in Geotech. Earthquake Engrg. and Soil Dynamics*, 1-7
- Martin, G. R., Finn, W. D. L. and Seed H. B. (1978): Effects of system compliance on liquefaction tests, *J. Geotechnical Engineering Div., ASCE*, 104(4), 463-479.
- Okamura, M., Ishihara, M., and Oshita, T. (2003): Liquefaction resistance of sand improved with sand compaction piles. *Soils and Foundations*, 43(5), 175-187.
- Okamura, M., Ishihara, M., and Tamura, K. (2006): Degree of Saturation and Liquefaction Resistances of Sand Improved with sand compaction piles, *J Geotechnical and Geoenvironmental Engrg., ASCE*, 132(2) , 258-264.
- Tokimatsu, K., Yoshimi, Y. and Ariizumi, K. (1990): Evaluation of liquefaction resistance of sand improved by deep vibratory compaction, *Soils and Foundations*, 30(3), 153-158.
- Tsukamoto, Y., Ishihara, K., Nakazawa, H., Kamada, K., and Huang, Y. (2002): Resistance of partially saturated sand to liquefaction with reference to longitudinal and shear wave velocities, *Soils and Foundations*, 42(6), 93-104.
- Yasuda, S., Kobayashi, T., Hukushima, Y., Kohari, M. and Simazaki, T. (1999): Effect of degree of saturation on the liquefaction strength of sand, *Proc. 34th Japanese Nat. Conf. Geotech. Engrg.*, 2071-2072.
- Yoshimi, Y., Tanaka, K. and Tokimatsu, K. (1989): Liquefaction resistance of a partially saturated sand, *Soils and Foundations*, 29(3), 157-162.

NONLINEAR BEHAVIOR OF TAIPEI SILTY CLAY UNDER IRREGULAR STRAIN LOADING

C.J. Lee¹⁾, and S.F. Sheu²⁾

1) Associate Professor, Department of Civil Engineering, National Central University, Taiwan

2) Graduate Student, Department of Civil Engineering, National Central University, Taiwan
cjleeciv@cc.ncu.edu.tw

Abstract: The nonlinear stiffness degradation of Taipei Silty Clay under cyclic strain loading was investigated based on a series of cyclic strain-controlled undrained triaxial shear tests. The Ramberg-Osgood formulation and the proposed degradation model are adopted to construct the initial and degraded backbone curves and associated with the unloading and reloading branches of cyclic loops. The proposed stiffness degradation model verified based on the results of three series of tests has capability to catch the softening or hardening behavior during the strain amplitude varied in the next cyclic sequence.

1. INTRODUCTION

One of basic problems that arise in the earthquake engineering and ocean engineering is the modeling of nonlinear soil behavior under the irregular cyclic loading. It is well known that soils exhibit pronounced nonlinear behavior under the shear loading. Published data show that soil response to cyclic loading ranges from virtually instantaneous to complete loss of strength due to liquefaction on loose sand and dramatically decreases in the strength on clayey soil (Moses, et al. 2003). Both earthquake loading and ocean wave loading are irregular and consist of a sequence of variable and non-symmetric cyclic loading amplitudes. They cause a continuous loss of stiffness and of strength with increasing both the level of shear strain amplitude and the numbers of loading cycle in the undrained condition for clayey soils. To evaluate the response of clay deposits and associated effects on the stability of supported structures in earthquakes or wave storms, it is necessary to know the accurate representation of cyclic stiffness degradation of and strength reduction of clays subjected to the irregular cyclic loading. This paper, based on the results of three series of strain-controlled undrained cyclic triaxial shear tests, introduces a stiffness degradation model to describe the cyclic behavior of normally consolidated cohesive soils under both the uniform cyclic loading and the irregular loading. It can be used on the 1-D ground response analysis.

2. STIFFNESS DEGRADATION MODEL FORMULATION

2.1 Stiffness Degradation On the First Cycle

The Ramberg-Osgood formulation (Richard & Abott, 1975), which has been widely used in describing the obtained stress-strain curve, is adopted to construct the initial backbone curve in this study. The equation of the initial backbone curve is:

$$\varepsilon_c = \varepsilon_y \left(\frac{\sigma_d}{E_{\max} \varepsilon_y} \right) \left(1 + \alpha \left| \frac{\sigma_d}{E_{\max} \varepsilon_y} \right|^{r-1} \right) \quad (1)$$

in which α and r are constants; ϵ_y is a reference axial strain; and ϵ_c and σ_d are the coordinates of the tips of the loop.

Hysteretic loops can be readily constructed by adopting the rules suggested by Masing after the initial backbone function is defined. These two original rules are stated as: (1) the Young's modulus of the first loading reversal is assumed to be the value equal to the initial tangent modulus for the initial backbone curve; and (2) the unloading or reloading curves are geometrically similar to the initial backbone curve, except that the scale is enlarged by a factor of two. Application of these two original rules allows the behavior under the symmetrical cyclic loading to be described by means of a single four-parameter analytical function, therefore, the equations of the reloading and unloading branches may be written as:

$$\epsilon \pm \epsilon_c = \epsilon_y \left(\frac{\sigma \pm \sigma_d}{E_{\max} \epsilon_y} \right) \left(1 + \frac{2\alpha}{2^r} \left| \frac{\sigma \pm \sigma_d}{E_{\max} \epsilon_y} \right|^{r-1} \right) \quad (2)$$

The values of the secant Young's modulus E_c associated with ϵ_c can be expressed as a function of these four parameters as follows:

$$E_c = \frac{E_{\max}}{1 + \alpha \left(\frac{\sigma_d}{E_{\max} \epsilon_y} \right)^{r-1}} \quad (3)$$

The normalized curve of E_c/E_{\max} plotted as a function of cyclic strain is commonly referred to as the Modulus Reduction Curve (Seed & Idriss, 1970). The initial backbone curve described by the loci of the tips of the first cyclic loop can be obtained from a series of undrained strain-controlled tests with different cyclic strain amplitudes or from a fast monotonous undrained compression test.

2.2 Stiffness Degradation Beyond the First Cycle

Pyke (1979) proposed two rules associated with original Masing rules as the extended Masing rules. He defined them as follows: (1) the unloading and reloading curves should follow the initial backbone curve if the previous maximum shear strain exceeded; and (2) if the current loading curve or unloading curve intersects that described by a previous one, the stress-strain relationship follows the previous curve. The nonlinear stress-strain model consists of (1) an initial backbone curve; and (2) the extended Masing rules to form arbitrary hysteretic loops may be used only to trace the response for a non-degraded material under cyclic loadings. However, clay structure deteriorates, pore water pressure changes, and consequently the clay stiffness and strength would decrease with the increase of numbers of loading cycle once the level of cyclic strain amplitude exceeds a threshold value.

To take the effect of the cyclic stiffness degradation into account, Idriss et al. (1978) proposed that the degraded backbone curves can be constructed by multiplying the ordinates of the initial backbone curve by a scaling factor called the degradation index, which is a good indicator to assess the degree of degradation of clay structure. The degradation index, δ_n , is defined as the ratio of the secant Young's modulus, E_n , on the N_{th} cycle to the secant Young's modulus, E_1 , on the first cycle. It is used to describe the evolution of the backbone curves during cyclic loading proceeding. Idriss et al. (1978) suggested that a degraded backbone curve could be attributed to any subsequent cyclic loop. In this manner utilizing the original two Masing rules in conjunction with the Ramberg-Osgood Formulation, the degraded backbone curve at the N_{th} cycle is written as:

$$\epsilon_c = \epsilon_y \left(\frac{\sigma_d}{\delta_n E_{\max} \epsilon_y} \right) \left(1 + \alpha \left| \frac{\sigma_d}{\delta_n E_{\max} \epsilon_y} \right|^{r-1} \right) \quad (4)$$

and the equations of the reloading and unloading branches are:

$$\varepsilon \pm \varepsilon_c = \varepsilon_y \left(\frac{\sigma \pm \sigma_d}{\delta_n E_{\max} \varepsilon_y} \right) \left(1 + \frac{2\alpha}{2^r} \left| \frac{\sigma \pm \sigma_d}{\delta_n E_{\max} \varepsilon_y} \right|^{r-1} \right) \quad (5)$$

From many results of uniform cyclic strain tests, a plot of $\log \delta_n$ versus $\log N$ is a straight-line (Idriss, et al. 1978; Vucetic, 1990; Sheu, 1992). The degradation index, therefore, can be related to the numbers of loading cycle under a given cyclic strain amplitude. That is

$$\delta_n = \frac{E_n}{E_i} = N^{-t} \quad (6)$$

The degradation parameter, t , which measures the rate of change of δ_n strongly depends on the cyclic strain amplitude and the prior stress history (OCR). In general, t consistently increases with increase of ε_c and decreases with increase of OCR for several different clays. Figure 1 displays a family of degraded backbone curves. The numbers of cycle needed to degrade a sample reaching the given degraded backbone curve (e.g. $\delta=0.8$) is obviously dependent on the level of cyclic strain amplitude. The smaller amplitude of cyclic strain necessitates the more numbers of strain cycle, on the contrary the larger amplitude of cyclic strain necessitates the less numbers of cycle, to bring a clay sample reaching the given degraded backbone curve.

Note that Eq.6 is inferred from the results of the uniform strain-controlled tests. It can be utilized to describe the degradation index δ_m at the M_{th} cycle in terms of the previous one δ_n at the N_{th} cycle as follows:

$$\delta_m = \delta_n \left[1 + (M - N) \delta_n^{1/t} \right]^{-t} \quad (7-a)$$

or

$$\frac{E_m}{E_n} = \frac{\delta_m}{\delta_n} = \left[1 + (M - N) \delta_n^{1/t} \right]^{-t} \quad (7-b)$$

in which E_m = the secant Young's modulus at the M_{th} cycle. Here E_m/E_n is termed as the degradation rate of secant modulus in the uniform cyclic strain tests. Accurately predicting δ_m by Eqs.7-a and 7-b are valid for any $M > N$ only in the cases of the uniform strain-controlled tests. Idriss et al. (1978) used Eq. 7 to predict δ_m in the transient loading cases. However, the greater difference between the measured and calculated value of δ_m was obtained in the case of very small ε_c following large cyclic strain or in the case of very large ε_c following a small cyclic strain. Therefore a more general equation for describing the change of the degradation index for both the uniform strain loading and the irregular loading still necessitates being derived in detail.

2.3 Proposed Modified Stiffness Degradation Model

Two assumptions are made to derive the modified cyclic stiffness degradation model to extend the results of controlled uniform strain tests to irregular loading conditions. (1) The samples would have the identical degradation potential of clay structure for the subsequent cyclic strains as long as it degraded to and stayed at the same degraded backbone curve, no matter how large the magnitude of cyclic strain or how many cycles it experienced previously. (2) If an extra cycle of different amplitude of cyclic strain applies to an already degraded sample, the final degradation index will depend only on the initial values δ_n and the level of the subsequent cyclic strain. This concept will be used to derive the modified cyclic stiffness degradation model to extend the results of controlled uniform strain tests to irregular loading conditions. Point A and Point B as shown in Fig. 2 define the tips of loops associated with the cyclic strain amplitudes of ε_a and ε_b on the first cycle. Assume that "Sample1" subjected to a uniform sequence of X cycles of strain amplitude of ε_a , and then the tip of loop degraded to Point A' that locates at the current degraded backbone curve (Curve II). After δ_{ax} is determined, E_{ax} can be easily calculated by definition as follows:

$$E_{ax} = \delta_{ax} E_{a1} \quad (8)$$

Here the first suffix denotes the level of strain amplitude, ϵ_a , and the second suffix denotes the numbers of cycle, X . So that E_{a1} is the secant Young's modulus corresponding to ϵ_a in the initial backbone curve and E_{ax} is the secant Young's modulus in the degraded backbone curve after the X_{th} cycle uniform strain amplitude of ϵ_a . The current degraded backbone curve (Curve II) can be constructed with Eq. 4.

Assume that "Sample2" has the identical soil property as "Sample1" and this sample also subjected to a uniform sequence of Z cycles of ϵ_b , the tip of loop (Point B as shown in Fig. 2) may degrade to Point B' that also locates at the same degraded backbone curve (Curve II) as Point A' locates. (Note: if $\epsilon_b < \epsilon_a$, then the numbers of cycle needed, Z , is larger than X). Although "Sample1" and "Sample2" experienced the different strain histories, they still have the identical degradation potential in the subsequent cyclic strain because they lie in the same degraded backbone curve II ($\delta_{ax} = \delta_{bz}$).

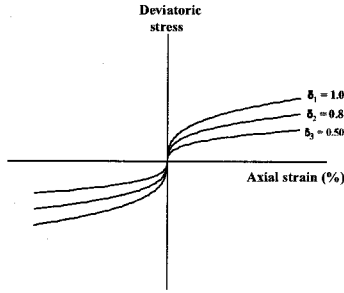


Figure 1 Family of degraded backbone curves

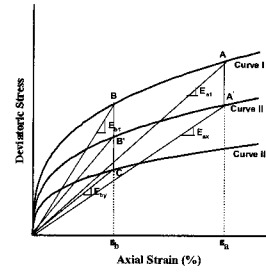


Figure2 Schematic illustration of stiffness degradation under cyclic loading

Now an extra cycle of different strain amplitude of ϵ_e , applies to "Sample1" (numbers of cycle from X increasing to $Y = X + 1$), the degradation index, δ_{ey} , for "Sample1" is obtained by definition. That is:

$$\delta_{ey} = \frac{E_{ey}}{E_{e1}} \quad (9)$$

where E_{ey} is the secant modulus corresponding to strain amplitude of ϵ_e at the Y_{th} cycle in the latest degraded backbone curve (Curve III) and E_{e1} corresponding to the same strain amplitude but in the initial backbone curve (Curve I). The degradation of secant modulus from the X_{th} cycle to the Y_{th} cycle for "Sample1" is obtained by Eq. 7-b. That is:

$$\frac{E_{ey}}{E_{ax}} = \frac{E_{ey}}{\delta_{ax} E_{a1}} = \left[1 + (Y - X) \delta_{ax}^{1/t_e} \right]^{-t_e} \quad (10)$$

where t_e is the degradation parameter corresponding to the cyclic strain level, ϵ_e , and it can be obtained from the plot of δ versus cyclic strain. Rearranging Eq.10, E_{ey} can be expressed as:

$$E_{ey} = E_{a1} \delta_{ax} \left[1 + (Y - X) \delta_{ax}^{1/t_e} \right]^{-t_e} \quad (11)$$

Substitute E_{ey} into Eq. 9 and if $Y = X + 1$ is assumed, then δ_{ey} can be written as:

$$\delta_{ey} = \delta_{ax} (1 + \delta_{ax}^{1/t_e})^{-t_e} \left(\frac{E_{a1}}{E_{e1}} \right) \quad (12)$$

By the same procedures of derivation as mentioned above, exactly the same expression as Eq. 12 can be also obtained for any sample degraded to the same degraded backbone curve (Curve II).

When the uniform cyclic strain tests (because of $\epsilon_e = \epsilon_a$, $t_e = t_a$ and $E_{a1}/E_{e1}=1$) are performed, just exactly the same expression as that proposed by Idriss et al. (1978) can be derived from Eq.12. That is:

$$\delta_{ey} = \delta_{ax} (1 + \delta_{ax}^{1/t_e})^{-t_e} = \delta_{ax} (1 + \delta_{ax}^{1/t_a})^{-t_a} \quad (13)$$

As small amplitude of ϵ_e following large amplitude of ϵ_a applies to a sample (since $E_{a1} < E_{e1}$ due to $\epsilon_a > \epsilon_e$, then $E_{a1}/E_{e1} < 1$), the value of δ_{ey} in Eq. 12 is smaller than that derived in the uniform cyclic strain test and the hardening behavior will occur. In contrast, as a large ϵ_e following a small ϵ_a applies to a sample (since $E_{a1} > E_{e1}$ due to $\epsilon_a < \epsilon_e$, then $E_{a1}/E_{e1} > 1$), the value of δ_{ey} is larger than that derived in the uniform cyclic strain test and the softening behavior will occur. The modulus ratio, (E_{a1}/E_{e1}), is capable of capturing the softening or hardening behavior of clay under the irregular loading. Both E_{a1} and E_{e1} can be easily obtained from the initial backbone curve corresponding to the level of cyclic strain amplitude. The proposed degradation model is simple in that the only additional component to the Idriss's model is the modulus ratio, which is capable of reflecting the effects of previous strain histories and the current level of cyclic strain amplitude. Hence Eq. 12 is the general equation to describe the degradation index for both the irregular loading and the uniform cyclic loading.

3. TEST PROGRAM AND PROCEDURES

The specimens utilized in the study have the following average physical properties: natural water content = 41%; Liquid Limit = 38%; Plastic Index = 21%; Unified Soil Classification = CL or ML. The specimen dimensions are 70 mm in diameter and 150 mm in height. In order to minimize the effect of sample disturbance, all the specimens were isotropically consolidated in a triaxial cell with a confined pressure of 226 kPa, and then cyclically tested in the undrained condition. Both the cyclic tests and the monotonic static shear tests were carried out, independently controlling the axial load and cell pressure.

Four series of tests were conducted. In Test series A and B, the frequency of cyclic strain was 0.1Hz and the sinusoid strain mode was applied by the computer controlled electro-hydraulic triaxial test system. Test Series A consisted of a total of six strain-controlled cyclic triaxial tests. Each cyclic straining test consisted of the stages of different consecutive cyclic strains. The amplitude of cyclic strain kept constant in each stage. It varied between 0.3% and 2.1% from one stage to another stage, the details are outlined in Table 1. There were 100 cycles in each stage. No break was allowed between any two stages or any two cycles. The test results of Test Series A are used to examine the characteristics of the initial backbone curve in the first cycle and the effects of degradation on the subsequent uniform cyclic straining.

In Test Series B, each cycle had the different cyclic strain amplitudes. The sequence of amplitudes of cyclic strain listed in Table 2 was repeated ten times without stopping the test. The results of Test Series B may display the softening or hardening effects for the clay under the non-uniform cyclic straining.

For field application, the loads and deformations vary throughout the duration of cyclic loading. Therefore, selecting a real earthquake history as the strain input to conduct the tests and then to evaluate the feasibility on predicting the behavior of clay under the irregular cyclic straining for the proposed model becomes necessary. The recorded free field acceleration history during the earthquake occurred on November 15th, 1985 was integrated twice to obtain the field displacement history. This earthquake caused considerable severe damages in the Taipei Basin. The displacement history tested in Series C was obtained by scaling the amplitudes of the real field displacement history without changing the original recorded wave pattern. The peak displacement is so determined as to test the sample being subject to 2.1% of maximum peak axial strain in the triaxial test. Fig. 3 shows the strain

history tested for Test B7-T3B.

Two static triaxial tests (i.e., monotonic loading with a strain rate of approximate 1%/min.) in Test Series **D** were also performed. Axial strains, deviatoric stresses and pore water pressures were continuously measured in all the tests.

Table 1 Strain Histories for Test Series A

4.2 Degradation of Backbone Curve

Idriss et al. (1978) used Eq. 7 to describe the stiffness degradation behavior of clay under cyclic loadings. The results shown in Fig.5 (hollow circles represent measured δ in this study and solid circles represent predicted δ with Eq. 7 indicate that some discrepancy between them is found if small amplitude of cyclic strain followed by a larger one or via versed. All the tests in Test Series A and B display the similar results. The reason of this discrepancy results from the hardening or softening occurring as long as the amplitude of cyclic strain changes. Therefore the details of the strain history prior to cycle N are reflected not only by δ_{n-1} but also by (E_{a1}/E_{b1}) . Some modification described in the previous section has been made to derive the general equation of stiffness degradation index to explain these characteristics.

The values of the measured δ and predicted δ with both Eqs.12 and 7 for Testt B6-T6B and Test B7-T3C are presented in Figs. 6 and 7, respectively. These figures indicate that the proposed model is capable of catching the softening or hardening behavior of clays as long as the strain levels changes on the subsequent cycles.

For an arbitrary irregular loading, such as real earthquake loading, it is convenient to evaluate the change of δ in between zero crossing (or for each half cycle). Thus, setting $(Y - X = 1/2)$, Eq.11 becomes

$$\delta_{by} = \delta_{ax} \left[1 + \frac{1}{2} \delta_{ax}^{1/t_b} \right]^{-t_b} \left(\frac{E_{a1}}{E_{b1}} \right) \quad (15)$$

in which t_b is the stiffness degradation parameter corresponding to a given strain level. Eq. 15 together with Eq. 14 constitutes the stiffness degradation model proposed herein for irregular loadings. It can be applied to any irregular loading to predict the decrease of δ at every zero crossing of the strain histories. Hence this model in conjunction with the initial backbone curve allows a complete description of nonlinear and degradation cyclic stress-strain behavior of a soft clay during irregular strain loading.

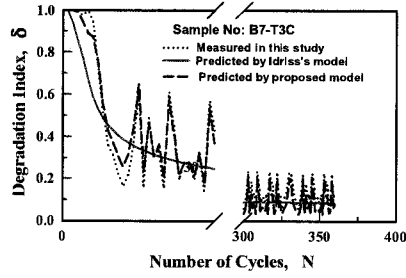


Figure 7 Comparison of measured δ and predicted δ both by the proposed model and Idriss's model under non-uniform cyclic strain loading

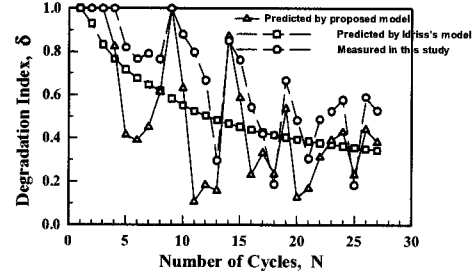


Figure 8 Comparison of measured δ and predicted δ both by the proposed model and Idriss's model under actual earthquake loading

5. SUMMARY AND CONCLUSIONS

A series of cyclic strain-controlled triaxial shear tests were performed in a systematic manner for Taipei silty clay. The Ramberg-Osgood equation, the proposed cyclic stiffness degradation model and the modified Massing Rules are adopted in this study. The following conclusions are given:

1. The modulus of reduction curve can be reasonably described by the Ramberg-Osgood equation. The parameters of the model can be obtained from a series of strain-controlled cyclic tests for Taipei Silty clay.
2. As larger amplitude of cyclic strain followed by a smaller one applies to a clay sample, stiffness of clay degrades less than it does in the uniform cyclic strain test. Therefore hardening behavior will occur. In contrast, smaller amplitude of cyclic strain followed by a larger one applies to a clay sample, stiffness of clay degrades more than it does in the uniform cyclic strain test. Therefore softening behavior will occur. Based on the concept in which δ_n may fully respond to the details of the strain history prior to the N_{th} cycle for the NC clay, the proposed cyclic stiffness degradation model is capable of arresting the softening or hardening behavior of clay in the irregular loading condition.

References:

STRENGTH AND DEFORMATION CHARACTERISTICS OF SOFT ROCKS FROM THE GUADALUPE TUFF FORMATION IN METRO MANILA WHEN SUBJECTED TO LARGE CYCLIC LOADING

D. Peckley Jr.¹⁾ and T. Uchimura²⁾

1) Graduate Student, Geotechnical Engineering Laboratory, University of Tokyo (UT), Japan

2) Assistant Professor, Geotechnical Engineering Laboratory, University of Tokyo (UT), Japan
daniel@geot.t.u-tokyo.ac.jp, uchimura@geot.t.u-tokyo.ac.jp

Abstract: Since capital allocation for seismic risk mitigation in developing countries like the Philippines is usually limited, any judicious and comprehensive mitigation program must involve ensuring certain, if not all, aspects of the program are cost-effective. One of the ultimate objectives of the present research is to assess whether foundations on the Guadalupe Tuff Formation (GTF), which underlies much of Metro Manila, Philippines, can be made more cost-effective considering a large-magnitude earthquake scenario. Presented in this paper are results of tri-axial cyclic loading tests on GTF soft rock samples. These results show that previous cyclic and creep loading histories do not have significant effects on strength and that slow loading rates, which have been employed on cyclic loading tests of soft rocks, can result in significantly larger residual deformations than that of actual loading rates during earthquakes. Noted also in the paper are some case studies showing that strength and deformation characteristics of soft rocks can be better evaluated under a “soil mechanics” framework rather than by a “rock mechanics” approach using the Hoek-Brown criterion, which is usually employed in practice for estimating the strength and deformation properties of the GTF.

1. INTRODUCTION

The Valley Fault System (VFS), which runs through Metro Manila, Philippines (**Figure 1**), is an active fault that can generate an earthquake with a magnitude of 7.2 (Bautista, 2004). A paleoseismic study on the fault that was jointly conducted by the USGS and the Philippine Institute of Volcanology and Seismology or PHIVOLCS (Nelson et al., 2000) indicated a recurrence interval of 200-400 years for magnitude 6-7 earthquakes over the past 1500 years. Considering the hazard posed by this fault, the Association of Structural Engineers of the Philippines (ASEP, 2001) classified the fault in the newly-adopted national structural code as a type ‘A’ seismic source, an active fault that can generate an earthquake of magnitude 7 or greater. Consequently, design seismic forces for structures within 5Km-10Km from the fault became significantly higher than design forces specified by previous editions of the national code. From **Figure 1** it can be noted that the area 5Km-10Km from the fault covers a significant portion of Metro Manila and includes the busy commercial and business districts (CBDs) of Makati, Ortigas Center and Fort Bonifacio.

In developing countries like the Philippines, capital allocation for disaster mitigation, whether in the public sector or the private sector, is usually very limited (Coburn et al., 1991). It should be noted, however, that protection of life and property from strong earthquakes does not always have to be costly. When designing a foundation for a large-scale structure, for example, this foundation can be made more cost-effective when more reliable characterization of both the seismicity of the site as well as the strength and deformation properties of the soil layers or rock formation at the site is available.

exceed 10MPa (Reyes, 2005). Based on unconfined compression tests of samples taken from 10 sites in Metro Manila and the nearby province of Laguna, Rayo and Zarco (2005) noted that strengths vary widely according to location, with some locations having an average UCS that are as low as 0.73MPa and some, around 3.5 MPa. At the excavation site located in Fort Bonifacio (**Figure 1**) where samples were taken for this research, UCS values varied from 0.65MPa to 8MPa; the mean was around 3MPa and the standard deviation was around 2MPa (Reyes, 2005).

According to Reyes (2005), the DVF has a prominent secondary structure composed of widely-spaced vertical joints. Furthermore, he has observed that there are zones with much closer joint spacing and that rocks in these zones are typically highly fractured. Slickensides and evidence of strike-slip movements have also been occasionally found.

3. ROCK MECHANICS OR SOIL MECHANICS?

In practice, the strength and deformation characteristics of the GTF are evaluated by a “rock mechanics” approach using the Hoek-Brown criterion (Hoek et al., 2002). It is assumed in rock mechanics that the behavior of a rock mass is largely governed by the joints and other discontinuities present in it; thus, the mass strength and deformation properties should be lower than those of an intact core sample to reflect the effect of these discontinuities. This assumption is valid for hard rock masses with intact core samples having unconfined compression strengths from 30MPa to more than 200MPa. For soft rocks, however, a number of case studies on actual full-scale behavior in Japan (Tatsuoka and Kohata, 1994; Kashima et al., 2000; Koseki et al., 2001; Tatsuoka et al., 2003) have shown that the effects of discontinuities are negligible.

According to the case studies reported by Tatsuoka and Kohata (1994) and Tatsuoka et al. (2003), reasonably accurate simulations of full-scale behavior were only possible when the data used are from (a) field seismic surveys that are conducted to estimate maximum deformation modulus and (b) relevant laboratory stress-strain tests on “undisturbed” core samples that are performed while taking into account strain-level and pressure-level dependencies of strength and deformation properties. It was also shown in these case studies that when simulations are based only on strength and deformation properties from unconfined compression tests of “intact” cores, actual field deformations can be grossly overestimated. These case studies include the following:

- 1) Sagami-hara Test Site near Tokyo, Japan as reported by Tatsuoka et al. (1997). At this site, a 50m deep shaft and a series of short tunnels were excavated into a sedimentary soft mudstone formation called the Kazusa Group to determine rational construction methods in a soft rock deposit and to investigate deformation characteristics of soft rock.
- 2) The settlements of Pier 2P and Pier 3P of the 3.91Km Akashi Kaikyo Bridge during construction as reported by Siddiquee et al. (1994, as cited by Tatsuoka and Kohata, 1994) and after the 1995 Kobe Earthquake as reported by Koseki et al. (1999) and Kashima et al. (2000) . Pier 2P is founded on a weakly-cemented gravel layer, underneath which is a soft sandstone formation. Pier 3P is directly founded on the soft sandstone formation.
- 3) Forty-five (45)-meter deep excavations into a soft sedimentary mudstone formation for 85,000 kiloliters and 200,000 kiloliters LNG tanks in Negishi, Yokohama as reported by Goto and Takahashi (1993, as cited by Tatsuoka and Kohata, 1994).
- 4) Displacements of Anchor 4A of the 918m Rainbow Bridge in Tokyo, which is on a soft sedimentary mudstone formation, as reported by Odagiri et al. (1993, as cited by Tatsuoka and Kohata, 1994).

Note that the locations of the aforementioned excavations and foundations are in a seismically active regions.

The tri-axial cyclic loading tests presented in this paper were carried out under a “soil mechanics” framework, following the recommendations by Tatsuoka et al. (2003) on measurements of stresses and strains in soft rocks.

4. TRI-AXIAL CYCLIC LOADING TESTS

Previous tests on soft rocks conducted by Nishi et al (1983, as cited by Tatsuoka et al., 2000), Tatsuoka et al. (2000), Hayano et al. (2001), Tatsuoka et al. (2003) and Bhandari and Inoue (2005) already established the rate-dependency of soft rocks under monotonic loading. In recent cyclic loading tests of natural soft rocks (Indo, 2001), however, it was implicitly assumed that the behavior under such loading is rate independent. In the tests that were conducted by Indo the loading rate that was applied was 0.01%/min, which is roughly equivalent to loading periods ranging from 3000s to 6000s.

4.1 Test Program

In the first series of tests that were conducted on the GTF soft rock specimen, one of the specific objectives was to evaluate loading rate effects on cyclic loading behavior, specifically on the accumulation of residual deformations.

The specimens were taken from a sandstone layer in an excavation site in Fort Bonifacio, Taguig, Metro Manila by block sampling. The sampling depth was around 12 meters from the existing ground elevation. The block samples were then packaged and shipped to the Geotechnical Engineering Laboratory of the University of Tokyo, Japan following the recommendations of ASTM D 5079-90 for critical care. The samples were cut and trimmed to L100mm x W60mm x H150mm nominal sizes using a rotary cutter. The unit weight of the samples was around 1.85g/cm³; moisture content was around 22%; and the mean diameter D_{50} was from 0.20mm to 0.25mm (after thorough crushing).

Figure 2 illustrates the set-up of the tests. To avoid bedding errors, Local Deformation Transducers or LDTs (Goto et al., 1991) were used to measure longitudinal and lateral deformations. Two 120mm LDTs were used to measure longitudinal (axial) deformations and were attached on the 60mm wide faces of the specimen. Six 70mm LDTs were used to measure lateral (horizontal) deformations and were arranged such that each of the 100mm wide faces of the specimen had three of these LDTs. To measure longitudinal (axial) load, a 50KN-capacity load cell installed inside the tri-axial cell was used to minimize errors due to friction along the loading shaft.

Initially, the loading system that was used in the tests was an automated clutch-gear system driven by an AC servo motor, as described by Santucci de Magistris et al. (1999). Having a maximum capacity of 50KN, this loading system is strain-controlled and the typical strain rates applied range from 0.001%/min to 0.1%/min. So far the maximum cyclic loading strain rate that was applied without compromising accuracy in amplitude was 1%/min, which was equivalent to a loading period T of around 60s.

Since the loading rates that can be employed using a clutch-gear system are significantly slower than actual loading rates during earthquakes, the hydraulic loading system at Koseki Laboratory in IIS,

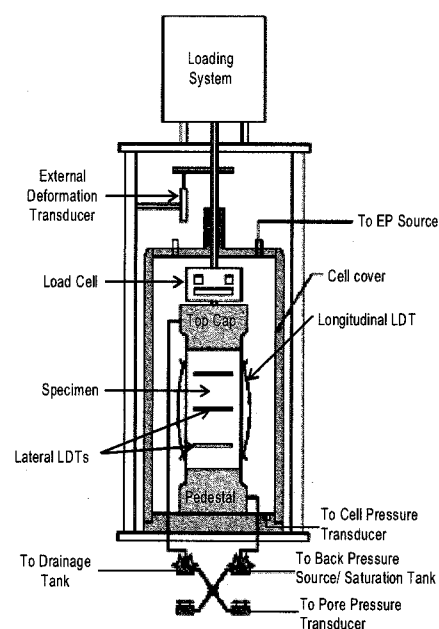


Figure 2. Schematic Diagram of Test Set-up

University of Tokyo was also used. Having also a maximum capacity of 50KN, this loading system is stress-controlled. The difficulties, however, with the use of this loading system are the following: (1) control of loading is not through a feedback system using the internal load cell, but through an external load cell connected to a separate computer-controller system; (2) over-shooting occurs in the 1st half-cycle of loading when the loading period is $T = 1$ s; and (3) the actual amplitude of loading can be significantly different from the input amplitude when the loading period is $T = 1$ s. To overcome items (1) and (3), preliminary tests to calibrate the input and actual amplitudes were carried out. To overcome item (2), the first half-cycle of loading was set to unloading then reloading.

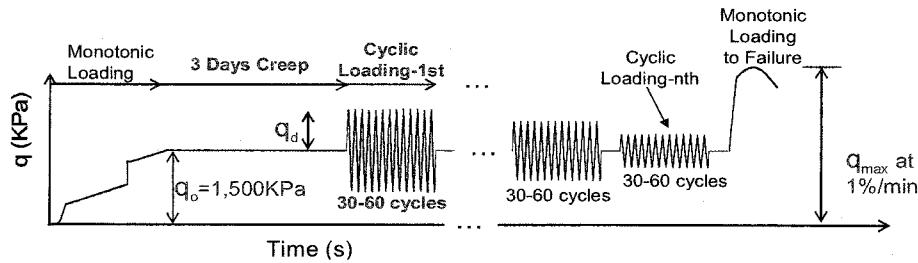


Figure 3. Loading Time Histories

Prior to loading, each specimen was consolidated at an isotropic pressure of 200KPa, the estimated insitu overburden pressure at the sampling site. The tests were unsaturated because the samples were taken above the water table, which was 20m below the existing ground surface. **Figure 3** shows the typical loading time history applied for each specimen. As shown in the figure, monotonic loading to a static stress condition $q_0 = 1500$ KPa was first applied to simulate the construction of the foundation. At the static state q_0 , creep for three days was applied prior to the application of cyclic loading, although this loading stage was not applied to the first two specimens that were tested for cyclic loading. Most of the specimens were subjected to more than one stage of cyclic loading, each with 30 cycles or 60 cycles. Between each stage, 30 minutes creep at the static state q_0 was applied. **Figure 4** shows the amplitude of the cyclic loading stages applied for each specimen. The last loading stage was monotonic loading to failure at 1%/min.

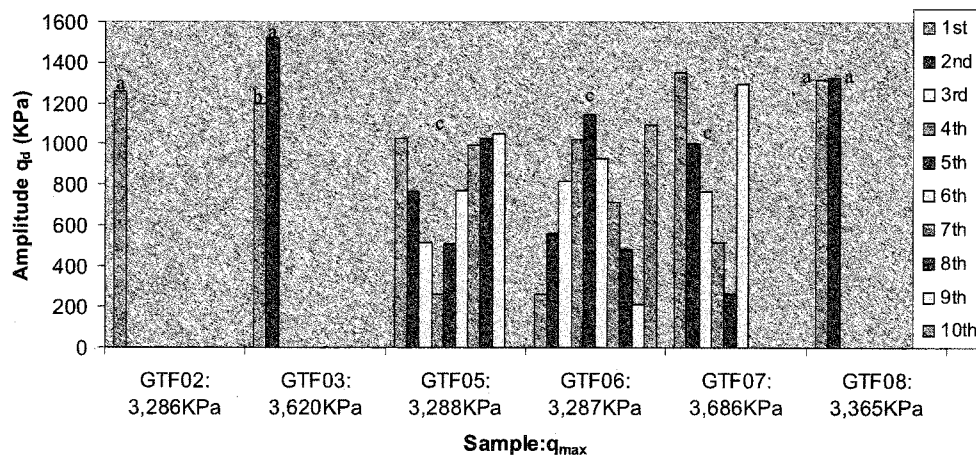


Figure 4. Amplitude of each cyclic loading stage and maximum deviator stress for each specimen; loading rates: 'a' – 1%/min(60s-73s); 'b' – .01%/min (6000s) ; 'c' – all loading stages at 1s

For specimens GTF02, GTF03 and GTF08, the automated clutch-gear loading system was used and the loading rates that were applied in the first stage of cyclic loading for these specimens were 1%/min ($T \sim 60$ s), 0.01%/min ($T \sim 6000$ s), and 1%/min ($T \sim 66$ s), respectively. For specimens GTF05,

GTF06 and GTF07, the hydraulic loading system was used and all cyclic loading stages were at a loading period $T = 1s$.

4.2 Test Results

Figure 4 also shows the maximum deviator stress q_{max} that were measured for each specimen. It can be noted from the values of q_{max} that despite the different loading histories that were applied to each specimen, the strength is essentially the same. These values are also practically the same as the strength obtained from a monotonic loading test of another specimen, which was around 3300KPa. The same observations were also noted in the tests performed by Indo (2001) and Bhandari and Inoue (2005).

Figure 5 compares the cyclic stress-strain curves of specimens GTF02 and GTF03. In both GTF02 and in the 1st cyclic loading stage of GTF03, 30 cycles were applied at almost the same amplitude. Note, however, that the loading rate for GTF02 was 100 times faster than that of GTF03. Due to this difference in loading rate, it can be readily observed that the cyclic stress-strain curves of the two are different, and that accumulated residual strain GTF03 after the 1st loading stage is larger than that of GTF02.

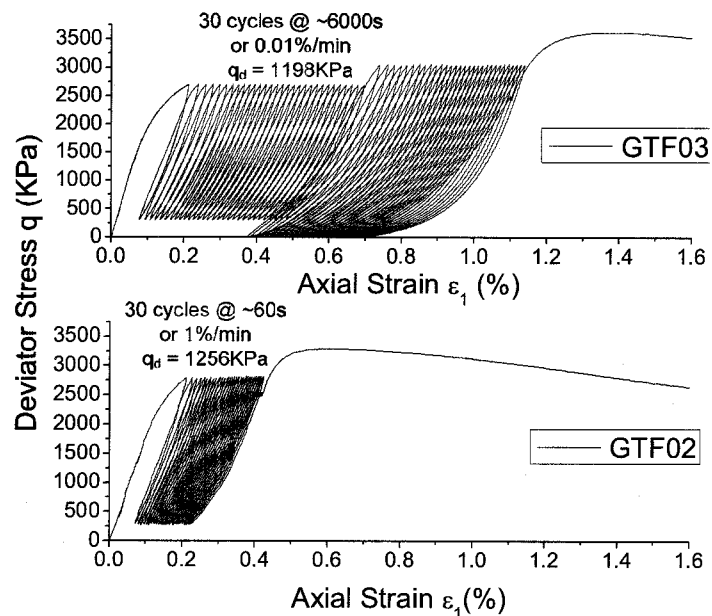


Figure 5. Cyclic stress-strain curves of GTF02 and GTF03

Figure 6, on the other hand, compares the cyclic stress-strain curves of GTF07 and GTF08. The amplitudes of the 1st stage of cyclic loading for both specimens are also almost the same but the number of cycles and loading rates are different. For GTF08, 30 cycles were applied at 1%/min or $T \sim 66s$. For GTF07, 60 cycles were applied at a loading period $T = 1s$. It can be observed from the figure that although the numbers of loading cycles are different for each specimen, the accumulated residual strains are almost the same. It can also be observed for both specimens that creep deformation at the static q_0 after three days is quite small compared to the deformations due to the large cyclic loading applied.

Figure 7 plots the accumulation of residual strain at the end of every cycle until the 30th cycle for GTF02, GTF03, GTF07 and GTF08. To take into account creep effects at the static state q_0 for GTF02 and GTF03 in this plot, the average creep loading time history of GTF05, GTF06, GTF07 and GTF08 was subtracted from the cyclic loading time histories of GTF02 and GTF03. It is clear from this figure that the slower the loading rate, the larger is the accumulated residual strain. It can also be surmised that the loading rates usually applied in cyclic loading tests of soft rocks, which range from 0.01%/min to 0.1%/min, can result in overestimated residual deformations.

5. CONCLUSIONS

From the preceding discussions, foundations on the Guadalupe Tuff Formation can be designed more cost-effectively even under a large earthquake scenario, when the following are considered:

- A “soil mechanics” framework is adopted in evaluating the strength and deformation properties of the soft rock layers of the formation, instead of a “rock mechanics” approach. As pointed out earlier, only in such a framework has actual full-scale behavior been simulated with reasonable accuracy. Thereby, the use of a “rock mechanics” approach can result in underestimation of strength and deformation properties of soft rock formations.
- Previous cyclic and creep loading histories do not have significant effects on strength.
- In the design of large-scale foundations, where residual deformations due to a large magnitude earthquake can become an issue, performing tests at loading rates commonly employed at present can result in significant overestimation of deformations. More accurate estimates of deformations can be obtained at loading rates similar to actual loading rates during earthquakes, e.g., a loading period $T = 1$ s.

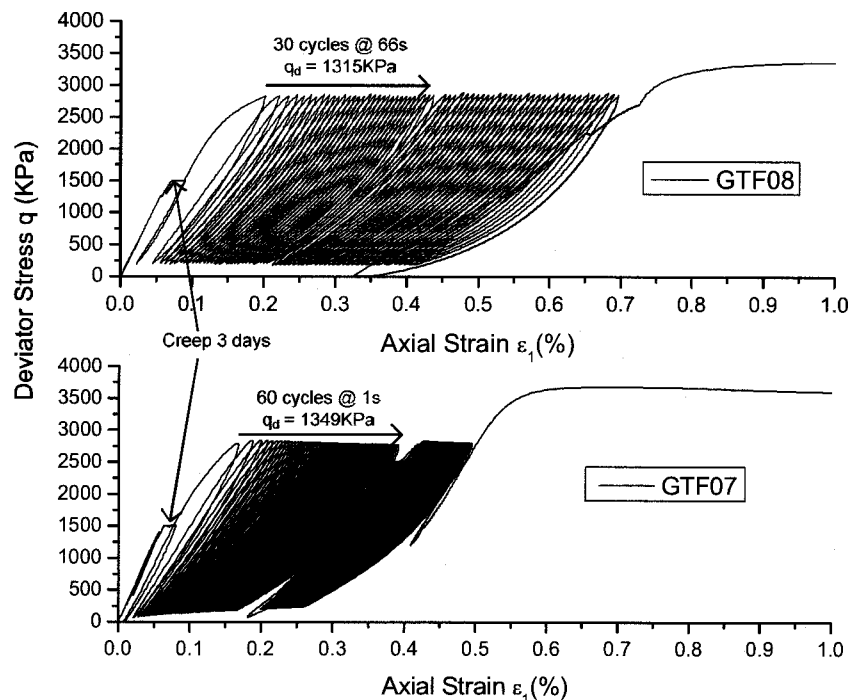


Figure 6. Cyclic stress-strain curves of GTF07 and GTF08

Acknowledgements:

The present research has been made possible through a scholarship grant that was awarded to the first author by the Japan Ministry of Education, Culture, Sport, Science, and Technology (MEXT). The authors are also grateful for the assistance of Engr. Wilson A. Sy of Aromin & Sy + Associates, Inc. in obtaining GTF soft rock samples from Fort Bonifacio, Metro Manila. Special appreciation is also extended to Prof. Junichi Koseki for allowing the authors to use the sample preparation equipment and hydraulic testing apparatus at the Koseki Laboratory, IIS, UT.

References:

- Association of Structural Engineers of the Philippines –ASEP (2001): National Structural Code of the Philippines 2001. Volume 1-Buildings, Towers, and other Vertical Structures. 5th edition. ASEP. Manila, Philippines.
- Bautista, M. P. (2004): Overview of the MMEIRS Project. [www.phivolcs.dost.gov.ph/clarification/Leyo's Letter.pdf](http://www.phivolcs.dost.gov.ph/clarification/Leyo's%20Letter.pdf)
- Bhandari, A. R. and Inoue, J. (2005): Experimental Study of Strain Rate Effects on Strain Localization Characteristics of Soft Rocks, *Soils and Foundations*, **45** (1), 125-140.
- Coburn, W. Spence, R. J. S, Pomonis, A (1994): Disaster Mitigation, 2nd edition, Cambridge Architectural Research Limited. Cambridge, United Kingdom.

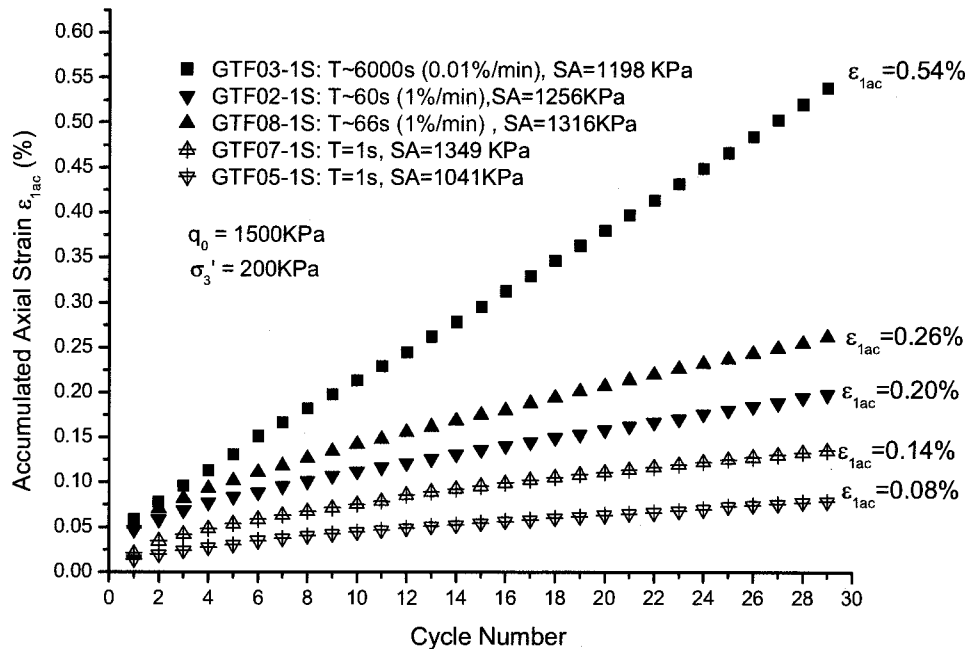


Figure 7. Residual Strain Accumulation after every cycle

- Hayano, K., Matsumoto, M., Tatsuoka, F. and Koseki, J. (2001): Evaluation of Time-dependent Deformation Properties of Sedimentary Soft Rock and their Constitutive Modeling, *Soils and Foundations*, **41** (2), 21-38.
- Goto, S., Tatsuoka, F., Shibuya, S., Kim, Y. S., and Sato, T. (1991): A simple gauge for local small strain measurements in the laboratory, *Soils and Foundations*, **31** (1), 169-180.
- Hoek, E., Carnaza-Torres, C.T., and Corkum, B. (2002): Hoek-Brown failure criterion 2002 edition, *Proc. North America Rock Mechanics Society Meeting*, Toronto.
- Indo, H. (2001): Deformation characteristics of sedimentary softrock by cyclic triaxial tests. Master of Engineering Thesis, University of Tokyo. (in Japanese).
- Kashima et al. (2000): Analysis of the Settlement of Pier 3P of the Akashi Kaikyo Bridge after the 1995 Hyogo Ken Nambu Earthquake, *Proc. 2000 JSCE Annual Conference, Sendai, Japan*. (in Japanese).
- Koseki, J., Moritani, T., Fukunaga, S., Tatsuoka, F. and Saeki, M. (2001): Analysis on Seismic Performance of Foundation for Akashi Kaikyo Bridge, *Proc. 2nd Int. Symposium Pre-failure Deformation Characteristics of Geomaterials (Jamiolowski et al. eds)*, Balkema, 1405-1412.
- Nelson, A. R. et al. (2000): Multiple large earthquakes in the past 1500 years on a fault in metropolitan Manila, The Philippines. *Bulletin of Seismological Society of America*, **90**, 73-85.
- Rayo, M. C. and Zarco, M. H. (2005): Characteristic Rock Mass Strength of the Guadalupe Tuff Formation, *Proc. PICE 2005 National Convention, Manila, Philippines*.
- Reyes, S. F. (2004): Personal communication.
- Reyes, S. F. (2005): Assessment of Geotechnical Conditions at Site of Proposed St. Luke's Medical Center, Bonifacio Global City, Taguig, Metro Manila.
- Santucci de Magistris, F., Koseki, J., Amaya, M., Hamaya, Sato, T. and Tatsuoka, F. (1999): A triaxial testing system to evaluate stress-strain behavior of soils for wide range of strain and strain rate, *Geotech. Testing J.*, **22** (1), 44-60.
- Tatsuoka, F., Hayano, K. Koseki, J. (2003): Strength and Deformation Characteristics of Sedimentary Soft Rocks in the Tokyo Metropolitan Area, *Characterization and Engineering Properties of Natural Soils (Tan et al. eds)*, Swets and Zeitlinger, 1461-1525.
- Tatsuoka, F. and Kohata, Y. (1994): Stiffness of Hard Soils and Soft Rocks in Engineering Applications, Keynote Lecture, *Proc. Int. Symposium of Pre-failure Deformation of Geomaterials (Shibuya et al. eds)*, Balkema, **2**, 947-1063.
- Tatsuoka, F., Ochi, K., Tsubouchi, T., Kohata, Y. and Wang, L. (1997): Experimental underground excavations in sedimentary softrocks at Sagami-hara, *Proc. Instn. Civ. Engrs. Geotech. Engng*, 206-223.
- Tatsuoka, F., Santucci de Magistris, F., Hayano, K., Momoya, Y., and Koseki, J. (2000): Some new aspects of time effects on the stress-strain behavior of stiff geomaterials, *The Geotechnics of Hard Soils-Soft Rocks (Evangelista and Picarelli eds.)*, Balkema, 1285-1372.
- Zanoria, E. S. (1988): The Depositional and Volcanological Origin of the Diliman Volcaniclastic Formation, Southwestern Luzon, Philippines, Master of Science in Geology Thesis, University of Illinois at Chicago.

DEVELOPING TIME VARYING WAVE TRANSMITTING BOUNDARIES USING JOINT TIME-FREQUENCY REPRESENTATION METHOD

A. Farahani¹⁾ and K. Konagai²⁾

1) Post Doctoral research fellow, Center for Urban Earthquake Engineering, Tokyo Institute of Technology, Japan

2) Professor, Dept. of Civil Engineering, University of Tokyo, Japan

farahani@cv.titech.ac.jp, konagai@iis.u-tokyo.ac.jp

Abstract: There are many methods to simulate wave propagation through half space in frequency and time domain. In this paper, an idea is proposed to use any kind of frequency dependent absorbing boundary for the far-field, but still holding the analysis kernel in time domain. If the frequency content of the outgoing waves is detected before hitting the frequency dependent absorbing boundaries, the boundaries have enough time for adaptation to absorb that range of frequency. For this purpose some benchmark nodes should be selected inside the near field. A frequency detector analyzes the displacement history of the benchmark nodes to detect the frequency content of outgoing waves. Then this information is transferred to the boundaries so that they are prepared to absorb these frequencies. The frequency detection analyzer is based on the Adaptive Optimal Kernel method, which has been developed for Time-Frequency Representation (TFR) analysis of signals.

1. INTRODUCTION

Numerical methods for the solution of wave problems in unbounded domains have been developed since the late 1960s. Among the pioneers were Zienkiewicz and Newton (1969), Ungless (1973), Bettles (1977,1992) and Lysmer and Kuhlemeyer (1969). Various methods have been proposed, such as boundary elements (Brebbia and Walker 1980), infinite elements, thin layer elements (Tajimi and Shimomura 1976) and non-reflecting viscous boundary method. Representation of signals in frequency domain is simpler and more common in practice than time domain. Hence, most of these methods have been developed in frequency domain and are limited to linear analysis. To solve nonlinear problems in unbounded media different methods are utilized, such as introducing the equations of motion for the far field directly in time domain (Wolf and Oberhuber 1985) or using Hybrid frequency-time domain analysis method and shifting between time and frequency repeatedly (Bernal and Youssef 1998) or transforming the frequency dependent impedance matrix of the far field into time (Kim and Yun 2000). It seems that the later is easiest to use, but still further approximation is required to convert the impedance matrix to simpler shapes to be transformable into time. The impedance matrix is approximated by polynomials and then transferred into time domain using Inverse Fourier Transformation (IFT) or Z-transformation (Wolf and Motosaka 1989). In this paper, the new idea is based on the evaluation of frequency-dependent absorbing boundaries in frequency domain and then transforming it into time domain as a piecewise constant variable. Therefore, the frequency content of outgoing waves should be evaluated in different intervals of time. In fact, due to uncertainty principle, if the resolution of spectrum in time domain increases, then the resolution in frequency domain will decrease and vice versa. A better way is to obtain response spectrum in a time interval and then make a judgment about dominant frequencies of that response (Cohen 1995). It should be noted that in this procedure, time interval is different from time step in dynamic analysis. For Time-Frequency Representation (TFR) part, Adaptive Optimal-Kernel Time-Frequency Representation of

signals is used (Baraniuk and Jones 1993, Jones and Baraniuk 1994,1995).

When a time-dependent disturbance exists in near field region, different waves with time-variable frequency contents hit the boundaries in different times. If the effective frequencies and their durations are calculated, the boundaries will be able to adjust their properties in those time intervals in order to be prepared to absorb the waves with those frequencies. The frequency content of waves can be detected with the help of benchmark nodes. By studying the short-time displacement-history of the benchmark nodes, it is possible to extract the dominant frequencies of the outgoing waves. Then, this information will be passed to the boundaries to become ready to absorb those waves.

In section 2 a simple frequency-dependent viscous absorbing boundary based on Lysmer and Kuhlemeyer (1969) method is introduced. The purpose of using this simple boundary is to pass Rayleigh waves that have the large portion of energy of propagating waves. By replacing this type of boundary with the more accurate frequency-dependent non-reflecting boundaries, better results for system's responses can be achieved. In section 3 the concept of TFR analysis is briefly reviewed. Then the application of TFR analysis in transforming frequency-dependent absorbing boundary into time domain is shown.

2. FREQUENCY-DEPENDENT VISCOUS ABSORBING BOUNDARY

The purpose of this section is to make a kind of viscous dashpot for the boundaries to absorb the energy of outgoing Rayleigh waves. By applying a harmonic point load on the surface of an elastic half space, the displacement field of the medium can be obtained (Sezawa 1930). That part of the displacement field, which is related to the Rayleigh waves traveling in positive X direction, can be expressed in frequency domain as follows:

$$\begin{aligned} U(k_R; Z) &= f(k_R; Z) e^{(i\omega t - k_R X)} \\ W(k_R; Z) &= g(k_R; Z) e^{(i\omega t - k_R X)} \end{aligned} \quad (1)$$

In which

$$\begin{aligned} f(k_R; Z) &= D \left(e^{-m k_R Z} - \left(\frac{2 m n}{n^2 + 1} \right) e^{-n k_R Z} \right) \\ g(k_R; Z) &= D \left(-m e^{-m k_R Z} + \left(\frac{2 m}{n^2 + 1} \right) e^{-n k_R Z} \right) \end{aligned} \quad (2)$$

$$\begin{aligned} \alpha &= \sqrt{\frac{1 - 2\nu}{2 - 2\nu}} & m &= \sqrt{1 - \alpha^2} V^2 \\ V &= \frac{C_S}{C_R} = \frac{0.87 + 1.12\nu}{1 + \nu} & n &= \sqrt{1 - V^2} \end{aligned}$$

U = Displacement in X direction
W = Displacement in Z direction
K_R = Wave number of Rayleigh wave
ν = Poisson's ratio of the medium
D = Constant value

C_S = S-Wave speed
C_R = R-Wave speed
ω = Frequency of outgoing Rayleigh wave
Z = Depth

Figure 1 shows an outgoing wave that hits a vertical boundary with viscous dashpots at an arbitrary

large distance from the source point of disturbance. Lysmer and Kuhlemeyer (1969) have shown that by minimizing the energy of reflected waves from this viscous boundary, the coefficients of dashpots can be calculated.

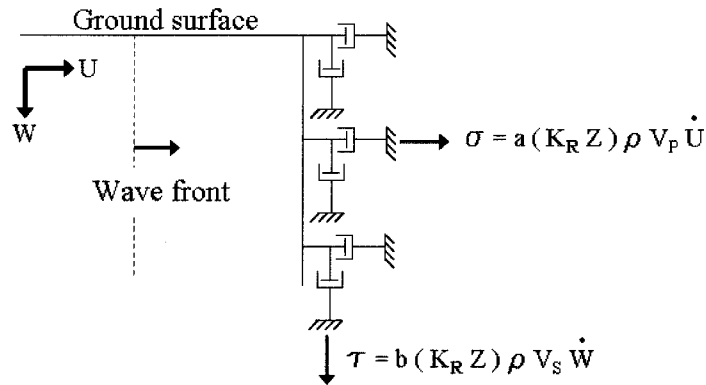


Figure 1 - Frequency and depth dependency of dashpot's coefficients at the boundary

In figure 1 , ρ is mass density of medium , V_p and V_s are the P-wave and S-wave velocities respectively and dot on the top of U and W shows derivative with respect to time. The coefficients for horizontal and vertical dashpots are

$$\begin{aligned} a(k_R Z) &= \frac{\eta}{\alpha} \left[1 - (1 - 2\alpha^2) \frac{g'(k_R Z)}{f(k_R Z)} \right] \\ b(k_R Z) &= \eta \left[1 + \frac{f'(k_R Z)}{g(k_R Z)} \right] \end{aligned} \quad (3)$$

Where $\eta = \frac{1}{V}$ and

$$\begin{aligned} f'(k_R; Z) &= D \left(-m e^{-m k_R Z} + \frac{2 m n^2}{n^2 + 1} e^{-n k_R Z} \right) \\ g'(k_R; Z) &= D \left(m^2 e^{-m k_R Z} - \frac{2 m n}{n^2 + 1} e^{-n k_R Z} \right) \end{aligned} \quad (4)$$

By using dashpots with the coefficients $a(K_R Z)$ and $b(K_R Z)$ at the vertical boundaries of the system, most of the energy of outgoing Rayleigh waves can be absorbed. The properties of these dashpots vary at different depths and frequencies. Sections 3 and 4 describe the procedure to use these dashpots in time domain.

3. JOINT TIME-FREQUENCY REPRESENTATION METHOD

Fast Fourier Transformation (FFT) method has shown its ability for solving many practical problems in engineering and sciences. Applying FFT on the vibration's time-history of a node produces the spectrum for the frequency content of that vibration. This spectrum shows the participation factors of each frequency in the total energy of the vibration. Although the participation factors reveal the distribution of the energy in frequency domain, but the distribution of the energy in time domain can not be achieved. In order to overcome this difficulty, many methods have been introduced. Gabor expansions and Short-Time

Fourier Transformation (Bastiaans 1985), Wigner distribution (Claasen and Mecklenbrauker 1980, Cohen 1989), Wavelet transformation (Daubechies 1990) and Adaptive Optimal Kernel method (Jones and Baraniuk 1995) are different methods to describe spectrum distribution in both frequency and time simultaneously. Among them, Adaptive Optimal Kernel (AOK) method seems to have less interference and noises. Hence, the last method (AOK) is used in this paper.

Finding the time-frequency distribution of the resultant signal $S(t) = S_1(t) + S_2(t)$ is required. $S_1(t)$ and $S_2(t)$ are two arbitrary signals which are concentrated in (t_1, ω_1) and (t_2, ω_2) respectively. The method is based on calculation of Ambiguity Function (AF) of the entire signal. The cross-correlation function of the resultant signal is:

$$R_{S_1, S_2}(t, \tau) = S_1\left(t + \frac{\tau}{2}\right) S_2\left(t - \frac{\tau}{2}\right) \quad (5)$$

Thus, time-dependent cross-correlation function is a function showing the relationship of a signal with a time shifted version of the other signal. Time-dependent power spectrum or cross Wigner-Ville Distribution (WVD) is the Fourier transformation of cross-correlation function:

$$WVD_{S_1, S_2}(t, \omega) = \int \left(S_1\left(t + \frac{\tau}{2}\right) S_2\left(t - \frac{\tau}{2}\right) e^{-i\omega\tau} \right) d\tau \quad (6)$$

If the Fourier transformation is taken with respect to variable t instead of τ , then the resultant spectrum is called cross Ambiguity Function.

$$AF_{S_1, S_2}(\vartheta, \tau) = \int \left(S_1\left(t + \frac{\tau}{2}\right) S_2\left(t - \frac{\tau}{2}\right) e^{-i\vartheta t} \right) dt \quad (7)$$

The Ambiguity Function of the resultant signal can be expressed as:

$$AF_S(\vartheta, \tau) = AF_{S_1, S_1}(\vartheta, \tau) + AF_{S_2, S_2}(\vartheta, \tau) + AF_{S_1, S_2}(\vartheta, \tau) + AF_{S_2, S_1}(\vartheta, \tau) \quad (8)$$

Figure 2 shows the three dimensional Ambiguity spectrum of the resultant signal. In this figure it can be seen that the first and second terms of (8) are located near the origin and the third and fourth interference-terms are located away from the origin. Jones and Baraniuk (1993) introduced a Gaussian kernel window function at the origin of the resultant spectrum to eliminate the un-wanted cross-correlation terms. If this window function is too wide then some part of the cross terms come into the result. If the window is too narrow then some part of the auto-correlation part is deleted. Thus, the kernel of this window should be optimized for the resultant signal to minimize the cross terms and maximize the auto terms. The window moves over time to produce time-dependent spectrum. That is why the method is called Adaptive Optimal Kernel method. Finally, the time-dependent spectrum can be calculated by applying two-dimensional Fourier transformation (Cohen 1966) on the weighted version of Ambiguity Function of the signal.

$$P(t, \omega) = \frac{1}{4\pi^2} \int_{-\infty}^{+\infty} \int_{-\infty}^{+\infty} AF_S(\vartheta, \tau) \Phi_{opt}(\vartheta, \tau) e^{(-i\vartheta t - i\omega\tau)} d\vartheta d\tau \quad (9)$$

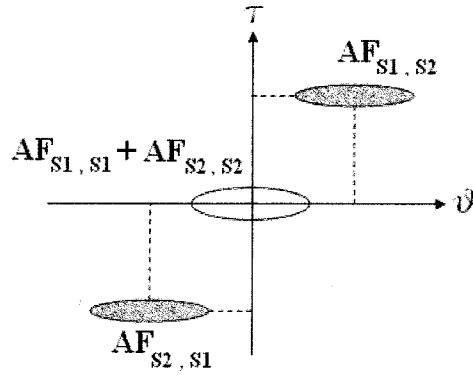


Figure 2 - Three dimensional Ambiguity Function spectrum

$\Phi_{\text{opt}}(\vartheta, \tau)$ is the kernel which should be optimized. Figure 3 shows an example for the application of AOK method on a time varying signal.

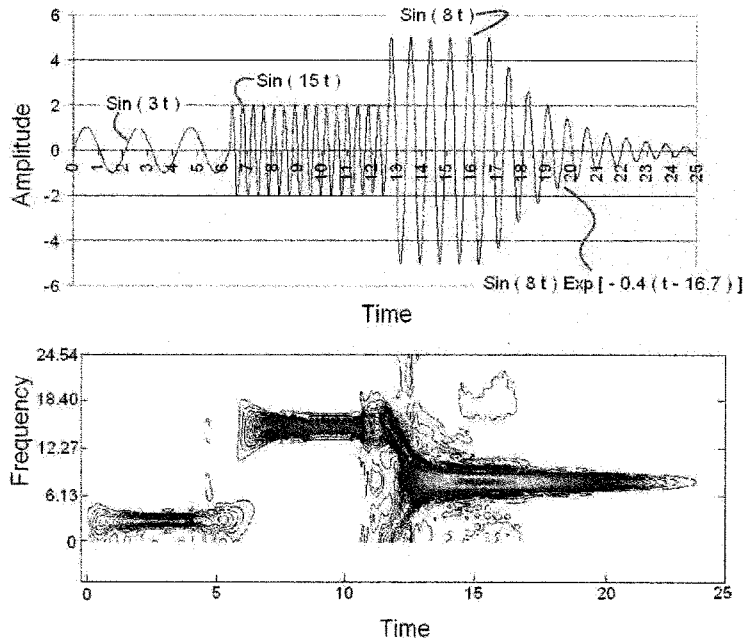


Figure 3 – Time varying spectrum of a non-stationary signal

The changes of frequency content of signals over time are detected well by using AOK method.

4. MEAN INSTANTANEOUS DAMPING

This section shows the method to detect frequency content of outgoing Rayleigh waves. Consider a semi-infinite medium shown in figure 4. Some benchmark nodes should be selected inside this medium in order to investigate the vibration behavior of waves. When these nodes are shaken by the outgoing waves, the TFR kernel detects the frequency content of the waves and passes these data to the boundaries. Then, the boundaries update their properties to absorb these waves with the specified frequencies.

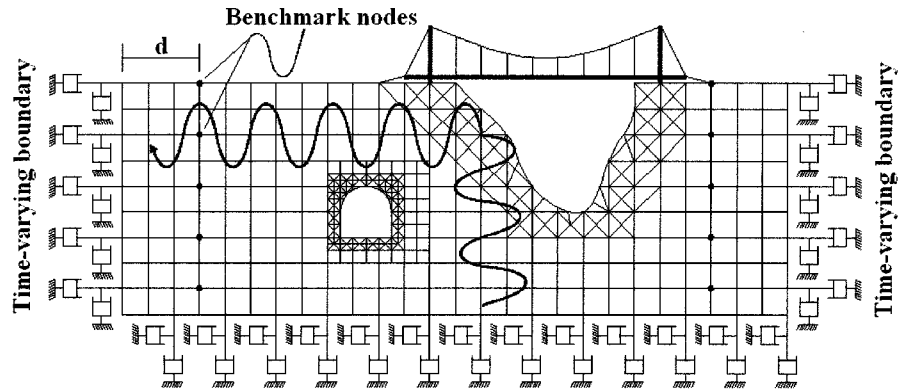


Figure 4 – Vertical time-varying boundaries for absorbing Rayleigh waves

As shown in previous section, the properties of vertical dashpots are function of their depths and frequency content. Because the outgoing waves are non-stationary and their frequencies evolve over time, hence the dashpots properties change when time passes.

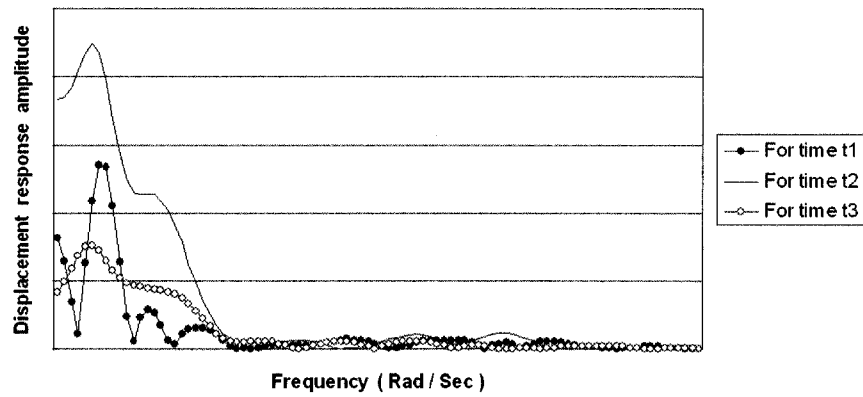


Figure 5 – Schematic time-varying displacement response spectrum of a benchmark node

To transform damping matrix into time domain the weighted average method is used. It has been shown (Farahani 2005) that in earthquakes signals, just a few frequencies are dominant at each time. It means that using the weighted average method for measuring mean instantaneous damping is acceptable.

$$[C]^{\Delta t} = \frac{\sum \left(\text{Amp}^{\Delta t}(\omega_i) [C(\omega_i)] \right)}{\sum \left(\text{Amp}^{\Delta t}(\omega_i) \right)} \quad (10)$$

In which

$[C]^{\Delta t}$ = mean instantaneous damping

$\text{Amp}^{\Delta t}(\omega_i)$ = displacement amplitudes at different frequencies for a specific time

$C(\omega_i)$ = damping at different frequencies for a specific time

Figure 5 shows the cross section of time varying spectrum at different times. In Figure 6, the mean instantaneous damping for a benchmark node is plotted. There should be a time delay between the times of frequency detection and boundaries updating. It is due to the distance d between benchmark nodes and boundaries.

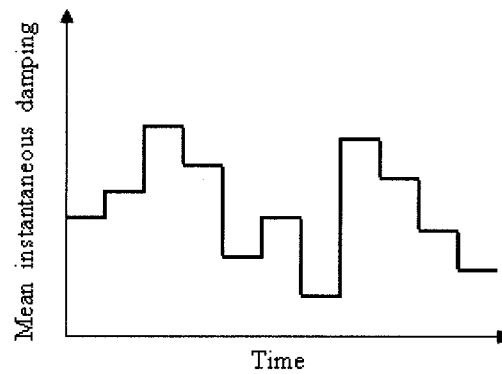


Figure 6 – Mean instantaneous damping diagram

5. EXAMPLE

In order to show the ability of the method to use frequency-dependent non-reflecting boundaries in time domain, a vertical point load on a half plane is simulated. Figure 7a shows the frequency content of the point load and figure 7b shows the displacement response of the upper right node on the ground surface. The result shows a good agreement between new method and the accurate model.

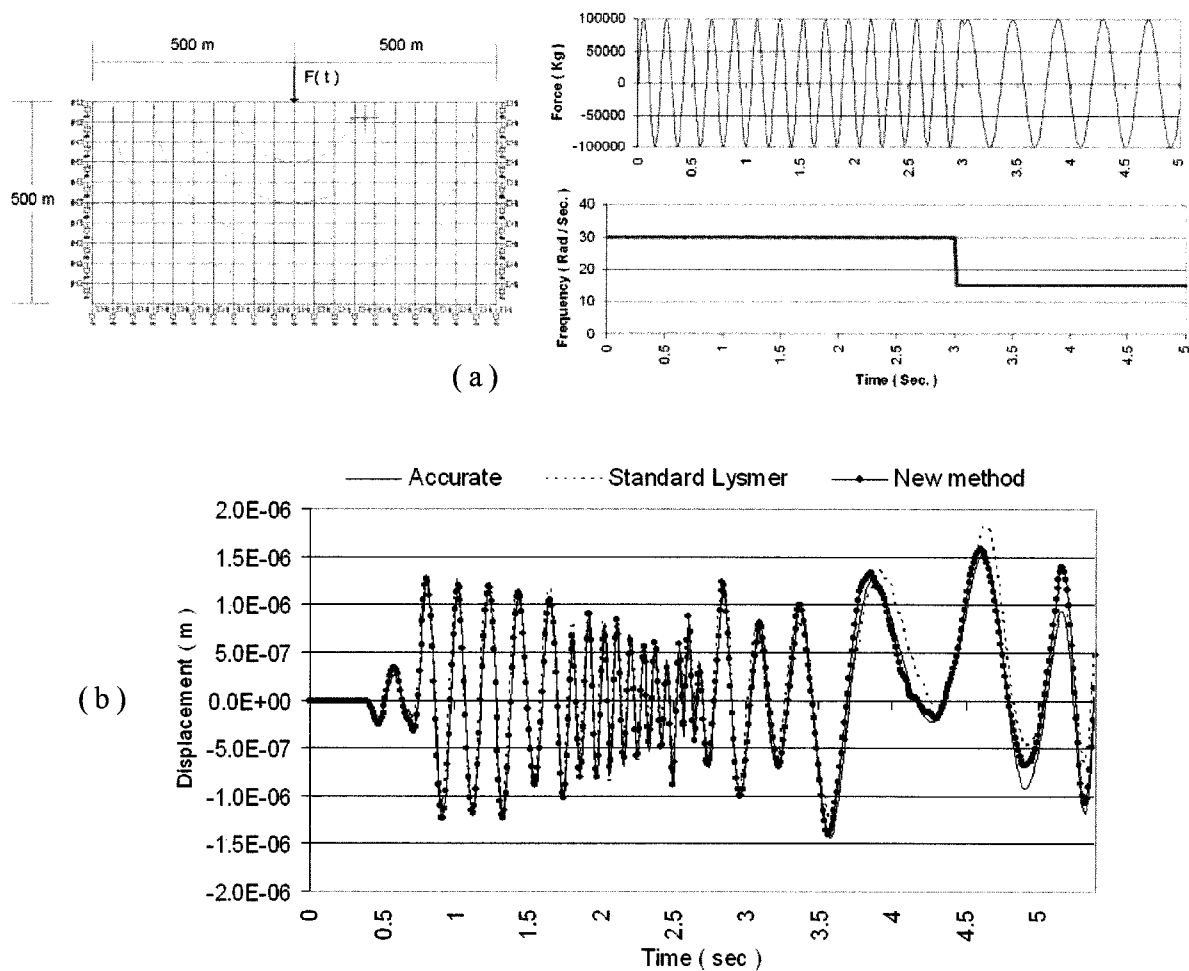


Figure 7 – Frequency content of a vertical point load and response of the system at the upper right node

6. CONCLUSIONS

The proposed method to model semi-infinite media in time domain is a combination of a simple frequency-dependent dashpot and the Adaptive Optimal Kernel method. This method can be improved when linking to more accurate non-reflecting boundaries like boundary elements or infinite elements. In some methods it is common to consider the real and imaginary parts of impedance matrix of far field as an equivalent stiffness and damping matrices in time domain respectively. This mixture is correct as far as steady state vibration is considered. But, for transient waves it produces inaccuracy, because the penetration of outgoing waves into the far field should be calculated. Linking the proposed method with infinite elements has ability to overcome the aforementioned difficulty.

Acknowledgements:

The authors would like to thank Prof. Jones from electrical department of University of Illinois at Urbana Champaign and Prof. Baraniuk from electrical department of Rice University for their invaluable guide in Joint Time-Frequency and Adaptive Optimal Kernel methods.

References:

- Baraniuk, R.G. and Jones, D.L. (1993), "A signal-dependent time-frequency representation: optimal kernel design," *IEEE Transactions on Signal Processing*, vol. 41, issue 4, 1589-1602.
- Baraniuk, R.G. and Jones, D.L. (1993), "A radially Gaussian, signal-dependent time-frequency representation," *Signal Processing*, vol. 32, 263-284.
- Bastiaans, M.J. (1985), "On the sliding-window representation in digital signal processing," *IEEE Transactions on Acoustics, Speech, and Signal Processing*, vol. 33, Issue 4, 868 – 873.
- Bernal, D. and Youssef, A. (1998), "A hybrid time frequency domain formulation for non-linear soil-structure interaction," *Earthquake Engineering and Structural Dynamics*, vol. 27, 673-685.
- Bettess, P. (1977), "Infinite elements," *International Journal for Numerical Methods in Engineering*, vol. 11, 53-64.
- Bettess, P. (1992), "Infinite elements," *CRC Press*.
- Brebbia, C.A. and Walker, S., (1980), "Boundary element techniques in Engineering," *Newnes – Butterworths*, London.
- Claasen, T.A.C.M. and Mecklenbrauker, W.F.G. (1980), "The Wigner distribution – A tool for time-frequency signal analysis," *Pillips Journal of Research*, vol. 35, 217-250.
- Cohen, L. (1966), "Generalized phase-space distribution functions," *Journal of Mathematical Physics*, vol. 7, 781-806.
- Cohen, L. (1989), "Time-frequency distribution – A review," *Proceeding of IEEE*, vol. 77, Issue 7, 941-981.
- Cohen, L. (1995), "Time Frequency Analysis," *Prentice Hall*.
- Daubechies, I. (1990), "The wavelet transform, time-frequency localization and signal analysis," *IEEE Transaction on Information Theory*, vol. 36, Issue 5, 961-1005.
- Farahani, A. (2005), "Joint Time-Frequency Representation of transient behavior of soil medium in Earthquakes," *PhD. Thesis, University of Tokyo, Civil Engineering Department*.
- Jones, D.L. and Baraniuk, R.G. (1994), "A simple Scheme for adapting Time-Frequency Representations," *IEEE Transactions on Signal Processing*, vol. 42, Issue 12, 3530-3535.
- Jones, D.L. and Baraniuk, R.G. (1995), "An adaptive optimal-kernel time-frequency representation," *IEEE Transactions on Signal Processing*, vol. 43, Issue 10, 2361-2371.
- Kim, D.K. and Yun, C.B. (2000), "Time-domain soil-structure interaction analysis in two-dimensional medium based on analytical frequency-dependent infinite elements," *International Journal for Numerical Methods in Engineering*, vol. 47, 1241-1261.
- Lysmer, J. and Kuhlmeyer, R.L. (1969), "Finite dynamic model for infinite media," *Proceedings of the American Society of Civil Engineers, Engineering Mechanics Division*, 859- 877.
- Sezawa, K. (1930), *Bulletin of the Earthquake Research Institute, University of Tokyo*, vol. 8, 59-70.
- Tajimi, H. and Shimomura, Y. (1976), "Dynamic analysis of soil – structure interaction by Thin Layered Element method," *Transaction of AIJ*, No. 243.
- Ungless, R.F. (1973), "An infinite finite element," *M.A.Sc. Thesis, University of British Columbia*.
- Wolf, J.P. and Oberhuber, P. (1985), "Non-linear soil-structure interaction analysis using green's function of soil in time domain," *Earthquake Engineering and Structural Dynamics*, vol. 13, 213-223.
- Wolf, John P. and Motosaka, M. (1989), "Recursive evaluation of interaction forces of unbounded soil in the time domain," *Earthquake Engineering and Structural Dynamics*, vol. 18, 345-363.
- Zienkiewicz, O.C. and Newton, R.E. (1969), "Coupled vibrations of a structure submerged in a compressible Fluid," *Proceeding of International Symposium on Finite Element Techniques, Stuttgart*, 1-15.

DEVELOPMENT OF SIMPLE, ECONOMIC AND EFFICIENT RETROFITTING METHOD FOR MASONRY BUILDINGS CONSIDERING LOCAL AVAILABILITY AND ACCEPTABILITY IN EARTHQUAKE PRONE REGIONS

K. Meguro¹⁾

*1) Professor, International Center for Urban Safety Engineering,
Institute of Industrial Science, The University of Tokyo, Japan
meguro@iis.u-tokyo.ac.jp*

Abstract: Masonry structures are widely used due to its low cost and construction easiness especially in developing countries. In spite of the efforts to provide guidelines for the construction of sound earthquake resistant houses, every year casualties due to collapsing masonry houses during earthquakes are reported. Although it is clear that retrofitting the existing housing stock is urgent, it has not been implemented extensively. To overcome this situation, retrofitting techniques involving inexpensive construction materials available in remote regions and low-skill labor as well as aggressive educational campaigns are needed. This paper presents an innovative retrofitting method for adobe/masonry houses, which consists of using polypropylene bands arranged in meshes. These bands, which are commonly used for packing, are resistant, inexpensive, durable and worldwide available.

1. INTRODUCTION

Masonry is a construction material widely used around the world due to its low cost and construction easiness. More than 30% of the world's population lives in a house of unbaked earth, which is one type of unreinforced masonry (Houben and Guillaud, 1989). During the last century, human casualties during earthquakes were mainly caused by structural damage, being the failure of unreinforced masonry structures responsible of more than 60% of them (Coburn and Spence, 1992). The vulnerability of masonry structures under seismic loads has being recognized long ago and efforts to provide guidelines for the construction of sound earthquake resistant houses have being remarkable. In spite of this, every year many casualties due to collapsing masonry houses during earthquakes are reported.

For strengthening unreinforced masonry houses in developing countries, a suitable retrofitting technique should guarantee not only its efficiency in terms of improvement of the seismic resistant characteristics of the structure (strength, ductility and energy dissipation). It should also be considered that: 1) the used material is economical and locally available and 2) no high labor skill is required. In this context, the use of polypropylene bands (PP-bands) arranged in a mesh fashion and embedded in a mud/mortar overlay is proposed. These bands, which are worldwide used for packing, are inexpensive, resistant, and easy to handle. The PP-band mechanical properties are shown in Figure 1.

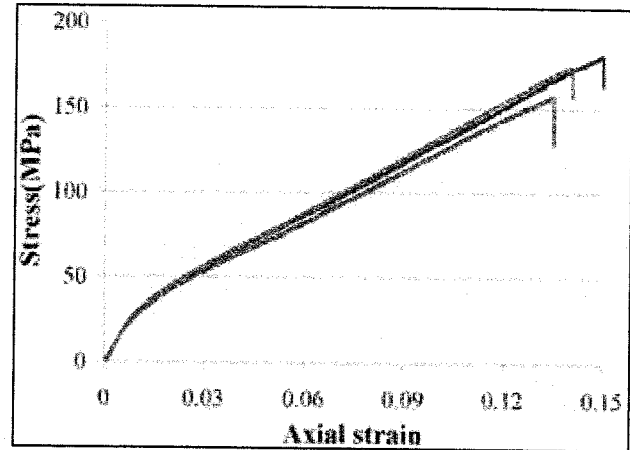
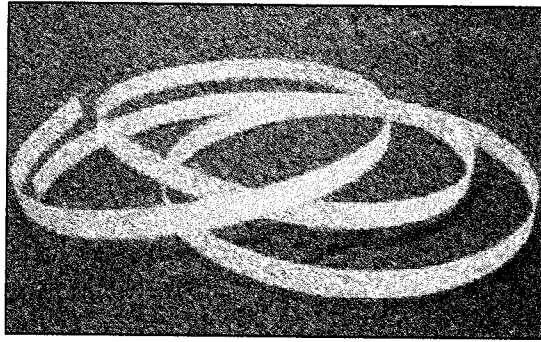


Figure 1. PP-band mechanical properties

2. INSTALLATION PROCESS

The PP-band mesh installation process is shown in Figure 1. It is simple and can be performed by the house owner himself. This is a critical requirement to promote safer building construction in developing countries.

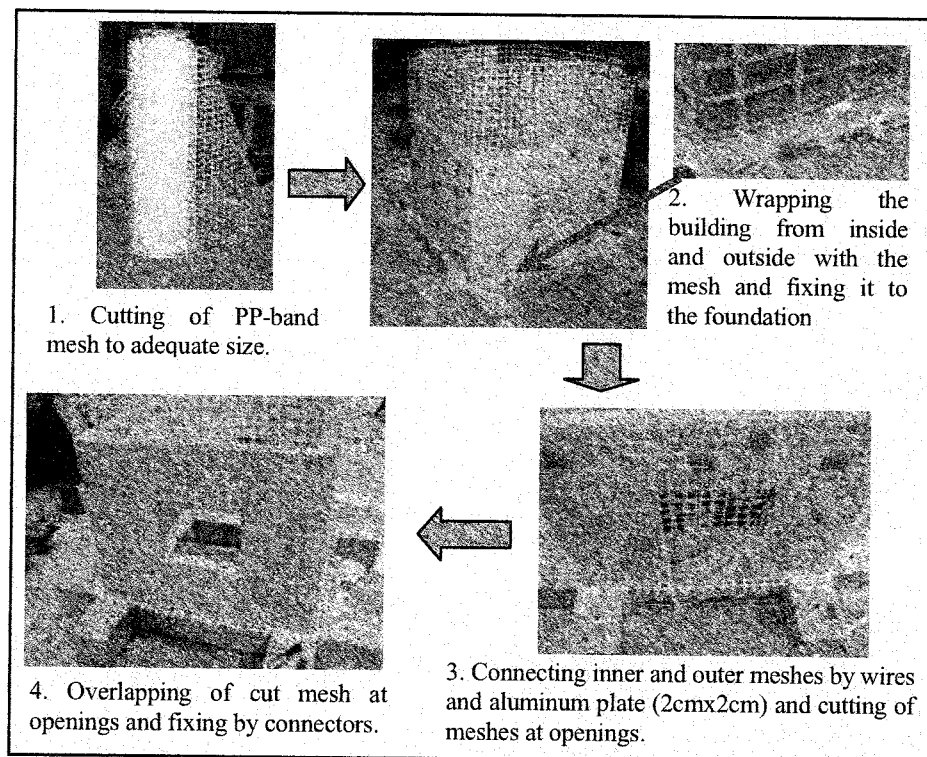


Figure 2. PP-band mesh installation process

3. EXPERIMENTAL VERIFICATION

The proposed technique was verified through several testing programs. These include element tests (in-plane and out-of-plane), in-plane static wall tests, scaled model shaking table tests, and full scale shaking table tests. In this paper, the first three will be reported.

3.1 Element test

Element tests on masonry wallettes, in-plane and out-of-plane, were carried out. A brief description of these experiments is presented here. For further details the reader is referred to Navaratnarajah S. et al (2005).

Figure 3 shows the in-plane test setup which is based on the ASTM E72 (1997). Figure 4 presents the comparison between the performances of non-retrofitted and retrofitted wallettes.

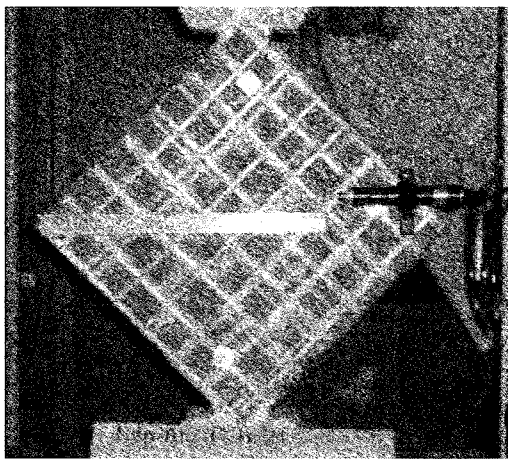


Figure 3. In-plane loading test

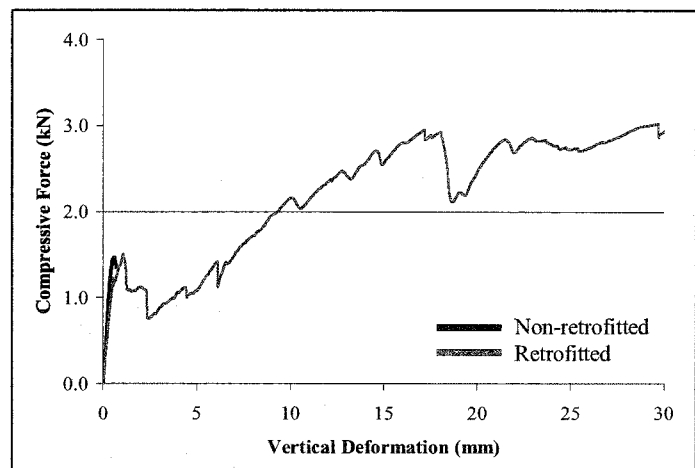


Figure 4. Comparison between non-retrofitted and retrofitted wallettes loaded in-plane.

The non-retrofitted wallette behavior is characterized by a brittle crack and a consequent sudden strength drop. On the other hand, the retrofitted specimen exhibited a ductile behavior because after the appearance of the first crack, the stresses were redistributed by the P-band mesh. As a whole, the retrofitted specimen was three times stronger than the non-retrofitted specimen and was kept as one unit for deformations equivalent to 45 times the initial crack deformation.

Figure 5 illustrate the out-of-plane loading test setup. Figure 6 shows the specimens after the test and the comparison of the load-deformation curves.

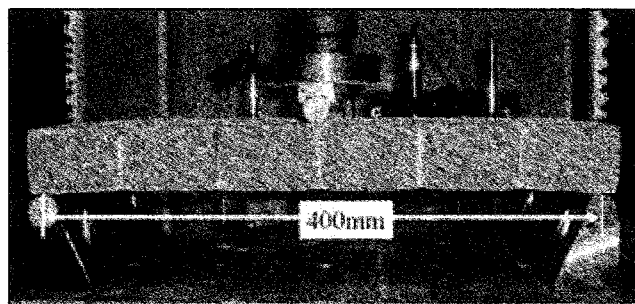
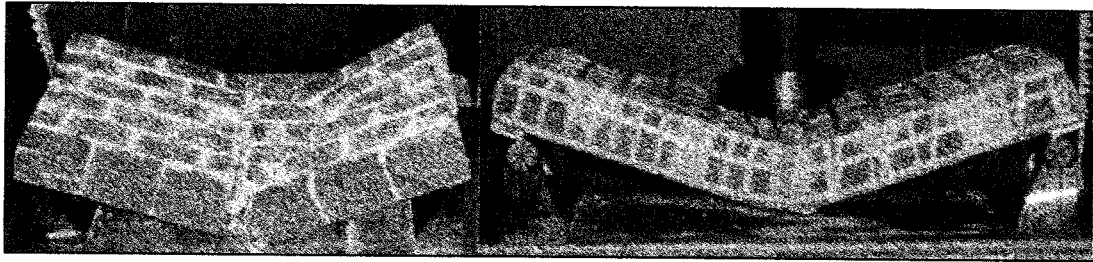
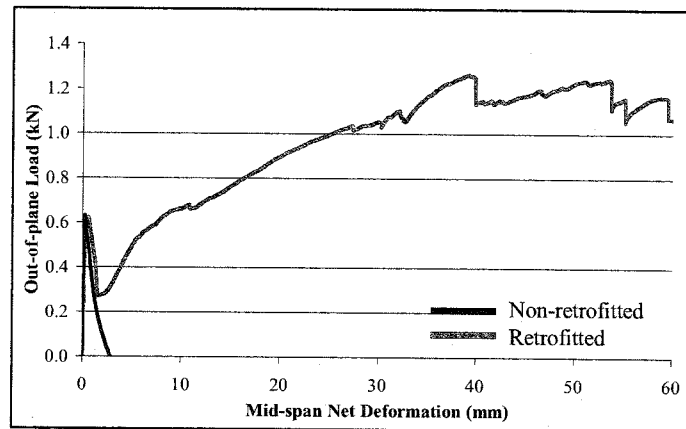


Figure 5. Out-of-plane test setup



(a) Specimens at the end of the out-of-plane test



(b) Test results

Figure 6. Out-of-plane test outcome

In the out-of-plane test the observed behavior was similar to the in-plane test, i.e. brittle failure for non-retrofitted specimens and ductile performance of the retrofitted specimens. In this case, the strength was twice higher and deformation capacity at least 49 times larger in the latter case.

3.2 In-plane static wall test

The detailed description of these tests may be found at Mayorca and Meguro (2003). The test setup is shown in Figure 7 and the crack patterns for non-retrofitted and retrofitted specimens are shown in Figure 8.

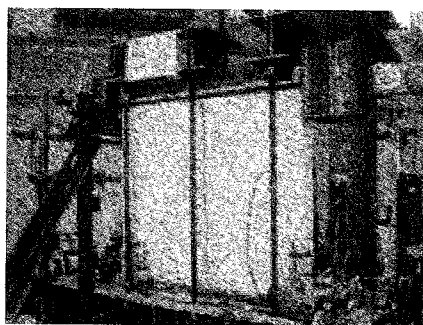
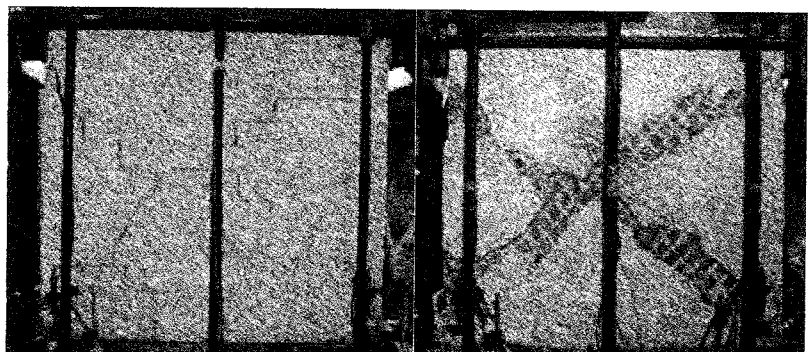


Figure 7. Test setup



(a) Non-retrofitted wall

(b) Retrofitted wall

Figure 8. Crack patterns after the test

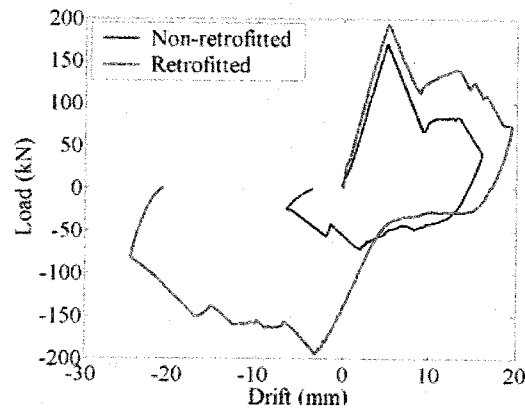
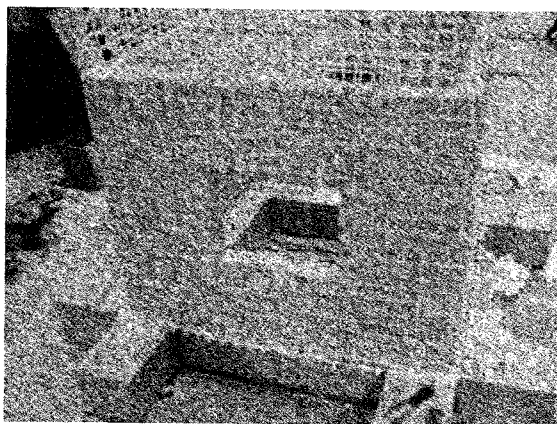


Figure 9. In-plane wall test results

The wall behavior was consistent with the observations of the element tests. The performance of the specimens, non-retrofitted and retrofitted, was similar up to the initial cracking. Once this was attained, the PP-band meshes of the retrofitted specimen redistributed the loads and as a result the strength and ductility of the specimens were increase by at least 1.5 and 2, respectively. As observed in the element tests, the non-retrofitted specimen cracks were concentrated whereas the cracks of the retrofitted one spread over a wider region due to the mesh effect.

3.3 Scaled model shaking table tests

Two models, a non-retrofitted and a retrofitted one, were built in the reduced scale 1:4 using bricks and cement lime mortar. The material strength was similar to those found in developing countries. The buildings' dimensions were 950x950x720 mm³ with wall thickness 50mm as shown in Figure 10. Sinusoidal motions of frequencies ranging from 2Hz to 35 Hz and amplitudes ranging from 0.05g to 1.4g were applied to obtain the dynamic response of both structures as shown in Figure 11. For more details on the test conditions the reader is referred to Meguro et al (2005).



Amplitude	Frequency (Hz)							
	2	5	10	15	20	25	30	35
1.4 g		59	58	57				
1.2 g		58	55	54	53			
1.0 g	62	52	51	50	49			
0.8 g	61	47	44	41	38	35	32	29
0.6 g	60	46	43	40	37	34	31	28
0.4 g	48	45	42	39	36	33	30	27
0.2 g	26	25	24	23	22	21	20	19
0.1 g	18	17	16	15	14	13	12	11
0.05 g	10	09	08	07	06	05	04	03
	01, 02							



 Loading steps for both non-retrofitted and retrofitted models
 Loading steps for retrofitted model after non-retrofitted model building collapsed

Figure 10. Retrofitted specimen for scaled model shaking table test.

Figure 11. Loading sequence for scaled shaking table test.

Initial crack patterns in both models, non-retrofitted and retrofitted, were similar. In the non-retrofitted specimen, few cracks propagated and widened in each successive loading. The specimen totally collapsed after Run 46. On the other hand, the retrofitted specimen exhibited widespread cracking. Loading proceeded until Run 60, i.e. 14 more runs than the non-retrofitted specimen. At this stage, almost all mortar joints were cracked. During shaking, sliding along mortar interfaces constituted an efficient energy dissipation mechanism. Figure 12 show the specimens' cracking pattern.

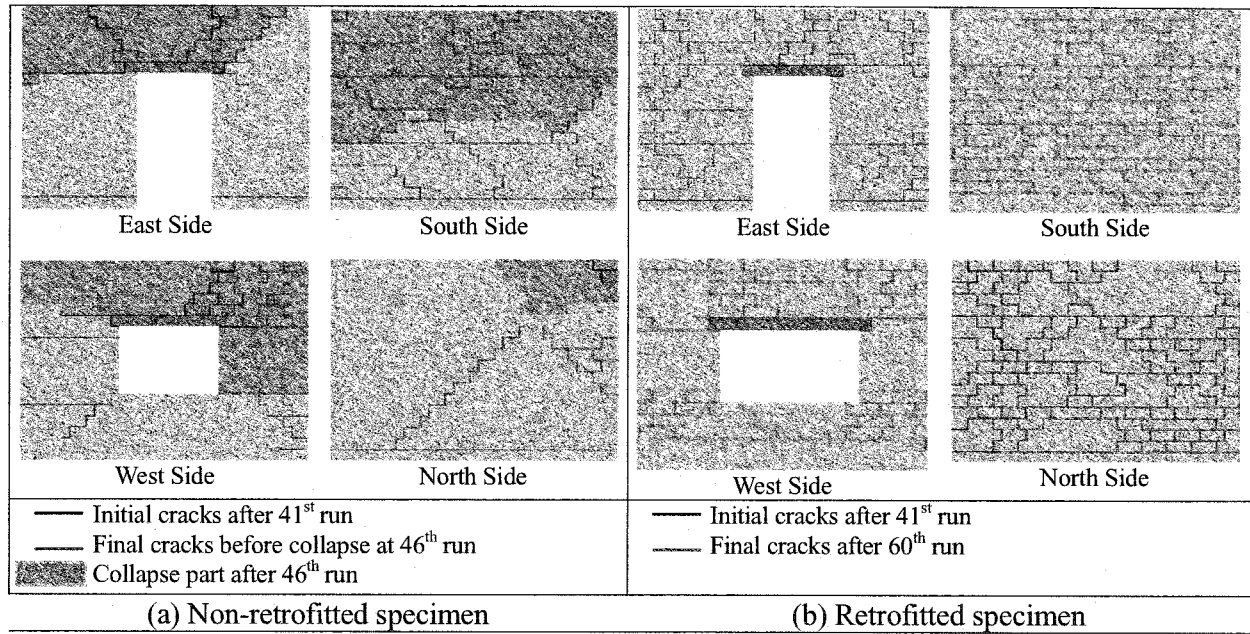


Figure 12. Cracking patterns of non-retrofitted and retrofitted specimens.

Figures 13 and 14 show the non-retrofitted and retrofitted specimens at the end of the tests. Even after Run 61, the retrofitted specimen had a life safety damage level compared to the total collapse exhibited by the non-retrofitted model based on the FEMA 356 (2000) definition. The JMA Intensities that the models were able to resist were 5- and 6+ for the non-retrofitted and retrofitted models, respectively.

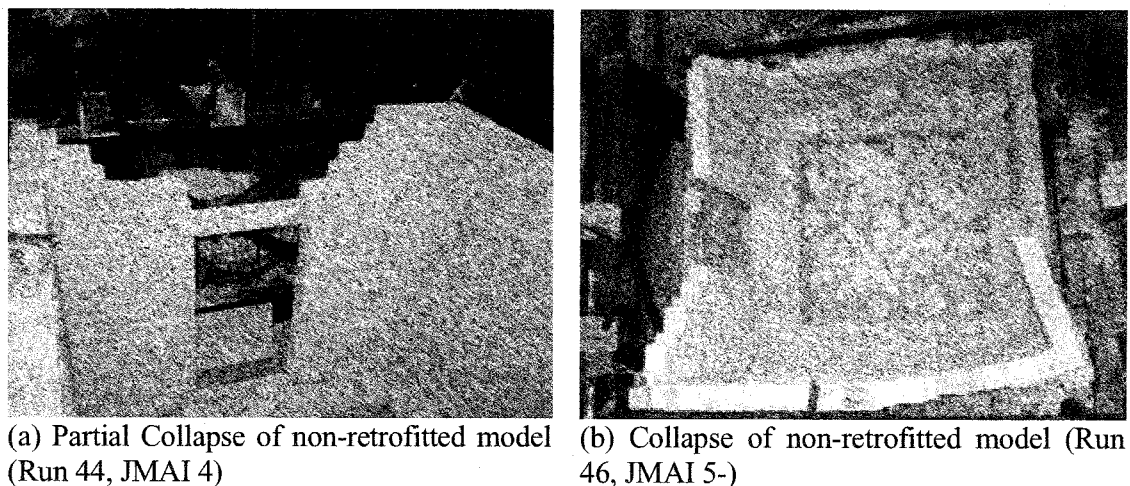


Figure 13. Non-retrofitted specimen after the test

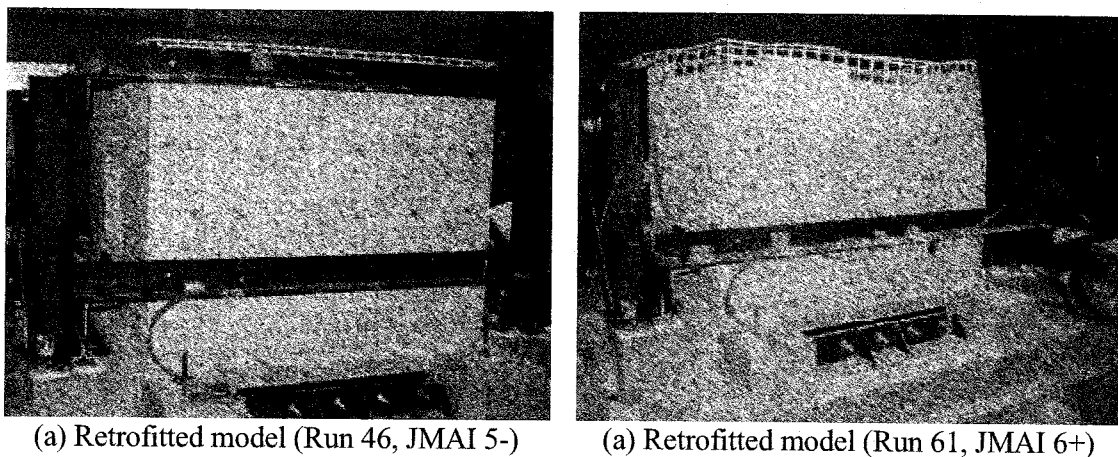


Figure 14. Retrofitted specimen after the test

4. CONCLUSIONS

An innovative retrofitting method for adobe/masonry houses, which consists of using polypropylene bands arranged in meshes is proposed to overcome the problem of low earthquake resistant houses in developing countries. The paper summarizes installation procedures, material properties and experiments carried out to verify the suitability of the proposed technique. Although cracking is not prevented by PP-band meshes, they efficiently increase the structure seismic capacity, particularly its ductility. The proposed retrofitting method improved the structure performance allowing a life safety damage level for a masonry structure subjected to a JMAI 6+ shaking.

Acknowledgements:

The authors acknowledge the support of Sekisui Jushi for the preparation of the PP-band meshes used in some of the reported experimental programs.

References:

- Houben H. and Guillaud, H. (1989) "Earth construction – A comprehensive guide." London: ITDG Publishing.
- Coburn A. and Spence R. (1992) "Earthquake Protection." West Sussex: John Wiley & Sons Ltd.
- Sathiparan, N., Mayorca, P., Nesheli, N., Guragain, R., and Meguro, K., (2005) "In-plane and Out-of-plane behavior of PP-band retrofitted masonry wallttes." *Proceeding of the 4th International Symposium on New Technologies for Urban Safety of Megacities in Asia*, Singapore.
- ASTM, E72 (1997) "Standard Test Methods of Conducting Strength Tests of Panels for Building Construction", American Society for Testing and Materials, Philadelphia, Pa.
- Meguro, K., Mayorca, P., Sathiparan, N., Guragain, R., and Nesheli, N., (2005) "Shaking table tests of ¼ small scaled masonry models retrofitted with pp-band meshes" *Proceeding of the 4th International Symposium on New Technologies for Urban Safety of Megacities in Asia*, Singapore.
- FEMA 356, (2000) "Prestandard and Commentary for the Seismic Rehabilitation of Buildings", Federal Emergency Management Agency

Vehicle Routing for Rescue Operation in Earthquakes

C.-F. Hsueh¹⁾ and H.-K. Chen^{2)*}

1) Assistant Professor, Department of Marketing and Distribution Management, Ching Yun University, Taiwan

2) Professor, Department of Civil Engineering, National Central University, Taiwan

cfhsueh@cyu.edu.tw, ncutone@ncu.edu.tw

Abstract: This paper shows that a special version of the real-time time-dependent vehicle routing problem with time windows and simultaneous delivery/pickup (RTTD-VRP-TWDP), along with our proposed two-phase solution algorithm, can be effectively applied to rescue operation in earthquakes. The illustrative example demonstrates that a suggested routing schedule can be immediately generated after the real-time delivery/pickup demands have appeared and/or the travel time has changed.

1. INTRODUCTION

Earthquake, one of natural disasters, can happen at any place and at any time and once happened, serious fatalities and property damages could result and continue for a period of time. It is apparent that the coordinated and orderly delivery/pickup of available resources helps to mitigate property damage and save lives. Without performing quick and appropriate rescue operation, the amount of losses could be worsened.

Relieving an earthquake disaster is not a simple task. It involves numerous relevant works such as constructing all relevant databases (stocking units, aid distribution centers, national transportation networks, search and rescue teams, etc) and the logistic coordination center. Critical to any disaster situation is to identify the resources needed at the site—i.e., the response team, equipment and commodities—and transport those resources to arrive at the right place and at the right time. However, it would be too ambitious to cover all relevant materials in one paper. Therefore, only emergency logistics is addressed in this paper.

The emergency logistics involves a planning time horizon. During a planning time horizon, the model assumes that delivery/pickup demand is known in the beginning of the current planning time horizon, and future delivery/pickup demand is forecasted for some commodities or emerged in a real time manner. Supply is limited and its availability is known for some time ahead due to the fact that prospective supply arrivals are usually known in advance. The priority of supply is principally given to the nodes with closer time windows.

To sum up, emergency logistics must take into account the following considerations during the rescue operation.

1. Once a disaster occurs, the road system in the affected area will be strictly controlled and under surveillance by the police officers and hence no driver can freely maneuver his/her vehicle from origin to destination. Therefore, the so-called user equilibrium (or Wardrop first principle) won't appear.

* Corresponding author

2. Time-dependent link travel times and delivery/pickup demands at nodes in the affected area may change in a real time manner; no prior information is available. It also implies that *any time algorithm* is essential for the emergency logistics problem as interruption of the scheduled plan can occur any time.
3. Each node has a time window defined by an upper limit beyond which the losses will get worse. The reason for not setting the lower limit is because a rescue team is assumed standby at the site all the time.
4. A dispatched vehicle must start its service upon arrival and continue its tour from the current node toward the next node right after the service has been completed. It is usually not allowed for a dispatched vehicle staying/idling at a node while there are still some nodes waiting for service.
5. Both delivery and pickup operations may be needed at a node.
6. A dispatched vehicle needs not to return to the depot by a time window or does not have to do so at all. Vehicles will wait at their last stop until they receive the next order from the logistics coordination center. In other words, “broken” tours that are not in closed circuit are also possible during the rescue operation.

The remainder of the paper will be organized as follows. In Section 2, the model formulation is described and the proposed solution algorithm is then elaborated. In Section 3. An illustrative example is provided in Section 4. Finally, a few closing remarks are given in Section 5.

2. MODEL FORMULATION FOR EMERGENCY LOGISTICS

In emergency logistics planning, a planner may not be aware of all information for route planning at the time the routing process begins. Moreover, information, including delivery/pickup demands and time-dependent travel times, may change after the initial routes are constructed, and such information cannot be known in advance. When a new node appears, the main task of the logistics coordination center is to include the new node into the current routing plan. Yet, if time dependent travel times have changed due to an unexpected incident(s), in order to fulfill time window constraints and achieve a lower travel cost objective, scheduled incoming nodes must be re-scheduled based on the position and loading of *en route* vehicles. The logistics coordination center needs a very quick answer in order to respond in real time to both the real-time delivery/pickup demands and time-dependent travel times.

To address emergency logistics in earthquakes, we will introduce the RTTD-VRP-TWPD problem. In order to capture the dynamic characteristics of the RTTD-VRP-TWPD, we employ the concept of time rolling horizon and hence adopt a series of mixed integer programming submodels to formulate the problem. Each submodel represents a *special* vehicle routing problem with time windows (VRPTW) at a particular point in time when travel times and/or delivery/pickup demands have changed. Each *special* VRPTW involves vehicles that may depart from current nodes (called critical nodes, not the actual depot) and visit other unserved nodes, because those vehicles are already on their routes when the travel times and/or delivery/pickup demands have changed. The goal of the RTTD-VRP-TWPD at any particular time is to find a set of minimum cost vehicle routes, which originate from the critical nodes (a critical node is defined as a node which is currently being serviced or to which a vehicle is heading) or the depot, $N_c(\tau) \cup \{0\}$, and visit each unserved node, $N_u(\tau)$. The reader may refer to Appendix A for a list of the notation used in this paper.

Whenever real-time delivery/pickup demands have appeared and/or time-dependent travel times have changed, the RTTD-VRP-TWPD needs to be solved within estimated computation time Δ , which is very close to zero, for an initial solution. Suppose τ is the time when the real-time information (i.e., travel times or delivery/pickup demands) becomes available plus an estimated

time to compute the model. At time τ , the RTTD-VRP-TWPD can be formulated as a mixed integer problem, as follows:

$$\min_{\{x_{ijk}\} \in \Omega} z(\tau) = \sum_{j \in N_u(\tau)} \sum_k \left(\sum_{i \in N_{cu}(\tau)} c_{ij}(d_i) x_{ijk} + c_{0j}(d_{0k}) x_{0jk} \right) \quad (1)$$

where Ω is the feasible region represented by the following constraints.

Flow Conservation Constraints:

$$\sum_j \sum_k x_{ijk} = 1 \quad \forall i \in N_{cu}(\tau) \quad (2)$$

$$\sum_i \sum_k x_{ijk} = 1 \quad \forall j \in N_u(\tau) \quad (3)$$

$$\sum_i x_{ihk} - \sum_j x_{hjk} = 0 \quad \forall h \in N_u(\tau), k \in K \quad (4)$$

$$\sum_j x_{ij\bar{k}_i} = 1 \quad \forall i \in N_c(\tau) \quad (5)$$

$$\sum_j x_{0jk} \leq 1 \quad \forall k \in K_0(\tau) \quad (6)$$

$$x_{ijk} \in \{0,1\} \quad \forall i \in N_{cu0}(\tau), j \in N_{u0}(\tau), k \in K \quad (7)$$

Time Window Constraints:

$$a_i \leq l_i \quad \forall i \in N_u(\tau) \quad (8)$$

Vehicle Capacity Constraints:

$$Q_{imk} \geq q_{im} \quad \text{if} \quad \sum_j x_{ijk} = 1 \quad \forall i \in N_u(\tau), m \in M, k \in K \quad (9)$$

$$\sum_m (Q_{imk} - q_{im} + \hat{q}_{im}) \leq C_k \quad \text{if} \quad \sum_j x_{ijk} = 1 \quad \forall i \in N_u(\tau), k \in K \quad (10)$$

Definitional Constraints:

$$a_j = d_i + c_{ij}(d_i) \quad \text{if} \quad x_{ijk} = 1 \quad \forall i \in N_{cu}(\tau), j \in N_u(\tau), k \in K \quad (11)$$

$$a_j = d_{0k} + c_{0j}(d_{0k}) \quad \text{if} \quad x_{0jk} = 1 \quad \forall j \in N_u(\tau), k \in K \quad (12)$$

$$d_i = \begin{cases} \max(\tau, a_i + s_i) & \text{if} \quad \sum_k x_{i0k} = 0 \\ \infty & \text{if} \quad \sum_k x_{i0k} = 1 \end{cases} \quad \forall i \in N_{cu}(\tau) \quad (13)$$

$$d_{0k} = \tau \quad \forall k \in K_0(\tau) \quad (14)$$

$$Q_{jmk} = Q_{imk} - q_{im} + \hat{q}_{im} \quad \text{if } x_{ijk} = 1 \quad \forall i \in N_u(\tau), j \in N_u(\tau), m \in M, k \in K \quad (15)$$

$$Q_{jmk} = \bar{Q}_{mk}(\tau) - q_{im} + \hat{q}_{im} \quad \text{if } x_{ijk} = 1 \quad \forall i \in N_c(\tau), j \in N_u(\tau), m \in M, k \in K \quad (16)$$

$$Q_{jmk} = \bar{Q}_{mk} \quad \text{if } x_{0jk} = 1 \quad \forall j \in N_u(\tau), m \in M, k \in K \quad (17)$$

The objective of the RTTD-VRP-TWPD, shown in Eqn (1), minimizes the total travel time of all tours. Note that the link travel time between any node i and depot 0 , $c_{i0}(d_i)$, is not included in the objective function, which will be further elaborated in Eqn (13). Eqn (2) requires that only one vehicle can leave from a critical node or unserved node i once. Eqn (3) denotes that only one vehicle can arrive at unserved node j once. Eqn (4) states that for each unserved node h , the entering vehicle must eventually leave this node. Eqn (5) requires that vehicle \bar{k}_i which has arrived at or is approaching a critical node must also leave this node once. Note that vehicle \bar{k}_i is known at time τ . Eqn (6) designates that each vehicle can leave the depot once at most. Eqn (7) designates x_{ijk} as a 0-1 integer variable. x_{ijk} equals 1 if vehicle k departs node i toward node j . Otherwise, x_{ijk} equals 0.

Eqn (8) requires that for each node, the service should take place no later than the end of its time window. Time window is set such that a vehicle must arrive before a time limit, which is predetermined according to the observed or predicted severity of losses on the spot. Eqn (9) indicates that if node i is serviced by vehicle k , i.e., $\sum_j x_{ijk} = 1$, then the remaining load of commodity m of vehicle k at node i must be greater than or equal to the demand of commodity m at node i . Eqn (10) indicates that if $\sum_j x_{ijk} = 1$, then the updated load of vehicle k at node i after delivery and pickup must be less than or equal to the full capacity of vehicle k .

Eqn (11) and Eqn (12) define the arrival time at node j . Eqn (13) defines the departure time at node i which is in the set of either critical or unserved nodes. If $i \in N_u(\tau)$ then the departure time is set as $d_i = a_i + s_i$. On the other hand if $i \in N_c(\tau)$, two scenarios must be further considered. (i) If node i is not the last node next to the depot, i.e., $\sum_k x_{i0k} = 0$, then the departure time is set as $d_i = \max(\tau, a_i + s_i)$. The only situation that the departure time will take on the value of τ is when the vehicle that is waiting at the last node i of a "broken" tour receives a new order from the logistic coordination center and must depart for the next node immediately. (ii) If node i is the last node next to the depot, i.e., $\sum_k x_{i0k} = 1$, then the departure time is set as $d_i = \infty$, where symbol ∞ refers to a big number. This logical expression is meant that link $i \rightarrow 0$ will never be traversed and therefore the link travel time between any node i and depot 0 , $c_{i0}(d_i)$, should not be included in the objective function. In other words, vehicle k will stay at the last node i next to the depot 0 until the next order from the logistics coordination center has been received. Eqn (14) defines the departure time at the depot. Eqn (15) states for unserved node i that if vehicle k is heading to node j , then the remaining load of commodity m of vehicle k at node j will be equal to the updated load of commodity m minus the delivery and plus the pickup at node i . Eqn (16) is identical to Eqn (15) except that the unserved nodes are substituted by the critical nodes. Eqn (17) defines the initial load of commodity m of vehicle k when dispatching from depot 0 .

3. SOLUTION ALGORITHM

We propose a two-phase heuristic comprising routes construction and routes improvement for the RTTD-VRP-TWPD. In Section 3.1 a systematic solution procedure, embedding both route construction and route improvement, is illustrated. An efficient strategy for route construction is proposed in Section 3.2.

3.1 Unified Framework of Solution Procedure

For solving real time operations, an *anytime* algorithm is desired. In other words, the solution procedure must have the ability to stop at any time and provide an acceptable solution. We describe a unified solution procedure for the RTTD-VRP-TWPD in the following. During the solution process, we constantly check whether (i) departure time for critical nodes is up, (ii) new delivery/pickup demand occurs, and (iii) time-dependent travel time has changed. The strategies of dispatching *en route* or on-call vehicles at the right time to the assigned nodes, reconstructing routes, improving the quality of the existing routes, and so forth, are repeatedly applied. Note that the computation time allowed for route construction and improvement is usually short due to the requirement of real-time response. It would be natural to adopt a “quicker” solution algorithm for use. In the following, the *insertion* method is used for route construction, while the *Or-opt* node exchange algorithm is adopted for route improvement.

3.2 Method for Route Construction

For the VRPTW, the insertion method has been proven effective in constructing static routes (Solomon, 1987). So we adopted the *insertion* method with modifications for route construction.

Note that applying the proposed algorithm to the RTTD-VRP-TWDP problem will result in “broken” tours, rather than commonly seen “complete” tours in most of VRP related problems. Without having to return to the depot, the vehicle can stay at the last node of the broken tour, waiting for the next order from the logistics coordination center and hence has more flexibility to rescue in earthquakes.

4. COMPUTATIONAL RESULTS

The test problem set used in Chen et al. (2005) is adopted with an additional column added to accommodate real-time delivery/pickup demands of each commodity. In Table 1 we only illustrate part of the testing results of the problem R103. It is assumed that two kinds of commodities are considered for delivery and/or pickup. The predictive traffic condition is characterized by a step-wise travel time function, which is exactly the same as the one used in Chen et al. (2005). During the rescue process, the number of unexpected road incidents or road recoveries is set as four, at each of which a new travel time function will result. The whole vehicle capacity is 200 for each vehicle, and the initial loads of a vehicle at depot are 80 percent of the whole vehicle capacity. In other words, 80 pallets for each commodity are loaded when a vehicle is departing the depot. Other information associated with each node is taken from Hsueh et al. (2006).

Table 1 Computational Results

Veh. No.	Route	Commodity 1			Commodity 2		
		\bar{Q}_{mk}	$\sum_i q_{im}$	$\sum_i \hat{q}_{im}$	\bar{Q}_{mk}	$\sum_i q_{im}$	$\sum_i \hat{q}_{im}$
1	0→27→52→18→60→83→8→46	80	40	25	80	28	36
2	0→28→26→12→80→68→29→24→55→25	80	35	77	80	84	37
3	0→89→6→94→96→99→59→95→97→93	80	113	43	80	28	104
:	:	:	:	:	:	:	:
16	0→69→88→62→84→5→17	80	26	41	80	52	28
:	:	:	:	:	:	:	:
19	0→53	80	0	14	80	13	0

Noticed that the proposed model and associated algorithm are very suitable for real time rescue operation since the response to the real time information (including most recent travel time information and pickup/delivery requests) of an earthquake can be made in a very short time (less than 1 second for a problem with 100 nodes). In Table 1, all nodes can receive proper relief goods by their desired time limits and the total routing cost is minimized as much as possible under the real time response requirement.

It is also worth mentioning that some relief goods or rescue equipments at a node may be no longer desired which can be picked up and made available to the following nodes of the same route. For example, the total delivery quantity of commodity 1 in vehicle 3 is 113 pallets, which is greater than its initial loads, 80 pallets, implying that at least some delivery demands are fulfilled by the pickup commodity from previous nodes of the same route.

5. CONCLUSIONS

In this paper, the RTTD-VRP-TWPD was studied and formulated as a mixed integer programming model, which accounts for real-time and time-dependent travel times, and real-time delivery/pickup demands. The results showed that, with our proposed model and algorithm, a suggested routing schedule can be immediately generated after the real-time delivery/pickup demands have appeared and/or the travel time has changed, which is of course critically required for the real time rescue operation.

Other contributions of the paper can be summarized as follows:

1. Real time information such as road incidents, road/bridge damage recovery or delivery/pickup request can be considered from time to time to regenerate a better route schedule in our model.
2. When a node which has been serviced needs further rescue, it will be regarded as a new demand and taken back to the unserved node list. This situation is quite common in rescue operation if the damage resulting from the earthquake continues.
3. Delivery and pickup demands are considered simultaneously. In addition, the relief goods or rescue equipments being picked up at one node can be reused by the following nodes of the same route.
4. Without having to return to the depot, a vehicle can stay at the last node of a broken tour to wait for the next order from the logistics coordination center, and hence has more flexibility to rescue in earthquakes.

5. A clear definition of critical node is proposed, which defines the scope of the remaining problem at a particular instant along the time horizon. The concept of critical nodes distinguishes the *real-time* VRPTW from the traditional VRPTW to a high degree.
6. The departure time at each node allows us eliminate numerous subtour (a circle disconnected from the depot) prevention constraints in the constraint set.

In the following, we also list few suggestions for future research.

1. Do optimal initial loads exist and, if so, how can they be optimally determined in a real time situation?
2. Hard time window constraints, if too tight, may cause some nodes being rejected. To cope with this problem, adopting soft time window constraints (that are associated the violation penalties) becomes a natural choice. Substituting the hard time window constraints by their “soft” counterpart within our proposed model structure is rather straightforward.
3. Supply shortages are not considered in this study. In fact, supply is limited in earthquakes. Therefore, optimally allocating supply to demanding nodes is also an important goal. Therefore, minimizing the sum of unsatisfied demand of all commodities throughout the planning horizon (Özdamar et al., 2004) should be also incorporated into the proposed model.
4. More efficient and accurate algorithms such as those including meta-heuristics for practical large-scale applications are needed which are subject to future research.

Acknowledgments:

We would like to thank the Center for Urban Earthquake Engineering (CUEE), Tokyo Institute of Technology, Japan, for supporting the corresponding author with round trip ticket and local expenses for attending the 3rd International Conference on Urban Earthquake Engineering.

References:

- Chen, H.K., Hsueh, C.F. and Chang, M.S. (2005), “The Real-Time Time-Dependent Vehicle Routing Problem,” *Transportation Research Part E*. (forthcoming)
- Hsueh, C.F., Chen, H.K. and Chou, H.W. (2006), “Vehicle Routing for Rescue Operation in Natural Disasters,” *Transportation Research Part E*. (submitted)
- Özdamar, L., Ekinçi, E. and Küçükyazacı, B. (2004), “Emergency Logistics Planning in Natural Disasters,” *Annals of Operations Research* 129, 217-245.
- Solomon, M.M. (1987). “Algorithms for the Vehicle Routing and Scheduling Problems with Time Windows Constraints,” *Operations Research* 35, 254-265.

APPENDIX A: NOTATION

Parameters and constants:

- Δ : estimated computation time for initial solution
- τ : time when real-time information (travel times or delivery/pickup demands) occurs plus an estimated computation time, Δ
- $c_{0j}(d_{0k})$: travel time between depot 0 and node j when vehicle k departs from the depot at time d_{0k}
- $c_{ij}(d_i)$: travel time between nodes i and j at departure time d_i
- C_k : full capacity of vehicle k
- l_i : ending time of time window at node i
- q_{im} : demand of commodity m to be delivered at node i
- \hat{q}_{im} : excess supply (or pickup demand) of commodity m to be picked up at node i
- \bar{Q}_{mk} : total loads of commodity m for vehicle k when dispatching from the depot
- $\bar{Q}_{mk}(\tau)$: remaining loads of commodity m for vehicle k at time τ
- s_i : service time at node i

Set of nodes:

- 0 : Depot designation
- $N_c(\tau)$: set of critical nodes at time τ ; critical node is defined as the node that the vehicle is staying at or on route to
- $N_u(\tau)$: set of unassigned (or unserved) nodes at time τ
- $N_{cu}(\tau)$: set of critical and unassigned nodes at time τ
- $N_{u0}(\tau)$: set of the depot and unassigned nodes at time τ
- $N_{cu0}(\tau)$: set of the depot, critical and unassigned nodes at time τ

Set of vehicles:

- K : set of all vehicles, which is the union of two sets, i.e., in the depot and *en route*
- $K_0(\tau)$: set of vehicles in the depot at time τ
- M : set of all commodities needed in the disaster area

Variable:

- a_i : time arriving at node i
- d_i : time to depart from node i
- d_{0k} : time for vehicle k to depart from the depot
- x_{ijk} : 1, if vehicle k departs node i toward node j ; 0, otherwise
- Q_{jmk} : remaining loads of commodity m when vehicle k arrives at node j

LEARNING DISASTER PREPAREDNESS AND RESPONSE THROUGH GAMING SIMULATION

T. Kikkawa¹⁾ and K. Yamori²⁾

1) Associate Professor, Faculty of Business and Commerce, Keio University, Japan

2) Associate Professor, Disaster Prevention Research Institute, Kyoto University, Japan

tompeikun@a3.keio.jp, yamori@drs.dprikyoto-u.ac.jp

Abstract: In this paper, the authors introduced three games they developed themselves: 'Crossroad,' 'Bosai Duck!' and 'Dai-Namajin.' 'Crossroad' is a table-top exercise to improve the ability to recognize and respond to disasters. The material on which the game is based was derived from our extensive focus-group interviews of individuals in Kobe, where the Great Hanshin-Awaji earthquake occurred on the 17th of January, 1995. 'Bosai Duck!' is a card game for young children to learn the 'first moves' to take in case of various hazards including natural disasters. 'Dai-Namajin' is a variation of the Game of the Goose ('Sugoroku' in Japanese) for players to learn how to be prepared when a major earthquake strikes Japan. From our experience in running these games, the authors concluded that gaming simulation could offer promising tools for disaster preparedness and response training.

1. INTRODUCTION

The Great Hanshin-Awaji earthquake occurred at 5:46 am on January 17, 1995. The earthquake was 7.2 in magnitude, and its epicenter was directly beneath Kobe, one of the largest cities in western Japan, with a population of 1.5 million. The damage was widespread in terms of lives, property, and infrastructure. More than 6,400 people were killed and 15,000 injured. At least 200,000 buildings were damaged or destroyed, 400,000 people were left homeless, and 240,000 people sought public shelter.

It is unlikely to be the last major earthquake in Japan. Japanese seismologists agree that, based on historical data, other catastrophic earthquakes will occur within the next 20 to 30 years. Although it seems reasonable to assume that the Japanese people have learned from the tragedy of the Great Hanshin-Awaji earthquake, the question of how much useful knowledge has actually been assimilated into Japanese society remains unclear. Interest in reducing the impact of an earthquake disaster seems to have faded rather quickly in recent years; in addition, there is the tendency for people to forget, generally, about the past in focusing on the present.

It is also true that the specific experience gained from the Great Hanshin-Awaji earthquake may not be consistently applicable to future earthquakes; there is no one 'correct' answer to any situation, particularly in the context of a disaster. The Great Hanshin-Awaji earthquake was so unprecedented that there were numerous immediate and irregular responses that cannot be generalized in relation to relatively frequent and more normal disaster situations. Furthermore, subsequent earthquakes such as the Chuetsu earthquake, which occurred in 2004, and the Fukuoka-ken Seiho-Oki earthquake, which occurred in 2005, raised new respective problems.

It is, therefore, not enough to simply learn lessons from the past but is necessary to proactively think about disaster preparedness and response. However, it is hard to find a way for people to do so. We believe that gaming simulation could be one possibility. In the present paper, we introduced three games we have developed: 'Crossroad,' 'Bosai Duck!' and 'Dai-Namajin.' In the following sections,

we will introduce 'Crossroad' in great detail, and then briefly introduce 'Bosai Duck!' and 'Dai-Namajin.'

2. 'Crossroad'

2.1 Overview of 'Crossroad'

'Crossroad' is a table-top exercise developed for the general public and for disaster response personnel in national and local government or non-governmental organizations, for the purpose of increasing their awareness of the problems faced in disaster situations.

'Crossroad' was designed to increase the awareness of serious problems or dilemmas faced in disaster response. Examples of typical decisions include whether or not to start distributing food if the supply is insufficient, or whether or not to build temporary housing in schoolyards for homeless victims if there is a shortage of sites elsewhere.

The first example describes a dilemma between need and equity distribution of food to the victims. If food is not distributed, none of the victims, including the more vulnerable children and the elderly, will eat and all of them will suffer greatly. On the contrary, if food is distributed, the imbalance between those who receive food and those who do not may cause conflict.

The second example, involving temporary housing, describes a dilemma between the needs of the victims and the needs of the school children, in that temporary housing has the potential to create negative impacts on the administration of a school. If schoolyards are used as temporary housing sites, the problem of homelessness for disaster victims can be solved in the short run. However, once temporary housing is in place, it then becomes more difficult for both the public administration and the victims to find new sites and move. From the perspective of educational administrators, these temporary housing structures displace school activities in the schoolyard and sometimes directly interfere with curricular activities. During the Great Hanshin-Awaji earthquake, responses to this problem differed in two of the affected cities. One city decided to use schoolyards as sites, but the other city made the decision not to use them.

Responses to this kind of complicated decision are usually difficult to convey and explain within a normal, lecture-style educational context. However, this type of learning can be facilitated within a game situation, especially since players share (sometimes non-verbally) their perspectives with other players during, and sometimes after, the game.

The episodes we used in the game were designed to be realistic and were derived primarily from our extensive focus-group interviews of individuals in Kobe. The records vividly described episodes which occurred during disasters; these episodes revealed complex dilemmas faced during disaster response. We selected 20 episodes to be used in the game; these episodes were presented on cards of approximately the same size as name cards (See Figure 1 for an example).

We also collected other episodes mediating dilemmas from other sources, such as newspapers and websites. These episodes were primarily descriptive of disaster preparedness; one example is the dilemma of whether or not to retrofit houses if it is very costly. Owing to time constraints, we tended to use 30 episodes (from an

City employee
who is in charge of
food distribution

There are approximately
30,000 victims in
evacuation centers. At
present, you have 20,000
meals available. There is
little chance of obtaining
additional meals.

Do you hand out
20,000 meals?

Yes (To hand out)
OR
No (Not to hand out)

[Kobe1008]

Figure 1 Example of cards:
'Crossroad'

approximately 110-episode total available) in each game, carefully selecting the episodes to fit the needs of the players.

During the game, a group of players read the episodes presented on the cards that described dilemmas faced in a particular disaster situation. Each episode required individual players to make an either-or decision about the situation, i.e., 'YES' or 'NO.' After reading the episode, the players voted simultaneously. For each episode, players who correctly predicted the majority opinion of the group gained a point.

One of the advantages of the game 'Crossroad' is that it can lead to increased awareness of different viewpoints and values, both during the game and through post-game discussions. Such awareness may help consensus building among individuals in both disaster-prone areas and in disaster situations, as well as in other, more general, situations in Japan.

2.2 Procedure

There are five to seven players to a game, with an odd number of players preferable for each group. Many groups can play simultaneously, as long as it does not become too noisy in the room.

At the beginning of a game, each player has exactly the same deck of ten episode cards at hand. S/he also has one 'YES' card and one 'NO' card. Within a group, any player can be the first player to arbitrarily choose to read the first episode card from her/his deck. Every episode card has the same format, consisting of three parts. The first part consists of a description of a certain role that is to be played when faced with a dilemma in a disaster situation. A short description of the situation follows. The third part consists of a description of both the 'YES' and 'NO' decisions. The following is an example of an episode card.

[Example]

You are: A city employee who is in charge of temporary housing.

Situation: A month has passed after an earthquake. You have been procuring sites for temporary housing for homeless victims. An additional hundred houses are still necessary, although there is a shortage of sites. Do you utilize schoolyards as sites?

Decision: YES (To utilize) or NO (Not to utilize)

Next, all the players predict the majority opinion of the group for each episode card. Each player puts either a 'YES' or a 'NO' card on the table, face down, in front of her/himself. The purpose is not for players to advance their own opinion but to predict that of others. After all of the players have put either a 'YES' or a 'NO' card on the table, they simultaneously turn the cards face up. Every player who correctly predicts the majority opinion gains a point. For example, if three out of five players vote 'YES' for an episode, each of the three players receives one point. A point is represented as a miniature blue *zabuton* (a Japanese traditional cushion) in this game. In other words, players who predict the majority opinion of the group gain a blue *zabuton*. The cushion has a symbolic meaning for many Japanese people, in that the *zabutons* on which traditional Japanese comedians sit during their performance are sometimes given to the person whose opinions are regarded with the most respect.

There is an additional way for players to gain points. If s/he is the only person in the group who predicts a different decision from the others, s/he can gain a gold *zabuton* as long as s/he can explain to the other players why s/he made that choice. Other players who predicted the majority opinion gain neither a blue nor a gold *zabuton* in this case. For example, when one player out of five chooses 'YES' and the other four players choose 'NO,' the 'YES' player gains a gold *zabuton*.

Although the point given to a gold *zabuton* is of the same value as that of a blue *zabuton*, and thus there is no advantage in explaining the reason for one's choice, the color difference may attract players and may provide some incentive for going after it.

Moving clockwise from the first player, players take turns reading cards until all are read. At the end of the game, when all ten episode cards have been read, the person who has the most *zabutons* (points) wins.

2.3 Major findings of running the game of ‘Crossroad’

Here, we introduce two of our studies in which we analyzed feedback of participants of ‘Crossroad.’

One study included 223 adults. Some of the participants were professionals with some expertise in disaster response. The evaluations are summarized in Table 1. As can be seen in the table, the responses were generally positive.

The responses to an open-ended question provided additional support; participants spontaneously wrote that the game was meaningful in that they were able to share a variety of opinions within the group, and improve their understanding of disaster preparedness and response.

The other study, consisting of 235 adult participants, focused on the yes-no responses to the dilemmas described in the cards. Interestingly enough, for some of the dilemmas, most participants agreed either yes or no, although the greatest proportion of them did not exceed by 80.0%. The dilemma was as follows:

You are: A city employee who is in charge of the mortuary.

Situation: You are laying out the remains. There have been increasing numbers of remains compared to the capability of the staff. You yourself are exhausted after several hours of work. Do you take a break?

Decision: YES (To take a break) or NO (Continue working)

Table 1 Evaluations of ‘Crossroad’ by participants

Was the game enjoyable?	%
Very enjoyable	62.33
Enjoyable	35.87
Not enjoyable	1.35
Do you think the game is a positive experience?	
Definitely yes	68.61
Yes	29.15
Not necessarily	1.79
Did you deepen your understanding of disasters?	
Definitely yes	49.78
Yes	43.95
Not necessarily	4.04
No	0.45
Do you think there are a wide variety of opinions to disaster preparedness and response?	
Definitely Yes	84.75
Yes	14.35
Not necessarily	0.45

Eighty percent of the participants replied 'yes' to this dilemma, whereas 20 percent of them replied 'No.'

There were, of course, other dilemmas for which the distribution of the yes-no responses were close to even. One example of them was whether to utilize schoolyards as temporary housing sites (See example of card in the section 2.2). Nearly 60 percent of participants replied 'yes,' while approximately 40 percent of them replied 'no' to the dilemma.

We do not intend to explore the correct answers to these dilemmas based on the above-mentioned data. Instead, additional analyses are necessary as to why people choose either yes or no to the situations presented in the cards. It should also be noted that further data are required for a more extensive investigation.

Although we have limited data so far, we would like to conclude that the game 'Crossroad: Kobe' can be a promising tool for disaster training, in that it improves awareness of the dilemmas that may be encountered both before and after a disaster. It also promotes an awareness of differences with respect to concerns, interests, and values among people that should be shared and, to some extent, accommodated through consensus building.

3. 'Bosai Duck!'

'Bosai Duck!' is a card game for young children between the ages of 4 and 10 to learn the 'first moves' to take in case of hazards. These cards include various kinds of disasters such as earthquakes and tsunami, lighting, traffic accidents, and so on. On the right face of each card, is an illustration of a hazard and, on the reverse side of the card is a picture of an animal demonstrating the first move to take in such a situation (See Figure 2 for an example).

Players are required to take the correct posture, i.e., the first move, as quickly as possible upon seeing the hazard card. In the card of earthquake as shown in Figure 2, the posture of ducking and covering one's head is required, as is demonstrated by the duck.

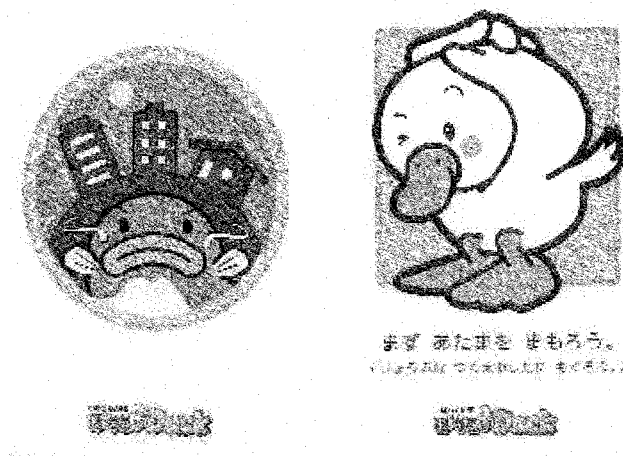


Figure 2 Example of cards: 'Bosai Duck!'

(left: hazard; right: first move illustrated by a picture of an animal)

4. 'Dai-Namajin'

'Dai-Namajin' is a variation of the Game of the Goose ('Sugoroku' in Japanese) for players to learn preparedness for impending earthquakes in Japan (See Figure 3). Each player in turn throws a die and moves the pawn according to the directions described in spaces on the game board. Each space corresponds to every month in a year. Disaster preparedness is explained in the spaces on the board, therefore, players will come to learn how to prepare for a disaster naturally by playing the game.

The rule of the game is quite similar to the Game of the Goose in the sense that the player who reaches the goal first wins. However, there is an exceptional rule in this game 'Dai-Namajin.' That is, whenever the die says one, the 'Dai-Namajin' (a kind of demon) pawn, which starts three spaces behind the players' pawns, moves one space. In that case, no players can move. Any player who is caught by the 'Dai-Namajin' loses the game. .

The name of the game 'Dai-Namajin' is named after that special pawn that chases after players' pawns. The 'Dai-Namajin' is symbolic of the impending earthquake in real life. A sense of urgency is implied in the rule of the game. A major earthquake will strike someday somewhere in Japan in the same way as the Dai-Namajin pawn is catching the player's pawn in the game.

5. CONCLUSIONS

From the experiences running the games introduced in this paper, we would conclude that the gaming simulation could be a promising tool for learning disaster preparedness and response. It can stimulate active participation, therefore, hopefully, leading to deeper understanding of disasters.

Note:

'Crossroad' is a registered trademark in Japan.

References:

- Kikkawa, T., Yamori, K., Ajiro, T., and Hayashi, H. (2004), "Crossroad:: Kobe: A training tool for disaster preparedness and response". In W.C. Kriz & T. Eberle (Eds.), *Bridging the gap: Transforming knowledge into action through gaming and simulation*. Pp.245-253. Munich, Germany: SAGSAGA
- Yamori, K., Kikkawa, T., and Ajiro, T. (2005) "Risk communication learned through gaming simulation: Introduction to 'Crossroad'". Kyoto, Japan: Nakanishiya Shuppan. (In Japanese)

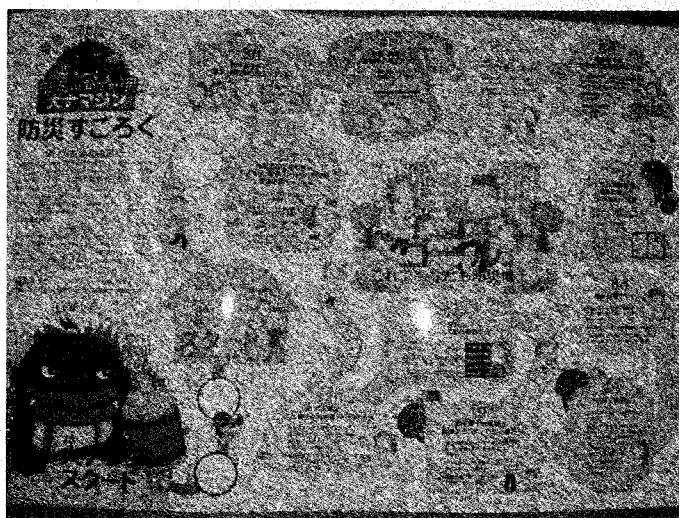


Figure 3 Board of the game 'Dai-Namajin'

RISK ASSESSMENT FOR TAIWAN RESIDENTIAL EARTHQUAKE INSURANCE POOL- MODELING AND APPLICATION

W. K. Hsu¹⁾, W. L. Chiang¹⁾, D. M. Hung²⁾, C. P. Tseng²⁾ and C. H. Tsai²⁾

1) Professor, Department of Civil Engineering, National Central University, Chungli, Taiwan, R.O.C.

2) Graduate Student, Department of Civil Engineering, National Central University, Chungli, Taiwan, R.O.C.

wenko@mail.educities.edu.tw, chiang@cc.ncu.edu.tw, s1342001@cc.ncu.edu.tw,

Abstract: Taiwan lies at earthquake-prone area. More than 200 sensible earthquakes occurred every year in Taiwan. Average annual loss due to 83 disastrous earthquakes since 1900 is about NT\$19 billion dollars which equals to 0.7% GDP. Therefore, the Taiwan Residential Earthquake Insurance Pool (TREIP) was created by the Taiwan Ministry of Finance (MOF) to facilitate a risk sharing mechanism between private insurance companies and the Government covering insured residential earthquake losses. In this paper, we have built up an event-based seismic hazard assessment and financial analysis model for earthquake disasters. As we know, low occurrence rate, tremendous loss and high uncertainty are characteristics of earthquake disasters. For the above issues, the model we built integrates knowledge from many fields including earth science, seismology, geology, risk management, structural engineering, the insurance profession, financial engineering and facility management. The model use the Monte Carlo simulation technology can construct an annual exceeding probability curve, which relates probability to size of loss, the specific event loss and allows for the evaluation of different insurance and reinsurance programs.

1. INTRODUCTION

Earthquake risk, a long-time concern in Taiwan, is increasingly being recognized as a concern in insurance industry and government. The Taiwan Residential Earthquake Insurance Pool (TREIP) was created by at April, 2002 the Taiwan Ministry of Finance (MOF) to facilitate a risk sharing partnership between private insurance companies and the Government covering insured residential earthquake losses. TREIP collects premium for the earthquake risk from the insurance companies and redistributes the premium to the various risk sharing entities (including itself). If losses occur, TREIP collects the appropriate funds from the risk sharing entities and reimburses the direct insurers for their payments to the policyholders.

We use the earthquake loss model to analysis the TREIP scheme to find out the loss exceeding probability curve, both the annual aggregate loss and standard deviation of loss for each layer. Use the analysis result, we can provide the TREIP how to modify the insurance scheme

2. INTRODUCTION FOR TAIWAN RESIDENTIAL EARTHQUAKE INSURANCE POOL

TREIP have 1,383,732 policies until September 31, 2005. The aggregate liabilities are NT\$ 1.8 trillions and take-up rate are 17.6%. TREIP collects premium for the earthquake risk from the insurance companies and redistributes the premium to the various risk sharing entities (including itself). If losses occur, TREIP collects the appropriate funds from the risk sharing entities and

reimburses the direct insurers for their payments to the policyholders.

The insurance scheme includes six layers is like the figure 1. The coinsurance in Taiwan retain the first NT\$ 2 Billions. Second layer is foundation layer. TREIP commissions the Central Re to be an administrator for the management of funds from the government to the private insurance and ultimately to policyholders. The third and fourth layer is reinsurance layer and the third layer had a Cat Bond for the first US\$ 100 million. The government then provides additional resources of NT\$ 10 billion in excess of NT\$ 40 billion.

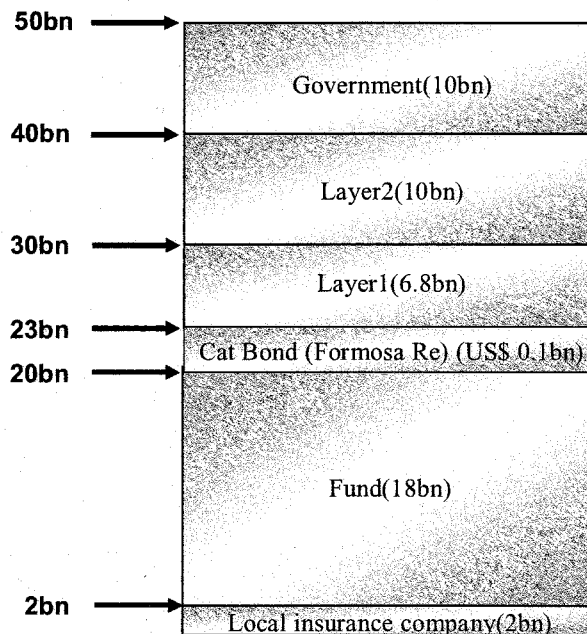


Figure 1 TREIP insurance scheme

There are about 7.6 millions buildings in Taiwan. According to the statistics from TREIP, we can establish the chart based on the building type and built year like following chart:

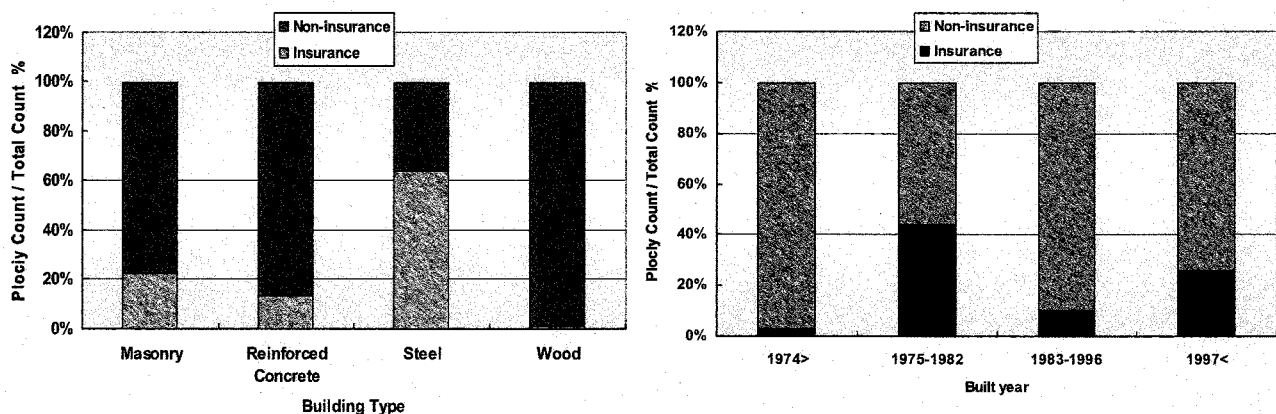


Figure 2 Statistics for non-insurance/insurance

For each policy, we can obtain the zip-code level location and characteristics of building such as building type, building height and built year. The premium for each policy are NT\$1459. Otherwise, the claim of TREIP policy will be paid in an amount equal to the policy limit (NT\$1.2 millions) if the building is no longer habitable or the damage ratio exceeds 50%. So we need to have a threshold trigger in the vulnerability analysis procedure.

The TREIP premium and expense flow diagram as figure 3 shows how the policy premium is collected from the insured and ultimately received by TREIP and how expenses are distributed.

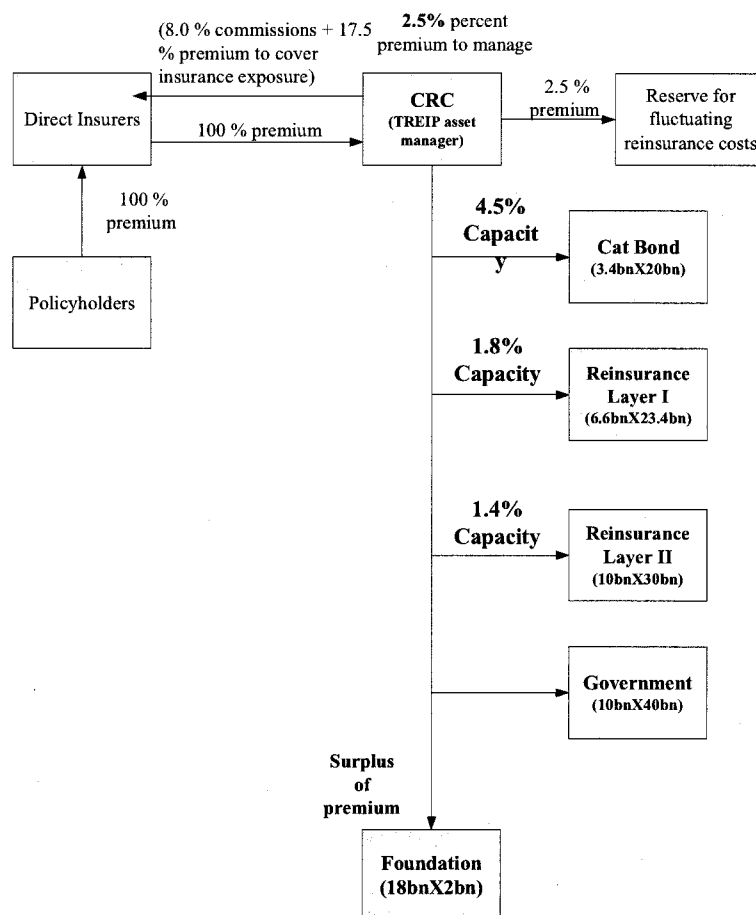


Figure 3 TREIP Premiums and Expense Flow Diagram

3. CATASTROPHE MODEL FOR EARTHQUAKE RISK

There are four primary components within earthquake loss assessment and management model. 1. Stochastic earthquake event generator, which uses a collection of relevant inventory and analysis parameters for the development of seismic damage assessment and loss estimation. 2. Hazard analysis procedure, can assess the intensity of ground shaking, maximum surface acceleration with the attenuation function in Taiwan and soil condition. 3. Vulnerability analysis procedure, can calculate the probability of different damage state to structural and content. 4. Financial analysis procedure, can assess loss include the direct and indirect economic losses. It also can provide the loss exceeding probability curve and dynamic financial analysis result. We would introduce how the primary components work in the following sections

3.1 Stochastic Earthquake Event Generator

An representative earthquake event set is important to an event-based earthquake model. For this reason, we collect the historical distribution of the epicenters of earthquakes in Taiwan during 1900 to 2004 from the Taiwan Central Weather Bureau. It includes 43 seismic zones, 21 shallow seismic sources, 7 deep seismic sources, and 15 subduction zone seismic sources (Cheng, 2002)[1]. There are also 42 active faults in the event generator (Taiwan Central Geological Survey, MOEA 2000)[2]. The

rate of occurrence of different magnitude events is estimated based on a Gutenberg-Richter³ (exponential) frequency-magnitude relationship. The earthquake occurrence rate is modeled by the Poisson model. There are 18,852 hypothetical earthquake events distributed across all sources in the generator and each event includes the parameters which the other analysis procedure need such as location, depth, magnitude, direction...etc.

3.2 Hazard Analysis Procedure

To assess the intensity of ground shaking for each simulated earthquake event is the purpose of the hazard analysis procedure. As described in the following diagram, we can calculate the Peak Ground Acceleration (PGA) for the location of the building. In analysis procedure, all crustal sources use the attenuation developed by Loh (2000)[4] while the subduction sources use Young et al. (1997)⁵. For the site effect, we also consider soil classifications are rock, weak rock / dense soil, stiff soil, and soft soil. Soil map inferred from the analysis of records of Free-field Strong-Motion Stations of Taiwan Central Weather Bureau and Geologic Map from Taiwan Central Geological Survey, MOEA . Geotechnical data is derived from geologic maps published by the Taiwan Ministry of Economic Affairs at 1:50,000 and 1:250,000 resolutions.

3.3 Vulnerability Analysis Procedure

According to the result of the hazard analysis procedure, we can obtain the capacity curve of building. Then, using the response spectral method described in the right diagram, a specific group of (S_d , S_a) can be determined. Finally, we can get the probability of each damage state of building. To Calculate the mean damage ratio and coefficient of variation to buildings, contents, and the resulting loss of use, the earthquake loss model includes four major elements: construction classes; occupancy classes; additional building classifications such as year built, number of stories, and seismic code zones. Based on the seismic resistance of buildings, vulnerability analysis procedure can assess the probability of each damage state to structure and content.

3.4 Financial Analysis Procedure

Before the beginning of the financial analysis, we must build the event loss table by the procedures we described above. As the described the following diagram, we can create the event loss table in the form include event id, annual mean rate and mean loss for each event.

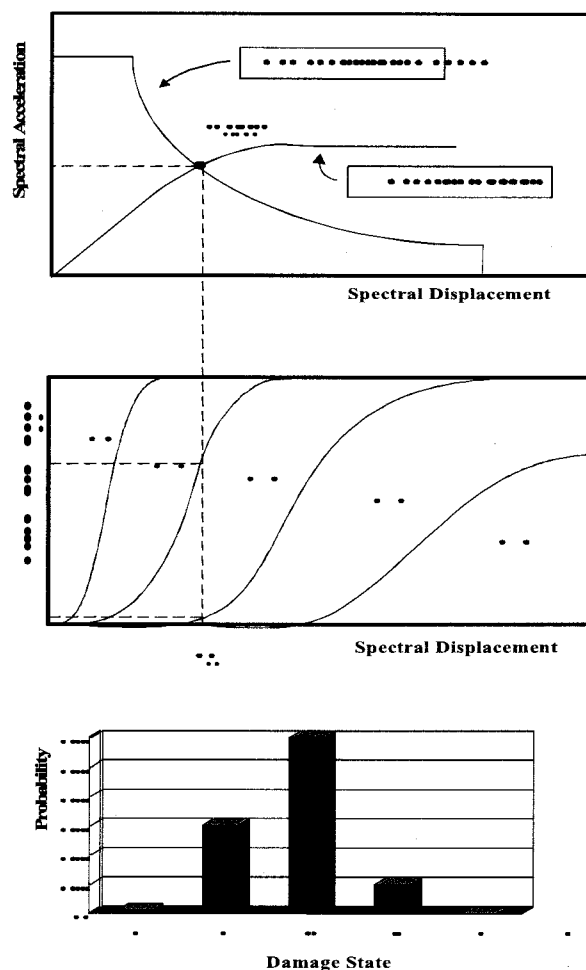


Figure 3 TREIP Determine the probability of each damage state

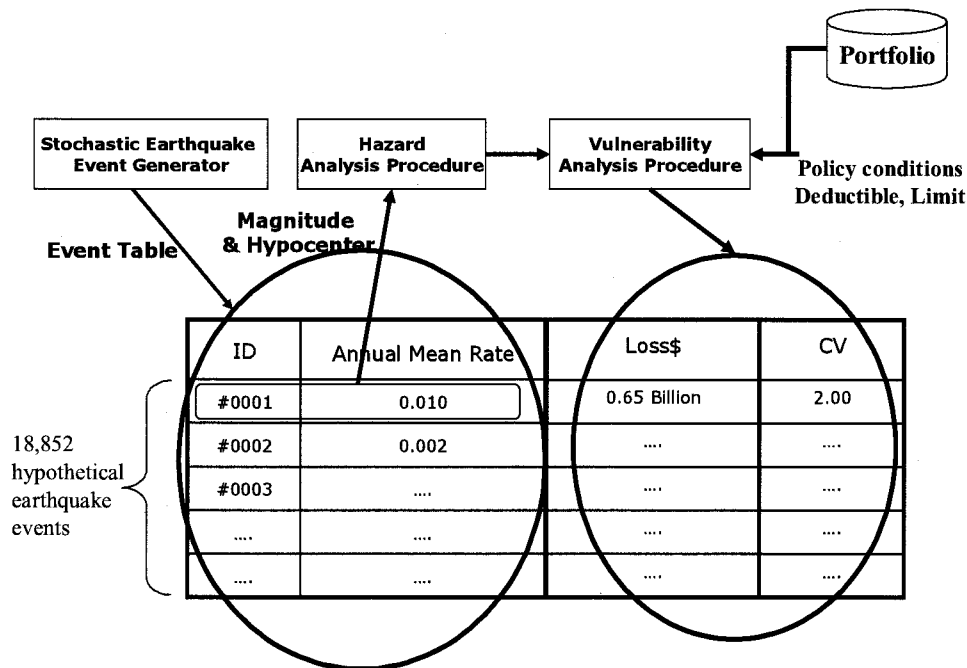


Figure 4 Building the event loss table

The direct and indirect economic losses caused by the simulated earthquakes can be estimated using the financial analysis procedure. Damage to assets is converted to monetary losses by ratio of repair/rebuilt cost. However, depending on the terms of the policy, the loss is shared by more than one party. This part of the modeling reflects the workings of a policy or treaty; it is included as an integral part of the overall modeling approach because of the intimate interaction between the insurance structure and damage to the physical buildings or assets.

After the event loss table was created, we can use the Monte Carlo simulation to establish aggregate or occurrence loss exceeding probability curve. First, we use the Poisson distribution to describe the earthquake occurrence times. According to the occurrence rate of each event, we can get the occurrence times N in every simulation and simulate the accumulative probability of severity distribution randomly. Therefore, we can generate the loss exceeding probability curve like the following diagram.

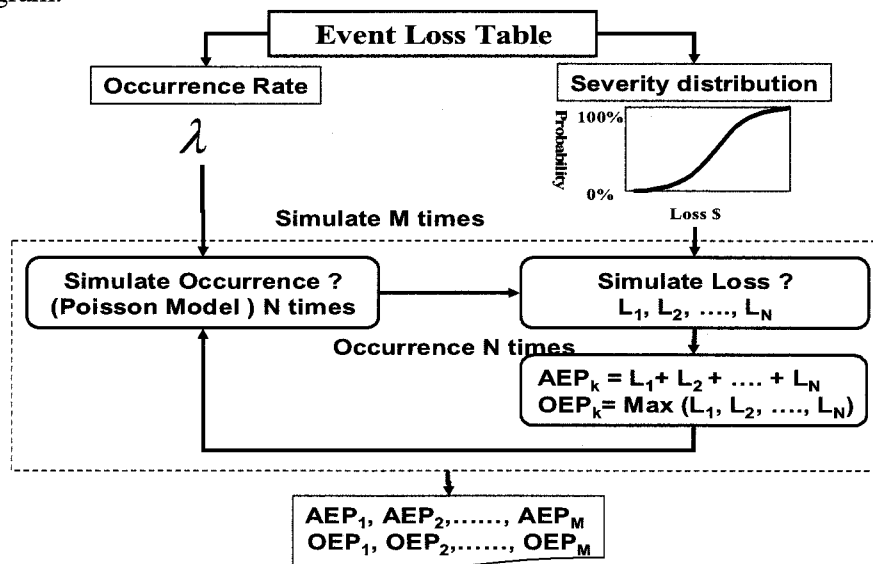


Figure 5 Building the aggregate/occurrence loss exceeding probability curve

When the losses for all locations in a portfolio are calculated, the financial analysis procedure allocates the losses to different participants, i.e., insured, insurer, and re-insurer through various insurance and treaty structures. Because there are many sources of uncertainty in modeling (from attenuation, vulnerability and incompleteness of data), the loss at the location level is treated as a random variable.

4. ANALYSIS FOR TREIP PORTFOLIO

With the parameters described above and TREIP portfolio, we can use the earthquake loss assessment and management model to simulate the loss exceeding probability curve and penetration probabilities for each layer like the charts below. In figure 6, we can see the loss ratio is about 3.75% based on 500 year return period. It means that it will occur once event of the loss ratio are greater than 3.75% in 500 year. In Table 1, it shows the current scheme can grantee the event loss in 276.0 years return period.

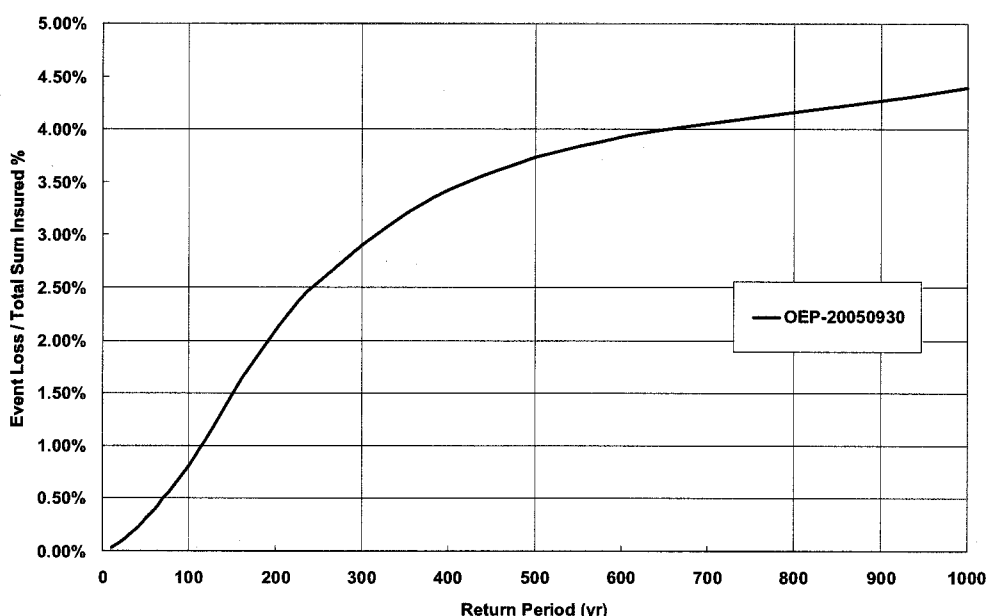


Figure 6 Loss exceeding probability curve

Table 1 Penetration probabilities and Return period in each layer

Layer	Attachment Point (NT\$ Billion)	Layer Amount (NT\$ Billion)	Penetration Probability (%)	Return Period (year)
-	50		0.36%	276.0
Government Grantee	40	10	0.46%	214.7
Second layer reinsurance	30	10	0.59%	168.9
First layer reinsurance	23.2	6.8	0.72%	137.7
Cat Bond	20	3.2	0.81%	123.0
Found	2	18	4.33%	22.6
Coinsurance	-	2	-	-

5. CONCLUSIONS

Because of the concern for uncertainty and engineering model, the earthquake loss assessment model can provide more information than the traditional method. For example, the loss exceeding probability curve can offer the policymaker to determine the earthquake protection capacity according to their tolerance of risk. On the other hand, the traditional method only can give us the single value for the possible maximum loss due to earthquake disaster.

To TREIP portfolio, current insurance scheme only can grantee the event loss occurs once in 276.0 years return period. TREIP can upgrade the earthquake protection capacity, but it also means the cost of insurance will increase. We can design several schemes and use the model we built to see how much the cost increase. Finally, the optimal solution will balance between the maximum earthquake protection capacity and minimum cost of insurance.

In this paper, we use Poisson model to simulate the occurrence rate of the stochastic earthquake event. As we know, Poisson model is a time-independent model. Nevertheless, the behavior which earthquake event occurs is time-dependent in fact. In the future, we should have a further research.

If we can establish the relations between the proportion of severity and damage state of the building, the model also can simulate the casualties according to earthquake event.

References:

-
- [1] Lin B. S, Lee C.T., Cheng C. T., "Strong Ground-Motion Attenuation Relationship for Subduction Zone Earthquakes in Taiwan", *9th Conf. on Geophysical Society, China*, 2002, 24-31.
 - [2] An introduction to active faults in Taiwan. (*Taiwan Central Geological Survey, MOEA*, 2000)
 - [3] Gutenberg, B., Richter, C. F., "Frequency of Earthquake in California", *Bull. Seism. Soc. Amer.* 1991, Vol. 34, p185~188.
 - [4] Loh, C.H. Z.K. Lee etc. "Ground Motion Characteristics of the Chi-Chi earthquake of September 21, 1999", *Journal of Earthquake Engineering and Structural Dynamics*, 2000, p 876-897.
 - [5] Young, "Subduction Slabs in Taiwan Region", *Jour. Geol. China*, 40, 1997, 653-670.

A PROPOSAL ON A METHOD TO DETERMINE RISK-BASED SEISMIC DESIGN LEVEL

M. Nakajima¹⁾, H. Morikawa²⁾ and K. Hirata³⁾

*1) Research Engineer, Civil Engineering Research Laboratory,
Central Research Institute of Electric Power Industry, Japan*

2) Associate Professor, Department of Built Environment, Tokyo Institute of Technology, Japan

*3) Senior Researcher, Civil Engineering Research Laboratory,
Central Research Institute of Electric Power Industry, Japan*

masato@criepi.denken.or.jp, morika@enveng.titech.ac.jp, hirata@criepi.denken.or.jp

Abstract: In performing “performance-based” seismic design, information on seismic risk evaluated from the stochastic method is necessary. For this purpose, some methods are proposed, and almost methods of them use seismic hazard curves as information on earthquake ground motions. However, we are afraid that the seismic hazard curves obtained from the conventional probabilistic seismic hazard analysis are not sufficient to evaluate seismic risk exactly. The purpose of this paper is to develop a method to determine a reasonable level for seismic design based on the evaluation method proposed by authors.

1. INTRODUCTION

For seismic design of civil engineering structures such as road bridges and dams, earthquake ground motions are sometimes prescribed by several levels of response spectra, and demanded design levels of the structures have been determined on the basis of deterministic fail-safe evaluation. However, such a conventional method for determining seismic design level may provide over or under value of an appropriate level from the following reasons:

- probabilistic seismic hazard is not taken into account explicitly,
- structural failure probability against limit states is not considered.

The objective of this paper is to develop a method to determine a reasonable level for seismic design stochastically.

For this purpose, we apply the hazard deaggregation and failure probability based on physics of structural models. First, the general framework for evaluating risk-based seismic design level is established. To represent the structural risk, we use the failure probabilities of structures which can be calculated by a method developed by authors. In the method, hazard-consistent earthquake ground motions are evaluated by incorporating deaggregation of seismic hazard and the PDF for the seismic response of a considering structure is determined on a basis of numerical model. From this, we introduce a “risk-based seismic design level” as the seismic design level with a value of structural failure probability.

Then, conducting numerical simulations for the northern part area of Japan, the two kinds of structural risk maps for the area are illustrated on the basis of the proposed method: one is a map which represents a geographical distribution of structural failure probability per year for assumed failure criteria (e.g., response acceleration, cumulative energy of elastic strain), the other is a map which represents regional distribution of limit intensity corresponding to structural failure probability per year.

2. PREVIOUS RESEARCHES

2.1 Seismic risk evaluation

Stochastic methods have been sometimes used to evaluate risk of target structures. In the case of risk evaluation by earthquakes, information on seismic hazard and information on structural fragility are necessary to evaluate seismic risk.

Conventional probabilistic seismic hazard analysis (PSHA) has been used to obtain information on intensity of earthquake ground motions and its frequency. This PSHA provides seismic hazard curves showing the relationship between the intensity of earthquake motions and its exceedance probability. The pioneering researches have been developed by Cornell (1968), Der-Kiureghian and Ang (1977).

Since we have unfortunately experienced many large earthquakes disaster, information about damaged structures have been accumulated. Fragilities is evaluated from statistics of the damaged structures by the earthquakes. However, the data of heavily damaged structures is not enough to obtain the statistics. Moreover, it is very difficult to estimate precisely fragilities of real structures because the original resistance of the structures to the earthquake ground motions is different from the resistance determined in the design.

2.2 Risk-based seismic design

Since the concept of “performance-based” design was proposed by Hamburger (1996), some studies have been made on stochastic seismic design method. For example, Hadjian proposed a framework to determine a design level using selection chart showing the relationship between mean return period and target damage index, which are obtained from the conventional seismic hazard curves and structural fragility curves (2001).

On the other hand, U.S.National Hazard Map was developed by U.S.Geological Survey (Frankel 1995, Frankel et al. 2000). Furthermore, another kind of seismic hazard map was made by Leyendecker et al. (2000). This map developed by Leyendecker et al. represents a regional distribution of ground motions by Maximum Considered Earthquake (MCE) to provide information for seismic design spectrum.

3. EVALUATION METHOD OF STRUCTURAL SEISMIC RISK

As is mentioned in the previous section, the conventional PSHA method uses single index of earthquake ground motion such as peak ground acceleration. From the conventional PSHA method, detailed information on earthquake ground motions cannot be obtained from the result. In order to overcome the problem, recently, several methodologies to determine scenario earthquakes based on PSHA have been proposed (e.g., Ishikawa and Kameda(1994), Kameda et al.(1997), McGuire (1995)). The concept is called “deaggregation of seismic hazard”, and the earthquake parameters represented by, for example, magnitude and distance for all seismic sources or for each seismic source, are evaluated as one characteristics of the concept.

3.1 Evaluation method of structural failure probability

To evaluate the failure probability, authors have proposed and developed a method on the basis of “deaggregation of seismic hazard” (Nakajima and Hirata 2004). The procedure of the proposed method is as follows:

STEP 1: The target area source is divided into two-dimensional meshes ($N=K \times L$). In this area, it is assumed that the hypocenters are distributed randomly. At a considering site, we

can obtain the probability density function (PDF) of the hypocentral distance R , $f_R(r)$ and PDF of earthquake magnitude, $f_M(m)$.

STEP 2: We discretize the (M, R) -space using $K \times L$ small areas with dimension $\Delta m \times \Delta r$ for magnitude and hypocentral distance, respectively. Hereafter, we call the small areas "bin".

Acceleration response spectrum $S_A^{i,j}(T)$ is determined corresponding to each bin (m_i, r_j) [$i=1,2,\dots,I$] [$j=1,2,\dots,J$], where i and j stand for the i -th and j -th bin with respect to the magnitude and the hypocentral distance, respectively. Then an earthquake wave consistent with the spectrum is generated. Furthermore, another two waves consistent with the spectra $S_v(i, j) \pm \exp(\sigma)$ are generated. The σ denotes a logarithm standard deviation of the spectra.

Then, we can generate KL earthquake ground motions, $x_{i,j}(t)$, which are consistent with the spectra $S_A^{i,j}(T)$ at a considering site. Furthermore, another more two sets of the motions consistent with the spectra $S_A^{i,j}(T) \pm \exp(\sigma)$ are generated.

STEP 3: Seismic response analyses of a structure are performed by using $i \times j \times 3$ earthquake waves. From this analysis, we can calculate a response such as maximum displacement, or cumulative energy of elastic strain, etc. For a pair of (i, j) , three values of the response index, $y_{i,j}^0, y_{i,j}^-, y_{i,j}^+$ which are obtained from the earthquake ground motions corresponding to $S_A^{i,j}(T)$, $S_A^{i,j}(T) - \exp(\sigma_b)$ and $S_A^{i,j}(T) + \exp(\sigma_b)$, respectively. Since the probability distribution of the index of the response is generally unknown, we introduce the three-points estimates method by Rosenblueth (1977) to estimate the mean and the standard deviation of $y_{i,j}$, $\mu_{y_{i,j}}, \sigma_{y_{i,j}}$.

STEP 4: The PDF of the structural response $y_{i,j}$ is determined from the parameters $\mu_{y_{i,j}}$ and $\sigma_{y_{i,j}}$ obtained at STEP3.

The conditional probability that the structural response exceeds a limit value of structural resistance C for an earthquake with magnitude m_i and hypocentral distance r_j : that is,

$$P_f^{i,j} \equiv \text{Prob}[y_{i,j} > C | m_i, r_j] \quad (1)$$

From this, the structural failure probability per year is obtained by the following equation;

$$P_{f/\text{year}} = \nu \sum_{i=1}^I \sum_{j=1}^J f_M(m_i) f_R(r_j) \text{Prob}[S > C | M_i, r_j] \Delta m \Delta r \quad (2)$$

where ν denotes the average number of earthquake occurrence per year in the target area source and $f_R(r)$ denotes PDF of the hypocentral distance R , respectively. In this equation, it is assumed that M and R are independent mutually.

It is easy to incorporate other earthquake occurrence models such as active faults models or inter-plate earthquake models from the following equation;

$$P_f = \nu \text{Prob}[S > C | M, r] \quad (3)$$

where ν denotes the earthquake occurrence rate per year and M and R denotes the characteristic magnitude and distance of the earthquake, respectively.

Hence, we can obtain the $P_{f/\text{year}}$ in a case where plural seismic sources are considered, by summing up the $P_{f/\text{year}}$ calculated from the above equation for each seismic source.

3.2 Method to determine risk-based seismic design level

As is described in previous sections, some attempts have been made on developing probability-based design. Uncertainties are considered in their proposes and one may say that their methods differ from the conventional design methods which are based on the deterministic evaluations. We, however, are afraid that they are not sufficient for practical purpose because they are generally based on only seismic hazard curves and fragility curves.

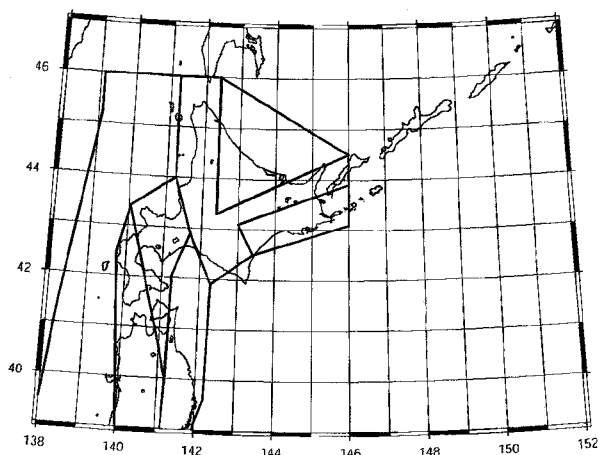


Figure 1 Area-source models

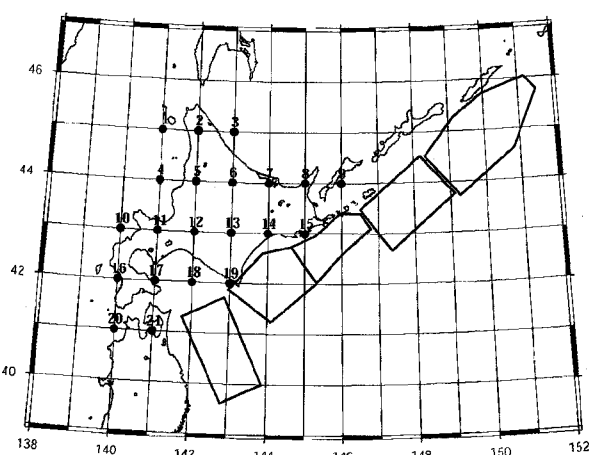


Figure 2 Inter-plate earthquake models

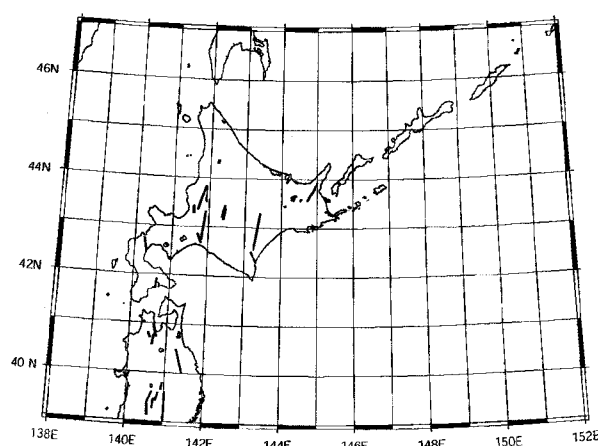


Figure 3 Active faults models

To overcome the problem, we propose a new method to determine seismic design level from the following points of view:

- the failure probability against the considered strength of structures can be previously evaluated,
- the needed strength for failure criterion in design can be determined corresponding to the prescribed failure probability. In this paper, we embody the above concept by representing seismic risk maps on the basis of the author's method (Nakajima and Hirata, 2004).

4. NUMERICAL EXAMPLES

To illustrate the method proposed in the previous section, some numerical simulations are carried out.

4.1 Target area

As a target area for numerical examples, the area covering Hokkaido and northern Tohoku, Japan are chosen to apply the proposed method. Twenty one sites are considered for numerical simulations, which are located at intersections of grid lines with one-degree intervals of latitude and longitude as shown in Fig.2.

Table 1 Parameters of earthquake occurrence models (Active faults and inter-plate earthquakes)

No.	Earthquake occurrence model	M_J	Return period (years)
1	Shibetsu fault zone	7.7	Unknown
2	Tokachi plain fault zone	8.0	17000 to 22000
3	Furano fault zone	7.2	4000 (West) 5000 to 20000 (East)
4	East Mshike falut zone	7.8	≥ 5000
5	Tōbetsu fault	7.0	7500 to 21500
6	East Ishikari fault zone	7.9	3300 to 6300
7	Kuromatsunai fault zone	7.3	3600 to 5000
8	Hakodate plain fault zone	7.0~7.5	13000 to 17000
9	East Aomori gulf fault zone	7.3	3000 to 6000
10	East Tsugaru fault zone	7.1~7.3	Unknown
11	Oritsume fault	7.6	Unknown
12	Off Tokachi EQ	8.1	77.4
13	Off Nemuro EQ	7.7	77.4
14	Off Shikotan island EQ	8.1	77.4
15	Off Etorofu island EQ	8.1	77.4
16	Off Northern Sanriku EQ	8.0	97.0

4.2 Earthquake occurrence models

To evaluate seismic hazard for the target area, three types of seismic sources i.e., area-sources, inter-plate large earthquakes occurring along Chishima Trough, and inland active faults are considered. The details of earthquake occurrence models are explained as below.

Fig.1 shows a polygon-shaped source-areas characterizing the earthquakes whose magnitude and locations can not be specified deterministically. In each area-source, it is assumed that magnitude-frequency relationship follows the Gutenberg-Richter's formula (Gutenberg and Richter, 1944) and earthquakes occur randomly and uniformly. Fig.2 shows fault plain of inter-plate earthquakes along Chishima Trough. The off Tokachi earthquake, off Nemuro earthquake, off Shikotan island earthquake, off Etorofu island earthquake and off northern Sanriku earthquake are considered. The models with characteristic magnitudes for the inter-plate earthquakes are set independently of the earthquakes in the area-source shown in Fig.2. The three dimensional shape of fault plane, such as area and slant, is considered for the inter-plate earthquakes. We adopt the active fault models shown in Fig.3, in which fault parameters are given as geographic shapes, magnitude, return period and so on. The detailed values of the earthquake parameters are released by the Headquarters for Earthquake Research Promotion, Japan (2005). From the reference, we employ the values of earthquakes listed in Table 1. It is assumed that earthquake occurrences are modeled by the stationary Poisson process in the time domain.

4.3 Models of earthquake ground motions

To prescribe the spectrum based on bin (M, R) as explained in Section 3, we employ the attenuation equation for acceleration spectrum, which is converted from the response spectrum by Nishimura et al. (2001).

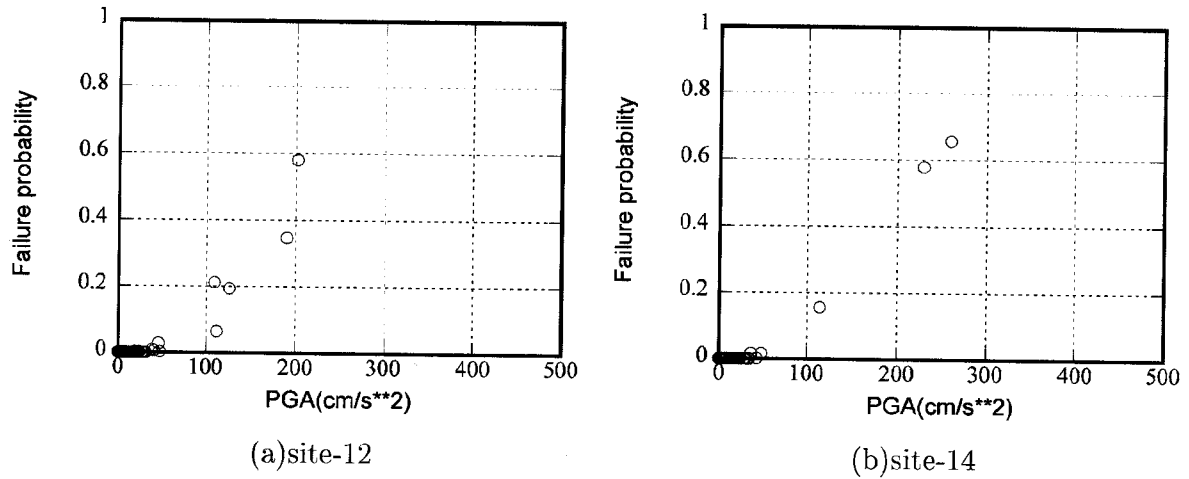


Figure 4 Examples of structural fragility evaluations (natural period:0.5s, yield strength:400(cm/s^2))

4.4 Structure model

In this example, a linear structure model is considered. As a linear structure model, SDOF system whose natural period is 0.5s and the damping ratio of 0.05 is given and we assume that structure failure occurs when response acceleration exceeds yielding seismic strength.

4.5 Seismic risk maps

Following the procedures mentioned in the previous section, structural failure probability per year at each point plotted in Fig.2 is calculated. Fig.4 shows the results examples of fragility evaluations, which can be obtained from the proposed method as secondary outputs. Using the results, we can obtain two kinds of seismic risk maps.

Fig.5 represents geographical distributions of structural failure probability per year in a case where the limit strength of the structure model is considered 400(Gal) and 800(Gal), respectively. From Fig.5(a), it is observed that the two small areas of seismic risk is high: one is the south-eastern Hokkaido and the other is the northern Aomori. However, the area with high seismic risk expands to western Hokkaido as shown in Fig.5(b) since the seismic hazard of some sites some are dominated by neighboring active faults. Furthermore, we can find that the difference between the highest seismic risk and the lowest within the target area enlarges.

Fig.6 is a map which represents regional distributions of limit intensity in a case where structural failure probability per year is considered 10^{-3} and 10^{-4} , respectively. From Fig.6(a), we can grasp that structures need the yield strength more than 500 (Gal) in the south-eastern area and in the northern Aomori. In a case where $P_{f/year}$ of 10^{-4} is considered, the needed strength of the structures can vary corresponding to the site location as shown in Fig.6(b).

The represented maps herein give information on seismic risk of structures, which can not be obtained from the conventional seismic hazard maps. Moreover, the appropriate level of seismic design can be prescribed reasonably.

5. CONCLUSIONS

We proposed a method to determine the seismic design level using seismic risk indices. Then, a numerical simulation is carried out to illustrate the applicability of the proposed method. The

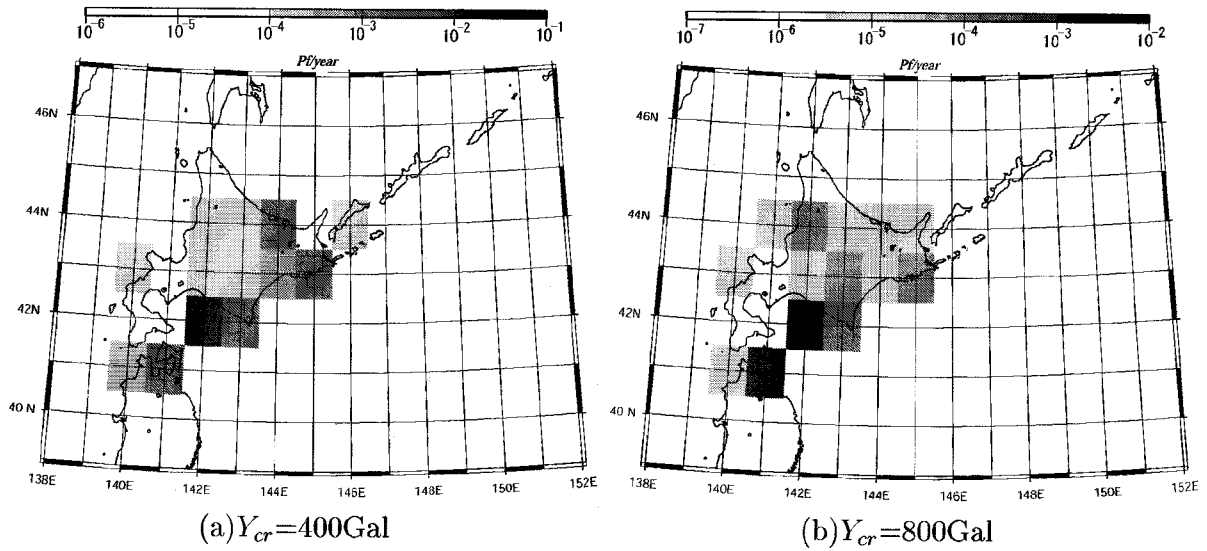


Figure 5 Seismic risk map in terms of P_f/year

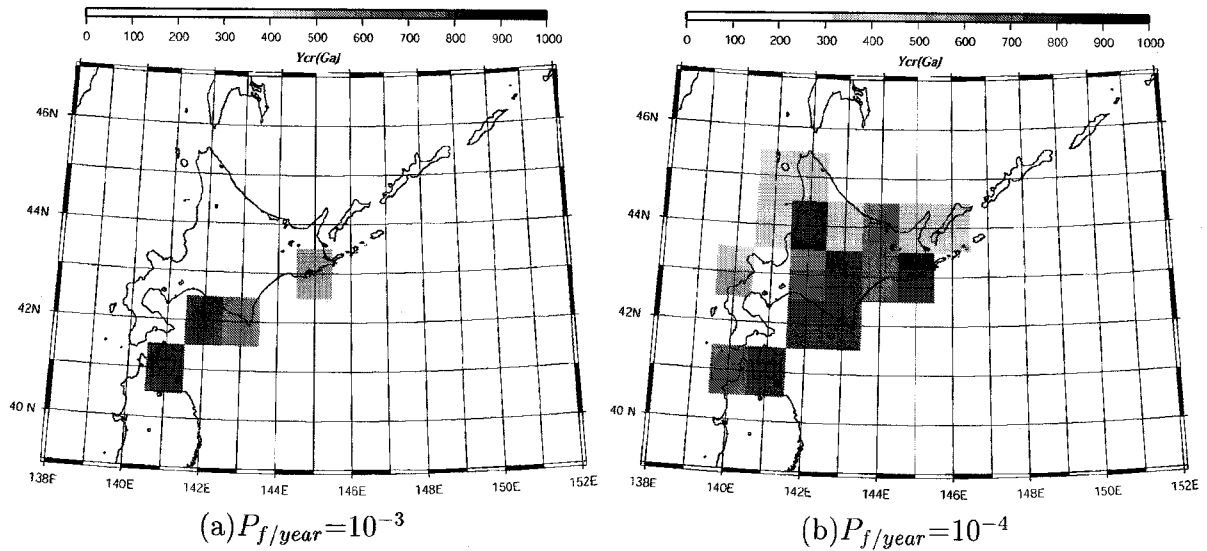


Figure 6 Seismic risk map using yield strength Y_{cr}

results of the simulation show that the regional variance of the seismic risk can be grasped from the two kinds of seismic risk maps.

As a result, it is concluded that the method developed herein can determine seismic design levels of structures reasonably and quantitatively from the stochastic point of view.

On the other hand, some problems to resolve are left: the uncertainties of structure parameters need to be considered. We will apply the proposed method to the MDOF systems and examine the practical usability of the method.

References:

- Cornell, C.A. 1968. Engineering Seismic Risk Analysis, *Bull. Seis. Soc. Am.*, Vol. 58, No. 5: 1583-1606.
- Der-Kiureghian, A. and A.H.S. Ang 1977. Probabilistic Procedures for Peak Ground Motions, *Journal of Structural Division*, ASCE, Vol. 105, No. ST11: 2293-2311.

- Frankel, A. 1995. Mapping seismic hazard in the central eastern United States, *Seism. Res. Lett.*, Vol.66, No.4: 8-21.
- Frankel, A.D., C.S.Muller, T.P.Barnhard, E.V.Leyendecker, R.L.Wesson, S.C.Harmsen, F.W.Klein, D.M.Perkins, N.C.Dickman, S.L.Hanson and M.G.Hopper, 2000. USGS National Seismic Hazard Maps, *Seism. Res. Lett.*, Vol.16, No.1: 1-19.
- Gutenberg, B. and C.F.Richter 1944. Frequency of earthquakes in California, *Bull.Seis.Soc.Am.*, Vo.34: 185-188.
- Hadjian, A.H. 2002 A general framework for risk-consistent seismic design. *Earthquake Engineering and Structural Dynamics*. Vol.31: 601-626.
- Hamburger, R.O., A.B.Court and J.R.Soulages 1996. Vision2000: A framework for performance based engineering practice, *EQE Review*, 1-7.
- Headquarters for Earthquake Research Promotion, Japan 2005. Report on General Seismic Hazard Map covering the whole of Japan (in Japanese)
- Ishikawa, Y. and H.Kameda 1994. Scenario Earthquakes vs Probabilistic Seismic Hazard Analysis, *Proceedings of the 6th International Conference on Structural Safety and Reliability*, Vol.3: 2139-2146.
- Kameda, H., Y.Ishikawa, T.Okumura and M.Nakajima 1997. Probabilistic Scenario Earthquakes -Definition and Engineering Applications-, *Journal of Structural Mechanics and Earthquake Engineering* No.577/I-41: 75-87 (in Japanese).
- Leyendecker, E.V., R.J.Hunt, A.D.Frankel and K.S.Rukstales 2000. Development of Maximum Considered Earthquake Ground Motion Maps, *Earthquake Spectra*, Vol.16, No.1: 21-40.
- McGuire, R.K. 1995. Probabilistic seismic hazard analysis and design earthquakes: closing the loop, *Bull. Seis. Soc. Am.*, Vol.85, No.5: 1275-1284.
- Nakajima, M. and K.Hirata 2004. Seismic Risk Evaluation Method of Structures Based on Deaggregation of Seismic Hazard, *13th World Conference on Earthquake Engineering*, Vancouver, Paper #3404.
- Nishimura, I., S.Noda, K.Takahashi, M.Takemura, S.Ohno, M.Tohdo and T.Watanabe 2001. Response Spectra for Design Purpose of Stiff Structures on Rock Sites, *SMiRT 16*, Washington DC, Paper#1133.
- National Research Institute for Earth Science and Disaster Prevention, Japan 2005 A Study on Probabilistic Seismic Hazard Maps of Japan, *Technical Note of the National Research Institute for Earth Science and Disaster Prevention* No.275
- Rosenblueth, E. 1975. Point estimates for probability moments, *Proc.Nat.Acad.Sci, USA*, Vol.72, No.10: 3812-3814.

CHANGES OF BUILDING USE AND STRUCTURE IN TOKYO 23-KU

Y. Meshitsuka¹⁾

1) Graduate Student, Tokyo Institute of Technology, Japan
meshi@mail.arch.titech.ac.jp

Abstract: The aim of this study is to detect zones where official treatments are needed. Transition matrices of use and structure of buildings were constructed. Future situations where it arrives when present tendency continues for a long time was estimated.

Following tendencies were observed. (1) Local difference of fire-spreading velocity ratio tends to decrease generally. (2) There is some possibilities that fire-spreading velocity ratio of zones which are surrounded by the zones of high level present fire-spreading velocity will increase exceptionally.

1. INTRODUCTION

1.1 Background

In an urban district where many old wooden buildings are included, it is a serious concern that their damage can be increased because of fire-spreading after big earthquake.

Although most of old buildings will be rebuilt to fire-proofed or fire-resistant buildings, some of them may be still remaining. In this case, it seems to be necessary to treat them officially. It is important for local administration to catch and estimate the situation of buildings renewal in each zone.

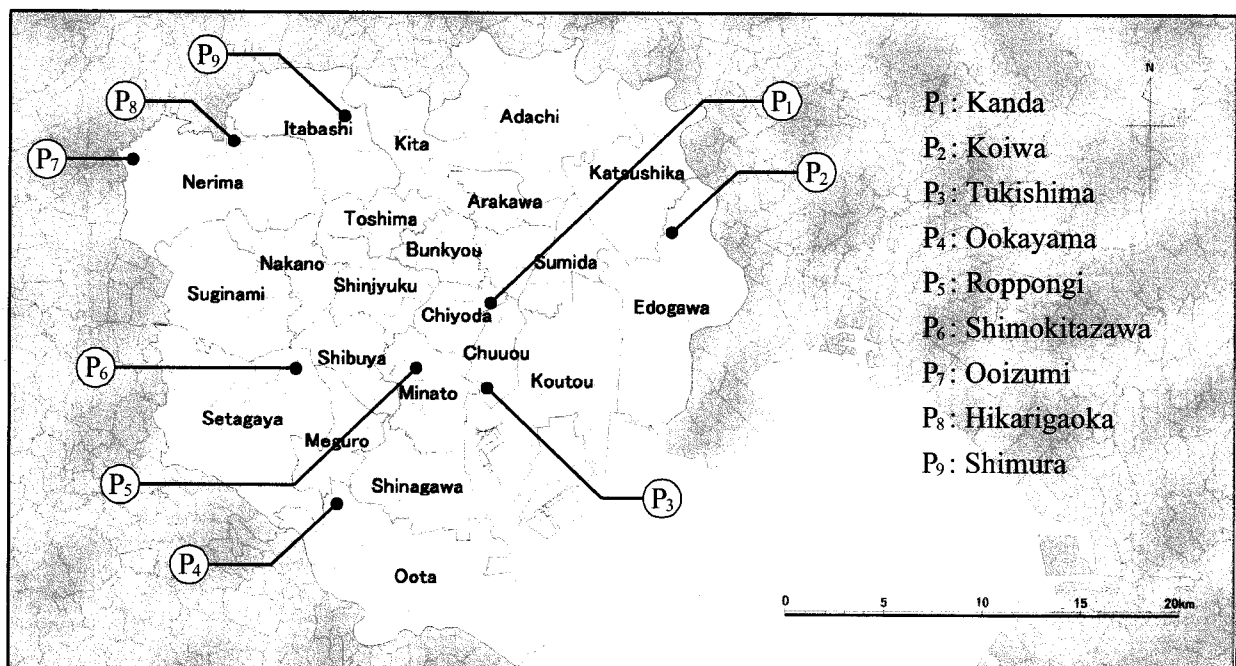


Figure 1 Targeted area

2. TARGETED AREA AND USED DATA

The area of Tokyo 23-ku was divided into 265 zones and used as the targeted area (Figure 1). The data used in this study is the building database of 1991 and 1996 which is the Urban Planning GIS of the Tokyo Metropolitan Government.

Table 1 Classification of building structure in Urban Planning GIS of Tokyo

Code	Class in Urban Planning GIS of Tokyo	Our classification
22	Wooden building (Mokuzo-tatemono)	S1
21	Fire-proof building (Bouka-tatemono)	S2
12	Semi-fire-resistant building (Jyuntaika-tatemono)	S3
11	Fire-resistant building (Taika-tatemono)	

Table 2 Classification of building use in Urban Planning GIS of Tokyo

Code	Class in Urban Planning GIS of Tokyo	Our classification
111	Government and municipal	Public (L)
112	Education and culture	
113	Medical and welfare	
114	Supply and disposal	
121	Office	Business (L)
122,123	Commerce	
124	Lodging, amusements	
125	Sports, show business	
131	Detached house	Housing (L)
132	Collective housing	
141,142	Factory	Industry (L)
143	Warehouse, transport	
150, etc.	Agriculture, etc.	Others (L)

This is a vector type data, and the shapes of buildings are related to the information of structure, use, area and number of floors. Structure of buildings is classified into 4 categories of Fire-resistant, Semi-fire-resistant, Fire-proof, and Wooden buildings in the original data. Fire-resistant and Semi-fire-resistant were treated as one category in this study (Table 1). Use of buildings is classified into 38 categories in the original data, but those were reclassified to the following 5 categories, Public, Business, Housing, Industry, and Others in this study (Table 2).

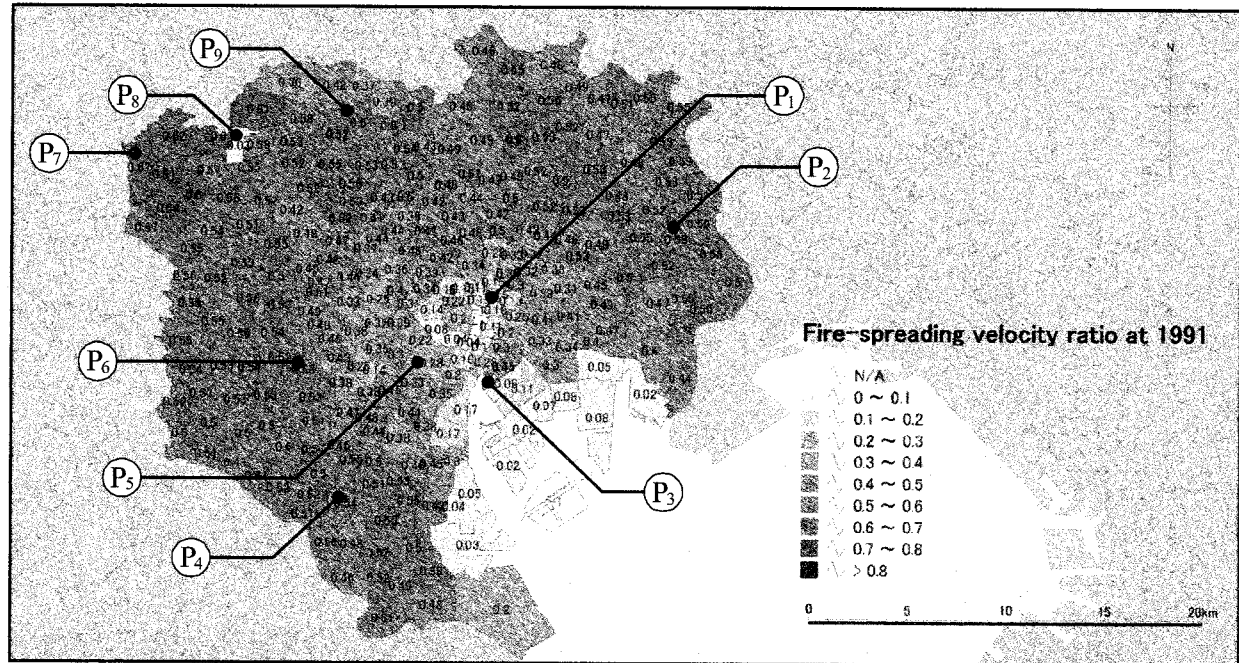


Figure 2 Fire-spreading velocity ratio at 1991

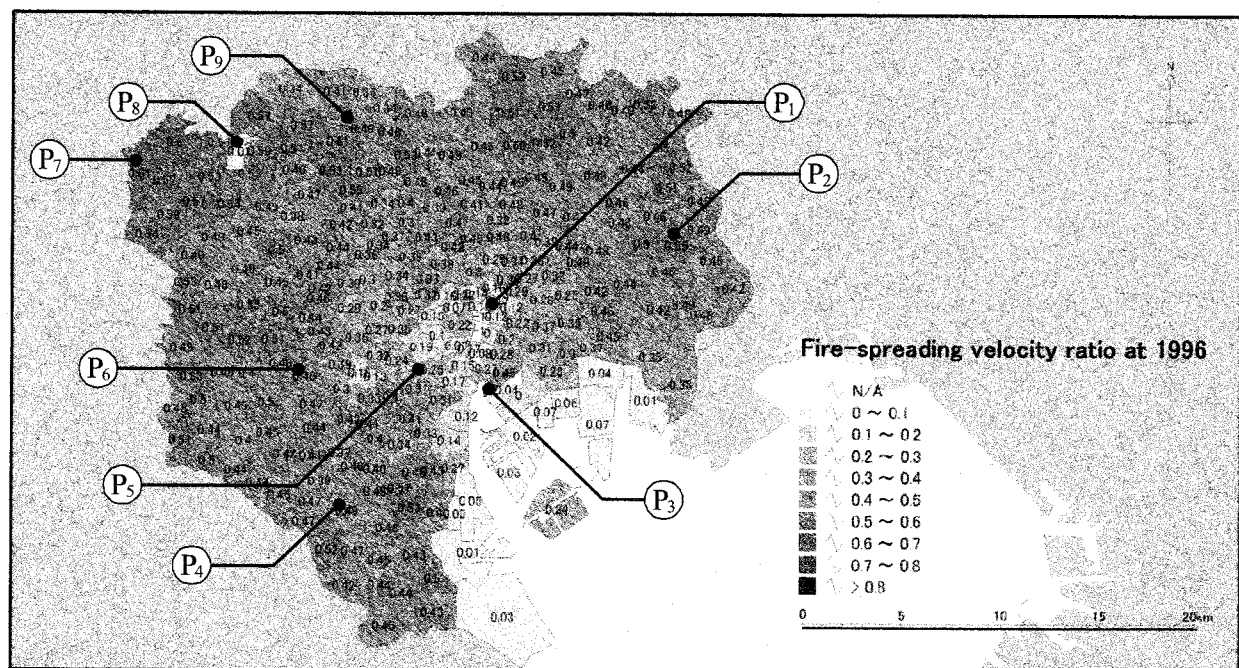


Figure 3 Fire-spreading velocity ratio at 1996

3. METHODS

3.1 Fire-spreading velocity ratio

There are many methods proposed for risk evaluation of fire-spreading, and the ones developed by Hamada (1951) are their typical examples. In this study, Fire-spreading velocity ratio as an evaluation index of the risk of fire-spreading by Hamada was used. This index may not be appropriate for the exact analysis because shapes and locations of buildings and cause of fire are not taken into consideration, but it must be still quite useful to obtain the general idea of fire-spreading velocity in the urban district.

Fire-spreading velocity ratio α is given by a following formula;

$$\alpha = \frac{a+b}{a+\frac{b}{0.6}}(1-c) \quad (1)$$

where a , b and c are ratios of wooden building (Mokuzo-tatemono), fire-proof building (Bouka-tatemono) and fire-resistant building (Taika-tatemono). They satisfy a following formula;

$$a+b+c=1. \quad (2)$$

Fire-spreading velocity ratio takes a value up to 1 from 0. When the value is close to 1, fire-spreading velocity are fast.

Fire-spreading velocity ratio of targeted areas at 1991 and 1996 are shown as Figure 2 and Figure 3. Generally, zones which close to the central district, such as P_1 and P_5 , had relatively low ratio, and zones which away from the central district, such as P_2 , P_4 , P_6 , P_7 , and P_9 , had relatively high ratio. It is interesting to note that there were some zones which are different from surrounding zones, such as P_3 and P_8 .

3.2 Transition matrix

Each building classify to one of m categories. $x_i(t) (i=1, \dots, m)$ is a ratio of the number of buildings of classification i in some zone at time t . Then $X(t)$ can represent the situation as follows;

$$X(t) = \begin{bmatrix} x_1(t) \\ \vdots \\ x_m(t) \end{bmatrix}. \quad (3)$$

In addition, p_{ij} is the probability of a zone where the class was type i at the time t changed to class j at the next time $t+1$. The transition matrix P from time t to time $t+1$ can be represented as follows;

$$P = \begin{bmatrix} p_{11} & \cdots & p_{i1} & \cdots & p_{m1} \\ \vdots & \ddots & & & \vdots \\ p_{1j} & \cdots & p_{ij} & \cdots & p_{mj} \\ \vdots & & & \ddots & \vdots \\ p_{1m} & \cdots & p_{im} & \cdots & p_{mm} \end{bmatrix}. \quad (4)$$

Then, $X(t+1)$ which represents a vector at the time of $t+1$ is represented as follows;

$$X(t+1) = PX(t). \quad (5)$$

When transition matrices are fixed regardless of the observation times, above formula can be rewritten as follows;

$$X(t+1) = PX(t) = \dots = P^{t+1}X(0). \quad (6)$$

Hence, if we know a situation at a certain point of time and the transition matrix of use and structure of buildings, it is possible to estimate the future situations of use and structure of buildings.

3.3 Estimation of converged situation by transition matrix

The eigenvalues of the transition matrix P include 1 because P is always satisfied with a following equation;

$$\sum_j p_{ij} = 1. \quad (7)$$

Therefore, there is an eigenvectors which satisfy following equation;

$$PX^* = X^*. \quad (8)$$

X^* is a convergent situation of P , and it shows a future situation that infinitely large number of transitions had been done.

4. APPLICATION

4.1 Transition matrix

In this study, each building was classified into 20 categories (= 4 use categories \times 5 structure categories). In order to measure category changes of each zone, two datasets of building shape at 1991 and 1996 were compared. Then, matrices which show tendencies of category change were constructed. Finally, eigenvectors of those matrices which show future situations of each zone were

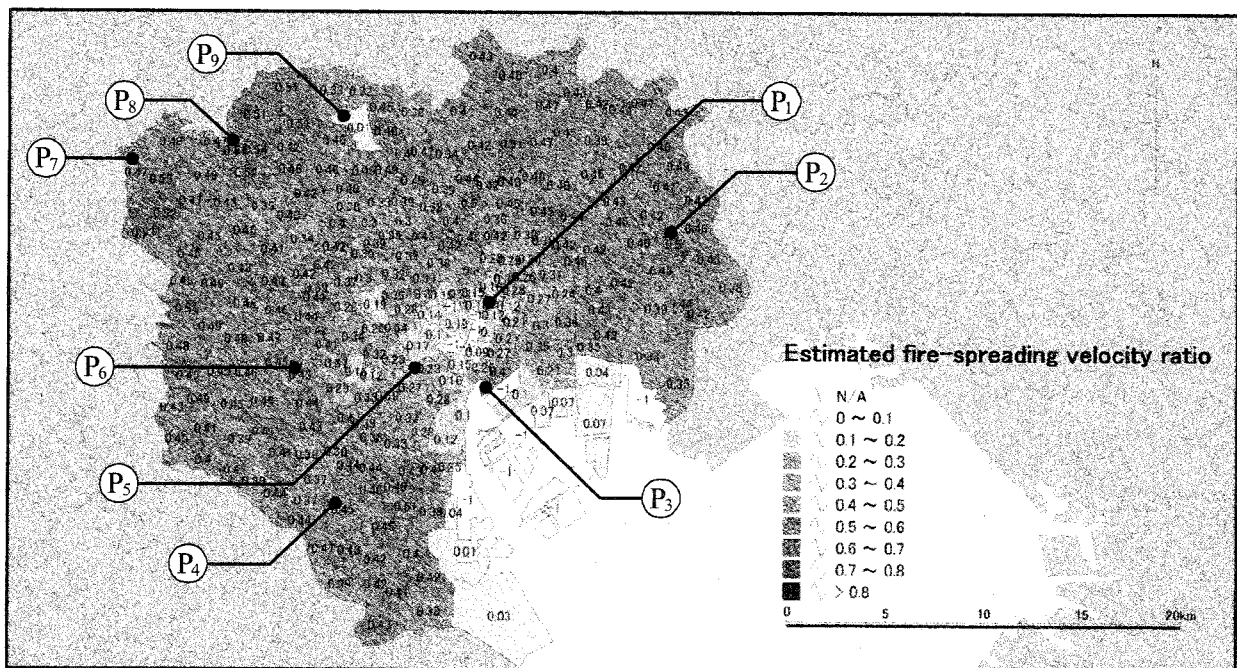


Figure 4 Fire-spreading velocity ratio of estimated future situations

calculated (Figure 4).

4.2 Converged situation of use and structure of buildings

Figure 4 shows estimated future situation. Following tendencies can be pointed out from these results.

- Generally, the ratio tend to decrease.
- The more faraway from central district, the bigger the reduction of its ratio.
- The differences of zones consequently become small.
- Though most zones whose present ratio are high have a certain reduction, such as P₂, P₄, and P₆, there are a few zones whose ratios increase, such as P₇ and P₈.
- There are some zones whose ratios maintain at present level, such as P₁, P₃ and P₅ It is noteworthy that P₃ maintain relatively high level.
- Though their present ratios are high, there are a few zones whose future ratios have great reduction, such as P₉.

From the above results, P₃, P₇ and P₈ were paid attention. P₃ is a zone where many buildings have been existing since old days. P₇ is a zone where land-use conversion to residential area from agricultural land are in progress. P₈ is a zone where fire-resistant buildings were already developed and called 'Danchi'.

4.3 Discussion

It is easy to pay attention to only to the zones whose fire-spreading velocity is already at high level. But according to the above results, it seems to be also necessary to pay attention to the zones whose fire-spreading velocity ratio will be high level ultimately even if its present fire-spreading velocity ratio is at low level.

5. CONCLUSIONS AND FUTURE DIRECTIONS

The aim of this study was to detect the zones where official treatments are needed. Transition matrices of use and structure of buildings were constructed. A situation where it arrives when present tendency continues for a long time is estimated.

Following tendencies was observed. (1) Local difference of fire-spreading velocity ratio tends to decrease generally. (2) There are some possibilities that fire-spreading velocity ratio of zones which are surrounded by the zones of high level present fire-spreading velocity will increase exceptionally.

However it is important to note that this method is only for the rough understanding, more detailed survey is required. Though only changes from buildings to buildings were counted in this study, changes between vacant lands and buildings should be counted for the exact discussion, and errors of this estimation must be checked.

References:

Minoru HAMADA : "Fire-spreading velocity", Research of fire, vol.1, Sagami publishing, 1951 (in Japanese)

DEVELOPMENT OF AN EFFECTIVE TOOL FOR VIRTUAL EXPERIENCE OF ENVIRONMENTAL HAZARD:

- A SURVEY OF DISASTER EDUCATION FACILITIES IN JAPAN

J. Ryu ¹⁾, M. Soeda ²⁾, and R. Ohno ³⁾

- 1) *Post-Doctoral Research Fellow, Center for Urban Earthquake Engineering (CUEE),
Tokyo Institute of Technology, Japan*
- 2) *Assistant Professor, Dept. of Interdisciplinary Graduate School of Science and Engineering,
Tokyo Institute of Technology, Japan*
- 3) *Professor, Dept. of Interdisciplinary Graduate School of Science and Engineering,
Tokyo Institute of Technology, Japan*
jaehoryu@enveng.titech.ac.jp, msoeda@n.cc.titech.ac.jp, rohno@n.cc.titech.ac.jp

Abstract: In order to mitigate the damage caused by the environmental hazard such as fire, earthquake, tsunami, it is important to educate the people about protecting themselves properly and effectively. In order to improve the disaster education and training skills as well as to propose an effective educational tool, first we have surveyed the contents and education program of some existing disaster education facilities in Japan. We chose several facilities in Kobe and Tokyo as the survey targets because of the experience and high potential of earthquake disaster. Furthermore, the urban area has a tendency of expanding the damage without proper preparedness against hazard. The contents, the art of exhibition and the disaster education program, were reviewed to propose the effective education methods including some applications with multimedia. From the result of the survey, we reached a conclusion that the intuitive and interactive tool is needed for effective disaster education, which has portability.

1. INTRODUCTION

The disaster education program for the member of community about environmental hazard such as fire, earthquake, and tsunami is very important because it is one of the effective ways to prepare for the disaster in our everyday life to mitigate the damage by disaster. The one of the effective methods to draw attention to disaster is showing the severely damaged scene with an explanation of the process how it happens. Therefore, the educatee would get powerful impression for memorization and understand the mechanism of disaster process, which will lead to prepare and to cope with the sudden outbreak of hazard situation.

Especially, the disaster preparedness education on earthquake is very important because its damage can be reduced quite a lot, if the daily preparedness is properly conducted. Since earthquake usually come to happen suddenly with no coping time to react, the daily preparedness for it is more important than other types of disaster. For example, the statistic analysis about the causes of injured people in Kobe earthquake in 1995 (Figure 1) shows the tumbling of furniture in house is the biggest one among the several reasons, which could be prevented by the daily carefulness or disaster awareness education program. The disaster education program using effective virtual reality tool will help to understand the educatee easily, which will result in the mitigation of damage by disaster.

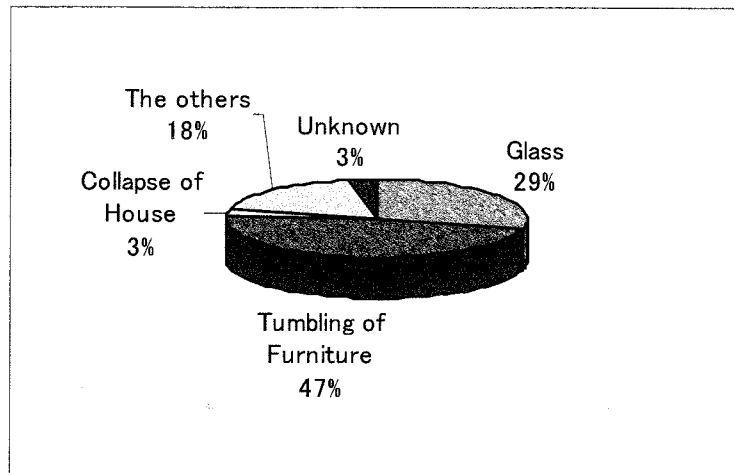


Figure 1 Causes of injury by the Kobe earthquake 1995
(Architectural Institute of Japan, 1996)

In order to propose an effective tool for virtual experience of environmental hazard, we need to understand the current state of educational and training program for environmental hazard prevention. In Japan, the major city like Tokyo makes great effort to inform the citizen about the environmental hazard through several disaster education facilities. These facilities play a central role in disaster education system that executes various kinds of training. Therefore, we expected to find some guidelines for development of a tool for environmental hazard education through an analysis of several representative facilities in Tokyo and Kobe.

2. SURVEY OF DISASTER EDUCATION FACILITIES

2.1 Target Facilities of Survey

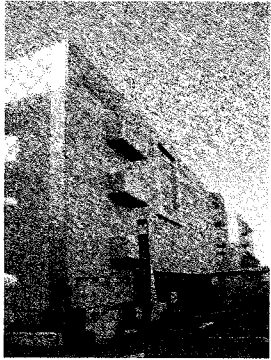

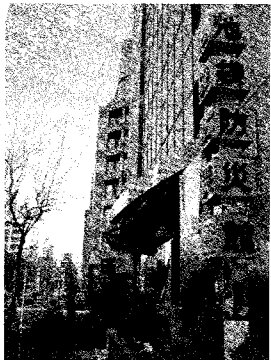

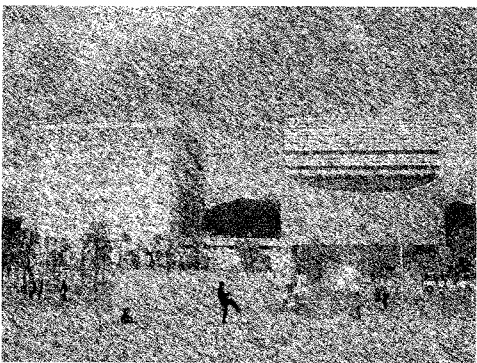
The target facilities of the present survey are the follows: Disaster Reduction and Human Renovation Institution in Kobe (DRI), Fire museum of Tokyo and three disaster education facilities (Ikebukuro center, Honjo center, Tachikawa center) in Table 1. These facilities are the leading public disaster education facilities that can represent the public education system of Japan. Through reviewing these facilities, we are expecting to obtain useful information for proposing new communication methods to educate the members of community.

Disaster Reduction and Human Renovation Institution (DRI) was established to pass on the experience and lessons learnt from the Great Hanshin-Awaji Earthquake to the future, and to contribute to the reduction of damage from coming disasters. The display contents are mainly concerned with the earthquake hazard and preparedness for that.

The other three life safety learning centers (Bosai-kan) are the disaster educational facilities in Tokyo where everyone can participate in and receive the training and information with techniques against disaster. The visitors can learn proper actions against earthquakes, successful evacuation, effective firefighting, first-aid treatment, and so on.

We visited these facilities, and participated in the several experience courses. The most of facilities provide the guidance program and free observation for the visitor.

Table 1 The Disaster Education Facilities

		
Tachikawa Center	Honjo Center	Ikebukuro Center
		
Fire Museum	Disaster Reduction and Human Renovation Institution	

2.2 Features of Disaster Education Facilities in Urban Area

At the surveying of disaster education facilities, we have focused on the communication tools of training process, mainly visual one, because the aim of this survey is to obtain useful knowledge for developing an effective tool that provides virtual experience of environment hazard.

Table 2 is the comparison of disaster education facilities from the several items that comprise the exhibit contents and education course. Usually, the movie contents were viewed first before starting the free look around other exhibit items because the visual demonstration has a merit of strong communication ability. Not only the movie but also the real object is used to give visitors with the image of severe damage by earthquake. Especially at the DRI in Kobe, they display the real wreckages from the earthquake disaster place to recall the fear of earthquake. And, photo images and small videos are installed near by wreckage to support the comprehension the disaster situation.

After experiencing the guide program of target facilities, we also found several common features in them to make an effective exhibition program. One of the features is the zoning plan (floor plan), which usually leads the visitors to the top floor first for watching the movie contents about disaster and to go down stairs for easy watching the exhibit items. For children, the centers specially make an effort to give interest to them such as making game-style education system including point-card and issuing a certification of disaster education. Usually, the children have some difficulties to understand the principle of environmental hazard and to learn the way of dealing with that situation. The game-style education method is interesting and effective way of attraction because the children like to compete with each other.

Table 2 Comparison of Disaster Education Facilities

Facilities	Visual Media	Exhibit Style Process	Pseudo-experience Equipment	Information Material
DRI (Kobe)	1.17 Theater, The Great Earthquake Hall	Guide & Free Viewing, 4F⇄3F⇄2F	Streets just after the Quake	Library for Earthquake-related
Fire Museum	-	Free Viewing, 7F⇄...⇄B1F	Miniature Fire Situation	Book & Video
Honjo Center	3D Theater	Guide & Free Viewing, 4F⇄3F⇄2F⇄1F	Earthquake, Fire & smoke, Typhoon & Heavy rain First Aid Training	Book & Video
Ikebukuro Center	-	Guide & Free Viewing, 5F⇄4F	Earthquake, Fire & smoke, First Aid Training	Video Room
Tachikawa Center	Disaster Mini Theater	Guide & Free Viewing, 2F⇄1F	Earthquake, Fire & smoke, First Aid Training	Book & Video

2.3 Hidden Factors of Effectiveness of Disaster Preparedness Education

Disaster Education program is carried out by instructors who is engaged in the facilities. From here, we can notice that human resource is another factor for the result of training program. Even though there is a same content of exhibit for the educatee and visitor, according to the instructor or guide, who is in charge of the program in the field, the quality of education become different. For example, who has the rich experience of disaster such as firefighter can understand the educatee with confirm knowledge and interesting episode. Also, the abundant know-how of education could be another skill for effective communication.

In the second place, the role of mass media like television has another impact for the educational result. For example, the television program "*The great earthquake must happen!*" of Asahi television program has great influence on the audience because it provided an easily understandable story and many common subjects of conversation between the watchers. Even though it is hard to measure the effectiveness of the program, its usefulness for disaster preparedness is undoubtable. This shows the visual media is useful as a risk communication tool.

3. TO IMPROVE THE EFFECTIVENESS OF DISASTER EDUCATION PROGRAM

The new media like the Internet and visual information of image is a very potential way of education for young students because it is easy to understand and to access. The survey by the R. Shaw (2004) shows the high preparedness of students who were received active ways of education through the conversation in family and community education. The result implies the effectiveness of spontaneous and active participation in disaster preparedness education.

According to B. Rohrmann (2000), there are three stages of socio-psychological model for risk communication process: *[Risk (Re)-Appraisal]* □ *[Decision for Preventative Action]* □ *[Risk-reducing Behavior]*. In these three stages, the final *Risk-reducing Behavior* is most important to reduce the damage from environmental hazard as well as natural disaster. To encourage the educatee reach to the last stage, the effective media is need to give the proper information. He also mentioned that practical experience might not be sufficient to ensure satisfactory results. Rather, a comprehensive theoretical framework is needed to guide risk communication efforts.

After surveying the facilities and interviewing some managers of the exhibition, we figure out these facts: (1) the visual contents is useful and effective for the education program, (2) there is a some request for the Potable VR system to show the visual contents to more students, (3) the interactive contents is needed to continued the interest of user which will lead more effective result of education. To satisfy the effective disaster education program, participant's interest and intuitive understand process is essential. At these aspects, the virtual reality technology is proper media to be used because the three-dimensional graphic presentation is interesting and easy to understand.

3.1 Portability of Education Tool for Broad Disaster Education

One of the requests for the effective disaster education is visual content for easy understand. To show the visual contents, the special system for display of graphic is necessary. Usually, the system is heavy and fixed one place because it is hard to move and reset the structure in other places. Therefore, the educatee must come to the heavy equipment room, which is one of the obstacles to the accessibility. Here is the problem of limited accessibility of the display system.

Potable VR system can be a solution for that kind of problem. The portability of VR system can broaden the number of participants who need the disaster education.

3.2 Contents of Education Tool (Detailed and Executable Instruction for Individual)

Another requests for the effective disaster education is interactive, interesting and intuitive contents for the long continued concern of it. To satisfy these requirements, the interactive VR system can be a potential proposal because there has been a quite progress in computer graphics of reality and real-time physical simulation. Also, adding to the VR system with multi-modal interfaces for the interaction such as locomotion (navigation), haptic (grasping & force) interface, and motion tracker could be the quite effective composition of system. By realizing the high presence sense and intuitive physics simulation with rich interaction will help to improve the result of the education program.

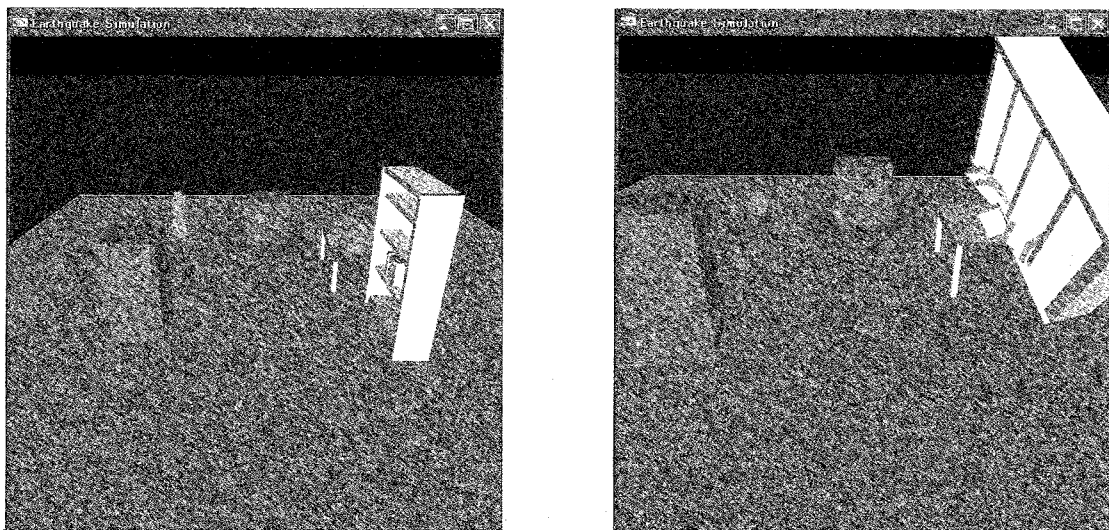


Figure 2. Earthquake Simulation by Real-time Physics Simulation

4. THE EFFECTIVENESS OF EDUCATION

Even though the disaster education facilities carry out the training program for citizen and student, still there is a doubt about the effectiveness of disaster education course for the participant. The natural disaster or environmental hazard is usually a sudden incident that is very hard to be predicted and controlled. Therefore, the experiment in limited condition is almost impossible.

One of the possible methods of investigation could be the questionnaire that compares the status of educatee between before and after education. Several previous studies such as Masuda et al. (1988) and Takimoto et al. (1999) carry the questionnaire method to evaluate the effectiveness of disaster education. Although they carried out the questionnaire about simple image, the effectiveness of the training through three-dimensional presentation such as virtual experience has not been discussed.

But, the effectiveness of virtual simulation was proved in the experiment carried by Bliss and Tidwell (1997). They executed an experiment about the firefighter to navigate a rescue route in an unfamiliar building with three conditions: Blueprint, Virtual Reality, or No Training. The results indicated that firefighter trained with virtual reality or blueprint performed a quicker and more accurate rescue than those without training. This result infers that the usefulness of the escape training or preparedness exercise using VR system.

5. CONCLUSIONS

We have surveyed several disaster education facilities in Kobe and Tokyo as the fundamental research for the construction of an effective tool that will help to make virtual experience and carry out education program for environmental hazard. From the analysis of the exhibit contents and training program, we had some useful findings for an effective tool for disaster education. The visual presentation has some merits of easy understanding and continued interest than literature presentation. The requirement for the interaction is important to derive a sustained interest and effective result from the education course. Especially for the children, the contents of education need to be the executable strategy in everyday life to get the instant comprehension and effective result. In the aspect of program management, the portable tool is another issue in order to broaden the participant of educatee. Furthermore, the experienced and well-trained educator or conductor is another factor that reinforce the effectiveness of the education. These findings will serve as guidelines for developing a new educational tool for the disaster education program.

Acknowledgements:

We thanks to the affiliate of disaster facilities for their kind cooperation and interviews.

References:

- Architectural Institute of Japan (1996), "Report of Damage Occurred Inside of Houses at Hashin-Awaji Great Earthquake," AIJ (Japaness)
- Shaw, R., Shiwaku, K., and Kobayashi, H. (2004), "Study on new system of earthquake disaster education at high school" (-analysis of factors affecting awareness in questionnaire survey targeted for high school students-), Journal of Environment Engineer, AIJ, No.585, 69-74. (Japaness)
- Rohrmann, B. (2000), "A socio-psychological model for analyzing risk communication process," The Australasian Journal of Disaster and Trauma Studies, Vol. 2000-2.

- Bliss, J. P., and Tidwell, P. D. (1997), "The effectiveness of virtual reality for administering spatial navigation training to firefighters," *Presence* Vol. 6, No. 1, 73-86.
- Masuda, H., Midorikawa, S., Miki, C., and Ohmachi, T. (1988), "Formative Process of Consciousness of Earthquake Preparedness and Evaluation of Effects of Earthquake Education," *Journals of the Japan Society of Civil Engineers* Vol. 398, I-10, 359-365. (Japaness)
- Takimoto, K., and Miura, F. (1999), "Development of Earthquake Preparedness Education Software for an Elementary And Junior Highschool Students and its Evaluation," *Journals of the Japan Society of Civil Engineers* Vol. 619, I-47, 155-167. (Japaness)

<http://www.tfd.metro.tokyo.jp/ts/museum.htm> : Fire Museum of Japan & Disaster preparedness Center

<http://www.dri.ne.jp/index.html> : Disaster Reduction and Human Renovation Institution of Kobe City

<http://www.disastereducation.org> : The National Disaster Education Coalition (NDEC) of USA

GLOBAL DISASTER DUE TO THE 2004 INDIAN OCEAN TSUNAMI

F.Imamura¹⁾, S.Koshimura²⁾, K.Goto³⁾, H.Yanagisawa⁴⁾ and Y.Iwabuchi⁴⁾

1) Professor, Disaster Control Research Center, Graduate School of Engineering, Tohoku University

2) Assoc. Professor, Disaster Control Research Center, Graduate School of Engineering, Tohoku University

3) Res.Assoc., Disaster Control Research Center, Graduate School of Engineering, Tohoku University

4) Graduate Students, Graduate School of Engineering, Tohoku University

imamura@tsunami2.civil.tohoku.ac.jp

Abstract: The typical mechanism of the generation and propagation of the tsunami is introduced and the damage due to it at each country are summarized to make the lessons for the tsunami mitigation in the future. And we investigated impact on not only coastal community but also the environment including the coral and vegetation through the field survey. The necessary research topics are discussed.

1. EARTHQUAKE AND TSUNAMI

A tsunami caused by a great earthquake occurred in Indian Ocean on 26 Dec. 2004 and hit more than 10 countries around the ocean including Indonesia, Sri Lanka, India, Thailand and etc., which resulted in a death toll of nearly 300,000 people and great economic losses. The whole world was heavily shocked by the precipitate tragedy.

The tsunami was to be a water wave train generated by impulsive disturbances of water surface due to the fault motion from the offshore of the northwestern Sumatra Island to Andaman sea off Myanmar, reaching 1,000 km where the Indian-Australia plate is subducting under the Eurasia one and several earthquakes followed by tsunamis with $M=8-8.5$ have happened, but not exceed $M=9.0$. This is the first earthquake more than 9.0 in Indian ocean. The tsunami generated in the trench propagating mainly toward east and westward direction because of the wave directivity of energy. When the tsunami reached the coast of Thailand and Malaysia around 500 km far from the source in the east passing through the Andaman sea, one toward the west propagating over the Indian sea arrived at the coast of India and Sri Lanka 1700 km far. Because the sea water depth in Andaman is shallow, 5-600 m in depth, and that in Indian ocean is deep, 4-5000 m in the depth, which change the traveling speed of the tsunami. However, the first tsunami in Thailand was to be pulled down, whereas that in Sri Lanka was to raise, which could be recorded at the tidal stations at each region and are reported by the eyewitness. This is because of the positive initial disturbance of sea bottom in west source and negative in east. Once tsunami waves reach shallow water, they transform dramatically, since the speed of a tsunami is a function of the water depth. But because its energy remains almost constant, the height of the wave grows tremendously in shallow water. The ranging of 10-48 m runup heights in the western shore of the Sumatra, 5-18 m in Thailand, and 10-15 m in Sri Lanka was measured.

Due to the Indian tsunami disaster on December 26, 2004, countries around the Indian Ocean were severely damaged. Rebuilding and recovery processes have been carried out with help from both national and international agencies. Meanwhile, the efforts are still in their initial stages. Many people have yet to re-establish secure livelihoods, and continue to need relief assistance. On country levels, environmental and disaster management programs are required for protection and prevention of future

disasters. Lessons of the catastrophe can be summarized into the following:

- Developing the monitoring and warning system with information technology evacuation system
- Integrated disaster mitigation program for each region to mitigate tsunamis as well as typhoons, erosion and flood.
- Data Base to compile the all available data; measured and observed, videos and photos, interview and media in newspaper
- International network for the community for research, education and Hazards map for society

The nature of damages by this earthquake is similar to the great earthquakes with magnitude over 8 which will occur along the Nankai Trough in Japan, but there epicenters are very close to the land. They will generate strong ground motion and great tsunami. We in Japan should remind that the similar damage due to the earthquake and tsunami should happen, so that the mechanism of them should be studied and the lessons should be shared.

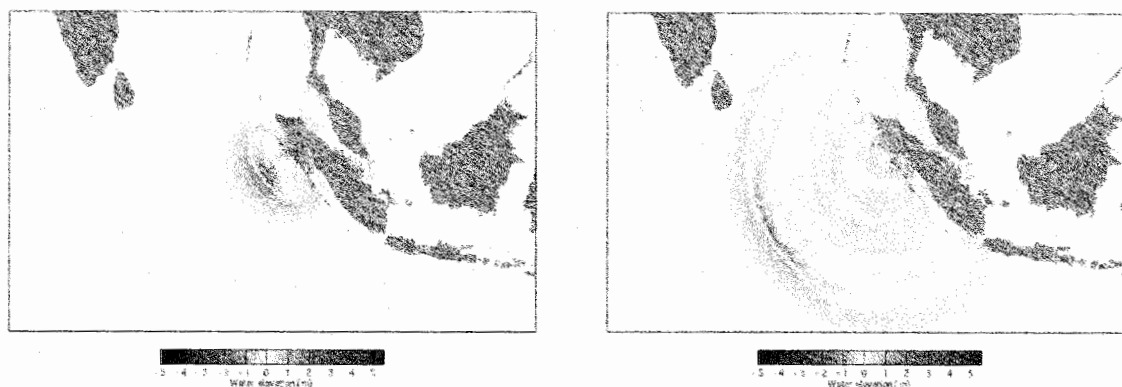


Figure 1 Propagation pattern of the tsunami 1 hour (left) and 2 hours (right) after the earthquake

2. FIELD INVESTIGATION

2.1 Field survey after the events

The international tsunami community conducts many field investigations immediately after an event: e.g. Nicaragua in 1992; Flores Island, Indonesia, in 1992; Okushiri Island, Japan, in 1993; East Java, Indonesia, in 1994; Shikotan Island, Russia, in 1994; Mindoro Island, Philippines in 1994; Irian Jaya, Indonesia, in 1996; Indian Ocean in 2004 [e.g. Yeh et al. (1993), Synolakis et al. (1995), Imamura et al. (1997)].

Members of the ITST (International tsunami Survey Team) decided that a field survey was necessary as soon as possible to try and determine the true value of the maximum run-up and to make an accurate map the run-up distribution along the coast. Subsequent investigations by international and locally-based scientists included two onshore investigations by international teams (the First and Second International Tsunami Survey Teams). The standard of the way of tsunami survey is compiled by IOC(1998). Another role of the ITST has been to advise the government and the survivors about the safety of this sector of coastline.

2.2 Damage in each country

The severest affected area of Indonesia is the Northern part of Sumatra, and it is reported that the coastal areas along the coast are completely destroyed by the strong shake and sudden attack of the big tsunami. The inland inundation mark was found up to 5 kilometers from the coast, and there were lot of debris such as pulled out trees, destructed house and ships carried out by the tsunami wave into the center of the city, which should increase the destructive power of the tsunami. It was observed that the tidal surge had reached over 40 meters-height on the hilly area where the tsunami run over the top of the peninsula with a saddle shaped hill. The damage in industrial area are found, which are oil tanks moved by the tsunami and erosion and destruction of harbor facilities.

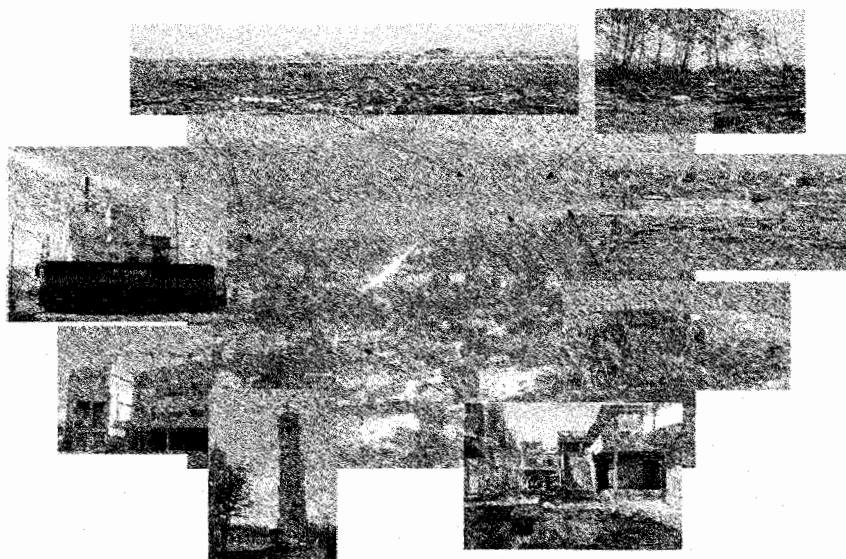


Figure 2 Several damage in the area of Banda Aceh, Indonesia

In Thailand and Malaysia, many sightseeing spots were damaged seriously and a large number of foreign visitors also became victim of the tsunami disaster. It was a sudden major disaster to the resorts. This is serious issue to mitigate the tsunami damage in the coastal area because the most of visitors have large variety on the nation, knowledge, and response for natural disaster. The tsunami warning system , transfer of the information, evacuation system are important issues to mitigate the damage.

In addition, India and Sri Lanka were seriously damaged. Especially, in Sri Lanka, the number of death toll became (raised) nearly 40,000. The East and South coast in Sri Lanka were totally damaged; besides Colombo, the South-West Sri Lanka had been damaged too, even though the coast is located in the back for the direction of tsunami propagation from the source. In the coastal areas, the community villages were totally destroyed; and the train that stopped for evacuating in emergency basis, had lost more than one thousand of people who were passengers and residents.



Figure 3 Damage including the train in the area of Kahawa, Sri Lanka

In The Republic of Maldives, at 9:00 AM (1:00 PM in Japan local time) on 26th December, tsunami attacked this region. Maldives is a group of about 1,200 coral islands, and its maximum height is only 1.8m. Almost all the roads in the capital city Male were flooded. There were no vacancies in hotels because it was Christmas vacation season (time). So, there had happened severe damage by that tsunami. There was no tsunami warning system in the Indian Ocean premises. In some coastal areas, the people could not feel ground motion; so, the inhabitants of that area were suddenly attacked.

3. EFFECTS OF TSUNAMI ON THE COASTAL ENVIRONMENTS

Large tsunami waves strongly affect the coastal environments, and damage severely to the agriculture and the fishery activities. For example, ponds for aquaculture are destroyed and trees are fell down by the impact of tsunami waves, and vegetations within the inundation area were blighted due to the salty seawater. Moreover, the sea bottom, coastal topography and river drastically change due to the erosion and re-sedimentation of the sea bottom and the beach sediments. A large amount of sediments are transported landward and cover the wide area of the coastal area to form the tsunami deposits. In order to mitigate damages on the coastal environments and to make a future disaster prevention plan for at-risk countries, detail survey for understanding the damage of coastal environments by the 2004 Indian Ocean tsunami is required. We conducted the field survey on coastal vegetation such as mangrove, sediments and coral rocks, and coastal topography.

3.1 Impact on green belt such as mangrove

The tsunami provide us with an unprecedented opportunity to evaluate the impact on the environment and to assess the role of mangrove forests in reducing impacts of tsunamis or storm surge. We have made initial comparison of pre-tsunami mangrove cover and post-tsunami destruction by using paired satellite images. Mangrove forests, in particular, shield coastlines by reducing wave amplitude and energy. Coastlines fringed by mangroves were strikingly less damaged than those where mangroves were absent or had been removed. Field observations indicate that mangroves also prevented people being washed into the sea, which was a major cause of death. In addition, mangroves trapped driftwood preventing property damage and injury to people Green belts of other trees, coastal dunes, and intact coral reefs performed similar functions. On the other hand, coastal vegetations would be fell down and pulled up by the strong tsunami impact, and fragments of fallen trees convert to the dangerous floating materials. We try to get a criteria of fell trees/mangrove due to the moment/force of the tsunami, which is necessary to discuss an effective tsunami disaster reduction plan that uses coastal

vegetations.

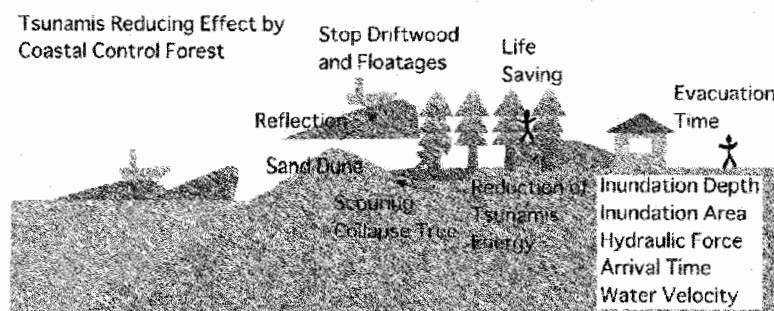


Figure 4 Functions and effect of coastal control forest to reduce a tsunami disaster

3.2 Tsunami deposits and blocks

A large tsunami can remove sediments from the sea bottom and the beach, and transport a large amount of sediments landward to form the tsunami deposits. Distribution of tsunami deposits and their sedimentological characteristics (e.g., thickness, grain size, sedimentary structures) are useful information to estimate the hydrodynamic force of the tsunami wave currents during their sedimentation. Thus, we preliminary investigated the distribution and their characteristics around the Khao Lak area. In Pakarang Cape near Khao Lak, there were abundant reef blocks, which were composed of fragments of coral up to 4 m in diameter. Reef blocks are scattered from 0 to about 400 m offshore and over a distance of about 1 km from north to south along the shore. No reef blocks are observed on land, suggesting that the hydrodynamic force of the tsunami wave currents have suddenly became weak near the shoreline. According to our field observation, flat, very shallow sea floor extends up to 300-600 m offshore from the high-tide line, and the gradient suddenly increased around the reef edge. We infer that tsunami waves probably impacted to the reef edge around 300-600 m offshore and transported reef blocks landward.

4. NECESSARY RESEARCHIN FUTURE

The following are the necessary points that we should consider to enhance the research activity of earthquake and tsunami disaster reduction;

- Partnership with the Asian countries.
- Strong cooperation with the institutes in Asian countries, such as: Indonesia, Thailand and Sri Lanka, etc., which suffered a great damage by the 2004 Sumatra Earthquake through meeting, exchange program, further cooperative works.
- Strong cooperation between many related institutes in various field, like: Science (hazard mechanism), Engineering (countermeasures) and Social science (recovery and reconstruction), etc.

Following are the research themes that we should take from now.

- Mechanism of huge earthquake and tsunami like the 2004 Sumatra type.
- Mechanism of damage and disaster due to huge earthquake and tsunami including new type damages.

- Technology development for disaster reduction development.
- Effective uses of Tsunami Warning System and Information Recognition, and Evacuation system as well.
- Recovery and reconstruction policy and plan; and a new city plan improving built environment for disaster reduction.
- Collection of basic data from wider areas and to establishment of its archives.
- Training and education system for the capacity building against earthquake and tsunami.

Acknowledgements:

The authors acknowledge support from special funds for promoting Science and Technology, Japan Ministry of Education, Culture, Sport, Science, and Technology (MEXT)

References:

- Imamura, F., D. Subandono, G. Watson, A. Moore, T. Takahashi, H. Matsutomi, and R. Hidayat, 1997: Irian Jaya Earthquake and Tsunami causes serious damage, *EOS Transactions*, AGU, Vol.78, No.19, p. 197 and pp. 201.
- IOC, 1998: *Post-Tsunami Survey Field Guide, Manual and Guides*, No. 37, UNESCO
- Synolakis, C., F. Imamura, Y. Tsuji, H. Matsutomi, S. Tinti, B. Cook, Y.P. Chandra, and M. Usman, 1995: Damage, conditions of East Java Tsunami of 1994 analyzed, *EOS Transactions*, AGU, Vol. 76, No. 26, p. 257 and pp. 261-262.
- Yeh, H., F. Imamura, C. Synolakis, Y. Tsuji, P. Liu, S. Shi, 1993: The Flores Island tsunamis, *EOS Transactions*, AGU, Vol. 74, No. 33, pp. 371-373..

ENVIRONMENTAL RESTORATION OF TSUNAMI IMPACTED INLAND WATER BODIES IN SRI LANKA

P.P. Gunaratna¹⁾

*1) Senior Lecturer, Department of Civil Engineering, University of Moratuwa, Sri Lanka
priyantha@civil.mrt.ac.lk*

Abstract: This paper describes the problems associated with inland water bodies, associated infrastructure and surrounding environment impacted in Sri Lanka following the tsunami disaster occurred on 26 December 2004. Based on assessment of present conditions development of environmental restoration plans for three selected sites are presented. The institutional arrangements necessary for implementation are also briefly highlighted.

1. INTRODUCTION

On 26th December, 2004, an earthquake originated in the Indian Ocean just north of Simeulue island off the western coast of northern Sumatra, Indonesia triggered propagation of a tsunami. This tsunami reached as much as 30 m in height at certain localities and devastated the coastal areas of Indonesia, Sri Lanka, South India, Thailand and some other countries in South Asia. The total death toll was estimated to be around 200,000 with massive scale destruction to coastal infrastructure and a multitude of adverse short term and long term impacts on environment.

In Sri Lanka, around 800 km of coastal stretch was affected covering 11 coastal districts (Figure 1). About 40,000 people were estimated to be killed with nearly 6,000 reported missing. The total population displaced was around one and half million. The damage to physical environment included building, transport, tourism, industrial, agricultural, health, defense, fisheries and port sectors (University of Moratuwa, 2005).

The tsunami has had impacts of varying magnitude and nature on streams, irrigation and drainage schemes, flood protection works, estuaries, lagoons and coastal wetlands. The resulting effect is both an obstruction to movement of water as well as degradation of water quality. The deposition of massive quantities of sea sand and intrusion of sea water rendered substantial extent of agricultural lands in coastal areas infertile. As the livelihood of a large community is affected by this environmental damage, it is of paramount importance to restore these water bodies, associated infrastructure and surrounding environment using appropriate technology, while avoiding further adverse impacts on environment.

This paper will focus on the post tsunami status of three selected sites in Sri Lanka comprising two coastal lagoons (Karagan Lewaya and Kalametiya Lagoon in the Hambantota district in the southern coast) and Pottuvil region in the east coast comprising several irrigation systems. The problems associated with these sites are typical of the impacts of tsunami on inland water bodies in Sri Lanka. The resulting environmental damage in terms of water and sediment quality, spread of alien plant species, debris accumulation, water stagnation and destruction to physical infrastructure is assessed.

Based on this assessment, site specific “Action Plans” for environmental restoration is developed. The contents of this paper are partly based on work carried out by the author as a Consultant to the Ministry of Environment and Natural Resources (MENR) of Sri Lanka.

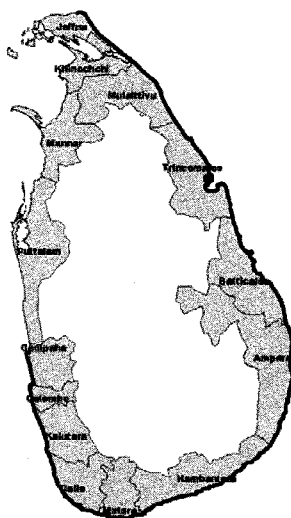


Figure 1 Coastal Area in Sri Lanka Affected by the Tsunami on 26 December 2004

2. PRE TSUNAMI STATUS IN AFFECTED ENVIRONMENT

2.1 Karagan Lewaya

Karagan Lewaya is a seasonally hyper-saline coastal lagoon situated within Hambantota district of the Southern Province of Sri Lanka immediately to the north-west of Hamabntota town (Figure 2). The term “Lewaya” stands for “saltern” indicating its past use for salt extraction, an activity which is virtually non-existent at present times. The lagoon covers an area 8.35 km² in extent and is 3.5 km long and 1.2 km wide. The average depth is about 0.9 m. Karagan Lewaya is considered as one of the best birdlife habitats of high conservation value found in Sri Lanka. Its importance as an area of special ecological interest is well emphasized by the inclusion in the Directory of Asian Wetlands (Hoffman, 1982).

The 58 km² undulating catchment of Karagan Lewaya includes dry zone scrub woodland, numerous village tanks, associated paddy, vegetable and forest plantations, a substantial part of Hambantota urban area and a strip of coastal sand dunes to the south. Fronting the dunes is a wide beach about 3 km long contained between rocky headlands. Bombuwetiya sea outlet canal just to the northeast of Hambantota town is the only connection between the lagoon and the sea, terminating with a gated control structure. This outlet is mostly blocked by a thick beach sand accumulation. It has been reported that in the high flood years of 1957 and 1969 this sand bar had to be breached to drain out lagoon water (Central Environmental Authority, Sri Lanka and Euroconsult, Netherlands, 1994).

2.2 Kalametiya Lagoon

Kalametiya lagoon is also situated in Hambantota district between the towns of Tangalle and Ambalantota (Figure 3). It is 6.06 km² in extent, comprising mainly marshland and mangroves. It can be roughly divided into a silted and well vegetated northern section and a southern part with open water surfaces with water depths generally less than 1 m. Kalametiya lagoon is connected with the neighbouring Lunama lagoon, 1.92 km² in extent, by a man-made channel about 2 km in length (Central Environmental Authority, Sri Lanka and Euroconsult, Netherlands, 1995).

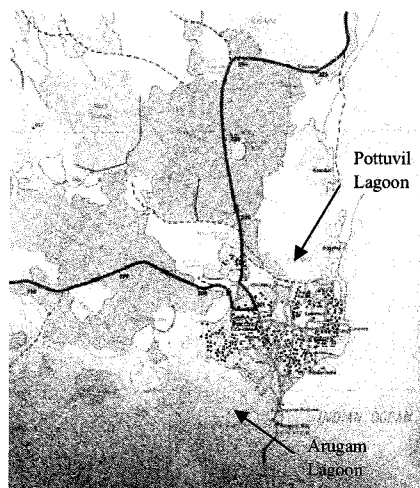


Figure 4 Pottuvil and Arugam Lagoons in Ampara District

3. IMPACT OF TSUNAMI

3.1 Karagan Lewaya

Karagan Lewaya was severely affected by sea water intrusion following tsunami hazard. About 5-6 m high tsunami waves hit the Hambantota area causing massive destruction of densely populated area at Hambantota town (Figure 5). The resulting debris, vehicles, and more than 1000 dead bodies were swept away by sea water into the Karagan Lewaya, necessitating a massive clearance effort. Bombuwetiya sea outlet canal was badly affected and the outlet structure was damaged and detached from the abutting high ground.

The ecosystem following the tsunami attack was markedly different (Figure 6) due to sudden change of salinity levels and bacterial decomposition was ceased to be occurring effectively. Bottom sediments were considerably agitated with changes in anoxic and oxic layers causing contaminant release. The data collected by the University of Moratuwa (UOM) in early April 2005 revealed that faecal contamination was very high. The high COD levels also indicated organic pollution. The uncleared debris is either partly or totally buried in the bottom sediments or in the form of floating material and scum. The nutrient pollution in stagnant water pools due to the presence of algae was evident. The dissolved oxygen levels which were already low prior to the occurrence of tsunami further declined, due to heavy load of debris especially biodegradable matter, which utilize oxygen for degradation. Several complaints of skin diseases had been reported indicating indiscriminate growth of disease causing microorganisms.

3.2 Kalametiya Lagoon

Kalametiya lagoon and the surrounding area were badly impacted by the tsunami causing extensive property damage and loss of human life (Figure 7). Tsunami inflicted heavy damage on the fishing community at Kalametiya. Almost the entire fleet of fishing boats and most of the fishing gear in the Kalametiya village were destroyed.

The beach strip dividing the Kalametiya lagoon from the ocean disappeared and the lagoon turned into another bay on the coastline with the sea entering it directly. However, the sand bar reformed within a short period of time restoring the pre-tsunami status. The deposition of marine sludge and sand in a salt marsh and grassland habitat bordering the lagoon resulted in the destruction

of vegetation in these habitats. Funneling of sea water from the lagoon outlet and the outlet canal partly damaged mangrove tree line bordering the lagoon. Sudden ingress of saline water resulted in destruction of certain plant species such as cattail reed and spreading of certain other salt water tolerant species such as invasive alien Prickly-pear cactus.

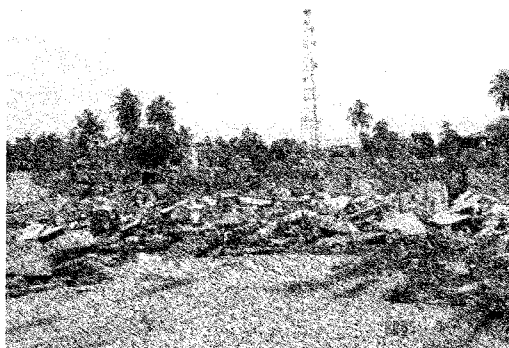


Figure 5 Hambantota Town Devastated by Tsunami



Figure 6 Tsunami Impact on Karagan Lewaya



Figure 7 Tsunami Impact on Kalametiya Lagoon

3.3 Irrigation Systems in Pottuvil Region

Ampara district, in the Eastern Province was the first to be struck by the tsunami wave as it approached the island. Due to generally flat coastal topography in this district, the sea intruded as much as 1.5 km inland from the shoreline, with severe impact in an 800 m strip. Within Ampara district, Pottuvil town and its surroundings were particularly affected, with over 400 deaths and irreparable damage to housing and other buildings.

Picturesque Arugam Bay, with its tourist facilities and the adjoining fishing village of Sinna Ullai, were badly affected with deaths of several tourists and local inhabitants. Along with the houses in Sinna Ullai, most hotels were also either completely destroyed or very badly damaged. Several coastal roads, bridges and causeways were severely damaged. A large section of the bridge at Arugam Bay was destroyed, and was re-opened only about 3 months later after Bailey bridge sections were installed by the Indian army.

The rice paddy cultivation in the area was severely affected. The significant and immediate negative effects on agriculture in the Pottuvil-Arugam Bay area, were salinization, water logging and sand deposition. Heavy rains immediately following the tsunami occurrence further aggravated the damage on irrigation and drainage systems. This rain intensified as the days passed by reaching about 350 mm as recorded at Ampara on 31 December 2004. With lagoon levels already high,

drainage canals blocked by sand deposition, the flood waters unable to pass freely into sea caused considerable damage to irrigation and drainage canals, canal structures, flood protection bunds and adjoining paddy fields (Figures 8 and 9). Some areas subjected to flooding, became permanent wetlands because of blocked drainage. In addition, many paddy fields were strewn with debris. The tsunami also badly damaged a number of farm and access roads and several anicut structures. The drainage channels conveying irrigation return flows to lagoons were silted up by the tsunami, and subsequently further damaged by the floods that followed.

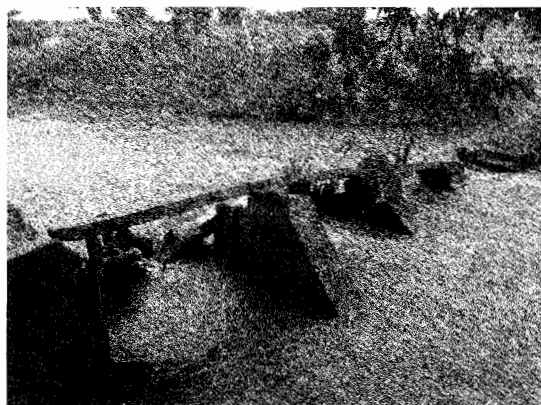


Figure 8 Tsunami Damaged Anicut Scheme –Pottuvil Region



Figure 9 Silted up Drainage Canal – Pottuvil Region

4. ENVIRONMENTAL RESTORATION

4.1 Karagan Lewaya

Following the emergency clean-up operations, which involved mainly recovery of human corpses, vehicles and large volume of debris from the water body, no further action had been taken to restore ecosystem of Karagan Lewaya even until late 2005. The problems of faecal contamination, depletion of dissolved oxygen and spread of pathogenic microorganisms further intensified with time. Another important aspect of tsunami damage was the decrease in flood control capacity of the lagoon due to deposition of large quantity of sediments brought in by the sea water.

Based on the observed status of environmental damage caused to Karagan Lewaya and its surroundings by October 2005 an Action Plan was developed for its restoration. In line with this Action Plan, University of Moratuwa (UOM) with financial assistance from Sri Lanka Red Cross has already commenced investigations and designs for environmental restoration. In the investigation phase field data collection and laboratory analysis to identify areas to be dredged, debris to be removed, disposal sites and methods of disposal are being looked into. The field work comprised water, bed sediment and core sediment sampling, identification and classification of debris. A lagoon bed contour survey was strongly recommended and would be undertaken during a dry weather period. The water and sediment samples are presently being laboratory analyzed to determine relevant quality parameters.

In the classification of debris, internationally accepted classification systems for immobilized waste by United States Environmental Protection Agency (USEPA), Victoria Environmental Protection Agency (EPA), Australia are to be used. The disposal area will be identified with due consideration to surface and groundwater drainage pattern. It is envisaged that removal of contaminated soil layer would involve around 300,000 m³ of dredging. Rehabilitation of the sea outlet canal and outlet structure is also another activity pending implementation.

After substantial dredging and debris removal, monthly inspection of water and sediment quality will be carried out under the supervision of UOM and Central Environmental Authority (CEA) of Sri Lanka staff for a minimum period of 6 months. In the absence of Sri Lankan standards for ambient water and sediment quality environmental monitoring will be based on internationally acceptable ANZECC (2000) standards. The performance of landfills will also be monitored for a minimum period of 6 months with reference to groundwater contamination by leachate through sampling of observation wells. This will ensure that water and sediment quality of the lagoon approach acceptable standards and landfills perform as designed.

4.2 Kalametiya Lagoon

Following the tsunami catastrophe, clean-up operations of the lagoon and surrounding environment to a certain extent has been carried out with the initiation of Non Governmental Organizations (NGOs). A substantial volume of debris had been removed. The damage to outlet canal was restored through the participation of local community. The eroded sand bar separating the lagoon from the sea has already reformed. The sea-shore vegetation in the affected beach would also be able to recover naturally from the remaining vegetation, within 1-2 years. The aquatic birds (including natives and migrants) observed in the lagoons, and the butterfly fauna associated with the terrestrial habitats should recover within a short period of time.

Based on above assessment of the lagoon environment, the two main remaining activities to be implemented under the proposed restoration programme were identified as removal and disposal of remaining debris within the lagoon limits and environmental monitoring of the lagoon. The debris removal will be confined to the dry areas and those contained at the water line. The biodegradable matter shall be allowed to dry up and subsequently disposed or burned. The other material could be disposed in properly engineered landfills.

Following the rapid salinization due to tsunami, some destruction of mangrove stand and spread of invasive plants had been noticed. The continuous ingress of freshwater flows would help to restore pre-tsunami conditions. However, monitoring of lagoon environment should be continued for some time particularly in reference to spread of alien plant species, natural restoration of reduced bird population and fish species. The monitoring programme should also focus on the issues which previously led to degradation of the lagoon such as accumulation of agro-chemical influx threatening eutrophication of surface waters, unplanned and uncontrolled development and bird hunting.

4.3 Irrigation Systems in Pottuvil Region

Following the tsunami and subsequent flood damage, restoration efforts had been undertaken by certain NGOs. ARCADIS Euroconsult (AEC) has made a significant contribution towards restoration of irrigation schemes and agricultural lands (ARCADIS Euroconsult et al. 2005). In the initial phase AEC successfully conducted a programme for removal of beach sand from paddy fields. Emergency repairs were also affected to damaged access roads to Navalaru anicut schemes. However, the condition of these roads has once again worsened and proper repair works are still pending. Under the technical supervision of Irrigation Department (ID) staff, rehabilitation of Panama left bank (LB) channel is in progress.

The restoration programme proposed will basically involve civil engineering construction work to rehabilitate identified elements in four tsunami and flooding affected irrigation schemes in the Pottuvil region. The main elements of work in these schemes were identified based on a preliminary damage assessment conducted by the Irrigation Engineer (IE) Pottuvil division and observations made by the author during site visits. In the initial phase it is necessary to conduct a comprehensive damage assessment by the technical staff attached to IE Pottuvil division. This damage assessment will provide necessary information for detailed design of rehabilitation work. The Action Plan developed for this region is presently under review by UNEP for possible funding.

5. IMPLEMENTATION ARRANGEMENTS

The proposed restoration plans will be implemented at district level with funding channeled through District Secretaries to respective institutions directly involved in the execution of works. The CEA under the direction of a National Coordinator for Post Tsunami Environmental Rehabilitation will coordinate the work with active participation of their regional office staff.

6. CONCLUSIONS

The problems associated with internal water bodies and associated infrastructure impacted by tsunami could be identified through detailed assessment of present conditions ascertained mainly through field inspections. While certain issues can be expected to be rectified through natural restoration process with time, development of well formulated site specific Action Plans are essential pre-requisites for reinstatement of pre-tsunami conditions.

Acknowledgements:

The author wish to acknowledge Ministry of Environment and Natural Resources and Central Environmental Authority of Sri Lanka for the assistance rendered in collecting the necessary information for developing environmental restoration plans presented in this paper. The author's special thanks also extends to Irrigation Department staff of Pottuvil Division, Sri Lanka, staff members at University of Moratuwa who were in different ways connected with restoration work following the tsunami disaster and several community members in affected regions who provided invaluable information. The financial support made available by the Center for Urban Earthquake Engineering (CUEE) in Tokyo Institute of Technology for his participation in this international conference is very highly appreciated.

References:

- Hoffman, T.W., (1982), "Provisional Inventory of Wetlands in Sri Lanka," *Loris*, Vol. 16, pp 94-96.
- Central Environmental Authority, Sri Lanka and EuroConsult, Netherlands (1994), "Wetland Site Report – Karagan Lewaya".
- Central Environmental Authority, Sri Lanka and EuroConsult, Netherlands (1995), "Wetland Site Report & Conservation Management Plan – Kalametiya and Lunama Kalapuwa's,"..
- University of Moratuwa (2005), "Rapid Environmental Assessment on Post-Tsunami Brown Environment – Final Report," Prepared for Ministry of Environment and Natural Resources, Sri Lanka.
- ARCADIS Euroconsult in collaboration with Rebuild Sri Lanka Trust & Central Environmental Authority, Sri Lanka (2005) "Environmental Assessment for Post Tsunami Rehabilitation – Assisting the Planning Process at Arugum Bay, Sri Lanka".
- Bambaradeniya, M., Perera, M.S.J., Rodrigo R.K., Samarawickrema, V.A.M.P.K. and Asela, M.D.C., (2005), "Impacts of the Recent Tsunami on the Lunama-Kalametiya Wetland Sanctuary", IUCN-The World Conservation Union, Sri Lanka County Office.

REPORT OF TWO FIELD VISITS TO ASSESS TSUNAMI DAMAGE IN SRI LANKA DUE TO THE SUMATRA-ANDAMAN EARTHQUAKE OF DECEMBER 26, 2004

A. C. Wijeyewickrema¹⁾, S. Inoue²⁾, H. Matsumoto³⁾, H. Miura⁴⁾, P. Gunaratna⁵⁾,
M. Madurapperuma⁶⁾ and T. Sekiguchi⁷⁾

1) Associate Professor, Department of Civil Engineering, Tokyo Institute of Technology, Japan

2) Research Associate, Department of Built Environment, Tokyo Institute of Technology, Japan

3) Research Scientist, Japan Agency for Marine-Earth Science and Technology, Japan

4) Postdoctoral Research Fellow, Center for Urban Earthquake Engineering, Tokyo Institute of Technology, Japan

5) Senior Lecturer, Department of Civil Engineering, University of Moratuwa, Sri Lanka

6) Former Graduate Student, Department of Civil Engineering, University of Moratuwa, Sri Lanka,

Graduate Student, Department of Civil Engineering, Tokyo Institute of Technology, Japan

7) Graduate Student, Department of Architecture and Building Engineering, Tokyo Institute of Technology, Japan

anil@cv.titech.ac.jp, shusaku@enveng.titech.ac.jp, hmatsumoto@jamstec.go.jp, hmiura@enveng.titech.ac.jp,
priyantha@civil.mrt.ac.lk, makmm@cv.titech.ac.jp, tsekiguc@mail.arch.titech.ac.jp

Abstract: The December 26, 2004 Sumatra-Andaman earthquake that had a magnitude of 9.0 was one of the largest earthquakes in the world since 1900. The devastating tsunami that resulted from this earthquake caused more casualties than any previously reported tsunami. The number of fatalities and missing persons in the most seriously affected countries were Indonesia - 167,736, Sri Lanka - 35,322, India - 18,045 and Thailand - 8,212. This paper describes two field visits to assess tsunami damage in Sri Lanka by a combined team of Japanese and Sri Lankan researchers. The first field visit from Dec. 30, 2004 – Jan. 04, 2005 covered the west, SW and south Sri Lanka and included the cities of Moratuwa, Beruwala, Bentota, Peraliya, Hikkaduwa, Galle, Thalpe, Matara, Tangalla and Hambantota. The objectives of the first field visit were to investigate the damage caused by the tsunami and to obtain eyewitness information about wave arrival times. The second field visit from March 10-18, 2005 covered the NE, east, SE and south Sri Lanka and included Trincomalee, Batticaloa, Arugam Bay, Yala National Park and Kirinda. The objectives of the second visit were mainly to obtain eyewitness information about inundation data and also to take relevant measurements using GPS instruments.

1. INTRODUCTION

The essential details of the Sumatra-Andaman earthquake are as follows: Magnitude: 9.0; Time: December 26, 2004 at 00:58:53 (Coordinated Universal Time); Local time at epicenter: December 26, 2004 at 7:58:53 AM; Location: 3.3°N 9.9°E; Depth: 33 km; Region: off the West coast of Northern Sumatra (USGS, 2004). Previous large earthquakes since 1900 with magnitudes ≥ 9.0 are, the 1960 Great Chilean earthquake (magnitude 9.5), the 1964 Prince William Sound, Alaska earthquake (9.2) and the 1952 Kamchatka earthquake (9.0), (USGS, 2006). The tsunami generated by the Sumatra-Andaman earthquake resulted in more casualties than any previous tsunami. Due to the earthquake and tsunami 167,736 people lost their lives or were reported missing in Indonesia. The other countries that reported a large number of fatalities or missing persons due to the tsunami were Sri Lanka – 35,322, India – 18,045 and Thailand – 8,212 (Appendix A). The location of the epicenter and surrounding countries are shown in Figure 1.

Northeast Indian Ocean Region Tectonic Setting

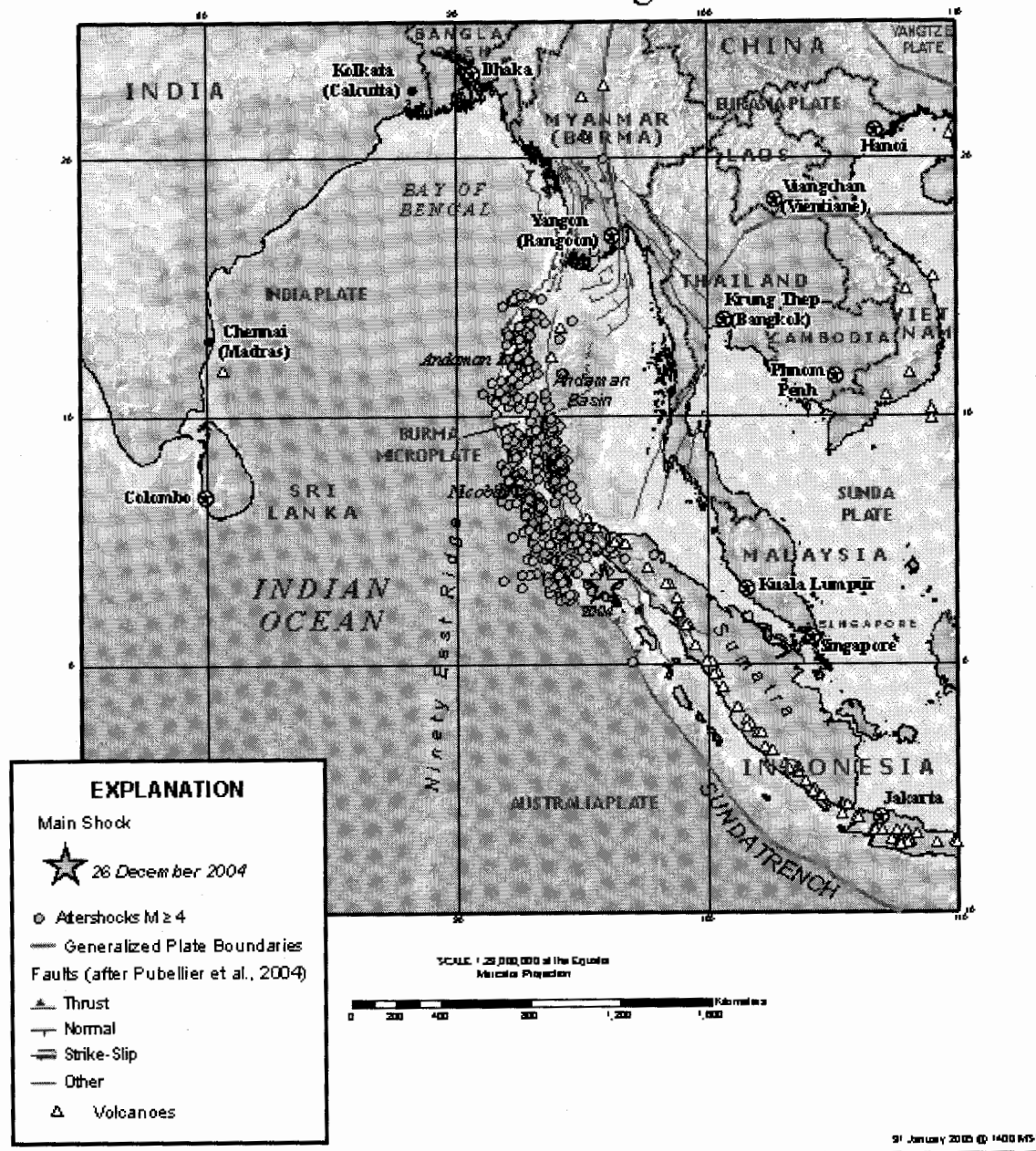


Figure 1. Epicenter of Sumatra-Andaman earthquake and surrounding countries (USGS, 2004).

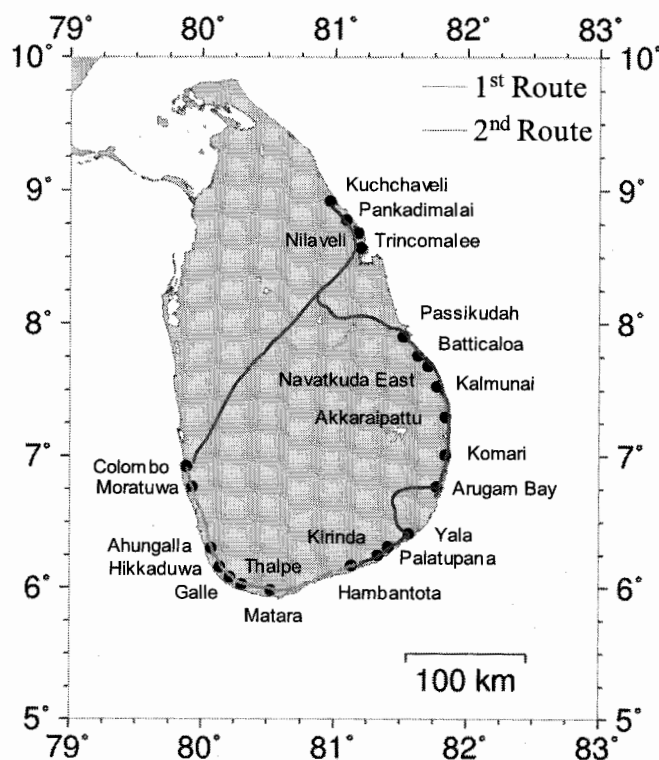


Figure 2. Field visit routes. 1st Route: Colombo, Moratuwa, Beruwala, Bentota, Peraliya, Hikkaduwa, Galle, Thalpe, Matara, Tangalla and Hambantota. 2nd Route: Colombo, Trincomalee, Kuchchaveli, Trincomalee, Polonnaruwa, Batticaloa, Arugam Bay, Yala National Park and Kirinda.

2. FIELD VISIT ROUTES AND TEAM MEMBERS

On the first field visit Anil C. Wijeyewickrema (ACW), Shusaku Inoue (SI) and Toru Sekiguchi (TS) arrived in Sri Lanka at 0020 on Dec. 30, 2004. The areas that were badly affected by the tsunami were the SW, S, SE, E and NE parts of Sri Lanka. Immediately after the tsunami, some sections of the main highway from Colombo to the South had been closed because of damage caused to the highway. But by Dec. 30 most sections of this highway were open. Priyantha Gunaratna (PG) and Manoj Madurapperuma (MM) joined the field survey. Due to inadequate information about the availability of food and drinking water in the tsunami-affected areas, all necessary supplies were purchased in Colombo and taken in the van.

The field visit commenced on Dec. 31 by going south along the main Colombo-Hambantota highway. The field visit route is shown in Figure 2. A section of the highway close to Peraliya where a train was swept off the train tracks by the tsunami was closed. A detour had to be made to arrive in Hikkaduwa, and then go north to Peraliya to inspect the train wreckage. On Dec. 31 night the team stayed at the faculty guesthouse of the University of Ruhuna which is located in Hapugala, East of Galle town. The next day the field visit continued from Galle up to Hambantota where the field visit ended, since the highway goes away from the coast at Hambantota. The van and the members of the field visit are shown in Figure 3(a). ACW, SI and TS left Sri Lanka at 0135 on Jan. 05, 2005.

On the second field visit ACW, SI, Hiroyuki Matsumoto (HM1) and Hiroyuki Miura (HM2) arrived in Sri Lanka at 2320 on March 10, 2005. PG and MM also joined the second field visit. The team shown in Figure 3(b) left Colombo on Mar. 11 and arrived late in the evening in Trincomalee and stayed the night at the National Aquatic Resources Research and Development

Agency (NARA) circuit bungalow in Trincomalee. The second field visit route is also shown in Figure 2. The team inspected Nilaweli, Kuchchaveli and Trincomalee on Mar. 12 and left Trincomalee for Polonnaruwa in the evening and stayed the night at the Hotel Sudu Araliya, Polonnaruwa. On Mar. 13 the team left for Batticaloa, inspected Pasikudah on the way, surveyed Batticaloa in the afternoon and stayed the night at Focus Rest and Banquet Hall, Batticaloa. The team left Batticaloa on Mar. 14 and inspected Kalmunai, Akkaraipattu and Komari on the way to Pottuvil and stayed the night at Hiltan Hotel, Arugam Bay, Pottuvil. On Mar. 15 the team left Arugam Bay for Tissamaharama via Monaragala, inspected Palatupana in the evening and stayed the night at Lake Side Tourist Inn, Tissamaharama. The team inspected Yala, Palatupana (again) and Kirinda on Mar. 16 and left Tissamaharama in the afternoon for Koggala and stayed the night at Koggala Beach Hotel, Koggala. On Mar. 17 the team proceeded to Colombo and stopped on the way to inspect Triton Hotel, Ahungalla. An account of the tsunami witnessed by a Triton Hotel guest is reported in Chapman (2004). ACW, SI, HM1 and HM2 left Sri Lanka at 2359 on March 18, 2005.



(a)



(b)

Figure 3. Field visit team members: (a) (from L to R) Rohana (driver), Manoj Madurapperuma, Shusaku Inoue, Priyantha Gunaratna and Anil C. Wijeyewickrema. In the inset is Toru Sekiguchi. (b) (from L to R) Priyantha Gunaratna, Anil C. Wijeyewickrema, Hiroyuki Miura, Manoj Madurapperuma, Shusaku Inoue and Hiroyuki Matsumoto.

3. SUMMARY OF THE TSUNAMI DAMAGE

The damage due to the tsunami observed on the first field trip is shown in Figs. 4-9. On the first field trip to the west, SW and south, it was observed that in general, the damage caused by the tsunami was most severe in regions between Galle and Hambantota and extended several hundred meters from the coast. However it was noted that the damage caused was not uniform with some areas having only, minor damage. Most of the houses that were damaged were masonry houses. But in some instances the more recently constructed houses seemed to have sustained less damage. Damage to houses have been mainly due to the tsunami wave pressure but some houses have been damaged due to boats, trees and vehicles that were swept away by the tsunami.

The Colombo-Matara rail tracks run mostly along the coast. Damage to the train tracks was observed in many places. The only train that was swept away was stopped between stations near Peraliya when the tsunami struck, and around 1,000 people are estimated to have lost their lives due to this incident (see Figure 6).

The damage observed on the second field trip is shown in Figs. 10-14.

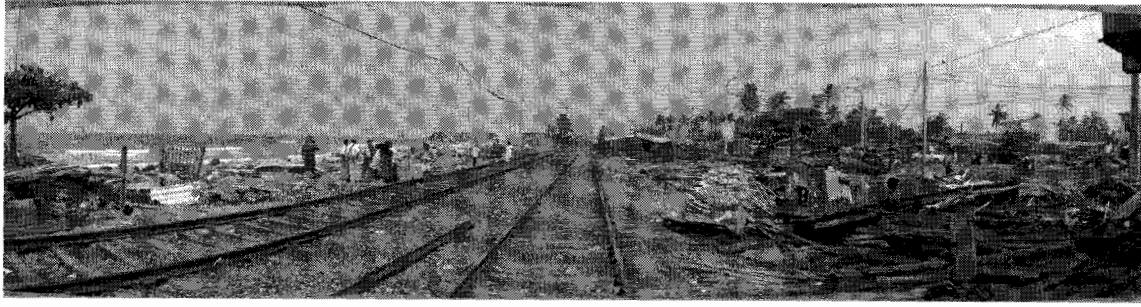


Figure 4. South Moratuwa: Tsunami came from the left, houses on both sides of the rail tracks were destroyed.



Figure 5. Hikkaduwa: Boat was swept into the hotel, outside wall of the hotel was broken, but the hotel was not destroyed.



Figure 6. Peraliya: Though this area is about 200 m from the coast, an express train was washed away by the tsunami and about 1,000 people lost their lives.



Figure 7. Talpe: An inland area away from the sea. The overturned lorry on the left was swept away from the right, where another lorry can be seen.

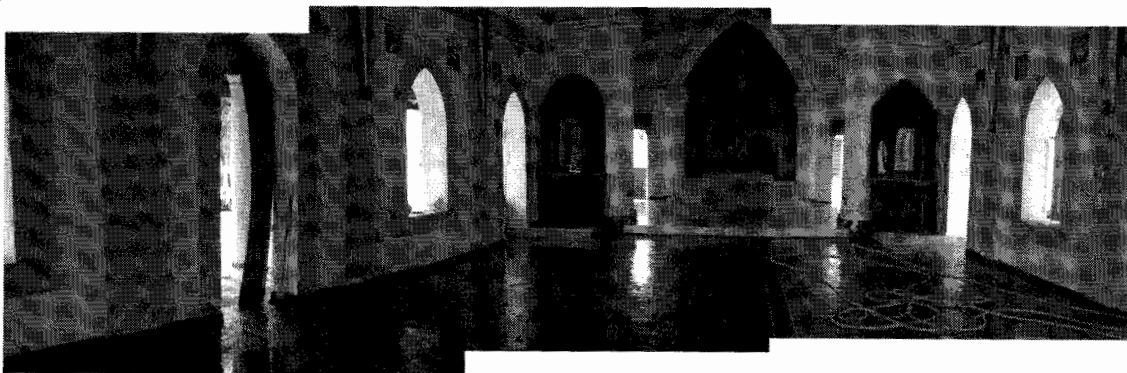


Figure 8. Matara: (Top) Inside of St. Mary's church which is located near the coast, the water level reached up to the feet of the crucifix. (Bottom) Coastal area outside the church, the bottom of the island was shaved by the tsunami.



Figure 9. Hambantota: Masonry houses located within a few hundred meters from the coast were completely destroyed, a few more recently constructed houses had less damage.

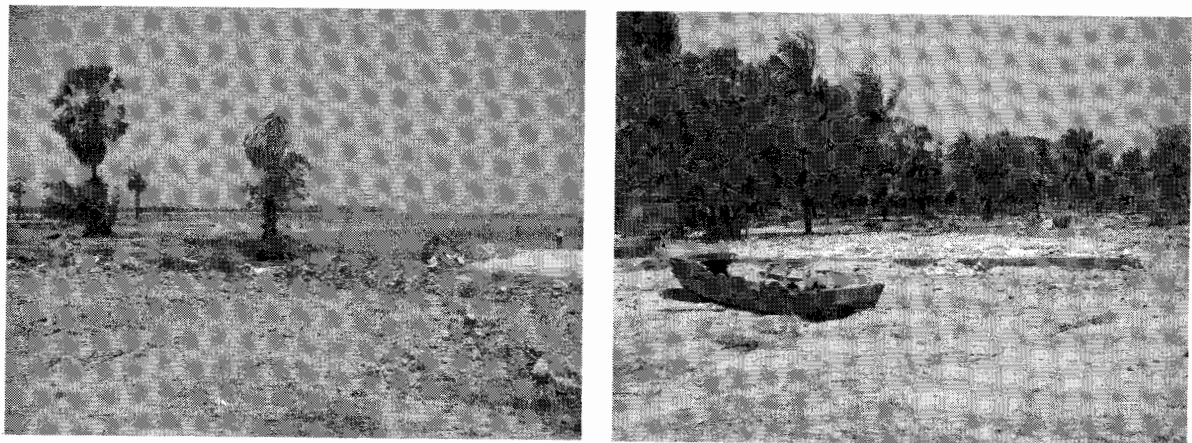


Figure 10. Passikudah: Many people on the east coast lost their lives due to the tsunami.

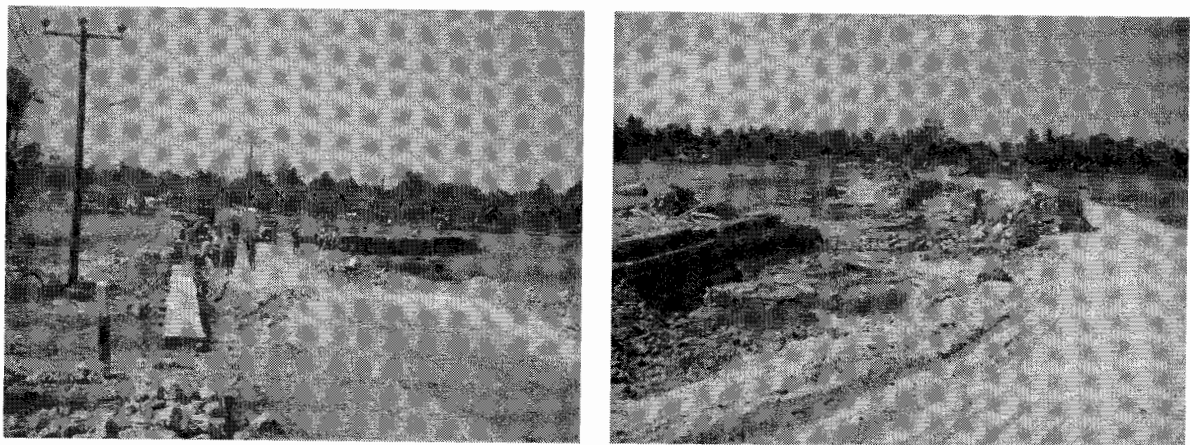


Figure11. Batticaloa: The tsunami swept into the Batticaloa lagoon from the right.

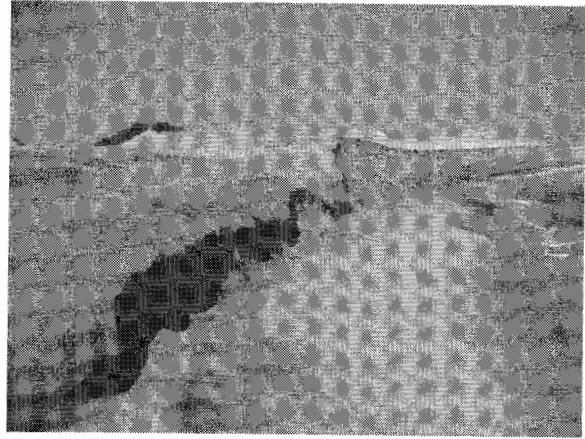
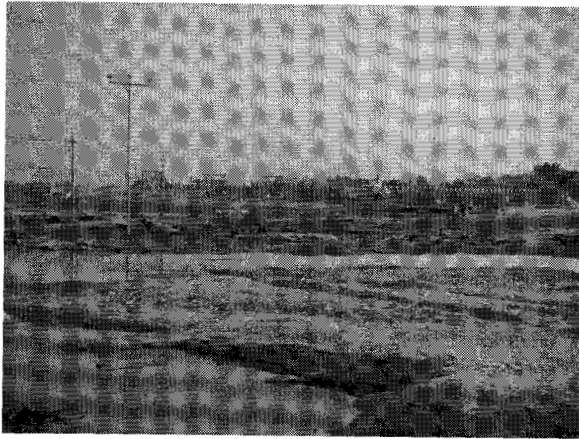


Figure 12. (a) Arugam Bay south of Pottuvil: Bridge on the right was damaged. (b) Palatupana: Natural sand dune formations protected the interior.

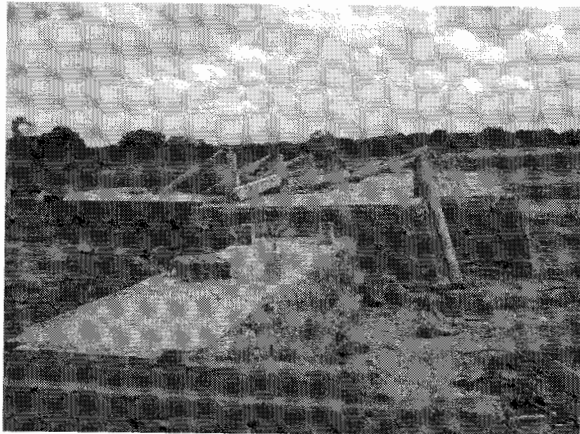


Figure 13. Yala National Park: Many tourists lost their lives at this location.



Figure 14. Yala Safari Hotel in Palatupana: This tourist hotel was completely destroyed.

4. CONCLUDING REMARKS

One of the main objectives of the first field survey was to interview people who had witnessed the tsunami and record their observations before they forget details such as arrival times. The arrival times obtained from this field trip are given in Inoue (2006). The eyewitness accounts of arrival times are not necessarily accurate as some witnesses did not have watches and some witnesses did not see all the waves. It is most likely that there were one or two waves before the biggest wave. Each wave period was about 30 minutes. Before the biggest wave arrived the water receded for several hundred meters in some locations and the wave height of the biggest wave is estimated to have been 5-6 meters. More details of the first field visit are given in Wijeyewickrema et al (2005).

The main objectives of the second visit were to obtain eyewitness information about inundation data and also to take relevant measurements using GPS instruments. A detailed report of the tsunami inundation area in the Batticaloa region is given in Miura (2006).

The team from Tokyo Institute of Technology that arrived in Sri Lanka in Dec. was the first international team of scientists to visit Sri Lanka to gather data about the effects of the tsunami. Other international scientific teams that arrived afterwards were from the USA led by Prof. Philip Liu (Cornell University) and Prof. Harindra Fernando (Arizona State University) and from Japan led by Prof. Yoshiaki Kawata (Kyoto University) and Prof. Fumihiko Imamura (Tohoku University).

Acknowledgements:

The advice and support of Prof. Tatsuo Ohmachi, COE Program Leader of CUEE and Prof. Kohji Tokimatsu, COE Program Sub-Leader of CUEE, is gratefully acknowledged. Financial support for the tsunami field surveys in Sri Lanka from the Center for Urban Earthquake Engineering (CUEE), Tokyo Institute of Technology, is gratefully acknowledged. SI and HMI are pleased to acknowledge financial support for the second field visit, from the Special Coordination Funds for Promoting Science and Technology from the Ministry of Education, Sports, Culture, Science and Technology (MEXT).

References:

- Chapman, C. (2004), "The Asian Tsunami in Sri Lanka: A Personal Experience", EOS, Vol. 86, No. 2, 13-14.
- Inoue, S., (2006), "Tsunami Arrival Time in Sri Lanka Due to the 2004 Sumatra Earthquake ", *Proceedings of the Third International Conference on Urban Earthquake Engineering*, March 6-7, Tokyo, Japan.
- Miura, M., (2006), "Extraction of Tsunami Inundation Area in the Eastern Part of Sri Lanka Due to the 2004 Sumatra Earthquake Using High-Resolution Satellite Images", *Proceedings of the Third International Conference on Urban Earthquake Engineering*, March 6-7, Tokyo, Japan.
- UN Office of the Special Envoy for Tsunami Recovery (2006),
<<http://www.tsunamispecialenvoy.org/country/humantoll.asp>>
- USGS (2004), "Magnitude 9.0 - SUMATRA-ANDAMAN ISLANDS EARTHQUAKE",
<<http://earthquake.usgs.gov/eqinthenews/2004/usslav/>>
- USGS (2006), "Largest Earthquakes in the World Since 1900",
<http://earthquake.usgs.gov/regional/world/10_largest_world.php>
- Wijeyewickrema, A. C., Inoue, S. and Sekiguchi, T., (2005), "Tsunami Damage in Sri Lanka Due to the Sumatra Earthquake of December 26, 2004 – Preliminary Reconnaissance", *Proceedings of the Second International Conference on Urban Earthquake Engineering*, March 7-8, Tokyo, Japan, pp. 181-191.

Appendix A: Fatalities and missing persons due to the Sumatra-Andaman earthquake

Country	Fatalities	Missing ¹	Total
Indonesia	130,736	37,000	167,736
Sri Lanka	35,322	-	35,322
India	12,405	5,640	18,045
Thailand ²	8,212	-	8,212
Somalia	78	211	289
Maldives	82	26	108
Malaysia	69	6	75
Myanmar	61	-	61
Tanzania	13	-	13
Seychelles	2	-	2
Bangladesh	2	-	2
Kenya	1	-	1
Total	186,983	42,883	229,866

(UN Office of the Special Envoy for Tsunami Recovery, 2006)

1. Some countries have not disaggregated between the deceased and the missing.
2. In Thailand, fatalities include 2,448 foreign tourists from 37 other countries.

TSUNAMI ARRIVAL TIME IN SRI LANKA DUE TO THE 2004 SUMATRA EARTHQUAKE

S. Inoue¹⁾, A. C. Wijeyewickrema²⁾, H. Matsumoto³⁾, H. Miura⁴⁾,
P. Gunaratna⁵⁾, M. Madurapperuma⁶⁾ and T. Sekiguchi⁷⁾

1) Research Associate, Department of Built Environment, Tokyo Institute of Technology, Japan

2) Associate Professor, Department of Civil Engineering, Tokyo Institute of Technology, Japan

3) Research Scientist, Japan Agency for Marine-Earth Science and Technology, Japan

4) Post-Doctoral Researcher, Department of Built Environment, Tokyo Institute of Technology, Japan

5) Senior Lecturer, Department of Civil Engineering, University of Moratuwa, Sri Lanka

6) Former Graduate Student, Department of Civil Engineering, University of Moratuwa, Sri Lanka,

Graduate Student, Department of Civil Engineering, Tokyo Institute of Technology, Japan

7) Graduate Student, Department of Architecture and Building Engineering, Tokyo Institute of Technology, Japan

anil@cv.titech.ac.jp, shusaku@enveng.titech.ac.jp, hmatsumoto@jamstec.go.jp, hmiura@enveng.titech.ac.jp,

priyantha@civil.mrt.ac.lk, makmm@cv.titech.ac.jp, tsekiguc@mail.arch.titech.ac.jp

Abstract: The Indian tsunami caused by the Sumatra-Andaman Islands earthquake of 26 December 2004 severely affected Sri Lanka, approximately 1500 km far west from the tsunami source. The post tsunami surveys in Sri Lanka by a combined team of Japanese and Sri Lankan researchers were carried out twice. The main objective of the surveys is to obtain eyewitness information, in particular tsunami arrival time. Many other survey teams have completed with respect to the tsunami height measurements, therefore the survey of tsunami arrival times is needed in order to understand the tsunami quantitatively. We estimated the tsunami arrival time in Sri Lanka from eyewitness accounts.

1. INTRODUCTION

The Sumatra offshore earthquake, which was the fourth largest earthquake in the world since 1900, occurred on December 26, 2004. The tsunami generated by the earthquake attacked many countries around the Indian Ocean, especially Bay of Bengal, and the damage due to the tsunami and the earthquake was severe. More than 230,000 people lost their lives.

Soon after the earthquake occurrence, we decided to conduct the field investigation in Sri Lanka which is the most damaged country next to Indonesia, although it is located about 1,500 km away from the epicenter (Fig. 1).

The field surveys were conducted twice. In the first we investigated Western and Southern coast of Sri Lanka from Dec. 29, 2004 to Jan. 5, 2005, and Northeast to Southeast part from Mar. 10 to 18, 2005 in the second trip (Fig. 2). Team members are as follows: Mr. Toru Sekiguchi from Tokyo Institute of Technology in Japan, and Dr. Priyantha Gunaratna, Mr. Manoj Madurapperuma from University of Moratuwa in Sri Lanka, and authors (Fig. 3). Mr. Sekiguchi joined the first trip and Dr. Miura and Dr. Matsumoto joined the second trip.

We gathered eyewitness accounts, tide gage data, wave height and inundation area in this field survey and in this paper we report the results of tsunami arrival time.

2. TSUNAMI ARRIVAL TIME IN SRI LANKA ESTIMATED FROM EYEWITNESS ACCOUNTS

Once huge tsunami occurred, several kinds of simulation are performed in late years. Researchers who perform it usually compare their simulation results with the wave heights and the arrival times recorded in tidal observation stations. However we did not have enough stations in Sri Lanka, which has sole station in Colombo, to obtain the demanded data along the coast with reasonable resolution. In this case we have no choice except for using the data acquired from field survey. Fortunately we could conduct our survey soon after tsunami occurrence and we hence focused on recording their experiences to grasp the arrival time before they forget its details. Though other research groups conducted field surveys, the information of the arrival time is less compared with that of the tsunami height. Tsunami consists of various waves and the maximum wave is only one of the waves. To comprehend tsunami phenomena, it is inadequate to understand only the maximum wave and it is also important to understand the other waves. In this section we discuss the tsunami arrival time in Sri Lanka estimated from their accounts and sole tidal observation station in Colombo.

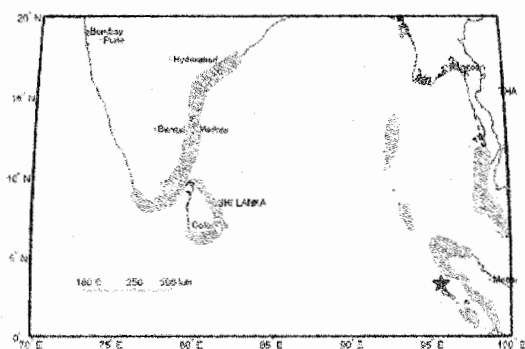


Figure 1 Epicenter of Sumatra earthquake and surrounding countries. Red shadowed portions are tsunami affected areas.

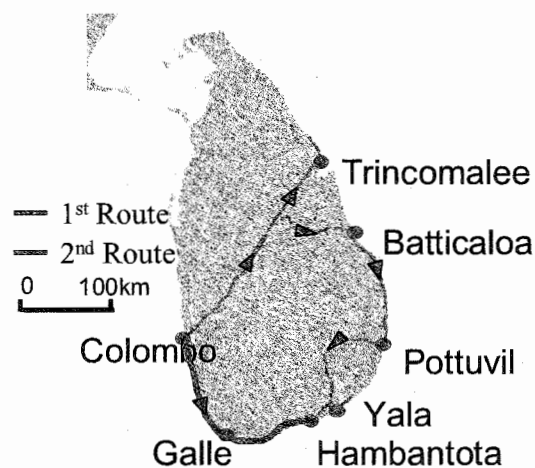


Figure 2 Field visit routes



Figure 3 Team members. Upper Left: 1st Trip. Lower Right: 2nd Trip.

We obtained many eyewitness accounts along the Sri Lankan coast from the tsunami survivors. When we interviewed them, I ask them to tell their own experience. The following accounts are examples obtained at Bentota and Seenigama.

An account we interviewed at Bentota was “A first wave began to come up at 9:55 and was inundated about 30m. The first wave came with about 4 times breaking water. After that, the wave went back to offshore about 500m at 10:00. The second wave came up at 10:30, and attacked the shore with breaking water and bad smell. The wave height was about 3m. The third wave came up at 11:30 which was the biggest wave. The third one broke the top of this roof (Fig. 4), and was inundated up to



Figure 4 We interviewed a local man in Benota. He said that the maximum wave attacked the top of this roof.

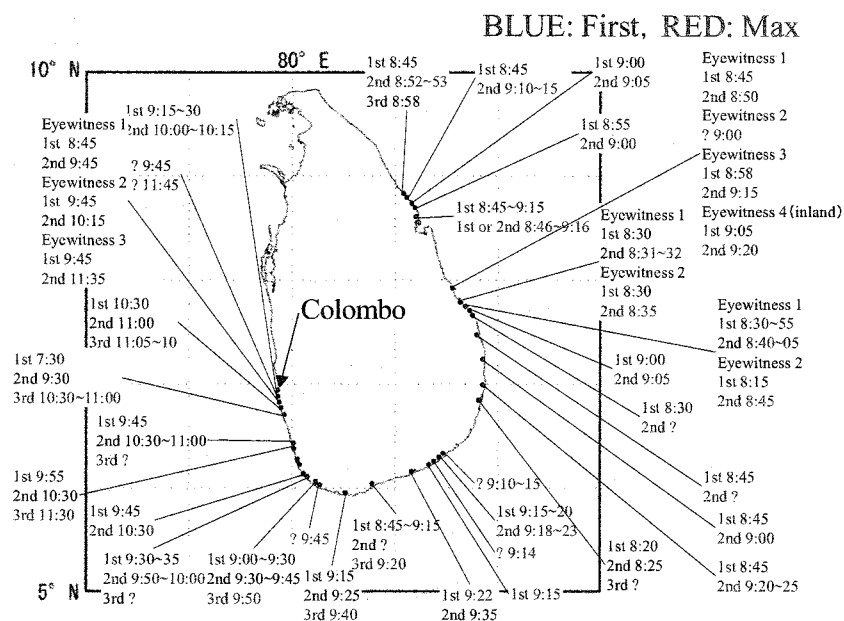


Figure 5 Tsunami arrival time obtained by eyewitness accounts. Blue letters show the first waves and red letters shows maximum waves.

national road. Its height was about 5m.”

From this eyewitness account, we estimated that the arrival time of the first wave was 9:55, the second one was 10:30 and third one was 11:30, and the third wave was maximum one in this area.

b) An account at Seenigama

An account at Seenigama was also “The first wave arrived at 9:45, and the train was derailed. The second wave, which was the biggest one, came at 10:30, and washed the train away.”

From the above account, we estimated that the arrival time of the first wave was 9:45 and the second one was 10:30, and the second wave was maximum one. In the same way, we estimated the

Tidal record in Colombo

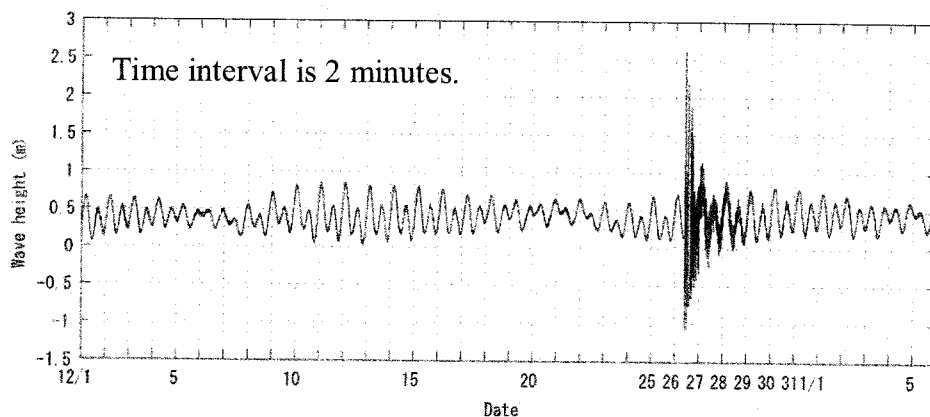


Figure 6 This record shows the water height in Colombo from Dec. 1 to Jan. 6.

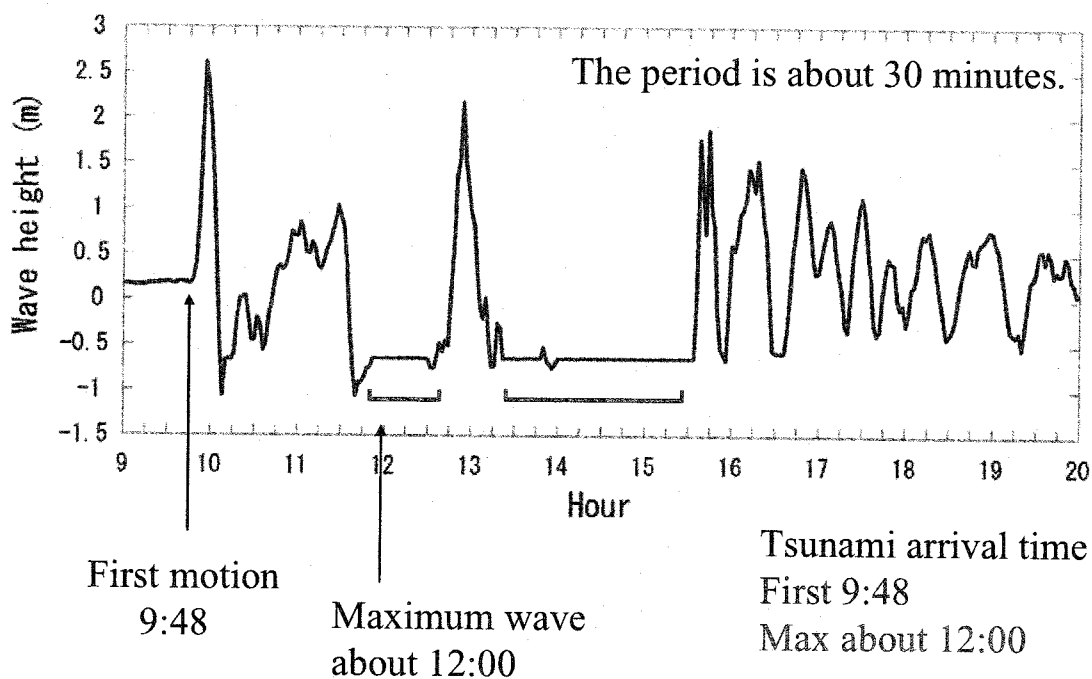


Figure 7 Tsunami record on Dec. 26 of the tidal record.

arrival time of each area from the eyewitness accounts of the local people (Fig. 5). Most likely there were one or two waves before the maximum one. Each wave period at the western coast was more

than 30 min and those at eastern coast was less than 30 min. Before the biggest wave, the sea retreated for several hundred meters in some locations. Though we showed the tsunami arrival time distribution in figure 5, the times in this map vary wildly even in the same area. We thought these reason as follows:

I. Some of them did not have their watches and depended on their sense of time.

All who we interviewed did not necessarily have their own watch when they experienced the tsunami. Some of them answered the arrival time by their feeling such as the second wave arrived about 5 minutes later from the first one.

II. They did not see all waves.

It is expected they did not see all waves. Some of them did not see the maximum wave because they escaped before and some of them did not see the first wave because they were not near the sea at that time. For that reason, the first wave or maximum wave of the eyewitness do not necessarily correspond to actual ones.

2.2 The Arrival time of first wave and maximum wave

To reduce the variety of the arrival time estimated from the eyewitness accounts, we removed strange data which is quite different from reliable data. Fortunately we have three more reliable data which are a tidal record of the sole tidal observation station in Colombo, a broken clock at the bus station in Hambantota and eyewitness accounts by Dr. Chapman (2005) who was in Sri Lanka.

Figure 6 shows the tidal record in Colombo on December 2004. Unusual wave height started on Dec. 26 is the tsunami and the sea water disturbance continued till Dec. 29. The record on Dec. 26 is enlarged in Fig. 7. The initial motion of the first wave is found clearly, and its time is 9:48. We can see lack of record in two parts. If the wave height at that time is less than that of first wave which is recorded perfectly, this instrument must record its wave height. We assumed that the maximum wave arrived at about 12:00.

In Hambantota, we could find the clock which was broken by the tsunami. It indicated 9:22 and the time corresponded to the arrival time of the maximum wave estimated from the accounts of a local man. According to his account, the first wave was the biggest wave among the waves attacked this harbor and the second wave was at 9:35.

The arrival time estimated from the account of Dr. Chapman is that the first wave arrived at 9:30, second one, which is the biggest, at 10:10 and third one at 11:10. We added these reliable data into the arrival time distribution map (Fig. 8).

Figure 9 shows the arrival time of the first and maximum waves. We removed strange data from Fig. 8 and compiled the figure. Wave front of the first wave offshore might be directed to NNW-SSE. Though the first tsunami arrival time varies in 10 to 15 min at near locations, the first wave arrived at the southern and the eastern coast at 8:30 to 8:45, and it arrived at the south and the western coast at 9:30 to 9:45. On the other hand, the maximum wave arrived at the western coast at 10:00 to 12:00 and the propagation velocity of the maximum one at the western coast is slower than that of the first wave. It is expected that tsunami wave were dispersed when the wave propagate along the coast.

3. CONCLUSIONS

After compiling two surveys, we could obtain some data of tsunami arrival times at the whole coast in Sri Lanka. The first wave arrived at 08:30 to 08:45 at the east coast, followed by the largest wave at 08:50 to 09:15. At most area at the east coast, the second wave was the largest. At the west coasts, on the other hand, the first wave arrived at 09:30 to 09:45, and the largest wave arrived at 10:00 to 12:00, that were the second or the third wave. Thus eyewitness accounts indicated that there were one or two waves before the arrival of the largest tsunami.

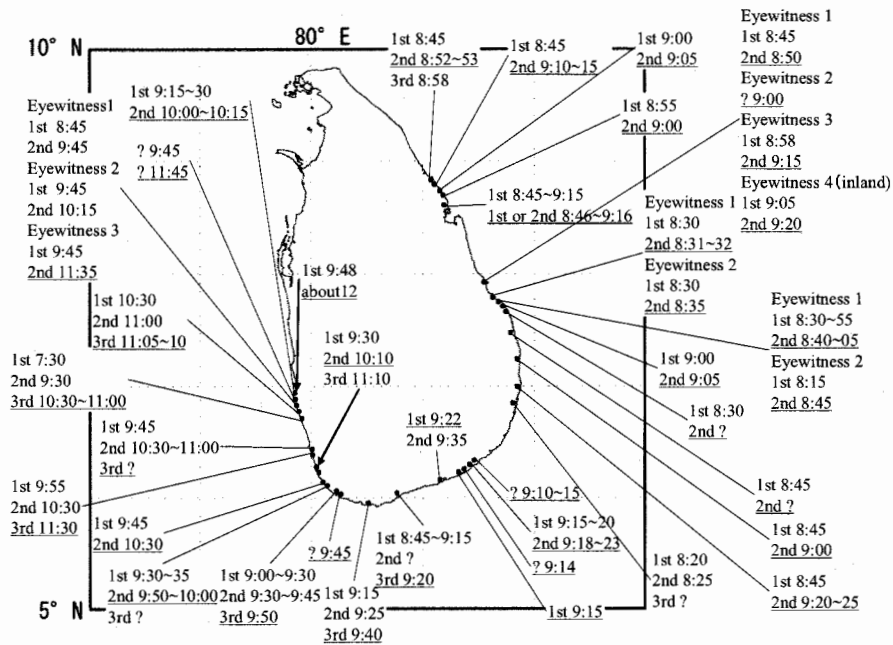
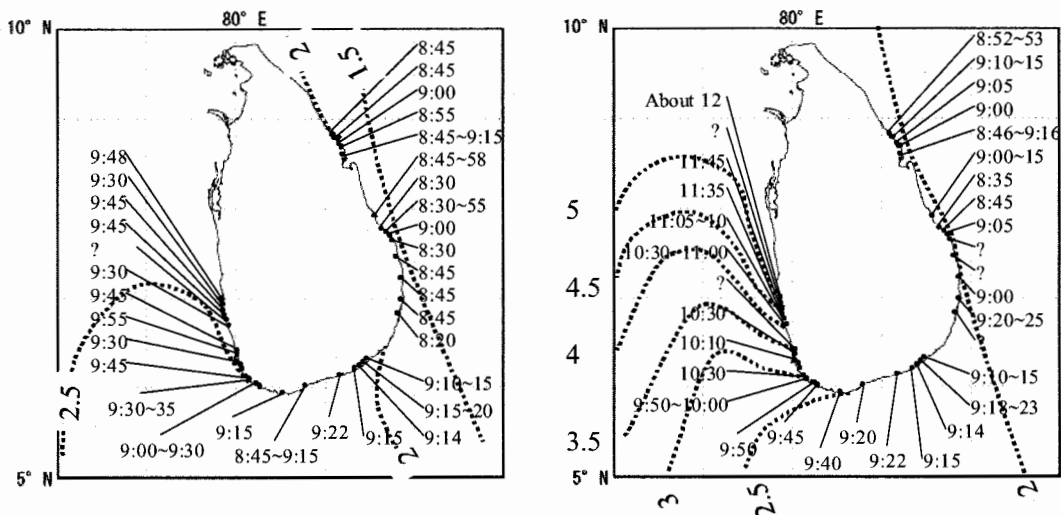


Figure 8 Tsunami arrival time distribution including more reliable data. Reliable data are written inside of Sri Lanka.



Arrival time of the first wave

Arrival time of the maximum wave.

Figure 9 Left figure: Arrival time of the first wave. Right figure: Arrival time of the maximum wave. Dotted lines are assumed wave fronts and numbers mean hours after the tsunami occurrence.

Acknowledgements:

Tide gauge data recorded at Colombo was provided by the National Aquatic Resources Research and Development Agency. This study was supported by both the 21st-century COE program and the Special Coordination Funds for Promoting Science and Technology, by Ministry of Education, Sports, Culture, Science and Technology.

References:

Chapman, C., The Asian tsunami in Sri Lanka: a personal experience, EOS trans., 86 (2), 13-14, 2005.

EXTRACTION OF TSUNAMI INUNDATION AREA IN THE EASTERN PART OF SRI LANKA DUE TO THE 2004 SUMATRA EARTHQUAKE USING HIGH-RESOLUTION SATELLITE IMAGES

H. Miura¹⁾ and S. Midorikawa²⁾

1) Post-Doctoral Research Fellow, Center for Urban Earthquake Engineering, Tokyo Institute of Technology, Japan

2) Professor, Center for Urban Earthquake Engineering, Tokyo Institute of Technology, Japan

hmiura@enveng.titech.ac.jp, smidorik@enveng.titech.ac.jp

Abstract: In order for efficient post disaster management, it is important to develop a methodology to capture affected areas from remote sensing data. Inundation of the tsunami generated by the 2004 Sumatra earthquake caused severe damage in coastal areas in Sri Lanka, located 1,500km away from the epicenter. A method for extraction of tsunami inundation area using high-resolution satellite images is examined in this study. Normalized difference vegetation index (NDVI) computed from the pre- and post-event satellite images is utilized since the vegetation in the affected area was remarkably decreased due to inundation of the tsunami. The ratio of the pixels whose NDVI is decreased after the event within a mesh area (20m x 20m) is examined. The average of the ratio in the inundated area shows 80% or more while that in the non-inundated area shows about 50-60%. The meshes whose ratios show more than 80% are extracted as inundation area. The result of the extraction seems to be similar with the actual inundation area by the field survey.

1. INTRODUCTION

In order for efficient relief activities and early-stage rehabilitation planning after large-scaled disaster, it is important to capture damage distribution immediately after the disaster. In tsunami disaster, grasp of area affected by inundation is necessary for the post damage assessment. Remote sensing data, especially high-resolution satellite image, would be useful to evaluate the inundation area since the data can capture the detailed land surface of vast areas. Recently, change detection techniques using satellite images have been proposed to comprehend damaged areas in disasters (e.g., Matsuoka and Yamazaki, 2004 and Kohiyama *et al.*, 2004).

The 2004 Sumatra earthquake caused catastrophic tsunami damage to the countries in the Indian Ocean. In Sri Lanka, located 1,500km away from the epicenter, the severe damage is observed at the coastal area. The number of deaths and damaged buildings due to the tsunami are more than 30,000 and 100,000, respectively (World Health Organization, 2005). After the disaster, many researchers have demonstrated the detection of the affected area from satellite images (e.g., Ramakrishnan *et al.*, 2005). However, techniques to evaluate inundation area using high-resolution satellite images have not been established because characteristics of images in actually affected area have not been examined in detail. In this study, a method for extraction of inundation area is examined using pre- and post-event high-resolution satellite images in Batticaloa, located in the eastern coastal area of Sri Lanka. The applicability of the method is discussed by comparing with the actual inundation area by field survey.

2. IKONOS IMAGES IN BATTICALOA, SRI LANKA

Figure 1(a) shows locations of Batticaloa and other major coastal cities in Sri Lanka. High-resolution satellite IKONOS image observed in Batticaloa one month after the earthquake as shown in Fig. 1(b). The spatial resolution of the image is 1m. The hatched areas in Fig. 1(b) indicate the built-up areas in the topographic map edited in 1985. The characteristics of the images are shown in Table 1. The pre-event images observed in 2000 and 2001 are employed in this study.

Close-up of the images in the severely damaged area is shown in Fig. 2. Figure 2(a-1) and (a-2) show the original images while Fig. 2(b-1) and (b-2) show distribution of NDVI (Normalized Difference Vegetation Index), which is defined as the difference in a pixel between the near infrared band image and the red band image divided by their sum. NDVI is related to the amount of biomass within a pixel and yields a number from -1 to $+1$ (Tucker, 1979). A higher NDVI indicates a higher density of green leaves. NDVI has been utilized as one of useful indices for change detection of land surface from remote sensing data (Singh, 1989 and Lu *et al.*, 2004). As shown in Fig. 2, NDVI is remarkably decreased in the post-event image because not only the buildings but also the vegetations are washed away or blighted due to the inundation of the tsunami. This suggests that the satellite images have the potential to extract tsunami inundation area by using the difference of NDVI observed before and after tsunami disaster.

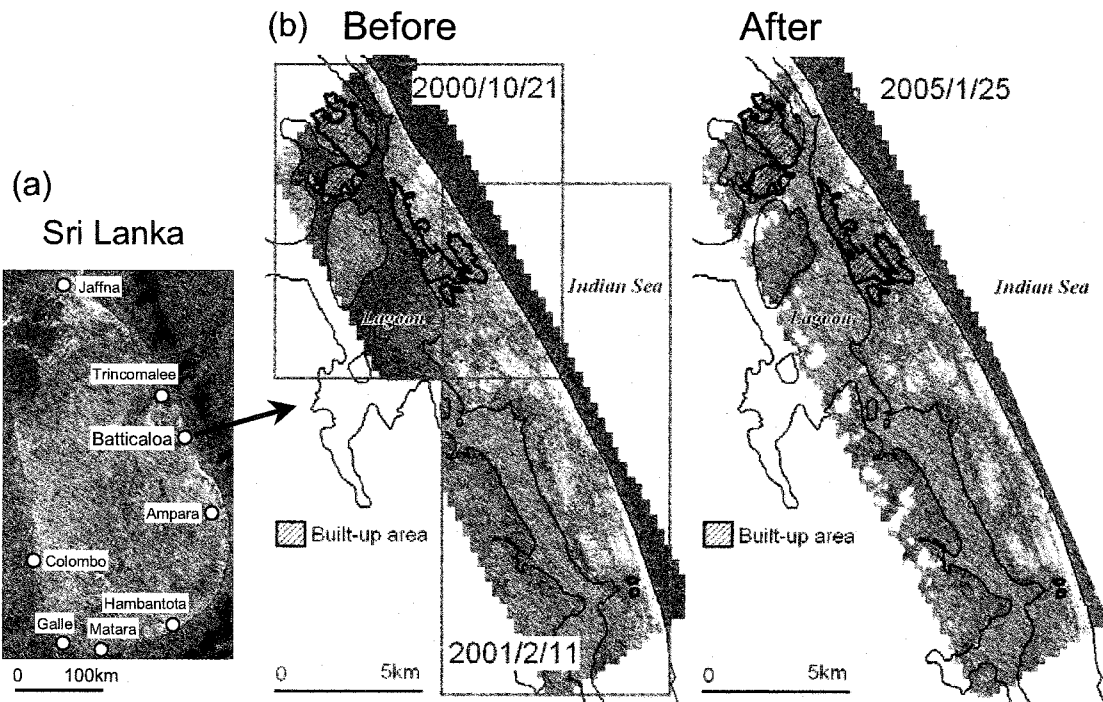


Figure 1 (a) Map of Sri Lanka, (b) IKONOS satellite images in Batticaloa.

Table 1 Characteristics of IKONOS images used in this study.

	Before		After
Date	21 Oct. 2000	11 Feb. 2001	25 Jan. 2005
Area size	67km ²	83km ²	125km ²
Spatial resolution	1m	1m	1m
Type of image	Pan-sharpen	Pan-sharpen	Pan-sharpen

Pan-sharpen : Blue, Green, Red, and Near infrared(NIR) band image

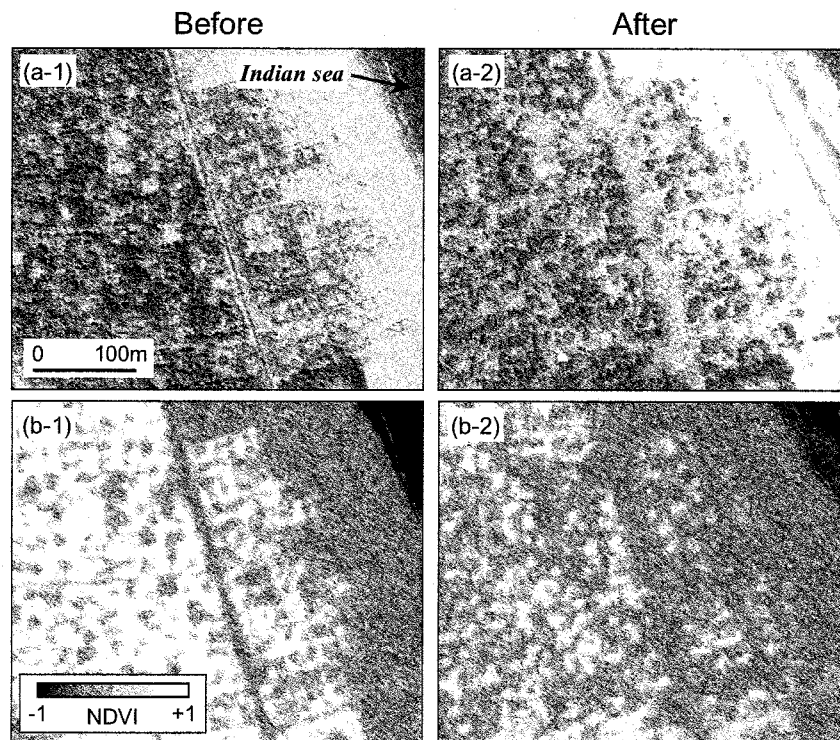


Figure 2 (a) Comparison of original image, (b) Comparison of NDVI image

3. EXTRACTION OF INUNDATION AREA FROM SATELLITE IMAGES

Figure 3 shows the flowchart of the analysis to extract the inundation area. After NDVI is computed from the satellite images observed before and after the disaster, the difference of NDVI in each pixel ($=D$) is calculated from these images. In order to avoid the change in the sea, the sea area is masked using the existing GIS data. It indicates that only the difference on the land is discussed in the analysis. Since the scale of the affected area would be large in the tsunami disaster, area-based change detection is more suitable to capture the inundation area rather than pixel-based change detection. The meshes whose size is 20m are constructed to examine the stochastic characteristics of the D values in a mesh. The stochastics in the actually inundated area are compared with those in the non-inundated area to discuss threshold value to discriminate inundation area from non-inundation area. The inundation area is extracted from the images using the threshold value.

The comparison of histograms of NDVI observed before and after the disaster is shown Fig. 4. Figure 4(a-1) shows the histograms of the images observed in 2000 and 2005, while Fig. 4(a-2) shows the histograms of the images observed in 2001 and 2005. The locations of the images are shown in Fig. 1(b). The histogram shows the data that are already masked in the sea area. The averages and their standard deviations are indicated in the figures. Significant difference of the shape of the histograms is not observed between the pre- and post-event images. It indicates that the seasonal change in NDVI is not remarkably observed in the area. Histograms of the D value are shown in Fig. 4(b-1) and (b-2). The averages of the differences are almost equal to zero. The shape of the histograms is similar to Gaussian distribution. When the D value shows larger than zero, the vegetation is decreased after the event in the pixel.

The schematic diagram of distribution of D value within a 20m-mesh is shown Fig. 5. D_P and D_N represent the pixels whose D value shows positive and negative, respectively. In the area inundated by the tsunami, percentage of D_P in a mesh would be increased. As shown by equation in Fig. 5, R_P defined as ratio of number of D_P to total pixels in a mesh is computed in each mesh.

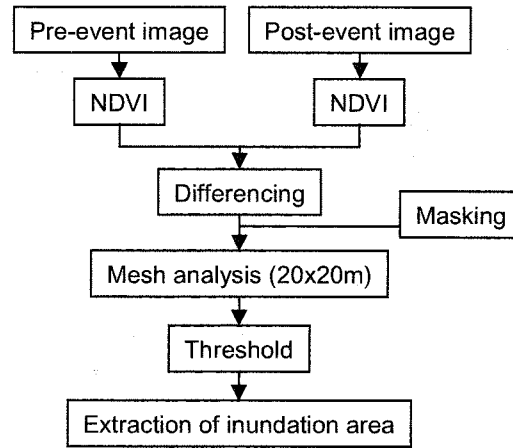


Figure 3 Flow for extraction of inundation area from satellite image

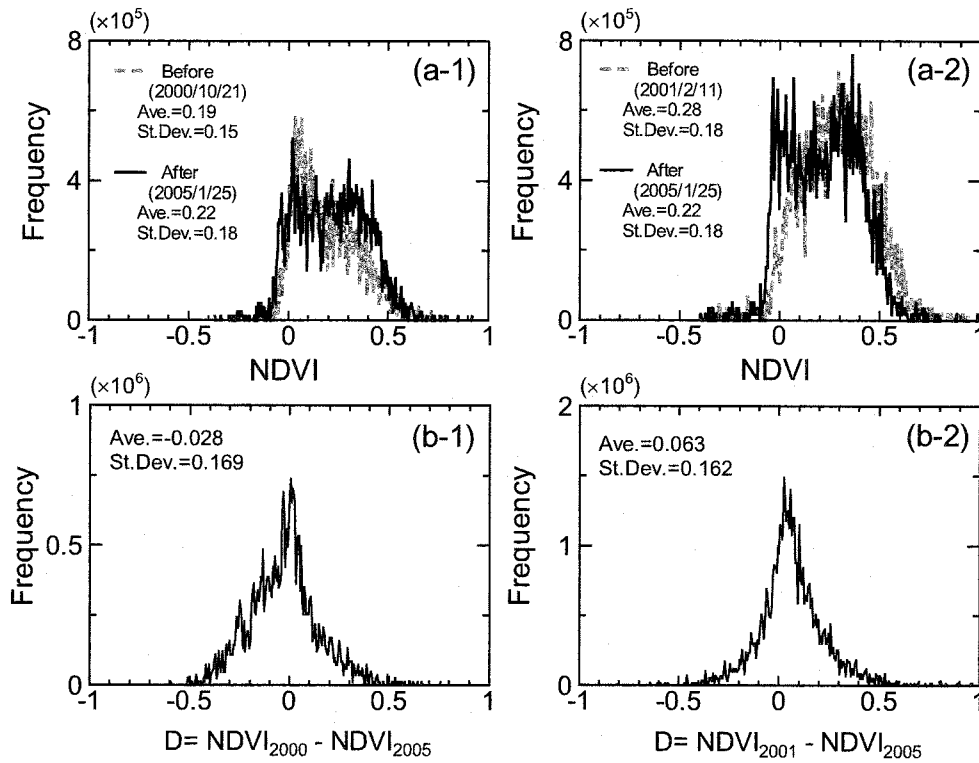


Figure 4 Comparison of histogram of NDVI before and after the disaster

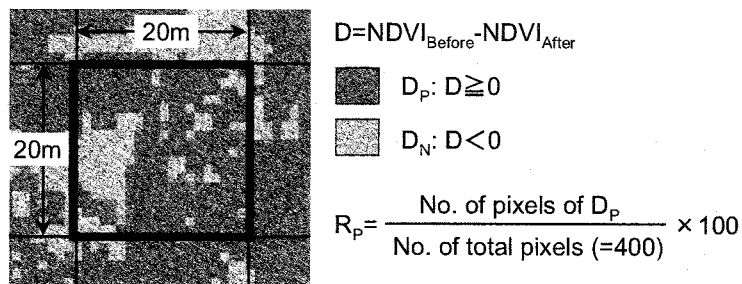


Figure 5 Schematic diagram for calculation of ratio to evaluate vegetation decrease

Figure 6(a) shows the distribution of inundation area in Batticaloa (Wijeyewickrema *et al.*, 2005). Solid circles indicate the survey point of the inundation boundary based on the evidences of the tsunami eyewitness. Open circles indicate the locations that other information such as inundation depth is obtained. According to the evidences, the tsunami crossed over into the western lagoon in the northern and southern survey points. Dotted line indicates the estimated inundation boundary based on the result of the survey. Solid lines show perpendicular lines to the coastline including the survey points of the inundation boundary.

Figure 7(a) shows the cross section of R_p along the solid line No.4. The area within the distance of 1,000m from the coastline was inundated on the line. R_p in the inundated area shows 80% or more while R_p in the non-inundated area shows around 60%. Figure 7(b) shows the comparison of R_p between the inundation area and the non-inundation area on the seven lines shown in Fig. 6(a). Circles and error bars represent the averages and the standard deviations of R_p on the line, respectively. On the other lines as well as the line No.4, the averages of R_p in the inundation area show 80% or more and the averages of R_p in the non-inundation area show 50 to 60%. It indicates that R_p in the inundation area shows higher than that in the non-inundation area.

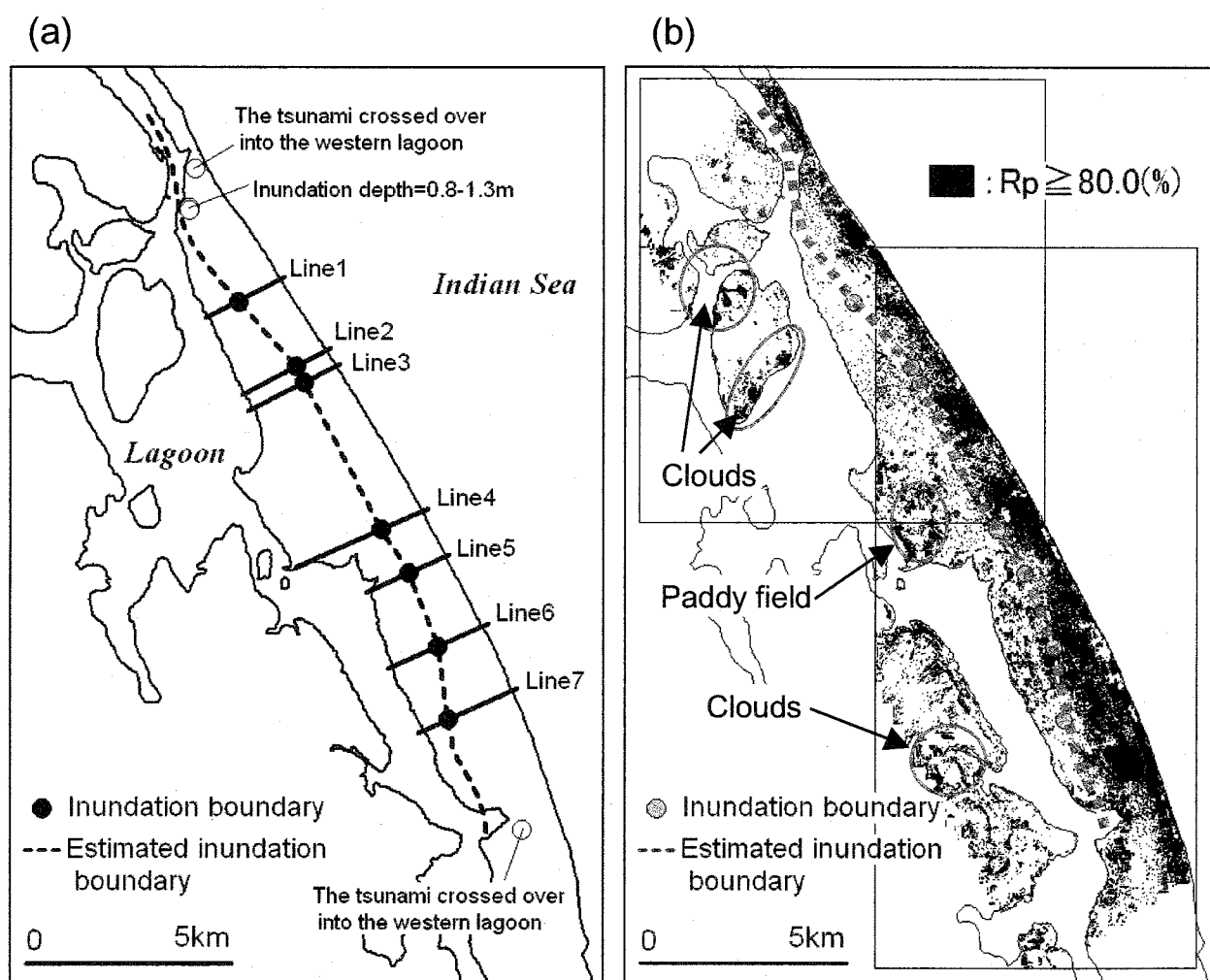


Figure 6 (a) Inundation area and perpendicular line on survey point
(b) Extraction of high R_p area from IKONOS images

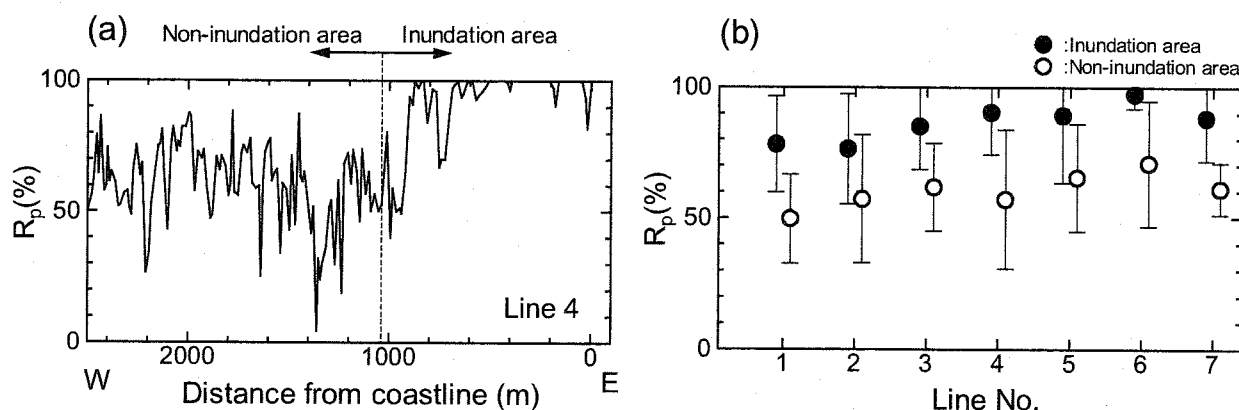


Figure 7 (a) Cross-section of R_p along the inundation survey line (Line 4) shown in Fig. 6 (a)
 (b) Difference of R_p in inundation area and non-inundation area

4. RESULT OF ANALYSIS

As shown in Fig. 7 (b), the mesh whose R_p show more than 80% is prone to be inundated by the tsunami. The meshes whose R_p is over 80% are regarded as the inundation area in this study. Figure 6(b) shows the result for the extraction of the inundation area. The blackened areas represent the locations of the extracted meshes. Thick dotted line in the figure indicates the inundation boundary. The result shows that the extracted meshes are mainly distributed in the eastern coastal area. The distribution of the densely extracted meshes seems to be similar with the actual inundation area. More meshes are extracted in the southern part than in the northern part. As shown in Fig. 1(b), the built-up areas in Batticaloa are concentrated in the northern area. The density of the vegetation in built-up areas would be relatively coarse because the land surface would be covered with buildings and other man-made structures. The change of vegetation in built-up areas would be small than that in other areas. It indicates that the extraction in densely built-up area would be underestimated compared with that in other areas.

As shown by solid circles in Fig. 6(b), the extracted meshes are distributed not only in the inundation area but also in non-inundation area. Figure 8(a-1) and (a-2) shows close-up of post-event IKONOS image and the distribution of D_p and D_N in cloud covered area. Blackened pixels and gray pixels in Fig. 8(a-2) represent pixels of D_p and D_N , respectively. Since land surface cannot be clearly observed on the cloud and its shadow area, NDVI shows apparently lower in the areas. Therefore, they are mis-detected as changed area. Figure 9(b-1) and (b-2) shows close-up of paddy field. The density of the vegetation in paddy field is seasonally changed because the land surface would be covered with the paddy during seasons of the growth while soil or water would be exposed during seasons of the rest. These results indicate that it is difficult to discriminate the seasonally changed area with tsunami inundation area.

In this study, threshold value of the extraction is determined by simply comparing the R_p in the inundation area with that in the non-inundation area. It may provide mis-detections in the seasonally changed area. In order to avoid these problems, image fluctuation in non-damaged area should be considered in the future works.

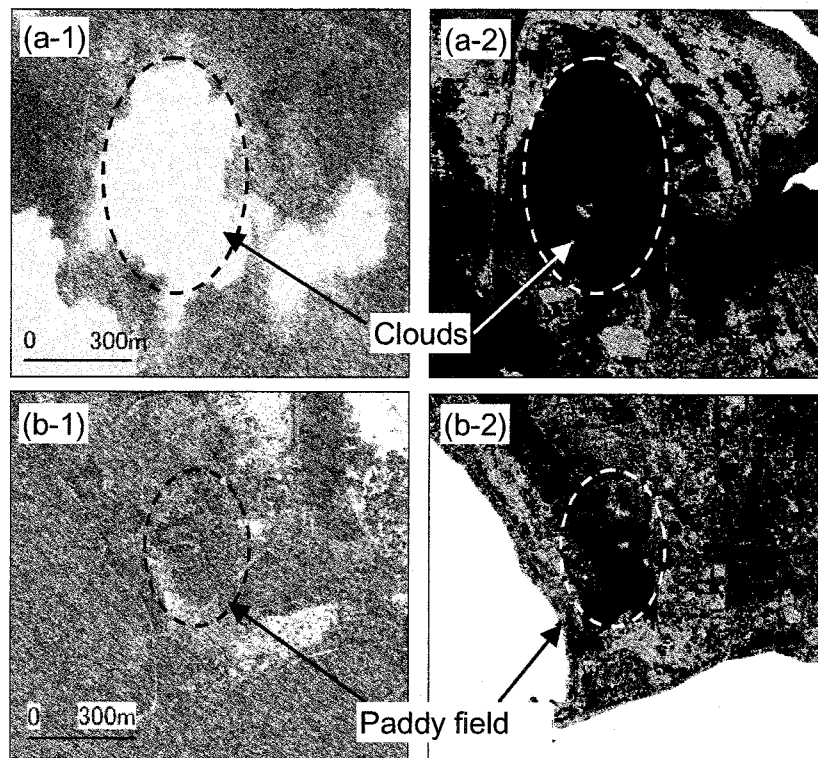


Figure 8 IKONOS image and distribution of D_P and D_N (Black: D_P , Gray: D_N)
(a) Cloud covered area, (b) Paddy field

5. CONCLUSIONS

A methodology to extract the tsunami inundation area from high-resolution satellite images is examined. Normalized difference vegetation index (NDVI) of the pre- and post-event IKONOS images is utilized in this method. The characteristics of the images observed in Batticaloa, Sri Lanka, where severe tsunami damage is observed due to the 2004 Sumatra earthquake are examined. In the heavily affected area, NDVI in the post-event image shows lower than that in the pre-event image because the tsunami washed away or blighted the trees and the grasses. The ratio of the pixels whose NDVI is decreased after the event within a mesh area (20m x 20m) is computed to conduct area-based analysis. Statistics of the ratios in the actually inundated area is compared with those in the non-inundated area. The results show that the averages of the ratio are about 80% in the inundated area while those are about 60% in the non-inundated area. The meshes whose ratio is more than 80% are extracted as the inundation area. The inundation area extracted from the satellite image is compared with the actual inundation area based on the field survey. The extracted area seems to be similar with the actual inundation area by the field survey. However, in cloud covered area and paddy field, it is difficult to discriminate the seasonal changed area from the inundated area.

Acknowledgements:

The authors are grateful to Assoc. Prof. Anil C. Wijeyewickrema (Tokyo Institute of Technology), Mr. Shusaku Inoue (Tokyo Institute of Technology), Dr. Hiroyuki Matsumoto (Japan Agency for Marine-Earth Science and Technology), Dr. Priyantha Gunaratna (University of Moratuwa), and Mr. Manoj Madurapperuma (University of Moratuwa) for helping the field survey.

References:

- Kohiyama, M., H. Hayashi, N. Maki, M. Higashida, H. W. Kroehl, C. D. Elvidge and V. R. Hobson (2004), "Early Damaged Area Estimation System Using DMSP-OLS Night-time Imagery", *International Journal of Remote Sensing*, Vol.25, No.11, pp.2015-2036.
- Lu, D., P. Mausel, E. Brondizio and E. Moran (2004), "Change Detection Techniques", *International Journal of Remote Sensing*, Vol.25, No.12, pp.2365-2407.
- Matsuoka, M. and F. Yamazaki (2004), "Use of Satellite SAR Intensity Imagery for Detecting Building Areas Damaged due to Earthquakes", *Earthquake Spectra*, Vol.20, No.3, pp.975-994.
- Ramakrishnan, D., S. K. Ghosh, V. K. M. Raja, R. V. Chandran, and A. Jeyram (2005), "Trails of the Killer Tsunami: A Preliminary Assessment Using Satellite Remote Sensing Technique", *Current Science*, Vol.88, No.5, pp.709-711.
- Singh, A. (1988), "Digital Change Detection Techniques Using Remotely-Sensed Data", *International Journal of Remote Sensing*, Vol.10, No.6, pp.689-1003.
- Tucker, C. J. (1979), "Red and Photographic Infrared Linear Combinations for Monitoring Vegetation", *Remote Sensing and Environment*, Vol.8, pp.127-105.
- Wijeyewickrema, A. C., S. Inoue, T. Sekiguchi, H. Miura, H. Matsumoto, P. Gunaratna and M. Madurapperuma (2005), "Tsunami Damage in Sri Lanka Due to the Sumatra Earthquake of December 26, 2004", *Proc. International Association of Seismology and Physics of the Earth's Interior (IASPEI) General Assembly*, Abstract No.5.
- World Health Organization (WHO) (2005), South Asia Tsunami Situation Reports 32 (1st February, 2005), http://www.who.int/hac/crises/international/asia_tsunami/sitrep/32/en/index.html.

EFFECT OF WAVE FREQUENCY DISPERSION IN THE INDIAN OCEAN TSUNAMI

Y. Shigihara¹⁾ and K. Fujima²⁾

1) *Research Associate, Dept. of Civil and Environmental Engineering, National Defense Academy, Japan*

2) *Professor, Dept. of Civil and Environmental Engineering, National Defense Academy, Japan*

shigi@nda.ac.jp, fujima@nda.ac.jp

Abstract: A numerical simulation that takes into account effect of wave frequency dispersion has been carried out in the Indian Ocean Tsunami in December 26, 2004. Proposed numerical method of leapfrog implicit scheme based on Shigihara et al. (2005) is applicable to the practical simulation. Regarding the runup to northwest coast of Sumatra Island, dispersion effect is negligible. In the west side of tsunami source, if the aim of simulation is the reproduction of detailed propagation process, dispersion effect should be considered in Sri Lanka. On the other hand, if only maximum runup height and tsunami arrival time is required, dispersion effect is possibly negligible.

1. INTRODUCTION

On December 26 00:58 (UTC), a great earthquake occurred off the coast of northern Sumatra, Indonesia. The tsunami accompanied with this earthquake propagated in the entire Indian Ocean, and attacked not only at the coast of Indonesia, but also at the coast of Thailand, Sri Lanka, Maldives and the east coast of Africa located several thousands kilo meters distance from the epicenter.

In the tsunami propagation over the distance, wave frequency dispersion effect (dispersion effect) plays an important role especially in the leading wave of a tsunami. Since the initial wave generated by the sea bottom uplift could have multiple amplitude and frequency components, the leading wave reveals its amplitude as a train of waves is being formed in its tail. Also if the waves propagate on a long shallow shelf, the soliton waves split due to interaction between non-linearity and dispersion effect. Although several studies have discussed the importance of dispersion effect in tsunami propagation, we do not have a standard numerical method for dispersive wave theory at the present. Fujima and Shigihara (2005) discussed the characteristics of some numerical schemes and equations, and proved that the leapfrog implicit method was accurate and stable. In addition, the selection of dispersion model (Boussinesq and Madsen-Sorensen) was appeared not to be so important if the grid size was practical. As the solution of this problem, Shigihara et al.(2005) proposed practical numerical method that the potential function of dispersive term is solved implicitly for the linear dispersive wave theory in the Cartesian coordinate.

This study aims to reproduce the Indian Ocean Tsunami of Dec. 26 with help of two different numerical models i.e., the shallow water theory and dispersive wave theory based on the Shigihara's numerical method for tsunami calculation. Using this model intended to uncover the implication of dispersion effects in tsunami propagation and runup process in this event.

2. NUMERICAL METHOD

2.1 Basic Equations and Numerical Procedure

The governing equations are Eqs.(1) to (4), where f_x and f_y are the convection and the other terms. In the dispersion terms, the effect of variation of water depth is assumed to be small.

$$\frac{\partial \eta}{\partial t} + \frac{\partial M}{\partial x} + \frac{\partial N}{\partial y} = 0 \quad (1)$$

$$\frac{\partial M}{\partial t} + gd \frac{\partial \eta}{\partial x} + f_x = h \frac{\partial \phi}{\partial x} \quad (2)$$

$$\frac{\partial N}{\partial t} + gd \frac{\partial \eta}{\partial y} + f_y = h \frac{\partial \phi}{\partial y} \quad (3)$$

$$\phi = \alpha h \frac{\partial^2 M}{\partial x \partial t} + \beta h \frac{\partial^2 N}{\partial y \partial t} + \gamma gh^2 \frac{\partial^2 \eta}{\partial x^2} + \delta gh^2 \frac{\partial^2 \eta}{\partial y^2} \quad (4)$$

$$\alpha h \frac{\partial^2 \phi}{\partial x^2} + \beta h \frac{\partial^2 \phi}{\partial y^2} - \phi = \alpha h \frac{\partial}{\partial x} \left[gd \frac{\partial \eta}{\partial x} + f_x \right] + \beta h \frac{\partial}{\partial y} \left[gd \frac{\partial \eta}{\partial y} + f_y \right] - \gamma gh^2 \frac{\partial^2 \eta}{\partial x^2} - \delta gh^2 \frac{\partial^2 \eta}{\partial y^2} \quad (5)$$

By substituting Eq.(2) and (3) into Eq.(4), definition of the potential function, the governing equation of the potential function is obtained as Eq.(5).

Numerical procedure is as follows:

- (1) Water surface elevation is computed explicitly through Eq.(1).
- (2) Potential function of dispersion term is solved implicitly through Eq.(5).
- (3) Discharge rate in x- and y-direction is solved explicitly through Eq.(2) and (3).

In procedure (2), because Eq.(5) is the differential equation of Poisson type, the computation can be conducted effectively by high-speed solver. The computation time is about 1/3 to 1/6 of that of simple SOR method. This numerical method is adaptable for the cases where there are nonlinear convection terms and the polar coordinates are used in the simulation. In the numerical simulation of two-dimensional case, the coefficients of dispersion terms were set as those of Boussinesq model (i.e., $\alpha = \beta = 1/3$, $\gamma = \delta = 0$), and the nonlinear terms were ignored. On the other hand in the shallow channel of one-dimensional case (details are in 2.2), the nonlinear terms as well as the bottom friction term are considered explicitly in the simulation.

2.2 Numerical Domains and Conditions

For the numerical computation, two cases of study have been carried out as follows: a) two-dimensional simulation in the Indian Ocean: two-dimensional deep ocean case, b) one-dimensional simulation Yala/Banda-Aceh; shallow channel cases. In all numerical simulation, the bathymetry is taken from GEBCO data bank using 1 min resolution. The bathymetric profile along transects (one-dimensional case) are obtained by linear interpolation from the GEBCO data bank. Initial condition or initial free surface deformation used in this study is given in details in Kowalik et al. (2005) according to the static dislocation formulae from Okada (1985).

In the two-dimensional deep ocean case, the computational domains is bounded by the window 70°E, 15°S to 100°E, 17°N (see Figure 1). For all boundaries, absorbing sponge layers are applied at the edge of numerical domain, on the other hand wall boundary condition is applied at the shore side. Model parameters for this case are given in Table 1. This computation aims to visualize the dispersion effect in deep sea of the Indian Ocean.

In the shallow channel cases, two places have been chosen, indicated by transects A-A and B-B in

Figure 1. One transect is located in the Northwest of Sumatra which was struck by a “near-field” tsunami. In contrast, the other one across the Bay of Bengal, Sri Lanka, which experienced a “far-field” tsunami. The numerical domains extend from 95.09°E, 5.47°N to 95.3°E, 5.47°N (A-A), and from 81.78°E, 6.35°N to 81.45°E, 6.35°N (B-B). At the offshore end of the channels the temporal variations of the free surface from two-dimensional computation are established as boundary forcing. This experiment is intended to investigate the implication of dispersion effect on the runup and the transformation of wave shape in the shallow region. Therefore, finer spatial resolution of 10 m is applied in both experiments to visualize the approach of the wave train to the shoreline. Model parameters for these cases are summarized in Table 1.

Table 1 Parameters for the numerical computation

Case	Dimension of computation	Δx	Δy	Δt
Deep Ocean	2D	1min	1min	3.0s
Shallow Channel	1D	10m	10m	0.1s

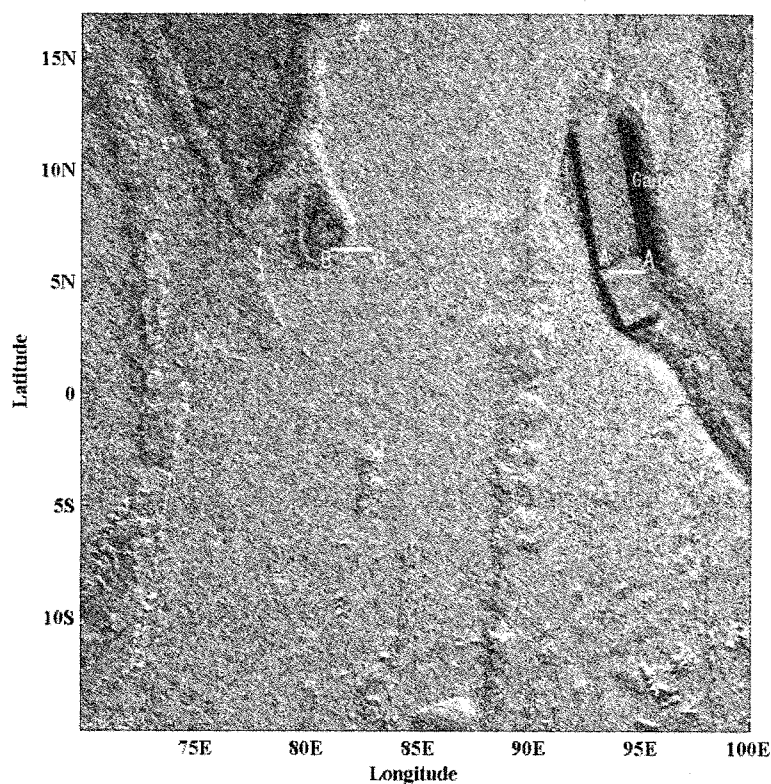


Figure 1 Bathymetry and initial free surface

3. RESULTS AND DISCUSSIONS

3.1 Dispersion Effect in Deep Ocean

Firstly, numerical results of the two-dimensional deep ocean case are discussed. Figure 2 shows wave pattern at time 2 h 21 min using Linear Shallow water Wave (LSW) and Linear Dispersive Wave (LDW) model. In the west side of tsunami source, e.g. Indonesia and Thailand, the dispersion effect is restricted. However, in the east and south side of the source, e.g. Sri-Lanka, Maldives and Diego Garcia, the effect is not so small. The LDW model results features a series of wave train behind the leading wave, the wave pattern is significantly different from that of LSW model. Since wave celerity of high-wavenumber component becomes small by the dispersion effect, the simulation with dispersion terms provided the first wave profile without high-wavenumber component. From Eqs. (3), (4) and (5), the magnitude of the dispersive term is proportional to the square of still water depth, then, the dispersion effect in the west and south side (4-5 km depth) is much stronger than that in the east side (several hundred meters depth). This reason and the longer distance propagation enhance the stronger dispersive effects in the west and south side.

Figure 3 indicates time history of free surface elevation at location of gauges in Figure 1. Wave front tip in all gauges show good agreement of the LSW and LDW model. At gauge 1 (west side from the source), agreement is very good due to the proximity of the gauge to the tsunami source, because there is no time to develop the dispersive waves. On the other hand at gauge 2 and 3 (east and south side), the dispersive waves are verified since the gauges are located farther away from the source. The SW model overestimates the leading wave height by 22% at gauge 2 and by 14% at gauge 3.

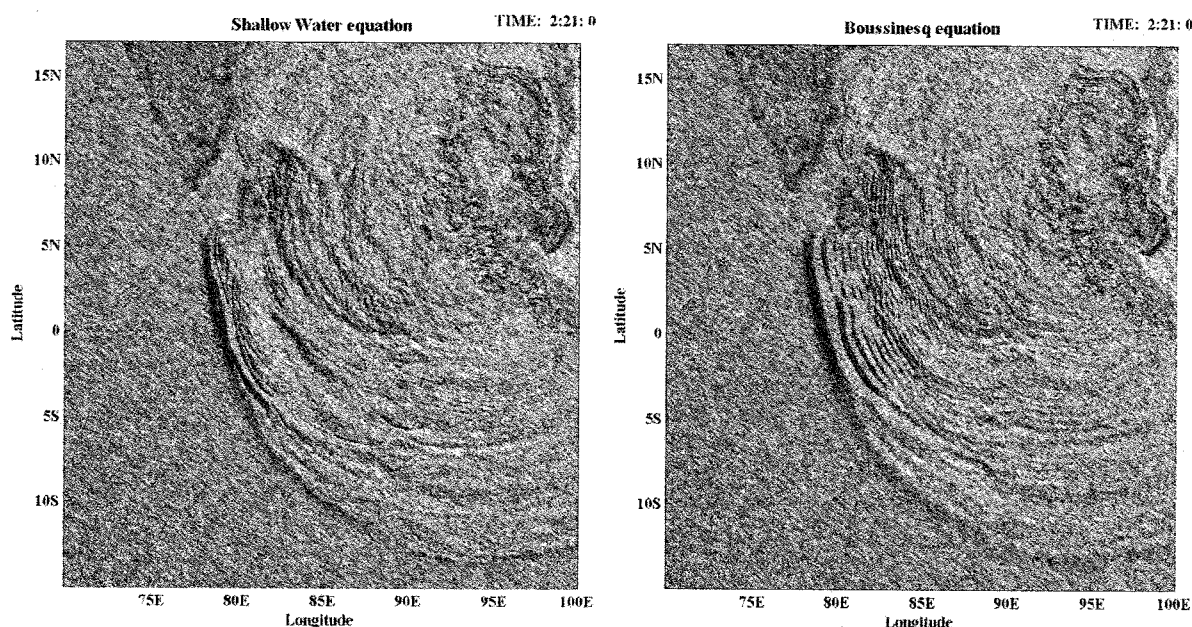


Figure 2 Comparison of water surface at 2 h 21 min. (left: LSW model, right: LDW model)

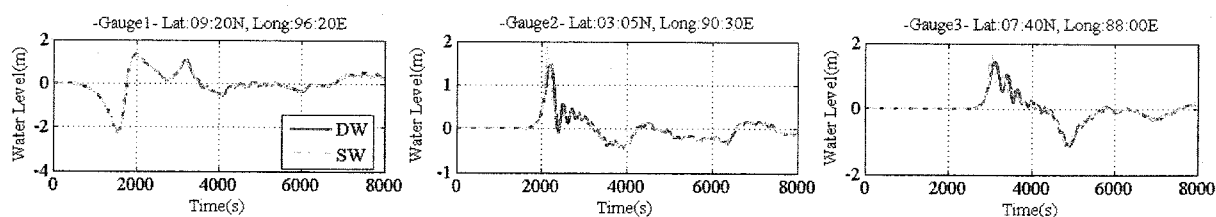


Figure 3 Comparison of water level at different locations

3.2 Transformation and runup of tsunami in coastal regions

Figure 4 and 5 indicate tsunami propagation and runup-rundown in the shallow water regions obtained by the Nonlinear Shallow water Wave (NLSW) and Nonlinear Dispersive Wave (NLDW) models using one-dimensional computation channels. From Figure 4, in Banda Ache where lies directly on the tsunami source of southern segment, free surface profile, runup timing and heights match very well regardless of models. Therefore regarding the runup to northwest coast of Sumatra island, dispersion effect can be negligible.

On the other hand, in Yala, wave pattern on the coastal shelf (panel of at 2h-5min in Fig. 5) is quite different due to the dispersion effect, however at 2h-19min the leading wave height of NLDW model goes to approach that of NLSW model. As a result at 2h-30min, the maximum runup height is almost the same in both models. However, at 3h-7min panel shows that the NLDW approach gives higher runup by the second wave than the NLSW approach, because such a different runup process might be caused by the dispersion effect. Therefore regarding the west side of tsunami source, if the aim of simulation is the prediction of detailed propagation process, dispersion effect should be considered in the simulation in Sri Lanka. Or again if only maximum runup height and tsunami arrival time is required in the tsunami simulation, dispersion effect is possibly negligible.

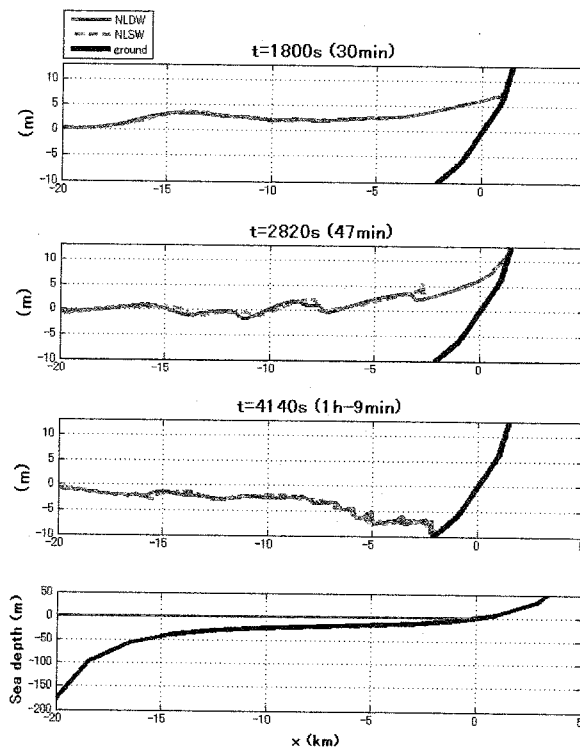


Figure 4 Tsunami runup and rundown at Northwest Sumatra (Banda Ache, transect A-A)

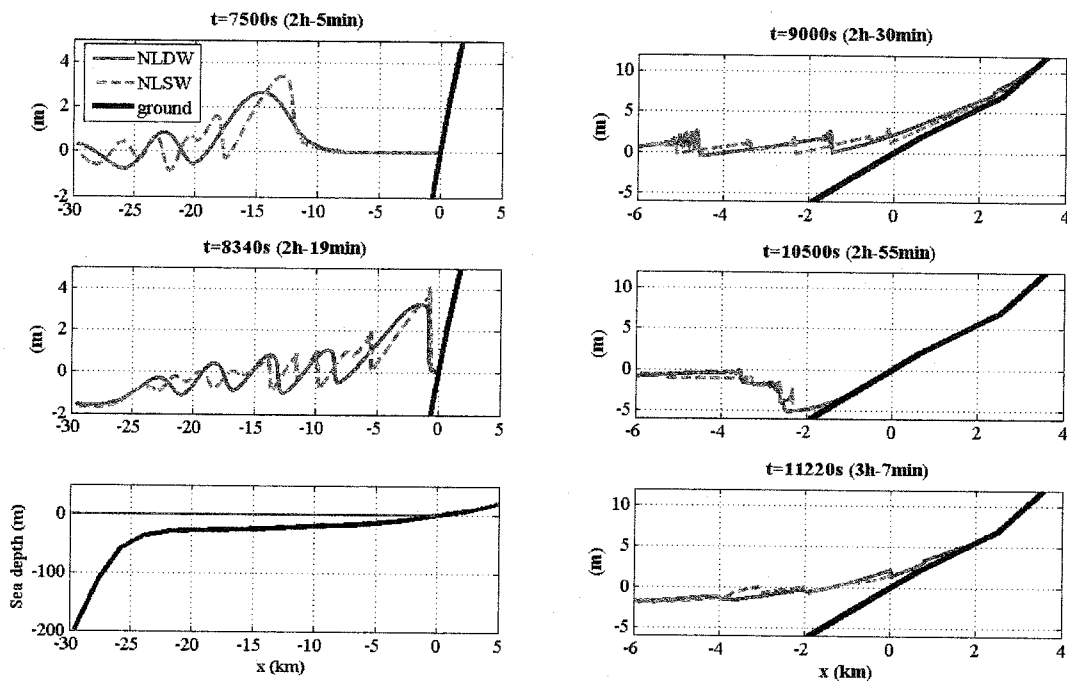


Figure 5 Tsunami propagation, runup and rundown at Yala (Sri Lanka, transect B-B)

4. CONCLUSIONS

A numerical simulation that takes into account effect of wave frequency dispersion has been carried out in the Indian Ocean Tsunami in December 26, 2004 in order to uncover the implication of dispersion effects in tsunami propagation and runup process. The proposed new model is applicable to the practical numerical simulation.

In the west side of tsunami source, e.g. Indonesia and Thailand, the dispersion effect is restricted, however, in the east and south side of the source, e.g. Sri-Lanka, Maldives and Diego Garcia, the effect is not so small. From the results of one-dimensional channel case, regarding the runup to northwest coast of Sumatra Island, dispersion effect is negligible. In the west side of tsunami source, if the aim of simulation is the reproduction of detailed propagation process, dispersion effect should be considered in Sri Lanka, or if only maximum runup height and tsunami arrival time is required, dispersion effect is possibly negligible.

Of course these conclusions are valid only in the present computation domain, the dispersion effect in the entire Indian Ocean is not checked at the present.

References:

- Fujima, K. and Shigihara, Y. (2005), "Adequate Numerical Scheme for Dispersive Wave Theory", *Proc. of Third International Conference on Asian and Pacific Coasts*, 977-987.
- Shigihara, Y., Fujima, K., Homma, M. and Saito, K. (2005), "Numerical Model of Linear Dispersive Wave Equation for the Practical Problem", *Proc. of Third International Conference on Asian and Pacific Coasts*, 998-1009.
- Kowalik, Z., Knight, W., Logan, T. and Whitmore, P. (2005), "Numerical Modeling of the Global Tsunami: Indonesia Tsunami of 26 December 2004", *Science of Tsunami Hazards*, **23** (1), 40-56.
- Okada, Y. (1985), "Surface deformation due to shear and tensile faults in a half-space", *Bulletin of the Seismological Society of America*, **75**, 1135-1154.

WHAT CAN WE DO FOR MINIMIZING TSUNAMI DISASTER?

S.I.Iwasaki

*National Research Institute for Earth Science and Disaster Prevention, Japan
cuh@bosai.go.jp*

Abstract: After 2004 Sumatra disasters, lack of early tsunami warning system (TWS) in Indian Ocean have been closing up as one of the main causes of large amount of loss of lives and properties. But, TWS is not a mighty counter measure against tsunamis. We must consider various things for activating TWS, such as limitation of TWS, capacity building for maintaining and operating TWS, promoting tsunami knowledge and awareness among the people, evacuation protocols including infrastructures etc. Considering the comparative rarity of tsunami in Indian Ocean, combination of TWS utilizing present resources and tsunami education for elementally school children is appropriate to minimize tsunami disasters as a cheap, sustainable and effective tsunami counter measures.

1. INTRODUCTION

Why the damages were so large by the 2004 Sumatra tsunami? Various reasons can be pointed out, tsunami and/or parent earthquake was so large, hard shaking was felt only very close to Banda Aceh due to the rapture process of the earthquake was slow, TWS was not installed in Indian Ocean and lack of tsunami knowledge among the people, that is, tsunami has great power, tsunami is very fast, tsunami would not finish just a one wave but continue for long time and sometimes the first wave is not the largest one etc. Then, what can we do for minimizing tsunami disaster? In this paper, I will clarify the reasons of heavy damages at first. Then, I will propose the needs of international tsunami warning system and education and/or educational program about tsunamis.

2. THE REASONS OF HEAVY DAMAGES

2.1 Generation Mechanism of the Tsunami and the Earthquake

The generation mechanism of the tsunami and the earthquake was not ordinary one. The areas generating seismic waves and tsunami were not the same (Satake, 2005, personal communication). Tanioka et al. (2006) stated that the rupture of the earthquake propagated about 1200 km toward north-northwest along the Andaman trough with

rather low rupture speed. Since, the total amount of deformation of sea bottom is a governing factor of tsunami generation. The slow rupture speed or the long duration of dislocation process of the earthquake means that the earthquake radiated rather low seismic energy compared with the tsunami wave heights. These kinds of earthquakes are called as “tsunami earthquakes” (Kanamori, 1972). Actually, hard shaking by the earthquake was only felt near Banda Aceh. Hard shaking is a natural precursor of tsunami. Ordinary, large number of people living close to the tsunami (earthquake) source would evacuate by hard shaking. Peculiar generation mechanism of the 2004 Sumatra tsunami is one of the main causes of heavy damages.

2.2 Lack of TWS in Indian Ocean

Fig.1 shows time tables of onset of the earthquake, arrival time of the tsunami to nations along Indian Ocean and times of warning issues by PTWC with the number of death, missing and displaced in each nations.

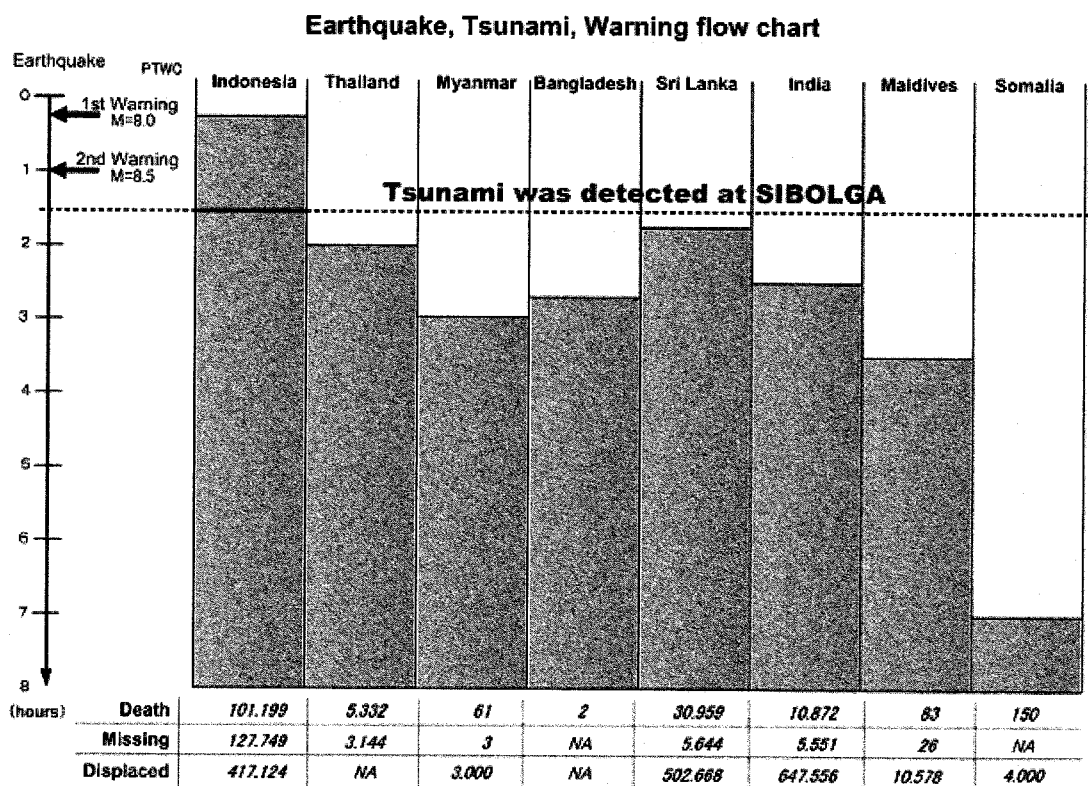


Figure 1 Earthquake, tsunami and warning flow chart

At 0059 (UTC) the earthquake occurred, just after 15minutes PTWC issued tsunami warning. But, PTWC only responsible for Pacific, the content of the warning issue did not raise attentions that tsunami threats existed. About one hour after the onset of the earthquake, PTWC revised warning. A part of the content of the warning is shown

below:

“THIS EARTHQUAKE IS LOCATED OUTSIDE THE PACIFIC.

NO DESTRUCTIVE TSUNAMI THREAT EXISTS FOR THE PACIFIC BASIN
BASED ON HISTORICAL EARTHQUAKE AND TSUNAMI DATA.

THERE IS THE POSSIBILITY OF A TSUNAMI NEAR THE EPICENTER”.

Again, this did not raise attentions and the tsunami has already attacked Banda Aceh. After one hour and half, tide gauge at Sibolga, Indonesia detected clear tsunami signal. But, this data was not telemetered.

According to the facts mentioned above, lack of TWS in Indian Ocean is also one of the main causes of large amount of victims living far from the tsunami source. But, one thing must be pointed out that people in Banda Aceh would not be survived.

3. THINGS MUST BE CONSIDERED FOR MINIMIZING TSUNAMI DISASTAERS

3.1 TWS Limitations

International TWS has two kinds of limitations, one is tsunami evaluation limitation and another one is time limitation. Explanation will be made by using PTWC (Pacific Tsunami Warning Center) procedures (PTWC, 2006)

For quick warning issue, PTWC evaluates tsunami threat based on seismological data at the first stage. Actually, about 90% of tsunami causes are earthquakes, but landslides, volcanic eruptions also generate tsunamis. And earthquake magnitude does not fully correspond to tsunami wave height. And as mentioned, there exist “tsunami earthquakes”, that is, tsunami wave heights are far large compared with parent earthquakes’ magnitudes. For exact tsunami evaluation, observation of tsunami itself is necessary. It means PTWC needs more time for exact warning. Finally, tsunami wave heights vary by local bathymetry and topography.

Ordinary, PTWC needs 15 minutes for warning issue. It means PTWC is sometimes not functioned for areas tsunami sources located very close to the coasts.

We must know these limitations of international TWS.

2.2 Problems of Maintaining and Operating TWS

One of the big reasons of large amount of loss of lives by The 2004 Sumatra tsunami is people living along the coasts of Indian Ocean did not know tsunamis. This is because tsunami is very rare phenomena in this region. Table 1 shows earthquakes whose tsunami magnitude (Abe, 1981) over 9 from 19th century. We experienced 10 gigantic earthquakes, but in Indian Ocean, the 2004 Sumatra is the first one. Table 2 shows earthquakes which caused damages near Sumatra, Indonesia. The latest one is 1907 event that claimed 400 casualties.

TWS hardware is mainly composed of seismographs and tide gauges which are well designed and distributed. It is very easy to understand that maintaining and operating TWS for tsunami watch and warning issue is difficult task in these regions. In particular, for tide gauges, versatile use is preferable. In Bay of Bengal, Storm surges are frequent natural hazards. Sea level rise, that enlarges vulnerability to coastal disasters and a kind of coastal hazards by itself, would be a big problem in near future. UHSLC (University of Hawaii Sea Level Center) had tide gauge network in Indian Ocean as a part of

GLOSS (The Global Sea Level Observing System) network at the time of 2004 Sumatra tsunami. Actually, ten or little more tide gauges recorded the tsunami. Since the tide gauges were designed to detect long term extremes represented by Sea Level Rise, these data were not telemetered. After the 2004 Sumatra tsunami, they slightly have changed data detection procedures to utilize the data to short extremes represented by tsunamis and storm surges. UHSLC has already transmitted tidal data to PTWC and JMA (Japan Meteorological Agency). Fig.2 is present status and future plan of tide gauge distribution in Indian Ocean administrated by UHSLC. For the tsunami warning, it is necessary to install additional tsunami gauges in the middle of Indonesia and Sri Lanka. But, we can make tide gauge network for TWS by minimum investment. And, the network would be used not only short extremes but for long extremes. It would resolve problems of maintaining and operating TWS for tide gauge stations.

Table 1 List of earthquakes whose tsunami magnitudes are over 9 from 19th century
(Originally this table was calculated and given by Prof. Abe (Tokyo Univ.),
adopted from DPRI home page, 2005)

1837	Valdivia, Chile	9.3
1841	Kamchatka	9.0
1868	Arica, Chile	9.0
1877	Iquique, Chile	9.0
1946	Aleutians	9.3
1952	Kamchatka	9.0
1957	Aleutians	9.0
1960	Chile	9.4
1964	Alaska	9.1
2004	Sumatra, Indonesia	9.1

Table 2 List of earthquakes that caused damages around south-west of Sumatra Island
(Original data was given in Solov'iev and Go (1975), adopted from DPRI home page, 2005)

Date	Lat.	Lon.	M	m
1797/02/10	0°N	99°E	8	3
1833/11/24	2.5°N	100.5°E	8.25	2.5
1843/01/05	1.5°N	98°E	7.25	2
1861/02/16	1°N	97.5°E	8.5	3
1907/01/04	1.5°N	97°E	7.5	2

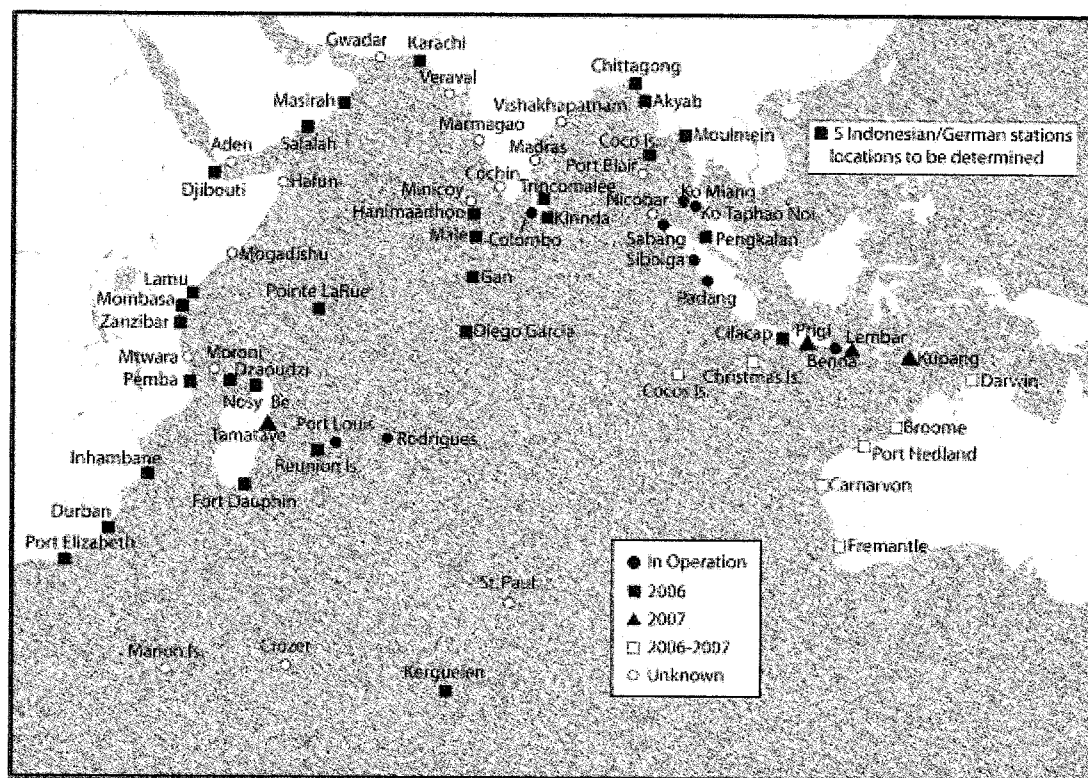


Figure 2 Present status and future plan of GLOSS tide station map
(by courtesy of Prof. Mark Merrifield, UHSLC)

2.3 Tsunami Educational Program

Who could have evacuated after receiving tsunami warning issue, if one have not have tsunami knowledge? I believe the answer is no. Tsunami knowledge is a key for activating tsunami warning issue. Kurita (2005) pointed out that the most useful information source soon after the tsunami was verbal communications with the families and neighbors. Continuous tsunami education and education program is necessary. I proposed that tsunami education to the elementally school children using text book. Year by year, the amount of the people who have tsunami knowledge will increase.

2.4 Evacuation Protocol (including infrastructures)

If TWS is installed and people well know about tsunami, it is not enough for saving lives. Tsunamis will attack any time and occasionally there is little time for evacuation and there is no place to evacuate. In Japan, tsunami evacuation is designed with the combination of hard wares and soft wares. Tide wall for prevent tsunami attack, evacuation terrace and building as a temporary evacuation place for those who living near the coasts, evacuation route equipped solar battery light are hard wares, examples are shown in Fig.3. Hazard map and pre-event planning and/or training according to the evacuation protocol are soft wares. These hard and soft wares must be arranged by local responsible authorities.

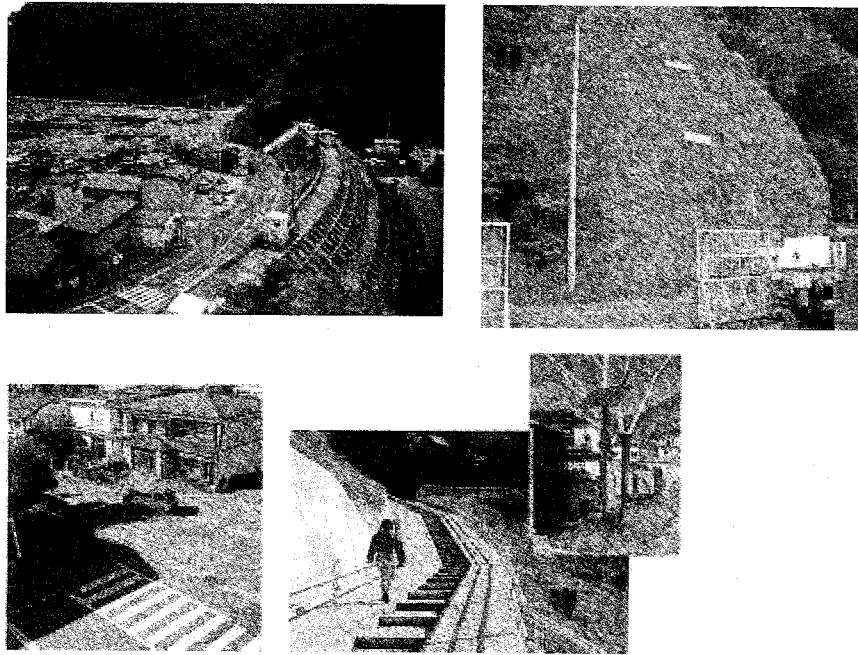


Figure 3 Various counter measures against tsunami in Japan. Upper left: Great tide wall. Upper right: Tsunami wave height symbols. Lower left: Corner cut out of the road. Lower right: Evacuation route to high ground with solar battery lightning system.

3. FINAL REMARKS

Making tsunami ready society is a hard task. We must consider not only installation of TWS but also measures for activating TWS.

Finally, I would like to point out two things. First one is summarized in Fig.4. The Figure shows the history of the occurrence of destructive tsunamis and warning system developments. All the time, the trigger was disasters. After receiving heavy damages, we realized the need of TWS. The 2004 Sumatra disaster is the same one. In future, we must reverse this order.

Another one is that tsunami education is a big problem not only to the Indian Ocean nations but also to Japan. As you know, Japan is the country that the word of tsunami came from. We have left tsunami records in written document forms. From these records, it was found that we have experienced 200 or more tsunamis in these 1300 years. Various counter measures can be seen in Japan. These counter measures can be called as "tsunami culture". But, Japan was attacked the 1960 Chilean Tsunami after 22 hours of the earthquake. This was a matter only 40 years ago. In 2004, the Off Kii Peninsula Tsunami occurred, at that time only 6% of the people evacuated after receiving the warning issue. Even in Japan, the situation was like that mentioned above. To introduce our tsunami culture to nations along Indian Ocean and make collaborations for making tsunami ready society is our responsibility and same time our hope as a part of Asian countries.

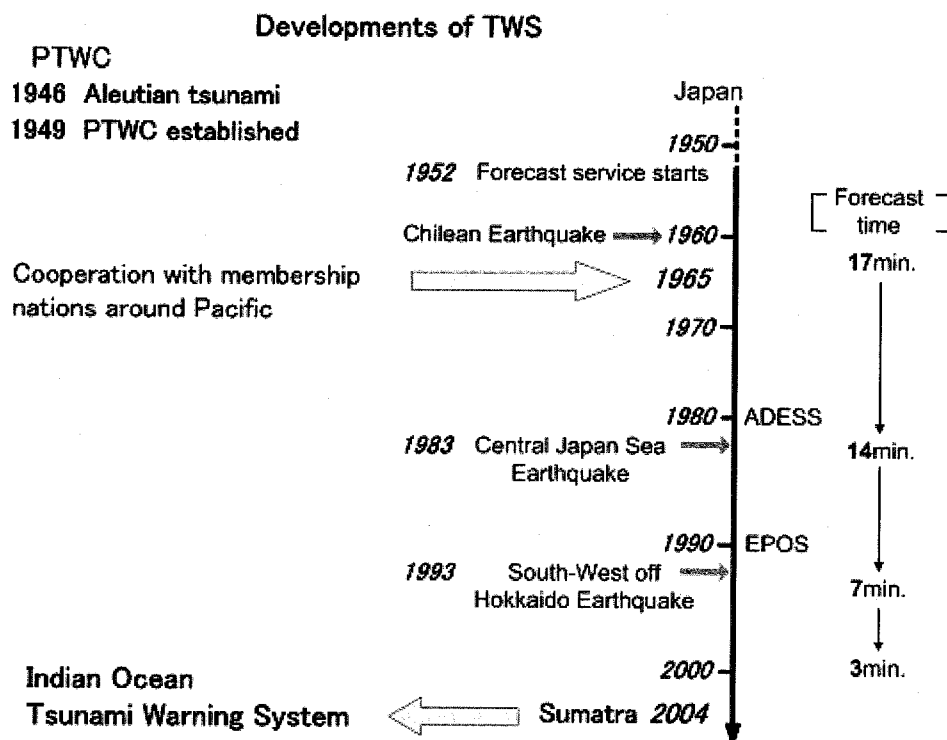


Figure 4 History of disasters and TWS installations and upgrades

References:

- Abe, K. (1981), "Physical size of tsunamigenic earthquakes of the northwestern Pacific", *Phys Earth Planet. Inter.*, **27**, 194-205..
- DPRI (2005), <http://www.drs.dpri.kyoto-u.ac.jp/sumatra/index-e.html>
- Kanamori, H. (1972), "Mechanism of tsunami earthquakes", *Phys Earth Planet. Inter.*, **6**, 246-259..
- Kurita, T., (2005), "Tsunami risk awareness in the affected communities", Proceedings of memorial conference on the giant earthquake and tsunami in Indian Ocean, P1-2-2-13.
- PTWC (2006): <http://www.prh.noaa.gov/ptwc/aboutptwc.htm>.
- Solov'iev S.L. and Ch. N. Go (1975), "Catalog of tsunamis on the western shore of the Pacific Ocean" Nauka, Moscow, 308p (in Russian)
- Tanioka, Y. *et al.* (2006), "Rupture process of the 2004 great Sumatra-Andaman earthquake estimated from the tsunami waveforms", *Earth Planets and Space*, in press.

ACCOUNTS AND MODELING OF THE OLD AND MODERN SUMATRAN TSUNAMIS FOR MITIGATION IN THE FUTURE

H. Latief¹⁾⁵⁾, D.H. Natwidjaya²⁾, H. Sunendar³⁾, A. R. Gusman³⁾, and Y. Tanioka⁴⁾

1) Senior Researcher, Study Program of Oceanography, Bandung Institute of Technology, Bandung, Indonesia

2) Senior Researcher, Research Center for Geotechnoogyl, Indonesian Institute of Sciences, Bandung, Indonesia

3) Assistant Research, Center for Marine and Coasta Developmnt, Bandung Institute of Technology, Bandung, Indonesia

4) Professor, Institute of Seismlogy and Volcanology, Graduate School of Geosciences Hokkaido University

5) Visiting fellow, Institute of Seismlogy and Volcanology, Graduate School of Geosciences Hokkaido University

hamzah@ppk.itb.ac.id, danny@geotek.lipi.id, haris@ppk.itb.ac.id, adit@ppk.itb.ac.id, tanioka@eos.hokudai.ac.jp

Abstract: The December 26, 2004 Aceh-Andaman megathrust earthquake and March 28, 2005 earthquake occurred along the interplate of Sumatra-Andaman where convergence area of the Indian and Australian plates are subducting beneath the Southeast Asian plate. The 2004 Aceh generated large tsunami and killed at least 283,000 people. Historically show that subduction earthquakes and associated tsunamis have occurred repeatedly along the Indian Ocean shores of Sumatra, and they are certainly will happen again. The March earthquake broke a part of the subduction zone that last ruptured in 1861 and 1907. Sooner or later the subduction zone will break again to the southeast, in the area where earthquakes of estimated magnitude 8.3 in 1797 and magnitude 8.7 in 1833 produced a destructive tsunami at west coast of Sumatra. This paper describes a historical earthquake and tsunami in the Sumatra region, and develop tsunami model for the 2004 Aceh Tsunami and 2005 Nias Tsunami. Furthermore for mitigation purpose we also develop the 1797 and 1833 Sumatra tsunamis with tsunami source base on coral microatoll models.

1. INTRODUCTION

On December 26, 2006 in the Sunday morning at 07:58:49 AM (00:58:49, UTC) the devastating megathrust earthquake occurred on the interface area of India plate subducts beneath the overriding Burma plate with seismic moment magnitude (M_w) = 9.1 to 9.3 and the March 28, 2005 (M_w =8.6) with the rupture a 1600 km-long occurred near Banda Aceh, Sumatra, and the rupture propagated to north along Andaman and Nicobar Islands (Lay, et al, 2005). The first one generated huge tsunami and attacked coastal area along the South and South East Asia and reached the Eastern part of Africa that caused 283,000 deaths. In Indonesia at least 113,500 people was killed, ten thousands were missing, and also ten thousands people injured.

Subduction earthquakes and associated tsunamis have occurred repeatedly along the Indian Ocean shores of Sumatra, historically are shown in Table 2 (Hamzah et al., 2000), and they are certain to do so again. The magnitude 8.6 earthquake of March 28, 2005 in Nias and demonstrated the worrisome potential for earthquakes farther to the southeast on the subduction zone marked by the Sunda trench. The March earthquake broke a part of the subduction zone that last ruptured in 1861 and 1907. Sooner or later the subduction zone will break again to the southeast, in the area where an earthquake of estimated magnitude 9 produced a destructive tsunami in 1833. This area at risk is located in along west coast of Sumatera. A tsunami perhaps as much as 10 m high struck Banda Aceh and vicinity in 1797. The tsunami associated with the 1833 earthquake appears to have struck the cities of Padang and possibly Aceh and Bengkulu (González, et. al, 2005). Other tsunamis that have struck Padang and other communities in Western Sumatra occurred in 1861, 1864, 1904, 1907, 1908, and 1964 (Natwidjaya, 2002). Much can be done to save lives in west coast Sumatra and other threatened coastal communities from their next near-source tsunami. As these preliminary steps are taken is to assess a potential of tsunami hazard by accounts and modeling of the tsunamis. Cases study for the old tsunamis are the 1797 and 1833 tsunamis and the modern tsunamis are the 2004 Aceh and 2005 Nias tsunamis.

2. TECTONIC SETTING, HISTORICAL EARTHQUAKES AND TSUNAMIS

The convergence of the plate boundaries in Sumatra region area is shown in Figure 1, where the Indian and Australian plates are subducting beneath the Southeast Asian plate. West Sumatra is an oceanic/continental plate boundary that consists of two fault systems, the mostly dextral strike-slip Sumatran fault system and a predominantly dipslip subduction interface [Fitch, 1972; McCaffrey, 1991 in Natawidjaya, 2002]. Oblique northward convergence of the Indian and Australian plates toward Southeast Asia occurs at about 60 mm/yr. The plate convergence partitions into trench-parallel slip that is being accommodated largely by the Sumatran fault and trench-perpendicular slip accommodated by the subduction interface [(Fitch, 1972; McCaffrey, 1991); in Natawidjaya, 2002]. Both the subduction zone at the Sunda trench and the Great Sumatran fault are seismically active. The Sumatran fault has generated nearly a dozen earthquakes, as well as many smaller events, over the past century as shown in Figure 1. The Sumatran subduction zone has produced two very large earthquakes in 1833 (M9) and in 1861 (M8.5). These dominate the historical seismicity of the subduction interface [(Newcomb and McCann, 1987) in Natawidjaya, 2002].

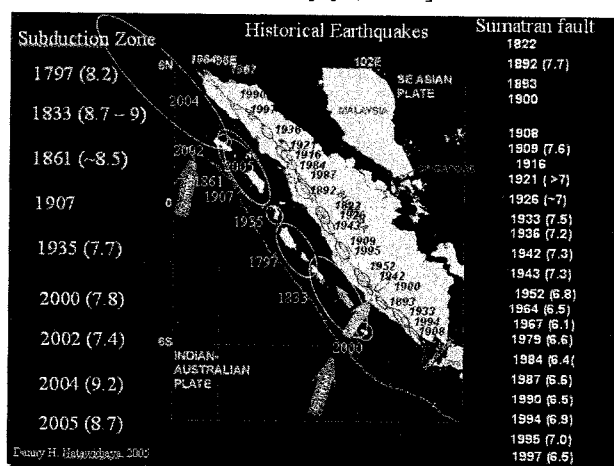


Figure 1 Tectonic map and major earthquake sources of the Sumatran plate margin

As historical earthquake and tsunamis in Indonesia where is including the Sumatran region have been studied by several researchers such as: Ibrahim et al. (1989) gave a statistics of earthquakes and found that at least 460 earthquakes greater than 4.0 have occurred every year which the percentage of the earthquakes in shallow, intermediate, and deep are 61%, 34% and 5% respectively and Utsu (1992) listed the destructive earthquakes in the world during the period of 1500-1992 (include Indonesia). Fauzi (1999) compiled the destructive earthquakes in Indonesia during period of 1800 to 1995, and then Hamzah et al. (2000), compiled the previous earthquake data reports and added with recent earthquake data. During the period of tabulation (1800

to 1998), at least 183 destructive earthquakes have occurred in the region, those have killed at least 11,000 people as shown in Table 1 (Hamzah et al., 2000). This catalog needs to update with more recent destructive earthquakes, such as the 2004 Aceh-Andaman and the 2005 Nias earthquakes. The large earthquake events in the Sumatra region have been plotted as shown in Figure 1 and some of them generated tsunamis, such as 1861, 1864, 1904, 1907, 1908, and 1964 Sumatran tsunamis. More detail studies about historical data and their earthquakes mechanism in the Sumatran region are described by Newcomb and McCann, (1987); Fauzi et al., (1996). The earthquake cycles of the Sumatran subduction interface by analysis evidences from coral microatolls have been reported by Sieh et al., (1999); Zachariasen et al., (1999); Zachariasen et al., (2000); and Natawidjaya (2002). Moreover the CalTech-LIPI (Sieh, et. al and Natawidjaya et, al) are still studying this area with installed GPS and seismograph.

As historical tsunamis in Indonesia include Sumatra, Berninghausen (1966) compiled the data of old tsunamis and seismic seiches from the regions facing the Indian Ocean, and Berninghausen (1969) also reported tsunamis and seismic seiches in the Southeast Asia. The work is continued by Cox (1970) by discussing the Berninghausen's reports. Iida (1983) compiled the data of old huge tsunamis in the world (include Indonesia) and Ismail (1989) listed the data of tsunamis in Indonesian region. However, mostly the old data before 1970 were not well reported and documented. The last 15 years tsunamis have studied and documented by International Tsunami Survey Team (ITST). Furthermore Hamzah, et al. (2000) described about the historical tsunami in Indonesia and the distribution of tsunamigenic earthquakes and volcanoes and their characteristics in space and time with proposed a tsunami catalog and zoning in Indonesia. The tsunami data are shown in the Table 2 (Hamzah, et. al, 2000). This catalog needs to update with more recent tsunamis. For the 2004 Aceh and the 2005 Nias tsunamis have been studied and well documented by the ITST and other researcher, and so far still many interesting topics need to study for both events.

3. TSUNAMI MODELING

We have been developing tsunami model by using TUNAMI-Code [Goto, C. and Ogawa, Y. (1992); Imamura, F. (1995)], for the recent tsunamis such as: the 2004 Aceh and the 2005 Nias tsunamis and also simulated the old tsunamis with cases study of the 1797 Padang and 1833 Bengkulu tsunamis.

3.1. Tsunami Model for the 2004 Aceh Tsunami and 2005 Nias Tsunami

Tsunami model for 2004 megatrust Aceh-Andaman (the 2004 Aceh Tsunami). The simulation area is designed as covered Northern part of the Indian Ocean ($75^{\circ}00'00''\text{E}$ - $105^{\circ}00'00''\text{E}$ and $5^{\circ}00'00''\text{S}$ - $25^{\circ}00'00''\text{N}$) as shown the bathymetry in Figure 2.a the mesh size are $3700 \times 3700 \text{m}^2$, number of grids is 900×900 . Reproduction time is 4 hours with time step is 3 seconds. Boundary condition at the coast as vertical wall is used. We have re-modeled the previous model based on a better earthquake source model, but still not the latest because of improve the tsunami sources. The tsunami sources base on Hirata model in Figure 2.b and applied into the model are shown in Figure 2.c. Wave pattern after 120 minutes propagated and the maximum wave (energy) distribution are shown in Figure 2.d and 2.e respectively. The tsunami heights in time function at the city of Banda Aceh and Loknga are shown in Figure 2.f. However, the model still could not simulate the highest tsunami in Loknga, western part of Aceh, so we plan to refine the model based on the latest tsunami sources with detail bathymetric and finest mesh size.

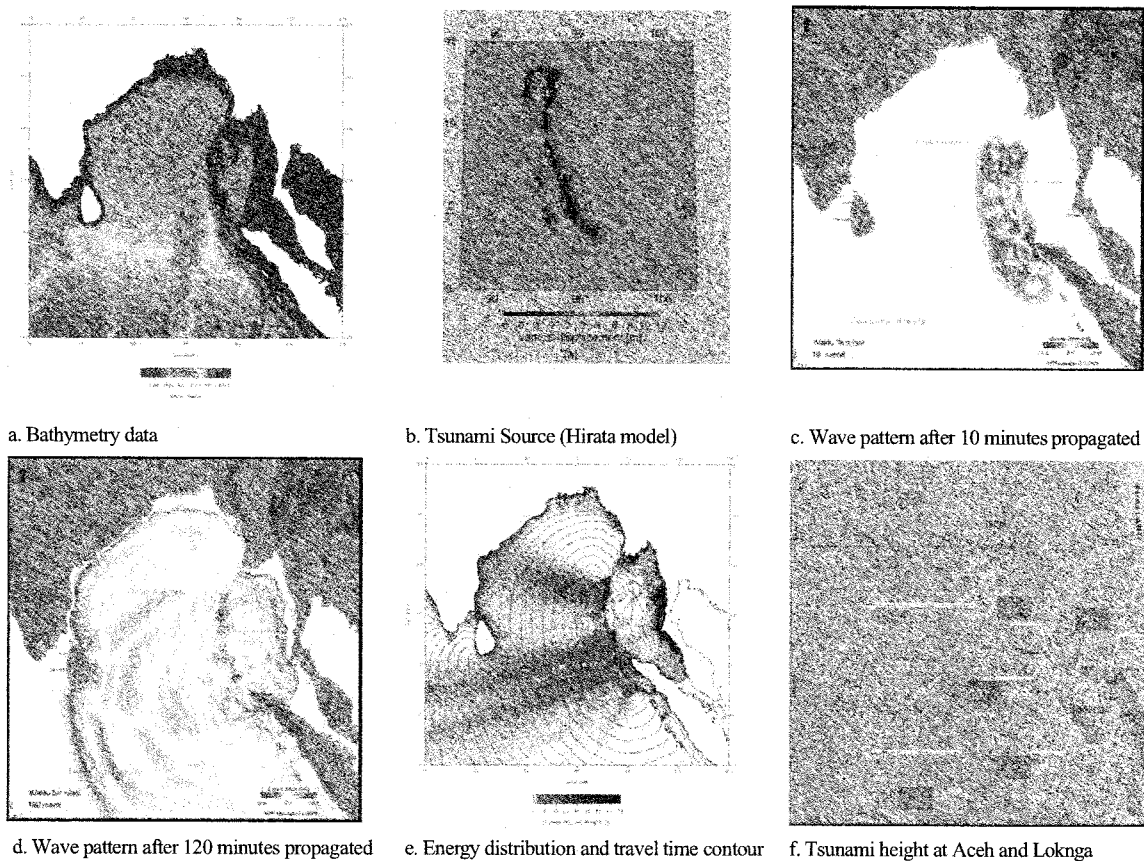


Figure 2 Tsunami simulation model for the 2004 Aceh event

Tsunami model for 2005 earthquake in Nias (the 2005 Nias Tsunami). The 2005 Nias tsunami is simulated with 2 (two) scenarios base on the configuration of the bathymetric and islands to see their effect to propagation, reflection and excitation of the waves

- Scenario-1 is real bathymetry and island near the rapture area as same bathymetric that used in the 2005 Aceh tsunami (Figure 2.a)
- Scenario-2 is consider no island near the rapture area (hypothetic bathymetry without Nias and Simelu Islands (Figure 3.a)

Both scenarios using the tsunami source as shown in Figure 3.b. This source is estimated base on the fault parameter from seismic analysis and verified with the GPS data (Natawidjaja et al, submitted to JGR). Tsunami pattern of Scenario-1 after propagated 10 and 120 minutes are shown Figure 3.c and 3.d respectively and the tsunami maximum (energy) distribution and travel time contour of scenario-1 and scenario-2 are shown in Figure 3.e and 3.f respectively. The results show that the 2005 Nias tsunami could not generated a big tsunamis as big as the 2004 Aceh tsunami because an initial tsunami of the 2004 Aceh tsunami located in deep waters but the 2005 Nias tsunami located in shallow waters and some part under Nias and Simeulu Islands.

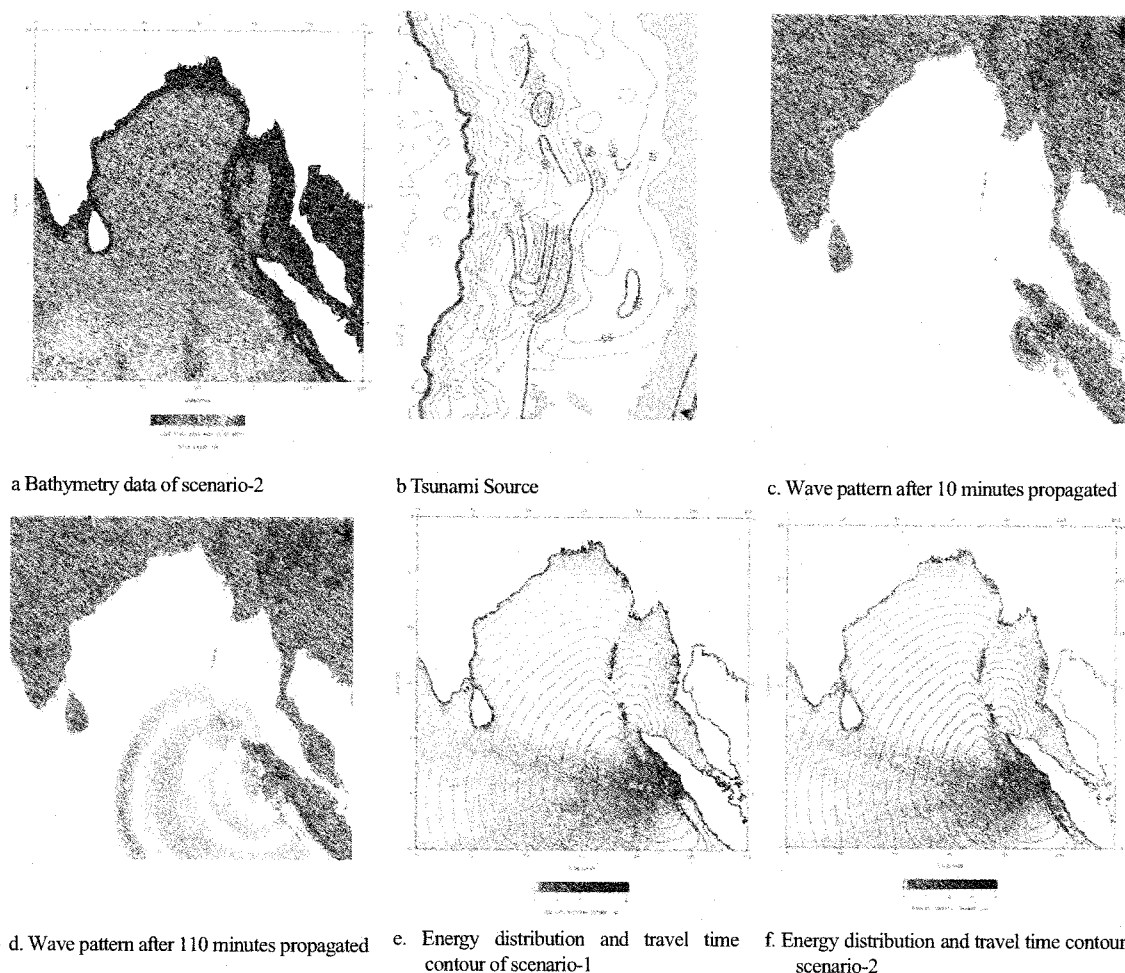


Figure 3 Tsunami simulation model for the 2005 Nias event

3.2. Tsunami Model for the 1797 Padang tsunami and the 1833 Bengkulu Tsunami

Tsunami model for 1797 megatrust events in Mentawai (The 1797 Padang tsunami). The 1797 Sumatran giant earthquake generated large tsunami that swept over Sumatran west coast. Historical notes indicate that tsunami height in Padang was 5 to 10 meters. We have developed the tsunami simulation based on the 1797 seismic source that we have modelled based on coral microatoll data are shown in Figure 4 (Natawidjaja et al, submitted to JGR). The results fit the historical data well. The bathymetry data and tsunami sources are shown in Figure 4.a and 4.b respectively. Figure 4.c shows the energy distribution and Figure 4.d,e,f, show the tsunami propagation. The time series of the 1797 tsunami height in Padang is shown in Figure.6 and the simulation of tsunami height and arrival time at several locations in west coast Sumatra are listed in Table1. The tsunami simulation shows that tsunami height in Padang could be as much as 9 meters (see Figure 6).

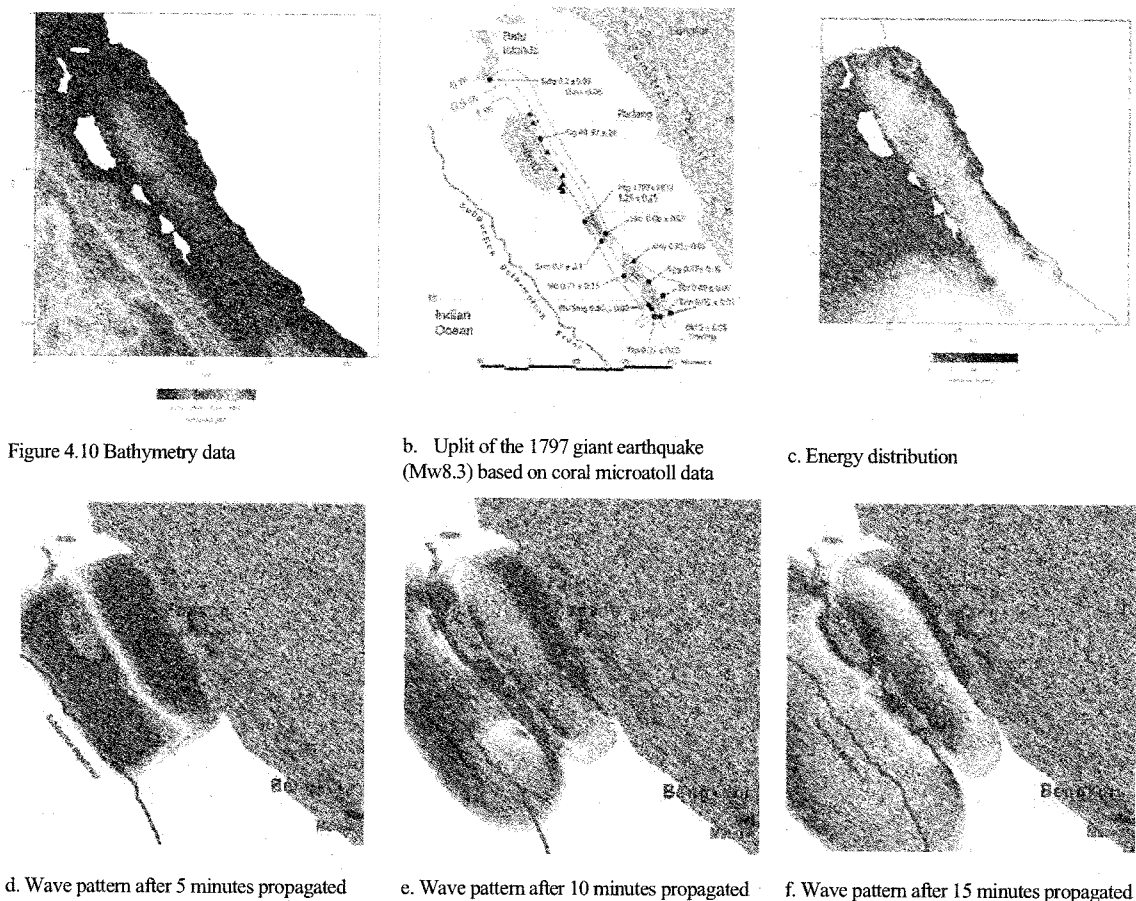


Figure 4 Tsunami simulation model for the 1797 event.

Tsunami Model for 1833 Megatrast events in Mentawai (the 1833 Bengkulu tsunami. We have also developed the tsunami simulation for the giant earthquake in 1833 in Pagai-Sipora region (Figure 5). The simulation is based on the 1833 rupture that we have modeled from coral microatoll data (Natawidjaja et al, submitted to JGR). The bathymetry data and tsunami sources from microatoll model are shown in Figure 5.a and 5.b respectively. Figure 5.c shows tsunami energy distribution and Figure 5.d,e,f show the tsunami propagations. The time series of the 1833 tsunami height in Padang is shown in Figure 6 and the simulation of tsunami height and arrival time at several locations in west coast Sumatra are listed in Table 1. The simulation shows that the 1833 event generates tsunami height about 3-4 meters in Padang (Figure 6 and Table 1), just as description in the historical notes. However, we will have to refine the tsunami simulation since it has not used the latest source model for the 1833 event.

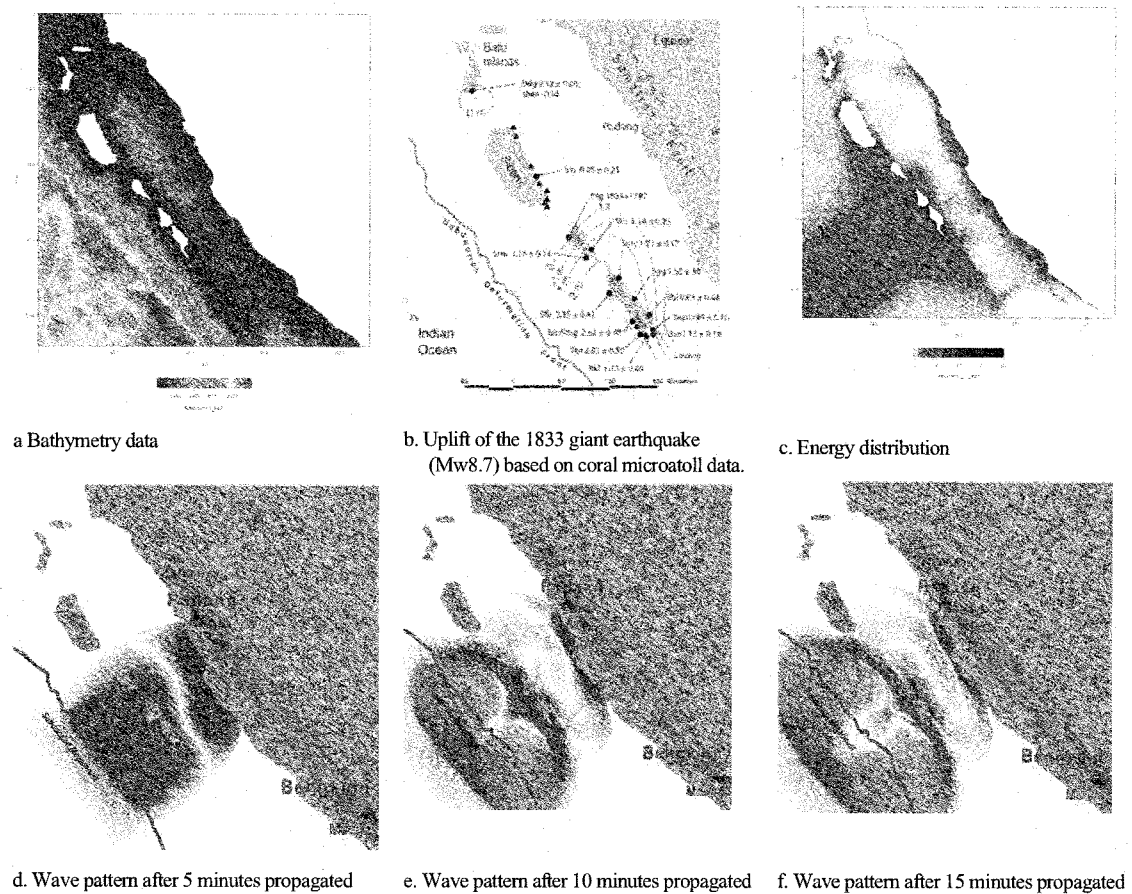


Figure 5 Tsunami simulation model for the 1833 event

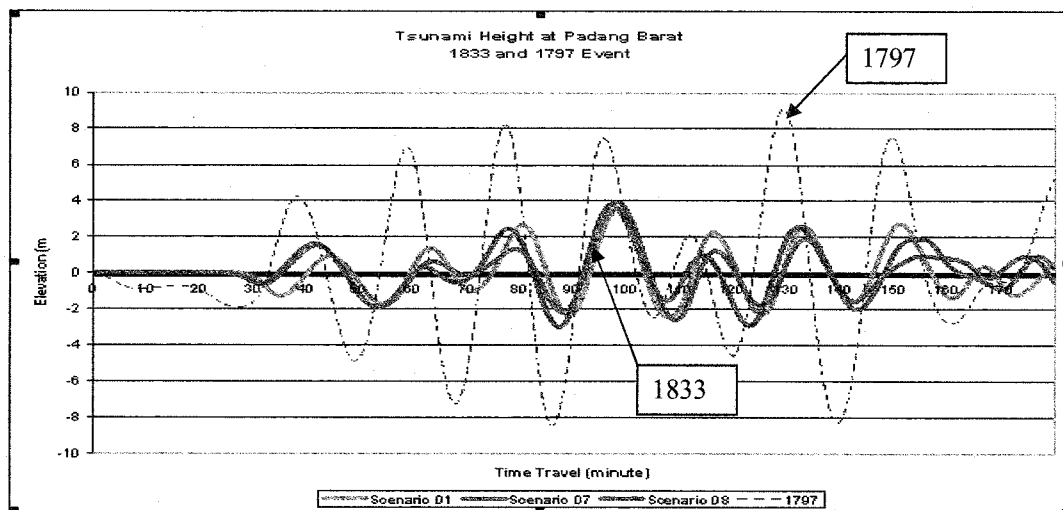


Figure 6 Estimated tsunami height in time series in Padang from the 1797 and 1833 events, modelled from seismic source models based on coral microatoll data.

Table1 Maximum tsunami heights and travel times at the several locations in the West Sumatra from tsunami simulation the 1833 and the 1797 events

Location	1833		1797	
	Maximum heights (m)	Travel time (mnt)	Maximum heights (m)	Travel time (mnt)
Pariaman	1.4	37	3.7	33
Padang Utara	2.2	39	5.2	37
Padang	3.9	42	9.0	38
Teluk Bayur	4.4	39	6.2	37
Painan	3.0	38	4.2	38
Bengkulu (a)	2.5	69	0.8	75
Bengkulu (b)	1.5	66	0.96	72
Manna	1.0	71	1.10	75

4. CONCLUSION AND RECOMMENDATION

Historical earthquake and tsunami show that the western coast of Sumatra is one of very front area. Sooner or later a big earthquake and tsunami will be attack this area, so need to analysis the evidences not only from coral microatolls, but also paleo-tsunami-sediment to estimate the earthquake and tsunami cycle.

Tsunami model of the 2004 Aceh event shows that the model still could not reconstructed the highest tsunami in Loknga, western part of Aceh, so need to refine the model based on the latest tsunami sources with considering slip distribution and using detail bathymetric and finest mesh size.

Tsunami model of the 2005 Nias event can simulate with reasonable result. These models (scenario-1 and scenario-2) show the effect of islands and shallow water depth give large contribution to reduce tsunami height. These models could not generated big tsunamis as big as the 2004 Aceh tsunami because an initial tsunami of the 2004 Aceh event is located in deep waters but the 2005 Nias tsunami located in shallow waters and some part of the rupture under Nias and Simeulu Islands.

The tsunami model of the 1797 shows that tsunami height in Padang could be as much as 9 meters, this results are well agree with the historical data. Then simulation of the 1833 event generates tsunami height about 3-4 meters in Padang, this also fit well with the description in the historical notes. However, we will have to refine the tsunami simulation since it has not used the latest source model for the 1833 event.

As these preliminary tsunami models are need to develop and improve the accuracy and then simulate inundation models for the big city along the west coast of Sumatra (i.e. Padang and Bengkulu) with multiple plausible earthquake scenarios. These tsunami simulations (and also historical tsunami data) are very usefully to improve the capabilities in defining the tsunami hazards for mitigation, and as input design parameter for engineering assessment to guide mitigation efforts.

Acknowledgements:

We would like to thanks to the Ministry of Research and Technology, Republic of Indonesia for funding our research trough RUTI Scheme, The Institute of Technology Bandung (ITB) through Riset Unggulan ITB and Study Program of Oceanography, ITB, Bandung for the research facilities. The first author would like to thanks to the Institute of Seismology and Volcanology (ISV), Hokkaido University, Japan, for the facilities and financial support during the first author is visiting and writing this paper at the ISV. Sincere thanks are extended to Professor Nobuo Shuto for his introduction to the field of tsunami when I first arrived in Tohoku University and my advisor Prof. Fumihiko Imamura (DCRC-Tohoku University) for his passion to discuss of my study. The authors acknowledge support from Tokyo Institute of Technology to present this paper.

References:

- Berninghausen, W.H. (1966), "Tsunamis and Seismic Seiches Reported from the Regions Adjacent to the Indian Ocean", *Bull. Seism. Soc. Am.*, 54, pp. 439-442.
- Berninghausen, W.H. (1969), "Tsunamis and Seismic Seiches of Southeast Asia", *Bull. Seism. Soc. Am.*, 59, pp. 289-297.
- Cox, D.C. (1970), Discussion of "Tsunamis and Seismic Seiches of Southeast Asia" by William H. Berninghausen, *Bull. Seism. Soc. Am.*, 60, pp. 281-287.
- Fauzi, R. McCaffrey, D. Wark, Sunaryo, and P. Y. Prih Harydi, (1996), "Lateral variation in slab orientation beneath Toba Caldera, northern Sumatra", *Geophys. Res. Lett.*, 23, 443-446.
- Fauzi, G. (1999): <http://www.gretchen.geo.rpi.edu/fauzi/rusak/txt/>
- Fitch, T. J., (1972), "Plate convergence, transcurrent faults, and internal deformation adjacent to Southeast Asia and the western Pacific", *J. Geophys. Res.*, 77(23), 4432-4460.
- Goto, C. and Ogawa, Y. (1992), "Numerical Method of Tsunami Simulation with the Leap-frog Scheme", Disaster Control Research Center, Faculty of Engineering, Tohoku University.
- González F., E. Geist, C. Synolakis, G. Crawford, B. Atwater, H. Latief, G.S. Prasetya, Y. Rizal (2005), "Tsunami Inundation Modeling and Mapping: Scenario-Based Hazard Assessment for Critical Coastal Urban Regions of Western Sumatra", a proposal to USAID.
- Hamzah, L., Puspito, N.T., and Imamura, F. (2000), "Tsunami catatlog and zones in Indonesia", *Journal of Natural Disaster Science*, v. 22, p. 25-43.
- Ibrahim, G., Untoro, M. Ahmad, and R. Hendrawan, (1989): Earthquake Statistics in Indonesia, Technical Report, Bandung Institute of Technology, Indonesia (in Indonesian).
- Imamura, F. (1995), "Tsunami Numerical Simulation with the Staggered Leap-frog Scheme (Numerical Code of TUNAMI-N1 and N2)", Disaster Control Research Center, Tohoku University, 33 pp.
- Ismail, S., (1989), "Tsunami in Indonesia", *Technical Report*, Meteorological and Geophysical Agency, Indonesia (in Indonesian).
- Lay, T., H. Kanamori, C.J. Amon, M. Nettles, S.N. Ward, R.C. Aster, S.L. Beck, S.L. Bilek, M.R. Brudzinski, R. Butler, H.R. DeShon, G. Eksrom, K. Satake, S. Sipkin, (2005), "The great Sumatra-Andaman earthquake of 26 December 2004". *Science*, 308: 1127-1133.
- McCaffrey, R., (1991), "Slip vectors and stretching of the Sumatran fore arc", *Geology*, 19, 881-884.
- Natawidjaya, D.H., (2002), "Neotectonics of Sumatran Fault and Paleogeodesy of the Sumatran Subduction Zone", *Doctor of Philosophy Thesis*, California Institute of Technology, Pasadena, California.
- Newcomb, K.R., and W.R. McCann (1987), "Seismic history and seismotectonics of the Sunda Arc", *Journal of Geophysical Research*, 92, 421-439.
- Sieh, K., S.N. Ward, D.H. Natawidjaya, and B.W. Suwargadi, (1999), "Crustal deformation at the Sumatran subduction zone", *Geophysical Research Letters*, 26 (20), 3141-3144.
- Utsu, T., (1992), "Catalog of Destructive Earthquakes in the World, 1500-1992", *Earthquakes Disaster Reduction Handbook*, International Institute of Seismology and Earthquake Engineering, Tsukuba Japan, pp. 1-24.
- Zachariasen, J., K. Sieh, F.W. Taylor, R.L. Edwards, and W.S. Hantoro, (1999), "Submergence and uplift associated with the giant 1833 Sumatran subduction earthquake: Evidence from coral microatolls", *Journal of Geophysical Research*, 104, 895-919.
- Zachariasen, J., K. Sieh, F.W. Taylor, and W.S. Hantoro, (2000), "Modern vertical deformation above the Sumatran subduction zone: Paleogeodetic insights from coral microatolls", *Bulletin of the Seismological Society of America*, 90 (4), 897-913.

PERFORMANCE AND DATABASE OF BUILDINGS IN THAILAND IN THE 2004 INDIAN OCEAN TSUNAMI

A. Ruangrassamee¹⁾ and P. Foytong²⁾

1) Assistant Professor, Department of Civil Engineering, Chulalongkorn University, Thailand

2) Graduate Student, Department of Civil Engineering, Chulalongkorn University, Thailand
fcearr@eng.chula.ac.th, ann_kung17@hotmail.com

Abstract: The 26 December 2004 Indian Ocean tsunami caused human loss and devastating damage to civil engineering structures along the west coast of southern Thailand. This damage was investigated with the goal of evaluating the performance of structures. Criteria for post-tsunami investigation were developed, and a database system was established to manage and present the data. A representative RC column's capacity to resist lateral forces was measured by a full-scale loading test to gain insight into the relationship between the observed damage and the actual structural performance.

1. INTRODUCTION

The tsunami caused human loss and devastating damage to civil engineering structures along the west coast of southern Thailand (TCLEE 2005 and Siripong et al. 2005). The damage ranged from zero for structures on higher ground to collapse for weak structures near the shoreline. A damage investigation was conducted to evaluate the performance of structures. These criteria, which were based on post earthquake evaluation, were designed to quantitatively evaluate tsunami-induced damage to buildings (AIJ 2000). An investigation form was used in the field to record damage data. A web-based database system was developed to manage and present these damage data and the corresponding photos. Damage data for 94 buildings are available on the website of the Center of Excellence in Earthquake Engineering and Vibration, Chulalongkorn University, Thailand. No database for the tsunami-induced damage to buildings in terms of damage or failure modes of structural components, design, and materials has been available so far.

To understand how a structural component resists lateral forces, a loading test was performed on an RC column that represents local construction practice. The test provided insight into the relationship between observed damage and actual performance.

2. FIELD DATA COLLECTION

To evaluate how buildings performed during the tsunami, a consistent format was used to gather basic structural information and record observed damage. Key aspects of the data collection are described below.

2.1 Location of Buildings

Building locations were measured by a portable global positioning system (GPS) receiver in the WGS84 datum. These locations are important for accessing buildings so a detailed investigation can be conducted later. Since it is time-consuming to measure the distance from a shoreline for each building in the field, GPS building locations are also useful for computing the distance from a shoreline by geographic information system (GIS) software.

2.2 Inundation Height

Because a tsunami usually leaves traces on the walls of most buildings, the inundation height for each building can be recorded. In this investigation, the inundation height was measured in reference to the ground floor.

2.3 Column and Beam Damage

Because columns are the primary members of a building, column damage can cause the whole building to collapse. Column damage was classified according to a damage index (DI) consisting of six categories, as shown in Table 1. The DI is based on the observed crack width in a column. Beam damage was classified according to four categories: no damage, cracking, spalling, and collapse.

Table 1 Column damage index DI (AIJ, 2000)

DI	Description
0	No cracks
1	Crack width < 0.2 mm; cracks are visible only at close range.
2	Crack width 0.2 mm to < 1.0 mm; cracks are obvious.
3	Crack width 1.0 mm to 2.0 mm; wide cracks with concrete spalling
4	Crack width > 2.0 mm; concrete spalling and exposed reinforcement
5	Buckling of reinforcement, crush of concrete core, or residual deformation are obvious.

2.4 Overall Damage

The overall damage was classified into four damage levels:

- a) no damage
- b) damage to secondary members (i.e., walls and roofs)
- c) damage to primary members, and
- d) collapse

Damage to primary members means that some columns or beams may crack or suffer some damage, but the whole structure does not lose its gravity-resisting capacity and is repairable.

3. DATABASE SYSTEM

A database system was developed to facilitate management of the collected damage data. The database is stored in Microsoft Access format and is interfaced with end users using Active Server Pages (ASP) which are server-side scripts developed by Microsoft. The records can be viewed, added, and deleted by any web browser, but only authorized users can add or delete records. Figure 1 shows a record accompanied by a photo. Damage data for 94 buildings are available on the website of the Center of Excellence in Earthquake Engineering and Vibration, Chulalongkorn University, Thailand at <http://evr.eng.chula.ac.th/earthquake/DamageSurvey/view.asp>. All of data required in the investigation form are also shown on the website.

In the database are 94 records of RC buildings; of these, 77 are in Kamala Beach (Phuket), and 17 are in Khaolak (Phang-Nga). Figure 2 shows the inundated area in Kamala Beach and the locations of the observed buildings. That area was inundated to a distance of about 600 m from the shoreline, and the locations of observed buildings range from the shoreline to the inundation boundary. Collapsed buildings were observed along the shoreline, whereas the buildings on higher ground suffered minor damage or no damage. Of the observed buildings, the greatest number were houses, most of which had one or two stories. Figure 3 shows the distribution of building damage. Notably, 77 out of 94 buildings suffered wall damage that was caused by the impact of the tsunami or debris.

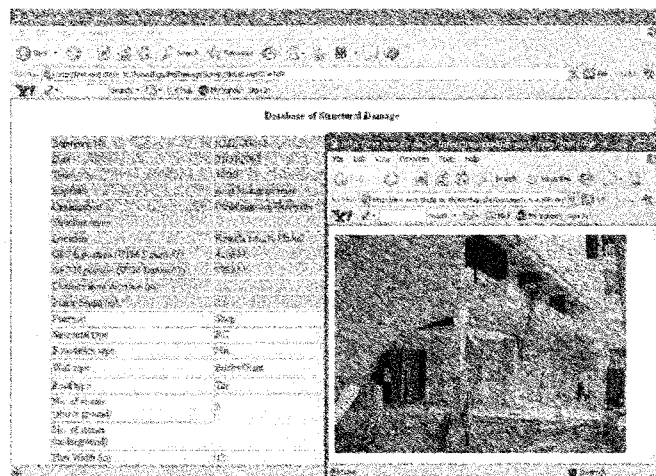


Figure 1 Sample page of the database record and an accompanying photo

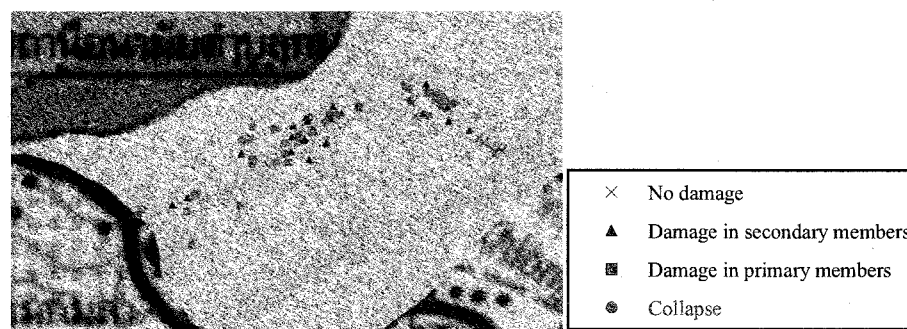


Figure 2 Locations of observed buildings in Kamala Beach, Phuket

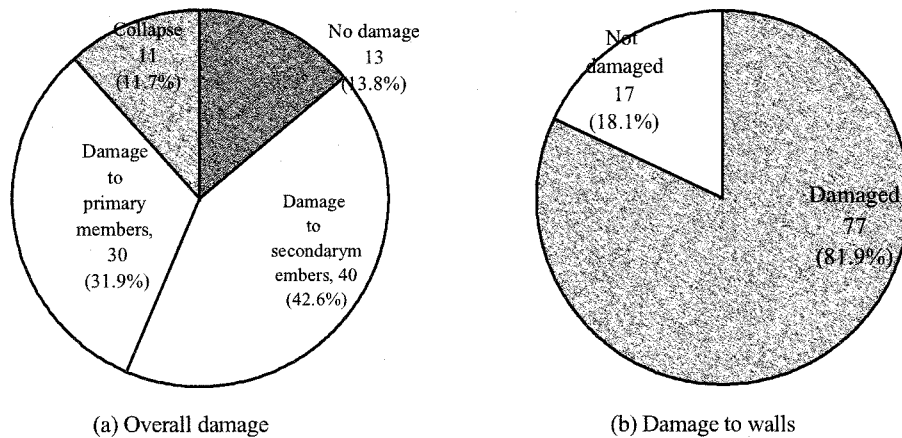


Figure 3 Distribution of damage to observed buildings

4. PERFORMANCE OF RC COLUMN UNDER LATERAL LOADING

In the buildings close to shorelines, most RC columns were damaged. In one-story and two-story buildings, columns whose section was 150 mm x 150 mm had DI values ranging from 0 to 5. To determine the lateral force capacity of this type of columns, a full-scale loading test was performed on a 150 mm x 150 mm RC column. The longitudinal reinforcement consisted of four 12-mm-diameter round bars. The lateral confinement was provided by rectangular ties made of 6-mm-diameter round bars equally spaced at 200 mm intervals along the column (Figure 4). The rectangular tie had a 90° hook at a corner, which is typical of local practice. The nominal yielding strength of a round bar is 240 MPa, and the strength of concrete on the test day was 17.4 MPa.

The column height in most buildings was about 2.6–2.8 m. The column specimen was set up by providing a footing at the base and applying a lateral load at 1.4 m above the base, resulting in a shear span ratio of 9.3. This represents an inflection point at the mid-height of the column. Axial force was applied to the column top by tension rods. The lateral load was monotonically applied by a 500-kN actuator under displacement control. The drift ratio that the crack pattern and crack width were recorded was evenly increased at intervals of 0.1% (for a drift ratio < 1.0%) and at intervals of 0.2% (for a drift ratio > 1.0%). The specimen was tested up to a drift ratio of 6.6%.

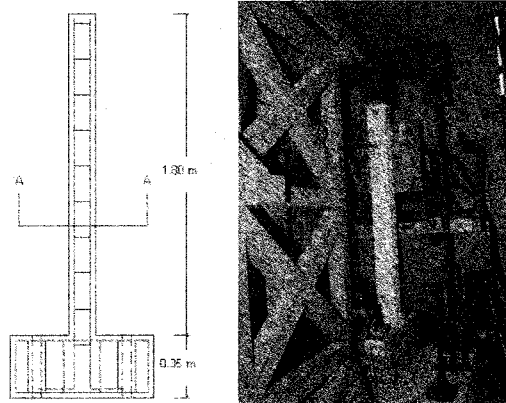


Figure 4 Setup for the full-scale loading test.

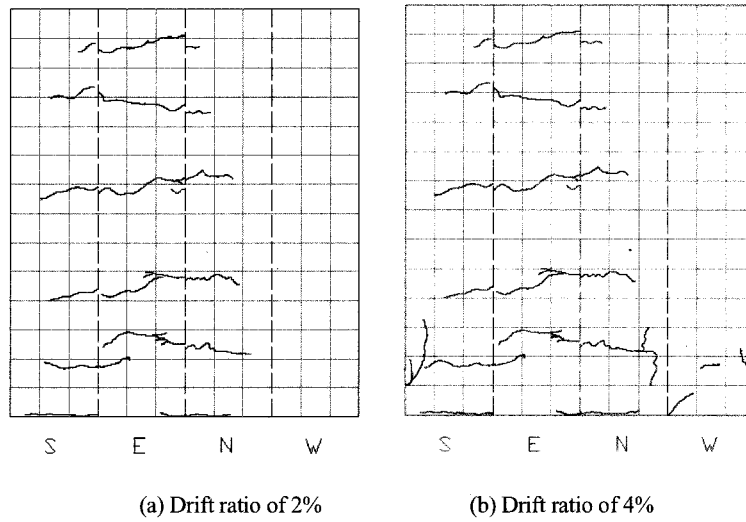


Figure 5 Crack patterns at different drift ratios

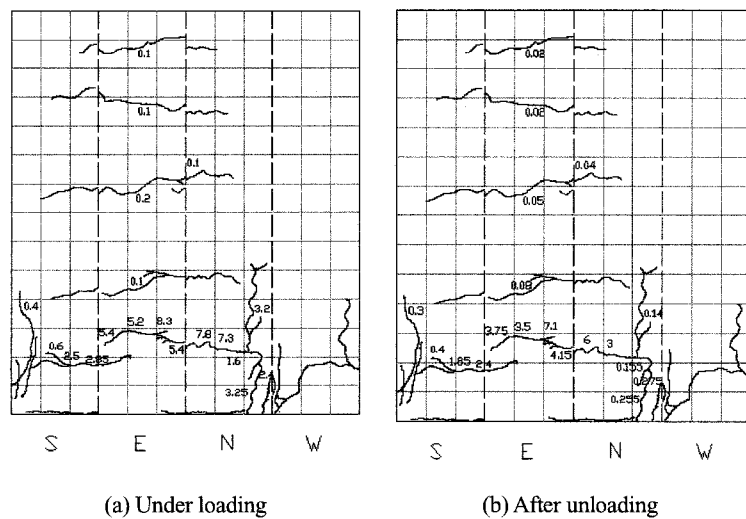


Figure 6 Crack widths at the final stage of testing

Since the actuator pushed the specimen to the west, horizontal tension cracks developed in the east face, and cracks extended to the north and south faces (Figure 5). At a drift ratio of 4%, cracks caused by concrete crushing were noticeable. Notably, even though the column is lightly confined by rectangular ties, no shear crack developed during the test. The slenderness of the column causes a moment to reach the moment capacity of the section before the shear capacity is reached. Longitudinal cracks became obvious at a drift ratio of 4%, indicating an onset of buckling of longitudinal reinforcement. In the investigation, the column DI was based on crack widths after unloading. The relation between crack widths under loading and crack widths after unloading is noteworthy. Figure 6 shows crack widths at a drift ratio of 6.6% under loading and after unloading. For crack widths < 2 mm, unloading causes a large percentage of crack closure.

Figure 7 shows the relation between the lateral force and the drift ratio. The maximum lateral force capacity is 6.9 kN at a drift ratio of about 3%. The lateral force drops to 80% of the capacity at a drift ratio of about 4.5%. Figure 8 shows how the maximum crack width depends on the drift ratio. The crack width increases exponentially with the drift ratio. At the maximum load corresponding to a drift ratio of 3%, the maximum crack width is about 1 mm.

In the post-tsunami investigation phase, crack width is one of the key parameters for identifying structural damage. Figure 9 shows the relation between the crack width and the normalized load which is the pre-peak lateral load normalized by the peak load. The crack width increases exponentially with a normalized load. The crack width C (mm) can be predicted as follows:

$$C = e^{-9.78+10\bar{L}} \quad (1)$$

where \bar{L} is a normalized load. One can estimate the probable applying load based on the measured crack width. And the probable load is a quantitative physical value for estimating damage. Notably, the crack width observed in the post-tsunami investigation is the crack width after unloading of tsunami forces. It is important to determine the relation between the crack width under loading and the crack width after unloading. Figure 10 shows the relation for the column at a drift ratio of 6.6%. The crack width after unloading C_{UL} (mm) may be predicted from

$$C_{UL} = 0.648C \quad (2)$$

Since the relation between the crack width under loading and the crack width after unloading was obtained at the final stage of the test when the column experienced a drift ratio of 6.6%, more study is required for other drift ratios.

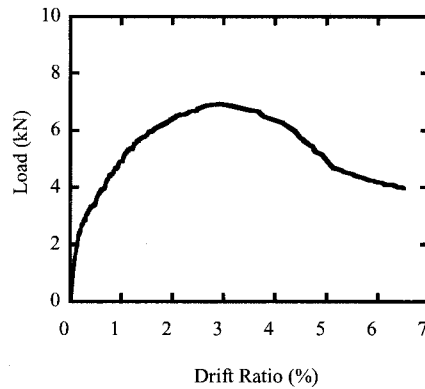


Figure 7 Lateral load versus drift ratio

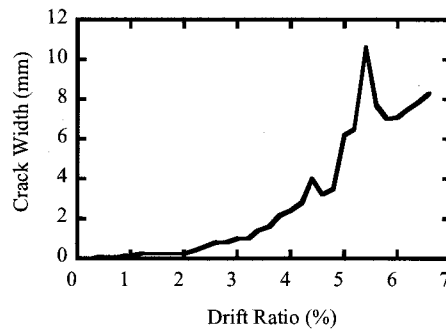


Figure 8 Maximum crack width versus drift ratio

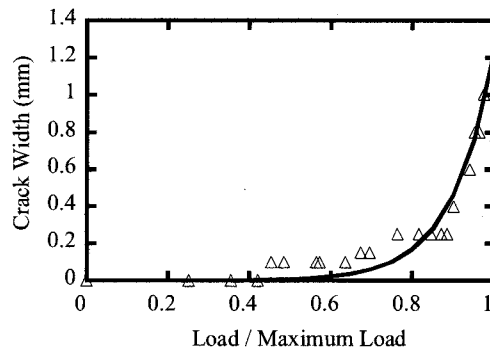


Figure 9 Maximum crack width versus normalized pre-peak load

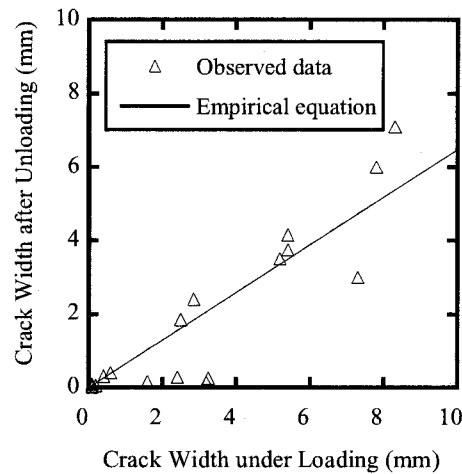


Figure 10 Crack width after unloading versus crack width under loading

3. CONCLUSIONS

The 26 December 2004 Indian Ocean tsunami caused human loss and devastating damage to civil engineering structures along the west coast of southern Thailand. The tsunami put a real test on tsunami resistance of buildings. Systematic and quantitative database is useful for evaluating the performance of buildings against tsunamis. A consistent format was developed and used to gather basic structural information and record observed damage. The damage to building components was categorized on the basis of general tsunami-induced damage observed. To facilitate data analysis and management, a database system was developed. The database was made available on a website for further utilization.

The damage to a typical RC column in the observed area was studied by performing a monotonic loading test. Since the crack width is an important parameter in post-tsunami investigation, its relation to the normalized load and the crack width under loading was clarified. On the basis of these findings, the observed damage can be quantified.

Acknowledgements:

The study could not have succeeded without the support of many people. The authors are grateful to the following groups: all the local people who shared the experience that they gained from their losses; Department of Marine and Coastal Resources, Ministry of Natural Resources and Environment; Department of Public Works and Town & Country Planning, Ministry of Interior Affairs; Public Works and Town & Country Planning Bureau in Phuket and Phang-Nga; Council of Engineers, Thailand; Chulalongkorn University, Thailand; Technical Lifeline Earthquake Engineering Committee, American Society of Civil Engineers; Earthquake Engineering Research Institute, USA; and the Institute of Civil Engineers, UK.

References:

- Technical Council on Lifeline Earthquake Engineering (TCLEE) (2005), "Sumatra-Andaman Islands Earthquake and Tsunami of December 26, 2004 - Lifeline Performance," American Society of Civil Engineers, TCLEE Monograph No. 29.
- Siripong, A., Choi, B. H., Vichiencharoen, C., Yumuang, S., and Sawangphol, N. (2005), "The Changing Coastline on the Andaman Seacoasts of Thailand from Indian Ocean Tsunami," *Proceedings of the Special Asia Tsunami Session at APAC 2005*, Jeju-do, Korea.
- Architectural Institute of Japan (AIJ) (2000), "Report on the Technical Cooperation for Temporary Restoration of Damaged RC School Buildings due to the 1999 Chi-Chi Earthquake," Tokyo, Japan.

PROBLEM AND IMPROVEMENT OF THE TSUNAMI WARNING SYSTEM

T. Takahashi

*Associate Professor, Department of Civil and Environmental Engineering,
Faculty of Engineering and Resource Science, Akita University, Japan
tomoc@ce.akita-u.ac.jp*

Abstract: To improve a disaster reduction system, reliable disaster information is required. In tsunami disaster, a tsunami warning system and a tsunami observation system should provide the important information for residents and administrations. Because Japan has been damaged by many tsunamis recurringly, the Japanese systems have been advanced. The tsunami warning system, however, has problems and they causes underestimation of tsunami disaster in some cases. The tsunami observation systems are not used effectively in the tsunami disaster reduction system. In this paper, the present tsunami warning system is reviewed and its problems are clarified. Furthermore, an improvement design of the tsunami warning system including the tsunami observation is discussed and its directivity is shown.

1. INTRODUCTION

On December 26, 2004 at 07:59 am (UTC 00:59 am), a giant earthquake occurred off the west coast of northern Sumatra, Indonesia. The giant earthquake generated a huge tsunami which was the third largest since 1900. This tsunami attack many countries in the Indian Ocean. With the exception of Indonesia, the Andaman Islands and Nicobar Islands, the tsunami, not the earthquake, caused all of the extensive damage. This was the greatest tsunami disaster in history.

In Japan, we had also many earthquake and tsunami disasters. Based on these disaster experiences, we have studied the tsunami disaster reduction system. Especially, the tsunami warning system and the tsunami observation system are advanced. Now we should support the tsunami disaster prevention in the Indian Ocean and other areas.

Structural mitigation measures such as a seawall, a tsunami breakwater and a water gate are effective in tsunami disasters. These hardware solutions, however, cannot completely prevent the damages. Non-structural mitigation measures are also necessary. One of the most effective software solutions is a tsunami evacuation. Residents must escape from coastal region right after an earthquake. To support the tsunami evacuation, simple and useful information about arriving tsunamis should be provided for the residents. And to provide the information, the tsunami warning system and the tsunami observation system play important roles. In the warning system, precise and prompt tsunami detection should be carried out, and observed tsunami data should be used to improve the tsunami disaster information.

In this paper, the present tsunami warning system and the observation system are reviewed and their problems are clarified. Furthermore, an improvement design of the tsunami warning system including the tsunami observation is discussed and its directivity is shown.

2. PROBLEM OF PRESENT TSUNAMI WARNING SYSTEM AND TSUNAMI OBSERVATION SYSTEM

2.1 The Relationship between Earthquake and Tsunami

Many geophysical phenomena, such as a volcano eruption, a submarine slide and a meteor impact, cause tsunamis. Most tsunamis, however, have been generated by earthquakes. Figure 1 shows a relationship between the earthquake and the tsunami. The earthquake generates a seismic wave and it propagates in the earth. The seismic wave causes damage to our society, but it is observed by a seismometer and we can study the mechanism of the earthquake using the data. When the earthquake is occurred in a sea area, it moves a seabed. This seabed displacement transfers sea water and generates a sea-surface change. It is a tsunami source.

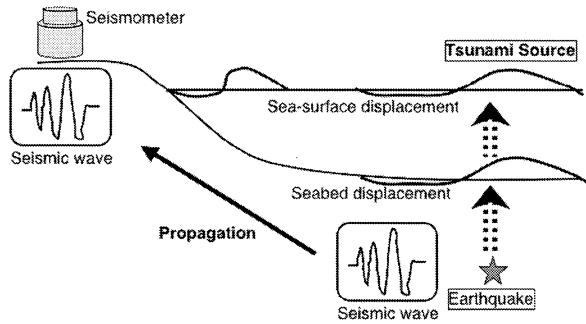


Figure 1 The Relationship between Earthquake and Tsunami

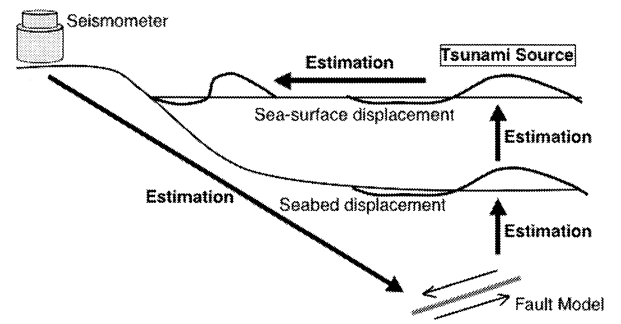


Figure 2 The Estimation Method of Tsunami in the Present Warning System

2.2 The Present Tsunami Warning System

Because many tsunamis are generated by large earthquakes, the present tsunami warning system is using a seismic wave to detect the tsunami generation as shown in Figure 2. The seismic wave observed by the seismometer on land has information about the hypocenter, and the fault model can be estimated by the seismic waves. The fault model gives a seabed displacement using the surface deformation models by Mansinha and Smylie (1971) and Okada (1985). If sea water above the seabed moves same as the seabed displacement, a sea surface displacement can be estimated. It is a tsunami source.

The tsunami warning system should provide information about tsunami waves arriving coastal areas and a numerical simulation of tsunami propagation is carried out. The tsunami source is used as an initial condition of the numerical simulation. A phenomenon of tsunami propagation is governed by the shallow water theory

$$\frac{\partial \eta}{\partial t} + \frac{\partial M}{\partial x} + \frac{\partial N}{\partial y} = 0 \quad (1)$$

$$\frac{\partial M}{\partial t} + \frac{\partial}{\partial x} \left(\frac{M^2}{D} \right) + \frac{\partial}{\partial y} \left(\frac{MN}{D} \right) + gD \frac{\partial \eta}{\partial x} + \frac{gn^2}{D^{7/3}} M \sqrt{M^2 + N^2} = 0 \quad (2)$$

$$\frac{\partial N}{\partial t} + \frac{\partial}{\partial x} \left(\frac{MN}{D} \right) + \frac{\partial}{\partial y} \left(\frac{N^2}{D} \right) + gD \frac{\partial \eta}{\partial y} + \frac{gn^2}{D^{7/3}} N \sqrt{M^2 + N^2} = 0, \quad (3)$$

Where η is the water surface elevation, M and N are velocity fluxes, D is the total depth, g is the gravity acceleration and n is the Manning's roughness coefficient. When the depth h is deeper than fifty meters, equations (2) and (3) are linearized as

$$\frac{\partial M}{\partial t} + gh \frac{\partial \eta}{\partial x} = 0 \quad (2')$$

$$\frac{\partial N}{\partial t} + gh \frac{\partial \eta}{\partial y} = 0. \quad (3')$$

Goto and Ogawa (1982) applied the Leap-Frog Scheme with the staggered grid to solve the governing equations. Especially, the upwind difference scheme was adapted for advection term in the shallow sea region.

2.3 The Problem of Present Tsunami Warning System

The present tsunami warning systems are operated by such institutions as the Japan Meteorological Agency (JMA), the Pacific Tsunami Warning Center (PTWC) and the West Coast and Alaska Tsunami Warning Center (WCATWC). These systems have been studied well and produced excellent results. However, there is a possibility of underestimation of a tsunami magnitude in some types of earthquake. The cases are an extra large earthquake like the 2004 Sumatra event, a tsunami earthquake like the slow earthquake and a large heterogeneity of tsunami source due to an asperity close to a coast.

Table 1 shows reports on the magnitude of the 2004 Sumatra Earthquake released by some institutes. WCATWC and PTWC issued an occurrence of the earthquake and warned a tsunami generation fifteen minutes after the main shock. Their swift analysis and reaction are excellent. The reported magnitude, however, was 8.0 and it was much smaller than the magnitude estimated now. M 9.0 was reported about 19 hours after the earthquake. This underestimation was not their failure and it shows an limitation of the tsunami detecting capacity of the present tsunami warning system. Especially, a difficulty in analyzing such the giant earthquake in a short time became obvious.

Table 1 A history of reported magnitude of the 2004 Sumatra Earthquake

Institute	Magnitude ^{*1}	Issued time (UTC) ^{*2}	Time after the event ^{*3}
WCATWC	M 8.0	12/26/2004 01:14	00:15
PTWC	M 8.0	12/26/2004 01:14	00:15
PTWC	M 8.5	12/26/2004 02:04	01:05
WCATWC	M 8.5	12/26/2004 02:09	01:10
USGS	M 8.5	12/26/2004 02:17	01:18
USGS	Mw 8.2	12/26/2004 02:23	01:24
Harvard Univ.	Mw 8.9	12/26/2004 05:26	04:27
Harvard Univ.	Mw 9.0	12/26/2004 20:02	19:03
WCATWC	M 9.0	12/27/2004 15:34	36:35
PTWC	M 9.0	12/27/2004 15:35	36:36

*1 "M" means that the type of magnitude was not shown in the e-mail.

*2 Where no issued time was shown in the e-mail, the posted time informed by the institute's SMTP server is used.

*3 The origin time of the earthquake is assumed to be 12/26/2004 00:59 UTC by USGS.

The underestimation for the giant earthquake was not only the magnitude but also the focal area of the earthquake. Because the seabed displacement is generated there, a reliability of the estimated tsunami source depends the focal area. Figure 3 shows the aftershock distribution of the earthquake by USGS and the region of aftershocks corresponds to the focal area. It was a extensive area of about one thousand kilometers from south to north along the Sunda Trench. However, right after the earthquake, the area was estimated as southern half area just close to Sumatra Island, and the actual area was studied after the tsunami arriving.

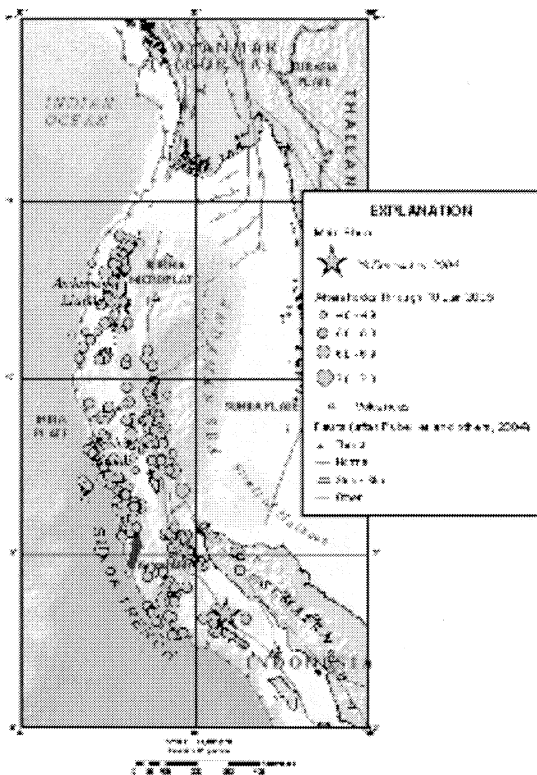


Figure 3 The Aftershock Distribution of the 2004 Sumatra Earthquake by USGS

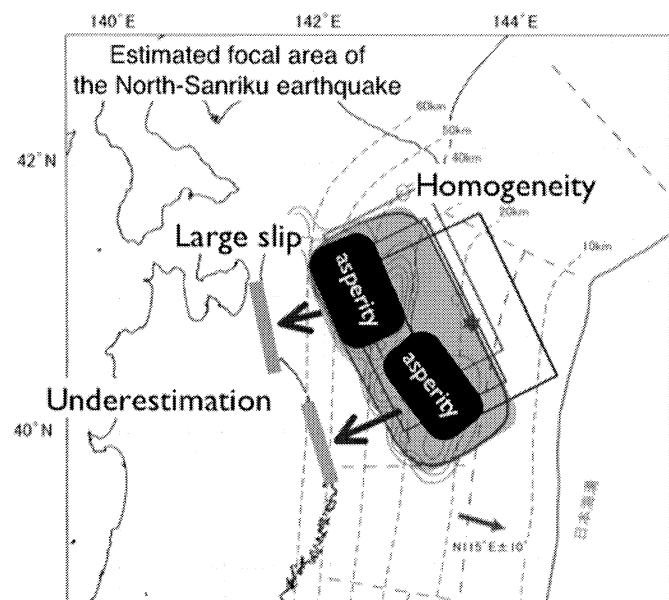


Figure 4 Underestimation due to the asperity

The second problem is underestimation for the tsunami earthquakes. The characteristic of the earthquakes is that its tsunami damage is much larger than a damage by ground motion. One of the typical tsunami earthquakes is the slow earthquake. The fault movement during the slow earthquake is very slow and it can not make a large ground motion. On the other hand, sea water movement is also slow and the focal area is large, then the tsunami is generated same as regular earthquakes. When the seismic wave is used to detect the tsunami source, its estimation of tsunami magnitude becomes underestimation.

Such underestimation of the present tsunami warning system is also occurred by the heterogeneity of tsunami source due to an asperity close to a coast. Figure 4 shows the estimated focal area off Sanriku, Japan. In the present tsunami warning system, a large rectangular area is assumed to move uniformly. However, if the asperities exist on the area, they generate larger tsunami waves there. Along the coastal area where the tsunami waves attack directly, the tsunami damage will be underestimated.

2.4 The Present Tsunami Observation System and its Problem

In Japan, the tsunami observation system has been studied well and has been established such as the Nationwide Ocean Wave Information Network for Ports and Harbours (NOWPHAS) operated by the Port and Airport Research Institute (PARI). Figure 5 shows the NOWPHAS network by Nagai (2002). The system has obtained many valuable data of past tsunamis and these data have contributed to a tsunami research. However, they are not yet sufficient for the tsunami generation detection, because they are located close to a coastal area and observe at each setup points. Many large tsunamis are generated along the plate boundary and their sizes get to a several hundred kilometers.

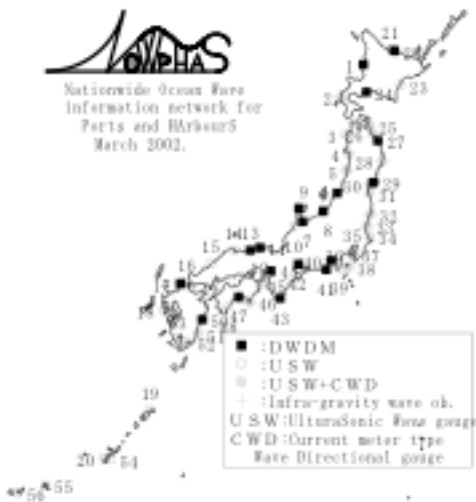


Figure 5 NOWPHAS Network
by the Port and Airport Research Institute

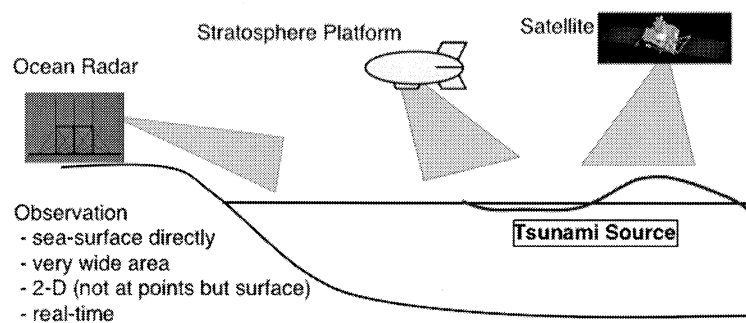


Figure 6 Tsunami Detecting System
Using Remote Sensing

3. IMPROVEMENT DESIGN OF TSUNAMI WARNING SYSTEM INCLUDING TSUNAMI OBSERVATION

There are many instructive systems in the tsunami disaster reduction and its research as mentioned above. They, however, have some problems and need to improve the tsunami detection performance for the advancement of tsunami disaster reduction. Because tsunamis are huge phenomena occurred far from coasts, it is important to observe a very wide area and measure a sea surface directly. Furthermore, the real-time and two-dimensional sensing is necessary to comprehend whole tsunami source and its propagation.

To realize these functions, a remote sensing technique should be applied. As the remote sensing platform to detect tsunamis, ocean radar, a stratosphere platform and an artificial satellite should be applicable as shown in Figure 6. Especially, the ocean radar is the most promising, because it has many advanced characteristics. The ocean radar has already been put to practice use in an ocean current observation. The United States has established many ocean radar and has a plan to increase the radar and to make its network. In Japan, some ocean radar has also been used to observe ocean currents. The second advantage of the ocean radar is a commercial price. The regular ocean radar can be purchased several hundred thousand US dollar. It is inexpensive compared to other observation systems. The largest advantage is about the maintenance of the system. Because the ocean radar sites on land and it is easy to maintain itself. When some troubles are happened, the easy access gives a prompt restoration. The disaster reduction system is required a stable operation.

The ocean radar can be associated with the NOWPHAS Network. Because NOWPHAS observes

velocities and water surface elevations at 54 points around the Japanese coast. These data are more accurate than the ocean radar's measurements and NOWPHAS data can improve a precision of the ocean radar data.

This proposed system is not designed to replace the present system, and it should be supplemented. In the disaster reduction system, a redundancy is important and it can actualize a robust system.

4. CONCLUSIONS

The present tsunami warning system and the observation system are reviewed and their problems are shown. Based on the problems, the improvement design of the tsunami warning system including the tsunami observation is proposed. It is the tsunami detecting system using remote sensing. Especially, the ocean radar has many advantages compared to other observation methods. This design, however, is still a concept stage and needs further research to realize the system.

References:

- Mansinha, L. and Smylie, D. E. (1971), "The Displacement of the Earthquake Fault Model", *Bulletin of the Seismological Society of America*, **161**, 1433-1400.
- Okada, Y. (1985), "Surface Deformation due to Shear and Tensor Faults in a Half-Space", *Bulletin of the Seismological Society of America*, **75**, 1135-1154.
- Goto, C. and Ogawa, Y. (1982), "Numerical Method of Tsunami Simulation with the Leap-Frog Scheme", Department of Civil Engineering, Tohoku University, translated for the TIME Project by Shuto, N.
- Nagai, T. (2002), "Development and Improvement of the Nationwide Coastal Wave Information Network", *Techno-Ocean 2002*, TI-1-2.

EARLY TSUNAMI FORECASTING USING REAL-TIME OFFSHORE OBSERVATORIES

H. Matsumoto¹⁾ and H. Mikada²⁾

1) Research Scientist, Deep-Sea-Research Dept., JAMSTEC, Japan

*2) Lecturer, Dept. Civil and Earth Resources Engineering, Kyoto University, Japan
hmatsumoto@jamstec.go.jp, mikada@kumst.kyoto-u.ac.jp*

Abstract: Tsunami early warning systems have been needed for those regions that have not experienced devastating tsunami disasters, such as the 2004 Indian tsunami. On 5 September 2004, two moderate-to-large earthquakes (M6.9 and M7.4) took place off Kii-peninsula of central Japan with 5 hours time interval, and both the earthquakes generated tsunamis affected along the coast nearby. We could successfully obtain water pressure fluctuations during the series of the earthquake by the offshore cabled observatory deployed off Muroto, approximately 200 km west of the epicenters, and we could resolved the tsunami signals obviously from the acquired dataset constraining by the tsunami computation. As a result, the offshore real-time cabled observatory could detect the tsunami waveforms 20 minutes before the first tsunami arrival at Muroto, the nearest coast line to the observatory. From a viewpoint of early tsunami forecasting and its warning strategies, the offshore-cabled observatory at Muroto would surely have a potential use for future regional tsunami disaster mitigation. We report the offshore tsunami observation, and then we show an offshore-cabled observatory can extremely contribute to the tsunami warning systems.

1. INTRODUCTION

The recent Sumatra-Andaman Sea earthquake has impacted us to be reminded an importance of tsunami warning. Offshore tsunami observatories have been established, that are including GPS buoy sensors at the sea surface, pressure sensor on the seabed telecommunicating to the surface buoy, and high frequency (HF) ocean radars on the coast. An offshore cabled observatory is a permanent observatory on the seabed, which is for the first deployed off Omaezaki, Japan in 1978. After then, similar systems have been established off Boso, off Izu peninsula, off Sagami, off Sanriku, off Muroto, and off Kushiro, covering seismogenic zones around Japan. Ocean bottom seismometers (OBSs) and tsunami meters (or pressure sensors) connecting by a submarine cable are monitoring seismic activities around the seismogenic subduction zone and detects precursory of subduction earthquakes and earthquake-accompanied tsunamis.

Japan Agency for Marine-Earth Science and Technology (JAMSTEC) has deployed an offshore cabled observatory off Muroto in 1997 (Fig. 1), followed by that off Kushiro-Tokachi, Hokkaido in 1999. In the meantime, two moderate-to-large earthquakes (M6.9 and M7.4) took place off Kii-peninsula of central Japan, and we could obtain offshore tsunami waveforms. Scientific uses of its waveforms such as geodetic and seismological purposes have been done by several groups (Baba *et al.*, 2005; Matsumoto and Mikada, 2005; Satake *et al.*, 2005). In the present paper, we report tsunami observation offshore, and we describe some notices for cabled observatory to use as an early tsunami warning system.

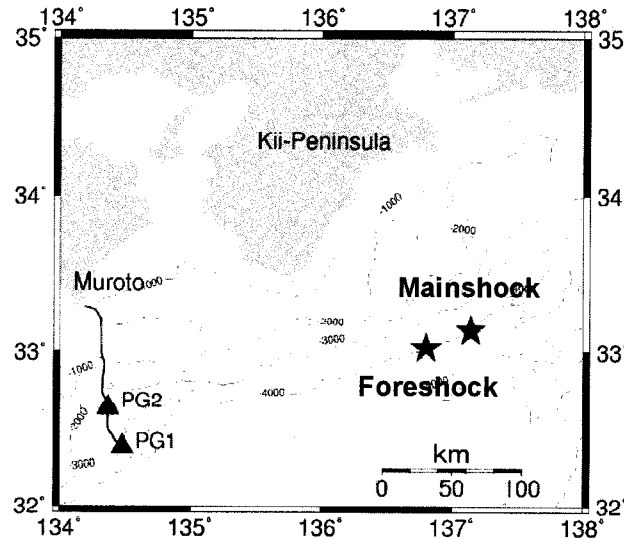


Figure 1 Location of the epicenters of the 2004 off Kii-Peninsula earthquakes. Stars indicate the epicenters of the fore- and the main-shocks. Triangles represent the ocean-bottom pressure gauges in the off Muroto cabled-observatory system, which are connected with the optical fiber cable (red line).

2. OFF KII-PENINSULA, JAPAN EARTHQUAKES OF 5TH SEPTEMBER 2004

Two earthquakes took place at 10:07 UTC and 14:57 UTC on 5 September 2004 off Kii-peninsula SW Japan, whose magnitude were estimated by 6.9 and 7.4, respectively. Two foci were determined to be 38 km and 44 km by Japan Metrological Agency (JMA), indicating both of them were intra-plate type earthquakes. The first earthquake of M6.9, followed by the second M7.4 earthquake took place about 40 km west. And its recurrent time was about 5 hours. We call these series of earthquakes as the foreshock and the mainshock hereafter (Fig. 1).

The seismic intensity in JMA scale during the foreshock was recorded by between I and V-, while the first tsunami warning was issued at 10:14 by JMA along the Pacific coast in SW Japan and expanded to Izu-Ogasawara Islands at 11:15. According the JMA report, some tide gauges observed tsunami signals from the foreshock. The highest tsunami wave observed by the tide gauge was 0.5 m at Kozu Island at 11:05. After the following sea surface movement, all of tsunami warnings were cancelled at 12:15.

For the mainshock occurred at 14:57, on the other hand, the largest seismic intensity was also V-, and JMA issued tsunami warning along the Pacific coast again at 15:01 for a few hours. The first arrival of tsunami was observed at the south of the Kii-peninsula at 15:17, its height was 0.9 m. After a few hours, all of warnings had been withdrawal. Detailed report of the tsunami was described in Koike *et al.* (2005).

3. OFFSHORE OBSERVATORY OFF MUROTO AND TSUNAMI DETECTION

Two pressure gauges, PG1 and PG2 are deployed at the water depth of 2340 m and 1555 m, respectively. These pressure gauges are located approximately 250 km from the epicenters of the Kii-peninsula earthquakes (Fig. 1). Figure 2 shows the observed pressure waveforms during the fore- and the main-shocks at PG1 and PG2. Significantly large-amplitude water pressure fluctuations were recorded at the time of the earthquakes because of the disturbances due to the incident seismic waves. Since the observed water pressures contain these high frequency noises during the earthquakes,

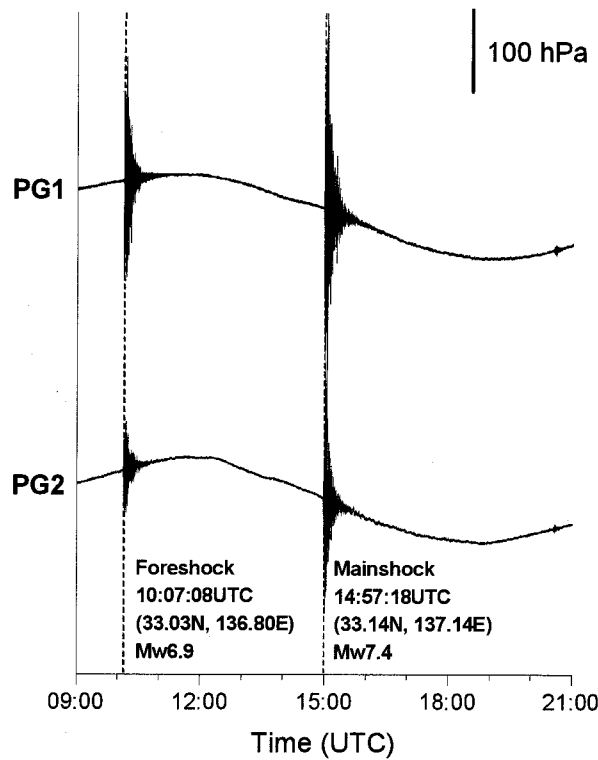
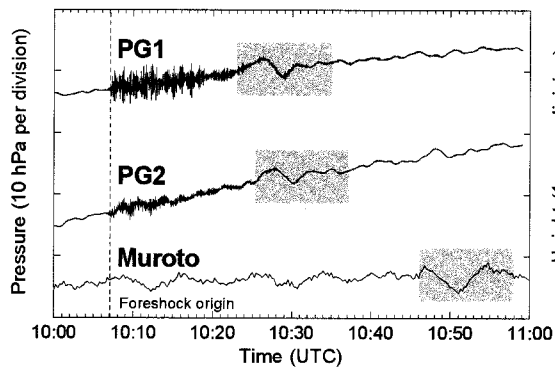


Figure 2 Pressure fluctuations at PG1 and PG2 during the series of the 2004 off Kii-peninsula earthquakes. The foreshock occurred at 10:07:08 UTC with its moment magnitude Mw 6.9, followed by the Mw7.4 mainshock at 14:57:18 UTC. Full water pressure waveforms have been recorded during the earthquakes.

(a) Fore-shock



(b) Main-shock

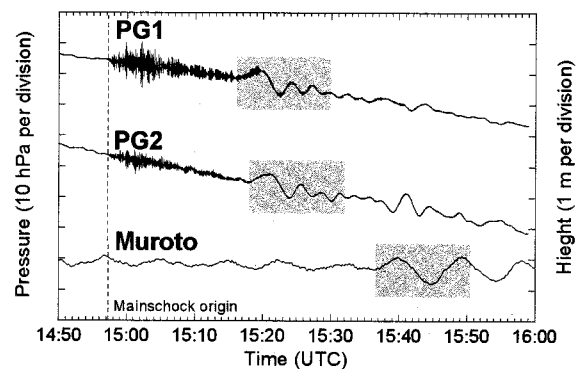


Figure 3 Water pressure waveforms applying the moving-average at 60 s (black lines) for (a) the fore-shock and (b) the main-shock (in hecto-pascal). Tidal waveforms at Muroto (blue lines) are also shown (in meter). Vertical dashed lines represent the origin time of the earthquakes. Shaded regions represent the first arrival tsunami detected. The first tsunami arrived at the offshore pressure gauges at 10:23 ~ and 15:16 ~ for the fore- and the main-shocks, respectively. The amplitude of tsunami by pressure gauges is less than 10 hPa (ca. 10 cm in water level), while the tsunami amplitude at Muroto is 0.5 m to 1 m by amplifying at the coast.

Table 1. Fault parameters of the fore- and the main-shocks

Fault parameters	Foreshock	Mainshock
Depth (km)	15.0	15.6
Strike (deg.)	71	135
Dip (deg.)	56	40
Rake (deg.)	75	123
Length (km)	50	70
Width (km)	30	40

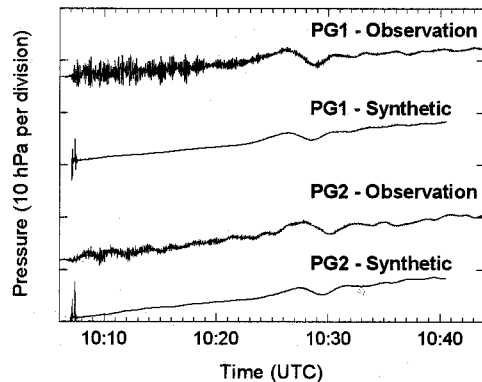
we attempt to remove them in the application of moving average at 60 s to the original dataset. The same procedure to remove seismic noise and to detect tsunami signal has been done by Hino *et al.* (2001) for a dataset from a cabled observatory at the off Sanriku, Japan earthquake in 1998. Two time series of water pressure during the fore- and the main-shocks at PG1 and PG2 thus derived are shown in Fig. 3. Although the observed waveforms are still accompanied by the large amplitude astronomical tidal waves and the high frequency seismic pressure vibrations, the tsunami components are visible in the waveforms. Long-period signals that could be regarded as tsunamis with periods of approximately 6 min and 7 min at the fore- and the main-shocks, respectively were derived in the waveforms.

We perceive that the first tsunami signals arrived at 10:23 and 10:25 at PG1 and PG2, respectively for the fore-shock, and at 15:16 and 15:18 at PG1 and PG2, respectively for the main-shock. We could detect the first arrivals for 20 min after the origin time of the earthquake. According to JMA report, the first tsunami was observed at 10:48 and 15:37 at Muroto that is the nearest tidal gauge station to PG2, i.e., the first tsunami arrived at Muroto 40 min after the earthquake. Thus, the cabled observatory could detect the first tsunami 20 min before the arrival at the coast station. For both PGs, the tsunami begins with a flood motion. Peak-to-peak amplitude of the observed tsunamis are to be approximately 4 hPa and 7 hPa at the fore- and the main-shocks for both PGs after the application of a 60 s moving average to the originals. Since 1 hPa in water pressure change corresponds to 1 cm in static water column, the observed peak-to-peak tsunami amplitude at the spots where PGs deployed could be estimated to be ca. 4 cm and 7 cm at the fore and the main-shocks, respectively, while the tide gauge at Muroto recorded peak-to-peak tsunami amplitude of about 0.5 m and 1 m at the fore- and the main-shocks, respectively.

4. NUMERICAL MODELLING OF PRESSURE WAVEFORMS

We computed pressure waveforms from the seismic fault model. The assumptions for the simulation are follows. We carried out the dynamic tsunami modeling presented by Ohmachi *et al.* (2001), in which the initial condition of the tsunami excitation caused due to dynamic motion of the ocean-bottom. Compressible ocean water as well as absolutely rigid ocean-bottom is assumed in the tsunami computation. We also computed the astronomical tidal wave using a method given by Matsumoto *et al.* (2000), and added it to our synthetic pressure waveform calculations. For building the synthetic pressure waveforms, we use the static vertical deformation of the ocean bottom estimated from the fault parameters shown in Table 1, and provide it to the bottom of water layer as a ramp-time

(a) Fore-shock



(b) Main-shock

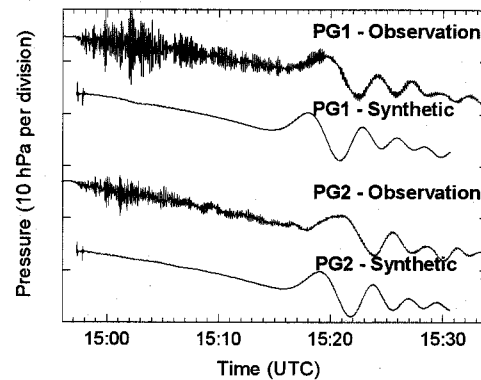


Figure 4 Comparison of the observed and computed pressure waveforms at PG1 and PG2 during (a) the foreshock, and (b) the mainshock. Black and red lines represent the observed and synthetic waveforms, respectively.

function with a 30 s rise-time as in the estimation of source-time function of the earthquake given by Yamanaka (2004). Although more realistic seismic source space-time functions may be employed in the computation, there is no difference in the simulation results for the tsunami component caused by the seismic faulting with its source time function of 30 s duration time (Matsumoto *et al.*, 2004). Hence, this assumption can be applied. To calculate water pressure, a finite different method (FDM) of the Navier-Stokes equation is numerically solved. The grid size are 1 km and 0.5 km in horizontal and vertical directions, respectively. The time step for the computation is 0.25 s to satisfy the stability criteria of the finite different method.

The synthetic pressure waveforms from the fault model are compared to the observation at PGs (Fig. 4) for the fore- and the main-shocks. At the beginning of the synthetic pressure waveforms, two pulses appear. These are caused by the very small deformation at PGs. The amplitudes of the tsunami components are computed from 10:25 and 15:15 for the fore- and the main-shocks. A few centimeters of the tsunami signals could be reproduced by the computations. Amplitudes of the tsunami signals are fit to the observations. Arrival times of the synthetics, however, are 1 to 2 min earlier than that of the observation. Some discrepancies between the observation and synthetic are still remaining, e.g., in arrival time, a simple 60 s moving average can introduce the tsunami signal, which can be done in real-time.

5. CONCLUSIONS

We report that two pressure gauges off Muroto successfully recorded water pressure fluctuations for a foreshock and a mainshock of the off Kii-peninsula earthquake of 5th September, 2004. Although there are still discrepancies with respect to the tsunami arrival time between the observed and synthetic waveforms for both mainshock.

The probability of the next megathrust Tonankai or Nankai, Japan earthquake taking place in the coming 30 years have been estimated more than 50%. The latest Tonankai and Nankai earthquakes about 60 years ago took place near the present sources, and we predict that the following tsunami inundates the southern coast of the SW Japan causing thousands of casualties.

Although the number of the permanent observatories of pressure gauges offshore is now very few, about 10 instruments installed around Japan, they could be used as a constraint to identify a fault plane

from two nodal planes in the source mechanism of off-shore earthquakes. Since high-precision water pressure measurements on the seafloor in the offshore detected the tsunami in 20 min before the arrival to the shore for the studies earthquake that took place beneath the central Nankai seismogenic zone, it might be proven that the offshore real-time cabled system off Muroto has a potential to be used in the tsunami disaster mitigation at the forthcoming Tonankai earthquake that could take place near the present tsunami sources.

Acknowledgements:

We used pressure gauges' dataset distributed by Submarine Cable Data Center, Japan Agency for Marine-Earth Science and Technology (JAMSTEC). Tide gauge record at Muroto was provided by Japan Meteorological Agency (JMA).

References:

- Baba, T., P. R. Cummins and T. Hori (2005), "Compound fault rupture of the 2004 Off Kii-Peninsula earthquake (M 7.4) inferred from tsunami waveform inversion with a new technique," *Earth Planets Space*, 57, 167-172.
- Hino, R., Y. Tanioka, T. Kanazawa, S. Sakai, M. Nishino, and K. Suyehiro (2001), "Micro-tsunami from a local interplate earthquake detected by cabled offshore tsunami observation in northeastern Japan," *Geophys. Res. Lett.*, 28, 3533-3536.
- Koike, N., T. Takahashi, K. Imai, Y. Tanioka, Y. Nishimura, K. Harada, S. Suzuki, K. Fujima, Y. Shigihara, Y. Namegaya, and S. Koshimura (2005), "Tsunami run-up heights of the 2004 off the Kii peninsula earthquakes," *Earth Planets Space*, 57, 157-160.
- Matsumoto, H., H. Mikada, T. Ohmachi, and S. Inoue (2004), "Tsunamis caused by slow seismic fault rupturing," *Ann. J. Coast. Eng. JSCE*, 51, 281-285 (in Japanese).
- Matsumoto, H. and H. Mikada (2005), "Fault geometry of the 2004 off the Kii peninsula earthquake inferred from offshore pressure waveforms," *Earth Planets Space*, 57, 161-166.
- Matsumoto, K., T. Takanezawa, and M. Ooe (2000), "Ocean tide models developed by assimilating TOPEX/POSEIDON altimeter data into hydrodynamical model: A global model and a regional model around Japan," *J. Oceanography*, 56, 567-581.
- Ohmachi, T., H. Tsukiyama, and H. Matsumoto (2001), "Simulation of tsunami induced by dynamic displacement of seabed due to seismic faulting," *Bull. Seism. Soc. Am.*, 91, 1898-1909.
- Satake, K., T. Baba, K. Hirata, S. Iwasaki, T. Kato, S. Koshimura, J. Takenaka, and Y. Terada (2005), "Tsunami source of the 2004 Off-Kii Peninsula earthquakes inferred from offshore tsunami and coastal tide gauges," *Earth Planets Space*, 57, 173-178.
- Yamanaka, Y. (2004), "Offshore Southeast of the Kii Peninsula Earthquakes," *EIC Seismological Note*, 152 and 153, (in Japanese).

Numerical Simulation of Tsunami Inundation in Urban Area

T. Hiraishi

*Head, Wave Division, Port and Airport Research Institute, Japan
hiraishi@pari.go.jp*

Abstract: The population and property in urban area facing to water front rapidly increases these days. Meanwhile the probability that a huge tsunami occurs in the Pacific Earthquake Rim area become very high. The huge damage might be generated in such urban coastal area when a gigantic tsunami attacks. The development of high accurate simulation model for tsunami inundation is needed because the tsunami mitigation like the establishment of evacuation route in the city should be planned with high accuracy. The paper describes a newly developed simulation model to estimate the inundation depth and speed of tsunami in the urban area.

1. INTRODUCTION

The 2004 Indian Ocean Earthquake Tsunami caused the gigantic hazard in the coastal areas. The tsunami hazard mitigation is necessary to reduce the human and housing damage in a future tsunami. Japan has been attacked by so many tsunamis in her history. The 1983 Nihonkai Earthquake Tsunami and the 1993 Hokkaido Nansei-oki Earthquake Tsunami left the devastated urban and fishery harbors and ruin villages. These tsunamis attacked the relatively populated areas where the residential houses and urban facilities are implemented with high density because of its concentrated property. The tsunami hazard risk, therefore, may vary according to the level of urbanization in the target areas. In Japanese cost, the urbanization in reclaimed lands and former beaches are carried out, while the probability of tsunami attack becomes higher because of the short return period.

The urbanized coastal areas usually have the high-rise building and underground facilities like parking lots, electric system and water suppliers etc. When tsunami inundate into the city area, such underground facilities become very risky because the tsunami flow may inundate from the ground entrance. We have a recent remarkable example of water inundation in underground floors in Masan city, Korea (Yasuda et al., 2004) in case of storm surge disaster. The underground floors were completely flooded even if the ground inundation depth was less than 50cm in the case. We should consider about the similar inundation case due to tsunami attacking a coastal urbanized area. The numerical expectation of ground flow also should be done in order to estimate the accurate tsunami flow speed on surface ground. The paper describes the physical and numerical experiment on tsunami inundation in a coastal urbanized area with an underground parking facility.

2. NUMERICAL MODEL

The nonlinear hydrodynamic effects like wave breaking, wave-structure interaction and

overflow should be estimated with high accuracy in the model to evaluate the flow propagation on the surface and underground spaces. The numerical model considering the both layer of water and air is suitable to represent the air bubble motion and air splash from a gap between water surface and board. The Multi-interfaces Advection and Reconstruction Solver (MARS-method)(Kunugi, 1997) is applied to estimate such water-air interaction in urban structures. The original 3-D flow model to calculate the Navier-Stokes model was improved the model to apply the wave variation in harbor with porous wave energy absorbing facilities Hiraishi et al. (2003).

Figure 1 shows an example of computational results by the MARS method. The horizontal distribution of water surface elevation at face of slit caisson type sea wall is indicated in the figure. The model is applicable to evaluate the variation of inundated water elevation on ground and in an underground space.

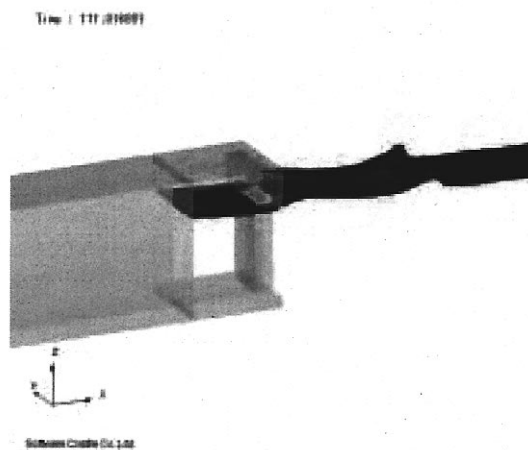


Figure 1 Water surface at sea wall in MARS-method

3. EXPERIMENTAL MODEL

As the target for study on flooded water in urban cities, the Port Side Zone in Yokohama city is employed. The area has been newly developed as an urban complex composed of high-rise apartment and office buildings. It faces to Tokyo-bay in which the occurrence probability of tsunami and storm surge is high and the risk analysis for disaster is urgently necessary. An underground public parking space is located in the center of target city. It is applicable to the model space in which the flow speeds and inundated depth variation is analyzed. **Figure 2** shows the bird-view image of the target urban area. The underground parking facility has the three flows and the slope is located in the entrance.

In the experiment, the model of target area with 1/50 scale is installed inside a new basin. The basin is named “Intelligent Basin for Maritime Environment”(The Port and Airport Research Institute) and equipped with the multi-directional wave and current generator. **Figure 3** shows the plane view of hydraulic model in the wave basin. The city model is implemented along the left side wall in the basin. The profile of overflowing water inside the target area is measured in water elevation and current meters. The duration for inundation is indicated in the contour maps in the figure.

The water level and flow velocity condition at the boundary of land and sea should be derived from the numerical simulation for tsunami propagation in the outer sea. The power and location of sea bed failure due to earthquake should be assumed on basis of the historical record of earthquakes and risk analysis. The failure model for 1923 Kanto Earthquake is

modified and the location of failure is varied along the trench on sea bed (Yasuda and Hiraishi, 2003). **Figure 4** shows the tsunami profile at the boundary wall computed in the non-linear tsunami generation and transfer model (Hiraishi, 2000). In the experimental condition, the original tsunami amplitude in harbor is 2.17m and it is assumed to approach in the high tide condition (H.W.L.=0.9m) The total water level is slightly larger than the averaged seawall crown height (2.63m). The modified tsunami height is 3.26m and it is 1.5 times larger than the original one. The tsunami period in the bay is 50min. The modified tsunami height at the model boundary becomes larger about 20min later than the beginning of tsunami profile generation.

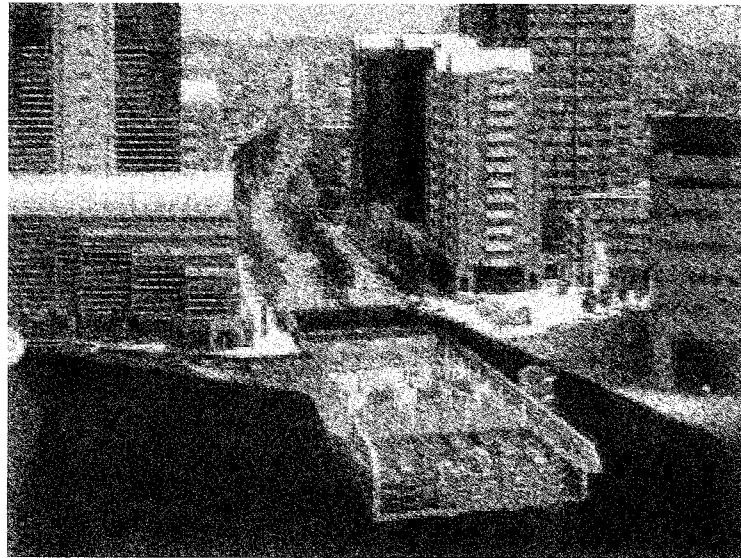


Figure 2 Image of coastal urban area with underground parking facility

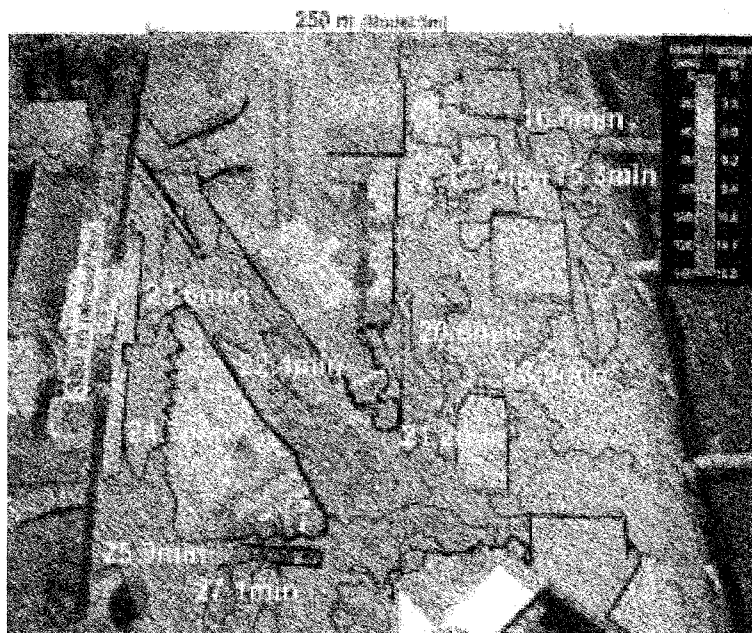


Figure 3 Experimental city model and arrival time of tsunami flow

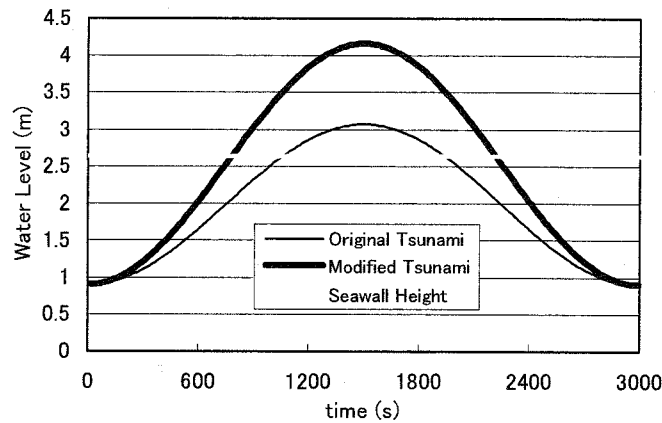


Figure 4 Tsunami profile at seawall

4. NUMERICAL RESULT AND ITS VERIFICATION

Figure 5 shows the snap shot of tsunami inundation situation in the urban area. The estimated inundation water depth and flow velocity agree with the measured ones in the hydraulic model test. **Figure 6** shows the snapshots of tsunami inundation into the underground parking space constructed in the target urban area. The numerical results in the underground tsunami activity demonstrated the flow velocity becomes very large at the entrance of underground floors and that the immediate evacuation is inevitable to reduce the tsunami disaster in coastal areas. A warning system to measure the variation of inundation water depth on surface may become effective to inform the risk of inundation to the underground residence.

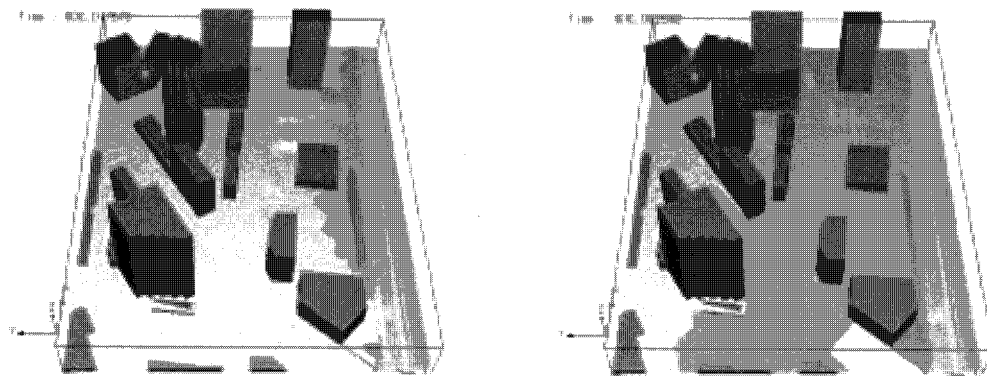


Figure 5 Numerically simulated tsunami inundation on surface (500 and 900s after the beginning of inundation)

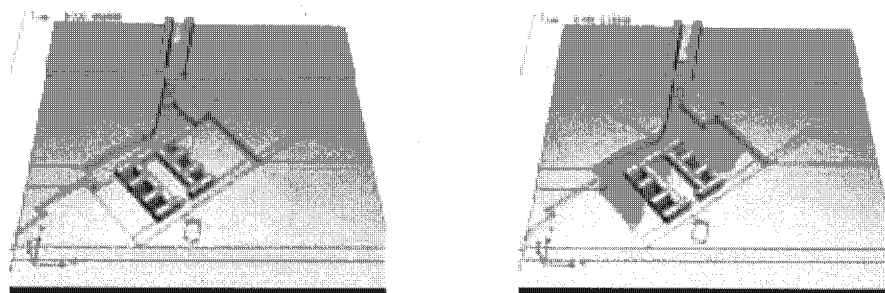


Figure 6 Tsunami inundation in underground parking space (1000 and 1100s after the beginning of inundation)

In order to verify the applicability of numerical simulation, we compared the inundating tsunami flow velocity estimated in the computation with those measured in the experiment. **Figure 7** shows the location of measurement points for tsunami flow velocity. The thermal type micro-current meters are employed for measurement. The location P.1(S) and P.2(U) corresponds to the measurement point for the surface flow at the entrance and the flow in underground floor respectively. P.3 and P.4 corresponds to the measurement point in the main road and a small street behind a tall building.

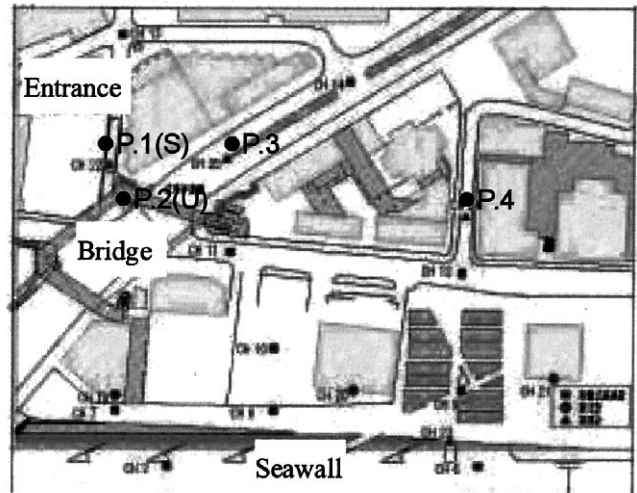


Figure 7 Location of current measurement point in target area

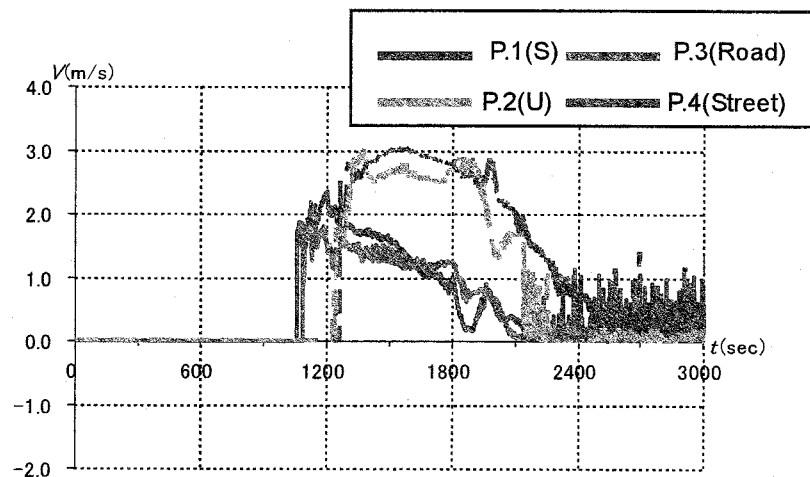


Figure 8 Variation of expected flow velocity due to tsunami

Figure 8 shows the variation of expected flow velocity in the measurement point. The inundating flow velocity becomes faster in the entrance and underground pass shown in the figure. The inundation risk in the underground area becomes higher than the surface facility because the inundating fast flow velocity makes the human evacuation much difficult.

The maximum flow velocity obtained in the experiment was analyzed using the current sensor data in the model test. **Figure 9** shows the flow velocity measured in the current sensors. The vertical axis corresponds to the flow velocity in the prototype dimension. The maximum current velocity in the measurement point P.1(S) becomes about 3m/s in the prototype. The measured velocity agrees to the estimated one in the entrance slope. The maximum velocity on the main road

(P.3) is about 2m/s and its value becomes equal to the expected velocity. In the experiment, the inundation depth of tsunami was measured in the target areas and their depths also agree well to the measured ones. Therefore the numerically simulated flow pattern is applicable to expect the flow situation in the tsunami inundation.

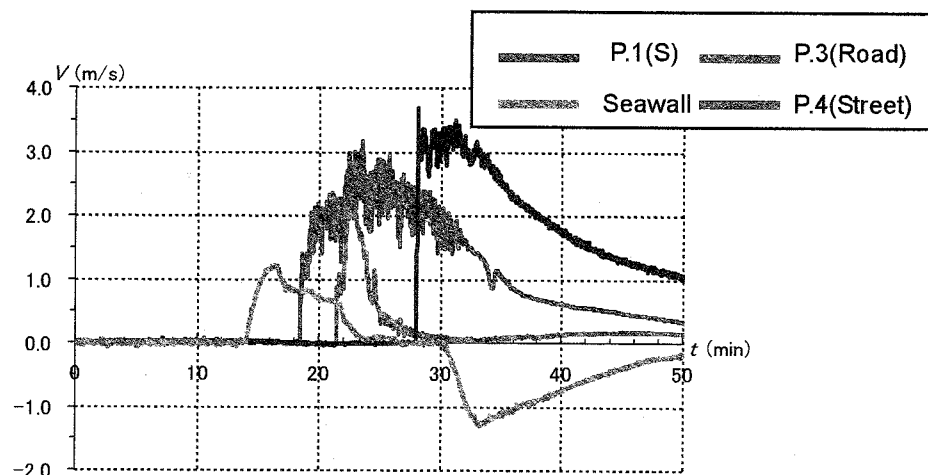


Figure 9 Variation of tsunami flow velocity measured in model test (indicated in the prototype)

5. CONCLUSIONS

The numerical model for tsunami inundation in the urban area employing the MARS method was described in the paper. The tsunami flow velocity estimated at the entrance of underground parking and main road agreed to them obtained in the model test with scale of 1/50. The numerical model is applicable to estimate the variation of tsunami inundation depth and flow velocity in the urban area facing to the sea.

References:

- Hiraishi, T.(2000), "Characteristics of Aitape Tsunami in 1998 Papua New Guinea", Report of the Port and Airport Research Institute, Vol.39, No.4, pp.23.
- Hiraishi T., Hirayama K., Kunisu H. and Nagase K. (2003), "Increase of Harbor Operation Rate by Long Period Wave Absorber", Long Wave Symposium, In parallel with the 30th IAHR Congress, pp. 91-100.
- Kunugi T. (1997), "Direct Numerical Algorithm for Multiphase Flow with Free Surface and Interface", Journal of Society of Japanese Mechanical Engineering, Vol.63, No.609, pp. 88-96.
- Yasuda T. and T. Hiraishi(2003),"Experimental Risk Assessment of Tsunami Inundation in Coastal Urban Area", Report of the Port and Airport Research Institute, Vol.42, No.3, pp.111-156.
- Yasuda T., T. Hiraishi, H. Kawai and K. Nagase (2004), "Numerical Analysis of Storm Surge Inundation in Masan, Workshop on Wave and Storm Surges around Korean Peninsula, pp.75-79.

DEVELOPMENT OF HIGH PERFORMANCE SIMULATOR FOR TSUNAMI BASED ON SHALLOW WATER EQUATIONS

R. Akoh¹⁾, S. Ii²⁾ and F. Xiao³⁾

1) Graduate student, Dept. of Energy Sciences, Tokyo Institute of Technology, Japan

2) Graduate student, Dept. of Energy Sciences, Tokyo Institute of Technology, Japan

3) Associate professor, Dept. of Energy Sciences, Tokyo Institute of Technology, Japan

g04m3101@es.titech.ac.jp, g04m3103@es.titech.ac.jp, xiao@es.titech.ac.jp

Abstract: Most of the existing numerical models for the simulation of Tsunami are based on the 2D shallow water equations. However, for many situations, it is necessary to use the 3D model in addition to the shallow water models to evaluate the damage in the coast region with a reliable accuracy. So, we propose the multi-scale warning system for Tsunami by coupling the 2D shallow water model and the 3D Navier-Stokes model that solves explicitly the free water surface to cover the physical phenomena that have diverse scales in both time and space. As a part of such a system, we, in this paper, present the formulation of the 2D shallow water wave model based on the CIP/MM-FVM with the MOC. In addition, we devise a numerical formulation for the source term that well preserves the hydrostatic balance. Finally, we apply the present model to the real-case simulation of "The 1993 Hokkaido-nansei-oki, Japan earthquake".

1. INTRODUCTION

Numerical simulation plays an essential role in the prevention and mitigation of the natural disasters caused by Tsunami and other violent oceanic waves, especially in providing warning forecasts immediately after the occurrence of an earthquake and in the assessment of the damage from a possible Tsunami. There are some widely used Tsunami models [1,2,3] based on 2D shallow water equations. However, it is still demanded to build more accurate numerical models that can provide not only numerical solutions with high accuracy to the 2D shallow-water-based systems but also the details of the direct water impact evaluated by 3D simulations of water fronts.

Toward the establishment of a reliable multi-scale Tsunami simulating and warning system, numerical models for different scales have been being developed based on the framework of CIP/MM FVM (Constrained Interpolation Profile/Multi-Moment Finite Volume Method) in our group. For the large-scale waves, we use 2D models based on the shallow water equations to predict the arrival time and the wave height of the Tsunami, which have been widely adopted in the existing models. For the small-scale waves, we use a 3D model based on the Navier-Stokes equations for the direct simulations of multi-phase fluids with free moving boundaries, to evaluate the impact of the water waves on the coastal structures. These components models are then coupled to cover the physical phenomena that have diverse scales in both time and space.

As one part of such a system, we, in the present study, propose the formulation for the shallow water wave model by applying the CIP/MM FVM with the theory of characteristics.

The non-conservative moments are computed by a semi-Lagrangian solution in terms of the characteristic velocities and the Riemann invariants, whereas the conservative moments are updated by a flux-based formulation. The resulting model is numerically accurate and robust. Additionally, a well-balanced numerical treatment of the source terms to include the effects of the topography of the seabed is also proposed to make the numerical model be ready for practical use.

2. CIP-CSL METHOD

In this section the essential aspects of the CIP-CSL methods [5,6] which are the advection schemes based on CIP/MM-FVM are briefly illustrated. More detailed description can be found in the references.

2.1 Definition of multi-moments

The 1D computational domain along x axis is partitioned into mesh cells of finite width. The VIA and the SIA degenerate to the line integrated average and the point value respectively. Assuming the i th cell is bounded by $[x_{i-\frac{1}{2}}, x_{i+\frac{1}{2}}]$, we defined the VIA of a field variable $\phi(x, t)$ over cell i as

$$\overline{v\phi}_i = \frac{1}{\Delta x_i} \int_{x_{i-\frac{1}{2}}}^{x_{i+\frac{1}{2}}} \phi(x, t) dx, \quad (1)$$

with $\Delta x_i = x_{i+\frac{1}{2}} - x_{i-\frac{1}{2}}$. The SIA is correspondingly the point value (PV) at the cell boundary

$$\overline{p\phi}_{i+\frac{1}{2}} = \phi(x_{i+\frac{1}{2}}, t). \quad (2)$$

2.2 Construct the interpolation function

With one cell-integrated average ($\overline{v\phi}_i$) and two point values at the cell boundaries ($\overline{p\phi}_{i-\frac{1}{2}}$, $\overline{p\phi}_{i+\frac{1}{2}}$) known, the CIP-CSL reconstructions can be made. To get rid of numerical oscillations associating the discontinuous solutions, like shock wave, we used CIP-CSL3 schemes to enforce the monotonicity. One may refer to the references for more details of the interpolation reconstructions.

2.3 Update of the moments

In the scheme based on multi-moment concept, different moments are temporally updated by different ways. In the CIP-CSL methods, the PV or the SIA, which needs not be exactly conserved, can be updated by a semi-Lagrangian method as

$$\overline{p\phi}_{i+\frac{1}{2}}^{n+1} = \Phi(x_{i+\frac{1}{2}} + \alpha), \quad \alpha = -u_{i+\frac{1}{2}} \Delta t; \quad (3)$$

where Φ is the interpolation function in the cell including the advection starting point.

The conservative moment, the cell-integrated average in 1D case, is updated by the following finite volume formulation in flux-form,

$$\overline{v\phi}_i^{n+1} = \overline{v\phi}_i^n - \frac{1}{\Delta x_i} \left(\int_{t^n}^{t^{n+1}} \mathbf{F}_{i+\frac{1}{2}} dt - \int_{t^n}^{t^{n+1}} \mathbf{F}_{i-\frac{1}{2}} dt \right). \quad (4)$$

In this scheme, the numerical flux in Eq.(4) at each cell boundary is computed by

$$\int_{t^n}^{t^{n+1}} \mathbf{F}_{i+\frac{1}{2}} dt = \int_{x_{i+\frac{1}{2}} + \alpha}^{x_{i+\frac{1}{2}}} \Phi(x) dx. \quad (5)$$

3. THE FORMULATIONS FOR SHALLOW WATER EQUATIONS

The mathematical model used in the 2D Tsunami simulator is based on the two-dimensional shallow water equations. The shallow water equations written in conservative form read :

$$\frac{\partial \mathbf{U}}{\partial t} + \frac{\partial \mathbf{F}}{\partial x} + \frac{\partial \mathbf{G}}{\partial y} = \mathbf{S}, \quad (6)$$

with

$$\mathbf{U} = \begin{bmatrix} h \\ hu \\ hv \end{bmatrix}, \mathbf{F} = \begin{bmatrix} hu \\ hu^2 + \frac{1}{2}gh^2 \\ huv \end{bmatrix}, \mathbf{G} = \begin{bmatrix} hv \\ huv \\ hv^2 + \frac{1}{2}gh^2 \end{bmatrix}, \mathbf{S} = \begin{bmatrix} 0 \\ S_x \\ S_y \end{bmatrix}. \quad (7)$$

where h is the water depth, u and v are the x and y components of flow velocity respectively, and g is the gravitational acceleration. \mathbf{S} is the source term including the bottom slope and slope friction.

3.1 Formulation for 1D shallow water equation without the source term

Without the source term, the one dimensional shallow water equations read as

$$\frac{\partial \mathbf{U}}{\partial t} + \frac{\partial \mathbf{F}}{\partial x} = 0, \quad (8)$$

with

$$\mathbf{U} = \begin{bmatrix} h \\ q \end{bmatrix}, \quad \mathbf{F} = \begin{bmatrix} q \\ q^2/h + \frac{1}{2}gh^2 \end{bmatrix}. \quad (9)$$

being the conservative variables and the fluxes. Denoted by $q(x, t)$ is the momentum.

Eq.(8) can be recast in its non-conservative form as

$$\frac{\partial \mathbf{U}}{\partial t} + \mathbf{A} \frac{\partial \mathbf{U}}{\partial x} = 0, \quad (10)$$

where the A is the Jacobian matrix of the flux function and defined as

$$\mathbf{A} = \frac{\partial \mathbf{F}}{\partial \mathbf{U}} = \begin{bmatrix} 0 & 1 \\ gh - u^2 & 2u \end{bmatrix}. \quad (11)$$

Owing to the hyperbolicity, the characteristic form of the shallow water equations can be derived as

$$\frac{\partial \mathbf{W}}{\partial t} + \Lambda \frac{\partial \mathbf{W}}{\partial x} = 0, \quad (12)$$

where the characteristic variables (or the Riemann invariants) are

$$\mathbf{W} = \begin{bmatrix} w_1 \\ w_2 \end{bmatrix} = \begin{bmatrix} c + \frac{1}{2}u \\ c - \frac{1}{2}u \end{bmatrix}, \quad (13)$$

where $c = \sqrt{gh}$ is the speed of the gravity wave. The diagonalized matrix is made up of the two characteristic speeds as

$$\Lambda = \begin{bmatrix} \lambda_1 & 0 \\ 0 & \lambda_2 \end{bmatrix} = \begin{bmatrix} u+c & 0 \\ 0 & u-c \end{bmatrix}. \quad (14)$$

Eq.(12), (13), (14) means that the solution at one point is determined from two characteristics along the characteristics lines C_1 and C_2 . If the variables at the upstream departure points of C_1 , C_2 are denoted by w_1 , w_2 , then ${}^p\bar{\mathbf{U}}_{i+\frac{1}{2}}^n$ are simply given by

$${}^p\bar{\mathbf{U}}_{i+\frac{1}{2}}^{n+1} = \begin{bmatrix} {}^p\bar{h}_{i+\frac{1}{2}}^{n+1} \\ {}^p\bar{q}_{i+\frac{1}{2}}^{n+1} \end{bmatrix} = \frac{1}{4g} \begin{bmatrix} (w_1 + w_2)^2 \\ (w_1 + w_2)^2(w_1 - w_2) \end{bmatrix}. \quad (15)$$

Then, once w_1 and w_2 are computed by the following semi-Lagrangian solutions, PV of the conservative variables at all cell boundaries can be directly found.

$$\begin{cases} w_1 = \mathcal{W}_1(x_{i+\frac{1}{2}} + \alpha_1), & \alpha_1 = -\lambda_{1i+\frac{1}{2}}\Delta t, \\ w_2 = \mathcal{W}_2(x_{i+\frac{1}{2}} + \alpha_2), & \alpha_2 = -\lambda_{2i+\frac{1}{2}}\Delta t. \end{cases} \quad (16)$$

Concerning the updating of the cell-integrated average values of the conservative variables, we integrated (8) over $[x_{i-\frac{1}{2}}, x_{i+\frac{1}{2}}]$ and $[t^n, t^{n+1}]$, yielding the following finite volume formulation in flux-form,

$${}^v\bar{\mathbf{U}}_i^{n+1} = {}^v\bar{\mathbf{U}}_i^n - \frac{1}{\Delta x_i} \left(\int_{t^n}^{t^{n+1}} \mathbf{F}_{i+\frac{1}{2}} dt - \int_{t^n}^{t^{n+1}} \mathbf{F}_{i-\frac{1}{2}} dt \right). \quad (17)$$

It is obvious that (17) exactly guarantees the conservation of ${}^v\bar{\mathbf{U}}$. The numerical flux in (17) at each cell boundary ($x = x_{i+\frac{1}{2}}$) is approximated as

$$\int_{t^n}^{t^{n+1}} \mathbf{F}(h, q)_{i+\frac{1}{2}} dt \approx \mathbf{F}(\bar{h}, \bar{q})_{i+\frac{1}{2}} \Delta t, \quad (18)$$

where $\Delta t = t^{n+1} - t^n$. The quantity $\bar{\phi}$ denotes the time integrated average (TIA) for time-evolution variable ϕ and defined as

$$\bar{\phi}_{i+\frac{1}{2}} = \frac{1}{\Delta t} \int_{t^n}^{t^{n+1}} \phi_{i+\frac{1}{2}} dt. \quad (19)$$

With the interpolation constructed in terms of the Riemann invariants for the semi-Lagrangian solution of the point values, we firstly evaluate the TIAs of the characteristic variables by averaging them along the characteristic lines in a similar way to (16) as

$$\begin{cases} \bar{w}_{1i+\frac{1}{2}}^n = \frac{1}{\Delta t} \int_{t^n}^{t^{n+1}} w_1 dt = \frac{1}{|\alpha_1|} \int_{x_{i+\frac{1}{2}}+\alpha_1}^{x_{i+\frac{1}{2}}} \mathcal{W}_1(x) dx, \\ \bar{w}_{2i+\frac{1}{2}}^n = \frac{1}{\Delta t} \int_{t^n}^{t^{n+1}} w_2 dt = \frac{1}{|\alpha_2|} \int_{x_{i+\frac{1}{2}}+\alpha_2}^{x_{i+\frac{1}{2}}} \mathcal{W}_2(x) dx. \end{cases} \quad (20)$$

After the TIAs of the characteristic variables are obtained by (20), the TIA of each conservative variables required in (18) is computed by

$$\overline{pU}_{i+\frac{1}{2}}^{n+1} = \frac{\left[\overline{th}_{i+\frac{1}{2}}^{n+1}\right]}{\left[\overline{tq}_{i+\frac{1}{2}}^{n+1}\right]} = \frac{1}{4g} \left[\frac{(\overline{tw}_{1i+\frac{1}{2}}^{n+1} + \overline{tw}_{2i+\frac{1}{2}}^{n+1})^2}{(\overline{tw}_{1i+\frac{1}{2}}^{n+1} + \overline{tw}_{2i+\frac{1}{2}}^{n+1})^2 (\overline{tw}_{1i+\frac{1}{2}}^{n+1} - \overline{tw}_{2i+\frac{1}{2}}^{n+1})} \right]. \quad (21)$$

Finally, VIA of the conservative variables are updated by (17) where the numerical fluxes are computed by (18), (20), and (21).

3.2 Formulation for the source term

If a numerical scheme does not preserve the fundamental balance between source term and flux gradient at the discrete level, it may result in spurious oscillations. In this paper, we construct the well-balanced formulation for the source term by the discretization for water surface $H(x, t) = h(x, t) + z(x)$, by using the Surface Gradient Method (SGM)[9].

3.3 Formulation for 2D shallow water equations

Extending the previous procedure to two dimensions can be simply implemented by dimensional splitting. In this paper, we apply VSIAM3 (Volume/Surface Integrated Average Multi-Moment Method)[7,8] which is the most simple multi-dimensional formulation of CIP/MM-FVM retaining VIA and SIA to be the dependent variables. One may refer to the references for details.

In addition, we apply the concept of effective area and volume fraction of fluid to include the effects of obstacles and complex boundaries.

4. NUMERICAL RESULTS

In this section, we present numerical results for several test problems for the 1-dimensional and 2-dimensional shallow water equations. In the computations, we apply CIP-CSL3 with MOC.

4.1 Test.1:1D dam-break flow

In the first numerical test, the one-dimensional dam-break is solved in a domain of $[0, 50]$. The mesh number is 201 and the time step is 0.02[s]. The initial conditions are

$$\begin{aligned} h_0(x) &= \begin{cases} 1.0[\text{m}] & 0.0 \leq x \leq 10.0, \\ 0.1[\text{m}] & 10.0 < x \leq 50.0, \end{cases} \\ u_0(x) &= \begin{cases} 2.5[\text{m/s}] & 0.0 \leq x \leq 10.0, \\ 0.0[\text{m/s}] & 10.0 < x \leq 50.0. \end{cases} \end{aligned} \quad (22)$$

After the instantaneous collapse of the dam, the numerical solution is computed until $t = 7.0[\text{s}]$.

Comparisons of the exact solutions with the simulated water depths h , and the velocity u are presented in Fig.1. It shows that the present formulation capture accurately the shock with correct speed within few mesh points. The rarefaction part is also accurately simulated.

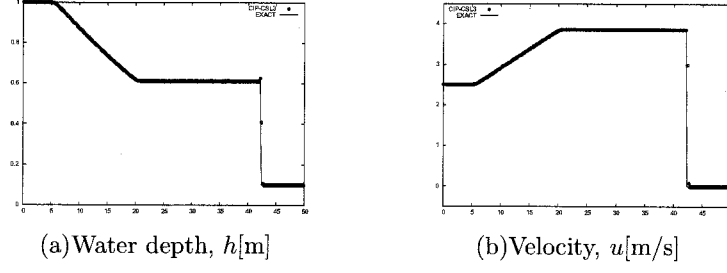


Figure 1: Test.1: Numerical Results at $t = 7.0[s]$ by CIP-CSL3 (circles) and exact solution (solid line).

4.2 Test.2:1D steady flow over the bump

The purpose of the second problem is to test the present formulation for source term in the case of steady flow over a bump. The bed level is given with

$$z(x) = \begin{cases} 0.25(1.0 + \cos(10.0\pi(x - 0.5))) & \text{if } 1.4 \leq x \leq 1.6, \\ 0.0 & \text{otherwise,} \end{cases} \quad (23)$$

in a domain of $[0, 50]$. The mesh number is 201 and the time step is $0.02[s]$. The initial conditions are

$$\begin{aligned} H_0(x) &= 1.0, \\ u_0(x) &= 0.0. \end{aligned} \quad (24)$$

Fig.2 show the total height $H[m]$ and the momentum $q[m^2/s]$ at $t = 0.2[s]$. From these results, we know that the present formulation for source term preserves exactly the balance between the source term and flux gradient.

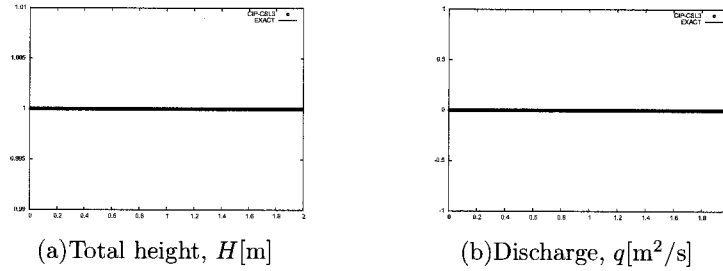


Figure 2: Test.2: Numerical Results at $t = 0.2[s]$ by CIP-CSL3 (circles) and exact solution (solid line).

4.3 Test.3:2D partial dam-break flow

In the third numerical test, the two-dimensional partial dam-break is solved in the domain of $[0, 200] \times [0, 200]$. The purpose of this problem is to test the present formulation for 2 dimensions and the treatment of barricades. The initial conditions are

$$\begin{aligned} h_0(x, y) &= \begin{cases} 10.0[m] & 0.0 \leq x \leq 100.0, \\ 5.0[m] & 100.0 < x \leq 200.0, \end{cases} \\ u_0(x, y) &= 0.0[m/s], \quad v_0(x, y) = 0.0[m/s]. \end{aligned} \quad (25)$$

The mesh number is 71×71 and the time step is $0.02[s]$.

Fig.3 show the bird's eye view and contour view of $h[m]$ at $t = 7.2[s]$. Compared with the reference solutions for this test case, the present results show a realistic behavior with adequate accuracy.

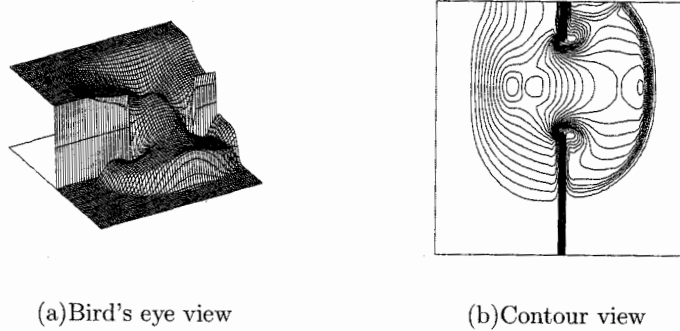


Figure 3: Test.3: Numerical Results at $t = 7.2[s]$ by CIP-CSL3

5. EXPERIMENT WITH REAL GEOGRAPHICAL DATA

As the final test, we computed the problem with a complex coastal-line and bottom topography based on the real geographical-data in Hokkaido region of Japan(Fig.4). In 1993, a big earthquake occurred in southwest of Hokkaido. This earthquake triggered a giant tsunami that caused serious damages.

It is well known that accurately determining the initial condition is very difficult. It arises another important issue in the tsunami simulation, and should be discussed separately. In this test, we used the initial condition provided by Dr. Inoue in Ohmachi laboratory, Tokyo Institute of Technology.

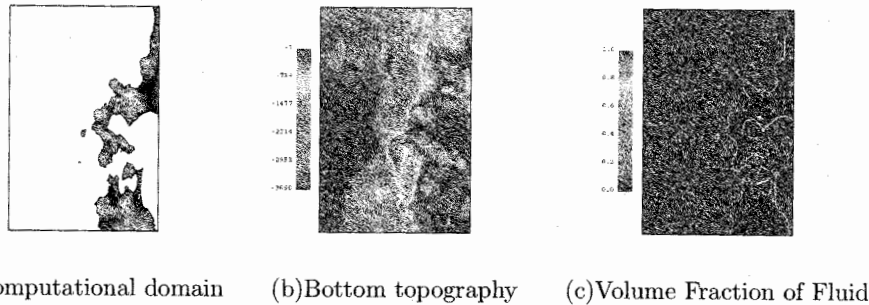


Figure 4: Experiments: Computational Conditions

Fig.5 show the numerical results of sea surface at $t = 0, 1000, 2000[s]$. From these results, the overall behavior of the surface waves have been captured with reasonable accuracy. We will further validate and improve the present models with more reliable conditions for real cases.

6. CONCLUSIONS

Making use of some state-of-the-art numerical formulations, we have constructed an accurate and robust numerical model for simulating the propagation of Tsunami based on the shallow water equations. The numerical model has been validated by some idealized and "real-case" numerical experiments, and the results are quite promising.

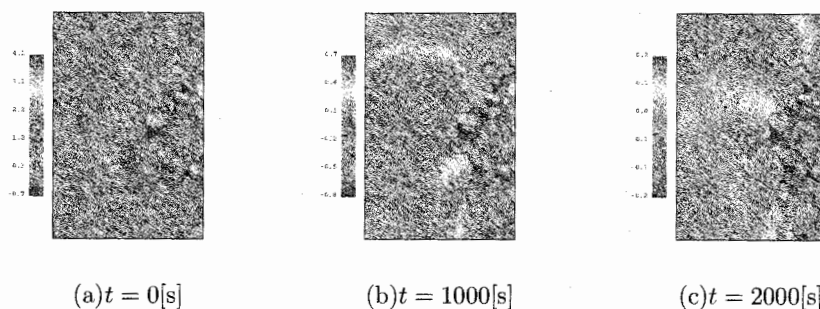


Figure 5: Experiments:Numerical Results of sea surface by CIP-CSL3

Further validations and applications of the present model are still needed. The coupling with the 3D Navier-Stokes model for free interface flows, which have been separately developed in our group, will be carried out to build an integrated system for evaluating various waves of different scales.

Acknowledgment:

We are very grateful for Dr. Inoue for providing the data for the real-case simulation on "The 1993 Hokkaido-nansei-oki, Japan earthquake".

References:

- [1] F. Imamura. (1995), "Tsunami Numerical Simulation with the staggered Leap-frog scheme (Numerical code of TUNAMI-N1 and N2)," School of Civil Engineering, Asian Inst. Tech. and Disaster Control Res. Cntr., Tohoku Univ.
- [2] C. Thaicharoen, S. Weesakul, A. D. Gupta. (2005), "TSUNAMI PROPAGATION TO THAILAND A CASE STUDY: PHI PHI ISLAND," MTERM International Conference, 06-10.
- [3] V. V. Titov, F. I. Gonzalez. (1997), "IMPLEMENATATION AND TESTING OF THE METHOD OF SPLITTING TSUNAMI (MOST) MODEL," NOAA Technical Memorandum ERL PMEL-112.
- [4] F. Xiao. (2005), "CIP/Multi-Moment Finite Volume Method", *J. Japan Soc. Comput. Engrg. Science*, Vol.10, 1243-1248.(in Japanese)
- [5] T. Yabe, R. Tanaka, T. Nakamura, F. Xiao. (2001), "Exactly conservative semi-Lagrangian scheme (CIP-CSL) in one dimension," *Mon. Wea. Rev.*, **129**, 332-344.
- [6] F. Xiao, T. Yabe. (2001), "Completely conservative and oscillation-less semi-Lagrangian schemes for advection transportation," *J. Comput. Phys.*, **170**, 498-522.
- [7] F. Xiao, A. Ikebata, T. Hasegawa, (2005), "Numerical simulations of free-interface fluids by a multi integrated moment method," *Comput. Struct.*, **83**, 409-423.
- [8] F. Xiao. (2006), "Unified formulation for compressible and incompressible flows by using multi-integrated moments : Multi-dimensional version for compressible and incompressible flows," *J. Comput. Phys.*, **213**, 31-56.
- [9] J. G. Zhou, D. M. Causon, C. G. Mingham, D. M. Ingram. (2001), "The Surface Gradient Method for the Treatment of Source Terms in the Shallow-Water Equations," *J. Comput. Phys.*, **168**, 1-25.
- [10] T. Ohmachi, H. Tsukiyama, H. Matsumoto. (2001), "Simulation of Tsunami Induced by Dynamic Displacement of Seabed due to Seismic Faulting," *Bulletin of the Seismological Society of America*, 91, 6, pp. 1898-1901.

STUDY ON THE OIL SPREAD CAUSED BY 1964 NIIGATA EARTHQUAKE TSUNAMI

Y. Iwabuchi¹⁾, S. Koshimura²⁾ and F. Imamura³⁾

1) Graduate Student, Department of Civil Engineering, Tohoku University, Japan

2) Associate Professor, Disaster Control Research Center, Tohoku University, Japan

3) Professor, Disaster Control Research Center, Tohoku University, Japan

d201yoko@tsunami2.civil.tohoku.ac.jp, koshimura@tsunami2.civil.tohoku.ac.jp, imamura@tsunami2.civil.tohoku.ac.jp

Abstract: We reviewed the process of complex tsunami disaster, focusing on the large spread of fire caused by the destruction of oil storage tank and tsunami inundation flow during the 1964 Niigata earthquake. Then, we propose a model to simulate the oil advection and diffusion on tsunami inundation flow by using 2-layer hydrodynamic model. The model is preliminarily tested in a simple numerical wave tank with discussions and future perspectives.

1. INTRODUCTION

The complex tsunami disaster due to floating objects driven by tsunami is concerned as a new aspect of tsunami disaster in a metropolitan coastal region. The most Commonly-observed feature of this complex tsunami disaster is that the destruction of the storage of flammable materials by the collision with tsunami-driven objects or by the hydrodynamic force of tsunami may result large spread of fire. As a result of destruction, the flammable material such as oil spills and ignited material is advected and diffused by the tsunami current in a harbor or inundation flow on a land.

Although every metropolitan coastal region is at risk of this disaster and the damage is significant, estimation of complex damage at the waterfront has not been carried out sufficiently. Current estimation method for tsunami damage is only based on counting the assets that is exposed against tsunami inundation zone. Thus, the qualitative features of the complex tsunami disaster is not well considered and contains lots of uncertainties.

In this paper, firstly we understand the process of complex tsunami disaster, focusing on the large spread of fire caused by the destruction of oil storage tank and tsunami inundation flow, that was occurred by the 1964 Niigata earthquake. The disaster process is reviewed by both reported facts in 1964 and numerical modeling of tsunami inundation within the port of Niigata. Then, we propose a model to simulate the oil advection and diffusion on tsunami inundation flow by using 2-layer hydrodynamic model. The model is preliminarily tested in a simple numerical wave tank with discussions and future perspectives.

2. TSUNAMI-CAUSED FIRE DURING THE 1964 NIIGATA EARTHQUAKE

The 1964 Niigata earthquake occurred in the boundaries of Asian and North-American plates at 13:02 on June 16th (JST). The tsunami accompanied this earthquake and affected the whole coast

along the Japan Sea. The maximum run-up height of 4.93m was measured at Kuwagawa, Niigata Prefecture. Liquefaction on the plane damaged buildings and bridges, and two events of fire were caused by oil leakage from the tanks (Iwabuchi and Imamura 2005). The first fire had no relation with the tsunami. However, the tsunami became the contributing cause of the second fire.

As shown in Figure 1, the shore protections at the dock were destroyed by the strong ground motion. Then, the tsunami attacked the dock, and the low land nearby was completely inundated. Figure 2 shows the extent of tsunami inundation and oil diffusion area on ground water due to liquefaction and sea water due to tsunami. Final inundation area in Niigata City became 56,000 by 1000 square meters. Since Yamanoshita area was involved in the liquefaction and the tsunami inundation zones, this area was inundated by sea water and heavy oil discharged from 100 oil storage tanks. 5 hours after the earthquake, the second fire occurred from the old oil plant where the inundation height reached 30-50 cm. The oil was widely floating on the inundation zone because lots of tanks and pipes were damaged by the strong ground motion. Spilled oil was diffused and advected over a wide area by the run-up flow. The original fire occurred in the diffusion area, in a distance of 30m from "No.33 oil tank" shown in Figure 1, but not in the spilled area. The fire continued for two weeks after the earthquake. It was believed that this area was burned by the second fire and resulted approximately 235 by 1000 square meters of the burned area.

Tsunami wash spilled oil inside the harbor and also residential area. Shore protection facilities became the entry pathway for sea water and oil. Initial spilled point were at the broken tanks of Showa Oil Co. and NIPPON Oil Co.. The river overflowed by ten-odd tsunami waves, and then washed into "Yamanoshita area" from both northern and southern part, in a pincer movement (Figure 2). The oil was floating on the inundation flow of approximately 1.5 meters as its depth. The floating oil in Yamanoshita area could be classified two types as spreading process. One was by oil diffusion which was transported with tsunami inundation flow before the fire occurred. The other was caused by a series of explosions from approximately a hundred of oil tanks, after the tsunami penetrated. Figure 3 is the interpreted process of the interaction of tsunami and oil. Photo 1 and 2 indicate diffusion oil on Shinano river. Photo-3 and 4 show residential areas which submerged with oil.

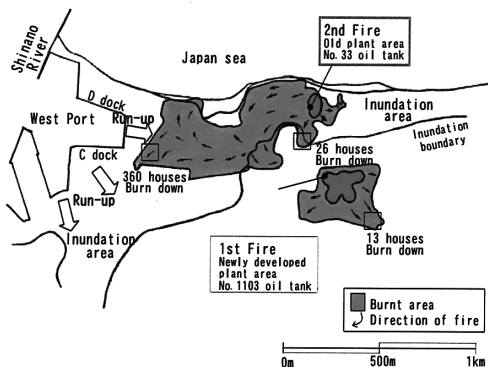


Figure 1 Oil Fires on Niigata Earthquake

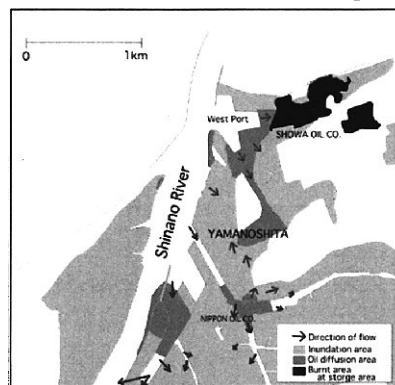


Figure 2 Inundation and Oil diffusion of Niigata City

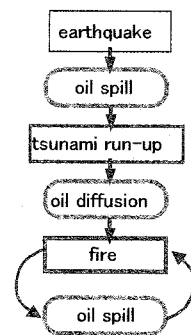


Figure 3 Interaction of tsunami and oil spread



Photo 1 The oil which flowed into Shinano River

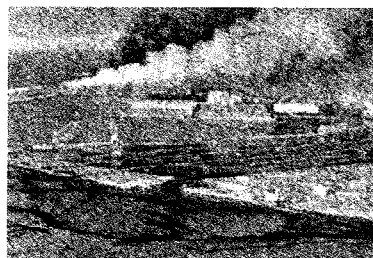


Photo 2 The oil which flowed into the harbor



Photo 3 Spreading of crude oil into residential area

Also, we discuss the sequence of oil spread and diffusion by using three aerial photographs taken during tsunami. Table 1 shows what the photographs contain in terms of the information of the sequence of the event. Those photos are focused on NIPPON OIL Co., LTD. and riverside area of branch of Shinano River. Figure 4 indicates the interpreted process of the large spread of fire. The NIPPON OIL Co. was located along the river. There was a paper industry within this area. Before the tsunami arrival, lots of wood were stocked as ingredient. Actually, within 15 minutes after earthquake occurred, two fires were ignited from both two plants. Oil leaked from broken tanks of NIPPON OIL Co. During initial 30 minutes after the quake, tsunami had not arrived yet. Photo 5 shows two fire events in the same area of Figure 4. Sea water with floating woods penetrated from branch of Shinano River to Yamanoshita area. Because of destruction of shore protection facilities, tsunami entered easily to the Yamanoshita residential area. The source of oil spill was at the broken tank of NIPPON OIL Co. Volume of crude oil from this tank was estimated approximately 5,000 kl. We can see, from the photos, the oil floated on the water surface of the river. And it went toward the north from the bank rip shown in Figure 4.



Photo 4 Adjacent residence for employees from tanks

Now, we focus on Photos 5 and 6. First thing we noticed was the movement of lumbers. The photos indicate that tsunami current transported those woods. Photo 5 was taken within 50 minutes after the earthquake. We can see that lumbers were already transported. In Photo 6, those lumbers were scattered. Then, we focus on spilled oil. The area of dark black in Photo 6 were presumed as oil diffusion area. The dark black area was also distributed on the land and in paper industry. As shown in Photo 7 which was taken 10 days later. The oil still remained at the branch of Shinano River.

Table 1 Information involved in aerial photographs

Stage	Time	Tsunami arrival	Oil diffusion	Scatter of woods	offer
Photo 5	June 16th, 13:20-13:45	1 st or 2 nd wave	Not found	Appeared	Mr. F. Yuminamochi
Photo 6	June 17th, 10:22	-	Appeared	Appeared	Kokusai Kogyo Co.
Photo 7	June 27th, 10:16	-	Appeared	Appeared	Asia Air Survey Co.



Photo 5 view of bank rip and two fires across the river (June 16th, 13:20-13:45)

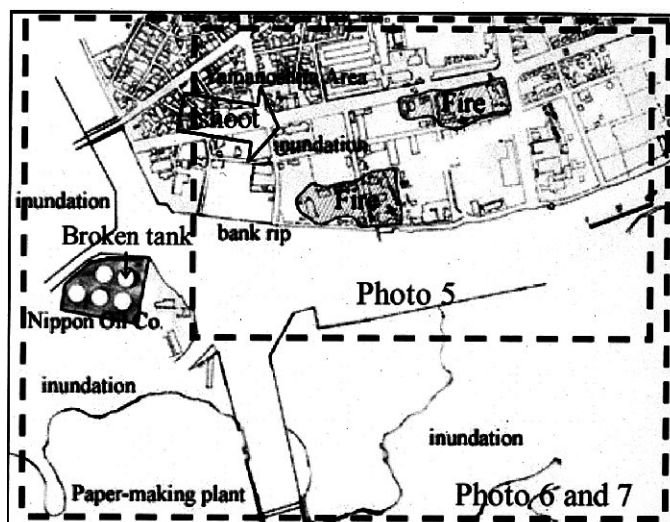


Figure 4 ancillary layout sketch of pictures



Photo 6 view of oil diffusion at 10:22 on June 17th

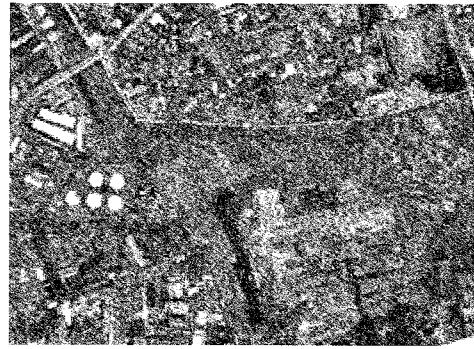


Photo 7 view of oil diffusion at 10:16 on June 27th

3. MODELING THE COASTAL INUNDATION OF THE 1964 NIIGATA EARTHQUAKE TSUNAMI

3.1 Modeling setup

As shown in Figure 5 and 6, five computational grids are nested, from tsunami source area to coastal area. Based on the parameters shown in Table 2, we estimate the vertical seismic deformation of the land and sea bottom by using the theory of *Mansinha and Smylie (1971)* to compute the static displacement. Table 3 is setting of grid in each area. Bathymetry data of region D and E, which is required for high-accuracy run-up simulation, was digitized from bathymetric charts published in 1964, because topographical change between 1964 and present is not negligible. By comparison of the bathymetry before and after the event, we found that, the sea bottom deformation was only upheaval. We decide the fault position to be consistent with the interpreted upheaval area. Tsunami numerical modeling was carried out according to the settings listed in Table 3.

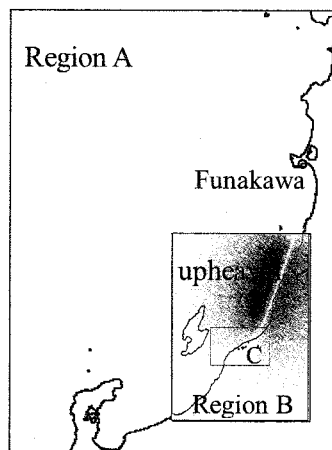


Figure 5 Initial profile of source deformation and division of region (A,B,C)

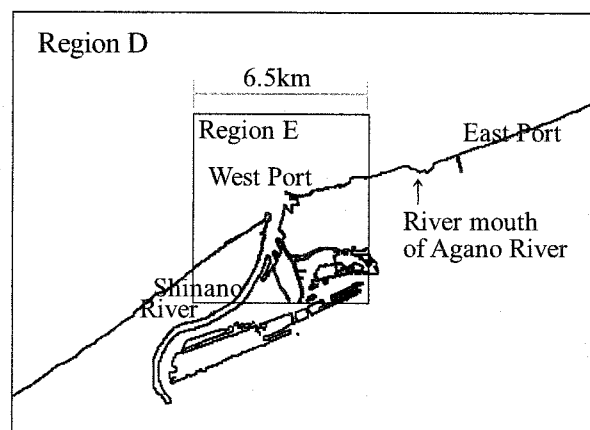


Figure 6 division of devastated area

Table 2 Fault parameters for the 1964 Niigata earthquake, Aki(1966)

D	θ	δ	λ	L	W	U
10	200	70	90	100	20	4

D is depth of the fault plane (km), θ is strike (degree), δ is dip (degree), λ is slip (degree), L and W are the strike length and downdip width (km) and U is dislocation (m).

Table 3 Settings of tsunami numerical model

Area Name	A	B	C	D	E
Grid size (m)	600	200	100	50	25
Governing Equation	Non-linear shallow water theory				
Differentiation scheme	Leap-frog scheme on Staggered grid				
Simulated Time & step	5h @ 0.25s				
At offshore	Non-reflecting plane	Connect water level and discharge			
At shoreline	Run-up				

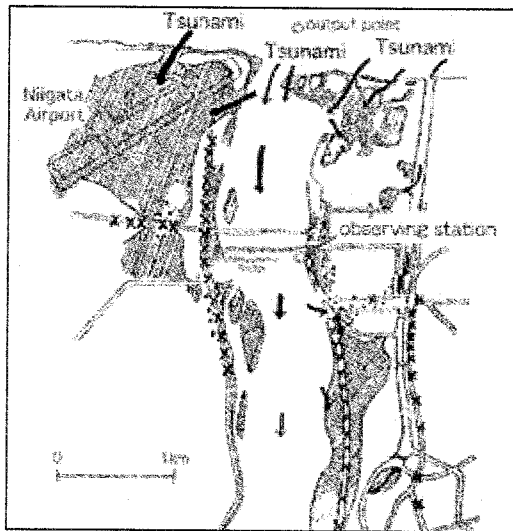


Figure 7 Station Matsugasaki and Run-up of Agano river

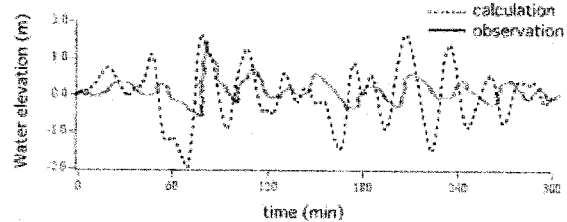


Figure 8(a) Station Matsugasaki

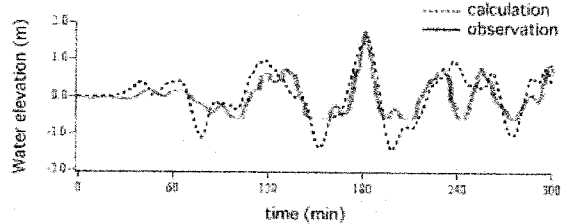


Figure 8(b) Station Funakawa

Figure 8 Comparison measured water level with that of computed at each location

3.2 Model results and discussions

Figure 8 shows comparison of observed and computed waveforms at Matsugasaki and at Funakawa. Tide record at Matsugasaki were obtained at the river mouth of Agano River (figure 7), the closest to the devastated area. The river channel and water depth of Shinano River in the bathymetry data were restored with map of surveying. However, water depth of Agano river were not restored as shown in Figure 6. The lacking part around the area significantly affects run-up. As shown in Figure 8, the mode result shows good agreement with the observed waveform in terms of arrival time of the first wave. However, negative water level is still overestimated. Figure 9 shows inundation area of calculation. Calculated inundation area is smaller then observed inundation area

which is shown in Figure 2. The calculated inundation area in Showa Oil Co. shows good agreement with observation. Because of uncertain phenomenon; destruction of shore protection and Liquefaction, are not considered, the calculation inundation are small. The river overflowed and then washed into "Yamanoshita area" from both northern and southern part. It is same as observation phenomenon.

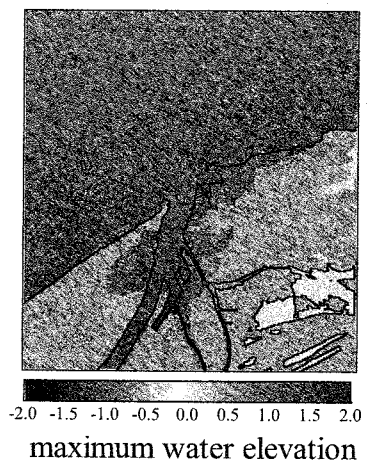


Figure 9 Inundation area in region E (calculation)

4. 2-LAYER MODEL FOR OIL SPREAD BY TSUNAMIS --- PRELIMINARY ANALYSIS

We carry out numerical experiment in 2D-sectional water tank to examine applicability of 2-layer model on run-up area. The governing equation of 2-layer model was derived from integrating Euler's equation for each layer. The boundary conditions were given at interface and water surface. The long wave approximation was assumed and vertical acceleration was set to 0, then, equations (1) to (6) were derived.

For oil layer

$$\frac{\partial}{\partial t}(\eta_1 - \eta_2) + \frac{\partial M_1}{\partial x} + \frac{\partial N_1}{\partial y} = 0 \quad (1)$$

$$\frac{\partial M_1}{\partial t} + \frac{\partial}{\partial x}\left(\frac{M_1^2}{D_1}\right) + \frac{\partial}{\partial y}\left(\frac{M_1 N_1}{D_1}\right) + g D_1 \frac{\partial \eta_1}{\partial x} - f_{inter} \bar{u} \sqrt{\bar{u}^2 + \bar{v}^2} = \nu \left(\frac{\partial^2 M_1}{\partial x^2} + \frac{\partial^2 M_1}{\partial y^2} \right) \quad (2)$$

$$\frac{\partial N_1}{\partial t} + \frac{\partial}{\partial x}\left(\frac{M_1 N_1}{D_1}\right) + \frac{\partial}{\partial y}\left(\frac{N_1^2}{D_1}\right) + g D_1 \frac{\partial \eta_1}{\partial y} - f_{inter} \bar{v} \sqrt{\bar{u}^2 + \bar{v}^2} = \nu \left(\frac{\partial^2 N_1}{\partial x^2} + \frac{\partial^2 N_1}{\partial y^2} \right) \quad (3)$$

For water layer

$$\frac{\partial \eta_2}{\partial t} + \frac{\partial M_2}{\partial x} + \frac{\partial N_2}{\partial y} = 0 \quad (4)$$

$$\frac{\partial M_2}{\partial t} + \frac{\partial}{\partial x}\left(\frac{M_2^2}{D_2}\right) + \frac{\partial}{\partial y}\left(\frac{M_2 N_2}{D_2}\right) + g D_2 \left(\alpha \frac{\partial D_1}{\partial x} + \frac{\partial \eta_2}{\partial x} - \frac{\partial h_1}{\partial x} \right) + \frac{\tau_x}{\rho_2} + \alpha f_{inter} \bar{u} \sqrt{\bar{u}^2 + \bar{v}^2} = 0 \quad (5)$$

$$\frac{\partial N_2}{\partial t} + \frac{\partial}{\partial x}\left(\frac{M_2 N_2}{D_2}\right) + \frac{\partial}{\partial y}\left(\frac{N_2^2}{D_2}\right) + g D_2 \left(\alpha \frac{\partial D_1}{\partial y} + \frac{\partial \eta_2}{\partial y} - \frac{\partial h_1}{\partial y} \right) + \frac{\tau_y}{\rho_2} + \alpha f_{inter} \bar{v} \sqrt{\bar{u}^2 + \bar{v}^2} = 0 \quad (6)$$

Additional character: 1: upper layer; 2: lower layer; h : still water depth; D : total water depth(= $h + \eta$); η_1 : oil surface level; η_2 : displacement of water level; M, N : discharge flux; g : gravity acceleration; ρ : density; $\alpha = (\rho_1 / \rho_2)$: density ratio; ν : horizontal diffusion coefficient; τ_x, τ_y : bottom friction; $INTF$: interfacial friction; f_{inter} : interfacial resistance coefficient; \bar{u}, \bar{v} : relative velocity in x and y direction, respectively; $DIFF$: Horizontal diffusion term;

In the model, to avoid numerical instability of moving boundary, which is the front of upper layer, the limitation of the thickness of oil is set to be 10^{-3} m, Spatial grid size and time step are selected as $\Delta x = 25$ m and $\Delta t = 0.1$ s, which satisfy the CFL condition. Table 4 indicates the overview of numerical wave tank and model description considered in the model.

Table 4 Condition of the calculation

Time step Δt	0.1 second
Grid size $\Delta x = \Delta y$	25 m
Size of 2D-sectional water tank	6525m \times 7025m.
angle of dip	1 : 0.007
water depth on flat	1.8 m
oil thickness	0.8 m
Input wave	Sine wave (Period T=7min, Amplitude =5m)

As the initial condition, we assume that the water layer already exists on the land because of liquefaction before tsunami arrival. Then, oil slick is set as 80cm on the water as the initial thickness. Tsunami propagates from the offshore and inundates on the land, and advects the oil on the water layer on the land. Figure 10 shows the snapshots of oil-tsunami advection at $t=450$ s, for $\alpha=0.91$, 0.7, and 0.5. The model case of $\alpha=0.91$ assumes the crude oil for upper layer and the sea water for lower layer.

Also, Figure 11 shows the snapshots of oil-tsunami advection, at $t=300$ and 500 s with the interfacial resistance coefficient $f_{inter}=0$, 0.01, and 0.1. In case of $f_{inter}=0$, elevation oil layer becomes sum of water elevation of 1-layer model and thickness of oil layer. At 300 seconds, oil slick is lifted up elevation. It indicate that transfer of kinetic momentum to upper is increased as f_{inter} is increasing, At 500 seconds, the tsunami is passing over the oil, the horizontal shift of the edge of run-up water is larger against f_{inter} is small.

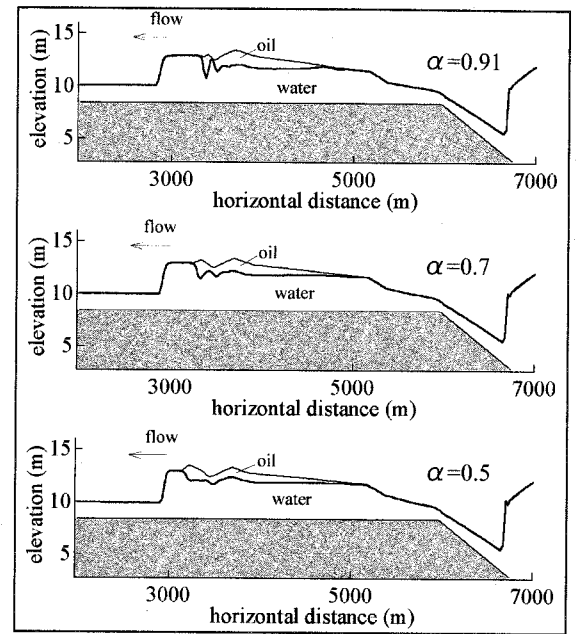


Figure 10 the edge of oil slick for each density ratio at 450seconds ($f_{inter}=0.01$)

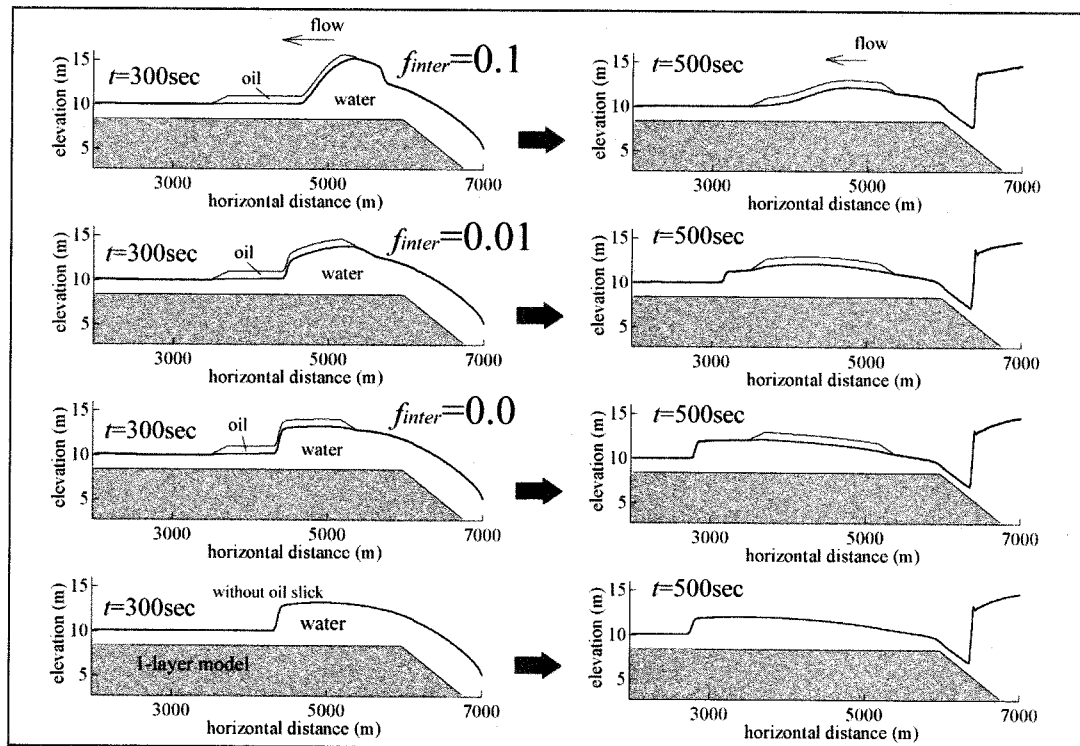


Figure 11 transfer of kinetic momentum from lower layer to upper layer

5. SUMMARY

We reviewed the disaster process of the large spread of fire during the 1964 Nigata earthquake with both reported facts in 1964 and numerical modeling of tsunami inundation. Then, we propose a model to simulate the oil advection and diffusion on tsunami inundation flow by using 2-layer hydrodynamic model. The model is preliminarily tested in a simple numerical wave tank. For the future, the model is extended to the actual topography to simulate the scenario of the water-oil advection by tsunami inundation flow as a significant aspect of complex tsunami disaster.

Acknowledgements:

The bathymetry data in this study were provided by Geographical Survey Institute and Ministry of Land, Infrastructure and Transport. We thank Hiroyuki Fujii, INA Corporation for his effort to make the bathymetry/topography grid of the studied area. Part of this study was financially supported by OBAYASHI Foundation.

References:

- Aki(1966a), "Generation and propagation of G waves from the Niigata earthquake of June 16,1964, Part 1. A statistical analysis." Bull. Earthq. Res. Ins., **44**, 23-72.
- Aki(1966b), "Generation and propagation of G waves from the Niigata earthquake of June 16,1964, Part 2. Estimation of earthquake moment, released energy, and stress-strain drop from the G wave spectrum. Bull. Earthq. Res. Inst., **44**, 73-88.
- L.Mansinha and D.E.Smylie (1971), "The displacement fields of inclined faults," Bull. Seism. Soc. Am. **61**, 1433-1440.
- Y.Iwabuchi and F. Imamura (2005), "Study on the oil spread and fire caused by a tsunami," Asian and Pacific Coasts, Jeju, Korea,471-474.

DAMAGE CONTROL SYSTEM USING PRESTRESSED CONCRETE MEMBERS WITH GRADED COMPOSITE STRANDS

S. Kono¹⁾, Y. Ichioka²⁾, F. Watanabe³⁾, M. Nishiyama⁴⁾ and S. Arakane⁵⁾

1) Associate Professor, Dept. of Architecture and Architectural Engineering, Kyoto University, Japan

2) Graduate Student, Dept. of Architecture and Architectural Engineering, Kyoto University, Japan

3) Professor, Dept. of Architecture and Architectural Engineering, Kyoto University, Japan

4) Associate Professor, Department of Global Environmental Engineering, Kyoto University, Japan

5) Structural Engineer, PC System Division, Sumitomo Steel Wire Corporation, Japan

kono@archi.kyoto-u.ac.jp, rc.watanabe@archi.kyoto-u.ac.jp, nabe@archi.kyoto-u.ac.jp, mn@archi.kyoto-u.ac.jp

Abstract: Graded Composite Strand (GCS) consists of two kinds of wires with different strengths. Low strength wires dissipate energy and high strength wires provide the restoring force. By post-tensioning beam-column joints with GSC's, construction of jointed hybrid system become greatly simplified. Cantilever beams with new types of GCS were tested to verify the increased efficiency of the hybrid joint system. The performance of tested specimens unfortunately was not as good as expected but clarified issues to be solved.

1. INTRODUCTION

Recent building structures are normally designed to respond nonlinearly under severe earthquakes. They have critical locations where the structural members deform or rotate beyond the linear limits. In precast concrete structures, the nonlinear locations are typically flexural plastic hinges in members or rotating joints in or between members. The global nonlinear seismic response of a structure depends on the response characteristics of the nonlinear locations. For seismic design, precast structural systems may be categorized into four types according to the behavior of the nonlinear locations; equivalent monolithic, jointed hybrid, jointed rotating, and foundation rocking.

If the nonlinear locations of a precast structure rotate by a mechanism of joint opening rather than by plastic hinging, the structure is categorized as a jointed system. In jointed systems nonlinear rotation is accommodated at a single crack or joint opening rather than over several cracks in a plastic hinge region. Jointed systems make use of either unbonded prestressing or dead load to provide a restoring force that counteracts seismic deformations. Jointed hybrid systems include special measures to provide energy dissipation similar to that occurring in equivalent-monolithic systems. The systems are called hybrids because they use the restoring-force characteristics of jointed-rotation systems combined with energy dissipation characteristics of equivalent monolithic systems.

A jointed hybrid moment resisting frame ordinarily has nonlinear locations at joints that open up at the ends of the beams. Unbonded post-tensioned tendons along the beam centerline, passing through the column, provides the restoring force. Mild steel reinforcement at the top and bottom of the beam section provides energy dissipation by yielding in tension and compression. The mild steel reinforcement is de-bonded for a specified length to control the reinforcement strain. The type of moment resisting frame system was shown to provide excellent performance in testing of a 5-story structure under the PRESSS program (Priestley et al. 1999) and has been used in California for

buildings up to 39 stories (Englekirk 2002).

Graded Composite Strand (GCS) consists of two kinds of wires with different strengths. Low strength wires dissipate energy and high strength wires provide the restoring force. By post-tensioning beam-column joints with GCS's, construction of the jointed hybrid system become greatly simplified. Using cantilever specimens with GCS's, Niwa et al. (1993) tested post-tensioned precast cantilever beams and found that specimens dissipated large amount of energy by yielding low strength wires and kept residual deformation small by elastic response of high strength wires. They used low strength wire (*L*-wire) with yield strength of 560 MPa and medium strength wire (*M*-wire) with yield strength of 1700 - 1770 MPa as shown in Figure 1(a). The obtained load-deflection relation is compared with that with ordinary 7-wire strand in Figure 2.

New types of GCS's were recently devised using higher strength wires (*H*-wire) with yield strength of 2110 MPa to increase the efficiency of GCS. GCS-H3L4, shown in Figure 1(b), consists of three *H*-wires and four *L*-wires and GCS-H1L6 consists of one *H*-wire and six *L*-wires. GCS-U, shown in Figure 1(c), does not use *H*-wires but consists of one seven *M*-wire strand and twelve *L*-wires surrounding *M*-wire strand. The central strand is de-bonded in an enclosed vinyl pipe with grease and *L*-wires are embedded directly in concrete. Prestressing force was introduced only to *M*-wires but not to *L*-wires.

In this study, these new types of GCS's are used in cantilever beams to verify the increased efficiency of the hybrid joint moment resisting frame with GCS's. The following two issues were focused.

- Beams with GCS's keep residual deformation small with enough amount of energy dissipation.
- Beams do not have severe damage since deformation concentrates at joints.

2. EXPERIMENTAL SETUP

Typical dimensions of five specimens are shown in Figure 3. Five specimens were identical except tendon type and locations that are shown in from Figure 3(b) through (e). Tendons with GCS-U were placed in the form and concrete of beam and stub was cast monolithically in B but beams and stubs were cast separately and post-tensioned through mortar joint for other four specimens.

Test variables are shown in Table 1. Initial prestressing forces were determined so that *L* wires yielded and *M*- or *H*-wires remained elastic. Material properties of concrete and mortar, mild steel reinforcement, and strand are given in Table 2. Loading system and protocol are shown in Figure 4. The specimen was rotated 90 degrees in the loading system and the load protocol was two cycles at rotation angles of 0.05, 0.1, 0.2, 0.4, 0.6, 0.8, 1.0, 2.0, 3.0, 4.0, 5.0 and 7.5 %.

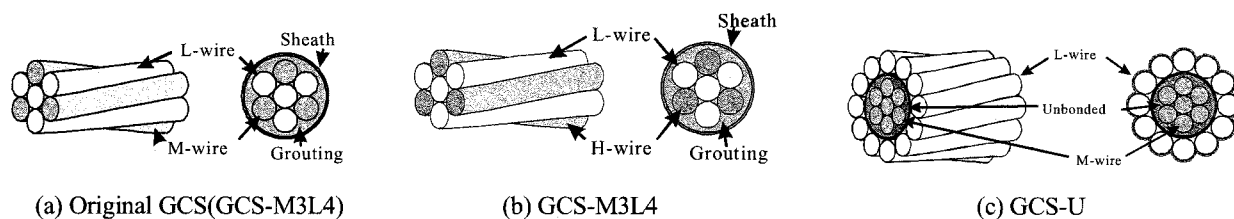


Figure 1 Configuration of different types of GCS's

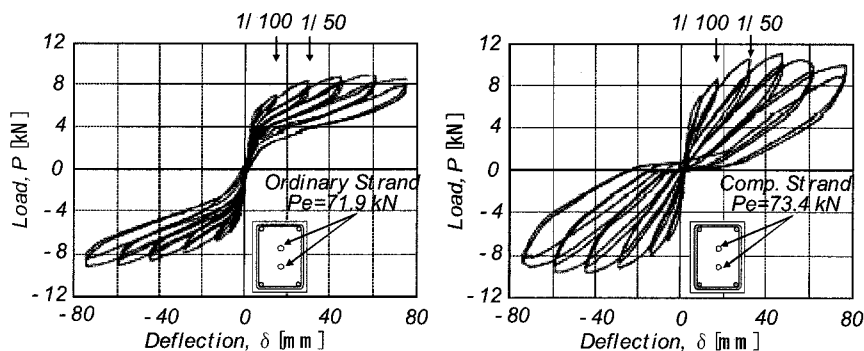
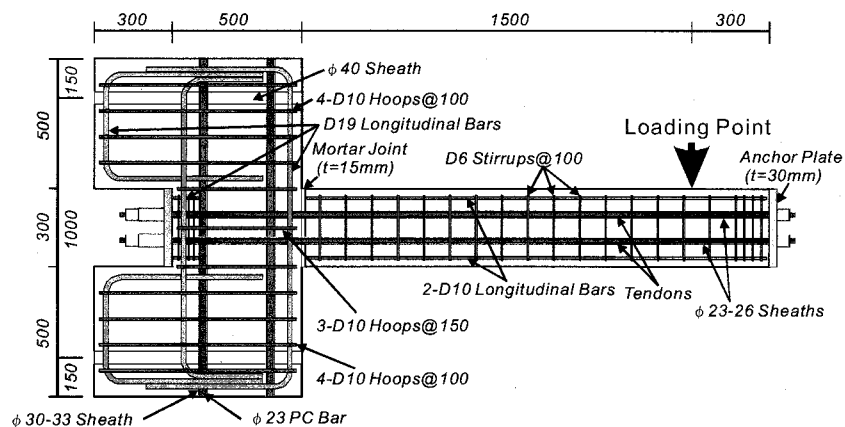
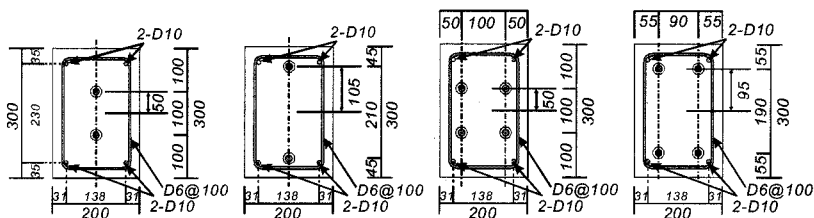


Figure 2 Load-deflection relations of previous experiment (Niwa et al. 1993)



(a) Specimen configurations



(b) A-1 and B

(c) A-2

(d) C-1

(e) C-2

Figure 3 Dimensions and reinforcing arrangement (Unit: mm)

Table 1 Test variables

Specimen	Strand		Prestressing force	
	Type	Components	P_i (kN)	$P_i / F_c b D$ (%)
A-1	Ordinary Strand	SWPR7B 15.2 (bonded)	200	6.4
A-2	Ordinary Strand	SWPR7B 15.2 (unbonded)	380	12.2
B	GCS-U	12-Mild Steel Wires 5.6 (bonded), SWPR7B 12.7 (unbonded)	200	6.4
C-1	GCS-H3L4	3-High Strength Wires 5.1 (bonded), 4-Low Strength Wires 5.1 (bonded)	320	10.3
C-2	GCS-H1L6	1-High Strength Wires 5.1 (bonded), 6-Low Strength Wires 5.1 (bonded)	300	9.6

P_i : total initial prestressing force, F_c : concrete compressive strength, b : beam width, D : beam depth

Table 2 Material properties

(a) Concrete

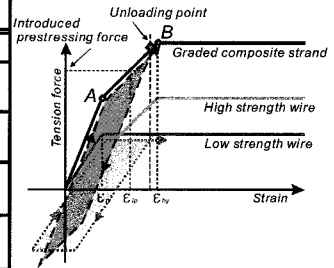
Location	Compressive strength (MPa)	Tensile strength (MPa)	Young's modulus (GPa)
Beam	51.8	3.1	28.4
Stub	60.3	2.7	31
Joint mortar	49.4	-	-
Grout mortar	45.4	-	-

(b) Mild steel reinforcement

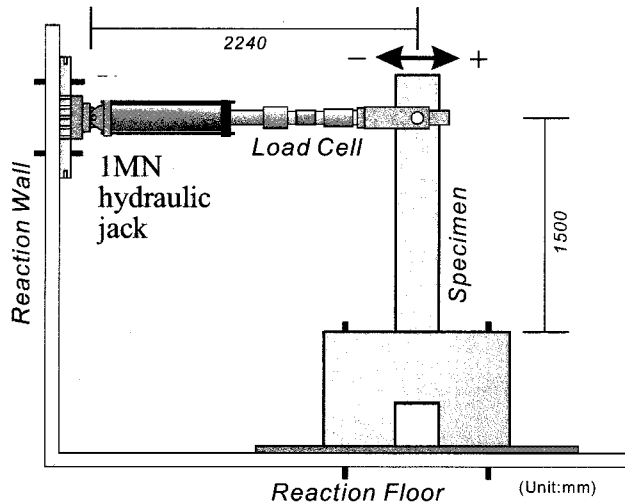
Type	Yield strength (MPa)	Tensile strength (MPa)	Young's modulus (GPa)
D6	370	519	173
D10	377	511	171
D19	346	539	159

(c) Strand

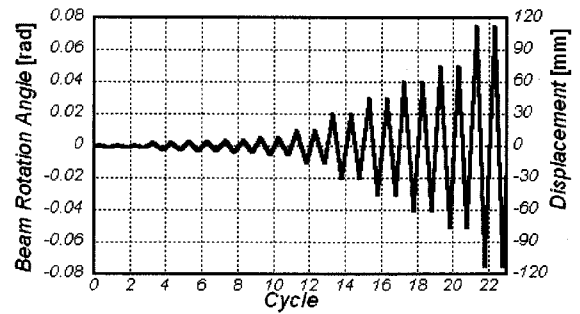
Specimen	Strand		Section area (mm ²)	Yield strength (MPa)	Tensile strength (MPa)	Young's modulus (GPa)
A-1&A-2	Ordinary Strand	SWPR7B 15.2mm	138.7	1700	1930	191
B	GCS-U	SWPR7B 12.7mm	98.7	1770	2720	193
	Central Strand					
	GCS-U	Low Strength Wire 5.6mm	24.6	560	610	195
C-1	GCS-H3L4	Point A *	140.7	560	1350	192
		Point B *		1220		
C-2	GCS-H1L6	Point A *	140.7	560	860	192
		Point B *		780		



*Point A and B indicates yielding points of L and H wires, respectively, in the right figure. Strengths and Young's modulus are converted using the section area.



(a) Loading setup



(b) Loading protocol

Figure 4 Loading setup and protocol

3. TEST RESULTS

Figure 5 shows load-rotation relations. All specimens showed residual deformation less than 5% of the peak value. A-1 and A-2 show typical hysteresis curves of beams with bonded and unbonded strands. It is noted that residual deflection of A-2 is extremely small. B shows a similar hysteresis curve with A-1. C-2 had relatively large residual deformation and *L*-wires fractured at $R = 3.0\%$. C-1 shows intermediate behavior between A-1 and C-2 in that dissipated energy was large with small residual deflection. Since grouting work was not successful for A-1, C-1 and C-2, energy dissipation for these specimens would have been larger. Consequently, as shown in Figure 6, equivalent damping ratios for these specimen did not increase compared with previous test results, shown in Figure 2(b), with the original GCS's. Although damping factors of C-1 and C-2 are larger than other specimens, they would have been large if the bond performance was better. B didn't show the increase of damping factor because *L*-wires didn't yield probably because bond characteristic of surrounding *L*-wires was not good.

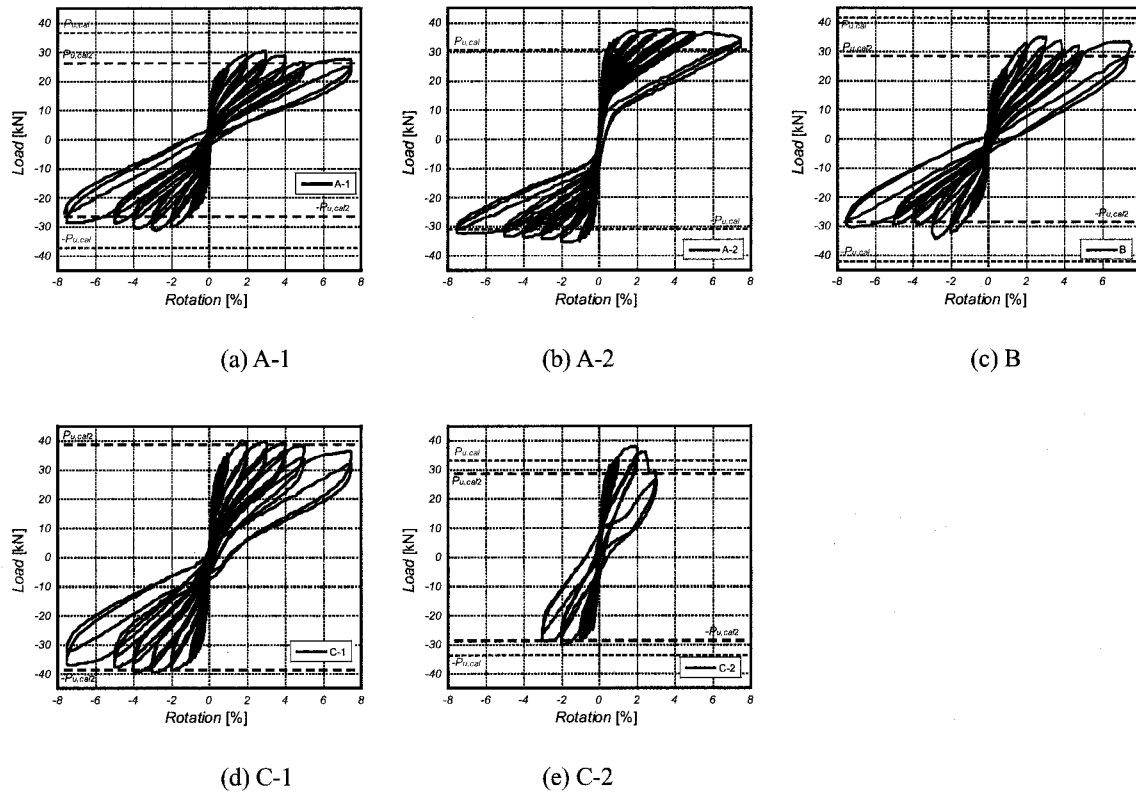
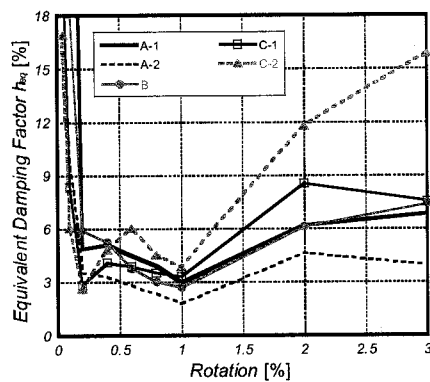
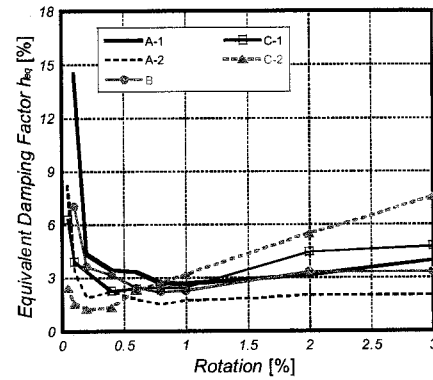


Figure 5 Load-rotation relations



(a) First loop

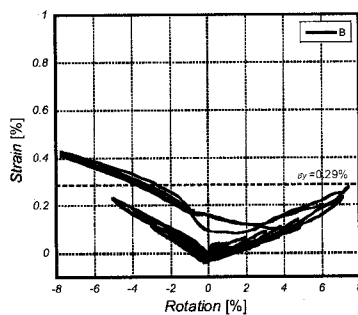


(b) Second loop

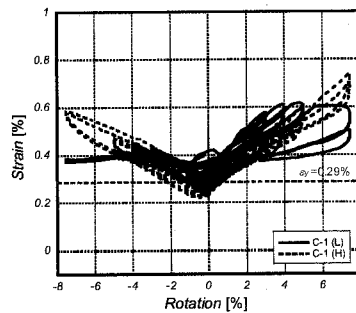
Figure 6 Equivalent damping factor-rotation relation

It was expected that *L*-wires would yield and *M*- or *H*-wires remained elastic. Figure 7 shows strain-rotation relations for B, C-1 and C-2. In B, *L*-wires, which were not prestressed, didn't yield leading to small equivalent damping factor. In C-1 and C-2, *L*-wires yielded at the early state of deformation.

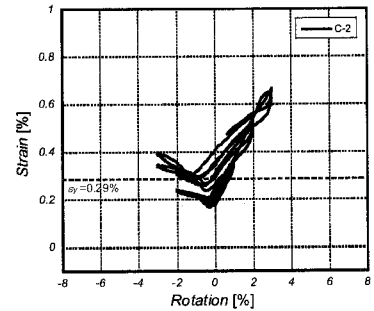
Figure 8 shows crack distributions at the ultimate state for C-1 and C-2 as representative specimens. The grid is drawn every 50 mm. They show quite minor damage even after experiencing rotation of 7.5%. In addition, most of crack widths were less than 0.3 mm at the peak of each loop and residual crack widths were less than 0.05 mm.



(a) *L*-wire of B

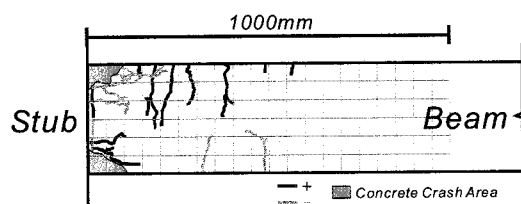


(b) *L*- and *H*-wires of C-1

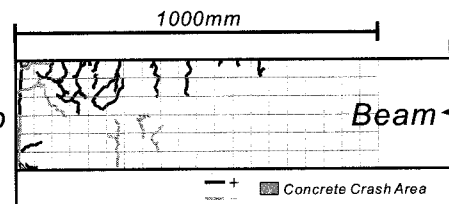


(c) *L*-wire of C-2

Figure 7 Strand strain-rotation relations



(a) C-1



(b) C-2

Figure 8 Cracks and damage of concrete at ultimate state

The Japanese guideline (AIJ 2003) gives Eq. (1) for the ultimate flexural moment capacity, $M_{u,cal}$.

$$M_{u,cal} = \frac{7}{8} a_t \sigma_y d + a_p \sigma_{pu} \left(d_p - \frac{d}{8} \right) \quad (1)$$

where d is the distance from extreme compression fiber to centroid of non-prestressed tension reinforcement, d_p the distance from extreme compression fiber to centroid of prestressed tension reinforcement, a_t the area of non-prestressed tension reinforcement, σ_y the nominal yield strength of non-prestressed tension reinforcement, a_p the area of prestressed tension reinforcement, and σ_{pu} the tensile strength of prestressed tension reinforcement at the ultimate state. It is assumed that $\sigma_{pu} = \sigma_{py}$ for bonded tendons and $\sigma_{pu} = 0.75\sigma_{pe} + 0.25\sigma_{py}$ for unbonded tendons where σ_{pe} is the effective prestressing stress of prestressed reinforcement and σ_{py} is the nominal yield strength of prestressed reinforcement.

$M_{u,cal}$ and experimental maximum moment capacity, M_u , are shown in Table 3. Except A-2, $M_{u,cal}$ were larger than M_u and Eq. (1) gave unsafe estimation. In the construction of specimens except A-2, grouting was not properly constructed and bond deterioration is considered to have occurred at the ultimate state. Therefore, by assuming that bond characteristics were intermediate values of perfect bond and unbond, σ_{pu} was modified as Eq. (2). The modified ultimate flexural moment capacity, $M_{u,cal2}$, were larger than M_u , as shown in Table 3.

$$\sigma_{pu} = 0.50\sigma_{pe} + 0.50\sigma_{py} \quad (2)$$

Table 3 Ultimate flexural moment capacity

Specimen	Experiment	Original AIJ		Modified calculation	
	M_u (kN.m)	$M_{u,cal}$ (kN.m)	$M_u / M_{u,cal}$	$M_{u,cal2}$ (kN.m)	$M_u / M_{u,cal2}$
A-1	45.3	55.2	0.82	39.3	1.15
	-47.0		0.85		1.20
A-2	56.6	45.7	1.24	-	-
	-47.0		1.03		
B	52.5	62.5	0.84	42.6	1.23
	-51.5		0.82		1.21
C-1	59.9	79.8	0.75	58.1	1.03
	-59.1		0.74		1.02
C-2	57.0	50.3	1.13	42.6	1.34
	-45.2		0.90		1.06

4. CONCLUSIONS

Experiment was conducted on cantilever beams with new types of GCS's and the following conclusions were obtained.

- Specimens with GCS-H series dissipated enough energy and their equivalent damping factor was about 10% at $R = 2.0\%$. C-1, with GCS-H3L4, kept residual deformation small and showed desirable behavior as planned. B, with GCS-U, unexpectedly didn't dissipate enough energy probably because bond characteristic of surrounding L -wires was not very good.

- Maximum and residual crack widths were very small and damage of concrete concentrated at the fixed end of beam. Critical damage of concrete was not seen until rotation of 7.5%.
- Ultimate flexural moment capacity may be calculated by considering bond deterioration of strand.

ACKNOWLEDGEMENT

This study was supported by Land, Infrastructure and Transportation Ministry (Principal investigator: Fumio Watanabe) and Ministry of Education, Culture, Sports, Science and Technology (No. 16360276, Principal investigator: Hitoshi Tanaka). The authors wish to express their appreciation for Neturen Co., Ltd. and DENKA by donating materials in experiment.

REFERENCES

1. Federation Internationale du Beton. *Seismic design of precast concrete building structures*, State-of-art report prepared by Task Group 7.3, FIB bulletin 27, October 2003.
2. Priestley, M.J.N., Sritharan, S., Conley, J.R. and Pampanin, S. "Preliminary results and conclusions from the PRESSS five-Storey Precast Concrete Test Building", *PCI Journal*, Vol. 44, No. 6, pp. 42-67, 1999.
3. Englekirk, R.E., "Design-Construction of the Paramount – A 39-story Precast Prestressed Concrete apartment Building" *PCI Journal*, Vol. 47, No. 4, pp.56-71, 2002
4. Architectural Institute of Japan. *Recommendations for Design and Construction of Partially Prestressed Concrete (Class III of Prestressed Concrete) Structures (in Japanese)*, 2003.
5. Niwa Y, et al. Energy Dissipating Precast-Prestressed Beam-Column Connection (in Japanese). *Summaries of Technical Papers of Annual Meeting Architectural Institute of Japan*, Vol. 2, pp. 535-536, 1993.
6. Jiang, L. H. et al. Hysteresis Behavior of Precast Beam-Column Joint Assemblages Post-tensioned by Composite Strands (in Japanese). *Summaries of Technical Papers of Annual Meeting Architectural Institute of Japan*, Vol. 2, pp. 1033-1036, 1994.
7. Yanaka H. et al. Study on Structural Performance of Precast Beam-Column Joint Assemblages Post-tensioned by Composite Strands (in Japanese). *Summaries of Technical Papers of Annual Meeting Architectural Institute of Japan*, Vol. 2, pp. 939-942, 1995.

TESTING ON 2-STORY AND 2-BAY REINFORCED CONCRETE FRAMES WITH SUBSTANDARD REINFORCING DETAILS

Y.C. Wang¹⁾, J.S. Huang²⁾, and B.C. Chen²⁾

1)Associate Professor, Department of Civil Engineering, National Central University, Taiwan

2)Former ME Students, Department of Civil Engineering, National Central University, Taiwan

wangyc@cc.ncu.edu.tw

Abstract: Simulated seismic load tests on a reinforced concrete 2-story and 2-bay frame with substandard reinforcing details in columns and beam-column joints are described. These substandard details are mainly lower concrete strength and less transverse reinforcement in base columns and beam-column joints. RC jacketing offers a versatility for retrofitting those deficient members. The improvement in columns and joints rehabilitated with RC jacketing, without dowel anchors into the concrete-to-concrete interface for preventing premature bond failure, is demonstrated. Results showed the prototype frame behaved as a typically non-ductile structure while the retrofitted frame with RC jacketing onto columns showed a superior seismic performance.

1. INTRODUCTION

The majority of structures in Taiwan do not meet current seismic code requirements, and many of these structures are vulnerable to damage and even collapse in an earthquake. Concerns about the seismic response of existing structures grew considerably and resulted in several programs to identify and mitigate seismic risk. The 1999 Chi-Chi earthquake provided renewed impetus for seismic rehabilitation of structures in Taiwan.

At least two significant challenges are posed by the goal to manage the seismic risk in Taiwan. The first of these is to identify those structures that pose the greatest threat to life and property and for which seismic upgrades can be implemented successfully. The second is to establish retrofit guidelines that not only represent current knowledge on retrofit design and construction practice, but that will also serve to educate the practicing engineer or other professional who may not have significant experience in seismic rehabilitation.

Some collaborated researches (Chang 2000, Hwang 2003, and Wang 2004a) onto the seismic evaluation and retrofit of non-ductile RC low-rise building frames typically constructed in Taiwan have been carried out. Those were aimed at providing the seismic assessment techniques of RC frames with and without in-filled brick and RC walls and finding the feasible retrofit schemes fit to local engineering practice. The authors in the paper have involved a series of investigations (Wang et al. 2003-2005) regarding non-ductile frames with RC jacketing since the past few years. Parts of

beam-column joint sub-assemblages had been tested as presented previously (Wang et al. 2003 and 2005). In the paper, the consecutive study on the behavior of non-ductile frames with substandard reinforcing details in columns and specially in beam-column joints was reported.

2. BEAM-COLUMN-JOINT SUBASSEMBLAGES

2.1 Objective

Seismic strengthening of weak beam-column-joint sub-assemblages has been studied experimentally by the authors (Wang et al. 2003) since 2002. Parts of results were presented in the previous CUEE conference (Wang et al. 2005).

Strengthening technique uses concrete jacketing. The retrofit aims to improve inadequate details such as lack of transverse joint reinforcement and insufficient shear strength of joint. The testing specimen of beam-column joint assemblages are chosen for an example as detailed in Figure 1 while the test set-up and loading sequences are presented in Figure 2.

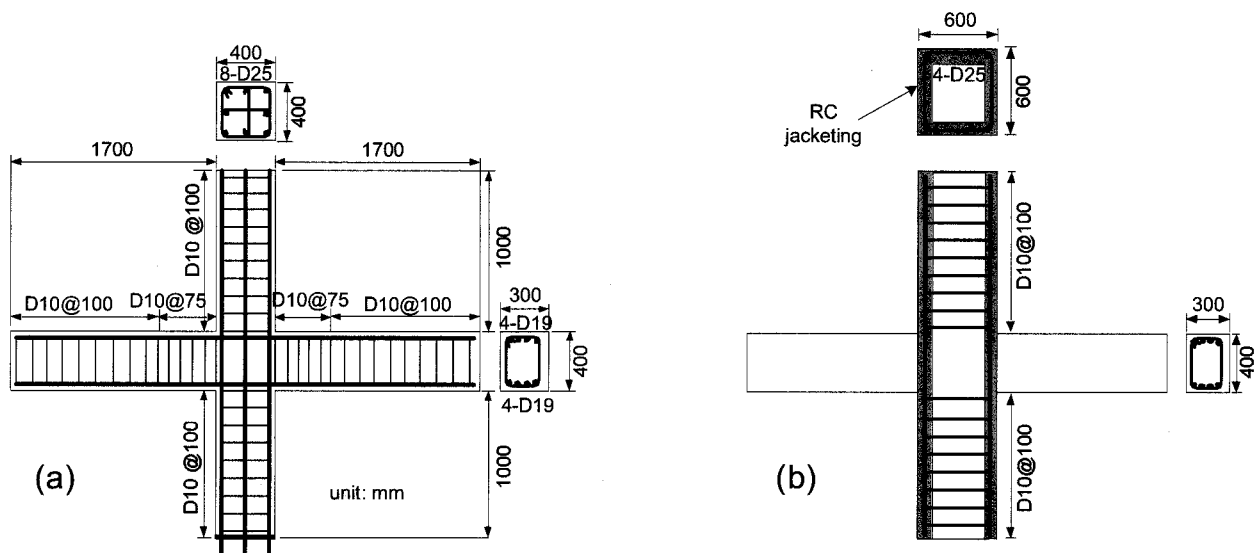


Figure 1 Details of Tested Beam-Column Joints: (a) As-built Unit JI1, and (b) RC Jacketed Unit JIR1.

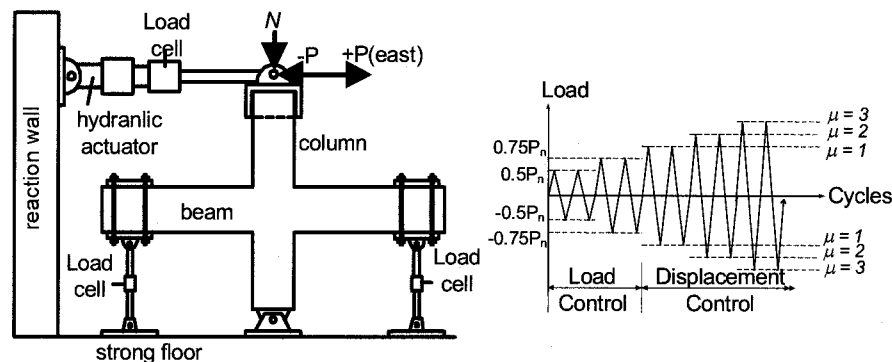


Figure 2 Test Set-up and Loading Sequence.

2.2 Significant Findings

The typical results of two reinforced concrete interior beam-column joints (see Figure 1) were tested: the specimen in its as-built form and the specimen retrofitted with a concrete column jacket. Concrete strength was 20 MPa for as-built units, but the concrete strength for the column jacket was 41 MPa.

Details of the original specimen include insufficient shear strength of joint and none of joint hoop. The prototype unit exhibited a joint shear failure mechanism. The nominal flexural strength of beam was never developed, indicating insufficient joint strength.

Retrofit specimen was strengthened by adding reinforced concrete column jacket with a thickness of 100 mm for each face (Figure 1). Column jacketing involved adding additional longitudinal steel along the entire length and through the existing slab. No anchors were installed between new and old concrete interface. As shown in Figure 3, the retrofit unit JIR1 developed higher strength and more ductile hysteretic behavior than the as-built unit JI1.

The test results showed that the shear strength of the non-ductile beam-column joints was efficiently enhanced by the concrete jacketing.

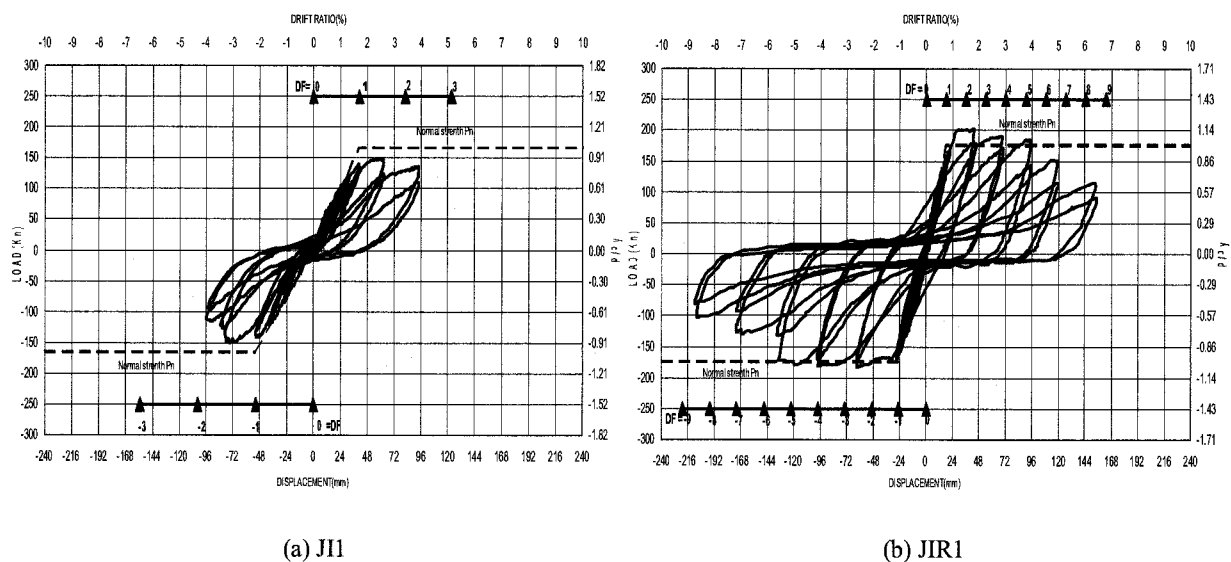


Figure 3 Test Results of Beam-Column Joint Sub-assemblages.

3. LOW-RISE RC BUILDING WITH DEFICIENCY IN BEAM-COLUMN JOINTS

3.1 Objective

Normally, experimental works were focused on the sub-assembly type as mentioned in previous Section 2. By means of testing on the large-scale 2-story and 2-bay frame, a more realistic behavior of the frame with non-ductile beam-column joints containing less or no horizontal shear reinforcement can be observed. Meanwhile, a retrofit scheme using RC jacketing may be criticized by strengthening

of the large-scale frame.

The research results can also be compared with the non-ductile frame retrofitted with the strengthening other than RC jacketing (Hwang et al. 2003). The advantages and disadvantages of the RC jacketing could be pointed out by the time.

3.2 Significant Findings

A two-story and two-bay non-ductile frame (NF) with substandard reinforcing details mainly in beam-column joints was tested to failure and then retested after retrofitting with RC jacketing (NF/rc). The test setup is shown in Figure 4. The reinforcing details for NF and NF/rc are presented in Figure 5. Concrete strength was 21 MPa for NF and 34 MPa for NF/rc.

Details of the original frame NF include the substandard reinforcing details in the beam-column joints without ties and the insufficient transverse reinforcement in the columns with unreliable 90 end hooks (Figure 5). The maximum force-carrying capacity developed by NF was 353 kN at about to 1% of story drift ration (Figure 6) and the joint shear failures were observed firstly in the interior joint located in the middle column

Based on the experimental observation, the retrofitting with RC jacketing is quite effective in increasing seismic strength for the low-rise RC buildings with substandard reinforcing details in the base columns and beam-column joints. Without unexpected failure occurred in mechanical bolted connectors, a higher story drift more than 3% could be developed.

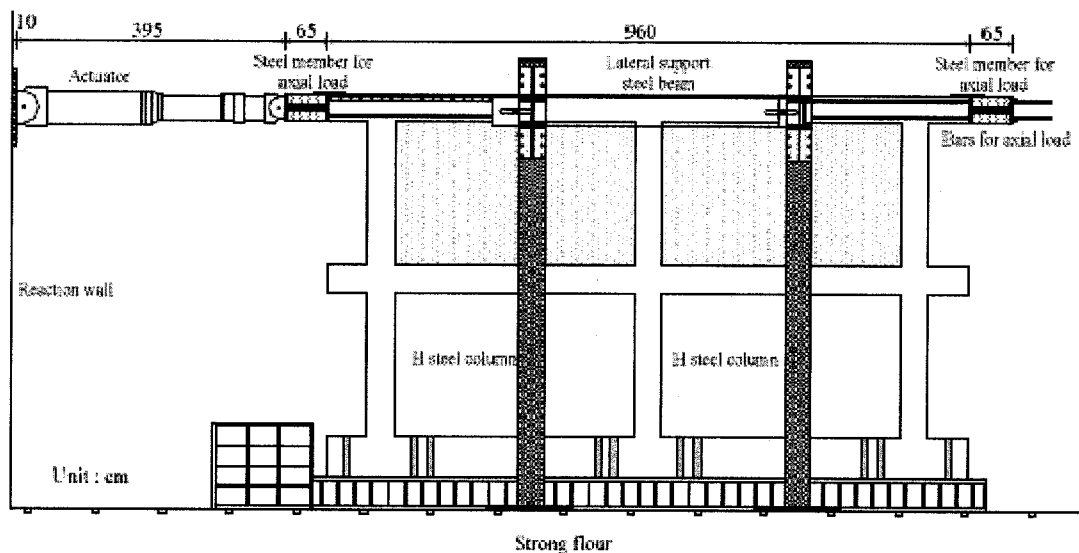
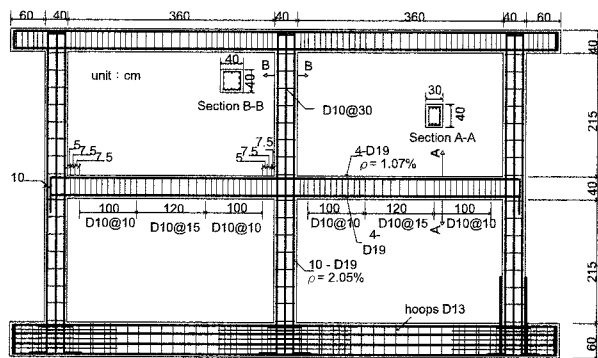
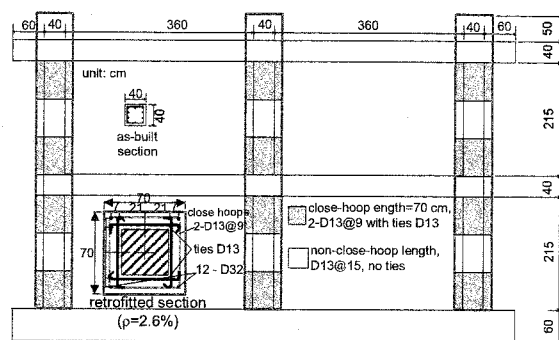


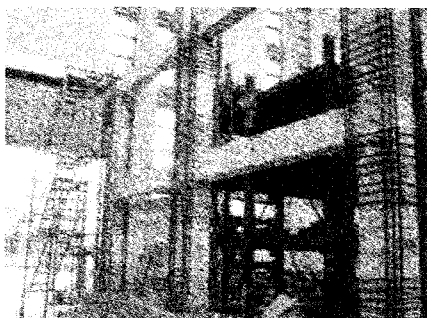
Figure 4 Frame Test Setup.



(a) Prototype Frame NF



(b) Retrofitted Frame NF/rc

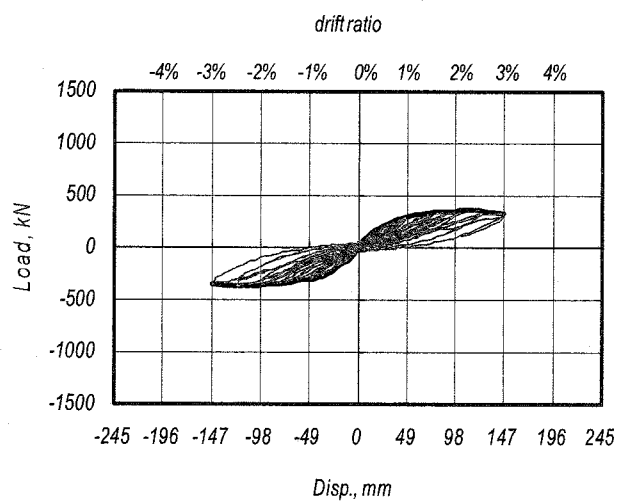


(c) Steel Details in NF/rc

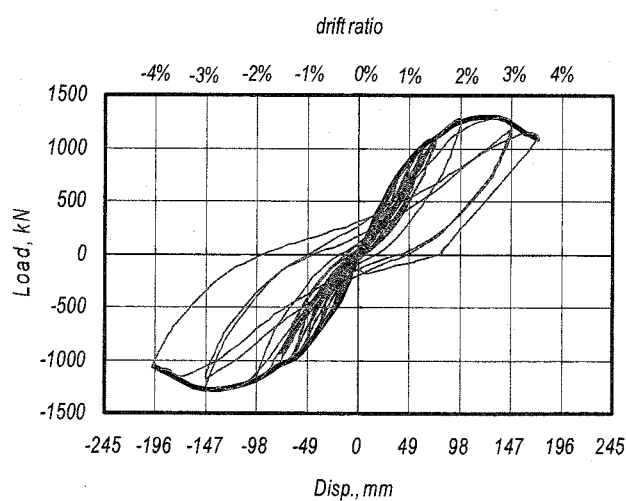


(d) Placing Concrete for NF/rc

Figure 5 Frame Details and Construction.



(a) NF



(b) NF/rc

Figure 6 Load Displacement Response of Test Frames.

4. CONCLUSIONS

For the experimental study on the non-ductile frame with substandard detailing in beam-column joints without ties, the main conclusions are presented as below. A worthy mention is that the concrete jacket without installing dowel anchors to as-built columns and joints, as a view of lowering labor work, was proposed by the authors and parts of results were described previously (Wang et al. 2005).

1. The design of RC jacketing mainly referred to recent RC standard code (ACI 318-05) is more acceptable to engineers.
2. Parts of design procedures not able to satisfy code requirements are provided by the authors. Such as, evaluation of beam-column joint strengths for prototype and jacketed units, and alternative layout of new lateral hoops in column jacketing area.
3. Unexpected failure due to the disconnection of mechanical bolted coupler was occurred at a higher story drift ratio 3%. It was believed that RC jacketing applied to columns can effectively improve the frame with substandard joint details to a ductile behavior.
4. Further tests for large-scale frames are needed to confirm the effects of layout of horizontal column hoops and the proposed design method of the RC jacketing.

Acknowledgements:

The research financial assistance provided by Taiwan National Science Council, Project No. NSC-93-2211-E-008-019, is gratefully acknowledged. The authors are also thanked for Japan CUEE to support the first author trip expense.

References:

- Chang, K. C. and F. S. Jong (2000), "Seismic Retrofit of Shear and Lap Splice of RC Rectangular Bridge Columns using FRP Laminates," *Report No. NCRE-00-034, National Center for Research on Earthquake Engineering*, Taipei, Taiwan. (in Chinese)
- Hwang, S. J. and H. B. Chang (2003), "Study on Seismic Behavior of Non-ductile Frame Retrofitted with RC Wing Walls," *National Center for Research on Earthquake Engineering*, Taipei, Taiwan. (in Chinese)
- Wang, Y. C., C. J. Kao, and C. T. Yang (2003), "Investigation on Shear Enhancement of Beam-Column Joint Retrofitted with RC Jacketing," *Journal of the Chinese Institute of Civil and Hydraulic Engineering*, 5(3), 521-530. (in Chinese)
- Wang, Y. C. and Huang, J. S. (2004a), "Test on the Seismic Performance of Two Story-Two Bay Reinforced Concrete Moment Resisting Frame," *Report of Department of Civil Engineering in National Central University*, Taiwan. (in Chinese)
- Wang, Y.C., and Lee, M.G. (2004b), "Rehabilitation of Nonductile Beam-Column Joint Using Concrete Jacketing," *Proceedings of 13th World Conference on Earthquake Engineering*, Paper No. 3159.
- Wang, Y.C., W.H. Ho, R.T. Ko, and T.F. Ya (2005), "Influence of Joint Concrete Interfacial Slip on the Seismic Response of Non-Ductile Frames Upgraded with RC Jacketing," *Second International Conference on Urban Earthquake Engineering*, March 7-8 2005, Tokyo, Japan.
- ACI Committee 318 (2005), "Building Code Requirements for Structure Concrete (ACI 318-05) and Commentary (ACI 318R-05)," *American Concrete Institute*.

MECHANICAL CHARACTERISTICS OF REINFORCED CONCRETE MEMBERS STRENGTHENED BY CARBON FIBER FLEXIBLE REINFORCEMENT

Y. Sato¹⁾ and A. Kobayashi²⁾

1) Associate Professor, Division of Built Environment, Hokkaido University, Japan

2) Manager, Nippon Steel Composite Co. Ltd., Japan

ysato@eng.hokudai.ac.jp, a-kobayashi@nick.co.jp

Abstract: Flexural-shear test of reinforced concrete beams and cyclic test of reinforced concrete columns strengthened by carbon fiber flexible reinforcement, CFFR which is a bundle of unidirectional carbon fiber inserted in a plastic tube were carried out. It is reported that the CFFR can improve shear capacity, ductility, and post-peak behavior of the RC members.

1. INTRODUCTION

In highly seismic region like Japan, design requires arrangement of congested lateral ties to confine lateral dilation of core concrete under reversed cyclic high shear force. Congestion of lateral tie, especially intermediate lateral tie reduces constructability and efficiency. As continuous fibers (carbon fibers) conduct electricity, its direct contact with steel might cause corrosion problem. As a probable solution to the aforementioned problems, a carbon fiber flexible reinforcement (CFFR) has been developed. The CFFR is a bundle of unidirectional carbon fiber inserted in a plastic tube. The tube with fibers is wound around the main reinforcement at the construction site, and then resin is injected into the tube to make Fiber Reinforced Polymer. Since CFFR is flexible before the resin injection, it can be easily arranged in a dense and even in a complicated pattern.

In this study, flexural-shear test of reinforced concrete beams and cyclic test of reinforced concrete columns strengthened by CFFR as intermediate shear reinforcement were carried out. The strengthening effect of the CFFR in the members and mechanical performance of the strengthened members are examined based on the experimental observation.

2. CARBON FIBER FLEXIBLE REINFORCEMENT

The carbon fiber flexible reinforcement is a tubular material consisting of a bundle of unidirectional carbon fiber covered with a plastic material as shown in Figure 1. It is intended primarily as a confinement for RC structures. A suitable clearance is provided between the reinforcing fiber bundle and the plastic covering. As liquid resin is injected into the clearance and hardens, the material becomes a unidirectional fiber-reinforced polymer.

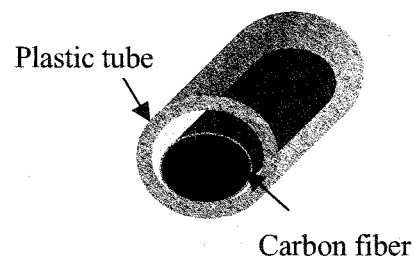


Figure 1 CFFR

Before resin is injected, CFRP is so flexible that it can be made any desired shape. Since CFRP can be easily wound at the construction site even in a complicated pattern, it can be expected that CFRP will not only facilitate bar arrangement but also increase the freedom of bar arrangement. The specifications of the CFRP used are shown in Table 1. The developed strength is 80 % of the strand strength of fiber itself.

Table 1 Components and Mechanical Properties of CFRP (Sugiyama et al. 1999)

Component	Tube	Material	PVC
		Thickness (mm)	1.0 or 2.5
	Fiber	Material	HT-Carbon fiber
		Number of strands	19
		Cross-sectional area (mm ²)	16.9
		Tensile strength (GPa)	5.00
CFRP (after resin impregnation)	Young's modulus (GPa)		265
	Tensile strength (GPa)		4.14
	Elongation (%)		1.6

3. SHEAR BEHAVIOR OF RC BEAM STRENGTHENED BY CFRP

3.1 Outline of Experiment (Kobayashi et al. 1999)

Four RC beams shown in Figure 2 were prepared. All specimens have D6 steel stirrups in the left span and D10 diameter steel stirrups in the right span at the spacing of 200 mm. Specimen SN-1 is a reference beam. In specimens SF-1 to SF-3, two CFRPs were wound around the steel stirrups as intermediate shear reinforcement (see Figure 2). The plastic tube wall thickness was approximately 2.5 mm for the CFRPs in specimen SF-1 and SF-2 while 1 mm for the CFRP in specimen SF-3.

After the CFRPs were wound around the steel stirrups, resin was injected into tubes. After the 24 hours the tubes were partly removed and strain gauges were attached to the exposed carbon fiber plastic bars and also the tubes at the ends of the CFRPs for specimen SF-2 and SF-3 were removed. The end portion of each CFRP was passed through a steel pipe with length of 300 mm and fixed to the pipe with injected grout. These pipes were anchored with a nut after concrete was placed. High-early strength cement was used for the concrete, with a target compressive strength of 29.4 MPa.

In the experiment, two-point concentrated loads were statically applied to each of the simply supported beam specimens. The load was increased in increments of approximately 10 kN.

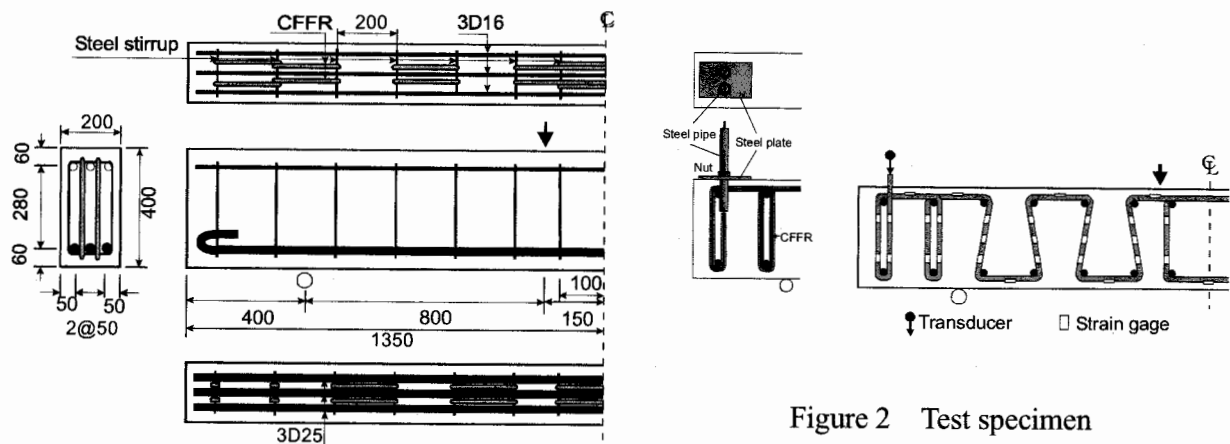


Figure 2 Test specimen

3.2 Cracking Pattern and Failure Mode

The maximum shear force is shown in Table 2. The crack patterns in each specimen are shown in Figure 3. In all specimens, a diagonal crack occurred at a load of 80 kN. In each of specimens SN-1, SF-2, and SF-3, the diagonal crack propagated into the compression zone as the applied force was increased. At the ultimate, the crack broke through the loading point, causing a diagonal tensile failure of the beam. For specimen SF-1, after diagonal crack reached the loading point, the load continued to be increased until the steel reinforcement in the compressive zone buckled.

Table 2 Experimental Results

Specimen	CFFR		Concrete	Maximum shear force V (kN)
	Tube thickness (mm)	Anchorage at end	Compressive strength (MPa)	
SN-1	-	-	26.6	119.6
SF-1	2.5	N	29.7	131.5
SF-2	2.5	Y	30.6	139.7
SF-3	1.0	Y	28.9	168.9

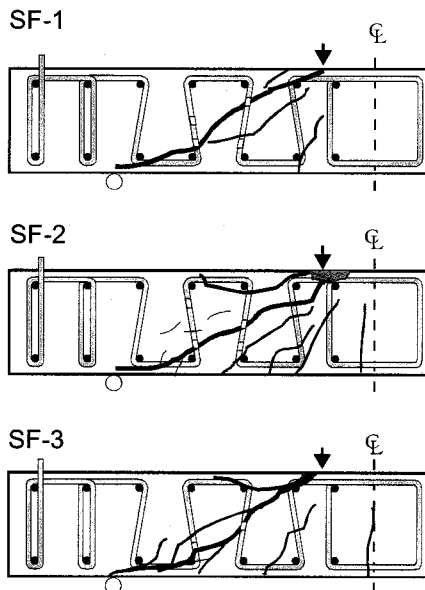


Figure 3 Crack Patterns

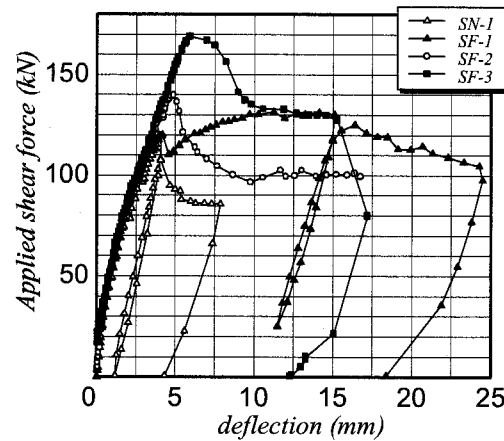


Figure 4 Relationships between Applied Shear Force and Deflection

3.3 Load-deflection Characteristics

Figure 4 shows the relationships between applied shear force and deflection for each specimen. Among the specimens with CFFR, anchoring the end of CFFR gives greater stiffness after the diagonal crack occurred. With the end of the CFFR anchored, the smaller tube wall thickness, the greater the stiffness of the beam. The same is true of the maximum load of the beam.

Specimen SN-1 sharply dropped to 90 kN after the diagonal crack broke through the compression zone under a shear force of approximately 120 kN. Specimen SF-1, by contrast, shows a very ductile deflection characteristics in which even after the diagonal crack broke through the compression zone under a shear force of approximately 120 kN, the shear force continued to increase until it began decreasing slowly from a peak of 130 kN. With specimens SF-2 and SF-3, the shear force began dropping from approximately 140 kN and 170 kN, respectively, at the same time that the diagonal crack broke through the compression zone.

3.4 Shear Resisting Characteristics

Shear force carried by steel stirrup and CFRP were calculated using strains where the diagonal crack was intersected. The variation of shear resisting forces is shown in Figure 5. With specimen SF-1 in which the CFRP was not anchored, the beam shear strength increased after the diagonal crack occurred at around 120 kN, because the shear force carried by CFRP increased. So after the maximum shear force, 131.5 kN was reached at a deflection of 11 mm, apparently, the specimen retained a shear strength approximately 130 kN until the deflection increased to 15 mm. With specimens SF-2 and SF-3, in which the ends of CFRP were mechanically anchored, the CFRP began producing its effect after the steel stirrups yielded. However the shear force carried by the CFRP remained very small. After the maximum shear force was reached, the shear force carried by CFRP began increasing. This explains why the CFRP could restrain a sharp decline in shear strength after the maximum shear force was reached. Thus, mechanically anchoring the ends of the CFRP made a difference in the pre- and post-peak behavior in load-deflection curve and shear force carried by the CFRP.

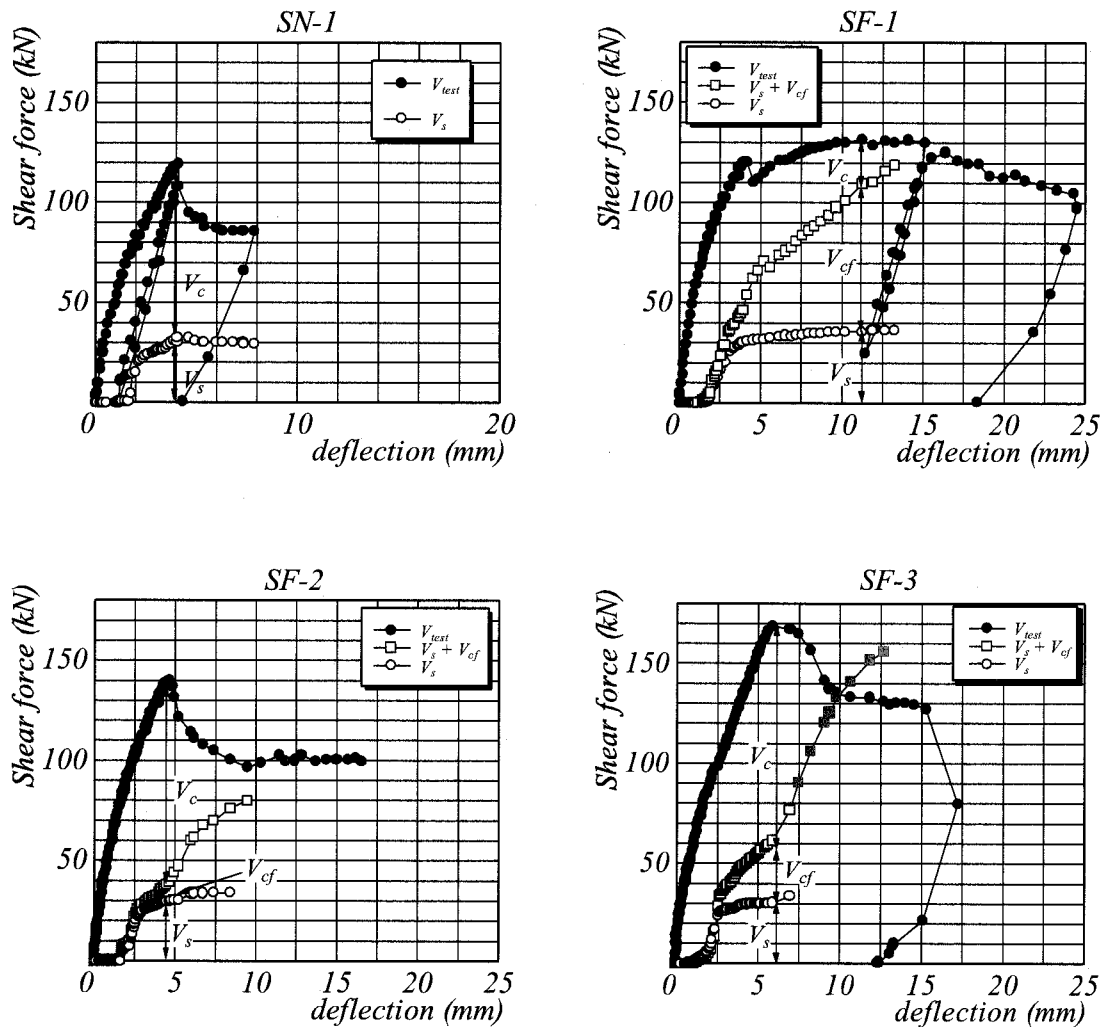


Figure 5 Variation of Shear Resisting Forces

4. DEFORMABILITY OF RC COLUMNS STRENGTHENED BY CFRP

4.1 Outline of experiment (Tuladhar et al. 2001)

Five column specimens were tested under the combination of flexure and shear. The size of all the columns were 350×350×1050 mm and that of footing to which it was monolithically attached were 900×900×800 mm (see Figure 6). All the columns contain the same amount of longitudinal reinforcement i.e., 8 D25 bars; 4 each on both sides. Minimum amount of steel shear reinforcement of 9 D10 stirrups @ 190mm c/c was provided. Besides the two reference columns S1 and S2, the two columns S3 and S4 containing additional 0.1% carbon fiber and the one column S5 containing additional 0.2% carbon fiber by volume were tested. The pattern of winding of CFRP around the main bar is shown in Figure 7. The mechanical properties of reinforcing bars and CFRP are shown in Table 3.

Pressure injection of resin took only 10 minutes after winding CFRP. When the resin hardened 24hours after the injection, the end portion of CFRP was passed through a steel pipe and fixed to the pipe with an expansive material mixed with 27% water by weight. It was then allowed to set for 24 hours. The steel pipes were anchored with washers and nuts to fix with column top surface after the concrete was placed.

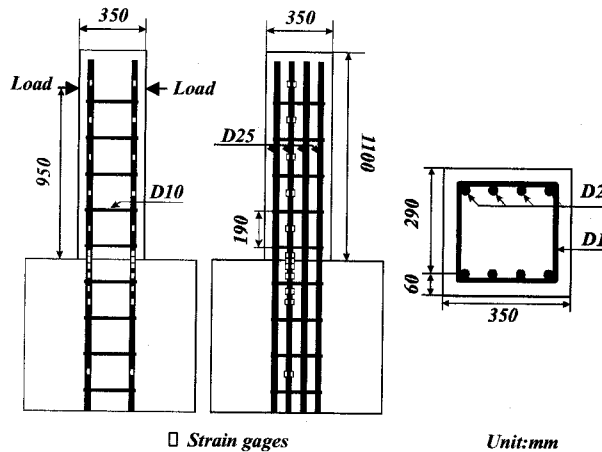


Figure 6 Arrangement of Steel Bars

Table 3 Experimental Parameters and Concrete Strength

Specimen	CFRP ratio p_{CFRS} (%)	Type of loading ¹⁾	Compressive Strength of concrete f'_c (MPa)
S1	-	A	44.7
S2	-	B	40.0
S3	0.1016	A	40.3
S4	0.1016	B	35.1
S5	0.2032	B	35.4

1) A: One-side cyclic loading
B: Reversed cyclic loading

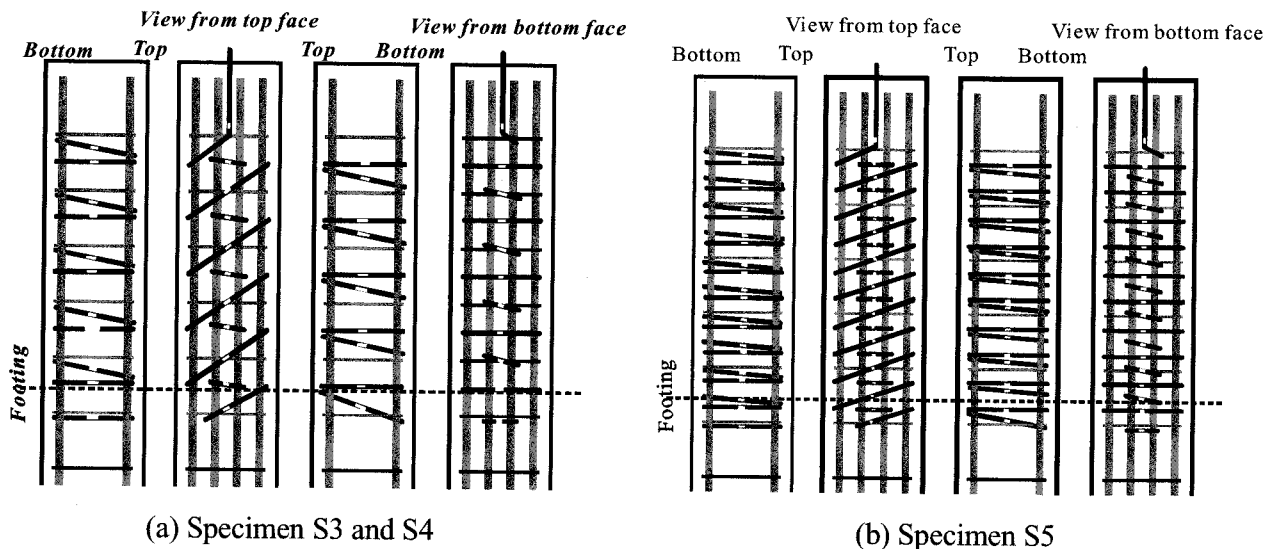


Figure 7 Arrangement of CFRP

4.2 Deformational Characteristics

The observed performance of each specimen is presented in the form of applied force vs. column tip deflection in Figures 8 through 10. The cyclic and reversed-cyclic hysteretic load-deflection relationship of the reference columns S1 and S2 suggest that the columns experienced rapid strength degradation due to insufficient confinement from the shear reinforcement. The specimen S2 even suffered from a huge damage with splitting along the longitudinal bar to the loading point. To such columns, which lack shear ductility, the authors introduced 0.1% volume fraction of carbon fiber as CFFR. Those columns are S3 and S4. Column S3, which was the companion for column S1, not only counteracted the degrading strength but also enhanced the ultimate deformation. Column S4, which is the companion for column S2, also counteracted the highly decayed strength in S2 with deformation enhancement. This demonstrates that addition of CFFR could effectively confine the core concrete with an introduction of its ductile fracture rather than quick extension and widening of CFFR and winding of diagonal crack loading to shear failure. Column S5 contains 0.2 % volume fracture of

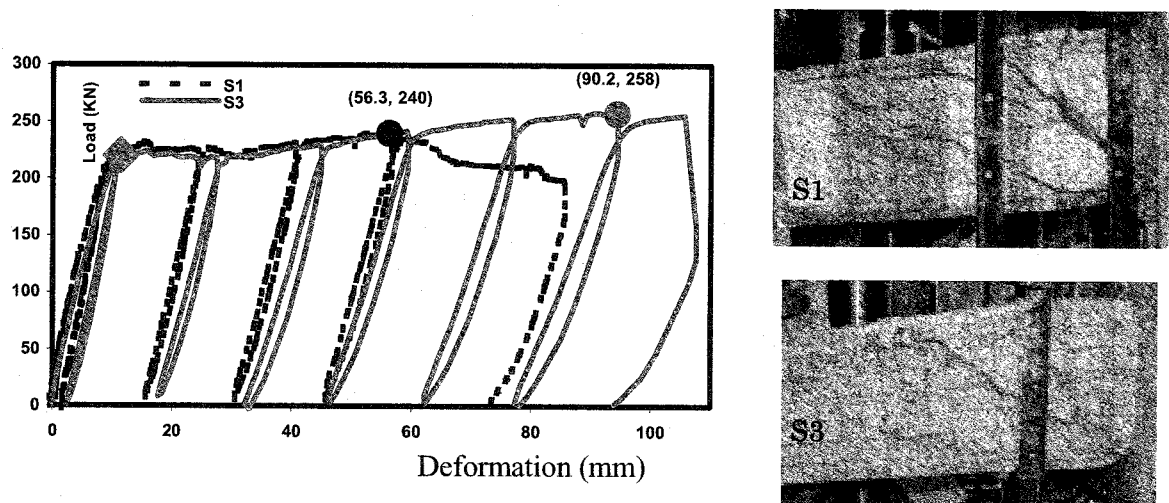


Figure 8 Load – Deformation Curves of Specimens S1 and S3

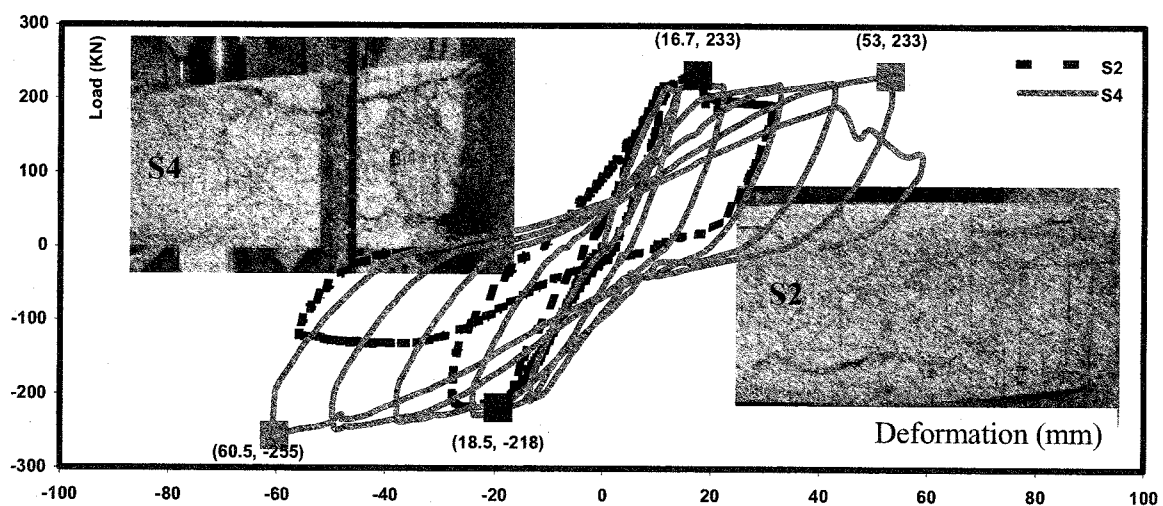


Figure 9 Load Deformation Curves of Specimens S2 and S4

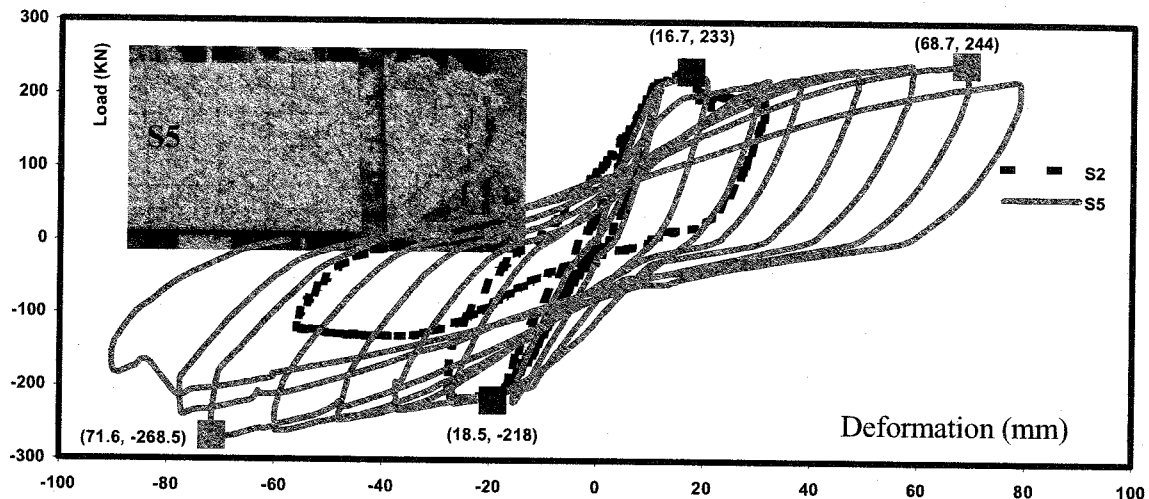
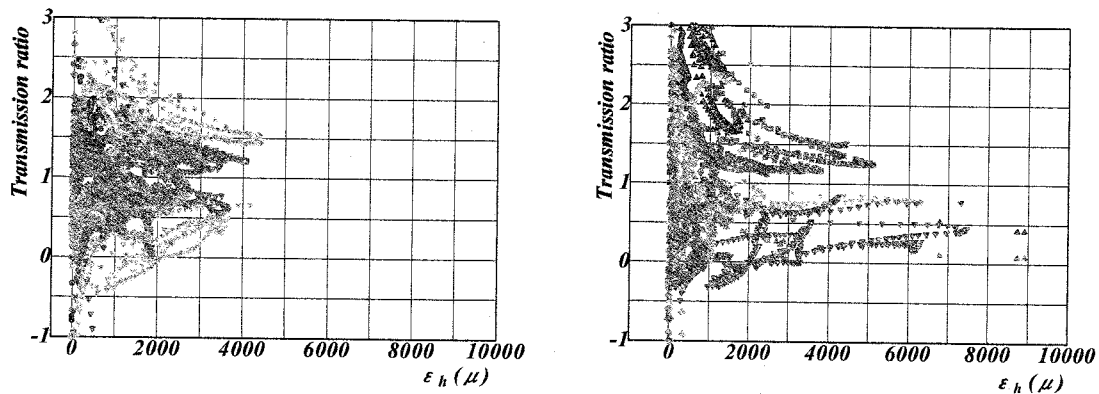


Figure 10 Load Deformation Curves of Specimens S2 and

carbon fiber as CFFR and was the companion to S2 and S4. It showed even further enhancement of shear strength and ultimate deformation. The superior performance of S5 over the companions indicates the greater confinement efficiency provided by the increment of amount of CFFR and the appropriateness of its winding pattern as well as the efficiency of the clamping system at its extremities. The CFFR could successfully provide the intended lateral confinement to the volumetric dilation of core concrete without any premature rupture.

4.3 Stress Transfer Characteristics at Bend-portion

The term transmission ratio is used for the ration of CFFR strains in horizontal part to its adjacent vertical part. Figures 11 and 12 show the verification of transmission ratio with the strain level for some typical bend portions. At low strain level, there is no any appreciable transmission and therefore the transmission ratio takes the extreme values. But at high strain level it becomes stable indicating that constant strain transmission occurs through the bend-portions. Even though the measured strain is initially negative, it always becomes positive stable at high strain level. The initial negative strains



(a) Left face

(b) Right face

Figure 11 Transmission Ratio for Outer CFFR of Specimen S4

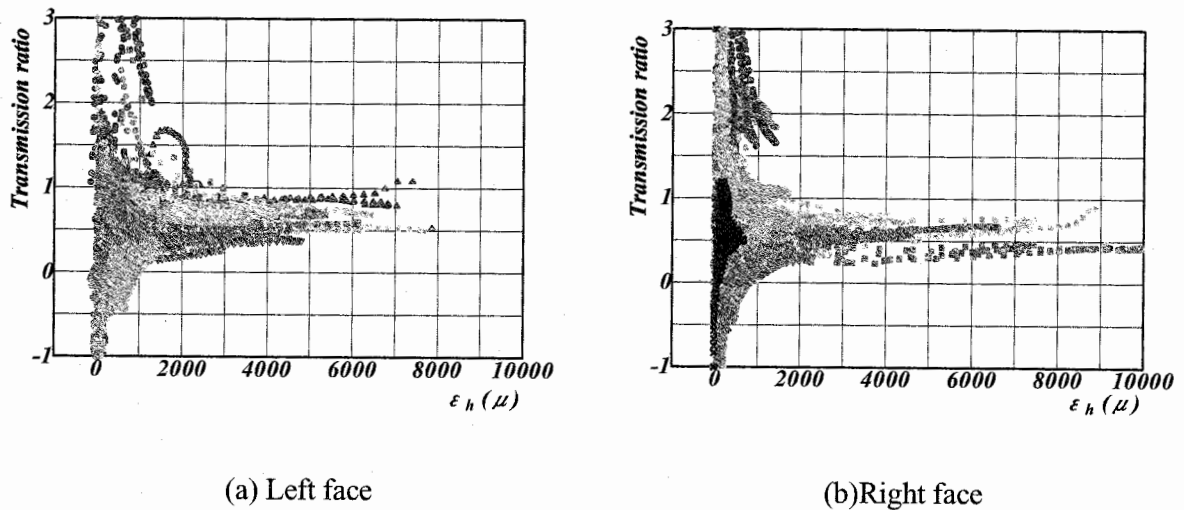


Figure 12 Transmission Ratio for Inner CFRP of Specimen S4

possibly might have been from the strain gauge locations in compressive side of CFRP curvature. The strain characteristics explored to interrelate the strains transmitted through the bend-portions indicates that the tensile force is transmitted through the CFRP efficiently. To develop quantitative evaluation method for strengthening effect of CFRP, the stress transfer mechanism must be clarified.

5. Conclusions

The conclusions obtained from the present experiment are summarized below.

- 1) By mechanical anchoring the end of the CFRP and reducing the tube wall thickness, it is possible to restrain the end of the CFRP from slipping and increase the strain distribution in the vicinity of the crack. This results in an improvement of the beam shear strength.
- 2) The CFRP can successfully provide the intended lateral confinement to the volumetric dilation of core concrete of RC column without any premature rupture.

References:

- Sugiyama, T. et al. (1999), "Development of Continuous Fiber Flexible Reinforcement," Fourth International Symposium on Fiber Reinforced Polymer Reinforcement for Reinforced Concrete Structures, SP-188, pp.13-22.
- Kobayashi, A. et al. (1999), "Study on Shear Strengthening of Beams Using Continuous Fiber Flexible Reinforcement," Proceedings of Fourth International Symposium on Fiber Reinforced Polymer Reinforcement for Reinforced Concrete Structures, SP-188, pp.195-207.
- Tuladhar, R. et al. (2001), "Deformational Characteristics of Reinforced Concrete Columns with Continuous Flexible Reinforcement," Proceedings of the Eighth East Asia-Pacific Conference on Structural Engineering and Construction, Paper No.1298.

CRACK TRACING PROCESS FOR SMEARED-CRACK-BASED NONLINEAR FEM

Y. Sato¹⁾, and K. Naganuma²⁾

1) Dept. of Urban and Environmental Engineering, Kyoto University, Kyoto 606-8501, Japan

2) Technical Research Institute, Obayashi Corporation, Tokyo 204-8558, Japan

satou@archi.kyoto-u.ac.jp, naganuma.kazuhiro@obayashi.co.jp

Abstract: A numerical process which traces crack propagation and evaluates crack width in reinforced concrete through post-crack stress redistribution is presented. The process iterates crack judgment and stress redistribution in the concrete and the steel in the main processing stage. This method explicitly gives the crack width by computing the bond behavior along reinforcing bars, without using any conventional tension-stiffening model. The process was incorporated with a two-dimensional finite element algorithm and example analyses were conducted for three RC columns. The analyses well predicted the crack propagations although some disagreements were found in the final crack condition with respect to the experimental observations.

1. INTRODUCTION

Conventional seismic design uses deformation indices that are, for instances, the storey drift or the ductility factor. The design procedure is developed based on an implicit assumption that these indices rationally represent seriousness of seismic damages induced to a structure. This assumption, however, is not always adequate, since the damage of each structural member probably varies even when a building is subjected to the same deformation level.

Recent progress in the nonlinear numerical analysis techniques for the RC, including the finite element method, enables prediction of crack propagation and maximum widths of the cracks. On the other hand, the building code is being transferred to the performance-based design, where evaluations of restoring force characteristics and structural damage are required. Hence, the crack width is becoming a possible design criterion as well as the conventional deformation indices.

From the viewpoint of the crack evaluation, finite element formulations are classified into the discrete-crack model and the smeared-crack model. The latter model includes difficulties to estimate the crack widths because of the nature of the formulation, while the former provides an explicit output of the crack width. The smeared-crack model, where cracked reinforced concrete is assumed as an orthogonal continuum, adopts average expressions of stresses and strains between smeared cracks. The smeared-crack model provides no explicit output of the crack widths, since number and spacing of the cracks are implicitly considered in the constitutive models. Nevertheless, the crack width can be evaluated in the smeared-crack based program by multiplying resulted principal tensile concrete strain by an effective length. Cervenka developed Crack Band Model, in which this effective length is given as a function of maximum aggregate size (Cervenka 1995), while Vecchio adopts crack spacing model in accordance with CEB-FIP Model Code (Vecchio 1986 and CEB-FIP 1978). Experimental observations, however, indicated that the crack spacing depends not only on the aggregate size or the bar arrangement, but also on conditions and hysteresis of internal/external loads. The cracks grow and increase through a number of stress redistribution processes under the transitional load condition. Thus the effective length is not constant, but changes depending on the external and internal conditions.

The authors developed a numerical process, which directly computes the stress redistribution processes due to the cracking in a structure. This process automatically recognizes the continuity of reinforcing bars in a finite element model and calculates the bond slips and the stresses between the concrete and the bars. Any prescribed tension-stiffening model is not used in the process because it directly computes all processes of the tension-stiffening mechanism. It is then incorporated with a smeared-crack-based finite element algorithm. The process traces the crack propagations and results in an explicit expression of the crack widths.

2. OUTLINE OF ANALYSIS PROCESS

The analysis process is classified into two parts:

2.1 Recognition of reinforcing bar continuity

A cracking in the concrete causes the bond slip along a reinforcing bar across the crack (Fig.1a). The length, along which the bond slip is induced, is defined as effective bond length l_b . The effective bond length covers several finite elements in a usual FE model. The numerical process therefore needs information of the adjacent elements, which contains the continuous bars. The proposed process includes a pre-processing routine to recognize and store the continuity of reinforcing bars automatically. The program judges a bar component as “continuous,” when the following conditions are satisfied:

- (i) Bar diameters coincide.
- (ii) Yield strength and elastic modulus of the bar coincide.
- (iii) Deviation of the bar orientation is less than 5 degrees.

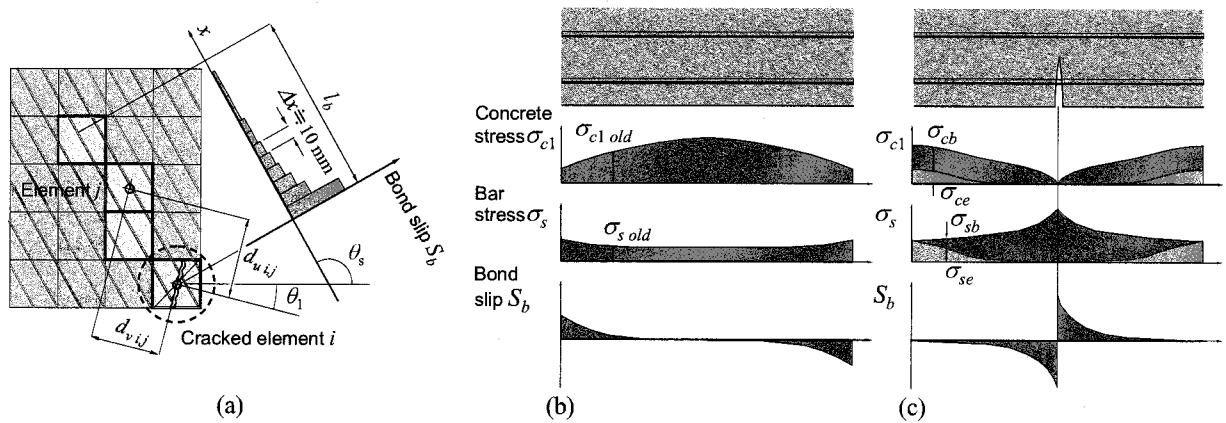


Fig.1 Stress redistribution process: (a) Elements subjected to stress redistribution; (b) Pre-crack stresses and slip; (c) Post-crack stresses and slip.

2.2 Stress redistribution

A conventional nonlinear FE program simultaneously judges cracking of elements at several points in each incremental step. On the other hand, the proposed process only judges one crack in an element, which yields maximum principal tensile concrete strain among uncracked elements. Then the process repeats the crack judgment and the stress redistribution in order of principal tensile concrete strain. Hence, the redistribution process is repeated as much as the number of newly cracked elements.

The tensile concrete stress after the redistribution is given as summation of the residual stress after stress release due to the cracking σ_{ce} , and the stress newly induced by the bond action σ_{cb} (Figs.

1b and 1c):

$$\sigma_{c1} = \sigma_{ce} + \sigma_{cb} \quad (1)$$

The residual stress σ_{ce} is computed by a procedure described in the authors' previous research (Sato 2005).

2. CONCRETE STRESS INDUCED BY BOND SLIP

Equation (2) gives concrete stress induced by the bond slip along the reinforcing bars (Sato 2002a).

$$\sigma_{cb\ new} = - \int_0^{l_b} \frac{4\rho\tau_b \cos^2(\theta_1 - \theta_s)}{d_b} dx \quad (2)$$

where

x = axis along bar ($x = 0$ at crack);
 ρ = reinforcement ratio; and
 τ_b = bond stress.

Equations (3) and (4) define a relationship between the bond stress and the slip along the reinforcing steel bar:

$$\tau_b = 2f'_t e^{\frac{\ln[(e-1)S_b/S_{by} + 1]}{(e-1)S_b/S_{by} + 1}} \quad (3)$$

$$S_{by} = 0.13 f'_t \quad (\text{mm, MPa}) \quad (4)$$

where

S_b = bond slip;
 S_{by} = bond slip corresponding to maximum bond stress; and
 f'_t = tensile strength of concrete.

Discretized calculation expressed by Eqs.(5) and (6) gives the bond slip.

$$[dS_b / dx]_{k+1} = [dS_b / dx]_k + \Delta x \tau_b / (E_s d_b) \quad (5)$$

$$S_{b,k+1} = S_{b,k} + \Delta x [dS_b / dx]_k \quad (6)$$

Where the subscript k denotes discretized part along x -axis, and E_s is elastic modulus of the bar. The calculation begins at crack ($x = 0$), and progresses with the discretized length of 10 mm. The calculation stops when the slip S_b becomes smaller than 10^{-6} mm, and the distance of this point from the crack is defined as the bond length l_b . Equation (7) gives relationships between the bar strain ϵ_s , the concrete strain along bar ϵ_c , and the bond slip S_b .

$$dS_b / dx = \varepsilon_s - \varepsilon_c \quad (7)$$

Equation (8) gives relationship between the crack width and the bond slip.

$$w_{cr} = S_{b1} + S_{b2} \quad (8)$$

Where S_{b1} and S_{b2} are bond slip at the left and the right surfaces of a crack. If more than one bar components run across a crack, then the slip of a component with the largest bond resistance is adopted. This component is selected using the bond-resistance coefficient C_B defined by Eq.(9).

$$C_B = \cos^2(\theta_1 - \theta_s) \rho E_s / d_b \quad (9)$$

A stress redistribution loop iterates calculations using the above equations until force equilibriums and deformation compatibilities are satisfied. Figure 2 outlines the calculation flow of stress redistribution.

3. EXAMPLE ANALYSIS

The proposed process was implemented into a non-linear FE program FINAL (Naganuma 2004). This section describes example analyses for three columns (Takami 2001 and Sugimoto 2003). Figure 3 shows FE meshes of the analyzed specimens while Table 1 summarizes the material properties. Table 2 shows the constitutive models used in the analyses.

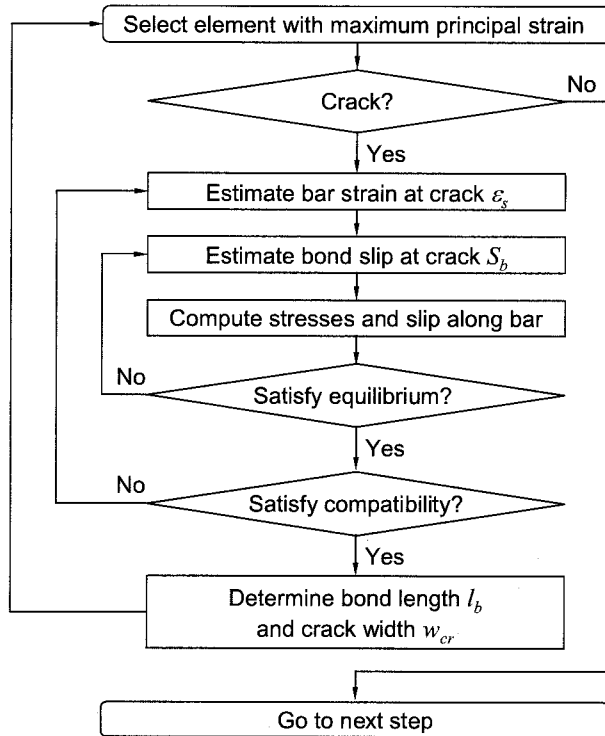


Fig.2 Computation flow

Table 1 Material properties

Concrete	Compressive strength f'_c	MPa	36.4
	Tensile strength f'_t	MPa	2.9
	Strain at peak ε_c	$\times 10^{-6}$	2716
Longitudinal bar	Number in 1st layer		4
	Number in 2nd layer		2
	Bar diameter d_b	mm	25
	Yield strength f_y	MPa	951
	Elastic modulus E_s	GPa	184
Hoop	Cross-sectional area ratio ρ_w	%	0.43
	Bar diameter d_{bw}	mm	10
	Yield strength f_{yw}	MPa	362
	Elastic modulus E_{sw}	GPa	193

Table 2 Constitutive models

Concrete	Orthotropic model
Compression curve	Naganuma 1995
Failure criterion	Kupfer 1973
Bond	Sato 2002a

The cross-section of the columns C4s-3-00, C4s-3-15 and C4s-3-30 was 305 mm×560 mm and the span 1410 mm. The columns were subjected to different axial force ratios, which were varied between 0.0, 0.15 and 0.30. Figure 4 presents a typical crack propagation observed in the test of Column C4s-3-00. Two cases of the analyses were conducted for each specimen with varying mesh density (fine mesh / coarse mesh). Total degrees of freedom (DOF) were 964 for the coarse mesh, and 2380 for the fine mesh. Tension cut-off assumption was adopted as the post-crack behavior for the analyses with the proposed process while a tension-stiffening model was used for the analyses with the conventional method.

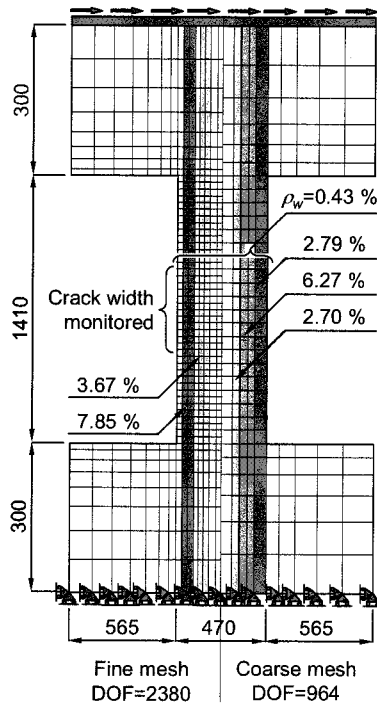


Fig.3 FE mesh of smeared-crack-based FEM

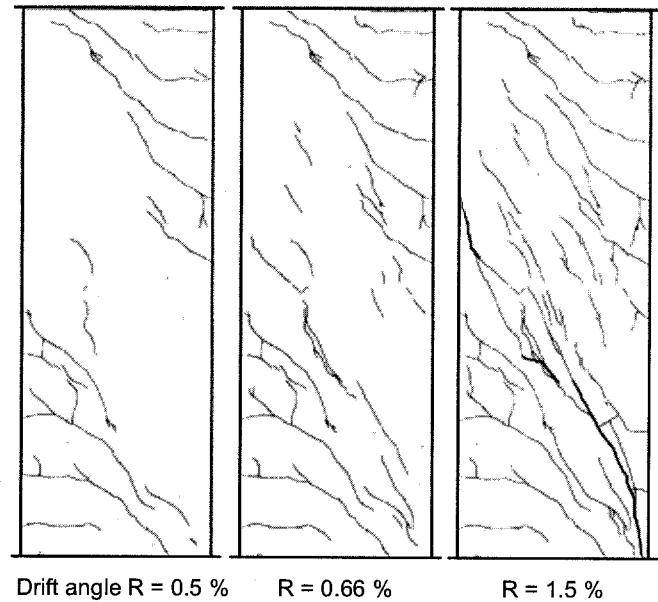


Fig.4 Experimental crack propagation of Column C4s-3-00

Shear stiffness of a cracked concrete was reduced based on Al-Mahaidi's equation (Al-Mahaidi 1979). This equation, however, was calibrated for a smeared-crack-based FE program, and is not compatible with the proposed process. Since the proposed process concentrates the shear deformation on the cracked element, it is needed to reduce the shear stiffness. Equations (10) and (11) modifies the shear stiffness reduction factor R_G of Al-Mahaidi's equation

$$R_{Gmod} = \frac{\varepsilon_n \sqrt{A_{elm}}}{w_{cr}} R_G \quad (\text{for cracked element}) \quad (10)$$

where

$$\begin{aligned} R_G &= 0.4 \varepsilon_{cr} / \varepsilon_n \\ \varepsilon_n &= \text{crack strain;} \\ \varepsilon_n &= \text{strain normal to crack;} \\ A_{elm} &= \text{area of element; and} \\ w_{cr} &= \text{crack width.} \end{aligned} \quad (11)$$

Figure 5 shows the computed crack propagation of Column C4s-3-00 by the fine mesh, at drift angles of 0.50 %, 0.66 % and 1.50 %. While the conventional method results in smeared cracks in

overall areas, the proposed process redistributes the crack series with uncracked spacings. At a drift angle of 1.5 %, however, induced cracks covered the uncracked spacings, resulting in a discrepancy between the analysis and the test. Figure 6 compares crack patterns in the clear spans of Columns C4s-3-00, C4s-3-15 and C4s-3-30 at a drift angle of 0.66 % between fine and coarse meshes. The process generally provides good simulations of the crack propagation under the variable axial force that the cracks grew steeper as the axial force became larger. However, crack conditions slightly vary depending on the mesh density: The area of the uncracked region tended to decrease when the columns were analyzed with the coarse mesh.

Figure 7a shows analyzed relationships between shear force and drift angle of the three columns. The analyses overestimated the maximum shear forces by 10 % up to 40 %.

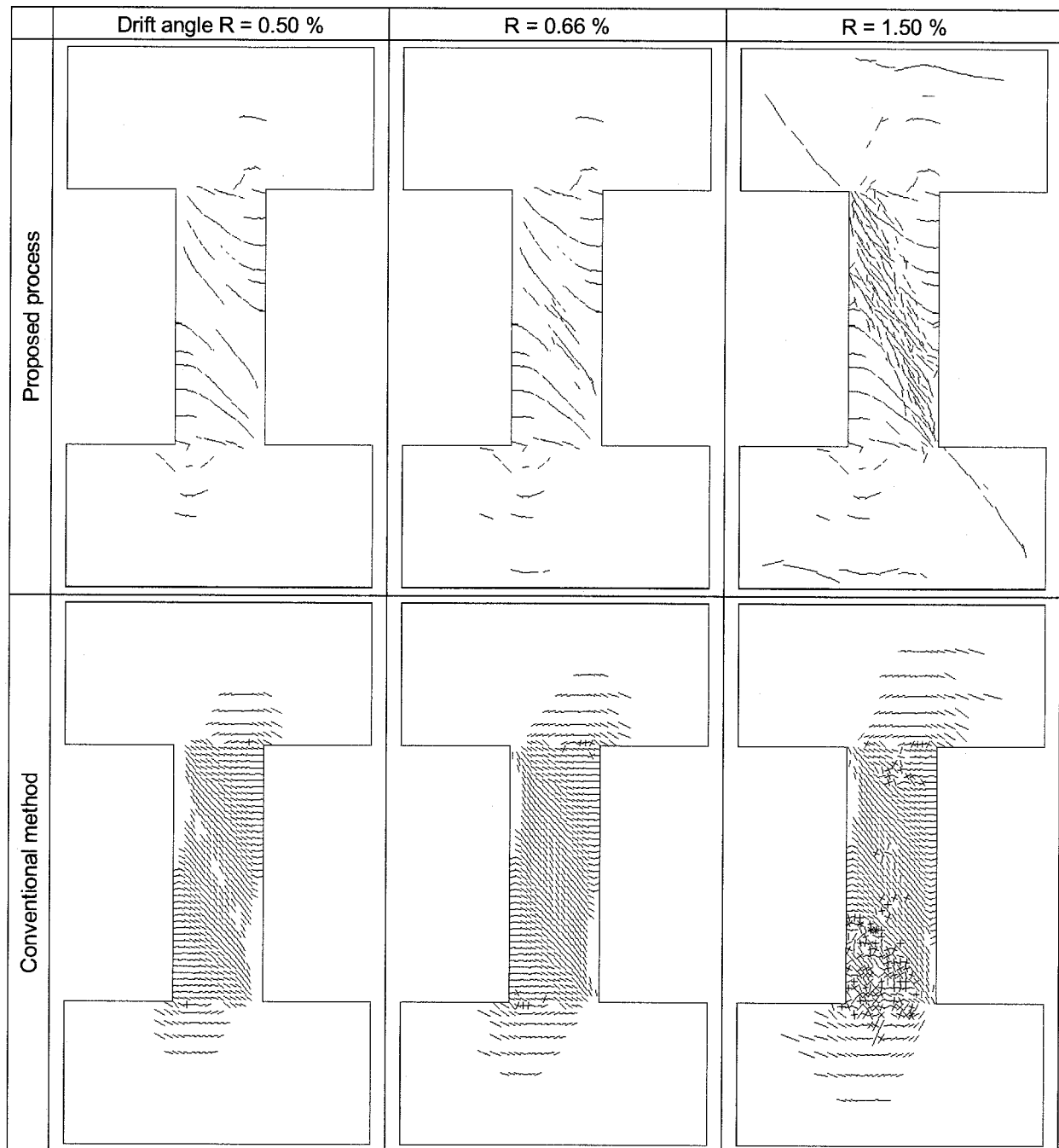


Fig. 5 Computed crack propagation of Column C4s-3-00

Figure 7c compares relationships between principal tensile concrete stress and strain in an element which yields the maximum crack width. The solid lines indicate the analyzed relationships given by the proposed process while the dotted lines indicate the conventional tension-stiffening model. The proposed process directly computed the tension-stiffening behaviors, which were accompanied with the redistribution processes. The model usually gave a smaller tensile stress (solid line) than the conventional model (dotted line) although the solid lines casually exceeded the dotted lines.

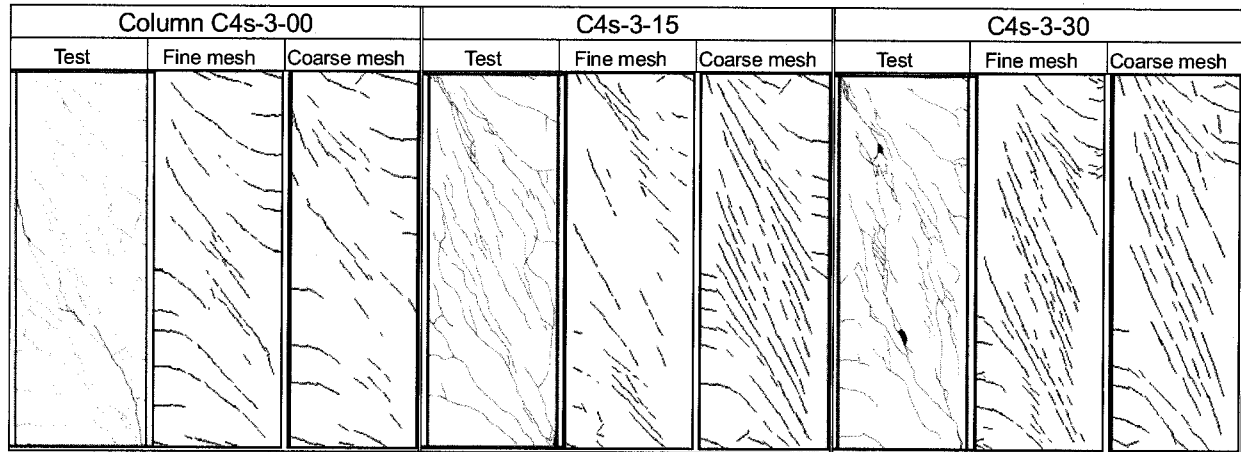


Fig. 6 Crack patterns in clear spans of Columns C4s-3-00, C4s-3-15 and C4s-3-30

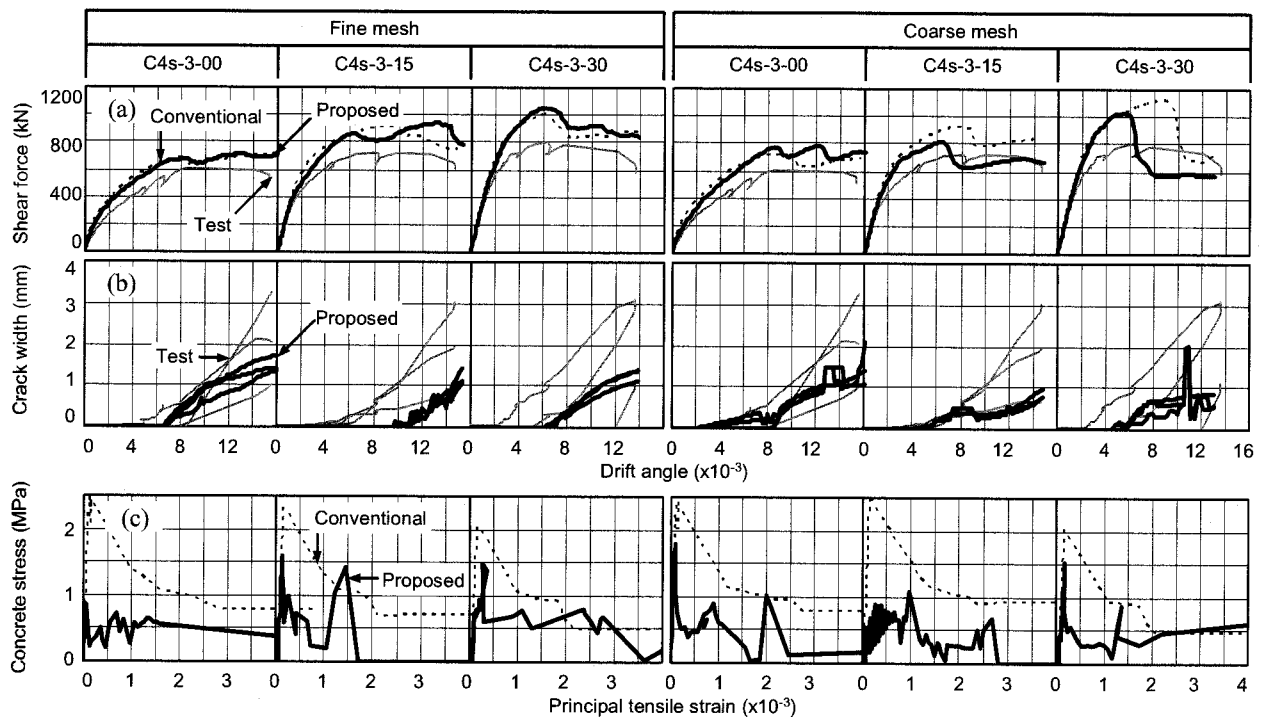


Fig.7 Analysis results of Columns C4s-3-00, C4s-3-15 and C4s-3-30: (a) Shear force-drift angle relation; (b) Crack width-drift angle relation; (c) Tension-stiffening characteristics.

Figure 7b compares the crack widths between tests and analyses. The gray liens indicate the largest three values among the crack widths at seven locations observed in the test. The solid lines

represent the largest three cracks among elements in the center region of the specimens (144 elements for the fine mesh, and 48 elements for the coarse mesh.) The crack widths observed in the test varies from 1 mm to 3mm. The computed ascending rate of the crack width to the drift angle agreed with the tests although the analyses underestimated the final crack widths.

3. CONCLUSIONS

This paper presents a numerical process, which directly computes the stress redistribution processes due to the cracking in a reinforced concrete structure. This process automatically recognizes the continuity of reinforcing bars in a finite element model and computes the bond slips and the stresses between the concrete and the bars. No prescribed tension-stiffening model is required in the algorithm because all processes of the tension-stiffening mechanism are directly computed.

The proposed process was then incorporated with a smeared-crack-based finite element algorithm and example analyses were conducted for three RC specimens. Crack conditions slightly vary depending on the mesh density: The uncracked area tended to decrease when the columns were analyzed with the coarse mesh.

Discrepancies were found in the final crack patterns and the crack widths between the tests and the analyses. although the computed crack propagation at smaller drift angles coincided with the test. It is thought that these discrepancies stemmed from inadequate consideration for the stress concentration at the crack tips.

Acknowledgements:

This research was funded by Grant-in-Aid for Scientific Research (No.16760454) of Japan Society for the Promotion of Science. The authors' grateful appreciation goes to Assoc. Prof. Minehiro Nishiyama of Kyoto University.

References:

- Al-Mahaidi, R.S.H. (1979) "Nonlinear Finite Element Analysis of Reinforced Concrete Deep Members." Report 79-1, Dept. Structural Engineering, Cornell Univ.
- CEB-FIP (1978) "Model Code for Concrete Structures: CEB-FIP International Recommendations, 3rd ed." Comité Euro-International du Béton, Paris, 348.
- Cervenka, V. and Pukl, R. (1995) "Mesh Sensitivity Effects in Smeared Finite Element Analysis of Concrete Structures." Proc. 2nd Int'l Conference on Fracture Mechanics of Concrete Structures (FRAMCOS 2):1387-1396, Ed. F. H. Wittmann, AEDIFICATIO, ETH Zürich, Switzerland.
- Kupfer, H. B. and Gerstle, K. H. (1973) "Behavior of Concrete under Biaxial Stress." J. Engrg. Mech. Div., ASCE, 99(EM4) 853-866.
- Naganuma, K. (1995) "Stress-Strain Relationship for Concrete under Triaxial Compression." J. Struct. Constr. Engng., 474, 163-170 (in Japanese.)
- Naganuma, K., Yonezawa, K., Kurimoto, O. and Eto, H. (2004) "Simulation of Nonlinear Dynamic Response of Reinforced Concrete Scaled Model Using Three-Dimensional Finite Element Method." 13th World Conference on Earthquake Engineering, Vancouver, B.C., Canada, Paper No. 586.
- Sato, Y. and Fujii, S. (2002a) "Local stresses and crack displacements in reinforced concrete elements." J. Struct. Engrg., ASCE, 128, 10, 1263-1271.
- Sato, Y. and Naganuma, K. (2005) "Crack Width Analysis Using Smeared-Crack-Based Finite Element Method." Proc. Annual Meeting, Architectural Institute of Japan, 23171-23172.
- Sugimoto, K., Kashiwase, T., Tuda, K. and Eto, H. (2003) "Evaluation Method for the Earthquake Resistant Performance of RC Buildings, Part 2 Investigation of Experimental Results of Columns and Beams." Proc. Annual Meeting Architectural Institute of Japan, C2, 143-144 (in Japanese.)
- Takami, S. and Eto, H. (2001) "Experimental Study on the Cracking Characteristic for RC Members." Proc. Annual Meeting Architectural Institute of Japan, C2, 485-486 (in Japanese.)
- Vecchio, F. J. and Collins, M. P. (1986) "The modified compression-field theory for reinforced concrete elements subjected to shear." ACI Struct. J., 83(2), 219-231.

SHEAR BEHAVIOR OF CONNECTING BARS ON PRECAST JOINT UNDER AXIAL TENSILE FORCE AND SHEAR FORCE FROM SEISMIC LOAD

K. Katori¹⁾, S. Hayashi²⁾ and H. Takagi³⁾

1) Assistant Professor, Structural Engineering Research Center, Tokyo Institute of Technology, Japan

2) Professor, Structural Engineering Research Center, Tokyo Institute of Technology, Japan

3) Associate Professor, Department of Architecture, Meiji University, Japan

katori@serc.titech.ac.jp, hayashi@serc.titech.ac.jp, htakagi@isc.meiji.ac.jp

Abstract: Dowel characteristic for connecting bars on precast joint under axial tensile force from seismic load is not made clear. In this paper the authors described an experimental study on behavior of shear behavior of connecting bars suffering both longitudinal tensile force and shear force. Ratio of tensile stress to yield strength of connecting bars, compressive strength of concrete and loading way shear force were selected as parameter of specimens. From experiments the following became clear that dowel strength of connecting bars reduced with growth of the ratio tensile stress to yield strength, and in the area that the ratio was nearly equal to 1 the formula proposed by Tassios gave larger calculations than experimental results. From that fact the authors lead that design method of precast joint in Japan had some problem about estimating shear strength of connecting bars suffering both longitudinal tensile force and shear force.

1. INTRODUCTION

Precast concrete structure has more useful merits on shortage of construction period, shortage of manpower for construction and high quality than those of cast-in-place reinforced concrete structures. But in seismic design in Japan precast structures has been required to use same recommendations as cast-in-place reinforced concrete structures.

In 2002 structural design guidelines for precast concrete connection emulating cast-in-place reinforced concrete was issued. In that guideline dowel design method for connecting bars suffering both longitudinal tensile force and dowel shear force was first mentioned. In that guideline it is written that dowel strength of connecting bars suffering both longitudinal tensile force and dowel shear force (V_u) should be calculated by Eq. (1) and Eq. (2) equation by using section area of connecting bar (A_s), tensile yield strength of connecting bar (f_y), compressive strength of concrete (f_c) and tensile stress of connecting bar (σ_s).

$$V_u = 1.65 \cdot A_s \cdot \sqrt{f_y \cdot f_c \cdot (1 - \alpha^2)} \quad (1)$$

$$\alpha = \sigma_s / f_y \quad (2)$$

Those equations were proposed by Tassios. But those equations have some problems such as followings,

- If α is equal to 1, V_u becomes 0. But even if α is equal to 1, connecting bar exists as rigid material, not as "very soft material". So connecting bar may have some strength for dowel force even if α is equal to 1. In fact Shinagawa and Kojima performed experiments and reported that though α is

equal to 1 connecting bar has dowel strength.

- Tassios performed experiments to confirm validity of Eq. (1) and Eq. (2). In general connecting bars suffering both longitudinal tensile force and dowel shear force may elongate on the point of joint area. But in those experiments connecting bars were not allowed to elongate longitudinally.

So the authors have thought that more research about Eq. (1) and Eq. (2) may be needed, and if any problem found, it is needed to make and propose another equations to calculate dowel strength of connecting bars suffering both longitudinal tensile force and dowel shear force.

In this research the authors performed experiments to confirm dowel strength of connecting bars suffering both longitudinal tensile force and dowel shear force and dowel characteristics of connecting bars. Those experiments also have purpose to get information to make another useful equations to calculate dowel strength of connecting bars suffering both longitudinal tensile force and dowel shear force.

2. SPECIMENS AND EXPERIMENTS

2.1 Specimens

Specimen's shape and reinforcement arrangement are shown in Fig. 1. And specimens name, parameters and mechanical properties of materials are shown in Table 1. Specimens were made as a element model of column-column joint on the 1st or 2nd story of frame-type high rise precast reinforced concrete building. But the authors have thought that the experimental results can be applied to of wall-beam joint of wall-type precast reinforced concrete building.

In real high rise building such as 15 stories, diameter of connecting bar of joint lower stories will be larger than 35mm, and large numbers of connecting bars will be arranged. But because of limit from loading system those specimens have only one piece of connecting bar. And also, diameter of connecting bar (d_b) became 16mm. D16 deformed bar fitting SD295 approved by JIS (Japan Industrial Standard) was used for connecting bar. Bar's rib was notched longitudinally in order to attach strain gages

In real joint shear keys will be arranged and shear reinforcement will be also arranged, but because removing any influence caused by such shear keys and shear reinforcements in order to simplify behavior of connecting bar, no shear key and shear reinforcement was arranged. In addition, Teflon sheet was put in order to remove influences caused by surface roughness of joint and chemical bond force of concrete.

Compressive strength of concrete ($\sigma_B=f_c$), ratio of tensile stress to yield strength of connecting bars ($\alpha=\sigma_s/f_y$) and loading way of shear force (cyclic or monotonic) are selected as parameter of specimens. α will be a most important parameter, so α was changed from 0 to 0.95.

Specimens were made by unique fabrication method shown in Fig. 2 to realize properties of precast structures.

Table 1 List of Specimens and Mechanical Properties of Materials for Specimens

Specimens' name	σ_B (N/mm ²)	f_y (N/mm ²)	A_s (mm ²)	Tensile Force for Connecting Bar N (kN)	$\alpha=\sigma_s/f_y$ $=N/(A_s f_y)$	Loading Way of Shear Force	V_u from Eq.(1) (kN)
36-0	30.2	347.2	151.6	0	0	Cyclic	25.6
36-25	29.1			13.2	0.25		24.3
36-50	28.0			26.3	0.50		21.4
36-75	29.6			39.5	0.75		16.8
36-95-c	30.0			50.0	0.95		8.0
36-95-m	26.7				0.95	Monotonic	7.5
60-95	63.1				0.95	Cyclic	11.6

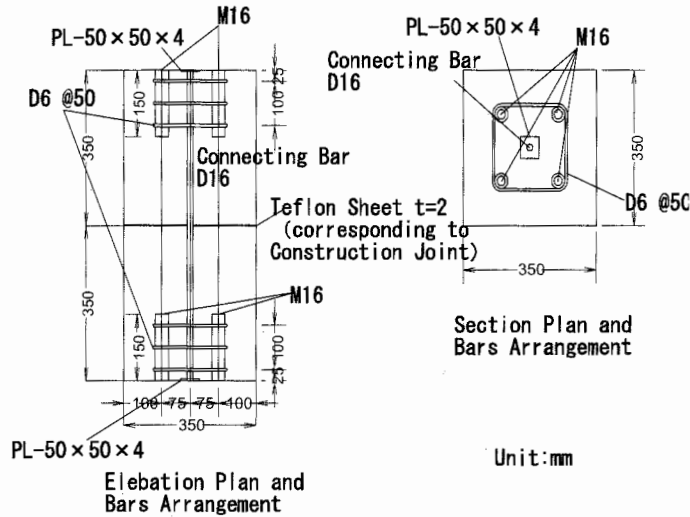


Figure 1 Specimen's shape and reinforcement arrangement

Shear-bending test of connecting bar for getting moment-curvature relationship was performed separately.

2.1 Loading Apparatus and program

Loading apparatus is shown in Fig.3. Specimen was set to reacting frame via slide needle bearing system, and link mechanism was attached to specimen for keeping upper part and lower part of specimen parallel. Longitudinal tensile force of connecting bar was loaded by 1500kN universal testing machine, and dowel force was loaded by 2 pieces of oil jacks.

Loading was performed by the following order,

- 1) Longitudinal tensile force was

loaded to connecting bar by pulling specimen by universal testing machine. Tensile force was kept constant automatically.

2) After loading tensile force for connecting bar, dowel force was loaded. Cyclic loading history was controlled by slip displacement between upper part lower parts of specimen. Turning displacement of loading history were selected to $\pm 0.5\text{mm}$, $\pm 0.8\text{mm}$, $\pm 1.6\text{mm}$, $\pm 3.2\text{mm}$, $\pm 8.0\text{mm}$ and $\pm 12.0\text{mm}$.

2. EXPERIMENTAL RESULTS AND DISCUSSIONS

2.1 Dowel Strength and Tassios's Value

2.1.1 Difference Caused by Longitudinal Tensile Force of Connecting Bar

Dowel force-slip displacement relationships are shown in Fig. 4 and experimental result is shown in Fig.5 and Table 2. In Table 2 "Dowel strength Q_d " is defined as shear force when connecting bar becomes bending yield at any point of strain gages, bending yield is judged by using results of Shear-bending test of connecting bar. The point when shear force reach to Q_d will correspond to the point of V_u calculated by Eq. (1) and Eq. (2).

From Fig.5 and Table 2, when tensile force becomes small, like as α is smaller than 0.25, V_u is probably corresponding to Q_d . But if α becomes larger than 0.5, V_u does not correspond to Q_d , and V_u becomes larger than Q_d . So it will be said that if longitudinal tensile force of connecting bar is small, Eq. (1) and Eq. (2) proposed by Tassios will give good calculated value of dowel strength of connecting bar, and if longitudinal tensile force of connecting bar becomes large, those equations will

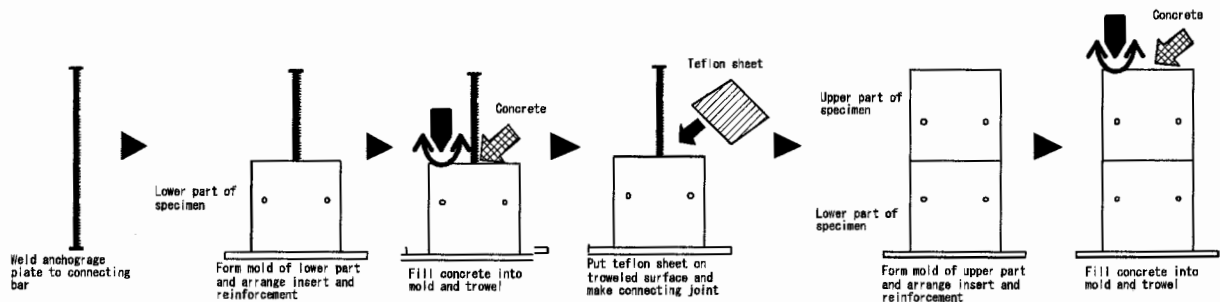


Figure 2 Making order of specimen

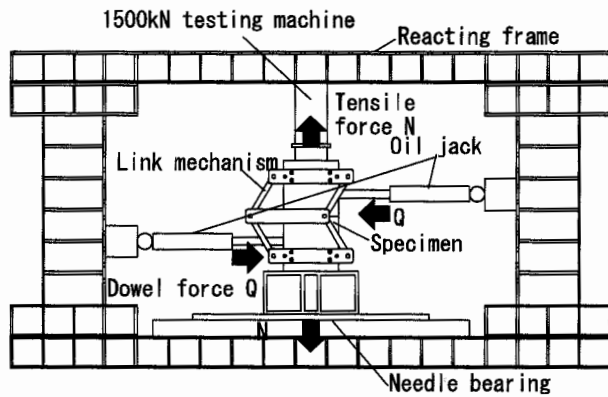


Figure 3 Loading apparatus

give unsuitable value of dowel strength of connecting bar.

Also from Fig. 5 plotted points of cubic mark, which are point for specimen made from normal strength of concrete and suffered to cyclic shear force, seem to form a curve, not form a line. It will be said that if equations proposed by Tassios need modified, they will need not a corrective coefficient but another term.

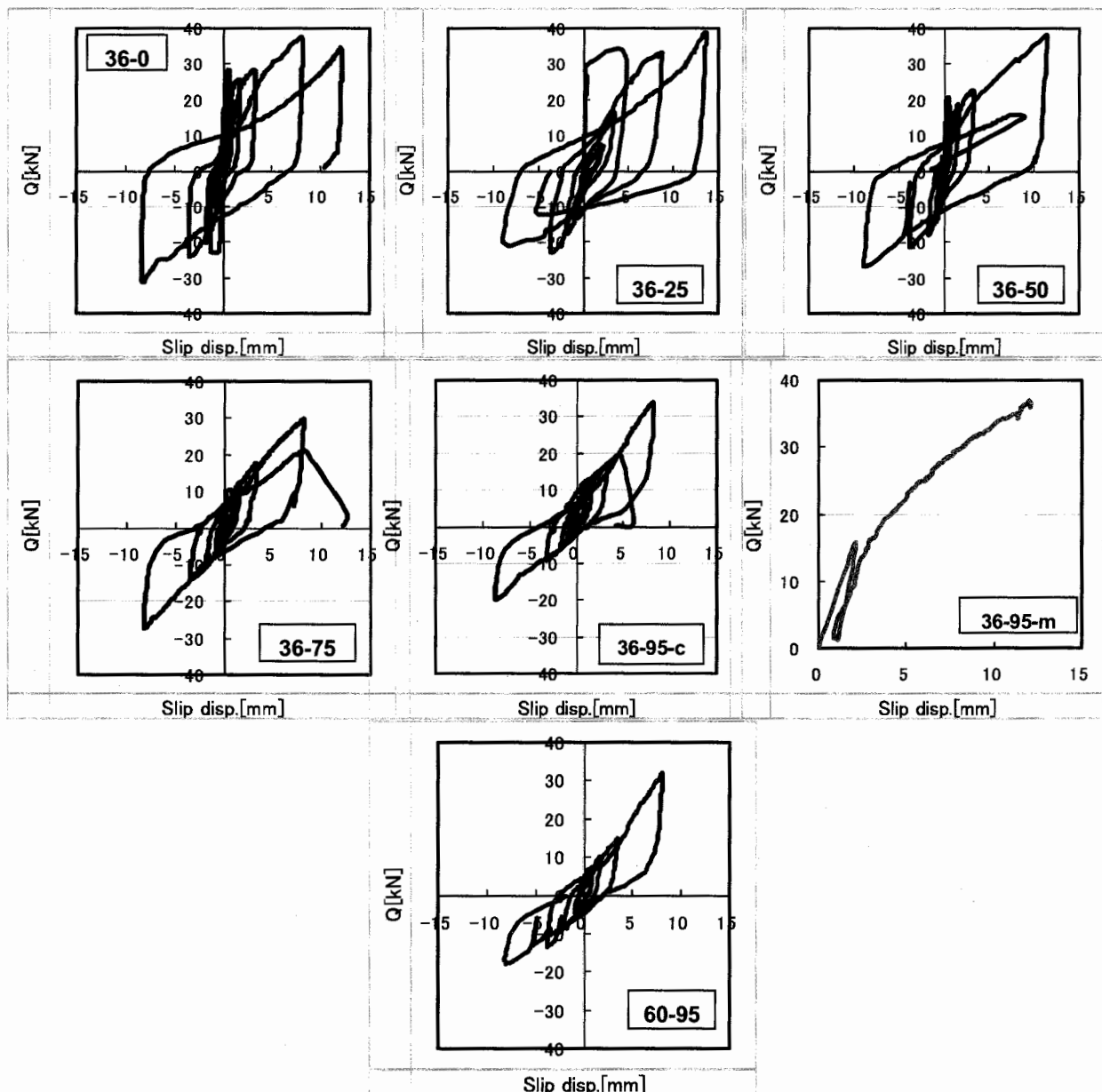


Figure 4 Dowel Force-Slip Displacement Relationship

Table 2 Experimental Result

Specimens' name	Dowel strength		Q_d/V_u	Maximum shear strength $Q_{max}(kN)$
	Q_d (kN)	Slip disp. when $Q=Q_d$ (mm)		
36-0	27.0	0.44	1.05	37.7
36-25	29.8	0.51	1.23	38.7
36-50	20.5	0.42	0.96	37.9
36-75	10.1	0.37	0.60	29.6
36-95-c	4.7	0.12	0.59	33.9
36-95-m	15.0	2.81	2.00	45.9
60-95	5.5	0.16	0.47	31.9

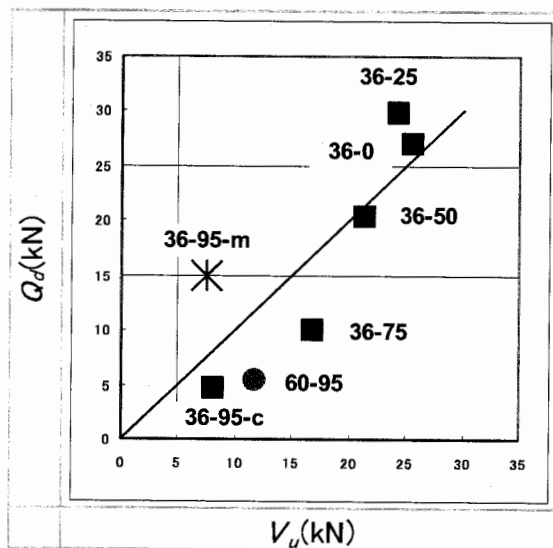


Figure 5 Relationship of Experimental Dowel Strength Q_d and Calculated Dowel Strength V_u

longitudinal tensile force of connecting bar, loading way of shear force and compressive strength of concrete may be needed for equations proposed by Tassios.

2.2 Moment Distribution of Connecting Bar Embedded into Concrete

2.1.1 Difference Caused by Longitudinal Tensile Force of Connecting Bar

Tassios led his proposed equations by using assumption that connecting bar embedded into concrete will act like pile embedded into cohesive soil on dowel action. From that assumption Tassios used moment distribution of free-headed pile in cohesive soil led by Broms as moment distribution of connecting bar. And Tassios assumed moment distribution of connecting bar shown in Fig. 6.

From Tassios's moment distribution, maximum bending moment of connecting bar embedded into concrete M_{max} will be calculated as follows;

$$M_{max} = 0.17 \cdot d_b^3 \cdot f_y \quad (3)$$

So in this experiment M_{max} may be calculated as follows;

2.1.2 Difference Caused by Shear Loading method

Plotted point for specimen "36-95-c" and "36-95-m" set quite another area. Equations proposed by Tassios have no term for shear force loading method, so Tassios's equation give same value for "36-95-c" and "36-95-m". So it will be said that Tassios's equations also need term or corrective coefficient for shear force

loading method.

2.1.3 Difference Caused by Compressive Strength of Concrete

Plotted point named "36-95-c" and "60-95" are for comparison of effect of compressive strength of concrete. From equations proposed by Tassios calculated value of dowel strength of "60-95" may become 1.45 times as much as that of "36-95-c". But from experimental result Q_d of "60-95" is probably same as that of "36-95-c". So it will be said that equations proposed by Tassios cannot express effect of compressive strength of concrete.

From results of those three sections above, it will be said that equations proposed by Tassios cannot express characteristics of dowel action of connecting bar loaded longitudinal tensile force exactly; Modifications about expressing effect of

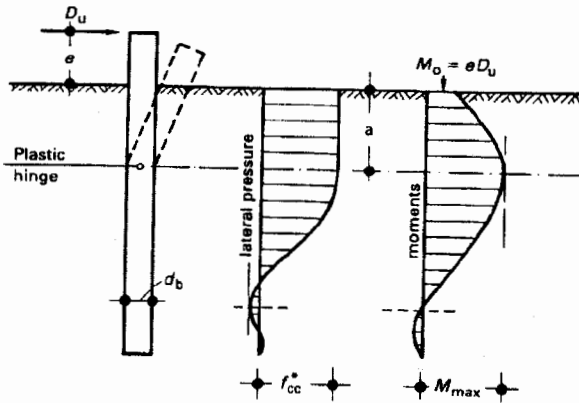


Figure 6 Moment Distribution of Pile Embedded into Soil (broms)

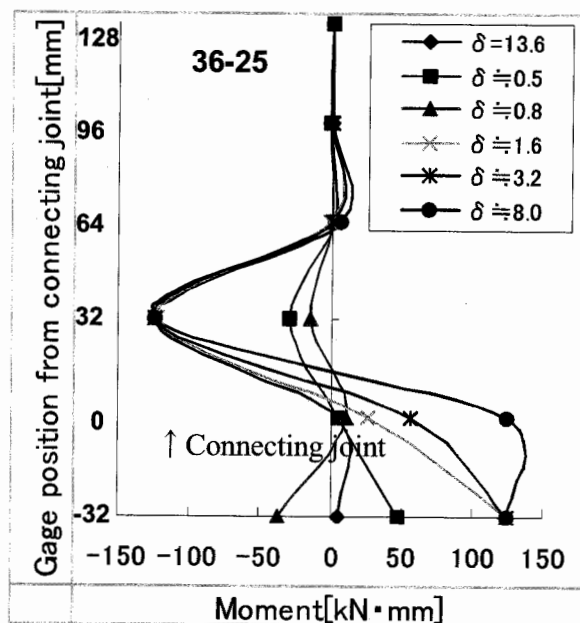


Figure 7 Moment Distribution of Connecting Bar from Experimental Result (36-25)

$$M_{\max} = 0.17 \times 16^3 \times 347.2 = 241752 (N \cdot mm) \\ = 241.8 (kN \cdot mm) \quad (4)$$

Moment distribution of specimen from experimental result is shown in Fig.7, for example distribution of "36-25" is shown. That figure shows that bending moment of connecting bar does not reach to moment value from Eq. (4). So it will be said that Broms's assumption cannot express moment distribution of connecting bar embedded into concrete, and also be said that Tassios's assumption for Eq. (1) and Eq. (2) have

problem about evaluating moment distribution of connecting bar.

The Authors would like to express that probing real moment distribution of connecting bar embedded concrete and loaded longitudinal tensile force and dowel shear force is important and needed to create another evaluating equation for dowel strength.

3. CONCLUSIONS

From experiments it have become that there are some problems about equations for evaluating dowel strength of connecting bar loaded longitudinal tensile force and dowel shear force proposed by Tassios. Especially when longitudinal tensile force becomes large, Tassios's equation gives smaller larger value than experimental results. It is necessary to create another equation, or modify Tassios's equations.

Acknowledgements:

The authors acknowledge support from Japan Ministry of Education, Culture, Sport, Science, and Technology (MEXT) for establishing the Center for Urban Earthquake Engineering (CUEE) in Tokyo Institute of Technology, support from Structural Engineering Research Center (SERC) in Tokyo Institute of Technology, and support from the grants-in-ade for scientific research of MEXT. The authors also acknowledge suggestion and information from Dr. Eiji MAKITANI, professor of Kanto-gakuin Univ., and great helps from Mr. Takeshi OHSAWA, Bachelor course student of Meiji Univ..

References:

- Shinagawa, K., Hibino, K., Takagi, N., and Kojima, T. (2005), "Influences of Tension Force of Longitudinal Bar on Dowel Action of RC Members", *Proceedings of the Japan Concrete Institute*, Japan Concrete Institute, 27(2), 793-798.
- Vintzeleou, E. N., and Tassios, T. P. (1986), "Mathematical Models for Dowel Action under Monotonic and Cyclic Condition", *Magazine of Concrete Research*, 38(134), 13-22
- Vintzeleou, E. N., and Tassios, T. P. (1987), "Behavior of Dowels Cyclic Deformations", *ACI Structural Journal*, American Concrete Institute, 84(S4), Jan.-Feb., 18-30
- Broms, B. B. (1964), "Lateral Resistance of Piles in Cohesive soils", *Proceedings of the American Society of Civil Engineers*, 90(SM2), 27-63

DEVELOPMENT OF RC FLAT BEAM AND COLUMN JOINT SYSTEM

K. Nishimura¹⁾, K. Takiguchi²⁾, H. Hotta³⁾, Y. Tsuneki⁴⁾, Y. Koitabashi⁴⁾, and N. Nakanishi⁴⁾

1) Assistant Professor, Dept. of Architecture and Building Engineering, Tokyo Institute of Technology, Japan

2) Professor, Dept. of Mechanical and Environmental Informatics, Tokyo Institute of Technology, Japan

3) Associate Professor, Dept. of Architecture and Building Engineering, Tokyo Institute of Technology, Japan

4) NIKKEN SEIKKEI, Japan

knishimu@tm.mei.titech.ac.jp, ktakiguc@tm.mei.titech.ac.jp, hotta@arch.titech.ac.jp,

tsuneki@nikken.co.jp, koitabashi@nikken.co.jp, nakanishin@nikken.co.jp

Abstract: A RC flat beam allows considerable latitude in building design if the beam and a normal column can be used in rigid frame construction. It is necessary to confirm load carrying capacity of this RC flat beam and column joint system because there are some fears indicated as follows.

1) Whether stress can be transmitted well between the beam and the column.

2) Whether bond of longitudinal bars of the column is sufficient in beam-column joint.

Additional reinforcements to strengthen beam end, which shifted plastic hinge of the beam at a distance from column surface, and more lateral confinements in connection were adopted as measures against the former problem. Spliced lapping bars of column at joint were adopted for the later one. Seven RC flat beam and column joint specimens were prepared for cyclic loading tests to examine above measures. And a specimen, which bonds of longitudinal bars of columns were removed in connection, was included in these seven specimens in order to examine effects of bond. As results, it can be said that RC flat beam and column joint system is possible.

1. INTRODUCTION

A reinforced concrete flat beam (RC flat beam), which has wider width than columns have and shorter depth than normal beams have, allows considerable latitude in building design if the beam and a normal column can be used in rigid frame construction. A stiffness of building will be secured to combine this RC flat beam and column joint system with wall structures and normal rigid frame. However, it is necessary to confirm load carrying capacity of this RC flat beam and column joint system because there are some fears indicated as follows.

1) Whether stress can be transmitted well between the beam and the column.

2) Whether bond of longitudinal bars of the column is sufficient in beam-column joint.

Additional reinforcements to strengthen beam end, which shifted plastic hinge of the beam at a distance from column surface, and more lateral confinements in connection were adopted as measures against the former problem. In addition, dense stirrups were placed between plastic hinge section and beam end not to crack in shear. Spliced lapping bars of column at joint were adopted for the later one.

Seven RC flat beam and column joint specimens were prepared for cyclic loading tests to examine above measures. And a specimen, which bonds of longitudinal bars of columns were removed in connection, was included in these seven specimens in order to examine effects of bond.

2. EXPERIMENTAL PROGRAM

2.1 Specimens

Seven specimens were prepared for the tests. Table 1 and 2 show dimension of specimens and mechanical properties of concrete and reinforcements. Parameters of the test were two types of position of connection and bar arrangements. Table 3 and Figure 1 show parameter and detail of specimens. Four of the specimens had connection with no eccentricity and three had connection with eccentricity, as shown in Figure 1.

The numbers in Table 3 correspond to the numbers in Figure 1. No.1 in Table 1, which is spliced lapping bar of 480mm length, is measure to secure bond of longitudinal bar of column in joint. No.2 is parameter to examine effect of bond. No.2 means whether bond of all longitudinal bars of column are removed in the range of connection, which is 160mm in length. No.3 to 5 are measures against problem of stress transmission between beam and column. No.3 is reinforcement of D13 with 180° hooks in both sides, which shift plastic hinge of beam at a distance from column surface. Figure 2 shows assumed plastic hinge section of specimens with and without additional reinforcement of beam end. No.4 means shear reinforcements are spaced 50mm or 100mm at beam end, "A." is 50mm space and "N. A." is 100mm space in Table 3. No.5 are D13 reinforcements lapping a wing part of beam at joint.

In summary, difference among RC-1, RC-2, and RC-3 on Normal Type, and between RC-5 and RC-6 on Eccentric Type, was bond of longitudinal bars of column in connection. RC-4 and RC-7 had no measure shown in Table 3.

The column of RC-1 was designed not to yield in ultimate condition, and the other specimens had same design of column as RC-1. A yield bending strength (AIJ, 1999) of column had more than 1.4 times of applied load when a bending moment at the assumed plastic hinge section was equal to a yield bending strength. The beams of specimens with additional reinforcements of beam end were designed to yield only at the assumed plastic hinge section. A yield bending strength at beam end had more than 1.4 times of applied load by placing additional reinforcements of beam end when a bending moment at the assumed plastic hinge section was equal to a yield bending strength. Dense stirrups were placed, which were spaced 50 mm, between the assumed plastic hinge section and beam end not to cracked in shear.

The bond of longitudinal bars of column in connection was examined whether the longitudinal bars and the spliced lapping bars of column satisfied Equation 21, Article 17, AIJ Standard for Structural Calculation of Reinforced Concrete Structures (AIJ, 1999). In this calculation, applied stress column end was computed on condition that beam yielded at assumed plastic hinge section. RC-1 [Normal type] and RC-5 [Eccentric type] satisfied this equation, RC-2 [Normal type] and RC-6 [Eccentric type] didn't, and RC-3 [Normal type] had no bond.

Table 1 Dimension of Specimens and Mechanical Properties of Concrete

Name of specimens	Dimension b x D[mm]		Main reinforcements		Shear reinforcement		Concrete Compressive strength [N/mm ²]
	Column	Beam	Column	Beam	Column	Beam	
RC-1 [Normal Type]	240 x 240	500 x 160	10-D13	16-D10	D6 @50		34.8
RC-2 [Normal Type]						D6 @50(column end)	32.6
RC-3 [Normal Type]						@100(both side)	34.2
RC-4 [Normal Type]						D6 @100	37.8
RC-5 [Eccentric Type]	240 x 240	500 x 160	10-D13	12-D10	D6 @50	D6 @50(column end)	37.7
RC-6 [Eccentric Type]						@100(both side)	38.1
RC-7 [Eccentric Type]						D6 @100	38.4

Table 2 Mechanical Properties of Reinforcements

	D6	D10	D13
Nominal section area [mm ²]	31.67	71.33	126.7
Yield strength [N/mm ²]	497 *	356	363
Tensile strength [N/mm ²]	675	509	515
Young's modulus [kN/mm ²]	198	194	192

*: 0.2 offset method

Table 3 Parameters of Specimens

Name of specimens	No.1: Spliced lapping bar of column	No.2: Bond of longitudinal bar of column in	No.3: Additional reinforcement at	No.4: Dense stirrup at beam end	No.5: More lateral confinement for eccentric type
RC-1 [Normal Type]	A.	N. R.	A.	A.	
RC-2 [Normal Type]	N. A.	N. R.	A.	A.	
RC-3 [Normal Type]	N. A.	R.	A.	A.	
RC-4 [Normal Type]	N. A.	N. R.	N. A.	N. A.	
RC-5 [Eccentric Type]	A.	N. R.	A.	A.	A.
RC-6 [Eccentric Type]	N. A.	N. R.	A.	A.	A.
RC-7 [Eccentric Type]	N. A.	N. R.	N. A.	N. A.	N. A.

A.: arranged, N. A.: not arranged. R.: removed, N. R.: not removed.

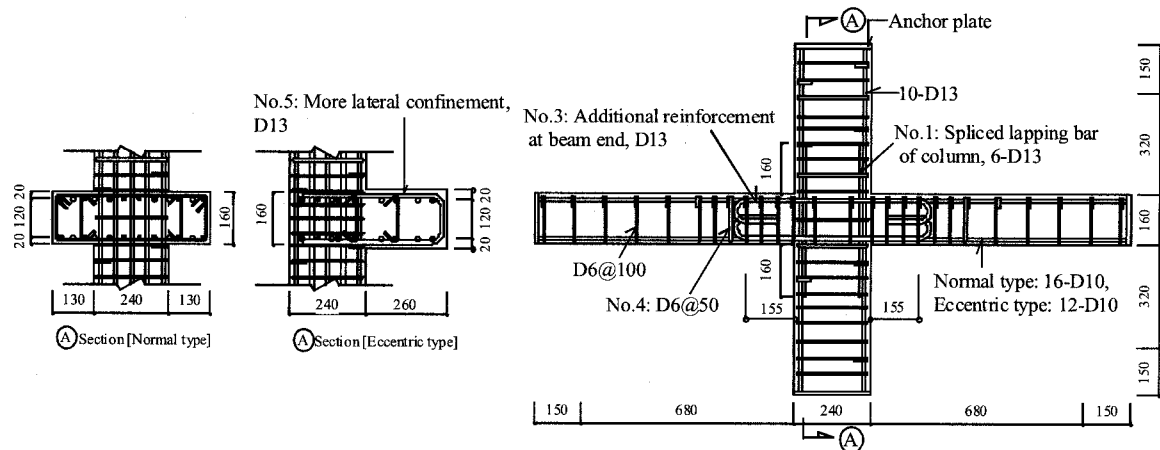


Figure 1 Detail of Specimens

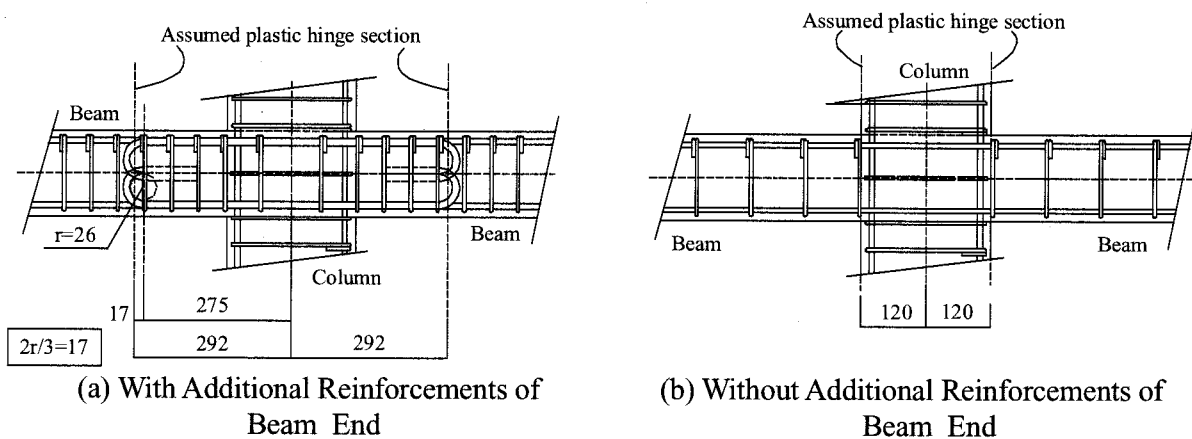


Figure 2 Assumed Plastic Hinge Section

2.2 Loading Setup and Loading Plan

As shown in Figure 3, the column was laid and supported. The beam was subjected to cyclic load by hydraulic jacks. Devices, which were called displacement restriction device in this paper, restricted displacement of orthogonal direction to loading direction at four points. The device consisted of a bar and a plate, which were fixed to a specimen and a loading frame, respectively. A Teflon sheet was fixed on the plate, and the bar, which point was a spherical surface, was touched to the Teflon sheet. As shown in Figure 4, displacement transducers measured displacements of loading point of beam, displacement of axis of column, deformation of column-beam connecting panel, and displacement of beam at 210mm from center of the connecting panel. The deformation of connecting panel were measured by displacement transducers that touched pieces of aluminum channels glued to beam nearby the column, as shown in Figure 3. Loading plan was shown in Figure 4, and all the specimens were tested in the same plan.

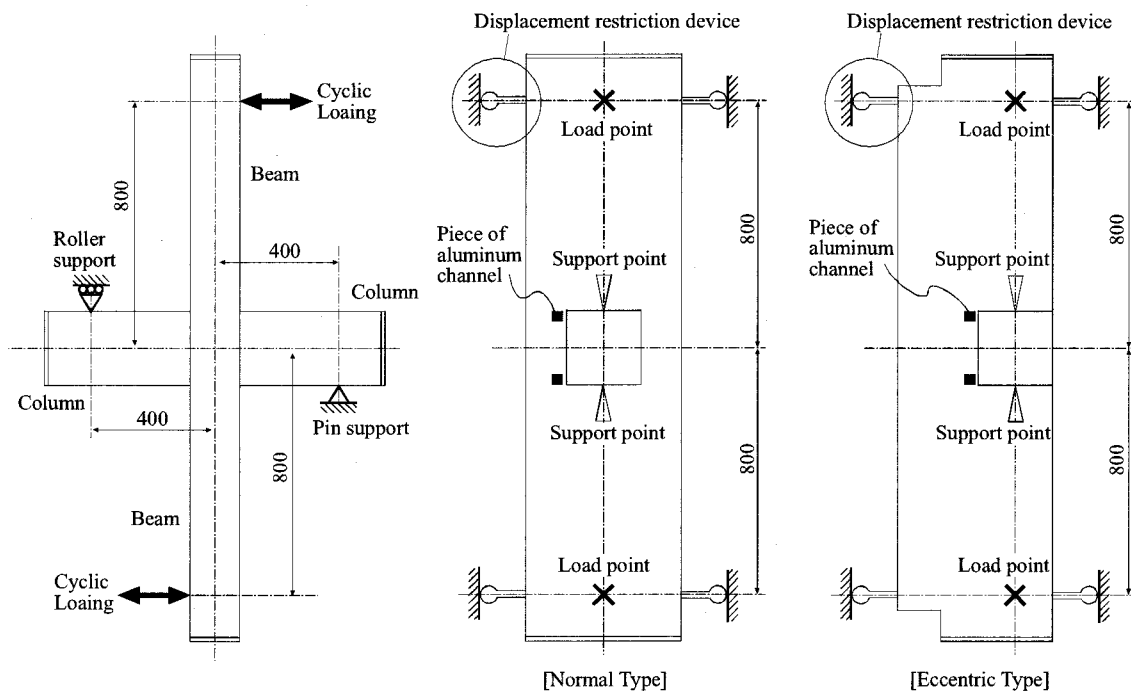


Figure 3 Loading Setup

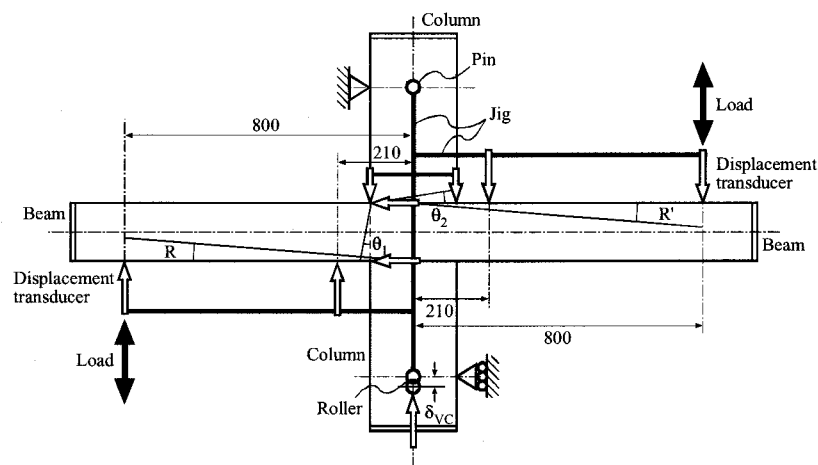


Figure 4 Measuring System

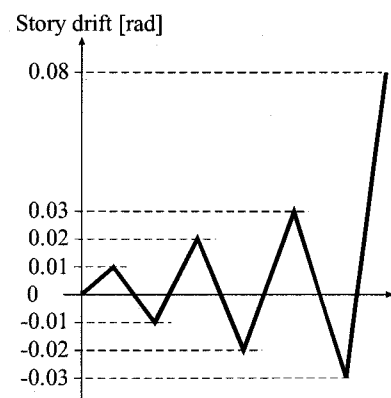


Figure 5 Loading Plan

3. TEST RESULTS AND CONSIDERATION

3.1 Restoring Force Characteristics

Figure 6 shows test results of seven specimens. Horizontal and vertical axis is story drift and shear force acted on column, respectively. Broken lines are ultimate bending strengths, which were computed based on yield bending strengths at plastic hinge section assumed as shown in Figure 2.

As shown in Figure 6, maximum strengths of all the specimens were more than calculated ultimate bending strengths, and the specimens didn't degraded its strength under large deformation. RC-1 and RC-5, which were taken all the measures shown in Table 3, showed good loops of flexural type. In this study, there were no remarkable difference between normal type and eccentric type specimens. It can be said that stress could be transmitted even if the position of connection was different.

The bond of column of RC-1, RC-2, and RC-3 was weaker in this order. As shown in Figure 6, stiffness became softer and slipping behaviors appeared clearer as the bond was weaker. Nevertheless, it can be considered these weren't fatal differences. These differences were caused by deformation at a column end that became larger as the bond was weaker because longitudinal bars of the column were pulled out from the connection.

On the other hand, RC-6 had weaker bond of longitudinal bars of column at the joint than RC-5. The story drift and shear load relationship of RC-6 almost agreed with that of RC-5. This result was different from normal type specimens. The eccentric type specimens had less main reinforcements in beam than the normal type specimens, and the columns of these two type specimens were designed in the same way. Therefore, stress acted on the longitudinal bars in the connection wasn't so high that the result of RC-6 wasn't different from that of RC-5 because applied loads to eccentric type specimens were lower than those to normal type specimens.

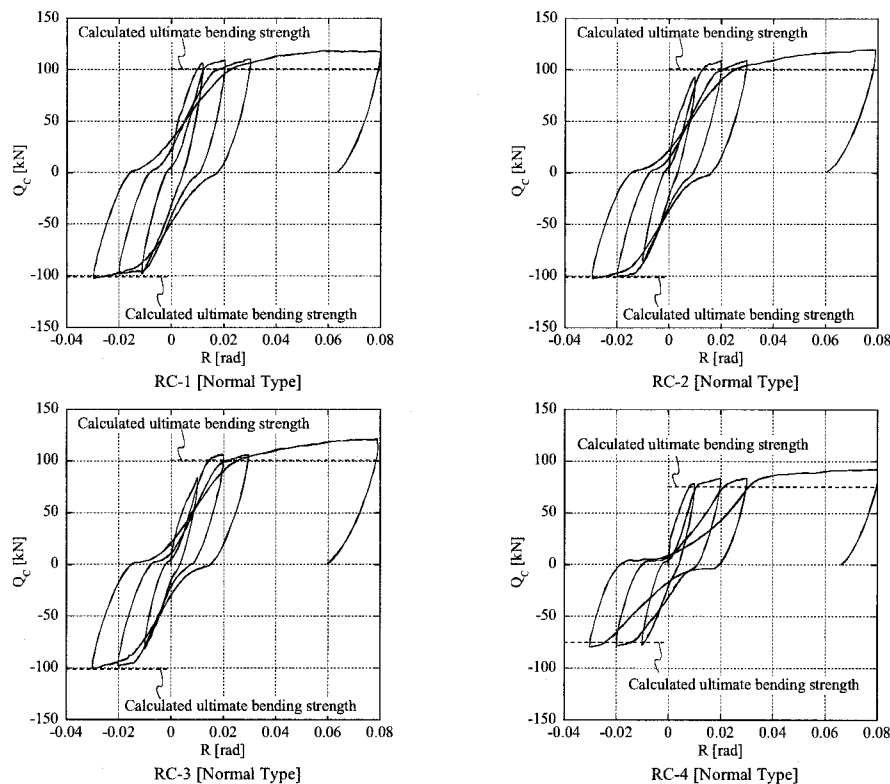


Figure 6 Story Drift and Shear Load Acted on Column Relationship of Normal Type

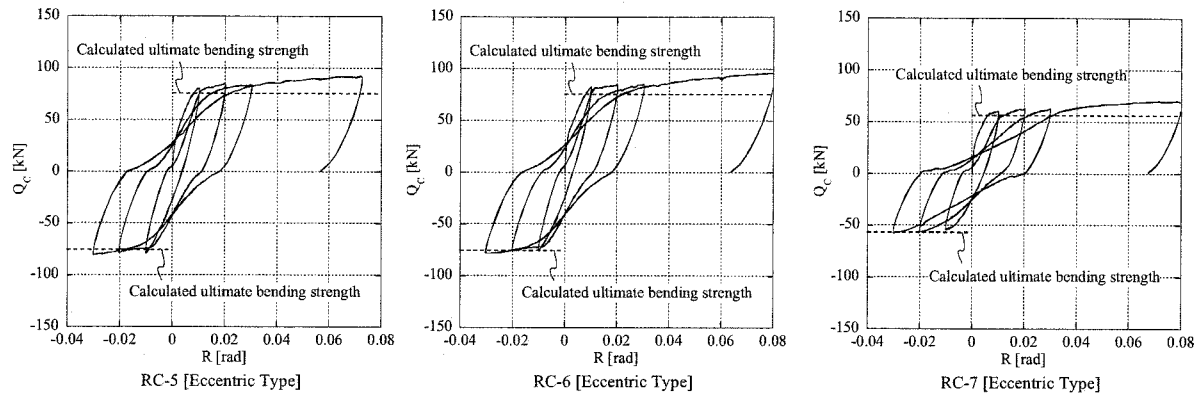


Figure 7 Story Drift and Shear Load Acted on Column Relationship of Eccentric Type

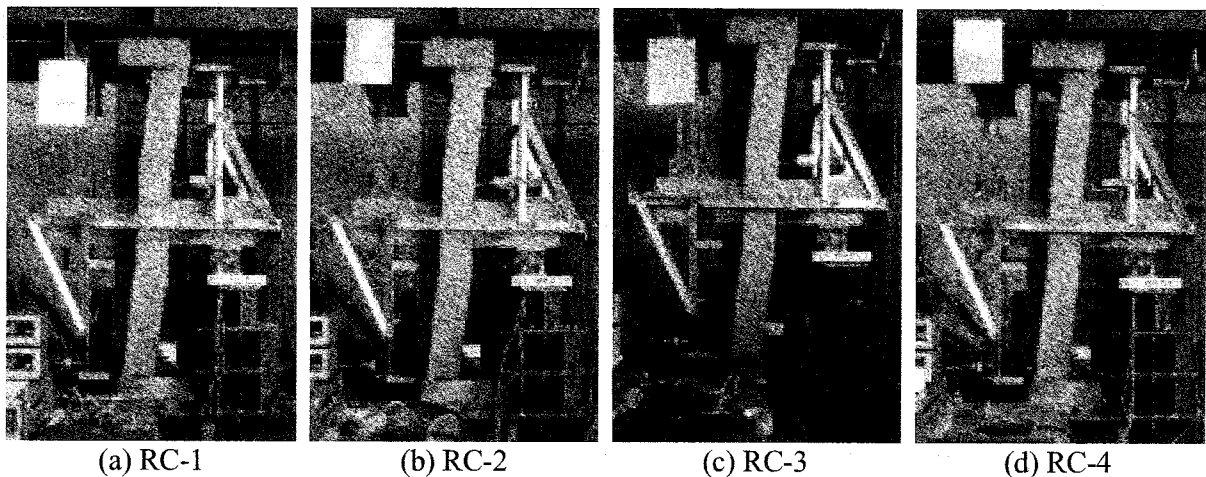
3.2 Property of Deformation and Damage

Figure 7 shows picture when the specimens deformed about 0.08rad. All the tests could be finished without a large torsional deformation.

The specimens placed additional reinforcement at beam end, which were five specimens except RC-4 and RC-7, had wide bending crack near the assumed plastic hinge section. These five specimens had bending crack at column end and a few shear crack in joint, but these cracks didn't expand so much. RC-4 and RC-7 had bending crack at column end and beam end, and wing parts of connection suffer damages. All the seven specimens had no shear crack on columns and beams.

There were no remarkable difference in damage and crack among RC-1, RC-2, and RC-3, and between RC-5 and RC-6, which had different condition of bond. These specimens had no fatal difference in the restoring force characteristics, as mentioned above. In this study, lack of bond in connection didn't have very bad effect on load carrying capacity and damage of the specimens. It is enough to examine the bond by Equation 21, Article 17, AIJ Standard for Structural Calculation of Reinforced Concrete Structures (AIJ, 1999). However, this problem need more consideration.

Figure 8 shows results of RC-1 that total story drift were divided into three components, which were story drifts by deforming beam, column, and joint, respectively. As shown in this figure, story drift of the beam-column joint was due to deformation of beam, and deformations of the column and the joint were a little. A little slipping behavior can be seen in Q_c - R_c relationship. The deformations of the joint and the column were measured through the pieces of aluminum channels that were pasted on the beam nearby the column, as shown in Figure 2. Therefore, it is considered that this slipping deformation was due to pulling out of longitudinal bars of column from the connection.



(a) RC-1 (b) RC-2 (c) RC-3 (d) RC-4

Figure 8 Picture of Normal Type Specimens at Maximum Deformation

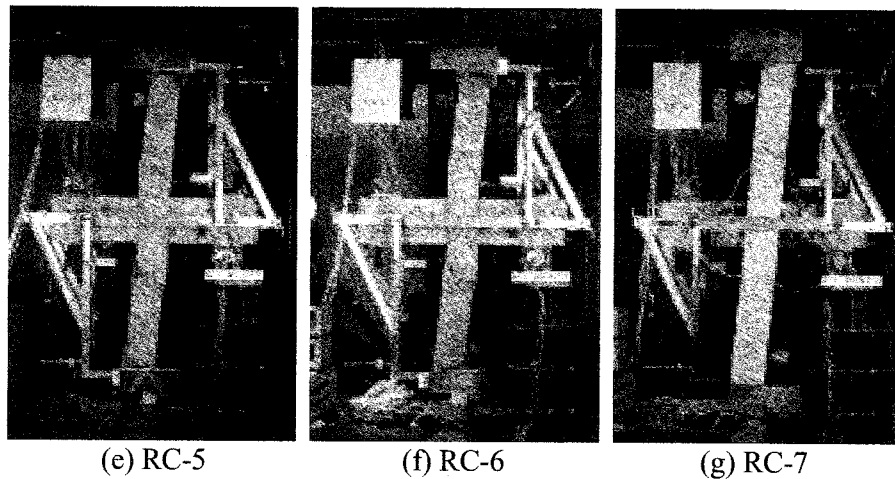


Figure 9 Picture of Eccentric Type Specimens at Maximum Deformation

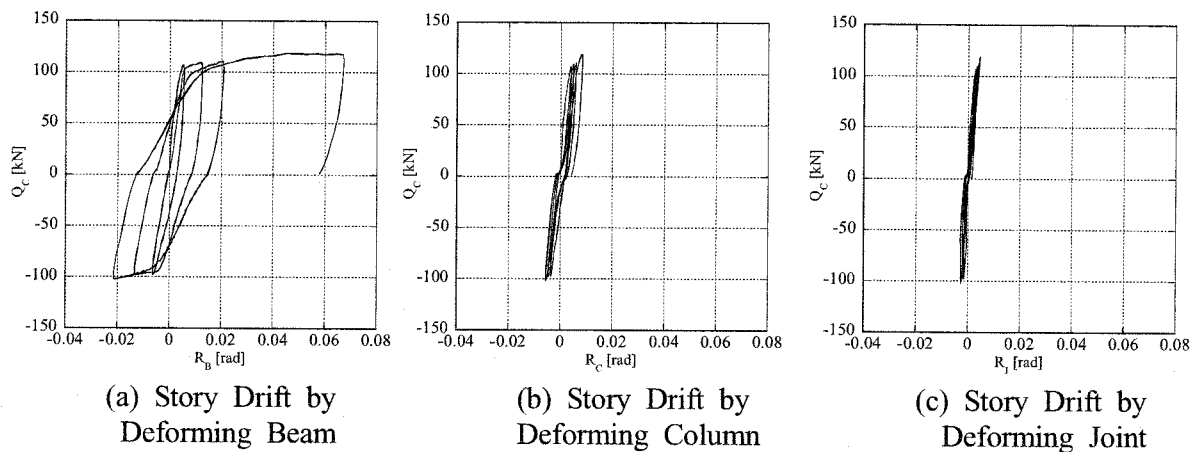


Figure 10 Story Drift of RC-1 divided into three components

4. CONCLUSIONS

In this study, seven RC flat beam and column joint specimens were subjected to cyclic loading tests to examine problems, whether stress can be transmitted well between the beam and the column, and whether bond of longitudinal bars of the column is sufficient in beam-column joint. As results, the following conclusion could be found.

1. RC flat beam and column joint system is possible.
2. Maximum strength can be expected to be calculated ultimate bending strength even if proportion of beam-column joint has fear of stress transmission.
3. The fears of this joint system appear in restoring force characteristics as slipping behavior.
4. Measures taken in this research, which are the additional reinforcements to strengthen beam end, the more lateral confinements, and the spliced lapping bars of column at joint, have good effects on load carrying capacity.
5. Measure that shift plastic hinge of beams at a distance from column surface is recommended.

References:

Architectural Institute of Japan (1999), "Standard for Structural Calculation of Reinforced Concrete Structures –Based on Allowable Stress Concept," Architectural Institute of Japan.

PERFORMANCE ASSESSMENT FOR REINFORCED CONCRETE BUILDINGS WITH SOFT FIRST STORIES

T. Nagae¹⁾

*1) COE researcher, Disaster Prevention Research Institute, Kyoto University, Japan
nagae@steel.mbox.media.kyoto-u.ac.jp*

Abstract: This study focuses on the seismic performances of the reinforced concrete buildings with the soft first stories, which are demanded especially in urban areas. The seismic responses of the soft-first-story buildings and the typical frame structures are statistically assessed based on the results of the dynamic response analyses. Eventually the mean annual frequencies that the maximum interstory drift ratios exceed the safety limit states are computed and compared.

1. INTRODUCTION

The residential buildings that have open spaces in the first stories are in great demand especially in urban areas. Architecturally it is very reasonable to allot such open spaces for parking lots and so on. As a result, the first stories become soft and weak relative to the other upper stories, since the first stories are composed of only the columns although the residential stories are divided by the rigid walls. Structurally those unbalances are unhealthy, and the soft-first-story buildings are well known for being susceptible to collapse through past big earthquakes.

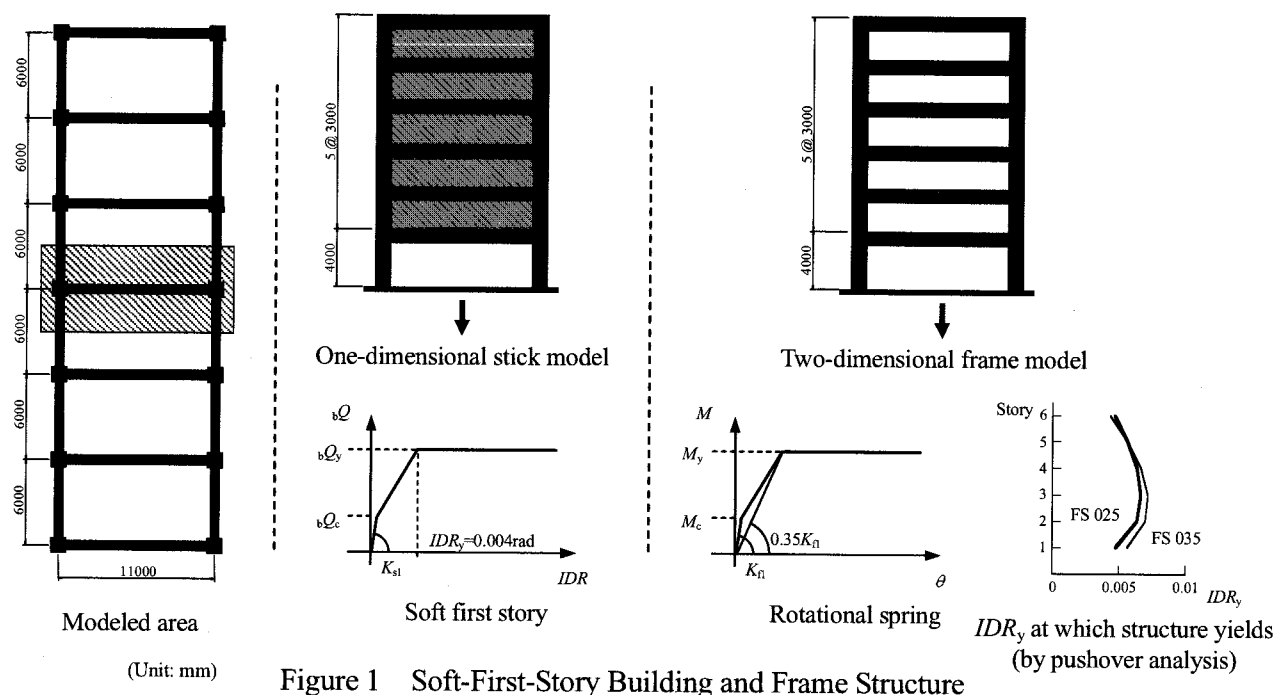
This study focuses on the design that controls the seismic responses of the first stories by the strengths and the deformation capacities. To assess the seismic performances of the structures, a probabilistic procedure is adopted based on the works by Shome and Cornell (1998) and Vamvatsikos and Cornell (2002). 'The probability that the seismic response exceeds the safety limit state is x % in 50 years', this expression is very clear and accessible to the residents. By comparing the performances of the soft-first-story buildings to those of the typical frame structures, the relative assessments for the soft-first-story buildings are also completed.

2. APPROACH FOR ESTIMATING THE PERFORMANCE OF STRUCTURE

2.1 Models for Dynamic Response Analyses

The six-story RC buildings shown in Figure 1 are considered. The analyzed cases consist of three soft-first-story buildings and two frame structures. The properties and the dimensions of the buildings are shown in Table 1. One interior frame of each building is assumed to represent the performance of the building, and the portion corresponding to the one frame is extracted.

For the soft-first-story buildings, the yield strength coefficients (the base shear coefficients at which the structures yield) of 0.35, 0.70 and 1.05 are selected. The structures are realized by stick models. The shear deformation and the flexural deformation of the each story are expressed by a shear spring and a rotational spring. The inelastic behaviors of the first stories are defined by applying



Takeda model (1970) to the relationships between the shear force and the interstory drift ratio. The initial stiffness K_{s1} is calculated by Eq. (1) estimating the flexural deformation of the two columns.

$$K_{s1} = 2 \cdot \left(\frac{12EI}{l^3} \right) \cdot L \quad (1)$$

where E is Young modulus, I is the moment of inertia of gross section, l is the clear span, L is the story height.

The crack strength bQ_c is calculated based on the flexural crack strength of the column subjected to the tension by the overturning moment of the structure. The interstory drift ratio corresponding to the yield strength is defined as 0.004 rad regardless of the size of the column, based on the work by Arzpeima and Kuramoto. (2003). The stiffness after the yield is defined as K_{p1} times 0.001.

Table 1 Assumed Cases

(1) Soft-First-Story Buildings

Cases	Yield strength coefficient	Columns of 1 st stories	Columns of 2 nd to 6 th stories	Beams of 2 nd - roof stories	Thickness of the walls	1 st mode periods (sec.)
SB 035	0.35	900 x 900	900 x 900	600 x 1000	200	0.20
SB 070	0.70	1050 x 1050	900 x 900	600 x 1000	200	0.17
SB 105	1.05	1200 x 1200	900 x 900	600 x 1000	200	0.15

(2) Frame Structures

Cases	Yield strength Coefficient	Columns of 1 st to 6 th stories	Beams of 2 nd story	Beams of 3 rd - 4 th stories	Beams of 5 th - roof stories	1 st mode periods (sec.)
FS 025	0.25	900 x 900	600 x 1100	600 x 1000	600 x 900	0.70
FS 035	0.35	900 x 900	650 x 1200	650 x 1100	650 x 1000	0.62

(Unit of dimensions: mm)

For the frame structure, the yield strength coefficients of 0.25 and 0.35 are selected. The structures are realized by two-dimensional frame models. The beams and the bottom ends of the columns are modeled as inelastic elements, and by making the other columns elastic, the complete mechanisms for the frame structures are guaranteed. The flexural deformations of the beams are concentrated to the rotational springs at the ends. The initial stiffness K_{fi} of the rotational spring is calculated by Eq. (2).

$$K_{fi} = \frac{6EI}{l} \quad (2)$$

The inelastic behaviours of the rotational springs are defined by Takeda model. The secant stiffness corresponding to the yield is defined as K_{fi} times 0.35. The yield moments of the hinges are decided so that all the hinges simultaneously yield at the assumed base shear under the pushover analysis based on the linear load distribution. The stiffness after the yield is defined as K_{fi} times 0.001.

The structures are damped by 5 % coefficient for the first mode, but the damping force of each member is changed in proportion to the instantaneous stiffness of the member. The P - D effects are considered using a geometric stiffness formulation.

2.2 Site Hazard and Ground Motion

The selected intensity measure IM is the peak ground acceleration PGA , whose hazard curve is available in Japan. In accordance with Eq. (3) shown in the Recommendations for Loads on Buildings (AIJ, 1993), the hazard curve $\lambda_{PGA}(x)$ is expressed by Eq. (4).

$$PGA = x = A_0 \left(\frac{1}{100\lambda_{PGA}(x)} \right)^{0.54} \quad (g) \quad (3)$$

$$\lambda_{PGA}(x) = 0.000527 \cdot x^{-1.85} \quad (4)$$

where A_0 is 200/980.

A set of 40 ground motions (Medina 2003) is used for the dynamic response analyses. The ground motions were recorded in various earthquakes in California. The sites are categorized as Type-D site of NEHRP ($183\text{m/sec} < V_s < 366\text{m/sec}$ or $15 < N < 50$, where V_s is shear wave velocity, N is N value of SPT test). The earthquake magnitudes are from 6.5 to 6.9, and the source-to-site distance ranges from 13 to 40 km, as shown in Figure 2 (1). The earthquakes with the large magnitude and the small

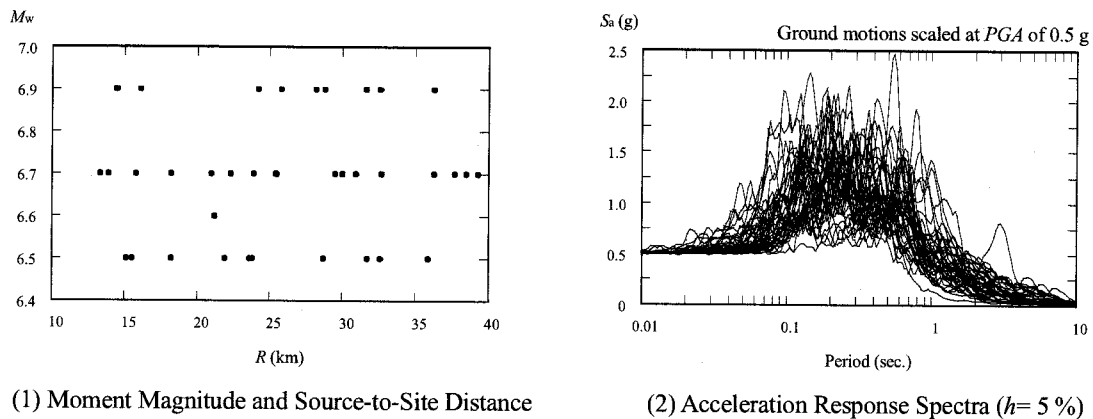


Figure 2 Ground Motions Used for Dynamic Response Analyses

source-to-site distance are adopted to consider the safety limit states of the structures. The acceleration response spectra of the selected ground motions are illustrated in Figure 2 (2).

2.3 Statistics of Results of Dynamic Response Analyses

The 40 results of the dynamic response analyses at given a PGA are shown by the plots in Figure 3 (1). The maximum interstory drift ratio IDR_{max} is adopted as an engineering demand parameter EDP to represent the seismic response. For the dispersed data, the statistics are conducted to the direction of EDP (to the lateral axis). Since the impacts of a few ground motions that produce extremely large deformations are apt to dominate the other results in the inelastic dynamic response analyses, the “counted” statistics are adopted. For the set of 40 ground motions, the average of the 20th and 21st sorted values is taken as median (50th percentile).

The median of the natural logarithm of the data $\text{Ln}(IDR_{max})^{50\%}$, and the equivalent dispersion δ_{eq} of the data are used as parameters in applying the lognormal distribution to the data. The equivalent dispersion δ_{eq} corresponds to the difference between the $\text{Ln}(IDR_{max})^{50\%}$ and the 16th percentile $\text{Ln}(IDR_{max})^{16\%}$, or the difference between the $\text{Ln}(IDR_{max})^{50\%}$ and the 84th percentile $\text{Ln}(IDR_{max})^{84\%}$. This is based on the assumption that the mean \pm one sigma (the standard deviation) is the 16 percentile or the 84 percentile in the normal distribution. Thus, δ_{eq} is calculated by Eq. (5).

$$\delta_{eq} = \frac{\text{Ln}(IDR_{max})^{84\%} - \text{Ln}(IDR_{max})^{16\%}}{2} \quad (5)$$

It should be noted that δ_{eq} is approximately the coefficient of variation of the data (Benjamin and Cornell 1970).

Figure 3 (2) shows the results of the incremental dynamic analyses, in which PGA is increased by 0.1 g to identify continuously the distribution of the responses. The 16th percentile, 50th percentile and 84th percentile curves are indicated with the bold lines.

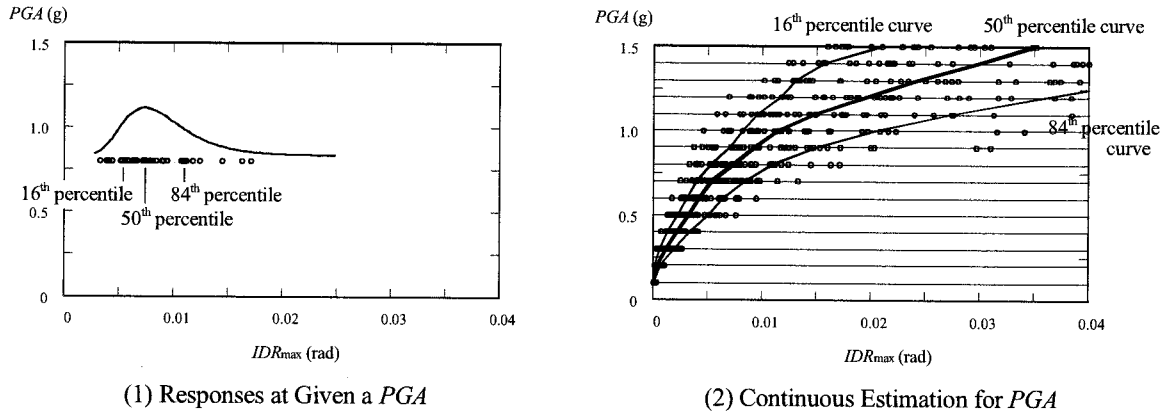


Figure 3 Statistics of Seismic Responses (SB 105)

3. COMPARISONS OF SEISMIC PERFORMANCES

3.1 Seismic Responses

Figure 4 (1) shows the 50th percentile curves of the responses (IDR_{max}), which represent the degree of vulnerabilities for PGA . In the case of the soft-first-story buildings, the seismic responses given PGA are effectively reduced by the increase of the yield strength. However, the slopes become gentle

in the range of IDR_{max} over 0.01 rad, although the slopes of the frame structures ascend linearly. Thus, it is suggested that the slopes of the curves are influenced by the differences of the redundancies depending on the mechanism types. Figure 4 (2) shows the relationships between δ_{eq} and 50th percentile of IDR_{max} . Although the tendency that δ_{eq} slightly increase with the increase of the IDR_{max} can be observed, δ_{eq} are between 0.3 and 0.7.

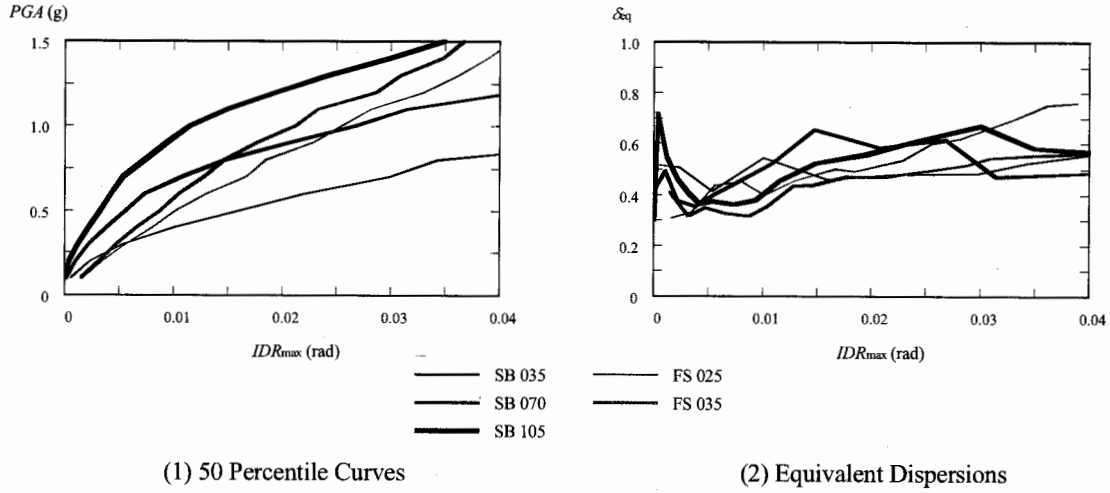


Figure 4 Parameters to Define Distributions of Seismic Responses

By using the two parameters mentioned above, the conditional probability that IDR_{max} exceeds idr at given PGA is obtained by Eq (6).

$$P[IDR_{max} > idr] = 1 - P[IDR_{max} \leq idr] = 1 - \Phi\left(\frac{\ln(idr) - \ln(IDR_{max})^{50\%}}{\delta_{eq}}\right) \quad (6)$$

Figure 5 shows the conditional probabilities that IDR_{max} exceeds 0.02 rad at given PGA . The selected $PGAs$ are 0.5, 0.8 and 1.2 g and corresponding to the return periods of 530, 1260 and 2660 years. It should be noted that the level of PGA considered in the code of Japan corresponds to 0.5 g. In that level, the conditional probabilities are kept very small (less than 0.5 %) except for the soft-first-story building with the yield strength coefficient of 0.35 and the frame structure with the yield strength coefficient of 0.25. However, the conditional probabilities become high as PGA becomes large. In the

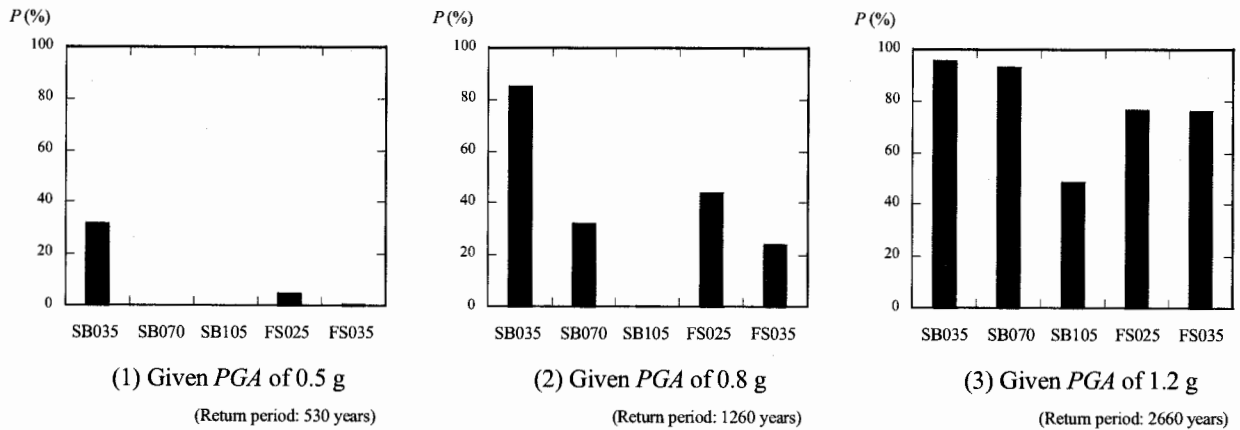


Figure 5 Conditional Probabilities of Exceeding 0.02 rad at Given PGA

case of PGA of 1.2 g, the probabilities that IDR_{\max} exceeds 0.02 rad ascend to more than 49%. Thus, it is suggested that if the design calls for the lower value of the probability that IDR_{\max} exceeds 0.02 rad given PGA of 1.2 g, the yield strength ratio of more than 1.05 is demanded in the case of the soft-first-story building.

The mean annual frequency that IDR_{\max} exceeds the specified value idr is calculated by Eq. (7).

$$\lambda_{IDR_{\max}}(idr) = \int_0^{\infty} P[IDR_{\max} > idr | PGA = x] d\lambda_{PGA}(x) \quad (7)$$

Eq. (7) consists of the slope of the seismic hazard curve in Eq. (4), which means the mean annual frequency of the occurrence of the event with PGA of x , and the conditional probability of the response in Eq. (6). Figure 6 shows the hazard curve for IDR_{\max} derived from Eq. (7). The mean annual frequencies given IDR_{\max} become smaller with the increase of the yield strength coefficient. For each, the mean annual frequency decrease as IDR_{\max} becomes larger, but the slope of the descent is steeper in the frame structures than in the soft-first-story buildings. This can be explained by the tendencies of 50th percentile curves (vulnerability curves) in Figure 4 (1).

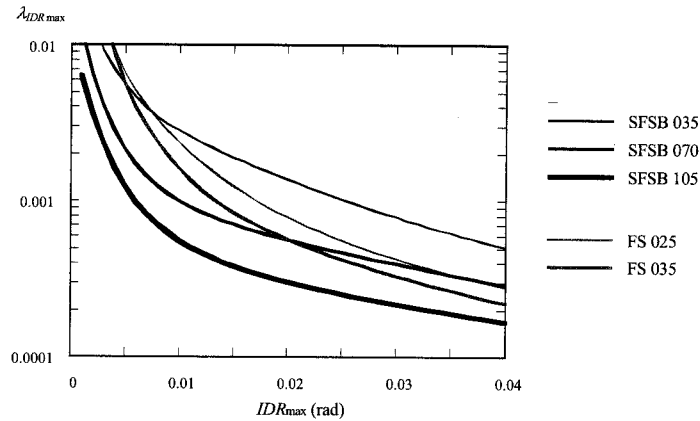


Figure 6 Hazard Curves of IDR_{\max}

3.2 Ultimate Deformation Capacity and Safety Limit State

The method to estimate the ultimate deformation capacity and the verification are shown in the Design Guideline Based on Ultimate Strength Concept (AIJ, 1990). Figure 7 shows the relationships

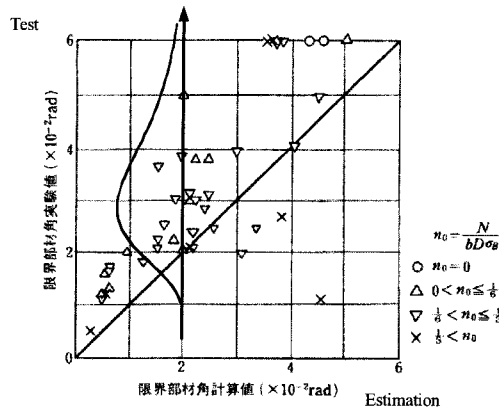


Figure 7 Verification of Estimated Ultimate Deformation Capacities (AIJ, 1990)

between the test results and the estimations in the guideline. The fragility curve of the ultimate deformation capacity $F(r)$ is defined by applying the lognormal distribution to the test results given the estimation. From the statistics of the all plots in Figure 7, the 50 percentile and δ_{eq} of the ratios of the test results to the estimations are obtained as 1.41 and 0.39, respectively. For the soft first story, the 50 percentile values are multiplied by l/L (where l is the clear span of the column, 3.0m, L is the story height, 4.0 m) to convert the maximum rotational angle of the column to the maximum interstory drift ratio IDR_{max} . For the frame structures, the maximum rotational angle of the beams is assumed to correspond to the maximum interstory drift ratio IDR_{max} .

Thus, the mean annual frequency that the response exceeds the safety limit state can be obtained by Eq. (8) that consists of the fragility curve based on interstory drift ratio $F(idr)$ and the slope of the hazard curve of IDR_{max} in Eq. (7).

$$\lambda_{Ru} = \int_0^{\infty} F(idr) |d\lambda_{IDR_{max}}(idr)| \quad (8)$$

Figure 8 shows the mean annual frequencies that the seismic responses exceed the safety limit state at given the estimation of the ultimate deformation capacity.

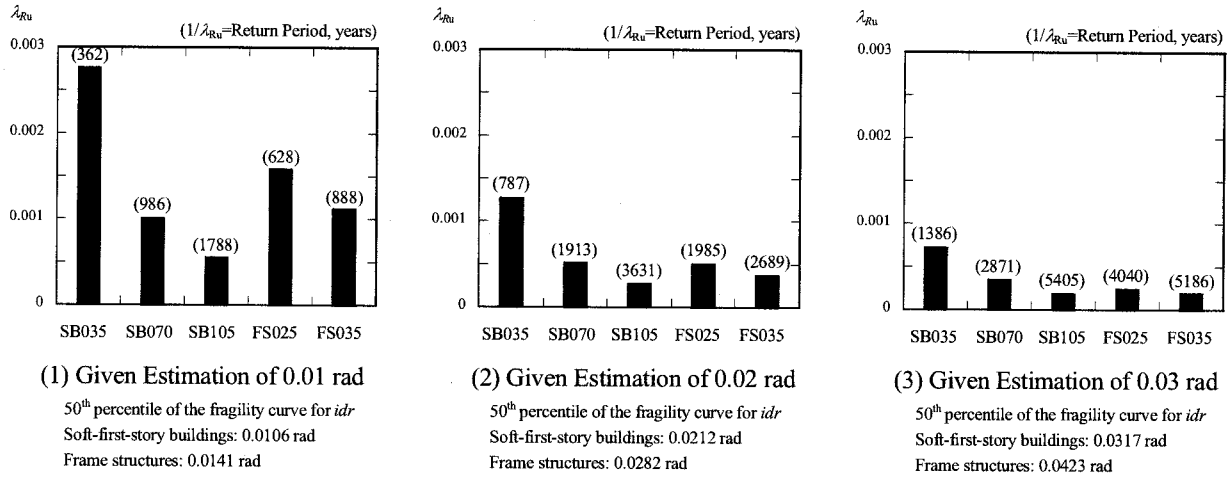


Figure 8 Mean Annual Frequencies of Exceeding Safety Limit States

In addition, the mean annual frequencies can be converted to the probabilities, assuming Poisson process. That is, the probabilities of exceeding the safety limit state in t years are given by Eq. (9).

$$P(\text{response} > \text{limit state}) = 1 - \exp(-\lambda_{Ru} \cdot t) \quad (9)$$

The results given t of 50 years are shown in Table 2. The design based on the probability can be conducted referring to this matrix. For example, if the design calls for less than 2 % chances of exceeding the limit states in 50 years, the soft-first-story building with the yield strength coefficient of 0.35 fails, and the soft-first-story building with the yield strength coefficient of 0.70 can succeed with the estimation of the deformation capacity of 0.03 rad. For the soft-first-story building with the yield strength coefficient of 1.05, the performances are competing with that of the frame structure with the yield strength coefficient of 0.35. However, the tendency can be observed that the differences between them become small as the given estimations of the deformation capacity become large.

Table 2 Probabilities of Exceeding Safety Limit States in 50 Years

Cases	Given Estimation of 0.01 rad	Given Estimation of 0.02 rad	Given Estimation of 0.03 rad
SB 035	12.9 %	6.2 %	3.5 %
SB 070	4.9 %	2.6 %	1.7 %
SB 105	2.8 %	1.4 %	0.9 %
FS 025	7.7 %	2.5 %	1.2 %
FS 035	5.5 %	1.8 %	1.0 %

4. CONCLUSION AND FUTURE DIRECTION

This study focused on the seismic performances of the soft-first-story buildings, which are in great demand in urban areas. The seismic performances were estimated through the probabilistic approach and compared to those of the typical frame structures. As a result, the possibility was suggested that the soft-first-story buildings can be designed with the same level of safety that the typical frame structures have, on the condition that the appropriate strength and the deformation capacity are given to the first story columns.

However, it should be noted that these performances are derived from the assumed condition. That is, the redundancies that come out after the safety limit state are not reflected in this estimating method. The increment of the response to that of *PGA* is more significant in the soft-first-story buildings than in the frame structures at around the safety limit state. Thus, the frame structures are expected to have advantages relative to the soft-first-story buildings in terms of the real collapsing point. The next step of this study is to identify the redundancies using the models that reflect the deteriorations of the strength.

Acknowledgements:

The author acknowledges the helpful suggestions and assistances of Professor Nakashima and Professor Suita of Kyoto University and Professor Hayashi of Tokyo Institute of Technology. The valuable comments of Professor Krawinkler of Stanford University are also appreciated.

References:

- AIJ (1990), "Design Guidelines for Earthquake Resistant Reinforced Concrete Buildings Based on Ultimate Strength Concept".
- AIJ (1993), "Recommendations for Loads on Buildings"
- Arzpeima, S. and Kuramot, H. (2003), "Effect of Varying Axial Forces in Columns on Earthquake Response of RC Piloti-Buildings", Proceedings of the Japan Concrete Institute, vol. 25, pp. 1309-1314.
- Benjamin, J.R. and Cornell, C.A. (1970), "Probability Statistics and Decision for Civil Engineers", McGraw-Hill, Inc., New York.
- Medina, R. (2003), "Seismic Demands for Nondeteriorating Frame Structures and Their Dependence on Ground Motions", Ph. D. thesis, Stanford University.
- Shome, N., and Cornell, C.A. (1998), "Earthquakes, Records, and Nonlinear Responses", Earthquake Spectra, 14 (3), 469-500.
- Takeda, T., Sozen, M. A., and Nielsen, N. N. (1970), "Reinforced Concrete Response to Simulated Earthquakes", Journal of the Structure Division, ASCE, ST12, pp. 2557-2573.
- Vamvatsikos, D., and Cornell, C.A. (2002), "Incremental Dynamic Analysis", Earthquake Engineering and Structural Dynamics, 31, 3, 491-514.

NONLINEAR ANALYSIS OF REINFORCED CONCRETE VIADUCTS BY 3D LATTICE MODEL

T. Miki¹⁾ and J. Niwa²⁾

1) Assistant Professor, Department of Civil Engineering, Tokyo Institute of Technology, Japan

2) Professor, Department of Civil Engineering, Tokyo Institute of Technology, Japan

mikitomo@cv.titech.ac.jp, jniwa@cv.titech.ac.jp

Abstract: Study on the seismic response of RC structures subjected to strong earthquake motion is presented. The dynamic analysis using a 3D lattice model is performed for the RC structures. The 3D lattice model can offer a reasonable prediction of the shear carrying capacity of RC columns and beams. The analytical targets are two RC columns used in the shaking table test and two RC viaducts damaged at the Hyogo-ken Nanbu Earthquake. The comparison between experimental results and predictions of the 3D lattice model reveals the reliability of the modeling on the seismic response of RC columns. In addition, the verifications show that the analysis can predict the failure mode observed in the field for the RC viaducts.

1. INTRODUCTION

The Hyogo-ken Nanbu Earthquake occurred at January 1995 caused the destructive collapse in various structures such as reinforced concrete (RC) structures. The observations followed this earthquake clearly show that the main causes of severe damage are caused by the overestimation for the load carrying capacity and the less ductility due to the insufficient amount of transverse reinforcement in the RC columns or beams. On the other hand, it is also noticed that there were many RC structures without almost any damages. The degree of structure damage differs due to the several factors even if the dimension of structures and the arrangement of reinforcement are almost identical. So far many investigations on the damage of the RC structures and the simulations for this earthquake have been carried out. The simulation to evaluate the seismic performance of the structures was performed mainly by the frame analysis based on a moment-curvature relationship or the analysis using a fiber technique. The shortcoming of these models is the difficulty in predicting the behavior in the post-peak region, especially, if a RC member fails in shear. In these models, moreover, the shear deformation and torsional behavior cannot be directly predicted because the in-plane deformation is not taken into account.

In this study, the 3D lattice model (Miki et al. 2004) is used to predict the seismic behavior of RC structures. The 3D lattice model is categorized as a macro-scopic truss approach and can offer the shear resisting mechanism of RC structural members appropriately. In this study, the seismic response of RC structures is evaluated by the nonlinear dynamic analysis using the 3D lattice model. Here, two RC columns used in the shaking table test and two RC rigid-framed viaducts damaged at the Hyogo-ken Nanbu Earthquake are selected as the analysis targets. In the dynamic analysis of the RC viaducts, the input ground motions at each site are estimated by the FDEL (Sugito et al. 1994). In the analysis, the interaction between the soil and the structures is not considered.

2. ANALYTICAL MODEL

2.1 Outlines of 2D Lattice Model

The 3D lattice model (Miki and Niwa 2004) is developed based on the concept of the 2D lattice model (Niwa et al. 1995). The 2D lattice model consists of members of concrete and reinforcement, as shown in Figure 1. The model in the figure shows the column subjected to load from left hand side. It is assumed that the cross section depth of the lattice model corresponds to the effective depth, d . With respect to the RC column, the concrete region is modeled into flexural compression members, flexural tension members, diagonal compression members, diagonal tension members, horizontal members and two arch members. The longitudinal and the transverse reinforcements are modeled into vertical and horizontal members, respectively. The characteristic of the 2D lattice model is to incorporate the diagonal tension members and the arch members of concrete into the modeling. The arch members connecting the nodes at the opposite diagonal corners between the loading point and the bottom of the column are arranged according to the direction of internal compressive stress flow.

Figure 2 is a schematic diagram of a RC column modeled by the 2D lattice model. The concrete region is divided into truss and arch parts. When the value of t is defined as a ratio of the width of the arch part to that of cross section, b and where $0 < t < 1$, the widths of the arch and truss parts are given by $b \times t$ and $b \times (1 - t)$, respectively. The value of t is determined based on the principle of minimum total potential energy for the 2D lattice model with the initial elastic stiffness. This means that any displacement satisfying the given boundary conditions minimizes the absorption of the total potential energy of an elastic system. The preliminary analysis using the 2D lattice model is carried out for a small displacement induced at the loading point, in which the value of t changes from 0.05 to 0.95 at intervals of 0.05.

2.2 Configuration of 3D Lattice Model

As an example of the 3D lattice modeling for a RC structural member, a RC column is shown in Figure 3. The 3D lattice model of the column consists of vertical and horizontal members of each material and diagonal and arch members of concrete. In the lattice model, a shear resisting mechanism is represented by arch and truss actions. It is assumed that the arch action in the shear resisting mechanism is defined by four arch members that connect the loading point with the bottom of the column at opposite corners. To represent the truss action, it is assumed that a 3D space is comprised of an orthogonal coordinate system defined by three planes that are x-y, y-z and z-x planes. Two crossing diagonal members are located on each truss plane to create a unit consisting of twelve diagonal

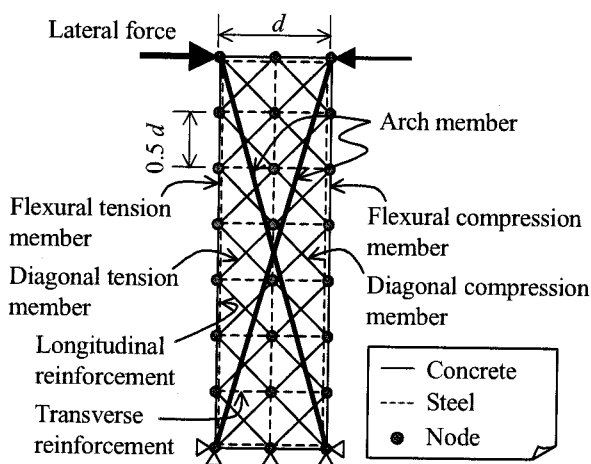


Figure 1 Outlines of 2D Lattice Model

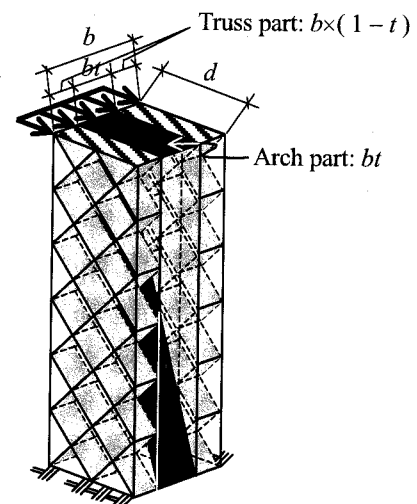


Figure 2 Schematic View of a RC Column Modeled by 2D Lattice Model

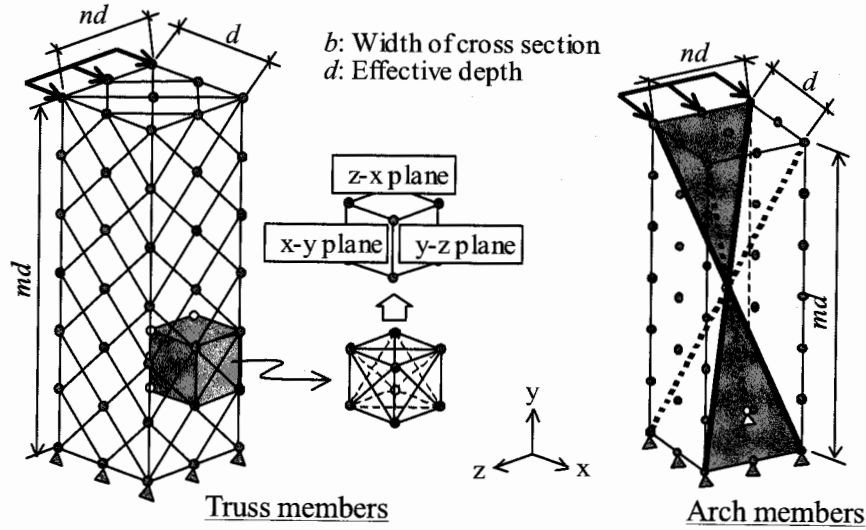


Figure 3 Discretization of Concrete Region in 3D Lattice Model

members on six truss planes, as shown in Figure 3. In each truss plane, the in-plane 2D constitutive law of concrete can be used, where consideration is given to the reduction of compressive strength of cracked concrete depending on transverse tensile strain (Vecchio and Collins 1986).

The cross-sectional area of the arch member can be calculated based on the assumption that the global stiffness of 3D lattice model is equivalent to one of 2D lattice model. Here, the ratios of the arch part width to the width and the depth in the cross section of the column are defined as t_b and t_d , respectively. With the determination of values of t in 3D lattice model, not only the width of cross-section of the column but also the depth of cross-section of the column is varied in the pre-analysis. In the 3D lattice mode the values of t_b and t_d are determined based on the theorem of minimization of the total potential energy.

2.3 Material Constitutive Models

In order to consider the effect of lateral confinement of concrete due to suitable arrangement of transverse reinforcement, the stress-strain relationship of confined concrete proposed by Mander et al. (1988) is applied to the diagonal compression members and the arch members. For cracked concrete, the compressive softening behavior of concrete proposed by Vecchio and Collins (1986) is considered. The ability of cracked concrete to resist compressive stress decreases as the transverse tensile strain increases. With the flexural compression member that is assumed to represent the cover concrete, the stress-strain relationship represented by the quadratic curve is used.

As for the flexural tension members of concrete, which are located near reinforcement, the concrete continues to contribute the tension force even after cracking due to the bond effect between the concrete and reinforcement. Therefore, the tension-stiffening model (Okamura and Maekawa 1991) is applied. On the other hand, for the diagonal tension members that consist of concrete far from reinforcement, after the crack occurs, the concrete can be assumed to show a tension strain-softening behavior. Hence, the tension softening curve, so-called 1/4 model (Rokugo et al. 1989), is applied. The fracture energy of concrete G_F , which is the area under the tension softening curve, is assumed to be 0.1 N/mm as a standard value of normal concrete.

The envelope stress-strain curve of reinforcing bar is modeled as bi-linear in which the tangential stiffness after yielding is $0.01E_s$, where E_s denotes Young's modulus. After yielding, the stiffness of the reinforcing bar decreases when the stress stage changes from tension to compression, while the similar behavior is observed when the stress stage changes from compression to tension. In the analysis, the numerically improved model of reinforcing bars (Fukuura and Maekawa 1997) is used to consider the

Bauschinger effect. In addition, in order to evaluate the buckling behavior of longitudinal reinforcing bars, the buckling model proposed by Dhakal (2000) is used. This model is characterized as the spatially averaged material model that accurately takes into account the inelastic behavior of buckling.

3. RC COLUMNS SUBJECTED TO SEISMIC BILATERAL LOADING

3.1 Outlines of Target RC Columns and Analysis procedure

In this section, the 3D lattice model is applied to the dynamic analysis of RC columns. The targets are large-scale RC columns used in the bilateral shaking table tests (Nishida and Unjoh 2004). The dimensions of the column are shown in Figure 4. The compressive strength of the concrete was 34.1 N/mm^2 and the yield strengths of the longitudinal and transverse reinforcements were 383 N/mm^2 and 350 N/mm^2 , respectively.

The input ground acceleration was the NS and EW components recorded at Takatori Station during the Hyogo-ken Nanbu Earthquake. The accelerations of EW and NS components were horizontally applied to the direction along the X and Y axes. Two kinds of maximum accelerations, 20 % and 100 % of original motion were used.

In the dynamic analysis, the 3D lattice model shown in Figure 5 is used. Regarding damping, in this study, the numerical damping of the Newmark method with factors $\beta = 0.36$ and $\gamma = 0.70$ is assumed as the time integration, while viscous damping is neglected. The time interval is set to be 0.01 second. The Newton-Raphson iteration method is adopted to iterate the calculation until an adequately converged solution is obtained. Here, the convergence tolerances for the out-of-balance force and energy are set to be 0.001 and 0.01, respectively.

3.2 Analytical Results and Discussion

The hysteresis loops that are the acceleration-horizontal displacement relationships at the center of gravity of a top weight are shown in Figure 6. The relationships are equivalent to that of lateral force-lateral displacement at the top of the column because the acceleration multiplied by the mass of a superstructure can be considered as the lateral force.

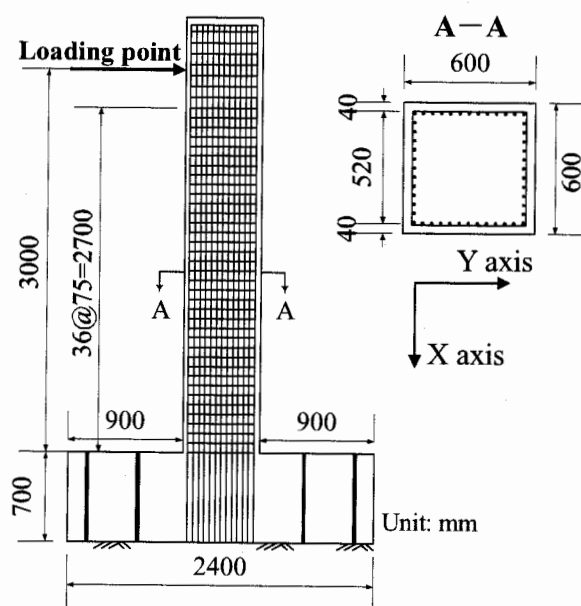


Figure 4 Details of Tested Column (Nishida and Unjoh 2004)

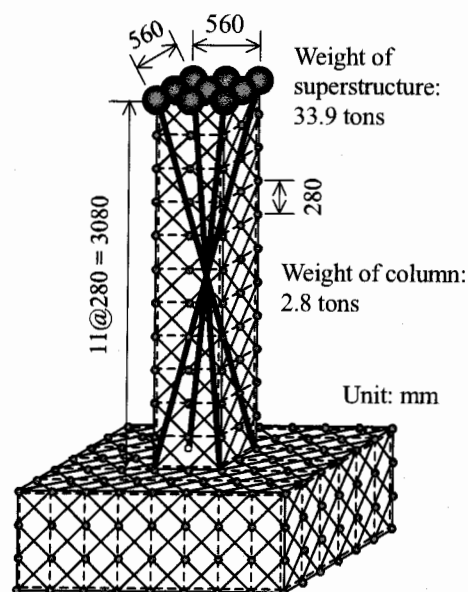


Figure 5 3D Dynamic Lattice Model

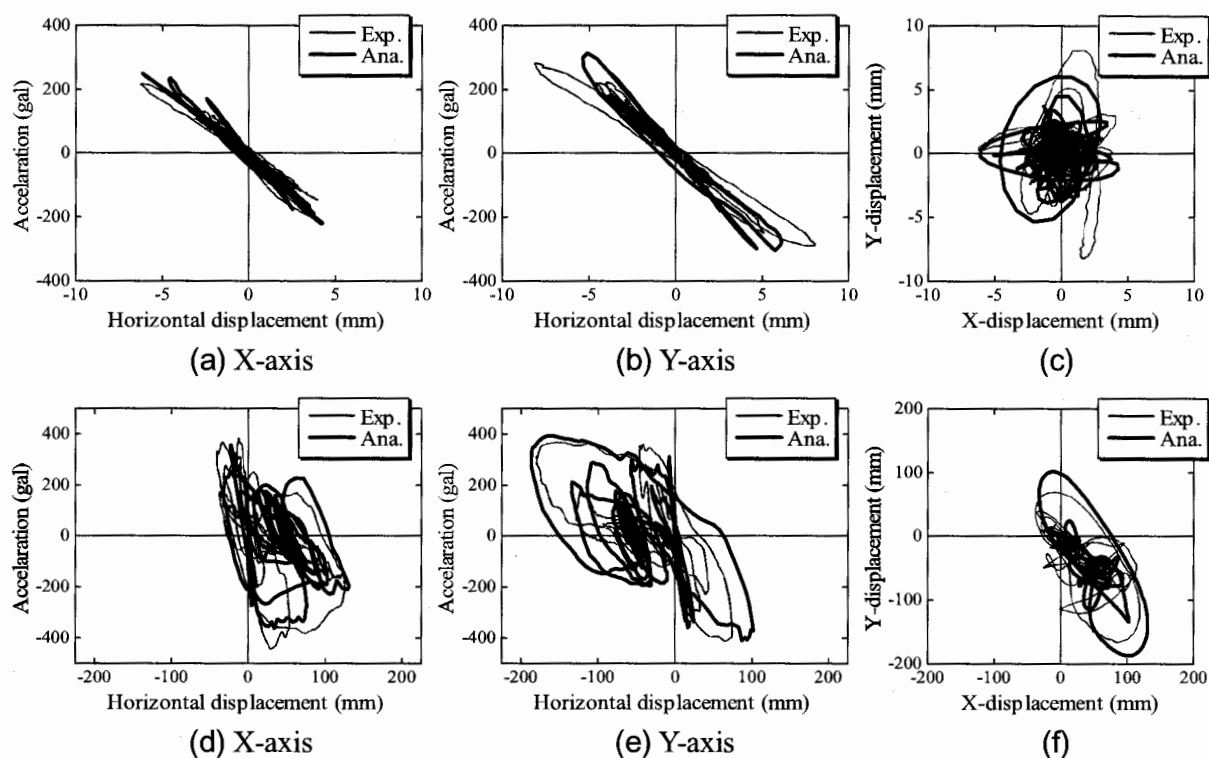


Figure 6 Results Observed in Shaking Table Test and Computed Using 3D Lattice Model Subjected to 20% Level Motion: (a) to (c); 100% Level Motion: (d) to (f)

For first low-level shaking, the experimental results are found to show linear response. As can be observed in Figure 6 (b), the response along the Y axis shows a small loop in the hysteretic response. This is due to minor cracks at the bottom of the column. The analytical results obtained from the 3D lattice model are in reasonably good agreement with the experimental results. The analytical initial stiffness is found to be slightly higher than the experimental results. This may be caused by the fact that the cylindrical strength of concrete is different from the actual strength of concrete used in the RC column. Even so, there is not huge difference in the elastic response range.

As for the full level motion, the analytical and experimental results are also found to show good agreement with each other. The hysteresis loops in the X and Y axes of the experiment and analysis show higher energy dissipation capacity. In the analysis, the buckling of longitudinal reinforcement takes place in the 280 mm range from the bottom of the column. This corresponds to the experimental results. Actually, a buckling length between 300 mm and 400 mm at the bottom of the column was observed in the experiment. Consequently, it is found that the cyclic loops in the acceleration-displacement curves show a decrease in the energy dissipation capacity after the buckling of longitudinal reinforcement occurs in both experiment and analysis.

4. DAMAGE ANALYSIS OF RC VIADUCTS

4.1 Target Structures and Analysis Procedure

The seismic performance evaluation is performed for two RC rigid-framed viaducts. They are beam-slab type rigid-frame with three-span columns. The actual damage conditions of two viaducts after the earthquake are shown in Figure 7 (Committee 311 2000). It was observed that there was the slight damage with crossed diagonal cracks at the upper column in the Shimokema R5 Viaduct. On the

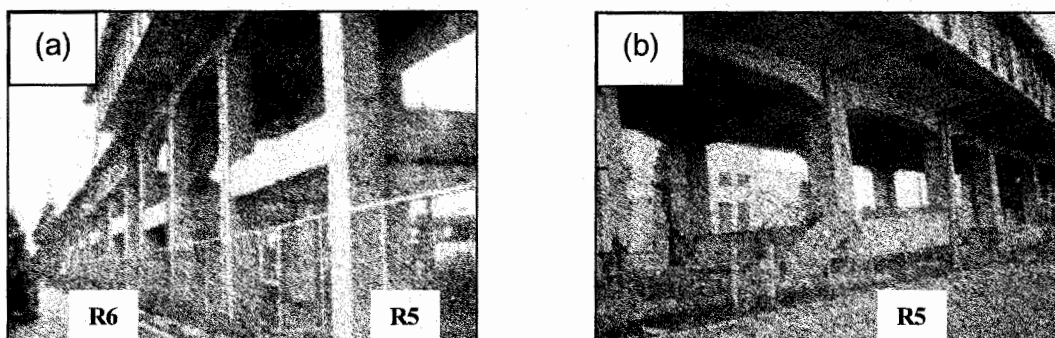


Figure 7 Damage Conditions in: (a) Shimokema R5 Viaduct and (b) Hansui R5 Viaduct

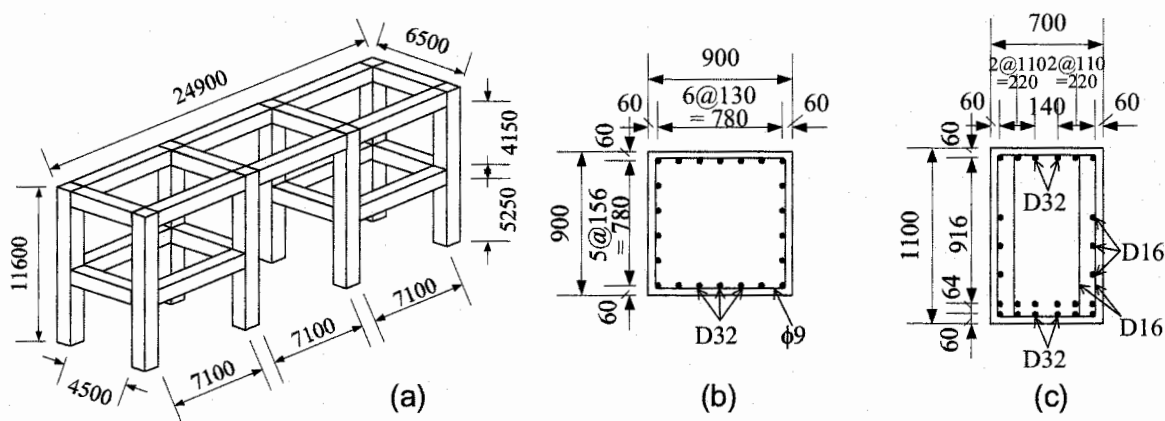


Figure 8 Shimokema R5 Viaduct: (a) 3D view, (b) Cross Section of the Column and (c) Cross Section of the Beam

other hand, in the Hansui R5 Viaduct, the severe shear failure with the collapse of columns and the drops of beams and slabs were observed. Figure 8 shows the dimension of the structure and arrangement of reinforcement in the Shimokema R5 Viaduct. The Hansui R5 Viaduct has similar dimension and arrangement of reinforcement as the Shimokema R5 Viaduct. The compressive strength of concrete of Shimokema R5 Viaduct was slightly stronger than that of Hansui R5 Viaduct. The material properties used in these two viaducts are summarized in Table 1.

The input ground motions determined by Frequency-Dependent Equi-Linearized technique, FDEL (Sugito et al. 1994) are used. The weight of a superstructure including the slab is assumed to be 7200 kN. The self-weight of viaduct is calculated by multiplying the volume of columns and beams by the specific gravities of concrete and reinforcement.

4.2 Seismic Response of RC Viaducts

Figure 9 shows the analytical results computed using the 3D dynamic lattice model for the Hansui R5 Viaduct. The analytical results of displacement time histories and particle traces of displacement at the mid-span of an upper beam in the transverse direction are also illustrated in the figure. With the Shimokema R5 Viaduct, the stable response during 10 seconds from the initial is predicted. In the analysis, the buckling of reinforcement takes place at the bottom of the lower column. It can be also observed that the buckling of reinforcement does not occur at both the top of the column and the each end of the beam. The cracks occur in the diaconal members of concrete at the upper and lower columns. This behavior corresponds to the actual observation after the earthquake as shown in Figure 7 (Committee 311 2000). On the other hand, the calculation is terminated due to the divergence in the case of the Hansui R5 Viaduct as shown in Figure 9. This is caused by the compressive softening of concrete in the diagonal and flexural members at the lower column. Actually, it was

Table 1 Material Properties of Concrete and Reinforcement

Name of viaducts	Concrete			Longitudinal reinforcement			Transverse reinforcement		
	f_c' (MPa)	f_t (MPa)	E_c (GPa)	f_y (MPa)	f_u (MPa)	E_s (GPa)	f_{wy} (MPa)	f_{wu} (MPa)	E_{ws} (GPa)
Shimokema R5	31.7	2.43	16.8	349	533	197	296	436	204
Hansui R5	29.1	1.27	18.4	322	521	203	263	380	183

Note: The properties of each material in the Shimokema R5 Viaduct was measured by the material of the structure sited near the target. With respect to the Hansui R5 Viaduct, the strength sampling from the target itself was measured.

observed in the Hansui R5 Viaduct that the severe shear failure at the lower columns took place that induced the drops of beams and slabs. It is also found that the direction, in which the beams and slabs dropped down after the lower column fails in shear, can be clearly estimated by the particle traces of displacement in Figure 9. As can be judged from the analytical results, the Hansui R5 Viaduct fails toward transverse direction during the displacement in longitudinal direction decreases. The information about the state of deformation after the structure fails in shear is beneficial in terms of the restoration after the earthquake.

4.3 Shear Failure Simulation of RC Viaducts

To verify the response of the Hansui R5 Viaduct where the calculation in the dynamic analysis is terminated by the divergence, the detailed analytical investigation is performed. With the Hansui R5 Viaduct, we focus on the elements of the lower column in the 3D lattice model. Figure 10 shows the stress-strain relationships of concrete flexural members and the strain time histories of concrete diagonal members. In the figure, the deformed shape of 3D lattice model for the Hansui R5 Viaduct is also illustrated. It can be observed that the analysis predicts the compressive softening behavior in diagonal and flexural members of concrete. The compressive softening behavior is observed in the elements A, B and C in the 3D lattice model, while the tensile strain of concrete increases in the element D. This is caused by that the externally applied energy due to the earthquake is locally consumed by the elements A, B and C. In addition, the element F at the surrounding portion releases the stored energy into the localizing elements. In this study, it is assumed that in the analysis the shear failure occurs at the column if the compressive softening behavior of concrete in the arch and diagonal members is predicted. Hence, the shear failure mode corresponds to the compressive softening of concrete in spite of the decrease in shear stresses transferred across diagonal cracks by the aggregate interlock. In this stage, since the widely opened diagonal crack occurs, the compressive strength of concrete decreases with the increase in the tensile strain perpendicular to the compressive direction. As a result of the consideration of this compressive softening, the analytical response in the post-peak becomes milder than that in the actual brittle behavior.

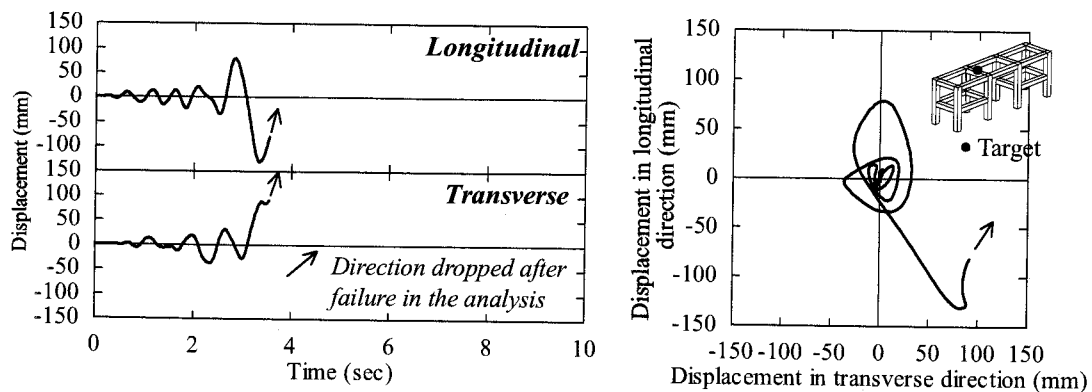


Figure 9 Response of Target Point at the Upper Beam in the Hansui R5 Viaduct

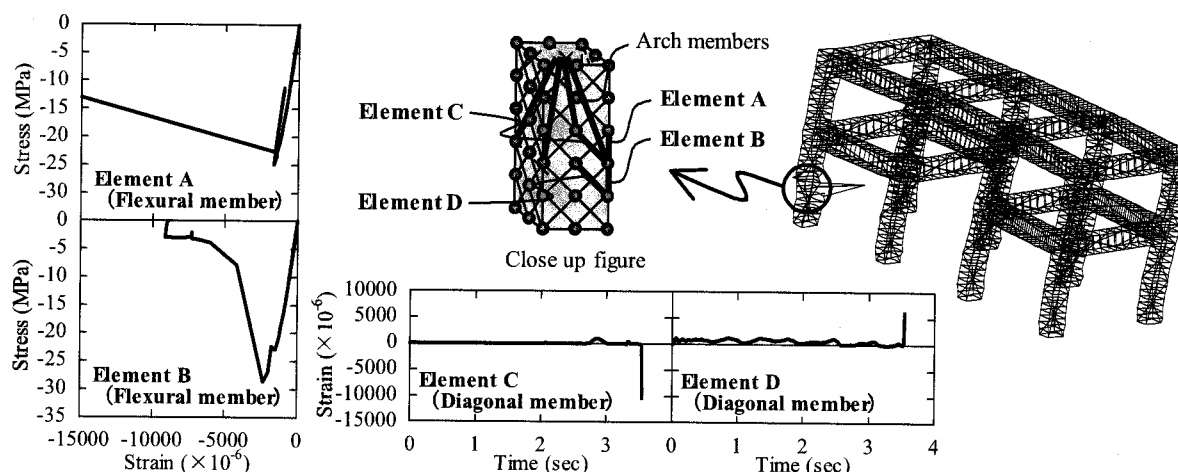


Figure 10 Computed Stress and Strain of Concrete Elements for Hansui R5 Viaduct

5. CONCLUSIONS

The nonlinear analyses of RC structures were performed using the 3D dynamic lattice model. The results of analysis for the RC columns prove that reasonable seismic behavior of the columns subjected to bilateral ground motion can be estimated. The calculated results show that the analysis considering the buckling behavior of longitudinal reinforcement can predict the post-peak response as well as the energy dissipation accurately. The comparisons between the prediction and the observations of actual damages of RC viaducts reveal the reliability of the 3D lattice model. It is also found that the analysis can predict damage conditions including both the buckling of longitudinal reinforcement in RC columns and the shear failure mode. Consequently, the verification in this study reveals the reliability of the 3D dynamic lattice model on the seismic response of RC structures within the scope from structural member level to whole structural system level.

References:

- Dhakal, R.P. (2000), "Enhanced Fiber Model in Highly Inelastic Range and Seismic Performance Assessment of Reinforced Concrete," Thesis (PhD), The University of Tokyo.
- Fukuura, N. and Maekawa, K. (1997), "Computational Model of Reinforcing Bar under Reversed Cyclic Loading for RC Nonlinear Analysis," *Journal of Materials, Concrete Structures and Pavements*, Japan Society of Civil Engineers, **564**(35), 291-295. (In Japanese)
- Mander, J.B., Priestley, M.J.N. and Park, R. (1988), "Theoretical Stress-strain Model for Confined Concrete," *Journal of Structural Engineering*, American Society of Civil Engineers, **114**(8), 1804-1826.
- Miki, T. and Niwa, J. (2004), "Nonlinear Analysis of RC Structural Members Using 3D Lattice Model," *Journal of Advanced Concrete Technology*, Japan Concrete Institute, **2**(3), 343-358.
- Niwa, J., Choi, I. C. and Tanabe, T. (1995), "Analytical Study for Shear Resisting Mechanism Using Lattice Model," *Concrete Library of JSCE*, Japan Society of Civil Engineers, **26**, 95-109.
- Okamura, H. and Maekawa, K. (1991), "Nonlinear Analysis and Constitutive Models of Reinforced Concrete," Gihodo-Shuppan.
- Rokugo, K., Iwasa, M., Suzuki, T. and Koyanagi, W. (1989), "Testing Method to Determine Tensile Strain Softening Curve and Fracture Energy of Concrete," *Fracture Toughness and Fracture Energy*, Balkema, 153-163.
- Sugito, M., Goda, H. and Masuda, T. (1994), "Frequency Dependent Equi-linearized Technique for Seismic Response Analysis of Multi-layered Ground," *Journal of Geotechnical Engineering*, Japan Society of Civil Engineers, **493**(27), 49-58. (In Japanese)
- Nishida, H. and Unjoh S. (2004), "Dynamic Response Characteristic of Reinforced Concrete Column Subjected to Bilateral Earthquake Grand Motions," *Proceeding of 13th World Conference on Earthquake Engineers*, 576.
- Vecchio, F.J. and Collins, M.P., (1986), "The Modified Compression Field Theory for Reinforced Concrete Elements Subjected to Shear," *ACI Journal*, **83**(2), 219-231.

COLLABORATIVE STRUCTURAL ANALYSIS SYSTEM BY LINKING SOPHISTICATED PROGRAMS THROUGH INTERNET

M. Tada¹⁾

*1) Associate Professor, Department of Architectural Engineering, Division of Global Architecture,
Graduate School of Engineering, Osaka University, Japan
tada@arch.eng.osaka-u.ac.jp*

Abstract: A collaborative structural analysis (CSA) system is proposed which utilizes beneficial features of existing individual structural analysis. In the CSA system, the equilibrium equation of the overall structural system is constructed in the host program running on a host computer, while critical parts of the structure are analyzed in station programs running on station computers. As the overall analysis progresses step by step, the necessary information, such as the displacements, restoring forces, and stiffness matrices, are exchanged between the different programs via the internet. This paper describes the framework and characteristics of the CSA system, and shows some analysis examples.

1. INTRODUCTION

Individual researchers have developed structural analysis programs and finite element analysis programs capable of simulating complex structural behavior, e.g., local buckling in steel members, composite action between concrete slabs and steel beams, and stress concentration at critical structural components. While the capacity of these detailed analysis programs is mostly limited to structural components, these existing programs can be utilized in a collaborative fashion to conduct highly sophisticated analyses of complex structural systems. Considering the independence of the individual programs and the fast data communication capability of the internet environment, a practical approach for combining multiple programs is to distribute the required tasks among multiple computers while exchanging the necessary data between the computers via the internet. A novel example of such a system is the collaborative structural analysis (CSA) system proposed by Tada et al. (2004a, and 2004b). The proposed CSA system constructs the equilibrium equation of the overall structural system in a “host” program running on the host computer, while critical parts of the analyzed structure (hereafter referred to as “substructures”) are analyzed with enhanced detail and accuracy in “station” programs running on station computers. As the overall analysis progresses, the necessary information such as the displacement vectors, restoring force vectors, and stiffness matrices are exchanged via the internet at each step. Unlike parallel computing, whose primary purpose is to increase the speed and capacity of the analysis, the CSA system aims to enable highly sophisticated structural analyses by combining beneficial features of multiple existing programs. This paper describes the framework and characteristics of the CSA system, and shows some analysis examples.

2. FRAMEWORK OF CSA SYSTEM

In the proposed CSA system, the global equilibrium equation for the overall structural system is constructed in the host program running on the host computer, while substructures are analyzed by station programs running on station computers as shown in Figure 1. The results obtained from the substructure analyses are fed back to the overall analysis via the internet. In the host program, the substructures are represented by dummy elements composed of a small number of DOFs associated with the boundaries of the element. In the station programs, the substructures are analyzed with enhanced detail and accuracy. During the course of the analyses, only the data associated with the boundaries of the substructures are exchanged between the host and station programs, thus the amount of data to be exchanged via the internet is minimized. The schematic procedure is summarized as follows:

- (1) Each station program constructs an initial stiffness matrix for the assigned substructure. The matrices are further reduced to condensed stiffness matrices associated with the DOFs at the boundaries. These condensed matrices are sent to the host program via the internet.
- (2) The host program transforms the local stiffness matrices from their respective local coordinate system to the global coordinate system, and then constructs the global stiffness matrix for the overall structural system.
- (3) The host program solves the global equilibrium equation to determine the global incremental displacements and the global restoring forces.
- (4) The host program transforms the global incremental displacement at the substructure boundaries from the global coordinate system to local coordinate systems, and then sends the displacement vectors to respective station programs.
- (5) Each station program analyzes the assigned substructure according to the incremental displacements. The updated stiffness matrices and the restoring force vectors at the boundaries are sent back to the host program.

The overall analysis is continued by repeating procedures (2) to (5) for each step.

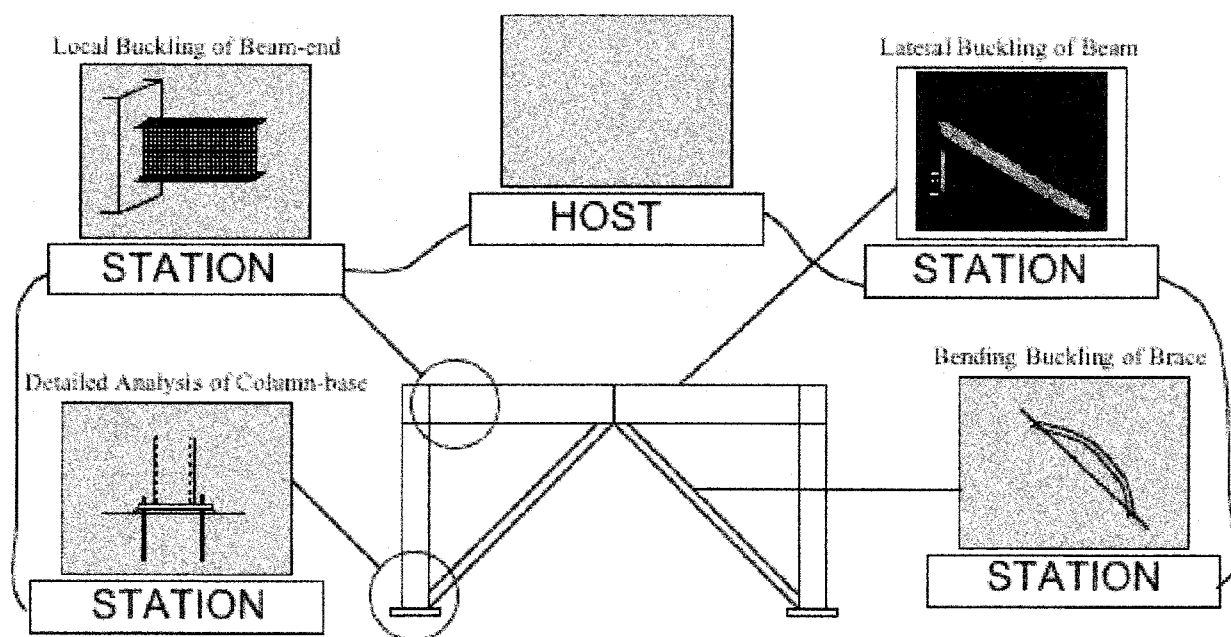


Figure 1 Collaborative Structural Analysis System which Utilizes Individual Analysis Program

The restoring forces at the boundaries transmitted from the station programs to the host program are used to calculate the imbalanced forces. The imbalanced forces are, in turn, treated as pseudo external forces in the immediately following step.

3. CHARACTERISTICS OF CSA SYSTEM

The proposed CSA system has the following characteristics:

- (1) The system enables collaboration among researchers by linking their programs through the internet. Participants to each project can be easily assembled according to the nature of the project.
- (2) Since the program developers need not share the source code or libraries to participate in a CSA project, copyrights owned by the program developers are securely protected.
- (3) It is easy to join a CSA project, since only minor modifications associated with input and output routines are needed.
- (4) Data exchange via the internet is easily accomplished because the CSA system uses the file and folder sharing protocol implemented in the operating system and a few FORTRAN77 commands.
- (5) Since a program operator cannot see analysis conducted in other stations, collaboration between all participating operators is essential in interpreting analysis results. On the other hand, if such collaboration is done, the programs are not used as black boxes.
- (6) It is preferable that the developers of each participating program join the CSA project to correctly modify the I/O routines and to study the analysis results. As stated above, interpretation of the analysis results rely on collaboration between participants.

4. ANALYSIS EXAMPLES

Analysis examples using the CSA system are shown.

4.1 Frame Analysis Combining Brace Buckling Analysis and Composite Beam Analysis (Tada and Kuwahara 2004a and 2004b)

Host program: NETLYS, Brace analysis program: NETLYS, Composite beam analysis program: COMPO.

Overview:

- (1) Programs that can analyze deteriorating behavior of brace buckling and concrete crushing were utilized.
- (2) Data associated with the DOFs at geometrical boundary of substructures and DOFs inside of substructures were transmitted. Thus, the deteriorating behavior could be analyzed by controlling an appropriate internal DOF.
- (3) In order to confirm the robustness of data transmission, the analysis tasks were distributed among 13 PCs in 10 organizations all over Japan. The pushover analysis with total 613 steps and 120 minutes were stably performed.

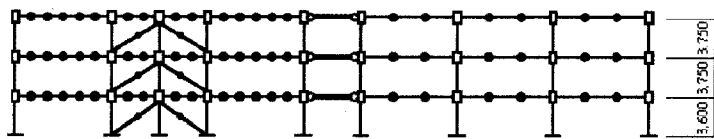


Figure 2 Analysis Object



Figure 3 Distribution of PCs

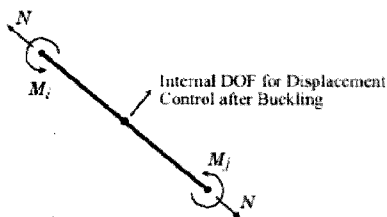


Figure 4 DOFs of Boundary

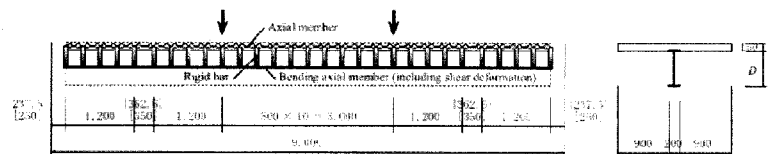
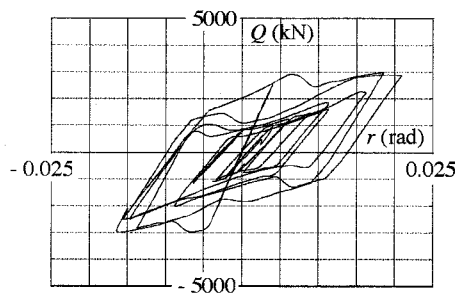
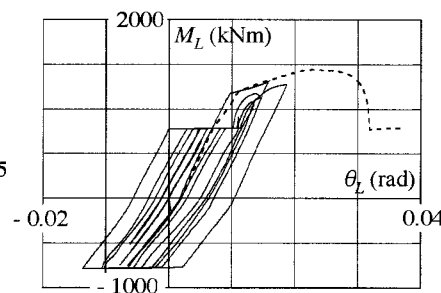


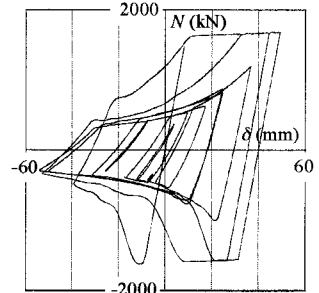
Figure 5 Structural Model for Composite Beam



(a) Story Shear - Drift Angle Relation



(b) Bending Moment - Rotation Relation of Composite Beam



(c) Axial Force - Elongation Relation of Brace

Figure 6 Results of Seismic Time History Analysis

4.2 Frame Analysis Combining Local Buckling Analysis and Composite Beam Analysis (Tada and Ohgami 2004)

Host program: NETLYS, Composite beam analysis program: COMPO, Local buckling analysis program: NASP (developed by Katsuki Ohgami of Nittetsu Plant Designing Corp.).

Overview:

- (1) The first challenge of combining programs developed by others.
- (2) The bottom segment of the first story columns were analyzed by NASP by which local buckling behavior could be considered, and all beams were analyzed by COMPO by which interaction between concrete slab and steel beam could be considered.
- (3) The program NASP is capable of conducting static analyses of thin-walled structures. In modeling a structure, the program uses a rectangular plane shell element with 8 nodes, and applies cubic functions for both in-plane and out-of-plane displacements. Each element has 40 DOFs; three displacements, four rotations, and one twist at corner nodes; and one boundary-parallel displacement and one in-plane rotation at mid-side nodes. Four rotations at corner nodes and in-plane rotation at mid-side nodes are the keys to establishing perfect compatibility between adjacent elements.

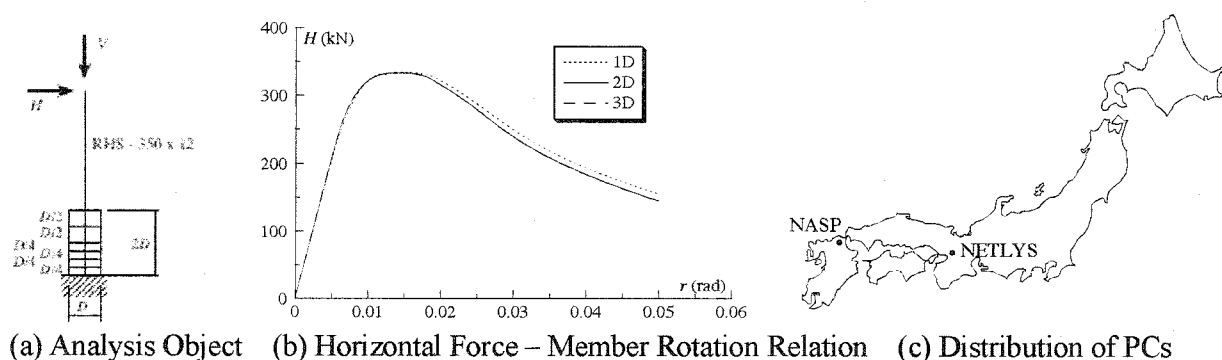


Figure 7 Preliminary Analysis of Cantilever Column Subjected to Constant Vertical Force and Incremental Horizontal Force

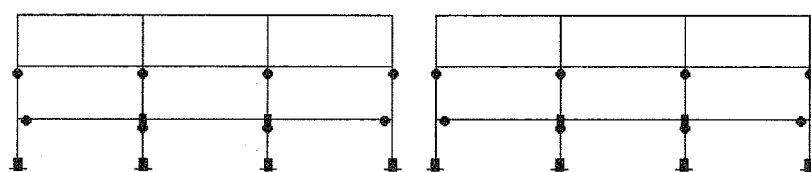


Figure 8 Plastic Hinges by Pushover Analysis

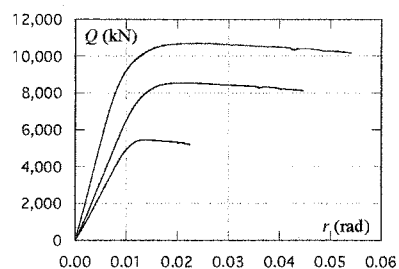


Figure 9 Story Shear - Drift Angle Relation

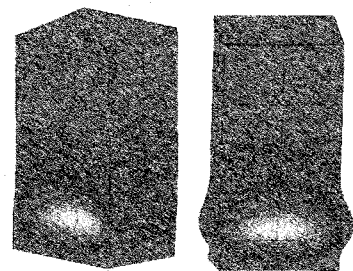


Figure 10 Local Buckling

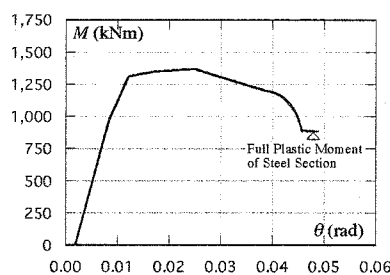


Figure 11 Bending Moment - Rotation Relation of Composite Beam

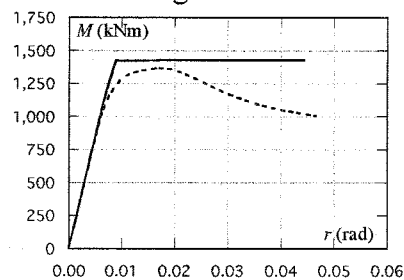


Figure 12 Bending Moment - Rotation Relation of Column Bottom

4.3 Frame Analysis Combining Exposed Column-Base Analysis Program and Composite Beam Analysis Program (Tada and Tamai 2005)

Host program: NETLYS, Composite beam analysis program: COMPO, Exposed column-base analysis program: NETBASE (developed by Hiroyuki Tamai of Hiroshima Institute of Technology).

Overview:

- (1) The program NETBASE can consider the change of rotational stiffness depending on axial force, and can express rotational slip hysteresis caused by plastic elongation of anchor bolts.
- (2) Pinching hysteresis in story shear versus drift angle relation and flag-type hysteresis in bending moment versus rotation relation at column-base were obtained.

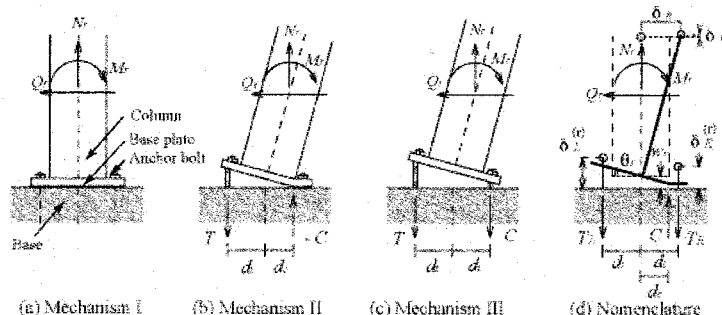


Figure 13 Mechanical Model of Exposed Column-Base

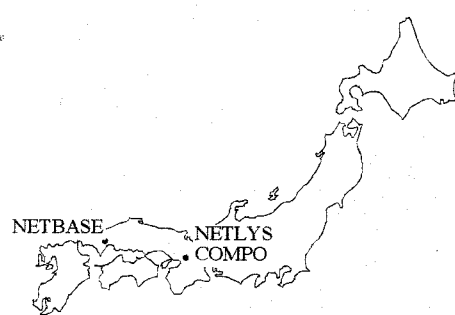


Figure 14 Distribution of PCs

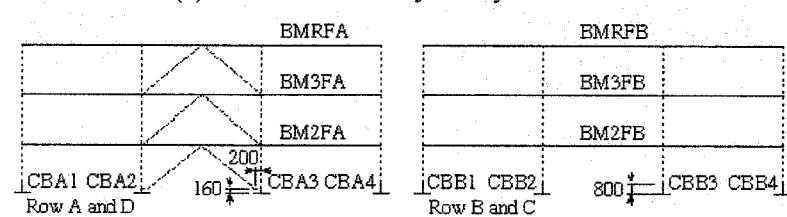
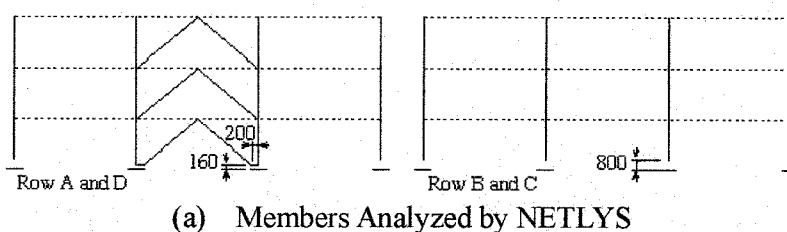


Figure 15 Braced Frame with Buckling Restrained Braces for Analysis

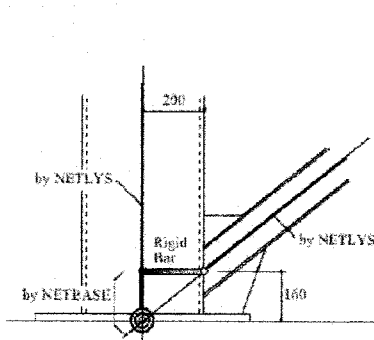


Figure 16 Brace Connecting Base

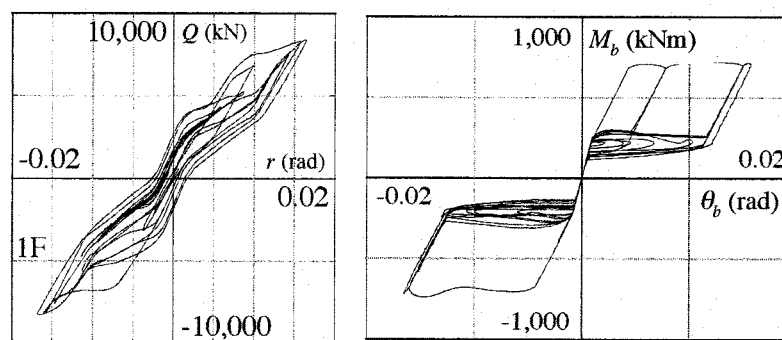


Figure 17 Results of Seismic Time History Analysis

4.4 Frame Analysis Combining Commercial FEM Program

Host program: NETLYS, Local buckling analysis program: ABAQUS.

Overview:

- (1) Operator splitting method was implemented to solve the equation of motion in the host program.
- (2) Owing to the implementation of OS method, stiffness matrices of substructures do not need to transmit. Only the restoring forces are necessary to transmit to host from station.
- (3) Commercial FEM program (ABAQUS) was combined to the hand made program (NETLYS).
- (4) Pseudo pushover analysis and seismic time history analysis were conducted for three story braced moment resistant frame.

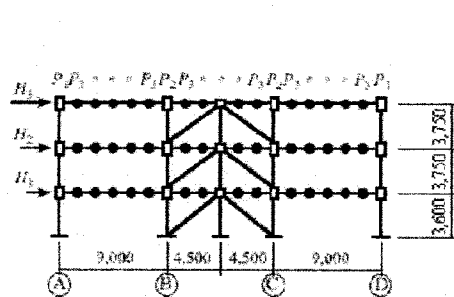


Figure 18 Analysis Object

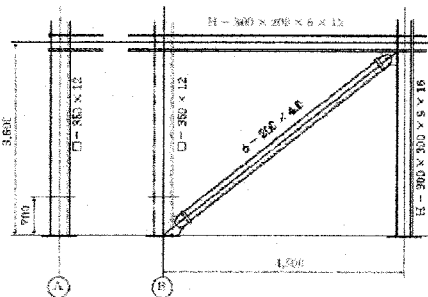


Figure 19 Detail of Tube-Brace

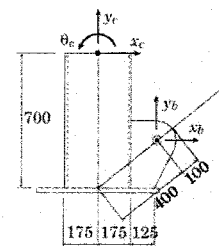


Figure 20 Substructure Analyzed by ABAQUS

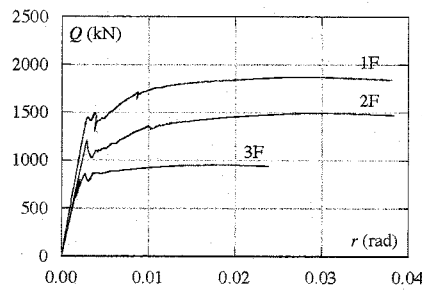


Figure 20 Story Shear - Drift Angle Relation by Pseudo Pushover Analysis

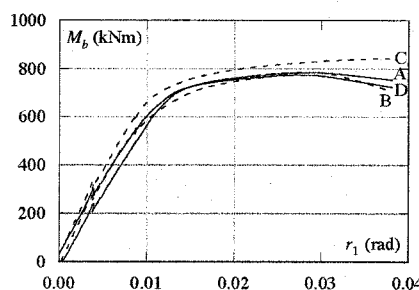


Figure 21 Moment - Rotation Relation of Column Bottom by Pseudo Pushover Analysis

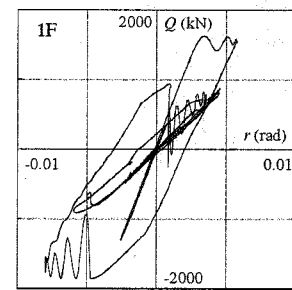
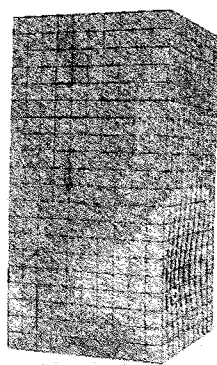
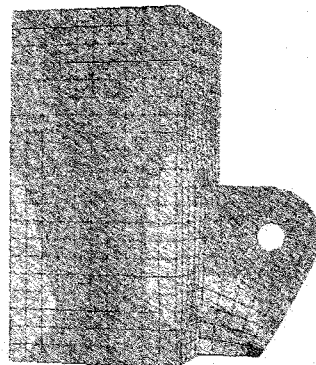


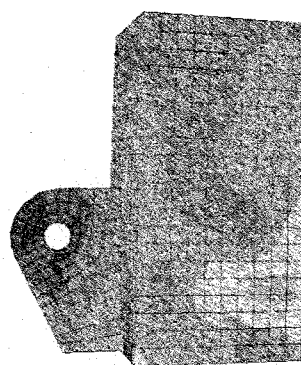
Figure 22 Story Shear - Drift Angle Relation by Seismic Time History Analysis



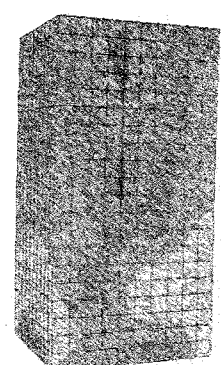
Column A



Column B



Column C



Column D

Figure 23 Out-of-plane Deformation at Column Bottom at the End of Pseudo Pushover Analysis

5. CONCLUSIONS

A collaborative structural analysis (CSA) system was proposed which utilizes beneficial features of existing individual structural analysis programs to perform highly sophisticated structural analyses. Examples of frame analyses (e.g., pushover analysis and seismic time history analysis) using the CSA system were described. In these examples, overall behavior of steel structures was analyzed, while bending buckling of braces, local buckling of column-bottom, composite action of beams, and flag-type behavior of exposed column-bases were analyzed with enhanced detail and accuracy in independent analysis programs. Thus, the proposed CSA system can be an effective tool for the collaboration of researchers in structural analyses.

Acknowledgements:

Financial support by the Ministry of Education, Culture, Sports, Sciences and Technology of Japan under Grant No. 16560498, and those by National Research Institute for Earth Science and Disaster Prevention for the NEES/E-Defense collaborative research, are gratefully acknowledged.

References:

- Tada, M. and Kuwahara, S. (2004a), "Basic Study on the System of Structural Analysis by Unifying Various Programs Through Internet", *Journal of Structural and Construction Engineering*, No.580, 113-120. (in Japanese).
- Tada, M. and Kuwahara, S. (2004b), "Fundamental Study on Unified Tool for Structural Analysis Using Network", *13th World Conference on Earthquake Engineering*, Paper No. 650, Vancouver.
- Tada, M. and Ohgami, K. (2004), "Internet-Based Numerical Analysis of Steel Building Frame in Collaboration of Frame Analysis and Local Buckling Analysis", *The 6th Korea-Taiwan-Japan Joint Seminar on Earthquake Engineering for Building Structures*, 201-206, Taipei.
- Tada, M. and Tamai, H. (2005), "An Overall Structural Analysis of Steel Frame Collaborating Composite Beam Analysis Program and Exposed Column Base Analysis Program", *The 7th Japan-Taiwan-Korea Joint Seminar on Earthquake Engineering for Building Structures*, 189-194, Seoul.

SEISMIC BEHAVIOR OF CONCRETE ENCASED STEEL COLUMNS SUBJECTED TO AXIAL LOAD AND BI-AXIAL BENDING

H.-L. Hsu¹⁾ and F.-J. Jan²⁾

1) Professor, Dept. of Civil Engineering, National Central University, Taiwan

2) M.S. Dept. of Civil Engineering, National Central University, Taiwan

t3200178@ncu.edu.tw

Abstract: This study is focused on the experimental evaluation on seismic performance of concrete encased steel columns. Relationships between members' seismic performance and structural parameters, such as the strength ratios of the sections' comprising components, and the magnitudes of bi-axial bending, were defined. It was found from the test results that member performance was governed by the strength of the comprising reinforced concrete when they were loaded in the sections' weak directions. Test results suggest that the strength ratio between the sections' strong and weak directions be adequately adjusted so that high member performance could be achieved. It is proposed in this study that the ratio be set to approximately 2.2 to optimize the member's seismic performance.

1. INTRODUCTION

Composite members comprising of wide-flange steels and reinforced concrete, defined as concrete encased steel columns hereafter, possess high load-carrying capacities and significant ductility, thus are effective forms for structures designed for earthquake-resistant purposes. For building frames subjected to earthquakes, particularly those acting at the non-principal axes of the structures, general loads, such as combined axial load and bending about the members' strong and weak axes, will be induced. Current studies on the seismic performance of such designs are mostly focused on the member behavior under axial load, flexural load or their combinations. Information on the member behavior under combined axial load and cyclic bi-axial bending is still limited (Lachance, 1982; Hsu, 1988; Munoz and Hsu, 1997; Kim and Lee, 2000; Qiu et. Al., 2002). In order to validate the effectiveness of such design, the member performance, such as the strength and ductility, under earthquake-induced combined axial load and bi-axial bending must be adequately defined.

In general, member performance under earthquake may be affected by the magnitudes of bi-axial bending as well as the strength ratios of the sections' comprising components. For example, effective structural designs of the sectional compositions usually suggest that bending about the section's strong axis with high sectional rigidity be adopted when single directional flexural load is considered. This situation may require amendments when bi-axial bending is imposed in the member, because composite section with extremely different flexural strength in the section's strong and weak axes will incur premature damage in the section's weak axis, and subsequently hamper the strength development and energy dissipation in the section's strong direction. Furthermore, the effect of bi-axial bending to the reduction of member performance will be amplified when the magnitude of the bi-axial bending is increased. In order to guarantee the design effectiveness, the relationship between member performance and the above-mentioned parameters must also be

calibrated.

This study is focused on the experimental evaluation on seismic performance of concrete encased steel columns. A series test of composite members subjected to various load combinations of axial load and bi-axial bending were conducted. Test results were used to define the relationships between member performance and the sectional compositions, and to establish guidelines for design applications.

2. EXPERIMENTAL PROGRAM

2.1 Specimens

Twenty-four composite specimens were fabricated for testing. Dimensions for all composite sections were 370mm x 370mm. In order to investigate the effect of component strength ratio on the seismic performance of composite members, six structural steel sections were used. They were JIS SS41 H100x100x6x8, H150x100x6x9, H150x150x7x10, H200x100x5.5x8, H200x150x6x9, and H200x200x8x12. The corresponding composite members using the above-mentioned steel sections were labeled series A, B, C, D, E, and F, respectively. Identical reinforcements were used in all specimens which comprising of four #6 deformed bars in the longitudinal direction and #3 deformed bars transversely. These compositions yielded various component strength ratios for the test specimens. Stirrup spacing was 100 mm within the confined zones and 150 mm in the non-confined zones. Yield strengths for the structural steel and longitudinal bars were 314 MPa and 543 MPa, respectively. Compressive strength of the concrete, determined from cylinder test, was 38 MPa.

In order to distinguish the member behavior under various load combinations so that adequate design references could be established, both monotonic and combined cyclic loadings were considered. The loading types were denoted M (Monotonic) and C (Cyclic), respectively. Besides the comprising structural steel, specimens were also categorized by the directions which loading was applied. For example, an X or Y was added to the specimen label when the member was laterally bent about the structural steel's (also the composite section's) strong or weak axis. Magnitudes of weak axis bending were also noted in the specimen labeling. They were denoted by the ratios between the applied bending and the nominal bending strength in the weak axis. For example, a specimen labeled with "25" indicated that a bending moment equaling 25% of the section's weak axis bending strength was applied to the member when the bi-axial bending was considered. In summary, an XAC25 indicated that the specimen was composed of H100x100x6x8 steel (A), subjected to cyclic (C) lateral load in the section's strong axis (X), and a 25% constant bending moment about the section's weak axis. Specimen labels and the corresponding load combinations were listed in Table 1.

2.2 Test Setup

Specimens were tested according to the desired load combinations. They included monotonic weak axis bending, combined axial load and cyclic strong axis bending, and combined axial load with various magnitudes of bi-axial bending. The purposes of the weak axis bending tests were to investigate the concrete damage pattern within the web regions of the structural steels and to quantify the weak-axis bending strength of the member, so that magnitudes of bi-axial bending could be determined. The combined axial load and bi-axial bending tests were used to evaluate the achievable member performance under earthquake. A constant axial load equaling 13% of each member's compressive strength was applied in the combined loading test.

Table 1 Label and Loading Combinations of Test Specimens

Specimen	Loading direction	Loading type	Magnitude of weak-axis bending (Myy/Moy)	$\frac{(Ms / Msrc)x}{(Ms / Msrc)y}$
YAM	Weak-axis bending	monotonic	--	2.20
YBM				2.82
YDM				3.65
YCM				1.74
YEM				2.04
YFM				1.50
XAC00	Strong-axis bending	cyclic	0.00	2.20
XBC00				2.82
XDC00				3.65
XCC00				1.74
XEC00				2.04
XFC00				1.50
XAC25	Bi-axial bending	cyclic	0.25	2.20
XBC25				2.82
XDC25				3.65
XCC25				1.74
XEC25				2.04
XFC25				1.50
XAC50	Bi-axial bending	cyclic	0.50	2.20
XBC50				2.82
XDC50				3.65
XCC50				1.74
XEC50				2.04
XFC50				1.50
Note: Ms: flexural strength of steel; Msrc: flexural strength of composite section; X: strong axis of section; Y: weak axis of section; Moy: weak axis flexural strength of composite section; Myy : magnitude of applied weak axis bending in bi-axial loading test				

Each specimen was rigidly fasten to a pair of stiffened platform at member bottom, and attached to a stiffened loading beam on the top, so that combined loads could be applied. The lateral load was generated by a servo-controlled hydraulic actuator with prescribed displacement history. The combined axial load and weak-axis bending was generated by an eccentrically placed hydraulic jack pushing against a stiffened reaction beam. The test setup is shown in Figure 1.

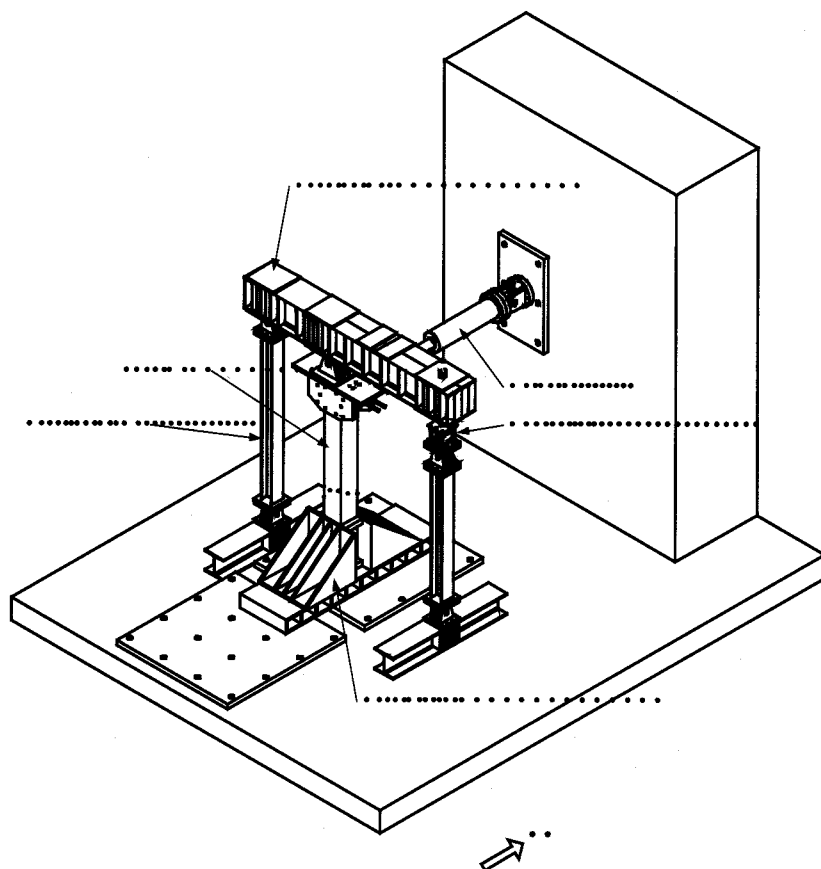


Figure 1 Test Set-up

3. FAILURE PATTERNS

3.1 Weak-axis Bending Tests

The load-displacement relationships for the members subjected to weak axis bending are shown in Figure 2. It was observed in the tests that similar yielding drifts for the specimens under weak-axis bending were achieved, approximately between 1% to 1.5%, and the drift at which ultimate strength was achieved was approximately 3%. Although these specimens exhibited similar yielding and ultimate drifts, their strength deterioration in the post-ultimate-strength stage was different. This phenomenon can be attributed to the ratios between the strengths of steel, M_s , and the composite section, M_{src} , in the loading direction, i.e. $(M_s/M_{src})_y$. Because when high steel flexural strength was used in the weak-axis of composite section, the higher member strength would induce heavier stress on the section, particular the concrete, as shown in Figure 3. This incurred higher crack potential in the core concrete, and subsequently larger strength deterioration when the concrete was damaged. It was found from the tests that the strength deterioration rates increased when the steel strength ratios in the weak axis were increased.

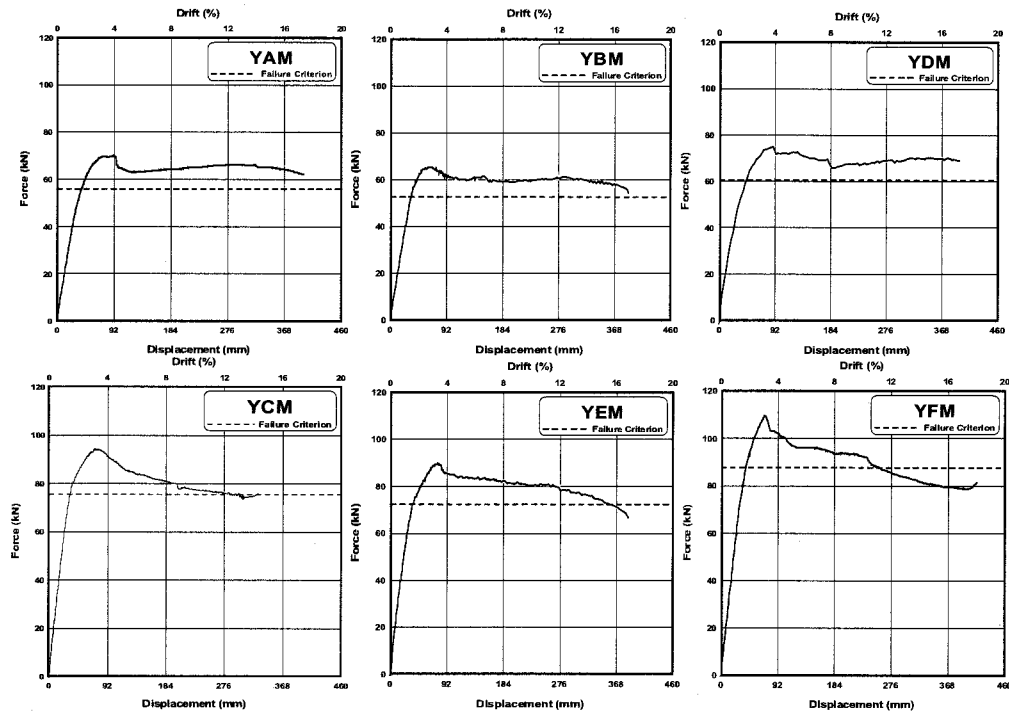


Figure 2 Load-displacement Relationships for Members Subjected to Weak-axis Bending

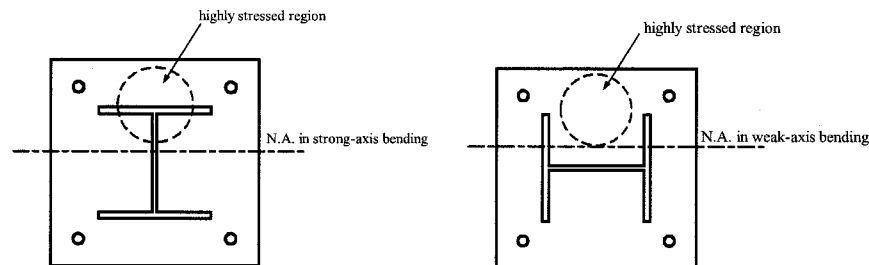


Figure 3 Different Failure Patterns Due to Various Loading Directions

3.2 Members Subjected to Combined Loading

For specimens subjected to combined axial load and cyclic lateral force in the strong axis, the member's ultimate strength was reached at drift ratio equaling 3%, and the longitudinal bar buckling was occurred at approximately 6% drift. In these cases, the member performance was governed by the formation of plastic hinge, and the failure pattern of the members shifted from concrete crushing to flexural damage when the section's steel strength ratio increased. Member performance was found to be increased when the sectional steel strength ratio increased. These results conformed with the concepts in beam-column designs, i.e. higher flexural strength in the direction of loading.

4. COMPARISONS AND INTERPRETATIONS OF TEST RESULTS

4.1 Interaction Equation

Composite member performance under combined axial load and bi-axial bending can be

affected by the loading types, i.e. monotonic or cyclic, as well as the magnitudes of combined loads. These parameters yield a highly nonlinear relationship among the applied loads. In general, they can be correlated by the following expression, as shown in Figure 4:

$$\left(\frac{P_n - P_{nb}}{P_0 - P_{nb}} \right) + \left(\frac{M_{nx}}{M_{nbx}} \right)^\alpha + \left(\frac{M_{ny}}{M_{nby}} \right)^\beta = 1 \quad (1)$$

In which, P_0 is the member's ultimate compressive strength; P_{nb} , M_{nbx} , M_{nby} are the nominal compressive strength, bending strengths about strong axis, and bending strength about weak axis, when uni-axial beam-column load was imposed. Similarly, P_n , M_{nx} , and M_{ny} are the achievable compressive, strong-axis bending, and weak-axis bending strengths when combined bi-axial loading was applied. In this equation, the values of α and β vary with the sectional compositions and the types of loading, thus can only be determined by the test results. Figure 5 shows the results obtained from the combined axial load and bi-axial bending tests. It can be found from the figure that the information can be adequately described by Equation (1) with α and β equaling 2.3. These values can be used for engineering practices, and can be further refined when more test information becomes available.

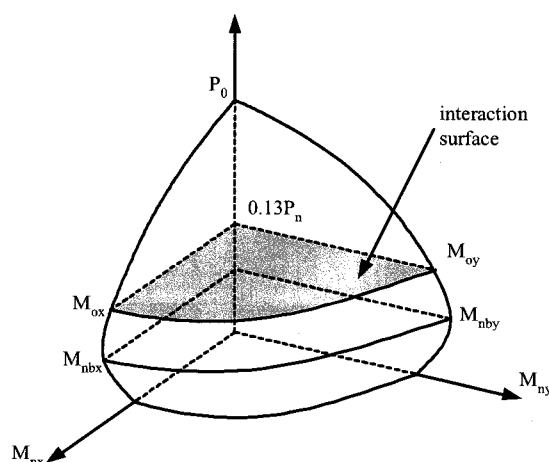


Figure 4 Interaction Between Axial Load and Bi-axial Bending

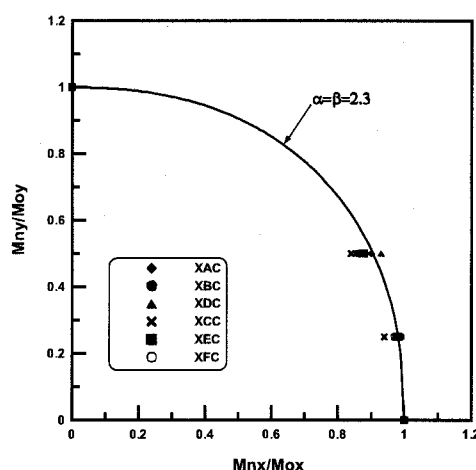


Figure 5 Interaction Coefficients for Members Subjected to Combined Loadings

4.2 Energy Dissipation

Figure 6 shows the typical hysteretic relationships for members subjected to various loading combinations. In order to evaluate the member performance under earthquake, the energy

dissipation of members tested under various load combination was further compared. Energy dissipation was evaluated by the cumulative area bounded by the hysteresis curves until member reached the failure stage. The failure criterion for the members in the combined axial load and bi-axial bending tests was defined by the state that member strength in the strong axis dropped to 80% of that of the corresponding member without weak axis bending. This criterion was set to investigate the effect of bi-axial bending in reducing the seismic performance of members. Figure 7 shows the normalized energy dissipation for the test specimens. It can be found from the figure that the members with extreme steel strength ratios between the composite section's strong and weak axes did not exhibit highest energy dissipating capability. Instead, a member with well-balanced steel strength ratio developed higher performance. This phenomenon can be interpreted by the stress level and the integrity of the section. For example, when a member with extremely high sectional steel strength ratio was loaded in the section's strong axis, excessive stress would occur in the section's core concrete, although the member possessed high resistance in that direction. This stress was amplified when further stress due to weak-axis bending was combined. Such phenomenon would incur premature failure in the core concrete and led to the low energy dissipating performance. On the other hand, for members with extremely low sectional steel strength ratio, the lateral load resistance was low, which resulted in poor hysteretic behavior. In either case, the member failed to develop significant seismic performance when the combined bi-axial load was presented. Therefore, it is suggested in this study that the sectional steel strength ratio be set to approximately 2.2 so that member performance could be optimized.

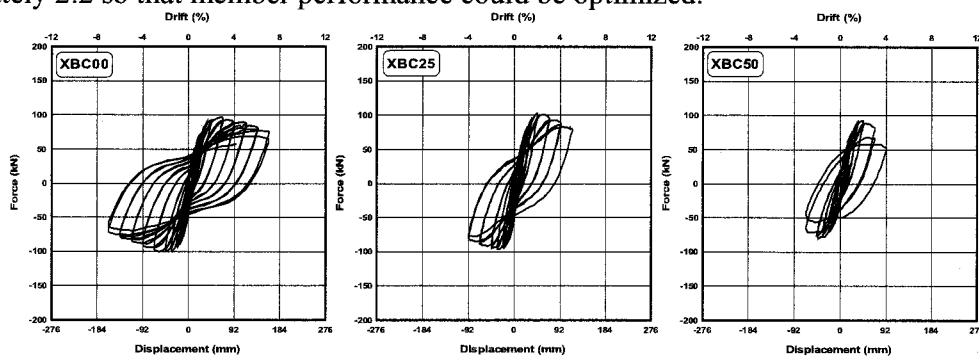


Figure 6 Typical Hysteretic Relationships for Members Subjected to Various Loading Combinations

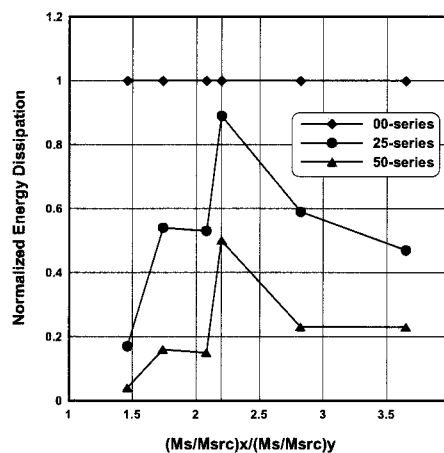


Figure 7 Normalized Energy Dissipation

5. CONCLUSIONS

This paper presents the test information of concrete encased steel columns subjected to various

combinations of axial load and bi-axial bending. Relationships between members' seismic performance and structural parameters, such as the strength ratios of the sections' comprising components, and the magnitudes of bi-axial bending, were defined. It was found from the test results that member performance was governed by the strength of the comprising reinforced concrete when they were loaded in the sections' weak direction. Test results suggest that the strength ratio between the sections' strong and weak directions be adequately adjusted so that high member performance could be achieved. It is proposed in this study that the ratio be set to approximately 2.2 to optimize the member's seismic performance.

Acknowledgements:

This study was partially supported by the National Science Council of the Republic of China under Grant No. NSC 92-2211-E-008-041, which is gratefully acknowledged.

References:

- Lachance, L. (1982), " Ultimate Strength of Biaxially Loaded Composite Sections," *Journal of the Structural Division- ASCE* , **108**(10), 2313-2329.
- Hsu, C.T.T. (1988), " Analysis and Design of Square and Rectangular Columns by Equation of Surface," *ACI Structural Journal*, **85**(2), 167-179.
- Munoz, P.R. and Hsu, C.T.T. (1997), "Biaxially Loaded Concrete-Encased Composite Columns : Design Equation," *Journal of Structural Engineering-ASCE*, **123**(12), 1576-1585.
- Kim, J.K. and Lee, S.S. (2000), "The Behavior of Reinforced Concrete Columns Subjected to Axial Force and Biaxial Bending," *Engineering Structures*, **22**(11), 1518-1528.
- Qiu, F., Li, W.F. , Pan, P., and Qian, J. (2002), "Experimental Tests on Reinforced Concrete Columns Under Biaxial Quasi-static Loading," *Engineering Structures*, **24**(4), 419-428.

CONTINUOUS COLUMN EFFECTS ON SEISMIC RESPONSE OF STEEL MOMENT FRAMES – IN PERSPECTIVE OF INSTANTANEOUS STABILITY

H. Tagawa¹⁾, G. MacRae²⁾, and L. Lowes³⁾

1) 21st Century COE Researcher, Tokyo Institute of Technology, Japan

2) Associate Professor, Dept. of Civil Engineering, University of Canterbury, Christchurch, New Zealand

3) Assistant Professor, Department of Civil Engineering, University of Washington, USA

htagawa@serc.titech.ac.jp, gregory.macrae@canterbury.ac.nz, lowes@u.washington.edu

Abstract: This paper introduces stability coefficients which represent the individual and combined effects of geometric ($P-\Delta$) and material nonlinearity on structural stability and, using the results of nonlinear dynamic time-history analysis, illustrates their individual and combined relationship to maximum interstory drifts and drift concentrations of three-, nine-, and twenty-story steel moment-resisting frames. It is found that the instantaneous material stiffness term decreases due to material inelasticity while the instantaneous geometric ($P-\Delta$) term generally increases due to drift concentrations during the earthquake. Also, as the continuous column stiffness increases, the $P-\Delta$ stability term decreases and the drift distributions become more uniform over structural height.

1. INTRODUCTION

When steel multi-story moment-resisting frames exhibit material yielding under moderate to severe earthquake loading, $P-\Delta$ effects may exacerbate yielding resulting in large maximum and residual drifts. Therefore, modern structural codes typically employ relatively simple models and prescribe limits beyond which $P-\Delta$ effects must be explicitly included in analyses. However, the interaction of material and geometric nonlinearity under dynamic earthquake loading is a complex phenomenon that is not captured accurately by simple models. Thus, the methods employed currently for assessment of $P-\Delta$ effects may underestimate these effects and, thereby, result in unconservative designs. To provide a basis for the research presented here, which seeks to develop improved methods for evaluating the impact of $P-\Delta$ effects, the following sections provide a review of the $P-\Delta$ effects and structural stability of SDOF and MDOF structures.

SDOF System

A SDOF system provides a simple model of a structure that can be used to investigate stability. The load-displacement backbone curve of a SDOF oscillator with a rigid column and a rotational spring at the base is shown in Figure 1. A number of researchers (e.g. Jennings and Husid, 1968, MacRae, 1994) have shown that the effect of the geometric nonlinearity on the oscillator response may be approximated as a reduction (1) in the lateral strength, V , of the oscillator at any displacement, Δ , by $P\Delta/L$, where P is the axial force on the column, and L is the column length, and (2) in the lateral stiffness of the oscillator by P/L . This effect can be defined in terms of the oscillator stiffness, in which case the initial, elastic stiffness of the oscillator considering $P-\Delta$ effects, K_{op} , is defined

$$K_{op} = K_o(1 - \theta_{SDOF}) \quad (1)$$

and the inelastic tangent stiffness considering P - Δ effects, K_p , is defined

$$K_p = K_o(r_o - \theta_{SDOF}) \quad (2)$$

where r_o is the material post-yield tangent stiffness ratio and θ_{SDOF} is a SDOF stability factor:

$$\theta_{SDOF} = \frac{P}{K_o L} \quad (3)$$

Also, employing the natural period of the SDOF oscillator, the SDOF stability coefficient, θ_{SDOF} , is defined

$$\theta_{MDOF}^{global} = 1 - \left(\frac{T_o}{T_p} \right)^2 \quad (4)$$

where T_o is the initial period, based on the stiffness of the structure neglecting P - Δ effects, and T_p is the initial period, based on the stiffness considering P - Δ effects.

Researchers (e.g., Jennings and Husid, 1968 and Miranda and Akkar 2003) have shown that for a given earthquake ground motion, the maximum displacement exhibited by a SDOF oscillator starts to increase rapidly once the post-elastic tangent stiffness, $K_o(r_o - \theta_{SDOF})$, or instantaneous eigenvalue becomes negative. Even for small negative post-elastic stiffnesses and low intensity earthquake ground motion, some earthquake ground motion records may result in structural collapse.

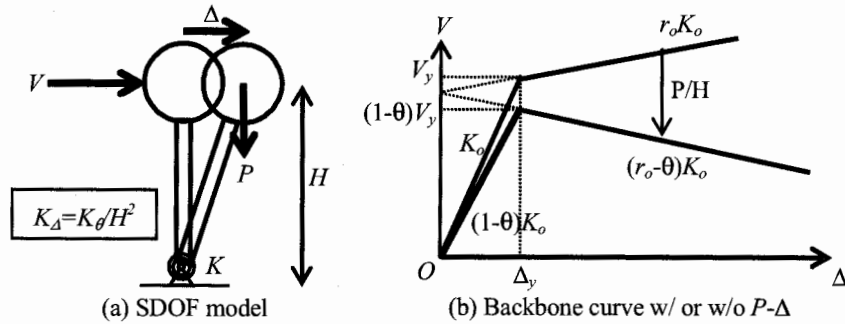


Figure 1: P - Δ effects on SDOF structural model

MDOF System

For MDOF structures, both local and global stability parameters have been proposed to assess stability. Many building design codes (e.g. IBC(ICBO, 2003)) use a local story-wise stability coefficient (Paulay, 1978):

$$\left(\theta_{MDOF}^{story} \right)_i = \frac{P_i \Delta_i}{V_i H_i} \approx \frac{P_i}{K_i^s H_i^s} \quad (7)$$

where, i is the story number, P_i is the total gravity load acting above the story, Δ_i is the elastic story drift (material and geometric nonlinearity are ignored in the analysis), V_i is the story shear, H_i is the story height, K_i^s ($\approx \Delta_i/V_i$) is the lateral stiffness of a story subassembly, H_i^s ($\approx H_i$) is the height of a story subassembly as shown in Figure 2.

While this local story-wise stability coefficient is simple and is appropriate for SDOF oscillators, recent research results suggest that it is not, in general, appropriate for MDOF oscillators. For MDOF systems, the story-wise stability coefficient follows from the assumption of a moment distribution in the frame in which points of contraflexure exist as mid-span of beams and columns. However, studies

show that if inelastic action occurs during an earthquake, contraflexure points move substantially (Paulay and Priestley, 1992).

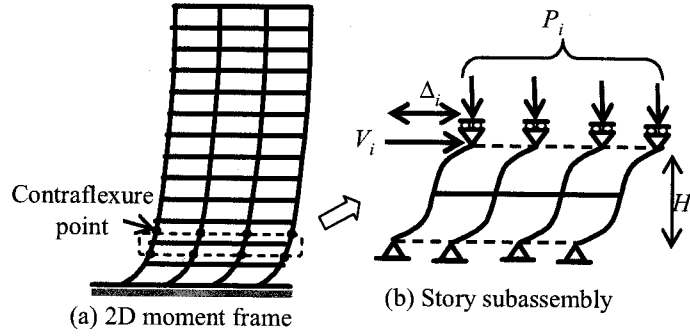


Figure 2: Single story sub-assembly used to compute the story-wise stability index

2. DEVELOPMENT OF STABILITY PARAMETERS

To provide a basis for investigating structural stability and determining the factors that control stability, a new, more sophisticated, method is developed as an extension of studies by Bernal (1992). This method is developed from the equations the dynamic motion of the full structure. The i^{th} -mode response of the structure, during a time increment dt , is defined

$$\{\phi_i(t)\}^T [M] \{\phi_i(t)\} d\ddot{\Delta}_{r,i} + \{\phi_i(t)\}^T [C] \{\phi_i(t)\} d\dot{\Delta}_{r,i} + \{\phi_i(t)\}^T ([K(t)] + [K_g]) \{\phi_i(t)\} d\Delta_{r,i} = -\{\phi_i(t)\}^T [M] \{\ell\} d\ddot{\Delta}_g \quad (10)$$

where $[M]$ is the mass matrix, $[C]$ is the viscous damping matrix, $[K(t)]$ is the tangent stiffness matrix at time t that is assumed to remain constant during the time increment dt , $[K_g]$ is the geometric stiffness matrix, $\{\ell\}$ is the influence vector, $d\ddot{\Delta}_g$ is the ground acceleration, $\{d\Delta_{r,i}\}$ is the incremental modal displacement, $\{\Phi_i(t)\}$ is the instantaneous i^{th} -mode shape, and $d\Delta_{r,i}$ is the incremental modal coordinate displacement. Taking a ratio of representative stiffness of the i^{th} -mode including P - Δ (in Equation 10) during an earthquake to that at the initial time and without P - Δ , the material, P - Δ , and the net stability coefficients, for the i^{th} -mode shape at an interest time are given by:

$$r_{MDOF,i}(t) = \frac{\{\Phi_i(t)\}^T [K(t)] \{\Phi_i(t)\}}{\{\Phi_{o,i}\}^T [K_o] \{\Phi_{o,i}\}} \quad (11)$$

$$\theta_{MDOF,i}(t) = -\frac{\{\Phi_i(t)\}^T [K_g] \{\Phi_i(t)\}}{\{\Phi_{o,i}\}^T [K_o] \{\Phi_{o,i}\}} \quad (12)$$

$$r_{net,i}(t) = r_{MDOF,i}(t) - \theta_{MDOF,i}(t) \quad (13)$$

Here, the same modal contribution factors should be used for the choice of the modal shape vectors. Also $[K_o]$ is an initial stiffness matrix. The i^{th} -mode instantaneous eigenvalue of the mass and stiffness matrices, $\Omega_i(t)$, which is a square of the instantaneous frequency, $\omega_i(t)$, is related to the stability coefficients as given by:

$$\Omega_i(t) = r_{net,i}(t) \cdot \frac{\{\Phi_{o,i}\}^T [K_o] \{\Phi_{o,i}\}}{\{\Phi_i(t)\}^T [M] \{\Phi_i(t)\}} = \omega_i(t)^2 \quad (14)$$

When the instantaneous eigenvalue of the structure becomes negative during an earthquake, which means that the instantaneous frequency becomes an imaginary value, the structure does not “oscillate” and tends to sway in one direction (Bernal 1998, Uetani and Tagawa, 1998, Araki and Hjelmstad, 2000). As a result, large maximum and residual story drifts tend to result.

3. 1D COUPLED SHEAR-FLEXURAL-BEAM MODELS

A series of dynamic analyses were performed of the 3, 9, and 20-story steel frames designed as part of the SAC study (FEMA-355C, 2000) chosen as the prototype structure. To reduce the computational demand of the analyses, a structure is represented by 1D coupled shear-flexural-beam model as shown in Figure 3. Nodes are located at floor levels in both elements. The shear-beam and flexural-beam elements are rigidly linked at each node. Tagawa (2005) provides a detailed discussion of the procedure employed to create a 1D model of a 2D frame.

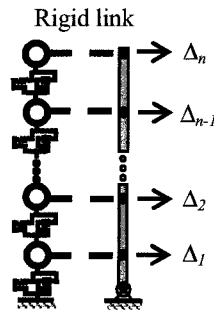


Figure 3: Configurations of 1D coupled shear-flexural-beam model.

4. EVALUATION OF STABILITY COEFFICIENTS AND FRAME RESPONSE

The results of dynamic analyses of 1D shear-flexural-beam models corresponding to the SAC 20-story frames were used to evaluate the proposed stability coefficients. The continuous column stiffness ratio, $\kappa_{c.c.}$, is computed as $\Sigma EI_{c.c.} / \Sigma EI_{moment}$, where ΣEI_{moment} is the total flexural stiffness of columns in the original moment frame at each story level, and $\Sigma EI_{c.c.}$ is the total flexural stiffness of the continuous columns. A value of $\kappa_{c.c.} = 0.8$ gives similar response to the actual frame during pushover and dynamic analyses. This ratio is varied to 0.1 and 100.

$\kappa_{c.c.} = 0.1$ (very small value)

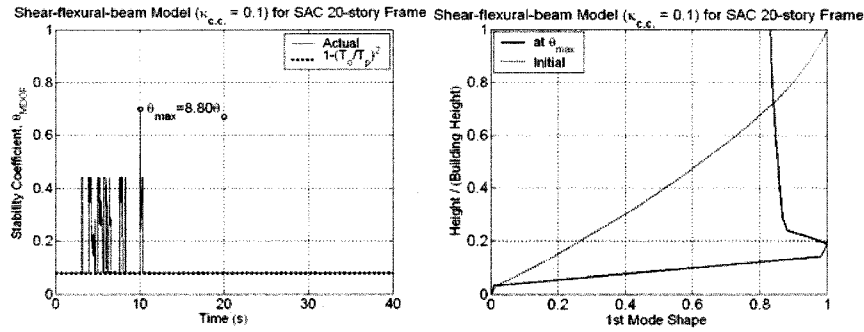
Figure 4(a) shows the time-history of θ_{MDOF} for 1D MDOF coupled model with $\kappa_{c.c.} = 0.1$ during the NF05 record (Somerville et al. 1997). The θ_{MDOF} becomes 880% of the initial elastic value due to very large drift concentrations at the maximum θ_{MDOF} as illustrated in Figure 4(a). The 1st-mode at the maximum θ_{MDOF} has large drift concentrations in the lower stories. Figure 5(a) shows time-history of r_{MDOF} and r_{net} during NF05. The r_{MDOF} decreases due to yielding but are always positive. However, r_{net} becomes negative as θ_{MDOF} becomes large. As a result, the instantaneous eigenvalue becomes negative as illustrated in Figure 5(b), which is likely to provide unstable behavior.

$$\kappa_{c.c.} = 0.8$$

Figure 6(a) shows the time-history of the 1st-mode θ_{MDOF} during the NF05 record. The θ_{MDOF} at the initial stage is similar to that calculated as $\theta_{MDOF}^{global} = 1 - (T_0/T)^2 = 0.0757$. As yielding progresses, however, θ_{MDOF} increases to approximately 214% of the initial value. This is because the 1st mode shape is changing during the ground motion. Figure 6 (b) compares the instantaneous 1st mode shape at the initial stage and that at the maximum θ_{MDOF} . Figure 7(a) and Figure 7(b) show the time-history of r_{MDOF} and r_{net} of the 1st-mode. The r_{MDOF} starts with a value of 1.0 and decreases to 0.455 due to yielding. The r_{net} starts with a value of 0.924 and decreases to 0.373 due to material yielding and increased $P-\Delta$. During the ground motion, r_{net} , and thereby the instantaneous eigenvalue, Ω , remain positive, which provides stable response.

$$\kappa_{c.c.} = 100 \text{ (very large value)}$$

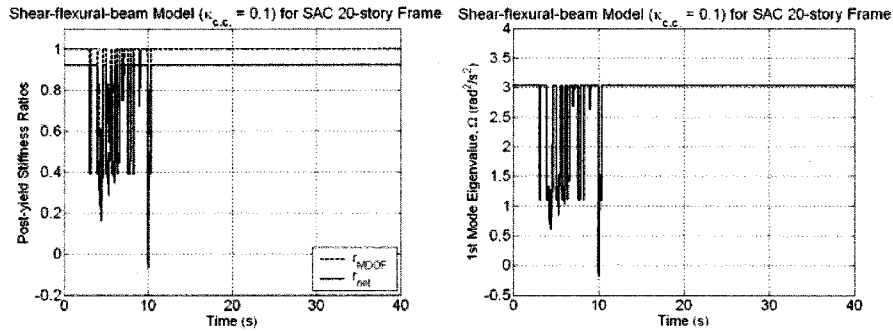
Figure 8(a) shows the time-history of θ_{MDOF} for 1D MDOF coupled model ($\kappa_{c.c.} = 100$) during the NF05 record. It is found that θ_{MDOF} is almost constant during ground motion. The θ_{MDOF} becomes 114% of the initial value. This is because the model has almost linear drift distribution during ground motion as shown in Figure 8(b). Figure 9(a) shows the time-history of r_{MDOF} and r_{net} during ground motion. It is found that r_{MDOF} decreases due to yielding but is always positive. Again, r_{net} remains positive as shown in Figure 9(b) providing stable response.



(a) $P-\Delta$ stability coefficient

(b) 1st-mode shape at θ_{MDOF}^{max}

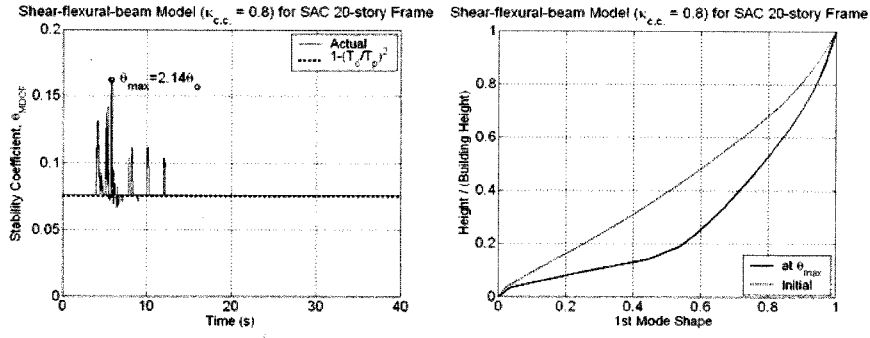
Figure 4: θ_{MDOF} , and 1st-mode shape at maximum θ_{MDOF} in 1D MDOF model ($\kappa_{c.c.} = 0.1$), NF05.



(a) Material and net coefficient

(b) 1st-mode eigenvalues

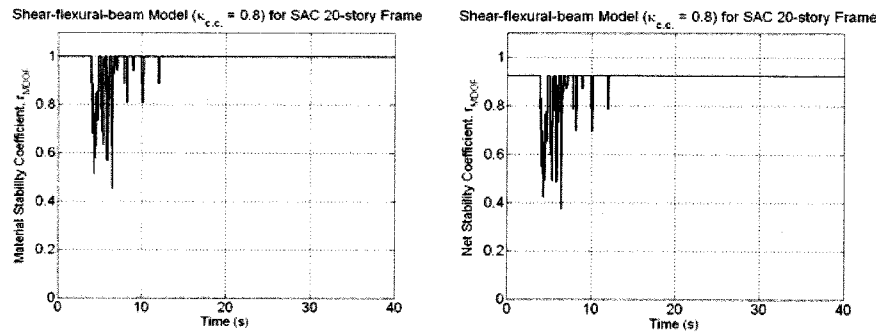
Figure 5: r_{MDOF} and r_{net} of the 1st-mode during NF05 in 1D MDOF coupled model ($\kappa_{c.c.} = 0.1$).



(a) P - Δ stability coefficients

(b) 1st mode shapes

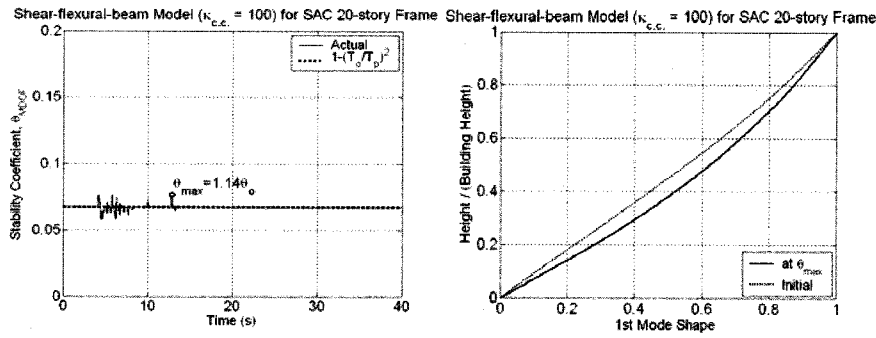
Figure 6: θ_{MDOF} and the 1st-mode at max θ_{MDOF} in 1D MDOF coupled model ($\kappa_{c,c} = 0.8$).



(a) Material stability coefficient

(b) Net stability coefficient

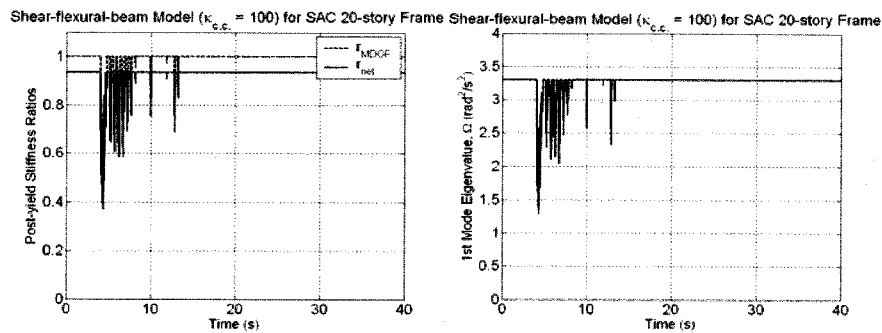
Figure 7: r_{MDOF} and r_{net} of the 1st-mode in 1D MDOF coupled model ($\kappa_{c,c} = 0.8$).



(a) P - Δ stability coefficient

(b) 1st-mode shape at θ_{MDOF}^{max}

Figure 8: θ_{MDOF} and the 1st-mode at max θ_{MDOF} in 1D MDOF coupled model ($\kappa_{c,c} = 100$).



(a) Material and net coefficients

(b) 1st-mode eigenvalues

Figure 9: r_{MDOF} and r_{net} of the 1st-mode in 1D MDOF coupled model ($\kappa_{c,c} = 100$).

Figure 10 compares the story drift angle time-history of the 1D MDOF coupled model with $\kappa_{c,c} = 0.1, 0.8$ and 100 . When $\kappa_{c,c} = 0.1$, the maximum and residual drift become very large due to negative instantaneous eigenvalue as shown in Figure 5. When $\kappa_{c,c} = 0.8$ and 100 , the maximum and residual drifts are smaller due to stable response provided by positive instantaneous eigenvalue as shown in Figures 7 and 9. However, when $\kappa_{c,c} = 0.8$, due to pulse characteristics of the near-fault ground motion, overall behavior is not oscillatory around the origin.

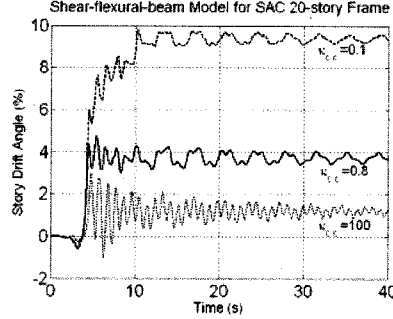
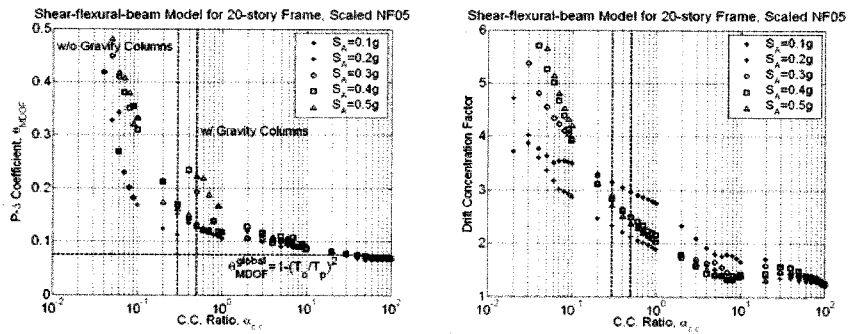


Figure 10: SDA history during NF05 in 1D MDOF coupled model ($\kappa_{c,c} = 0.1, 0.8$, and 100).

5. CONTINUOUS COLUMN EFFECTS ON STABILITY COEFFICIENTS

Figures 11(a) and (b) show the maximum θ_{MDOF} and drift concentration factor (DCF) during the scaled NF05 ground motions for 1D 20-story coupled model with various continuous column stiffness ratio, $\alpha_{c,c}$. ($= EI_{fi}/(H_i^3 K_{o,i})$, where E is the elastic modulus, I_{fi} is the moment of inertia of all the continuous columns in the structure at the height of the i^{th} story subassembly, H_i is the i^{th} story subassembly height, and $K_{o,i}$ is lateral initial stiffness of the i^{th} story subassembly). The maximum θ_{MDOF} significantly decreases to $\theta_{MDOF}^{global} = 1 - (T_o/T_p)^2 = 0.0752$ as $\alpha_{c,c}$ increases. The maximum θ_{MDOF} becomes almost 200% of θ_{MDOF}^{global} when $\alpha_{c,c}$ is 0.3 . The DCF decreases and approaches unity as $\alpha_{c,c}$ increases. The gravity columns decrease slightly the maximum θ_{MDOF} and DCF as shown by the vertical lines in Figure 11.



(a) Maximum $P-\Delta$ coefficients

(b) Minimum net coefficient

Figure 11: Maximum θ_{MDOF} and DCF in 1D models with various $\alpha_{c,c}$ for 20-story frame.

6. CONCLUSIONS

Stability coefficients were proposed that characterize the impact of material and geometric nonlinearity on the net instantaneous stability of a MDOF structure. Dynamic analyses of the 3-, 9-, 20-story steel frames were conducted using simple models. Major findings are:

- (1) The proposed net stability coefficient, r_{net} , provides a method for quantifying the potential for unstable response, and the proposed material, r_{MDOF} , and P - Δ , θ_{MDOF} , describe the impact of material and geometric nonlinearity on system stability.
- (2) For a regular steel moment frame, the P - Δ stability coefficient increases due to drift concentration indicating that the yielding structure is more susceptible to P - Δ effects than the original elastic structure.
- (3) As the continuous column stiffness increases, the P - Δ stability coefficient decreases and approaches the global stability index, and also the drift concentration decreases.

References:

- Adam, C., Ibarra, L., and Krawinkler, H. 2004. Evaluation on P-Delta Effects in Non-deteriorating MDOF Structures from Equivalent SDOF Systems, 13th WCEE, Vancouver, B.C., Canada, August.
- Araki, Y. and Hjelmstad K., 2000. Criteria for Assessing Dynamic Collapse of Elastoplastic Structural Systems, Earthquake Engineering and Structural Dynamics, Vol. 29.
- Bernal, D. 1998., Instability of buildings during seismic response, Engineering Structures, 20(4-6).
- Chung, B.T., 1993. The Influence of P-Delta Effects on the Seismic Design of Structures, School of Engineering Report No. 538, University of Auckland, September.
- FEMA-355C, 2000. State of the Art Report on Systems Performance of Steel Moment Frames Subject to Earthquake Ground Shaking, the SAC Joint Venture for the FEMA, Washington, DC.
- MacRae, G., 1994. P- Δ Effects on SDOF Structures in Earthquakes, Earthquake Spectra, Vol. 10, No. 3.
- Miranda, E. and Akkar, S., 2003, Dynamic Instability of Simple Structural Systems, Journal of Structural Engineering, ASCE, Vol. 129, No. 12.
- Somerville, P., Smith, N., Punyamurthula, S., and Sun, J., 1997. Development of ground motion time histories for phase 2 of the FEMA/SAC steel project, Rep. No. SAC/BD97/04, SAC Joint Venture, Sacramento, California.
- Tagawa, H., 2005. Towards an Understanding of Seismic Response of 3D Structures – Stability & Reliability, Partial Requirement for Doctoral Thesis, University of Washington, Seattle.
- Uetani, K. and Tagawa, H., 1998, Criteria for Suppression of Deformation Concentration of Building Frames under Severe Earthquakes, Engineering Structures, Vol. 20.
- Paulay, T., 1978. A Consideration of P-Delta Effects in Ductile Reinforced Concrete Frames, Bulletin of the New Zealand National Society for Earthquake Engineering, Vol. 11, No.3, September.
- Paulay, T. and Priestley, M. J. N., 1992. Seismic Design of Reinforced Concrete and Masonry Buildings, Wiley and Sons, New York.

DEVELOPMENT OF LINK-TO-COLUMN CONNECTIONS FOR STEEL ECCENTRICALLY BRACED FRAMES

T. Okazaki¹⁾ and M. D. Engelhardt²⁾

1) Assistant Professor, Dept. Civil Engineering, University of Minnesota, Minnesota, U.S.A.

2) Professor, Dept. of Civil, Architectural, and Environmental Engineering, University of Texas at Austin, Texas, U.S.A.
tokazaki@umn.edu, mde@mail.utexas.edu

Abstract: The link-to-column connection is a critical element affecting the safety and performance of seismic-resistant steel eccentrically braced frames (EBFs). In the US, the AISC *Seismic Provisions for Structural Steel Buildings* requires that satisfactory performance of link-to-column connections be verified by testing under a prescribed loading protocol. To-date, very few link-to-column connection details have passed these testing criteria. Consequently, the availability of link-to-column connection details with demonstrated satisfactory performance remains a largely unsolved problem for construction of EBFs in the US. The writers recently completed a program of pilot tests on link-to-column connections, using welded details that are intended for shop welding. These tests have shown excellent connection performance, satisfying the performance requirements of the AISC *Seismic Provisions*. This paper will describe the development of these connection details, provide a summary of test results, and discuss the design implications of this research program.

1. INTRODUCTION

An important and largely unsolved problem in the design of seismic-resistant steel eccentrically braced frames (EBFs) is the development of a suitable link-to-column connection detail. The link-to-column connection must sustain very large shear forces and bending moments while accommodating large inelastic rotations. EBFs are most commonly designed using shear yielding links, in which the link length e is less than approximately $1.6M_p/V_p$. M_p is the plastic moment capacity of the link section, and V_p is the plastic shear capacity. For a shear yielding link, the link-to-column connection may be required to sustain shear forces on the order of $1.5V_p$, a moment on the order of M_p and a cyclic inelastic rotation angle on the order of 0.08 rad (Popov and Engelhardt 1988). Developing connection details that can sustain these demands without fracture remains an important challenge for researchers and designers.

In the US, design and detailing requirements for EBFs are specified in the 2005 AISC *Seismic Provisions for Structural Steel Buildings* (AISC 2005). The requirements for link-to-column connections are stated as a performance specification, in which the connection must be capable of sustaining the required inelastic rotation angle under cyclic loading, while maintaining a shear resistance equal to at least the nominal shear strength of the link. Further, the ability of a link-to-column connection detail to satisfy these performance requirements must be demonstrated by large-scale tests, using a loading protocol specified in Appendix S of the 2005 AISC *Seismic Provisions*. In the case of a shear yielding link, the link-to-column connection must sustain an inelastic rotation angle of at least 0.08 rad when tested using the cyclic loading protocol in Appendix S. When the connection reaches 0.08 rad of inelastic rotation, the shear resistance of the connection must still

be at least V_p of the link. Note that in the 2005 AISC *Seismic Provisions*, the loading protocol specified for testing link-to-column connections was modified from earlier editions of the AISC *Seismic Provisions*, based on studies by Richards and Uang (2003).

In an attempt to identify economical link-to-column connection details that satisfy the performance requirements of the AISC *Seismic Provisions*, an extensive series of experimental and analytical studies was recently conducted by the authors (Okazaki 2004, Okazaki et al. 2004, Okazaki and Engelhardt 2005). This investigation evaluated three different link-to-column connection configurations, and employed improved welding practices and details (use of toughness rated electrodes, removal of backing bars and weld tabs, etc.) based on post-Northridge moment connection research. The three connection configurations tested in this investigation were largely intended to be constructed as field-welded connections, as is the common practice in US building construction. The choice of connection configurations were based on successful moment connection details developed in the SAC program (FEMA 2000), modified for use in EBFs based on finite element analyses (Okazaki 2004, Okazaki and Engelhardt 2006). Ultimately, however, very few of the specimens tested in this program satisfied the performance requirements of the AISC *Seismic Provisions*. One of the conclusions of this investigation was that connection details that perform well in moment frames may perform quite poorly when used for link-to-column connections. The results also emphasized the large force and deformation demands placed on link-to-column connections, and the difficulty in finding connection details that can sustain these demands.

Thus, at present, the development of an EBF link-to-column connection detail that satisfies the performance requirements of the AISC *Seismic Provisions* remains a largely unsolved problem in the US. In fact, the commentary to the 2005 AISC *Seismic Provisions* advises designers to avoid EBF configurations with links attached to columns until further research has been conducted to identify suitable details.

In continuing research on link-to-column connections, the writers recently developed and tested a simple welded connection detail, which in limited testing, successfully satisfied the requirements of the 2005 AISC *Seismic Provisions*. This detail is suitable primarily only for shop welding. As noted above, link-to-column connections are normally field welded in US practice. Nonetheless, the proposed detail showed outstanding performance in laboratory testing, and may be a viable connection detail for EBF construction.

This paper describes the proposed link-to-column connection detail. The performance of the detail in laboratory testing is then presented, followed by a discussion of design implications.

2. PROPOSED CONNECTION DETAIL

The fundamental concept of the shop welded link-to-column connection is illustrated in Figure 1. In this approach, the link is shop welded to the column, and a brace stub is shop welded at the link end. The brace and beam segment outside of the link are then connected in the field using bolted splices. While such “column-tree” approaches are not normally used in US practice, this approach offers some particular advantages in EBFs. Both the link-to-column connection and the brace-to-link connection can be constructed in the shop, in a single assembly. Further, the beam segment outside of the link need not be the same wide flange section as the link, thereby alleviating a common design problem in EBFs. Disadvantages may include difficulties in shipping the column-link assembly to the job site, and the additional cost of the bolted splices in the beam and brace.

As shown in Figure 1, the connection detail between the link and column consists simply of double-sided fillet welds on the link flanges and on the link web. There is no special end preparation required of the link. That is, there is no need to cut bevels in the link flanges or to cut weld access holes, as is the case with complete joint penetration groove welds.

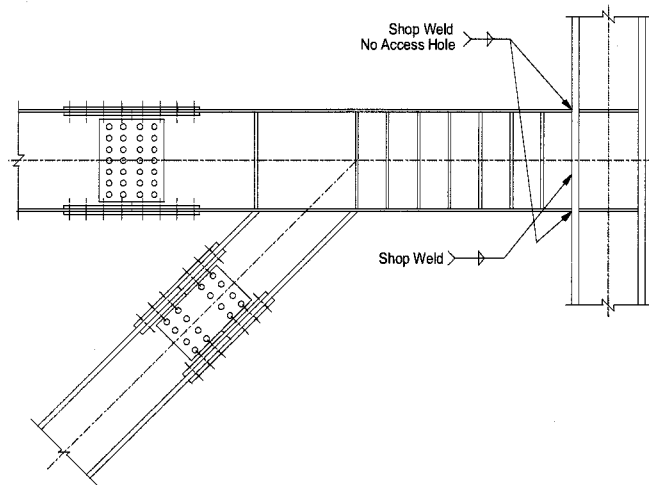


Figure 1 Overall view of shop welded link-to-column connection.

The concept of the fillet welded link-to-column connection was motivated by successful tests of a similar detail in an investigation by Okazaki et al. (2005). In this investigation, links were subject to cyclic loading to study flange buckling and flange slenderness limits. Consequently, it was necessary to be able to test links without premature failure of the link end connections. For these tests, links were fillet welded to heavy end plates, which in turn, were bolted to a test frame (Okazaki et al. 2005). The sizes of fillet welds was chosen to be 1.5 times the thickness of the connected link flange or web, and were made using the shielded metal arc welding (SMAW) welding process. Further, small weld tabs were placed at the outer edges of the link flanges for run-off the link flange to end plate fillet welds. This connection detail was developed by trial and error in the laboratory. It was not intended to represent a realistic link end connection, but was simply developed to permit laboratory testing of links without the occurrence of link end connection failure. This detail was used successfully in over fifty link tests. Based on this successful experience, the concept of the shop welded link-to-column connection was developed, and evaluated in a limited number of pilot tests. Further details of the connection and test program are described in the following section.

3. DESCRIPTION OF EXPERIMENTAL PROGRAM

A series of four link-to-column connection tests were conducted for a preliminary performance evaluation of the shop welded detail. The specific objectives of these tests were as follows:

- Determine if the fillet weld detail will perform satisfactorily when the link is welded directly to a column flange rather than to a thick end plate.
- Determine if the fillet weld detail will perform satisfactorily when welding is done using the gas shielded flux cored arc welding process (FCAW-GS) rather than SMAW. FCAW-GS is more commonly used for shop welding by US fabricators than SMAW.
- Determine if the fillet weld size can be made smaller than 1.5-times the connected plate (link flange or web) thickness.
- Determine if the double-sided fillet weld for the link flange can be replaced with a detail consisting of a partial joint penetration groove weld made from the outer side of the flange, combined with a fillet weld placed on the inside face of the link flange. For links with thick flanges, this detail may permit considerable savings in welding.

The test setup used for the link-to-column connection tests was the same setup used for previous tests by Okazaki. Full details of the setup are described in Okazaki (2004) and in Okazaki and Engelhardt (2005) and are not repeated here. A typical specimen consisted of a column with an attached link. The end of the link away from the column was welded to a heavy end plate, which in turn, was bolted into the test frame.

Table 1 lists basic properties of the links used in the four test specimens. The links were constructed of either W18x40 or W10x68 sections of A992 steel. The column section used for all specimens was a W12x120 of A992 steel. All links were 980 mm in length, placing all specimens in or near to the shear yielding range. Also listed in Table 1 is the link target plastic rotation γ_p as defined by the 2005 AISC *Seismic Provisions*. The link must achieve this target plastic rotation without failure of the link-to-column connection to satisfy the connection performance requirements of the provisions.

The basic connection detail and welding process used for each specimen is listed in Table 2. Specimens 1 and 2 used double-sided fillet welds sized to be approximately 1.5 times the connection flange or web thickness. The only difference between these two specimens was the welding process; SMAW for Specimen 1 and FCAW-GS for Specimen 2. These specimens were intended to evaluate the suitability of FCAW-GS welding for this application. Specimen 3 was also welded using FCAW-GS, just like Specimen 2. However, the double-sided fillet welds on Specimen 3 had a leg size approximately equal to the thickness of the connected flange or web. This specimen was designed to evaluate the feasibility of using smaller sized fillet welds.

Table 1 Link sections used for test specimens.

Specimen	Link Section	Link length, e	$e/(M_p/V_p)$	Target γ_p
		mm		rad.
1 to 3	W18x40	980	1.70	0.075
4	W10x68	980	1.33	0.080

Table 2 Specimen connection and welding details.

Specimen	Welding process and electrode	Connection detail
1	SMAW with E7018	Double sided fillet welds: 19 mm fillets on flanges; 13 mm fillets on web
2	FCAW-GS with E70T-9	Double sided fillet welds: 19 mm fillets on flanges; 13 mm fillets on web
3	FCAW-GS with E70T-9	Double sided fillet welds: 13 mm fillets on flanges; 8 mm fillets on web
4	FCAW-GS with E70T-9	Flange: partial pen weld from outside and fillet weld on the inside face; Web: 17 mm double-sided fillet weld

Figure 2 illustrates connection details for Specimen 1 to 3. An additional feature of these details is the use of weld run-off tabs at the outer edges of the link flanges. The thickness of the tabs was approximately the same as the flange thickness. The tabs provided an area to terminate the fillet welds, and prevented undercut at the flange edges. The tabs were left in-place upon completion of welding. The beneficial effects of these tabs were observed in earlier tests by the authors (Okazaki 2004, Okazaki et al. 2005). The fillet weld on the top side of a link flange, along with the weld run-off tabs are visible in the photo in Figure 3.

For links with thick flanges, providing double-sided fillet welds with a leg size equal to 1.5 times the flange thickness can result in exceedingly large and costly fillet welds. For such cases, an alternative detail was developed, and tested on Specimen 4. The details for this specimen are shown in Figure 4. The W10x68 used for Specimen 4 is a shallower section compared to the W18x40 used for

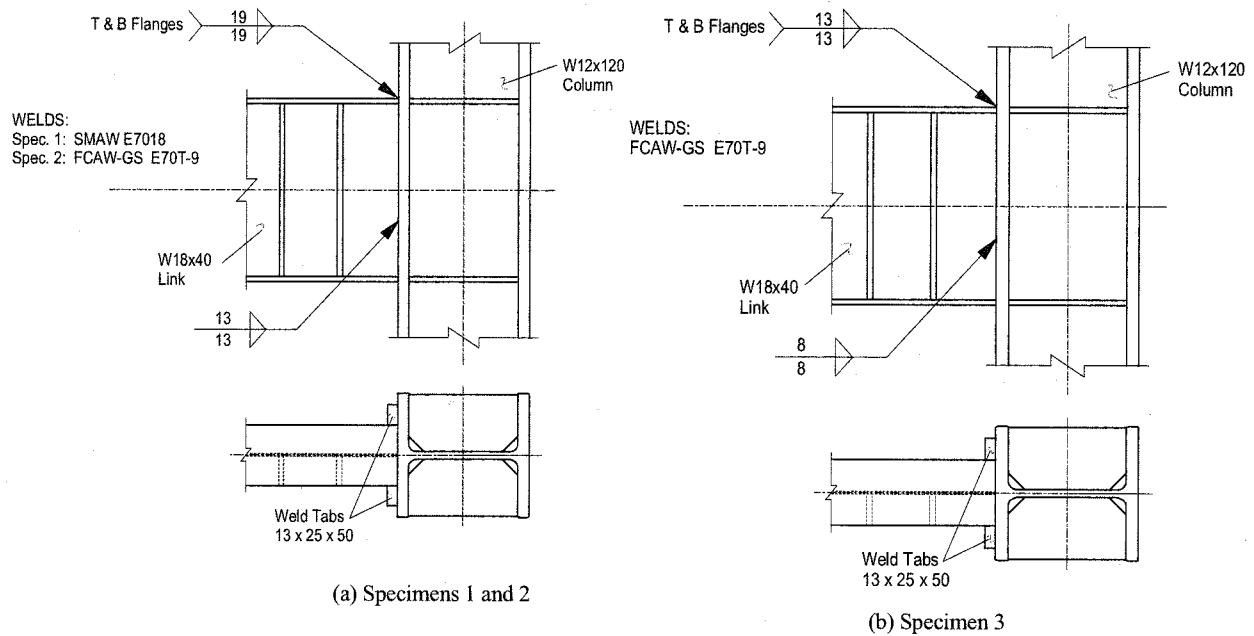


Figure 2 Connection details for Specimens 1 to 3.

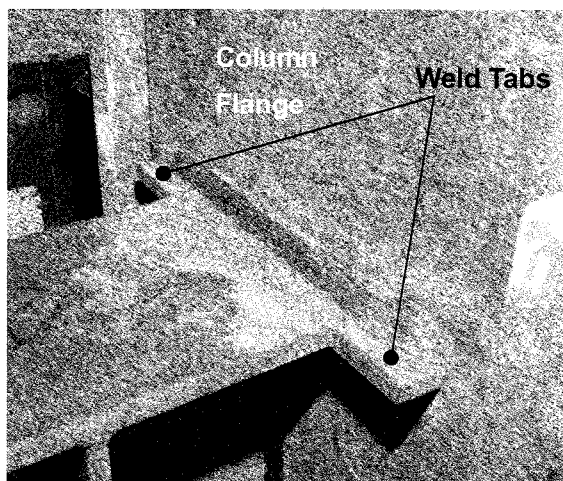


Figure 3 Specimens 1 to 3: typical link flange fillet weld.

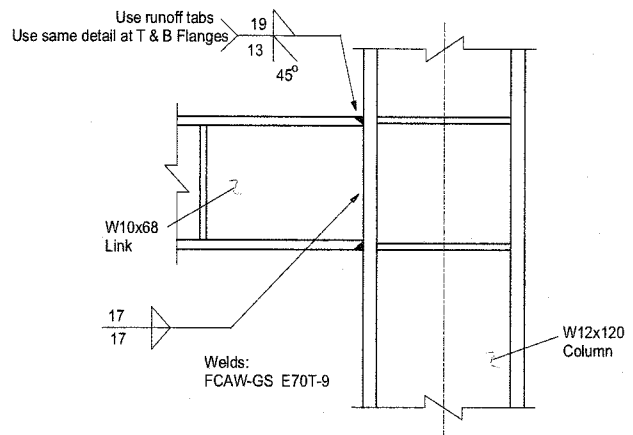


Figure 4 Connection detail for Specimen 4.

Specimens 1 to 3. For Specimen 4, the link web was welded to the column using double-sided fillet welds sized for 1.5 times the web thickness, similar to Specimens 1 and 2. However, for the link flange, a partial joint penetration groove weld was used. A bevel was made from the outer surface of each flange. The bevel angle was 45-degrees, and the bevel was nearly the full thickness of the flange. A small land was left on the flange, with a height of about 6 mm. Consequently, the weld was close to being complete joint penetration, except there was no open root, and no backing bars required.

On the inside face of each link flange, a fillet weld was placed, with a leg size equal to the flange thickness. Weld run-off tabs were placed at the outer edges of the link flanges, and were angled to match the bevel angle of the groove. The fillet welds on the inside face of the link flanges were also extended over these tabs. The tabs were left in-place after completion of welding. A photo of the link flange weld and run-off tabs are shown in Figure 5.

Specimen 1 was welded using the SMAW process with E7018 electrodes. This welding process and electrode were used in the previous successful end plate welded connections used by Okazaki et al.

(2005) and was repeated here for Specimen 1 for consistency and comparability with these past tests. SMAW with E7018 electrodes can provide very high levels of notch-toughness (Johnson 2000), but is generally not favored in fabrication practice due to very low deposition rates, and consequent high cost. The remainder of the specimens were welded using the FCAW-GS process with E70T-9 electrodes. This process and electrode is more commonly used by US fabricators due to higher deposition rates. The notch toughness values for these welds may not be as high as the SMAW E7018 welds. Nonetheless, the FCAW-GS E70T-9 welds still provide high levels of notch-toughness, and satisfy the requirements of *demand critical* welds in the 2005 AISC *Seismic Provisions*, which is the most restrictive category of welding requirements.

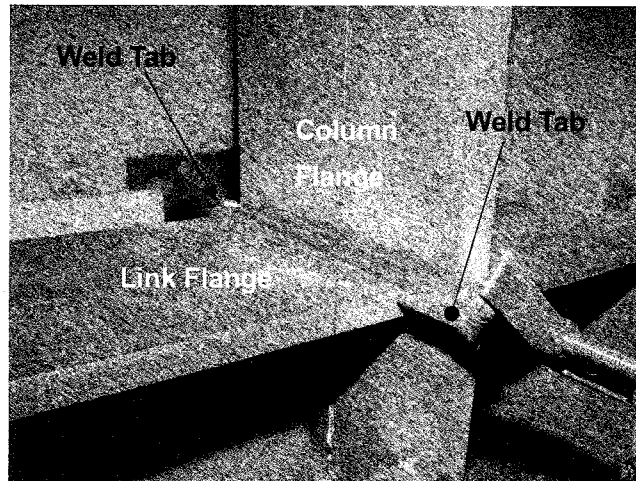


Figure 5 Flange weld and weld run-off tabs for Specimen 4.

4. TEST RESULTS

All four specimens were tested using the cyclic loading protocol specified in Appendix S of the 2005 AISC *Seismic Provisions*. In each case, cyclic loading was continued until the shear resistance of the specimen was severely deteriorated, due to the occurrence of fracture at the link-to-column connection, or within the link itself. That is, all specimens were tested essentially to complete failure. Key results for each specimen are summarized in Table 3.

Table 3 Summary of test results.

Specimen	Target γ_p rad.	Test γ_p rad.	Failure Mode
1	0.075	0.11	Fracture at link flange to column connection (fracture primarily in link flange base metal near fillet weld)
2	0.075	0.095	"
3	0.075	0.057	"
4	0.080	0.096	Fracture of link web at stiffeners (no distress at link-to-column connection)

The column labeled "Test γ_p " lists the actual plastic rotation achieved by each specimen. This was determined as the plastic rotation developed for one full cycle of loading, prior to the shear resistance of the specimen degrading below the nominal shear strength of the link. As an example, the hysteretic response of Specimen 1 is shown in Figure 6. This figure shows a plot of link shear force versus link

plastic rotation angle. The vertical dashed lines show the target plastic rotation for this specimen (0.075 rad.) and the horizontal dashed lines show the nominal shear strength of the W18x40 link (710 kN). The last full cycle of loading corresponded to a plastic rotation angle of ± 0.11 rad. In the next cycle of loading, the shear strength of the specimen deteriorated quickly, dropping below the nominal shear strength of the link. The cause of this strength deterioration was fracture of the link flange near the fillet weld to the column flange. Figure 7 provides a view of the fractured link flange. This specimen showed outstanding overall performance. The target plastic rotation angle of 0.075 rad. was achieved, and was in fact exceeded by about 45-percent. Consequently, the link-to-column connection of Specimen 1 satisfied the performance requirements of the 2005 AISC *Seismic Provisions*. Observe also the full and stable hysteretic loops exhibited by Specimen 1; one of the hallmarks of a well detailed shear yielding link.

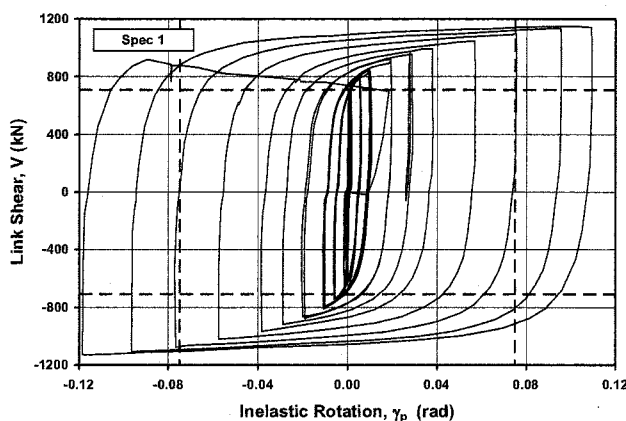


Figure 6 Hysteretic response of Specimen 1.

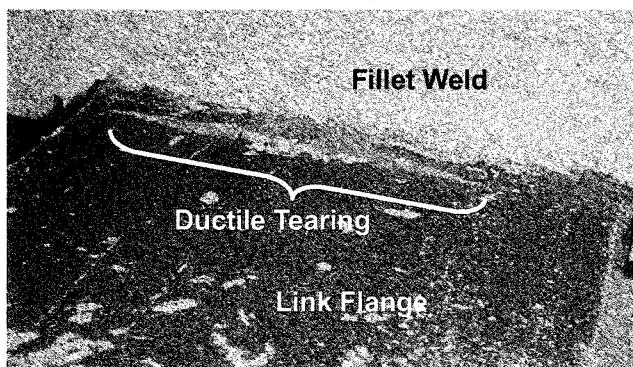


Figure 7 Fracture of link flange in Specimen 1.

Specimen 2 was nominally identical to Specimen 1, except for the welding process used to fabricate the link-to-column connection. This specimen developed somewhat less plastic rotation than Specimen 1 prior to link flange fracture, but still exceeded the target plastic rotation. The results of Specimen 2 suggest that satisfactory connection performance can be achieved by the FCAW-GS process with E70T-9 electrodes.

Specimen 3 was similar to Specimen 2, except that smaller fillet welds were used. As indicated in Table 3, this specimen did not achieve the target plastic rotation angle, indicating that fillet welds with a leg size equal to the thickness of the connected flange are not adequate.

Specimen 4 showed outstanding performance, achieving a plastic rotation angle well in excess of the target value. This specimen ultimately failed by fracture of the link web, with the fracture initiating at the termination of a fillet weld connecting a link web stiffener to the link web. This failure mode has

been commonly observed in recent tests on shear links (Okazaki et al. 2005). When the link web fracture occurred, there was no sign of fracture initiation or any other form of distress at the link-to-column connection. Consequently, the partial penetration weld detail used for this specimen performed very well.

5. CONCLUSIONS

This paper summarized a pilot test program on link-to-column connections. The details tested were intended primarily for shop welding application. Observations from this test program are as follows:

- The simple detail of welding the link to the column using double-sided fillet welds performed well. Successful specimens used a fillet weld leg size approximately equal to 1.5 times the thickness of the connected link flange or web.
- The use of the FCAW-GS welding process with E70T-9 electrodes resulted in satisfactory performance.
- The use of the alternative link flange weld detail that combined a partial joint penetration groove weld with a fillet weld also showed satisfactory performance.

The limited number of tests conducted in this research program, combined with a large number of successful tests on a similar detail by Okazaki et al. (2005) suggest that the shop welded link-to-column connection details described herein can provide excellent performance. Further research and testing would be desirable to confirm this performance over a wider range of link sections.

Acknowledgements:

Funding for this research was provided by the American Institute of Steel Construction (AISC). The advice and support of Tom Schlafly of AISC is greatly acknowledged. The writers are also grateful for the advice and assistance provided by Chia-Ming Uang, Tom Sabol, Subhash Goel and Keith Landwehr.

References:

- AISC. (2005), "Seismic provisions for structural steel buildings," *Standard No. ANSI/AISC 341-05*. American Institute of Steel Construction, Chicago.
- FEMA. (2000), "Recommended seismic design criteria for new steel moment frame buildings," *Report No. FEMA 350*, Federal Emergency Management Association, Washington DC.
- Johnson, M. (2000), "State of the art report on welding and inspection," *Report No. FEMA 355B*, Federal Emergency Management Association, Washington DC.
- Okazaki, T. (2004), "Seismic performance of link-to-column connections in steel eccentrically braced frames," *PhD dissertation*, University of Texas at Austin.
- Okazaki, T., Engelhardt, M.D., Nakashima, M., and Suita, K. (2004), "Experimental study of link-to-column connections in steel eccentrically braced frames," *Proceedings: 13th World Conference on Earthquake Engineering*, Vancouver. August 1-6, 2004.
- Okazaki, T., Arce, G., Ryu, H., and Engelhardt, M.D. (2005), "Experimental study of local buckling, overstrength and fracture of links in EBFs," *Journal of Structural Engineering*, American Society of Civil Engineers, 131(10), 1526-1535.
- Okazaki, T., and Engelhardt, M.D. (2005), "Seismic performance of link-to-column connections in steel eccentrically braced frames," *Proceedings: Second International Conference on Urban Earthquake Engineering*, March 7-8, 2005, Tokyo, Japan.
- Okazaki, T. and Engelhardt, M.D. (2006), "Finite element simulation of link-to-column connections in steel eccentrically braced frames," *Proceedings: 8th National Conference on Earthquake Engineering*, San Francisco. April 18-22, 2006.
- Popov, E. P. and Engelhardt, M.D. (1988), "Seismic eccentrically braced frames," *Journal of Constructional Steel Research*, 10, 321-354.
- Richards, P. and Uang, C.-M. (2003), "Development of testing protocol for short links in eccentrically braced frames," *Report No. SSRP-2003/08*, Department of Structural Engineering, University of California, San Diego.

DYNAMIC TESTS OF STEEL FRAMES WITH COLUMN UPLIFT FOR SEISMIC RESPONSE REDUCTION

T. Ishihara¹⁾, M. Midorikawa²⁾, T. Azuhata¹⁾, and A. Wada³⁾

1) Senior Researcher, Building Dept., National Institute for Land and Infrastructure Management, Ministry of Land, Infrastructure and Transport, Japan

2) Professor, Division of Architectural and Structural Design, Graduate School of Engineering, Hokkaido University, Japan

3) Professor, Structural Engineering Research Center, Tokyo Institute of Technology, Japan

ishihara-t92hd@nilim.go.jp, midorim@eng.hokudai.ac.jp, azuhata-t92ta@nilim.go.jp, wada@serc.titech.ac.jp

Abstract: The seismic responses of the base plate yielding systems are examined comparing with those of the fixed base system by shaking table tests, which are carried out using a three-story, one-by-two bay braced steel frame of two thirds scale. The total height of the frame is 5.3 meters. The yielding base plates are attached at the bottom of each column at the first story of the test frame. Three types of base plates with different thicknesses are installed in the test frame. The earthquake ground motion used for the tests is the record of the 1940 El Centro NS component whose time scale is shortened to $1/\sqrt{2}$. The maximum input accelerations are adjusted in several levels to examine the responses of each system. From the test results, it is concluded that the base plate yielding systems can reduce effectively the seismic responses of steel frames.

1. INTRODUCTION

It has been pointed out that the effects of rocking vibration (uplift motion) may reduce the seismic damage of buildings subjected to strong earthquake ground motions (Rutenberg et al. 1982, Hayashi 1996). Based on this knowledge, we are now developing the rocking structural systems that can cause rocking vibration under appropriate control during earthquakes (Midorikawa et al. 2002, Azuhata et al. 2002).

One of the rocking systems under development has yielding base plates at the bottom of each steel column of the first story. When the weak base plates yield due to tension of column during a strong earthquake motion, the structure causes rocking vibration.

In this paper, shaking table tests are carried out to examine the seismic responses of this type of rocking systems (base plate yielding systems) comparing with those of the fixed base system.

The basic idea of the base plate yielding systems is illustrated in Figure 1.

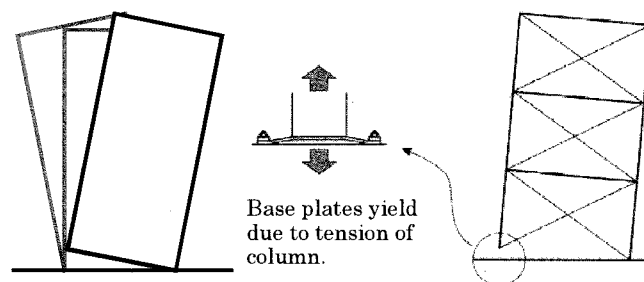


Figure 1 Base Plate Yielding System

When we apply the base plate yielding system to real structures, we must adjust the mechanical characteristics of the base plate such as stiffness and yield strength, so that the building structures can cause rocking vibration. Therefore we need to grasp the relation between the mechanical characteristics of the base plates and the critical base shear initiating uplift response. A simplified method to grasp this relation is proposed and the applicability of this method is verified (Azuhata et al. 2002).

2. TEST FRAME AND TEST PROCEDURES

A three-story, one-by-two bay braced steel frame of two thirds scale was tested on the shaking table at the National Research Institute for Earth Science and Disaster Prevention in Tsukuba, Japan. The test frame is composed of moment-resisting steel frames and structural components such as yielding base plates attached to the bases of the frames and bracing members of prestressing steel bar (tensile strength: 980 MPa) as shown in Figures 2 and 3.

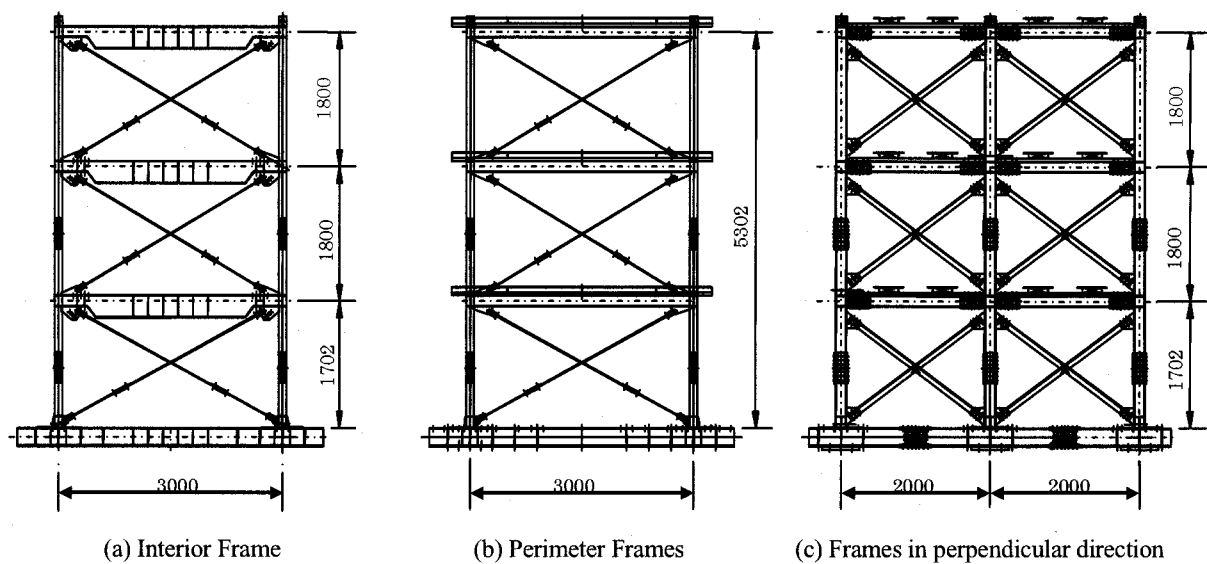


Figure 2 Test Frame

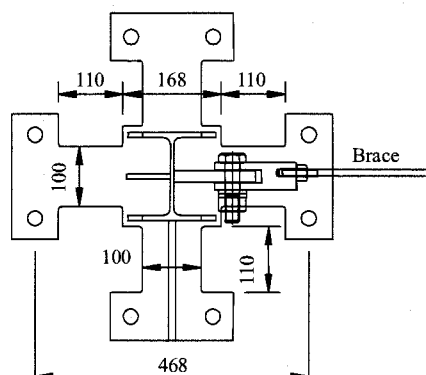


Figure 3 Yielding Base Plate

The total height of the frame is 5.3 meters. Story heights are 1.7 meters at the first story and 1.8 meters at the second and third stories. Every floor plan is 3 by 4 meters. In the test direction, the span is 3 meters. The mass of each floor and the cross sections of members are shown in Tables 1 and 2,

respectively.

The yielding base plates are installed at the bottom of each column at the first story of the test frame as shown in Figure 3. Three types of base plates with different strength are used in the test. The thicknesses of the base plates are 6 mm and 9 mm. Mechanical characteristics of base plates are listed in Table 3. In this paper, the test frame with base plate thickness of 6 mm is referred to as BP6 model, the test frame with base plate thickness of 9 mm referred to as BP9 model, and the fixed base test frame referred to as F model, respectively. The base plate of BP6 and BP9 models has four wings that are 110 mm in length and 100 mm in width. The test frame, whose base plates have two wings of 9mm thickness, is referred to as BP9-2 model.

Table 1 Mass of Floor

Floor	Mass [t]
Roof	4.6
3	5.2
2	5.2

Table 2 Cross Sections of Members

Member	Size [mm]
Column	H-148x100x6x9
Beam	H-150x150x7x10
Brace	ϕ -11

Table 3 Mechanical Properties of Base Plate

Model	JIS	Yield Stress [MPa]
BP6	SS400	330
BP9, BP9-2		292

The test frame is vibrated only in one horizontal direction, which coincides with the strong axis of columns. The earthquake ground motion used for the tests is the record of the 1940 El Centro NS component whose time scale is shortened to $1/\sqrt{2}$. The maximum input accelerations are adjusted in several levels to examine the responses of each model.

3. TEST RESULTS

Figure 4 shows the time history of uplift displacement responses of BP9-2 model under the maximum input acceleration of 5.84 m/s^2 . The peak uplift displacement reaches about 10 mm. The rocking vibration occurs definitely in the test frame.

Figure 5 shows the time history of shears at the bottom of columns of BP9-2 model. The shear from the west to the east indicates a positive value as shown in the Figure. The shears are calculated by summing up the shears from column and brace based on the measured strains. The shear is transmitted effectively at the base even when the column uplifts.

Figure 6 shows the relations between the maximum responses and the input acceleration of each model. The base shears of all models are not so different when the input acceleration is smaller than 1.0 m/s^2 . When the input acceleration becomes larger than 2.5 m/s^2 , the base shears of BP6, BP9 and BP9-2 models are about 120 kN and the rate of increase becomes small drastically. Furthermore the base shears of BP6 and BP9-2 models are much smaller than those of extrapolated values of F model shown by dotted line in the figure.

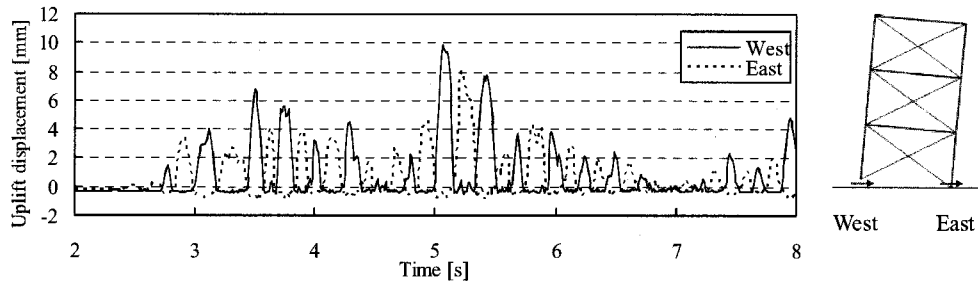


Figure 4 Time History of Uplift Displacement Responses of BP9-2 model
(Maximum Input Acceleration: 5.84 m/s^2)

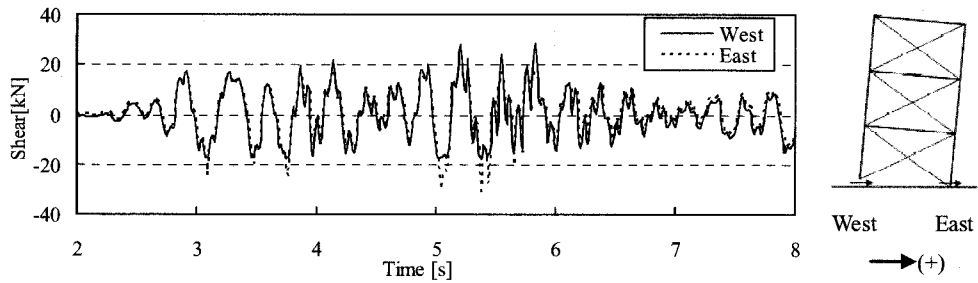
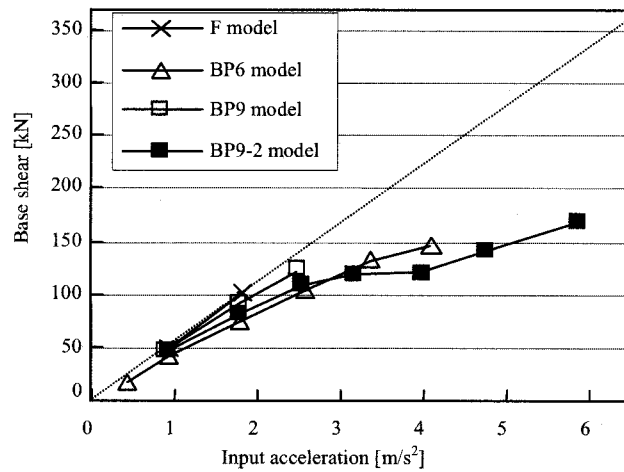
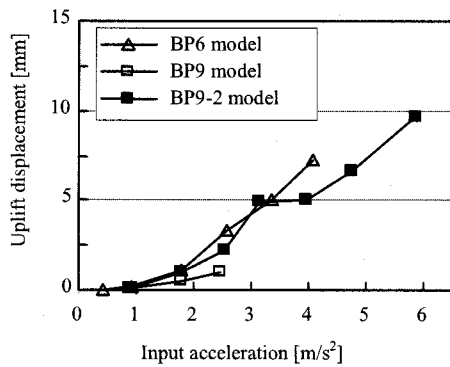


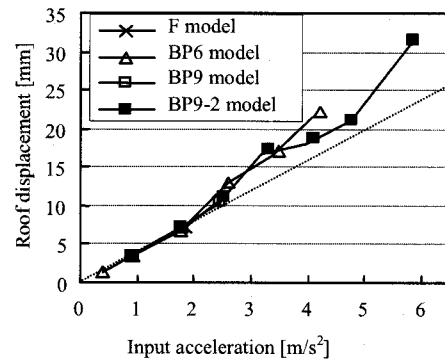
Figure 5 Time History of Shears at the bottom of columns of BP9-2 model
(Maximum Input Acceleration: 5.84 m/s^2)



(a) Base Shear



(b) Uplift Displacement



(c) Roof Displacement

Figure 6 Maximum Responses versus Maximum Input Acceleration

The uplift responses are very small when the maximum input acceleration is nearly up to 1.0 m/s^2 . As the input acceleration becomes larger, the uplift displacements increase monotonically. When the input acceleration becomes about 3.0 m/s^2 , the uplift displacements of BP9 and BP9-2 models reach about 5 mm.

The roof displacements of BP6 and BP9-2 models are not much different from the extrapolated one of F model up to the maximum input acceleration of 5.0 m/s^2 .

Figure 7 shows the story shear distribution along the height. When the maximum input acceleration is 0.9 m/s^2 , story shears of all models are not so different at each story. When the input acceleration becomes 3.5 m/s^2 , seismic response reduction effect of rocking structural systems is clearly observed and all story shears of BP6 and BP9-2 models are smaller than the extrapolated shears of F model.

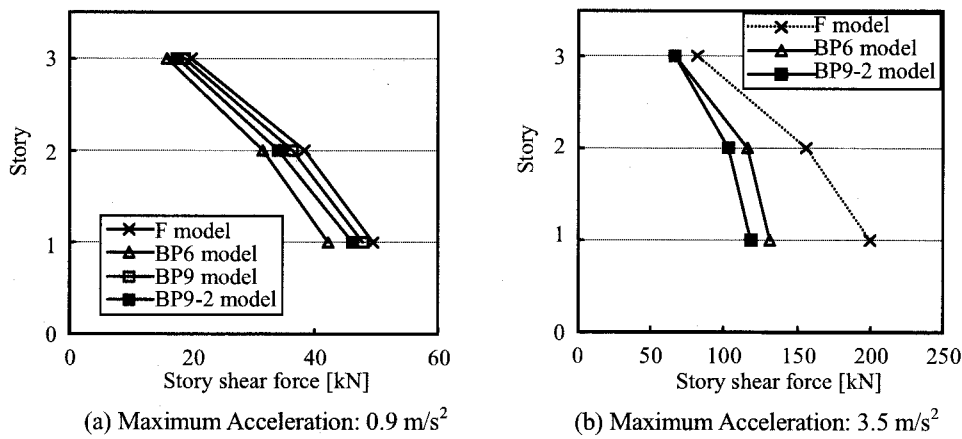


Figure 7 Maximum Story Shears

Figure 8 shows the relations between the maximum axial forces of columns and input acceleration. The variable ranges of axial forces are symmetrical in tension and compression when the input acceleration is small. On the other hand, the variable axial force in compression is larger than that in tension after the uplift motion occurs under larger input. Though the impact at landing after an uplifting motion affects the compressive forces of columns, they hardly exceed the extrapolated values of F model shown by dotted lines in the figure.

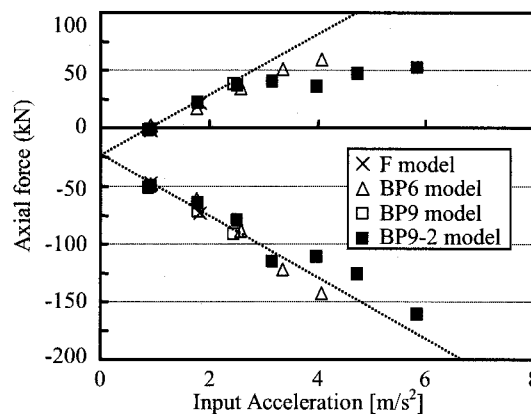


Figure 8 Maximum Axial Forces of Columns versus Maximum Input Acceleration

4. CONCLUSIONS

The seismic responses of the rocking structural systems with yielding base plates were examined comparing with those of the fixed base system by shaking table tests. The results of this study are summarized as follows:

- 1) Yielding base plates are successfully applicable to put structural rocking systems into practice.
- 2) The base plate yielding systems are able to reduce effectively the seismic responses.
- 3) The shear at the bottom of the column is transmitted reliably through the yielding base plate even when the column uplifts.
- 4) Though the impact at landing after an uplifting motion affects the compressive forces of columns, they hardly exceed the extrapolated values of the fixed base system.

Acknowledgements:

This work has been carried out under the US-Japan cooperative structural research project on Smart Structure Systems. The authors would like to acknowledge all project members for their useful advice and suggestions.

References:

- Azuhata, T., Midorikawa, M., Ishihara, T. & Wada, A. (2002), "Shaking Table Tests on Rocking Structural Systems with Base Plate Yielding", *Proc. of Structural Engineers World Conference 2002*, T2-7-a-2.
- Hayashi, Y. (1996), "Damage reduction effect due to basement uplift of buildings", *J. Struct. Constr. Eng.*, Architectural Institute of Japan **485**, 53-62. (In Japanese)
- Midorikawa, M., Azuhata, T., Ishihara, T., Matsuba, Y., Matsu-shima, Y. & Wada, A. (2002), "Earthquake response reduction of buildings by rocking structural systems", *Proc. SPIE, Smart Structures and Materials 2002*, 4696, 265-272.
- Rutenberg, A., Jennings, P. C. & Housner, G. W. (1982), "The response of Veterans Hospital Building 41 in the San Fernando Earthquake", *Earthquake Engineering and Structural Dynamics*, **10**(3), 359-379.

SEISMIC BEHAVIOR OF BEAM-COLUMN CONNECTIONS BASED ON DAMAGE-CONTROLLED-DESIGN

S. Kishiki¹⁾, S. Yamada²⁾, T. Takeuchi³⁾, and A. Wada⁴⁾

1) Graduate Student, Tokyo Institute of Technology, Japan

2) Associate Professor, Integrated Research Institute, Tokyo Institute of Technology, Japan

3) Associate Professor, Department of Civil Engineering, Tokyo Institute of Technology, Japan

4) Professor, Integrated Research Institute, Tokyo Institute of Technology, Japan

kishiki@serc.titech.ac.jp

Abstract: After the 1995 Kobe earthquake, a remarkable number of researches have been conducted on the beam-column connections. Those results have improved welding practices using higher material toughness and geometrical modification in the welded connections. Although the improved connections showed sufficient rotation capacity, little attention has been paid to repairing damage after an earthquake. At the stage of seismic design, it is important to consider restoring structures immediately. The purpose of this study is to propose new ductile MRF connections, which realize not only seismic performance but also easy repairing after an earthquake. In this paper, cyclic loading tests were conducted to evaluate composite effects on the new connection, and to compare damage to concrete slab with conventional connection. The test results indicated that the plastic rotation capacity of the new connection was hardly affected by the presence of concrete slab, and the new connection was beneficial in reducing damage to concrete slab.

1. INTRODUCTION

In the Northridge and Kobe earthquakes, some buildings lost structural functions, although many buildings avoided collapse as to save human life. The loss caused the termination of social and industrial activities, and severe economic loss. At the stage of seismic design, it is important to consider restoring structures immediately after an earthquake.

Today, most of high-rise buildings are designed according to the Damage-Controlled-Structure (Wada et al., 1992). This system consists of a mainframe and dampers as shown in Figure 1. The mainframe only supports gravity and can remain in the elastic range during an earthquake, because dampers absorb the input energy of the earthquake. Therefore, the structures designed based on the Damage-Controlled-Structure can be used continuously by repairing or exchanging dampers. However, in urban areas, most of steel structure buildings are low-rise or medium-rise without dampers. In the case of these buildings, naturally, energy absorption of an earthquake must be expected with plastic rotation of beam-ends. In the earthquakes mentioned above, many steel structure buildings suffered damage at the beam-end welded connection, and some fractures of beam-bottom-flange occurred at the connections. After the earthquakes, a remarkable number of studies have been made on the beam-end connections in the U.S. and Japan. Those results improved welding practices using higher material toughness and geometrical modification of the weld access hole in Japan. And the reduced beam section (RBS) has been proposed in the U.S. However, the improved details and the proposed designs are based on plastic deformation capacity at the welded beam-end or near here. Consequently, those have not considered the repairing of damage parts. The purpose of this study is to propose new

ductile steel MRF connections, which realize not only structural performance (deformation capacity) but also easy repairing after an earthquake. Moreover the structural performance and the easy repairing were verified from quasi-static cyclic tests.

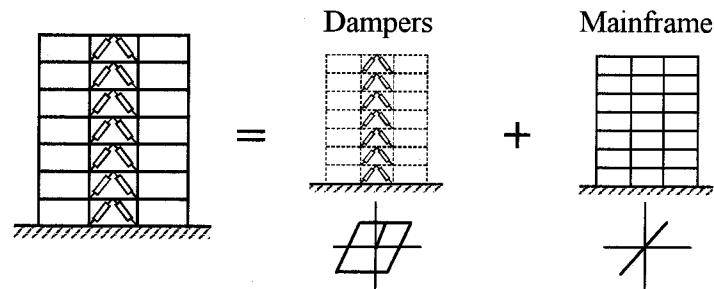


Figure 1 Damage-Controlled-Structure (Wada et al., 1992)

2. NEW DUCTILE MOMENT RESISTING BEAM-ENDS CONNECTIONS

It is important to realize structural performance and easy repairing, because conventional dampers, which are wall type, brace type, and shear link type, cannot be applied to low-rise and medium-rise steel structure buildings. Owners and designers like large windows (spaces).

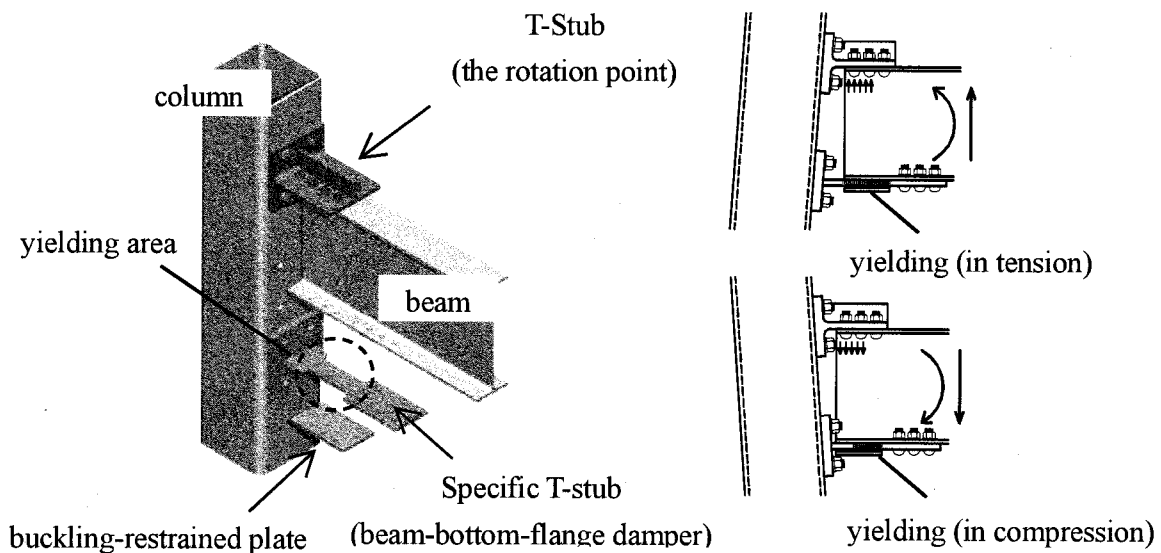


Figure 2 New MRF Connection based on Damage-Controlled Design

There are two conditions that must be met to make structures easy repairable. One of them is to constitute structures using exchangeable members. The other is limiting damage to some of these exchangeable elements as the Damage-Controlled-Structure mention above. New beam-end connection, which satisfies the two conditions, is shown in Figure 2. In the proposed connections, seismic damage (plastic deformation) is limited to specific T-stubs at the beam-bottom-flange. Consequently, plastic deformations are limited to the specific T-stubs at the beam-bottom-flange during an earthquake, and by repairing or exchanging the specific T-stubs, the steel structure buildings can be used continuously. Naturally, the specific T-stubs are not conventional because they have to show same stable behavior in tension and compression. In other words, they have to work as the

hysteretic dampers (the beam-bottom-flange dampers). The specific T-stubs have buckling-restrained weak-section on the flat-plate in Figure 2, and detail of the buckling-restrained method will be described later.

3. TEST PLANNING

3.1 Test Specimen and Test Set-up

A consist comparison was used for all specimen to evaluate composite effects. The tests were cantilever beam, cyclic-loading tests with a stiff, strong column as seen in Figure 3. Two pairs of specimen were tested. Each pair consisted of a bare steel specimen and similar specimen with a concrete slab attached. In the first pair, a conventional welded connection was applied. In the second pair, the proposed connection was investigated. Overall details are complied in Table 1.

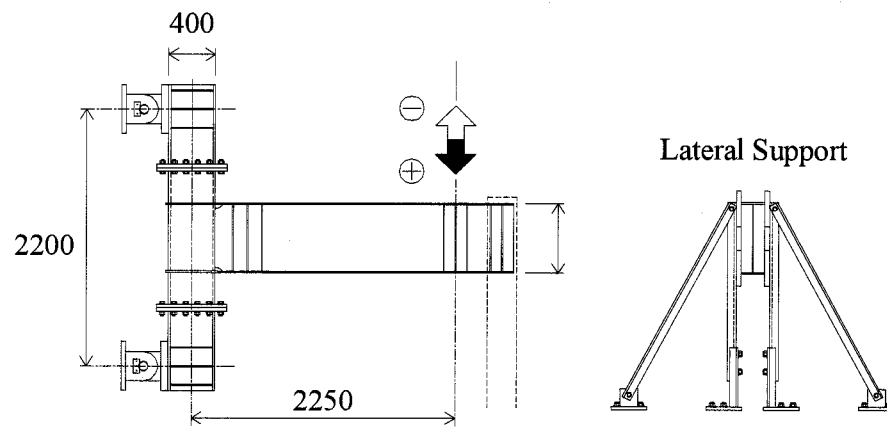


Figure 3 Test Specimen and Test Set-up (unit : mm)

Table 1 Specimen List

Specimen	Connection Detail	Composite or Bare Steel
W_B	conventional welding	bare steel
W_C	conventional welding	composite
T_B	with beam-bottom-flange damper	bare Steel
T_C	with beam-bottom-flange damper	composite

3.2 Beam, Column, and Connection

Beam with both connections was made of section (depth \times flange width \times web thickness \times flange thickness) of 600 \times 200 \times 9 \times 12. Column with the beam-bottom-flange dampers was H-shaped, and made of section of 400 \times 400 \times 16 \times 19. Steel grades JIS SS400 were chosen for flange and web of beam and column. Column with conventional welded connections was made of cold-formed square-tubes, and had section (width \times width \times thickness) of 400 \times 400 \times 19. Both columns were used to provide strong column, weak beam action and to provide for a strong panel zone. As shown in Table 2, mechanical properties were obtained from tensile coupon tests according to JIS-1A.

Details of beam-end connection are shown in Figure 4. The conventional welded connection referred to as a “through-diaphragm connection” is used (Nakashima et al., 1998). A beam was shop-welded by complete joint penetration (CJP) groove welds. Welds in the conventional connection

were made using the gas metal arc welding (GMAW) with CO₂ shielding was used to fabricate the welded joints of test specimens. A solid electrode designated as YGW-11 with a diameter of 1.2mm was used for all welding. Backing bars and weld tabs were left in place for the conventional connection.

In the new connection, the yield strength of the beam-bottom-flange damper was designed weaker than those of beam, column, and the T-stub at the beam-top-flange to keep the other member in the elastic range. The steel material used for the beam-bottom-flange dampers was the low yield point (LYP) steel. Mechanical properties of the LYP steel are shown in Table 2. Note that Young's modulus and Poisson's ratio of the LYP steel are identical to those of conventional structural steels.

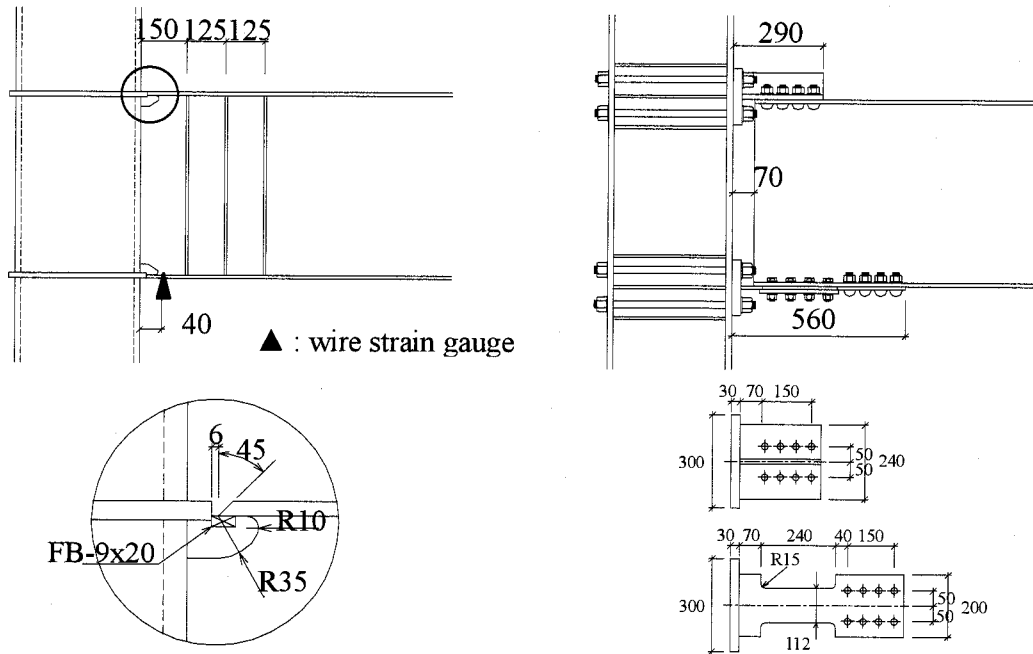


Figure 4 Details of Beam-End Connection (unit : mm)

Table 2 Mechanical Properties of Steel Plate

Sample plate & Thickness	Grade	Yield Strength [MPa]	Tensile Strength [MPa]	Elongation [%]
Beam-flange	SS400	279	429	31
Beam-web		296	435	33
Box Column	BCR295	388	439	27
Dampers	LYP225	244	298	39

3.3 Buckling-Restrained Method for the Beam-Bottom-Flange Damper

Detail of buckling-restrained method for the beam-bottom-flange dampers is shown in Figure 5. Yield area of the dampers was put between the beam-bottom-flange and the buckling-restrained plate. Unbounded material for removing friction has to be stuck on the yield area of the dampers. The buckling-restrained plate and beam-bottom-flange were connected through rings by high strength bolts. 2mm out-of-plate clearance was obtained by setting up the ring, because the yield area of the damper

had a thickness of 12mm and the rings had a thickness of 14mm.

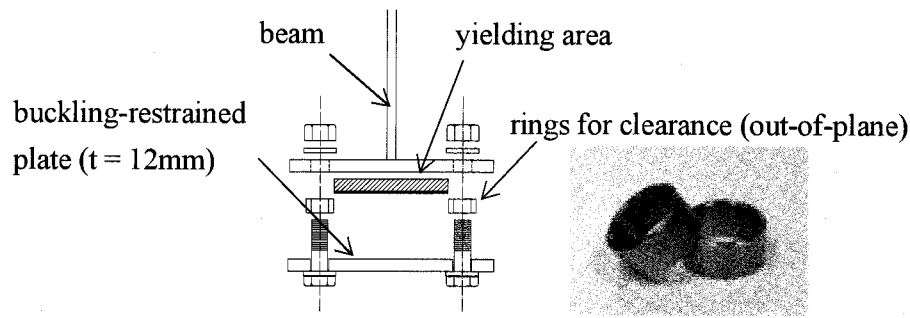


Figure 5 Detail of Buckling-Restrained for the Beam-Bottom-Flange Damper

3.4 Concrete Slab

Shear studs, which had a diameter of 19mm and a height of 80mm, welded in 140mm pitches. Wire-meshes were placed 25mm and 115mm above the beam-top-flange. Concrete, which had a thickness of 130mm, was placed on the beam-top-flange without metal deck sheets. Material properties of concrete shown in Table 3 were obtained from concrete cylinder tests on the same day of the cyclic loading tests.

Table 3 Mix Proportion and Compression Test (Concrete Slab)

W / C [%]	Sand [%]	weight per unit volume [kg/m ³]				
		water	cement	fine	coarse	admixture
55.5	47.5	162	292	863	968	0.73

Compression Test (average)

Young's modulus : 2.5×10^4 MPa]

Compressive Strength : 16.5 [MPa]

3.5 Loading Program

Quasi-static loading was carried out following to the loading program shown in Figure 6. The loading program was based on the rotation angle of beam, which were 1/100, 1/50, 1/33, and 1/25 radian. The cantilever beam had a length from the face of the column to the center of the load, L . The total tip deflection was due to elastic and plastic flexural deflection of the beam, δ . The rotation angle of beam can be found out by dividing the total tip deflection by L .

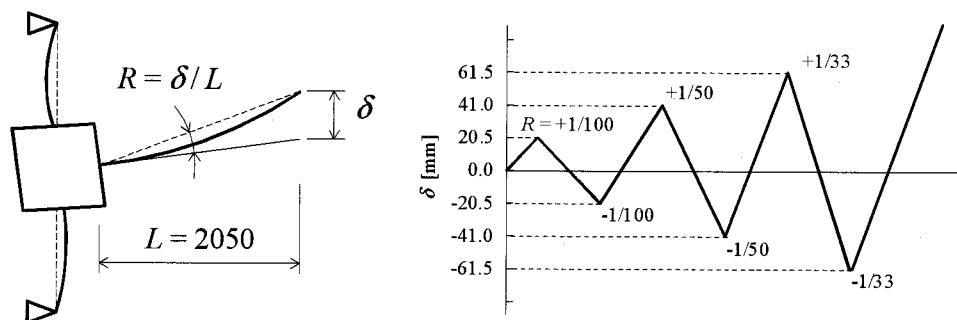


Figure 6 Loading Program

4. TEST RESULTS AND CONSIDERATION

4.1 Specimen Performance

The shear force versus the rotation angle of the beam is plotted for all specimens in Figure 7. Although specimen W_B and W_C ultimately failed during the cycles of 0.03 radian amplitude, W_C failed earlier than W_B. Failure mode of W_B was lateral buckling of beam. On the other hand, that of W_C was fracture of beam-bottom-flange near the toe of the weld access hole. It meant that the sudden change in geometry at the toe of the weld access hole caused a stress (and strain) concentration. The reason why the failure mode changed from lateral buckling to beam-bottom-flange fracture was that concrete slab resisted compression and the tensile strain at the beam-bottom-flange increased.

Although cracks were observed at the yielding area of the beam-bottom-flange damper, specimen T_B and T_C did not ultimately fail during the cycles of 0.05 radian amplitude. Composite action led to a roughly 98% increase in initial stiffness and 20% increase in yield strength. Nevertheless, T_B results, especially plastic rotation capacity, were very similar to T_C.

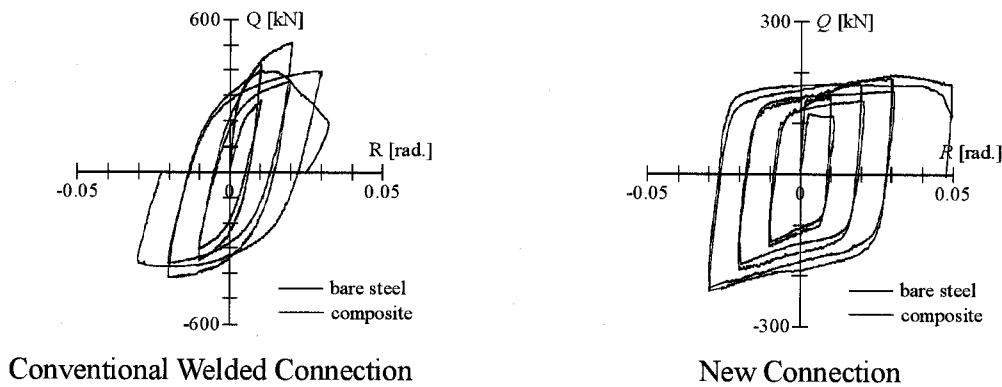


Figure 7 Specimen Performance (Shear Force (Q) versus Rotation Angle (R))

4.2 Composite Effects (especially, an increase in strain of beam-bottom-flange)

In the conventional welded connection (W_B and W_C), strain gauges were glued on the beam-bottom-flange as shown in Figure 4, in order to observe composite effects. In the new connection, an axial deformation of the beam-bottom-flange damper was measured by displacement transducers, and axial strain can be obtained by dividing the axial deformation by a length of the yielding area. Strain hysteresis of the beam-bottom-flange and the dampers are shown in Figure 8. In the conventional welded connection, composite action led to a roughly 50% increase in the tensile strain by the presence of concrete slab. In other words, the plastic deformation capacity of the conventional connection was affected by the presence of concrete slab. To opposite side of that, the symmetrical strain hysteresis was observed in the beam-bottom-flange damper. Further, the plastic strain at the beam-bottom-flange damper was increase by only 10%, indication that the new connection was hardly affected by the presence of concrete slab.

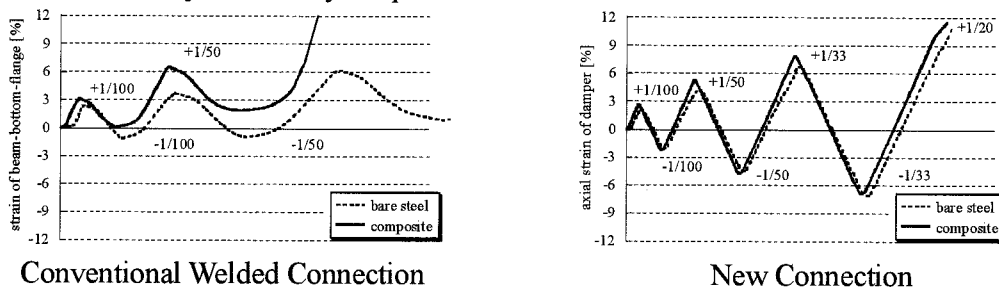


Figure 8 Strain of Beam-Bottom-Flange

4.3 Damage to Concrete Slab (crack pattern and maximum crack width)

Crack pattern and crack width were observed and written down, in order to grasp damage to concrete slab, when the rotation angle of the beam reached to 0, $-1/200$, $-1/100$, and $-1/50$ radian. Crack pattern and crack width obtained from the tests are shown in Figure 9. In the conventional welded connection specimen, cracks occurred on the entire slab. To the contrary, in the new connection, cracks were concentrated near the face of column where the beam-bottom-flange damper attached. The reason why cracks were concentrated near there was that plastic deformation was limited to the beam-bottom-flange damper.

When an attention is paid to the maximum crack width of both connections, it can be found out that the maximum crack width of the conventional connection specimen is gradually growing by subjected to cyclic loadings. To the contrary, the maximum crack width of the new connection specimen is hardly growing at the same rotation angle of beam (for example, $1/100$ radian). Further, when the rotation angle of beam changes from $1/100$ to $1/50$, the maximum crack width becomes twice. It indicates that there is a correlation between the maximum crack width and the axial strain of the damper (the axial deformation of the damper). Therefore, in this paper, the maximum crack width and the axial deformation of the damper are related by a calculation model shown in Fig.10. In Fig.9 (b), the red broken line is evaluation value, which is calculated by using the model and an experimental data of the axial deformation of the damper. The evaluation value of the maximum crack width is in good agreement with the experimental value.

5. CONCLUSIONS

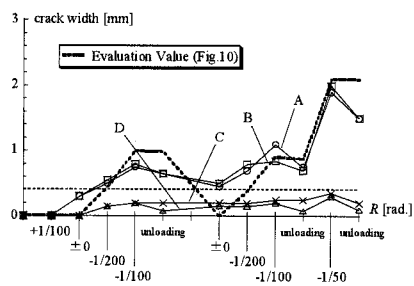
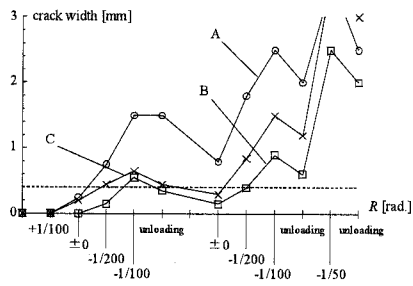
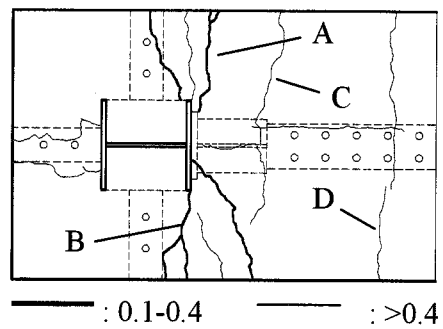
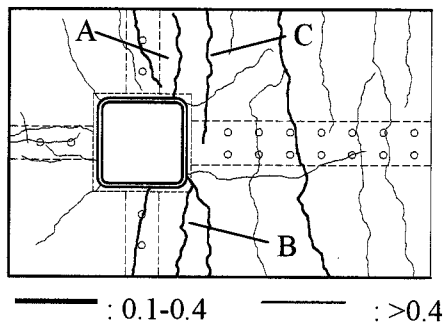
This paper presents an experimental study on new MRF connections designed to restrict damage to specific connection elements (T-stubs) placed at the beam-bottom-flange. Especially, composite effects and damage to the concrete slab were addressed in these tests. Composite action led to a roughly 98% increase in initial elastic stiffness and 20% increase in yield strength. Meanwhile, the plastic strain at the specific connection elements was increased by only 10%, indicating that the plastic rotation capacity of the connections was hardly affected by the presence of the concrete slab. And the feature of the design forcing the connection to rotate about the beam-top-flange was beneficial in reducing damage to the concrete slab (cracks).

Acknowledgements:

The author would like to thank the following for their assistance in conducting the experiments: Mr. Kazuaki Suzuki, Dr. Eiichiro Saeki in Nippon Steel Corporation, Mr. Daisuke Uehara, Mr. Tsugutomo Okayasu (former graduate student) in Tokyo Institute of Technology.

References:

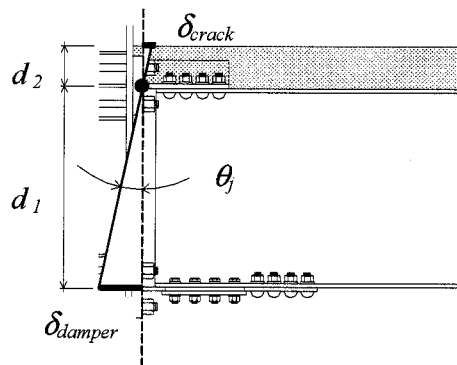
- Nakashima, M., Suita, K., and Maruoka, Y. (1998), "Tests of Welded Beam-Column Subassemblies 1 Performance," *Journal of Structural Engineering*, American Society of Civil Engineers
- Wada, A., Conner, J.J., Kawai, H., Iwata, M., and Watanabe, A. (1992), "Damage Tolerant Structure," *5th U.S.-Japan Workshop on the Improvement of Building Structural Design and Construction Practice*



Conventional Welded Connection

New Connection

Figure 9 Crack Pattern and Maximum Crack Width



$$\delta_{crack} = \delta_{damper} \frac{d_2}{d_1}$$

Figure 10 Calculation Model for Evaluation Maximum Crack Width of Concrete Slab

STUDY ON FRACTURE AND ULTIMATE PERFORMANCE OF STEEL BEAM-TO-COLUMN CONNECTIONS

Y. Matsumoto

*Associate Professor, Department of Architecture and Building Science, Yokohama National University, Japan
yuka@arc.ynu.ac.jp*

Abstract: The deformation capacity of fractured member tends to have large dispersion, and it is difficult to verify the reliability and applicability of empirical knowledge. That is partly because the deformation capacity depends on the strain distribution in longitudinal direction as well as the fractured section's performance. In this study, the full-scale test results of previous researches were evaluated in terms of strain hardening level in order to investigate the fractured section's performance exclusively. As the result, it was confirmed that material toughness or current improved scallop was effective to prevent the deterioration of strain-hardening in fractured flanges. Without the deterioration, the approximate method provided satisfactory estimation of beam's deformation capacity.

1. INTRODUCTION

The prevention of premature fracture at beam-to-column connection is a major issue for the structural design of moment resistant steel frames. In Japan, many research organizations have performed plenty of full-scale subassembly's tests, especially after Hyogoken-Nanbu earthquake. Because the experimental data has large dispersion, however, it is difficult to verify the reliability and applicability of empirical knowledge by comparing with the other test series.

The ultimate capacity of fractured member depends on various factors, such as scale, geometric discontinuity, material property and loading speed. Therefore, certain degree of dispersion is unavoidable. However, there is some scope to improve the evaluation method of member's performance. Generally, the ultimate performance of beam is evaluated in terms of deformation capacity. The deformation depends on the strain distribution in longitudinal direction as well as the fractured section's performance, so the information of un-fractured part's behavior is included. Therefore, the maximum moment capacity at beam end is more suitable indicator in order to investigate fractured section's performance exclusively and clarify the fracture mechanism.

The aim of this study is to investigate the fracture at beam end reported by previous researches and to derive the common tendency. For this purpose, the strain-hardening level of specimen was evaluated, and its correlation with various factors was examined.

2. METHOD OF STUDY

2.1 Outline of design practice and concept of this study

The shop-welded beam-to-column connections shown in figure 1 are adopted for moment resistant frames in Japan. Figure 1 (a) shows the prevalent connection type with rectangular hollow section

column and through diaphragm. The beam's flange is connected to the diaphragm by groove weld, and the beam's web is connected to column's flange by fillet weld. The connection types shown in figure 1 (b) and (c) are adopted for welded built-up column and H-shaped column, respectively.

Generally, the flange's fracture starts from stress concentration points at the scallop tip or the run-off tabs. The scallop and out-plane deformation of column's flange reduce the moment capacity of the beam's web, and this phenomenon increases stress and strain in flanges.

The estimation method of maximum moment at beam end, ${}_jM_u$, was proposed in the design recommendation of Architectural Institute of Japan (AIJ, 2001).

$${}_jM_u = {}_jM_{fu} + {}_jM_{wu} \quad (1)$$

where ${}_jM_{fu}$ and ${}_jM_{wu}$ are maximum moment of flanges and web, respectively.

$${}_jM_{fu} = b_f \cdot t_{bf} (d_b - t_{bf}) \sigma_{fu} \quad (2)$$

where b_f , t_{bf} , d_b and σ_{fu} are beam flange's width, thickness, depth and tensile strength, respectively.

$${}_jM_{wu} = m \cdot Z_{wpe} \cdot \sigma_{wy} \quad (3)$$

where m , Z_{wpe} and σ_{wy} are coefficient to consider the out-plane deformation of column flange, plastic section modulus calculated in consideration of the section loss by scallop and yield point stress of web, respectively.

The web's moment capacity was experimentally evaluated in previous researches (Matsumoto et al. 1999 and Okada et al. 2002). The experimental moment capacity, M_{wp_ex} , is compared with ${}_jM_{wu}$ obtained by equation (3) in figure 2. The M_{wp_ex} is corresponding to the ${}_jM_{wu}$, and it is conceivable that equation (3) provides appropriate estimations. On the other hand, equation (2) is based on the hypothesis that the maximum stress of fractured flange reaches the tensile strength obtained by coupon test, and the premature deterioration because of brittle fracture is ignored. Therefore, the fractured flange's resistance to brittle fracture is able to be evaluated in terms of $M_{max}/{}_jM_u$, the ratio of experimental maximum moment M_{max} to ${}_jM_u$ obtained by equation (1), (2) and (3). If $M_{max}/{}_jM_u$ is lower than 1, the strain hardening of flanges doesn't reach the level of σ_{fu} .

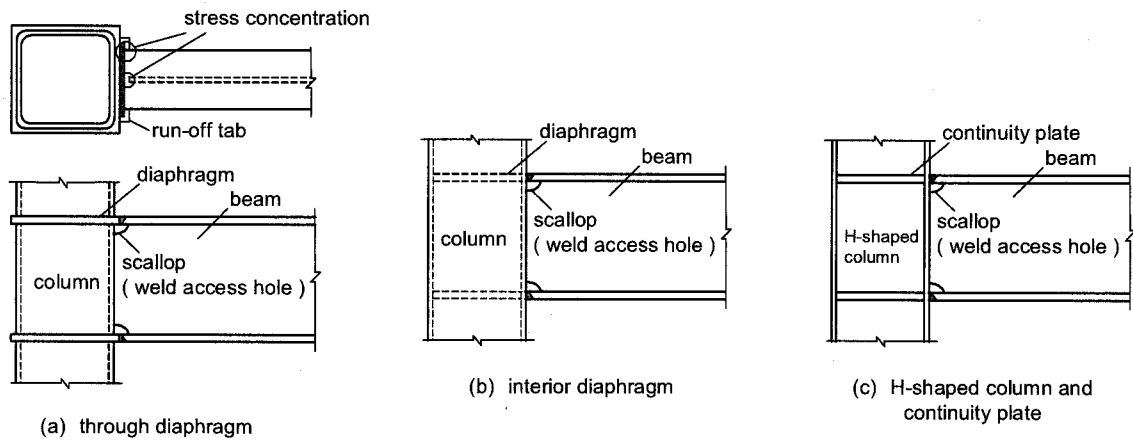


Figure 1 Connection Type of Moment Resistant Frame in Japan

It is important for structural design to identify the condition that keeps M_{max} higher than jM_u and prevents the underestimation of beam's ultimate performance. The relation between M_{max}/jM_u and various factors was investigated in the following sections.

2.2 Specimens of Previous Researches

Referring to journals issued by AIJ or Japanese Society of Steel Construction (JSSC) from 1991 to 2002, a total of 166 full-scale test specimens were taken as objects in this study. The following points were considered in sorting these specimens.

- Tensile strength of beam flange satisfies the specification of JIS SS400 or SM490.
- The ultimate behavior is fracture at beam end.
- The material toughness of fracture starting point, whether it is base metal, welding metal or heat affected zone, is identifiable.

Table 1 shows the number of specimens, n , according to connection type shown in figure 1. Table 2 shows the distribution of beam's depth and thickness of flange. Table 3 shows the distribution of material strength of beam's flange.

Generally, the brittle fracture is triggered by ductile crack which is generated at the scallop tip or the run-off tabs, and the condition of these spots is an important issue. Figure 3(a) shows the prevalent scallop shape before Hyogoken-Nanbu earthquake. Figure 3 (b) and (c) shows improved scallop intended to mitigate the geometrical notch effect and stress concentration. Especially, type (b) is recommended in JASS6 (AIJ 2002). Figure 3 (c) shows non-scallop type.

Steel run-off tab is conventionally remained after welding. As improved method, steel tab is removed or flux tab is adopted in stead of steel tab.

The connection detail is categorized according to the scallop type and run-off tab. Table 4 shows the specimen's number of each group.

Table 1 Connection Type

Connection Type	n
Rectangular hollow section column with through diaphragm	115
Rectangular hollow section column with interior diaphragm	42
H-shaped section column with continuity plates	9

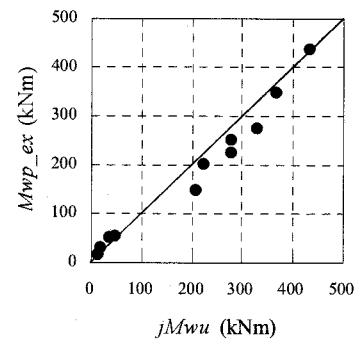


Figure 2 The Estimation of Web's Moment Capacity

Table 2 Beam's Section

d_b (mm)	n	t_{bf} (mm)	n
$d_b \leq 450$	53	$t_{bf} \leq 16$	32
$450 < d_b \leq 500$	57	$16 < t_{bf} \leq 19$	23
$500 < d_b \leq 550$	5	$19 < t_{bf} \leq 22$	15
$550 < d_b \leq 600$	51	$22 < t_{bf} \leq 25$	68
		$25 < t_{bf}$	28

Table 3 Material Strength

σ_{fy} (N/mm ²)	n	σ_{fu} (N/mm ²)	n
$\sigma_{fy} \leq 275$	4	$\sigma_{fu} \leq 450$	18
$275 < \sigma_{fy} \leq 300$	30	$450 < \sigma_{fu} \leq 475$	19
$300 < \sigma_{fy} \leq 325$	11	$475 < \sigma_{fu} \leq 500$	2
$325 < \sigma_{fy} \leq 350$	55	$500 < \sigma_{fu} \leq 525$	65
$350 < \sigma_{fy} \leq 375$	43	$525 < \sigma_{fu} \leq 550$	41
$375 < \sigma_{fy} \leq 400$	10	$550 < \sigma_{fu} \leq 575$	16
$400 < \sigma_{fy}$	13	$575 < \sigma_{fu}$	5

Table 4 Connection Detail

Scallop	Run-off Tab	n
Conventional (SC)	steel	42
	steel-removed	12
	flux	33
Improved (IS)	steel	22
	steel- removed	5
	flux	20
Non-Scallop (NS)	steel	30
	steel- removed	2
	flux	-

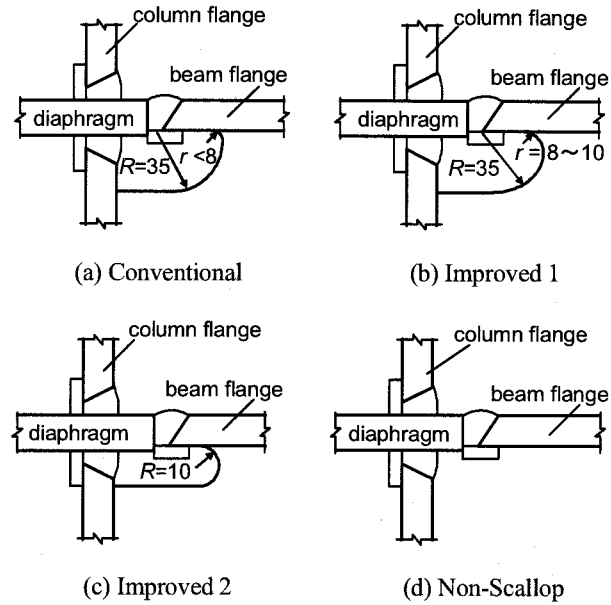


Figure 3 Scallop Type

Another point of view is loading speed. 144 tests were static loading, and 22 tests were dynamic loading. The maximum strain rate of flange was approximately 10-100%/sec.

3. RESULTS

3.1 Effect of fracture mode

Fracture modes are categorized into “brittle” and “ductile.” The brittle mode in this study is defined as one of the following cases.

- The depth of ductile crack that triggered the brittle fracture is less than 3mm.
- The author remarks that the ductile fractured surface is invisible without scope.
- It is conceivable from the photo or sketch in paper that the fractured surface is equivalent to the above two cases.

The starting point of brittle fracture is crack at the scallop tip for almost all specimens categorized as brittle mode. The ductile mode is defined as the case in which deeper ductile crack was propagated than those of the brittle one. Some specimen's fracture mode is not identifiable.

Figure 4(a) shows the relation of M_{max}/M_u and Charpy dissipated energy at fractured area, vEt , in case of static loading. The temperature of Charpy impact test is equivalent to those of the full-scale test. When vEt is less than 50J, every specimen's fracture mode is brittle, and M_{max}/M_u is scattered form 0.8 to 1.2. On the other hand, when vEt is more than 50J, the fracture mode is mainly ductile and M_{max}/M_u of most specimens reaches 1. This tendency is observed more remarkably in case of dynamic loading, which is shown in figure 4(b). Therefore, strain-hardening level is susceptible to the particular condition in case of brittle fracture, and it is reasonable to control the fracture mode in order to establish a reliable estimation method of ultimate performance.

3.2 Effect of Connection details

Figure 5 shows the relation of M_{max}/M_u and vEt according to the connection details. When vEt is less than 50J, M_{max}/M_u is lower than 1 in considerable specimens with conventional scallops. On the other hand, almost specimen's M_{max}/M_u reaches 1 when vEt is higher than 50J. This tendency means that tough material prevented the deterioration of strain-hardening in spite of geometrical notch effect.

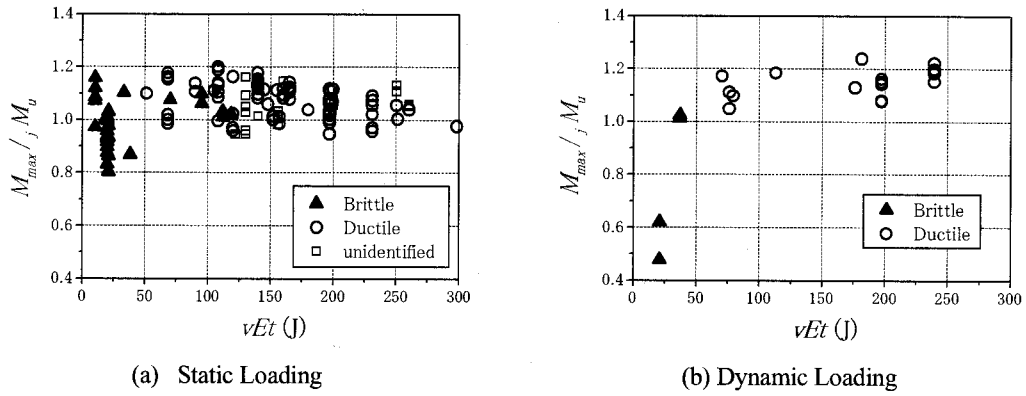


Figure 4 Relation of Strain-Hardening and Material Toughness According to Fracture Modes

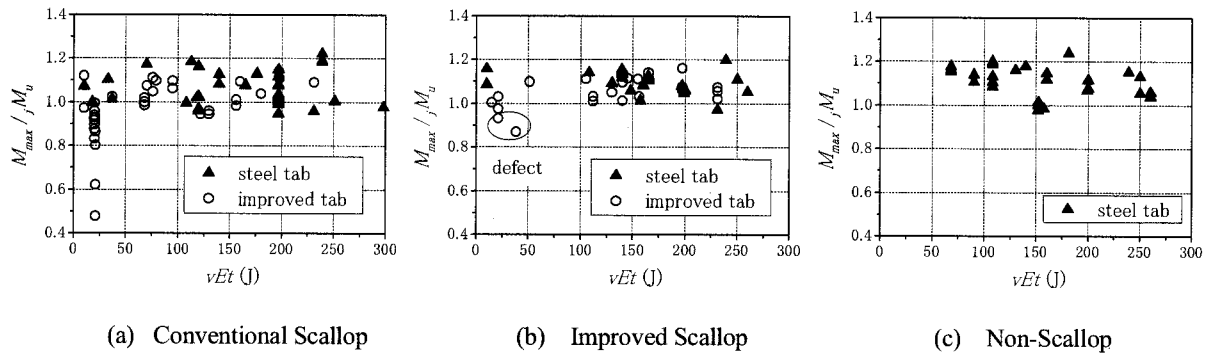


Figure 5 Relation of Strain-Hardening and Material Toughness According to Connection Details

It seems from figure 5 (a) that the strain-hardening deteriorated in specimens with improved tabs. However, conceivably run-off tab didn't have any practical effects because brittle mode was mainly caused by crack at scallop tip.

Figure 5 (b) shows the case of improved scallop. The marks in circle indicate the specimens in which defects were found around scallop tips. Except for the specimens with defects, almost all specimens' M_{max}/M_u reach 1 regardless of vEt . Therefore, the deterioration of strain-hardening was mitigated when the geometrical notch at scallop tip was eliminated.

Figure 5(c) shows the case of non-scallop. Every specimen's vEt is higher than 50J, and almost all specimens' M_{max}/M_u reach 1.

As a result, it was confirmed that material toughness or current improved scallop is effective to mitigate the deterioration of strain-hardening and prevent the underestimation of section's ultimate capacity. In case of improved scallop, careful manufacture is required.

Because the brittle mode caused by run-off tab occurred in very few specimens, the effect of run-off tab wasn't observed clearly. The condition of this area is so complicated because of weld defect, slit and distribution of material property that further researches are required.

3.3 The Estimation of Deformation Capacity

It is crucial to ensure that the maximum strength of connection exceeds the member's yield strength in order to develop the member's plastic deformation before the connection's fracture. In AIJ recommendation, the design criterion for beam end is based on the concept that the ratio of M_u to beam's general yield moment, M_p , is corresponding to the beam's deformation capacity (AIJ 2001). Akiyama described the concept by modeling the moment-rotation curve as bi-linear shown in figure 6, and approximate method of maximum rotation was proposed (Akiyama et al. 1997).

$$\theta_{max} - \theta_p = \frac{M_{max} - M_p}{D_{st}} \cong \frac{M_{max} - M_p}{0.03D} \quad (4)$$

where θ_p , θ_{max} , D and D_{st} are elastic rotation corresponding to M_p , maximum rotation, elastic gradient and second gradient of $M-\theta$, respectively. When ${}_jM_u$ is substituted for M_{max} and the equation is divided by θ_p , plastic deformation capacity ratio under monotonic loading, η_{pM} , is estimated as follows.

$$\eta_{pM} = \frac{\theta_{max}}{\theta_p} - 1 = \frac{D}{M_p} \cdot \frac{{}_jM_u - M_p}{0.03D} = \frac{1}{0.03} \left(\frac{{}_jM_u}{M_p} - 1 \right) \quad (5)$$

Because almost all tests were cyclic loading, the experimental η_{pM} should be evaluated based on a hystereses law in order to verify the reliability of this method. For this purpose, the specimens whose loading sequences were described in detail were selected among those in the preceding sections.

The following equations were proposed in order to describe the relation among η_{pM} , $\bar{\mu}_p$ which is ratio of plastic amplitude to θ_p and number of cycles until fracture, N_f (Ichinohe et al. 2000).

$$N_f = \frac{\eta_{pM}}{\bar{\mu}_p} \left(\frac{\eta_{pM}}{\bar{\mu}_p} - 1 \right)^{\frac{2}{3}} \quad (\bar{\mu}_p \leq \frac{\eta_{pM}}{2}) \quad (6)$$

$$N_f = \frac{\eta_{pM}}{\bar{\mu}_p} \quad (\bar{\mu}_p > \frac{\eta_{pM}}{2}) \quad (7)$$

The experimental η_{pM} is obtained by applying the equation (6), (7) and Miner's law to the loading sequence until fracture.

Figure 7 shows the relation of experimental η_{pM} and estimated one obtained by equation (4) and (5). The mark \times indicates the case in which M_{max} is lower than ${}_jM_u$. Except for these specimens, experimental η_{pM} exceeds estimated one. Although the data shows large dispersion, the approximate method provided satisfactory estimation in order to prevent unexpected fracture. Meanwhile, this figure shows that it is essential to keep M_{max} higher than ${}_jM_u$ by some limitations for material or details.

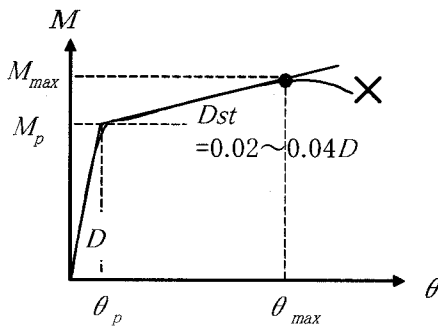


Figure 6 Model of $M-\theta$ relation

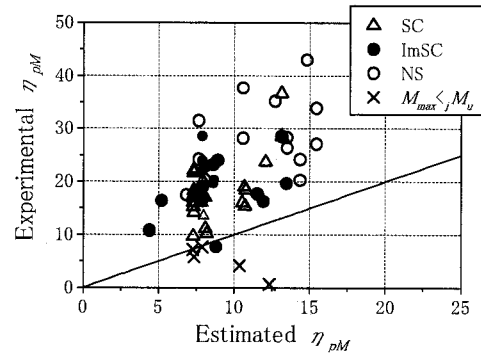


Figure 7 The estimation of deformation capacity

4. CONCLUSIONS

The full-scale test results of previous researches were evaluated in terms of M_{max}/M_u , which represents the strain hardening level in fractured flanges. The relation between M_{max}/M_u and various factors was investigated in order to identify the condition that keeps M_{max} higher than M_u and prevents the underestimation of beam's ultimate performance. As the result, it was confirmed that material toughness or current improved scallop mitigated the deterioration of strain-hardening in fractured flanges. When M_{max} was higher than M_u , the approximate method provided satisfactory estimation of beam's deformation capacity

References:

- Architectural Institute of Japan (2001), "Recommendation for Design of Connections in Steel Structures"
- Matsumoto, Y., et al. (1999), "Relation between Deformation Capacity of Beam at Steel Beam-to-Column Connection and Joint Efficiency," *J. Struct. Constr. Eng.*, AIJ, No.523, 117-124.
- Okada, K., et al. (2002), "Relationship between Joint efficiency and strain concentration rate of H-shaped Steel Beam," *Summaries of Technical Papers of Annual Meeting*, AIJ, c-1,749-750.
- Sayanagi, M. et al. (1991), "The Behavior of RHS-Column to H-Shaped Beam Connections with Interior Diaphragms (Part 1)," *Proc. of Architectural Research Meetings*, AIJ Kinki Branch, No.31, 329-332.
- Sonoda, R. et al. (1992), "The Behavior of RHS-Column to H-Shaped Beam Connections with Interior Diaphragms (Part 2)," *Proc. of Architectural Research Meetings*, AIJ Kinki Branch, No.32, 265-268.
- Nakagomi, T. et al. (1992), "Effect of Scallop at Beam-End on Mechanical Behaviors of H-shaped Steel Beams Connected to H-shaped Column," *J. Struct. Constr. Eng.*, AIJ, No.432, 51-59.
- Yabe, K. et al. (1992), "Effect of Scallop at Beam-End on Mechanical Behaviors of H-shaped Steel Beams Connected to Box Column," *J. Struct. Constr. Eng.*, AIJ, No.440, 125-132.
- Tanaka, T. et al. (1993), "The Behavior of RHS-Column to H-Shaped Beam Connections with Through Diaphragms (Part 6)," *Proc. of Architectural Research Meetings*, AIJ Kinki Branch, No.33, 209-212.
- Tabuchi, M. et al. (1993), "Improvement on Scallop Shape in RHS Column-to-H Beam Connections by Welding," *J. Constructional Steel*, JSSC, Vol.1, 65-72.
- Ishii, T. et al. (1993), "Influence of Geometrical condition of Weld Access Hole on the Deformation capacity of Flange at Welded Beam End Connection," *Summaries of Technical Papers of Annual Meeting*, AIJ, c, 1255-1256.
- Makishi, T. et al. (1993), "Experimental study on the Deformation capacity of Welded Beam End Connection without Weld Access Hole (Part 1, 2)," *Summaries of Technical Papers of Annual Meeting*, AIJ, c, 1257-1260.
- Yamamoto, N., et al. (1993), "Influence of Weld Access Hole on the Fracture of Flange at Welded Beam End Connection," *J. Structural Engineering*, AIJ, JSCE, Vol.39B, 493-506.
- Inoue, K., Kohzu, I. et al. (1997), "Full-Scale Test on Plastic Rotation Capacity of Steel Wide-Flange Beams Connected with Square Tube Steel Columns (Part1-4)," *Steel Construction Engineering*, JSSC, Vol.4, No.16, 27-87. (in Japanese)
- Nakagomi, T. et al. (1997), "Study on Beam-End Details for the Method of Non-Scallop on Beam-to-Column Welded Joints," *J. Struct. Constr. Eng.*, AIJ, No.498, 145-151.
- Akiyama, H., et al. (1998), "Study on Fracture of Beam-to-Column Connections by means of Full Scale Shaking Table Test," *J. Struct. Constr. Eng.*, AIJ, No.512, 165-172.
- Saragai, Y., et al. (1998), "Effects of Beam-End Details on Structural Behaviors at Steel Beam-to-Column Connections," *Summaries of Technical Papers of Annual Meeting*, AIJ, c-1,373-374.
- Kikukawa, S., Mukai, A. et al. (1998), "Fracture Behavior of Beam-to-column Connections with Low Toughness Steel (Part 1-6)," *Summaries of Technical Papers of Annual Meeting*, AIJ, c-1,407-418.
- Akiyama, H., et al. (1999), "Transition from Ductile Fracture to Brittle Fracture of Full Scale Beam-to-Column Connections Caused by Temperature", *J. Struct. Constr. Eng.*, AIJ, No.522, 105-112.
- Kikukawa, S., Ishii, T. et al. (1999), "Fracture Behavior of Beam-to-column Connections (Part 1, 2)," *Summaries of Technical Papers of Annual Meeting*, AIJ, c-1,473-476.
- Azuma, K. and Suzuki, T. (1999), "Fracture Behaviour of Built-up H-Shaped Beams Connected to Box Column," *Summaries of Technical Papers of Annual Meeting*, AIJ, c-1,477-478.
- Emoto, D. et al. (1999), "Effects of Beam Flange width-thickness ratios on Beam Flange Fracture Caused from Scallop Tip," *Proc. of Architectural Research Meetings*, AIJ Kinki Branch, No.39, 245-248.
- Harada, Y., et al. (2000), "Experimental Study on Brittle Fracture in Beam-to-Column Connections," *J. Struct. Constr. Eng.*, AIJ, No.535, 141-148.
- Kawanori, A. and Kohzu, I. (2000), "Study on Mechanical Property of Site Welding type Beam-to-Column Connection

- (Part1)," *Steel Construction Engineering*, JSSC, Vol.7, No.28, 71-85.
- Nakagomi, T., et al.(2001),"Experimental Study on Effect which Mechanical Property of Beam Material gives to Deformation Capacity of Beam to Column Welded Connection," *J. Struct. Constr. Eng.*, AIJ, No.540, 111-117.
- Nakagomi, T. et al. (2001),"Experimental Study on the Effects of Beam-End Details for the Non-Scallop Method on Deformation Capacities of Beam-to-Column Welded Joints," *J. Struct. Constr. Eng.*, AIJ, No.546, 121-128.
- Matsumoto, Y., et al. (2002), "Fracture of Beam-to-Column Connections Simulated by Full-Scale Shaking Table Test and Evaluation of Deformation Capacity," *J. Struct. Constr. Eng.*, AIJ, No.560, 181-188.
- Architectural Institute of Japan (2002), "JASS6 Structural Steelwork Specification for Building Construction"
- Akiyama, H., and Yamada, S. (1997), "Estimation of Earthquake Resistance of the Moment Resistant Steel Frames under the Hyogoken-Nanbu Earthquake," *J. Struct. Constr. Eng.*, AIJ, No.501, 151-157.
- Ichinohe, Y. and Kuwamura, H. (2000),"Effects of Deflection Amplitude on brittle fracture of steel members – Research on Steel Fracture Part3 –, " *J. Struct. Constr. Eng.*, No.534, 145-151.

PROPOSAL OF A REMOTE BRIDGE MONITORING SYSTEM FOR DAMAGE DETECTION

E. Sasaki¹⁾, C. Miki²⁾, M. Tohmori³⁾, Y. Ishikawa⁴⁾, and S. Miyazaki⁴⁾

1) Associate Professor, Faculty of Environment and Information Sciences, Yokohama National University, Japan

2) Professor, Department of Civil Engineering, Tokyo Institute of Technology, Japan

3) Graduate Student, Department of Civil Engineering, Tokyo Institute of Technology, Japan

4) Research and Development Headquarters, NTT DATA CORPORATION, Japan

esasaki@cvg.ynu.ac.jp, miki@cv.titech.ac.jp, tohmori@cv.titech.ac.jp,

ishikawayuj@nttdata.co.jp, wakamatsus@nttdata.co.jp

Abstract: Based on the lessons from the 1995 Hyogo-ken Nanbu Earthquake, it has been important to establish a bridge monitoring system that can detect damage level immediately after earthquakes and can judge whether the route can be open to the traffic or not. In this study, a new remote bridge monitoring system was proposed and a prototype system was actually developed. The proposed monitoring system consists of fiber optic sensors directly connected fiber optic information network and diagnosis and alarm functions. The arrangement of the sensors was proposed to detect the damage based on the investigations on the damage in bridges in the Hyogo-ken, Naubu Earthquake. Finally, the functions of the prototype system were verified by a loading test of modeled elevated bridges system.

1. INTRODUCTION

In the Hyogo-ken Nanbu Earthquake, many structures including bridges were damaged (Japanese Society of Civil Engineers, 1997). The investigations on the damage revealed that if the damage due to the earthquake was detected and the damage level of each route was diagnosed immediately after the earthquake, rescue operation and transportation of relief goods could have been efficient and the secondary damage could have been reduced.

In addition, when earthquakes over a certain level occur, road administrators must check the damage by visual inspection with the route closed to the traffic. If the damage in bridges can be detected by a monitoring system from a remote station, time up to the reopen to the traffic can be reduced. Even if the visual inspection is needed, the inspection can be efficient because the damaged bridges could be listed by the monitoring system.

In Japan, fiber optic information network was already set by the government along almost all the major national highway roads for the maintenance of them. In order to utilize the network, one of the authors proposed a remote bridge monitoring system (Miki et al, 2001) and developed an automatic vehicle weights analysis system (Miki et al, 2004). However, these investigations also revealed that devices using power sources at the site have the disadvantage of the weakness against dust, power cuts, and thunderbolts. Therefore, the authors attempted to apply fiber optic sensors that have strong advantages of durability (Kobayashi et al, 2003). They also don't need power sources at the site because the laser can be sent from a remote place, and they are promising sensors (Tsuda et al, 2005) for bridge monitoring for long term.

In this study, a new remote bridge monitoring system was proposed, and the prototype system was developed and verified by experiments using modeled elevated bridges. In the proposed monitoring

system, fiber optic sensors directly connected to fiber optic information network were arranged to detect various types of bridge damage due to earthquakes, and the developed diagnosis and alarm functions were installed. The proposed monitoring system is aiming to diagnose the damage of bridges and to show the proper traffic control level from the four levels of “No traffic is allowed”, “Only emergency and rescue vehicles can pass carefully”, “The maximum speed is limited”, and “No restriction (Open to any traffic)”. The selection and the arrangement of sensors is the key issue in this study. In the following chapters, the selection of sensors was discussed, and the arrangement of sensors was proposed based on the investigations on the damage due to the Hyogo-ken Nanbu Earthquake.

2. SELECTION OF FIBER OPTIC SENSORS

As fiber optic sensors, several types have been developed. In this study, FBG (Fiber Bragg Grating) sensors and OTDR (Optical Time Domain Reflectometer) sensors were focused on. FBG sensors can measure strain dynamically at 250 Hz or more of sampling frequency at multiple points by connecting the sensors. Recently, FBG sensors have been used to develop new sensors like accelerometers (Mita et al, 2003) and AE sensors (Tsuda, 2003).

On the other hand, OTDR system can detect the occurrence of bending or breakage of fiber and the location of the damage by analyzing the optical power reduction. Also, OTDR system can use for long distance over 10km as well as FBG sensors.

In this study, in order to detect damage due to earthquakes, FBG sensors and OTDR system were applied by considering their characteristics as mentioned above. Accurate displacement meters were developed by using FBG sensors, and they can measure the displacements between bridge girders immediately by their dynamic measuring ability. The arrangement of the displacement meters was discussed in the next chapter. As for OTDR system, the application to detect the occurrence of extraordinary damage such as large movement or falling of bridges is suitable.

The developed displacement meters using FBG sensors and the FBG analyzer used in this study are shown in Figure 1 and Figure 2. The capability of the FBG analyzer is shown in Table 1. In addition, the used OTDR analyzer is shown in Figure 3.

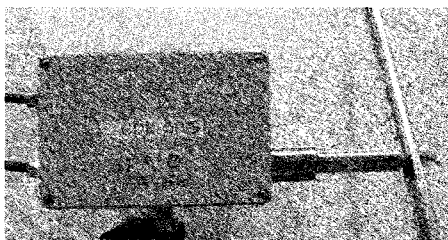


Figure 1 FBG Displacement Meter (Capacity: 50mm)

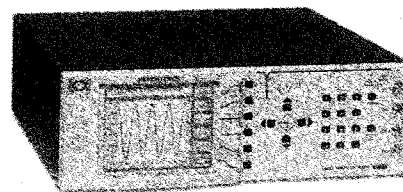


Figure 2 FBG Analyzer

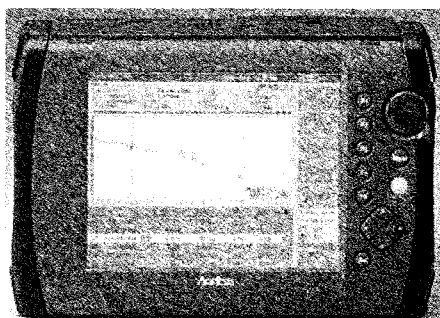


Figure 3 OTDR Analyzer

Table 1 Capability of Used FBG Analyzer

Number of Channels	4
FBG Connection Capacity	512 (128/Channel)
Bragg Wavelength Range (nm)	1520-1570
Resolution (pm)	1
Scanning Frequency (Hz)	250
Working Temperature (degree of Celsius)	-10 to 40

3. PROPOSAL OF SENSOR ARRANGEMENTS FOR DAMAGE DETECTION

3.1 Investigations on Bridge Damage due to Earthquakes

According to the investigations on the damage in bridges in the Hyogo-ken Nanbu Earthquake (Japanese Society of Civil Engineers, 1999), various bridge damage modes were observed, and they were assorted into two groups of “Primary Damage” and “Secondary Damage”. Considering the causal relationship between the damage modes, a damage tree diagram as shown in Figure 4 can be arranged. In Figure 4, it can be found that the modes of pier movements, pier settlements, pier inclinations, shoe failures are connected to most of the modes, so if they can be detected, other related modes can be evaluated through the damage tree diagram. In this study, the damage modes of pier movements, pier settlements, pier inclinations, shoe failures as well as girder movements are referred to the key modes. In addition, as an extraordinary damage mode, falling of girders should be considered.

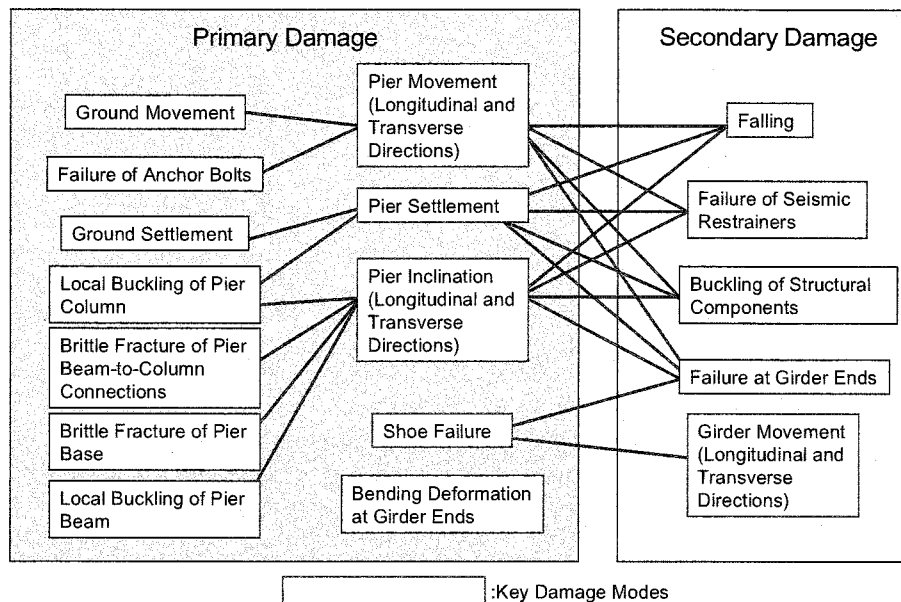


Figure 4 Damage Tree Diagram

3.2 Proposal of Sensor Arrangement

Basically, in order to diagnose the damage of bridges and to determine the proper traffic control level, it is effective to measure the relative displacements in three directions between two bridges in case of continuous multi-spanned bridge structures or between a bridge and abutments in case of a single spanned bridge and the relative displacement between the target bridge and piers in case of continuous multi-spanned bridge structures. In the following discussions, the case of continuous multi-spanned bridge structures is considered because in case of a single spanned bridge, the proposed idea can be applied easily. For usual service conditions, road administrators have the control levels for each of the relative displacements in the vertical, transverse, and longitudinal directions to avoid traffic accidents. Therefore, the traffic control levels determined after the damage detection due to earthquakes can be set based on such relative displacement control levels.

In this study, the sensor arrangement shown in Figure 5 was proposed. The relative displacements between bridges at the joints in the three directions marked “X” in the longitudinal direction, “Y” in the transverse direction, and “Z” in the vertical direction will be measured by FBG displacement meters. In addition, the relative displacements between bridges and piers marked “L” is also measured by FBG displacement meters. The values for the traffic control levels can be changed up to the road administrators’ decisions. In addition, falling of girders will be detected as well as the location of falling by OTDR system as shown in Figure 5 and Figure 6, respectively. In this study, the

arrangement of optical fiber lines for OTDR was also proposed. If an extreme displacement of bridge girders occurs, optical fibers will be bent by a bar installed on the girders, and the bending of fibers will be detected together with the location of the damage.

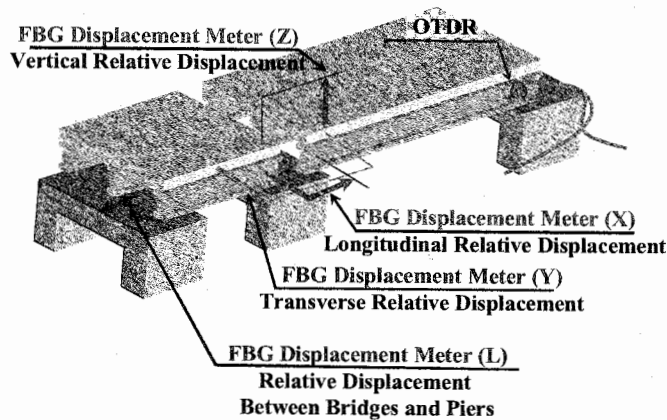


Figure 5 Proposed Sensor Arrangement

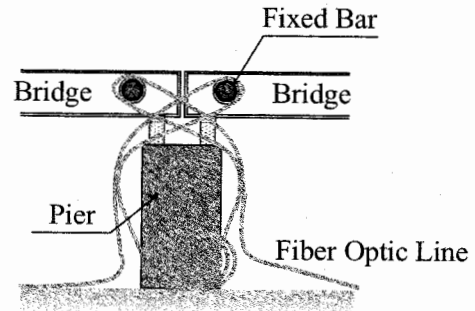


Figure 6 Proposed Sensor Arrangement for OTDR

From the above-mentioned discussions, it was pointed out that the detection of the key modes is important. The authors investigated on the relationship the proposed sensor arrangement and the detection of the key modes. Figure 7 shows the sensors that respond in case of the occurrence of each of the key modes marked by a circle. It can be concluded that the key modes can be analyzed by the responses of sensors including sensors on neighbor joints of damaged parts of bridges.

		X	Y	Z	L
Sensors on A Damaged Pier	Longitudinal Girder Movement	○		○	○
	Transverse Girder Movement	○	○		
	Longitudinal Pier Movement				○
	Transverse Pier Movement	○	○		
	Longitudinal Pier Inclination	○			○
	Transverse Pier Inclination	○	○		
	Pier Settlement	○		○	○
Sensors on The Neighbor Pier	Longitudinal Girder Movement	○		○	○
	Transverse Girder Movement	○	○		
	Longitudinal Pier Movement	○			○
	Transverse Pier Movement	○	○		○
	Longitudinal Pier Inclination	○		○	○
	Transverse Pier Inclination	○	○	○	
	Pier Settlement	○		○	○

Figure 7 Responses of Sensors due to the Key Damage Modes

4. DEVELOPMENT AND VERIFICATION OF A PROTOTYPE MONITORING SYSTEM

4.1 Developed Prototype Monitoring System

In this study, a prototype remote monitoring system was actually developed. It consists of four major parts of “sensor part”, “transmission part”, “measuring part”, and “diagnose and alarm part” to simulate actual applications (Figure 8). In the sensor part, selected sensors were used in the proposed arrangement. The transmission part is long fiber optic lines. This time the 10 kilometer length fiber lines were applied. In the measuring part, a PC connected to a FBG analyzer and a OTDR analyzer measures automatically. Finally, the diagnose and alarm part is built in the same PC, and from the measured data, damage levels and traffic control levels are analyzed and shown on the screen of the PC (Figure 9). The analyzed traffic control level is shown in different colors for each of the four levels of “No traffic is allowed (Red)”, “Only emergency and rescue vehicles can pass carefully (Orange)”, “The maximum speed is limited (Yellow)”, and “No restriction (Open to any traffic) (Green)”.

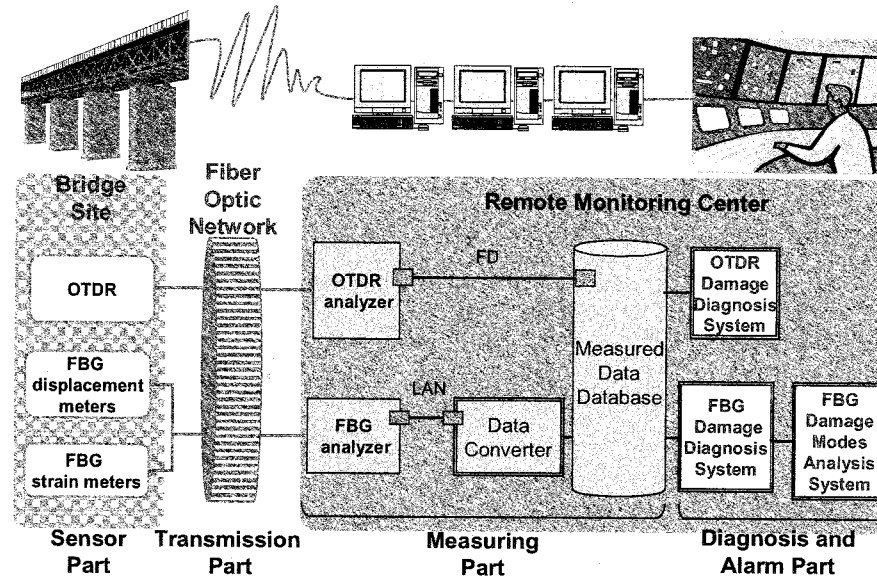
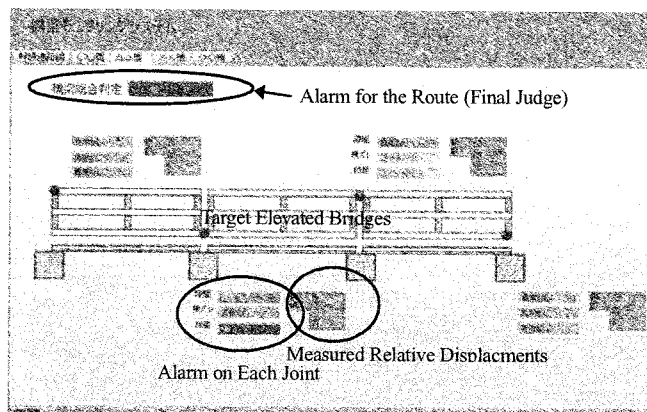
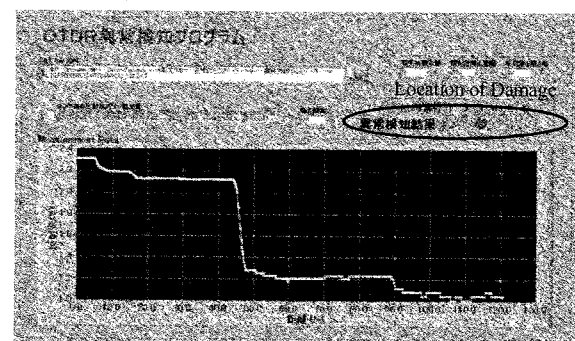


Figure 8 Prototype System



(a) FBG system



(b) OTDR system

Figure 9 Screen of Diagnosis and Analysis Results

4.2 Verification of Prototype Monitoring System

In order to verify the developed prototype monitoring system, a loading and fracture tests of modeled elevated bridges were conducted. Figure 10 shows the modeled elevated bridge system and the test setup. The bridge system consists of 3 girder bridges and 4 piers models as about one twentieth of actual typical structures. In the elevated bridge structures including piers, FBG displacement meters and OTDR sensors were set according to the proposed arrangement (Figure 11 and Figure 12). Through the 10 kilometer transmission fiber optic lines, data was measured and analyzed by a PC. In the loading test, lateral displacement was given with the increment of 5mm on one of the middle piers up to the fracture of the pier at the displacement of 175mm. For this test, considering the size, the values for the traffic control levels were set as shown in Table 2.

Table 2 Values for Determination of Traffic Control Levels

Traffic Control Level*	1	2	3	4
X (mm)	up to 1.0	up to 2.0	up to 3.0	up to 4.0
Y (mm)	up to 1.0	up to 2.0	up to 3.0	up to 4.0
Z (mm)	up to 1.0	up to 1.5	up to 2.0	up to 3.0

*1: No Restriction, 2: The Maximum Speed is Limited,
3: Only Emergency and Rescue, 4: No Traffic is Allowed

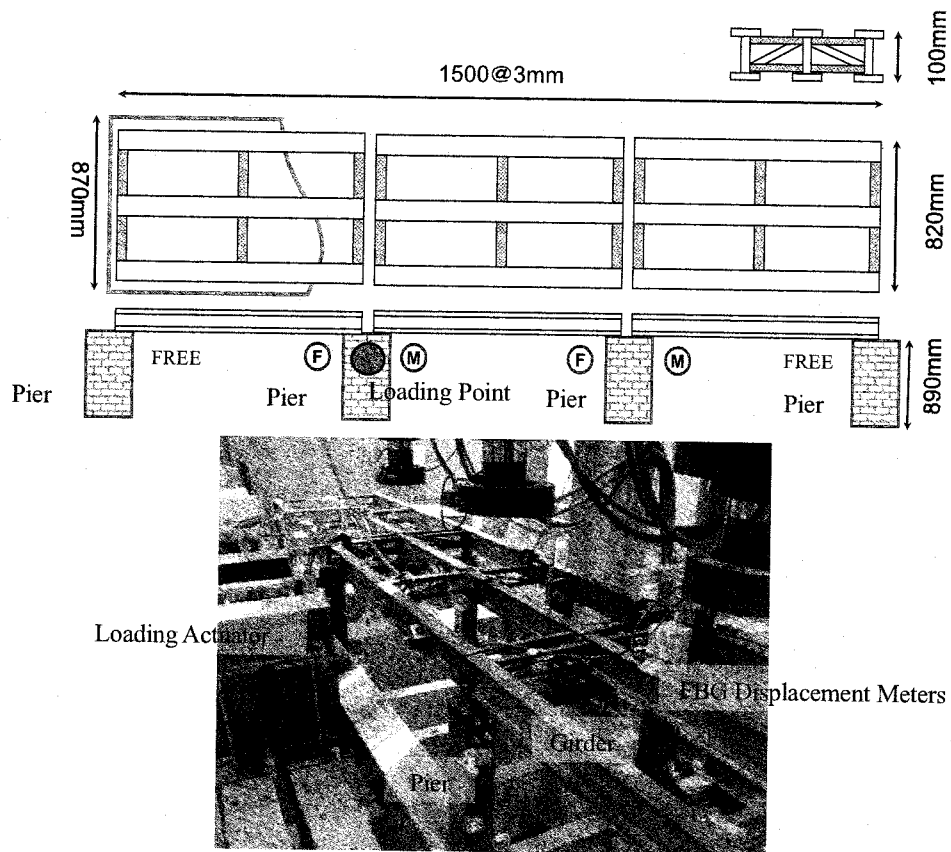


Figure 10 Modeled Elevated Bridges and Test Setup

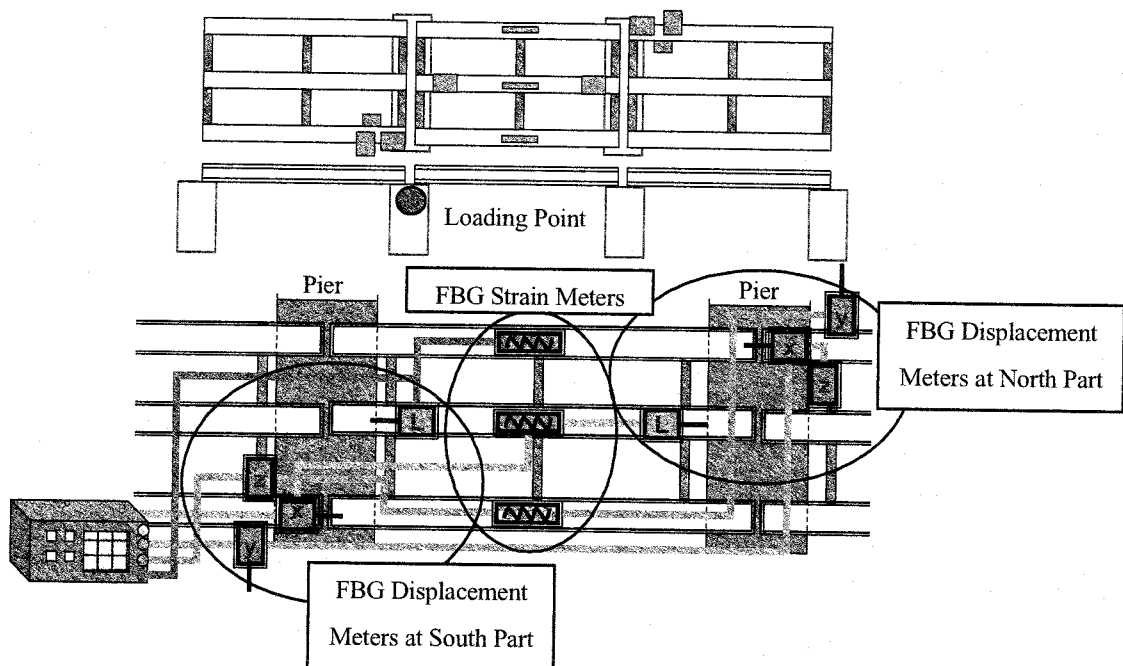


Figure 11 FBG Sensors Arrangement on Modeled Bridges

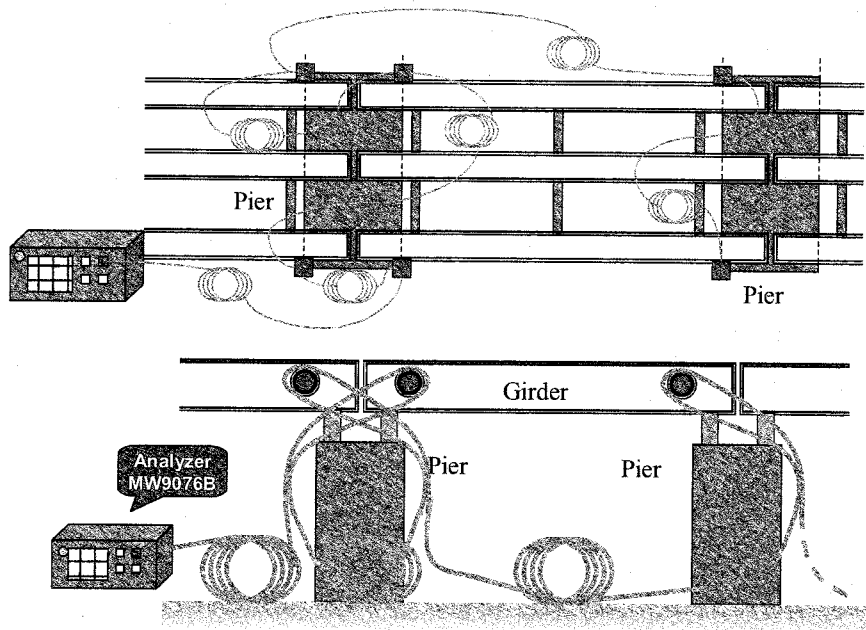


Figure 12 OTDR Arrangement on Modeled Bridges

During the loading tests, at the displacement of 95mm, one end of a girder bridge fell down from the neighbor pier of the loaded pier, the loaded pier was fractured at the displacement of 150mm, and the girder bridge fell down at the displacement of 175mm. Figure 13 shows the displacements measured by FBG displacement meters, and the displacements changed at 95mm, at 150mm, and at 175mm. Figure 14 shows the diagnosis and alarm analysis results based on the FBG displacement meters, and it was confirmed that the function of the diagnosis and alarm worked properly. Large displacement of the girder bridge was also detected by the diagnosis and alarm based on OTDR system as shown in Figure 9(b).

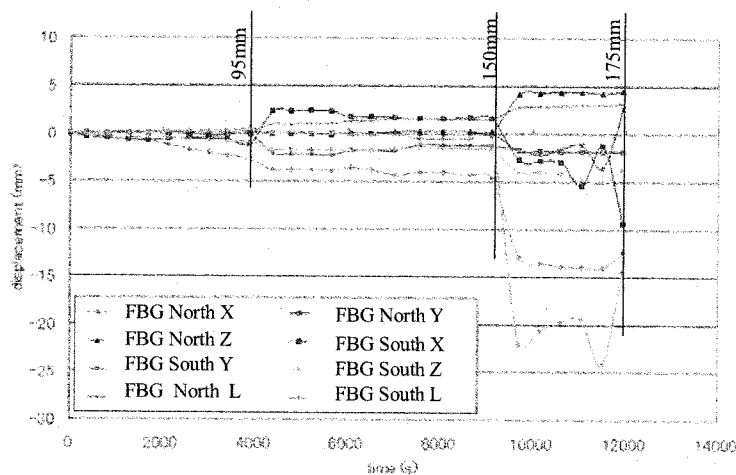
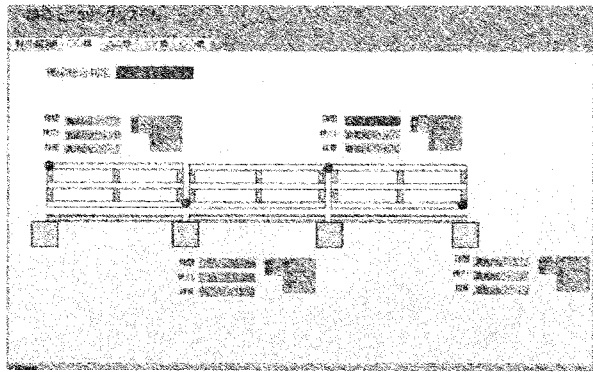
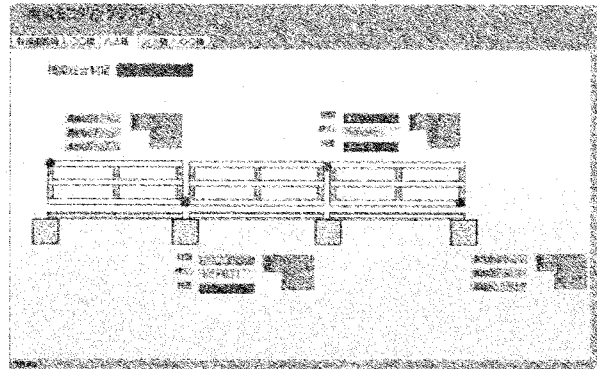


Figure 13 Changes of Displacements Measured by FBG Displacement Meters



(a) At the Displacement of 100mm



(b) At the Displacement of 160mm

Figure 14 Damage Detection by FBG System

5. CONCLUSIONS

In this study, a new remote bridge monitoring system utilizing fiber optic sensors directly connected to fiber optic information network was proposed as an effective system to detect damage levels to show the proper traffic control levels. Through the verification tests using the developed prototype system and the modeled elevated bridges, it was shown that the damage can be detected by the proposed sensor arrangement from a remote place 10 kilometers apart from the bridges, and that the diagnosis and alarm functions worked as expected.

References:

- Japanese Society of Civil Engineers, Committee of Steel Structures (1995), "Survey Reports on Safety of Steel Structures".
- Miki, C., Mizunoue, T., and Kobayashi, Y. (2001), "Monitoring System of Bridge Performance with Fiber-Optic Communications Net, *Journal of Construction Management and Engineering, Japanese Society of Civil Engineers*, 686/VI-52, 31-40.
- Kobayashi, Y., Miki, C., and Tanabe, A. (2003), "Long-Term Monitoring of Traffic Loads by Automatic Real-Time Weigh-in-Motion", *Journal of Structural Mechanics and Earthquake Engineering, Japanese Society of Civil Engineers*, 773/I-69, 99-111.
- Kobayashi, Y., Miki, C., and Sasaki, E. (2003), "Development of Weigh-In-Motion System Utilizing FBG Sensor", *Journal of Applied Mechanics, Japanese Society of Civil Engineers*, 6, 1009-1016.
- Tsuda, H. (2005), "Development of Fiber Bragg Grating Sensors for Structural Health Monitoring", *Journal of the Japanese Society of Non-Destructive Inspection*, 54(2), 71-75.
- Kazama, H. and Mita, A. (2003), "Micro Vibration Sensor System using Fiber Bragg Grating", *Journal of Applied Mechanics, Japanese Society of Civil Engineers*, 6, 993-1000.
- Tsuda, H. (2003), "AE Measurement Using Fiber Bragg Gratings", *Journal of the Japanese Society of Non-Destructive Inspection*, 52(10), 539-542.
- Japanese Society of Civil Engineers, Committee of Steel Structures (1999), "Actual Conditions and Analysis of Damaged Steel Structures in Hanshin-Awaji Earthquake Disaster".

SHAKE TABLE TESTS OF REINFORCED CONCRETE BRIDGE COLUMNS THAT MITIGATE RESIDUAL DISPLACEMENTS FOLLOWING EARTHQUAKES

J. Sakai¹⁾, and S. A. Mahin²⁾

1) Research Engineer, Earthquake Engineering Research Team, Public Works Research Institute, Japan

*2) Professor, Dept. of Civil and Environmental Engineering, University of California at Berkeley, USA
sakai55@pwri.go.jp, mahin@ce.berkeley.edu*

Abstract: To minimize residual displacements of reinforced concrete columns following extreme earthquakes, a design is proposed whereby a longitudinal prestressing tendon replaces some of usual longitudinal reinforcing bars. The seismic performance of such partially prestressed, reinforced concrete columns is investigated through a series of quasistatic analyses followed by earthquake simulator tests. The quasistatic analyses explore optimal combinations of design parameters: configuration of tendons, unbonding of tendons, magnitude of prestress force, amount of prestressing tendons and amount of longitudinal reinforcement. Based on the design recommendations from the analytical investigations, two reinforced concrete bridge column models are designed, constructed and then tested on a shake table. The earthquake simulator tests demonstrate that a partially prestressed, reinforced concrete column performs well under strong earthquake excitations. With the proposed structure, a post-earthquake permanent deformation is significantly reduced while similar maximum response displacements and similar damage at the plastic hinge region are observed.

1. INTRODUCTION

In recent years, reinforced concrete bridge columns with high ductility capacity are designed and constructed in regions of high seismicity to avoid collapse of the supported bridge during strong ground shaking (California Department of Transportation 2001, Japan Road Association 2002). While such conventionally designed reinforced concrete bridge columns are likely to ensure life safety, large residual displacements may exist following extreme earthquakes, necessitating long-term closure of highways while expensive repairs or even complete replacement is carried out. Thus, mitigation of such post-earthquake residual displacements of bridge columns has become a major concern.

Recent research in Japan has begun to explore methods for mitigation of the post-earthquake residual displacement of reinforced concrete bridge columns (Ikeda 1998, Zatar and Mutsuyoshi 2000, Iemura et al. 2002). These studies suggest that the use of prestressing tendons or unbonded high strength bars can be a good means for reducing residual displacements. While results to date are promising, general recommendations have not yet to be developed regarding the optimal characteristics of the column to achieve desired seismic performance including reduced residual displacements. Additionally, the seismic performance under multi-directional excitation of such structures has not yet been investigated.

The research presented in this paper is part of a larger experimental and analytical investigation to enhance the performance of reinforced concrete bridges. A new method for reducing residual displacements of reinforced concrete bridge columns has been developed whereby a single bundle of unbonded prestressing tendon is incorporated at the center of the cross-section of a lightly reinforced

concrete column (Sakai and Mahin 2004a & 2004b). This paper presents a series of quasistatic analyses for such reinforced concrete columns with unbonded prestressing tendons to investigate the hysteretic response, followed by a series of earthquake simulator tests under multi-directional loading to validate the effectiveness of this approach in improving seismic performance.

2. BRIDGE COLUMNS THAT MITIGATE POST-EARTHQUAKES RESIDUAL DISPLACEMENTS

To investigate the hysteretic behaviors of reinforced concrete bridge columns, a series of quasistatic cyclic analyses was conducted. The hysteretic behavior is idealized with fiber elements. The results (Sakai and Mahin 2004a) demonstrated that quasistatic residual displacements of reinforced concrete columns decrease when (1) the amount of longitudinal reinforcement is relatively small, and (2) the magnitude of axial force is relatively large. To satisfy these conditions, a structure is proposed whereby unbonded prestressing tendons replace some of longitudinal mild reinforcement of a conventional reinforced concrete column.

Primary design parameters of the proposed column are: (1) configuration of tendons, (2) unbonding of tendons, (3) magnitude of prestressing force, (4) amount of prestressing tendons, and (5) amount of longitudinal reinforcement. The optimal combinations of the parameters are explored based on the design criteria listed below:

- 1) residual displacement is small enough compared to the conventionally designed column,
- 2) ductility capacity is similar to that of the conventionally designed column,
- 3) flexural strength is similar to that of the conventionally designed column,
- 4) energy dissipation capacity is not too small, and
- 5) prestressing tendons remain elastic during excitation.

Figure 1 shows cross sections of columns with tendons considered in this study. The configuration of the tendons is set up as follows: first, half of the usual rebar is replaced with prestressing tendons and the diameter of the configuration of the tendons changed to 1.67 m to 0 m; the total area of tendons is kept constant at half of the total area of the usual reinforcement of the conventional column. The analyses (Sakai and Mahin 2004a & 2004b) suggest that:

- 1) when a tendon is placed at the center of the cross section, and the tendon is debonded from concrete, the column has a similar skeleton curve of lateral force versus lateral displacement hysteresis to that of the conventional column while the residual displacement is reduced,
- 2) when prestressing force increases, maximum flexural strength increases. The residual displacement tends to decrease with a larger prestressing force; however, too large prestressing force results in even larger residual displacement due to premature crushing of concrete. An optimal prestressing force is one to two times of that induced by the dead load,
- 3) a larger amount of prestressing tendons tends to increase post-yield stiffness, and
- 4) a larger amount of longitudinal reinforcement increases flexural strength, energy dissipation capacity, post-yield stiffness, but also increases residual displacement.

The analyses also demonstrate that the hysteretic behaviors of the proposed columns can be easily controlled by selecting appropriate design parameters. **Figure 2** shows hystereses of some of the proposed columns, which have an unbonded center tendon as shown in **Figure 3**. **Table 1** summarizes design variables of the columns shown in **Fig. 2**. Here ρ_l and ρ_{ps} are the longitudinal reinforcement ratio and the area ratio of prestressing tendon to concrete, respectively. α_{total} represents a total axial force ratio, which is defined in Eq. (1).

$$\alpha_{total} = \frac{P + P_{ps}}{f'_{co} A_g} \quad (1)$$

where P is the axial force at the bottom due to the dead load of the top mass and column, P_{ps} is the prestressing force, f'_{co} is the cylinder strength of concrete, and A_g is the gross section area.

Column A has small amounts of both mild reinforcement and tendon with a large prestressing force, which results in very small residual displacement with small post-yield stiffness and energy dissipation capacity. Column B has a similar total steel ratio ($\rho_l + \rho_{ps}$) with a 3-times axial force compared to the conventional design, which results in a similar skeleton curve to the conventional column with small residual displacements. Column C has a relatively large amount of mild reinforcement with zero prestress, which results in a large post-yield stiffness with large residual displacements. According to the design criteria shown above, Column B has the best hysteretic performance.

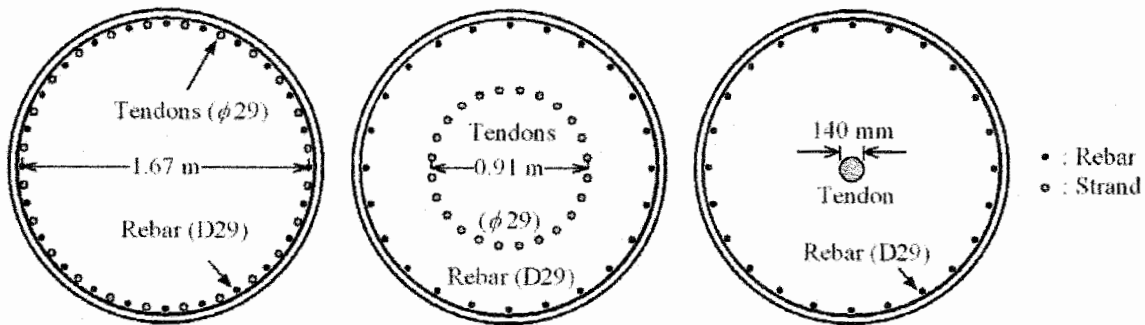


Figure 1 Cross Sections of Columns with Tendons

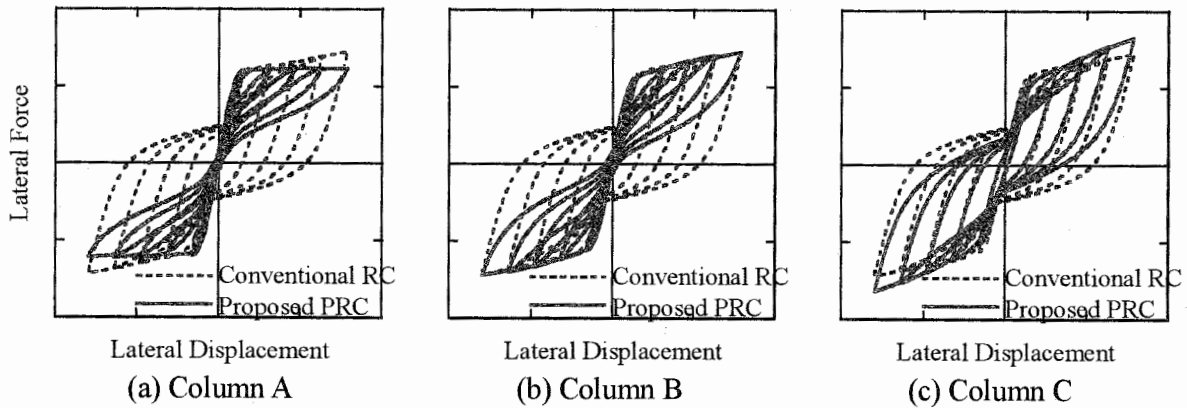


Figure 2 Quasistatic Hysteretic Behaviors of Proposed Columns

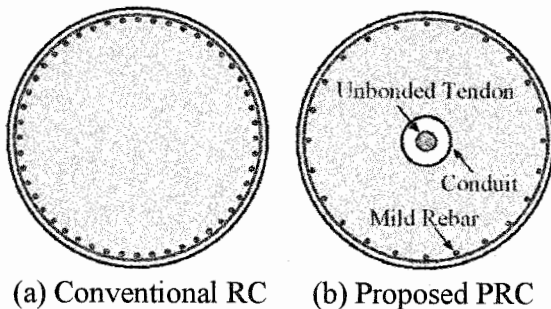


Figure 3 Cross Sections

Table 1 Design Parameters

	ρ_l	ρ_{ps}	α_{total}
Conventional RC	1.18%	-----	5%
Column A	0.18%	0.29%	20%
Column B	0.35%	0.88%	15%
Column C	0.92%	0.88%	5%

3. EARTHQUAKE SIMULATOR TESTS

To access the seismic performance of the proposed design, a series of earthquake simulator tests

was conducted with a shake table of the Earthquake Engineering Research Center, University of California, Berkeley. **Table 2** and **Figure 4** show the specimens tested in this study. A scaling factor of 4.5 is assumed for the specimens. The diameter of the specimens is 406 mm, and the height from the bottom of the column to the center of gravity of the top mass is 2.44 m, resulting in an effective aspect ratio of 6. The cylinder strength of concrete is 41.7 MPa. The specimens support concrete blocks that idealize the inertia mass and dead load from a superstructure as shown in **Photo 1**.

Table 2 Specimens

Specimen	Description	f'_{co} (MPa)	ρ_l (%)	ρ_{ps} (%)	P (kN)	P_{ps} (kN)	α_{total} (%)	Tendon size
RC	Conventional design	41.7	1.19	-----	291	-----	5.4	-----
PRC	Proposed design	41.7	0.66	0.62	291	379	12.4	32 mm (1-1/4")

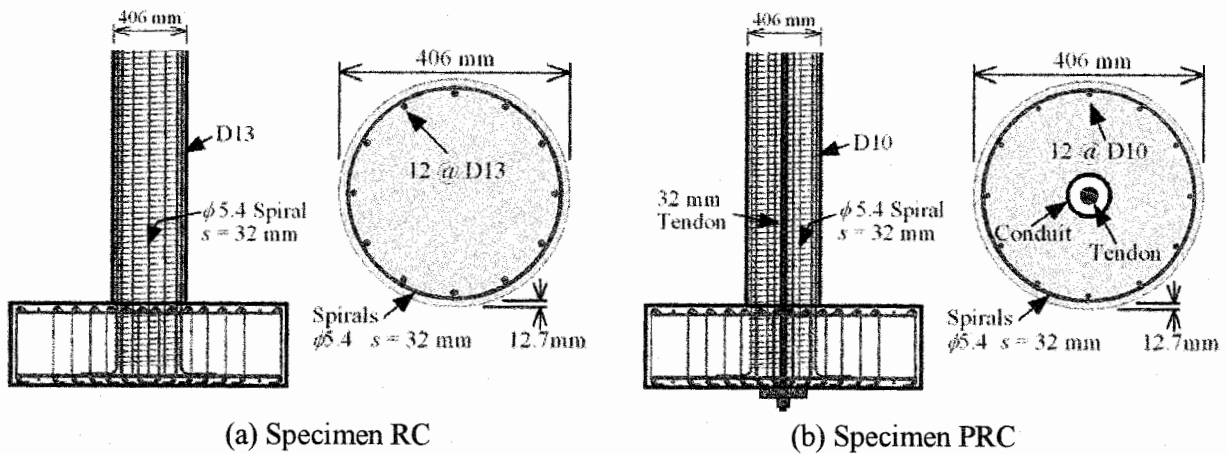


Figure 4 Specimens

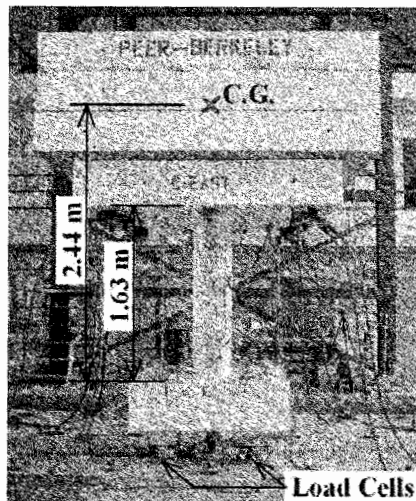


Photo 1 Test Setup

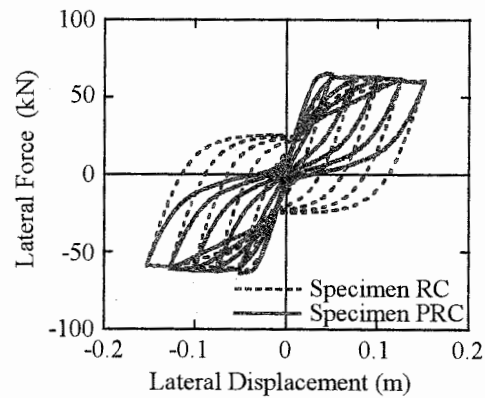


Figure 5 Quasistatic Behavior of Specimens

Specimen RC represents at reduced scale a reinforced concrete bridge column, as commonly constructed in California, USA. The specimen is reinforced longitudinally with 12 No. 4 (13-mm diameter) deformed bars, providing a longitudinal reinforcement ratio, ρ_l , of 1.19%. W3.5 (5.4-mm diameter) spirals are used to confine the concrete core, spaced at a 32-mm pitch, resulting in a volumetric ratio, ρ_s , of 0.76%, which results in the ultimate ductility capacity of 7.8. Grade 60 bars

are used for the mild longitudinal reinforcement, while Grade 80 wire ($f_y = 607$ MPa) is used for the spirals. The Grade 60 No. 4 bars have a yield strength of 491 MPa, and an ultimate strength of 728 MPa.

The design parameters for Specimen PRC were determined based on results of a series of quasistatic analyses. The quantity of longitudinal reinforcement was reduced by about half compared to Specimen RC by using a smaller rebar (No. 3, 10-mm diameter, deformed bars), but a single 32-mm diameter prestressing tendon was placed in an ungrouted conduit at the center of the column to provide nearly the same total longitudinal reinforcement ratio as in Specimen RC. The same spiral reinforcement to Specimen RC is used for Specimen PRC. A prestressing force of 379 kN is applied to the column, resulting in a total axial force ratio, α_{total} , of 12.4%. The Grade 60 No. 3 bars have a yield strength of 488 MPa, and an ultimate strength of 792 MPa. The yield and ultimate strength of the tendon are 1024 MPa and 1169 MPa, respectively.

Figure 5 shows computed quasistatic hysteresses of the specimens when they are loaded uni-directionally. The PRC specimen is expected to have a strongly origin-oriented tendency upon unloading.

Figure 6 shows the test input signals. The two horizontal components of a modified motion recorded in Los Gatos during the 1989 Loma Prieta, California, earthquake (Somerville et al., 1997) are selected because large residual displacements are predicted for Specimen RC by nonlinear dynamic analyses. Records are scaled using a time scale factor equal to the square root of the length scale factor ($= 2.12$) considering the similitude requirements, and then, band pass filtered to remove low and high frequency components because of the performance characteristics of the earthquake simulator.

Four intensities of ground motion are imposed in the tests. These levels are denoted herein as elastic, yield, design and maximum level tests. Scale factors for the amplitudes of four level tests are 7%, 10%, 70% and 100%, respectively. The first two levels are intended to check the instrumentation and data acquisition system, and to provide information on the dynamic response of the specimens under excitations representative of moderate earthquakes. The design and maximum level tests investigate nonlinear dynamic response of the specimens. The intensity of the excitations are set in order to develop a displacement ductility of about 4 during the design level tests, and a displacement ductility of 8 during the maximum level test (approximately the ultimate capacity of the specimen).

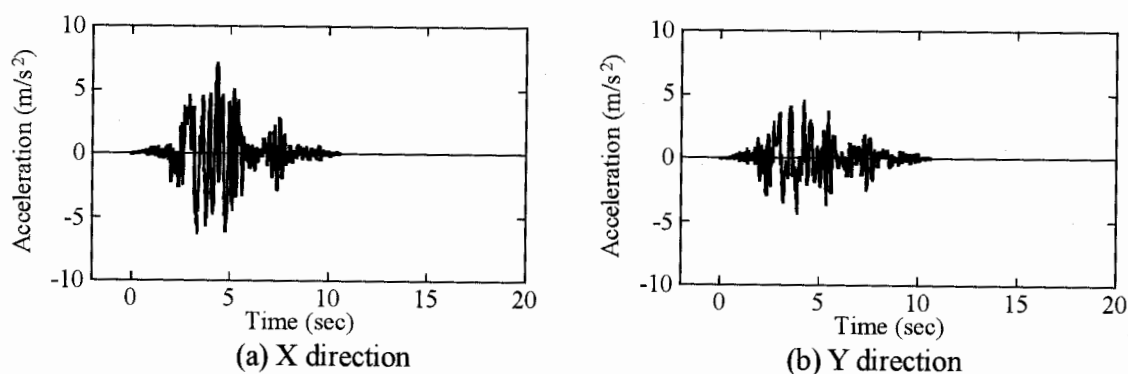


Figure 6 Input Ground Motion (Los Gatos Record, 1989 Loma Prieta Earthquake)

4. DYNAMIC RESPONSE OF SPECIMENS RC AND PRC

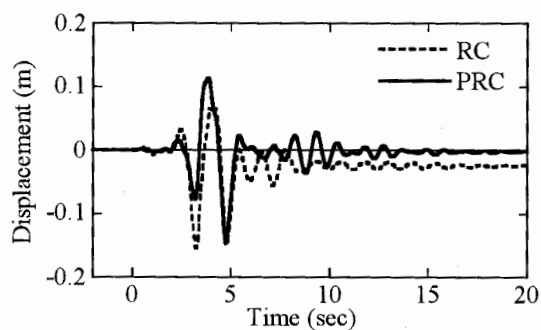
Figure 7 compares the displacement response at the center of gravity of the top mass subjected to the design level ground motion, and **Table 3** shows maximum and residual displacements during the design level tests. The results from the maximum level tests are also shown in the table. The

displacements are expressed as distances from the origin in **Table 3** while the displacements are shown in each principal direction in **Fig. 7**.

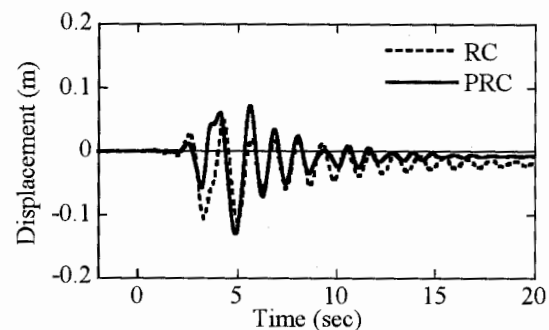
The maximum displacements in the X direction of the specimens are 0.155 m and 0.147 m, respectively, which occurs around 4.8 seconds. About the same time, the specimens reach the maximum distances from the origin, which are 0.187 m and 0.189 m (ductilities of about 7.5). Although both specimens have similar peaks, Specimen RC has a residual displacement of 0.031 m, which exceeds the yield displacement by 20%, whereas Specimen PRC has a residual displacement of only 0.008 m. The physical damage in both columns was minor after these tests, consisting of moderate spalling of the concrete covers as shown in **Fig. 8**. This implies that even if a larger axial force is induced in the proposed column due to prestress, the local damage is similar to a conventional design with an appropriate confinement.

Table 3 Maximum and Residual Distances of Specimens RC and PRC

Specimen	Design Level (70%)		Maximum Level (100%)	
	Maximum Response	Residual Deformation	Maximum Response	Residual Deformation
RC	0.187 m	0.031 m	0.349 m	0.285 m
PRC	0.189 m	0.008 m	0.323 m	0.107 m

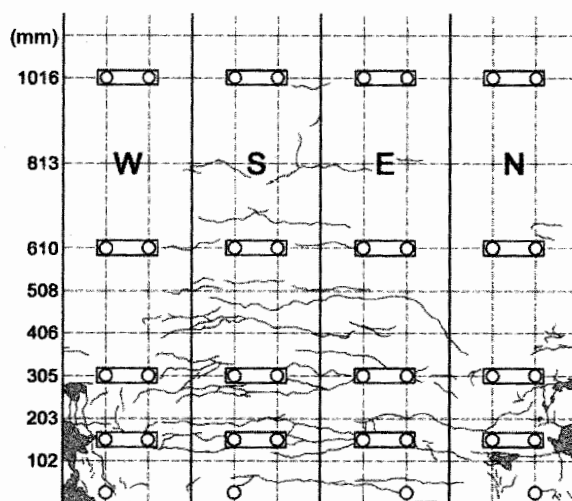


(a) X direction

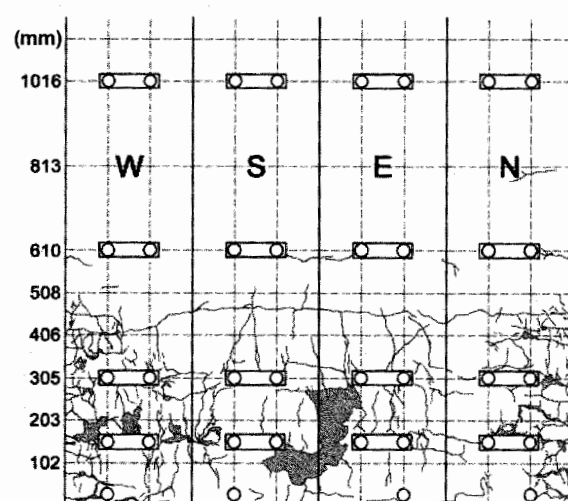


(b) Y direction

Figure 7 Response Displacement at C.G of Mass Blocks (Design Level Test)



(a) Specimen RC



(b) Specimen PRC

Figure 8 Local Damage of Specimens after Design Level Test

Figure 9 shows the displacement response at the top mass subjected to the maximum level ground motion, and **Photo 2** shows residual displacements of the specimens after the maximum level test. The maximum displacement ductility factors attained by Specimens RC and PRC are 14 and 13, respectively. These are very large, far exceeding the computed capacities. The residual displacement of Specimen RC is 0.285 m, which is more than 10 times of the yield displacement, while that of Specimen PRC is only 38% of that of Specimen RC, which proves the effectiveness of the proposed method on mitigation of the residual displacement following extreme earthquakes.

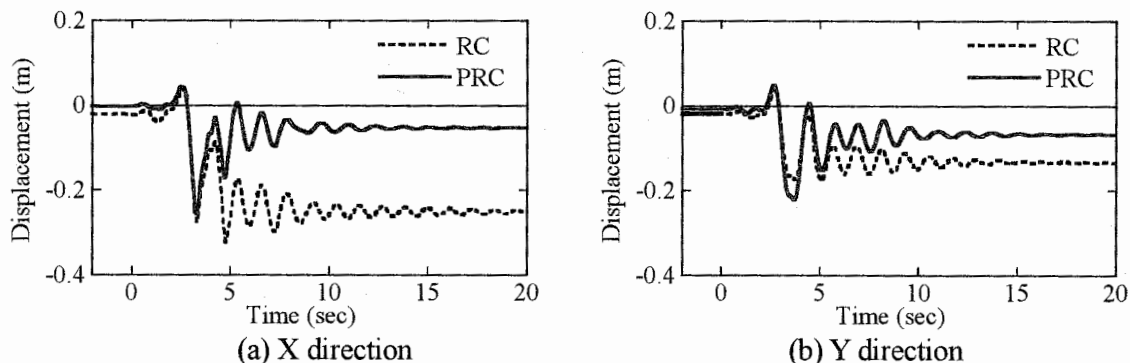
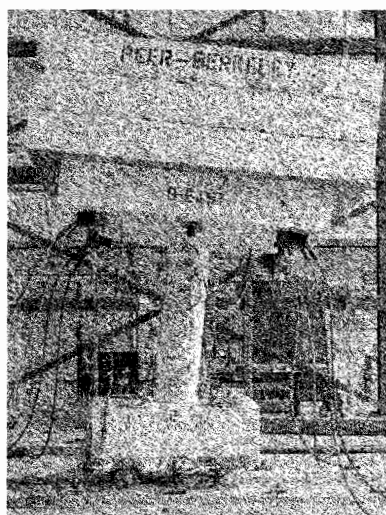
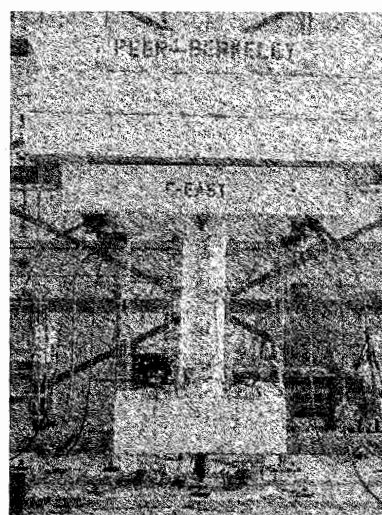


Figure 9 Response Displacement at C.G of Mass Blocks (Maximum Level Test)



(a) Specimen RC



(b) Specimen PRC

Photo 2 Residual Displacements of Specimens after Maximum Level Test

5. CONCLUSIONS

To mitigate post-earthquake residual displacements of reinforced concrete bridge columns, a design is proposed. To investigate the seismic behavior of the proposed design, a series of earthquake simulator tests have been conducted. Below are the conclusions determined from the study:

- (1) A design is proposed whereby an unbonded longitudinal prestressing tendon replaces some of usual longitudinal mild reinforcing bars to mitigate residual displacements of reinforced concrete columns. The proposed column has a similar flexural strength and ductility capacity with reduced residual displacement compared to the conventional design. The hysteretic behaviors of the proposed columns can easily be controlled by selecting appropriate design parameters.

- (2) The earthquake simulator tests validate that the origin-oriented benefit of providing an unbonded prestressing tendon at the center of the column cross-section. After a design level ground excitation, the residual displacement of the conventionally designed RC specimen is more than the yield displacement, while that for the partially prestressed, reinforced concrete (PRC) specimens is reduced by 75%. The peak displacement responses of RC and PRC specimens are similar for the same shaking.
- (3) The local damage at the plastic hinge region is similar for the conventional RC specimen and the proposed PRC specimen for the same shaking. This implies if an appropriate confining reinforcement is provided, the local damage is similar even with a larger axial force due to prestress.

Acknowledgements:

Support for this work was provided in part by the Earthquake Engineering Research Centers Program of the National Science Foundation, under Award Number EEC-9701568, through the Pacific Earthquake Engineering Research Center (PEER). The findings, observations and conclusions contained herein, however, are those of the authors and do not necessarily represent those of the sponsoring organizations. The thoughtful help and advice provided by the staff of the Pacific Earthquake Engineering Research Center and by Andres Espinoza, a graduate student researcher, are gratefully appreciated.

References:

- California Department of Transportation (2001). *Seismic Design Criteria Ver. 1.2.*, California, USA.
- Iemura, H., Takahashi, Y. and Sogabe, N. (2002). "Innovation of High-Performance RC Structure with Unbonded Bars for Strong Earthquakes." *J. Struc. Mech. Earthq. Engrg.*, Japan Society of Civil Engineers, No. 710/I-60, pp. 283-296. (in Japanese)
- Ikeda, S. (1998). "Seismic Behavior of Reinforced Concrete Columns and Improvement by Vertical Prestressing." *Challenges for Concrete in the Next Millennium, Proc. of XIIIth FIP Congress*, Vol. 1, pp. 879-884, Balkema Rotterdam, Netherlands.
- Japan Road Association (2002). *Design Specification of Highway Bridges. Part V: Seismic design*, Japan (in Japanese).
- Sakai, J. and Mahin, S. A. (2004a). "Analytical Investigations of New Methods for Reducing Residual Displacements of Reinforced Concrete Bridge Columns." *PEER-2004/02*, Pacific Earthquake Engineering Research Center, Univ. of California at Berkeley, USA.
- Sakai, J. and Mahin, S. A. (2004b). "Mitigation of Residual Displacements of Circular Reinforced Concrete Bridge Columns." *Proc. of 13th World Conference on Earthquake Engineering*, CD-ROM No. 1622, Vancouver, Canada.
- Somerville, P., Smith, N. Punyamurthula, S. and Sun, J. (1997). "Development of Ground Motion Time Histories for Phase 2 of The FEMA/SAC Steel Project." *Report SAC/BD-97/04*, SAC Joint Venture, California, USA.
- Zatar, W. A. and Mutsuyoshi, H. (2000). "Reduced Residual Displacements of Partially Prestressed Concrete Bridge Piers." *Proc. of 12th World Conference on Earthquake Engineering*, CD-ROM No. 1111, Auckland, New Zealand.

NONLINEAR SEISMIC RESPONSE CONTROL OF ISOLATED BRIDGES USING MR DAMPERS

T. Y. Lee¹⁾ and K. Kawashima²⁾

1) Assistant Professor, Department of Civil Engineering, National Central University, Taiwan

2) Professor, Department of Civil Engineering, Tokyo Institute of Technology, Japan

tylee@cv.titech.ac.jp, kawashima@cv.titech.ac.jp

Abstract: The effectiveness of a semi-active control method using magnetorheological (MR) dampers on reducing the deck displacement of the isolated bridges, which exhibit nonlinear responses at both the columns and isolators under near-field ground motions, is studied. The sliding mode control algorithm is utilized to command the MR dampers. A five-span viaduct with high-damping-rubber bearings is analyzed to evaluate the control performance. The results show that the semi-active control using MR dampers is capable of providing the similar performance by the active control. The semi-active control based on the sliding mode control algorithm achieves outstanding control performance through comparison with the semi-active control based on the LQR control algorithm.

1. INTRODUCTION

The isolators in bridge structures are effective in mitigating the induced seismic force by a shift of natural periods. However, the deck displacement becomes excessively large when a bridge is subjected to a ground motion with large intensity or unexpected characteristics. Such a large displacement may result in the higher-than-expected seismic force due to the pounding of decks and the $P-\delta$ effects. Semi-active control systems have the major advantages of the versatility and adaptability of active control systems without requiring large energy supply, and have the reliability of passive control systems. In the previous studies (e.g. Kawashima 1994, Yang 1995a), semi-active control systems were studied to effectively reduce seismic responses of isolated bridges. However, the isolators were regarded as either nonlinear elements or hysteretic elements in only several studies with all the columns being assumed to behave linearly. In reality, the columns may exhibit hysteretic behavior under extreme excitations. Hence it is emphasized in this study to reduce the deck displacement of isolated bridges with nonlinearity at both the columns and isolators by using semi-active control technology.

Magnetorheological (MR) dampers are utilized as the semi-active device in this study. The clipped optimal control algorithm base on the LQR control has been adopted mainly to command MR dampers in control of linear structures (Dyke 1996). Although studies on seismic response control for linear structures have been performed by a number of researchers, few control methods for nonlinear structures have been developed (e.g. Yang *et al.* 1994, 1995b). It is noted that sliding mode control can provide remarkable seismic control effect. Therefore, the application of the semi-active control using MR dampers based on the sliding mode control algorithm to nonlinear isolated bridges is investigated in this study. A five-span viaduct with high-damping-rubber bearings is analyzed to evaluate the control effectiveness. The results reveal that the MR damper can trace most of the control forces demanded by the sliding mode control algorithm as well as the LQR control algorithm. The control

performance on reducing the deck displacement is outstanding using the semi-active control based on the sliding mode control algorithm as compared with the semi-active control based on the LQR control algorithm.

2. ANALYTICAL MODEL AND CONTROL ALGORITHMS

Assuming the deck of a typical isolated bridge is rigid in the longitudinal direction, a column with the effective deck mass on the top can be taken apart as a unit for seismic analysis, as shown in Fig. 1. For study of control effectiveness, the column-isolator-deck system may be idealized as a two degree of freedom lumped-mass system. A control device is set between the deck and the column.

The column and the isolator are assumed to behave nonlinearly, and the damping of the system is assumed as linear viscous herein. The equations of motion of the isolated bridge system may be expressed as

$$\mathbf{M}\ddot{\mathbf{x}}(t) + \mathbf{C}\dot{\mathbf{x}}(t) + \mathbf{F}[\mathbf{x}(t)] = \boldsymbol{\eta}\ddot{\mathbf{x}}_g(t) + \mathbf{H}U(t) \quad (1)$$

in which $\mathbf{x}(t)$, $\dot{\mathbf{x}}(t)$, $\ddot{\mathbf{x}}(t)$ are the displacement, velocity and acceleration vectors; $\ddot{\mathbf{x}}_g(t)$ is the absolute ground acceleration; \mathbf{M} and \mathbf{C} are mass and damping matrices, respectively; $\mathbf{F}[\mathbf{x}(t)]$ is the nonlinear stiffness vector; $U(t)$ is the control force generated by the control device, and $\boldsymbol{\eta}$ and \mathbf{H} are the location matrices of the excitation and the control force, respectively.

The equations of motion by Eq. (1) can be written based on a state space formulation as

$$\dot{\mathbf{Z}}(t) = \mathbf{g}[\mathbf{Z}(t)] + \mathbf{B}U(t) + \mathbf{W}\ddot{\mathbf{x}}_g(t) \quad (2)$$

where $\mathbf{Z}(t) = [\mathbf{x}(t) \ \dot{\mathbf{x}}(t)]^T$ is a space-state vector; $\mathbf{g}[\mathbf{Z}(t)]$ is a nonlinear function of $\mathbf{Z}(t)$. \mathbf{g} , \mathbf{B} and \mathbf{W} are defined as follows:

$$\mathbf{g}[\mathbf{Z}(t)] = \begin{bmatrix} \dot{\mathbf{x}} \\ -\mathbf{M}^{-1}[\mathbf{C}\dot{\mathbf{x}}(t) + \mathbf{F}[\mathbf{x}(t)]] \end{bmatrix}; \quad \mathbf{B} = \begin{bmatrix} 0 \\ \mathbf{M}^{-1}\mathbf{H} \end{bmatrix}; \quad \mathbf{W} = \begin{bmatrix} 0 \\ \mathbf{M}^{-1}\boldsymbol{\eta} \end{bmatrix} \quad (3)$$

2.1 Sliding Mode Control

In sliding mode control, the response trajectory is driven toward the sliding surface by the designed controller, where the motion on the sliding surface defined by $\mathbf{S} = \mathbf{0}$ is stable, and then it is maintained on the sliding surface. Define the sliding surface \mathbf{S} as a linear function of state vector \mathbf{Z} such that

$$\mathbf{S} = \mathbf{P}\mathbf{Z}(t) \quad (4)$$

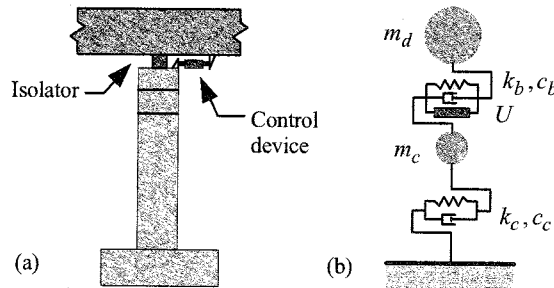


Figure 1. Analytical idealization: (a) analytical unit of column, and (b) 2DOF system.

In the design of the sliding surface, the nonlinear structure is linearized to the initial condition $\mathbf{Z} = 0$ and the external excitation \ddot{x}_g is neglected. The sliding surface can be determined using the pole assignment method or the LQR method (Yang 1995b). To design the controller, the following Lyapunov function is considered

$$\Gamma = 0.5\mathbf{S}^T\mathbf{S} \quad (5)$$

The sufficient condition for the sliding mode to occur is given by $\dot{\Gamma} = \mathbf{S}^T\dot{\mathbf{S}} \leq 0$. Substituting Eq. (4) into Eq. (5), taking the derivative and using the state equations of motion by Eq. (2), a possible continuous controller, which does not have undesirable chattering effect and whose control force is continuous, is given by (Yang 1995b)

$$U(t) = \alpha G - \delta \lambda \quad (6)$$

where $G = -(\mathbf{PB})^{-1}\mathbf{P}(\mathbf{AZ} - \mathbf{f} + \mathbf{E})$; $\lambda = \mathbf{S}^T\mathbf{PB}$. Both α and δ are specified by designers with $0 \leq \alpha \leq 1$.

2.2 LQR Optimal Control

The LQR optimal control is referred for comparison. In this control algorithm, the control force $U(t)$ in Eq. (1) is obtained by minimizing the quadratic function, over the duration of the excitation, as

$$J = \int_0^{t_f} [\mathbf{Z}^T(t)\mathbf{Q}\mathbf{Z}(t) + RU^2(t)]dt \quad (7)$$

in which \mathbf{Q} is a (4×4) symmetric positive semidefinite weighting matrix and R is a positive weighting scalar.

The optimal solution that minimizes the performance index by Eq. (7), is obtained under the constraint of the state equations of motion by Eq. (2) as follows (Yang 1992)

$$U(t) = -0.5R^{-1}\mathbf{B}^T\bar{\mathbf{P}}\mathbf{Z}(t) \quad (8)$$

in which $\bar{\mathbf{P}}$ is the solution of Ricatti equation $\Lambda_0^T\bar{\mathbf{P}} + \bar{\mathbf{P}}\Lambda_0 - 0.5\bar{\mathbf{P}}\mathbf{B}R^{-1}\mathbf{B}^T\bar{\mathbf{P}} = -2\mathbf{Q}$. Note that the constant Ricatti matrix $\bar{\mathbf{P}}$ is obtained by linearizing the structure at $\mathbf{Z} = 0$ as $\Lambda_0 = \partial\mathbf{g}(\mathbf{Z})/\partial\mathbf{Z}|_{\mathbf{Z}=0}$ and neglecting the earthquake excitation \ddot{x}_g .

3. SEMI-ACTIVE CONTROL

The semi-active control utilizing MR dampers is investigated in this study. Although the MR damper model proposed by Spencer et al. (1997) based on the Bouc-Wen hysteretic model can describe the MR damper behavior precisely, it is difficult to obtain an explicit demanded current from the model when the control force is given from control algorithms. Thus, the MR damper model consisting of only friction damping force and viscous damping force, which are functions of current, is used herein as (Ruangrassamee and Kawashima 2001)

$$V(t) = f_m(t) + c_m(t)\dot{x}_m(t) \quad (9)$$

where $V(t)$ is the exerting damping force; f_m and c_m are assumed as the forms of

$$f_m(t) = f_{m1} + f_{m2}I(t); \quad c_m(t) = c_{m1} + c_{m2}I(t) \quad (10)$$

where $f_{m1}, f_{m2}, c_{m1}, c_{m2}$ are the identified parameters of the MR damper; $I(t)$ is the regulable current.

In semi-active control, the MR damper is expected to provide the demanded control force $U(t)$

by Eq. (6) or Eq. (8). Equating the demanded control force by Eq. (6) or Eq. (8) and the exerting damping force from the MR damper by Eq. (9) yields the demanded current. It is noted that the control force cannot be commanded directly but the current has to be regulated in the MR damper to achieve various damping force levels. The external energy required for such control is generally much smaller than that required for the active control. Therefore, the MR damper not only changes arbitrarily the damping force depending on the feedback structural responses to resemble an active system but also functions as a passive energy dissipater.

3. TARGET ISOLATED BRIDGE AND RESPONSE SIMULATIONS

A typical isolated viaduct designed based on Japan Design Specifications of Highway Bridges is analyzed to investigate the effectiveness of structural control as shown in Fig. 2 (Japan Road Association 1996). The superstructure consists of a five-span continuous deck with a total length of $5 \times 40 \text{ m} = 200 \text{ m}$ and a width of 12 m, which is supported by four reinforced concrete columns and two abutments. Five high-damping-rubber isolators per column support the deck.

The effective mass of deck and column are 600 ton and 243.15 ton, respectively. The column and isolator are assumed to be perfect elastoplastic and bilinear elastoplastic, respectively. The initial stiffness of the column and isolator is 112.7 MN/m and 47.6 MN/m, respectively while the yielding displacement is 0.0309 m and 0.016 m, respectively. The ratio of the post-yielding to pre-yielding stiffness of the isolator is 0.19. The first and second natural periods of the isolated bridge with the initial elastic stiffness are 0.86 sec and 0.24 sec, respectively. The damping ratios of the system are assumed 2% for both modes. In simulation, the isolated bridge is subjected to two near-field ground motions recorded at JMA Kobe Observatory in the 1995 Kobe, Japan earthquake and Sun-Moon Lake in the 1999 Chi-Chi, Taiwan earthquake as shown in Fig. 3. The Bouc-Wen hysteretic model (Wen 1976) is used to simulate the restoring force of both the column and the isolator.

The MR damper model by Eq. (9) proposed by Ruangrassamee and Kawashima (2001) is based on a small-scale MR damper. For application to real bridges, the large-scale MR damper behavior modeled by Yang, G. *et al.* (2002) based on the Bouc-Wen hysteretic model is utilized for reference. Through the least-squares fit of a straight line, a large-scale MR damper model with four segments by

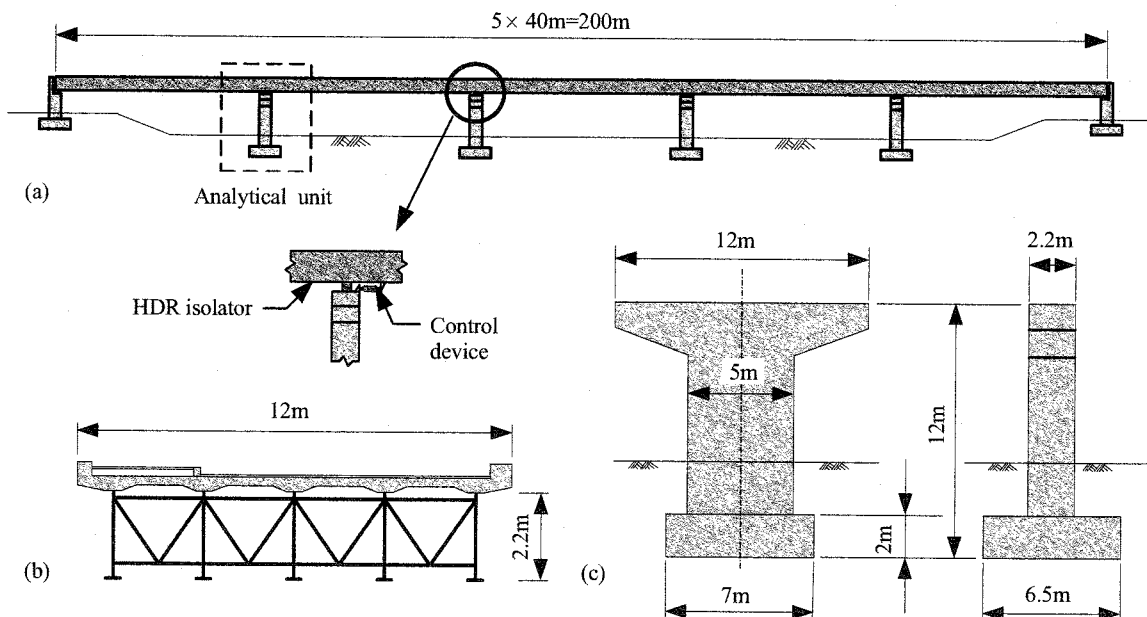


Figure 2. An isolated viaduct: (a) elevation, (b) superstructure, and (c) column.

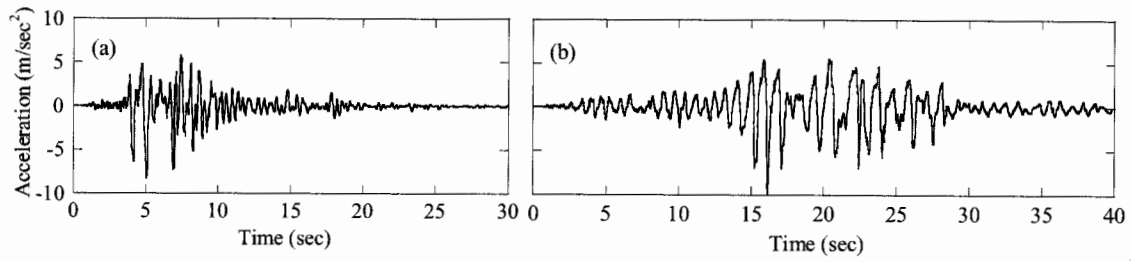


Figure 3. Ground motion records: (a) JMA Kobe observatory, and (b) Sun-Moon Lake.

Eq. (9), which approximates the behavior of the large-scale MR damper proposed by Yang, G. *et al.*, is determined.

The large-scale MR damper is commanded based on the sliding mode control algorithm to apply the semi-active damping force to the isolated bridge. The pole assignment method is adopted to determine the sliding surface by Eq. (4), where the poles are -30 and $-10 \pm 25i$. The δ and α in Eq. (6) are assumed to be unity and 0.059, respectively. Figure 4 compares the control force and the deck displacement among uncontrolled, active controlled and semi-active controlled under Sun-Moon Lake ground motion. The applied current of the MR damper is also presented here. As observed from Fig. 4, the control forces from the actuator under the active control and from the MR damper under the semi-active control are virtually the identical except at few instants. The deck displacement is significantly reduced in both the active and semi-active controlled systems and it is slightly smaller in the semi-active controlled system than in the active controlled system. The hysteretic loops of the isolator and the column are presented in Fig. 5, which shows that the maximum isolator and column displacement are drastically reduced under both control strategies. The hysteretic loops are similar under the active control and the semi-active control. The values corresponding to the peak control

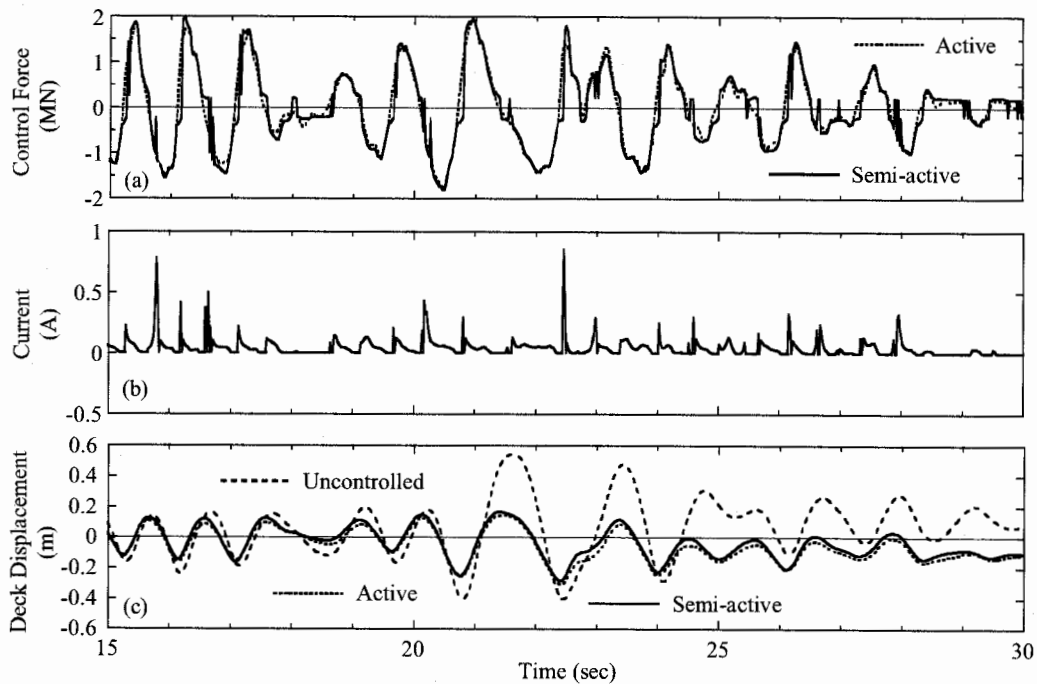


Figure 4. Comparison between active control and semi-active control using a MR damper: (a) control force, (b) applied current of the MR damper, and (c) deck displacement.

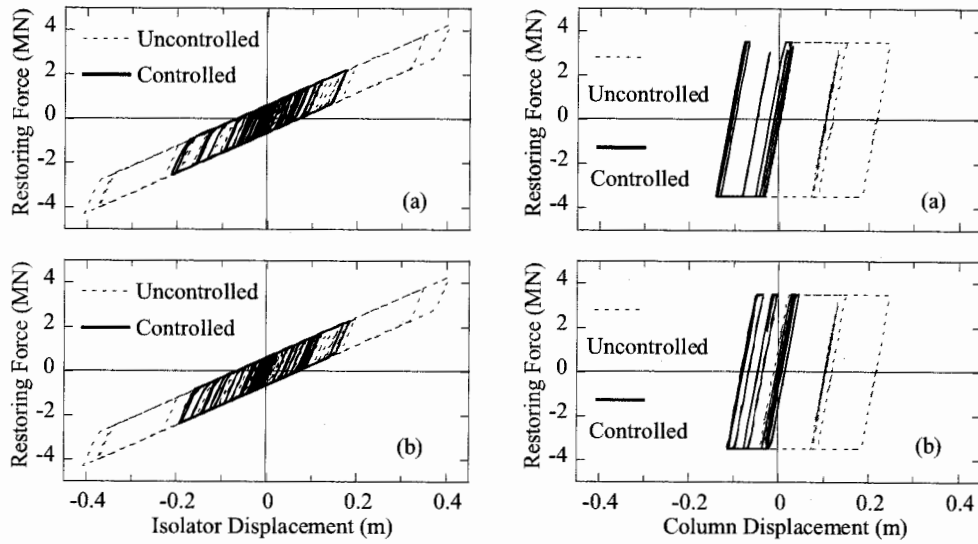


Figure 5. Hysteretic loops of the isolator and the column: (a) active control, and (b) semi-active control using a MR damper.

force and responses in Figs. 4 and 5 are available in Table 1. Also, it can be observed from Table 2 that the semi-active control based on the sliding mode control provides comparable control performance to the active control under JMA Kobe ground motion.

Instead of the sliding mode control algorithm, the LQR optimal control algorithm is applied to command the MR damper for comparison. The weighting matrix \mathbf{Q} in Eq. (7) is assumed as a diagonal matrix with the diagonal elements $Q_{ii} = [1, 1000, 1, 1]$, which achieves better performance in reducing the deck displacement through a parametric study. The weighting R in Eq. (7) is assumed to be 3×10^{-12} such that the peak control force is almost equal to that based on the sliding mode control algorithm. Tables 1 and 2 present the peak control forces and responses under the active control and the semi-active control based on the LQR control algorithm. As shown in Tables 1 and 2, the peak responses are almost identical under both the active control and the semi-active control, which display that the semi-active control using the MR damper performs quite close effect to the active control. However, the semi-active control based on the sliding mode control algorithm presents more effective performance on reducing the deck displacement than the semi-active control based on the LQR control algorithm. It is also observed that the semi-active control based on the LQR control causes much larger residual displacement than the uncontrolled under Sun-Moon Lake ground motion, which likely develops extreme inelastic response in structures.

4. CONCLUSIONS

The effectiveness of a semi-active control method using magnetorheological (MR) dampers in reducing the deck displacement of the isolated bridges, which exhibit nonlinear responses at both the columns and the isolators under near-field ground motions, was studied. The sliding mode control algorithm was utilized to command the MR dampers. The control performance of the semi-active control based on the sliding mode control algorithm was investigated through comparison with that based on the LQR control algorithm. Analyzed was a five-span viaduct with HDR isolators. The following conclusions may be drawn from the results presented herein.

(1) The semi-active control using MR dampers is effective in reducing the peak deck displacement of

Table 1 Peak control force and peak responses under Sun-Moon Lake record

Control method	Control force (kN)	Deck displacement (m)	Isolator ductility	Column ductility	Column residual displacement (m)
No control	-	0.55	25	8.0	0.11
Sliding mode control					
Active control	1965	0.31	13	4.5	0.10
Semi-active control	1964	0.29	12	3.7	0.08
LQR optimal control					
Active control	1975	0.37	11	8.3	0.22
Semi-active control	1954	0.37	11	7.7	0.21

Table 2 Peak control force and peak responses under JMA Kobe record

Control method	Control force (kN)	Deck displacement (m)	Isolator ductility	Column ductility	Column residual displacement (m)
No control	-	0.24	14	1.6	0.02
Sliding mode control					
Active control	1941	0.12	8	1.4	0.01
Semi-active control	1987	0.14	7	2.6	0.05
LQR optimal control					
Active control	1939	0.17	8	2.1	0.03
Semi-active control	1929	0.17	8	2.2	0.04

nonlinear isolated bridges under near-field ground motions.

(2) The MR damper is capable of tracing most of the control forces demanded by the sliding mode control algorithm as well as the LQR optimal control algorithm such that the semi-active control using the MR damper provides the comparable control performance to the active control.

(3) The control performance in reducing the deck displacement is outstanding by using the semi-active control based on the sliding mode control algorithm as compared with the semi-active control based on the LQR control algorithm.

Acknowledgements:

The authors acknowledge the support to the first author during the doctoral study from the Center for Urban Earthquake Engineering (CUEE) in Tokyo Institute of Technology, Tokyo, Japan.

References:

- Dyke, S.J., Spencer, B.F., Sain, M.K., and Carlson, J.D. (1996), "Modeling and Control of Magnetorheological Dampers for Seismic Response Reduction," *Smart Materials and Structures*, **5**, 565-575.
- Japan Road Association (1996), "Design Specifications of Highway Bridges, Part V Seismic Design," Tokyo, Maruzen.
- Kawashima, K., and Unjoh, S. (1994), "Seismic Response Control of Bridges by Variable Dampers," *Journal of Structural*

- Engineering, ASCE, **120**(9), 2583-2601.
- Ruangrassamee A., and Kawashima, K. (2001), "Semi-Active Control of Bridges with Use of Magnetorheological Dampers," *Smart Materials and Structures*, **10**, 323-332.
- Spencer, M.K., Dyke, S.J., Sain, M.K. and Carlson, J.D. (1997), "Phenomenological Model of a Magnetorheological Damper," *Journal of Engineering Mechanics, ASCE*, **123**(3), 230-238.
- Wen, Y.K. (1976), "Method for Random Vibration of Hysteretic System," *Journal of Engineering Mechanics Division, ASCE*, **102**(EM2), 249-263.
- Yang, G., Spencer, B.F., Carlson, J.D. and Sain, M.K. (2002), "Large-Scale MR Fluid Dampers: Modeling and Dynamic Performance Considerations," *Engineering Structures*, **24**, 309-323.
- Yang, J.N., Li, Z., and Vongchavalitkul, S. (1992), "A Generalization of Optimal Control Theory: Linear and Nonlinear Control," NCEER-92-26, National Center for Earthquake Engineering Research, State University of New York at Buffalo, USA.
- Yang, J.N., Wu, J.C., Kawashima, K., and Unjoh, S. (1995a), "Hybrid Control of Seismic-Excited Bridge Structures," *Earthquake Engineering and Structural Dynamics*, **24**(11), 1437-1451.
- Yang, J.N., Wu, J.C. and Agrawal, A.K. (1995b), "Sliding Mode Control for Nonlinear and Hysteretic Structures," *Journal of Engineering Mechanics, ASCE*, **121**(12), 1330-1339.

CYCLIC ELASTO-PLASTIC BEHAVIOR OF BUCKLING-RESTRAINED BRACE MEMBERS

A. Kasai¹⁾, T. Usami²⁾, and M. Kato³⁾

1) Assistant Professor, Dept. of Civil Engineering, Nagoya University, Japan

2) Professor, Dept. of Civil Engineering, Nagoya University, Japan

3) Mitsubishi Heavy Industry Co., Ltd., Japan

kasai@civil.nagoya-u.ac.jp, usami@civil.nagoya-u.ac.jp, motoki_kato@mhi.co.jp

Abstract: This study is aimed at developing a simple analysis model which can predict the cyclic behavior of buckling-restrained braces. For this purpose, the brace characteristic and elasto-plastic behavior under monotonic loading are investigated by means of FEM analysis. Moreover, the results of cyclic analysis are compared with experimental data. As a result, core plate behavior that the fundamental mode is moved to higher modes owing to contacting with mortar, is reproduced and it is found that buckling does not occur. Cyclic loading analysis shows that the brace has stable load-displacement relation in both the tension and compression fields and the results are well agreed with experimental results.

1. INTRODUCTION

After the Hyogoken-Nanbu Earthquake in 1995, the way of adopting members that absorb the seismic energy of structures is very effective in the fact that they have the ability of absorbing seismic energy constantly. According to the researches in the past, if the energy-absorbed members are installed in the main part of a structure, almost damages concentrate in their members and as a result the residual displacement of whole system including the main structure is significantly larger than normal main structure. Therefore, setting up sacrificial members to absorb seismic energy in that part results in decreasing residual deformation of main members and easier repairing of structures.

Brace members who are used as diagonal members of frame structures are adopted widely towards structures such as high-rise buildings in the building engineering field. But their strength falls suddenly because of the buckling phenomenon when they are compressed axially. It is difficult not only to select the suitable sectional form, but also to build structures possessing stiffness and strength expected.

To overcome this weak point, the buckling-restrained brace that is covered with restraining part made of a frame and mortar is recommended (Fig. 1). In this figure, (b) shows conceptual composition of the buckling-restrained brace; (c) gives three examples of the sectional form. Restraining the buckling of brace not only reduces lateral deflection, but also supplies similar load-displacement characteristic in compression to that in tension. In short, this method makes it possible both to raise the ability absorbing the seismic energy remarkably and to simplify the hysteresis. Because of these reasons, a number of studies on the buckling-restrained brace have been carried out in the building engineering field. A type of structural configuration in which a flat steel brace is covered with soft rubber acting as unbonded material, and restrained by the reinforced concrete wall has been proposed by Yoshino et al. (1971). The experiment using similar composite wall, carried out by Wakabayashi et al. (1973), was succeeded in observing spindle shape load-displacement relation under cyclic loading of large amplitude. Moreover, a method that flat steel brace builds in reinforced concrete wall has

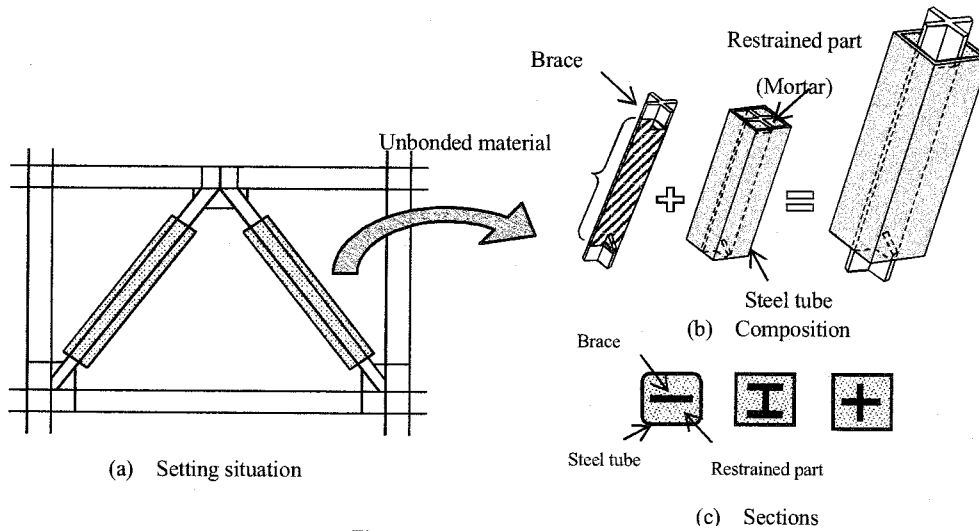


Figure 1 Buckling-restrained brace

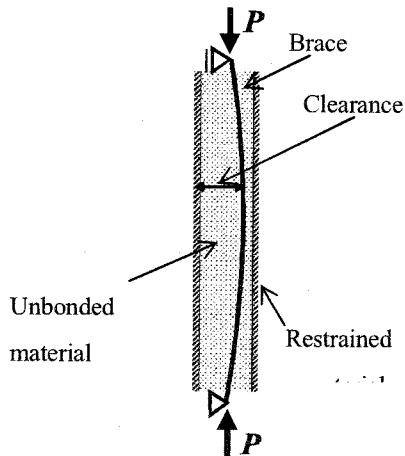


Figure 2 Simple beam model

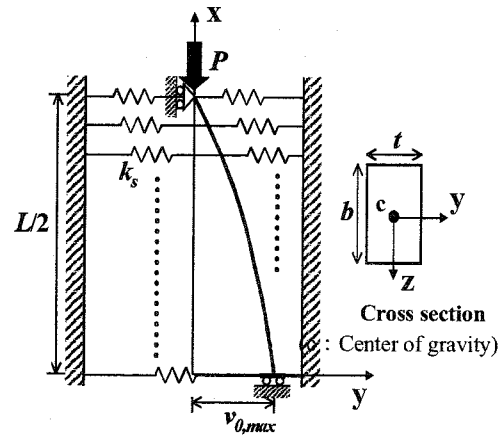


Figure 3 Analytical model

made progress to the buckling-restrained brace as a wire rod was reported by Fujimoto et al. (1988) and Nakao et al. (1990, 1991). Furthermore, the performance of the buckling-restrained brace as a seismic element was evaluated by Iwata et al. (2000).

Although the seismic performance of the buckling-restrained brace has been experimentally confirmed by many researchers, numerical studies are very few. Even in the limited analytical studies, numerical effort dealing with the reproduction of the experimental behavior is not available. Therefore, this study is aimed at developing a simple analytical model which can predict the cyclic elasto-plastic behavior of buckling-restrained brace.

2. NUMERICAL METHOD

2.1 Outline of analytical model

The brace as shown in Fig.1(a) can restrain the buckling of core plate, because the deformation of core plate are grown in the space filled in the unbonded material, and then contacts with the restraining part. That is to say, the behavior of the buckling-restrained brace can be considered as a problem dealing with contact phenomenon between the brace and the restraining part. Most of buckling-restrained braces are made by putting unbonded material around the brace and then filling

restraining material such as mortar between the brace and steel tube that is used as a cover. It is considered that the clearance between the brace and the restraining part closely re-lates to initial deflection. In this study, since the stiffness of the unbonded material is much less than that of the restraining part, the surface of restraining part was assumed as rigid wall and initial deflection was assumed with moderate clearance. The analytical model considered is a two-dimensional simply supported beam model as shown in Fig. 2, and half model is adopted because of its symmetry. In this model, the surface of the restraining part is represented as rigid body, and the lateral resistance of the unbonded material is modeled as finite springs (Fig. 3). The ABAQUS program is used in this analysis. Two-dimensional beam elements based on Ti-moshenko beam theory are used for the brace. The rectangular section form is selected to model the flat steel brace. And a two-node rigid element R2D2 is employed as rigid wall, and a two-node spring element SPRING2 is used to model springs. Moreover, finite sliding contact formulation based on Lagrangian multiplier technique available in the ABAQUS is defined in the analysis.

Both beam and rigid elements are divided into 40 at the same interval, and the position of each node in the X direction is defined to be equal (the coordinate of this analysis is shown in Fig. 3). Spring elements are defined to connect beam and rigid points, and to act for only y-axis direction. As for the boundary conditions of the present model, the displacement in the y-axis direction is fixed at top node, and both the displacement X direction and the rotation in the Z direction which is perpendicular to the X-Y plane are fixed at bottom node.

2.2 Modeling of unbonded element

As mentioned above, the lateral resistance characteristic of unbonded material is modeled as finite springs. Normally, coating materials or adhesive tapes and so on, which are very thin, are used as un-bonded materials. This is why there are many un-known points about the stiffness of unbonded materials. Actually it is very difficult to exactly define the stiffness of those springs. Therefore, the spring stiffness, k_s , is calculated by using a parameter in terms of a relative ratio to the bending stiffness of the brace.

For deciding the constant, k_s , the problem as shown in Fig. 4 was consulted because of the core plate supported by unbonded material continuously. Firstly, a ratio of stiffness K_{unbond} to the stiffness K_{brace} was decided as Eq. (1):

$$\alpha = \frac{K_{unbond}}{K_{brace}} \quad (1)$$

Deflection on the center of core plate is restraint by unbonded material. This can be explained as Eq. (2):

$$v_1 = \frac{1}{1 + \alpha} \cdot v_0 \quad (2)$$

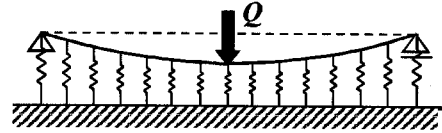


Figure 4 Successive supported beam

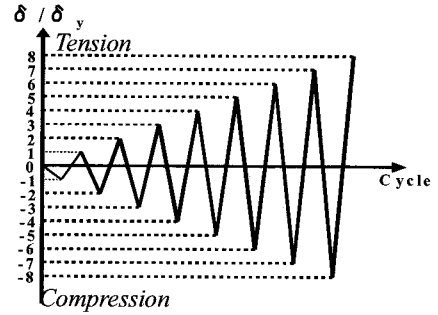


Figure 5 Cyclic loading pattern

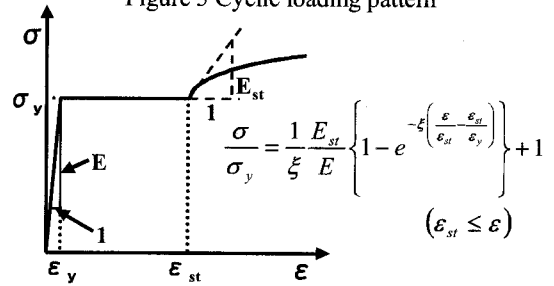


Figure 6 Stress-strain model for steel

where v_1 = deflection of core plate restraint by un-bonded material and v_0 = pure deflection of core plate. The restraint plate is govern by Eq. (3):

$$EI \frac{d^4 v}{dx^4} + cv = 0 \quad (3)$$

where E = Young's modulus, I = moment of inertia and c = spring constant per unit length. Constant c can be calculated from Eqs. (1) – (3). Because discrete springs are used in modeling unbonded material in this analysis, the length supported by a spring is L/m ($m = 40$ in this study). Accordingly, the spring constant is obtained as $c \cdot L/m$. It should be noted that the spring constant at the bottom node is half of this value, because the half model is used.

2.3 Dimensions of analytical models

Table 1 shows dimensions and model parameters of analytical models together with their theoretical yield load P_y and Euler's buckling load P_{cr} . In this table, λ is the slenderness ratio defined by L/r where r is the radius of gyration. Moreover, the width b and length L are kept constant as 90mm and 4000mm, respectively.

According to the past study performed by Iwata et al. (2000), the width of the unbonded material is set to be 1 mm. Initial deflection v_0 is assumed to be sine-wave with its maximum value of 0.5mm which is half of the unbonded material's thickness.

Table 1 Dimensions and Parameters

λ	P_y (kN)	P_{cr} (kN)	t (mm)	α	c (MPa)	k_s (N/mm)
100	3120	2510	138.6	0	0	0
				1/10	0.158	7.92
				1/5	0.317	15.9
				1/2	0.746	39.8
200	1560	315	69.3	0	0	0
				1/10	0.0198	0.990
				1/5	0.0397	1.98
				1/2	0.0995	4.98
				1	0.200	10.0
				10	2.27	113
400	779	39.3	34.6	0	0	0
				1/10	0.00247	0.124
				1/5	0.00494	0.247
				1/2	0.0124	0.620
*Length of brace : L = 4,000mm, Width of section : b = 90mm Divided number : m=40						

Table 2 Material Properties

Steel Type	σ_y (MPa)	E/E_{st}	ϵ_{st}/ϵ_y	E (GPa)	ξ	ν
SS400	250	40	10	205	0.06	0.3

2.4 Loading method and stress-strain model for steel

In this study, the brace is loaded by controlling X-directional displacement at the top point of analytical model. Two types of loading patterns (i.e. monotonic and cyclic loading) are considered (see Fig. 5).

An elasto-plastic relation with strain-hardening region as shown in Fig. 6 is employed in the mono-tonic analysis. The material properties of a mild steel SS400 are given in Table 2. In the cyclic analysis, a modified two-surface model (2SM) is employed (Shen et al. 1995).

3. NUMERICAL RESULTS

3.1 Monotonic analysis

Shown in Fig. 7 are load-displacement relations from monotonic analyses of steel flat braces under compression or tension, and a buckling-restrained brace under compression in the case of $\lambda = 200$ and

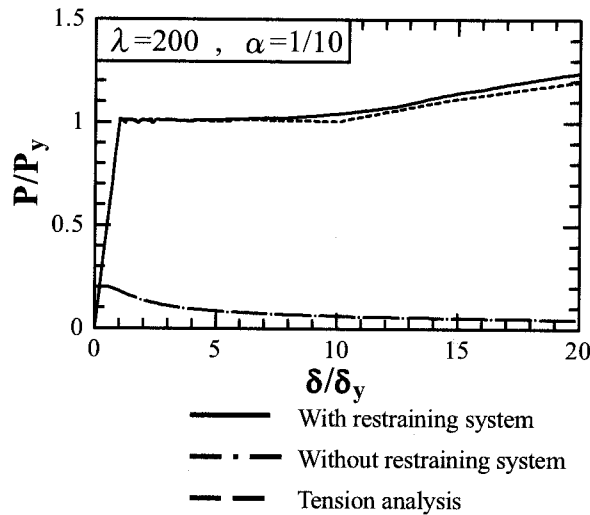


Figure 7 Load-displacement relation
(Monotonic loading)

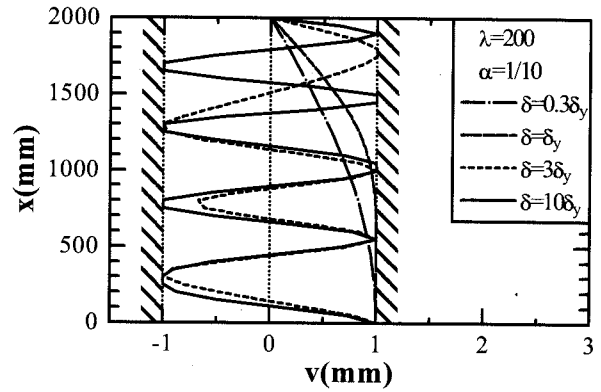
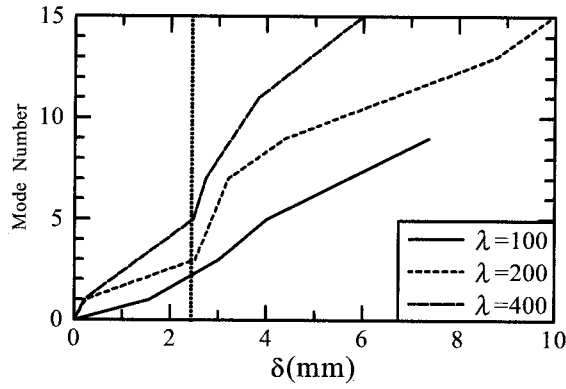
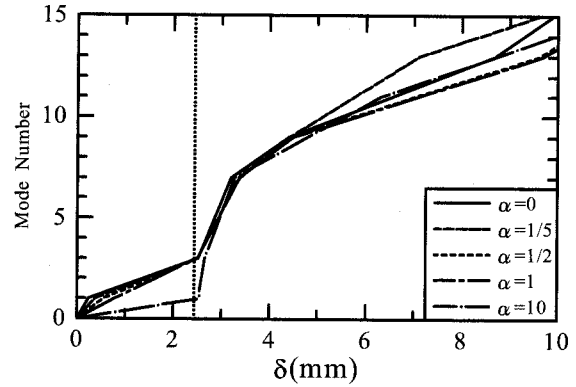


Figure 8 Deformation of the brace
(Monotonic loading)



(a) For the slenderness ratio



(b) For the stiffness ratio

Figure 9 Comparison of Deformation

$\alpha = 1/10$. In this figure, vertical axis is the load divided by the yield load, while horizontal axis is the displacement non-dimensionalized by the yield displacement. It is noted that compressive field is taken as positive in the compression analysis and tension field is taken as positive in the tension analysis.

In the analysis of compressing the brace alone, where no restrain to the buckling is provided, the load drops immediately before yielding because of the buckling. Whereas in the compressive analysis of the buckling-restrained brace carried out by using the present analytical model, no decrease in the strength is observed and the load-displacement relation is close to that of the tension analysis.

The same behavior is consistent with all the cases of $\lambda=100$, 200 and 400. Therefore, it is appropriate to use the analytical model developed in this study in order to simulate stable load-displacement relation of the buckling-restrained brace subjected to monotonic loading.

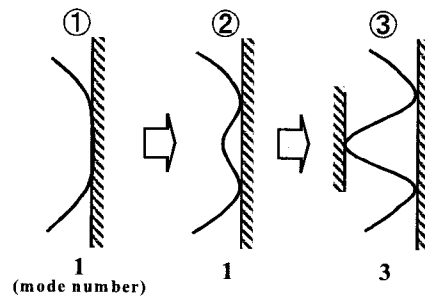


Figure 10 Definition of the mode number

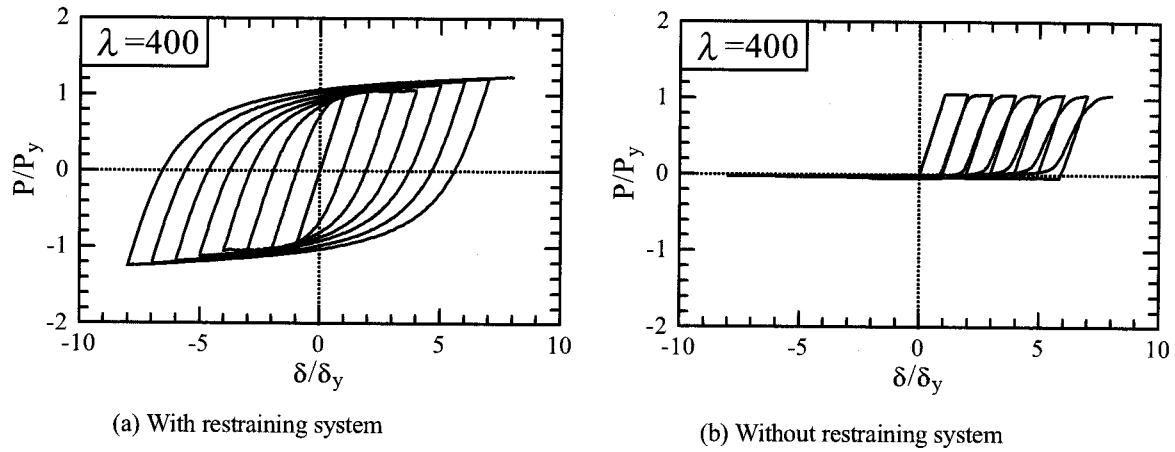


Figure 11 Load-displacement relation (Cyclic loading)

Shown in Fig. 8 is the deformation of the brace under monotonic loading for a case of $\alpha=1/10$ and $\lambda=200$, corresponding to axial displacements at $0.3\delta_y$, δ_y , $3\delta_y$, and $10\delta_y$. Fig. 9 shows comparisons of deformation modes where (a) is for the slenderness ratio λ , and (b) for the stiffness ratio α . The mode number is defined as the number of points contacting with the wall. This number increases when the points separated from the wall contacts with the reverse wall (see Fig. 10).

In Fig. 8, the brace is deformed along the wall after contacting it, and then moves to higher modes. This behavior is predominant after yielding as is seen from the difference between $\delta=\delta_y$ and $\delta=3\delta_y$. The deformation behavior moving to the higher mode can be recognized from Fig. 9. The brace is deformed easily when the slenderness ratio is larger, but the deformation is almost the same when α is less than 1. This is because the stiffness of the un-bonded material is much less than that of the brace. Thus, it can be concluded that the effect of the un-bonded material stiffness on the deformation of the brace is very small.

3.2 Cyclic analysis

The load-displacement relation obtained from the cyclic analysis of the buckling-restrained brace is shown in Fig. 11 in the case of $\lambda = 400$, where (a) is obtained using the present analytical model, and for comparison (b) represents analytical result of the brace alone. Both the vertical and horizontal axes are defined in the same way as in the case of monotonic analysis, and tension field is taken as positive here.

From Fig. 11(b), the behavior of the brace alone in the compressive field is very weak because of the buckling. However, the load-displacement relation of the buckling-restrained brace is very stable in both the compression and tension fields as can be seen from Fig. 11(a). Also in the cases of $\lambda=100$ and $\lambda=200$, similar stable behaviors are obtained. There-fore, the developed analytical model can also be used to predict the stable load-displacement relation of the buckling-restrained brace under cyclic loading.

Table 1 shows dimensions and model parameters of analytical models together with their theoretical yield load P_y and Euler's buckling load P_{cr} . In this table, λ is the slenderness ratio defined by L/r where r is the radius of gyration. Moreover, the width b and length L are kept constant as 90mm and 4000mm, respectively.



Photo 1 Testing system

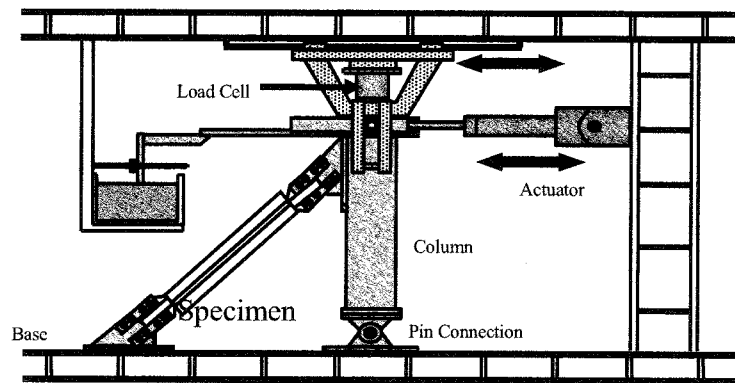


Figure 12 Conceptual scheme of testing system

Table 3 Dimensions and material properties of test specimen

Parameters						
λ	L	b (mm)	t (mm)			
553	1355	100	8.49			
Material properties						
Steel Type	σ_y (MPa)	E/E _{st}	ϵ_{st}/ϵ_y	E (GPa)	ξ_F	ν
SS400	306	74	12	213	0.06	0.29

4. COMPARISON WITH EXPERIMENTAL RESULTS

4.1 Outline of experiment

Pilot experiments of the buckling-restrained brace are recently carried out at Nagoya University in 2002 (see Photo 1). The testing system used in this study is shown in Fig. 12. The test specimen is set up so that the vertical angle can become 45° . The lower end of the specimen is fixed at the base, and the up-per end is set to the column. The axial displacement of the specimen is given by the horizontal displacement of the actuator and the rotation of pin end of the column. Dimensions of test specimen are shown in Table 3.

4.2 Comparisons between test and analysis

The load-displacement relations from both the experiment and analysis are shown in Fig. 13. It is found that analytical results show good agreement with the experiment. Furthermore, the experimental results are explained in detail by Usami et al. (2003).

5. CONCLUSIONS

Main findings obtained from the present study are summarized as follows.

- 1) A simple analytical model which can predict both the monotonic and cyclic behaviors of the buckling-restrained brace is developed.
- 2) The brace is easy to deform when the slenderness ratio is larger, and the effect of the unbonded material stiffness is very small.
- 3) The comparison between the analysis and experiment shows that the analytical model developed in this study is of good accuracy in predicting the inelastic behavior of the buckling-restrained brace.

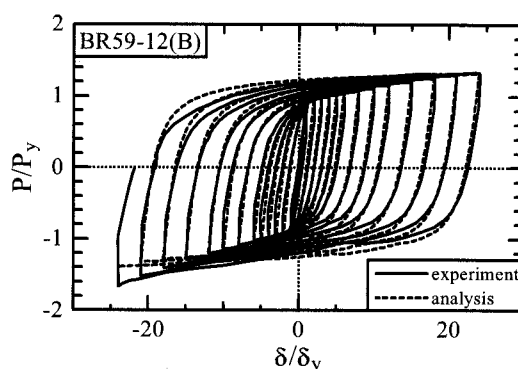


Figure 13 Hysteresis curve

References:

- Fujimoto, M., Wada, A., Saeki, E., Watanabe, A., and Hitomi, Y. (1988.), A study on the unbonded brace encased in buckling-restraining concrete and steel tube," *Journal of Structural Engineering*, Vol.34B, AIJ,249-258(in Japanese).
- Iwata, M., Murai, M., Kato, T., Ogawa, H., and Wada, A. (2000), Buckling-restrained braces as hysteretic dampers (Part1,Part2), *Summaries of technical papers of annual meeting architectural institute of Japan*, Struct.-CU,921-924(in Japanese).
- Matsumoto, N., Okano, M., Arita, H., Sogabe, M., Wakui, H., Ohuchi, H., and Takahashi, Y. (1999), "Seismic behavior of railway viaducts with steel damper and braces," *Journal of Structural Engineering* Vol.45A, 1411-1422(in Japanese).
- Matsumoto, N., Sogabe, M., Okano, M., Wakui, H., and Ohuchi, H. (2000), "A study on improvement for seismic behavior of railway viaducts using steel damper and braces," *Journal of Structural Engineering* Vol.46A, 547-554(in Japanese).
- Nagao, T. and Takahashi, S. (1990), "A study on the elasto-plastic behavior of unbonded composite bracing (Part1)," *Journal of Structural Construction Engineering*, AIJ, No.422, 105-115(in Japanese).
- Nagao, T. and Takahashi, S. (1991), "A study on the elasto-plastic behavior of unbonded composite bracing (Part2)," *Journal of Structural Construction Engineering*, AIJ, No.422, 45-56(in Japanese).
- Saeki, M., Maeda, Y., Nakamura, H., Midorikawa, M., and Wada, A. (1995), "Experimental study on practical-scale unbonded braces," *Journal of Structural Construction Engineering*, AIJ, No.476, 149-158(in Japanese).
- Saeki, M., Maeda, Y., Iwamatsu, K., and Wada, A. (1996), "Analytical study by finite element method and comparison with experiment results concerning buckling-restrained unbonded braces," *Journal of Structural Construction Engineering*, AIJ, No.484, 111-120(in Japanese).
- Saeki, M., Maeda, Y., Iwamatsu, K., and Wada, A. (1996), "Analytical study on unbonded braces fixed in a frame," *Journal of Structural Construction Engineering*, AIJ, No.489, 95-104(in Japanese).
- Shen, C., Mamaghani, I. H. P., Mizuno, E., and Usami, T. (1995), "Cyclic behavior of structural steels. Theory," *J. Engng. Mech.*, ASCE, 121(11), 1165-1172.
- Usami, T., Kasai, A., Kato, M. (2003), "Behavior of buckling-restrained brace members," *Proc. of Fourth International Conference on behavior of steel structures in seismic areas*.
- Wakabayashi, H., Nakamura, T., Kashiwara, A., Morizono, T., and Yokoyama, H. (1973), "Experimental study on cyclic elasto-plastic property of precast concrete panel including insulation braces," *Summaries of technical papers of annual meeting architectural institute of Japan*, Struct., 1041-1044(in Japanese).
- Yoshino, T., Karino, Y., Kuwabara, T., and Soumura, Y. (1971), "Experimental study on structural wall including braces," *Summaries of technical papers of annual meeting architectural institute of Japan*, Struct., 403-404(in Japanese).

DUCTILITY OF WELDED JOINTS WITH WEAKER WELDING MATERIAL

A. Tanabe¹⁾ and M. Kato²⁾

1) Research Associate, Department of Civil Engineering, Tokyo Institute of Technology, Japan

2) Student, Department of Civil Engineering, Tokyo Institute of Technology, Japan

tanabe@cv.titech.ac.jp -

Abstract: Bridge high-performance steel (BHS) is being developed. BHS has a problem about under-match welded joint. The under-match welded joints are joints with weaker weld metal. It has been showed that under-match welded joints have enough tensile strength but low elongation capacities because of constraint due to stress triaxiality in weld metal. Thus, evaluations of stress triaxiality, constraint effects, tensile strength and elongation are carried out by solid FEA and tensile test. In this study, it was proposed that strain fraction as the index of constraint effects. FEA results show that highest triaxiality and constraint effects occur at the center of welded metal, and that stress triaxiality and constrain effects are not directly connected. Furthermore, it also showed that the constraint effect increase just after weld metal yielding, and then it takes peaks and it gradually decrease. Tensile tests of under-match welded joints with/without reinforcement showed that only the specimen of 20% under match without reinforcement shows the significant low elongation. Therefore we may say that if reinforcement exists, under-match welded joints had enough elongation because critical sections were base metal (outside of weld metals), and that 10% under match welded joint is applicable even if the reinforcement was removed.

1. INTRODUCTION

Bridge High-performance Steel, BHS500 and BHS700, is developing now (Miki et al. 2003, Miki 2005). BHS has many features: high strength, high weldability, high corrosion toughness, high fracture toughness, etc. BHS is designed for the super structure of bridges, however it is considered to use BHS for substructures such as frame piers, because of its high performance. However, in order to use BHS for substructures, seismic performance is also required; because BHS was designed for use in elastic region (post yielding behavior was not considered). Moreover, there is a high possibility of under-match welded-joints, because of its high strength. The under-match welded joints are welded joint with lower strength welding material than base-metal.

When external force was applied to under-match welded joints, weld metal yield first and the weld metal is constrained by non-yielded base metal. Stress triaxiality is introduced by this constraint (HENry and Luxmoore 1997, Hancock et al. 1993). Stress triaxiality is defined as Equation (1).

$$Triaxiality = \frac{\sigma_m}{\sigma_{eff}} = \frac{\frac{1}{3}(\sigma_{xx} + \sigma_{yy} + \sigma_{zz})}{\frac{1}{\sqrt{2}} \left[(\sigma_{xx} - \sigma_{yy})^2 + (\sigma_{xx} - \sigma_{zz})^2 + (\sigma_{yy} - \sigma_{zz})^2 \right]^{1/2}} \quad (1)$$

Where, σ_m : hydrostatic mean stress, σ_{eff} : von Misses Equivalent Stress.

Satoh and Toyoda (1971) showed that the under-match welded joint have almost same tensile strength as usual welded joints due to constraints by stress triaxiality. However, it was also pointed that under-match welded joint have a tendency of low elongation. Elongation is one of important post-yielding behavior and it is required to achieve high seismic resistance due to prevention of brittle failure. Thus, evaluation of the elongation of under-match welded joints is important, because if it as high elongation, it also have high energy absorption due to high strength.

This study aims to evaluate the performance of under-match welded joints. Finite Element Analyses (FEA) with solid elements were carried out in order to investigate triaxiality and constraint in under-match welded joints. The parameters of the FEA are under-matching ratio. Then the tensile strength and elongation of under-match welded joints were evaluated by tensile tests.

2. FINITE ELEMENT ANALYSIS

In order to know the detailed condition of stress and strain in under-match welded joints, solid finite element analysis was carried out. In this analysis, triaxiality, constraint and elongation were considered.

2.1 Proposal of Strain fraction

Constraint due to strength mismatching is usually evaluated with stress triaxiality. However the stress triaxiality is index by stress, thus there is a possibility that stress triaxiality does not reflect constraint effect properly. Thus, this study proposes strain fraction as an index of constraint and it is also evaluated. The strain fraction is defined as Equation (2) .

$$\text{Strain Fraction} = \frac{\epsilon_{trans}}{\epsilon_{xx}} \quad (2)$$

Where, ϵ_{trans} : transverse component of strain, ϵ_{xx} : longitudinal component of strain.

The strain fraction is equal to poison's ratio in elastic region, 0.5 in plastic region if there is no constraint, and about 1.0 under plane strain condition. Constraint effects may reduce the fraction of strain, thus the strain fraction can be used as an index of constraints due to triaxiality.

2.2 Analysis Conditions

Main parameter of the analysis is under-matching ratio of yielding point. Three under-matching ratios were evaluated: Even-match (0% under-match), 10% under-match and 20% under-match. In addition, existence of reinforcement and plastic hardening ratio were also considered as parameters.

In this study, butt welded joints are evaluated. Fig. 1 shows the FEM model of but welded joint. By considering symmetry, 1/8 model with 3 mirror conditions was used. The shape of fusion line was determined to simulate typical X-groove welded joint. Displacement was input at model end.

ABAQUS (ABAQUS.Inc 2005) was used as analysis code. Table 1 shows the list of material property for the analyses. Kinematic hardening was used. The yielding point of base metal is 500Mpa and the yielding points of welded metals are 500, 450 and 400 MPa.

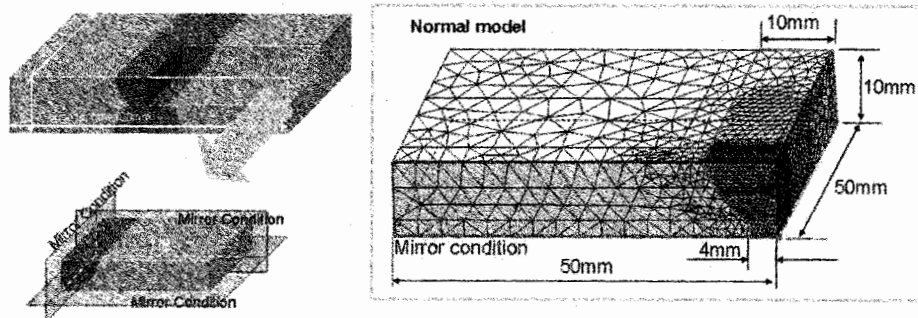


Figure 1 FEM mode

Table1 Material property for FEM

Material	Yielding Point (MPa)	Young's modulus (GPa)	Poisson's ratio	Strain Harding Ratio (GPa)
Base metal	500	20	0.3	2
Weld metal (Even-match)	500			
Weld metal (10% under-match)	450			
Weld metal (20% under-match)	400			

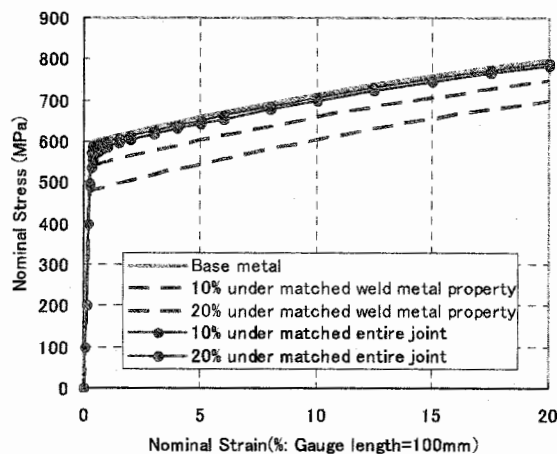


Figure 2 Nominal Stress-Nominal Strain Relationship

2.3 Analysis results

Figure 2 shows the relationships of nominal stress and nominal strain (gauge length 100mm). Material properties were also shown in this figure for comparison. In spite of under-matching, 10% and 20% under-match types have only small differences from even-match type. This fact means that welded joint may have enough tensile strength even in case of under-match welded joint.

Triaxiality was shown in Figure 3. High triaxiality was observed in the center of weld metal. The change of triaxiality at the center of weld metal is also shown in Figure 3. The stress triaxiality of 20% under-match model reduced after the yielding of weld metal.

Figure 4 shows strain fraction for width direction. High constraint occurred along fusion line and the highest constraint occurred at the center of specimen. Figure 5 show the relationship between strain fraction and nominal strain at the center of weld metal, next of fusion line (weld metal and base metal) and base metal. These figures indicate that constrain effects were appeared in weld metal after the yielding.

These result showed that the behavior of triaxiality and strain fraction have contrast. Thus, we may say that the reduction of stress-triaxiality after the yielding is came from constrain effects.

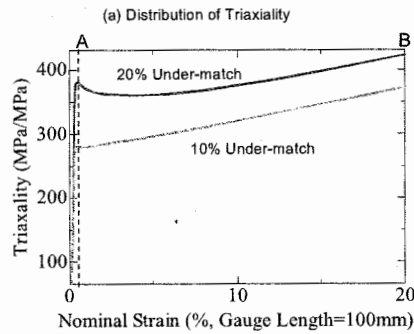
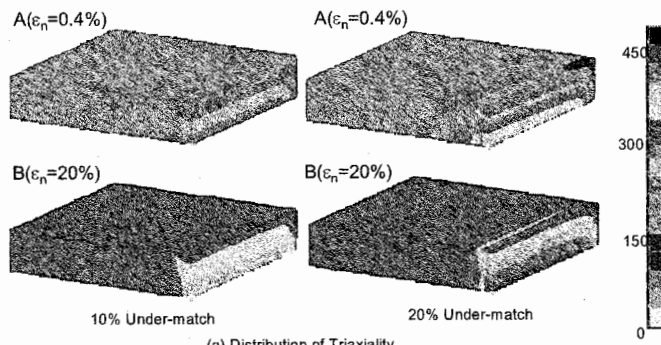


Figure 3 Triaxiality

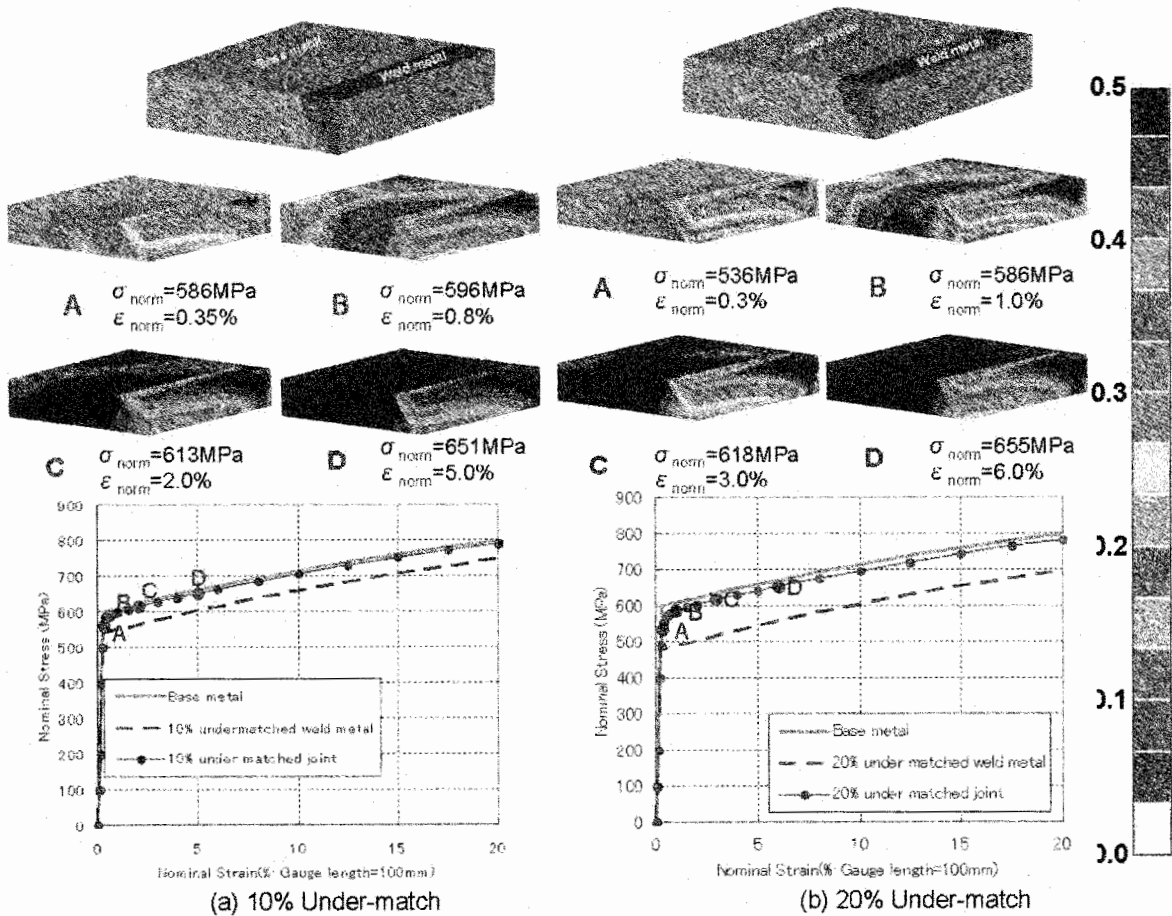


Figure 4 Fraction of Strain ($\epsilon_{width} / \epsilon_{longitudinal}$)

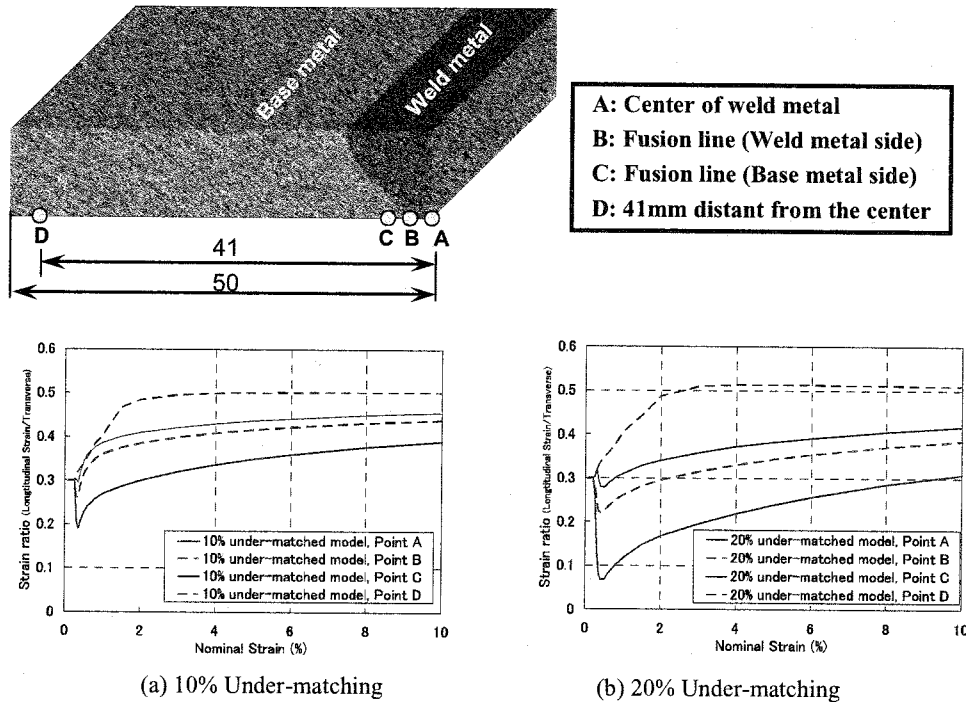


Figure 5 Fraction of Strain -- Nominal Strain Relationship

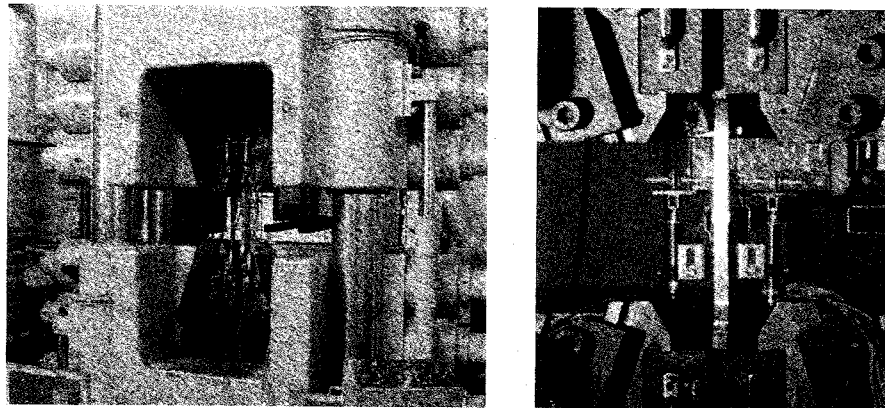


Figure 6 Test Setup

3. TENSILE TEST

3.1 Test setup

In order to evaluate the actual elongation of under-match welded joints, tensile tests were carried out. Main parameter is under-match ratio. Actual welded joints usually have reinforcement and existence of reinforcement may prevent strain concentration due to additional cross section. Therefore, existence of reinforcement is also considered as a parameter.

Tensile tests were carried out by 400ton tensile test machine. Test setup is shown in Figure 6. Table2 shows the list of specimens. Total 6 specimens were tested. Table4 shows the material properties for tensile test specimens.

Figure 7 shows the dimension of specimens. Satoh and Toyoda (1971) showed that the width of specimen should be wider than 5 times of plate thickness in order to achieve enough tensile

strength. The width of specimen was determined by following the specification of JIS #7 tensile test specimen (it was expired on 31 Dec 2004) in order to achieve width requirement. In case of no-reinforcement specimen, plate thickness was 18 mm because of removing reinforcement. Arrangement of strain gauge and extensometer is shown in Figure 8.

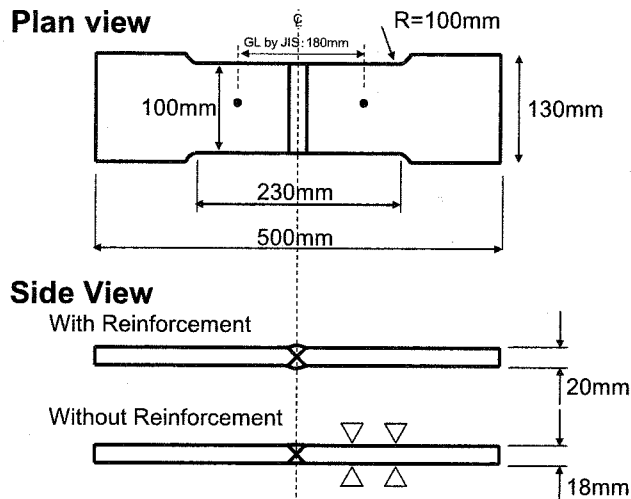


Figure 7 Dimension of Specimens

Table2 List of Specimens

Name	Under-match ratio	Reinforcement
UR00-R	0	With
UR10-R	10%	With
UR20-R	20%	With
UR00-N	0	Without
UR10-N	10%	Without
UR20-N	20%	Without

Table3 Welding Conditions

	Weld metal	Heat input (kJ/mm)	Desired YP (MPa)
Even	SF-60L	1.84	610
10% Under	SF-60	2.2	550
20% Under	YM-28S	1.69	490

Table4 Material Properties for Tensile Test

	Spec	YP(MPa)	TS(MPa)	Elongation(%)	Note
Base Metal	BHS500	611	691	36	from mill sheet
Weld Metal (even)	SF-60L	580	640	24	from spec
Weld Metal (10% Under)	SF-60	550	605	26	from spec
Weld Metal (20%Under)	YM28-S	480	540	33	from spec

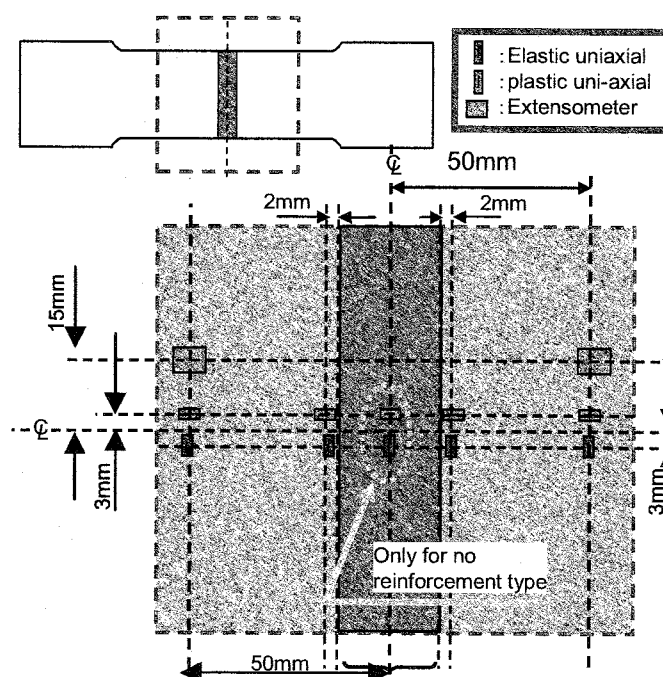
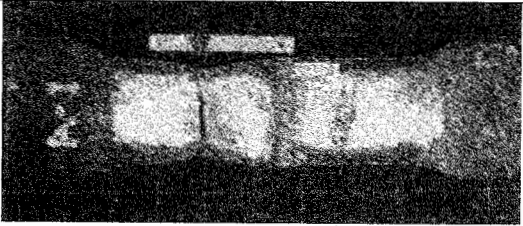
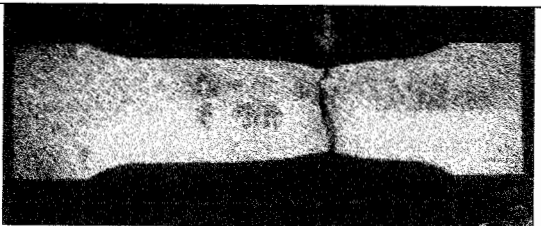
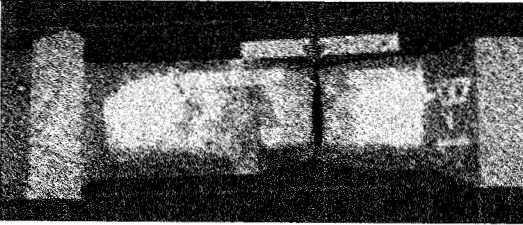
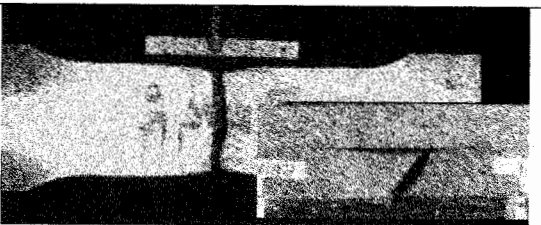
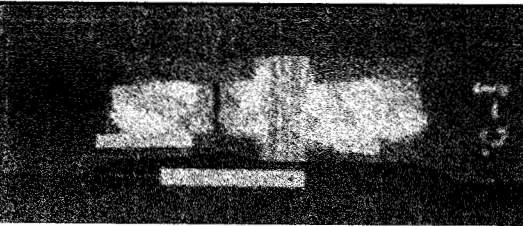
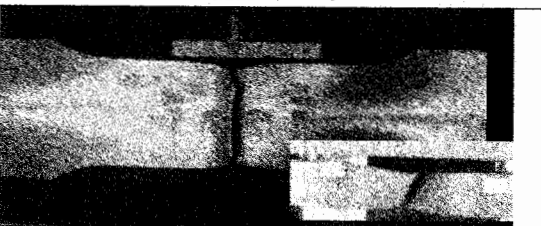


Figure 8 Arrangement of strain gauge and extensometer

3.2 Test result and discussion

Table5 shows the location of the section of failure. Table6 shows the tensile test result. Figure 9 shows the comparison of tensile strength, and Figure 10 shows the comparison of elongation. Figure 9 indicates that under-matching have small effects on the tensile strength. This is same tendency of Satoh and Toyoda's experimental results. In case of 20% under-matching without reinforcement specimen, elongation was significantly lower than others. Comparison with Table5 revealed that reason of low elongation of 20% under-match without reinforcement specimen was failure in weld metal. These facts also indicate that if reinforcement exists, welded joint may have enough elongation and tensile strength even 20% under-match weld joint, and that in case of no reinforcement, 10% under-match welded joint may allowable.

Table5 Location of Failure

	With Reinforcement	Without Reinforcement
Even	 Base metal	 Base metal
10% Under	 Base metal	 Fusion Line
20% Under	 Base metal	 Weld metal

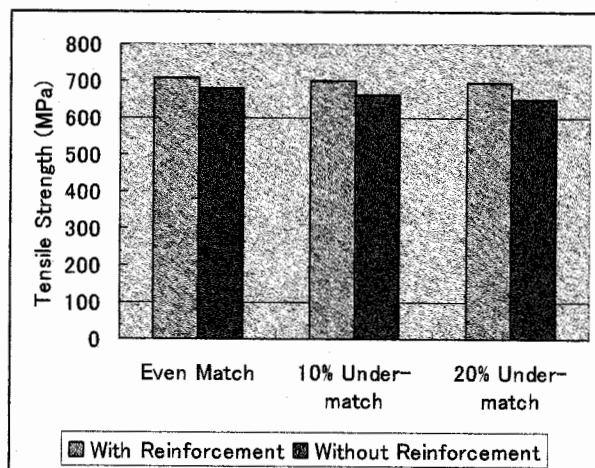


Figure 9 Comparison of Tensile Strength

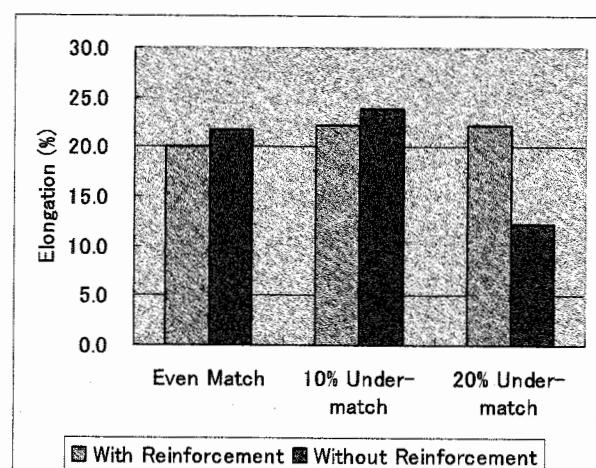


Figure 10 Comparison of Elongation

Table6 Tensile Test Result

Specimen	TS (MPa)	YP (MPa)	Elongation (%)
UR00-R	708.3	619	20.0
UR10-R	700.7	572	22.2
UR20-R	694.2	583	22.2
UR00-N	678.4	587	21.7
UR10-N	660.9	561	23.9
UR20-N	652.0	538	12.2

4. CONCLUDING REMAKS

4.1 Conclusions

The following results were obtained by this study.

- 1) Under-matched welded joint had enough elongation, which specified in JIS, if the joint have reinforcement, because the failure was not occurred in weld metal.
- 2) 10% under-match welded joint was allowable because it pass the criteria by JIS.
- 3) The highest triaxiality was occurred in under-match welded joint at the center of weld metal and it reduces just after yielding.
- 4) Strain fraction shows that constrain effects have a peek after the yielding ant it makes contrast with stress triaxiality. .

4.2 Future works

This study showed the possibility of the application of BHS for earthquake critical structures such as bridge piers. However, low cycle fatigue toughness is also required for seismic resistance. Therefore evaluation of low cycle fatigue performance is required.

References:

- Miki, C., Ichikawa, A., Kusunoki, T. and Kawabata, F. (2003) "Proposal of New High Performance Steels for Bridges (BHS500, BHS700)", *Journal of Structural Mechanics and Earthquake Engineering*, Japan Society of Civil Engineers, 738, 1-10
- Miki, C. (2005) "BHS: High Performance Steels for Bridges", *Bridge and Foundation Engineering*, Kensetsutosho, 39(8), 41-43
- Henry, B. S. and Luxmoore, A. R. (1997) "The stress triaxiality constraint and the Q-value as a ductile fracture parameter", *Engineering Fracture Mechanics*, 57(4), 375-390
- Hancock, J. W., Reiter, W. G. and Parks, D. M. (1993) "Constraint and toughness parameterized by T.", *Constraint Effects in Fracture*, ASTM STP1171, American Society for Testing and Materials, 21-40
- Satoh, K. and Toyoda, M. (1971) "Effect of Mechanical Heterogeneity on the Static Tensile Strength of Welded Joints", *Journal of the Japan Welding Society*, 40(9), 885-900
- ABAQUS.Inc (2005) "Analysis User's Manual"

EFFECT OF NEAR-FIELD GROUND MOTIONS ON THE INELASTIC FORCE AND DISPLACEMENT DEMAND OF BRIDGE STRUCTURES

G. Watanabe¹⁾ and K. Kawashima²⁾

1) Research Associate, Department of Civil Engineering, Tokyo Institute of Technology, Japan

*2) Professor, Department of Civil Engineering, Tokyo Institute of Technology, Japan
gappo@cv.titech.ac.jp, kawasima@cv.titech.ac.jp*

Abstract: In the force-based seismic design of bridge structures, the displacement reduction factor has an important role in the determination of inelastic displacement demand of bridge structures. Evaluation of the modification factors have been conducted by many researchers. On the other hand, the near-field ground motions resulted in the severe damage to the bridge structures in the last decade. The importance of the directivity of near-field ground motions and long pulsive ground motions has been recognized. A special emphasis of this paper is placed on the effect of near-field ground motions on the inelastic force and displacement demand.

1. INTRODUCTION

In the force-based seismic design of bridge structures, the force reduction factor has an important role in the determination of inelastic force demand of a bridge structure. Previous researchers conducted a comprehensive statistical study of constant ductility force reduction factor (Miranda and Bertero 1994). However, in spite of the importance in seismic design, less attention has been paid to large dispersion of the force reduction factors depending on ground motions.

On the other hand, the lateral displacement demand has not been taken into account in the force-based seismic design (Bommer and Elnashai 1999, Miranda and Ruiz-Garcia 1999, Ruiz-Garcia and Miranda 2003). Although the excessive nonlinear displacement response of a deck result in the failure of the superstructures due to the pounding between the adjacent decks and the failure of the restrainers, failure has not been taken into account. Since the maximum nonlinear displacement of a bridge deck and the residual displacement affect the retrofit and the serviceability after an extreme earthquake, to control the seismic damage of a structure, an adequate estimation of lateral displacement demand of the structure that exhibits non-linear behavior is also required. This paper discusses the lateral displacement demand of bridge structures based on the analysis of SDOF system.

In the last decades, a number of near-field ground motions have been recorded. Since near-field ground motions resulted in severe damage to bridge structures, interest has been generated the mechanism of generation (Somerville et al. 1996, Kamae, Irikura and Pitarka 1998) and the effect on the seismic response. From the previous researches, the importance of the directivity of near-field ground motions and longer period impulsive ground motions are considered. A special emphasis of this paper is provided on the effect of near-field ground motions on the inelastic force and displacement demands of bridge structures.

2. NONLINEAR RESPONSE AND MODIFICATION FACTORS FOR NEAR-FIELD GROUND MOTION

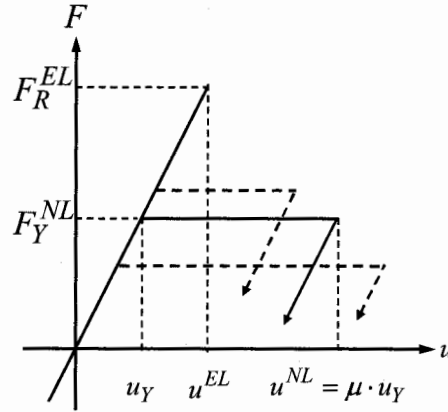


Figure 1 Elastic Response vs. Inelastic Response for SDOF systems

2.1 Definition of Modification Factors

In the preliminary seismic design of structures, the force reduction factor R_μ and displacement amplification factor D_μ can be used to assess the force and displacement demands from elastic response spectra. If one idealizes a structure in terms of a single-degree-of-freedom (SDOF) oscillator with an elasto-plastic model as shown in Figure 1, the force reduction factor R_μ and the displacement amplification factor D_μ may be defined as

$$R_\mu(T, \mu_T, \xi_{EL}, \xi_{NL}) = F_R^{EL}(T, \xi_{EL}) / F_Y^{NL}(T, \mu_T, \xi_{NL}) \quad (1)$$

$$D_\mu(T, \mu_T, \xi_{EL}, \xi_{NL}) = u^{NL}(T, \mu_T, \xi_{NL}) / u^{EL}(T, \xi_{EL}) \quad (2)$$

where T : natural period, F_R^{EL} and F_Y^{NL} : maximum restoring force in an oscillator with a linear and an elasto-plastic model, respectively, μ_T : target ductility factor, and ξ_{EL} and ξ_{NL} : damping ratio assumed in the evaluation of linear and bilinear response, respectively. In the present study, it was assumed that $\xi_{EL} = 5\%$ and $\xi_{NL} = 2\%$ (Watanabe and Kawashima 2001). Thus $R_\mu(T, \mu_T, \xi_{EL}, \xi_{NL})$ and $D_\mu(T, \mu_T, \xi_{EL}, \xi_{NL})$ are represented as $R_\mu(T, \mu_T)$ and $D_\mu(T, \mu_T)$ hereinafter.

The natural period T may be evaluated based on the yield stiffness of columns. Representing u_y as the yield displacement where the stiffness changes from the initial stiffness to the post-yield stiffness, a target ductility factor μ_T may be defined based on the yielding displacement u_y as

$$\mu_T = u_{\max T} / u_y \quad (3)$$

where $u_{\max T}$ is a target maximum displacement of an oscillator. The post-yield stiffness is assumed to be zero in the present study. Force reduction factors and displacement amplification factors were evaluated for target ductility factor, μ_T of 2, 4, 6 and 8 assuming an elastic perfect-plastic bilinear hysteresis. The natural periods range from 0.1 to 4.0 seconds (Watanabe and Kawashima 1999).

2.2 The Data Set of Ground Motions

The present study is based on 150 recorded ground motions. These records are classified into two categories depending on the distance from the fault D_{CF} . Hence, 60 records for near-field ground motions ($D_{CF} < 10\text{km}$) and 90 for middle-field ground motions ($10\text{km} \leq D_{CF} < 40\text{km}$) are used, respectively. These records are non-uniformly distributed over the entire magnitude range from $M = 5.3$ to 8.1 and the peak ground acceleration range from 0.9 to 17.5 m/sec^2 as shown in Figure 2.

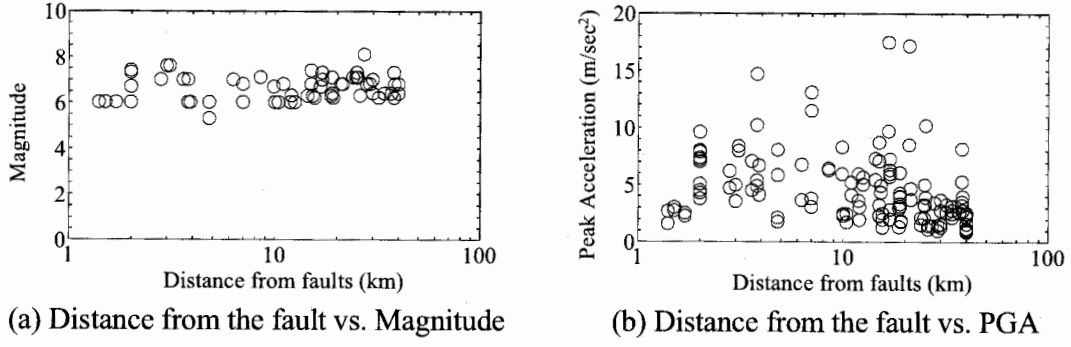


Figure 2 Data set of ground motion in the present study

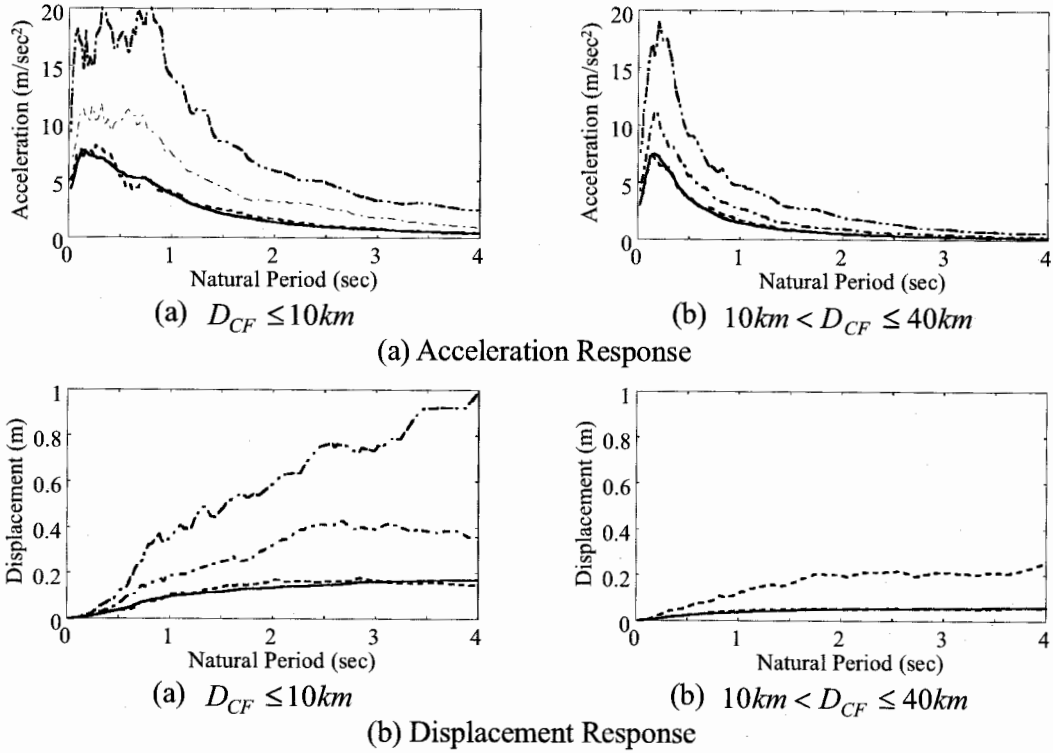


Figure 3 Response Spectra for each category of ground motions

Figure 3 shows the mean value of elastic acceleration and displacement spectra for the two categories of ground motions. The acceleration response spectra for the data set of ground motions with $10km < D_{CF} \leq 40km$ have obvious peaks at 0.2 sec. On the other hand, the mean acceleration response spectra for $D_{CF} \leq 10km$ are wide-band spectra. The displacement response spectra for $D_{CF} \leq 10km$ are much larger than those spectra for $10km < D_{CF} \leq 40km$.

The response spectra with the probability of non-exceedance are also shown. The probability of non-exceedance $p_r(X)$ (D'Ambrisi and Mezzi 2005) is the probability that the estimators X does not exceed a certain value of b . It may be defined as

$$p_r(X) = 1 - P(X \leq b) = 1 - \int_{-\infty}^b p(X) dX \quad (4)$$

where $p(X)$ is the probability of occurrence of the estimators.

As shown in Figure 3(a), the acceleration response spectra with $p_r = 0.5$ for $D_{CF} \leq 10km$ and $10km < D_{CF} \leq 40km$ exhibit the similar trend, and the peak level is $7.5 m/sec^2$. The peak level of acceleration response spectra with $p_r = 0.9$ reaches $20 m/sec^2$, which is equivalent to elastic seismic force level in the current seismic code. On the other hand, the displacement response with $p_r = 0.9$ for $D_{CF} \leq 10km$ is 4 times larger than that for $10km < D_{CF} \leq 40km$ in the $T = 0.1-1.0$ sec period range.

3. MODIFICATION FACTORS FOR NEAR-FIELD GROUND MOTIONS

Figure 4 and 5 show the modification factors, R_μ and D_μ , for each category of ground motions. Only the results for $\mu_T = 4$ and 8, as shown in Figure 4 and 5, are presented here since the results for other target ductility factors exhibit similar characteristics. It can be seen that scattering of the modification factors depending on ground motion is so significant. For example at natural period of 1.0 second, the force reduction factor varies from 1.9 to 8.6 depending on ground motion for $\mu_T = 4$ for near-fault ground motions, the displacement amplification factors range from 0.46 to 2.1.

Figure 6 shows the mean and coefficient of variation. The mean spectra of modification factors reach some certain value for the natural period longer than 2.0 sec, the mean values for this range are roughly independent of the fault distance D_{CF} . For the natural period range shorter than 0.7 sec, however, the difference due to D_{CF} is so significant. Coefficients of variation of R_μ and D_μ are quite large, however the scatterings of modification factors are independent of the period, especially for natural period range longer than 1.0 sec.

It is apparent that such a large scattering of the modification factors result in a large change of sizing of a structure in seismic design. Obviously smaller force reduction factors should be assumed to provide conservative design.

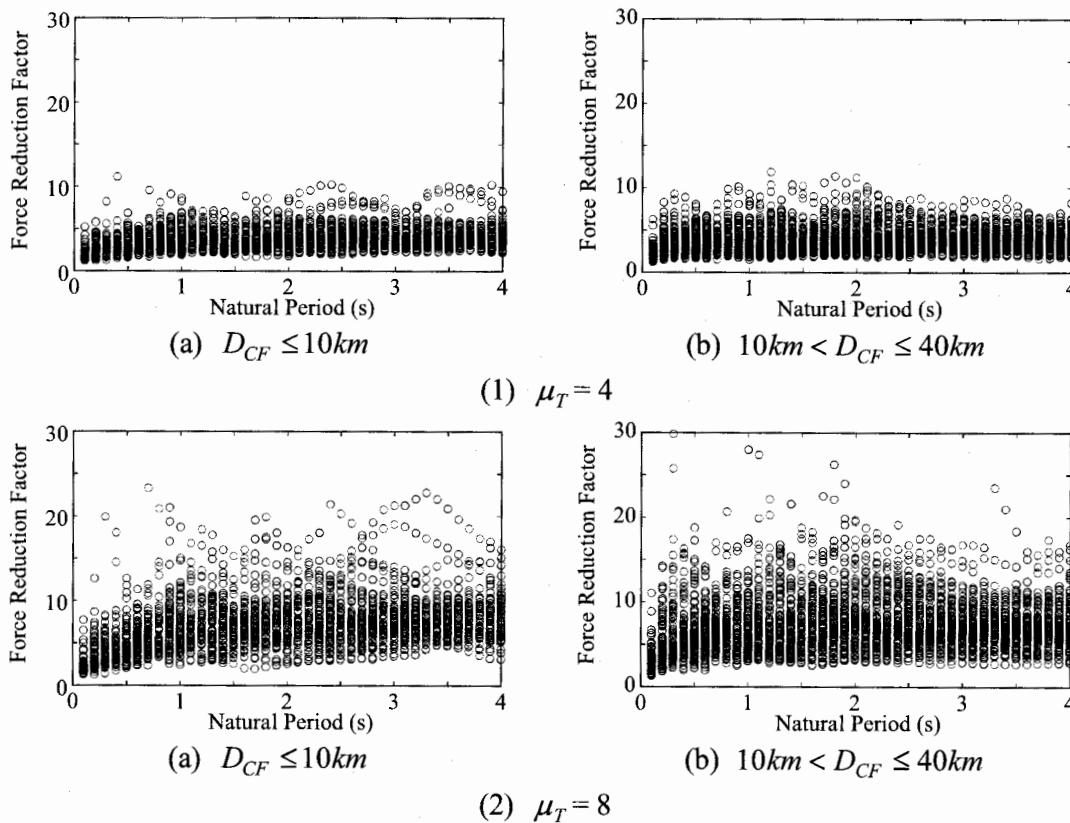
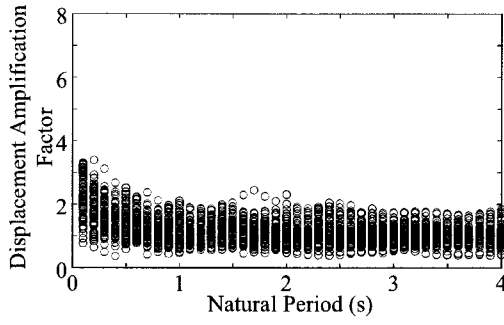
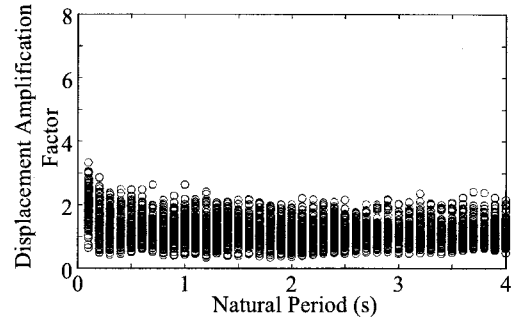


Figure 4 Computed Force Reduction Factor

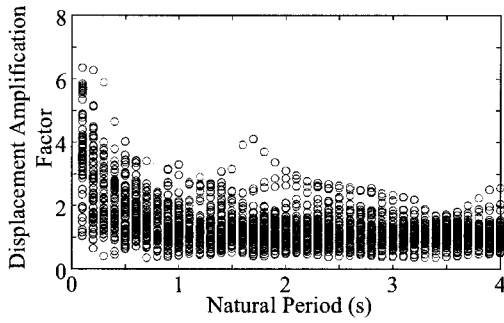


(a) $D_{CF} \leq 10\text{km}$

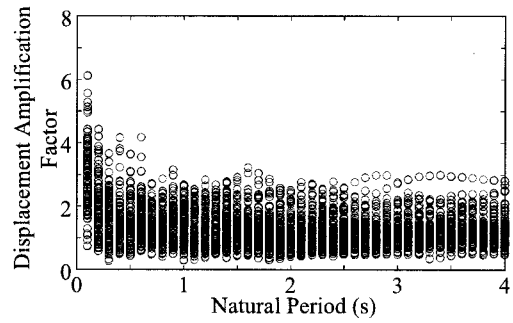


(b) $10\text{km} < D_{CF} \leq 40\text{km}$

(1) $\mu_T = 4$



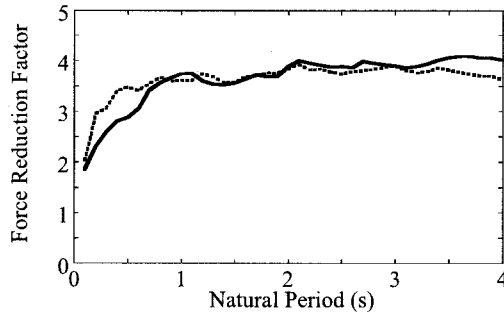
(a) $D_{CF} \leq 10\text{km}$



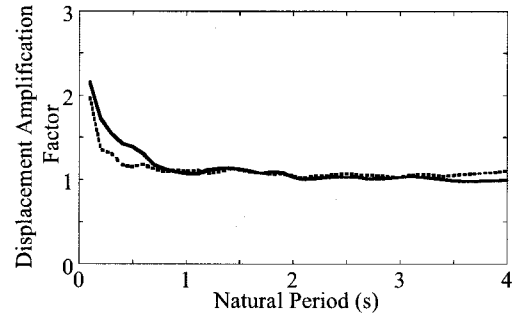
(b) $10\text{km} < D_{CF} \leq 40\text{km}$

(2) $\mu_T = 8$

Figure 5 Computed Displacement Amplification Factor

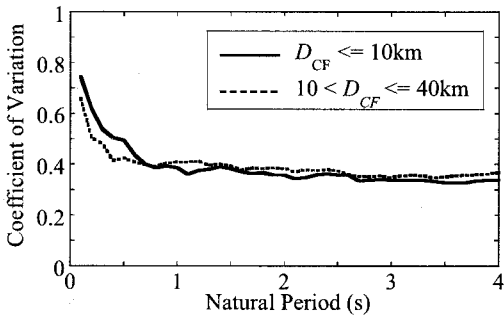


(a) Force Reduction Factor

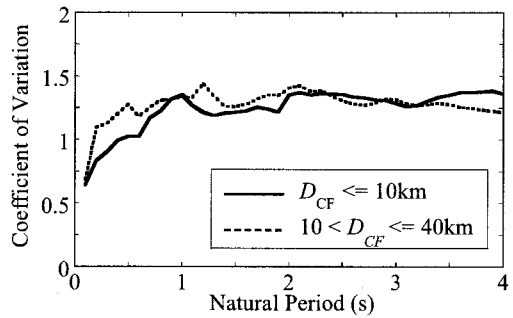


(b) Displacement Amplification Factor

(1) Mean value of modification factors



(a) Force Reduction Factor



(b) Displacement Amplification Factor

(2) Coefficient of variation of modification factors

Figure 6 Mean and Coefficient of variation of R_μ and D_μ for $\mu_T = 4$

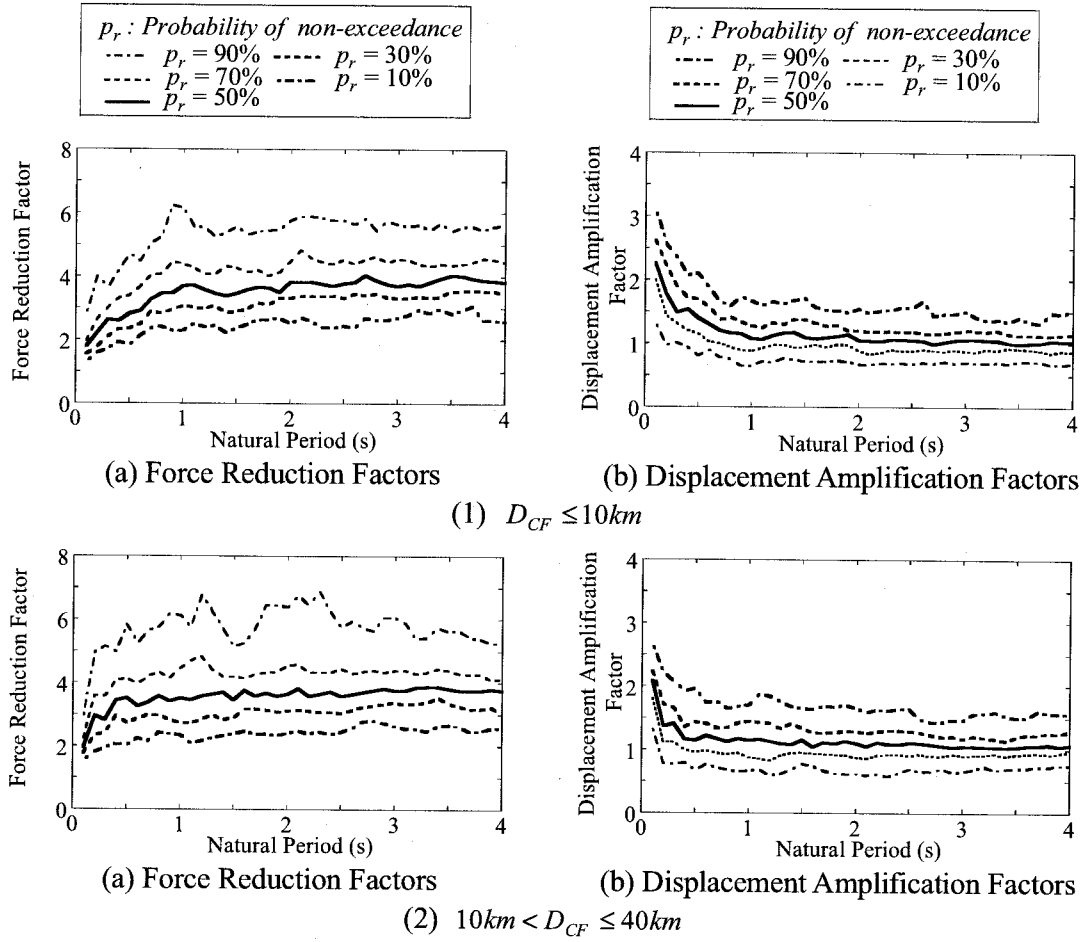


Figure 7 Modification Factors depending on the probability of non-exceedance ($\mu_T = 4$)

4. EVALUATION OF MODIFICATION FACTORS

Figure 7 shows modification factor spectra characterized by probability of non-exceedance, $R_\mu(p_r = \alpha)$ and $D_\mu(p_r = \alpha)$. For structural design applications, the target design value of modification factors should not be mean value, but a value which safely evaluates the force and displacement demands should be used. Thus, a value of R_μ with a non-exceedance probability significantly smaller than 0.5 should be used. On the other hand, a value of D_μ with p_r significantly larger than 0.5 should be used.

To measure the scattering of modification factors, a ratio of computed force reduction factor with a non-exceedance probability, $R_\mu(p_r = \alpha)$, and the mean value of computed force reduction factor, $mean(R_\mu)$, is defined as,

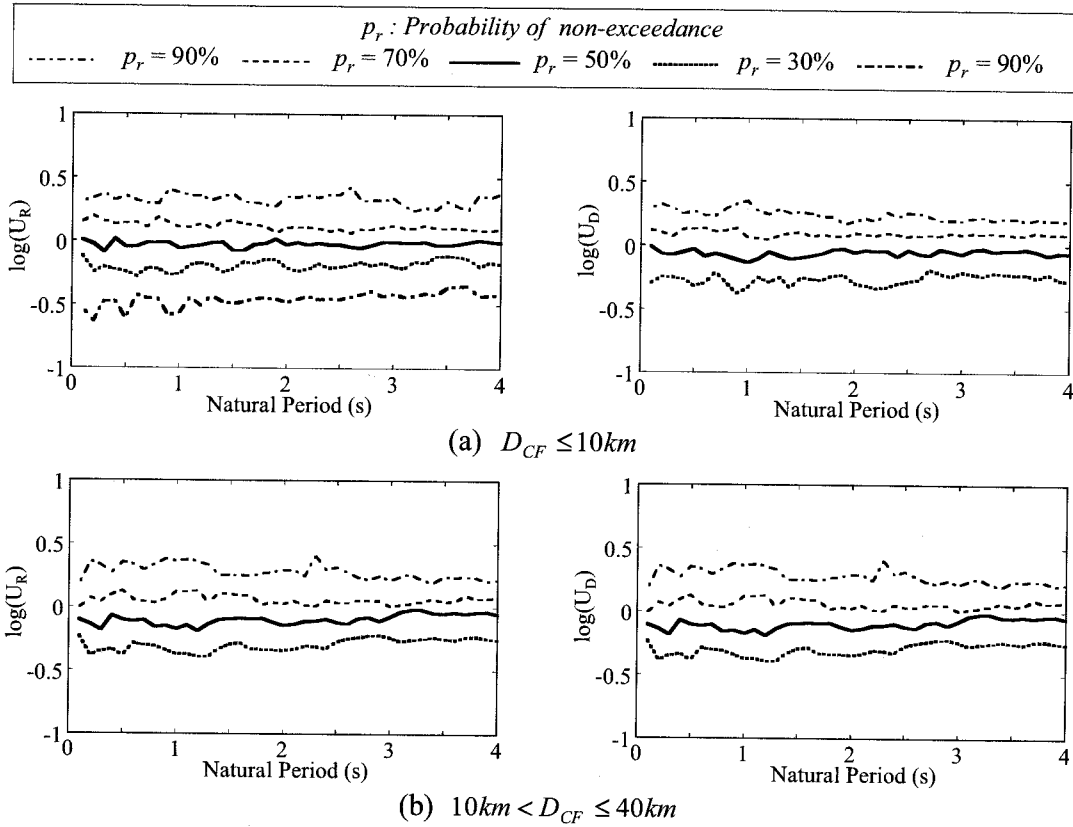
$$U_R = R_\mu(p_r = \alpha) / \text{Exp}(\text{mean}(\log(R_\mu))) \quad (5)$$

in the same manner, a ratio U_D is defined as,

$$U_D = D_\mu(p_r = \alpha) / \text{Exp}(\text{mean}(\log(D_\mu))) \quad (6)$$

$\log(U_R)$ and $\log(U_D)$ are distributed as shown in Figure 8. Since the variation of $\log(U_R)$ and $\log(U_D)$ depending on the natural period are small, the scatterings of $\log(U_R)$ and $\log(U_D)$ are roughly independent of the period and fault distance, D_{CF} .

Figure 9 shows the probability of $\log(U_R)$ and $\log(U_D)$ for all natural period range. In order to



(1) Force Reduction Factors

(2) Displacement Amplification Factors

Figure 8 Distributions of Force Reduction Factors and Displacement Amplification Factors

identify the probability distribution function (PDF) of $\log(U_R)$ and $\log(U_D)$, nonlinear regression analysis is conducted. Since the normal distribution can well represent PDF of $\log(U_R)$ and $\log(U_D)$, R_μ and D_μ exhibit the lognormal distribution.

Figure 10 shows the cumulative probability of U_R and U_D . 60 % of data set of R_μ and D_μ are distributed within the range 0.75 – 1.3 times of around the mean value of computed R_μ and D_μ .

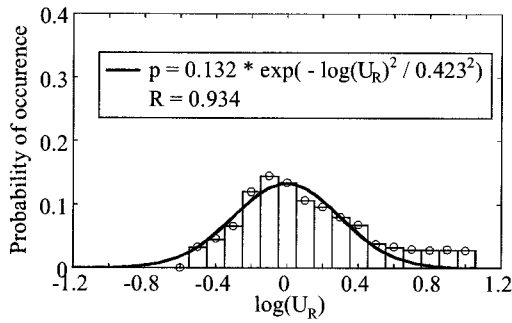
5. CONCLUSIONS

An analysis was conducted for the force reduction factor based on response of SDOF oscillator using 150 free-field ground motions. Based on the analysis presented herein, the following conclusions may be deduced:

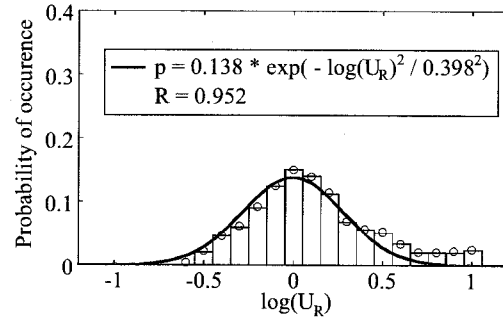
- 1) Since a large scattering of the ground motions induces to extensively change nonlinear response of a structure in seismic design, modification factors distributes with a large scattering.
- 2) Such a large scattering of the modification factors result in a large change of sizing of a structure in seismic design. Thus smaller force reduction factors and larger displacement amplification factors should be assumed to provide conservative design.
- 3) Modification factors exhibit the lognormal distribution, and 60 % of data set of modification factors are distributed within the range 0.75 – 1.3 times of around the mean value of computed modification factors.

References:

- Miranda, E. and Bertero, V.: Evaluation of Strength Reduction Factors for Earthquake Resistant Design, Earthquake Spectra, Vol.10, No.2, pp.357-379, 1994.
- Bommer, J. J. and Elnashai, A. S.: Displacement Spectra for Seismic Design, Journal of Earthquake Engineering, Vol.3,

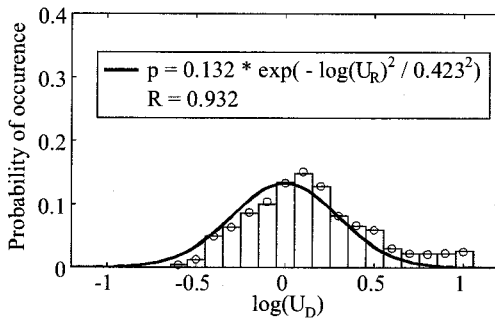


(a) $D_{CF} \leq 10\text{km}$

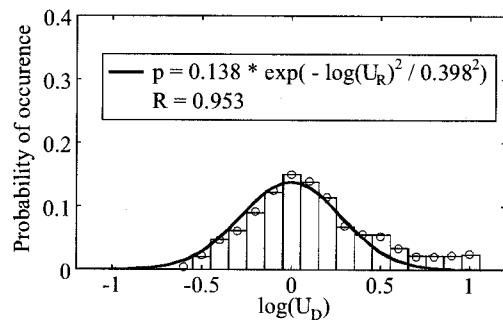


(b) $10\text{km} < D_{CF} \leq 40\text{km}$

(1) Force Reduction Factor



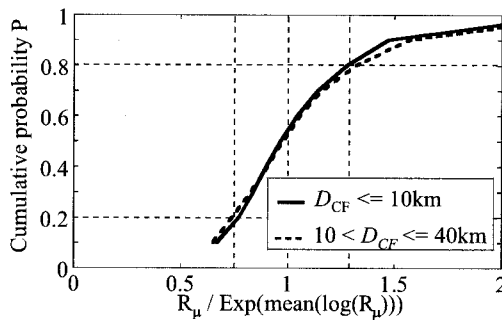
(a) $D_{CF} \leq 10\text{km}$



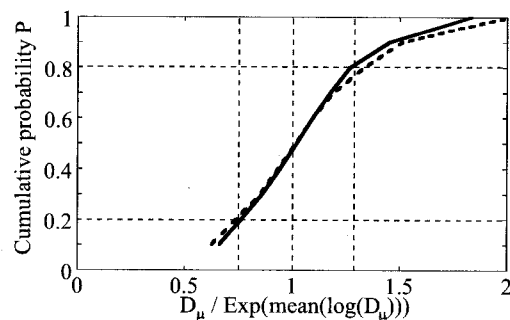
(b) $10\text{km} < D_{CF} \leq 40\text{km}$

(2) Displacement Amplification Factor

Figure 9 Distributions of $\log(U_D)$ and $\log(U_R)$



(a) Force Reduction Factors



(b) Displacement Amplification Factors

Figure 10 Distributions of Force Reduction Factors and Displacement Amplification Factors

No.1, January, pp.1-32, 1999.

Miranda, E. and Ruiz-Garcia, J.: Evaluation of Approximate Methods to Estimate Maximum Inelastic Displacement Demands, *Earthquake Engineering and Structural Dynamics*, John Wiley & Sons, 31, 539-560, 1999.

Ruiz-Garcia, J. and Miranda, E.: Inelastic Displacement Ratios for Evaluation of Existing Structures, *Earthquake Engineering and Structural Dynamics*, John Wiley & Sons, 32, 1237-1258, 2003

Watanabe, G., and Kawashima, S. (2001), "Evaluation of Force Reduction Factor in Seismic Design," *Structural Engineering and Earthquake Engineering*, Proc. JSCE, No. 682/I-56, 115-128.

Somerville, P. G., C. Saikia, D. J. Wald, and R. Graves.: Implications of the Northridge earthquake for strong motions from thrust faults, *Bulletin Seismic Society of America*, vol. 86, pp.115-125, 1996.

Kamae, K., K. Irikura and A. Pitarka.: A technique for simulating strong ground motion using hybrid Green's function, *Bulletin of the Seismological Society of America*, Vol.88, pp.357-367, 1998.

D'Ambrisi. A and Mezzi M.: A probabilistic approach for estimating the seismic response of elasto-plastic SDOF systems, *Earthquake engineering and structural dynamics*, Vol. 34, ISSUE 14, pp. 1737-1753, 2005.

SEISMIC RESISTANCE EVALUATION OF BEAM-TO-CIRCULAR COLUMN CONNECTIONS OF STEEL BRIDGE FRAME PIERS WITH CIRCULAR COLUMN

K. Kinoshita¹⁾ and A. Tanabe²⁾

1) *Doctoral Student, Department of Civil Engineering, Tokyo Institute of Technology, Japan*

2) *Assistant Professor, Department of Civil Engineering, Tokyo Institute of Technology, Japan*
kinoshita@cv.titech.ac.jp, tanabe@cv.titech.ac.jp

Abstract: In this research, seismic resistance of beam-to-circular column connections of steel bridge frame piers with circular column was examined analytically. Four actual steel bridge piers with circular column, which have general shape type of the beam-to-circular column connection respectively, were selected and evaluated. The focus was on the strain at beam-to-circular column connections. FEM earthquake response analyses indicated that the plastic strain at the beam-to-circular column connections of all types was not significant from the point of view of low cycle fatigue without welded defects. However, it should be noted that over 1.0% strain occurred at the corner of the beam-to-circular column connections, where the weld defects exist.

1. INTRODUCTION

During the Great Hanshin Earthquake of 1995, steel bridge piers suffered damage, such as local buckling (JSCE 1995). After the Great Hanshin Earthquake, a large number of research investigations were immediately established to evaluate the seismic resistance of steel bridge piers (PWRI 1999). As the result of those investigations, several types of seismic retrofits were recommended and performed, such as installing additional longitudinal ribs, placing concrete in the piers (PWRI 1999 and Imamura et al. 1999). Although seismic retrofits can improve seismic performance very much, there are unretrofitted beams and beam-to-column connections.

Recently, in the Metropolitan expressway system, fatigue cracks on the steel bridge frame piers have been reported. Most of those fatigue cracks occurred at the corners of the beam-to-column connections. Previous study clarified that the main causes of fatigue cracks were the existence of weld defects in the welded joints of the beam-to-column connections and the occurrence of the high stress concentration due to the shear-lag phenomenon (Miki et al. 2002). Generally, the existences of the weld defects can be causative of fatigue because of the stress concentration around their defects. Unfortunately, these defects were made not only by poor welding but also by no concern about such a fatigue problem in the past. This problem is critical, for the existences of the defects have a possibility of causing damage such as not only high cycle fatigue during service condition, but also low cycle fatigue and brittle fracture during earthquake. Therefore, the strain at the beam-to-column connections during earthquakes should be evaluated accurately.

In this research, earthquake response FEM analyses were conducted to obtain the strain at the beam-to-circular column connections of the steel bridge frame piers.

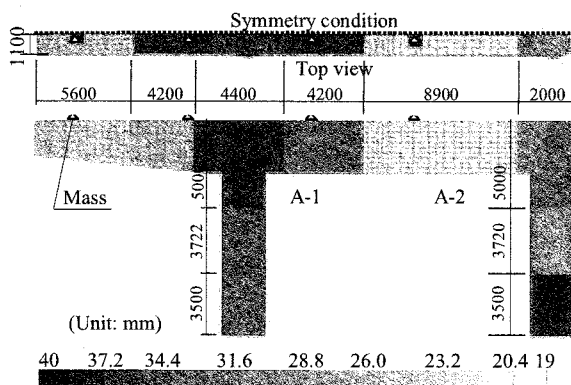


Figure 1 Shape and Thickness distribution of Model A

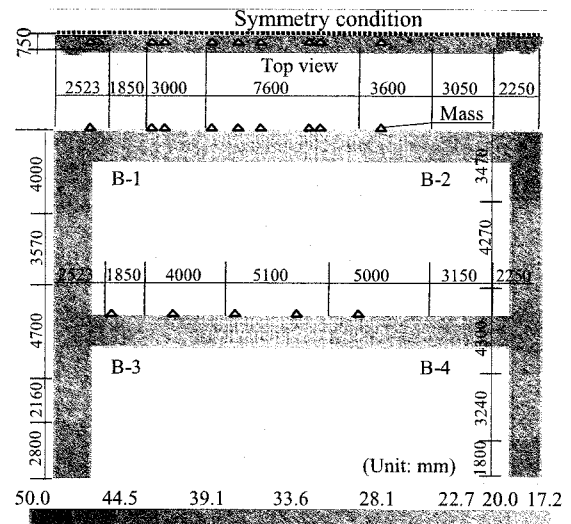


Figure 2 Shape and Thickness distribution of Model B

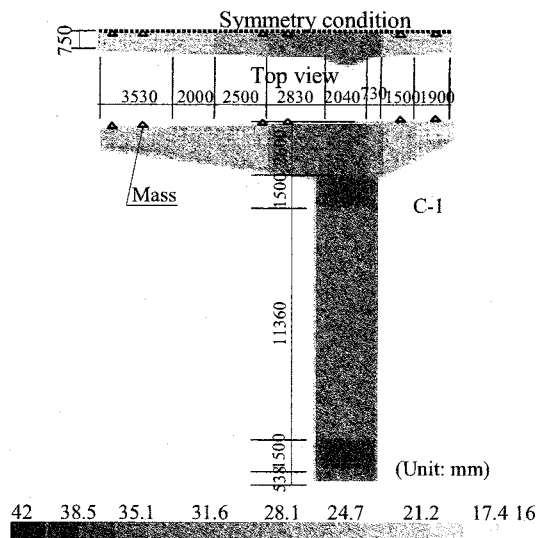


Figure 3 Shape and Thickness distribution of Model C

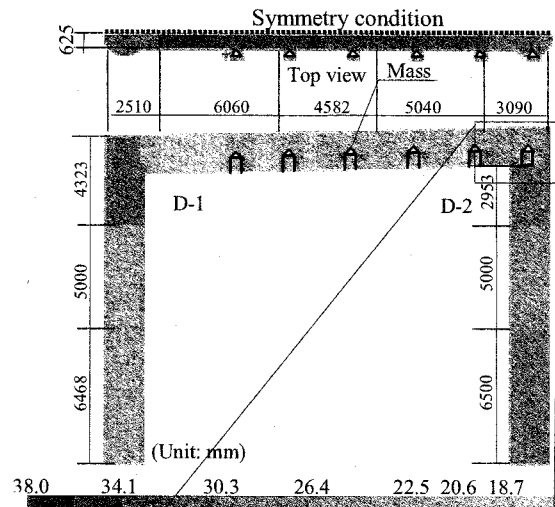


Figure 4 Shape and Thickness distribution of Model D

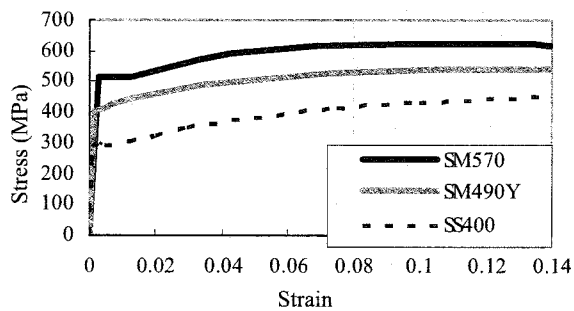


Figure 5 Stress-Strain curve of Steel

2. ANALYSIS CASES AND CONDITIONS

Target models are shown in from Figure 1 to Figure 4. Each model was selected as a general shape of beam-to-circular column connection. Model A is single layer type with one side cantilever beam of the steel bridge frame pier. Model B is double layer type of the steel bridge frame pier. Model C is single pier type of the steel bridge pier. Model D is single layer type of the steel bridge frame pier. The beam-to-circular column connections of Model A are A-1, A-2, and Model B are B-1 B-2, B-3, B-4, and Model C are C-1, and Model D are D-1, D-2. Here, panel of D-2 is not the circular column.

Target models were modeled by shell element. The symmetry condition was used, and bases of columns were fixed. Mass elements were used to consider the weight of the superstructure. Earthquake motions were applied as inertial forces. To consider dead load of steel bridge frame piers and the superstructures, vertical inertial forces as gravity were taken into account. Stress-Strain curves of steels used in FEM model shown in Figure 5. The combined hardening of isotropic and kinematics hardening was used. As great earthquakes, East-West and Up-down components of acceleration waves of JMA-Kobe and JR-Takatori record were used for in the dynamic analyses. Rayleigh-dumping, which is defined as Eq. (1), was used. The first and second angle frequencies were calculated by the modal analyses.

$$[C] = \alpha[M] + \beta[K] \quad (1)$$

$$\alpha = \frac{2\omega_1\omega_2(h_1\omega_2 - h_2\omega_1)}{\omega_2^2 - \omega_1^2} \quad (2)$$

$$\beta = \frac{2(h_2\omega_2 - h_1\omega_1)}{\omega_2^2 - \omega_1^2}$$

where, $[C]$ is dumping matrix, $[M]$ is mass matrix, $[K]$ is Stiffness matrix, ω_1 , ω_2 are the angle frequency of each mode, and h_1 , h_2 are dumping factors for each mode ($=0.02$).

3. DYNAMIC RESPONSE ANALYSIS RESULTS AND CONSIDERATION

Figure 6, 7, 8 and 9 shows the deformation and the plastic strain distribution of the beam-to-circular column connections when maximum response displacement occurred at each model. Figure 10, 11, 12 and 13 shows the time history of the strain of the beams at the corner of beam-to-circular column connection of each model, where the weld defects exist. As the dynamic analysis results of each model, the largest strain results at beam-to-circular column connection in both wave cases of each model were shown. The results of Model A, Model B, Model C and Model D show the JMA-Kobe case, the JMA-Kobe case, the JR-Takatori case and the JR-Takatori case, respectively.

From Figure 6, 7, 8 and 9, we can see that the plastic strain occurred at connection between the beam flange and the circular column plate in each beam-to-circular column connection. From Figure 10, 11, 12 and 13, the maximum plastic strain of the beam-to-circular column connections of each model, except for D-2, was over 1%. The plastic strain result at the corner of the beam-to-circular column connection of D-2 was largest in other results. The panel of D-2 is not the circular column and it is close to the shape of the beam-to-box column connection. Thereby, large plastic deformation might occur at that connection. For that reason, we excluded the results of D-2 from the consideration.

From the dynamic analysis results, we found out that the plastic strain was confirmed at the beam-to-circular column connections of all types. In addition, it should be noted that over 1.0% strain occurred at the corner of the beam-to-circular column connections, where the weld defects exist.

JSCE (2000) indicates strain conditions during earthquakes. The strain condition during the Level 1

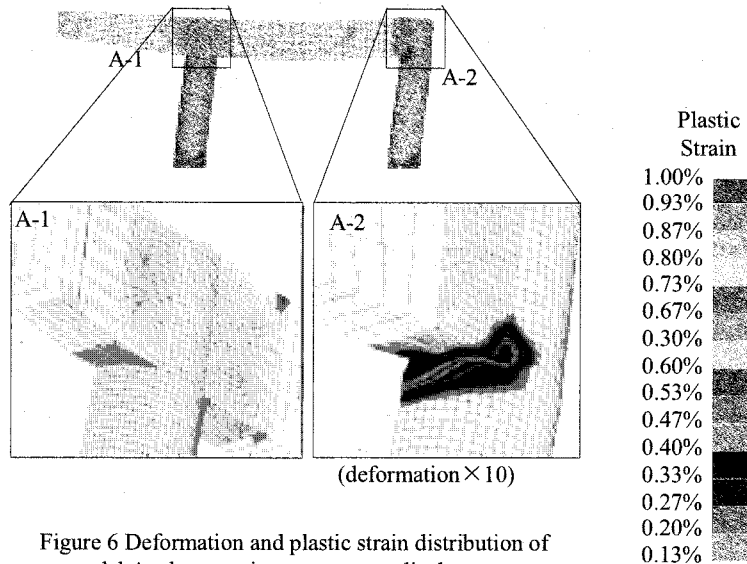


Figure 6 Deformation and plastic strain distribution of model A when maximum response displacement

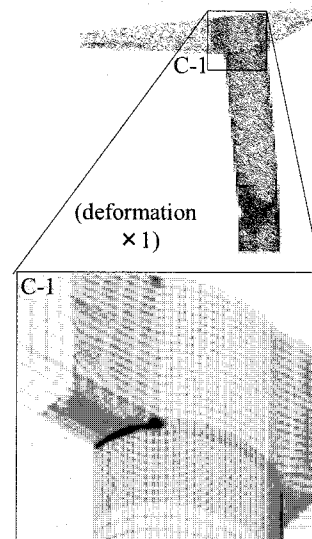


Figure 8 Deformation and plastic strain distribution of model C when maximum response displacement

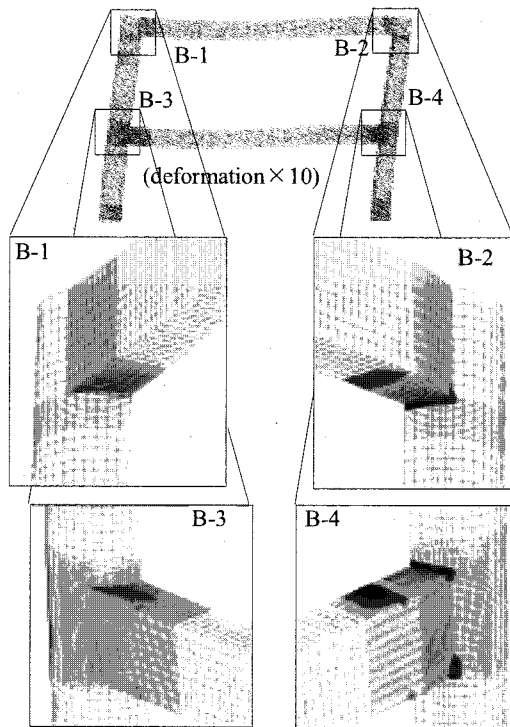


Figure 7 Deformation and plastic strain distribution of model B when maximum response displacement

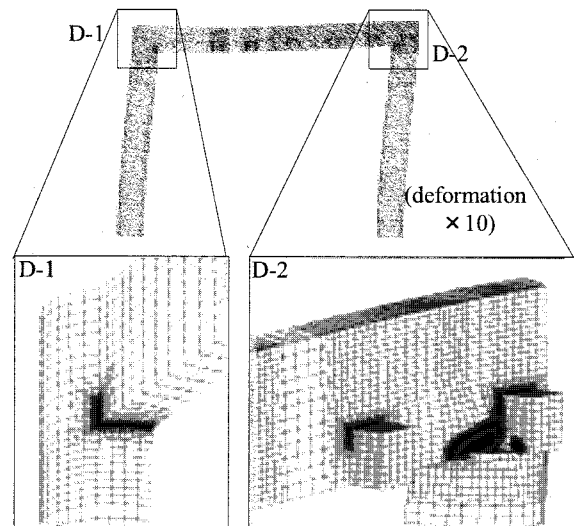


Figure 9 Deformation and plastic strain distribution of model D when maximum response displacement

earthquake and the Level 2 earthquake is 1% under 30 cycles per 3 earthquake, and 10% under 5 cycles per 1 earthquake, respectively. Therefore, the dynamic analysis results of the strain at the corner of the beam-to-circular column connections were close to the strain condition during the Level 1 earthquake and much smaller than that of the Level 2 earthquake.

On the other hand, the existences of the defects can be causative of low cycle fatigue because of the stress concentration around the defects. In the earthquake design recommendation of gas pipeline (The Japan Gas Association 1986), welded parts of the gas pipeline require not exceeding the 0.5% strain under 50 cyclic conditions. Hence, over 1.0% strain at the corner of the beam-to-circular column

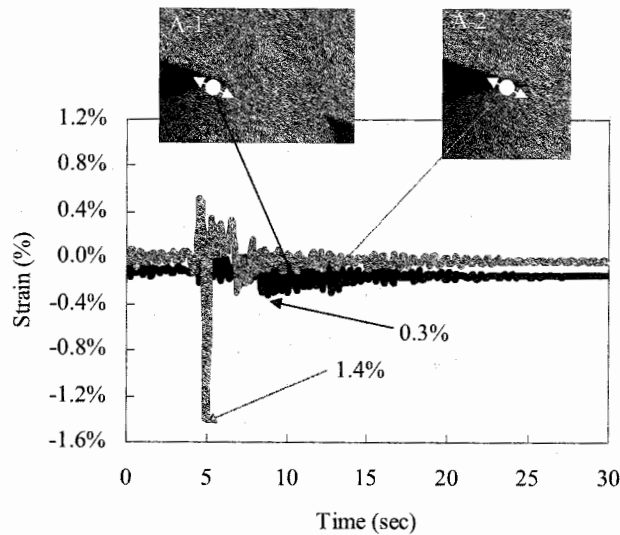


Figure 10 Time history of strain at the corner of the beam-to-circular column connection of model A

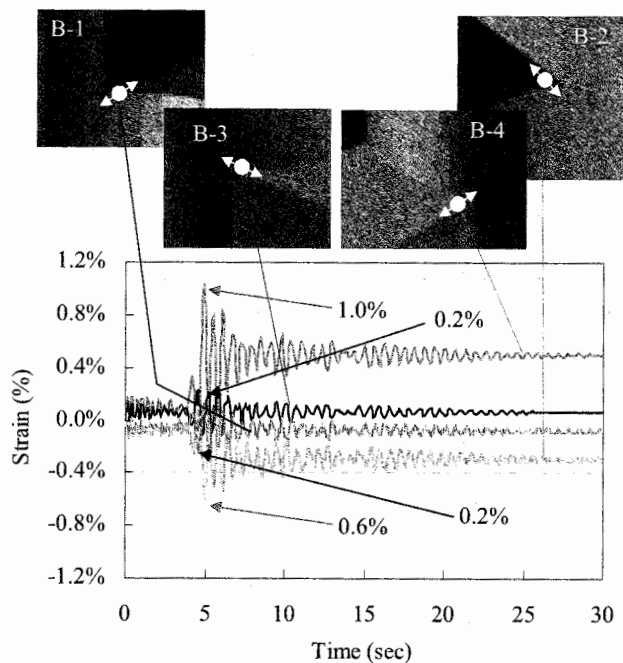


Figure 11 Time history of strain at the corner of the beam-to-circular column connection of model B

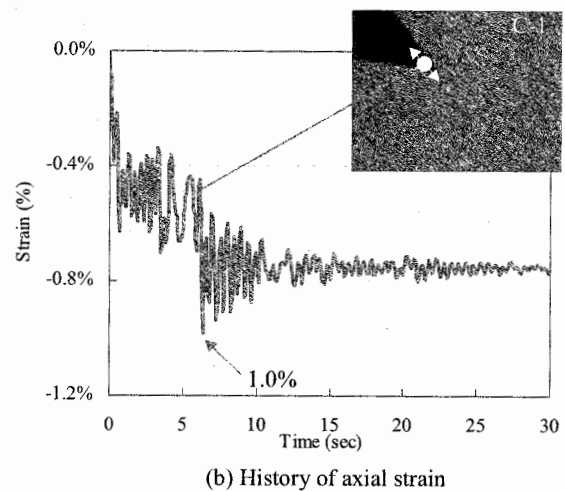


Figure 12 Time history of strain at the corner of the beam-to-circular column connection of model C

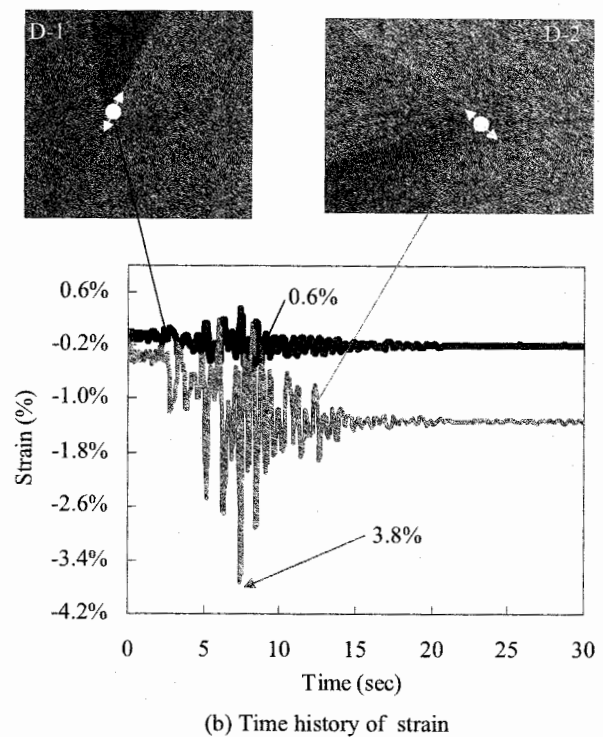


Figure 13 Time history of strain at the corner of the beam-to-circular column connection of model D

connections may be relatively large in case that the welded defects exist there. Therefore, it can be said that we have to carefully evaluate the seismic resistance of the beam-to-circular column connections from the point of view of low cycle fatigue with respect to the relationship between the existence of the welded defects and the stain at the corner of the beam-to-circular column connections.

4. COMPARISON BETWEEN THE BEAM-TO-BOX COLUMN CONNECTION AND BEAM-TO-CIRCULAR COLUMN CONNECTION

Figure 14 shows the time history of the strain at the corner of the beam-to-box column connection. This result referred a previous research (Sasaki et al. 2004). It is obvious that the strain at the corner of the beam-to-box column connection is much larger than that of the beam-to-circular column connection.

This may be led by two reasons. The first reason is the design calculation of the shear-lag stress of the beam-to-circular column connection. There is the assumption of the design calculation of the shear-lag stress, which assumption is replacing the circular column with the box column. The second reason is the difference of the structural detail. Figure 15 shows the plastic strain distribution of the beam-to-box column connection and the beam-to-circular column connection. By comparing the results of them, we found out the difference of the plastic strain distribution. In case of the beam-to-circular column connection, the plastic strain occurred immediately not only at the corner but also at the center of that connection as shown in Figure 15(b). On the other hand, in case of the beam-to-box column connection, large plastic strain occurred at the corner of that connection very locally as shown in Figure 15(a). Sasaki et al. (2001) indicated that in elasto-plastic region, strain concentration by shear-lag phenomenon was not observed. Thus, it is estimated that due to the immediate occurrence of the plastic strain not only at the corner but also at the center of beam-to-circular column connections, the strain at the corner of the beam-to-circular column connection was smaller than that of the beam-to-box column connections.

5. CONCLUSIONS

The conclusions of this research can be summarized as follows.

1. From the earthquake response FEM analyses, the strain occurring at the beam-to-circular column connections during the large earthquakes was not significant from the point of view of low cycle

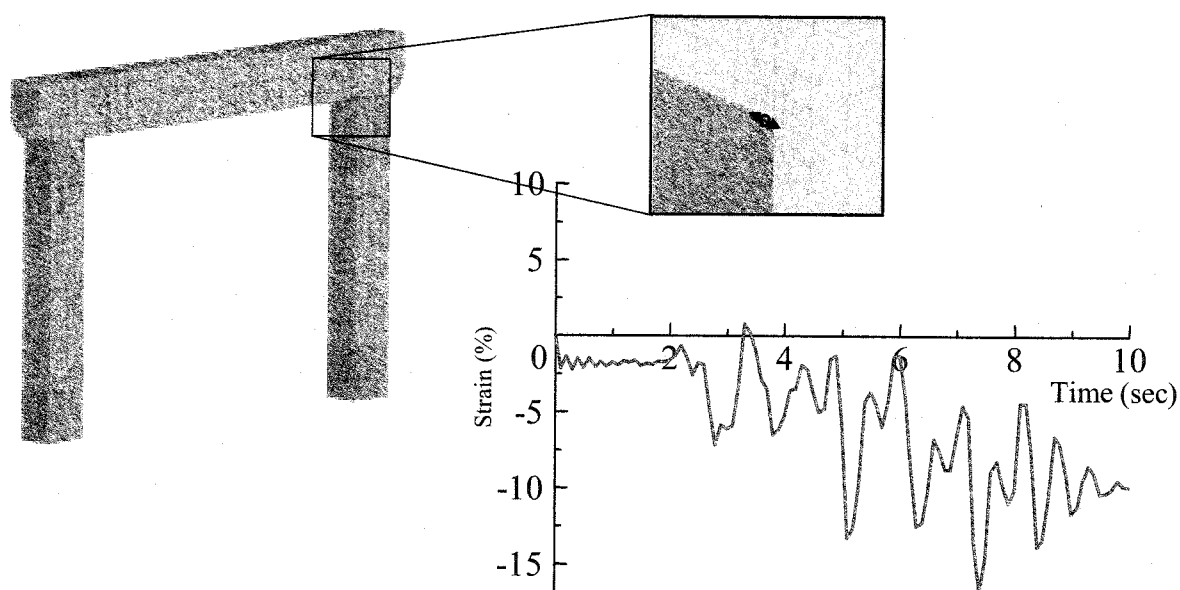


Figure 14 Time history of strain

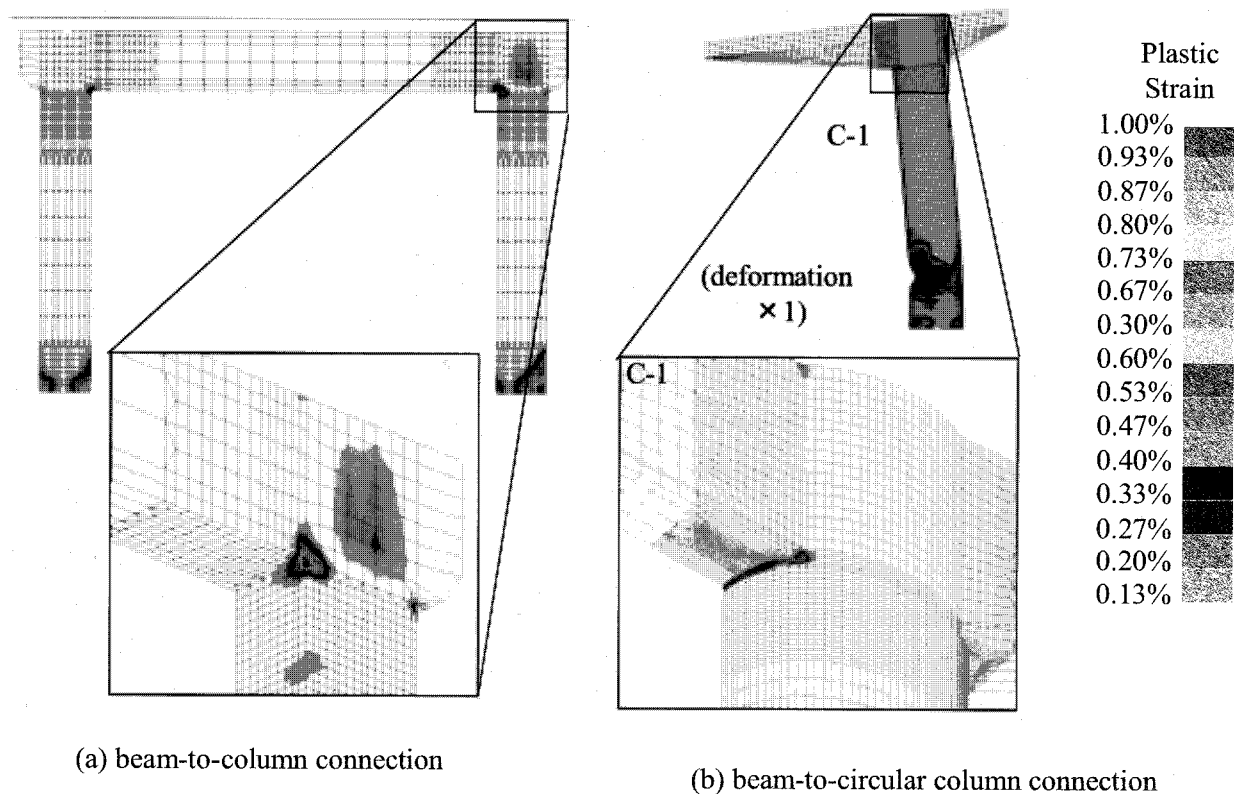


Figure 15 Plastic strain distribution

fatigue without the welded defects.

2. However, it should be noted that over 1.0% strain occurred at the corner of the beam-to-circular column connections, where the weld defects exist.
3. The strain at the corner of the beam-to-circular column connection was smaller than that of the beam-to-box column connections. This reason was estimated from the difference of the design and the structural detail.

References:

- JSCE, Committee of Steel Structures. (1995) "Survey Reports on Safety of Steel Structures"
- PWRI (1999) "Summary of the Cooperation Research on the Seismic Limit State Design of Highway Bridge Piers"
- Imamura, K., and Takahashi, M. (1999) "Retrofitting of Existing Piers in Metropolitan Expressway", *Bridge and Foundation Engineering*, Vol. 33, 163-165.
- Miki, C., Ichikawa, A., Sakamoto, T., Tanabe, A., Tokida, H. and Shimoizato, T. (2002) "Fatigue Performance of Beam-to-Column Connections with Box Sections in Steel Bridge Frame Piers", *Journal of Structural Mechanics and Earthquake Engineering*, No.710, pp361-371.
- Japan Road Association (1998) "Design Specifications of Highway Bridges, Part V, Seismic Design"
- Sasaki, E., Miki, C., Ichikawa, A., Takahashi, K. (2004) "Behavior of Steel Bridge Frame Piers during Earth-quakes", *Journal of Structural Engineering, JSCE*, Vol. 50A, p1467-1477.
- JSCE, Special Committee Relating Seismic Design Method of Infrastructures. (2000) "Third suggestion and explanation relating seismic design method of infrastructures"
- The Japan Gas Association (1986) "The Earthquake Design Recommendation of Gas Pipeline"
- Sasaki, E., Miki, C., Ichikawa, A., Takahashi, K. (2001) "Influences of stiffening methods on elasto-plastic behavior of beam-to-column connections of steel rigid frame piers", *Journal of Structural Mechanics and Earthquake Engineering*, 689, 201-214.

RESPONSE ANALYSIS OF BRIDGES SUPPORTED BY C-BENT COLUMNS

S. Nagata¹⁾, and K. Kawashima²⁾

1) Graduate Student, Department of Civil Engineering, Tokyo Institute of Technology, Japan

2) Professor, Department of Civil Engineering, Tokyo Institute of Technology, Japan

nseiji@cv.titech.ac.jp, kawashima@cv.titech.ac.jp

Abstract: C-bent columns exhibits complicated seismic behavior due to the eccentricity. The eccentric moment results in extensive failure in the eccentric compression side of the columns under a strong excitation, and this failure mode results in a large residual displacement. To clarify the seismic performance of bridges supported by C-bent columns, a dynamic response analysis on five-span continuous bridge consisting of fixed steel bearings, C-bent columns is conducted. In addition, effectiveness of rubber bearings in mitigation of the residual displacement of C-bent columns is clarified based on the analysis.

1. INTRODUCTION

In urban areas, there exist various unique structures which require special consideration in seismic design due to their irregular structural placement. One such structure is a single column with the lateral beams being longer in one side than the other. They are called C-bent columns or inversed L-shaped columns. In C-bent columns, an eccentricity between the column center and the point where the deck weight applies results in a static eccentric moment. The eccentric moment results in more extensive failure in the eccentric compression side than the tension side of the columns under a strong excitation, and this failure mode results in a large residual displacement. To clarify the effect of the eccentricity on the seismic performance of RC C-bent columns, experimental investigations on model columns have been conducted (Kawashima et al. 2003). In this study, to clarify the seismic performance of bridge supported by C-bent columns, a dynamic response analysis is conducted on a bridge system including a superstructure, bearings, columns, and foundations. This paper shows a series of the analytical investigations.

2. TARGET BRIDGES

Figure 1 shows a target bridge consisting of a five-span continuous deck supported by RC C-bent columns and pile foundations. This bridge is 150-meter long and composed five equal spans. Each span is 30 m long and 12 m wide. The superstructure is composite type and supported by six piers with 10-meter height. The columns have a 3.4 m x 3.4 mm square cross section. The shear- span ratio is 3.7. Axial stress at the plastic hinge region of the columns resulted from the dead weight of the superstructure is 0.86 MPa. The eccentricity between the column center and the deck center e is 4.3 m.

The footing is 2.5 m thick, 8.5 m long and 8.5 m wide. Nine 17 m long cast-in-place reinforced concrete piles with a diameter of 1.2 m support a footing. The columns and the foundations are

designed based on the current seismic design codes (JRA 2002) under Type-I (middle-field) and Type-II (near-field) ground motions at a site corresponding to the moderate ground condition (Type-II Ground Condition).

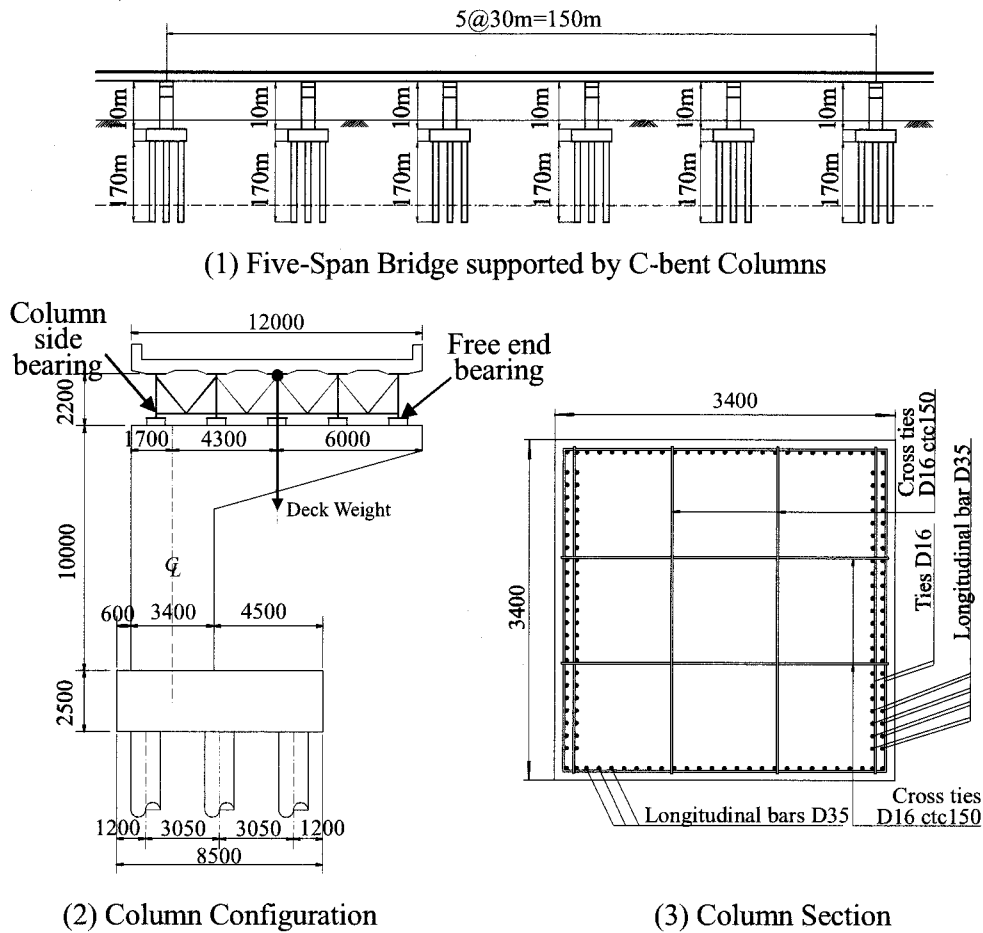


Figure 1 Target Bridge

Based on Figure 1(3), 35 mm diameter deformed longitudinal bars with a nominal strength of 295 MPa (SD295A) are provided in double at not only the eccentric tension side but also the eccentric compression side in the column. The longitudinal reinforcement ratio is 1.21 %. 16 mm diameter deformed tie bars (D16SD295A) are provided at 150 mm interval for the entire column height. Tie bars are provided in the inner longitudinal bars as well. The volumetric tie reinforcement ratio is 0.76 %. Concrete strength of the columns is 21 MPa.

First, five fixed steel bearings assumed to be employed at the top of each pier to support the deck. Then the steel bearings are assumed to be replaced with 129 mm thick, 850 mm long and 850 mm wide rubber bearings. The lateral stiffness of the rubber bearing is 5.63 MN/m. The leftmost bearing and the right most bearing shown in Figure 1(2) are defined hereinafter as the column side and the free end bearings, respectively.

3. ANALYTICAL IDEALIZATION

To simulate the seismic response of the bridge, both superstructure and substructure are idealized by finite elements as shown in Figure 2. The deck and the column body other than the plastic hinge are

idealized by linear beam elements. The plastic flexural deformation of the columns at the plastic hinge region is idealized by a fiber element. The plastic hinge length L_p is assumed a half of the column width (JRA 2002). Pier cracking torsional stiffness of the plastic hinge region of is assumed to be 20 % of that full section which is determined based on the experimental results (Kawashima et al. 2003, Nagata and Kawashima et al. 2005).

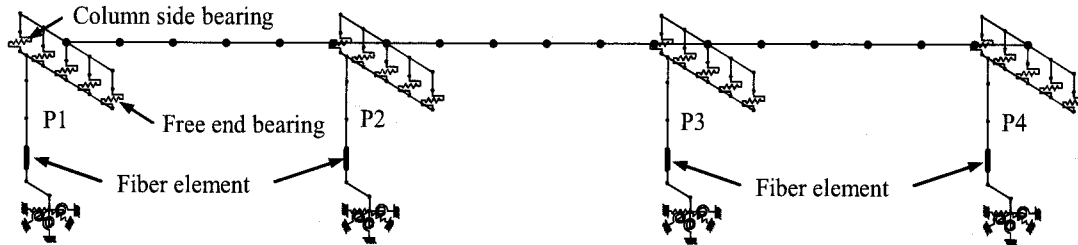
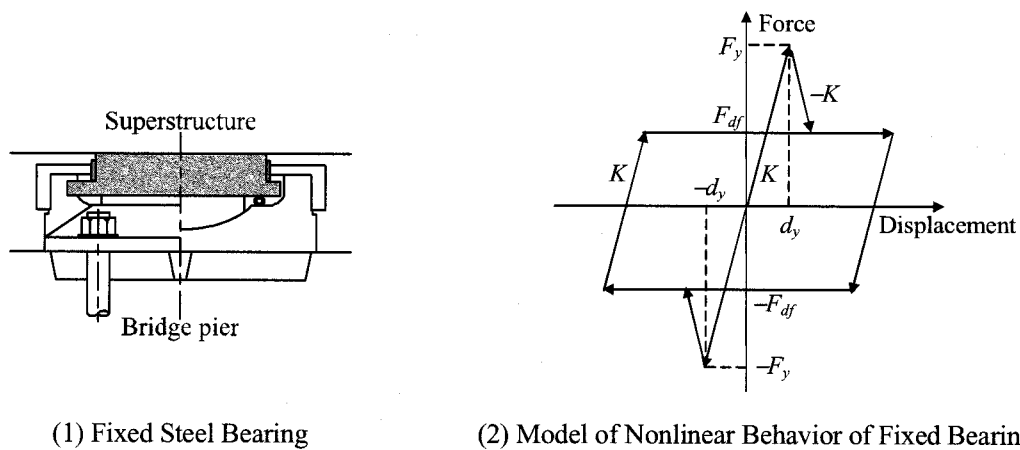


Figure 2 Analytical Idealization of the Target Bridge



(1) Fixed Steel Bearing

(2) Model of Nonlinear Behavior of Fixed Bearing

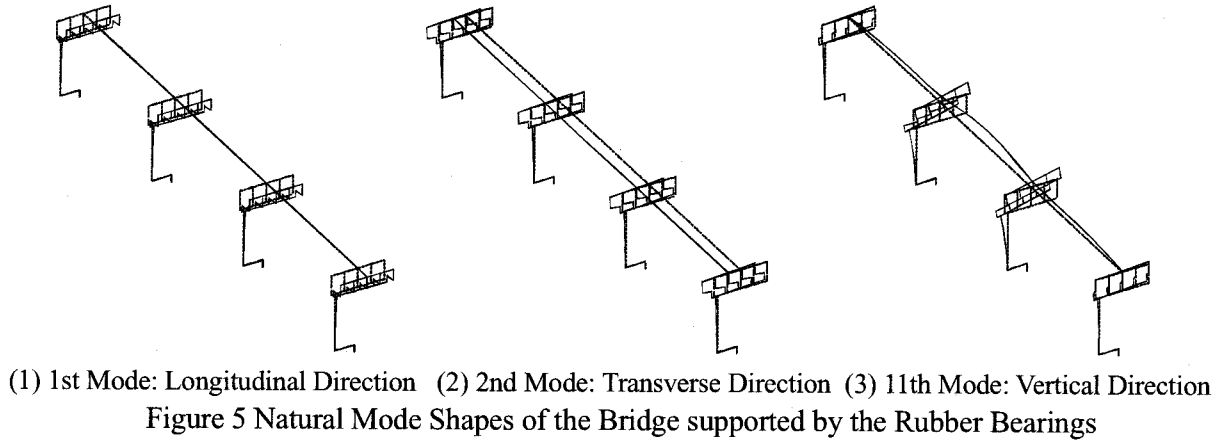
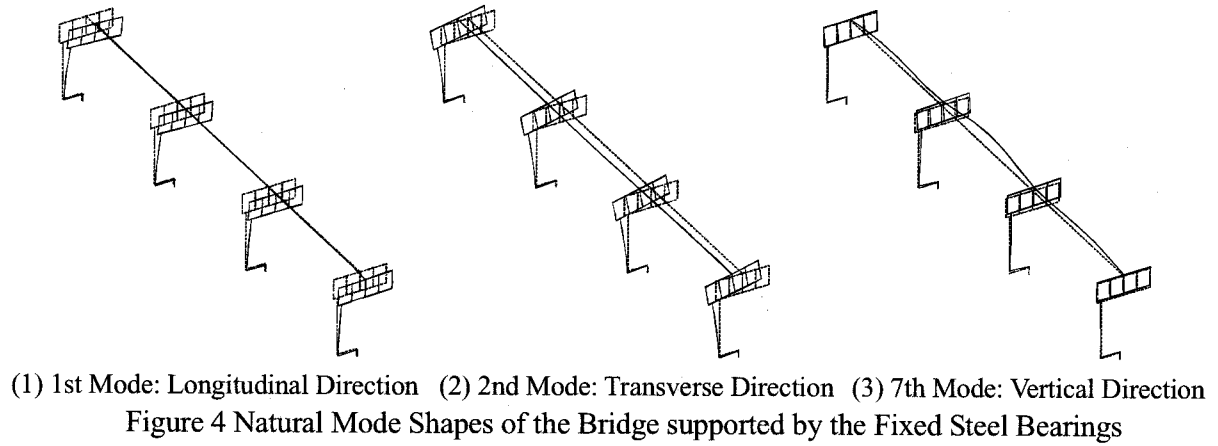
Figure 3 Fixed Steel Bearing and Its Nonlinear Model

In the fiber element, the stress vs. strain relation of confined concrete is idealized by a model by Hoshikuma and Kawashima et al. (Hoshikuma and Kawashima et al. 1997). and unloading and reloading hysteresses are idealized based on a model by Sakai and Kawashima (Sakai and Kawashima 2000). Furthermore, the modified Menegotto-Pinto model is used to idealize the stress vs. strain relation of the reinforcements (Menegotto and Pinto 1973, Sakai and Kawashima 2003).

The fixed steel or rubber bearings are modeled by a set of spring elements in the longitudinal and transverse directions. The fixed steel bearings are first assumed to be used. Although the deck and the fixed bearings restrained the seismic torsion of the C-bent columns, the columns may slightly rotate during an earthquake. This slight rotation of the columns may result in larger lateral displacement in the column side bearing than the free end bearing, which results in a larger reaction force in the bearing at the column side than the other side. Thus an analysis which includes the effect of bearing failure is conducted. To include the nonlinear behavior of the steel bearings, a model proposed by Tirasit and Kawashima (Tirasit and Kawashima 2005) is used. Figure 3 shows the configuration of the fixed steel bearing and the nonlinear hysteretic model. The fixed steel bearing is assumed to behave elastically before failure. The strength F_y of a fixed steel bearing is evaluated as

Table 1 Natural Periods of the Bridges

(1) Bridge supported by the Fixed Steel Bearings				(2) Bridge supported by the Rubber Bearings			
Mode no.	Direction	Natural Periods (s)	Effective mass ratio (%)	Mode no.	Direction	Natural Periods (s)	Effective mass ratio (%)
1	Longitudinal	0.58	71	1	Longitudinal	0.95	49
2	Transverse	0.51	56	2	Transverse	0.91	42
7	Vertical	0.22	44	11	Vertical	0.26	30



$$F_y = 1.7k_h R_{DL} \quad (1)$$

in which k_h : the seismic coefficient and R_{DL} : the reaction in bearing due to dead weight of superstructure. After failure displacement d_y , the fixed bearing is assumed to suffer damage and its lateral force capacity decreases and becomes dependent on the friction force F_{df} between the upper and the lower parts of bearing. The friction force is assumed as

$$F_{df} = \mu R_{DL} \quad (2)$$

where μ : the friction coefficient which is assumed to be 0.15 in both transverse and longitudinal directions, and R_{DL} : the reaction in bearing due to dead weight of the superstructure.

To study the application of rubber bearing for the bridge supported by C-bent columns, the five steel bearing are replaced with five rubber bearings. The rubber bearings are modeled by a linear

spring with a lateral stiffness of 5.63 MN/m in the longitudinal and transverse directions.

To analyze the seismic response of the bridge under three-directional excitation, NS, EW and UD components of JMA Kobe ground accelerations are imposed to the analytical models in the longitudinal, transverse and vertical directions simultaneously. The constant acceleration is assumed in each step of numerical integration and time step interval of integration is 0.001 sec.

The natural periods and the effective mass ratios of the bridges supported by the fixed steel and rubber bearings are shown in Table 1. The natural mode shapes of the bridges are presented in Figures 4 and 5. The fundamental modes of both bridges are in the longitudinal direction. The fundamental periods are 0.58 seconds and 0.95 seconds in the bridges supported by the fixed steel and rubber bearings, respectively.

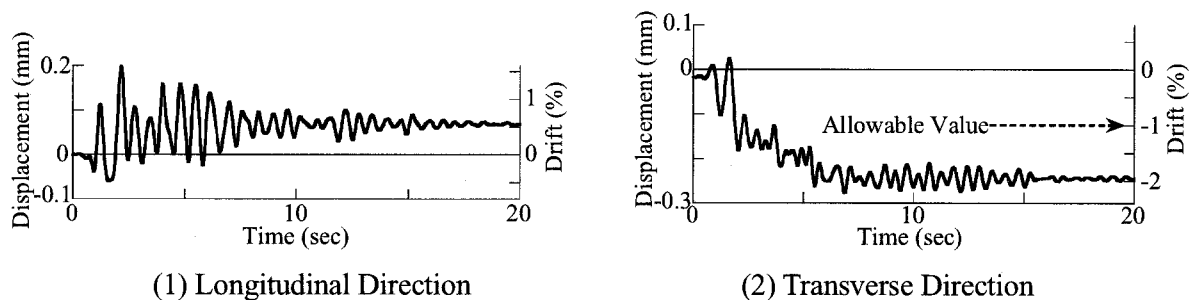


Figure 6 Displacement Response of the Bridge supported by the Steel Bearings

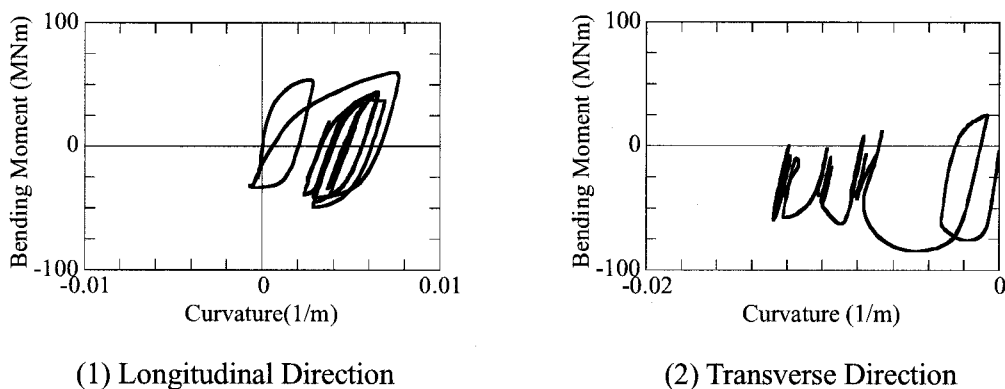


Figure 7 Moment vs. Curvature Hystereses of the Column with the Steel Bearings

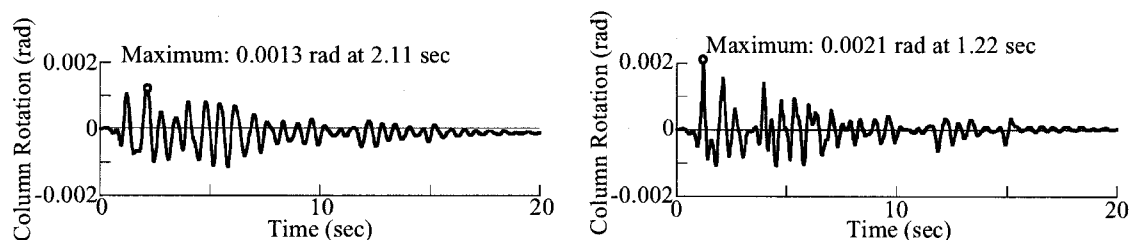


Figure 8 Rotation of the Bridge Column supported by the Steel Bearings

4. SEISMIC PERFORMANCE OF BRIDGES SUPPORTED BY FIXED STEEL BEARINGS

Because stiffness of the superstructure is so large that the seismic response of all the columns is quite similar. Thus the analytical results of one column (P1) are presented here. Figure 6 shows the

displacement response of the deck center of the column in the longitudinal and transverse directions. The maximum displacement in the longitudinal direction is +1.6 % drift at 2.3 sec, and the residual displacement after the excitation reaches 0.6 % drift. The most important feather of the C-bent columns is the accumulation of residual displacement in the transverse direction due to the column eccentricity. The maximum displacement in the transverse direction is -2.2 % drift at 7.1 sec, and the residual displacement after the excitation is -2 % drift, which exceeds the acceptable value (1% drift).

The bending moments vs. curvature hysteresses at the plastic hinge region in the column in the longitudinal and transverse directions are shown in Figure 7. Based on the hysteresses in the transverse direction, post-yield stiffness at negative side (eccentric compression side) is quite small, and plastic deformation accumulates in this direction. The maximum curvature is -0.014 /m in the transverse direction, while it is 0.008 /m in the longitudinal direction.

Although the deck is fixed by the steel bearings to the C-bent columns, the columns slightly rotate under strong excitation. Figure 8 shows the rotation of the bridge column P1 around its axis. The result which takes into account damage of the fixed steel bearings as will be described later is also presented in this figure for comparison. The maximum rotation of the column is 0.0013 radian at 2.3 sec.

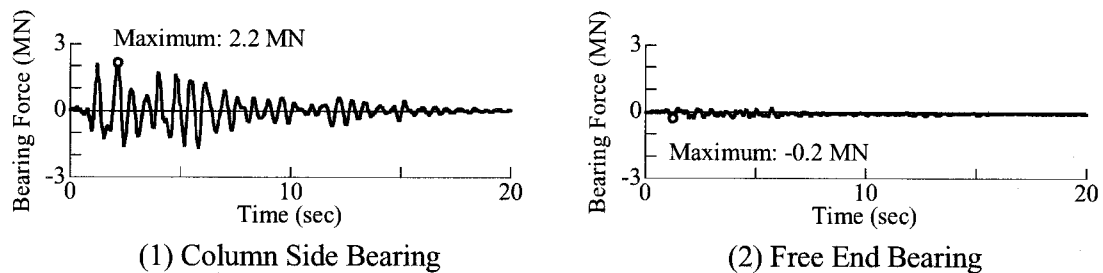


Figure 9 Bearing Force of the Fixed Bearings at the Column side and the Free End

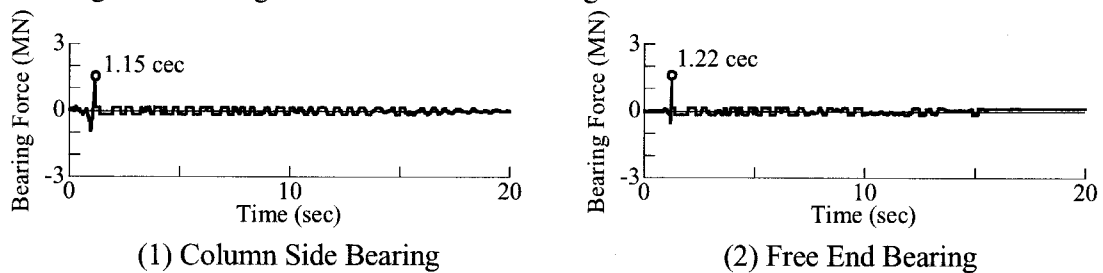


Figure 10 Bearing Force of the Damaged Fixed Bearings at the Column Side and the Free End

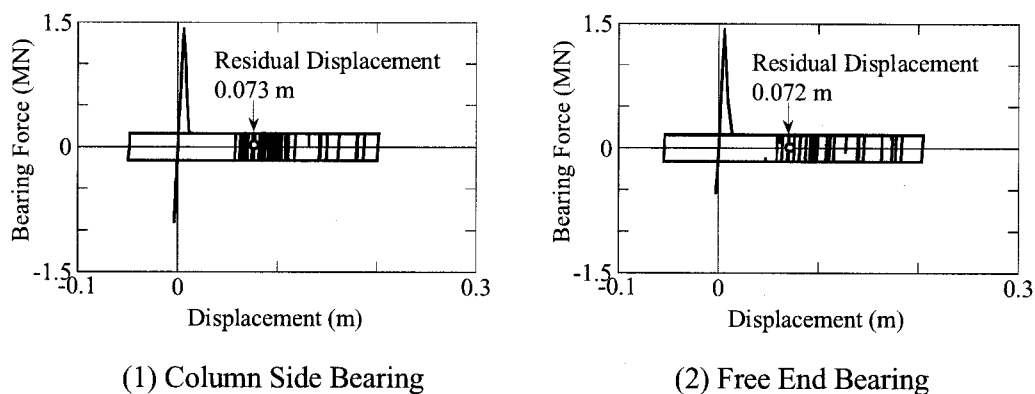


Figure 11 Hysteresses of Damaged Steel Bearing in the Longitudinal Direction

As described above, this slight rotation of the columns results in a larger bearing displacement in the column side bearing than the free end bearing, which likely causes undesirable damage in the column side bearing. Comparison of the bearing lateral reaction forces between the column side bearing and the free end bearing is shown in Figure 9. It is obvious that the bearing force is much larger at the column side than that at the free end. The maximum forces are 2.21 MN and -0.21 MN in the bearings at column side and the free end, respectively. Therefore the bearing lateral strength demand should be carefully evaluated by an analysis on the total bridge system including a deck, bearings, C-bent columns and foundations.

An analysis which takes into account damage of the fixed steel bearings is conducted. The analytical results of column P1 are presented here. The bearing lateral reaction forces in the column side bearing and the free end bearing are compared in Figure 10. The lateral reaction force of the column side bearing first reaches the maximum strength (1.43 MN) at 1.15 sec, and then it deteriorates significantly due to failure of the bearing. At 1.22 sec, the reaction force of the free end bearing reaches the maximum strength, and it deteriorates significantly. From 1.15 sec and 1.22 sec, the column side and free end bearings exhibit hysteretic behavior, respectively, as shown in Figure 11.

This failure of the fixed steel bearings allows increase of the column rotation around its axis as shown in Figure 9. The maximum rotation is 0.0021 radian at 1.22 sec, which is 62 % larger than the rotation obtained by the analysis without damage of the bearings. The rotation of the column increases significantly from 1.15 sec corresponding to the failure of the column side bearing, and the rotation reaches maximum value (0.0021 radian) at 1.22 sec corresponding to the failure of the free end bearing.

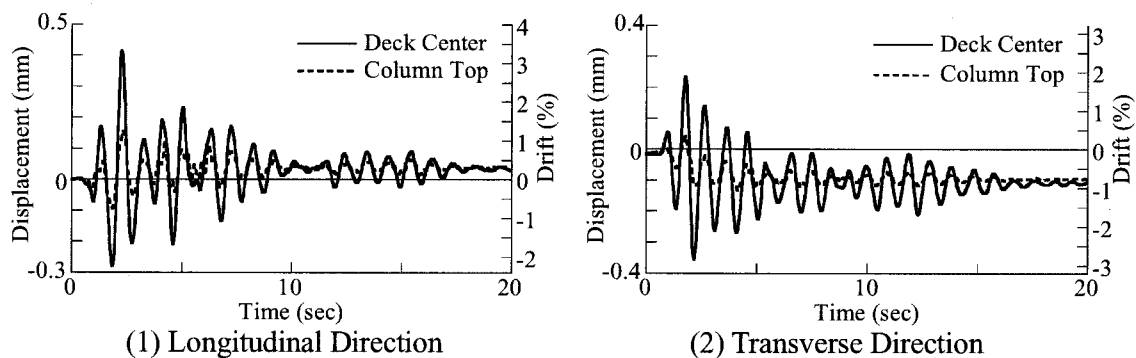


Figure 12 Displacement Response of the Bridge supported by the Rubber Bearings

5. EFFECT OF DAMAGE OF FIXED STEEL BEARINGS

The five steel bearing are replaced with rubber bearings with a lateral stiffness of 5.63 MN/m as presented above. Figure 12 shows displacement response of the deck center and the column top of the column P1. The maximum displacement of the deck is 3.2 % and -2.9 % drifts in the longitudinal and transverse directions, respectively, while the maximum displacement of the column top is 1.2 % and -1.1 % drifts in the longitudinal and transverse directions, respectively. The residual displacement of the deck center after the excitation reaches 0.3 % and -0.9 % drift in the longitudinal and transverse directions, respectively, which are smaller than the acceptable value (1 % drift). The accumulation of the residual displacement is less significant, because use of the rubber bearing decreases the plastic deformation of the columns.

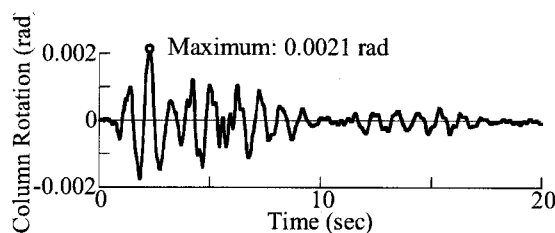


Figure 13 Rotation of the Bridge Column with the Rubber Bearings

Although a rubber bearing is effective to mitigate the residual displacement, use of the rubber bearing increases the rotation of C-bent columns around their axis compared to use of fixed bearings as shown in Figure 13. The maximum rotation is 0.0022 radian at 2.3 sec, which is 69 % larger than the rotation obtained by the analysis with steel bearings (see Figure 8(1)). Thus the rotation of the C-bent columns should be carefully evaluated in the seismic design.

6 CONCLUSIONS

To clarify the seismic performance of a bridge supported by C-bent columns, dynamic response analysis was conducted on a total bridge system. Based on the analytical results presented herein, the following conclusions may be deduced.

- 1) If we consider the response of a total bridge system, seismic torsion of the C-bent columns depends on the supporting conditions of the deck by bearings.
- 2) For a bridge supported by steel bearings, special consideration should be given in the design of steel bearings because the lateral reaction force induced in the bearing is larger in the column side than the other side. If the reaction force of the bearings exceeds their strength capacity and the bearings exhibit nonlinear behavior, this increases the rotation of C-bent columns around their axis.
- 3) When the deck is fixed by steel bearings, a large residual displacement, which exceeds the acceptable value, likely to develop due to the eccentricity of the columns. A rubber bearing is effective to mitigate plastic deformation of columns as well as the residual displacement. However, use of the rubber bearing increases the rotation of the columns around their axes.

References:

- Kawashima, K., Watanabe, G., Hatada, S. and Hayakawa, R. (2002), "Seismic Performance of C-bent Columns based on a Cyclic Loading Test," *J. Structural Mechanics and Earthquake Engineering*, JSCE, No. 745/I-65, pp. 171-189, 2003.
- Japan Road Association: *Part V seismic design, design specifications of highway bridges*, Maruzen, Tokyo, Japan, 2002.
- Hoshikuma, J., Kawashima, K., Nagaya, K. and Taylor, A. W.: Stress-Strain Model for Confined Reinforced Concrete in Bridge Piers, *J. Structural Engineering*, ASCE, 123(5), pp. 624-633, 1997.
- Sakai, J. and Kawashima, K.: An Unloading and Reloading Stress-Strain Model for Concrete confined by Tie Reinforcements, *Proc. 12th World Conference of Earthquake Engineering*, No. 1432 (CD-ROM), Auckland, New Zealand, 2000.
- Menegotto, M. and Pinto, P.E.: Method of Analysis for Cyclically Loaded R.C. Plane Frames including Changes in Geometry and Non-Elastic Behavior of Elements under Combined Normal Force and Bending, *Proc. IABSE Symposium on Resistance and Ultimate Deformability of Structures Acted on by Well Defined Repeated Loads*, pp. 15-22, 1973.
- Sakai, J. and Kawashima, K.: Modification of the Giuffre, Menegotto and Pint model for unloading and reloading paths with small strain variations, *J. Structural Mechanics and Earthquake Engineering*, JSCE, No. 738/I-64, 159-169, 2003.
- Tirasit, P. and Kawashima, K.: Seismic Torsion Response of Skewed Bridge Piers, *J. Earthquake Engineering*, No. 28, Perper No.116 (CD-ROM), 2005.

MATLAB-BASED HEALTH MONITORING SYSTEM FOR BUILDINGS AND ITS DATA MANAGEMENT SYSTEM

A. Mita¹⁾, T. Inamura²⁾, and S. Yoshikawa²⁾

1) Professor, Dept. of System Design Engineering, Keio University, Japan

2) Graduate Student, Dept. of System Design Engineering, Keio University, Japan
mita@sd.keio.ac.jp, mushina8@hotmail.com, yoshikawashirou@hotmail.com

Abstract: A health monitoring system based on MATLAB Web Server is proposed and its prototype system is developed. In order to acquire the response data automatically a simple sensor system was also developed. It transfers the data automatically through the Internet and is configurable through the network. The system is now under operation to identify the research needs and the right direction for evolution.

1. INTRODUCTION

Structural health monitoring (SHM) systems that monitor the condition of buildings and infrastructures in order to promptly and quantitatively evaluate risks due to their deterioration or large earthquakes are promising for prolonging the lives of buildings while keeping them in healthy conditions. The proposal of feasible SHM systems that can evaluate the safety and reliability of buildings and ensure the asset value is thus urgently demanded. As damage detection methods have been studied extensively, the technology pool for SHM has been widened and deepened. However, in the course of developing such a system, it has been recognized that the establishment of a database that provides the statistical information on many structures is one of the most important issues for utilizing the sophisticated tools effectively.

Although many researchers have advocated the necessity of such a database for gathering building information, designers and contractors are kind of reluctant to reveal the information to third parties. In addition, it is not easy to set a foot in a building which is mostly private-owned. In contrast, the purchasers, users or owners of buildings keep eager to know the safety and reliability of their properties. Thus, the needs for the SHM systems vary widely depending on which stakeholder initiates it even for a particular building.

Given these backgrounds, an SHM study group in the Consortium for Building Research and Development was newly established to promote the use of SHM. The SHM study group initiated the use of the SHM system presented in this paper. The system has been developed at Mita laboratory, Keio University and it acquires on-line building data by using automatic sensor systems and upload tools. Eight buildings are currently monitored using the system at this moment.

We use the sensor system being developed and the MATLAB-based server developed by us. The MATLAB Web Server is an ideal deployment tool to develop a Web application for release of the identified results as we already have many damage detection tools coded for MATLAB. For example, the story stiffness is identified using complex modal properties obtained by numerical algorithm for subspace state space system identification. This algorithm is implemented to the system.

2. MATLAB-BASED HEALTH MONITORING SYSTEM

2.1 System Outline

The outline of the MATLAB-based health monitoring system is depicted in Figure 1. The data obtained at a building is automatically transmitted to the server through the Internet when the monitored response exceeds the prescribed trigger level. The trigger setup and other configurations for the sensor system can be done through this server so that the users of the sensors do not need to configure the sensors at each building. The software architecture for the data transfer and configuration is presented in Figure 2. In addition to this software, the upload software was prepared for manual upload of the data where the sensing system had been installed for other purposes. Transmitted or uploaded data are stored in the designated directories and added to file selection menus for evaluation of health status.

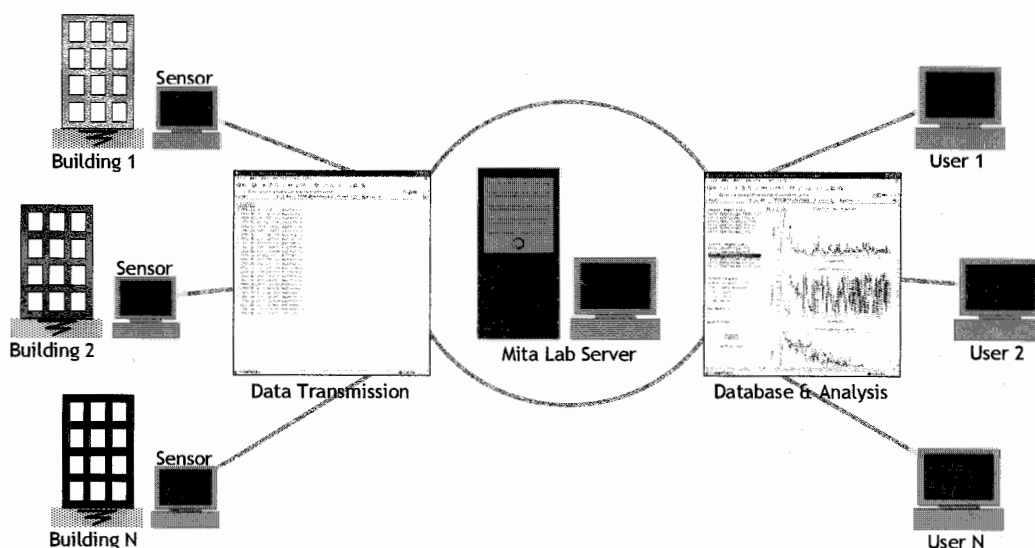


Figure 1: Outline of MATLAB-based health monitoring system.

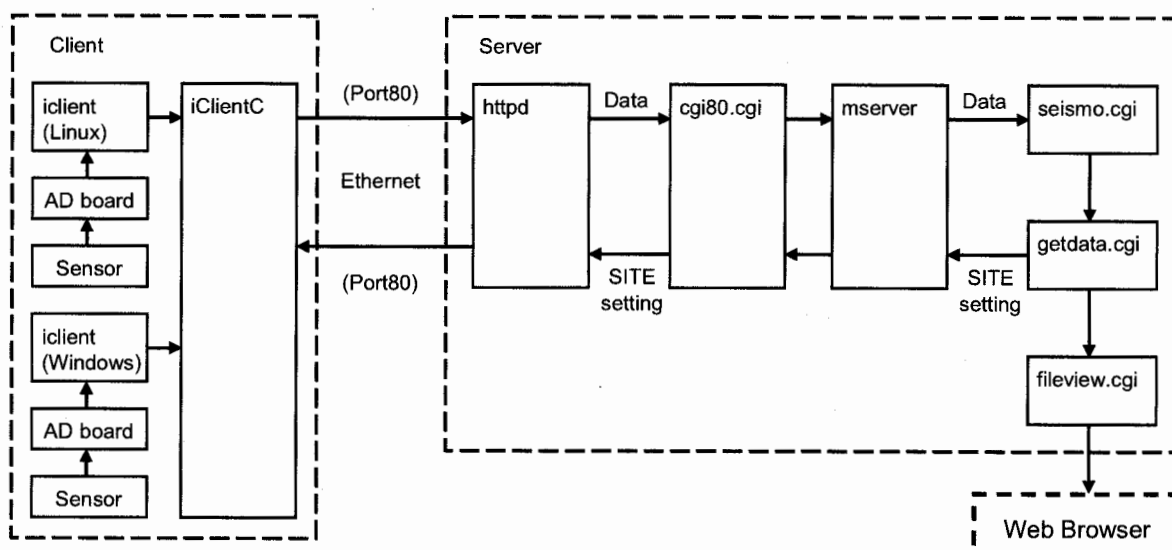


Figure 2: Software architecture for data transfer and configuration

2.2 Data Format and Data Evaluation

The acquired data need to be accompanied with the meta-data that explain the relevant information of the data such as date, location, building name, sensor name, trigger and so on. The minimum information of the data was decided embedding in the name of the file as defined by:

sname_yyyymmddhhmmss_chname.txt

where:

sname:	name of building
yyymmddhhmmss:	year, month, day, hour, minute, second
chname:	channel name such as accrflx+

In each file, the physical value of the data at each time step is stored in one column. If the sensor has three outputs, the corresponding number of files should be 3. The meta-data is currently stored as a plane text file. They will be stored in the relational database in the next version. We are currently testing the mechanism to automatically transfer the meta-data related to the sensor systems that are stored in the memory of the sensor systems in XML formats.

The MATLAB Web Server was employed for data evaluation as shown in Figure 3. The stored data are processed using the applications developed at our laboratory. The MATLAB Web Server bridges web server and MATLAB and works as an API. The applications are a combination of MATLAB m-files, HTML input documents, HTML output documents, and graphics. The applications for health evaluation had been developed to be used off-line. They can be used for the MATLAB Web Server by adding the code to accept input from a HTML input document and to return the results to the HTML output document. Thus, accumulated resources can be effectively used. The MATLAB application resides on the server machine so that the users of health monitoring system do not need to know the MATLAB itself. They do not need the license of the software.

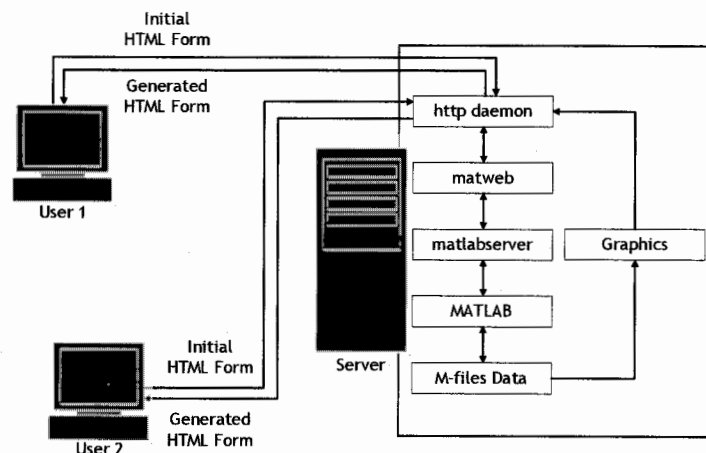


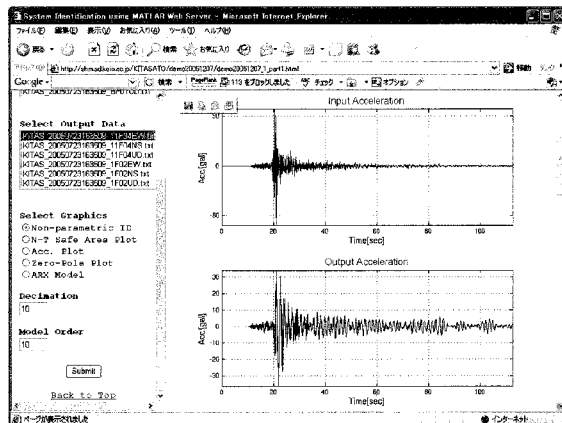
Figure 3: MATLAB web server

3. PROTOTYPE SYSTEM

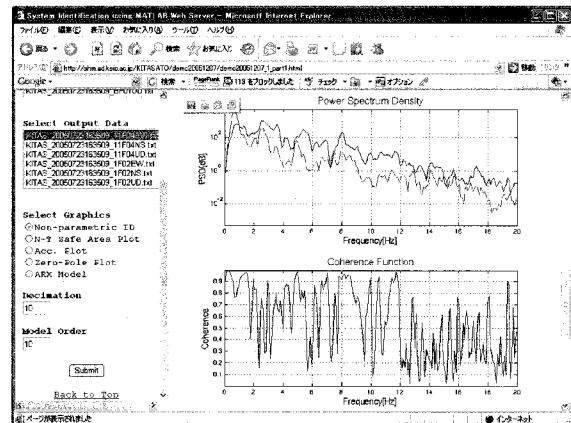
A prototype system was constructed for eight buildings. This time, only one site has the automatic sensor system. The rest of buildings use existing monitoring systems so that the selected data were uploaded to our server. The system is opened for the limited participants who agreed to provide the observed data. The system requires the standard authentication process for the access.

3.1 Standard Tools

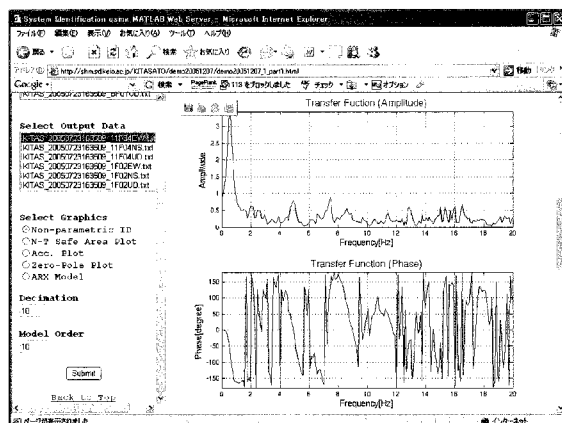
The views on the web-server are listed in Figure 4 for a base-isolated building for the earthquake occurred on July 23, 2005. The standard view tools include time histories, power spectrum density and coherence functions, transfer functions and parametric system identification using ARX models. Users can arbitrarily set the decimation rate and model orders. From the set of views we can evaluate the basic dynamic characteristics of the building during this moderate earthquake.



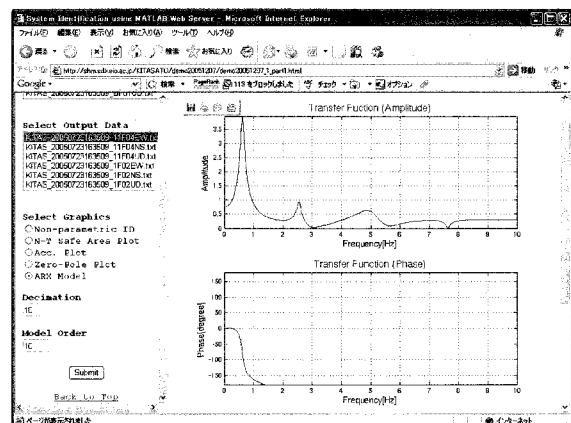
(a) Acceleration in time histories



(b) Power spectrum and coherence functions



(c) Transfer functions



(d) ARX System Identification

Figure 4: Standard tools for data evaluation.

3.2 Damage Index Example

As an example of damage indexes, the story stiffness of a building was employed. The algorithm used here requires a complex mode shape of any order (Yoshimoto et al., 2005). Assuming the steady state motion in the depicted mode, the story stiffness is estimated. In order to test the performance of the implemented algorithm, a test structure consisting of four floors shown in Figure 5 was prepared. As the damaged case, four leaf springs used as the columns for the second story were cut at the bottom and top parts. The photo of the damaged leaf springs is shown in Figure 6. Five accelerometers were used to observe acceleration response of all the floors including the base. The modal parameters were identified using the base acceleration as an input and the four acceleration data at each floor as outputs. The subspace identification method was applied for the one-input and four-output system. The story stiffness was identified based on those modal parameters. An example of acceleration data in the

damaged case is shown in Figure 7.

The estimated natural frequencies and damping ratios are shown in Table 1. We can observe that the 1st natural frequency fell about 7% compared with the healthy case by the damage introduced to the columns on the second floor. On the other hand, for the 2nd natural frequency, there is almost no change between the healthy case and the damaged case. This fact is confirmed from the transfer functions plotted in Figure 8. It is noted that the horizontal axis of the transfer functions is “period(s)” so that the most right peaks indicate the first modal frequencies for the healthy and damaged cases. The mode shapes also shown in Figure 8 include the information of the location and the degree of the damage in this structure. The damage degrees identified from the 1st mode and the 2nd mode are plotted in Figure 9. It is clearly understood that the stiffness of the second story was indeed reduced due to the damage. However, the results of the 3rd and 4th stories show the increase of the stiffness. This is not the desired scenario for this case. The method may need more robustness to clearly depict the damaged stories with more confidence.

In Figure 10, an example of desired view for showing the damage degree and location is depicted. Although, many sophisticated damage detection algorithms have been developed, complicated indexes are not appropriate for users of the buildings. We need to develop the communication tools to narrow the gaps between professional engineers and the public. The developed MATLAB-based health monitoring system can be a promising test bed for verifying the newly proposed or developed damage detection algorithms. The most sophisticated algorithm may not be necessarily the best tool for convincing the public that some danger due to the damage exists.

Table 1: Estimated modal parameters

MITAL	Healthy		Damaged	
	Frequency f [Hz]	Damping h [%]	Frequency f [Hz]	Damping h [%]
1st mode	1.50	3.2	1.39	2.0
2nd mode	3.84	3.3	3.82	4.8

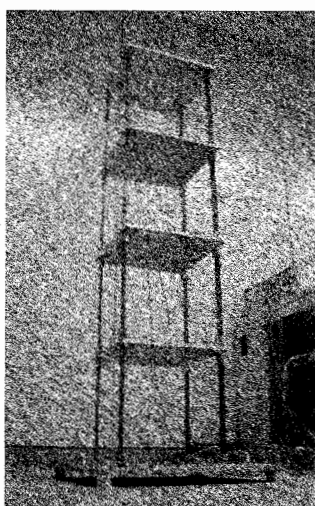


Figure 5: Test structure

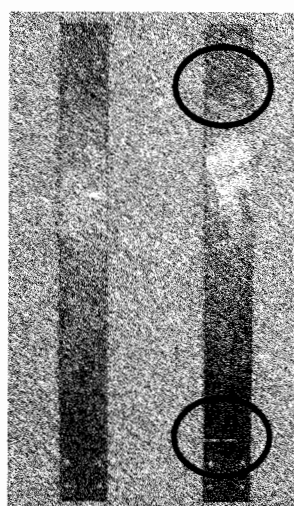


Figure 6: Leaf spring (L: healthy, R: damaged)

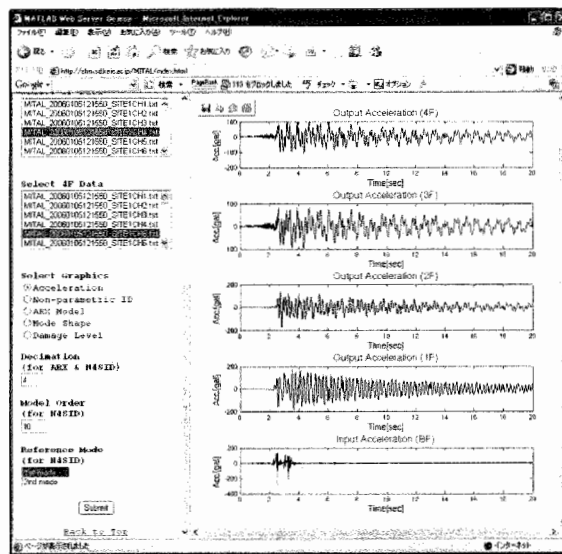


Figure 7: Time histories obtained from 4-story test model.

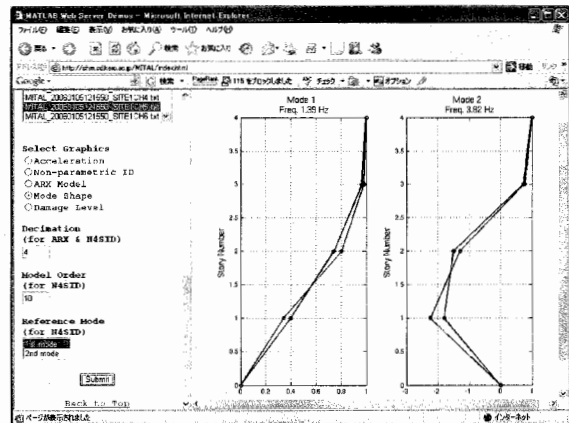
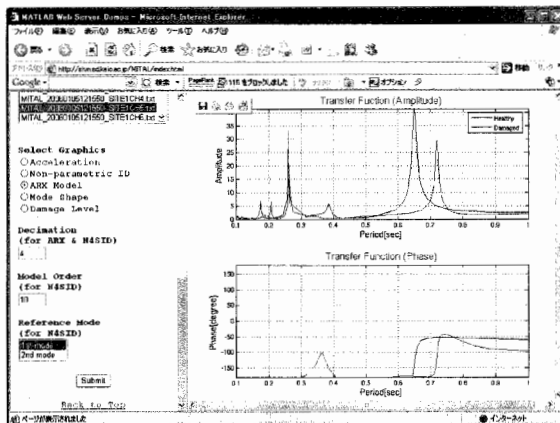


Figure 8: Transfer functions and mode shapes for healthy and damaged models.

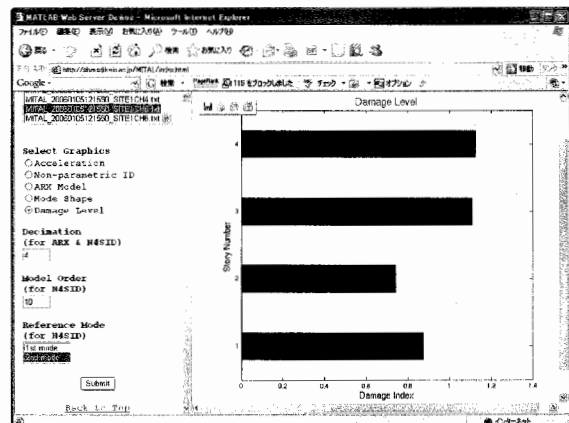
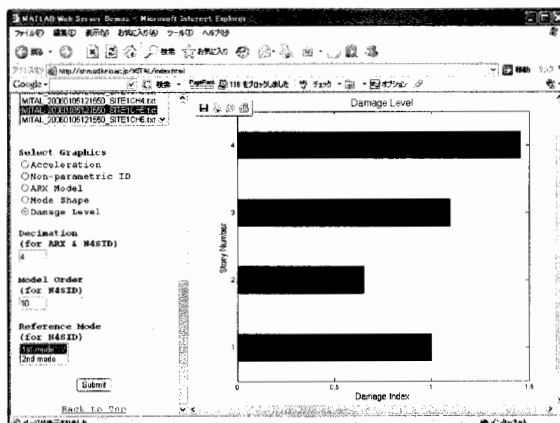


Figure 9: Story stiffness identified from 1st mode(left) and 2nd mode(right).

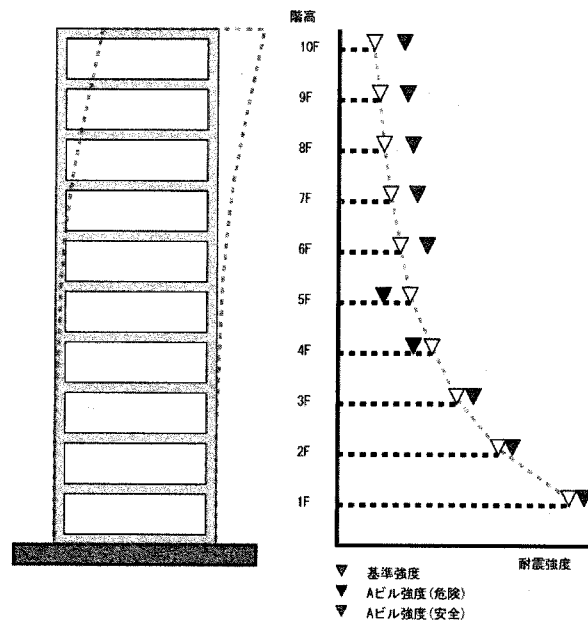


Figure 10: Desired view for showing damage degree and location.

4. CONCLUSIONS

A MATLAB-based health monitoring system was proposed and its prototype system has been developed. The system includes the automatic sensor system that transfer the data from the sensor through the Internet and the configuration of the system can be easily modified via the MATLAB-based health monitoring system. The data transferred by the sensor system is managed by the data server based on the meta-data relevant to the acquired data. The automatic sensor network may contain the configuration data in XML formats to be stored in the relational database to ease the management of the whole system.

The prototype system provides the standard evaluation tools to show time histories, power spectrum, transfer functions and modal information. Though the current system provides the algorithm to locate and quantify the damage in some story, the robustness of the results was found to be improved.

The system presented here is a good test bed to evaluate the damage identification methods and data management algorithms for further promotion of such a system. The system should be evolved to meet the requirements from the public to provide easy understanding of the views without the engineering knowledge of the background information on the buildings. It is our hope to use the system to prolong the lives of buildings with healthier conditions.

Acknowledgements:

The authors acknowledge support from Japan Ministry of Education, Culture, Sport, Science, and Technology (MEXT) for the COE program System Design: Paradigm Shift from Intelligence to Life (CUEE) at Keio University. The partial support from MEXT through grant-in-aid (No. 17360274, PI: Akira Mita) is also appreciated. The authors would like to express their thanks to member of SHM study group in the Consortium for Building Research and Development for providing their valuable data to our server.

References:

Yoshimoto, R., A. Mita and K. Okada, "Damage Detection of Base-Isolated Buildings Using Multi-Inputs Multi-Outputs Subspace Model Identification," *Earthquake Engineering & Structural Dynamics*, Vol. 34, No. 3, 307-324 (2005).

SEISMIC RETROFIT OF EXISTING BUILDING WITH HYSTERETIC DAMPERS

T. Takeuchi¹⁾, K. Yasuda¹⁾, K. Yuasa¹⁾, M. Iwata²⁾

1) Associate Professor, Dept. of Architecture and Building Eng., Tokyo Institute of Technology, Japan

tтору@arch.titech.ac.jp

2) Professor, Dept. of Architecture and Building Eng., Kanagawa Univ., Japan

Abstract: The authors have proposed the concept of integrated facade engineering, which treats architectural design, structural and environmental design combined together, and improving seismic performance of existing buildings with energy dissipation elements in attached facades. In this paper, the practical application of this concept to the aged concrete building is reported, which requires improvement in seismic performance allowing continuous tenant occupancy along the retrofit works.

1. INTRODUCTION

Seismic performances of buildings in Japan have large varieties depends on construction ages, because of seismic design code have been changed continuously along earthquake experiences. Especially buildings built before 1971 does not have enough hoop re-bar in columns, and have high risks of shear failure in the case of severe earthquake. Large amount of such buildings have been still existing and used in Japan, and early retrofit treatments are required. However such retrofit work is often difficult for the continuous occupation requirements and destruction of building appearances. For solving these problems, the authors have proposed the concept of “Integrated Façade”, which treats structural retrofit, facade design and environmental design combined together, including improvements on seismic performances using energy dissipation devices (Figure 1).

In this paper, this concept is applied to a practical existing building (Figure 2), and detailed structural design and effect of elasto-plastic energy dissipation braces are discussed. For seismic retrofit, Seismic Index “ I_s ” is commonly used for judging requirement for seismic retrofit in Japan. However, the relationship between I_s value and seismic performance is not necessarily clear when energy dissipation devices are applied. In this project, the energy dissipation devices are designed to satisfy the I_s requirement, and the seismic performance improvement is analytically evaluated together with detail of façade design and retrofit work process.

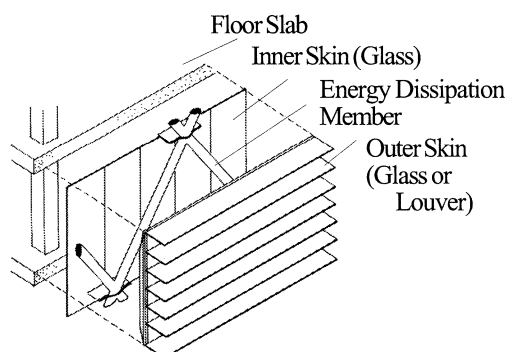


Figure 1. Concept of “Integrated Façade”

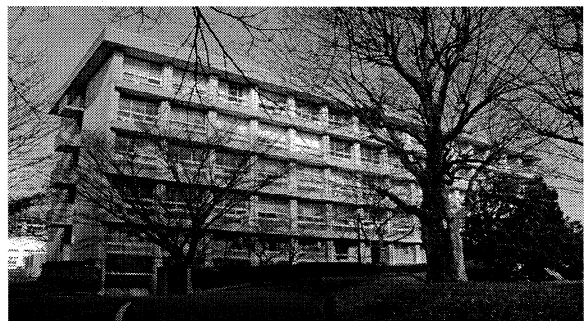


Figure 2. T.I.T. Midorigaoka-1st Bdg. before Retrofit

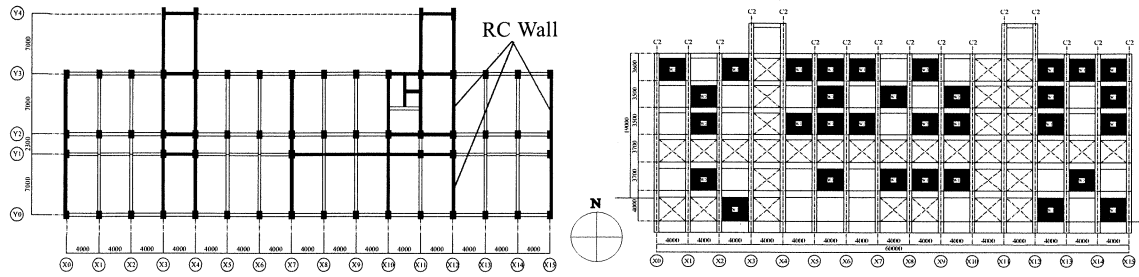


Figure 3. Plan and Elevation of Midorigaoka-1st Building

Table 1. I_s Indexes in E-W direction before Retrofit

Fr	C	F	E_0	S_D	T	I_s	$C_T \cdot S_D$	
5F	1.50	1.00	0.87	1.00	0.95	0.83	0.87	OK
4F	0.97	1.00	0.61	1.00	0.95	0.58	0.61	NG
3F	0.65	1.00	0.45	1.00	0.95	0.43	0.45	NG
2F	0.42	1.00	0.32	0.85	0.95	0.26	0.27	NG
1F	0.58	1.00	0.50	1.00	0.95	0.48	0.50	NG
BF	0.48	1.00	0.48	1.00	0.95	0.46	0.48	NG

2. BUILDING PROFILE

Midorigaoka-1st building in Tokyo Institute of Technology is 6-story RC building designed in 1966 before the revision of Building Code of Japan in 1971. This revision strengthen the requirements on shear re-bar in columns to satisfy bending failure, following many less-ductile shear failures in Tokachi Earthquake in 1968. The plan and elevation of the building are shown in Figure 3. The building has 23.3m x 60m square plan with cores for stairs and W.C.. Horizontal stability for N-S direction is secured by RC walls, and structural system for E-W direction is composed of moment frames with beams and columns in 4-m spans. For evaluating this structure, three types of following ultimate strength indexes on E-W direction are calculated.

(a) I_s indexes in each story are calculated using 3-D push-over analyses. Estimated values are shown in Table 1 and Figure 4. Values in E-W direction are much less than target value of 0.7 and minimum value is 0.27 in 2nd floor. These values are converted to shear force-deflection relationship estimating $F=1.0$ as story drift angle of 1/250, and $F=2.0$ as story drift angle of 1/150.

(b) Addition of crack strength and ultimate strength of columns and walls calculated by A.I.J. recommendations. The lower values of bending failure or shear failure of columns and walls are added up in each story using these equations. For column, the following equations are given.

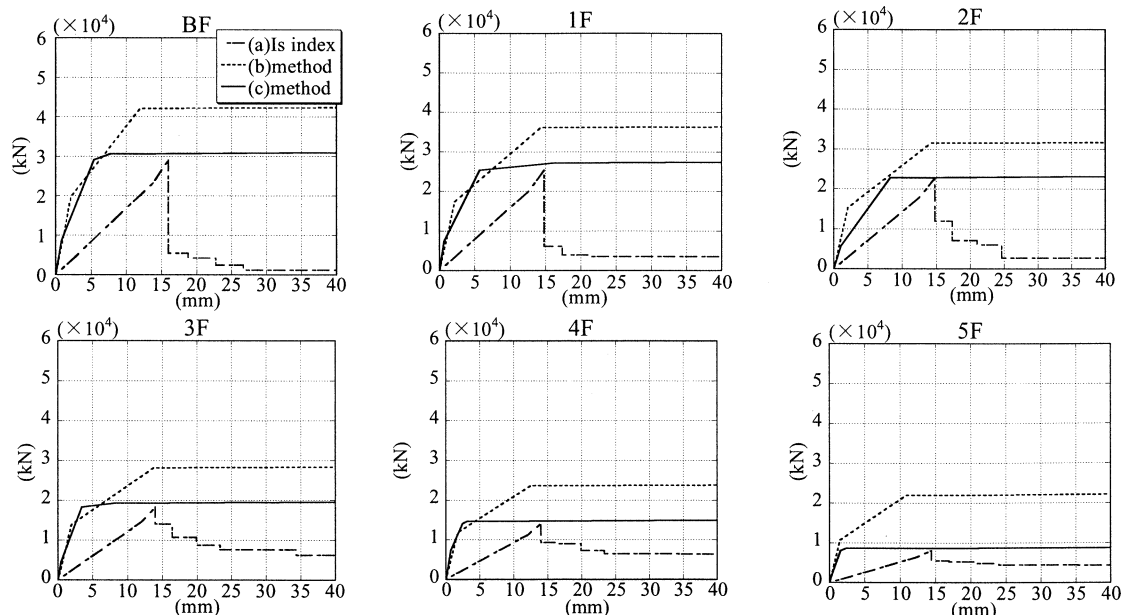


Figure 5. Shear Force-Deflection Relationship before Retrofit

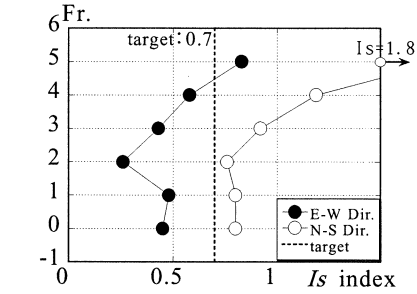


Figure 4. I_s Indexes before Retrofit

$$\text{Bending crack moment: } M_{cr} = 0.56 \sqrt{\sigma_B} Z_e + \frac{ND}{6} \quad (1)$$

$$\text{Ultimate bending moment: } M_u = 0.8 a_t \sigma_y d + 0.5 ND \left(1 - \frac{N}{bD\sigma_B} \right) \quad (2)$$

$$\text{Shear crack strength: } Q_{cr} = \frac{0.065 k_c (50 + \sigma_B)}{M/(Qd) + 1.7} bj \quad (3)$$

$$\text{Ultimate shear strength: } Q_{cr} = \left\{ \frac{0.053 p_t^{0.23} (18 + \sigma_B)}{M/(Qd) + 0.12} + 0.85 \sqrt{p_w \sigma_y} + 0.1 \sigma_0 \right\} bj \quad (4)$$

where, Z_e : equivalent section modulus, σ_B : strength of concrete, N : axial force, Q : shear force, D : depth, b : width, d : effective depth, $j = (7/8)d$, a_t : tension re-bar area, $p_t = a_t/bD$, p_w : shear re-bar ratio, σ_y : yield strength of re-bar, $k_c = 0.72$, $\sigma_0 = N/bD$.

(c) Shear force-deflection relationship of each story is estimated by push-over analyses with 3-D model using each member's load-deflection relationship calculated in (b).

Obtained shear force-deflection curves by each method are shown in Figure 5. For ignoring 3-D effects as axial deformation of column and beams, or rocking action of walls, strength (b) has higher than others, however, strength (c) is consistent with strength (a). These indicate I_s indexes well estimate ultimate strength, however, the stiffness until the ultimate strength is not corresponding.

3. RETROFIT CONCEPT

The retrofit concept is shown in Figure 6. The lower floors (BF-2F) of the building are class rooms, which are free in summer seasons and replacement of windows are possible. Columns in these floors are reinforced by carbon fiber sheets, preventing shear failure and improving deformation capacities. Their having not enough strength yet, additional Buckling Restrained Braces (BRB) are attached on facades. The upper floors (3F-5F) of the building are continuously occupied by laboratories, only works from outside being permitted, additional BRB are simply attached. Used types of braces are shown in Figure 7, and improved I_s values are shown in Table 2 and Figure 8. Three

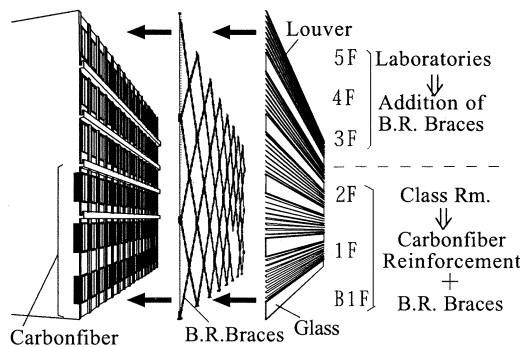
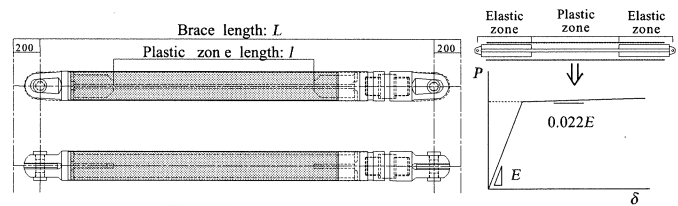


Figure 6 Retrofit Concept

Table 2. I_s Indexes in E-W direction after Retrofit

Fr	C	F	E ₀	S _D	T	I _s	C _T · S _D	
5F	1.63	1.00	0.95	1.00	1.00	0.95	0.95	OK
4F	1.28	1.00	0.81	1.00	1.00	0.81	0.81	OK
3F	1.13	1.00	0.79	1.00	1.00	0.79	0.79	OK
2F	0.82	1.00	0.51	0.84	1.00	0.88	0.43	OK
1F	0.79	1.00	0.31	1.00	1.00	0.75	0.31	OK
BF	0.70	1.00	0.34	1.00	1.00	0.79	0.34	OK



	Mark	Size	Strength (kN)
B.R. Brace	RB1	PL-19×152	650
	RB3	PL-32×153	1102
	RB4	PL-40×159	1431
Ordinary Brace	H1	H 200×200×8×12	706
	H2	H 250×250×9×14	1352

Figure 7 Buckling Restrained Braces

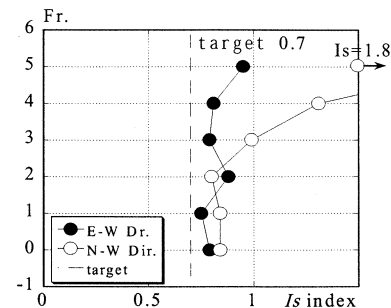


Figure 8. I_s Indexes after Retrofit

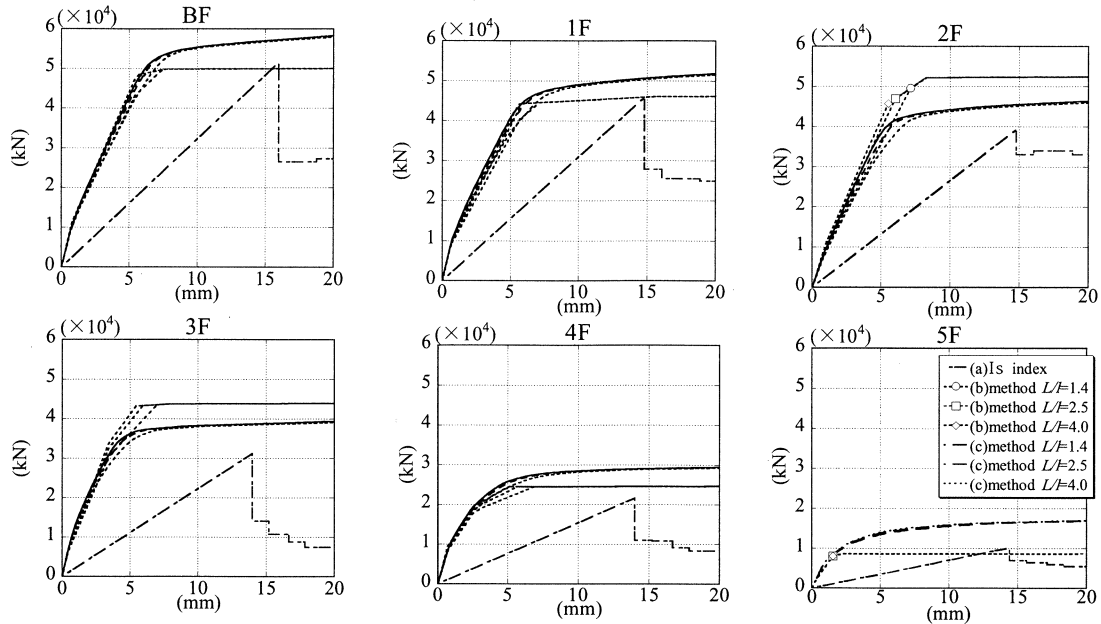


Figure 9. Shear Force-Deflection Relationship after Retrofit

types of BRB whose plastic zone length ratio L/l defined in Figure 7 are changed by $L/l=1.4, 2.5, 4.0$, and ordinary H-section braces whose buckling strength are equivalent to BRB yield strength is also studied. The improved shear force-deflection curves in each floors calculated by the method (a)-(c) are shown in Figure 9. The relationship between calculation methods are similar to Figure 5, however, the ultimate strength in the lower floors are increased by almost double. The effects of plastic zone length are observed as the difference of yield drifts.

4. REDUCED MOCK-UP FRAME EXPERIMENT

For verifying the evaluated hysteretic characteristics, reduced mock-ups of 2nd floor frame before retrofit and after retrofit are fabricated, and cyclic loading tests are carried out. The test

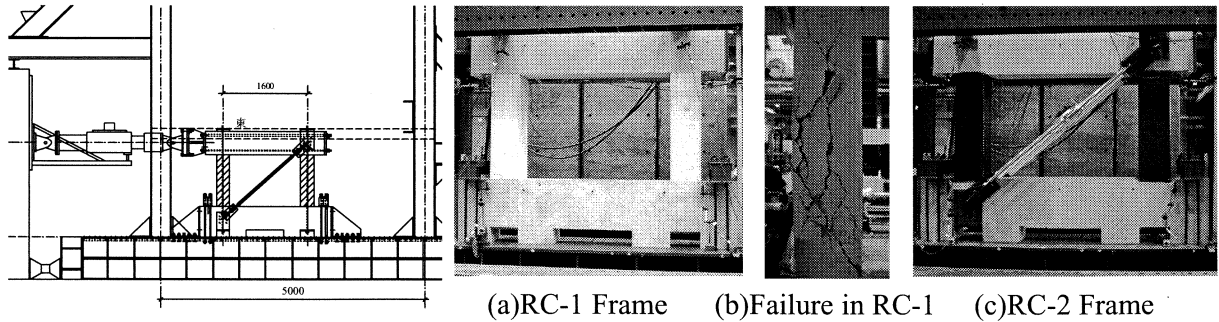


Figure 10. Test Configuration

Figure 12. Specimen Frames

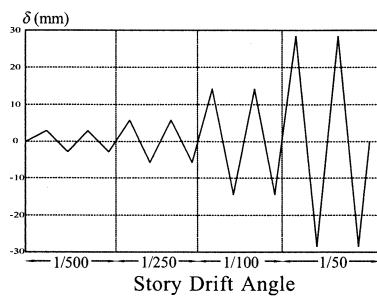
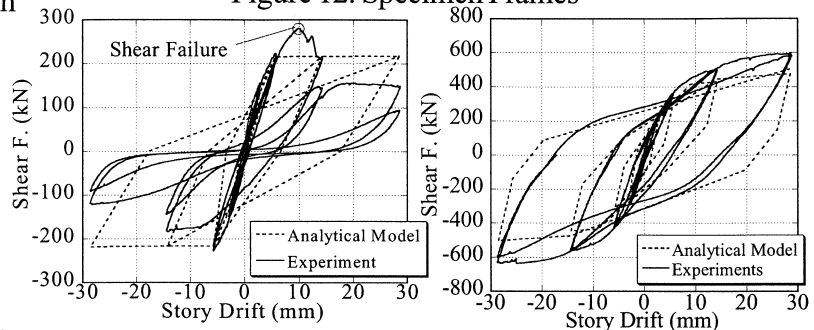


Figure 11. Loading Program



(a) RC-1 (before retrofit)

(b) RC-2 (after retrofit)

Figure 13. Hysteresis Loops before and after retrofit

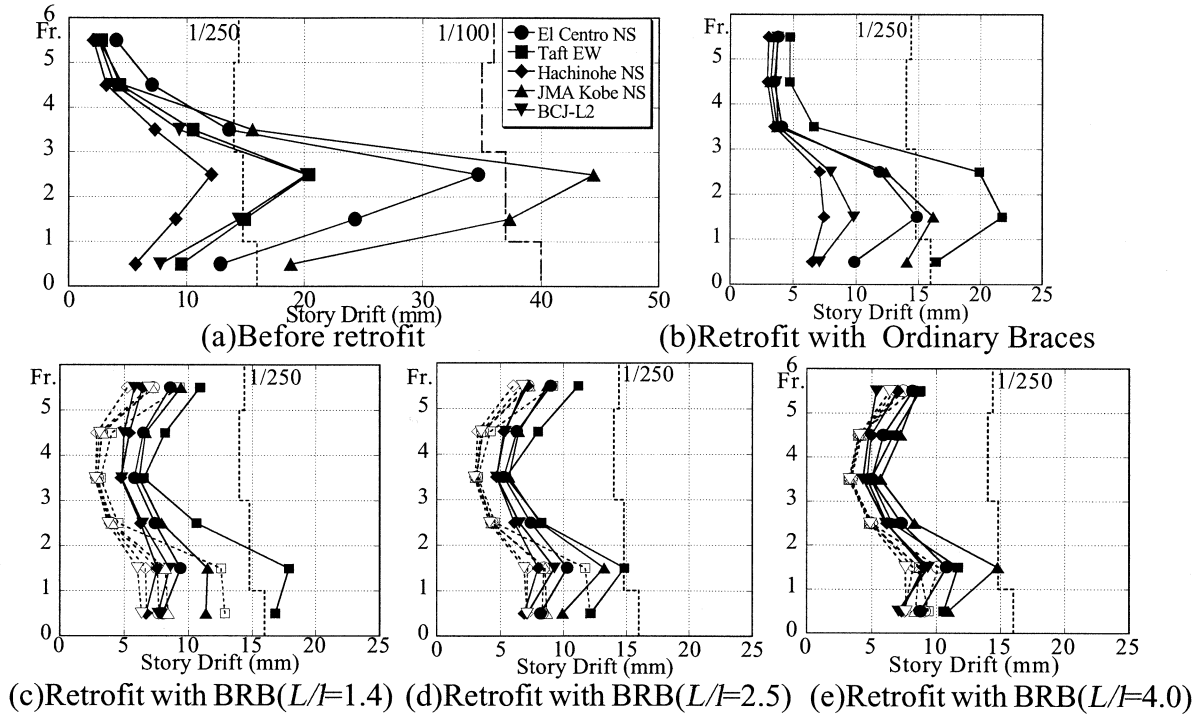


Figure 14. Maximum Story Drift Response with Each Braces

configuration is shown in Figure 10, and Loading program is shown in Figure 11. Appearance of each specimen is shown in Figure 12. They are modeled by 1/2.5 scales with the same criteria as real building, with axial force introduced to columns by PC bars. Obtained hysteretic loops are shown in Figure 13. Frame before retrofit (RC-1) started shear failure at 1/200 story drift angle, then lost bearing capacity drastically by each cycle (Figure 13(a)). On contrary, frame after retrofit, which is reinforced by carbon fiber and BRB did not cause shear failure, showed stable hysteretic loops up to cycles 1/50 story drift angle (Figure 13(b)). Analytical hysteretic loops by method (b) and Takeda model are shown in Figure 9 with dotted lines, which are considered to well express the test results. However, analytical model does not express the strength reduction of RC-1 after 1/250 story drift angle.

5. SEISMIC PERFORMANCE IMPROVEMENT BY RETROFIT

Using hysteresis model confirmed in Chap. 4., the effect of retrofit on the seismic performance of the building is checked by time-history analyses. Seismic waves of EL CENTRO NS, TAFT EW, HACHINOHE NS, and JMA KOBE NS with maximum velocity of 50cm/s, and artificial wave BCJ-L2 are applied to the 3-D models of the buildings. Figure 14 shows the maximum story drifts of each type of models. Figure 14 (a) shows the response of the building before retrofit, whose maximum drift exceeds 1/100 angle. Considering the results of the mock-up test, the building is expected to collapse with the shear failure at 2nd floor columns in real situation. Figure 14 (b) indicates the response with ordinary H-section braces, which cause partial buckling and some of the maximum drift exceeds 1/250. With these drift, non-structural walls will lose their strength and severe damages are expected. This results means the performance of strength-based retrofit might not be enough for $V_{\max}=50\text{cm/s}$ earthquake even satisfying $I_s=0.7$. Figure 14 (c)-(e) shows the response with BRB in various plastic zone length. When plastic zone length ratio L/I increases, the response is reduced, and $L/I=4.0$ satisfies maximum story drift being less than 1/250, and almost no damage. This results indicates the performance of energy dissipation members is more effective than ordinary braces, even for the same I_s values.

In Figure 14(c)-(e), the results lead by simple shear-mass models with (b) method are also shown in dotted lines. These results are much less than the results by 3-D models, which indicates the

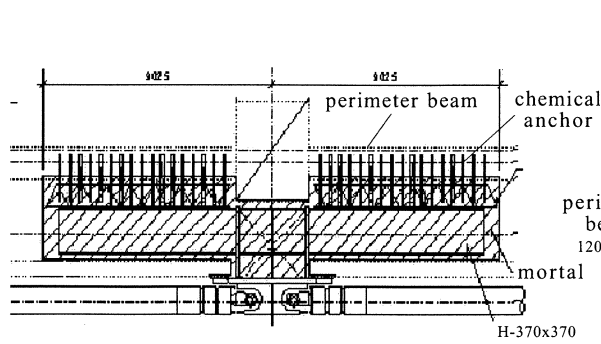


Figure 15. Design of the Connection

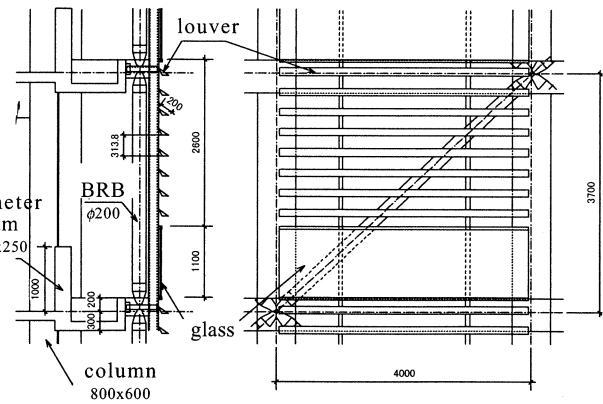


Figure 16. Design of the Skin

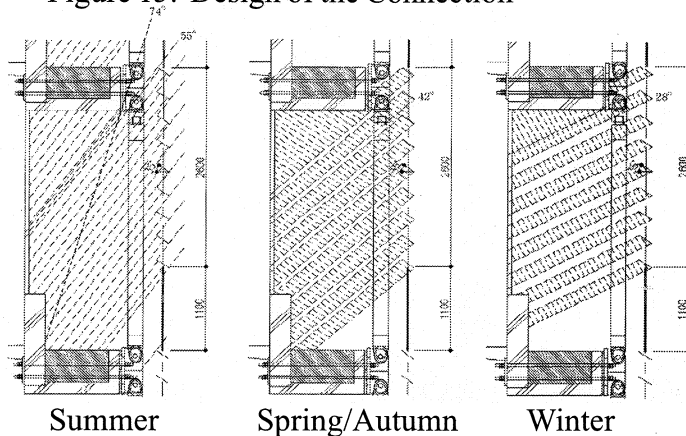


Figure 17. Effect of Louver and Glass

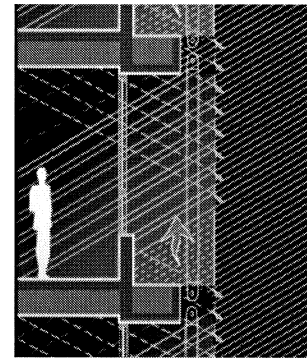


Figure 18. Light Reflection by Louver

evaluation with simple model ignoring axial deformation of column, beams and connections, or rocking action of braces often lead to over-estimation for the effect of the retrofit.

6. DESIGN OF THE CONNECTION AND SKIN

The connections between additional BRB and existing building need to transfer maximum 2000kN of horizontal force each, and should not obstruct inner occupancy. For satisfying these conditions, detail as shown in Figure 15 is applied. Firstly, shear anchor-bolts enough to transfer expected shear force are drilled on perimeter beams from outside only. Then corresponding H-section transfer steel beams with shear-studs are inserted in eaves, and fixed to perimeter beams by injecting mortar in-between. The steel beams have brackets sticking out from eaves, and BRB are connected to these brackets.

Seismic retrofit often destroys building facade design, and no function for reducing the environmental impact. In this project, following the concept of “Integrated facade”, additional skins composed of louver and glass are attached on BRB. Facade configuration is shown in Figure 16. The louvers are placed on upper parts of each story, and glass panels are placed on lower parts. They protect BRB from summer heats and rains, and the louvers are effectively cut the summer sun into the room. In winter, sunshine reaches to the inner room through the gap of the louver, and also heats the eave surface through the glass. They create the double-skin effect, and increase the temperatures in perimeter zones. The each louver section is also designed to reflect indirect sunshine effectively into the room (Figure 18). Also the appearance of the building is improved by these skins. Figure 19 shows the appearances of facade after retrofit, and Figure 20 shows the elevation of the building. The real size mock-up for the facade is also fabricated, as shown in Figure 21.

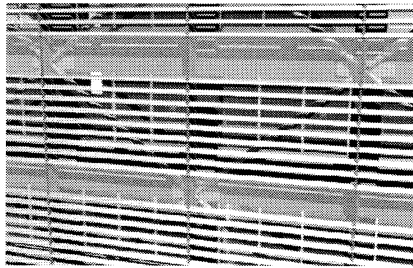


Figure 19. Facade Appearance

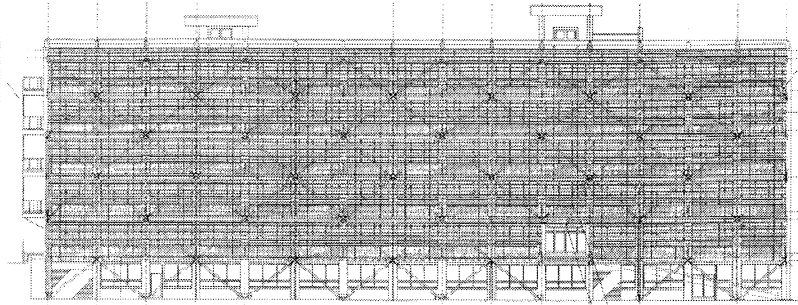


Figure 20. Elevation of the Building after Retrofit

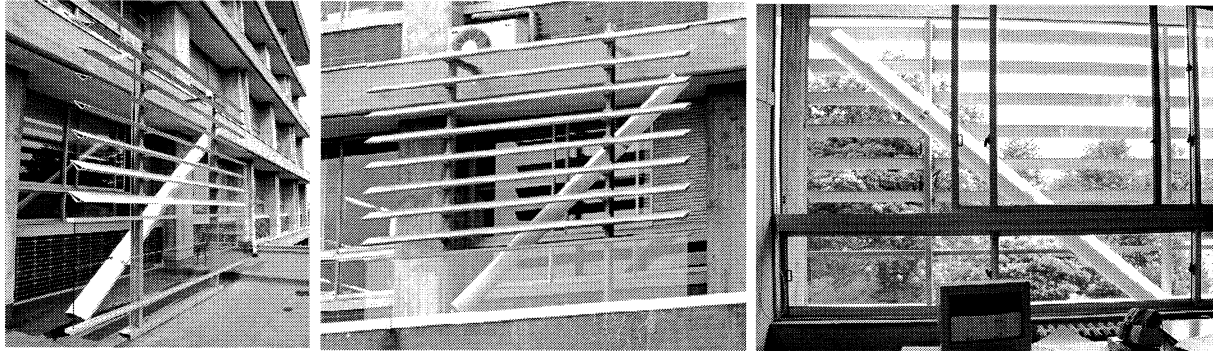


Figure 21. Mock-up of Louver and Glass

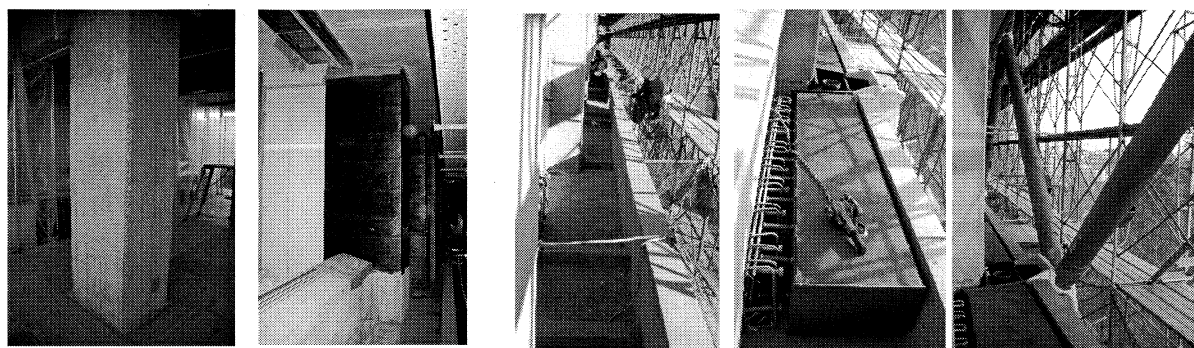
7. RETROFIT WORK PROCESS

The retrofit works for Midorigaoka-1st building has started in July 2005, and expected to be finished in March 2006. The time-schedule for retrofit work is shown in Table 3. Within the table, occupancy ratio of tenant in the building is shown. In the second month after start construction, works with noise and vibration as drilling or smashing are carried out, and some tenant were moved to other building and occupancy ratio were decreased to 60%. However, after this month the occupancy ratio are kept in the same ratio.

In Figure 22, process of retrofit works is shown. (a) is carbon-fiber reinforcement on columns, and (b) is the setting of the connection for Buckling Restrained Braces. (c) (d) is the attachment of the braces and building elevation before attaching the louver. The work is carried out within ordinary retrofit cost and schedule because of no additional piles are required.

Table 3. Retrofit Work Time-schedule

		2005													
		8			9			10			11			12	
Topics		Air conditioner removal			start of 2nd semester						Noise protection sheet removal				
Smash & Drill		Entrance			Roof			Connections							
Column reinforcement	2F				Carbon fiber			Window sash							
	1F							Carbon fiber			Window sash				
	BF				Carbon fiber						Window sash				
Stud					South Elev.			North Elev.							
W.C.											East W.C. renovation				
Occupancy ratio	5F	83.3%	67.8%	67.8%	67.8%	58.3%	58.3%	58.3%	58.3%	58.3%	50.0%	50.0%	50.0%	50.0%	
	4F	85.7%	85.7%	71.4%	71.4%	71.4%	71.4%	71.4%	71.4%	71.4%	71.4%	71.4%	71.4%	71.4%	
	3F	100.0%	100.0%	87.5%	87.5%	75.0%	62.5%	50.0%	50.0%	50.0%	50.0%	50.0%	50.0%	50.0%	
	total	88.2%	82.4%	73.5%	70.6%	67.6%	64.7%	61.8%	61.8%	61.8%	58.8%	58.8%	58.8%	58.8%	



(a) Carbon Fiber Reinforcement

(b) Setting Brace Connections



(c) Brace Attachment



(d) Facade with Buckling Restrained Braces

Figure 22. Retrofit Work Process

8. CONCLUSIONS

The concept of “Integrated facade” is applied to practical building with poor seismic performance designed in 1966, and improvement using elasto-plastic energy dissipation members are attempted. As results of mock-up experiments and analyses, seismic performance of the building is expected to be improved drastically and damage-controlled design against Level-2 earthquake are achieved. Actual retrofit work is proceeding on schedule, and expected to be completed by April 2006.

Acknowledgement:

This study is partially supported by Grants-in-Aid for Scientific Research, by the Ministry of Education, Science and Culture (B-1, No.16360283).

References:

- Takeuchi, T., Koyano, K., Iwata., M. (2005), “Studies on Integrated Facade Engineering -Analyses on existing facades-”, *J. Environ. Eng., AIJ, No.592*, pp.97-104
- Takeuchi, T., Koyano, K., Yasuda. K., Yuasa, K., Iwata., M. (2006), “Studies on Integrated Facade Engineering - Proposal for integrated facade and its evaluation-”, *J. Environ. Eng., AIJ, No.601*, pp.81-88
- The Japan Disaster Prevention Association (1989), “Recommendation for Seismic Retrofit for Reinforced Concrete Buildings”
- AIJ Standard for Structural Calculation of Reinforced Concrete Structures -Based on Allowable Stress Concept-, (rev.1999)
- Takeda, T., M.A. Sozen, N.N. Nielsen (1970), “Reinforced Concrete Response to Simulated Earthquakes”, *Proc. ASCE, Vol.96, No.ST12, Dec. 1970*, pp.2557-2573

PREDICTION FOR CUMULATIVE PLASTIC DEFORMATION OF DAMPER IN ELASTO-PLASTICALLY DAMPED STRUCTURE

H. Ito¹⁾ and K. Kasai²⁾

1) Graduate Student, Dept. of Built Environment, Tokyo Institute of Technology, Japan

*2) Professor, Structural Engineering Research Center, Tokyo Institute of Technology, Japan
ihiroshi@enveng.titech.ac.jp, kasai@serc.titech.ac.jp*

Abstract: This paper discusses simplified theory on cumulative damage prediction for elasto-plastic damper under earthquake ground motion. The theory is based on the seismic behavior of single-degree-of-freedom (SDOF) elasto-plastically damped structure, cumulative plastic deformation of damper can be clearly expressed as a function of stiffness parameter, ductility demand, natural period of structure and duration of earthquake ground motion. The relationship between cumulative plastic deformation and maximum deformation is also clarified. Accuracy of proposed prediction method is demonstrated via numerous time history simulations using a wide range of SDOF models.

1. INTRODUCTION

Passively-controlled building structures have become a common practice in Japan, taking full advantage of various energy dissipation devices developed recently. Especially, passively-controlled structure with elasto-plastic (EP) dampers, such as buckling-restrained brace, has gained widespread practical applications. The EP dampers substantially reduce building drifts and member forces by adding hysteretic damping and stiffness to the structure under earthquake ground motion. The performance of EP damper is closely related to its maximum deformation capacity of EP damper and cumulative plastic deformation capacity, but design method considering such an aspect has not been proposed to-date.

The objective of this paper is to propose a simplified theory on cumulative damage prediction for elasto-plastic damper under earthquake ground motion, and to verify accuracy of the proposed theory. The proposed theory is based on the seismic behavior of single-degree-of-freedom (SDOF) elasto-plastically damped structure, cumulative plastic deformation of damper can be clearly expressed as a function of natural period of structure and duration of earthquake ground motion, which haven't been considered exactly by Akiyama et al (1999) and Ogawa et al (2002), as well as stiffness parameter and maximum ductility factor. The relationship between cumulative plastic deformation and maximum deformation is also clarified. Accuracy of proposed prediction method is demonstrated via numerous time history simulations using a wide range of SDOF models.

2. CUMULATIVE PLASTIC DEFORMATION OF SDOF EP SYSTEM

2.1 Analytical Model

As shown in Figure 1, SDOF model of EP system consists of mass and two springs, which

represent EP damper and frame, connected in a row to the mass. EP damper is modeled as elasto-perfectly-plastic with elastic stiffness K_d , yield deformation u_{dy} , yield strength F_{dy} ($=K_d \times u_{dy}$) and maximum ductility factor μ_d , whereas frame behaves linearly with elastic stiffness K_f (Figure 2(a),(b)). Thus, maximum displacement of system u is identical to the one of frame u_f , and one of damper u_d , moreover maximum ductility factor μ and yield deformation u_y of system are identical to those of damper μ_d , u_{dy} , respectively. Fundamental vibration period and damping ratio of frame are defined as T_f and h_0 . Elastic stiffness $K_f + K_d$ and fundamental vibration period T_0 of EP system are given by Eq. 1(a)-(c).

$$K_0 = K_f + K_d, \quad T_0 = \sqrt{p} \cdot T_f, \quad p = \frac{K_f}{K_f + K_d} \quad (1a-c)$$

where p = ratio of post-yield stiffness to elastic stiffness of system.

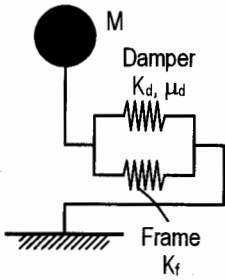


Figure 1
SDOF Model
of EP System

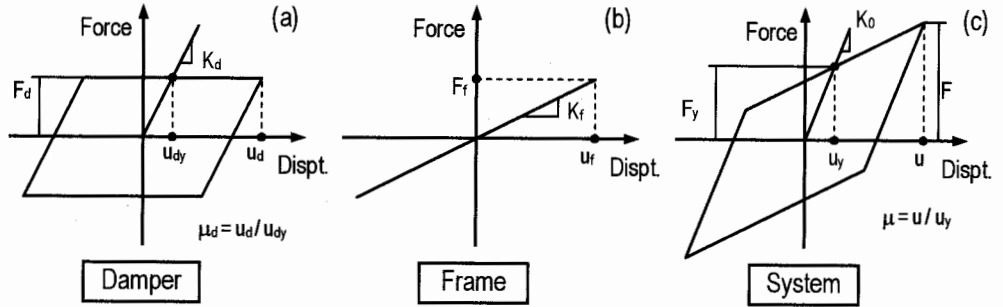


Figure 2 Force – Displacement Characteristic
(a)Damper, (b)Frame and (c)System

Cumulative deformation ductility factor of damper η , which is an index of cumulative energy dissipation of damper, is defined as follows.

$$\eta = \sum \Delta \mu \quad (2)$$

where $\Delta \mu$ = deformation ductility factor in each half cycle (Figure 3).

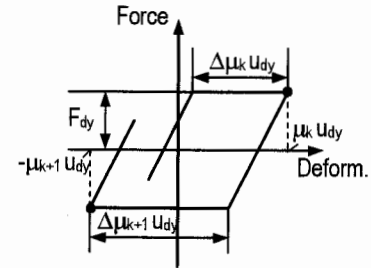


Figure 3 Deformation Ductility
Factor of Damper in Each Half Cycle

2.2 Analysis Parameters

In order to grasp the relationship between cumulative plastic deformation and maximum deformation of damper, numerous time history simulations using SDOF model are carried out. In this numerical study, 8 post yield stiffness ratios $p=0.001, 0.01, 0.1, 0.2, 0.5, 0.8, 0.95$ and 0.999 , 4 maximum ductility factors $\mu=2, 4, 8$ and 15 , 6 natural vibration periods of system $T_0=0.3, 0.5, 1.0, 2.0, 3.0$ and 4.0 sec and 14 earthquake ground motions are considered. Thus, $2688 (=8 \times 4 \times 6 \times 14)$ cases in total are verified. Table 1 shows the input maximum acceleration, record length and duration of 14 earthquake ground motions used in this study. The duration of earthquake ground motion t_d is defined as cumulative duration, which is the time interval during which the central 90% of the contribution to the integral of the square of the acceleration takes place (Trifunac & Brady, 1975). Initial viscous damping ratio $h_0=0.02$ is considered for all cases.

Table 1 List of Earthquake

Observed Earthquake	Max. Acc. (cm/sec ²)	Record Length (sec)	Duration (sec)	Artificial Earthquake	Max. Acc. (cm/sec ²)	Record Length (sec)	Duration (sec)
El Centro NS	341.7	53.7	24.4	BCJ-L2	346.6	120.0	65.3
El Centro EW	210.1	53.5	24.5	Hachinohe EW	435.1	60.0	49.2
Taft N021E	152.7	54.4	30.5	JMA Kobe NS	539.8	60.0	14.8
Taft N111E	175.9	54.4	28.8	Tohoku Univ. NS	371.0	60.0	30.4
Hachinohe NS	229.7	51.0	28.4	El Centro NS	524.7	53.7	41.4
Hachinohe EW	180.2	51.0	24.8	Taft N111E	548.5	54.4	41.5
JMA Kobe NS	820.6	30.1	8.1				
JMA Kobe EW	619.2	30.1	9.5				

2.3 Analysis Results

The relationship between cumulative deformation ductility factor η and maximum ductility factor $(\mu-1)$ of EP damper can be clarified by investigating complex effects of key parameters such as p , μ , T_0 and t_d . Figure 4 plots value of $\eta/(\mu-1)$ against p for different μ , T_0 and earthquakes. As can be seen in Figure 4, as long as p is lower than 0.2, value of $\eta/(\mu-1)$ almost doesn't change regardless of μ . On the contrary, as the p , μ get higher, value of $\eta/(\mu-1)$ tends to increase strongly in each Figure. Figure 5(a)-(c) shows time history of displacement and force of damper in case of $p=0.1$, 0.8 and 0.999. As p gets higher, which means as K_d/K_f gets lower, the system behaves linearly due to less energy dissipation by damper, therefore η -value also becomes greater as shown in Figure 5(d).

In addition, by comparing Figure 4(a) and (c), as well as Figure 4(b) and (d), the relation between value of $\eta/(\mu-1)$ and T_0 suggests that value of $\eta/(\mu-1)$ especially increases in short period structure. The most likely reason is that, under earthquake excitation, short period structure vibrates many more cycles in inelastic state than long period structure, as shown in Figure 6(a)-(d). Moreover, it can be seen that value of $\eta/(\mu-1)$ by artificial earthquakes is somewhat higher than by observed earthquakes (Figure 4(a) and (b), Figure 4(c) and (d)). This is why duration of artificial earthquakes is longer than observed earthquakes as shown in Table 1.

Therefore, in estimating cumulative deformation ductility factor of damper η , it is important to consider complex effects, including the number of cycles in inelastic state, plastic deformation in each cycle, as well as factors such as p , μ , T_0 and t_d .

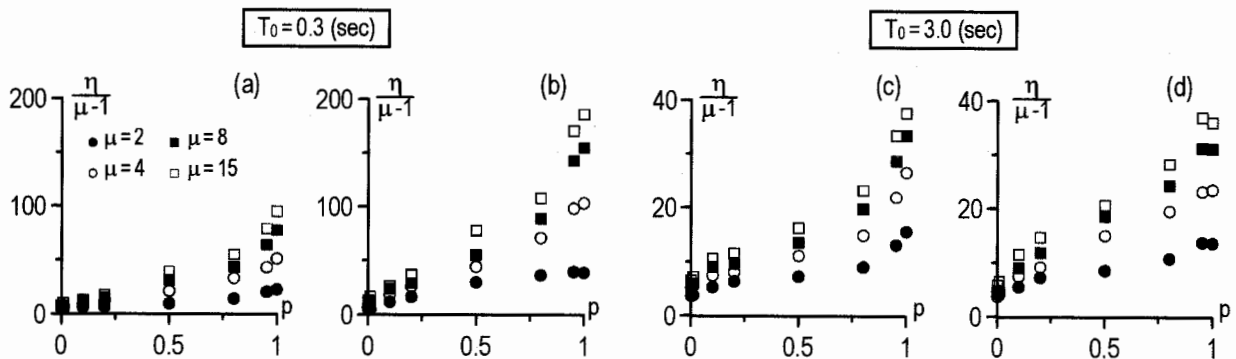


Figure 4 Relationship between $\eta/(\mu-1)$ and p for Different μ , T_0 and Earthquakes ((a),(c): Mean of 8 Observed Earthquakes, (b),(d): Mean of 6 Artificial Earthquakes)

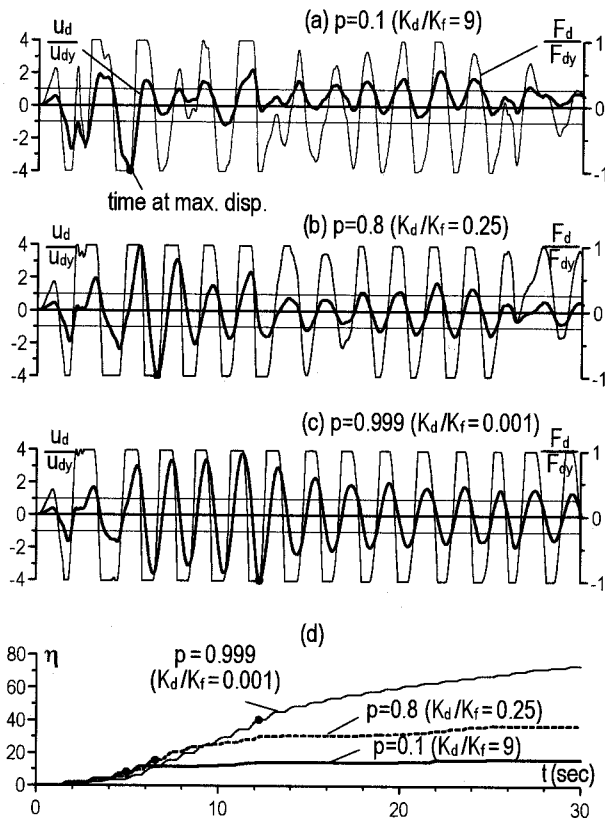


Figure 5 Time History of Displacement, Force and Cumulative Plastic Deformation of Damper with Various p - values (El Centro NS, $T_0 = 2\text{sec}$, $\mu = 4$)

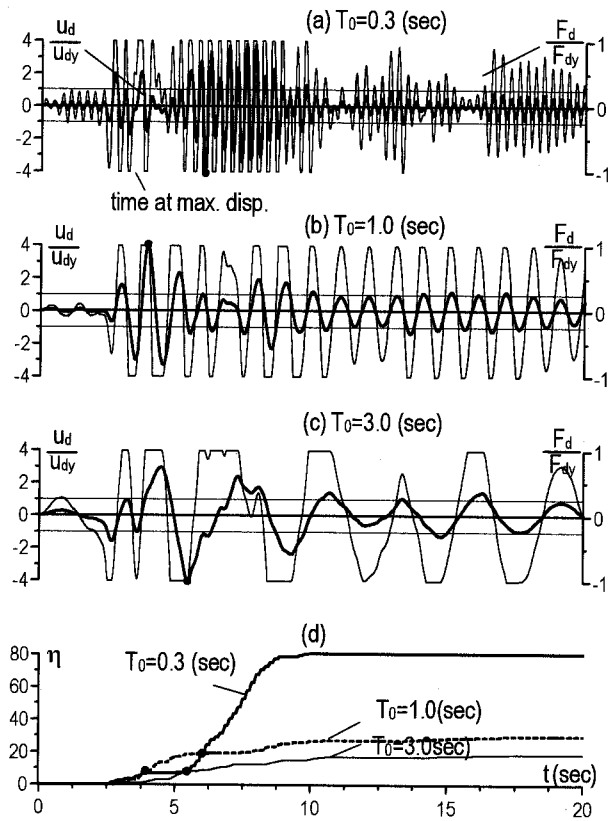


Figure 6 Time History of Displacement, Force and Cumulative Plastic Deformation of Damper with Various T_0 - values (JMA Kobe NS, $p = 0.8$ ($K_d/K_f = 0.25$), $\mu = 4$)

3. PREDICTION OF CUMULATIVE PLASTIC DEFORMATION OF SDOF SYSTEM

3.1 Proposed Theory for Prediction

Based on trend of analysis results of SDOF EP system (section 2.3), this section proposes prediction theory for cumulative deformation ductility factor η of damper, given maximum ductility factor μ . The proposed theory is considered complex effects, including the number of cycles in inelastic state, plastic deformation in each cycle, as well as factors such as p , μ , T_0 and t_d .

Procedure to obtain the formula for prediction of cumulative deformation ductility factor η of damper is summarized in sequence of steps below:

1. Investigate relation between the total time the system in inelastic state and duration of earthquake ground motion t_d .
2. Investigate relation between the total number of cycles the system in inelastic state and the total time in inelastic state.
3. Investigate the maximum plastic deformation in all the half cycle.
4. Investigate the relation between plastic deformation and corresponding number of cycles.
5. Calculate the cumulative plastic deformation as an integral value of the product of plastic deformation and corresponding number of cycles.

Consequently, the formula for prediction of cumulative deformation ductility factor η of damper is obtained as follows.

$$\eta = \frac{1+\sqrt{p}}{3} \left[(1+\sqrt{p})(\mu-1)^2 + \frac{t_d}{T_0} \frac{0.3 T_0^{1/3} (\mu-1)^{3/2} \exp(0.55 T_0^{1/4} p)}{1-0.18(1-p)\ln(T_0)} \right] \quad (3)$$

Therefore, the formula for relationship between cumulative deformation ductility factor η and maximum ductility factor $(\mu-1)$ of damper is also obtained by dividing Eq. 3 by $(\mu-1)$.

$$\frac{\eta}{\mu-1} = \frac{1+\sqrt{p}}{3} \left[(1+\sqrt{p})(\mu-1) + \frac{t_d}{T_0} \frac{0.3 T_0^{1/3} (\mu-1)^{1/2} \exp(0.55 T_0^{1/4} p)}{1-0.18(1-p)\ln(T_0)} \right] \quad (4)$$

3.2 Trends of Cumulative Plastic Deformation

Figure 7 plots $\eta/(\mu-1)$ against p for different $\mu=2, 4, 8$ and 15 , $T_0=0.3, 1.0$ and 3.0 , and $t_d=15, 30$ and 60 by the proposed theory (Eq. 4). It can be seen that the proposed theory (Eq. 4) can express successfully trends of analysis results (section 2.3), which are the strongly increase η -value in case of short period structure and long-duration earthquake, as well as behavior of low-stiffness and low-yield-strength damper.

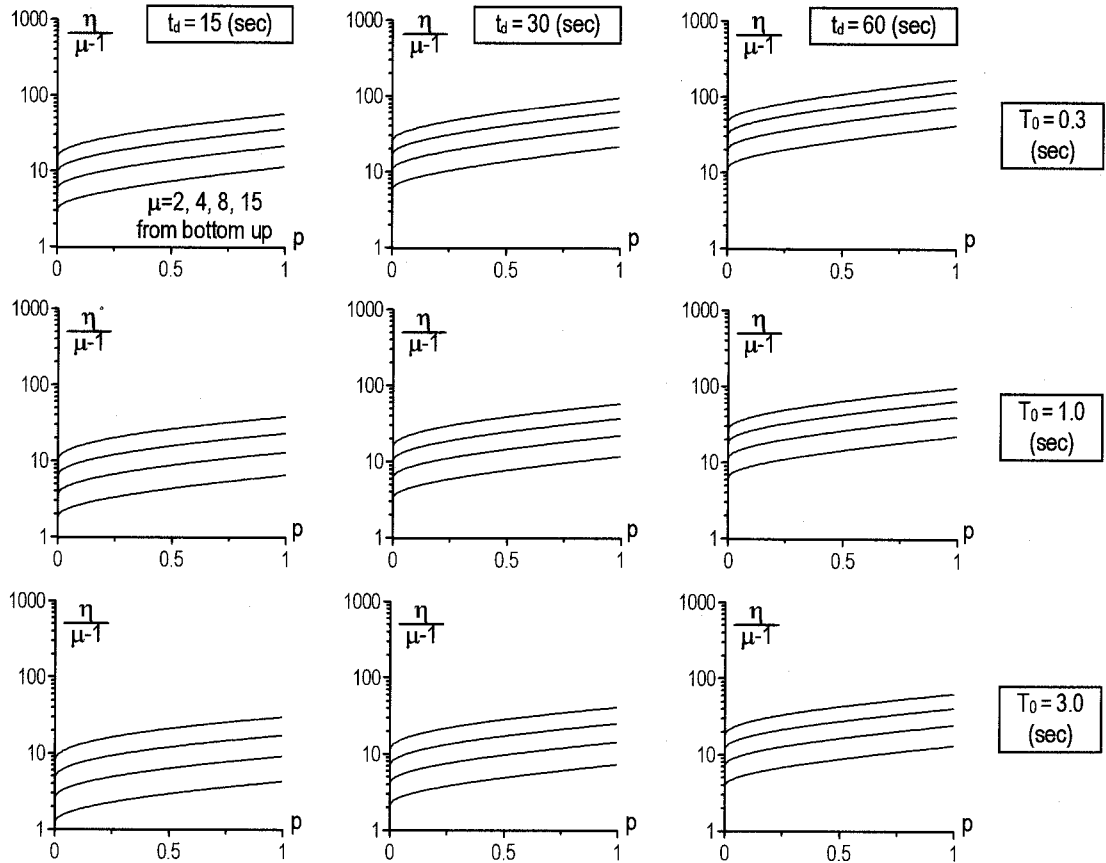


Figure 7 Relationship between $\eta/(\mu-1)$ and p for Different μ , T_0 and t_d by Proposed Theory (Eq. 4)

4. VALIDATION STUDY OF RELATIONSHIP BETWEEN CUMULATIVE PLASTIC DEFORMATION AND MAXIMUM DEFORMATION OF SDOF EP SYSTEM

4.1 Other Methods Proposed in the Past

Akiyama et al (1999) and Ogawa et al (2002) proposed prediction theories for cumulative plastic deformation and maximum deformation based on total energy balance under earthquake excitation. Akiyama proposed the formula (Eq. 5) for the relationship between $\eta/(\mu-1)$ and p , which is also shown in Figure 8(a).

$$\frac{\eta}{\mu-1} = 4 + \frac{\mu p}{1-p} \quad \left(\frac{\mu p}{1-p} \leq 1 \right), \quad \frac{\eta}{\mu-1} = 8 \quad \left(1 < \frac{\mu p}{1-p} \right) \quad (5a,b)$$

As it can be seen in Eq. 5 and Figure 8(a), $\eta/(\mu-1)$ doesn't change as long as $1 < \mu p/(\mu-1)$. Thus, the strongly increase of the ratio $\eta/(\mu-1)$ along with the increase of p and μ is neglected by Akiyama's formula.

On the contrary, Ogawa didn't express η as a function of μ in predicting seismic response but only considering total energy balance and distribution of energy in each cycle, from there the relationship between $\eta/(\mu-1)$ and p shown in Figure 8(b),(c) is developed. In prediction theory proposed by Ogawa, the higher p and μ get, the more value of $\eta/(\mu-1)$ get, moreover value of $\eta/(\mu-1)$ increases sharply as long as $p > 0.8$. In addition, as shown in Figure 8(b),(c), value of $\eta/(\mu-1)$ by near field earthquake with short duration is less than by other earthquake.

The most difference between the proposed method in this paper (chapter 3) and above mentioned methods is the appropriate consideration of effects caused by natural period of structure and duration of earthquake.

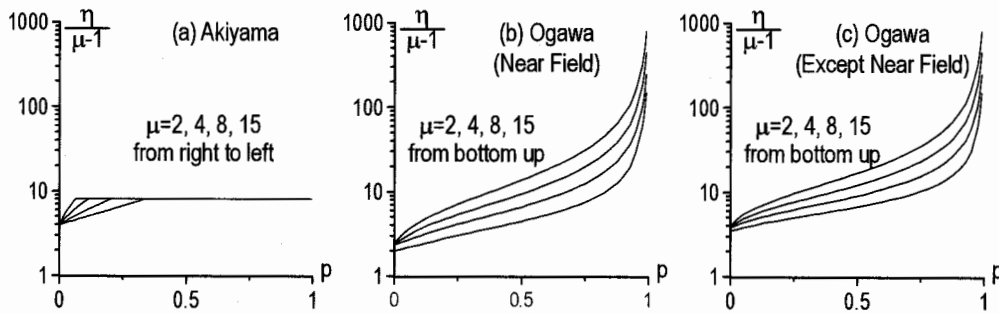


Figure 8 Relationship between $\eta/(\mu-1)$ and p for Different μ by Other Methods

4.2 Validation of the Proposed Method

Validation study for the proposed method is carried out using a wide range of EP SDOF models that introduced in section 2.2 (2688 cases in total), the accuracy of estimated η -value is verified with time history analysis results. In estimating η -value by Ogawa's method, 3 JMA Kobe earthquakes (2 observed and 1 artificial) are considered as "near field earthquake". Instead of calculating the bias a and dispersion σ as the median and standard deviation of $\eta(\text{prediction})/\eta(\text{analysis})$, a and dispersion σ can equivalently be obtained by performing a one-parameter log-log linear least squares regression of $\eta(\text{prediction})$ on $\eta(\text{analysis})$. The regression model is expressed " $\ln(\eta(\text{prediction})) = \ln(a) + \ln(\eta(\text{analysis})) + \ln(\varepsilon)$ ", where a is regression parameter and ε is the random error in $\eta(\text{prediction})$ given $\eta(\text{analysis})$ with median 1 and dispersion σ .

Figure 9 and Table 2 show accuracy of each method for different T_0 , it can be seen that the proposed method gives quite good estimation regardless of T_0 , while the accuracy of the other

methods is low and dependent on T_0 .

Therefore, in estimating the relationship between cumulative deformation ductility factor and maximum ductility factor of damper, it is quite important to consider the effects by natural period of structure and duration of earthquake, as well as stiffness balance and maximum ductility factor of damper.

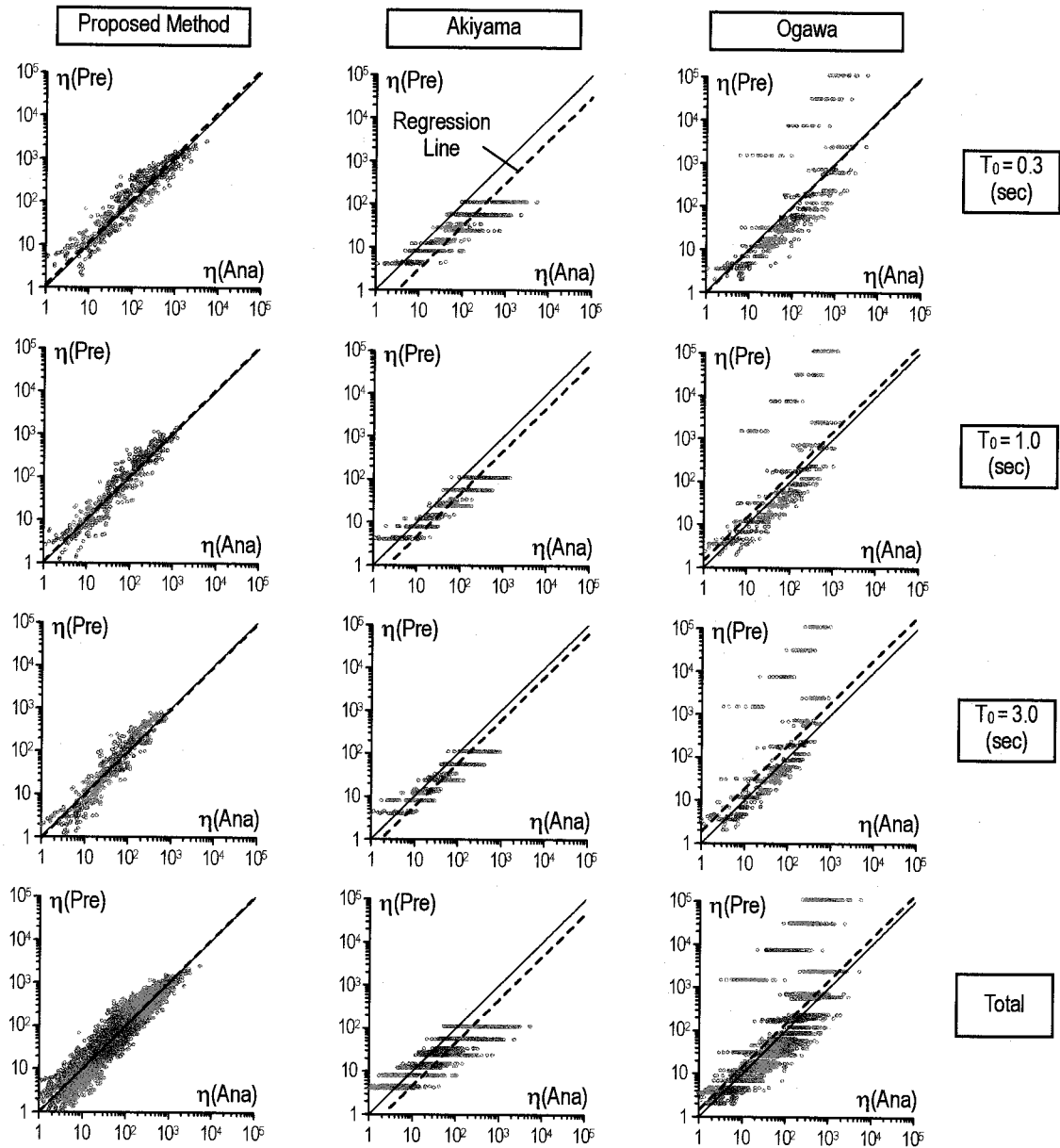


Figure 9 Comparison Prediction Methods with Analysis Results of Cumulative Deformation Ductility Factor η for Different T_0

Table 2 Accuracy of the Methods in Prediction of Cumulative Deformation Ductility Factor η for Different T_0
(Upper: Bias a , Lower: Dispersion σ)

	Total	$T_0=0.3$ (sec)	$T_0=0.5$ (sec)	$T_0=1.0$ (sec)	$T_0=2.0$ (sec)	$T_0=3.0$ (sec)	$T_0=4.0$ (sec)
Proposed Method	1.024 (0.583)	1.155 (0.618)	1.101 (0.550)	1.072 (0.561)	0.951 (0.600)	0.950 (0.597)	0.921 (0.528)
Akiyama	0.471 (0.801)	0.307 (0.930)	0.365 (0.847)	0.468 (0.718)	0.532 (0.724)	0.608 (0.650)	0.645 (0.621)
Ogawa	1.468 (1.765)	0.956 (1.692)	1.137 (1.703)	1.459 (1.817)	1.658 (1.722)	1.895 (1.799)	2.011 (1.739)

5. CONCLUSIONS

This study is aimed to develop the prediction method for cumulative plastic deformation of damper in elasto-plastically damped structure. The proposed method is based on the behavior of SDOF EP system subjected to earthquake ground motion. The conclusions are as follows:

1. The prediction theory for cumulative plastic deformation of damper is developed, by considering stiffness parameter, maximum ductility factor, natural period of structure and duration of earthquake ground motion.
2. Cumulative plastic deformation of damper increases strongly with short period structure and long-duration earthquake, as well as with low-stiffness and low-yield-strength damper.
3. The proposed method can be applied to long earthquake records, by considering factors such as natural period of system and duration of earthquake.

The proposed theory is also applied to multi-degree-of-freedom (MDOF) EP system, accuracy of this theory is validated.

Acknowledgements:

The Ministry of Education, Science and Culture provided support for this study in the form of Grants-in-Aid for Scientific Research. The authors gratefully acknowledge the support.

References:

- Trifunac, M.D. and Brady, A.G. (1975), "A Study on Duration of Strong Earthquake Ground Motion," *Bulletin of the Seismological Society of America*, **65**(3), 581-626.
- ITO, H., and Kasai, K. (2005), "Statistical Investigation on Cumulative Plastic Deformation of Elasto-Plastically Damped Structures," *Summaries of Technical Papers of Annual Meeting*, Architectural Institute of Japan, B2, 331-332.
- Takahashi, M., and Akiyama, H. (1999), "The Maximum Displacement and Energy Response of Multi-Story Frames under Earthquakes," *Journal of Structural Engineering*, Architectural Institute of Japan, 515, 59-66.
- Ogawa, K. and Hirano, T. (2002), "Ductility Demanded of Hysteretic Dampers," *Journal of Structural Engineering*, Architectural Institute of Japan, 558, 197-204.

SEISMIC ISOLATION STRUCTURES IN JAPAN

M.Ohmiya¹⁾ and T.Teramoto²⁾

1) Research associate, Department of Architecture, Faculty of Engineering Course, Tokyo University of Science, Japan

2) Professor, Department of Architecture, Faculty of Engineering Course, Tokyo University of Science, Japan

mohmiya@rs.kagu.tus.ac.jp, teramoto@rs.kagu.tus.ac.jp,

Abstract: Based on the performance evaluation sheets released by the official evaluation organizations, the database of about 1200 seismic isolation buildings was created. Based on this, we have tried to research the change and tendency of the structural characteristics according to the years. As a result, the number of evaluated buildings per a year has a downward tendency after the peak of 1996. The structural systems are the reinforced concrete at about 70% and the main building-usage is the apartment house. The building height and the average usual pressure of isolators have a upward tendency. The natural period of the buildings tends to the longer period.

1. INTRODUCTION

The seismic isolation building in Japan initiated from the Yachiyo-dai-house in 1982, and about 1200 seismic isolation buildings have been constructed by present. Although the performance demands to seismic isolation members or seismic isolation buildings are diversified, the investigations and researches on these structural characteristics of the existing seismic isolation buildings are not sufficient. Then, in order to grasp the time history of the structural characteristics of seismic isolation buildings, we made up the isolation-buildings database from the " Performance evaluation sheet " that is officially published by the performance evaluation organizations.

And the tendency grasp of many data was performed for the main examination items, which are the building-heights, structure systems and main uses etc. of the series change in time, and which are the dynamic properties such as the natural periods and the maximum base shear coefficients etc..

2. OUTLINE OF DATABASE

Based on the published performance evaluation sheets¹⁾ of isolation-buildings, the data items (about 100 items) were taken up, and the database was created. The number of inputted buildings is 1179 buildings (including 47 high-rise isolation-buildings), which the official evaluation organizations checked from April 1986 to December 2004. The main official evaluation organizations are the Building Center of Japan, Japan ERI Inc., and the General Building Research Corporation of Japan. In addition, the low-rise houses of seismic isolation are not included in this database.

3. VARIOUS CHARACTERISTICS CHANGE AT THE TIME

3.1 Number of Isolation-Buildings and Structural Systems

The time history for the number of evaluated buildings is shown in Figure 1. The

isolation-buildings total number from June 1986 to December 2004 is 1179 buildings. Until 1994, the number of annual evaluated buildings remained in several buildings from the starting year of 1986. However, after the Hyogoken-Nanbu earthquake in 1995, the number of evaluated buildings increases rapidly and the number of evaluated buildings in 1996 had become 227 buildings per year. The number of evaluated buildings was decreasing every year after 1997. In addition, because the building permissions for isolation-buildings were simplified and was not required to be evaluated getting the special minister-permission by the ministerial notice in October 2000 accompanying Japanese Building Standard Law revision. The number of evaluated buildings started to decrease in 2000 and afterwards.

About structural systems, the reinforced concrete structure (RC) occupies 76% of the whole and, subsequently the composite structure (SRC) is 11%, and the steel structure (S) is 8%. A big change is not appeared at the structural system rate in 1995 and afterwards.

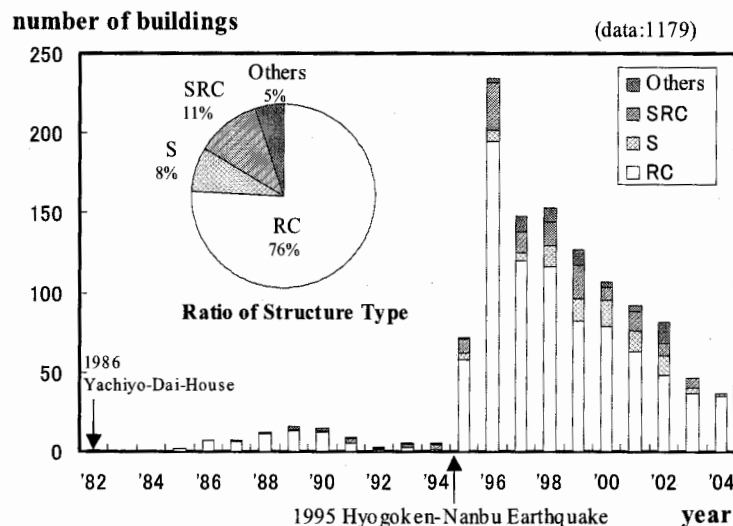


Figure1 Time history of Number of Evaluated Buildings and Structure Types

3.2 Main Building-Usage

Time history of main building-usages and the ratio are shown in Figure 2. Main building-usages are apartment houses as 41%, offices as 14%, complex institutions as 13% and hospitals as 10%. A big change is not appeared at the main building-usage rate in 1995 and afterwards. In the main building-usages for every structural system, the apartment houses of the RC structure were the about half of main usages, and the offices were accounted for about 40 percent in the S structure and the SRC structure.

3.3 Building Height

Time history of building-heights is shown in Figure3. The highest building-height has been increasing every year. High-rise isolation-buildings should have received the official structural evaluation as the high-rise building in addition to the isolation building. The number of the high-rise isolation-buildings exceeding the height of 60m is 47 in 2004. The highest building-height is 152m (an apartment house of RC structure), and the number of the RC structure isolation building is increasing.

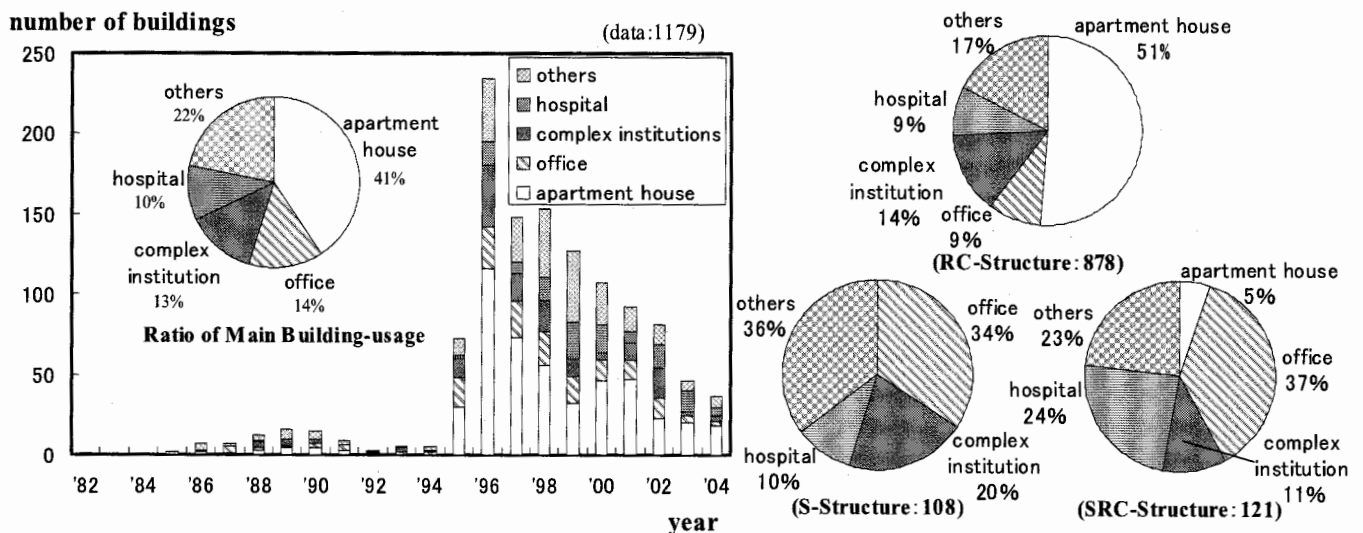


Fig.2 Time History of Main Building-usage

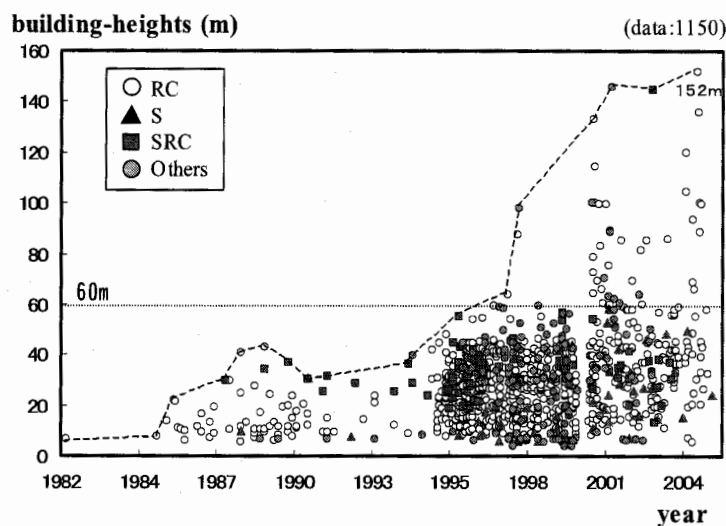


Fig.3 Time History of Building-Heights

4. SEISMIC ISOLAION TYPE AND SEISMIC ISOLATION

4.1 Seismic Isolation Type

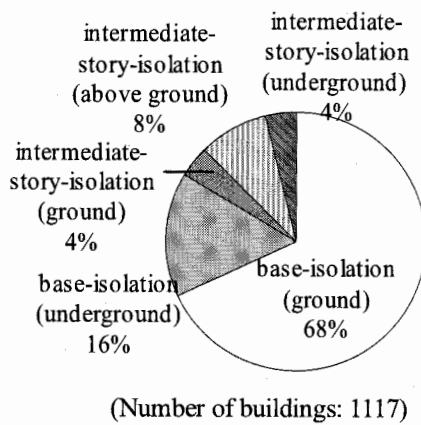
Seismic isolation type rates are shown in Figure 4. The base-isolation type (including the ground-base-isolation and the underground-base-isolation) is 84% and the intermediate-story-isolation type (including three types) has become 16%. The differences arising from the structural system and the main building-usages were not looked at in the seismic isolation type.

4.2 Isolator

The rates of the various used isolators are shown in Figure5. In this figure, when two or more isolators are used together, each is inputted as one affair. The laminated rubber isolators are the natural rubber laminated rubber isolator (NRB), the laminated rubber isolator with lead plug (LRB), and the high damping laminated rubber isolator (HDR). The laminated rubber isolators occupy 81% of the whole. The sliding isolators are the stiff-sliding isolator (SI) and elastic sliding isolator (SIR), and the sliding isolators occupy 14%. The differences arising from structural systems were not looked at from the isolator use rate.

The average usual pressure of the isolator and the building-height are shown in Figure6. The

average usual pressure has the tendency to increase when the building-height increase. The average value of average usual pressure is 107 kgf/cm^2 (10.5 N/mm^2) in the building lower 60m, and is 77.8 kgf/cm^2 (7.62 N/mm^2) in the building equal or higher 60m. The isolator average usual pressure of high-rise isolation-building has the tendency to have the higher pressure.



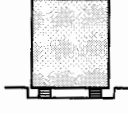
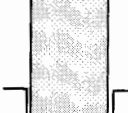
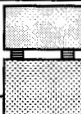
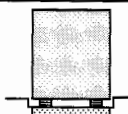
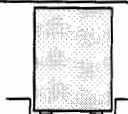
	above ground	ground	underground
base-isolation		 base-isolation (ground)	 base-isolation (underground)
intermediate-story-isolation	 intermediate-story-isolation (above ground)	 intermediate-story-isolation (ground)	 intermediate-story-isolation (underground)

Fig.4 Seismic Isolation Type Rates

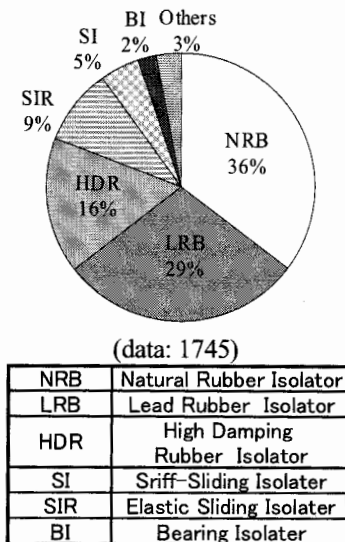


Fig.5 Rates of Various Used Isolators

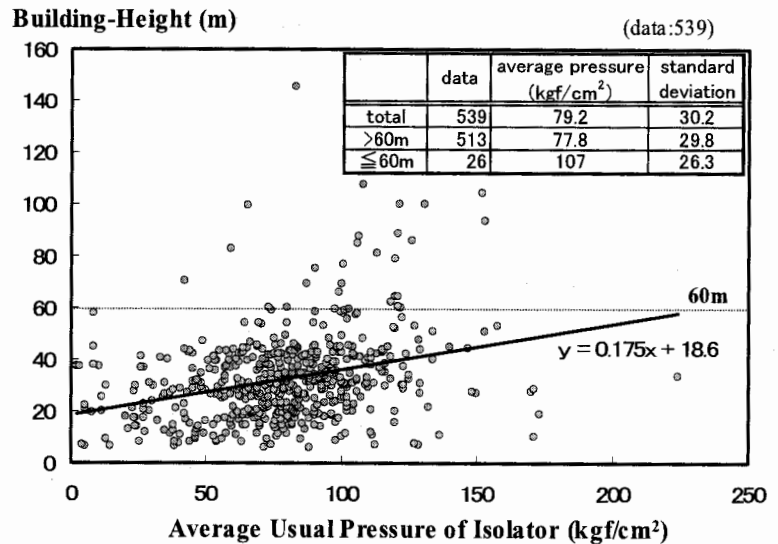


Fig.6 Average Usual Pressure of Isolator and Building-Height

4.3 Damper

The use rates of various dampers are shown in Figure 7. The histresis dampers are the steel-bar damper (SD), the lead damper (LD) and others. The histresis dampers occupy 80% of the whole. The viscous dampers, such as the oil damper (OD) and the viscous damper (VD), occupy 17%. For the structural system, the use rate of the oil damper to be as high as 34% was seen in the steel structure. The difference in use proportion of RC-structure and SRC-structure was less.

Figure 8 shows the time history of the use rates of dampers. Although many single type or multi types use of the histresis dampers are existed until 2000, the single type use of the viscous damper is increasing a little in 2000 and afterwards.

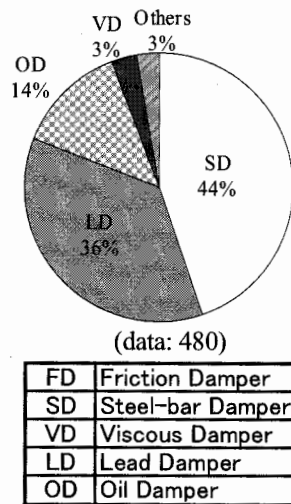


Fig.7 Use Rates of Various Dampers

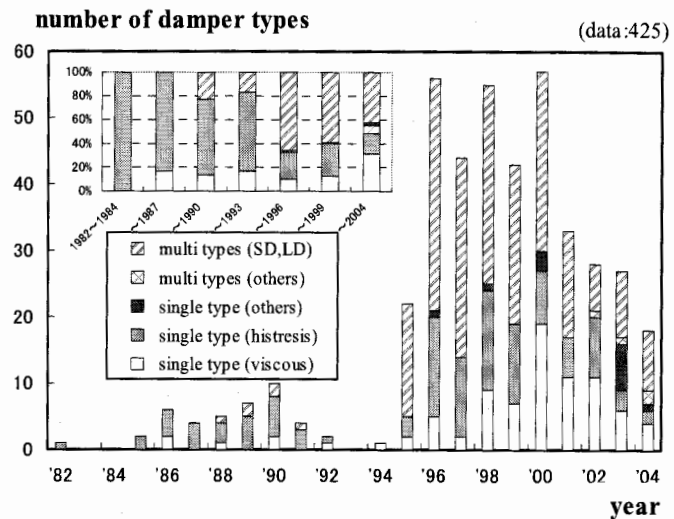


Fig.8 Time History of Use Rates of Dampers

5. DYNAMIC CHARACTERISTICS

5.1 Restoring Force Characteristics of Seismic Isolation Member and Upper Structure

The restoring force characteristic rates of seismic isolation members are shown in Figure 9, and the restoring force characteristic rate of the upper structure for every structural system is shown in Figure 10 to Figure 12. In the restoring force characteristic of seismic isolation members, the modified bi-linear model (MB) is 36% that is the most used one. The bi-linear model (B) is 25%, the linear model (L) is 11% and the tri-linear model (T) is 9%.

About the upper structure, the tri-linear model is the most as 39% and the degrading model (DT) is 25% and the linear model is 20%. In the steel structure, the linear model is 52% that is the half of the whole and the tri-linear model is 21% and the bi-linear model is 8%. About SRC structure, it is the almost same tendency as RC structure.

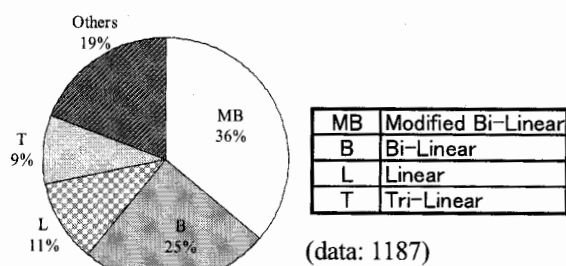


Figure9 Restoring Force Characteristic Rates of Seismic Isolation

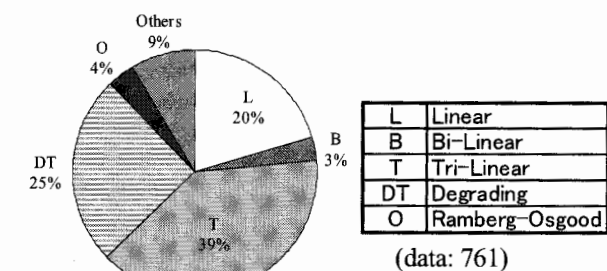


Figure10 Restoring Force Characteristic Rate of Upper Structure (RC-Structure)

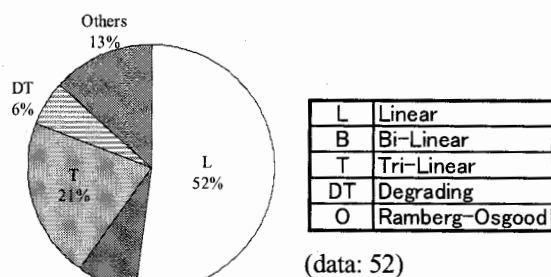


Figure11 Restoring Force Characteristic Rate of Upper Structure (S-Structure)

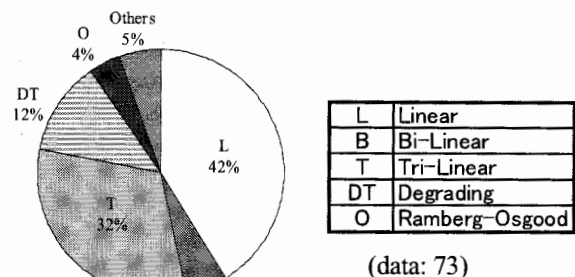


Figure12 Restoring Force Characteristic Rate of Upper Structure (SRC-Structure)

5.2 Natural Period

The time history of the 1st natural period T_1 (at the level-2 earthquake-input) is shown in Figure 13. Level-2 earthquake motion is the input level supposing the big earthquake that happens very rarely, and it is thought that the hysteresis damper of a isolation-building should yield at this time. For this reason, it can be considered mostly that the natural period at the level-2 earthquake-input is the natural period by isolators only. As for the natural period, the tendency to have the longer value is seen when the time passed, and according to linear approximation, the amount of increases of the natural period has become 0.16 seconds per a year. The difference in the natural periods by structural systems is not seen.

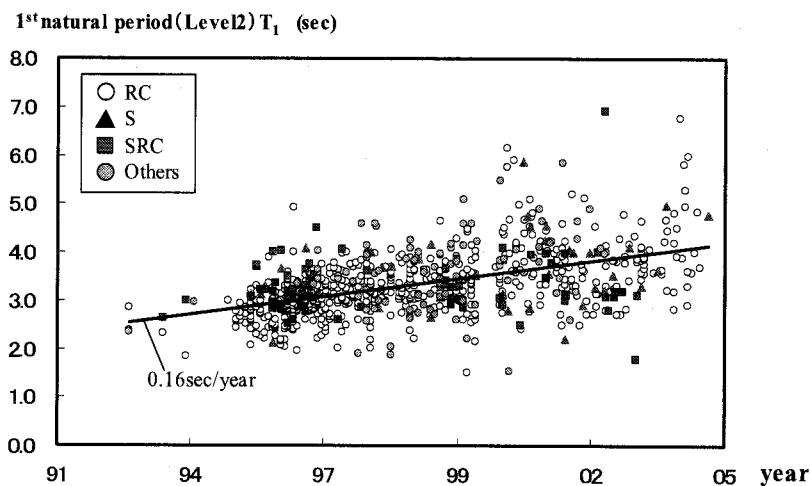


Figure13 Time History of the 1st Natural Period T_1 (at the level-2 earthquake-input)

5.3 Natural period and Maximum Shear Force Coefficient

The relation between the maximum shear force coefficients C_1 and the 1st natural periods T_1 at the level-2 earthquake-input is shown in Figure 14. The relation between the shear force coefficient C_1 and the natural period T_1 is expressed with the equation $C_1 = \alpha / T_1$. The value of the coefficient α by the average approximation is set to 0.38, and almost all data is distributed between $\alpha = 0.20$ and 0.55.

The frequency distribution of the natural period T_1 and the maximum shear force coefficient C_1 is shown in Figure 15 and Figure 16. The average of the natural period T_1 is 3.33 seconds, and the about 80% buildings are distributed at from 2.5 seconds to 4.0 seconds. The natural periods exceeding 4.0 seconds formed 13% of the whole. The average value of the shear coefficient C_1 is 0.12, and about 80% buildings are distributed at from 0.08 to 0.16.

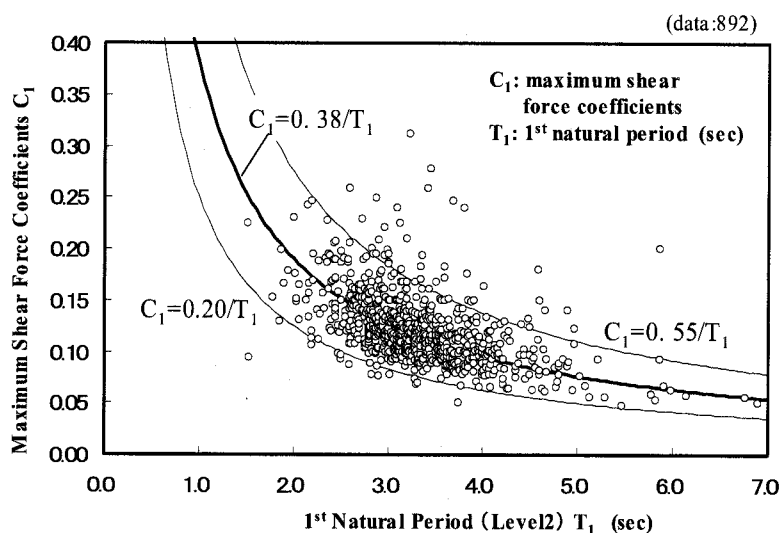


Figure14 Maximum Shear Force Coefficients C_1 and 1st Natural Periods T_1 (at the level-2 earthquake-input)

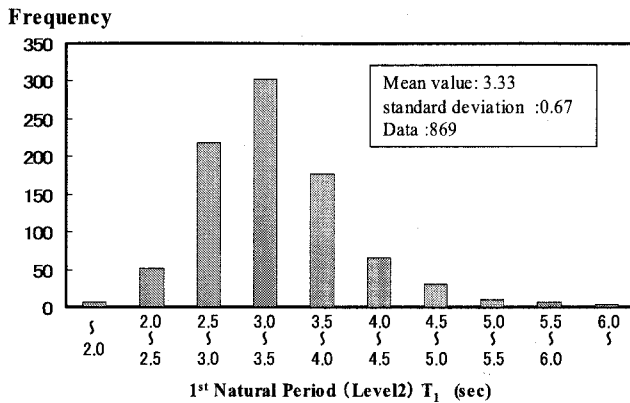


Figure15 1st Natural Period T_1 (Level-2)

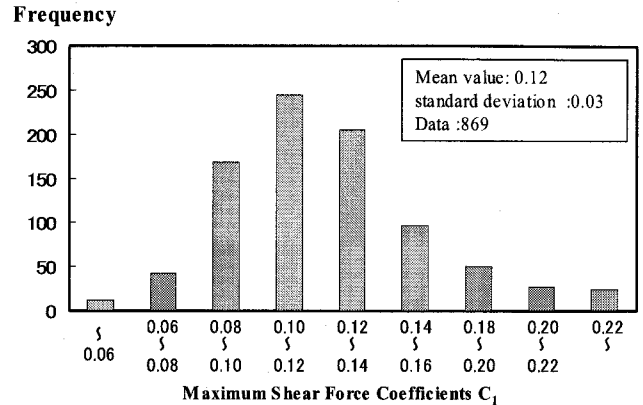


Figure16 Maximum Shear Force Coefficient C_1

5.4 Maximum Response Displacement and Allowable Displacement

In Figure 17, the allowable displacement of seismic isolation story is shown. In Figure 18, the maximum response displacement (Level-2) is shown. The average value of allowable displacements is 43.0cm and has been designed to distribute from 30cm to 60cm in many buildings. The average of the maximum response displacements is 29.6cm, and the response value has become 40cm or less in 88% of building.

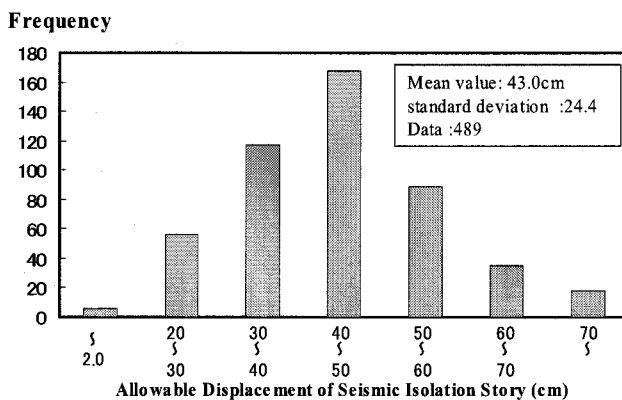


Figure17 Allowable Displacement of Seismic Isolation Story

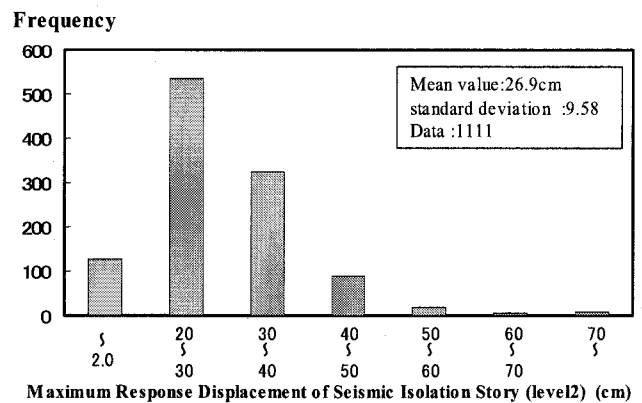


Figure18 Maximum Response Displacement of Seismic Isolation Story (Level-2)

5.5 Maximum Response of Upper Structure

In Fig19, the maximum top accelerations of the upper structures are shown. In Figure20, the maximum base shear coefficients of the upper structures are shown. In Figure21, the maximum story drift angles are shown. The average value of the maximum top acceleration is 221 cm/s^2 , and maximum response acceleration is controlled to the value under 300 cm/s^2 in 86% of building. From Figure 20, the average shear force coefficient is 0.13 and the shear force coefficients are distributed between 0.08 and 0.14. From Figure 21, the average value of the maximum story drift angle is $1/1742$, and the story drift angle is controlled to $1/200$ or less in 96% of buildings at the time of the level-2 earthquake-input.

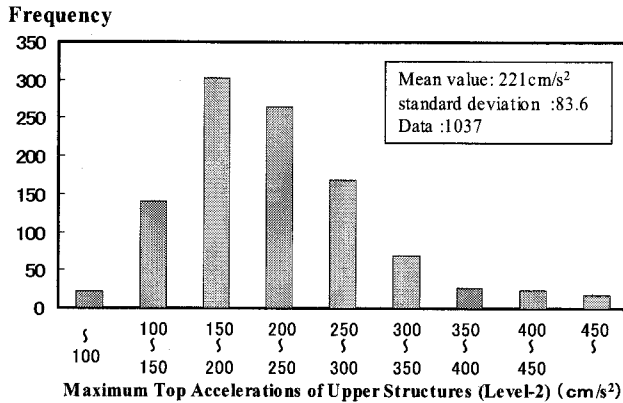


Figure19 Maximum Top Accelerations of Upper Structures (Level-2)

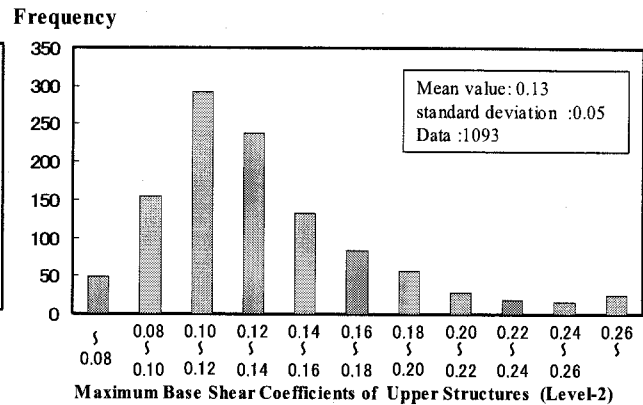


Figure20 Maximum Base Shear Coefficients of Upper Structures (Level-2)

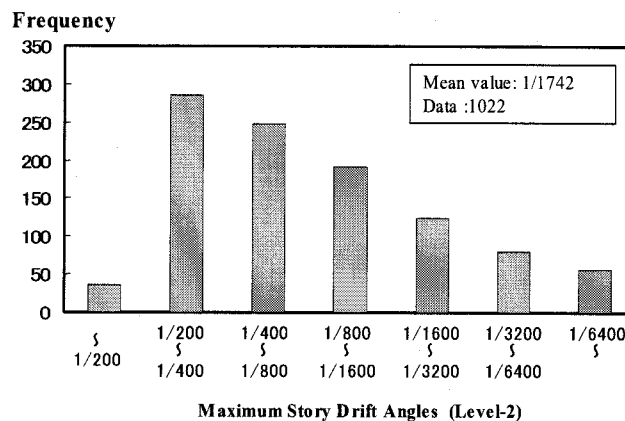


Figure21 Maximum Story Drift Angles (Level-2)

6. CONCLUSION

The database was created for the about 1200 seismic isolation buildings which have received the evaluation at the official evaluation organization in Japan, and the tendency grasp was performed about the structural characteristics at series change of the time. As a result, the following knowledge was acquired.

- (1) The number of evaluated buildings is decreasing in recent years after the peak of 1995.
- (2) By structural systems, the reinforced concrete structure (RC) is most popular and, as for main building-usages, the apartment house occupies about 40%.
- (3) The building heights are increasing and also the isolators are changing into higher usual pressure in connection with this.
- (4) As for the natural period, the tendency to be longer is seen every year, and the average value is 3.33 seconds.

References:

- 1) Building Center of Japan, "Building letter ", 1987.8-2005.8

FUNDAMENTAL STUDY ON EFFECT OF DAMPING ON DISTRIBUTION OF STORY SHEAR COEFFICIENT

Y. Ooki¹⁾, K. Kasai²⁾, T. Igusa³⁾, and T. Shimoda⁴⁾

1) *Research Assoc., Structural Engineering Research Center, Tokyo Institute of Technology, Japan*

2) *Professor, Structural Engineering Research Center, Tokyo Institute of Technology, Japan*

3) *Professor, Department of Civil Engineering, Johns Hopkins University, U.S.A.*

4) *Graduate Student, Dept. of Build Environment, Tokyo Institute of Technology, Japan*

ooki@serc.titech.ac.jp, kasai@serc.titech.ac.jp, tigusa@jhu.edu

Abstract: The effect of damping is not considered in Japanese static design force and it is required to examine the damping effect on story shear for the reasonable design of the passively controlled buildings. Non-Classically damped 5, 10, and 30-story buildings are considered and distribution of maximum story shear of those structures is evaluated by CQC modal combination method applying the ideal design seismic spectrum. From these results, a coefficient is proposed, which modify the story shear coefficient in Japanese seismic code. Furthermore, the stiffness of braces whose effect should be included in really existing passively controlled buildings are considered. The proposed formula is revised and comparison with the result of CQC modal combination shows good agreement under various damping distribution and brace stiffness condition.

1. INTRODUCTION

In seismic design, designers can decide static lateral force when base shear and distribution of seismic force pattern are given. In Japanese seismic code, story shear coefficient is indicated and used to initial design and so on. In this formula, the characteristics of the highly damped buildings are not considered, but it is often applied correspondingly to design of the passively controlled building under the present situation. For the reasonable seismic design of the building with high damping, it is needed to examine the effect of damping on the seismic force pattern.

In Japan, using the real-valued modal combination method, Ishiyama (1986) proposed the story shear coefficient which comprehends the formula of Japanese seismic code and can extend to the building with extremely non-uniform stiffness distribution. In this study, non-classically damped structures representing the passively controlled building are examined using the complex-valued modal combination method. In order to pay careful attention to the effect of damping, an ideal stiffness and mass distribution is applied.

2. BUILDING MODELS AND ANALYTICAL METHOD

2.1 Multi-Story Kelvin Model

In this study, at the beginning, 5, 10, and 30-story Kelvin models are examined (Model A, Fig. 1). For the simple procedure of the analysis, mass for i -th story (m_i , $i = 1, 2, \dots, n$) is uniformly

given along height of the building. i -th story stiffness, k_i is decided so that the building under the static lateral force given by Japanese seismic code shows uniformly distributed inter-story drift. Natural period of the first mode of 5, 10, and 30-story model are 0.56, 1.1, and 3.3 second, respectively.

Regarding the i -th story additional damping c_i , it is given by using $\eta_i = c_i \omega_1 / k_i$ (ω_1 = natural circular frequency obtained by real-valued mode). η_i corresponds to the loss factor of the viscoelastic system and it represents the fatness of the i -th story hysteresis under sinusoidal excitation. The first story loss factor η_1 , is set to 0, 0.05, 0.1, 0.2, and 0.4, and distribution of η_i along height of the building is linearly changing using the parameter $\zeta = \eta_n / \eta_1$ (Fig. 2(a)). Especially in the case of $\zeta = \eta_n / \eta_1$, the model is regarded as the classically damped system. In Fig. 2(b)–(d), actual distribution of damping c_i is shown, and the initial structural damping is applied by Rayleigh damping in which the first and second mode damping factor are set to 0.02.

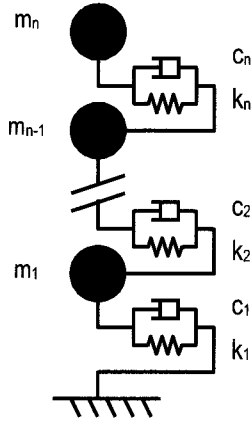


Figure 1 Multi-Story Kelvin Model

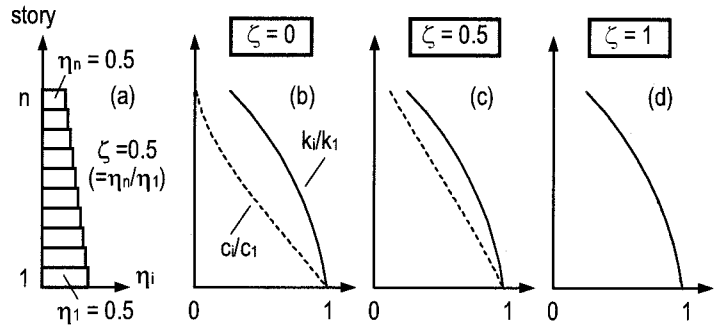


Figure 2 Distribution of Stiffness and Damping

2.2 Modal Combination Method (CQC Method)

Since the building models are the non-classically damped system, the eigenvalue problem of Eq. (1) is solved to obtain the j -th modal parameters indicated from Eq. (2) to Eq. (5). \mathbf{M} , \mathbf{C} , and \mathbf{K} in Eq. (1) are mass, damping, and stiffness matrix, respectively.

$$\mathbf{A}\boldsymbol{\Psi}_j = \mu_j \boldsymbol{\Psi}_j, \quad \mathbf{A} = \begin{bmatrix} \mathbf{0} & \mathbf{I} \\ -\mathbf{M}^{-1}\mathbf{K} & -\mathbf{M}^{-1}\mathbf{C} \end{bmatrix} \quad (1a, b)$$

$$\mu_j, \quad \boldsymbol{\Psi}_j = \begin{Bmatrix} \boldsymbol{\Phi}_j \\ \mu_j \boldsymbol{\Phi}_j \end{Bmatrix} \quad \text{eigenvalue and eigenvector} \quad (2a, b)$$

$$\omega_j = |\mu_j| \quad \text{natural circular frequency} \quad (3)$$

$$h_j = -\frac{\text{Re}(\mu_j)}{\omega_j} \quad \text{damping factor} \quad (4)$$

$$\varepsilon_j = \frac{\boldsymbol{\Phi}_j^T \mathbf{M} \mathbf{r}}{\boldsymbol{\Phi}_j^T (\mathbf{K} - \mu_j^2 \mathbf{M}) \boldsymbol{\Phi}_j} \mu_j, \quad \mathbf{r} = \begin{Bmatrix} 1 \\ \vdots \end{Bmatrix} \quad \text{participation factor} \quad (5)$$

Maximum responses of the building are evaluated by CQC modal combination method (Igusa 1984, 2005). For example, j -th modal transfer function of i -th inter-story displacement Z_j under sinusoidal excitation $\ddot{x}_g = -e^{i\omega t}$ is evaluated as follows;

$$Z_j = d_j \left[\text{Re}(\mathbf{q}_i^T \boldsymbol{\Phi}_j \boldsymbol{\varepsilon}_j \bar{\boldsymbol{\mu}}_j) H_j - \text{Re}(\mathbf{q}_i^T \boldsymbol{\Phi}_j \boldsymbol{\varepsilon}_j) i \omega H_j \right], \quad d_j = \begin{cases} 2 & (0 \leq h_j < 1) \\ 1 & (h_j = 1) \end{cases} \quad (6)$$

$$H_j = \frac{1}{\omega_j^2 - \omega^2 + 2i\omega\omega_j h_j} \quad (7)$$

If the second inter-story displacement is required, \mathbf{q}_i is given as follows;

$$\mathbf{q}_2^T = [-1 \quad 1 \quad 0 \quad \dots]$$

Using ρ_{jk} and ρ'_{jk} , which are the correlation coefficients between j -th and k -th SDOF response displacement and velocity, respectively, the maximum inter-story displacement $R_{i,\max}$ is evaluated.

$$R_{i,\max}^2 = \sum_j \sum_k d_j d_k \left\{ \rho_{jk} \text{Re}(\mathbf{q}_i^T \boldsymbol{\Phi}_j \boldsymbol{\varepsilon}_j \bar{\boldsymbol{\mu}}_j) \text{Re}(\mathbf{q}_i^T \boldsymbol{\Phi}_k \boldsymbol{\varepsilon}_k \bar{\boldsymbol{\mu}}_k) S_{d,j} S_{d,k} + \rho'_{jk} \text{Re}(\mathbf{q}_i^T \boldsymbol{\Phi}_j \boldsymbol{\varepsilon}_j) \text{Re}(\mathbf{q}_i^T \boldsymbol{\Phi}_k \boldsymbol{\varepsilon}_k) S_{v,j} S_{v,k} \right\} \quad (8)$$

$$\rho_{jk} = \frac{8\sqrt{\omega_j^3 \omega_k^3 h_j h_k} (\omega_j h_j + \omega_k h_k)}{(\omega_j^2 - \omega_k^2)^2 + 4\omega_j \omega_k (\omega_j h_k + h_j \omega_k)(\omega_j h_j + h_k \omega_k)}, \quad \rho'_{jk} = \frac{h_j \omega_k + h_k \omega_j}{h_j \omega_j + h_k \omega_k} \rho_{jk} \quad (9)(10)$$

where $S_{d,j}$ and $S_{v,j}$ are j -th displacement and velocity spectrum, respectively.

Maximum story shear force $Q_{i,\max}$ is the combination of the elastic and damping component, and the story shear coefficient C_i is obtained using Eq. (13).

$$Q_{i,\max}^2 = \sum_j \sum_k d_j d_k (\rho_{jk} D_{ij} D_{ik} S_{d,j} S_{d,k} + \rho'_{jk} V_{ij} V_{ik} S_{v,j} S_{v,k}) \quad (11)$$

$$D_{ij} = k_i \text{Re}(\mathbf{q}_i^T \boldsymbol{\Phi}_j \boldsymbol{\varepsilon}_j \bar{\boldsymbol{\mu}}_j) + c_i \text{Re}(\mathbf{q}_i^T \boldsymbol{\Phi}_j \boldsymbol{\varepsilon}_j \bar{\boldsymbol{\mu}}_j \boldsymbol{\mu}_j) \quad (12a, b)$$

$$V_{ij} = k_i \text{Re}(\mathbf{q}_i^T \boldsymbol{\Phi}_j \boldsymbol{\varepsilon}_j) + c_i \text{Re}(\mathbf{q}_i^T \boldsymbol{\Phi}_j \boldsymbol{\varepsilon}_j \boldsymbol{\mu}_j)$$

$$C_i = Q_i / \sum_{k=i}^n W_k, \quad W_i = m_i g \quad (13)$$

2.3 Design Spectrum

The design spectrum shown in Fig. 3 is applied as the seismic excitation to the models. Story shear coefficient of the building can be evaluated by CQC modal combination method without using the time-history analysis.

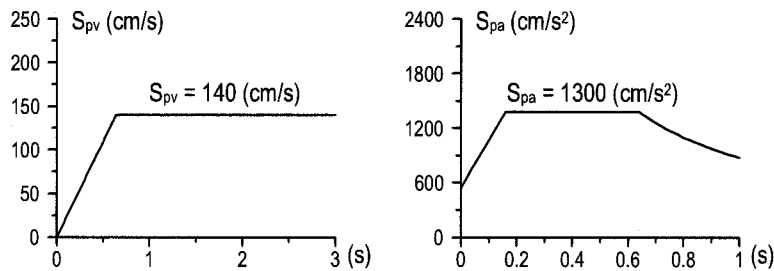


Figure 3 Design Spectrum

3. NUMERICAL RESULTS AND DISCUSSIONS

3.1 Modal Frequency and Damping Factor

Fig. 4 shows the relationship between modal damping factor h_j and circular frequency ω_j by changing the case of ζ (= distribution of damping along height). Damping factor h_j increases almost linearly with the modal circular frequency. However, those of higher modes are decreasing as the decrease of ζ , and the trend is significant when the η_1 (= loss factor of the first story) is large.

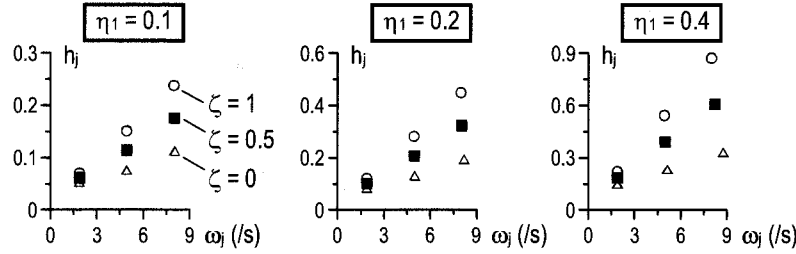


Figure 4 Relationship between Damping factor h_j and Circular Frequency ω_j (Model A)

3.2 Effect of Damping on Story Shear

Fig. 5 shows the changing of distribution of the maximum story shear with increase of η_1 . In this figure, distribution of the first mode is shown, and as η_1 increases, the contribution gradually dominates around the top. This is caused by the fact that the damping factors of higher modes become quite large as shown in Fig. 4.

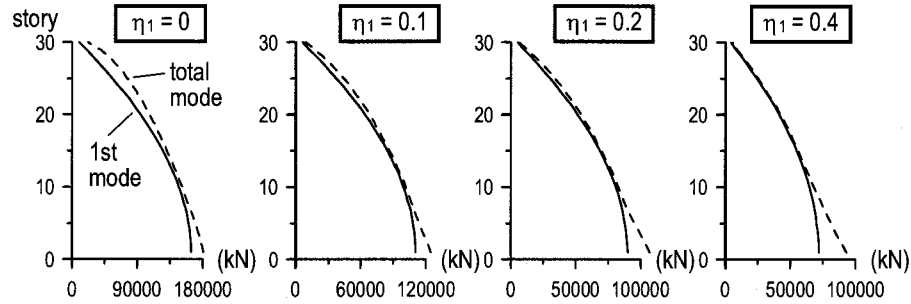


Figure 5 Distribution of Maximum Shear Force (Model A, $\zeta = 0.5$)

Fig. 6 shows the story shear coefficient obtained from Fig. 5. In this figure, the story shear coefficient given by the Japanese seismic code is also shown and it is called A_i -Distribution. A_i -Distribution represents those like a normalized absolute acceleration under the earthquake and includes the parameters T_1 = first mode's natural period and α_i = normalized weight, but does not consider the effect of damping.

$$A_i = 1 + \left(\frac{1}{\sqrt{\alpha_i}} - \alpha_i \right) \frac{2T_1}{1 + 3T_1}, \quad \alpha_i = \frac{\sum_{k=i}^n W_k}{\sum_{k=1}^n W_k} \quad (14)$$

Fig. 6 shows relationship between ξ_i ($= 1 - \alpha_i$) and distribution of story shear coefficient ($= C_i/C_1$). When $\eta_1 = 0$, that is, additional damping is zero, C_i/C_1 shows almost same shape as A_i -Distribution. Since A_i -Distribution was the average of the numerical results of buildings subject to various earthquakes, this seems an appropriate result. C_i/C_1 around the top decreases with the additional damping, and linearly distributes along building height. This trend is significant especially in high-rise building.

As indicated above, original A_i -Distribution cannot reproduce the behavior of Model A. In the next section, the damping effect will be installed to the story shear coefficient.

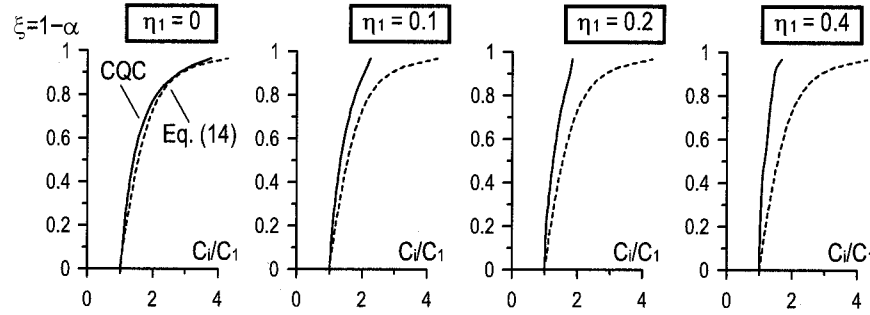


Figure 6 Distribution of Story Shear Coefficient (Model A, $T_1 = 3.3$, $\zeta = 0.5$)

3.3 Modified Story Shear Coefficient

From the above-mentioned reason, the original story shear coefficient is modified using the coefficient β .

$$A'_i = 1 + \left(\frac{1}{\sqrt{1 - \beta \xi_i}} - (1 - \beta \xi_i) \right) \frac{2T_1}{1 + 3T_1} \quad (15)$$

$$\beta = - \left\{ (0.337 \log T_1 + 0.468) \zeta^{3/4} + 0.191 \log T_1 + 0.352 \right\} \eta_1^{3/4} + 1 \quad (16)$$

where β is a reduction function, which consists of T_1 , ζ , and η_1 . Fig. (7a) shows the change of β with the first story loss factor η_1 by ranging distribution ($= \zeta$). β is obtained using the least square method as compared with Eq. (15) and numerical results. And most suitable function is selected considering the trend of parameter T_1 , ζ , and η_1 . If the additional damping is zero ($\eta_1 = 0$), A'_i corresponds with original A_i -Distribution.

Eq. (16) is verified using the four kinds of artificial earthquakes which have similar shape of response spectrum. Time-history results are compared with proposed equation shown in Fig. 8 and they match with each other very well.

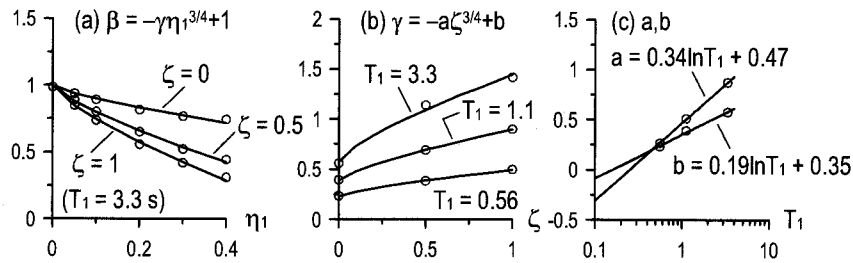


Figure 7 Coefficient β and Its Components (Model A)

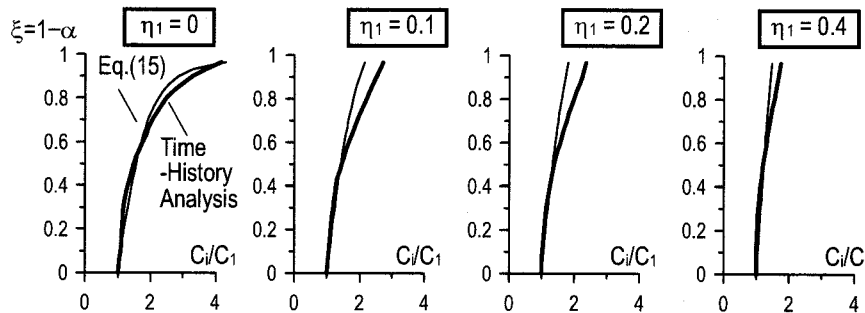


Figure 8 Comparison with Time-History Analysis (Model A, $T_1 = 3.3$, $\zeta = 0.5$)

4. EFFECT OF BRACES IN SERIES

4.1 Modal Properties of Models with Added-Component

A really existing passively controlled building has dampers supported by brace members, and approximately, the brace and damper are modeled as the spring and dashpot, respectively. From the reason mentioned above, the spring in Model A is expected to be connected to the dashpot in series to examine the actual situation of the buildings. The portion connecting in series are so called add-components. In this section, Model B and Model C with different added-component type are examined (Fig. 9) and these have equivalent story stiffness k_i and damping η_i to Model A. The effect of the brace is considered by ranging the parameter $c_{di}\omega_1/k_{bi} = 0.05, 0.1$, and 0.5 , where c_{di} = damping caused by dampers and k_{bi} = brace stiffness. The way to obtain the k_i and η_i from k_{fi} = frame stiffness, k_{di} = damper stiffness, k_{bi} , and c_{di} is given by JSSI Manual (2005)

Fig. 9 shows the relationship between damping factor h_j and circular frequency ω_j . Up to third mode, modal circular frequency of Model B is almost same as Kelvin model (Model A) as well as Model C. However, as compared with Model A, damping factors of higher modes decrease significantly when $c_{di}\omega_1/k_{bi}$ is large. It is interesting that Model B and Model C show similar trend on not only ω_j , but also h_j if they have same k_i , η_i , and $c_{di}\omega_1/k_{bi}$.

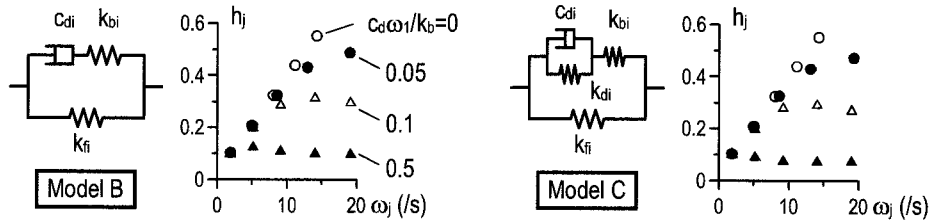


Figure 9 Models Including Added-Component (Model B and C) and Relationship between Damping factor h_j and Circular Frequency ω_j ($\eta_1 = 0.2$, $\zeta = 0.5$)

4.2 Revision of Proposed Story Shear Coefficient

Fig. 10 shows the C_i/C_1 of Model C. Since the damping factors of higher modes are small under large $c_{di}\omega_1/k_{bi}$ ($= 0.5$), the contribution of those modes on story shear are insignificant, and distribution of story shear coefficient comes close to original A_i -distribution (Eq. 14). As shown here, clearly, $c_{di}\omega_1/k_{bi}$ has considerable influence on the damping characteristic of the models. It also affects distribution of story shear coefficient of the building. Then Eq. (16) for multi-story Kelvin model (Model A) is revised here to include the effect of $c_{di}\omega_1/k_{bi}$.

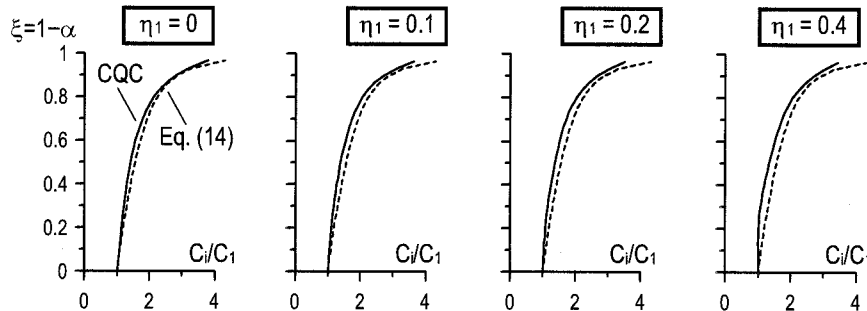


Figure 10 Distribution of Story Shear Coefficient (Model C, $T_1 = 3.3$, $\zeta = 0.5$, $c_{di}\omega_1/k_{bi} = 0.5$)

Fig. 11 shows the change of the parameters included in β with $c_{di}\omega_1/k_{bi}$ and equations of approximate curves are as follows;

$$\beta = -\left\{ (aa \log T_1 + ab) \zeta^{3/4} + ba \log T_1 + bb \right\} \eta_1^{3/4} + 1$$

$$\begin{cases} aa = -0.387(c_d \omega_1 / k_b)^{0.119} + 0.337, & ab = -0.401(c_d \omega_1 / k_b)^{0.285} + 0.468 \\ ba = -0.238(c_d \omega_1 / k_b)^{0.190} + 0.191, & bb = -0.424(c_d \omega_1 / k_b)^{0.412} + 0.352 \end{cases} \quad (17)$$

It is found that these parameters drastically decrease with $c_d \omega_1 / k_{bi}$ and then β successively comes close to 1.0. This means that the seismic force pattern is close to the case of ordinary buildings when the brace stiffness is relatively small. To reduce the seismic force around the top, adequate brace stiffness is requested in design.

In Fig. 12, story shear coefficient obtained from CQC modal combination and proposed formula are compared and they are corresponding very well.

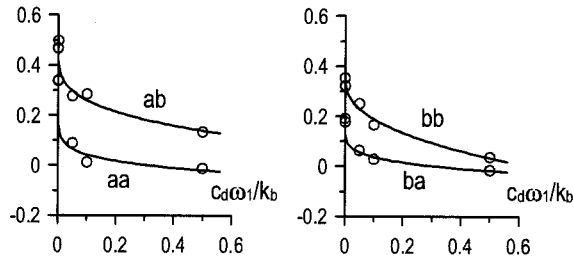


Figure 11 Relationship between β and $c_d \omega_1 / k_{bi}$ (Eq. 17, Model C)

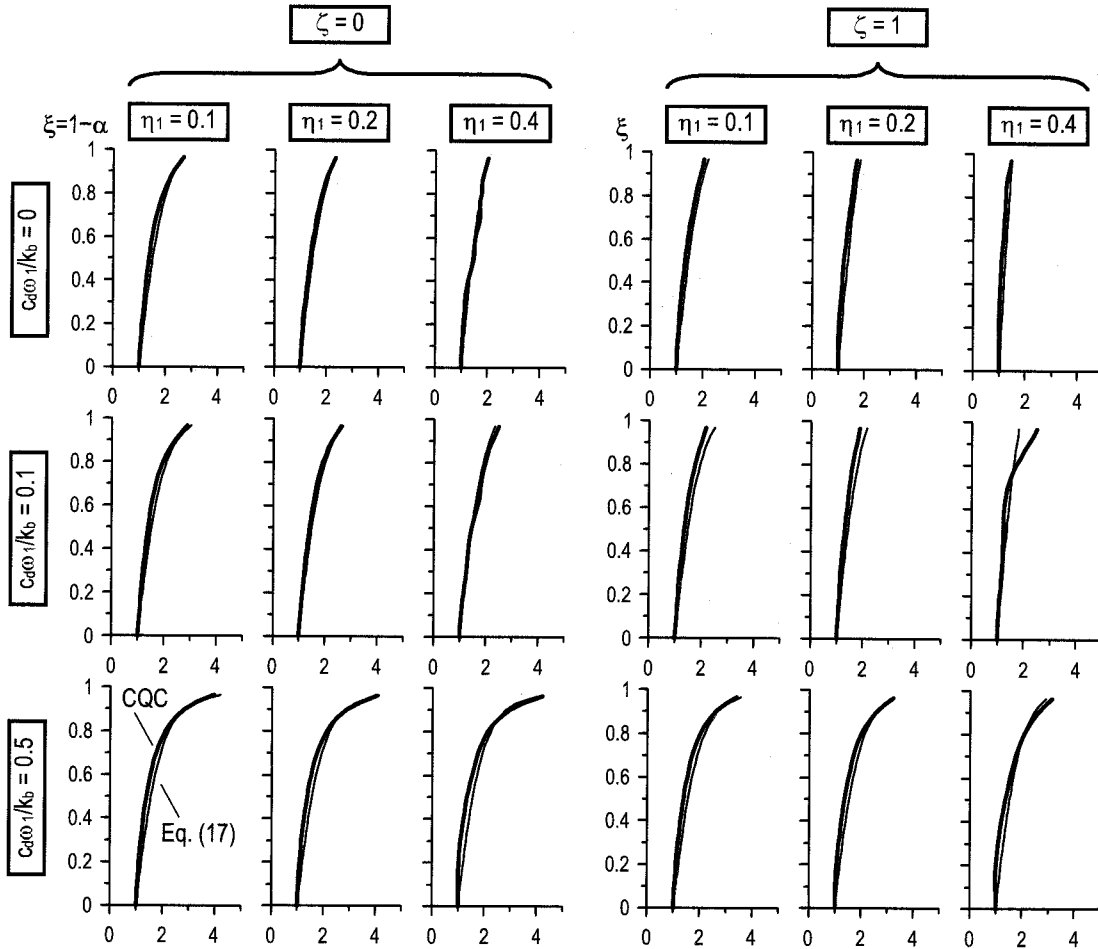


Figure 12 Comparison with CQC Modal Combination (Model C, $T_1 = 3.3$)

5. CONCLUSIONS

The effect of damping on story shear coefficient was examined using non-classically damped Kelvin models. The response was evaluated using CQC modal combination method and the design spectrum, and the first mode was found to dominate when the model had large damping. This made distribution of story shear coefficient straight and A_i -Distribution given by Japanese seismic code was modified to consider the damping effect.

Furthermore, the spring was connected in series to the dashpot of Kelvin model and the effect on modal properties was examined. The parameter $c_{di}\omega_1/k_{bi}$ had influence on story shear and the proposed story shear coefficient was revised to include the effect. Finally, story shear coefficient obtained from CQC modal combination and proposed formula is compared under various damping distribution and brace stiffness condition. The validity was confirmed and the proposed equation would contribute to seismic design of passively controlled buildings.

References:

- Ishiyama, Y. (1986), "Distribution of Lateral Seismic Forces along the Height of a Building", BRI Research Paper, (120)
- Igusa, T., Der Kiureghian, A., and Sackman, J.L. (1984), "Modal Decomposition Method for Stationary Response of Non-Classically Damped Systems" *Earthquake Engineering and Structural Dynamics*, **12**, 121-136
- Igusa, T., Kasai, K., and Yamashita, T. (2005), "Effects of Non-Classical Damping in Passively Controlled Structures", *Proc. of International Symposium on Earthquake Engineering Commemorating Tenth Anniversary of the 1995 Kobe Earthquake (ISEE Kobe 2005)*
Kobe and Awaji, January 13-16, 2005
- Japan Society of Seismic Isolation (2005), "Manual for Design and Construction of Passively-Controlled Buildings (2nd Edition)" (in Japanese)
- Architectural Institute of Japan (2004), "Recommendations for Loads on Buildings", (in Japanese)
- Yamaishita, T., Ito, S., Mukai, Y., and Inoue, Y. (2000), "Estimation for Effective Design Story-Shear Force Distributions of Building Structures Installed Interstory Hysteretic Damper", *Journal of Structural Engineering*, Architectural Institute of Japan, **46B**, 365-374 (in Japanese)

EVALUATION ON ASEISMIC PERFORMANCE OF HYBRID TYPE OF BASE-ISOLATION SYSTEM WITH POWERED-MASS COUPLERS DAMPER

Y. Mukai

Associate Professor, Faculty of Human Life and Environment, Nara Women's University, Japan
mukai@cc.nara-wu.ac.jp

Abstract: Effectiveness of a "Powered-Mass Couplers Damper (PMC)" system which is installed in the base-isolation story of seismic isolating building is investigated. In this study, performance of the PMC damper which is equipped in the base-isolation story as a damping device is evaluated by comparison with case when the viscous damper is used. To improve aseismic efficiency of the seismic isolating buildings, optimal designing method of this hybrid type which has the base-isolator and PMC damper is proposed and seismic isolating effects of this system are evaluated through numerical studies. Multi-mass system is used as a numerical model of a seismic isolating building to estimate seismic-isolated effects of the upper structures. As a result, it is assured that the PMC can effectively used to reduce resonant responses of the seismic isolating building without spoiling vibration isolating efficiency for the acceleration responses.

1. INTRODUCTION

Seismic isolating buildings are generally designed by considering a balance between prolonging effect of natural period of a structural system to decrease seismic input and a damping efficiency to control deformation of a base-isolation story. When the vibration period of input motions is enough short from the natural period of the structural system, seismic input is isolated from those excitations and acceleration responses can be effectively reduced. In the other hand, damping devices in the base-isolation story are required to reduce the resonant amplitude when the vibration period close to the natural period of the structural system is included in the input motions. Although, it is well-known problem that viscous damping takes into deterioration in vibration isolating effects for high-frequency (short vibration period) of input motions (Clough and Penzien 1975), "Tuned Mass Dampers (TMD)" can be used as a damper which has different energy absorption mechanism to overcome for those problem (Iwanami and Seto 1981). However, to install the TMD as providing enough effect to shift with viscous dampers, considerable large volume of additional mass is required.

An "Active Powered-Mass Couplers Damper (PMC)" system is introduced as an advanced damper which is providing equivalent efficiency with the TMD system even if volume of the additional mass is reduced (Mukai 2004, Mukai and Fujimoto 2005). In this paper, the PMC is applied as a response control device to improve aseismic efficiency of the base-isolation building. The PMC is assembled by a moving-mass installed in an isolated story and dual connecting members to both the upper structure and the basement. One of connecting side with the main structure is composed by damper and spring elements (this set of connecting members is called an "upper coupler" in the followings). The set of the moving-mass and the upper coupler is configured and designed as a TMD. The other connecting member of the basement side (this connecting member is called a "lower coupler" in the followings) is designed as to apparently generate "negative stiffness". When the lower coupler has the negative stiffness, it is considered that motion of the part of the TMD can be amplified. This

operation may give virtual effect as if the volume of the moving-mass is increased, accordingly, negative stiffness of the PMC can take the place of the control force by large volume of the additional mass required on the TMD. To install "negative stiffness", actuator is equipped on the lower coupler and it is theoretically assumed that the PMC is actively controlled on line. When a mechanism which can generate hysteretic property including "quasi-" negative stiffness is used, it seems that affinity performance can be also gained on the PMC with lower coupler of a semi-active or a passive lower coupler type. Appropriate designing method of the PMC is proposed by using the general tuning theory for TMD systems. In the following sections, fundamental mechanism and synthesis of the PMC are described, and control effects by installing the PMC to the seismic isolating building are numerically evaluated.

2. DESIGN OF POWERED-MASS COUPLERS DAMPER

In this section, synthesis of the PMC system is summarized. The configuration of the PMC is expressed as that a moving-mass of a mass damper system is additionally connected to the basement by the member with negative stiffness. Accordingly, the PMC can be tuned by considering optimal design for the additional mass damper system equipped to the main structural system. By applying the theory of "fixed point" (which is generally utilized to synthesize structural control system by interaction of the dual-mass such as a TMD or a jointing damper for coupled structures), the optimal design method of the PMC is conducted (Hartog 1956, Iwanami et al. 1986).

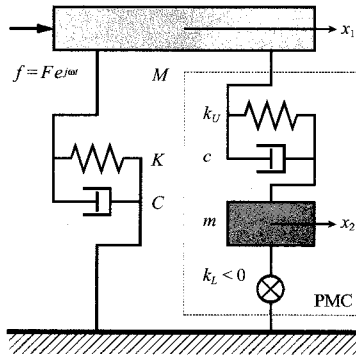


Figure 1 Mechanical Model of the PMC
Equipped to SDOF Structural System

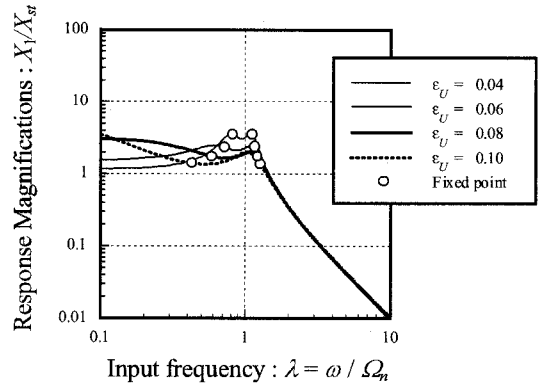


Figure 2 Response Magnifications
(Influence of the upper coupler : ϵ_U)

2.1 Equations of motion of the control system

Mechanical model of the structural system that the PMC is installed is shown in Figure 1. This structural model has two degrees of freedom. M and K mean mass and stiffness of the main structure of SDOF system (which is corresponding to the seismic isolating building), and m is mass of the sub structural system (which is corresponding to the additional mass included to the control device of the PMC). This sub system is connected to the main system by the upper coupler which have stiffness k_U and viscous damping c , and also connected to the basement by the lower coupler which has stiffness k_L . It is assumed that the stiffness of the lower coupler virtually has a negative stiffness and that the negative stiffness can be generated by a certain mechanical device such as actuators ($k_L < 0$).

When the main system of the structural model as shown in Figure 1 is subjected by an external excitation $f (= Fe^{j\omega t})$, equations of motion of this structural system can be represented as follows.

$$M\ddot{x}_1 = -Kx_1 + k_U(x_2 - x_1) - C\dot{x}_1 + c(\dot{x}_2 - \dot{x}_1) + f, \quad m\ddot{x}_2 = -k_U(x_2 - x_1) - c(\dot{x}_2 - \dot{x}_1) - k_L x_2 \quad (1)$$

In which, x_1 and x_2 mean the displacements of the main system and the sub system, respectively. The response in the steady state of x_1 and x_2 for the external excitation f are represented as follows.

$$x_1 = X_1 e^{j(\omega t + \phi_1)} = \bar{X}_1 e^{j\omega t}, \quad x_2 = X_2 e^{j(\omega t + \phi_2)} = \bar{X}_2 e^{j\omega t} \quad (2)$$

Where \bar{X}_1 and \bar{X}_2 denote the complex amplitudes of x_1 and x_2 , X_1 and X_2 denote the maximum amplitude, and ϕ_1 and ϕ_2 denote the angular difference of phase with the external excitation f . By using the Eqs. (2) for the Eqs. (1), \bar{X}_1 and \bar{X}_2 can be solved as follows.

$$\bar{X}_1 = \frac{-m\omega^2 + (k_U + k_L) + j\omega c}{\Delta(\omega)} F, \quad \bar{X}_2 = \frac{k_U + j\omega c}{\Delta(\omega)} F \quad (3)$$

Where,

$$\Delta(\omega) = \begin{vmatrix} -M\omega^2 + (K + k_U) + j\omega(C + c) & -(k_U + j\omega c) \\ -(k_U + j\omega c) & -m\omega^2 + (k_U + k_L) + j\omega c \end{vmatrix} \quad (4)$$

By considering the Eqs. (3) and (4), the maximum amplitude of the main system X_1 can be described as follows.

$$X_1 = \sqrt{\frac{\{-m\omega^2 + (k_U + k_L)\}^2 + (\omega c)^2}{|\Delta(\omega)|}} F \quad (5)$$

Where,

$$|\Delta(\omega)| = \{(-M\omega^2 + K)(-m\omega^2 + k_U + k_L) - mk_U\omega^2 + k_U k_L - \omega^2 Cc\}^2 + \{- (M + m)\omega^2 + K + k_L\}^2 (\omega c)^2 + (-m\omega^2 + k_U + k_L)^2 (\omega C)^2 \quad (6)$$

By using the Eqs. (5) and (6), a dimensionless response transfer function (X_1 / X_{st}) can be represented as Eqs. (7) and (8), in which $X_{st} (= F/K)$ means the static deformation of the main system under the external load F .

$$\frac{X_1}{X_{st}} = \sqrt{\frac{(\varepsilon_U + \varepsilon_L - \mu\lambda^2)^2 + (2\mu\zeta\lambda)^2}{A}} \quad (7)$$

Where,

$$A = \{(1 - \lambda^2)(\varepsilon_U + \varepsilon_L - \mu\lambda^2)^2 - \mu\varepsilon_U\lambda^2 + \varepsilon_U\varepsilon_L - 4\mu\zeta Z\lambda^2\}^2 + \{1 - (1 + \mu)\lambda^2 + \varepsilon_L\}^2 (2\mu\zeta\lambda)^2 + (\varepsilon_U + \varepsilon_L - \mu\lambda^2)^2 (2Z\lambda)^2 \quad (8)$$

In the Eqs. (7) and (8), the following dimensionless quantities are used.

- $\mu = m/M$: mass ratio of the sub system for the main structural system,
- $\varepsilon_U = k_U / K$: stiffness ratio of the upper coupler,
- $\varepsilon_L = k_L / K$: stiffness ratio of the lower coupler,
- $\Omega_n = \sqrt{K/M}$: angular frequency of the main structural system,
- $\lambda = \omega / \Omega_n$: input frequency ratio,
- $\zeta = c / 2m\Omega_n$: damping ratio of the sub system,
- $Z = C / 2M\Omega_n$: damping ratio of the main structural system.

2.2 Tuning of the PMC with the fixed point method

In the following, it is assumed that the main structural system is regarded as the mass-spring model and that the damping of the main system C is considered as zero. Under this condition, the response

transfer function (X_1 / X_{st}) of the Eq. (7) can be modified to the following expression.

$$(X_1 / X_{st})^2 = \frac{B_1 + B_2 \zeta^2}{D_1 + D_2 \zeta^2} = \frac{B_2 \{(B_1 / B_2) + \zeta^2\}}{D_2 \{(D_1 / D_2) + \zeta^2\}} \quad (9)$$

Where,

$$B_1 = (\varepsilon_U + \varepsilon_L - \mu \lambda^2)^2, \quad B_2 = (2\mu \lambda)^2, \\ D_1 = \{(1 - \lambda^2)(\varepsilon_U + \varepsilon_L - \mu \lambda^2)^2 - \mu \varepsilon_U \lambda^2 + \varepsilon_U \varepsilon_L\}^2, \quad D_2 = \{1 - (1 + \mu) \lambda^2 + \varepsilon_L\}^2 (2\mu \lambda)^2 \quad (10)$$

When the condition $B_1/B_2 = D_1/D_2$ is supposed in the Eq. (9), the response transfer function of the main system (X_1 / X_{st}) can be represented as not including the relation with the damping ratio ζ . Accordingly, by considering the condition $B_1/B_2 = D_1/D_2$ in the Eq. (9), a quadratic equation for λ^2 can be gained. Let denote two solution for this quadratic equation λ_P and λ_Q ($\lambda_P < \lambda_Q$), those are corresponding to two fixed points P and Q which is invariable to difference of the damping ratio ζ . At this, $(X_1 / X_{st})^2$ can be simply represented as B_2/D_2 under the condition $B_1/B_2 = D_1/D_2$. By applying the fixed point method, the "Optimal tuning" can be provided as the condition that the values of response magnification factors at the fixed points P and Q become equal height. Namely, the optimum tuning of the PMC can be derived as the relation between the stiffness of the upper coupler and the lower coupler [Condition of the optimal tuning of the PMC].

$$\varepsilon_L = \mu - (1 + \mu)^2 \varepsilon_U \quad (11)$$

At this point, the value of the frequency ratio $\lambda_P (= \lambda_P^2)$ and $\lambda_Q (= \lambda_Q^2)$ and the values of response magnification factor at the fixed points P and Q can be expressed as follows.

$$\lambda_P, \lambda_Q = 1 - (1 + \mu) \varepsilon_U \mp (1 + \mu) \varepsilon_U \sqrt{1 / \mu(2 + \mu)} \quad (12)$$

$$(X_1 / X_{st})^2 \Big|_{\lambda_P, \lambda_Q} = \{1 / (\mu - \varepsilon_U)\} \sqrt{\mu(2 + \mu)} \quad (13)$$

As the next step to apply the fixed point method, "Optimal damping" condition is considered so that peaks of the response transfer curves appear at the neighbor of the fixed points. When the peaks of the response transfer curves appear at the two fixed point P and Q, the following condition is required.

$$\partial^2 (X_1 / X_{st}) / \partial (\lambda^2) \Big|_{\lambda_P, \lambda_Q} = 0 \quad (14)$$

By considering this condition for the Eq. (7) and by solving for the damping ratio ζ , two solutions ζ_P and ζ_Q can be gained. At this point, since the peaks of the response transfer curves can not appear in the both of the two fixed points P and Q at the same time, the average of ζ_P and ζ_Q is regarded as the most suitable condition for the optimal damping of the sub system. Namely, the following condition can be derived [Condition of the optimal damping of the PMC].

$$\zeta = \sqrt{\frac{\{(3 + 2\mu) - (1 + \mu)(5 + 2\mu)\varepsilon_U\} \varepsilon_U^2}{4[\mu(2 + \mu) - 2\mu(1 + \mu)(2 + \mu)\varepsilon_U - (1 + \mu)^2 \{1 - \mu(2 + \mu)\} \varepsilon_U^2]}} \quad (15)$$

2.3 Synthesis of the upper coupler of the PMC

"Optimal tuning" of the PMC (the Eq. (11)) is the condition to design the value of the lower coupler's negative stiffness ε_L by using the parameters m and ε_U . "Optimal damping" of the PMC (the Eq. (15)) is the condition to design the value of the upper coupler's damping ζ by using the

parameters m and ε_U . As the final step to design the PMC, those parameters μ (mass ratio) and ε_U (stiffness ratio of the upper coupler) should be determined. At this point, when the mass ratio may be voluntarily selected by engineering designers, the "Optimal stiffness" condition of the upper coupler should be required to design the whole of the PMC system. Accordingly, the synthesis for the stiffness ratio of the upper coupler ε_U is considered in the followings.

At this point, when the case of $\lambda = 0$ is considered in the Eq. (7), the response transfer function of the main system (X_1 / X_{st}) is converging to value invariable to difference of the damping ratio ζ (this point is called an "invariable point R" in the followings). Figure 2 show the response transfer curves which considers difference of the parameters ε_U (those cases corresponding to $\mu = 0.01$). As seen in Figure 2, when the value of ε_U is enlarged, it is found that the response magnification factor of the invariable point R (which appears at $\lambda = 0$) increases and the fixed points P and Q are slipped out from the peak positions of the response transfer curves. By considering those tendencies, it is proposed that the invariable value at the point R should be equal to or lower than the value of the fixed points P and Q. When the invariable point R is not lower than the fixed points P and Q, the maximum response appears at the frequency distant from the λ_P and λ_Q , and the PMC may be out of tuning from the optimal damping conditions. Accordingly, the condition of the "Optimal stiffness" is supposed as that the invariable value at the point R has equal height for the fixed points P and Q. The following relation is proposed to satisfy this condition.

$$\{1/(\mu - \varepsilon_U)\} \sqrt{\mu(2 + \mu)} = (\varepsilon_U + \varepsilon_L) / (\varepsilon_U + \varepsilon_L + \varepsilon_U \varepsilon_L) \quad (16)$$

In the Eq. (16), the left side is the invariable value at the invariable point R which is given by $\lambda = 0$ in the Eq. (7) and the right side is the fixed points P and Q which is given by $B_1/B_2 = D_1/D_2$ in the Eq. (9). By solving the Eq. (16) for ε_U and by using the Eq. (11), the following condition can be gained [Condition of the optimal stiffness of the PMC].

$$\varepsilon_U = \frac{2\mu\sqrt{2 + \mu}}{(1 + \mu)\sqrt{\mu}\{(1 + \mu) + \sqrt{\mu(2 + \mu)} + \sqrt{9 + 2\mu(4 + \mu)} - 2(3 + \mu)\sqrt{\mu(2 + \mu)}\}} \quad (17)$$

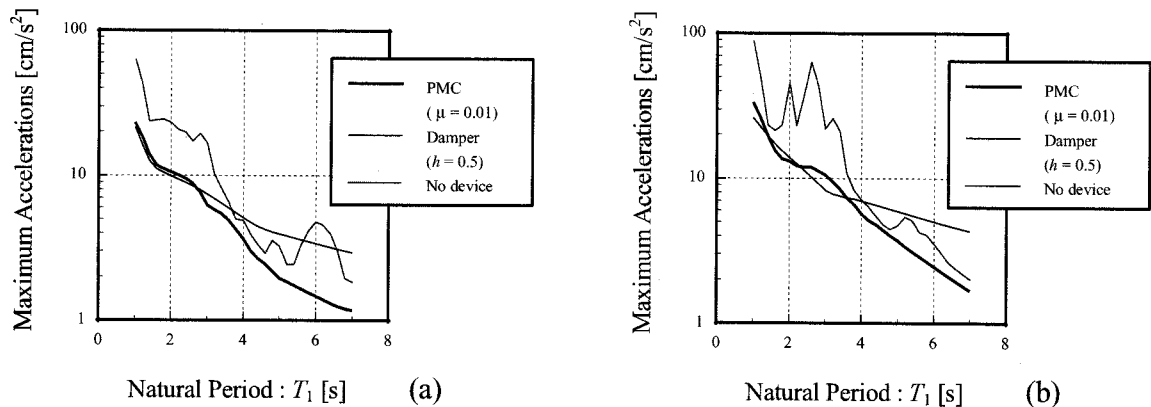


Figure 3 Maximum Acceleration Response : (a) El Centro NS, and (b) Hachinohe NS

3. NUMERICAL EVALUATION OF PMC FOR SEISMIC EXCITATIONS

Control effects on the hybrid system of the seismic isolation building and the PMC are investigated through numerical simulations. In the numerical model which is shown in Figure 1, the first natural period of the main structural system T_1 is given as the parameter ($T_1 = 1.0 - 7.0$ [s]). For

each models of the main structural system with different natural period T_1 , three cases which are no device, the PMC ($\mu = 0.01$) installed and the viscous damper ($h = 0.5$) installed on the isolated story are compared. El Centro NS and Hachinohe NS are used as input of exciting motions to evaluate seismic responses (the maximum acceleration of those input motions are reduced to 30 [cm/s²]).

Figure 4 (a) and (b) show the spectrum properties of the maximum acceleration responses on the main structural system excited by the inputs of El Centro NS and Hachinohe NS, respectively. By considering those figures, deterioration of vibration isolating effect for accelerations can be recognized on the case of the viscous damper installed by exceeding the boundary nearly $T_1 = 3 - 4$ [s]. On the other hand, when the PMC is installed to the isolated story, it is assured that acceleration responses can be effectively reduced without deterioration of vibration isolating effects.

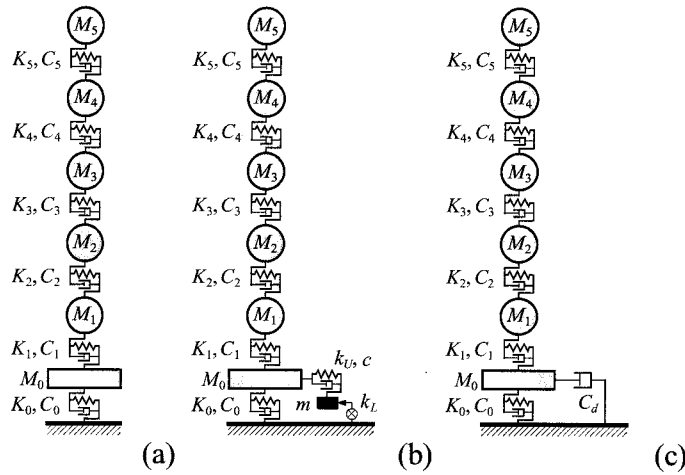


Figure 4 Hybrid Type of Base-Isolation Models : (a) No Device, (b) PMC-Installed, and (c) Viscous Damper-installed

4. SEISMIC ISOLATING EFFECTS ON MULTI-MASS STRUCTURAL SYSTEM

To evaluate seismic isolating effect of hybrid mechanism of the base-isolation system (which is modeled to multi-mass structural system) and the PMC system, 6-stories of structural model which has isolated-story on the bottom (as seen in Figure 4 (a)) is considered as a "base-isolation model". In this model, the bottom story with single-mass is an "isolated-story" and the upper structure with 5-mass is an "upper building". The mechanical properties of the PMC in the hybrid type of base-isolation system are designed as the following procedures.

Step-1) At first, system matrix of the "base-isolation model" which has 6-stories is represented in a modal coordinate, by using generalized mass M_0^* and generalized stiffness K_0^* corresponding to the first mode, equivalent single-mass substitution model is generated (in which damping of the structural system is neglected).

Step-2) The PMC system is set up on this equivalent single-mass system, and equivalent 2-mass system is generated as like to Figure 1 (it is regarded as $M = M_0^*$, $K = K_0^*$ in this figure). The mechanical property of the sub-system (the part of the PMC) is tuned by using design equations, the Eqs. (11), (15) and (17) (it is supposed that the volume of the mass of the PMC is designed in advance).

Step-3) In the 2-mass model which is designed at Step-2), the part of main mass (equivalent single-mass model for the base-isolation building) is replaced to the original 6-stories model, that is, 7-stories structural model is composed as seen in Figure 4 (b). At this point, the mechanical property of PMC (k_U , c_U and k_L) is remained to the same values which are determined at Step-2).

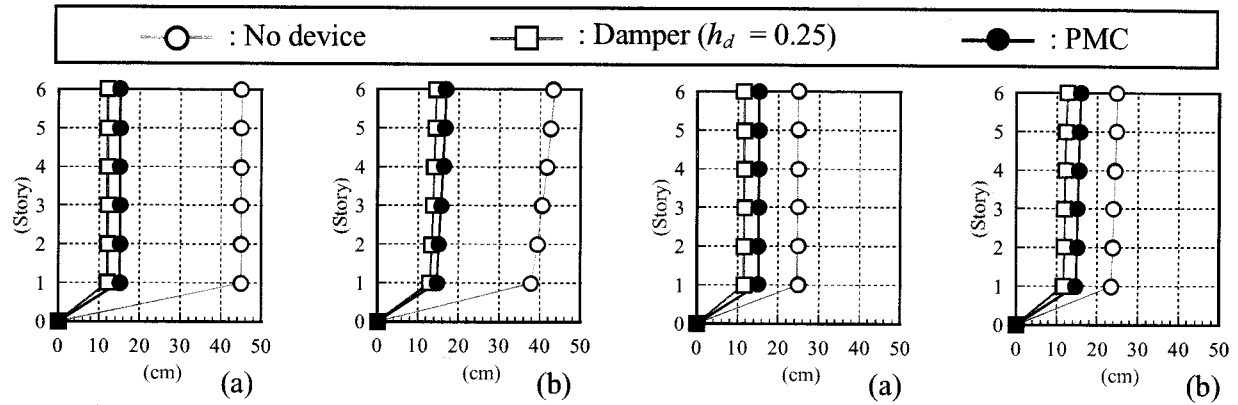


Figure 5 Horizontal Displacements ($T_f = 3$ [s]):
(a) $T_1 = 0.1$ [s], and (b) $T_1 = 1.0$ [s]

Figure 6 Horizontal Displacements ($T_f = 5$ [s]):
(a) $T_1 = 0.1$ [s], and (b) $T_1 = 1.0$ [s]

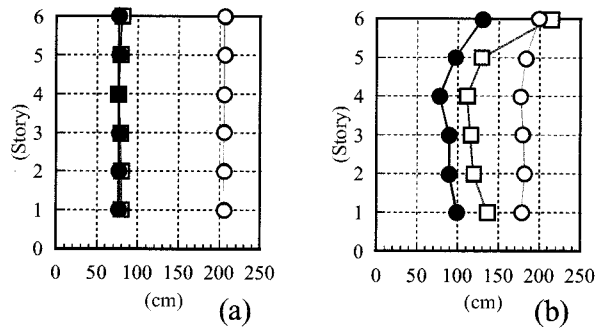


Figure 7 Accelerations ($T_f = 3$ [s]):
(a) $T_1 = 0.1$ [s], and (b) $T_1 = 1.0$ [s]

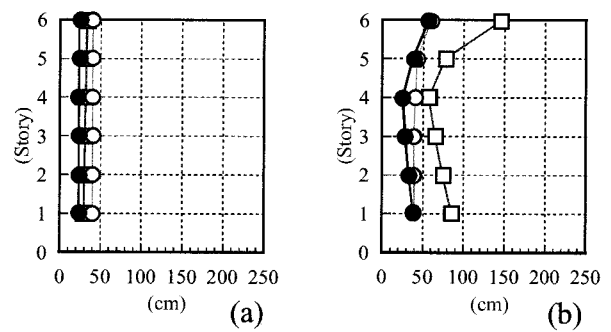


Figure 8 Accelerations ($T_f = 5$ [s]):
(a) $T_1 = 0.1$ [s], and (b) $T_1 = 1.0$ [s]

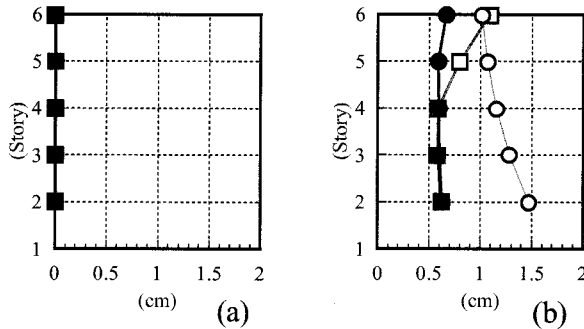


Figure 9 Inter-story Deformations ($T_f = 3$ [s]):
(a) $T_1 = 0.1$ [s], and (b) $T_1 = 1.0$ [s]

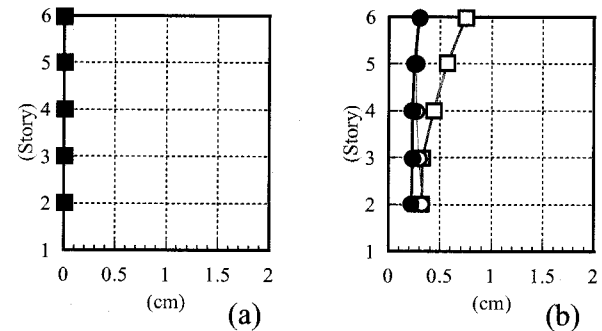


Figure 10 Inter-story Deformations ($T_f = 5$ [s]):
(a) $T_1 = 0.1$ [s], and (b) $T_1 = 1.0$ [s]

Every mass of the base-isolation model (from M_0 to M_5) have unit value and is uniformly distributed. Stiffness of the upper structure (from k_1 to k_5) has the distribution which is designed as that the first model shape is proportional to the reversed triangular form. Two kinds of models of the 5-mass upper structure (excepting base-isolation story) are evaluated, and the first natural periods of those 5-stories models T_1 (which is called "upper building's period" in the followings) are 0.1 and 1.0 [s]. Damping of those 5-stories upper structure is supposed as proportional type with stiffness and damping ratio for the first vibration mode is considered as $h_1 = 0.01$. Stiffness of the base-isolation story is determined as follows. At first, the whole mass of the 6-stories of base-isolation structure is regarded as a single-mass and it is supposed that this single-mass is supported by single-spring which is corresponding to the base-isolator. Two kinds of base-isolators are evaluated, so that the natural periods of those single-mass systems T_f (which is called "base-isolator's period" in the following) are designed as 3.0 and 5.0 [s]. Damping of the base-isolation story is determined as that those

single-mass models have $h_f = 0.01$ of damping ratio.

In the following case studies, 3 kinds of response control systems with different damping mechanism on the base-isolation story are investigated. Those are "No device" (Model-1; as seen Figure 4 (a)), "PMC-installed" (Model-2; as seen Figure 4 (b)) and viscous "Damper-installed" (Model-3; as seen Figure 4 (c)), respectively. In Model-2, the additional mass of the PMC is designed by $\mu = 0.01$ ($m / \Sigma M$). In Model-3, the additional damping which is installed in the base-isolation story is given by $h_d = 0.25$ of damping ratio (which is determined "base-isolator's period" and stiffness of the isolated-story). EL Centro NS (which has $341 \text{ [cm/s}^2\text{]}$ of the maximum acceleration) is used as an examining input motion.

Figure 5, 7 and 9 are seismic responses (those are the maximum values of horizontal displacement, acceleration, and inter-story deformation, respectively) for the case for the "base-isolator's period" $T_f = 3 \text{ [s]}$, and Figure 6, 8 and 10 are seismic responses for the case for $T_f = 5 \text{ [s]}$. In those figure, (a) and (b) are corresponding to the cases for $T_1 = 0.1$ and 1.0 [s] , respectively. As seen in Figure 5 and 6, it is assured that both the PMC and viscous damper can give similar control effects for reducing the horizontal displacements of the base-isolators. Even if the base-isolator's periods are different, close tendency can be recognized for each case which has the different upper structural model ($T_1 = 0.1$ and 1.0 [s]). On the other hand, when responses of acceleration and inter-story deformation are focused, significant differences are observed by comparing Figure 7 and 9 with 8 and 10. In the case for $T_1 = 0.1$ of the upper structure, those responses can be controlled to almost same level in each model which is Model-1, 2 or 3. However, in the case of $T_1 = 1.0$, those responses of the Model-3 is increasing by comparing with Model-1 or 2 in the case of the "base-isolator's period" $T_f = 5 \text{ [s]}$. It is recognized that the PMC can not cause such deterioration of seismic isolation effects as that appear in viscous Damper-installed model at both cases of base-isolator's period $T_f = 3$ and 5 [s] .

5. CONCLUSIONS

In this paper, the "Powered-Mass Couplers (PMC)" damper system is proposed and the optimal designing method of the PMC is derived by applying the theory of the fixed points. To consider advantageous of applying the PMC as the "damping" device for the vibration isolating system, the control effects of the PMC is compared with viscous damping effects through numerical simulations. As a result, it is assured that the PMC can effectively perform to improve the vibration isolating effects of the seismic isolation system.

Acknowledgements:

This research was partially supported by Ministry of Education, Culture, Sport, Science, and Technology of Japan under Grant-in-Aid for Young Scientists B (No.17760455) for 2005. The author would like to appreciate for financial support. And also, the author acknowledge to Mr. Masaki Fjimoto for having cooperated in this study.

References:

- Clough, R.W. and Penzien, J. (1975) "Dynamics of Structures, International Student ed," McGraw-Hill Kogakusha, 64-69.
- Iwanami, K. and Seto, K. (1981) "An Investigation of the Vibration Isolation Equipped with Dual Dynamic Dampers as a Damping Element," *Bulletin of the JSME*, **24**(197), 2013-2019.
- Mukai, Y. (2004) "Development of Active Powered-Mass Couplers by Utilizing Negative Stiffness," *Proceedings of International Symposium on Network and Center-Based Research for Smart Structures Technologies and Earthquake Engineering (SE'04)*, 127-132.
- Mukai, Y. and Fujimoto, M. (2005) "Application of Active Powered-Mass Couplers to Improve Aseismic Efficiency on Vibration Isolating Systems," *Theoretical and Applied Mechanics Japan*, **54**, 115-122.
- Hartog, J.P.D. (1956) "Mechanical Vibration, 4th ed.," McGraw-Hill, 93-106.
- Iwanami, K., Suzuki, K., and Seto, K. (1986) "Studies of the Vibration Control Method of Parallel Structures (The Method by the Theory of P, T, Q)," *J. of the JSME C-52*(484), 3063-3072 (in Japanese).

PERFORMANCE-BASED SEISMIC PROVISIONS FOR SEISMICALLY ISOLATED BUILDINGS IN JAPAN

M. Midorikawa¹⁾, M. Iiba²⁾, N. Koshika³⁾, and N. Kani⁴⁾

1) Professor, Division of Architectural and Structural Division, Hokkaido University, Japan

2) Research Coordinator, National Institute for Land and Infrastructure Management, Japan

3) Senior Manager, Kobori Research Complex, Kajima Corporation, Japan

4) Executive Director, Japan Society of Seismic Isolation, Japan

midorim@eng.hokudai.ac.jp, iiba-m92hx@nilim.go.jp, koshika@krc.kajima.co.jp, kani@jssi.or.jp

Abstract: The Building Code of Japan has been changed from the former prescriptive type into a performance-based type in June, 2000. This paper presents the basic concept and the evaluation procedures of seismic provisions for seismically isolated buildings against major earthquake motions newly introduced to the Building Code of Japan in October, 2000. The basic concept of seismic design spectrum for major earthquake motions is: 1) the basic design spectra defined at the engineering bedrock, and 2) the evaluation of site conditions from geotechnical data of surface soil layers. The evaluation procedures apply the equivalent single-degree-of-freedom (ESDOF) system, equivalent linearization and response spectrum analysis. The principle of evaluation procedures is that the predicted response values should not exceed estimated limit values. The evaluation criteria of each portion of a building are: 1) the isolation system shall be designed so that the maximum response displacement does not exceed the design limit displacement, and 2) the structure above the isolation system and the foundation and structural elements below the isolation system shall be designed so that the working stress does not exceed the allowable stress. The scope of application of the provisions is: 1) buildings not exceeding 60 meters in height, and 2) base isolation buildings on the soil layers excluding very soft soil layers.

1. INTRODUCTION

The Building Code of Japan (the Building Standard Law of Japan) has been revised from the former prescriptive type into a performance-based type in June, 2000. The details of the basic concept of performance-based seismic and structural code proposed by the Building Research Institute (BRI) are discussed elsewhere (Hiraishi et al. 2000, Midorikawa et al. 2000, Kuramoto et al. 2000).

The revised code have also introduced the new provisions for seismically isolated buildings (MLIT 2000a) in October, 2000. This provision provides the seismic evaluation procedures of seismically isolated buildings applying the ESDOF system, equivalent linearization and response spectrum analysis. The structural evaluation procedures in the provisions are applied for the design of a seismically isolated building provided that the height of the structure is equal to or less than 60 meters, that the structure is located on the site of soil layers excluding very soft soils, and that the isolators and dampers of the isolation system meet the criteria prescribed (MLIT 2000b). Before the issue of this provision, all seismically isolated buildings were required to receive a technical review by the appraisal committee in the Building Center of Japan and the special permission from the Ministry of Land, Infrastructure and Transport.

This paper presents the simplified evaluation procedures in the provisions for seismically isolated buildings (MLIT 2001, BRI et al. 2001). The procedures using the response spectrum analysis obtain

directly the response shear and displacement from an ESDOF system with equivalent linear spring and damping derived from the characteristics of the isolation system. A seismically isolated building is reduced to an ESDOF system assuming that the superstructure is rigid. The response of an ESDOF system is predicted using the response spectrum on the basis of the seismic ground motion considering the amplification of the site soil conditions.

2. EVALUATION PROCEDURES OF SEISMIC GROUND MOTION

2.1 Seismic Ground Motion and Surface-soil-layer Amplification Factor

The seismic ground motion used for the evaluation is the site specific motion of an extremely rare earthquake which is expected to occur once in approximately 500 years. A soil layer whose shear wave velocity is equal to or more than about 400 m/s is assumed to be the engineering bedrock. The basic acceleration response spectrum S_0 of the seismic ground motion at the engineering bedrock is shown in Figure. 1 and given in the following expression:

$$\begin{aligned} S_0 &= 3.2+30T & \text{for } T \leq 0.16 \\ S_0 &= 8.0 & \text{for } 0.16 < T \leq 0.64 \\ S_0 &= 5.12/T & \text{for } 0.64 < T \end{aligned} \quad (1)$$

where, T : natural period (s), and, S_0 : basic acceleration response spectrum (m/s^2).

The response spectrum at the engineering bedrock is applied in the design of all buildings such as conventionally designed buildings (MLIT 2000c) and seismically isolated buildings (MLIT 2000a). Multiplying the response spectrum at the engineering bedrock by the surface-soil-layer amplification factor G_s as shown in Figure 2, the response spectrum at the ground surface S_a is obtained as shown in Figure 3 and expressed in Equation (2).

$$S_a = G_s Z S_0 \quad (2)$$

where, S_a : acceleration response spectrum at ground surface (m/s^2), G_s : surface-soil-layer amplification factor, and, Z : seismic zone factor of 0.7 to 1.0

The amplification factor G_s are evaluated by the accurate or simplified procedures (MLIT 2000c). G_s to be determined here is the ratio of response spectra. Practically, the accurate procedures considering the strain-dependent properties of soils are available for a seismically isolated building whose fundamental natural period is 2 to 4 seconds as shown in Figures 2 and 3. G_s is calculated based on the strain-dependent shear stiffness (or shear wave velocity) and damping ratio of surface soil layers as follows:

$$\begin{aligned} G_s &= G_{s2} \frac{T}{0.8T_2} & \text{for } T \leq 0.8T_2 \\ G_s &= \frac{G_{s1} - G_{s2}}{0.8(T_1 - T_2)} T + G_{s2} - 0.8 \frac{G_{s1} - G_{s2}}{0.8(T_1 - T_2)} T_2 & \text{for } 0.8T_2 < T \leq 0.8T_1 \\ G_s &= G_{s1} & \text{for } 0.8T_1 < T \leq 1.2T_1 \end{aligned} \quad (3)$$

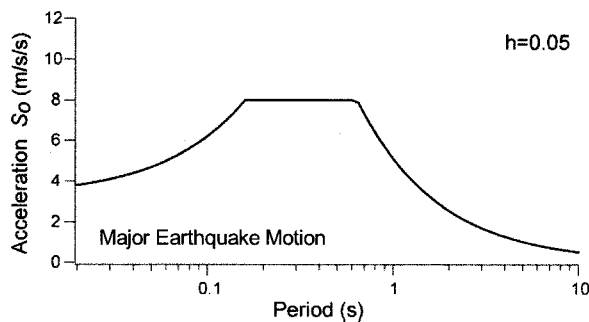


Figure 1 Basic Acceleration Response Spectrum at Engineering Bedrock S_0

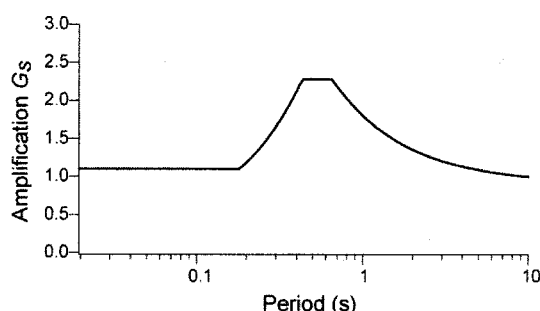


Figure 2 Amplification Factor of Surface Soil Layers G_s

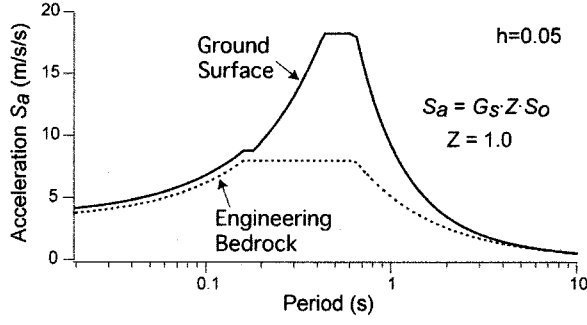


Figure 3 Acceleration Response Spectrum at Ground Surface

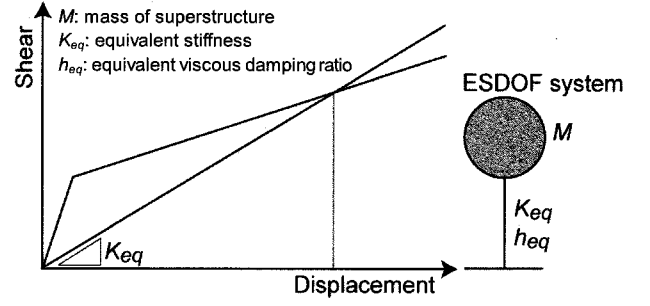


Figure 4 Model of Seismically Isolated Structure

$$G_s = \frac{G_{s1} - 1}{\frac{1}{1.2T_1} - 0.1} \frac{1}{T} + G_{s1} - \frac{G_{s1} - 1}{\frac{1}{1.2T_1} - 0.1} \frac{1}{1.2T_1} \quad \text{for } 1.2T_1 < T$$

where, G_s : surface-soil-layer amplification factor, G_{s1} : G_s value at the period of T_1 , G_{s2} : G_s value at the period of T_2 , T : natural period (s), T_1 : predominant period of surface soil layers for the first mode (s), and, T_2 : predominant period of surface soil layers for the second mode (s). Minimum value of G_s : 1.2 for $T \leq 1.2T_1$ and 1.0 for $1.2T_1 < T$.

2.2 Evaluation of Surface-soil-layer Amplification Factor

a) Modeling of surface soil layers

The surface soil layers are reduced to an equivalent single soil layer. Consequently, the soil layers including the engineering bedrock are reduced to the equivalent two-soil-layer model.

The characteristic values of the equivalent surface soil layer are expressed as follows:

$$V_{se} = \frac{\sum V_{si} d_i}{H}, \quad \rho_e = \frac{\sum \rho_i d_i}{H}, \quad h_e = \frac{\sum h_i W_{si}}{\sum W_{si}}, \quad H = \sum d_i \quad (4)$$

where, V_{se} : equivalent shear wave velocity of surface soil layers (m/s), ρ_e : equivalent mass density of surface soil layers (kg/m^3), h_e : equivalent damping ratio of surface soil layers, H : total thickness of surface soil layers (m), V_{si} : shear wave velocity of soil layer i (m/s), d_i : thickness of soil layer i (m), ρ_i : mass density of soil layer i (kg/m^3), d_i : thickness of soil layer i (m), h_i : viscous damping ratio of soil layer i , and, W_{si} : potential energy of soil layer i .

h_e in Equation (4) represents the averaged value of the equivalent viscous damping ratio of equivalent surface soil layer. Finally, the viscous damping ratio h_{se} of the equivalent surface soil layer is estimated by Equation (5) at the final step of iteration in the calculation, considering the scattering of damping ratios.

$$h_{se} = 0.8 \frac{\sum h_i W_{si}}{\sum W_{si}} \quad (5)$$

b) Predominant periods and amplification factors

The first and second predominant periods, T_1 and T_2 , and amplification factors, G_{s1} and G_{s2} , of the equivalent surface soil layer are obtained by the following equations:

$$T_1 = \frac{4H}{V_{se}}, \quad T_2 = \frac{T_1}{3}, \quad G_{s1} = \frac{1}{1.57h_{se} + \alpha}, \quad G_{s2} = \frac{1}{4.71h_{se} + \alpha}, \quad \alpha = \frac{\rho_e V_{se}}{\rho_b V_{sb}} \quad (6)$$

where, α : wave impedance ratio, ρ_b : mass density of engineering bedrock (kg/m^3), and, V_{sb} : shear velocity of engineering bedrock (m/s).

3. EVALUATION PROCEDURES OF SEISMIC RESPONSE

3.1 Basic Concept

Assuming the superstructure to be rigid compared to the isolation system, a seismically isolated building is considered to be an ESDOF system with spring and damper at the seismic isolation level. The relationship of shear and displacement of the seismic isolation system is modeled by the bi-linear property as shown in Figure 4, and it is expressed as the capacity spectrum in Figure 5. The equivalent stiffness and damping ratio of the isolation system is obtained on the basis of the design limit displacement δ_s . Accordingly, the demand spectrum is available for an isolated building in the form of acceleration-displacement response spectrum. The response shear Q and response displacement δ are obtained at the intersection of the demand and capacity spectra as shown in Figure 5.

3.2 Response of Isolation System

The load-deformation relationships of typical isolation system components such as isolators and dampers are shown in Figure 6. The design limit displacement of each component is obtained by multiplying the ultimate displacement δ_u of each component by the following safety factor β :

- $\beta = 0.8$ for elastomeric isolators,
- $\beta = 0.9$ for sliding and roller bearings, and,
- $\beta = 1.0$ for dampers and restorers.

The design limit displacement δ_s of the seismic isolation system is determined by the minimum value of $\beta \delta_u$ for every component in the isolation system.

The design natural period T_s of an isolated building is calculated by the equivalent stiffness K_{eq} of the isolation system corresponding to the design limit displacement δ_s .

$$T_s = 2\pi \sqrt{\frac{M}{K_{eq}}} \quad (7)$$

where, T_s : design natural period of an isolated building (s), M : mass of superstructure (kg), and, K_{eq} : equivalent stiffness of seismic isolation system at δ_s as shown in Figure 7 (kN/m).

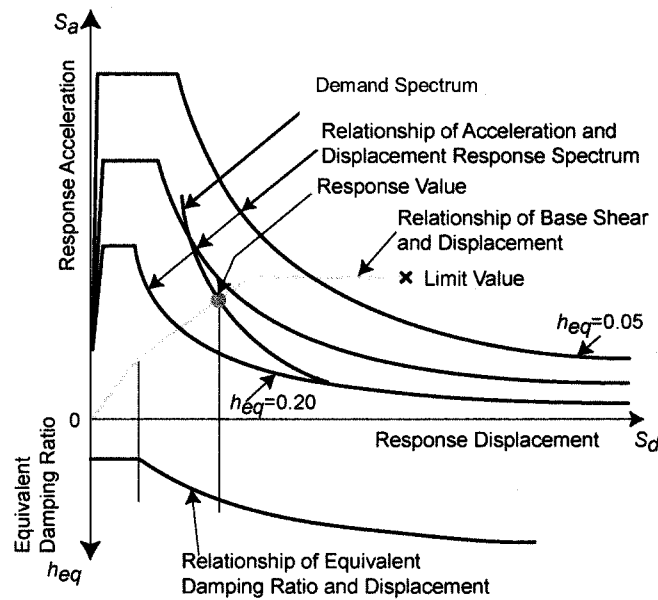


Figure 5 Response Shear and Displacement in Demand and Capacity Spectra

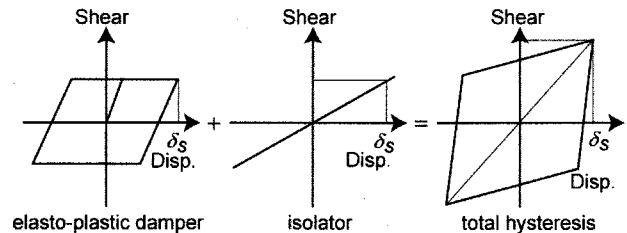


Figure 6 Load-deformation Curves of Elements and Total Hysteretic Curve of Seismic Isolation System

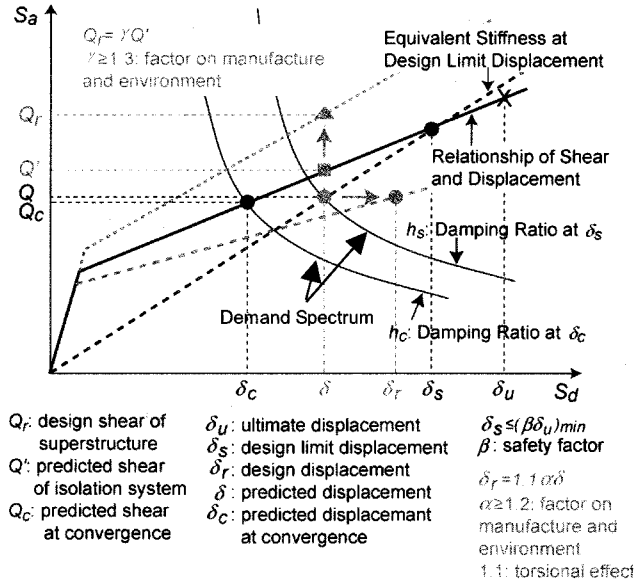


Figure 7 Prediction of Response of Seismically Isolated Building by Demand Spectrum for h_{eq} and Capacity Spectrum

The response of a seismically isolated building is predicted using the demand spectrum for h_{eq} and the capacity spectrum as shown in Figure 7. If necessary, the convergent values of the response shear and displacement can be obtained by iteration.

The basic design shear of an isolated building is determined by Equation (8) considering that T_s is longer than 0.64 seconds.

$$Q = M S_a \quad (8)$$

where, Q : basic design shear of an isolated building (kN), M : mass of superstructure (kg), $S_a = F_h G_s Z S_0$: response spectrum at ground surface (m/s^2), F_h : acceleration reduction factor regarding the equivalent viscous damping ratio $h_{eq} = h_d + h_v$ of an isolated building, not less than 0.4, defined by Equation (9a), G_s : amplification factor of equivalent surface soil layer, not smaller than 1.0, Z : seismic zone factor of 0.7 to 1.0, and, $S_0 = 5.12/T_s$: acceleration response spectrum at the engineering bedrock for $T_s > 0.64$ (m/s^2).

The acceleration reduction factor F_h is given according to the equivalent viscous damping ratio h_{eq} shown in Figure 8, which is the summation of equivalent viscous damping ratios, h_d and h_v , of elasto-plastic dampers and fluid dampers given by Equations (9b) and (9c), respectively.

$$F_h = \frac{1.5}{1 + 10(h_d + h_v)} \quad (9a)$$

$$h_d = \frac{0.8 \sum \Delta W_i}{4\pi \sum W_i} \quad (9b)$$

$$h_v = \frac{1}{4\pi} \frac{T_s \sum C_{vi}}{M} \quad (9c)$$

where, F_h : acceleration reduction factor, h_d : equivalent viscous damping ratio of elasto-plastic dampers, h_v : equivalent viscous damping ratio of fluid dampers, ΔW_i : dissipation energy of an elasto-plastic damper as shown in Figure 9 ($\text{kN} \cdot \text{m}$), W_i : potential energy of an elasto-plastic damper shown in Figure 9 ($\text{kN} \cdot \text{m}$), and, C_{vi} : viscous damping coefficient for equivalent velocity V_{eq} (m/s), given by Equation (10), of a fluid damper as shown in Figure 10 ($\text{kN} \cdot \text{s/m}$).

$$V_{eq} = 2\pi \frac{\delta_s}{T_s} \quad (10)$$

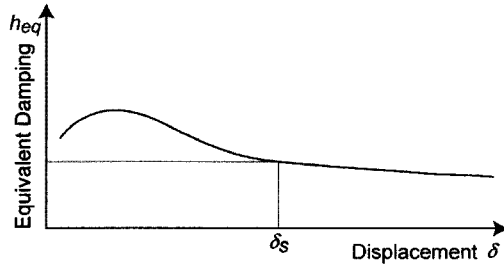


Figure 8 Relationship between Equivalent Damping h_{eq} and Displacement

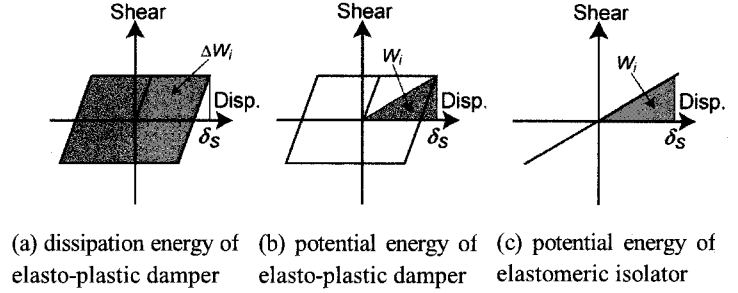


Figure 9 Dissipation Energy and Potential Energy of Elasto-plastic Hysteretic System

δ_s : design limit displacement of a seismic isolation system, and, T_s : design natural period of an isolated building.

The factor of 0.8 in Equation (16) is introduced to estimate the difference between the stationary and nonstationary vibration. Figure 11 shows the comparison of response displacements calculated by the time history response analysis and the procedures presented in this paper. In this comparison, three synthesized earthquake ground motions are used that are compatible with the acceleration response spectrum with 5 % critical damping ratio specified in the Building Code of Japan as shown in Figure 1. The analytical model is a single-degree-of-freedom system assuming the superstructure to be rigid. Four types of isolation systems are adopted such as; 1) lead rubber bearings with rubber shear modulus of 0.4 N/mm², 2) lead rubber bearings with rubber shear modulus of 0.6 N/mm², 3) high damping rubber bearings, and 4) natural rubber bearings with steel and lead dampers, corresponding to numerals in circles in Figure 11.

The capacity spectrum in Figure 7, the relationship of base shear and displacement of an ESDOF system, is affected by stiffness hardening and/or softening of seismic isolation components influenced by aging degradation, temperature change, and tolerance of manufacture. The response displacement at the center of gravity at the isolation level, δ_r' , is obtained by Equation (11b). Furthermore, the effect of accidental eccentricity between the centers of gravity and stiffness, that is not expected in the design, shall be considered. In this case, the response displacement at the peripheral of the building is increased. Considering accidental eccentricity factor of 1.1, the design response displacement δ_r is obtained by Equation (11a).

$$\delta_r = 1.1 \delta_r' \quad (11a)$$

$$\delta_r' = \alpha \delta \quad (11b)$$

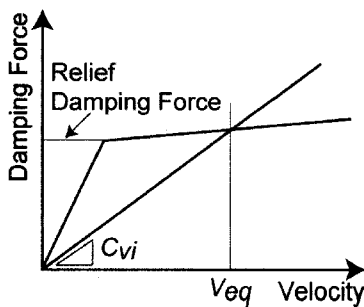


Figure 10 Damping Coefficient C_{vi} and Equivalent Velocity V_{eq} for Fluid Damper

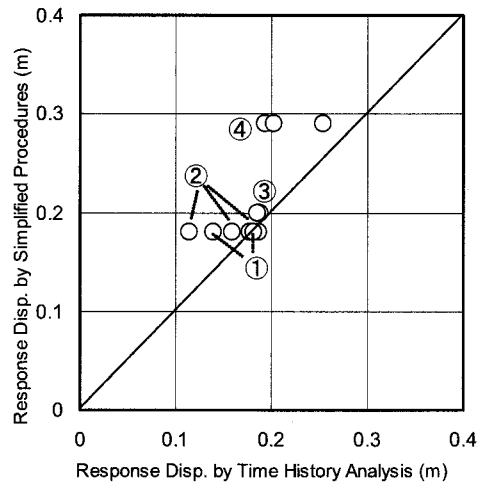


Figure 11 Comparison of response displacements calculated by simplified procedures and time history analysis

where, δ_r : design response displacement (m), α : influence factor by softening of stiffness of elastomeric isolators influenced by temperature, dispersion of manufacture, and aging, not less than 1.2, and,

$$\delta = \frac{Q}{K_{eq}} : \text{averaged response displacement at the center of gravity (m).}$$

The response displacement δ_r shall not exceed the design limit displacement δ_s .

The story shear distribution of the superstructure is obtained by the following formula, using shear force of dampers, Q_h and Q_v , and shear force of isolators, Q_e , as the seismic story shear coefficients C_{ri} including distribution profile in height A_i .

$$C_{ri} = \gamma \frac{\sqrt{(Q_h + Q_e)^2 + 2\varepsilon(Q_h + Q_e)Q_v + Q_v^2}}{Mg} \cdot \frac{A_i(Q_h + Q_v) + Q_e}{Q_h + Q_v + Q_e} \quad (12)$$

where, C_{ri} : design story shear coefficient of superstructure, γ : influence factor by stiffness hardening of seismic isolation components influenced by aging degradation, temperature change, and tolerance of manufacture, not less than 1.3, Q_h : shear force of elasto-plastic dampers (kN), Q_e : shear force of isolators (kN), $Q_v = C_v \cdot V$: shear force of fluid dampers (kN), $C_v = \sum C_{vi}$: viscous damping coefficient of fluid dampers (kN·s/m), C_{vi} : viscous damping coefficient of a fluid damper as shown in Figure 8 (kN·s/m), $V = 2\sqrt{(Q_h + Q_e)\delta}/M$: response velocity at isolation system level, δ : average response displacement at the center of gravity (m), M : mass of superstructure (kg), ε : superposition factor of different types of dampers, 0.5 when the response velocity of the seismic isolation system is larger than the relief velocity of fluid dampers, and 0 when the response velocity of the seismic isolation system is equal to or less than the relief velocity of fluid dampers,

$$A_i = 1 + \left(\frac{1}{\sqrt{\alpha_i}} - \alpha_i \right) \frac{2T_{ds}}{1 + 3T_{ds}} : \text{story shear distribution factor along the height of superstructure,}$$

α_i : ratio of weight above i -th story divided by total weight of superstructure, and, T_{ds} : design fundamental natural period of superstructure (s).

The factor ε in Equation (12) is introduced to consider the phase difference of response shears between fluid dampers and elasto-plastic dampers/isolators.

The design story shear Q_{db} of the substructure in Equation (13a) is obtained from the summation of the design shear force Q_{iso} at the seismic isolation level given by Equation (13b) and the design inertia force Q_b of the foundation itself given by Equation (13c).

$$Q_{db} = Q_{iso} + Q_b \quad (13a)$$

$$Q_{iso} = \gamma \sqrt{(Q_h + Q_e)^2 + 2\varepsilon(Q_h + Q_e)Q_v + Q_v^2} \quad (13b)$$

$$Q_b = 2k M_b g \quad (13c)$$

where, Q_{db} : design story shear of substructure (kN), Q_{iso} : design story shear of superstructure at isolation level (kN), Q_b : design inertia force of foundation (kN), M_b : mass of base and foundation (kg), k : seismic coefficient below ground, given by Equation (14),

$$k \geq 0.1 (1 - D/40) Z \quad (14)$$

D : depth from ground, maximum 20 meters, Z : seismic zone factor, and, g : acceleration of gravity.

4. SUMMARY AND CONCLUSIONS

The Building Code of Japan has been changed from the former prescriptive type into a performance-based type in June, 2000. Presented are the basic concept and the evaluation procedures of seismic provisions for seismically isolated buildings against major earthquake motions newly introduced to the revised Building Code of Japan in October, 2000.

The scope of application of the evaluation procedures is: 1) buildings not exceeding 60 meters in height, and 2) base isolation buildings on the soil layers excluding very soft soils.

The basic concept of seismic design spectra for major earthquake motions is: 1) the basic design spectra defined at the engineering bedrock, and 2) the evaluation of site conditions from geotechnical data of surface soil layers. The design criteria of each portion of seismically isolated buildings are: 1) the isolation system shall be designed so that the maximum response displacement does not exceed the design limit displacement, and 2) the structure above the isolation system and the foundation and structural elements below the isolation system shall be designed so that the working stress does not exceed the allowable stress.

An ESDOF system, equivalent linearization and response spectrum analysis are applied in the evaluation procedures of seismically isolated buildings. The evaluation procedures introduced make it simple to predict the maximum structural response against major earthquake motions without time history analyses.

Acknowledgements:

This manuscript was stimulated by the authors' participation as the members of the "Examination Committee on Performance-based Provisions for Seismically Isolated Buildings" established at BRI, where they have shared their opinions, comments and discussions with other members. The authors would like to express their gratitude towards all of them. They would also like to specially thank Prof. Akira Wada of Tokyo Institute of Technology, Prof. Tetsuo Kubo of Nagoya Institute of Technology, and Dr. Tatsuya Azuhata of BRI for their participation as the members of the Committee.

References:

- Hiraishi, H., Midorikawa, M., Teshigawara, M., Gojo, W. and Okawa, I. (2000), "Development of Performance-based Building Code of Japan -Framework of Seismic and Structural Provisions-," *Proc. 12th World Conference on Earthquake Engineering*, Paper ID 2293.
- Midorikawa, M., Hiraishi, H., Okawa, I., Iiba, M., Teshigawara, M., Isoda, H. (2000), "Development of Seismic Performance Evaluation Procedures in Building Code of Japan," *Proc. 12th World Conference on Earthquake Engineering*, Paper ID 2215.
- Kuramoto, H., Teshigawara, M., Okuzono, T., Koshika, N., Takayama, M. and Hori, T. (2000), "Predicting the earthquake response of buildings using equivalent single degree of freedom system," *Proc. 12th World Conference on Earthquake Engineering*, Paper ID 1093.
- Ministry of Land, Infrastructure and Transport (2000a), "Notification No.2009-2000, Technical Standard for Structural Specifications and Calculation of Seismically Isolated Buildings," (in Japanese).
- Ministry of Land, Infrastructure and Transport (2000b), "Notification No.1446-2000, Technical Standard for Specifications and Quality of Structural Materials," (in Japanese).
- Ministry of Land, Infrastructure and Transport, Building Research Institute, Japan Conference of Building Officials, Japan Society of Seismic Isolation, and Building Center of Japan (2001), "Commentary on Technical Standards and Calculation Procedures of Seismically Isolated Buildings," Kogaku-tosho (in Japanese).
- Building Research Institute, Japan Society of Seismic Isolation, and Kenchiku Kenkyu Shinko Kyokai (2001), "Technical Background of the Provisions of Seismically Isolated Buildings in the Revised Building Standard Law of Japan," Gyosei (in Japanese).
- Ministry of Land, Infrastructure and Transport (2000c), "Notification No.1457-2000, Technical Standard for Structural Calculation of Response and Limit Strength of Buildings," (in Japanese).
- Ministry of Land, Infrastructure and Transport (1980), "Notification No.1793-1980, Technical Standard for Calculation of Seismic Story Shear Distribution Factor along the Height of a Building Structure, etc.," (in Japanese).

RESIDUAL SEISMIC CAPACITY OF CONCRETE BLOCK INFILLED RC FRAMES: CRACK DEVELOPMENT MECHANISM OF CONCRETE BLOCK WALL

Y. Nakano¹⁾ and H. Choi²⁾

1) Professor, Institute of Industrial Science, The University of Tokyo, Japan

2) Graduate Student, Graduate School of Engineering, The University of Tokyo, Japan

iisnak@iis.u-tokyo.ac.jp, choiho@iis.u-tokyo.ac.jp

Abstract: In this study, concrete block infilled reinforced concrete frames for school buildings in Korea are tested under cyclic loadings, and a simplified model is proposed to investigate the relationship between residual crack widths in concrete block wall and frame's residual deformations. Although the measured crack widths in concrete block walls are much smaller than the residual deformations, a simplified model proposed in this paper considering flexural and shear deformation distribution of columns can rationally reproduce the measured crack widths. The relationship between crack widths in concrete block wall and frame's residual deformations is further investigated and their ratio is found to lie approximately in the range of 0.2 to 0.3. This result implies that the residual deformation of frames can be estimated from crack widths in concrete block wall.

1. INTRODUCTION

After an earthquake, the major concerns to damaged buildings are their safety/risk to aftershocks, quantitative damage assessment to evaluate their residual seismic capacity and to identify necessary actions on the damaged buildings. Post-event damage evaluation is therefore essential for quick recovery of damaged communities as well as pre-event seismic evaluation and strengthening of vulnerable buildings. Few investigations on unreinforced masonry walls, however, have been made to quantitatively identify their damage level and criteria to judge necessary actions for their continued use, repair and rehabilitation although their damage has been often found in the past damaging earthquakes.

In this study, concrete block (CB) infilled RC frames for school buildings in Korea, where CB walls are typically unreinforced, are experimentally investigated to develop pre- and post-earthquake seismic evaluation method. In the tests, full-scale, one-bay, single-story specimens having different axial loads in columns and different opening configurations in walls are tested under cyclic loadings, and the contribution of CB walls to overall behaviors is examined. Furthermore, crack patterns and widths in walls and frames which may be of great significance for post-event damage assessment are carefully observed, and the measured results in CB wall are compared to those estimated by a simplified model proposed in this paper.

2. OUTLINE OF EXPERIMENT

2.1 Test Specimen

Figure 1 shows a standard design for Korean school buildings in the 1980s (The Ministry of Construction and Transportation 2002). As can be found in this figure, CB walls are commonly used

as partition walls or exterior walls in Korean school buildings. In this study, 4 specimens representing a first or fourth story of 4 story RC school buildings are tested under cyclic loadings. They are infilled wall type 1 (IW1) assuming a first story, infilled wall type 2 (IW2) assuming a fourth story, and wing wall type (WW) and partial height wall type (PW) both having an opening in the wall. The axial force applied in each column is 720 kN (4 N/mm^2) for specimens IW1, WW, and PW while 180 kN (1 N/mm^2) for IW2.

The design details of specimen IW1 are shown in Figure 2. Since seismic design provisions for buildings were introduced in 1988 in Korea, the model structures studied herein are not designed to seismic loads. Therefore, they have (1) large spacing of hoops (300 mm) and (2) 90-degree hooks at both ends of hoops as shown in the figure. Specimens IW1, WW, and PW have the identical re-bar arrangement in columns but different wall arrangement, while IW2 has fewer re-bars than other 3 specimens. Concrete block units are laid in the RC frame after concrete is hardened.

2.2 Test Setup and Test Program

Figure 3 shows the elevation view of the loading system. Cyclic lateral loads are applied to each specimen through a loading beam tightly fastened to the specimen. Figure 4 shows the loading history, where a peak drift angle R is defined as “lateral deformation (δ_p) / column height (=2,400 mm)”. As shown in the figure, peak drift angles of 0.1, 0.2, 0.4, 0.67, 1.0, and 2.0% are planned and 2.5 cycles for each peak drift are imposed to eliminate one-sided progressive failure (unsymmetric failure pattern in positive or negative loadings). A constant axial load of 1,440 kN (720 kN for each column) is applied to specimens IW1, WW and PW while 360 kN (180 kN for each) to specimen IW2.

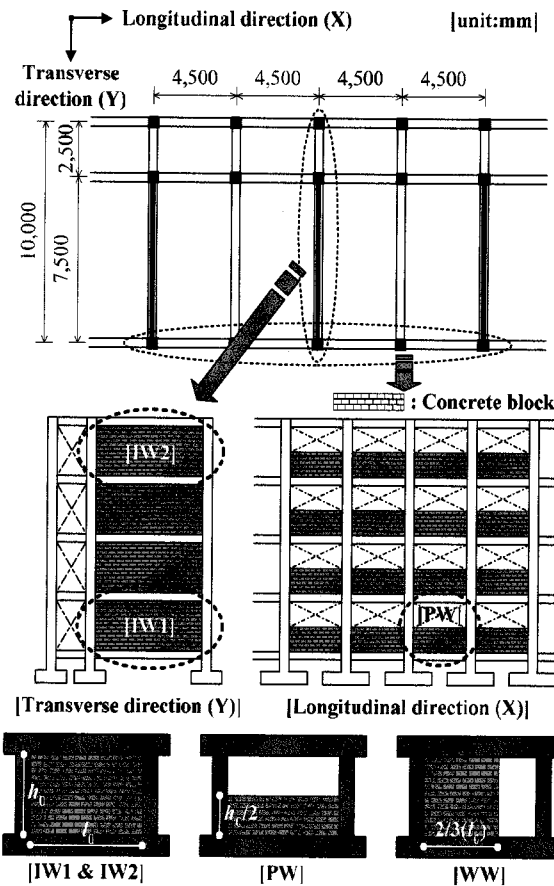


Figure 1 Standard design of Korean school buildings in the 1980s and specimen configuration

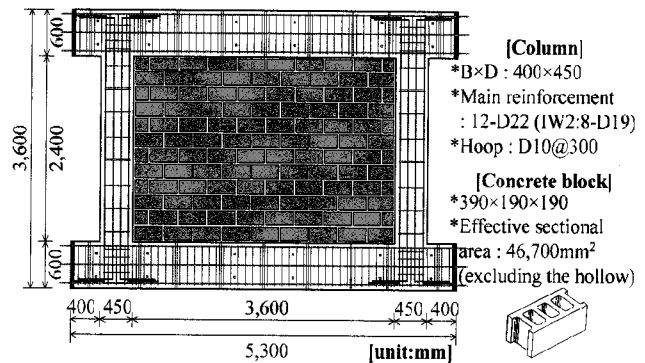


Figure 2 Detail of specimen (IW1)

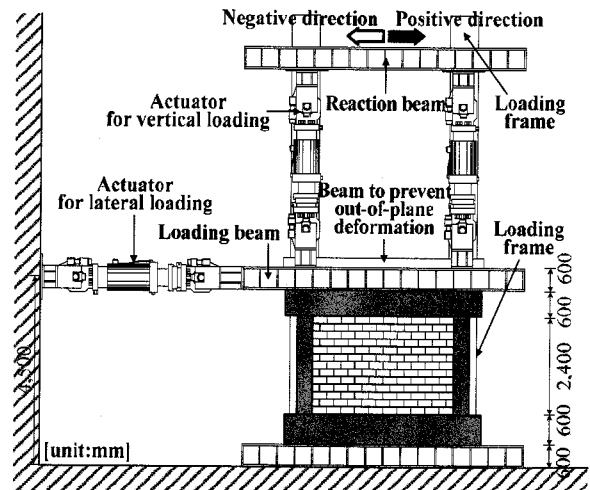


Figure 3 Test setup

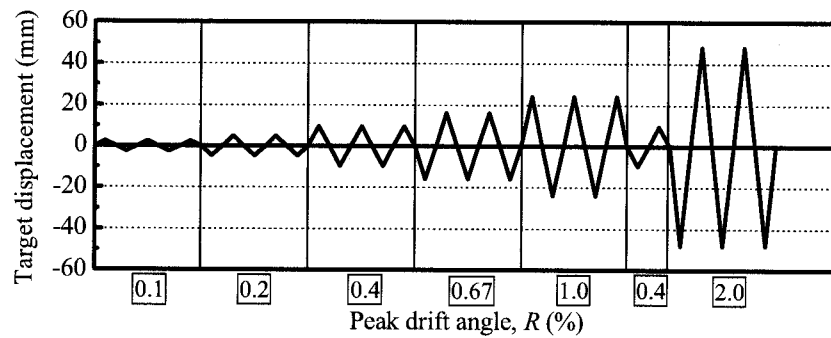


Figure 4 Loading history

3. CRACK WIDTHS AND RESPONSE OF SPECIMENS

3.1 Measurement of Crack Width

Cracks in members after an earthquake are visible and essential evidence of damage that can be found at the building site, and they often provide valuable information regarding the response that the building has experienced and its residual capacity. To investigate the relationship between crack width and residual capacity, crack widths in RC columns and CB walls are carefully measured at peak loads and unloaded stages. Figure 5 shows the measurement points in columns and walls made in this study.

The widths of flexural and shear cracks observed at the top and bottom of each column are visually measured with crack scales. Since crack widths are not necessarily uniform along the crack, its major width which is deemed to be largest along a crack is measured. It should also be noted that the width perpendicular to the crack is measured.

All visible cracks in the head joints found in stair-stepped diagonal cracks running through the CB wall are also measured to record the lateral dislocation of CB units (see Figure 5(a)) while several cracks in the bed joints of one continued crack are measured to investigate a rotational behavior of wall (see Figure 5(b)). In the following sections, crack widths measured in the head joints of CB walls of specimens IW1 and IW2 are investigated to understand the relationship between observed cracks and frame's behavior.

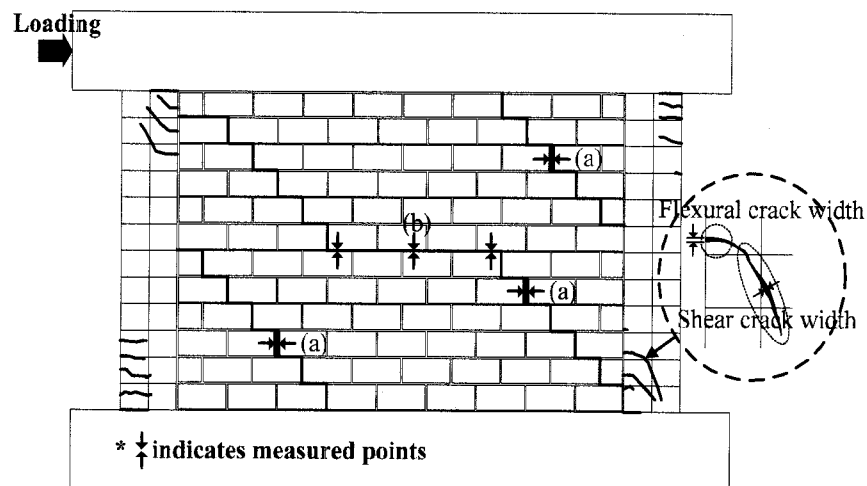


Figure 5 Schematic illustration of crack pattern and measured points

3.2 Residual Crack Width in CB Wall

The residual deformation (δ_0), total residual crack width ($\Sigma_{\max} W_0$) measured in CB wall, and their ratio $[\Sigma_{\max} W_0 / \delta_0]$ at unloaded stages after each first cycle in the positive domain are plotted for specimens IW1 and IW2 with respect to the peak drift angle in Figure 6. In this figure, $_{\max} W_0$ is defined as the maximum residual crack width, as is shown (a) in Figure 5, in the head joints of a continued stair-stepped diagonal crack. When the CB wall has more than one major stair-stepped diagonal crack, $_{\max} W_0$ can be found along each continued crack and the sum of $_{\max} W_0$ ($= \Sigma_{\max} W_0$) is then calculated. The ratio $[\Sigma_{\max} W_0 / \delta_0]$ of specimen IW1 differs from that of IW2 over the peak drift angle R smaller than 0.2% and larger than 1.5%. The results can be attributed to the following observations.

- (1) The ratio tends to be dependent on crack inspectors especially when the deformation is small (i.e., $R \leq 0.2\%$) since the observed crack widths are around 0.1mm which would be the limit for visual inspections. The calculated ratio is therefore sensitive to the measurement error and may not be consistent in the small drift range along different specimens.
- (2) The crack widths in CB wall significantly increases after $R = 1.4\%$ in IW1 due to extensive shear cracks in columns, while IW2 performs well even in such a large deformation. The ratio is therefore higher in IW1 than in IW2.

It should also be noted that the ratio $[\Sigma_{\max} W_0 / \delta_0]$ is approximately in the range of 0.2 to 0.3 over the peak drift angle larger than 0.2% and much smaller than 1.0. The reason can be found in the following section.

3.3 Estimation of Measured Residual Crack Width in CB Wall by Simplified Model

(1) General assumptions

In order to investigate the crack development mechanism and to estimate the residual crack width in CB wall, the following assumptions are made.

- 1) The residual deformation (δ_0) of frame can be approximated by the sum of residual flexural deformation (δ_{f0}) and residual shear deformation (δ_{s0}) of column as shown in Figures 7(a) and (b). (i.e., $\delta_0 = \delta_{f0} + \delta_{s0}$)

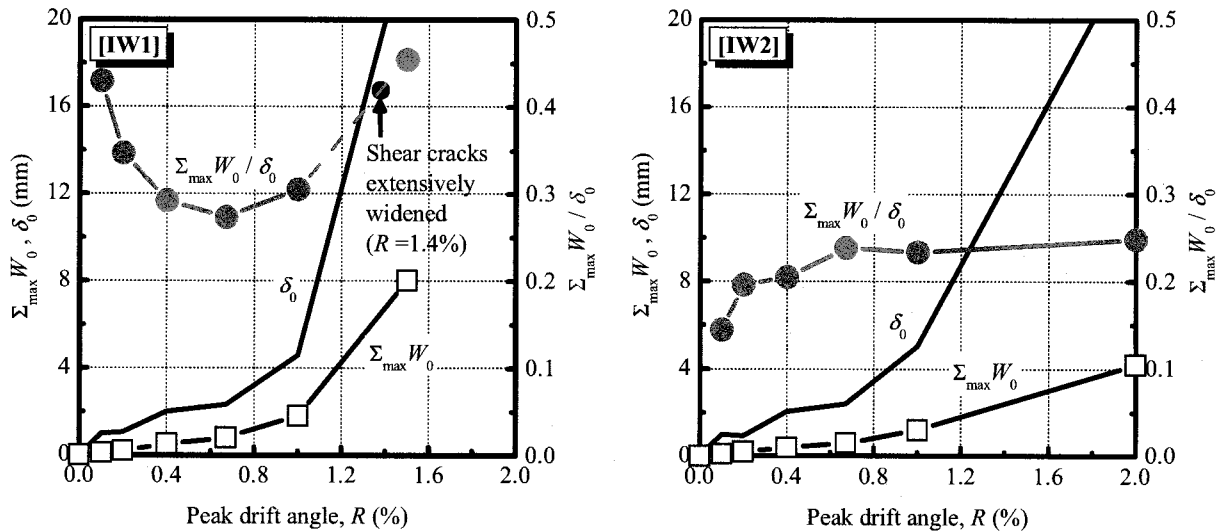


Figure 6 δ_0 , $\Sigma_{\max} W_0$ and $[\Sigma_{\max} W_0 / \delta_0]$ (CB wall) vs. peak drift angle R

- 2) Cracks in head joints of CB wall result from the discrepancy of deformation distribution along its height in each column.

If each column has an identical anti-symmetrical flexural deformation and distribution as shown in Figure 7(a), no discrepancy should be found in the CB wall's clear span length l_{0i} along column height (i.e., $l_{01} \approx l_{02} \approx l_{03}$). Since a similar flexural deformation distribution is observed in each column during tests, no major cracks due to flexural deformation are expected.

The shear deformation distribution along its height in each column, however, is not obviously identical as shown in Figure 7(b), since the deformation due to shear cracks concentrates on the bottom of compression column and the top of tensile column resulting from a compressive strut action as can be found in specimens IW1 and IW2 (see Figure 8). This may cause the discrepancy of lateral deformation distribution in CB wall along column height (i.e., $l_{01}' \neq l_{02}' \neq l_{03}'$). The maximum discrepancy, which may be simply expressed by the residual shear deformation (δ_{s0}) as shown in Figure 7(b), then needs to be consistent with crack widths in head joints resulting in high correlation between the residual shear deformation (δ_{s0}) and total crack width in CB wall ($\Sigma_{\max} W_0$).

Bearing in mind that the flexural deformation may highly contribute to the overall deformation of long columns but that the flexural deformation, as is described earlier, may not cause major cracks in head joints, the ratio $[\Sigma_{\max} W_0 / \delta_0]$ can be expected to be small as demonstrated in Figure 6. Based on studies by Maeda et al.(2000), AIJ Guidelines define the relationship between residual crack width and residual deformation for RC members (AIJ 2004). However, few researches on the relationship for RC frames and/or CB wall infilled frames have been yet made to date. It is therefore of great interest and significance to investigate the applicability of analogous relationship to CB

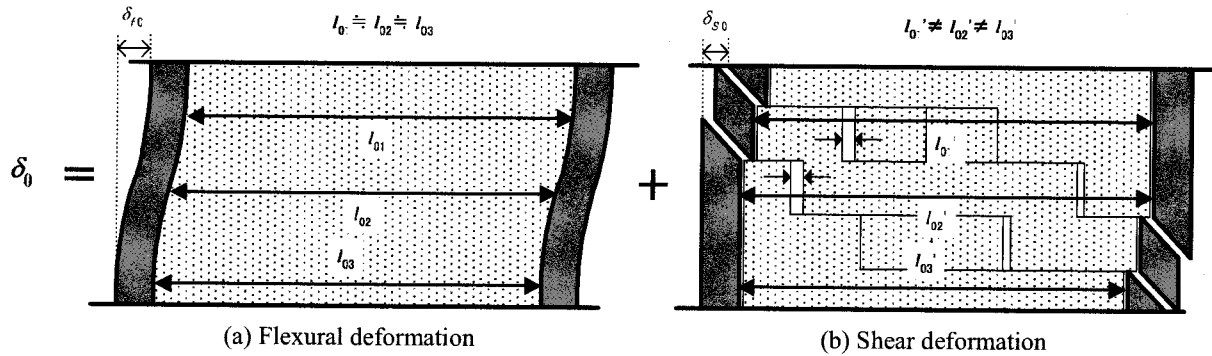


Figure 7 Deformation of column and CB wall

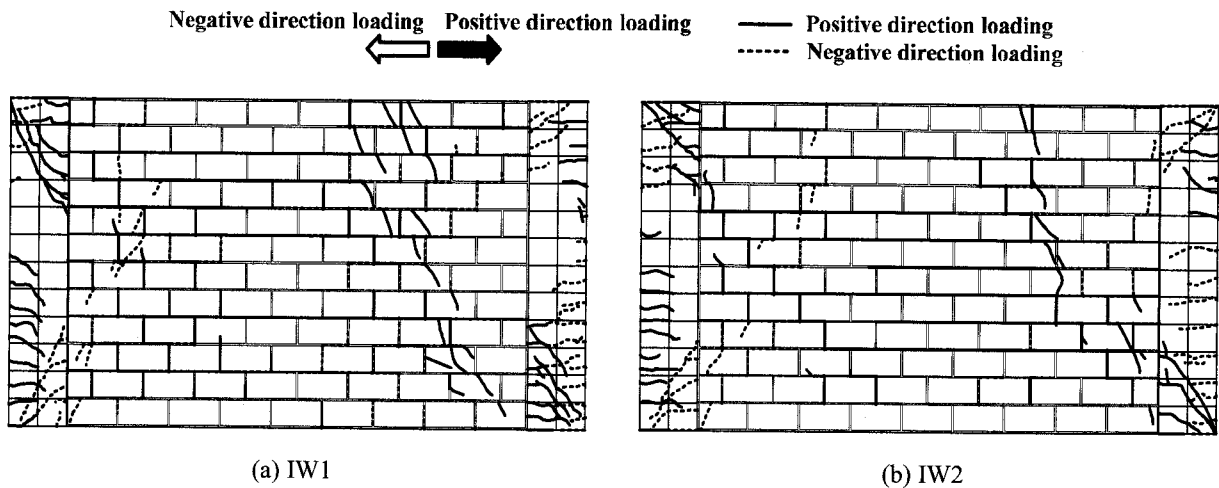


Figure 8 Cracks in RC columns and CB wall at the 1st cycle with peak drift angle of +1.0%

wall infilled frames. In the subsequent discussions, a simplified model considering the discrepancy of flexural and shear deformation distribution is proposed to estimate the crack width in CB wall, and the correlation between measured and estimated results is discussed.

(2) Crack width due to flexural deformation

Figure 9 shows the outline of the simplified model studied herein. The residual flexural deformation, ${}_t\delta_{f0}$ and ${}_c\delta_{f0}$, of each column can be approximated using the average total residual flexural crack width at the top and bottom of column as shown in equations (1) and (2) (AIJ 2004), where “t” and “c” denote “tension side” and “compression side”, respectively. The maximum discrepancy between two columns due to residual flexural deformation distribution, which causes minor cracks in head joints as discussed earlier, is assumed herein to develop in the mid-height of column ($h_0/2$) as shown in equation (3).

$${}_t\delta_{f0} = {}_tR_{f0} \cdot h_0 = \frac{1}{D-x} \cdot \left(\frac{\Sigma {}_tW_{f0,T} + \Sigma {}_tW_{f0,B}}{2} \right) \cdot h_0 \quad (1)$$

$${}_c\delta_{f0} = {}_cR_{f0} \cdot h_0 = \frac{1}{D-x} \cdot \left(\frac{\Sigma {}_cW_{f0,T} + \Sigma {}_cW_{f0,B}}{2} \right) \cdot h_0 \quad (2)$$

$$\Sigma_{\max} W_{f0} = \left(\frac{\Sigma {}_cW_{f0,B} - \Sigma {}_tW_{f0,B}}{D-x} \right) \cdot \frac{h_0}{2} \quad (3)$$

where,

- ${}_t\delta_{f0}, {}_c\delta_{f0}$: residual flexural deformation of tension and compression side column, respectively (see Figure 9(a))
- ${}_tR_{f0}, {}_cR_{f0}$: residual flexural rotation angle of tension and compression side column, respectively (see Figure 9(a))
- $\Sigma {}_tW_{f0,T}, \Sigma {}_tW_{f0,B}$: total residual flexural crack width of top and bottom in tension column, respectively (measured)
- $\Sigma {}_cW_{f0,T}, \Sigma {}_cW_{f0,B}$: total residual flexural crack width of top and bottom in compression column, respectively (measured)
- D : column depth (=450 mm)
- x : distance from extreme compression fiber to neutral axis (0.2 D (= 90 mm) is assumed herein)
- h_0 : column clear height (= 2,400 mm)
- $\Sigma_{\max} W_{f0}$: total residual crack width in CB wall due to the discrepancy of flexural deformation distribution

(3) Crack width due to shear deformation

The residual shear deformation, ${}_t\delta_{s0}$ and ${}_c\delta_{s0}$, of two RC columns can be approximated based on the measured total residual shear crack width of each column as shown in equations (4) and (5) (AIJ 2004). The total residual crack width in CB wall due to different residual shear deformation distribution between tension and compression side column can be estimated using the average total residual shear crack width as shown in equation (6).

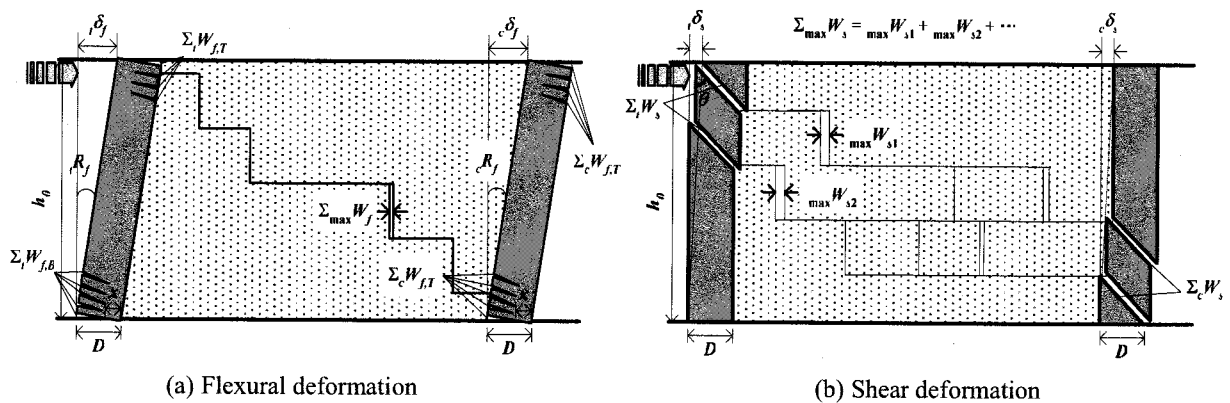


Figure 9 Simplified model of column and CB wall

$${}_t\delta_{s0} = \Sigma {}_tW_{s0} \cdot \cos \theta \quad (4)$$

$${}_c\delta_{s0} = \Sigma {}_cW_{s0} \cdot \cos \theta \quad (5)$$

$$\Sigma_{\max} W_{s0} = \frac{{}_c\delta_{s0} + {}_t\delta_{s0}}{2} \left(= \frac{(\Sigma {}_cW_{s0} + \Sigma {}_tW_{s0}) \cdot \cos \theta}{2} \right) \quad (6)$$

where,

${}_t\delta_{s0}, {}_c\delta_{s0}$: residual shear deformation of tension and compression side column, respectively (see Figure 9(b))
 $\Sigma {}_tW_{s0}, \Sigma {}_cW_{s0}$: total residual shear crack width of tension and compression side column, respectively (measured)
 θ : angle between shear crack and vertical direction of column (45-degree angle is assumed herein)
 $\Sigma_{\max} W_{s0}$: total residual crack width in CB wall due to the shear deformation distribution

(4) Total crack width in CB wall

As shown in equation (7), the total residual crack width in CB wall, $\Sigma_{\max} W_0$, can be calculated using crack widths defined in equations (3) and (6).

$$\Sigma_{\max} W_0 = \Sigma_{\max} W_{f0} + \Sigma_{\max} W_{s0} = \left(\frac{\Sigma {}_cW_{f0,B} - \Sigma {}_tW_{f0,B}}{D - x} \right) \cdot \frac{h_0}{2} + \frac{(\Sigma {}_cW_{s0} + \Sigma {}_tW_{s0}) \cdot \cos \theta}{2} \quad (7)$$

Figure 10 shows the residual deformation δ_0 and δ_{f0} with respect to the peak drift angle, where δ_{f0} is assumed to be the average of ${}_t\delta_f$ and ${}_c\delta_f$ at unloaded stages derived from equations (1) and (2). Since major wide cracks are selectively measured after 1.0% drift, δ_{f0} is plotted up to 1.0 %. As is anticipated in 3.3 (1), δ_{f0} mainly contributes to the overall residual deformation δ_0 . It is also interesting to point out that the ratio of crack widths $\Sigma_{\max} W_{f0}$ to δ_{f0} is relatively small, which is consistent with the results shown in Figure 6. This is mainly because the flexural deformation distribution along their height of two boundary columns does not differ much (i.e., $l_{01} \approx l_{02} \approx l_{03}$) and therefore leads to minor cracks in head joints.

Figure 11 shows the estimated crack widths in CB wall at unloaded stages obtained from equation (7) together with measured results. The estimated results (shown in circle : -○-) slightly overestimate the measured results (shown in square : -□-) since all cracks developed in CB wall are not perfectly measured during tests. The estimated results, however, generally compare well with the measured results and the proposed model shown in Figure 9 successfully explains the crack

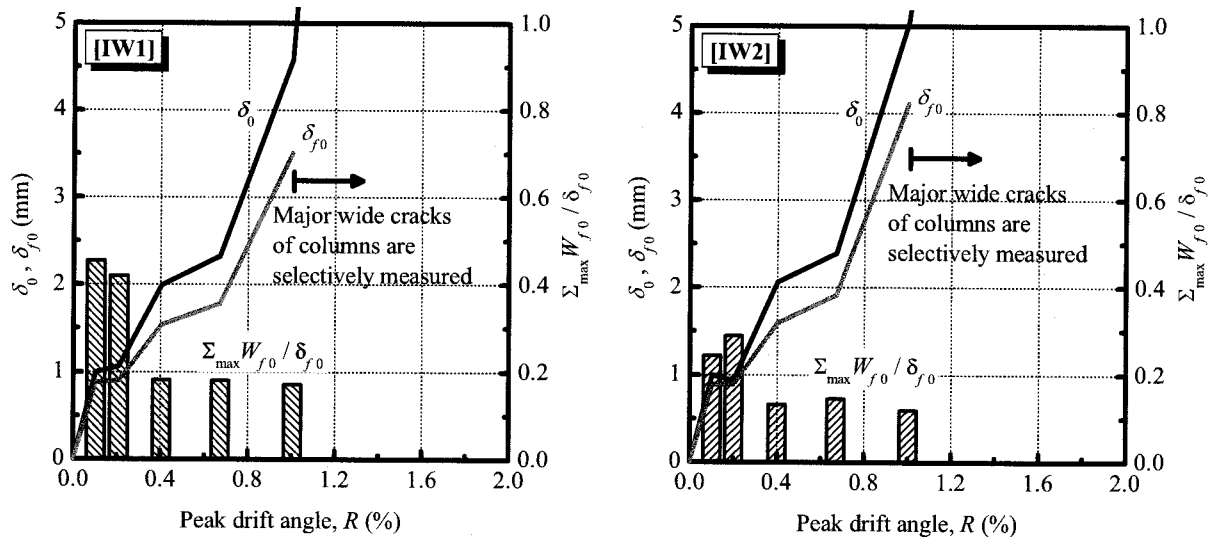


Figure 10 δ_0 , δ_{f0} and $[\Sigma_{\max} W_{f0} / \delta_{f0}]$ vs. peak drift angle R

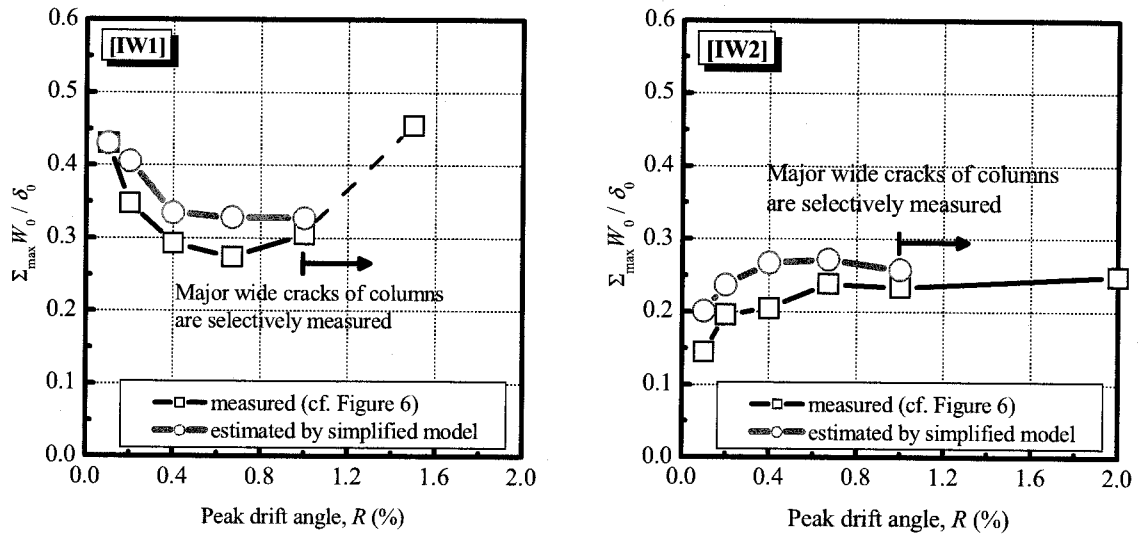


Figure 11 $[\Sigma_{\max} W_0 / \delta_0]$ vs. peak drift angle R (in positive loading)

development mechanism of CB wall studied herein. This result implies that the residual deformation δ_0 of frames as well as RC members can be estimated from crack widths $\Sigma_{\max} W_0$ observed in CB wall based on the ratio $[\Sigma_{\max} W_0 / \delta_0]$. The residual seismic capacity, therefore, could be evaluated through previously estimated δ_0 if the typical hysteretic characteristics of CB wall infilled frame are given.

4. CONCLUSIONS

Concrete block (CB) infilled RC frames for school buildings in Korea are tested under cyclic loadings, and a simplified model is proposed to investigate the relationship between residual crack widths in CB wall and residual deformation. The results can be summarized as follows.

- (1) The measured ratio $[\Sigma_{\max} W_0 / \delta_0]$ for specimens IW1 and IW2 lies approximately in the range of 0.2 to 0.3 before the specimen extensively fails in shear.
- (2) Although the ratio above is much smaller than 1.0, a simplified model proposed in this paper considering flexural and shear deformation distribution of columns can rationally reproduce the measured results.
- (3) The results described above imply that the residual deformation δ_0 of frames can be estimated from crack widths $\Sigma_{\max} W_0$ observed in CB wall based on the ratio $[\Sigma_{\max} W_0 / \delta_0]$. The residual seismic capacity, therefore, could be evaluated through previously estimated δ_0 if the typical hysteretic characteristics of CB wall infilled frame are given.

Acknowledgements:

The research reported herein was performed in cooperation with Professor Waon-Ho Yi of the Kwangwoon University and Dr. Sang-Hoon Oh of RIST (Research Institute of Industrial Science and Technology) in Korea. The authors express their deepest gratitude to all these supports without which the test could not be accomplished.

References:

- The Ministry of Construction and Transportation (2002), "A Study on the Seismic Evaluation and Retrofit of Low-rise RC Buildings in Korea," pp. 113-155.
- M. Maeda, M. Bunno and M. Nagata (2000) "A Study on the Damage Level Estimation of RC Buildings Based on Residual Seismic Capacity of Members," *Proceedings of the Japan Concrete Institute*, Vol.22, No.3, pp. 1447-1452.
- AIJ (2004), "Guidelines for Performance Evaluation of Earthquake Resistant Reinforced Concrete Buildings (Draft)," pp. 155-161.

SEISMIC RESPONSES OF STRUCTURES SUBJECTED TO ARTIFICIAL GROUND MOTIONS GENERATED USING 1D, 2D AND 3D GROUND MODELS

H.T. Chen¹⁾, Y.C. Wang²⁾ and D.S. Juang³⁾

1) Associate Professor, Department of Civil Engineering, National Central University, Taiwan

2) Graduate Student, Department of Civil Engineering, National Central University, Taiwan

3) Professor, Department of Civil Engineering, National Central University, Taiwan

chenht@cc.ncu.edu.tw

Abstract: Using the spectrum-compatible artificial earthquake motion as the input motion, in this paper a three-dimensional nonlinear finite element model is used to compute the surface ground motions which are subsequently used as the input motions for the seismic response analyses of a ten-story building. The differences among the ground motions generated using the 1D, the 2D and the 3D ground models and their effects on the seismic responses of the building are then explored. It is found that the seed number affects the characteristics of the artificial earthquakes significantly. For a soil stratum with an improved zone of finite dimension, the 2D analysis gives the largest surface ground motion, while the 1D analysis gives the smallest surface ground motion. In the dynamic analysis of a building located on top of an improved soil zone, if the input ground motion is computed using the 1D analysis, then the response will be underestimated; thus, for such a case, the surface ground motion must be obtained using the 2D or the 3D analyses if the design ground motion is specified at the engineering bedrock.

1. INTRODUCTION

The performance objectives associated with different severities of earthquake have to be selected when implementing a performance-based design. To ensure that the designed structure can meet these performance objectives, the analytical techniques, which allow one to predict degrees of damage in the various elements based on the inelastic demands predicted for these elements, must be adopted. One method is the so-called pushover approach which consists of performing a series of incremental nonlinear static analyses on the structural model. It has been reported that if the response of the structure is dominated by the first mode, this approach can give a reasonable estimate of inelastic demand distributions and damages in the structure; however, for the long period structures, the estimate of damages made using this approach is poor (Hamburger 1996). The other method is the nonlinear dynamic time-history analysis which is more complex to perform and time-consuming and is deemed to be able to give accurate predictions if the assumed constitutive relations for structural elements reflect their true behaviors. However, in the nonlinear dynamic analysis a time history of earthquake motion must be selected to serve as the input for the analysis. As stated in FEMA368 (2000), the earthquake motion actually recorded at the site can be used as the input motion for the analysis; however, if there is no recorded earthquake motion, the artificial earthquake motion generated by enveloping the design spectrum can also be adopted. In Japan, instead of providing the design forces, the newly developed performance-based seismic design code for buildings gives two design spectra at engineering bedrock (Midorikawa et al. 2003). Apparently, due to the lack of strong ground motion records at sites, in most nonlinear dynamic time-history analyses, the

spectrum-compatible artificial earthquake ground motions have to be generated.

Pappin et al. (2000) investigated the effects of site response on performance-based design for 2 levels of seismic ground motion and 3 different actual soil profiles using the nonlinear 1D ground model. They found that regardless of the soil type of the site, the performance-based design will cause the 'no collapse' requirement to dominate the seismic design in the regions of low to moderate seismicity, while in the regions of high seismicity, the 'immediate occupancy' requirement will dominate the seismic design for the low period structures located on soft or loose soil sites. The performance-based seismic design code for buildings in Japan, in addition to giving the design spectra at engineering bedrock, also provides the design spectrum at ground surface which is also derived using the 1D soil profile (Midorikawa et al. 2003). Although using the 1D model to compute the surface ground motions is easy to implement, it has long been recognized both from the theoretical analyses and the field observations that the surface topography, the subsurface topography and the lateral inhomogeneities in the properties of the site can alter the motions significantly, as compared with the results of the 1D model which assumes the soil layers to be horizontal (Chen and Ho 2000, Semblat et al. 2002). Using ten spectrum-compatible artificial earthquakes with ten seed numbers for random number generator subroutine, Chen and Ou (2004) studied the seismic responses of a 10-story steel structure located on top of a region of soil improvement. Both the 1D and the 2D ground motion analyses are performed and the computed surface motions were used as the input to conduct the seismic responses of the building. They found that the surface ground motions of the 2D analysis are larger than those of the 1D analysis, the seed number has significant effects on the maximum story drift ratio and the dynamic seismic responses of the selected building will be underestimated if the input ground motion is computed using the 1D analysis.

However, for a soil stratum with a zone of improvement it is essentially a three-dimensional problem. Thus, using the spectrum-compatible artificial earthquake motion as the input motion, in this paper a three-dimensional nonlinear finite element model is used to compute the surface ground motions which are subsequently used as the input motions for the seismic response analyses of a building. The differences among the ground motions generated using the 1D, the 2D and the 3D ground models and their effects on the seismic responses of a ten-story building are then explored.

2. METHOD OF ANALYSIS

The methodology adopted in this study consists of three stages: (1) the artificial earthquake motion compatible with a selected design spectrum specified at the engineering bedrock is generated, (2) the artificial earthquake motion generated in step (1) is then used as the input motion for the surface ground motion calculation using a three-dimensional finite element model, and (3) the nonlinear dynamic time-history analysis is subsequently performed using the surface motion computed in step (2) as the input motion.

2.1 Generation of Artificial Earthquake

Many methods have been proposed for generating artificial earthquakes. In this study the one adopted is to express the acceleration in terms of complex exponentials as

$$a(t) = f(t) \sum_{k=0}^n A_k \exp(i(\omega_k t + \phi_k)) \quad (1)$$

where $a(t)$ is the acceleration, A_k the k th Fourier amplitude, ϕ_k the k th Fourier phase angle, ω_k the selected frequency and $f(t)$ the envelope function which approximately envelopes the time history of the entire earthquake record and represents the nonstationary property of earthquake motion. However, observing the close correlation between the shape of distribution of difference of Fourier

phase angles for any two consecutive frequencies and the wave shape of an earthquake motion, Ohsaki (1979) proposed the so-called “phase difference method” in which the independent random numbers are assigned for the desired numbers of phase difference. Assuming $\phi_1=0$, the k th Fourier phase angle is then computed using

$$\phi_{k+1} = \phi_k + \Delta\phi_k \quad k=0,1,2,\dots,n-1 \quad (2)$$

Shown in Fig. 1 is the shape of distribution of difference of Fourier phase angles adopted in this study; in the figure, T_R is the rise time to reach the full amplitude, T_L is the time to decrease the amplitude, T_D is the duration of the motion and NDIF is the number of the intervals used to obtain the corresponding accumulated function. This approach do not need $f(t)$ as shown in equation (1) and is shown to have the uniform convergence. In this study, a program NCUARTEQ (Wang 2000) based on the “phase difference method” is used for generating the spectrum-compatible earthquake motions. The ω_k is chosen arbitrarily to cover the entire frequency range of the design spectrum. During the iterative process, the quantities ω_k and ϕ_k remain unchanged, while only the A_k is adjusted so that the response spectrum of the generated artificial earthquake motion can envelope the design spectrum. It is also noted that we adopt the criterion listed in Standard Review Plan (NRC 1989) where the calculated response spectrum of the artificial earthquake is considered to envelope the design spectrum when no more than five points and no more than 10% of the value below the design spectrum.

The Level 2 design spectrum at engineering bedrock given in the performance-based seismic design code for buildings in Japan is adopted. This spectrum (unit: cm/sec^2) is defined as follows where T is the period.

$$0.64 \leq T < 5.0 \quad S_0 = 512/T \quad (3a)$$

$$0.16 \leq T < 0.64 \quad S_0 = 800 \quad (3b)$$

$$T < 0.16 \quad S_0 = 320 + 3000T \quad (3c)$$

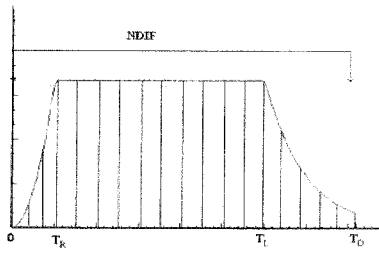


Figure 1 Distribution of Phase Difference

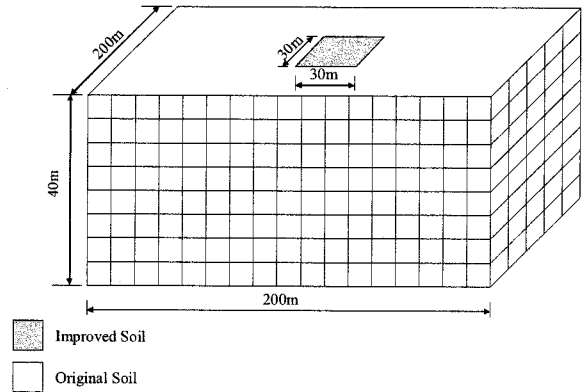


Figure 2 3D Finite Element Ground Model

2.2 Analysis of Seismic Ground Motion

In this study the seismic ground response is computed using the program NCULIQUID3 (Chen 2002) which is a three-dimensional nonlinear effective stress finite element program based on Biot's equations. In this program the soil displacement and the pore pressure can be obtained directly from the solutions of equations. The constitutive relation for soil is the cap model (Sandler et al. 1976) and the pore pressure model developed according to the cap model is the one proposed by Pacheco (1989). In addition, the viscous boundary accounting for two-phase nature of soil is used to model

the lateral infinite extent of soil stratum (Akiyoshi et al. 1994). A note is to be made that no effect of underground water is considered in this study.

Shown in Fig. 2 is the hypothetical three-dimensional ground model employed in this study. The shaded region is the improved construction site and the improvement is made such that its shear wave velocity changes from 170m/sec to 300m/sec. The depth of soil stratum is 40m and the width of improvement region is 30m x 30m x 20m. Through the convergence test runs, as shown in Fig. 3, it is found that when the boundary of domain of analysis is set up at a location of 100m from the center of the model (indicated as 40x40x8 in the figure), the response spectrum of the surface ground motion converges and this is the size of the finite element model used in this study. Although three components of motions on the ground surface can be obtained from the finite element model, in order to compare with the 1D and the 2D results, only the horizontal motion which is parallel to the input motion at the bedrock is considered. The ground motion at the center of improved-zone surface is used as the input for the dynamic analysis of a building. Table 1 describes the parametric values of the ground model. These properties are exactly the same as those used for the 1D and the 2D finite element models in Chen and Ou's study (Chen and Ou 2004)

Table 1 Parametric Values for Soil Stratum

	Original soil	Improved soil
Shear-wave velocity (m/sec)	170	300
Poisson ratio	0.44	0.46
Mass density (t/m^3)	1.9	2.1
Cohesion (kN/m^2)	12	100.5
Friction angle (degree)	10	26.7
Cap model parameter R	4.0	1.6
Cap model parameter W	0.18	0.18
Cap model parameter D ($1/kN$)	5×10^{-6}	5×10^{-6}

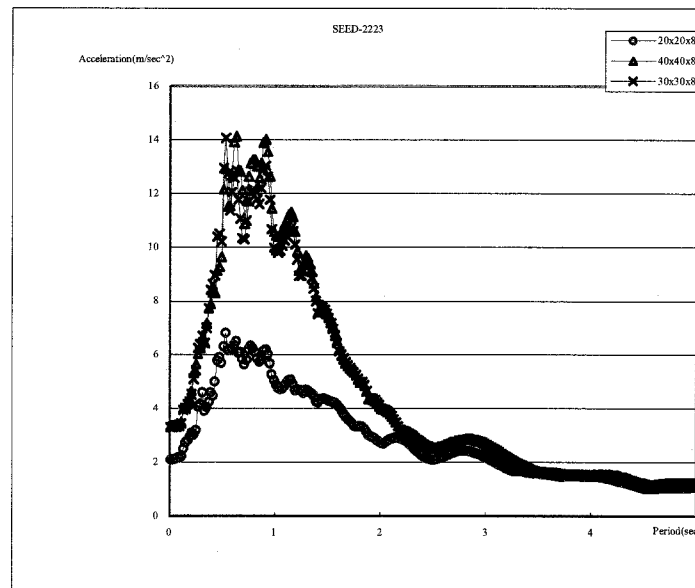


Figure 3 Convergence Study for Determining the Size of Domain of Analysis

2.3 Seismic Analysis of Building

The nonlinear dynamic analysis of building in this study is performed using the program

Raumoko-3D which is developed by Prof. Carr of University of Canterbury (Carr, 2000). This program is versatile and can perform the static analysis, the linear and the nonlinear dynamic time-history analysis, the modal analysis and the static pushover analysis for the three-dimensional structures.

The building investigated is a 10-story steel building which has 3 bays on each side. Except the first story which has a height of 4.5m, all other stories have the same height of 3.5m. This building is designed according to the seismic design code of Taiwan and has been used in the other study (Chen, 1994). Figure 4 shows its plane view and side view. The bi-linear behavior is assumed for the nonlinear behavior of the members and the joints are taken as rigid. The periods of the first two modes are 1.607 seconds and 1.461 seconds, respectively. The Rayleigh damping with 5% damping for the first two modes are used.

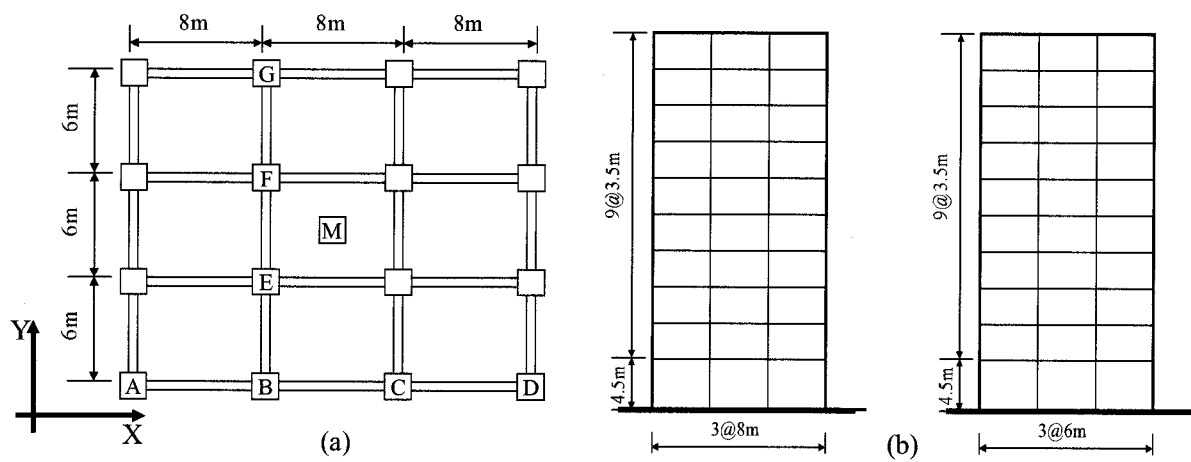


Figure 4 Building Model: (a) Top View, and (b) Side View

3. RESULTS AND DISCUSSIONS

3.1 Artificial Earthquakes

It is known that there are infinite numbers of artificial earthquakes which can be generated to envelope the same design spectrum. In order to investigate the effects of these earthquakes on the seismic responses of buildings, Chen and Ou (2004) generated ten artificial earthquakes using the following numbers as the seed numbers for the random number generator subroutine: 10579, 123, 130579, 2223, 2459, 290197, 5791, 6079, 7983 and 8953, to generate the distribution of phase differences associated with $T_R=5.0$ seconds, $T_L=15.0$ seconds, $T_D=20.48$ seconds and $NDIF=100$. Figure 5 shows the response spectra of the artificial earthquakes generated using the seed numbers 130579 and 123, which envelope the design spectrum denoted as the dash line. Their results also showed that the time to reach the maximum acceleration varies significantly with the seed number, indicating that the seed number plays an important role in generating the spectrum-compatible artificial earthquakes.

3.2 Response Spectra from 1D, 2D and 3D Analysis

In the seismic ground motion analysis the 1D analysis is frequently performed because of its easy implementation. However, for the case where a portion of ground is improved, it becomes essentially a three-dimensional problem. In such a situation both the 1D and the 2D conditions are violated and whether the 1D and the 2D analyses are still applicable needs further investigation.

Shown in Fig. 6 are the response spectra computed from the surface motions at the center of the

surface of improved soil zone as described in the section 2.2. These ground motions are obtained using the 1D, the 2D and the 3D analyses. It can be seen that the response spectra for the surface ground motions are influenced by the seed numbers. For the case using the seed number 123, the peak value is at period of 1 second, while for the case using the seed number 130579 its peak value is at period about 0.4 seconds; in addition, the significant difference can also be observed for the peak values.

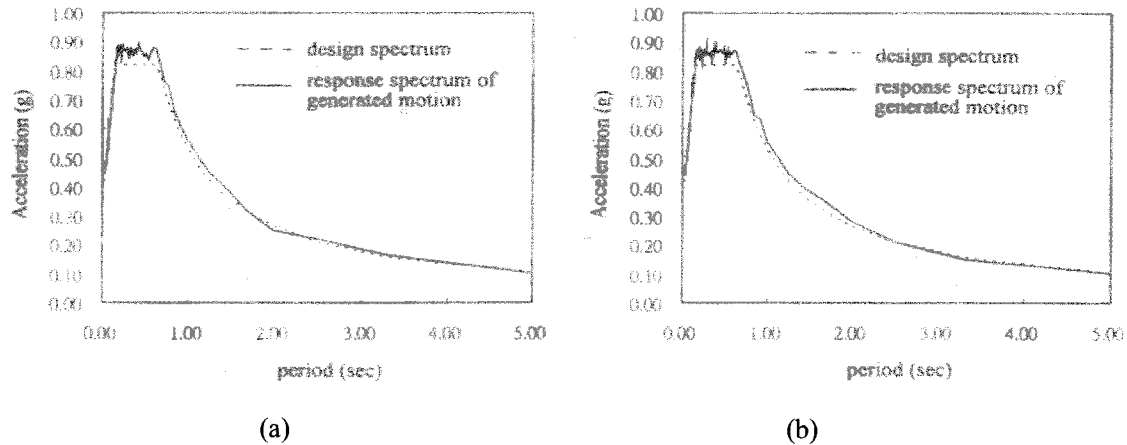


Figure 5 Design spectrum enveloped by generated artificial earthquakes (Chen and Ou, 2004):
(a) Seed Number 123, and (b) Seed Number 130579

On the other hand, the response spectra of the 1D analysis are very different from those of the 2D and the 3D analyses with the spectral values of the 2D analysis being the largest and those of the 1D analysis being the smallest over the periods below about 3 seconds. The reason for such a difference is that in the 1D analysis the improved soil zone is assumed to extend laterally to infinity and during the strong earthquake most of the wave energy is trapped at the bottom soft soil region and dissipated by the nonlinear soil behavior; for the 2D analysis the improved soil zone is surrounded by the soft soil region and “floats” on top of the soil stratum during the strong earthquake, resulting in larger ground motions, while in the 3D analysis the propagation of wave in the third direction dissipates a little more energy than the 2D analysis, rendering smaller responses. Despite this, for the periods above 1.8 seconds, there is almost no difference between the 2D and the 3D analyses.

From the above discussions, it can be concluded that for the case of a soil stratum with an improved zone and the surface ground motion is desired over that zone, it will be inappropriate to perform the 1D ground motion analysis.

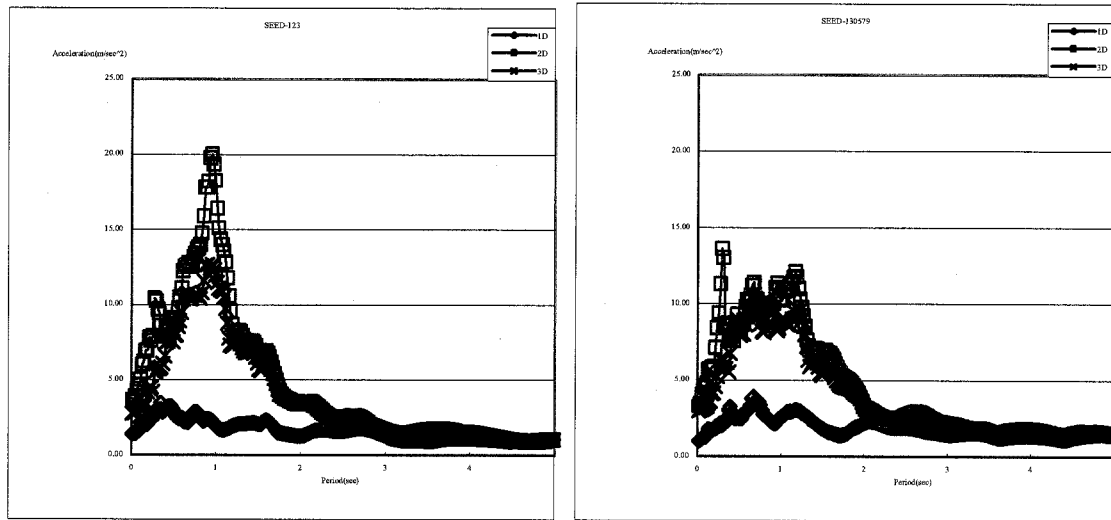
3.3 Dynamic Responses of Building

Figure 7 depicts the maximum story drift ratios for the ten-story building described in the section 2.3 using the surface ground motions computed from the 1D, the 2D and the 3D analyses as the input motions. In the figure the lines with rhombus mark, square mark and cross mark are the results using the ground motions from the 1D, the 2D and the 3D analyses, respectively. Again it can be seen that the seed number affects the seismic responses significantly.

For both the seed numbers considered, as expected, the input motion from the 1D analysis gives the smallest maximum drift ratio, the difference being about 3 times as compared with the values of the 2D analysis. For the case of seed number 123, the ground motion from 2D analysis will predict the larger maximum drift ratios for stories between 4 and 8 than those from the 3D analysis, while the trend is reversed for the other stories. For the case of seed number 130579, the ground motion from the 2D and the 3D analyses do not show significant differences, as compared with the results for the

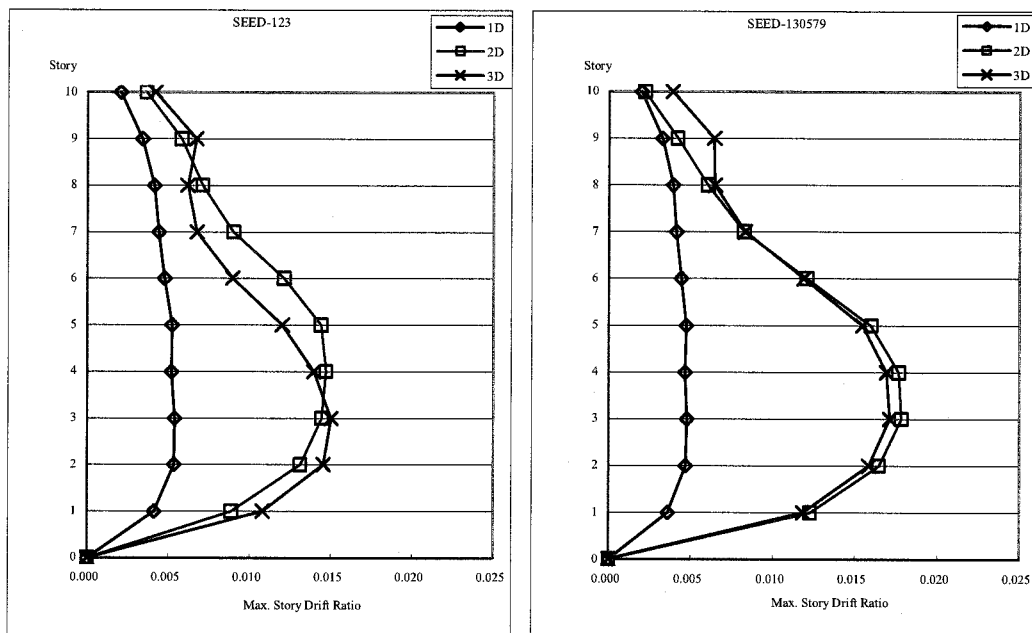
case of seed number 123. However, it can also be observed from the figure that the larger maximum story drift ratio is predicted for the artificial earthquakes using the seed number 130579.

Thus, it clearly indicates that in the dynamic analysis of a building located on top of an improved soil zone, if the input ground motion is computed using the 1D analysis, then the response will be underestimated. Thus, for such a case, the surface ground motion must be obtained using the 2D or the 3D analyses if the design ground motion is specified at the engineering bedrock.



(a) (b)

Figure 6 Response spectra of surface ground motions from 1D, 2D and 3D analyses:
(a) Seed Number 123, and (b) Seed Number 130579



(a) (b)

Figure 7 Maximum story drift ratio using motions computed from 1D, 2D and 3D analyses:
(a) Seed Number 123, and (b) Seed Number 130579

4. CONCLUSIONS

Using the spectrum-compatible artificial earthquake motion as the input motion, in this paper a three-dimensional nonlinear finite element model is used to compute the surface ground motions which are subsequently used as the input motions for the seismic response analyses of a ten-story building. The differences among the ground motions generated using the 1D, the 2D and the 3D ground models and their effects on the seismic responses of the building are then explored. It is found that the seed number affects the characteristics of the artificial earthquakes significantly. For a soil stratum with an improved zone of finite dimension, the 2D analysis gives the largest surface ground motion, while the 1D analysis gives the smallest surface ground motion. In the dynamic analysis of a building located on top of an improved soil zone, if the input ground motion is computed using the 1D analysis, then the response will be underestimated; thus, for such a case, the surface ground motion must be obtained using the 2D or the 3D analyses if the design ground motion is specified at the engineering bedrock.

Acknowledgements:

This research is sponsored by the National Science Council, Taiwan, Republic of China under the grant no. NSC 91-2211-E08-020. The Authors would like to express their appreciation for the NSC's support.

References:

- Hamburger, R.O. (1996), "Implementing Performance Based Seismic Design in Structural Engineering Practice," *Proceedings of 11th World Conference on Earthquake Engineering*, Paper No. 2121.
- FEMA 368, NEHRP (2000), "Recommended Provisions for Seismic Regulation for New Buildings," Federal Emergency Management Agency.
- Midorikawa, M., Okawa, I., Iiba M., and Teshigawara, M. (2003), "Performance-Based Seismic Design Code for Buildings in Japan," *Earthquake Engineering and Engineering Seismology*, 4(1), 15-25.
- Pappin, J.W., Lubkowski, Z.A., and King, R.A. (2000), "The Significance of Site Response Effects on Performance Based Design," *Proceedings of 12th World Conference on Earthquake Engineering*, Paper No. 1192.
- Chen, H.T. and Ho, J.C. (2000), "Effects of Ground Water on Seismic Response of Basin," *Proceedings of 12th World Conference on Earthquake Engineering*, Paper No. 0770.
- Semblat, J.F., Dangla, P., Kham, M., and Duval A.M. (2002), "Seismic Site Effects for Shallow and Deep Alluvial Basins: In-Depth Motion and Focusing Effect," *Soil Dynamics and Earthquake Engineering* 2002. 22, 849-854.
- Ohsaki, Y. (1979), "On the Phase Difference of Phase Content in Earthquake Ground Motions," *Earthquake Engineering and Structural Dynamics*, 7, 427-439.
- Wang, J.M. (2000), "The effect of Phase Angle of Spectrum-Compatible Artificial Earthquake on the Floor Response Spectra," *Master Thesis*, Department of Civil Engineering, National Central University, Chungli, Taiwan (in Chinese).
- Standard Review Plan (1989), US Nuclear Regulatory Commission, Rev.2.
- Chen, W.H. (2000), "Effectiveness of Diaphragm Wall in Reducing the Potential of Soil Liquefaction Induced by Earthquakes," *Master Thesis*, Department of Civil Engineering, National Central University, Chungli, Taiwan (in Chinese).
- Sandler, I.S., Dimaggio, F.L., Baladi, G.Y. (1976), "Generalized Cap Model for Geological Materials," *Journal of Geotechnical Engineering Division*, ASCE 1976. 102(7), 683-699.
- Pacheco, M.P. (1989), "Pore Pressure Predictions in Finite Element Analysis," *International Journal for Numerical and Analytical Methods in Geomechanics*, 13, 477-491.
- Akiyoshi, T., Fuchida, K., Fang, H.L. (1994), "Absorbing Boundary Conditions for Dynamic Analysis of Fluid-Saturated Porous Media," *Soil Dynamics and Earthquake Engineering*, 13, 387-397.
- Carr, A.J. (2000), "Raumoko3D - Inelastic Dynamic Analysis," Department of Civil Engineering, University of Canterbury, New Zealand.
- Chen, F.S. (1994), "Seismic Design and Analysis of Steel Structure Installed with ADAS Device," *Master Thesis*, Department of Civil Engineering, National Central University, Chungli, Taiwan (in Chinese).
- Chen, H.T. and Ou, G.Y. (2004), "Seismic Responses of Structures Subjected to Artificial Ground Motions Generated Using 1D and 2D Ground Model," *Proceedings of 13th World Conference on Earthquake Engineering*, Paper No. 1765.

EQUIVALENT SINGLE-STORY MODEL FOR MULTI-STORY UNSYMMETRIC FRAME BUILDINGS WITH ELASTO-PLASTIC SEISMIC CONTROL DEVICES

K. Fujii¹⁾

*1) Research Associate, Department of Department of Architecture, Faculty of Science and Engineering,
Tokyo University of Science, Japan
kfujii@rs.noda.tus.ac.jp*

Abstract: In recent years, the seismic rehabilitation of existing buildings using energy dissipative devices have been widely studied. To understand the behavior of multi-story unsymmetric buildings with such seismic control devices, nonlinear time-history analysis of three-dimensional frame building model based on each member element is the most rigorous solution. However it is often too complicated and it may not be suitable for the parametric study to determine the optimum amount and location of such seismic control devices. Therefore the simplified model would be useful for such parametric study.

In this paper, the simplified 1-mass 3-degree-of-freedom model, named Equivalent Single-Story Model, is proposed for multi-story unsymmetric buildings with regular elevation. In the examples, the nonlinear response of 7-story unsymmetric frame building models with ductile structural walls rehabilitated by elasto-plastic brace-type seismic control devices are shown.

1. INTRODUCTION

It is well accepted that unsymmetric buildings are vulnerable to earthquakes. This is because the excessive deformation may occur at the flexible and/or weak side frame due to the unfavorable torsional effect. This may lead to the premature failure of brittle members and finally to the collapse of whole buildings. In general, the excessive deformation at the flexible and/or weak side frame can be reduced by relocation of frames and/or members. However it may not be feasible for existing buildings because such relocation may be difficult due to architectural and functional constraints.

In recent years, the seismic rehabilitation of existing buildings using energy dissipative devices has been widely studied, and the seismic behavior of unsymmetric buildings with viscous viscoelastic and elasto-plastic devices have been investigated by some researchers (Goel, 1998, 2000, 2004, Lin and Chopra 2001, and De la Llera et al. 2005). To understand the behavior of multi-story unsymmetric buildings with such seismic control devices, nonlinear time-history analysis of three-dimensional frame building model based on each member element is the most rigorous solution. However it is often too complicated and it may not be suitable for the parametric study to determine the optimum amount and location of such seismic control devices. Therefore the simplified model would be useful for such parametric study.

In this paper, the simplified 1-mass 3-degree-of-freedom model, named Equivalent Single-Story Model, is proposed for multi-story unsymmetric buildings with regular elevation. In the examples, the nonlinear response of 7-story unsymmetric reinforced concrete frame building models with ductile structural walls rehabilitated by elasto-plastic brace-type seismic control devices are shown.

2. DESCRIPTION OF EQUIVALENT SINGLE-STORY MODEL

The building model considered in this study is a N -story unsymmetric frame model with regular elevation as shown in Fig. 1. In this paper, the following assumptions are made in the building model: 1) each floor has the same configuration in plan and member location, 2) the center of mass of all floor diaphragms lie on the same vertical axis, 3) each floor has the same radius of gyration r about the center of mass as expressed in Eq. (1), 4) all frames are oriented either in the X- or Y-direction that is mutually orthogonal.

$$r = \sqrt{I_1/m_1} = \sqrt{I_2/m_2} = \dots = \sqrt{I_N/m_N} \quad (1)$$

Where m_i and I_i are the mass and moment of inertia of i -th floor, respectively. The equation of motion of N -story unsymmetric frame model can be written as Eq. (2).

$$\mathbf{M}\ddot{\mathbf{d}} + \mathbf{C}\dot{\mathbf{d}} + \mathbf{f}_R = -\mathbf{M}(\mathbf{a}_X \cdot \mathbf{a}_{gX} + \mathbf{a}_Y \cdot \mathbf{a}_{gY}) \quad (2)$$

$$\mathbf{M} = \begin{bmatrix} \mathbf{M}_0 & \mathbf{0} & \mathbf{0} \\ \mathbf{0} & \mathbf{M}_0 & \mathbf{0} \\ \mathbf{0} & \mathbf{0} & \mathbf{I}_0 \end{bmatrix}, \mathbf{M}_0 = \begin{bmatrix} m_1 & & 0 \\ & \ddots & \\ 0 & & m_N \end{bmatrix}, \mathbf{I}_0 = \begin{bmatrix} I_1 & & 0 \\ & \ddots & \\ 0 & & I_N \end{bmatrix} = r^2 \mathbf{M}_0 \quad (3a, 3b, 3c)$$

$$\mathbf{C} = \begin{bmatrix} \mathbf{C}_{XX} & \mathbf{C}_{XY} & \mathbf{C}_{X\theta} \\ \mathbf{C}_{YX} & \mathbf{C}_{YY} & \mathbf{C}_{Y\theta} \\ \mathbf{C}_{\theta X} & \mathbf{C}_{\theta Y} & \mathbf{C}_{\theta\theta} \end{bmatrix}, \mathbf{d} = \begin{bmatrix} \mathbf{x} \\ \mathbf{y} \\ \theta \end{bmatrix}, \mathbf{f}_R = \begin{bmatrix} \mathbf{f}_{RX} \\ \mathbf{f}_{RY} \\ \mathbf{f}_{MZ} \end{bmatrix}, \mathbf{a}_X = \begin{bmatrix} 1 \\ 0 \\ 0 \end{bmatrix}, \mathbf{a}_Y = \begin{bmatrix} 0 \\ 1 \\ 0 \end{bmatrix} \quad (4a, 4b, 4c, 4d, 4e)$$

Where \mathbf{M} is the mass matrix and \mathbf{C} is the damping matrix of N -story unsymmetric building model and assumed proportional to the stiffness matrix; \mathbf{f}_R is the restoring force vector at the center of mass of floor diaphragms; \mathbf{d} is the displacement vector at the center of mass of floor diaphragms; \mathbf{a}_{gX} and \mathbf{a}_{gY} are ground acceleration in X- and Y-direction, respectively. It is assumed that the displacement vector \mathbf{d} can be approximated as Eq. (5a) even if the buildings oscillate beyond the elastic range.

$$\mathbf{d}^T = \left\{ \Gamma_{s1} \Phi_{s1}^T X_1^*, \Gamma_{s1} \Phi_{s1}^T Y_1^*, \Gamma_{s1} \Phi_{s1}^T \Theta_1^* \right\}, \Gamma_{s1} = \Phi_{s1}^T \mathbf{M}_0 \mathbf{1} / \Phi_{s1}^T \mathbf{M}_0 \Phi_{s1} \quad (5a, 5b)$$

Where $\Gamma_{s1} \Phi_{s1}$ is the deflection shape vector. By substituting Eq. (5a) into Eq. (2), Eq. (6) is obtained.

$$\begin{cases} \mathbf{M}_0(\Gamma_{s1} \Phi_{s1}) \ddot{X}_1^* + \mathbf{C}_{XX}(\Gamma_{s1} \Phi_{s1}) \dot{X}_1^* + \mathbf{C}_{XY}(\Gamma_{s1} \Phi_{s1}) \dot{Y}_1^* + \mathbf{C}_{X\theta}(\Gamma_{s1} \Phi_{s1}) \dot{\Theta}_1^* + \mathbf{f}_{RX} = -\mathbf{M}_0 \mathbf{1} a_{gX} \\ \mathbf{M}_0(\Gamma_{s1} \Phi_{s1}) \ddot{Y}_1^* + \mathbf{C}_{YX}(\Gamma_{s1} \Phi_{s1}) \dot{X}_1^* + \mathbf{C}_{YY}(\Gamma_{s1} \Phi_{s1}) \dot{Y}_1^* + \mathbf{C}_{Y\theta}(\Gamma_{s1} \Phi_{s1}) \dot{\Theta}_1^* + \mathbf{f}_{RY} = -\mathbf{M}_0 \mathbf{1} a_{gY} \\ \mathbf{I}_0(\Gamma_{s1} \Phi_{s1}) \ddot{\Theta}_1^* + \mathbf{C}_{\theta X}(\Gamma_{s1} \Phi_{s1}) \dot{X}_1^* + \mathbf{C}_{\theta Y}(\Gamma_{s1} \Phi_{s1}) \dot{Y}_1^* + \mathbf{C}_{\theta\theta}(\Gamma_{s1} \Phi_{s1}) \dot{\Theta}_1^* + \mathbf{f}_{MZ} = 0 \end{cases} \quad (6)$$

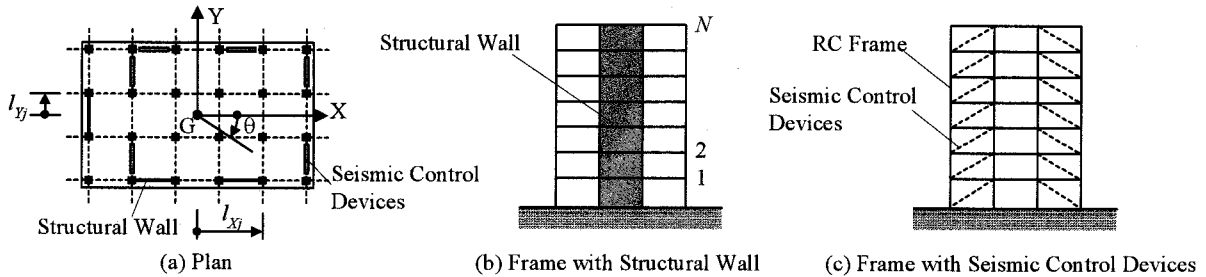


Figure 1 Multi-Story Unsymmetric Frame Building Model with Seismic Control Devices

By multiplying $\Gamma_{S1}\Phi_{S1}^T$ from the left side of Eq. (6), the equation of motion of Equivalent Single-Story Model is obtained as Eq. (7).

$$\mathbf{M}_T \ddot{\mathbf{d}}_T + \mathbf{C}_T \dot{\mathbf{d}}_T + \mathbf{f}_{RT} = -\mathbf{M}_T (\mathbf{a}_{TX} \cdot a_{gX} + \mathbf{a}_{TY} \cdot a_{gY}) \quad (7)$$

$$\mathbf{M}_T = \begin{bmatrix} M_{T1}^* & 0 & 0 \\ 0 & M_{T1}^* & 0 \\ 0 & 0 & I_{T1}^* \end{bmatrix} = \begin{bmatrix} \Gamma_{S1}^2 (\Phi_{S1}^T \mathbf{M}_0 \Phi_{S1}) & 0 & 0 \\ 0 & \Gamma_{S1}^2 (\Phi_{S1}^T \mathbf{M}_0 \Phi_{S1}) & 0 \\ 0 & 0 & \Gamma_{S1}^2 (\Phi_{S1}^T \mathbf{I}_0 \Phi_{S1}) \end{bmatrix} \quad (8)$$

$$\mathbf{C}_T = \begin{bmatrix} \Gamma_{S1}^2 (\Phi_{S1}^T \mathbf{C}_{XX} \Phi_{S1}) & \Gamma_{S1}^2 (\Phi_{S1}^T \mathbf{C}_{XY} \Phi_{S1}) & \Gamma_{S1}^2 (\Phi_{S1}^T \mathbf{C}_{X0} \Phi_{S1}) \\ \Gamma_{S1}^2 (\Phi_{S1}^T \mathbf{C}_{YX} \Phi_{S1}) & \Gamma_{S1}^2 (\Phi_{S1}^T \mathbf{C}_{YY} \Phi_{S1}) & \Gamma_{S1}^2 (\Phi_{S1}^T \mathbf{C}_{Y0} \Phi_{S1}) \\ \Gamma_{S1}^2 (\Phi_{S1}^T \mathbf{C}_{0X} \Phi_{S1}) & \Gamma_{S1}^2 (\Phi_{S1}^T \mathbf{C}_{0Y} \Phi_{S1}) & \Gamma_{S1}^2 (\Phi_{S1}^T \mathbf{C}_{00} \Phi_{S1}) \end{bmatrix} \quad (9)$$

$$\mathbf{d}_T = \{X_1^* \quad Y_1^* \quad \Theta_1^*\}^T, \mathbf{f}_{RT} = \{R_{X1}^* \quad R_{Y1}^* \quad M_{Z1}^*\}^T \quad (10a, 10b)$$

$$\mathbf{a}_{TX} = \{1 \quad 0 \quad 0\}^T, \mathbf{a}_{TY} = \{0 \quad 1 \quad 0\}^T \quad (11a, 11b)$$

Where M_{T1}^* and I_{T1}^* are the equivalent mass and equivalent moment of inertia for Equivalent Single-Story Model, respectively; \mathbf{f}_{RT} is the equivalent restoring force vector at the center of mass of floor diaphragms; \mathbf{d}_T is the equivalent displacement vector at the center of mass. The equivalent displacement of j -th frame in X- and Y-direction, d_{Xj}^* and d_{Yj}^* , are defined as Eq. (12), and the equivalent restoring force of j -th frame in X- and Y-direction, Q_{Xj}^* and Q_{Yj}^* , are defined as Eq. (13), respectively.

$$d_{Xj}^* = \Gamma_{S1} \Phi_{S1}^T \mathbf{M}_0 \mathbf{d}_{Xj} / M_{T1}^*, d_{Yj}^* = \Gamma_{S1} \Phi_{S1}^T \mathbf{M}_0 \mathbf{d}_{Yj} / M_{T1}^* \quad (12a, 12b)$$

$$Q_{Xj}^* = \Gamma_{S1} \Phi_{S1}^T \mathbf{f}_{RXj}, Q_{Yj}^* = \Gamma_{S1} \Phi_{S1}^T \mathbf{f}_{RYj} \quad (13a, 13b)$$

Where \mathbf{d}_{Xj} and \mathbf{d}_{Yj} are the displacement vector of j -th frame in X- and Y-direction, respectively; \mathbf{f}_{RXj} and \mathbf{f}_{RYj} are the restoring force vector of j -th frame in X- and Y-direction, respectively. The equivalent displacement of j -th frame in X- and Y-direction, d_{Xj}^* and d_{Yj}^* , can be expressed as Eq. (14).

$$d_{Xj}^* = X_1^* + l_{Yj} \Theta_1^*, d_{Yj}^* = Y_1^* - l_{Xj} \Theta_1^* \quad (14)$$

Where l_{Yj} and l_{Xj} are the distance from the center of mass to the j -th frame in X- and Y-direction, respectively. The equivalent restoring force of j -th frame in X- and Y-direction, Q_{Xj}^* and Q_{Yj}^* , can be expressed as Eq. (15).

$$Q_{Xj}^* = Q_{Xff}^* + Q_{Xdj}^*, Q_{Yj}^* = Q_{Yff}^* + Q_{Ydj}^* \quad (15)$$

$$Q_{Xff}^* = \Gamma_{S1} \Phi_{S1}^T \mathbf{f}_{RXff}, Q_{Yff}^* = \Gamma_{S1} \Phi_{S1}^T \mathbf{f}_{RYff} \quad (16a, 16b)$$

$$Q_{Xdj}^* = \Gamma_{S1} \Phi_{S1}^T \mathbf{f}_{RXdj}, Q_{Ydj}^* = \Gamma_{S1} \Phi_{S1}^T \mathbf{f}_{RYdj} \quad (17a, 17b)$$

Where Q_{Xff}^* and Q_{Yff}^* are the equivalent restoring force of reinforced concrete frame (RC frame + structural wall) at j -th frame in X- and Y-direction defined as Eqs. (16a) and (16b), respectively; Q_{Xdj}^* and Q_{Ydj}^* are the equivalent restoring force of seismic control devices at j -th frame in X- and Y-direction defined as Eqs. (17a) and (17b), respectively; \mathbf{f}_{RXff} and \mathbf{f}_{RYff} are the restoring force vector of reinforced concrete frame (RC frame + structural wall) at j -th frame in X- and Y-direction,

respectively; \mathbf{f}_{RXdj} and \mathbf{f}_{RYdj} are the restoring force vector of seismic control devices at j -th frame in X- and Y-direction, respectively. The equivalent restoring force vector of Equivalent Single-Story Model, \mathbf{f}_{RT} , can be expressed as Eq. (17).

$$\mathbf{f}_{\text{RT}} = \begin{Bmatrix} R_{X1}^* \\ R_{Y1}^* \\ M_{Z1}^* \end{Bmatrix} = \begin{Bmatrix} \sum \mathcal{Q}_{Xj}^* \\ \sum \mathcal{Q}_{Yk}^* \\ \sum \mathcal{Q}_{Xj}^* \cdot l_{Yj} - \sum \mathcal{Q}_{Yk}^* \cdot l_{Xk} \end{Bmatrix} = \begin{Bmatrix} \sum (\mathcal{Q}_{Xff}^* + \mathcal{Q}_{Xdj}^*) \\ \sum (\mathcal{Q}_{Yfk}^* + \mathcal{Q}_{Ydk}^*) \\ \sum (\mathcal{Q}_{Xff}^* + \mathcal{Q}_{Xdj}^*) \cdot l_{Yj} - \sum (\mathcal{Q}_{Yfk}^* + \mathcal{Q}_{Ydk}^*) \cdot l_{Xk} \end{Bmatrix} \quad (17)$$

The equivalent restoring force-equivalent displacement relationship of reinforced concrete frame and seismic control devices can be determined based on planer pushover analysis of each frame. In this paper, the pushover analysis is carried out considering the lateral force distribution regulated by Japanese Building Code, which is called A_i -force distribution and defined Eq. (18).

$$A_i = 1 + \left(\frac{1}{\sqrt{\alpha_i}} - \alpha_i \right) \cdot \frac{2T}{1 + 3T}, \alpha_i = \frac{W_i}{W} \quad (18a, b)$$

Where A_i is the design lateral shear distribution factor (design story shear divided by the weight above i -th story W_i), W is the total weight of building and T is the design natural period. The deflection shape vector $\mathbf{1}_{s1}\Phi_{s1}$ is assumed invert triangular shape to determine the properties of the Equivalent Single-Story Model.

3. BUILDING AND GROUND MOTION DATA

3.1 Building Data

Buildings investigated in this paper are two seven-story unsymmetric buildings as shown in Fig. 2. The first building is referred to as Model-O, which is the building model without any seismic control devices, and the second building is referred to as Model-S, which is the same structure as Model-O except seismic control devices: in Model-S, the brace-type elasto-plastic seismic control devices are installed as shown in Fig. 2(b). Their story height is 4.05m for the first story and 3.60m for upper stories. Their floor mass m_i and moment of inertia I_i are assumed 450ton and $3.19 \times 10^4 \text{tom}^2$, respectively. The compressive strength of concrete σ_B is assumed 45N/mm^2 , and SD390 ($\sigma_y = 390 \text{N/mm}^2$) is used for the longitudinal reinforcement and SD295 ($\sigma_y = 295 \text{N/mm}^2$) is used for the shear reinforcement. The dimension of the beams, columns and structural walls are the same in the whole building: sections of the beams and columns are $500 \text{mm} \times 700 \text{mm}$ and $650 \text{mm} \times 650 \text{mm}$, respectively, and the thickness of the structural wall is 250mm. The reinforcements of concrete

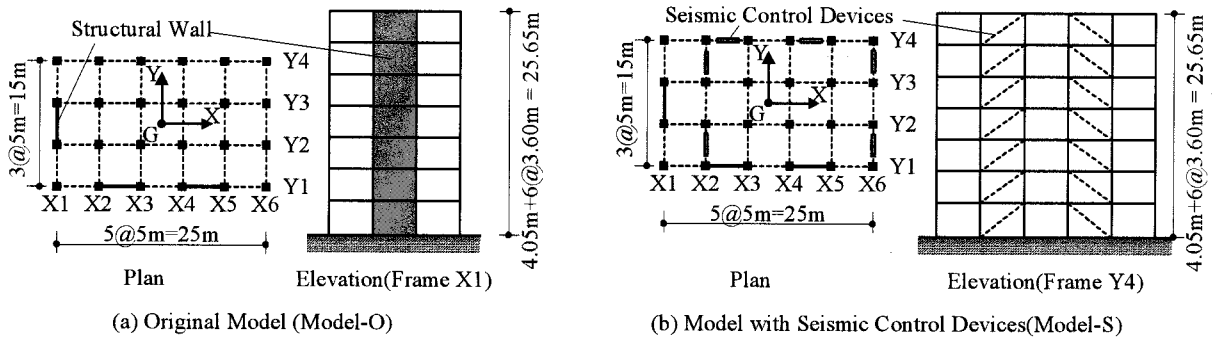


Figure 2 Model Structures

sections are determined so that the potential hinges are located at all beam-ends and bottoms of columns and structural wall in the first story, and shear reinforcement are provided enough to prevent premature shear failure. The crack moment M_c and yield moment M_y of each concrete member are calculated according to AIJ Design Guideline (AIJ, 1999). The base shear coefficient obtained from planar pushover analysis, which is the value when roof displacement reaches 1% of whole height, is 0.625 for X-direction and 0.531 for Y-direction.

The yield strength of the seismic control devices in first story is determined so that the contribution to story shear strength in each frame is $0.06W$, and the vertical distribution of seismic control devices in each story is assumed to be proportional to the design story shear coefficients A_i defined by Eq. (18). The dimensions of those seismic control devices are determined assuming that the yield stress of material used for seismic control devices is 100N/mm^2 .

The building structures are modeled as pseudo-three dimensional models: the floor diaphragms are assumed rigid in their own planes, and no out-of-plane stiffness, and the frames oriented in X- and Y-directions are modeled independently. All concrete beams, columns and structural walls are modeled as one-component model with nonlinear flexural spring at both ends and nonlinear shear spring at the middle of line element. To determine the flexibility of nonlinear flexural springs, anti-symmetric curvature distribution is assumed for beam and column, while uniform curvature distribution is assumed for structural wall. Figs. 3(a), (b) and (c) show the envelope curve of force-deformation relationship of each nonlinear spring. The envelopes are assumed symmetric in both positive and negative loading directions. For column and structural wall, their axial behavior is assumed elastic and no interaction is considered for axial-bending and bi-axial bending. Muto hysteretic model (Muto 1973) is employed for flexural spring with one modification as shown in Fig. 4: the unloading stiffness after yielding stage is modified as it decreases with proportional to $\mu^{-0.5}$ (μ : ductility ratio of flexural spring). Origin-oriented model is employed for shear spring of structural wall. The shear springs of beams and columns are assumed to be elastic.

The seismic control devices installed in Model-S are modeled as brace model with nonlinear axial spring and pins at both ends. Fig. 3(d) shows the envelope curve of force-deformation relationship of nonlinear spring. Normal bi-linear model is employed for seismic control devices.

Table 1 compares the natural periods of models obtained from (1) frame model and (2) Equivalent Single-Story Model. As shown in this table, the natural periods of Equivalent Single-Story Model is very close to those of frame model. Therefore it is expected that the nonlinear response of

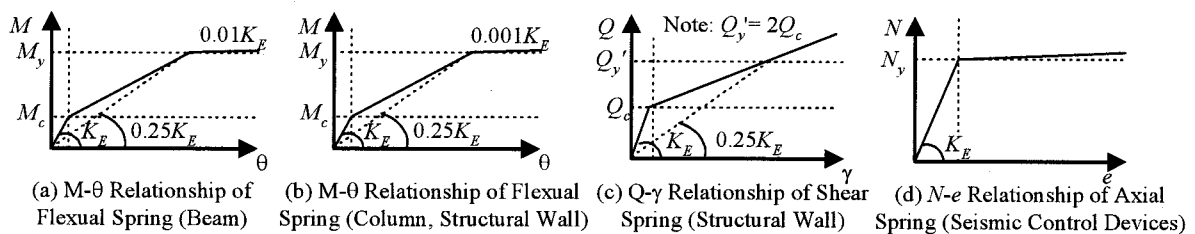


Figure 3 Envelope of Force-Deformation Relationship of Nonlinear Springs

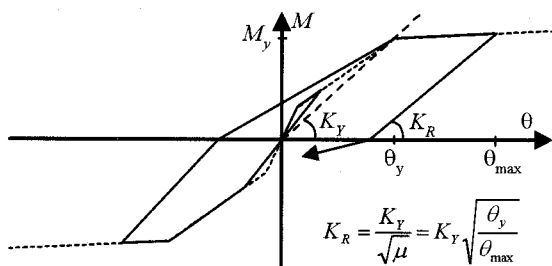


Figure 4 Hysteretic Model for Flexural Spring

Table 1 Natural Periods of Models

		Natural Periods		
		$T_1(\text{s})$	$T_2(\text{s})$	$T_3(\text{s})$
Model-O	(1)	0.434	0.333	0.232
	(2)	0.432	0.341	0.233
	(2)/(1)	0.996	1.024	1.004
Model-S	(1)	0.372	0.313	0.223
	(2)	0.370	0.319	0.223
	(2)/(1)	0.995	1.019	1.000

Note: (1) Frame Model, (2) Equivalent Single-Story Model

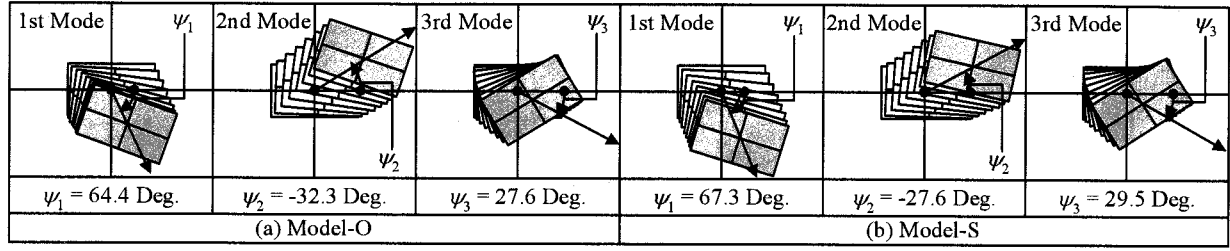


Figure 5 Mode Shapes in Elastic Range (Frame Model)

frame model can be approximated by the proposed Equivalent Single-Story Model.

Fig. 5 shows the mode shapes of frame models in elastic range. In this figure, the principal directions of the i -th modal response obtained by Eq. (19) are also shown.

$$\tan \psi_i = - \frac{\sum_j m_j \phi_{Yji}}{\sum_j m_j \phi_{Xji}} \quad (19)$$

Where the $\phi_i^T = \{\phi_{X1i} \cdots \phi_{XNi} \quad \phi_{Y1i} \cdots \phi_{YNi} \quad \phi_{\Theta 1i} \cdots \phi_{\Theta Ni}\}$ is the i -th natural mode of frame model. In this paper, the principal direction of modal response is defined as the direction that produces the largest i -th modal mass ratio. As shown in this figure, the difference of the principal directions in Model-O and Model-S is negligibly small.

3.2 Ground Motion Data

In this study, the earthquake excitation is considered bi-directional in X-Y plane, and three sets of artificial ground motions are used. The first 40.96 seconds ($2^{12} = 4096$ data, 0.01 second sampling) of two horizontal components (major and minor horizontal component) of the following records are used to determine phase angles of the ground motion: El Centro 1940 (referred to as ELC), Tohoku University 1978 (TOH), and Fukiai 1995 (FKI). Target elastic spectrum of “major” components with 5% of critical damping $S_A(T, 0.05)$ is determined by Equation (20):

$$S_A(T, 0.05) = \begin{cases} 4.8 + 45T & \text{m/s}^2 \quad T < 0.16s \\ 12.0 & 0.16s \leq T < 0.864s \\ 12.0 \cdot (0.864/T) & T \geq 0.864s \end{cases} \quad (20)$$

Where T is the natural period of the SDOF model. In this study, the target spectrum of “minor” components is reduced 0.67 from Eq. (20). Table 2 shows the set of artificial ground motions. Elastic acceleration response spectra of artificial ground motions with 5% of critical damping are shown in Fig. 6. In this paper, the “major” components are applied in the same direction as the principal direction of the first modal response of Model-O, while the “minor” components are applied in the

Table 2 Set of Artificial Ground Motion

	Max. Acc. (m/s ²)	
	“Major” component	“Minor” component
ELC	5.091	3.625
TOH	5.248	3.495
FKI	6.039	3.652

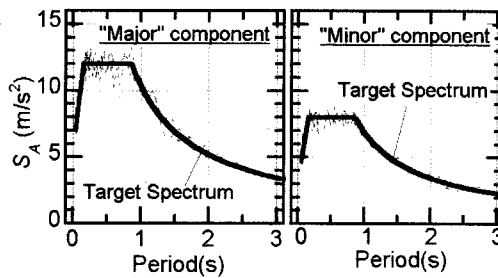


Figure 6 Elastic Response Spectra

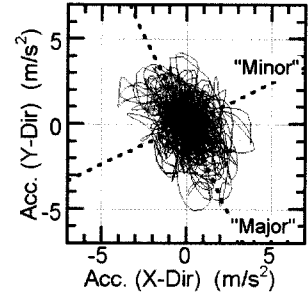


Figure 7 Orbit of Artificial Ground Motion

direction that lies at right angle with “major” components. Fig. 7 shows the orbit of the set of artificial ground motion obtained from TOH.

3.3 Numerical Analysis Procedure

In this study, the damping matrix is assumed proportional to the instant stiffness matrix without seismic control devices and 3% of the critical damping for the first mode. Newmark- β method ($\beta = 1/4$) is applied in numerical integrations. The time increment for numerical integration is 0.002 sec. The unbalanced force due to stiffness change is corrected at a next time step during analysis.

4. ANALYSIS RESULTS

Fig.8 shows the peak drift at frame X1, X4 and frame Y1 and Y6 of Model-O and Model-S (phase angle of input artificial ground motion: TOH). As shown in this figure, the seismic control devices installed in Model-S is significantly effective for the reduction of peak drift; the largest peak drift of Model-O is 2.51%, while that of Model-S is 1.22%. This figure also shows the peak drift estimated by the Equivalent Single-Story Model; the estimated peak drift are based on the pushover analysis results corresponds to the peak equivalent displacement d_{Xj}^* and d_{Yj}^* . This figure shows that Equivalent Single-Story Model can satisfactorily estimate the peak drift of frame model.

Figs. 9 and 10 show the comparisons of the peak drift at frame and cumulative plastic ductility ratio of seismic control devices η_D , respectively, estimated from the Equivalent Single-Story Model and those from frame model. The cumulative plastic ductility ratio of seismic control devices η_D estimated by the Equivalent Single-Story Model are based on the pushover analyses results and calculated from Eqs. (21) through (23).

$$\eta_{DXi,j} = \frac{W_{DXi,j}}{N_{yDXi,j} e_{yDXi,j}}, W_{DXi,j} = \left(W_{D0Xi,j} / \sum_i W_{D0Xi,j} \right) \cdot W_{DXj}^*, W_{DXj}^* = \int Q_{Xj}^* d_{Xj}^* \quad (21a, b, c)$$

$$\eta_{DYi,j} = \frac{W_{DYi,j}}{N_{yDYi,j} e_{yDYi,j}}, W_{DYi,j} = \left(W_{D0Yi,j} / \sum_i W_{D0Yi,j} \right) \cdot W_{DYj}^*, W_{DYj}^* = \int Q_{Yj}^* d_{Yj}^* \quad (22a, b, c)$$

$$W_{D0Xi,j} = \begin{cases} N_{yDXi,j} (e_{DXi,j} - e_{yDXi,j}) & e_{DXi,j} > e_{yDXi,j} \\ 0 & e_{DXi,j} \leq e_{yDXi,j} \end{cases}, W_{D0Yi,j} = \begin{cases} N_{yDYi,j} (e_{DYi,j} - e_{yDYi,j}) & e_{DYi,j} > e_{yDYi,j} \\ 0 & e_{DYi,j} \leq e_{yDYi,j} \end{cases} \quad (23a, b)$$

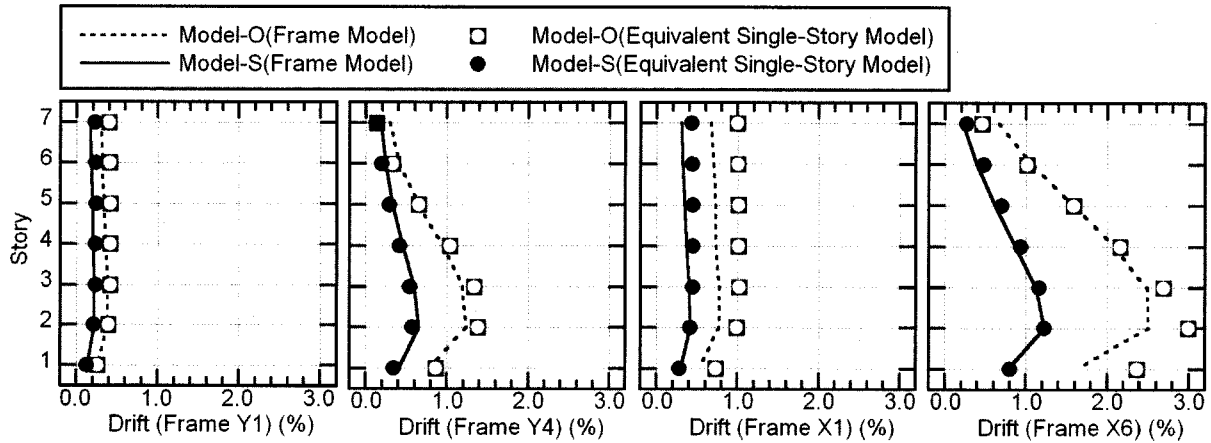


Figure 8 Peak Drift of Frame Y1, Y4, X1 and X6 (Phase angle of input artificial ground motion: TOH)

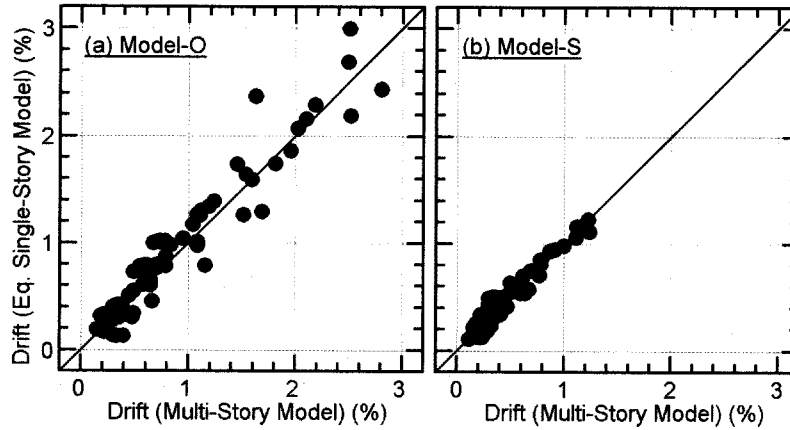


Figure 9 Comparisons of Peak Drift

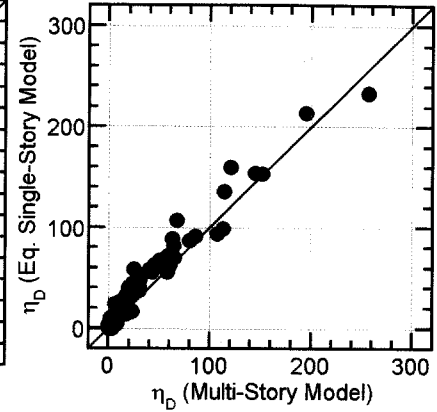


Figure 10 Comparisons of η_D

Where η_{DXij} and η_{DYij} are the predicted cumulative plastic ductility ratio of seismic control devices at i -story in j -th frame in X- and Y-direction, respectively; N_{yDXij} and N_{yDYij} are the yield axial strength of seismic control devices at i -story in j -th frame in X- and Y-direction, respectively; e_{yDXij} and e_{yDYij} are the yield axial deformation of seismic control devices at i -story in j -th frame in X- and Y-direction, respectively; e_{DXij} and e_{DYij} are the predicted axial deformation of seismic control devices at i -story in j -th frame in X- and Y-direction, respectively, obtained from pushover analysis; W_{DXj}^* and W_{DYj}^* are the dissipated energy seismic control devices at j -th frame in X- and Y-direction, respectively, obtained from Equivalent Single-Story Model. These figures show that Equivalent Single-Story Model proposed in this paper can predict the peak drift of frame and also the cumulative plastic ductility ratio of seismic control devices with good accuracy.

5. CONCLUSIONS

In this paper, the simplified 1-mass 3-degree-of-freedom model, named Equivalent Single-Story Model, is proposed for multi-story unsymmetric buildings with regular elevation, and the results of nonlinear time-history analysis of 7-story unsymmetric reinforced concrete frame building models with ductile structural walls rehabilitated by elasto-plastic brace-type seismic control devices obtained from three-dimensional frame building model are compared with those of proposed model. The results show that the proposed simplified model can satisfactorily estimate the response of three-dimensional frame building model.

References:

- Goel, R.K. (1998), "Effects of supplemental viscous damping on seismic response of asymmetric-plan systems", *Earthquake Engineering and Structural Dynamics*, Vol. 27, No. 2, 125-141.
- Goel, R.K. (2000), "Seismic behaviour of asymmetric buildings with supplemental damping", *Earthquake Engineering and Structural Dynamics*, Vol. 29, No. 4, 461-480.
- Goel, R.K. (2004), "Seismic response control of irregular structures using nonlinear dampers", *Proceedings of the 13th World Conference on Earthquake Engineering*, Paper No. 3242.
- Lin, W. and Chopra, A.K. (2001), "Understanding and predicting effects of supplemental viscous damping on seismic response of asymmetric one-storey systems", *Earthquake Engineering and Structural Dynamics*, Vol. 30, No. 10, 1475-1474.
- De la Llera, J. C., Almazán J. L., and Vial I. J. (2005), "Torsional balance of plan-asymmetric structures with friction dampers: analytical results", *Earthquake Engineering and Structural Dynamics*, Vol. 34, No. 9, 1089-1108.
- Architectural Institute of Japan, (1999), "Design Guidelines for Earthquake Resistant Reinforced Concrete Buildings Based on Inelastic Displacement Concept", 1999.8 (Japanese)
- Muto, K., Hisada, T., Tsugawa, T., and Bessho S. (1973), "Earthquake Resistant Design of a 20 Story Reinforced Concrete Buildings", *Proceedings of the 5th World Conference on Earthquake Engineering*, 1960-1969

SPECTRUM-BASED PREDICTION RULE FOR PEAK STRUCTURAL RESPONSES OF SDOF SYSTEM POUNDING AGAINST RIGID STRUCTURES

T.B. Tran¹⁾ and K. Kasai²⁾

1) Post-doctoral Fellow, Structural Engineering Research Center, Tokyo Institute of Technology, Japan

2) Professor, Structural Engineering Research Center, Tokyo Institute of Technology, Japan

tthbinh@enveng.titech.ac.jp, kasai@serc.titech.ac.jp

Abstract: A spectrum method is proposed for predicting peak responses of a building that pounds against rigid adjacent structure(s) during an earthquake. This paper studies pounding problem fundamentally, in which the building is modeled as a SDOF system, while adjacent structures are considered rigid. Pounding is simulated using contact elements comprising of a spring and a dashpot (viscoelastic element). Based on free vibration and harmonic vibration both involving pounding, the equivalent period and damping of the SDOF system are obtained and used to predict peak displacements as well as collision force. Accuracy of the proposed method is demonstrated by mean of validation study that uses a variation of the structural properties, contact element properties, and six artificial earthquakes scaled to approximate the elastic design spectrum.

1. INTRODUCTION

1.1 Structural Pounding Problem

Pounding between adjacent buildings due to earthquake has been reported as one of the causes of severe structural damages (Bertero 1986, Rosenblueth and Meli 1986, Kasai and Maison 1997). This seismic hazard occurs mainly in highly constructed area where the separation distance is insufficient to accommodate the peak relative displacement between buildings (Kasai and Tran 2004, 2005).

Earthquake-induced structural pounding has been studied mostly using SDOF and a few with MDOF model. The collision between two buildings is often simulated by the use of contact elements, which become active only when contact is detected. Several types of contact elements such as linear spring, bilinear spring, nonlinear spring (Hertz law of contact), linear viscoelastic, or nonlinear viscoelastic elements have been used for pounding simulation (Wolf and Skrikerud 1980, Anagnostopoulos 1988, Chau and Wei 2001). Since most of the past studies concentrated into the mechanics of the systems examined, they are lack practical application for structural pounding.

Some authors have proposed simplified methods for this problem, such as, by linearizing the SDOF system pounding against rigid structure(s), equivalent stiffness was derived in different means from its hysteresis and was used to predict peak responses (Miller and Heidari 1986, Iwan 1977, Kasai and Patel 1990). These approaches, however, lack simplicity as well as sufficient verifications of accuracy. Moreover, they consider only a linear contact spring with no energy dissipation.

1.2 Objectives and Scopes

The objective is to propose simplified methods for estimating peak responses of buildings subjected to pounding. In this paper, the pounding problem is studied fundamentally, in which a building is modeled as the SDOF system, while adjacent buildings are considered rigid. Viscoelastic contact element is used, and a wide range of its stiffness and damping considered. Formulas for

equivalent period and damping of the SDOF system under pounding are presented, and they are combined with elastic response spectra to obtain peak responses. The method proposed is easy to use, and is applicable to both the harmonic and earthquake ground motions. The method is validated over numerous combinations of the structural properties, contact element properties, and earthquakes.

The study can be applied for the assessment of the peak responses which are required for preliminary design purposes. The proposed method also serves as a basic method that will be extended for a wide variety of pounding situations involving not only SDOF systems but also MDOF systems.

2. MODELING OF POUNDING PROBLEM

Consider a SDOF system with mass m , stiffness k , and viscous damping coefficient c . It pounds against adjacent rigid wall(s) when absolute magnitude of displacement, $|u(t)|$, exceeds either separation distance s^+ (> 0) on the right side, or s^- (> 0) on the left side.

Viscoelastic contact elements on the right and left sides have stiffnesses k_s^+ and k_s^- , damping coefficients c_s^+ and c_s^- , respectively.

The system is considered to be in *state 1* when not in contact and *state 2* when in contact with the wall. Elastic force F_e and damping force F_d are governed by u and \dot{u} as follows

$$F_e = ku, \quad F_d = c\dot{u} \quad (\text{State 1: } -s^- \leq u \leq s^+) \quad (1a,b)$$

$$F_e = ku + k_s^+(u - s^+), \quad F_d = (c + c_s^+)\dot{u} \quad (\text{State 2: } u > s^+) \quad (1c,d)$$

$$F_e = ku + k_s^-(u + s^-), \quad F_d = (c + c_s^-)\dot{u} \quad (\text{State 2: } u < -s^-) \quad (1e,f)$$

Clearly, stiffness and damping are added by the contact element when the state changes from 1 to 2; Hereby define the stiffness increase ratio κ^+ and κ^- , as well as damping increase ratio ζ^+ and ζ^- .

$$\kappa^+ = 1 + k_s^+/k, \quad \zeta^+ = 1 + c_s^+/c \quad (2a,b)$$

$$\kappa^- = 1 + k_s^-/k, \quad \zeta^- = 1 + c_s^-/c \quad (2c,d)$$

Let call vibration frequency of the system at state 1 as no-pounding vibration frequency ω_{np} , $\omega_{np} = \sqrt{k/m}$, and those at state 2 as pounding vibration frequencies ω_{pd}^+ and ω_{pd}^- . Hereafter, subscript 'np' and 'pd' stand for 'no pounding system' and 'pounding system', respectively. Thus,

$$\omega_{pd}^+ = \sqrt{\frac{k + k_s^+}{m}} = \sqrt{\kappa^+} \omega_{np}, \quad \xi_{pd}^+ = \frac{c + c_s^+}{2m\omega_{pd}^+} = \frac{\zeta^+}{\sqrt{\kappa^+}} \xi_{np} \quad (3a,b)$$

$$\omega_{pd}^- = \sqrt{\frac{k + k_s^-}{m}} = \sqrt{\kappa^-} \omega_{np}, \quad \xi_{pd}^- = \frac{c + c_s^-}{2m\omega_{pd}^-} = \frac{\zeta^-}{\sqrt{\kappa^-}} \xi_{np} \quad (3c,d)$$

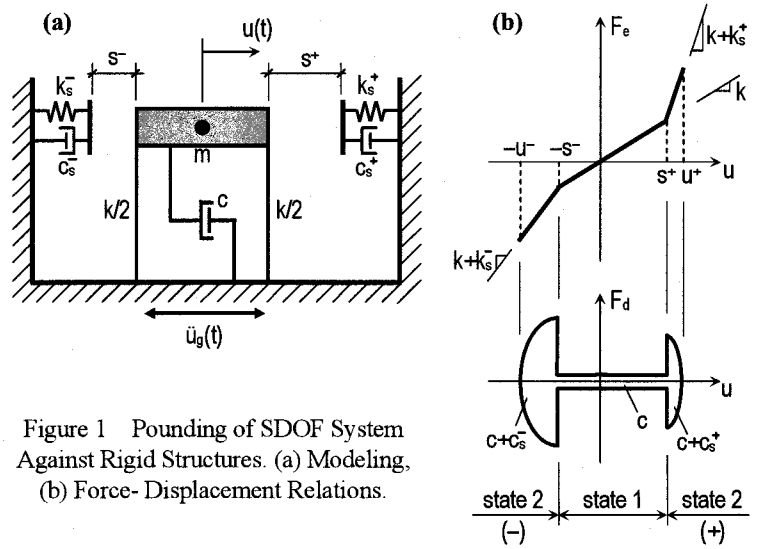


Figure 1 Pounding of SDOF System Against Rigid Structures. (a) Modeling, (b) Force- Displacement Relations.

3. FREE VIBRATION WITH POUNDING

3.1 Equivalent Vibration Period

At time $t = 0$, displacement $u = 0$ and velocity $\dot{u} = \dot{u}_{\max}$ are considered. Magnitude of \dot{u}_{\max} is given and $\dot{u}_{\max} > \omega_{np} s^+, \omega_{np} s^-$ so that displacement exceeds the separation distances. Considering undamped free vibration (Weaver et al. 1990), the vibration duration on each side can be obtained as follows

$$\Delta t^+ = \frac{T_{np}}{\pi} \left[\sin^{-1} \frac{\omega_{np} s^+}{\dot{u}_{\max}} + \frac{1}{\sqrt{\kappa^+}} \tan^{-1} \sqrt{\kappa^+ \left\{ \left(\frac{\dot{u}_{\max}}{\omega_{np} s^+} \right)^2 - 1 \right\}} \right] \quad (4a)$$

$$\Delta t^- = \frac{T_{np}}{\pi} \left[\sin^{-1} \frac{\omega_{np} s^-}{\dot{u}_{\max}} + \frac{1}{\sqrt{\kappa^-}} \tan^{-1} \sqrt{\kappa^- \left\{ \left(\frac{\dot{u}_{\max}}{\omega_{np} s^-} \right)^2 - 1 \right\}} \right] \quad (4b)$$

where $T_{np} = 2\pi / \omega_{np}$. Consequently, equivalent vibration period T_{eq} is defined as

$$T_{eq} = \Delta t^+ + \Delta t^- \quad (5)$$

Above equations can still be used for one-side also. For pounding at right only, Δt^+ is obtained from Eq. 4a; in contrast, $\Delta t^- = 0.5T_{np}$ instead of Eq. 4b is obtained, by setting $s^- = u^-$ and $\dot{u}_{\max} = \omega_{np} u^-$ (see Sec. 3.2) in Eq. 4b. Similarly for pounding at left, $\Delta t^+ = 0.5T_{np}$ instead of Eq. 4a.

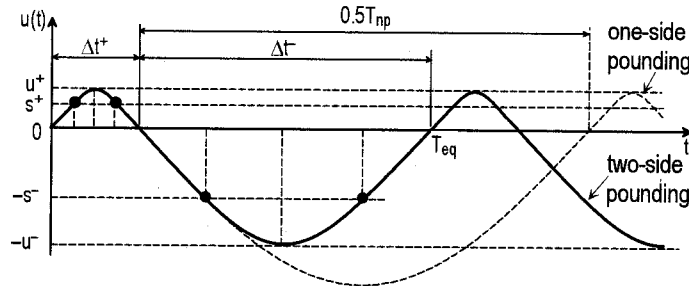


Figure 2 Time History of Undamped Free Vibration

3.2 Peak Displacement and Peak Velocity Relationship

The absolute values of positive and negative peak displacements, u^+ and u^- , can be expressed with \dot{u}_{\max} as follows

$$u^+ = s^+ \left[1 - 1/\kappa^+ + \sqrt{\{1/\kappa^+ - 1 + (\dot{u}_{\max} / \omega_{np} / s^+)^2\} / \kappa^+} \right] \quad (6a)$$

$$u^- = s^- \left[1 - 1/\kappa^- + \sqrt{\{1/\kappa^- - 1 + (\dot{u}_{\max} / \omega_{np} / s^-)^2\} / \kappa^-} \right] \quad (6b)$$

When pounding occurs only on the left side, peak displacement u^+ on the right side is expressed simply as $u^+ = \dot{u}_{\max} / \omega_{np}$, by setting $\kappa^+ = 1$ in Eq. 6a. Similarly, u^- when pounding on the right side only can be expressed as $u^- = \dot{u}_{\max} / \omega_{np}$ by setting $\kappa^- = 1$ in Eq. 6b.

Using Eq. 6 on the other hand, \dot{u}_{\max} can be expressed by either u^+ or u^- as follows:

$$\dot{u}_{\max} = \omega_{np} u^+ \sqrt{1 + (1 - s^+ / u^+)^2 \{(\kappa^+)^2 - 1\}} = \omega_{np} u^- \sqrt{1 + (1 - s^- / u^-)^2 \{(\kappa^-)^2 - 1\}} \quad (7)$$

4. HARMONIC VIBRATION WITH POUNDING

4.1 Equivalent Damping Ratio

Equivalent damping ratio ξ_{eq} is based on harmonic vibration and resonant state, where the excitation period T coincides with T_{eq} . The equation of motion at resonant state is given as:

$$m\ddot{u} + F_d(\dot{u}(t)) + F_e(u(t)) = -m\ddot{u}_{g0} \sin(2\pi t / T_{eq}) \quad (8)$$

In this section, T_{eq} , Δt^+ , Δt^- , u^+ , and u^- are assumed to be given and hold the relationship expressed by Eqs. 4 to 6. Such relationship from undamped vibration would hold even when damping exists, since it is governed by stiffness rather than damping. Displacement $u(t)$ is approximated in order to simplify calculation of hysteretic energy, which comprises two distinct half-sinusoidal curves with vibration frequencies $(\pi/\Delta t^+)$, $(\pi/\Delta t^-)$ for each side, respectively. Thus, energy E_D^+ dissipated by the viscous elements for $u(t) > 0$ (Fig. 3c) and energy E_D^- for $u(t) < 0$ are calculated respectively as

$$E_D^+ = c \frac{(\pi u^+)^2}{2\Delta t^+} \left[1 + \frac{2c_s^+}{\pi c} \left\{ \cos^{-1} \frac{s^+}{u^+} - \frac{s^+}{u^+} \sqrt{1 - \left(\frac{s^+}{u^+} \right)^2} \right\} \right] \quad (9a)$$

$$E_D^- = c \frac{(\pi u^-)^2}{2\Delta t^-} \left[1 + \frac{2c_s^-}{\pi c} \left\{ \cos^{-1} \frac{s^-}{u^-} - \frac{s^-}{u^-} \sqrt{1 - \left(\frac{s^-}{u^-} \right)^2} \right\} \right] \quad (9b)$$

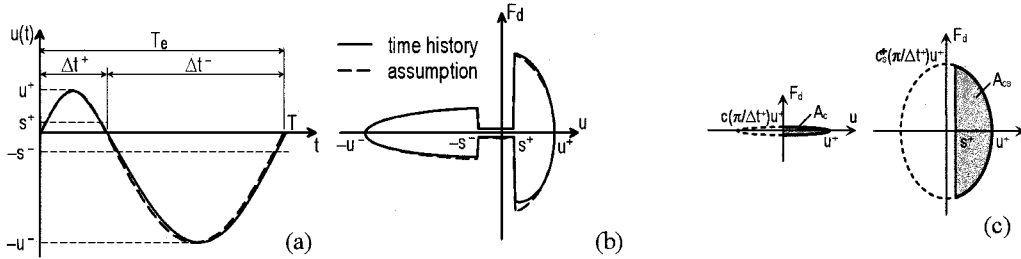


Figure 3 Steady State Response of Two-Side Pounding: (a) Time History, (b) F_d - u Relationship, (c) Calculation of Hysteretic Energy

Strain energy E_s on each side is assumed to be equal, and can be calculated using stiffnesses and peak displacements (Fig. 1b)

$$E_s = \frac{1}{2} k [1 + (\kappa^+ - 1)(1 - s^+/u^+)^2] (u^+)^2 = \frac{1}{2} k [1 + (\kappa^- - 1)(1 - s^-/u^-)^2] (u^-)^2 \quad (10a,b)$$

Based on these, equivalent damping ratio at resonance is given by

$$\xi_{eq} = \Delta \xi^+ + \Delta \xi^-; \quad \Delta \xi^+ = \frac{E_D^+}{4\pi E_s}, \quad \Delta \xi^- = \frac{E_D^-}{4\pi E_s} \quad (11a-c)$$

if pounding is on positive side only, set $s^- = u^-$ in Eq. 9b and use $\Delta t^- = 0.5T_{np}$ (Sec. 3.1), we have $\Delta \xi^- = 0.5\xi_{np}$. Similarly, if pounding is on negative side only, set $s^+ = u^+$ in Eq. 9a and use $\Delta t^+ = 0.5T_{np}$, we have $\Delta \xi^+ = 0.5\xi_{np}$.

4.2 Numerical Experiments of Harmonic Vibration

Numerical experiments are conducted using harmonic ground acceleration $\ddot{u}_{g0} \sin(2\pi t/T)$, where $\ddot{u}_{g0} = 0.6g = 588 \text{ cm/s}^2$ and T is varied over a wide range. We consider a system with $m = 50 \text{ ton}$, $k = 1973.92 \text{ kN/m}$, $c = 12.57 \text{ kN}\cdot\text{s/m}$. Therefore, $T_{np} = 1 \text{ s}$, $\xi_{np} = 0.02$, and peak steady state displacement of the no-pounding system at resonant excitation ($T = T_{np} = 1 \text{ s}$) is $u_{np} = \ddot{u}_{g0} / 2\omega_{np}^2 \xi_{np} = 3.72 \text{ m}$.

Both two-side pounding and one-side pounding are considered. For two-side pounding, separation distance is set equal on both sides, thus, $s^+ = s^- = s$. Four different values of $s = 0, 0.5, 1$, and 4 m are considered. For contact element, $k_s = 5921.76 \text{ kN/m}$ ($\kappa = 4$, and $T_{pd} = 0.5 \text{ s}$) is used, and c_s varied to consider 4 values of $\xi_{pd} = 0.01 \sim 0.40$ (Figs. 4, 5). Respective values of coefficient of restitution e (Anagnostopoulos 1988) are also shown. By varying excitation frequency $\omega (= 2\pi/T)$ and conducting time-history analysis, steady state displacement spectra are plotted in Figs. 4 and 5.

Fig. 4 shows two-side pounding cases, whereas Fig. 5 shows u^+ and u^- spectra of one-side pounding, respectively. For $s = 4 \text{ m}$ ($> u_{np} = 3.72 \text{ m}$), pounding is avoided and spectrum curves are identical irrespective of different ξ_{pd} -values, one-side or two-side pounding. Some comments follow for the case of $s = 0$: the system with two-side pounding (Fig. 4) will have vibration period of T_{pd} and damping ratio ξ_{pd} of the linear systems (Eq. 4). The system with one-side pounding (Fig. 5), in addition to the peak of harmonic response, the peak of so-called subharmonic response appears at twice the resonant frequency of the pounding system with $s = 0$ (Wolf and Skrikerud 1980). However, the subharmonic response does not seem to have any significant effect.

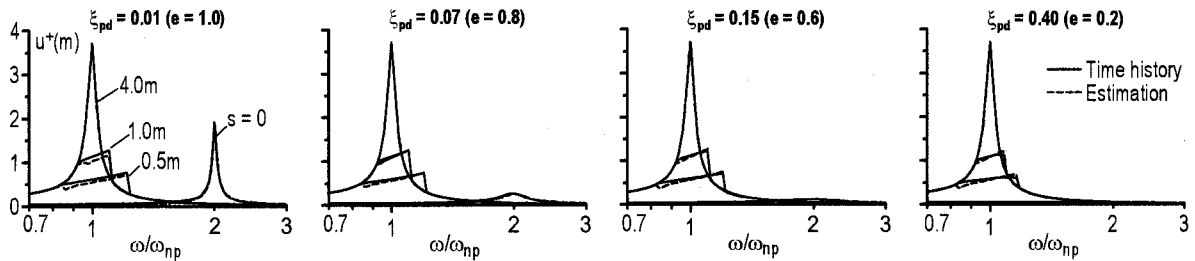


Figure 4 Displacement Spectra of Two-Side Pounding

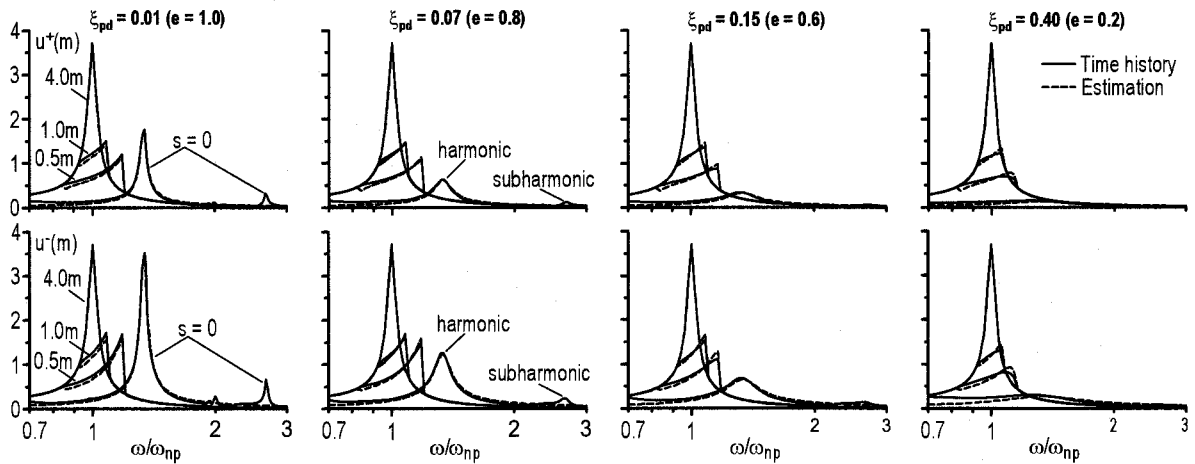


Figure 5 Displacement Spectra of One-Side Pounding

4.3 Prediction of Peak Harmonic Responses

This section presents a simplified method to estimate maximum response. The u^+ and u^- (Sec. 4.2) are estimated from Eq. 6, if \dot{u}_{\max} is given. It is assumed that \dot{u}_{\max} represents the peak velocity of an equivalent linear system having T_{eq} and ξ_{eq} (Eqs. 5, 11). But the T_{eq} and ξ_{eq} depend on \dot{u}_{\max} . Accordingly, iterations must be performed to obtain the value \dot{u}_{\max} . The method is summarized as follows: after setting initial values $T_{eq}^{(1)} = T_{np}$ and $\xi_{eq}^{(1)} = \xi_{np}$, the i -th iteration process is described below

- 1) Estimate $\dot{u}_{\max}^{(i)}$ (Eq. 12), and u^+ and u^- (Eq. 6).
- 2) Estimate $T_{eq}^{(i+1)}$ and $\xi_{eq}^{(i+1)}$ (Eqs. 5, 11).
- 3) Estimate $\dot{u}_{\max}^{(i+1)}$ (Eq. 12), and if $\dot{u}_{\max}^{(i+1)} \approx \dot{u}_{\max}^{(i)}$, the process ends.
- 4) Use accelerated estimate $\dot{u}_{\max}^{(i+1)} = (\dot{u}_{\max}^{(i+1)} + \dot{u}_{\max}^{(i)})/2$ and go to 1).

Note that $\dot{u}_{\max}^{(i)}$ is
$$\dot{u}_{\max}^{(i)} = \omega \ddot{u}_{g0} / \sqrt{((\omega_{eq}^{(i)})^2 - \omega^2)^2 + (2\xi_{eq}^{(i)} \omega_{eq}^{(i)} \omega)^2} \quad (12)$$

In order to assess the accuracy of the method, the values u^+ and u^- obtained from time history are utilized to obtain $\dot{u}_{\max}^{(1)}$ (Eq. 7). Then steps 2), 3), and 1) are followed and the results without further iterations are compared with the time-history analysis results (broken lines in Figs. 4,5). For both two-side and one-side pounding cases, the estimated curves match very well with exact ones from numerical analysis, especially near the peak of each curve.

5. PREDICTION OF SEISMIC POUNDING RESPONSES

5.1 Spectrum-Based Prediction of Peak Seismic Responses

The method proposed in Sec. 4.3 is also used for estimation of peak displacements caused by seismic pounding. However, instead of Eq. 12, \dot{u}_{\max} is estimated by using elastic design velocity spectrum. Using design spectrum, \dot{u}_{\max} still depends on equivalent T_{eq} and ξ_{eq} , and is expressed as

$$\dot{u}_{\max} = S_{pv}(T_{eq}, \xi_{eq}) = D_{\xi} \cdot S_{pv}(T_{eq}, \xi_{np}), \quad D_{\xi} = \sqrt{\frac{1 + \alpha \xi_{np}}{1 + \alpha \xi_e}} \quad (13a,b)$$

in above expression D_{ξ} = scaling factor for taking into account the effect of damping on spectra, where α depends on each particular earthquake. Some values of α are listed in Table 2 for several artificial earthquakes used in this study.

Using the peak displacements obtained after iteration, peak collision force will be calculated approximately as the square root of the sum of the peak forces developed in contact element's spring and dashpot element (Fig. 3c). Accordingly, the peak collision force developed when pounding on the right or left side will be written respectively as

$$F_c^+ = \sqrt{[k_s^+(u^+ - s^+)]^2 + [c_s^+(\pi / \Delta t^+) u^+]^2 [1 - (s^+ / u^+)^2]} \quad (14a)$$

$$F_c^- = \sqrt{[k_s^-(u^- - s^-)]^2 + [c_s^-(\pi / \Delta t^-) u^-]^2 [1 - (s^- / u^-)^2]} \quad (14b)$$

5.2 Validation of the Method

The validation study includes both one-side pounding and two-side pounding that considers same contact elements on both sides. For each pounding incident, it uses 8 systems with different T_{np} (Table 1) but having same $\xi_{np} = 0.02$. For each system, separation distances are varied through 10 values of separation ratios $s/u_{np} = 0.1$ to 1.0 at an increment of 0.1 . Two different cases of contact element stiffness are considered: in stiff contact case the contact element is much stiffer than the system's stiffness; while in soft contact case the contact element is assumed quite flexible such that $\kappa = 4$ for all systems (Table 1). For each analysis case above, dashpot of contact element is chosen to simulate three values of coefficient of restitution, $e = 0.9, 0.6$ and 0.2 .

For time-history analysis, 6 artificial earthquakes (Table 2) are considered in both positive and negative directions. These artificial earthquakes, which are scaled to Level 2, have similar spectrum characteristics and similar to the elastic design spectrum. Thus, results obtained from numerical

analysis can be used for investigating the accuracy of the proposed method. Fig. 6 shows the pseudo velocity spectra of these earthquakes (2% damping ratio), it also shows the elastic design spectrum that has pseudo velocity $S_{pv} = 140$ cm/s in the constant velocity domain (from 0.64 s).

Table 1 Systems Used in Validation Study.

System	1	2	3	4	5	6	7	8
T_{np} (s)	0.4	0.8	1.2	1.6	2.0	2.4	2.8	3.2
Stiff Contact Case	T_{pd} (s)	0.1	0.16	0.2	0.2	0.2	0.24	0.28
	κ	16	25	36	64	100	100	100
Soft Contact Case	T_{pd} (s)	0.2	0.4	0.6	0.8	1.0	1.2	1.4
	κ	4	4	4	4	4	4	4

Table 2 Artificial Earthquakes and α

Earthquake	α
Hachinohe EW	75
JMA Kobe NS	25
Tohoku NS	75
El Centro NS	55
Taft N111E	75
BCJ-L2	75

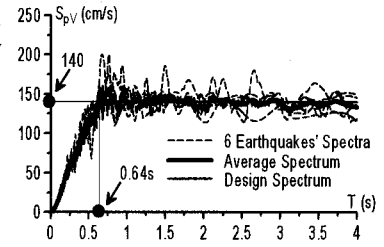


Figure 6 Spectra of Artificial Eq. and Design Spectrum.

The accuracy of the proposed method in estimating peak displacement is demonstrated through ratios between estimated and respective time-history analysis results. The graphs in Fig. 7 show the mean and standard deviation of these ratios vs. separation ratios, for each value of coefficient of restitution e . Thus, each value at a separation ratio is calculated from 96 ratios [8systems \times 6earthquakes \times 2directions].

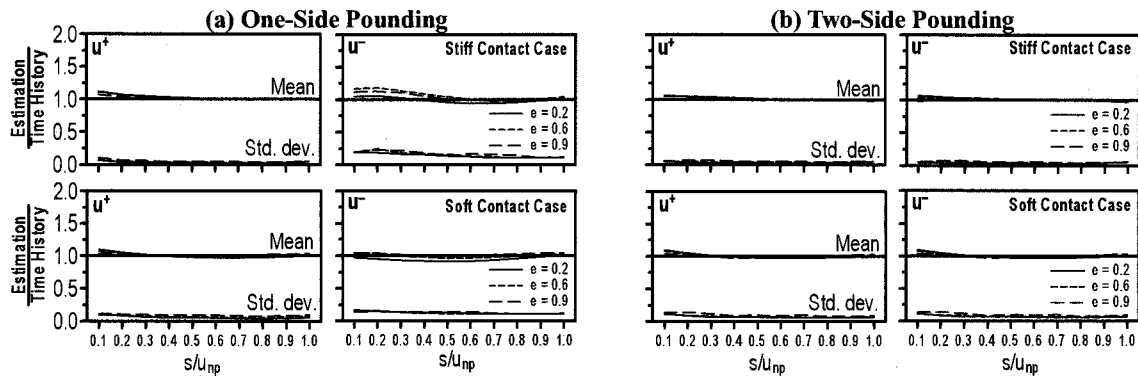


Figure 7 Accuracy of Estimated Peak Displacement.

For one-side pounding, Fig. 7a shows very close results between time-history analysis and estimation for u^+ , ratios for u^- are slightly scattered at s/u_{np} small but most of them still distributes near 1.0. Accuracy of the method does not significantly change between soft and stiff contact case. Similarly to results of one-side pounding, the proposed method predicts very well peak displacement

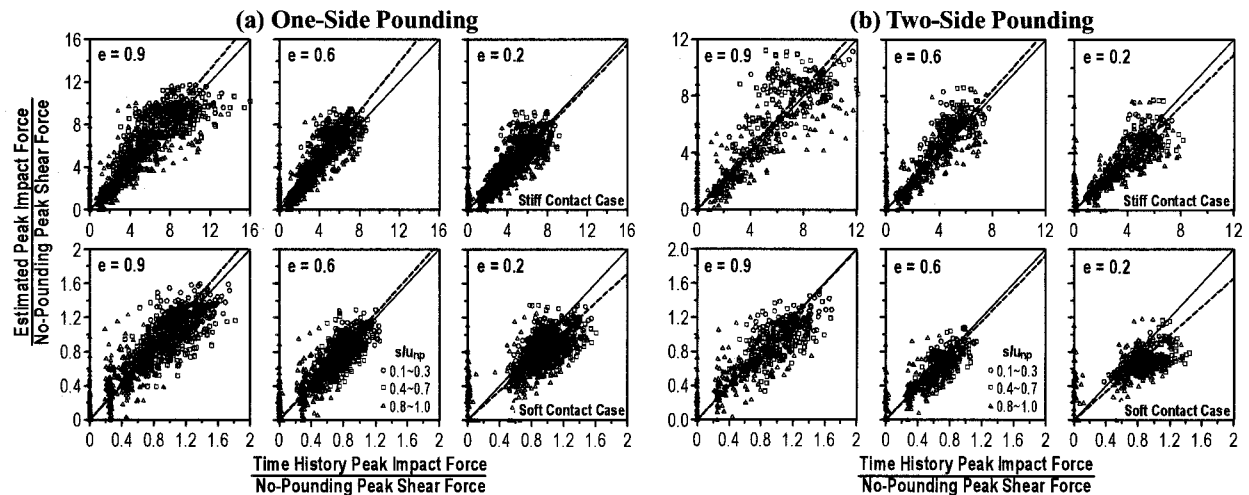


Figure 8 Accuracy of Estimated Peak Collision Force.

of symmetric two-side pounding (Fig. 7b).

Peak collision force is normalized with the respective peak shear force that would develop in the system if pounding did not occur (i.e. $k \cdot u_{np}$). Such normalized forces estimated by the proposed method are plotted against the accurate time-history analysis result in Fig. 8, where each data point corresponds to one analysis case. These graphs show good estimation, especially for pounding with small coefficient of restitution and soft contact element. This can be understood because contact element with large damping can effectively dissipate energy, while soft contact element reduces collision force.

6. CONCLUSIONS

This paper proposed the new spectrum-based prediction rule to estimate peak structural responses of a SDOF system pounding against rigid structures. The conclusions are as follows

(1) Collision is modeled using viscoelastic elements. This idealization is consistent with SDOF system used and appears adequate for study the effects of pounding on the overall building responses.

(2) The spectrum-based prediction rule is based on analytical solution of free vibration and harmonic vibration of the system to obtain equivalent period and damping, and uses them together with elastic design spectrum for estimation of peak responses.

(3) Using 6 artificial earthquakes that resemble the elastic design spectrum, the method is validated through extensive numerical experiments. The applicability of the method is shown and the correlation of estimated peak responses to time-history analysis results is very satisfactory.

The proposed method will serve as a basis that will be extend for structural pounding between two SDOF systems, as well as pounding of MDOF systems.

Acknowledgements:

The Ministry of Education, Science and Culture provided support for this study in the form of Monbu Kagakusho Scholarship given to the second author. The authors gratefully acknowledge the support.

References:

- Anagnostopoulos, S.A. (1988), "Pounding of Buildings in Series during Earthquakes," *Eq. Eng. Struct. Dyn.*, 16: 443-456.
- Bertero, V.V. (1986), "Observation of Structural Pounding," *Proc. International Conference: the Mexico earthquake-1985*, ASCE, 264-278.
- Chau, K.T. and Wei, X.X. (2001), "Pounding of Structures Modeled as Non-Linear Impacts of Two Oscillators," *Earthquake Eng. Struct. Dyn.*, 30: 633-651.
- Iwan, W.D. (1977), "Predicting Earthquake Response of Resiliently Mounted Equipment with Motion Limiting Constraints," *Proc. 6th WCEE* Vol. III: 3292-3297.
- Kasai, K. and Maison, B.F. (1997), "Building Pounding Damage During The 1989 Loma Prieta Earthquake," *Engineering Structures*, Vol.19, No.3, 195-207.
- Kasai, K. and Patel, D. (1990), "A Proposed Method of Evaluating Response for a Type of Collision between Adjacent Buildings," *Report No. IIT-CE-90-02*, Structural Engineering Series, Illinois Institute of Technology.
- Kasai, K. and Tran, T.B. (2004), "A Simplified Method to Predict Peak Value and Trend of Seismic Relative Motion Between Adjacent Buildings," *J. Struct. Constr. Eng.*, AIJ, No. 582: 47-55.
- Kasai, K. and Tran, T.B. (2005), "Simplified Method to Predict Relative Motion between Two Inelastic Structures Subjected to Time-Lagged Base Motions," *J. Struct. Constr. Eng.*, AIJ, No. 594: 75-83.
- Miller, R.K. and Heidari, M.A. (1986), "Approximate Analysis of Earthquake Response of Impacting Structures," *Proc. 8th WCEE*: 363-370.
- Rosenblueth, E. and Meli, R. (1986), "The 1985 Earthquake: Causes and Effects in Mexico City," *Concrete Journal*, American Concrete Institute, Vol.8, No.5, 23-24.
- Weaver, W. JR., Timoshenko, S.P., and Young, D.H. (1990), "Vibration Problems in Engineering," 5th Ed., John Wiley & Sons, US.
- Wolf, J.P. and Skrikerud, P.E. (1980), "Mutual Pounding of Adjacent Structures during Earthquakes," *Nuclear Eng. Design*, 57: 253-275.

SEISMIC SHUTOFF CHARACTERISTICS OF INTELLIGENT GAS METER DEPLOYED FOR INDIVIDUAL CUSTOMERS

Y. Maruyama¹⁾, F. Yamazaki²⁾, K. Nabana³⁾, and A. Yamauchi³⁾

1) Research Associate, Dept. of Urban Environment Systems, Chiba University, Japan

2) Professor, Dept. of Urban Environment Systems, Chiba University, Japan

3) Center for Disaster Management and Supply Control, Tokyo Gas Co., Ltd., Japan

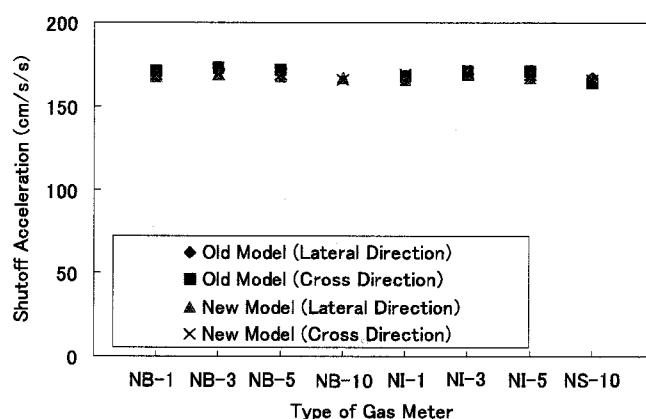
ymaruyam@tu.chiba-u.ac.jp, yamazaki@tu.chiba-u.ac.jp, k-nabana@tokyo-gas.co.jp, akko@tokyo-gas.co.jp

Abstract: After the 1995 Kobe earthquake, countermeasures against earthquakes got higher priority than before. As one of such earthquake countermeasures, Tokyo Gas Co., Ltd. introduced an earthquake monitoring and rapid damage assessment system called SUPREME. This system has been under operation since 2001. The intelligent gas meters have been deployed for 9.7 million customers in the area where Tokyo Gas Co., Ltd. provides the service. The gas meter stops gas supply if earthquake motion exceeds a certain level. SUPREME has a subsystem to estimate the number of gas meters which stop gas supply because of an earthquake. However, the accuracy of estimation by this subsystem is not good because the characteristics of gas supply shutoff by the intelligent gas meter are not so clear. In this study, to improve the accuracy of estimation, the characteristics of gas supply shutoff by the intelligent gas meter are investigated based on shaking table tests and the questionnaire survey among employees of Tokyo Gas Co., Ltd.

1. INTRODUCTION

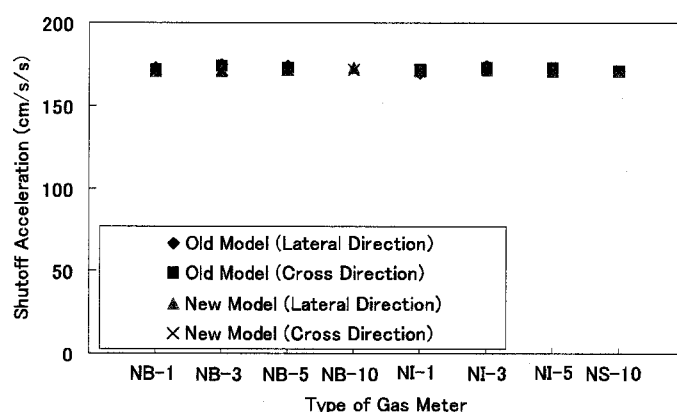
The 1995 Kobe earthquake caused serious damage to various infrastructures and buildings in the highly populated area of central-western Japan. The gas system in this area was also seriously affected (Oka, 1995; Yamazaki and Tong, 1996). After this earthquake, countermeasures against earthquakes got higher priority than before. As one of such earthquake countermeasures, Tokyo Gas Co., Ltd. introduced an earthquake monitoring and rapid damage assessment system (Yamazaki *et al.*, 1994; Yoshikawa *et al.*, 1995), SIGNAL (Seismic Information Gathering and Network Alert), with 331 SI-sensors in 1994. Expanding SIGNAL into a much denser seismic monitoring network with about 3800 SI-sensors, SUPREME (Super-Dense Real-time Monitoring of Earthquakes) has been under operation since 2001 (Yamazaki *et al.*, 2001). The SI sensors (Katayama *et al.*, 1988) measure the peak ground acceleration (PGA) and spectrum intensity (SI) at district regulator stations. The data from the network will be used for an early damage assessment of the city gas network of Tokyo Gas Co., Ltd. and the results will serve as important information for the decision making of the gas supply suspension.

The intelligent gas meters have been deployed for 9.7 million customers. The gas meter stops gas supply if earthquake motion exceeds a certain level. It is designed to shut off gas supply if the peak acceleration is in the range of 150-250 cm/s². SUPREME has a subsystem to estimate the number of gas meters which stop gas supply because of an earthquake. However, the accuracy of estimation by this subsystem is not good because the characteristics of gas supply shutoff by the intelligent gas meter are not very clear. Therefore, the subsystem sometimes overestimates the number of gas meters that shut off gas supply, and sometimes underestimates it.



Old Model: Until February 2003
New Model: From March 2003

(a) 0.3 s



Old Model: Until February 2003
New Model: From March 2003

(b) 0.7 s

Figure 1 Shutoff Acceleration of Various Types of Intelligent Gas Meters Conducted by Producteers (Sinusoidal waves with the period of 0.3 s and 0.7 s were applied.)

In this study, to improve the accuracy of estimation, the characteristics of gas supply shutoff by the intelligent gas meter are investigated based on the shaking table tests and the questionnaire survey among employees of Tokyo Gas Co., Ltd.

2. INVESTIGATION OF SEISMIC SHUTOFF CHARACTERISTICS OF INTELLIGENT GAS METER BASED ON SHAKING TABLE TESTS

2.1 Shutoff Characteristics under Sinusoidal Wave

Intelligent gas meters are designed to shut off gas supply if the acceleration in the range of 200-250 cm/s^2 is detected. The makers of gas meter are conducting product tests. In the tests, gas meters are subjected to sinusoidal waves with the period of 0.3 s and 0.7 s. Figure 1 shows the average cutoff accelerations among various types of intelligent gas meters. This figure suggests that the shutoff acceleration does not depend on the type of intelligent gas meters. The shutoff acceleration under sinusoidal wave with the period of 0.3 s is almost equal to that under sinusoidal wave with the period of 0.7 s. However, in the product testing, only two periods are adopted as the period of the applied sinusoidal waves. Therefore, for a further investigation of seismic shutoff characteristics of intelligent gas meter, it is necessary to consider the shutoff acceleration of gas meters subjected to sinusoidal

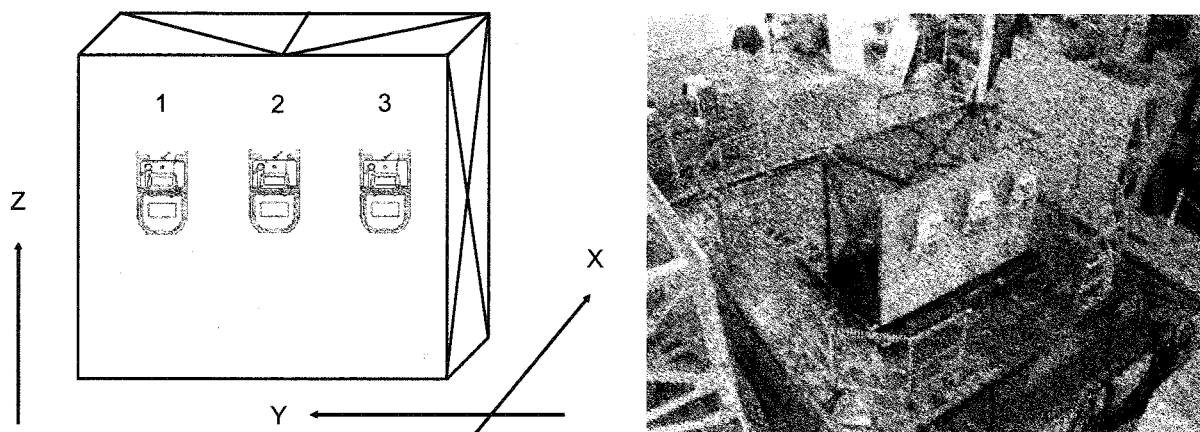


Figure 2 Shaking Table Test of Intelligent Gas Meters

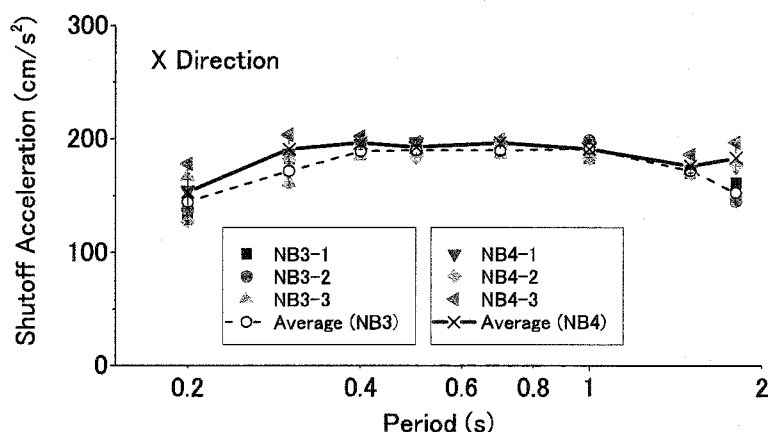


Figure 3 Shutoff Accelerations with respect to the Periods of Sinusoidal Waves Applied to the X Direction

waves with various periods.

In this study, a series of shaking table tests of intelligent gas meters was conducted. The shaking table possessed by Pipeline Technology Center, Tokyo Gas Co., Ltd. was employed in the experiment. The sinusoidal waves with the period of 0.2-1.8 s were applied to the gas meters fixed on the wall (Fig. 2). The amplitudes of sinusoidal waves increase with the interval of 5 cm/s^2 . The change of power voltage associated with the shutoff by gas meter was detected, so that the time when the gas meter shut off gas supply could be identified exactly. Two types of gas meters, which are NB-3 and NB-4, were used in the experiment. Three gas meters of each type were subjected to excitation.

Figure 3 shows the relationship between the period of applied sinusoidal waves and shutoff acceleration of intelligent gas meters. In the experiment, the sinusoidal waves were applied to the X direction (Fig. 2). According to the figure, the shutoff accelerations with the periods of 0.2 s and 1.8 s are a little smaller. However, the shutoff accelerations with the periods of 0.3-1.5 s are almost constant, and the shutoff acceleration is about 190 cm/s^2 . The differences between the shutoff accelerations of NB-3 type gas meter and those of NB-4 type were not observed in the period range, but the shutoff acceleration of NB-3 type is smaller than that of NB-4 type when the period of sinusoidal wave is equal to 1.8 s.

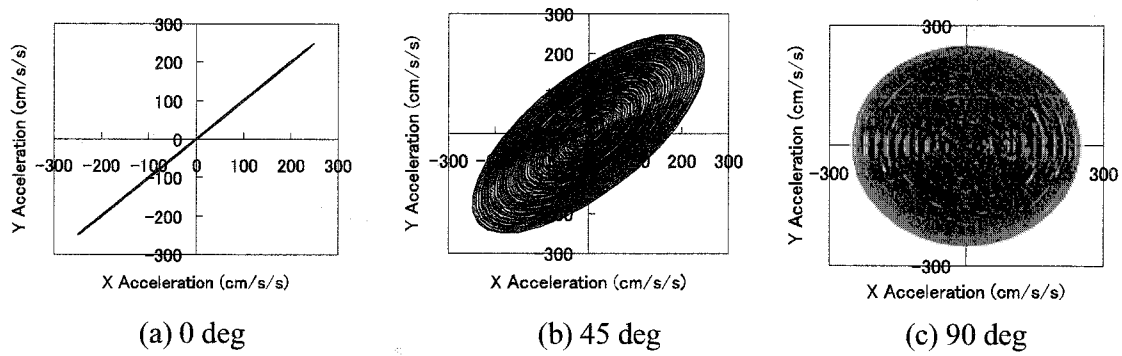


Figure 4 Orbits of Applied Accelerations to Intelligent Gas Meters (Two Directional Shaking)

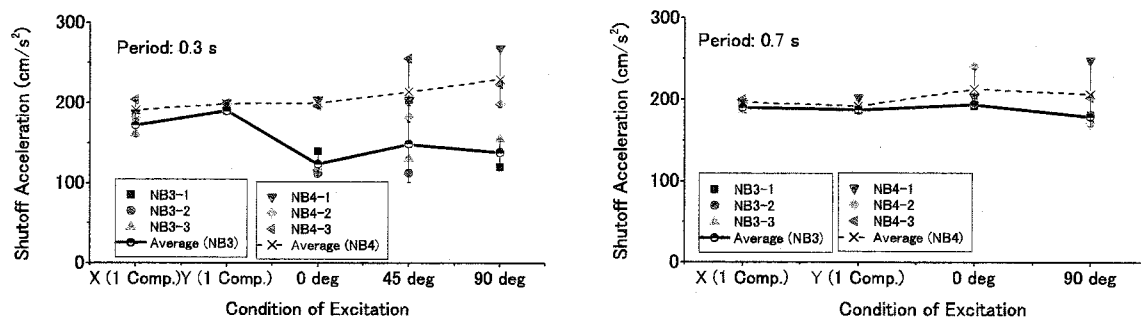


Figure 5 Shutoff (Resultant) Accelerations of Intelligent Gas Meters under Two Directional Excitations

The direction dependency of shutoff acceleration was investigated by applying sinusoidal waves to the two horizontal directions (X and Y axes). The phase lag was set to be 0 deg, 45 deg ($\pi/4$) and 90 deg ($\pi/2$), respectively (Fig. 4). Figure 5 shows the shutoff acceleration of intelligent gas meters with respect to the phase lag between the sinusoidal wave of X direction and that of Y direction. The shutoff acceleration of NB-3 type of gas meter depends on the condition of shaking when the period of the applied sinusoidal wave is set to be 0.3 s. In other cases, the shutoff accelerations are almost constant regardless of shaking condition.

2.2 Shaking Table Tests using Actual Seismic Motions

To evaluate the characteristics of seismic shutoff of intelligent gas meters revealed in the previous section, four sets of actual seismic motion records were used as input motions in the shaking table tests. Figure 6 shows the acceleration time histories used in this study: 1) the Kobe Marine Observatory record of Japan Meteorological Agency (JMA) in the 1995 Kobe earthquake, 2) the K-NET Tomakomai record in the 2003 Tokachi-Oki earthquake, 3) the K-NET Yokaichiba record in the North-eastern Chiba Prefecture earthquake (April 11, 2005), and 4) the Miyako-cho Tokyo Gas seismic observation station record in the North-western Chiba Prefecture earthquake (July 23, 2005). The Tomakomai record was selected as the typical long-period record. On the contrary, the K-NET Yokaichiba record was employed as the short-period seismic motion. The peak ground acceleration (PGA) of the record, which is obtained as the resultant of two horizontal components, was scaled to be 130-250 cm/s^2 . The scaled seismic motions were applied to the intelligent gas meters.

Table 1 shows the number of gas meters which shut off gas supply because of ground shaking. It should be noted that the K-NET Tomakomai record whose PGA is equal to 130 cm/s^2 could not be

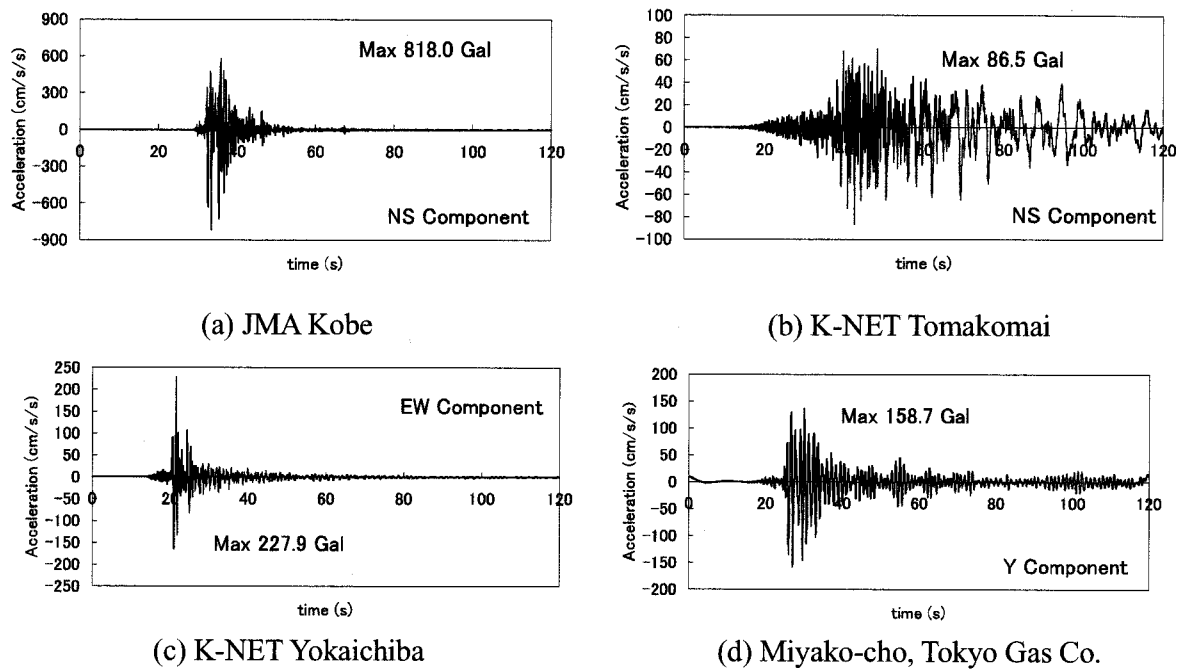


Figure 6 Acceleration Time Histories used in the Shaking Table Tests

Table 1 The number of intelligent gas meters which shut off gas supply during the shaking table test

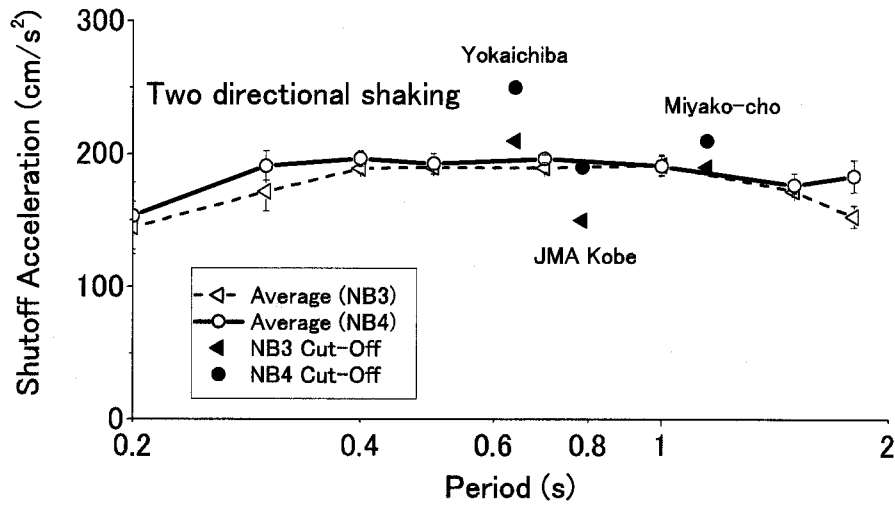
PGA (cm/s ²)	JMA Kobe		Miyako-cho, Tokyo Gas		K-NET Yokaichiba	
	NB-3	NB-4	NB-3	NB-4	NB-3	NB-4
130	0	0	—	—	—	—
150	3	0	—	0	—	—
170	3	0	0	0	0	0
190	—	3	3	2	1	0
210	—	—	—	3	3	1
230	—	—	—	—	—	1
250	—	—	—	—	—	3

applied to the shaking table because of the limitation of actuators. Therefore, the result under the K-NET Tomakomai record is not listed in Table 1. The gas meters did not shut off gas supply under the non-scaled K-NET Tomakomai record. According to the result, the gas meters of NB-3 type shut off gas supply under smaller seismic motion than those of NB-4 type especially for the JMA Kobe record.

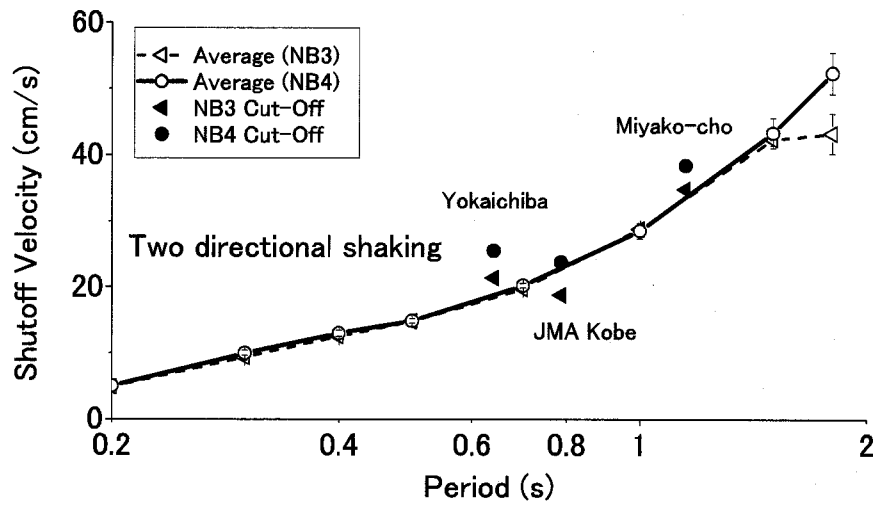
Figure 7 compares the results of shaking table tests using sinusoidal waves and actual ground motion records. The period of seismic motion was determined by Eq. (1).

$$T = 2\pi \frac{PGV^*}{PGA^*} \quad (1)$$

where T is the period of seismic motion. PGA^* and PGV^* are the peak ground acceleration and the peak ground velocity by the resultant of two horizontal components, respectively. Figure 7 illustrates the shutoff accelerations and shutoff velocities when all the three gas meters shut off gas supply under seismic motion. According to the figure, the shutoff acceleration under the K-NET Yokaichiba record



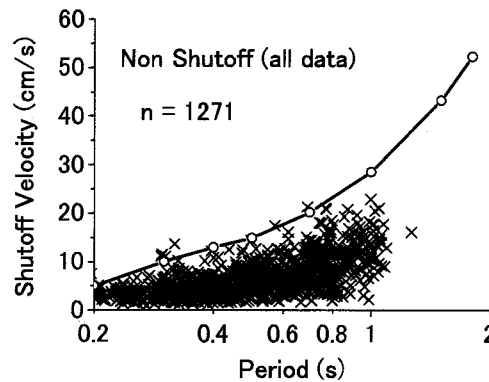
(a) Shutoff Acceleration



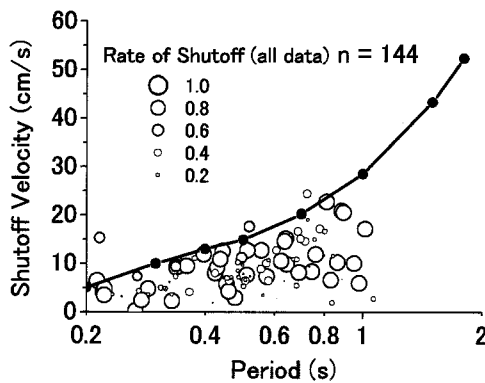
(b) Shutoff Velocity

Figure 7 Comparisons of the Shutoff Accelerations and the Shutoff Velocities between under Seismic Motions and Sinusoidal Waves

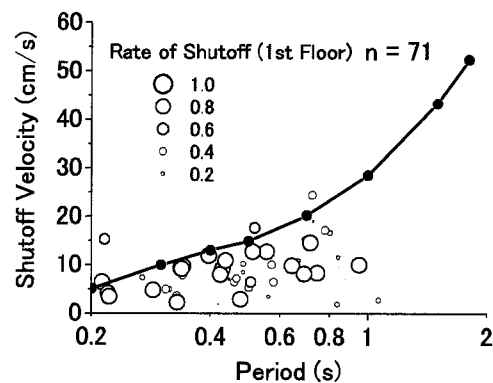
is larger than that obtained under sinusoidal waves. As is mentioned before, the K-NET Yokaichiba record was selected as an example of short-period record. The peak ground acceleration is dependent on the short-period components of ground excitation. This indicates that the intelligent gas meters may not be sensitive to the short-period ground motions. When the PGV is used to show the shutoff of the gas meters (Fig. 7(b)), the results obtained from the seismic motions coincide with those obtained from sinusoidal waves. The PGV does not depend on the short-period components of ground motion, so the results under the K-NET Yokaichiba record show good agreement with those under sinusoidal waves.



(a) Non-shutoff



(b) Ratio of Shutoff (All Data)



(c) Ratio of Shutoff (1st Floor)

Figure 8 Relationship between the Period of Seismic Motion and the PGV Allocated to the Responders of the Questionnaire Survey

3. QUESTIONNAIRE SURVEY ON SEISMIC SHUTOFF OF INTELLIGENT GAS METERS

On July 23, 2005, the North-western Chiba Prefecture earthquake occurred. The JMA magnitude of this earthquake was 6.0. The Tokyo Metropolitan area suffered from this earthquake, and the lifelines, especially, train services and road traffic networks stopped because of the earthquake.

The intelligent gas meters perceived the seismic motion, and they shut off gas supply. In order to reveal the effects of seismic motion to the shutoff behavior of intelligent gas meters, the questionnaire survey was conducted for employees of Tokyo Gas Co., Ltd. In the questionnaire, the responders were asked to answer the address of residence, what floor they live on, and whether the gas meter stopped due to the earthquake or not.

From the addresses of responders, the seismic intensity was allocated using the nearest record of SI-sensors deployed by Tokyo Gas Co., Ltd. In SUPREME, the spectrum intensity (SI) and the PGA recorded by SI-sensors can be monitored and gathered at an early stage of the earthquake. Therefore, these two seismic indices were adopted in the analysis. The SI was converted to the PGV using the relationship by Tong *et al.* (1994) shown in Eq. (2).

$$SI = 1.18PGV \quad (2)$$

The period of seismic motion was determined by Eq. (1). Figure 8(a) shows the relationship between

the period of seismic motion and the PGV for the gas meters that did not shut off gas supply. Figure 8 (b) and (c) show the relationship between the period and PGV for the gas meters that shut off gas supply. The size of the circle means the rate of shutoff by gas meters in Fig. 8(b) and (c). The ratio of shutoff was calculated based on the all data (located within 500 m from the nearest seismic observation station) of the questionnaire survey in Fig. 8(b). Figure 8(c) shows the ratio of shutoff calculated from the results of the responders who live on the 1st floor of an apartment building or in two or one storied house. In Fig. 8, the results of the shaking table test using the sinusoidal waves are also illustrated.

According to the figure, the symbols that show the non-shutoff gas meters are mainly concentrated in the lower part of the line drawn from the results of the experiments. The symbols in Fig. 8(b) spread out comparing with the result of Fig. 8(c). This is because the seismic responses of the buildings affect the behavior of shutoff characteristics of intelligent gas meters. This suggests that the effects of the structural response to seismic motion should be considered to predict the number of shutoff gas meters.

4. CONCLUSIONS

In this study, to investigate the characteristics of seismic shutoff of intelligent gas meters, a series of shaking table tests were conducted. The intelligent gas meters were subjected to the sinusoidal waves with various periods and four sets of actual seismic motion records. According to the results, the characteristics of seismic shutoff of gas meters estimated by applying sinusoidal waves coincided with the results of experiments under actual seismic records. The questionnaire survey to reveal the characteristics of seismic shutoff during the 2005 North-western Chiba Prefecture earthquake was conducted among the employees of Tokyo Gas Co., Ltd. The results of the questionnaire survey were compared with those of the shaking table tests. To predict the number of intelligent gas meters that detect the seismic motion, the seismic response of structures and the spatial distribution of seismic intensity should be considered in proper manner.

Acknowledgements:

The authors appreciate Mr. M. Mitsuya and Mr. H. Sugahara, Pipeline Technology Center, Tokyo Gas Co., Ltd., for their efforts in the shaking table tests.

References:

- Katayama, T., Sato, N. and Saito, K. (1988), "SI-sensor for the identification of destructive earthquake ground motion." *Proc. of the 9th World Conference on Earthquake Engineering*, 7, 667-672.
- Oka, S. (1995), "Damages of gas facilities by great Hanshin earthquake and restoration process," *Proc. of the 6th U.S.-Japan Workshop on Earthquake Disaster Prevention for Lifeline Systems*, 253-269.
- Tong, H., Yamazaki, F., Sasaki, H. and Matsumoto S. (1994), "A relationship between seismic ground motion severity and house damage ratio," *Proc. of the Ninth Japan Earthquake Engineering Symposium*, 2299-2304.
- Yamazaki, F. and Tong, H. (1996), "Damage and restoration of natural gas system in the 1995 Kobe Earthquake." *The 1995 Hyogoken-Nanbu Earthquake -Investigation into Damage to Civil Engineering Structures-*, Japan Society of Civil Engineers, 219-227.
- Yamazaki, F., Noda, S. and Meguro, K. (1998), "Developments of early earthquake damage assessment systems in Japan." *Structural Safety and Reliability: Proceedings of the 7th International Conference on Structural Safety and Reliability*, 1573-1580.
- Yamazaki, F., Shimizu, Y., Nakayama, W., Koganemaru, K., Ishida, E. and Isoyama, R. (2001), "New development of super-dense seismic monitoring and damage assessment system for city gas networks." *Proceedings of the 8th International Conference on Structural Safety and Reliability*, CD-ROM, 8p.
- Yoshikawa, Y., Kano, H., Yamazaki, F., Katayama, T. and Akasaka, N. (1995), "Development of SIGNAL: An early warning system of city gas network." *Proc. of 4th U.S. Conference on Lifeline Earthquake Engineering*, ASCE, 160-167.

A SHAKING TABLE TEST OF 2 STORY R/C FRAMES WITH PARTIAL WALLS INDEPENDENT FROM COLUMNS

H. Hotta¹⁾ and T. Nakajima²⁾

1) Associate Professor, Dept. of Architecture and Building Engrg., Tokyo Institute of Technology, Japan

2) Graduate Student, Dept. of Architecture and Bld. Engrg., Graduate School, Tokyo Institute of Technology, Japan
hotta@arch.titech.ac.jp, tnakj3@mail.arch.titech.ac.jp

Abstract: Walls connected to the upper and the lower beams and apart from the both side columns, called briefly “partial walls” in this paper, are popular exterior walls in Japanese condominium. The influence of shear failure of those walls on the behavior of the structure is investigated through a shaking table test by means of two numbers of 2 story R/C frames with 1/8 scale as specimens. As a conclusion of this study, a result obtained by a simple seismic response analysis for single degree of freedom model with tri-linear restoring force characteristic which approximates static test result well explains the response obtained from the shaking table test, and shear failure of a wall makes the story drift at the story where the failed wall exists progress more than other story.

1. INTRODUCTION

Walls connected to the upper and the lower beams, however, apart from the both side columns, briefly called “partial walls” in this paper, are very popular as exterior walls in a large number of buildings, especially in apartment houses in Japan. In many cases, they had not been regarded as structural elements, because they did not satisfy the requirements for bearing walls, and their presence had been ignored in structural calculation until about decades ago for a long time. However, if slightly, they have a certain lateral stiffness and strength, therefore they have some influence on the structure, and it is necessary to grasp it adequately, and that become more important in a recent performance based design.

In the previous paper presented in the 1st International conference conducted by CUEE, we reported the influence of the flexural yield type walls and concluded that elongation of the walls due to flexural yielding sometimes influenced much to the strength themselves and the behaviors of the beams connected to them. This paper deals with a case that the walls expected to fail with shear failure mode prior to yield due to bending. In this case, it is considered that there is some fear that brittle failure of a wall at a certain story may cause the story collapse.

The method of the investigation is a shaking table test, because the brittle behavior should be grasped in a dynamic test. The testing machine is the one designed and produced in CUEE in 2004 and it contains a one-directional sliding table with 100cm×120cm rectangular area and an actuator with the max. loading capacity of 500kN and the max. velocity of 50cm/s, as shown in Fig.1. The design full payload is 5tons.



Figure 1 Photographic view of testing machine

2. SPECIMENS AND TESTING METHOD

2.1 Specimen

Two specimens as illustrated in Fig.2, in which a typical one with 12cm wide partial walls is illustrated, were provided for the shaking table test. They are 1/8 scale model of actual dimensions and have span length of 80cm and story height of 40cm. There is a partial wall at mid-span at every story. The members, that is, columns, beams, and partial walls have the dimensions as described in Table 1 and as detailed in Fig.3. The difference between two specimens is only width of the partial wall. One has 12cm wide walls and another has 15cm wide ones. The walls are designed to fail due to shear before flexural yielding and hoop ratio of the wall is 0.6%. By contrast, the beams and the columns are sufficiently strengthened against shear. The frame is designed based on 'weak beam and strong column concept' when the presence of the walls is ignored, however, the column does not have more than enough strength, therefore there is minute provability that the story collapse will occur at the story where the wall fails formerly due to shear. Mechanical properties of the concrete and the reinforcement are shown in Table 2.

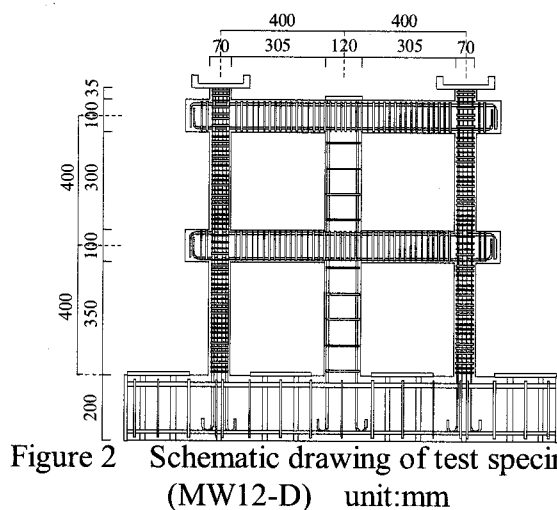


Figure 2 Schematic drawing of test specimen (MW12-D) unit:mm

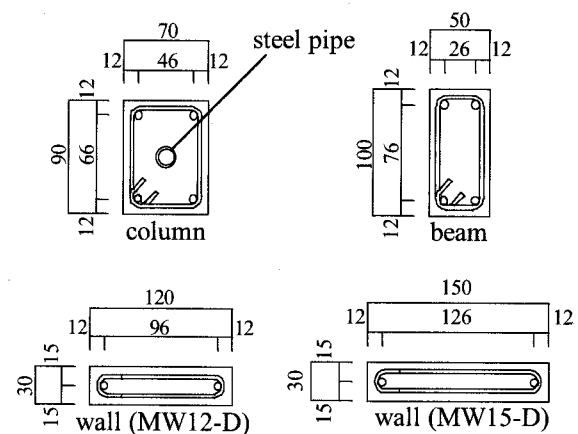


Figure 3 Section of members unit:mm

Table 1 Section detail of members

Specimen		MW12-D	MW15-D
column	b×D(mm)	90×70	
	Main reinforcement	4-D6 $p_g=2.01(\%)$	
	Hoop reinforcement	2-3 ϕ @15 $p_w=1.05(\%)$	
beam	b×D(mm)	50×100	
	Main reinforcement	4-D6 $p_g=2.53(\%)$	
	Hoop reinforcement	2-3 ϕ @18 $p_w=1.57(\%)$	
wall	b×D(mm)	30×120	30×150
	Main reinforcement	2-D6 $p_g=1.76(\%)$	2-D6 $p_g=1.41(\%)$
	Hoop reinforcement	2-3 ϕ @79	$p_w=0.6(\%)$

Table 2 Mechanical properties of concrete and reinforcing bars

Concrete			
Age	Compressive strength(MPa)	Tensile strength(MPa)	Young's modulus(Mpa $\times 10^3$)
29	30.0	2.96	27.2
Reinforcing bars			
Size	Yield strength(MPa)	Tensile strength(MPa)	Young's modulus(Mpa $\times 10^3$)
D6	334	495	197
3#	493	663	201

2.2 Method of loading and measuring

The outline of the setup is illustrated in Fig.4. Because the specimen is a small scale model, some additional mass is required. In this test, four steel plates with 1m square and about 6cm thick are used as the additional mass, which are illustrated in the figure as hatched square. How the mass is connected to the specimen is detailed in Fig.5. A H-shaped beam is set at the top of the specimen and connected with the top of the column by pin connections. The additional mass, namely, steel plates are fastened by PC bars, and the block of the plates is attached at the lower surface of the H-shaped steel. The total mass of the plates, the H-shaped steel and so on is 1.97tons and its center of gravity is almost coincident with the central point of the second story beam. The H-shaped steel above mentioned also plays the role of restricting axial elongation of the wall. By this restriction, it is considered that the specimen shows almost the same behavior as lower 2 stories of a middle-rise building shows. The axial force of the columns due to the mass is shorter than design axial compression of 0.15 bDFc(18.6kN), therefore the lack is filled up by pulling PC bars vertically running through the center of the columns.

The measuring responses are as follows: absolute acceleration at every story including the ground(the upper surface of the stub), absolute acceleration of the additional mass, absolute horizontal displacement of every story including the ground(both the stub and the shaking table), axial elongation of the columns and the walls and the axial force of the columns induced by the PC bars.

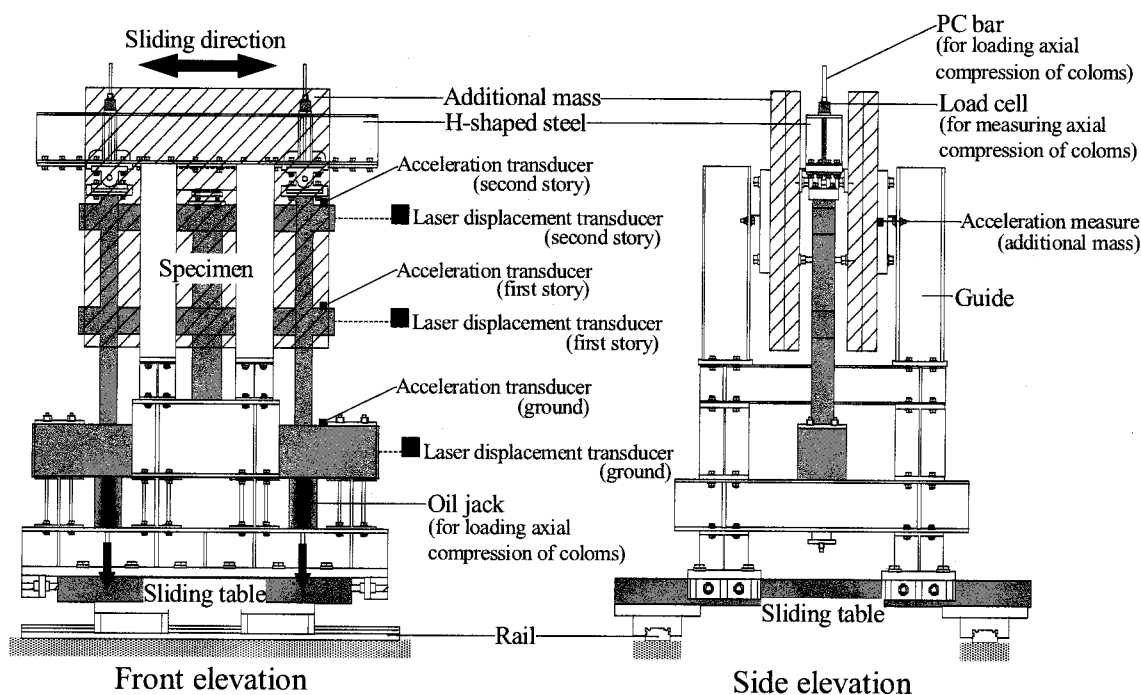


Figure 4 Schematic drawing of loading setup and measuring

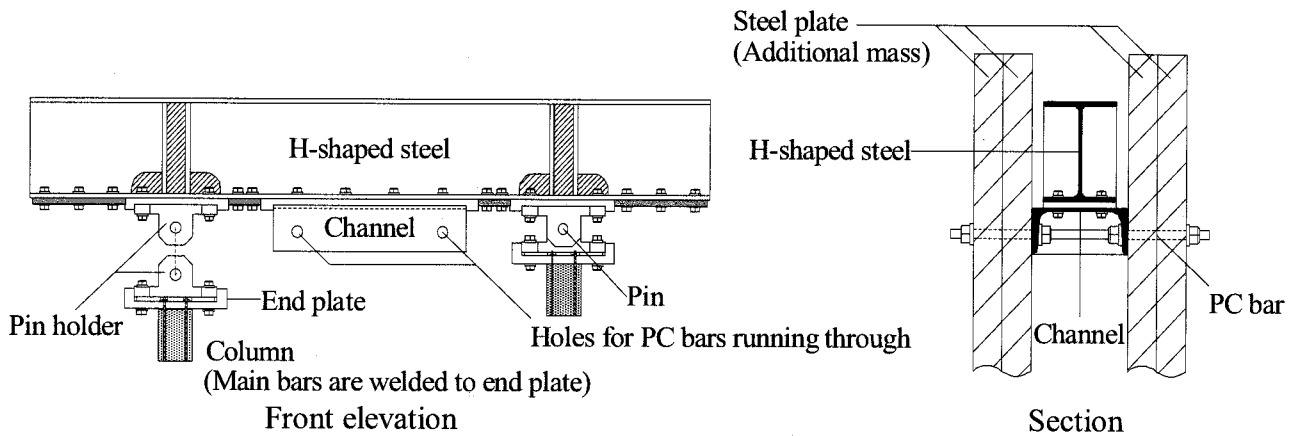


Figure 5 Detailed drawing of connection to specimens of additional mass

2.3 Input ground motion and pre-analysis to decide compression ratio of time axis

Input ground motion is NS component of JMA KOBE wave. As the size of the specimen is 1/8 times as large as a practical frame, amplitude of the wave is reduced to 1/8, however, the compression ratio of time axis should not be obeyed $1/8^{0.5}$ rule because the additional mass is not enough to satisfy the law of similarity of stress.

In order to decide the compression ratio of time axis, a simple pre-analysis was carried out. The analytical model was a SDOF model having the mass of 1.97tons and an elastic-plastic spring. The restoring force characteristic of the spring is two kinds of tri-linear model with different ultimate strength(type 1 and 2), as shown in Fig.6, which approximate static test results for the specimens with the same dimension as the one's for the shaking table test as shown in Fig.7. Type 1 corresponds to the frame with sound walls and Type 2 corresponds to the one without walls or with almost completely failed walls. Fig.8 shows the analytical results in the case the time axis is compressed to 3/10. As shown in the Fig.8, Type1 do not reach the maximum strength, however, Type 2 goes over the max. strength and considerably go into inelastic region. In the case of more compression ratio, both shows inelastic behavior, and in the case of less compression ratio, both shows almost elastic behavior, therefore, the compression ratio of 3/10 is considered to be adequate. The natural period of the specimen including the additional mass is about 0.10sec., therefore the specimen corresponds to buildings with natural period of 0.33sec., namely, 5-6 story buildings in actual size.

Run table is shown in Table 3. A typical input ground motion (Kobe $\times 1.0$) is same as shown in the left most figure in Fig.8.

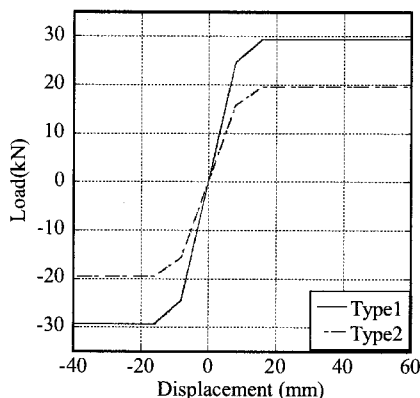


Figure 6 Skeleton characteristic of elastic-plastic spring SDOF model

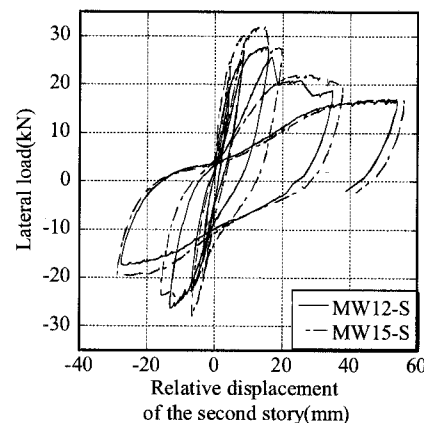


Figure 7 Static test results

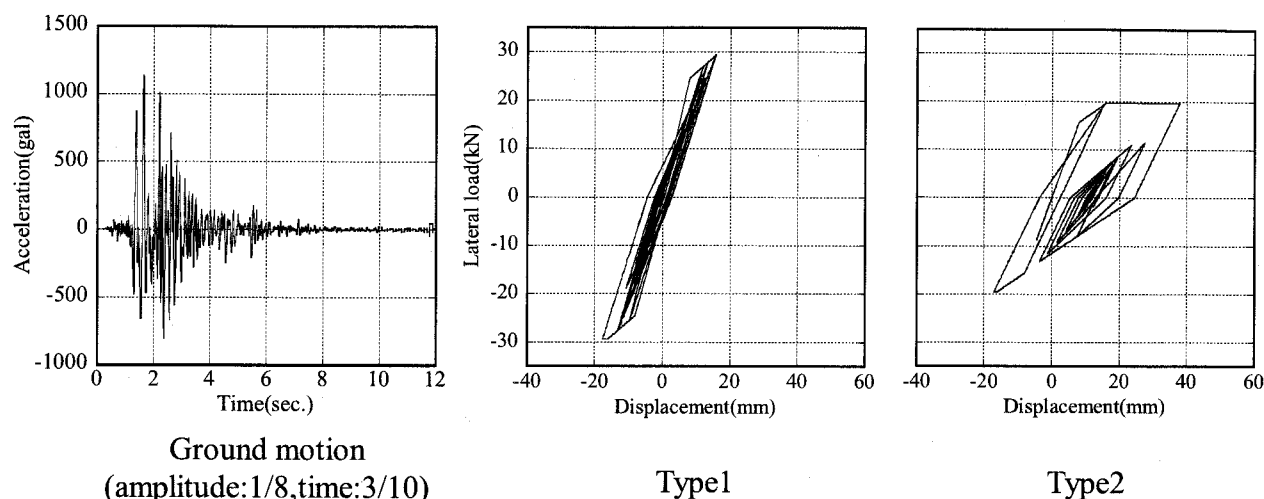


Figure 8 Results through pre-analysis

Table 3 Run table of shaking table test

Run	MW12-D	MW15-D
1	Kobe \times 0.1	Kobe \times 0.1
2	Kobe \times 0.3	Kobe \times 0.3
3	Kobe \times 0.5	Kobe \times 0.5
4	Kobe \times 0.7	Kobe \times 0.7
5	Kobe \times 1.0	Kobe \times 1.0
6	Kobe \times 1.2	Kobe \times 1.2
7	Kobe \times 0.5	Kobe \times 0.5
8	Kobe \times 0.7	Kobe \times 0.7
9		Kobe \times 1.0
10		Kobe \times 1.2

3. TEST RESULTS

3.1 Performance of testing machine

As a typical example, in the case of Run 6 for the specimen MW12-D, measured horizontal displacement of the stub of the specimen is compared with the control signal for the actuator in Fig.9. They are almost coincident with each other, therefore, it can be said that the performance of the machine is excellent and rocking vibration is ignorable.

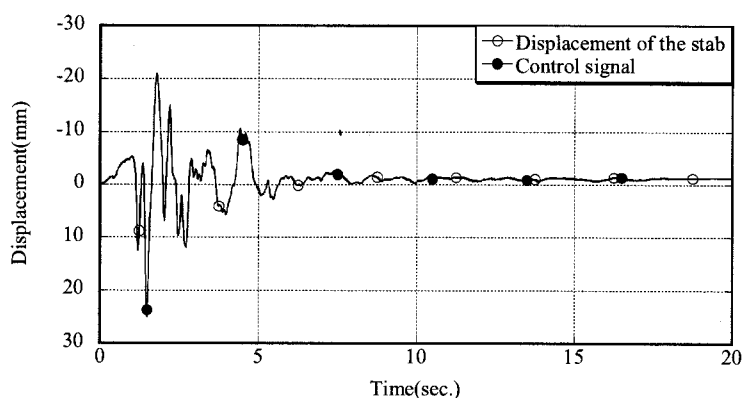


Figure 9 Comparison of measured displacement and control signal

3.2 Hysteresis of lateral force-displacement for several input level of ground motion

The relationships between the lateral force and the displacement are shown in Fig.10 for several input level, Run-4, -5, -6 and Run-8. In the figure, the lateral force means the one obtained by multiplying the recorded absolute acceleration of the additional mass by the mass of 1.97tons, which is equivalent to the sum of restoring force and damping force, and the displacement is the relative displacement between the stub and the second floor.

Until Run-3, both specimens showed almost elastic behavior. During Run-4 in which 70% of JMA KOBE wave was inputted, the both specimens went into inelastic region and hysteresis loop gradually shifted to slip type. As for Run-5 (100% of JMA KOBE), a number of shear cracks are observed in the walls after shaking for both the specimens, however, they had not yet experienced the strength degradation due to shear failure of the walls. This result is approximately coincident with the analytical one. During Run-6 (120% of JMA KOBE), the walls at both the stories were failed due to shear in both the specimens. As shown in Fig.11, it can be recognized that the elongation of the walls rapidly decreased after the time indicated by dots ● and ○, and then did not change after that, therefore, it is considered that the walls were failed at the time indicated by the dots, respectively. According to the above consideration, as for the specimen MW12-D, the wall at the lower story failed at first (1.53sec) and then the upper story wall failed (1.61sec), and as for MW15-D, the upper wall failed at first (1.53sec) and then the lower one (1.63sec.) The difference of the time the wall failed between the upper and the lower wall is about 0.1sec, and the both failure occurred in the same loop of the hysteresis. As for Run-8, both specimens exhibited considerable slip behavior, and the restoring force did not reach the remaining lateral strength of the specimens. The specimens still had an ability to stand by themselves against dead load after all runs.

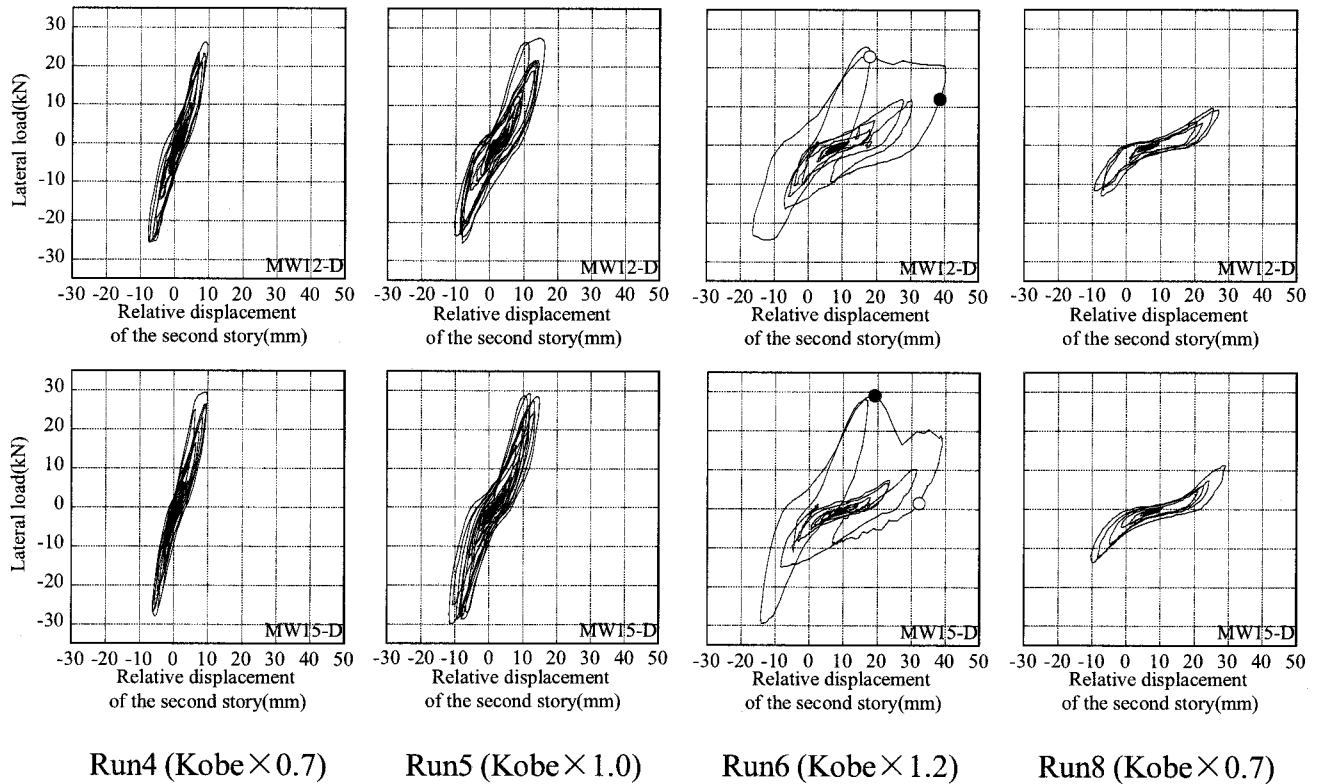


Figure 10 The relationships between the lateral force and the displacement
(upper:MW12-D , lower:MW15-D)

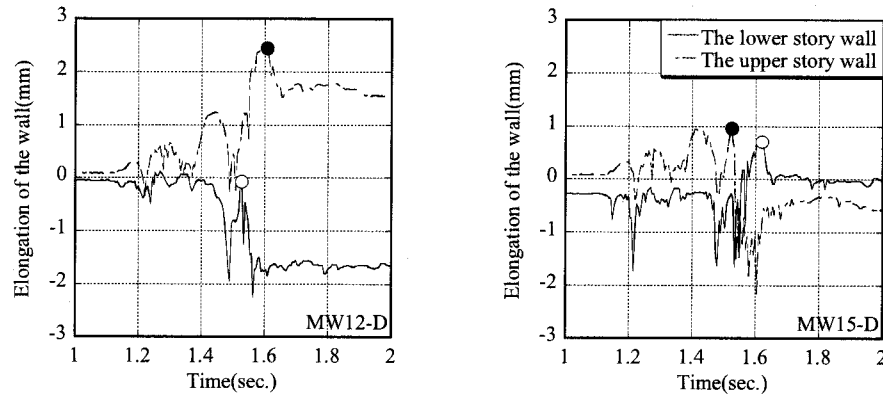


Figure 11 Time history of the elongation of the walls (Run6)

3.3 Risk of story collapse

Story drift angle of the first story is compared with that of the second story in Fig.12. As for all specimens, it is recognized that the story-drift at the story where the wall failed former rapidly increased compared with the other during two times of the shear failure of the walls. In these specimens, they occurred in a very short period of 0.1sec and the columns were designed still little stronger than the beams, therefore, the influence of the brittle behavior of the wall is limited small. The reason two failure occurs in a short period can be considered that shear failing of one wall releases the restriction of the elongation for the other wall, and that weaken the shear strength of the wall, however, if less stronger columns are used, the attention should be continuously paid on this problem, because there is still some fears the brittle failure of the wall eventually cause story collapse.

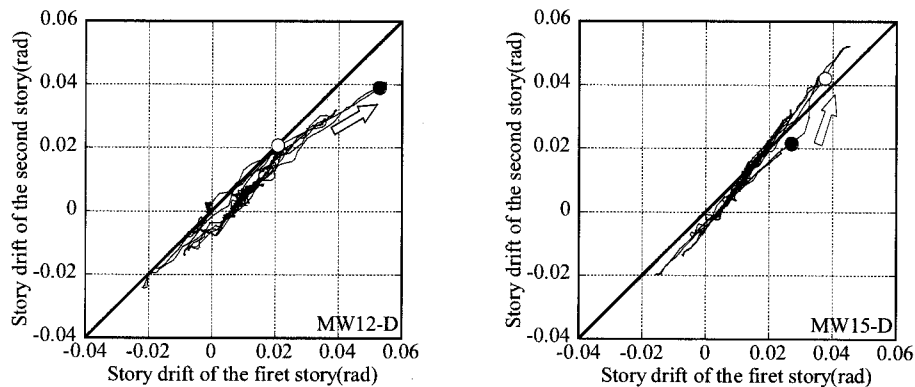


Figure 12 Relationship between story drift of the second story and the first story

3.4 Equivalent damping ratios

Equivalent damping ratio evaluated each half loop as shown in Fig.13 is plotted in Fig.14 for both the specimens. Strictly speaking, this equivalent damping ratio includes the ordinary viscous damping ratio because the lateral force is the sum of restoring force and damping force in the hysteresis previously described in 3.2. The horizontal axis of Fig.14, namely, x_{max} corresponds to that in Fig.13 and it is almost equivalent to the lateral displacement of the story when x_{max} is smaller than about 10mm, therefore the plots in Fig.14 are the equivalent damping ratios before the wall fails. In spite that the walls do not fail, they exhibited 0.1 and more. The damping ratios for the specimen MW12-D are totally higher than those for MW15-D.

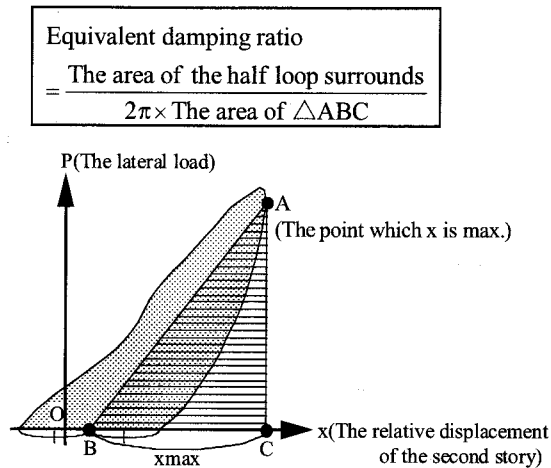


Figure 13 How evaluate equivalent damping ratio

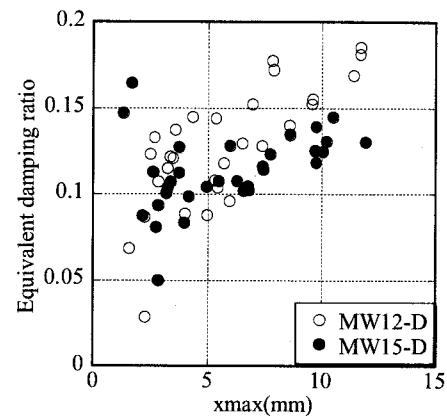


Figure 14 Relationship between equivalent damping ratio and xmax

4. CONCLUSIONS

A shaking table test is carried out for 1/8 scale R/C frames with “partial walls” which is apart from side columns and designed to fail due to shear before flexural yielding. The conclusions of this study can be summarized as follows.

- 1) A result obtained by a simple seismic response analysis for single degree of freedom model with Tri-linear restoring force characteristic which approximates static test result well explains the shaking table test result.
- 2) Shear failure of a wall makes the story drift at the story where the failed wall exists progress more than other story. However whether that cause the story collapse has not clarified yet. It is necessary to do continuous investigation on this issue.
- 3) Equivalent damping ratio more than 0.1 is expected for RC frames with the partial walls before exhibiting the ultimate lateral strength.

Acknowledgements:

The authors wish to express special thanks to graduate and undergraduate students in Prof. Hotta's laboratory for supporting the experiment from making the specimens to carrying out the test. This study was supported by Grants-in-Aid for General Scientific Research (#17560498) from the Ministry of Education, Science, Sports and Culture and Technology, Japan.

References:

- Hotta H. and Tsunoda T. (2004), “An experimental study on influence of mullion-type wall of predominant bending failure in reinforced concrete frame”, *Proc. of the 1st international conference on urban earthquake engineering*, Yokohama, Japan, 105-111
- Hotta, H. and Tsunoda T. (2004), “An experimental study on influence of mullion-type wall of predominant bending failure in load-carrying capacity and deformation efficiency of reinforced concrete frame”, *Journal of Structural and Construction Engineering (Transaction of Architectural Institute of Japan)*, 582, 131-136. (in Japanese)
- Hotta, H. and Kimura T. (2005), “An Analytical study on influence of multi-story mullion-type walls of predominant bending failure in reinforced concrete structure”, *Journal of Structural and Construction Engineering (Transaction of Architectural Institute of Japan)*, 591, 123-128. (in Japanese)

Earthquake Response Monitoring of Traditional Japanese Timber Pagoda

K. Fujita¹⁾, T. Hanazato²⁾ and I. Sakamoto³⁾

1) Assistant Professor, Department of Architecture, Tokyo Metropolitan University, Japan

2) Professor, Mie University, Japan

3) Professor, the University of Tokyo, Japan

fujita-kaori@c.metro-u.ac.jp, hanazato@arch.mie-u.ac.jp, sakamoto@buildcon.arch.t.u-tokyo.ac.jp

Abstract: Traditional timber pagodas in Japan are believed to have high seismic performance, because there is no document of a pagoda, which was destroyed by earthquake. The vibration characteristic of traditional timber pagodas in Japan is discussed based on the results of earthquake monitoring and micro tremor measurement. The experiment was subjected to a newly built timber pagoda, which was built by applying traditional structural system. The natural frequency of vibration showed displacement dependence due to the influence of non-linearity of the structure. The second and third modes of vibration were observed prominently by earthquake response. The damping factor ranged from 1% to 8%, values of which are relatively large compared to ordinary timber structures. But as the values range widely and shows no definite relation with the maximum displacement, further discussion is necessary in order to verify the energy dissipation of timber pagodas.

1. INTRODUCTION

Traditional timber pagodas in Japan are believed to have high seismic performance. This is because there is no documented record of a multi story timber pagoda, which collapsed by earthquake hazard, in spite of their height and low rigidity. The seismic performances of timber pagodas have been an interest to seismologists as well as structural engineers, and many analytical studies have been operated and hypotheses proposed. The seismic performance of traditional timber pagodas has not yet been clarified quantitatively, because of the lack of experimental data.

The object of the research is to clarify the seismic performance of traditional timber pagoda based on the results of recent earthquake response monitoring in comparison with preceding micro tremor measurement and free vibration test.

1.1 TRADITIONAL TIMBER PAGODAS

Timber pagodas are monuments worshipping the bone of Buddha, and have been constructed in Japan since the 6th century, when Buddhism reached our country. Although the style was imported from China through Korea, only a few timber pagodas are left in both countries. Numerous pagodas have been constructed during the course of our history but the structural system has not changed fundamentally.

The height of five storied timber pagodas range from 15 meter to over 50 meter. The structure has a square and symmetrical plan, usually three spans by three spans. The aspect ratio has a tendency to increase and the structure becomes slender for newer pagodas. The structural system of timber pagodas in Japan is composed of the center column and the surrounding multi story frame as shown in Figure1. The center column is structurally independent of the surrounding frame structure, and is based on the foundation or on top of the beam of the first floor or suspended from the frame. On top of the center column, metal ornamentation called the *sourin* is installed. The columns of the surrounding frame are all based on top of the beam of the lower story, and have small aspect ratio.

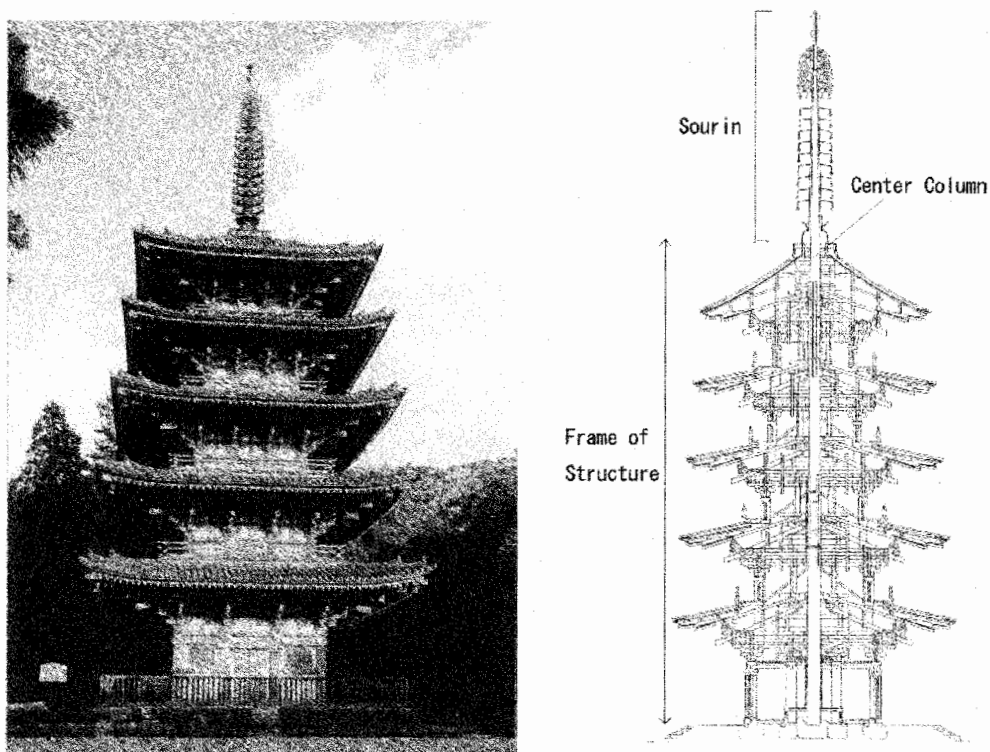


Figure 1 Example of the Section and Picture of Five Storied Pagoda (Daigo-ji Pagoda)

1.2 STRUCTURAL CHARACTERISTIC OF TIMBER PAGODAS

Many seismologists as well as structural engineers have discussed the seismic performance of traditional timber pagodas. The oldest experimental research was done by Omori[1], who conducted micro tremor measurements on six timber pagodas. Theoretical and analytical researches were operated by Sano and Taniguchi [2] and Sezawa and Kanai [3]. At the 2nd WCEE, which took place in Japan, Tanabashi gave a lecture on the earthquake resistance of traditional timber structures in Japan. He reviewed the preceding theories and pointed out that the assumed high earthquake resistance of traditional five storied pagodas are due to their structural damping and scale effect [4]. Umemura pointed out that the earthquake resistance of timber pagoda is due to small aspect ratio of the columns of the surrounding frame, the quantity of the horizontal members on each floor and the damping effect of the brackets [5]. Shiga and Shibata performed micro tremor measurement on a newly constructed

five-storied timber pagoda [6], [7]. Experimental research was done by Kanai and Yamabe et.al [8] who determined the vibration characteristics of twelve timber five storied pagodas by micro tremor measurement. Kubota and Yamabe conducted structural analysis on a timber pagoda and pointed out that the timber pagodas do not have high seismic performance without considering the effect of friction [9]. Micro tremor measurements on three-storied as well as five-storied timber pagodas were conducted by Nishizawa[10] and Kawai, Maekawa and Uchida[11] to clarify the fundamental vibration characteristics. Structural design of a timber pagoda based on earthquake response analysis was carried out by Hanazato and Sakamoto[12]. Micro tremor measurement was also performed on aforesaid timber pagoda and the results compared with the analyses [13]. The correlation between historic earthquakes, which occurred near the pagoda, and the resulting damage was investigated by the authors[14]. The seismic performances of five-storied pagodas are revealed statistically. Seven documented damages at five five-storied pagodas were found, the amount of which are comparatively scarce to the earthquakes that took place. The natural frequencies of five storied timber pagodas obtained by preceding researches are shown in relation with the height of the frame (Figure 2). The methods of experiment are micro tremor measurements. The results show that the natural frequencies of five storied timber pagodas range from 0.5Hz to 1.2Hz. The natural frequency of vibration is in inverse proportion to the square of the height of the structure.

From the results of preceding researches the earthquake resistance of traditional timber pagodas is generally high, due to the fact that many of the timber pagodas have experienced severe earthquakes during their lifetime while their damage by earthquake is scarce. The natural period of vibration of five-storied timber pagodas range from 0.8s to 2s. The characteristic structure system of the timber pagodas, such as the brackets, center column and short thick surrounding columns are expected to be efficacious to earthquake resistance.

The determined natural frequency of vibration in the first mode and the height of the frame of Tsu-kanon pagoda is compared with the results of the preceding research. The frame of Tsu-Kanon pagoda, which was subjected to the experiment is approximately 13meters in height and the determined natural frequency was 1.5 Hz. As the structure is small and newly built the consequent natural frequency is large. On the assumption that the natural frequency of vibration is in inverse proportion with the square of the height, the determined value is consistent with the result of the preceding researches.

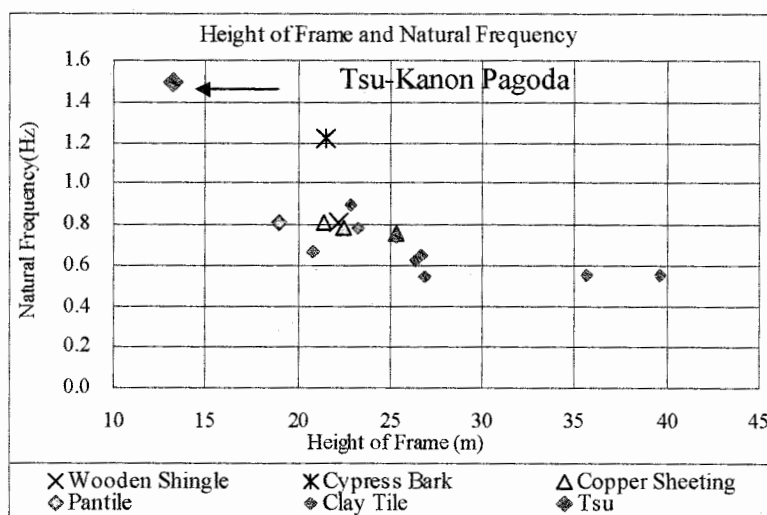


Figure 2 Relation of the Height of Frame and Natural Frequency of Five storied Pagodas

3. EARTHQUAKE RESPONSE MONITORING OF TSU-KANON PAGODA

3.1 METHOD OF EXPERIMENT

The experiment was subjected to a newly built timber pagoda called *Keinichi san Kannon-ji Taihou-in Five storied Pagoda* (hereafter *Tsu Kanon Pagoda*) situated in *Tsu city, Mie Prefecture*, which is the central part of Japan. The *Tsu Kanon Pagoda* was constructed in May, 2001. The plan and section of the pagoda are shown in Figures 3 and 4. The building was newly built by applying traditional timber structural system. The building is approximately 21m to the top of the *sourin*, the frame is 13m in height, 5m by 5m in plan. The structure is built on reinforced concrete foundation, the center column is set on a foundation stone installed on top of the RC foundation. All the timber used in the structure is cypress. The calculated weight of the structure was approximately 733 kN in total as shown in Table1.



Figure 3 Picture of Tsu Kanon

Table1 Weight of Pagoda	
	Weight (kN)
Center Column	7.5
5Fl	112
4 Fl.	101
3 Fl	105
2 Fl	112
1 Fl	296
Total	733

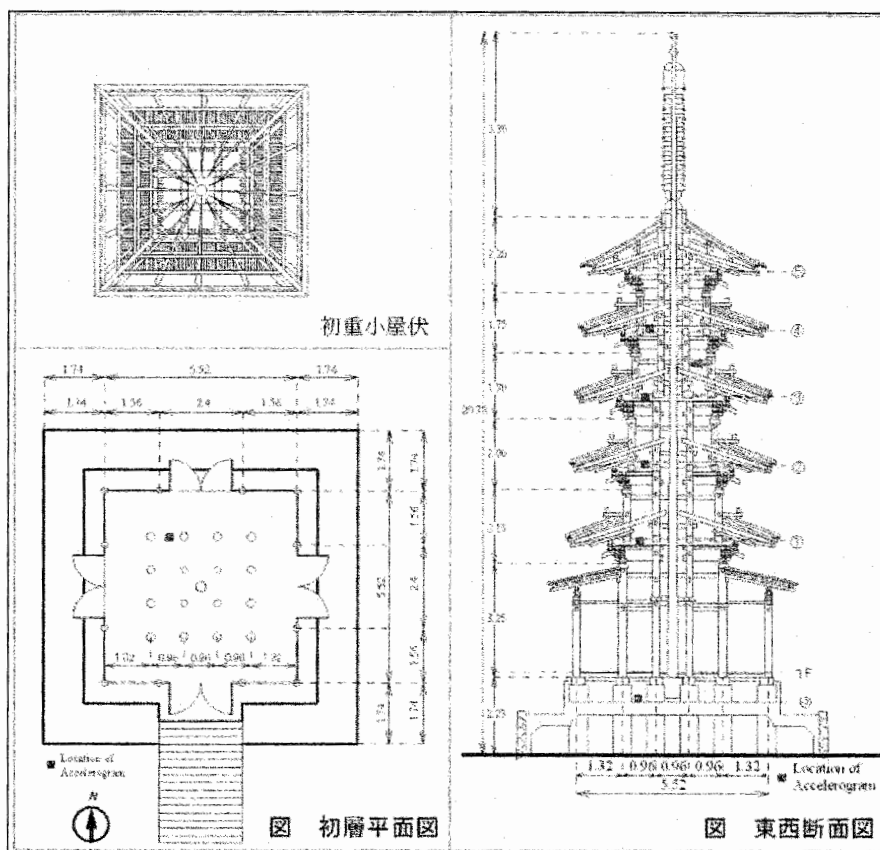


Figure 4 Plan and Elevation of Tsu Kanon Pagoda

Strong motion accelerograms are installed in the pagoda and earthquake response monitoring is under operation. The devices were first set in July, 2002 on the foundation and the beam of third story, each with two channels in the horizontal direction. On September 2002 two accelerograms were added on the first and fourth stories, each one horizontal direction (EW). On August 2003 two more accelerograms were added on the first and fourth story, each in the NS horizontal direction. The location of the accelerometer is shown in the plan and section. The sampling frequency was 100Hz,

duration of measurement 60 seconds. High pass filter of 0.02Hz is used. Micro tremor measurement and free vibration tests were conducted on September 2002 and December 2003. Data samples were measured for 60s by 100Hz, three times in each horizontal direction.

3.2 MEASURED EARTHQUAKE RESPONSE

Approximately 120 earthquake responses have been recorded at the Tsu Kanon Pagoda as of May 2005. The largest measured earthquake was the 2004 South Eastern Off Kii Peninsula Earthquake (23:57 September 5th, 2004, M7.1). Seismic intensity 4 was observed in Tsu city, on the JMA scale. Figure 5 shows the Kii peninsula with the epicenters of the earthquake together with two sequential earthquakes, which took place the same day. At the Tsu-Kanon Pagoda maximum input acceleration of 122 Gal was observed. Table 3 shows the maximum values recorded at each observed point. The observation points in the Table correspond with those shown in Figure 4.

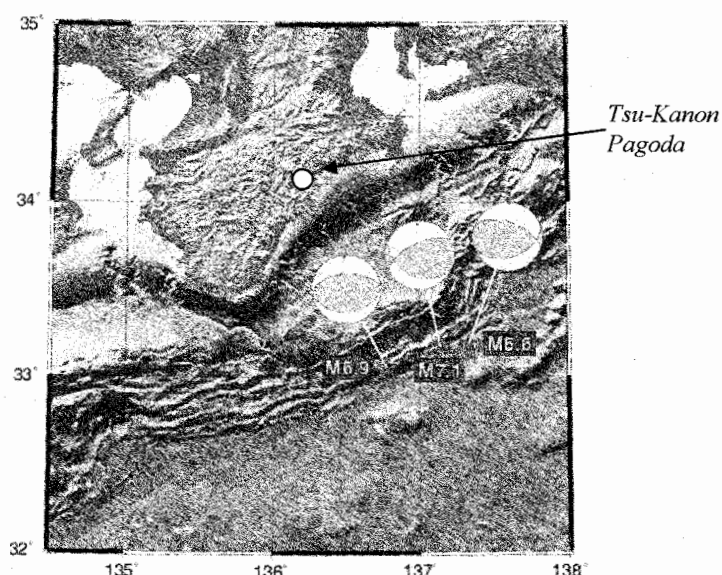


Figure 5 2004 Off Kii Peninsula Earthquake (National Research Institute for Earth Science and Disaster Prevention)

Table3 Maximum Values of September 5th, 2004 Ise Earthquake

	NS			EW		
	Acceleration	Velocity	Displacement	Acceleration	Velocity	Displacement
	Gal	kine	cm	Gal	kine	cm
④4 th FL	91	11.9	4.15	96	9.4	2.94
③3 rd FL	82	10.8	3.88	169	11.5	2.80
①1 st FL	106	9.3	3.29	264	13.6	2.67
Foundation	112	6.5	2.93	122	7.4	2.35

Figure 6 shows the Fourier transform of the input acceleration record. The prominent frequency can be seen at 2.98 Hz in the EW direction. The transfer function from the foundation to the beam of each floor determined from the results of the micro tremor measurement and earthquake response is shown in Figure 7 and 8 respectively. The natural frequencies of vibration were approximately 1.49Hz (first mode), 4.2Hz(second mode) and 7.2Hz(third mode). The values did not differ for NS and EW

direction, resulting from the symmetrical plan. The response amplitude of the second and third modes are substantially large compared to the first mode by earthquake response. This tendency was observed for earthquake response but was not observed for micro tremor measurement nor free vibration tests.

Figure 9 shows the relation of the ratio of amplitude of the second mode to the first mode and the measured wind velocity at the time of the earthquake. The vertical axis shows the ratio of amplitude of the first mode A1 to the second mode A2. The horizontal axis shows the wind velocity measured at the time of the earthquake. The result shows that ratio A2/A1 is larger when the wind velocity is smaller. The amplitude of second mode is predominant when the wind velocity is small and the response of the structure is genuinely by earthquake.

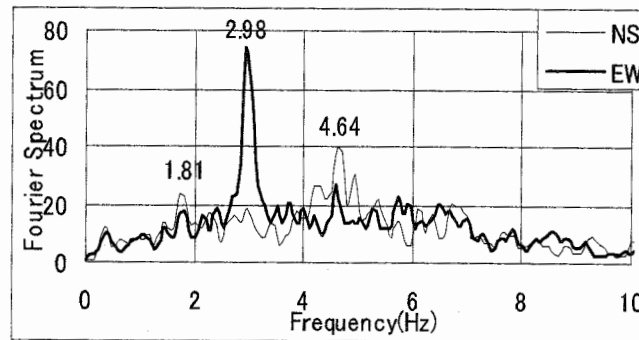


Figure 6 0409052357 50-70s Fourier Spectrum

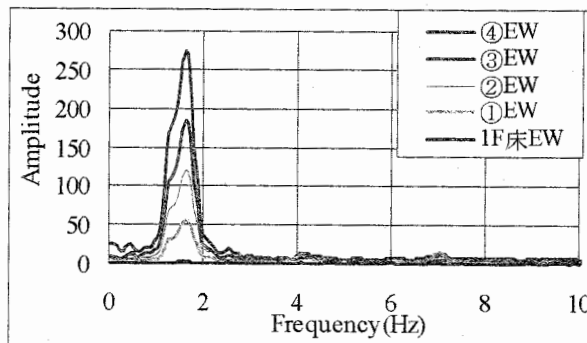


Figure 7 Transfer Function (Micro Tremor)

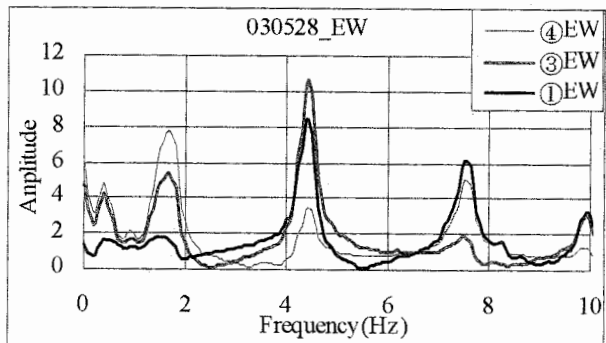


Figure 8 Transfer Function (Earthquake Response)

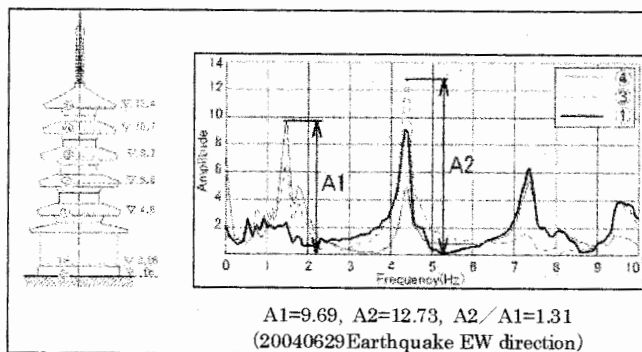


Figure 9 Response amplitude of First and Second modes

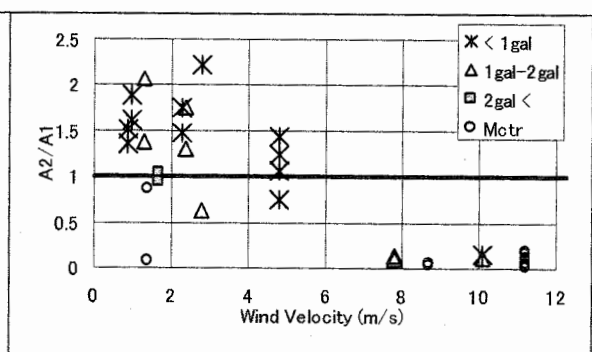


Figure 10 Response amplitude and wind velocity

The natural frequency of vibration in the first mode determined from the micro tremor, free vibration and earthquake monitoring is shown in relation with the measured maximum horizontal displacement of the beam of the fourth floor (Figure 11). The natural frequency of vibration was determined from the transfer function from foundation to the beam of the fourth story as shown in prior Figure 7 and 8. The figure indicates that the natural frequency of vibration in the first mode is dependent on the maximum horizontal displacement. From the results of the micro tremor measurement and free vibration tests the maximum displacement is approximately 0.01mm and the natural frequency range from 1.4Hz to 1.7Hz, but as the displacement increase the frequency reaches 1.2 Hz due to the strong non-linearity characteristic of timber structures.

The damping factor determined by curve fitting method is shown in relation with the maximum displacement of the fourth story in Figure 12. From the result of micro tremor measurement the damping factor was approximately 1%, which is consistent with those of the preceding experimental research. The results of the earthquake response were 2.5% to 8%, values of which are relatively large compared to ordinary timber structures. But as the values range widely and shows no definite relation with the maximum displacement, further discussion is necessary in order to verify the energy dissipation of timber pagodas.

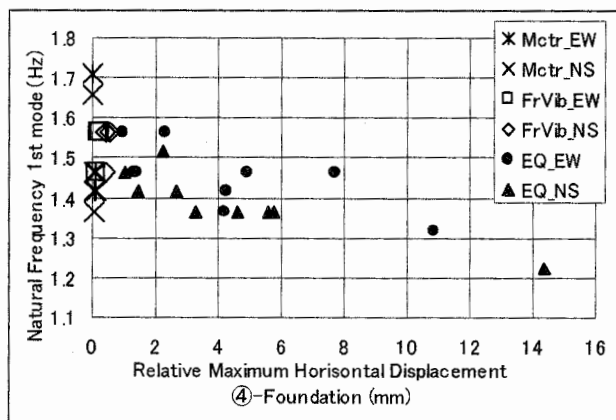


Figure 11 Natural Frequency (1st) and Displacement

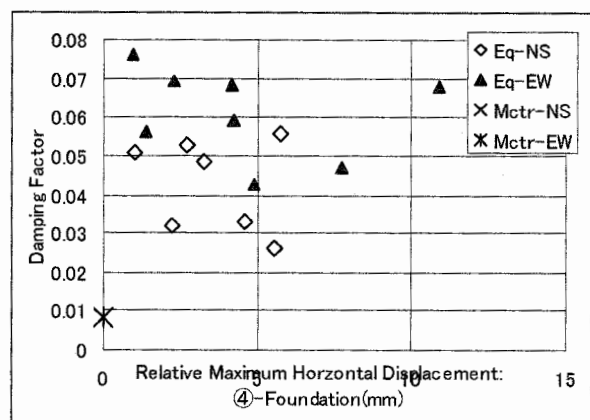


Figure 12 Damping Factor and Maximum Displacement

4. CONCLUDING REMARKS

The seismic performance of traditional timber five-storied pagoda is discussed based on the results of earthquake response monitoring and micro tremor measurement. The experiment was subjected to a newly built five-storied timber pagoda in Japan. The fundamental vibration characteristics are determined. The natural frequency of vibration is dependent on the maximum horizontal displacement due to the influence of non-linearity of the structure. The second and third modes of vibration were observed prominently by earthquake response. The damping factor was approximately 1% from micro tremor measurement, the result of which is consistent with those of the preceding experimental research. From the results of the earthquake response the damping factor ranged from 2.5% to 8%, values of which are relatively large compared to ordinary timber structures. But as the values range widely and shows no definite relation with the maximum displacement, further discussion is necessary in order to verify the energy dissipation of timber pagodas.

Acknowledgment:

The authors wish to express their sincere gratitude to the Chief priest of the Tsu-Kanon Temple Mitsuo Iwatsuru, chairman of the Imuraya Confectionery Masakatsu Imura, Mr. Yanagisawa of Taisei Cooperation for their generosity and help, without which this experiment would never have been realized.

References

1. Fusakichi OMORI: On the Vibration of Five Storied Pagoda, Journal of Architecture and Building Science Vo.414, pp.219-227, 1921.4 (in Japanese)
2. Toshikata SANO and Tadashi TANIGUCHI: General Theory of Earthquake resistant Structures, Iwanami-zensho 30, Iwanami Book Co., Ltd, 1934 (in Japanese)
3. Katsutada Sezawa, Kiyoshi Kanai: On The Seismic Vibrations of a Gozyunoto (Pagoda), Earthquake Research Institute, 1936 (in Japanese)
4. Ryo Tanabashi: Earthquake Resistance of Traditional Japanese Wooden Structures, The Lecture of 2W.C.E.E, 1960.
5. Kai UMEMURA: Earthquake and Buildings, Extension Lectures of the University of Tokyo 24 Earthquake, Publication of the University of Tokyo, p77-106, 1976 (in Japanese)
6. Toshio SHIGA and Akinori SHIBATA et.al : Vibration Measurement of Newly Built Conventional Building Style Five Storied Pagoda, Japan Institute of Architecture Northeastern Division 1986.11 (in Japanese)
7. Toshio SHIGA et.al : Vibration Measurement of Newly Built Conventional Building Style Five Storied Pagoda (Part2), Japan Institute of Architecture Northeastern Division 1987.11 (in Japanese)
8. Katsuyoshi YAMABE and Kiyoshi KANAI: Study on the Aseismic Properties of Gzyunotos (Pagodas), Journal of Nihon Daigaku Vol.21 No.2, 1988.12 (in Japanese)
9. Hiroyuki KUBOTA and Katsuyoshi YAMABE: Earthquake Resistance of Five Storied Pagodas – Examination by Earthquake Response Analysis- Annual meeting of Architectural Institute of Japan, P801-802, 1991.9 (in Japanese)
10. Hidekazu NISHIZAWA: Vibration Measurement of Timber Multi Storied Pagodas, Kyoto University, 1994
11. Naohito KAWAI, Akito UCHIDA and Hideyuki MAEKAWA, Dynamic Characteristics of Traditional Wooden Buildings Part2-6, 1997-1999, Annual meeting of Architectural Institute of Japan (in Japanese)
12. Toshikazu HANAZATO, Yukio OGIWARA, Masahiro INAYAMA, Isao SAKAMOTO et.al: Structural Design of Traditional Wooden Five-Storied Pagoda, AIJ Journal of Technology and Design No.7, pp.33-38, 1999.2 (in Japanese)
13. Toshikazu HANAZATO, Kaori FUJITA, Isao SAKAMOTO et.al: Dynamic Behavior of Traditional Timber Five-Storied Pagoda – Measurement of Microtremor and Free Vibration at Newly-Built Pgoda-, 11th Japan Earthquake Engineering Symposium, 2002.11, CDR (in Japanese)
14. Kaori FUJITA, Mizuho OYAMA, Toshikazu HANAZATO and Isao SAKAMOTO, Vibration Characteristics of Traditional Five Storied Pagodas, 11th Japan Earthquake Engineering Symposium, 2002.11, CDR (in Japanese)
15. Kaori FUJITA, Toshikazu HANAZATO and Isao SAKAMOTO, Earthquake Response Monitoring and Seismic Performance of Five Storied Timber Pagodas, 13th World Conference on Earthquake Engineering, Aug. 2004

LESSONS LEARNED FROM RECENT EARTHQUAKE DISASTERS - FOR MEGA-CITIES ON HUGE SEDIMENTARY BASINS -

K. Seo¹⁾, K. Motoki²⁾, and K. Eto³⁾

1) Professor, Dept. of Built Environment, Tokyo Institute of Technology, Japan

2) Research Associate, Dept. of Built Environment, Tokyo Institute of Technology, Japan

3) Earthquake Engineer, Tokyo Soil Research, Co., Ltd., Japan

seo@enveng.titech.ac.jp, kmoto@enveng.titech.ac.jp, eto@tokyosoil.co.jp

Abstract: Recent earthquake disasters since 2003 in Japan were reviewed for practical considerations in mega-cities like Tokyo and Taipei, in the future. Tomakomai in Hokkaido, located on a thick sedimentary basin, suffered a heavy damage on huge oil tanks because of long period earthquake motions during the 2003 Tokachi-Oki earthquake. Chuetsu district in Niigata suffered very serious problems due to a series of heavy rain, earthquakes and heavy snow from the summer of 2004 through the winter of 2005. The 2005 Fukuoka-Oki earthquake brought additional subjects due to the failure of non-engineering parts of modern structures. Such recent experiences should be taken into account in the disaster mitigation program for Tokyo and other mega-cities.

1. INTRODUCTION

We are really afraid a major earthquake which may take place around Tokyo and Yokohama in the near future. It is true that as much as efforts will be made for the reduction of expected damage. Because we can estimate some probable seismic sources, we have amount of borehole data, and we have made deep underground structural surveys. Therefore we can make hazard mapping for some expected future earthquakes. But how about risk evaluation? It may be possible of course, if we can prepare simplified models describing vulnerable conditions those might be scattered around the huge city area. Unfortunately we are not sure that such evaluation does work so well. Therefore we need to find helpful aspects through as much as experiences in the past.

In this paper, the following three earthquakes will be focused, such as the 2003 Tokachi-Oki earthquake, the 2004 Niigata-Chuetsu earthquake, and the 2005 Fukuoka-Oki earthquake. The authors believe that some of important aspects, which could be found in these earthquakes, might be very useful when we talk about the future earthquakes in Tokyo and other mega-cities.

2. THE 2003 TOKACHI-OKI EARTHQUAKE

The M8 Tokachi-Oki earthquake of September 26, 2003, took place in the Pacific subduction zone and hit Tokachi district, the southern Hokkaido. It was almost similar with the previous one in 1952. The damage including liquefaction and tsunami appeared along the south coast of Hokkaido, but the further remarkable aspect was the appearance of long period motions around Tomakomai city in the Yufutsu plain. Sloshing phenomenon, a kind of resonance phenomenon between long period ground motions and liquids in oil tanks, was observed in this area because there was an industrial region with full of huge oil tanks. Many tanks showed overflow of oils and two of them got fire.

The point is that a basin shaped thick deposits excited such long period motions in spite of far distance of about 250km from the epicenter. It is quite easy to imagine that the Kanto plain including Tokyo and Yokohama will meet with the similar problem if we have M8 earthquake. During the 1923 Kanto earthquake with M7.9, there were no huge oil tanks and no tall buildings to be resonated with such long period motions. The experience during the 2003 M8 earthquake might bring us some estimation about long period ground motions in the future M8 earthquake in Tokyo and Yokohama area.

3. THE 2004 NIIGATA-CHUETSU EARTHQUAKE

The M6.8 earthquake of October 23, 2004, attacked Chuetsu area, the central district of Niigata prefecture. Damaged area distributed some parts in local cities and towns in flat level, but most of the cases in villages scattered among the mountain districts. Therefore amounts of land failures disturbed the traffics. Totally collapsed houses were found and seismic intensity 7, as the maximum in Japanese scale, was observed around the focal region. Number of deaths counted 40 not only because of collapsed houses but exhaustion and illness after the earthquake. JR Super Express named Shin-kan-sen suffered heavy damage including a derailment, destructions of columns, and failures in tunnels. It was just by chance that such failures did not kill any people. After two months, heavy snow covered whole parts of the damaged area for more than three months with the thickness of 3m or more. Such difficult condition disturbed the recovery and countermeasures very hard.

Although the situation in Niigata looks quite different from that in Tokyo area, we must be very careful to find useful aspects for the future M7 earthquakes around Tokyo. Take the M6 earthquake of July 23, 2005, that happened near Tokyo, for example. Whole of trains and subways in and around Tokyo did not work for a few hours to several hours. Elevators in buildings showed big problems including 44 collapse, 78 shut people inside, 64,000 stopped among 227,000 in total.

4. THE 2005 FUKUOKA-OKI EARTHQUAKE

The M7 earthquake of March 20, 2005, hit Fukuoka city and neighboring districts of the northern Kyushu Island. The seismic activity of the district has been recognized as one of the lowest zones in Japan. Therefore seismologists concerning with the earthquake prediction had to lose confidence. Anyway damage was not so hard unlike the Niigata-Chuetsu earthquake, except a small island very close to the focal region.

Fukuoka city has 1.3 million in population and 70 percent of citizens are living in residential tall buildings. Failures in such buildings brought a big problem although most of the damage was non-structural one. For example, non-structural walls suffered heavy shear failures and fixed entrance doors. Therefore residential people could not make urgent evacuation at all. Two buildings separated with expansion joints showed pounding each other, and a piece of concrete wall with 500kg in weight fell down from the 10th floor to the entrance floor on the ground level. As there was no description about such matters in Japanese Building Code, concerning officials and construction companies did not want to take any kinds of responsibilities. So residential people had to solve these difficult problems by themselves.

5. DISCUSSION AND CONCLUDING REMARKS

After reviewing such recent experiences, although individual subjects mentioned above are not enough to imagine the every case for mega-cities like Tokyo and Caracas, we can find some important aspects to be considered.

When local governors want to prepare practical hand manuals for emergency activities, they will need a hypothetical scenario that shows what will happen in their territory along the time.

It will be sure that the most fundamental basis should be prepared based on theoretical and empirical estimation such as hazard mapping, vulnerability evaluation and risk assessment. But in spite of such efforts, they will never accomplish everything. Problems always happen with unexpected ways. Therefore we hope that the important aspects as new findings experienced in the past earthquake disasters could be applied to the future preparedness.

Here the authors would like to list up the following aspects for the countermeasures about future earthquakes those will take place in mega-cities like Tokyo and Yokohama.

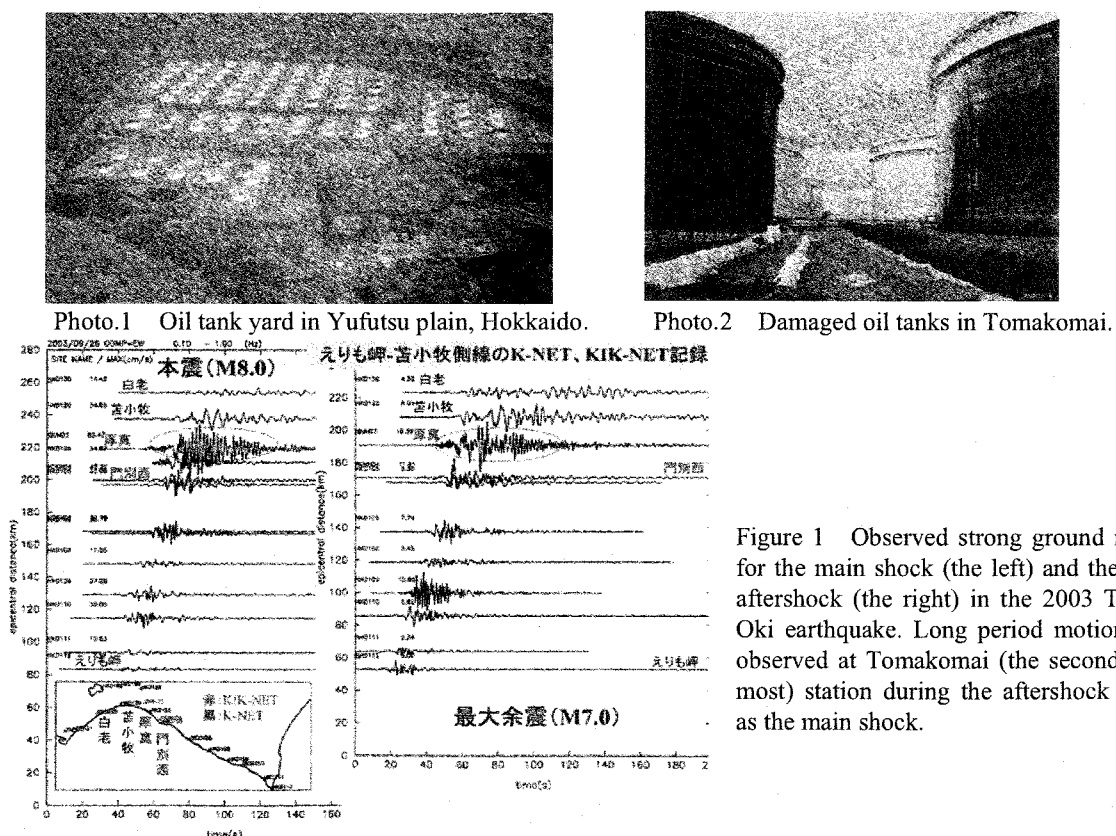
- 1) It is quite easy to imagine that Tokyo and Yokohama will meet with long period earthquake motions if there is M8 earthquake. In the case of the Kanto plain including Tokyo, Yokohama and Chiba, the predominant period could be from 6 seconds to 10 seconds. Huge oil tanks, long bridges, and tall buildings will have very serious problem by getting such special ground motions.
- 2) M7 earthquakes, if the epicenter is very close, will be strong enough to bring a heavy damage to mega-cities. Infrastructures including transportation systems and communication systems will have serious problem, although they might not be collapsed.
- 3) Buildings and houses will have non-structural failures also in M7 earthquakes, even if they are not collapsed. Such failures, those could be seen in the Fukuoka-Oki earthquake, will disturb citizens to keep living in mega-cities.

Acknowledgements

The authors of this paper have finished the survey in Tomakomai area, but are still making field surveys in Niigata-Chuetsu district and in Fukuoka city. They would like to express their sincere appreciations to amounts of residents, officials and companies. They were very kind to accept interviews and to provide useful materials, photos and other information, in spite of their very hard situation just after the earthquake disasters. Strong motion records, in K-NET and KIK-NET, were offered by National Research Institute for Earth Science and Disaster Prevention (NIED).

References

SEO, K.: Reports on damage investigations for the 2003 Tokachi-oki earthquake, for the 2004 Niigata-Chuetsu earthquake, and for the 2005 Fukuoka-oki earthquake; Research Reports on Earthquake Engineering, Center for Urban Earthquake Engineering (CUEE) and lecture notes with PPT, Tokyo Institute of Technology, 2004-2005 (in Japanese)



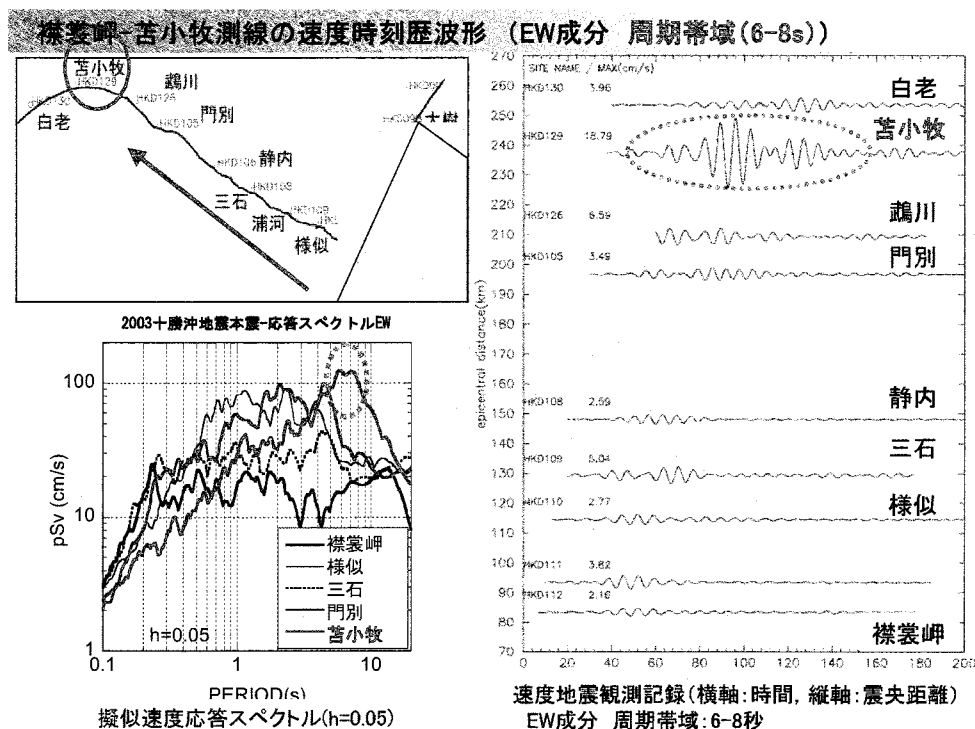


Figure 2 Long period strong motions during the 2003 Tokachi-Oki earthquake.

Right upper figure shows the propagation path of principal seismic waves from the epicenter toward Tomakomai direction. Right lower figure shows response spectra with 5% damping for each station. Long period component is predominant at Tomakomai (dotted circle). Left figure shows velocity motions filtered with the band between 6 to 8 seconds. The second uppermost motion is for Tomakomai (dotted circle).

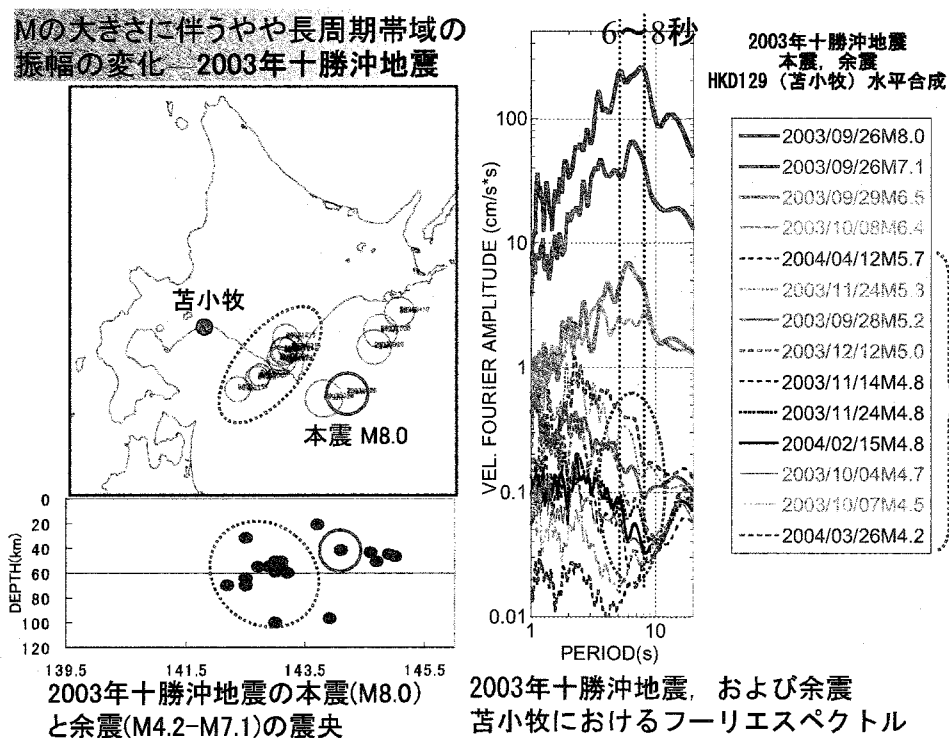


Figure 3 Distribution of aftershocks (the left) and individual Fourier spectrum at Tomakomai (the right).

It can be seen that the predominant component from 6 to 8 seconds at Tomakomai looks quite stable even in small aftershocks. Such features can be explained as the site effect of Tomakomai region located in the thick sedimentary basin.

Mの大きさに伴うやや長周期帯域の振幅の変化
伊豆諸島付近の地震 K-NET鎌倉、川崎、木更津観測点

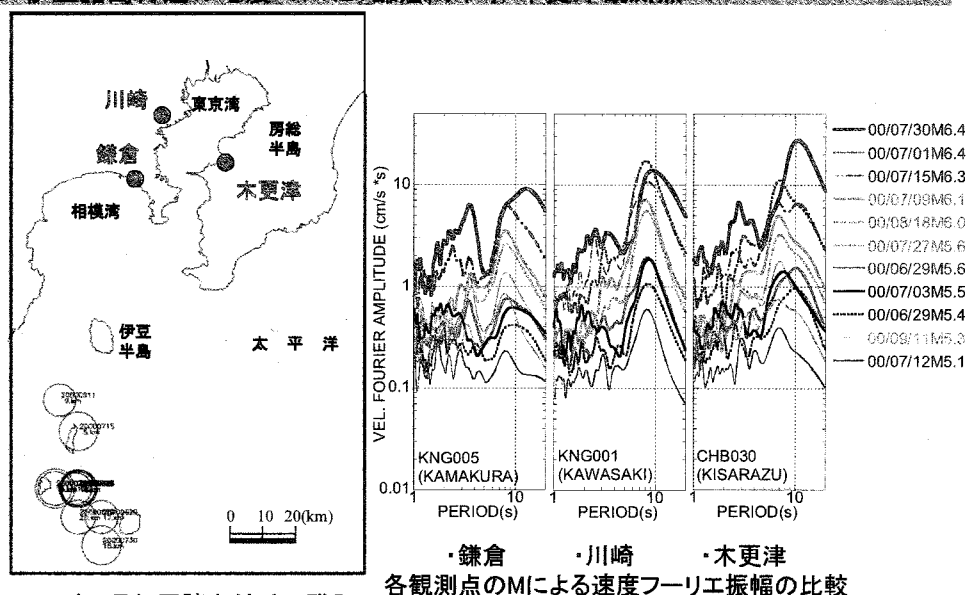


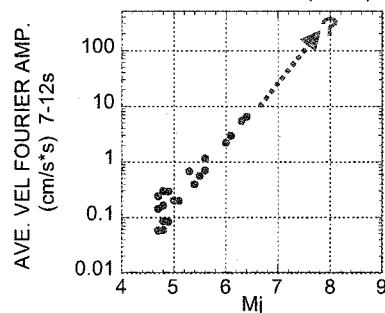
Figure 4 Long period earthquake motions observed in the Kanto plain.

The long period components are observed in every station in the plain mainly during very shallow earthquakes those took place around Izu peninsula (the left). In such cases, the magnitudes of earthquakes are not the matter to have long period components (the right).

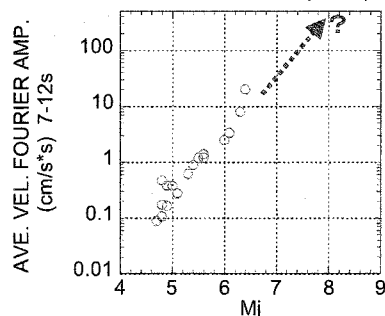
苫小牧、鎌倉、木更津における卓越周期帯域の平均振幅とMの関係

伊豆諸島付近の震央とする地震(M4.5~M6.4)

鎌倉($\Delta=70\sim140\text{km}$) 周期7~12秒
• KNG005 (7-12s)

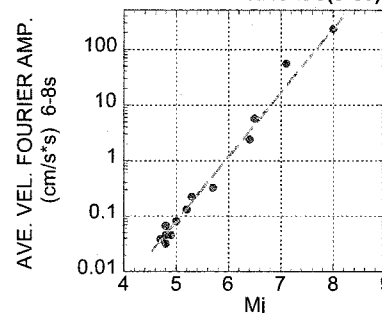


木更津($\Delta=110\sim150\text{km}$) 周期7~12秒
○ CHB030 (7-12s)



2003年十勝沖地震 (M4.6~M8.0)

苫小牧($\Delta=130\sim240\text{km}$) 周期6~8秒
• HKD129(6-8s)



同震源域からの地震観測記録
から確認された事

・地震動の平均振幅値は、
Mが1大きくなると、約10倍(?)

Figure 5 Comparison of long period earthquake motions between the Kanto district (the left upper: Kamakura, the left lower: Kisarazu) and Tomakomai (the right). We have already observed M8 motions at Tomakomai but not yet in the Kanto plain. We are going to estimate M8 motions there with the experience obtained at Tomakomai. It looks almost ten times difference in amplitude between M7 and M8 earthquakes.

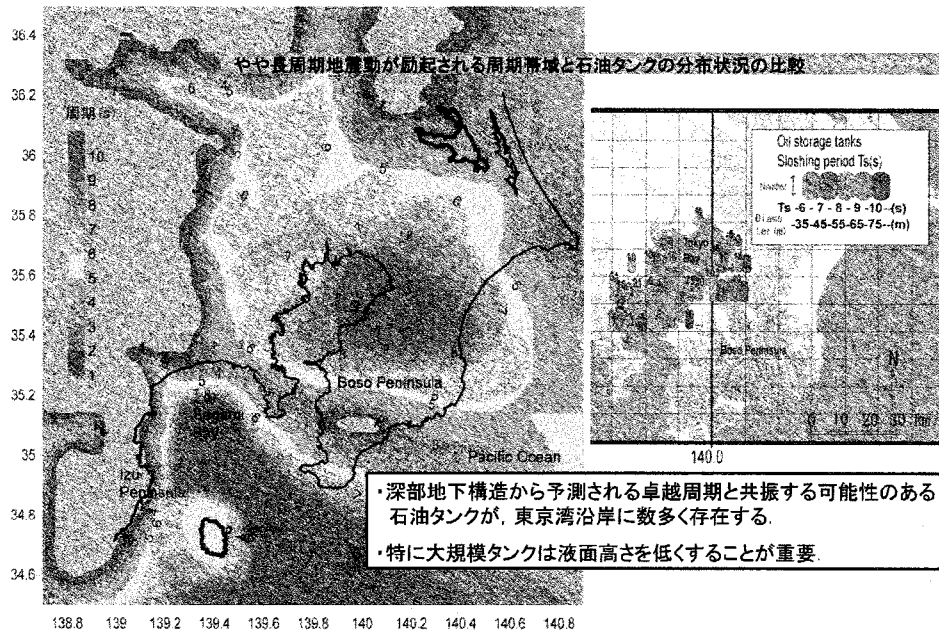


Figure 6 Predominant period evaluation based on deep underground structures in the Kanto plain (the left) and distribution of existing huge oil tanks in the Tokyo bay area (the right). We are very afraid the resonance between the long period motions and oil tanks.

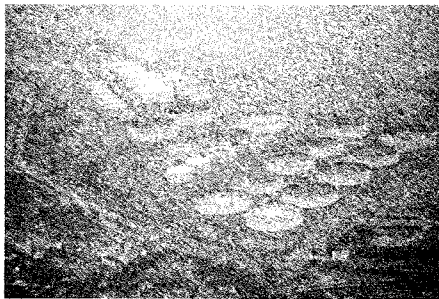
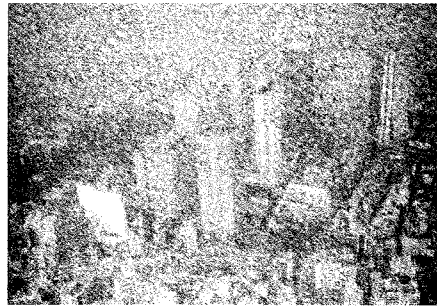
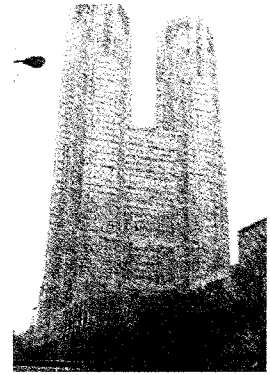


Photo.3 Oil tanks in the Tokyo bay area.



Photos.4-5 Tall buildings in Shinjuku area, Tokyo Metropolis.



川口町中心部の被害



Photo.6 Damage in the central region of Kawaguchi town.

山古志村役場から見た油伏(ゆふ)集落の惨状



Photo.7 Land failures in Yamakoshi village.

The 2004 Niigata-Chuetsu earthquake with M6.8 hit the Chuetsu district of Niigata prefecture. The district consists of local cities on the flat plain along the Shinano River and amount of small villages scattered in the Uonuma Mountain. Intensity 7 in Japanese scale was observed in Kawaguchi town very close to the focal region.



Photos.8-10 Failures of JR-Shin-kan-sen during the 2004 Niigata-Chuetsu earthquake.

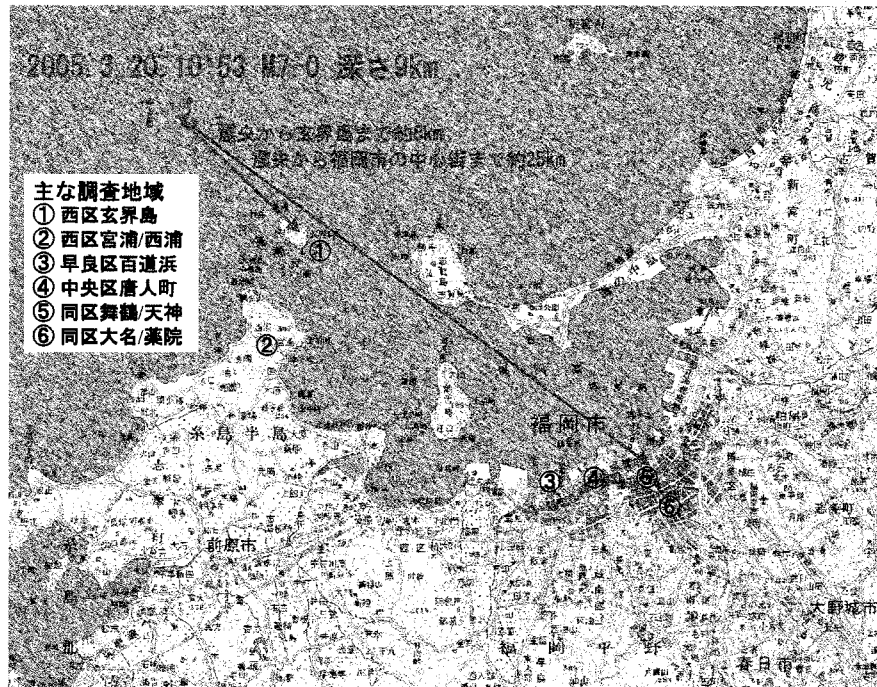


Figure 7 Map showing the epicenter and damaged area for the 2005 Fukuoka-Oki earthquake.



Figure 8 The Kego active fault crosses the central region of Fukuoka city. Principal damage appeared along the eastern edge of the fault although the fault itself did not work during the earthquake.

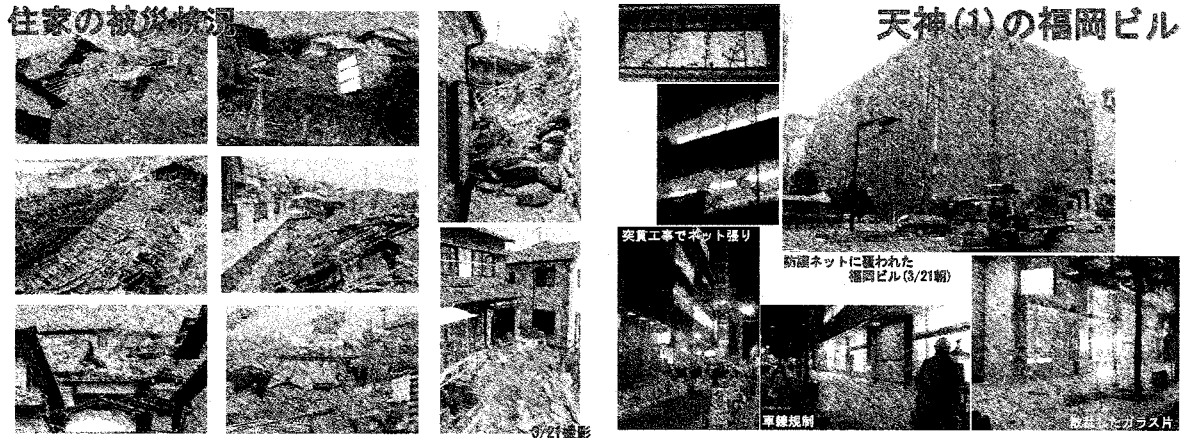


Photo.11 Damage in Genkai island close to the epicenter. Photo.12 Damage of window glasses in Fukuoka city.

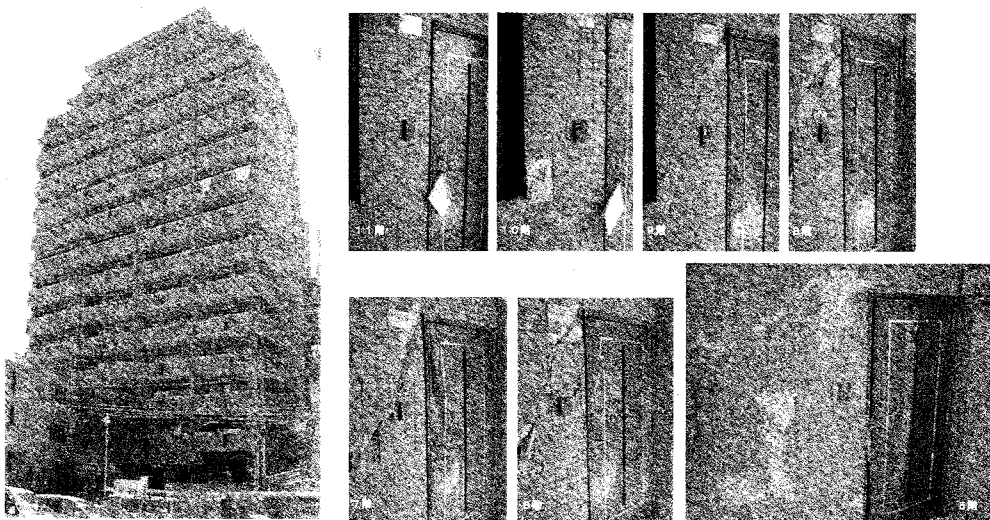
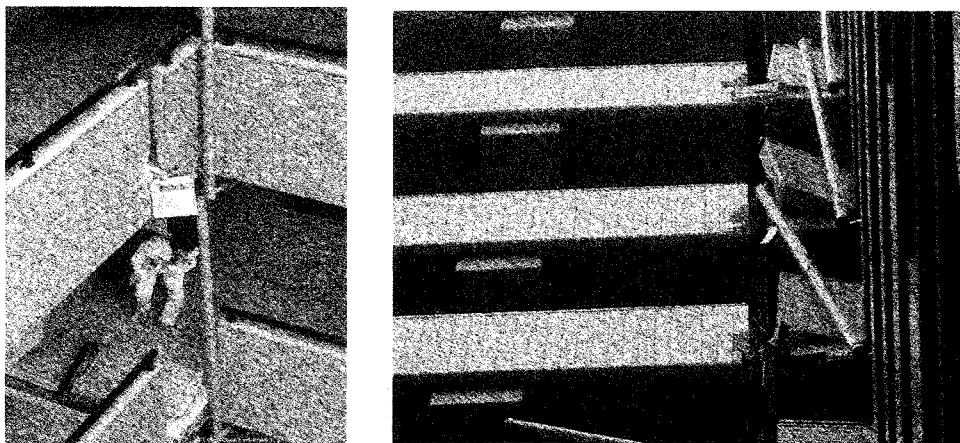


Photo.13 Damage of non-structural walls collapsed entrance doors in a residential building in Fukuoka city.



Photos.14-15 Expansion joints in a residential building showed pounding each other.

It was quite lucky that no one was killed by such damaged structures, although one old woman was killed on a street by a fallen brick fence. But the possibility looks very high that amount of unexpected failures, such as falling window glasses, fixed entrance doors, and falling piece of heavy concrete, might kill the people in the central city areas.

JOINT INVERSION OF RECEIVER FUNCTION AND RAYLEIGH-WAVE PHASE VELOCITY FOR ESTIMATION OF S-WAVE VELOCITY OF SEDIMENTARY LAYER IN NIIGATA, JAPAN

H. Yamanaka¹⁾ and T. Kurose²⁾

1) Associate Professor, Dept. of Environmental Science and Tech., Tokyo Institute of Technology, Japan
yamanaka@depe.titech.ac.jp

2) Graduate Student, Dept. of Environmental Science and Tech., Tokyo Institute of Technology, Japan
(Present: CRC Solutions Corp.)

Abstract: In this study, we propose a joint inversion method, using genetic algorithms, to determine the S-wave velocity structure of deep sedimentary layers from receiver functions and surface-wave phase velocity. Numerical experiments with synthetic data indicate that the proposed method can avoid the trade-off between shear-wave velocity and thickness that arises when inverting the receiver function only, and the uncertainty in deep structure from surface-wave phase velocity inversion alone. We apply the method to receiver functions obtained from earthquake records, and Rayleigh-wave phase velocities obtained from a microtremor array survey in the Niigata Plain, Japan. The basement depth in the estimated subsurface structure is approximately 7km.

1. INTRODUCTION

The S-wave velocity structure in sedimentary layers, down to the basement with an S-wave velocity of about 3 km/s, is essential information for precisely estimating or predicting strong-motion characteristics during earthquakes. To explore S-wave velocity structure of deep sedimentary layers, inversion of surface-wave phase velocities obtained from a microtremor array survey was developed (Horike, 1985; Okada, 2003). The method has been established as a convenient and low-cost method of providing an S-wave profile of deep sediments for engineers in earthquake engineering through many actual applications in large basins (e.g., Yamanaka and Yamada, 2002).

The microtremor array method utilizes dispersion of surface waves, commonly Rayleigh waves, contained in observed microtremor array data. In order to determine accurately a profile from near-surface to basement by this technique alone, microtremors must be observed over a broad frequency range, and phase velocity must be estimated precisely over this range, because deeper structure influences surface-wave dispersion at longer periods. However, the period range of observed microtremor data is generally limited because of the inherent small amplitude of long-period microtremors, and the limited array aperture.

A receiver-function method was originally developed to explore the S-wave velocity structure of the crust and mantle, using mainly broadband earthquake records (Langston, 1979). The method uses seismic phases generated from P-S conversions and multiple reflections at velocity discontinuities. Inversion of the receiver function (Owens et al., 1984) is an established method that many researchers use to explore the crust and mantle (e.g., Darbyshire et al., 2000; Priestley et al., 1988). Recently, the receiver function has been also attracting attention in earthquake engineering, as a method of estimating basement depth using the arrival time difference between direct P and P-S converted waves (Kobayashi et al., 1998). The inversion method of the receiver function was also proposed by Owens

et al. (1984) using a damped least-squares technique. In the least-squares technique, we may sometimes have practical difficulties from numerical instability and dependence of initial model on the choice of initial model. These difficulties are also met in the phase velocity inversion in the microtremor array exploration. In order to avoid these problems, global optimization algorithms, such as genetic algorithms and simulated annealing, were applied to inversion of the receiver function and phase velocity inversion (e.g., Shibutani et al., 1996; Yamanaka, 2005). Furthermore, it is well known that there must be a trade-off between shear-wave velocity and thickness in inversion of receiver functions (Ammon et al., 1990). In order to avoid this problem, Julia et al. (2000) performed a joint inversion of the receiver function with surface-wave group velocities, in crust and mantle studies.

In this study, we propose a joint inversion method, using genetic algorithms, to estimate the shear-wave velocity structure of deep sedimentary layers from receiver function and surface-wave phase velocity data. We discuss the applicability of the method, trade-off relation between parameters, and the uniqueness of the inversion result, using numerical experiment and analysis of actual observed data.

2. JOINT INVERSION METHOD

Here we present our joint inversion method for receiver function and Rayleigh-wave phase velocity data obtained at a common site. We use a genetic algorithm to infer a 1D S-wave velocity profile of the subsurface layers that can fit the two data. The GA that we implemented was similar to that of Yamanaka and Ishida (1996), which adopted a binary coding and introduced an elite selection and dynamic mutation, except for the definition of misfit, which is to be minimized in the inversion.

The dimensions and number of the receiver function and phase velocity data are different from each other. Therefore, the data must be reduced to dimensionless form in order to invert them simultaneously. In this study, the objective function (goodness of fit) for the receiver function ϕ_{RF} , and that for the phase velocity ϕ_{ph} , are defined as the sum of squared differences between the observations and calculated values, normalized by the standard deviation and divided by the number of data as shown in Equation (1).

$$\begin{aligned}\phi_{RF} &= (1/N_{RF}) \sum [\{ R_{obs}(t_i) - R_{cal}(t_i) \} / \sigma_{RF}(t_i)]^2 \\ \phi_{ph} &= (1/N_{ph}) \sum [\{ C_{obs}(T_j) - C_{cal}(T_j) / \sigma_{ph}(T_j) \}]^2\end{aligned}\quad (1)$$

Here, N_{RF} and N_{ph} are the number of data, and $\sigma_{RF}(t_i)$ and $\sigma_{ph}(T_j)$ are the standard deviations of the observed receiver function $R_{obs}(t_i)$ at time t_i and the observed phase velocity $C_{obs}(T_j)$ at period T_j , respectively. The objective function ϕ to be minimized in the joint inversion is defined as the average of the two misfits;

$$\phi = (\phi_{ph} + \phi_{RF})/2 \quad (2).$$

In the joint inversion, parameters of the subsurface structure at a target site are determined so that the misfit defined by Equation (2) will be minimized. Theoretical receiver function and Rayleigh-wave phase velocity are calculated using P- and S-wave velocities, thickness, and density of each layer in a flat-layered model. However, S-wave velocity and thickness are the most influential quantities (e.g., Horike, 1985). Therefore, S-wave velocity and thickness of each layer are parameterized in the inversion. P-wave velocity is calculated from S-wave velocity using an empirical relationship established from velocity data in deep sediments in Japan (Kitsunezaki et al., 1990). Densities are fixed at constant values. The theoretical receiver function, $R_{cal}(t_i)$, and the theoretical phase velocity, $C_{cal}(T_j)$, in Equation (1) are calculated by the methods of Haskell (1962) and Haskell (1960), respectively.

In the GA implementation, the population size and rates of crossover and mutation are set to be 30, 0.7, and 0.01, respectively. Each parameter was coded into an 8-bit binary string. Selection was performed according to a roulette rule. The inversion result was evaluated after 10 repetitions of a 100-generation calculation with different seeds of random number generator. Further details of the parameters in the GA can be seen in Yamanaka and Ishida (1996).

3. NUMERICAL EXPERIMENTS

A subsurface structural model used in the numerical experiment is shown in Figure 1. This is a typical model of deep sedimentary layers down to basement, where S-wave velocity is 3.0 km/s, in a large basin, such as the Kanto basin, Japan (Yamanaka and Yamada, 2002). Synthetic receiver function values and fundamental-mode Rayleigh-wave phase velocities for the model were calculated, and contaminated with random noise, uncorrelated with each other, as shown in Figures 2(a) and 2(b). These synthetic data were used in the numerical test. The noise added to the receiver function lies in the range of ± 0.2 from the synthetics, while we added 10% noise to the phase velocity. As explained earlier, phase velocity data are not always perfectly observed in an actual microtremor survey. Therefore, we used only the phase velocities at periods shorter than 4.5 s in the test, as shown in Figure 2(a). In the calculation of the synthetic receiver function, the incident angle of the P-wave at the top of basement was set to be 40° , and a band-pass filter in the period range from 0.5 s to 5.0 s was applied. We also assumed a frequency-independent Q-value to be defined by 1/15 of P- or S-wave velocity in m/s. Standard deviation of the receiver function, σ_{RF} in Equation (1), was set to be 0.2 uniformly, while that of the phase velocity, σ_{ph} , was set to be 10% of the noisy synthetic value. The cases of individual inversions for the phase velocity and receiver function were also tested for comparison. In the individual inversions, each misfit value in Equation (1) is minimized in the same way of the joint inversion. Search limits for S-wave velocities and thicknesses of each layer are also shown in Table 1.

Table 1 Model parameters and search areas in numerical experiments

Layer	True model			Search area	
	Vs km/s	H km	ρ t/m ³	Vs km/s	H km
1	0.6	0.3	1.8	0.3-0.8	0.1-1.0
2	1.0	1.0	2.0	0.8-1.8	0.1-1.5
3	1.8	0.7	2.3	1.5-2.0	0.1-1.5
4	3.0	∞	2.5	3.0	-

S-wave profiles obtained from the joint and individual inversions are compared with the true model in Figure 1. The comparison of the test data and the synthetics obtained from the joint inversion result is shown in Figures 2(a) and 2(b). The results of the joint inversion are in better agreement with the true model than the result of individual inversion of either the phase velocity only or receiver function only. The difference in basement depth between the true model and the individual inversion of phase velocity data is quite large. The model from the individual inversion of the receiver function data also differs from the true model in the S-wave velocity of the first layer. Because each individual inversion attempts to find an optimum model to satisfy the contaminated data without any other constraints, the results of the individual inversions are quite different from the true model. On the other hand, the model obtained from the joint inversion is not widely different from the true model. This indicates that the joint inversion tries to find the optimum model referring to the two datasets. This shows that the contribution from the receiver function data in the joint inversion performs a constraining role in the resultant model. Consequently, the joint inversion of receiver

function and surface-wave phase velocity data can reduce the effects of noise contained in each dataset. It is also noted that the joint inversion reconstruct the true model without the phase velocity data in enough long-period range more than 4.5 s.

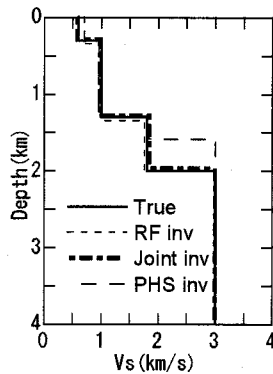


Figure 1 Comparison of true model and inverted models.

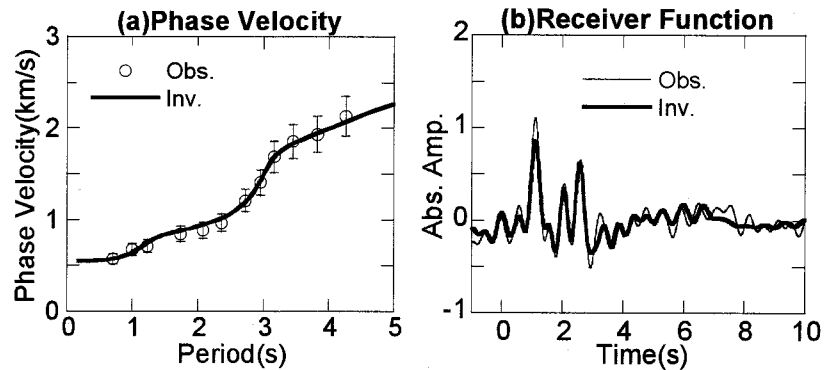


Figure 2 Comparison of receiver function and Rayleigh wave phase velocity for true model and inverted model.

4. APPLICATION OF JOINT INVERSION TO ACTUAL DATA

We applied the joint inversion method to receiver function and phase velocity data observed in the Niigata plain, Japan. In the area, sloshing of oil in huge oil storage tanks was observed during the 1983 Nihonkai-chubu earthquake with M of 7.7. Kudo and Sakaue (1984) indicated that long-period ground motion excited in the deep sedimentary layers in the Niigata plain is responsible for the sloshing. We try to infer S-wave velocity profile in the Niigata plain to provide subsurface structural information for understanding such a long-period motion in the area.

Rayleigh-wave phase velocity data were obtained from a microtremor array survey performed in the area (Kurose et al., 2000). Location of the site is shown in Figure 3. They temporarily installed vertical seismometers in two arrays with different sizes as shown in Figure 4. The estimated Rayleigh-wave phase velocity at periods from 1 to 7 s is shown in Figure 5. They also estimated an S-wave velocity profile from a genetic inversion of the Rayleigh-wave phase velocity. The resulting S-wave velocity profile is depicted in Figure 6. The figure also shows the S-wave profile estimated from an analysis of surface waves in earthquake records in the Niigata city (Kudo and Sakaue, 1984). Since the phase velocity in the microtremor array exploration is limited in long-period range, the basement depth from the phase velocity inversion is shallower than that by Kudo and Sakaue (1984) as can be seen in Figure 6.

We used earthquake records observed at the Niigata Observatory of the Japan Meteorological Agency for calculating the receiver function, because many earthquake records have been accumulated through long-term observation. The epicenters of the earthquakes used in the calculation are also shown in Figure 3. The water-level method of calculating receiver functions (Langston, 1979) was applied to the data in the first 10 s from the onset of the P-wave in these records. The receiver function obtained from averaging the results of the 5 events are shown in Figure 7. A band-pass filter, with a period range from 0.5 to 5.0 s, was applied during the calculations. A distinct phase can be seen at 3.3 s from the P-wave onset in the observed receiver functions. It is considered that the phase represents a P-S converted wave generated at the sediment/basement interface. We calculated theoretical receiver functions for the two previous models in Figure 6. The incident angles calculated

for the events are assumed to be 35° in the calculation. Figure 8 compares the calculated receiver functions with the observed one. The model for the S-wave profile from the microtremor array observation shows a similar distinct phase, although the arrival times do not agree with the observation. On the other hand, the overall features of the observed receiver function including absolute values are similar to theoretical one for the model by Kudo and Sakaue (1984).

In the joint inversion of the phase velocity and the receiver function, we assume a 5-layer model. The search spaces of the parameters are listed in Table 2. Figure 9 shows the S-wave velocity model obtained from the joint inversion. The basement depth for the model is much deeper than those in the previous work in Figure 6. Figures 10(a) and 102(b) show the comparisons between the observations of receiver function and phase velocity and the values calculated from the inverted model. The model can explain not only almost all of the major phases of the observed receiver function but also almost all of the observed phase velocity data.

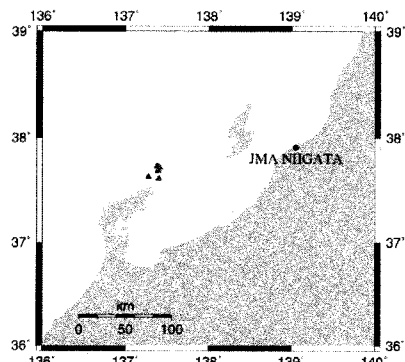


Figure 3 Map for earthquake station in Niigata with epicenters used in calculation of receiver function

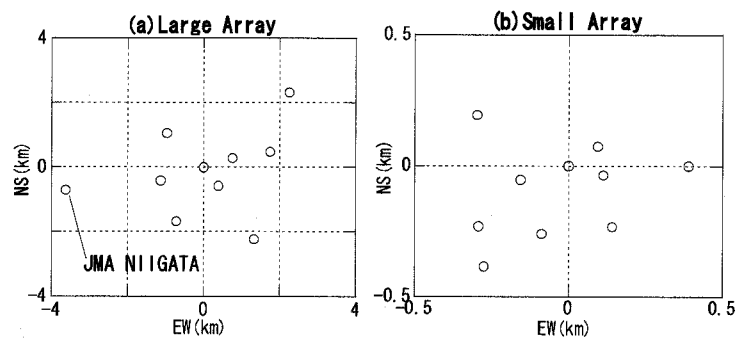


Figure 4 Array configurations in microtremor array explorations in Niigata area

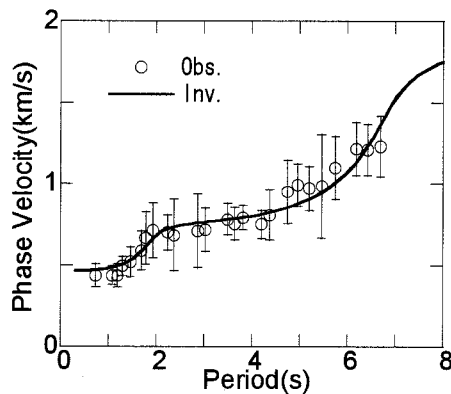


Figure 5 Comparison of observed phase velocity with calculated one for model from individual inversion by Kurose et al (2000).

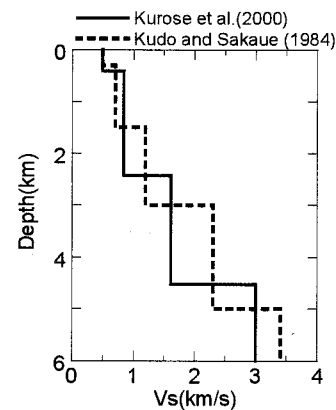


Figure 6 Comparison of models from individual inversion and by Kudo and Sakaue (1984).

Table 2 Search areas in inversion of observed data in Niigata

Layer	ρ t/m ³	Vs km/s	H km
1	1.7	0.3-0.6	0.2-0.6
2	2.0	0.6-1.0	1.0-2.5
3	2.2	1.0-1.8	1.0-2.5
4	2.4	1.8-2.6	1.5-3.5
5	2.5	3.0	-

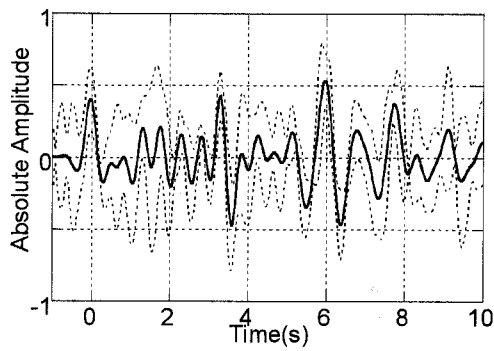


Figure 7 Receiver function observed at Niigata JMA station.

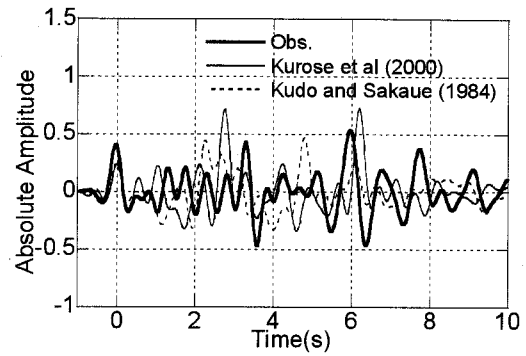


Figure 8 Comparison of observed receiver function with theoretical ones for models by Kurose et al (2000) and Kudo and Sakaue (1984).

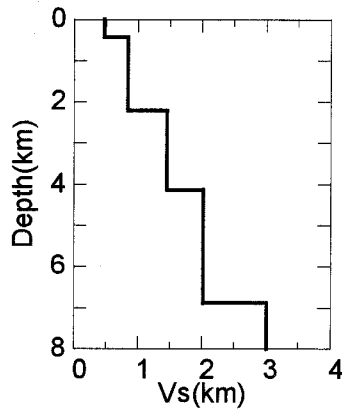


Figure 9 S-wave velocity profiles at Niigata station from joint inversion

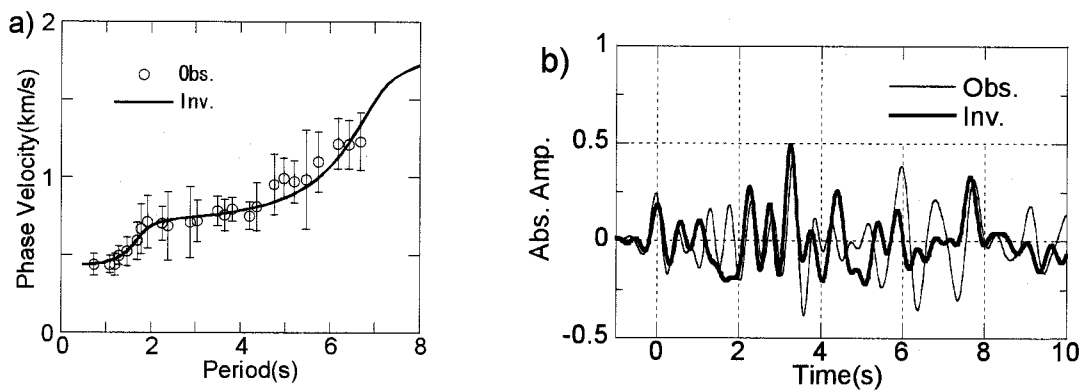


Figure 10 Comparison of observed phase velocity and receiver function with calculated ones for model from joint inversion at Niigata.

5. CONCLUSIONS

In this study, the method of joint inversion of receiver function and surface-wave phase velocity data, using genetic algorithms, was proposed to estimate a shear-wave velocity structure for deep sedimentary layers. Numerical experiments indicated that the proposed method could avoid the trade-off relation in modeling receiver function data only. This method is also effective in reducing uncertainty in deep structure when modeling only surface-wave phase velocity data over a limited period range. We apply the method to observed data in the Niigata plain, Japan, and proposed an S-wave model of deep sediments. In applying the joint inversion method to actual data at a site without any information on subsurface structure in advance, a priori assumptions are important in successful determination of an S-wave velocity profile. For example, the number of layers is one of the critical parameters. Empirical relationships between velocities of P- and S-waves are also one of the important assumptions in this joint inversion.

Acknowledgements:

Earthquake records used in this study were obtained by the Japan Meteorological Agency. This study is partly supported by a Grant-in-Aid for General Scientific Research (#14206081, #15510147) and Special Project for Earthquake Disaster Mitigation in Urban Areas from Japanese Ministry of Education, Culture, Sport, Science, and Technology.

References:

- Ammon, C.J., Randall G.R., and Zandt, G. (1990), On the nonuniqueness of receiver function inversion, *Journal of Geophysical Research*, **95**, 15303–15318.
- Darbyshire, F.A., Priestley, K.F., White R.S., Stefansson, R., Gudmundsson G.B., and Jakobsdottir, S.S. (2000), Crustal structure of central and northern Iceland from analysis of teleseismic receiver functions, *Geophysical Journal International*, **143**, 163–184.
- Haskell, N.A. (1960), The dispersion of surface waves in multilayered media, *Bulletin of the Seismological Society of America*, **50**, 657–679.
- Haskell, N.A. (1962), Crustal reflection of plane P and SV waves, *Journal of Geophysical Research*, **67**, 4751–4767.
- Horike, M. (1985), Inversion of phase velocity of long-period microtremors to the S wave velocity structure down to the basement in urbanized areas, *Journal of Physics of the Earth*, **33**, 59–96.
- Julia, J., Ammon, C.J., Herrmann, R.B., and Correig, A.M. (2000), Joint inversion of receiver function and surface wave dispersion observations, *Geophysical Journal International*, **143**, 99–112.
- Kitsunezaki, C., Goto, N., Kobayashi, Y., Ikawa, T., Horike, M., Saito, T., Kurota, T., Yamane, K., and Okuzumi, K. (1990), Estimation of P- and S- wave velocities in deep soil deposits for evaluating ground vibrations in earthquake, *Journal of the Japan Society for Natural Disaster Science*, **9**, 1–17 (in Japanese).
- Kobayashi, K., Uetake, T., Mashimo, M., and Kobayashi, H. (1998), An investigation on detection method of P to S converted waves for estimating deep underground structures, *Journal of Structural and Construction Engineering, Architectural Institute of Japan*, **505**, 45–52 (in Japanese).
- Kudo, K., and M. Sakaue (1984), Oil-sloshing in the huge tanks at Niigata due to the Nihonkai-chubu earthquake of 1983, *Bull. Earthq. Res. Inst.*, **59**, 361–382 (in Japanese).
- Kurose, T., H. Yamanaka, and Y. Kinugasa (2000), An estimation of shear wave velocity structure of Niigata plain by microtremor array observations, Abstract 2000 Japan Earth and Planetary Science joint meeting, Sg001 (in Japanese).
- Langston, C.A. (1979), Structure under Mount Rainier, Washington, inferred from teleseismic body waves, *Journal of Geophysical Research*, **84**, 4749–4762.
- Okada, H. (2003), The microtremor survey method: Society of Exploration Geophysicists.
- Owens, T.J., Zandt, G., and Taylor, S.R. (1984), Seismic evidence for an ancient rift beneath the Cumberland Plateau, Tennessee: A detailed analysis of broadband teleseismic P waveforms, *Journal of Geophysical Research*, **89**, 7783–7795.
- Priestley, K.F., Zandt, G., and Randall, G.E. (1988), Crustal structure in Eastern Kazakh, U.S.S.R from teleseismic receiver function, *Geophysical Research Letters*, **15**, 613–616.
- Shibutani, T., Sambridge, M., and Kennett, B. (1996), Genetic algorithm inversion for receiver functions with application to crust and uppermost mantle structure beneath Eastern Australia, *Geophysical Research Letters*, **23**, 1829–1832.
- Yamanaka, H., and Ishida, H. (1996), Application of genetic algorithms to an inversion of surface-wave dispersion data: *Bulletin of the Seismological Society of America*, **86**, 436–444.

- Yamanaka, H. and N. Yamada (2002). Estimation of 3D S-wave velocity model of deep sedimentary layers in Kanto plain, Japan, using microtremor array measurements, *Butsuri-Tansa (Geophysical exploration)*, **55**, 53-66 (in Japanese).
- Yamanaka, H (2005), Comparison of performance of heuristic search methods for phase velocity inversion in shallow surface wave methods, *Journal of Environmental and Engineering Geophysics*, **10**, 163-173.

A METHOD FOR ESTIMATION OF 2-D SUBSURFACE STRUCTURE USING GRAVITY AND MICROTREMOR DATA SIMULTANEOUSLY

K. Sakai¹⁾ and H. Morikawa²⁾

1) Graduate Student, Department of Built Environment, Tokyo Institute of Technology, Japan

2) Associate Professor, Department of Built Environment, Tokyo Institute of Technology, Japan

sakaik@enveng.titech.ac.jp, morika@enveng.titech.ac.jp

Abstract: Earthquake ground motions are influenced by parameters of ground structure such as layer thickness, P-wave velocity, S-wave velocity and density. Thus, to estimate detailed subsurface structure is important for earthquake hazard mitigation. For this purpose, many geophysical survey technique has been proposed, though, they have merits and demerits with respect to some specific features, for example, costs, resources, labors, accuracy, and so on. To obtain the precise model of ground structure, it is effective to combine the merits from the different techniques. We propose a joint inversion method using gravity and microtremors data: it is noted that we can obtain the density structure from the former and the velocity structure from the later. To confirm the appropriateness of the proposed method, we apply the method to the synthetic data and actual observation data. From the results, we confirmed that the method can provide a reasonable model of ground structure.

1. INTRODUCTION

Characteristics of strong motion are affected by 3-D subsurface structure. Thus, it is important to estimate the subsurface structure, in order to consider the earthquake disaster and its mitigation. The geophysical survey technique such as seismic refraction and reflection, microtremor and gravity surveys can be used to estimate the subsurface structure. The seismic refraction and reflection survey can provide good information about the ground structure, while this type of survey requires much cost and labor for the observation. Simple observation systems can be used for the microtremor and gravity surveys and the data of microtremors and gravity can be obtained anytime and anywhere. The microtremor and gravity surveys, however, cannot provide a unique solution for the ground structure because there are so many local minimum solutions in the process to find the ground structure by means of an inversion technique. Furthermore, we often face the problem that a model of the ground structure, which is obtained through observation data based on one physical values, does not satisfy observation data on other physical values. To avoid these problems and to obtain more precise model of ground structure, we propose a joint inversion method using microtremor and gravity data.

2. JOINT INVERSION METHOD

2.1 Joint Inversion Method using Bouguer Anomaly and Phase Velocity

It is known that microtremor and gravity data depend strongly on the velocity structure and density structure, respectively. Thus, ground structures estimated from the microtremor and

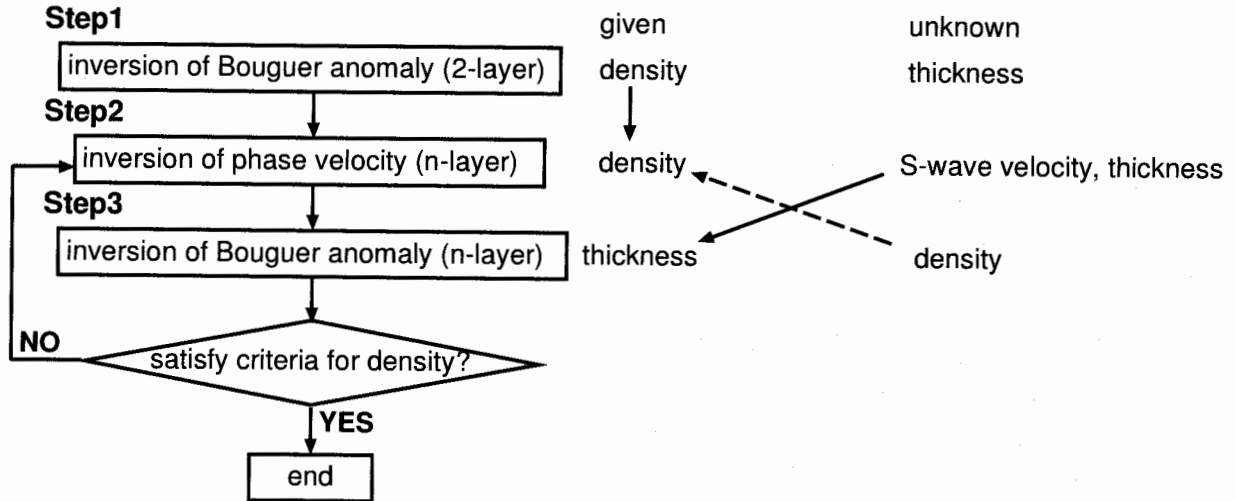


Figure 1 Procedure of joint inversion using Bouguer anomaly and phase velocity

gravity data show good resolution for the velocity and density, respectively. We employ advantages of microtremor and gravity survey technique for the proposed method.

Figure 1 shows the procedure of the proposed method. Step 1: two-layered (sediment and basement) model is estimated from the inversion of Bouguer anomaly, which is computed from gravity data. On this step, the thickness of the sedimentary layer is unknown and the density is appropriately given. Step 2: n-layered model is estimated from the inversion of the phase velocities which are obtained through the array observation of microtremors. On this step, the thickness and S-wave velocities of each layer are unknown and density is given as the value which is used the previous step. For the P-wave velocity, the regressive relationships between the P- and S-wave velocities are used. Step 3: n-layered model is estimated from the inversion of Bouguer anomaly. On this step, density is unknown and thickness of each layer is interpolated using the values which is obtained at the array observation sites for microtremors on the previous step. After the calculation of Step 3, the values of the density on Step 2 and 3 are compared. In a case where the differences between these two values of density are enough small, the calculation is terminated. In the other case, the procedure of calculation goes back to Step 2 and the values of density obtained at Step 3 are applied to the inversion on Step 2. We may find a model of the ground structure through the iteration of Step 2 and Step 3.

2.2 Joint Inversion Method including the horizontal/vertical spectral ratio (H/V)

In the method proposed at Figure 1, we have to carry out the array observations at many sites to ensure the accuracy of the estimated ground structure. We have sometimes the situations that it is difficult to complete the array observation because of various reasons. For this, we expand the method to apply the horizontal/vertical spectral ratio (H/V) of microtremors. H/V can be obtained from the observation of three components of the microtremors at a single site. This means that the H/V is obtained much easier than phase velocity. Figure 2 shows the procedure of the modified joint inversion method including the H/V. While the inversion method of Figure 2 is almost same as that of Figure 1. We insert the procedure for the inversion of the H/V after the Step 2 to handle the H/V. On this step, only the thickness of each layer are unknown and the densities and S-wave velocities are given, because we should reduce the unknown parameters to avoid the instability of the inversion process for H/V. Afterward the inversion of gravity data is held as Step 4.

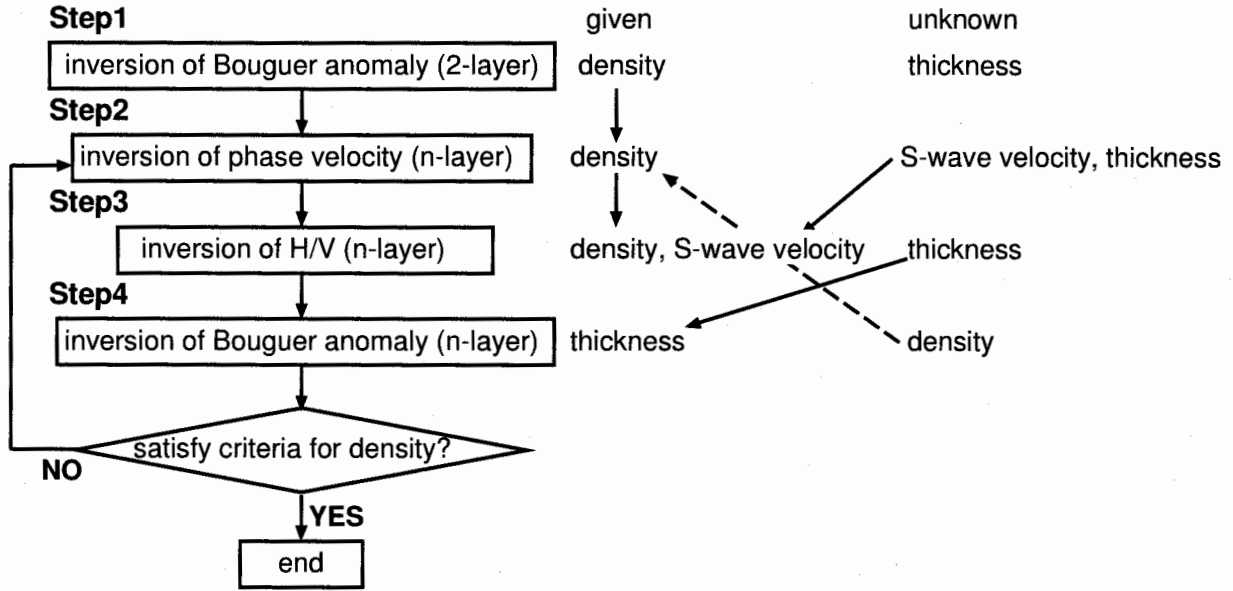


Figure 2 Procedure of joint inversion including the H/V

3. NUMERICAL SIMULATION

3.1 Joint Inversion using Bouguer Anomaly and Phase Velocity

To discuss the appropriateness of the proposed method, numerical simulation is conducted. First, we examine the joint inversion method of Bouguer anomaly and phase velocity. Let us consider a ground structure with four layers. The structural model, which we used for the numerical simulation, is shown in Figure 3. We set 13 observation sites of every 1km (0–12, A–F of Figure 3) for the gravity survey and 6 sites of every 2km (A–F of Figure 3) for the array observation of microtremors. The phase velocities (Haskell 1953) and Bouguer anomaly (Talwani *et al.* 1960) at the observation sites are calculated analytically from the considering ground structure.

For the inversion of Bouguer anomaly (2-layer) on Step 1, we apply the following formula (Komazawa 1998):

$$D^{(n+1)} = D^{(n)} + 0.75 \times \frac{(\Delta g^{(n)} - g^{res})}{2\pi G\rho}, \quad (1)$$

where G is the universal constant of gravitation, ρ is difference of density between basement and sediment, g^{res} is observed Bouguer anomaly, $D^{(n)}$ is depth to the gravity basement at n -th iteration and $\Delta g^{(n)}$ is Bouguer anomaly calculated analytically from $D^{(n)}$. To find the optimal S-wave velocities and thickness of each layer on Step 2, the sum of squares of differences between the observed and analytical phase velocity is minimized using the quasi-Newton method. We use the nonnegative values for the unknown parameters as the constraint. On Step 3, to obtain the optimal densities for each layer, we minimize the sum of squares of differences between the observed and analytical Bouguer anomaly under the constraint of $1.0 \leq \rho_j \leq 3.0(t/m^3)$, where ρ_j is density at j -th layer. For this the technique of sequential quadratic programming is used. A cubic spline function is employed to interpolate the shape of layer boundary using the thickness of each layer at the observation sites of microtremors (Koketsu *et al.* 1992).

Following the above procedure, 50-time iterative calculations from Step 2 (inversion of phase velocity) to Step 3 (that of Bouguer anomaly) is proceeded. Figure 4 shows the values of density at each iteration and Figure 5 shows the values of misfit f_V and f_H for S-wave velocity

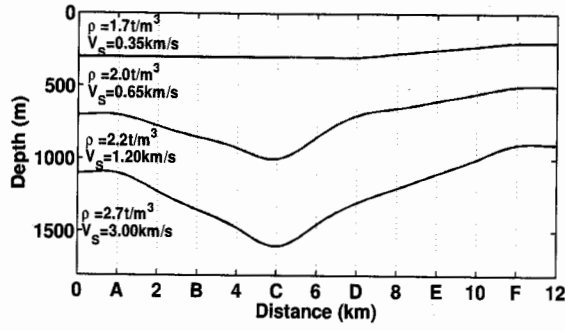


Figure 3 A model of ground structure for numerical simulation.

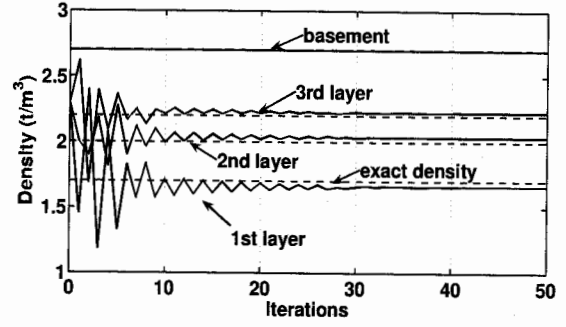


Figure 4 Variation of density by iteration.

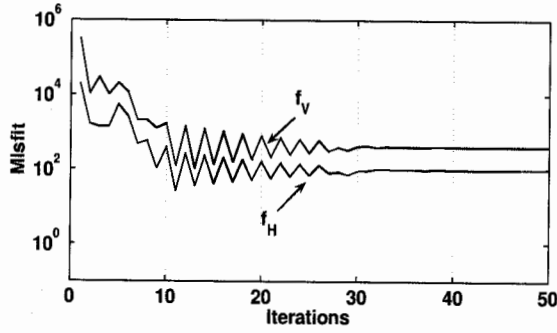


Figure 5 Variation of misfits by iteration.

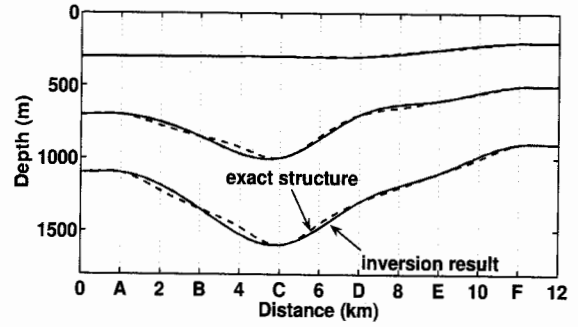


Figure 6 Estimated subsurface structure.

V_S and thickness H , respectively, which are defined by the follows:

$$f_V = \frac{\sum_{i=1}^L \sum_{j=1}^M [V_S^{ans}(x_i, j) - V_S^{inv}(x_i, j)]^2}{L \times M} \quad (2)$$

$$f_H = \frac{\sum_{i=1}^L \sum_{j=1}^{M-1} [H^{ans}(x_i, j) - H^{inv}(x_i, j)]^2}{L \times (M - 1)}, \quad (3)$$

where $V_S^{ans}(x_i, j)$ and $H^{ans}(x_i, j)$ stand for the exact values of V_S and H of j -th layer at site i , $V_S^{inv}(x_i, j)$ and $H^{inv}(x_i, j)$ for the estimated values by the inversion, and L and M for the numbers of observation sites and layers, respectively. Figure 6 shows the subsurface structure obtained through 50-time iterative calculations.

As shown in Figure 4, the values of density at each layer is converged to the closed value of exact solution. The misfit of thickness and S-wave velocity (Figure 5) decrease with the number of iteration. The estimated structure (Figure 6) is almost same as the exact structure. Therefore, the appropriateness of the proposed method is confirmed.

Although the estimated subsurface structure and density are almost same as exact solution, estimated structure does not coincide definitely the exact solution. We assume that the slight difference between the estimated and exact solutions is caused by the error of interpolated shape for layer boundary. To confirm this, we consider a slightly modified model of ground structure whose boundary can be represented by the cubic spline functions, because we applied the cubic spline functions to interpolate the shape of boundary. The proposed method is applied to the modified model and the optimal solution for the ground structure is obtained as shown in Figure 7. From this figure, it is observed that the obtained structure coincides with the exact solution. This means that the estimated structure depends on the accuracy of the interpolation of the boundary shape and the proposed method can provide the good estimation in a case where we apply the appropriate function for the interpolation.

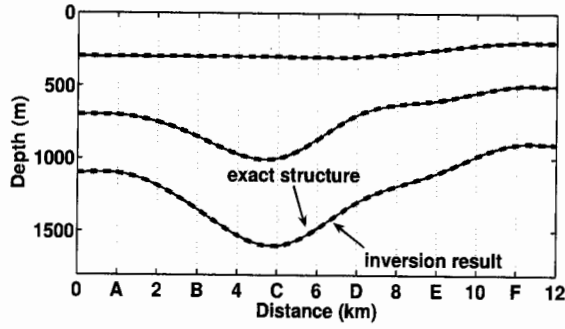


Figure 7 Estimated subsurface structure (subsurface structure can express spline function)

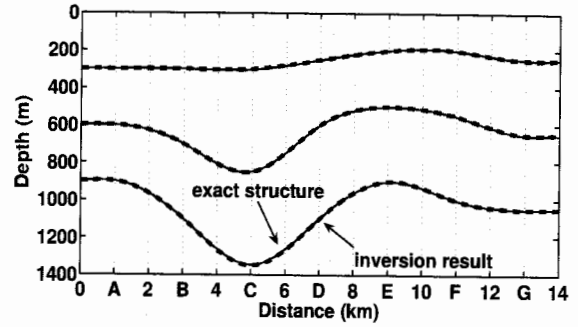


Figure 8 Estimated subsurface structure (including the H/V)

3.2 Joint Inversion including the H/V

We examine the appropriateness of the method of inversion including H/V. We introduce the data set of H/V instead of the data of the phase velocities obtained from the array observations of microtremors. We have the observation data of gravity at 15 sites of 0 to 14 and A to G, phase velocities at 2 sites of B and F, and H/V at 5 sites of A, C, D, E and G shown in Figure 8. As the handling the H/V, we minimize the sum of the squares of differences between the observed and analytical H/V. To minimize the sum, we used the technique of grid search. As the result, we can obtain the exact solution of the ground structure as shown in 8 under the less information of the phase velocities. Therefore, we confirmed that the H/V can perform efficiently to estimate the ground structure.

4. INVERSION OF OBSERVED DATA

4.1 Joint Inversion using Bouguer Anomaly and Phase Velocity

To verify the applicability of the proposed method, we apply the method shown in Figure 1 to actual data observed at the Yumigahama Peninsula, Tottori.

Generally, the actual data are contaminated by the various noise and the ground structure is not so homogeneous as the ideal model presented in the numerical examples. Thus, to avoid these problems, to ensure the stability of the calculation and to keep the simplicity of the analysis, the procedure of the analysis and inversion techniques at each step of the procedure are modified. After the inversion of phase velocity (Step 2), we insert a new step. To be homogeneous layers, the S-wave velocities are averaged with respect to sites for each layer as follows:

$$V_S(j) = \frac{1}{L} \sum_{i=1}^L V_S(x_i, j). \quad (4)$$

Using the values of $V_S(j)$, then the inversion of phase velocity is carried out. On this step, the only thickness of each layer is unknown and averaged S-wave velocity and Bouguer anomaly is carried out. For the inversion of the phase velocity and Bouguer anomaly, we use the technique of the genetic algorithm (Yamanaka *et al.* 1996) and grid search, respectively.

The upper and lower bounds in the search spaces of the parameters are listed in Table 1. Two different functions to interpolate the layer boundary are conducted: one is a cubic spline function (Case 1) and the other is a function which is generated by a modification of the shape of gravity basement (Case 2).

Table 1 Search space for the joint inversion of phase velocity and Bouguer anomaly (Yumigahama, Tottori).

Layer	V_S (km/s)	ρ (t/m ³)	H (m)
1	0.35–0.45	1.70–2.05	10–500
2	1.50–1.70	2.05–2.30	50–1000
3	2.30–2.50	2.30–2.60	50–1500
4	3.18–3.22	2.70	∞

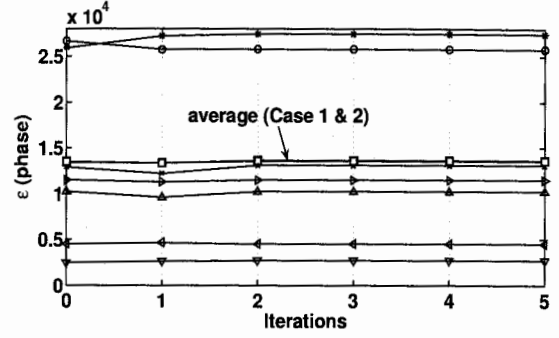


Figure 9 The misfit of the phase velocity.

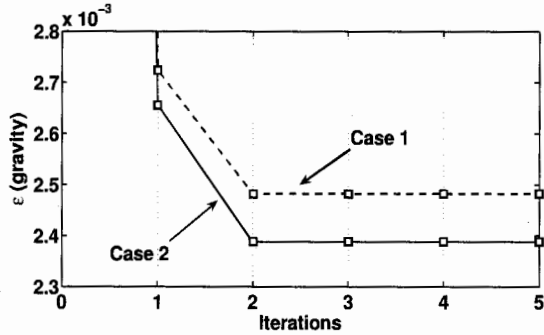


Figure 10 The misfit of the Bouguer anomaly.

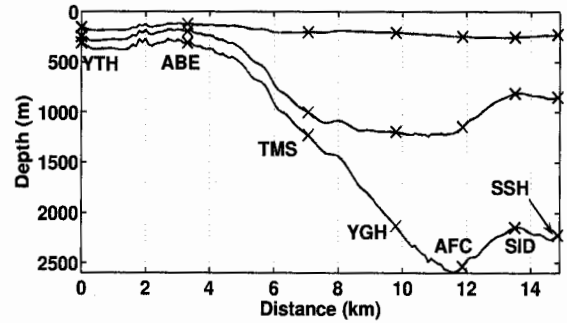


Figure 11 Estimated subsurface structure.

Using above inversion technique, we proceed 5 times iterative calculation from Step 2 (inversion of phase velocity) to Step 3 (inversion of Bouguer anomaly) of Figure 1. Figures 9 and 10 show the squared misfits of the phase velocity and the Bouguer anomaly at each iteration, respectively. As shown in Figure 9, the misfits of the phase velocities is almost constant through the iterations. While the misfit of the Bouguer anomaly (Figure 10) is drastically reduced by the joint inversion. This means that the proposed method can provide a better solution for the subsurface structure than the solution obtained by the one of the phase velocities and Bouguer anomaly. As shown in Figure 10, furthermore, Case 2 provides a better solution than Case 1. From this, it is observed that a shape function based on the gravity basement is more suitable than cubic spline function for the interpolation of the layer boundary.

Figure 11 shows the estimated subsurface structure after iterative calculation. The estimated structure agrees with the subsurface structure estimated by the seismic reflection survey.

4.2 Joint Inversion including the H/V

Gravity and microtremors are observed at the Tsukuba, Ibaraki. We apply the method including the process of the H/V inversion (Figure 2) to the observed data. We applied the modified procedure and inversion techniques for the analysis which are described in the previous section. Furthermore, the objective function for the H/V inversion is also modified as the follows:

$$\epsilon(H/V) = \frac{1}{2}[(f_{obs}^{peak} - f_{cal}^{peak})^2 + (f_{obs}^{dip} - f_{cal}^{dip})^2] \rightarrow \min, \quad (5)$$

where f_{obs}^{peak} and f_{obs}^{dip} stand for peak and dip frequencies for fundamental mode of the observation data, respectively, and f_{cal}^{peak} and f_{cal}^{dip} for ones obtained through the analytical calculation based on the structure model. Since the H/V inversion is affected negatively by the noise, we reduced the target for fitting to ensure the numerical stability.

Table 2 Search space for the joint inversion of phase velocity and Bouguer anomaly (Tsukuba).

Layer	V_S (km/s)	ρ (t/m ³)	H (m)
1	0.26–0.30	1.80–2.00	10–100
2	0.40–0.46	1.90–2.10	10–300
3	0.65–0.70	2.00–2.40	50–600
4	3.29–3.31	2.63	∞

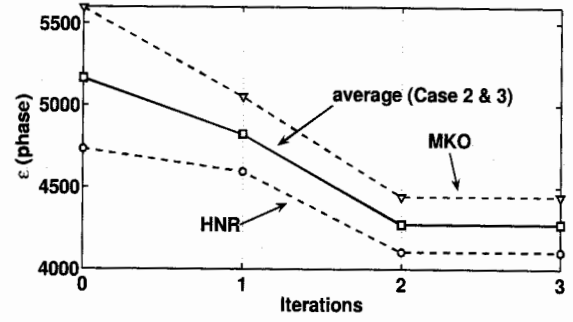


Figure 12 The misfit of the phase velocity.

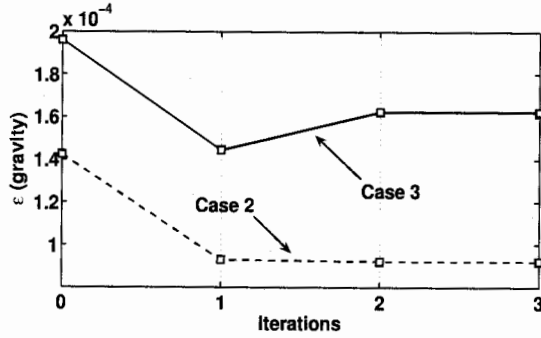


Figure 13 The misfit of the Bouguer anomaly.

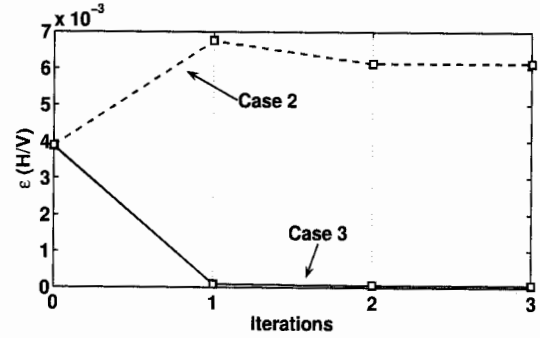


Figure 14 The misfit of the H/V.

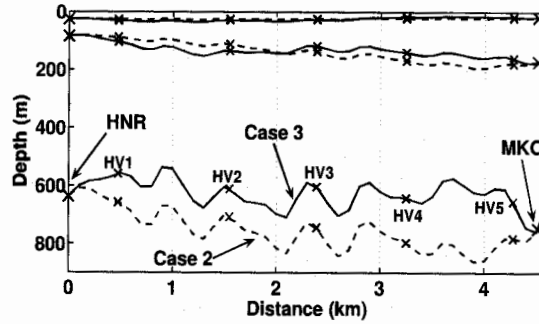


Figure 15 Estimated subsurface structure.

The upper and lower bounds in the search spaces of the parameters are also listed in Table 2. For the interpolation of the layer boundary, we use the function obtained from the shape of the gravity basement.

Using above inversion technique, we proceed 3 times iterative calculation from Step 2 (inversion of phase velocity) to Step 4 (that of Bouguer anomaly) of Figure 2. Figures 12, 13 and 14 show the misfits to the phase velocity, the Bouguer anomaly and the H/V, respectively. Case 2 in these figures shows the result of inversion without the H/V, while Case 3 shows that with the H/V. Figure 15 shows the estimated subsurface structure after iterative calculation.

As shown in Figures 12 and 13, the misfits of the Bouguer anomaly and the phase velocities are reduced by the procedure. The misfit of Case 3 for the Bouguer anomaly is larger than Case 2. This result seems to show that the process of H/V inversion blocks the accurate estimation of the density structure. It is noted that the misfit of Case 3 for H/V is smaller than Case 2 as shown in Figure 14. This means that the obtained model of the subsurface structure can satisfy the velocity structure. In this case, we should consider the trade-off between the

accuracy of density and velocity structures. For example, in a case where we apply the model to the numerical simulation of the seismic wave fields, the accuracy of the velocity structure precedes the density one. Since the priority depends on the situation or objective to use the model of subsurface structure, we cannot decide uniquely the best model. In our case, we apply mainly the model to the numerical simulation of the earthquake ground motion. Thus, the solution of Case 3 in Figure 15 may be useful for our objective. Actually, the result of Case 3 agree with the profile obtained from the seismic reflection survey.

5. CONCLUSIONS

We proposed a joint inversion method using gravity and microtremor data to obtain precise model of subsurface structure. Through the results obtained from the inversion of numerical and actual data, we confirmed that the proposed method can provide the reasonable model of the ground structure. Furthermore, it is observed that the data of H/V perform efficiently for the method.

References:

- Haskell, N. A. (1953), "The dispersion of surface waves on multilayered media", *Bulletin of the Seismological Society of America*, 43, 17-34.
- Koketsu, K. and Higashi, S. (1992), "Three-Dimensional Topography of the Sediment/Basement Interface in the Tokyo Metropolitan Area, Central Japan", *Bulletin of the Seismological Society of America*, 82, 2328-2349.
- Komazawa, M. (1998), "Gravity survey", *Handbook of Exploration Geophysics*, 433-471.
- Talwani, M. and Ewing, M. (1960), "Rapid computation for gravitational attraction of three-dimensional bodies of arbitrary shape", *Geophysics*, 25, 203-225.
- Yamanaka, H. and Ishida, H. (1996), "Application of genetic algorithms to an inversion of surface-wave dispersion data", *Bulletin of the Seismological Society of America*, 86, 436-444.

ESTIMATION OF S-WAVE VELOCITY MODEL IN THE WESTERN COASTAL PLAIN OF TAIWAN

C. M. Lin¹⁾, K. L. Wen²⁾ and T. M. Chang³⁾

1) PhD Candidate, Institute of Geophysics, National Central University, Taiwan

2) Professor, Institute of Geophysics, National Central University, Taiwan

*3) Associate Research Fellow, National Center for Research on Earthquake Engineering, Taiwan
cheminlin@gmail.com, wenkl@earth.ncu.edu.tw, tmchang@ncree.org.tw*

Abstract: Western coastal plain borders on the west of western foothills which is a fold-and-thrust zone and one of the major seismic zones in Taiwan. The earthquakes from western foothills often cause a lot of disaster in coastal plain, like 1999 Chi-Chi earthquake. We conducted array measurements of microtremors at seven sites in western coastal plain in Taiwan. At each site, four arrays with difference apertures are performed. F-K analysis was used to obtain the phase velocity dispersion curves. After inversion of dispersion curves, the S-wave velocity structures under all sites were estimated. We could roughly describe the variation of shallow shear wave velocity structures in the western coastal plain of Taiwan.

According to the previous studies, the inversion of dispersion curves in the frequency range from 0.1 to 5 Hz can completely estimate shear wave velocity models down to the depth of 3 km. The results of all sites which we desired correctly reflect the S-wave velocities and depths of main interfaces including the tops of Pliocene and Miocene. Peikang High apparently dominates the S-wave velocity structure in western Taiwan. Therefore, the S-wave velocity of Dongshih at the depth about 1 km is higher than that of other sites. And the depths of major interfaces are shallowest near Peikang High and dip to north, east and south. Besides, the variation of S-wave velocity at Yijhu is similar to Dongshih, because the Yijhu hinge fault which is the southern boundary of Peikang High cross this area. Residual gravities and seismic surveys show that there are a lot of complex structures including normal faults and anticlines in this area.

1. INTRODUCTION

Western coastal plain in Taiwan is a important economic zone with a lot of population. This area borders on the west of western foothills which is a fold-and-thrust zone and one of the major seismic zones in Taiwan. The earthquakes from western foothills often cause a lot of disaster in coastal plain, like 1999 Chi-Chi earthquake. To reduce the loss of life and property from strong ground shaking, it is necessary to estimating site-effect and theoretical simulation of strong motion.

For the theoretical simulation or prediction of strong motion, it is important to get information of underground structure, especially for S-wave velocity of sedimentary layers. A Rayleigh-wave inversion technique using array records of microtremors has been emphasized as one of useful methods to obtain S-wave velocity models (e.g. Horike, 1985; Matsushima and Okada, 1990; Sato et al., 1991). This method is based on the assumption that microtremors are dominated by Rayleigh-waves. Therefore, array measurement of microtremors can estimate phase velocities from vertical components of array records of microtremors. Then, the dispersion curves suited to the studying sites are solved to estimate the structures by the Rayleigh-wave inversion. However, the structures obtained by this method are average within the array. It is not suitable to apply this method to sites where the velocity structure is sharply varying in horizontal direction.

In this study, we conducted array measurements of microtremors at seven sites in western Taiwan to obtain the S-wave velocity structures. And we try to discuss this result with previous studies for constructing the suitable shear wave velocity model of western coastal plain in Taiwan.

2. ARRAY MEASUREMENT OF MICROTREMORS

We conducted array measurements of microtremors at seven sites including Lugang, Erlin, Huwei, Dongshih, Taibao, Yijhu and Jiali in the western coastal plain in Taiwan (Figure 1). At each site, we performed four arrays (S, M, L and XL arrays) with difference apertures. Every array at the same site consisted of 10 seismometers distributed over three concentric circles with one common station at the center for frequency-wavenumber (F-K) spectral analysis (e.g. Horike, 1985; Kawase et al., 1998). Table 1 shows the approximate radius of four arrays. And the real radius would be changed slightly because of the difficulty of field work. Figure 2 shows the array configuration of XL array at Lugang as an example. The relative coordinates of stations are measured by the total station except the stations 1 km away measured by GPS system.

The seismometers we used are the three-component velocity sensors with the flat amplitude in the frequency range from 0.07 to 100 Hz. The sampling frequency of array measurements is 100Hz. The lengths of continuous recording time are various between 20 minutes to 6 hours according to the aperture of array.

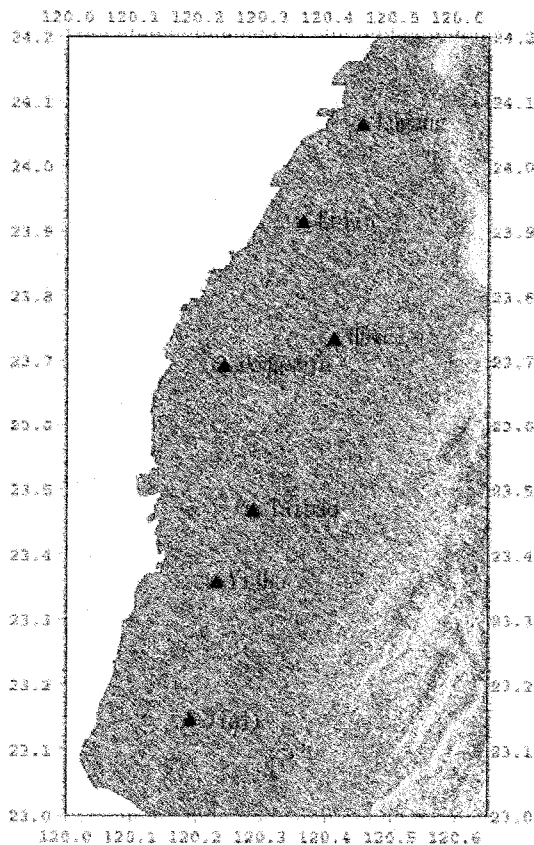


Figure 1 The distribution of the seven sites for array measurements of microtremors in western Taiwan.

Size	Radius of inner circle	Radius of middle circle	Radius of outside circle
S	8m	16m	32m
M	32m	64m	128m
L	128m	250m	500m
XL	250m	500m	1km

Table 1 The approximate radius of all arrays.

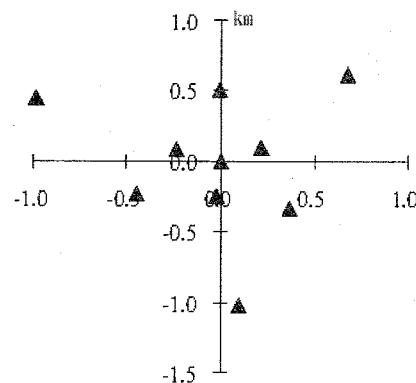


Figure 2 The array configuration of XL array at Lugang.

3. DETERMINATION OF THE S-WAVE VELOCITY STRUCTURE

The waveforms of vertical components are divided into time windows with the lengths of 20.48, 40.96 and 81.92 sec by 2 sec moving windows for F-K analysis. Phase velocities obtained from different lengths of time windows are estimated by F-K spectral analysis based on the maximum likelihood method (Capon, 1969). And the propagation directions are also obtained from the F-K spectra. Figure 3 shows the phase velocities with different signs representing different apertures of arrays and different colors representing different lengths of time windows at Lugang. According to the results of phase velocities, we determined the dispersion curves by picking the reasonable and suitable phase velocities. Figure 4 shows dispersion curves of all sites. It is apparent that the estimated dispersion curves slightly vary from site to site.

Before inversion of S-wave velocity structures, we have to decide the initial models which dominate the correctness of results for all sites. In this study, we applied genetic algorithms (GA) to searching the appropriate initial models. Figure 5 shows the best twenty results of GA searching for the initial model of Lugang. According to the results of GA, we decided the initial models without some apparent faults for inversion.

Finally, the conventional surface waves inversion (Herrmann, 1987) are used to invert the S-wave velocity structures by dispersion curves. We also test the sensitivity of all layers and leave out the immaterial layers to emphasize the major interfaces of velocity structures. Figure 6 shows the observed and theoretical dispersion curves of all studying sites in period domain. At all sites, the fitness between the observed and theoretical dispersion curves is certainly good. And the shear wave velocity structures of inversion results are shown in Figure 7.

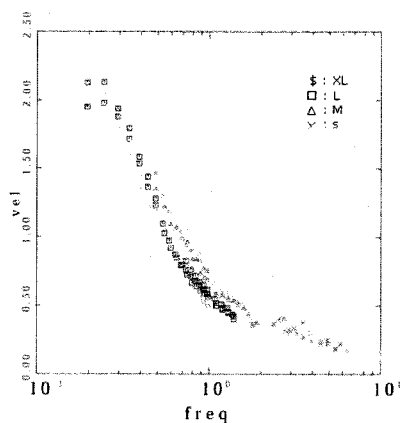


Figure 3 The phase velocity at Lugang.

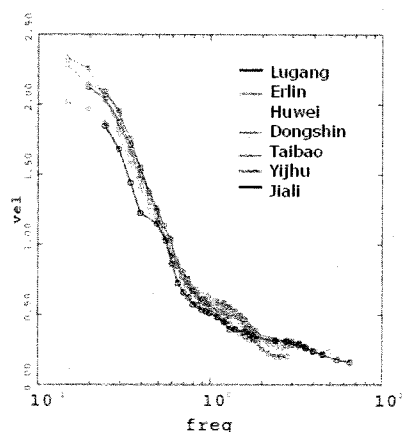


Figure 4 The dispersion curves obtained from F-K spectral analysis at all sites.

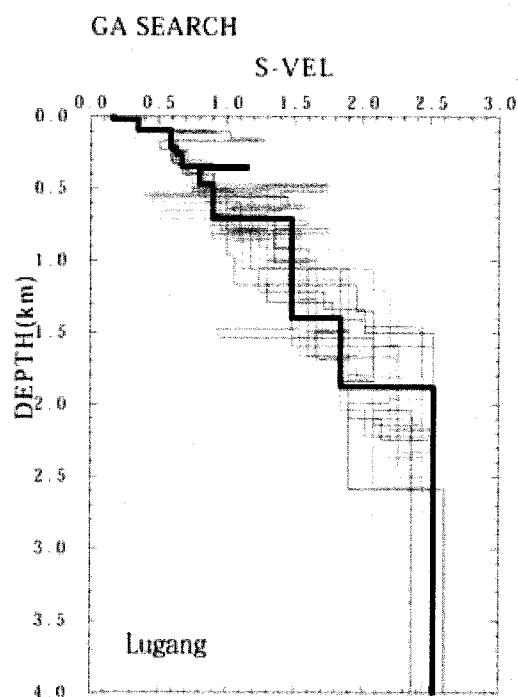


Figure 5 The best twenty results of GA searching at Lugang.

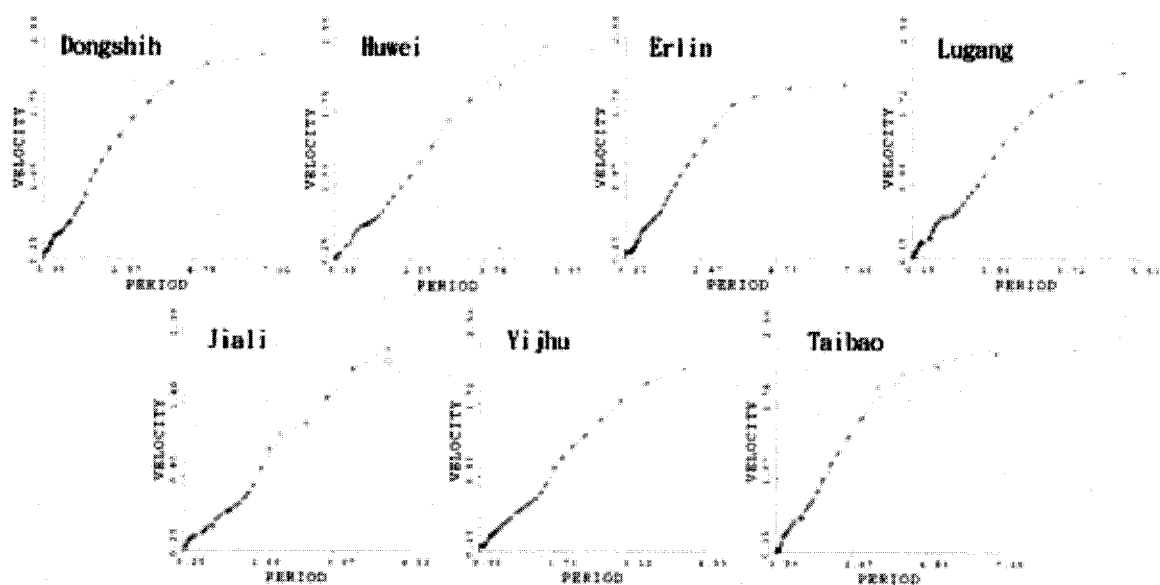


Figure 6 The observed (black circles) and theoretical (line) dispersion curves of seven sites in period domain.

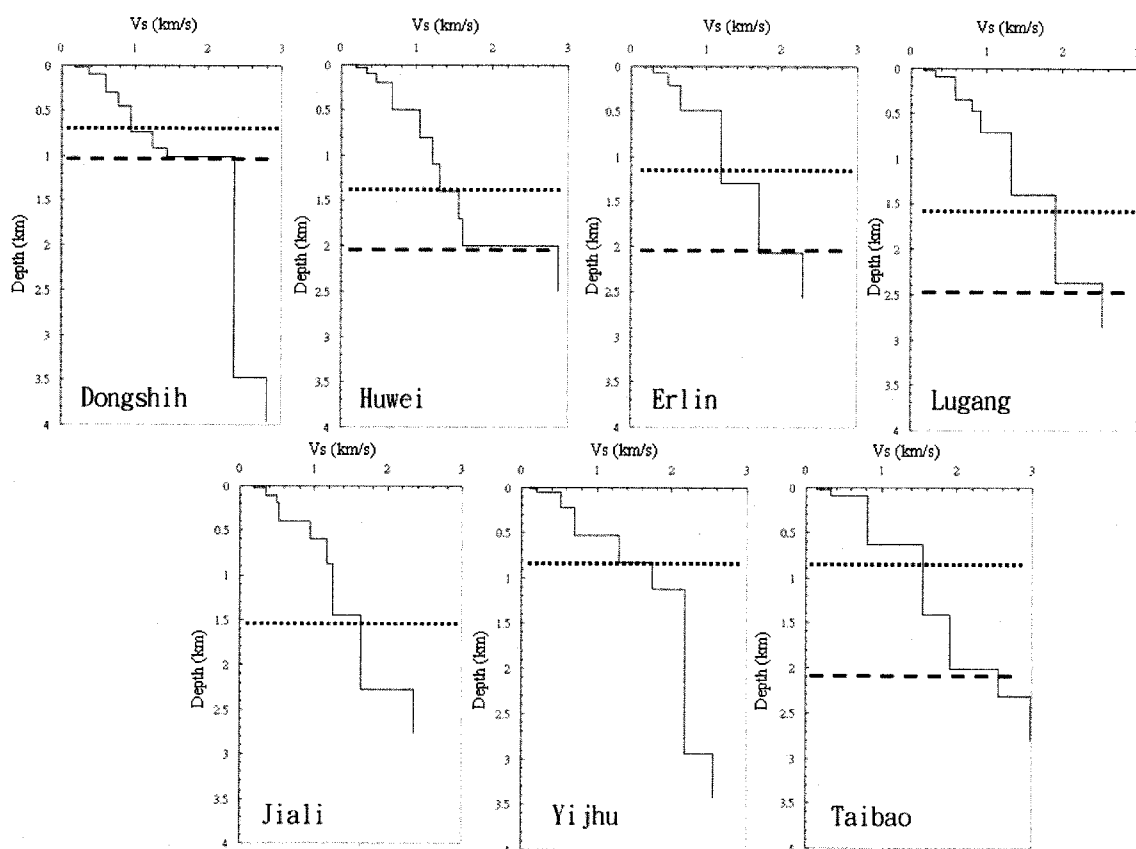


Figure 7 The shear wave velocity models obtained by inversions of dispersion curves at all sites. The depths of the top of Pliocene indicated by dotted lines and the depths of the top of Miocene indicated by dash lines are based on the seismic survey.

4. DISCUSSIONS

In the results of S-wave velocity models, the trends and variations of velocities at all sites are alike with some different depths of interfaces. But, the results of Dongshih and Yijhu present higher velocities than other sites under about 1 km. According to the seismic survey in previous studies, the depths of major interfaces under western Taiwan including the tops of Pliocene and upper Miocene are shallowest near Peikang High and dip to north, east and south (Pan, 1967; Pan, 1968; Chen, 1978). We draw these interfaces on Figure 7 for comparison. The dotted lines indicate the depths of the top of Pliocene, and the dash lines indicate the depth of the top of Miocene in Figure 7. But, the information about the depths of the top of Miocene at Yijhu and Jiali are deficient. It is apparent that the velocity structures we preferred at all sites reflect these two major interfaces. Therefore, the shear wave velocity structure of Dongshih presents the highest velocity. And the variations of depths of these two interfaces are also shown on our results.

Furthermore, the Yijhu hinge fault which is the southern boundary of Peikang High cross through Yijhu. There are a lot of complex structures including normal faults and anticlines at Yijhu according to the residual gravities and seismic survey (Hu and Hsu, 1988). Because of the complex structures, the S-wave velocity model at Yijhu is apparently higher than other sites based on the assumption of F-K analysis.

In this few years, well drillings of TSMIP (Taiwan Strong Motion Instrumentation Program) stations are performed and the V_p and V_s are measured by P-S logging. But, the depths of these wells are all just 40 to 70 meters. The logging data of TSMIP stations within a distance of 5 kilometers from each studying sites are selected except Lugang which is without suitable stations. Figure 8 is the comparison between the results of inversion on near surface and the logging data of TSMIP stations. It shows that the S-wave velocities of inversions agree with the V_p and V_s of well loggings.

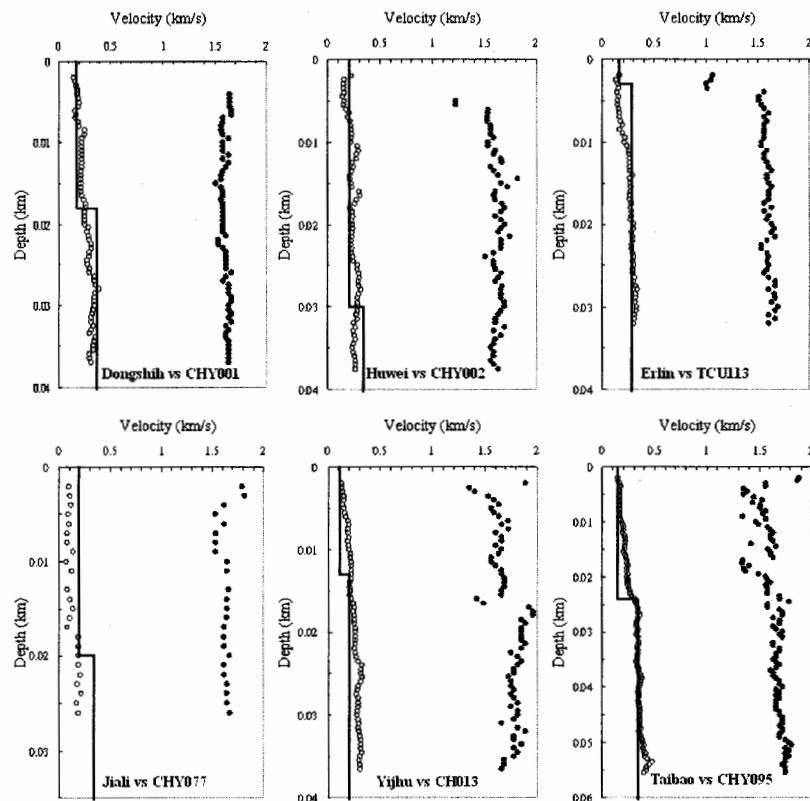


Figure 8 The comparison between the results of inversion on near surface (line) and the V_p (black circle) and V_s (open circle) of logging data at TSMIP stations within a distance of 5 kilometers from each studying sites.

5. CONCLUSIONS

In this study, array measurements of microtremors at seven sites are conducted in western coastal plain in Taiwan to determine the dispersion curves in frequency range from 0.1 to 5Hz. After inversion, we completely estimated the shear wave velocity structures from near surface to the depth of 3 kilometers. The results of S-wave velocity models correctly reflect the depths of major interfaces. Peikang High apparently dominates the shear wave velocity structures in western Taiwan. Therefore, the S-wave velocity of Dongshih in the depth about 1 km is higher than that of other sites. And the variation of S-wave velocity at Yijhu is similar to Dongshih because of the underground complex structures.

Acknowledgements:

The well logging data were provided from National Center for Research on Earthquake Engineering, ROC. This study is supported by National Science Council, ROC, under the grant no. NSC94-2116-M-008-005.

References:

- Capon, J. (1969), "Investigation of long-period noise at the large aperture seismic array," *J. Geophys. Res.*, **74**, 3182-3194.
- Chen, J. S. (1978), "A comparative study of the refraction and reflection seismic data obtained on the Changhua Plain to the Peikang Shelf, Taiwan," *Petrol. Geol. of Taiwan*, **15**, 199-217.
- Herrmann, R. B. (1987), "Surface wave inversion," *Computer program in seismology*, Vol. 4, Saint Louis University.
- Horike, M. (1985), "Inversion of phase velocity of long-period microtremors to the S-wave-velocity structure down to the basement in urbanized area," *J. Phys. Earth*, **33**, 59-96.
- Hu, C. C., and Hsu, H. H. (1988), "Application of linear inversion to the geophysical data interpretation for petroleum evaluation of the Chiayi coastal plain," *Petrol. Geol. of Taiwan*, **24**, 96-122.
- Kawase, H., Sato, T., Iwata, T., and Irikura, K. (1998), "S-wave velocity structures in the San Fernando and Santa Monica areas," *Proc. Of the 2 International Symposium on Effects of Surface Geology on Seismic Motions*, Tokyo, Japan, Vol. 2, 733-740.
- Matsushima, T., and Okada, H. (1990), "Determination of deep geological structures under urban areas using long-period microtremors," *ButsuriTansa*, **43**, 21-33.
- Pan, Y. S. (1967), "Interpretation and seismic coordination of the Bouguer gravity anomalies over west-central Taiwan," *Petrol. Geol. of Taiwan*, **5**, 99-115.
- Pan, Y. S. (1968), "Interpretation and seismic coordination of the Bouguer gravity obtained in southwestern Taiwan," *Petrol. Geol. of Taiwan*, **6**, 197-207.
- Sato, T., Kawase, H., Matsui, M. and Kataoka, S. (1991), "Array measurement of high frequency microtremors for underground structure estimation," *Proc. Of the 4 International Conference on Seismic Zonation*, Odawana, Japan, Vol. 2, 409-416.

EFFECTS OF LATERAL RESPONSE OF EMBEDDED FOOTING ON PILES

S. Tamura¹⁾ and K. Tokimatsu²⁾

1) Associate Professor, DPRI, Kyoto University, Japan

2) Professor, Tokyo Institute of Technology, Japan

tamura@sds.dpri.kyoto-u.ac.jp, kohji@o.cc.titech.ac.jp

Abstract: This paper examines earth pressure acting on an embedded footing and its effects on pile forces, based on both liquefaction and non-liquefaction tests using a large-scale laminar shear box. The following conclusions are drawn: (1) The total earth pressure in the non-liquefaction tests tends to be out of phase by 180 degrees with the superstructure inertia, reducing the shear force and bending moment at the pile head; (2) The total earth pressure in the liquefaction tests tends to be in phase with the superstructure inertia, making the bending moment at the pile head large; and (3) The total earth pressure in the liquefaction tests tends to increase, when the excess pore water pressure in the liquefied soil decreases.

1. INTRODUCTION

Extensive soil liquefaction that occurred on the reclaimed land areas of Kobe during the 1995 Hyogoken-Nambu earthquake caused vital damage to pile foundations. Over the past decade, a considerable number of studies have been conducted on the failure mechanism of piles, based on the field investigations (Oh-Oka et al., 1998, Tokimatsu et al., 1998), centrifuge tests (Sato et al., 1995, Horikoshi et al., 1998) and numerical analyses (Miyamoto et al., 1997, Fujii et al., 1998). Many efforts have also been made on the evaluation of the horizontal subgrade reaction of piles (Wilson et al., 2000, Tokimatsu et al., 2002) as well as of the inertial and kinematic interaction of soil-pile-structure systems (Murono et al., 2000). In contrast, little attention has been given to dynamic earth pressure acting on an embedded footing and its effects on the failure mechanism of piles.

To qualitatively investigate the effects of inertial and kinematic forces, several series of large-scale shaking table tests were conducted on soil-pile-structure systems with dry sand (Tokimatsu et al. 2004) and with saturated sand (Tamura et al. 2000). Total earth pressure acting on the embedded footing was evaluated in the tests. The objective of this paper is to examine the effects of the total earth pressure on the piles forces in both non-liquefaction and liquefaction tests.

2. SHAKING TABLE TESTS

2.1 Model Preparation

This paper presents in detail the earth pressure acting on an embedded footing based on the results of two shaking table tests with dry sand (case DBL after Tokimatsu et al. 2004) and with saturated sand (case SBL after Tamura et al. 2000), as shown in Fig. 1. The tests were performed at NIED (National Research Institute for Earth Science and Disaster Prevention) in Tsukuba, Japan, using a large-scale laminar shear box of 4.6 or 6.1 m in height, 3.5 m in width and 12.0 m in length (shaking direction) mounted on the shaking table. The soil used for case DBL was Nikko Sand ($e_{\max}=0.96$, $e_{\min}=0.57$, $D_{50}=0.31\text{mm}$, $F_c=5.4\%$). The relative density of the dry sand deposit was about 80%.

The soil profile in case SBL consists of two layers including a 4.5 m layer of Kasumigaura sand ($e_{\max}=0.98$, $e_{\min}=0.65$, $D_{50}=0.42$ mm) with a shear wave velocity of 90 m/s, which is underlain by a 1.5 m layer of gravel with $V_s = 230$ m/s. The water level was located at about GL-0.5 m. The relative density of the saturated sand deposit was about 35-50%.

A 2x2 steel pile was used for all the tests. The piles had a diameter of 16.5 cm, a thickness of 0.37 cm and a flexural rigidity EI of 1259 kNm². The pile heads were rigidly linked to the footing, while their tips were connected to the laminar shear box by hinges. The footing was modeled with a rigid steel box of 2.5 m (length) x 1.8 m (width) x 0.6 m (height) and embedded 0.5 m in the dry sand. The mass of the superstructure was 14200 kg and that of the footing was 2100 kg. The natural period of the superstructure under fixed footing conditions was about 0.7 s for case DBL, which was longer than the natural period of the ground. The natural period of the superstructure in case SBL was about 0.8 s, which is longer than that of the ground before liquefaction but shorter than that after liquefaction.

All the tests were excited by RINKAI92, which is a synthesized ground motion for the Tokyo Bay area. The amplitude of the motion was scaled to 240 cm/s². Acceleration, displacement, excess pore water pressure and strain of the piles were recorded during the tests.

2.2 Dynamic Response of Soil-Pile-Superstructure System

Figure 2 shows the vertical distributions of the excess pore water pressure in case SBL. The excess pore water pressure begins to increase at 8 seconds. The upper part of the saturated sand layer liquefied at about 10 seconds and the lower part liquefied at 20 seconds. Figure 3 shows acceleration and displacement time histories of superstructure and ground surface, as well as those of input accelerations, relative displacement between footing and ground surface, total earth pressure and bending moment at the pile head in cases DBL (Tokimatsu et al. 2004) and SBL (Tamura et al. 2002a). The displacements were calculated by the double integration of the accelerometer recordings. The total earth pressure, P can be evaluated by,

$$P = Q - F \quad (1)$$

in which Q = the sum of shear forces at the pile heads and F = the sum of the inertial forces of the superstructure and footing (Tamura et al. 2002a).

The superstructure acceleration and the ground surface acceleration in case DBL are smaller than those in case SBL, even though the input acceleration time history in case DBL is similar to that in case SBL. This indicates that the soil liquefaction reduces the superstructure and ground surface acceleration. On the other hand, the relative displacement, and bending moment at the pile head in case DBL are apparently smaller than those in case SBL. It is in-

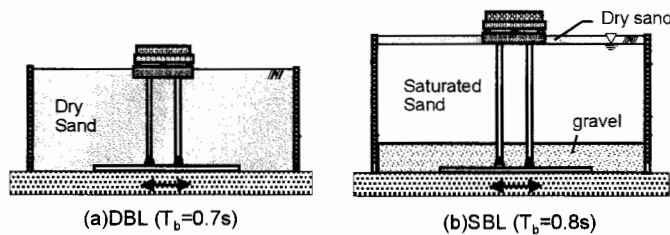


Figure 1 Test models (Tokimatsu et al., 2004, Tamura et al., 2000)

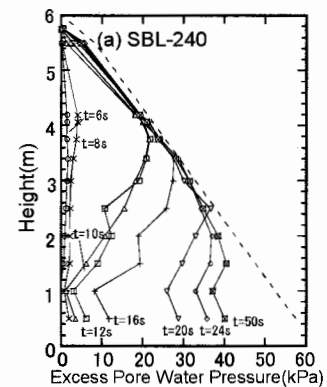


Figure 2 Vertical distribution of excess pore water pressure

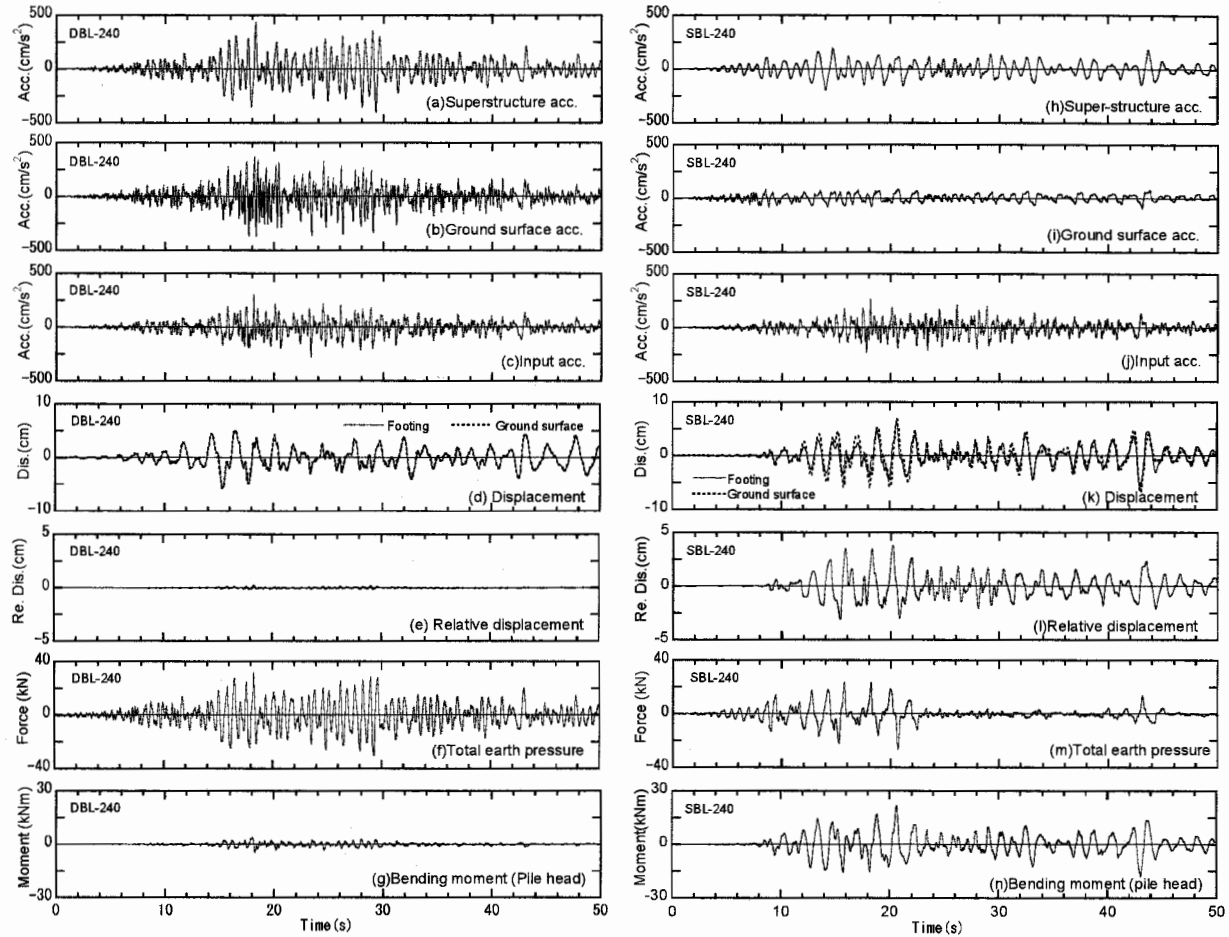


Figure 3 Time histories in shaking table tests

interesting to note that bending moment at the pile head in case DBL is much smaller than that in case SBL, even though the superstructure inertia in case DBL is larger than that in case SBL.

2.3 Relation between Relative Displacement and Earth Pressure

Figure 4 shows the relations between the relative displacement and the total earth pressure. The relations between the two are elliptical in shape all the time in case DBL. The relation is also elliptical until 8 seconds in case SBL. It becomes nonlinear with the development of the pore water pressure from 8 to 20 seconds. The total earth pressure gets small with cyclic loading from 20 to 50 seconds. Although the relative displacement in case SBL is an order magnitude larger than that in case DBL, the total earth pressure amplitudes in case SBL tend to be smaller than that in case DBL.

To investigate the mechanism of earth pressure in case SBL, the time histories of the total earth pressure and the excess pore water pressure ratio, u/σ_v' at GL.-1.8m from 15 to 22 seconds are shown in Fig. 5. The instance when the total earth pressure reaches a local maximum coincides with the instance when the excess pore water pressure reaches a local minimum. This indicates that the effect of excess pore water pressure change on the total earth pressure is significant. The relation between the excess pore water pressure ratio and the total earth pressure from 10 to 50 seconds is shown in Fig. 6. The total earth pressure tends to increase, when the excess pore water pressure decreases. This suggests that the mechanism of the earth pressure in case DBL is different from that in case SBL as shown in Fig. 7. In the case of non-liquefaction test, a soil wedge, according to the Mononobe-Okabe method, is formed by a failure surface starting at the heel of the wall and ex-

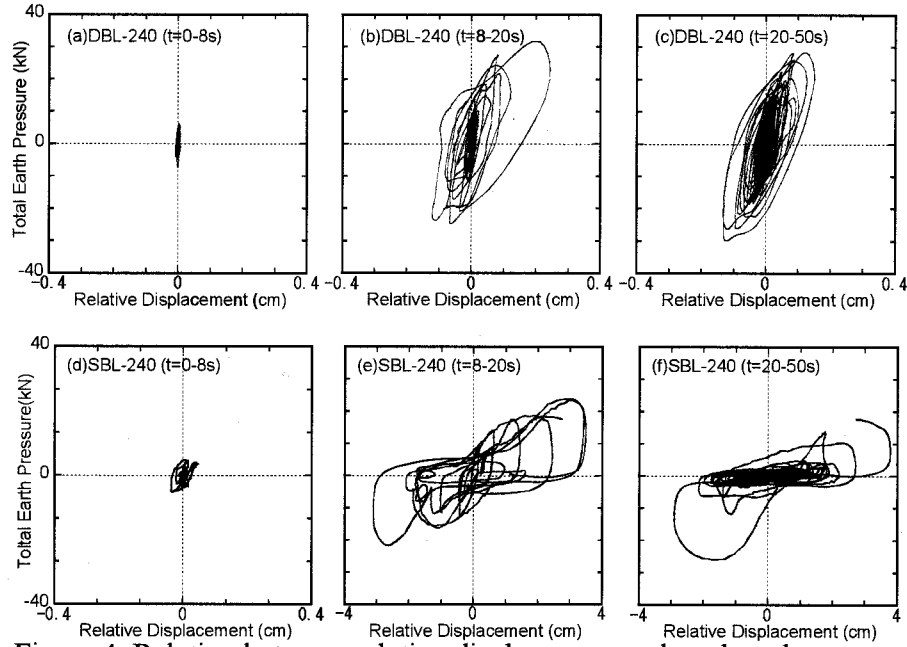


Figure 4 Relation between relative displacement and total earth pressure

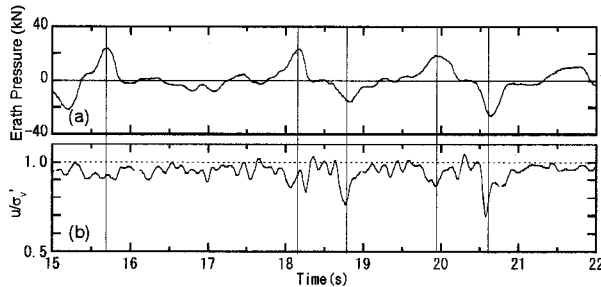


Figure 5 Time histories of total earth pressure and excess pore water pressure ratio (SBL)

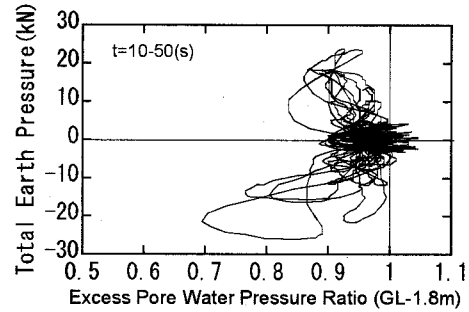


Figure 6 Relation between total earth pressure and excess pore water pressure ratio (SBL)

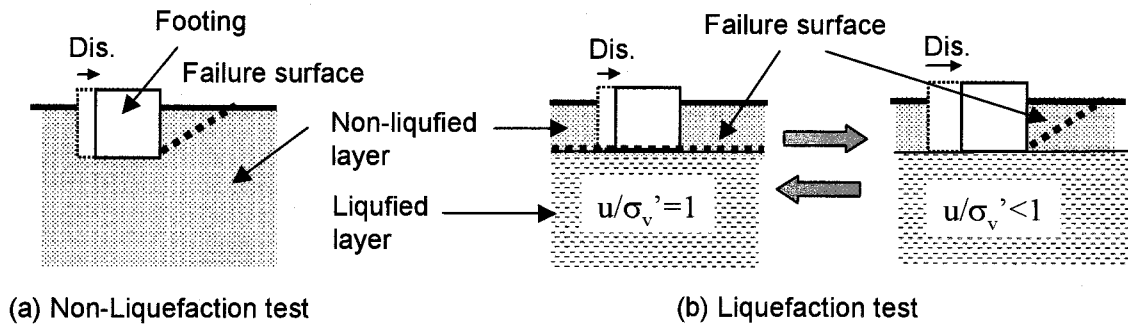


Figure 7 Mechanism of earth pressure acting on embedded footing

tending to the free surface of the soil. In the case of liquefaction test, the shear force between the non-liquefied layer and liquefied layer becomes extremely small when u/σ'_v of the liquefied soil is 1. Therefore, a failure surface occurs between the two layers and the earth pressure is small in spite of comparatively large relative displacement. The shear force between the two layers increases, when u/σ'_v of the liquefied soil is less than 1. Similar to the non-liquefaction test, a failure surface starting at the heel of the wall and extending to the free surface of the soil occurs.

3. EFFECTS OF TOTAL EARTH PRESSURE ON PILE FORCES

3.1 Effects of Superstructure Inertia and Total Earth Pressure on Pile Forces

Figure 8 shows superstructure inertia, total earth pressure and shear force at pile head when the bending moment at pile head reaches its maximum in cases DBL and SBL. The superstructure inertia and the total earth pressure in case DBL are larger than those in case SBL. On the other hand, the shear force at pile head in case DBL is smaller than that in case SBL. The difference between cases DBL and SBL is the phase between the superstructure inertia and the total earth pressure. The total earth pressure is out of phase by 180 degrees with the superstructure in case DBL. The total earth pressure is in phase with the superstructure in case SBL. Therefore, the shear force at pile head in case DBL is smaller than that in case SBL. This indicates that the phase between superstructure inertia and total earth pressure is the key to discussing the pile forces.

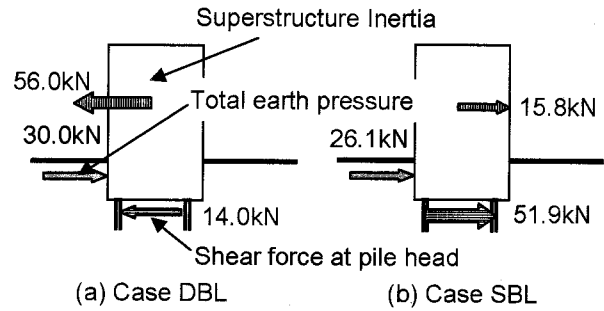


Figure 8 Superstructure inertia, earth pressure and shear force at maximum bending moment

3.2 Phase between Superstructure Inertia and Total Earth Pressure

A method for estimating the phase between superstructure inertia and total earth pressure has been proposed by Tamura et al. (2002b), based on the natural period of the superstructure under fixed footing condition T_b , the predominant period of the ground T_g , the soil displacement ΔS , and the footing displacement ΔB .

- If $T_b < T_g$ and $\Delta S > \Delta B$, the total earth pressure tends to be in phase with the superstructure inertia (Fig. 9 (a)). Thus, the bending moment at the pile heads increases due to the total earth pressure.
- If $T_b > T_g$ and $\Delta S > \Delta B$, the total earth pressure tends to be out of phase by 180 degrees with the superstructure inertia (Fig. 9 (b)). Thus, the bending moment at the pile heads decreases due to

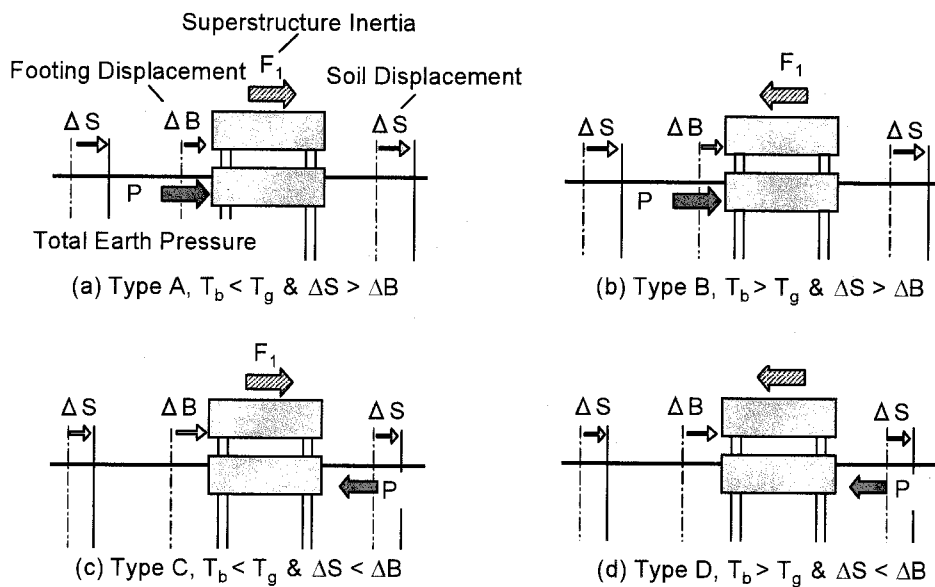


Figure 9 Phase between superstructure inertia and total earth pressure

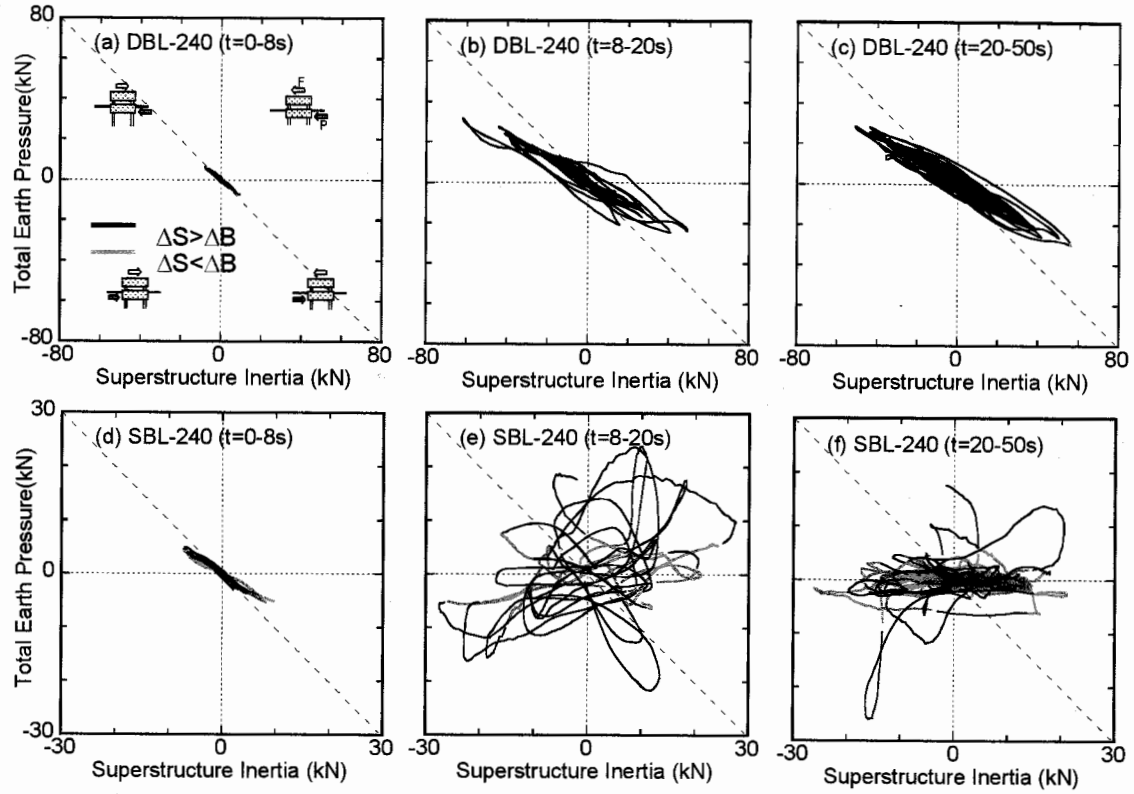


Figure 10 Relation between superstructure inertia and total earth pressure

the total earth pressure.

c) If $T_b < T_g$ and $\Delta S < \Delta B$, the total earth pressure tends to be out of phase by 180 degrees with the superstructure inertia (Fig. 9 (c)). Thus, the bending moment at the pile heads decreases due to the total earth pressure.

d) If $T_b > T_g$ and $\Delta S < \Delta B$, the total earth pressure tends to be in phase with the superstructure inertia (Fig. 9 (d)). Thus, the bending moment at the pile heads increases due to the total earth pressure.

To investigate the effects of the total earth pressure on the bending moment at the pile head, the phase between the total earth pressure and the superstructure inertia in cases DBL and SBL are shown in Fig. 10. The data fallen in the first and third quadrants show that the total earth pressure tends to be in phase with the superstructure inertia, while those in the second and fourth quadrants show that the total earth pressure tends to be out of phase by 180 degrees with the soil inertia. A gray line in the figure shows that the soil displacement ΔS is smaller than the footing displacement ΔB , while a black line shows that ΔS is larger than ΔB .

In case DBL, most of the test data fall in the second and fourth quadrants. This indicates that the total earth pressure is out of phase by 180 degrees with the superstructure inertia. A black line is dominant, indicating that ΔS tends to be larger than ΔB when the total earth pressure reaches its peak. Considering that T_b is longer than T_g , conditions in case DBL corresponds to Type B in Fig. 9. The expected phase between the superstructure inertia and the total earth pressure agrees with the test result.

In case SBL, the total earth pressure tends to be out of phase by 180 degrees with the superstructure inertia until 8 seconds. The phase is similar to that in case DBL. The total earth pressure, which is equivalent to about 60-70 percent of the superstructure inertia, counteracts the inertial force transmitted from the superstructure to the pile heads. Therefore, the bending moment is very small until 8 seconds as shown in Fig. 3(n). It is unclear whether ΔS is larger than ΔB or ΔS is smaller than ΔB .

The relations between the two changed after 8 seconds, significantly. The total earth pressure tends to be in phase with the superstructure inertia. Therefore, the bending moments increase rapidly after 8 seconds as shown in Fig. 3(n). ΔS tends to be larger than ΔB when the total earth pressure reaches its peak. In addition, T_b is shorter than T_g due to the liquefaction. These conditions correspond to Type A in Fig. 9. The method as shown in Fig. 9 gives a reasonable explanation of the difference in earth pressure between the different tests.

4. CONCLUSION

This paper examines earth pressure acting on an embedded footing and its effects on pile forces, based on both liquefaction and non-liquefaction tests using a large-scale laminar shear box. The following conclusions are drawn:

- (1) The total earth pressure in the non-liquefaction tests tends to be out of phase by 180 degrees with the superstructure inertia, reducing the shear force and bending moment at the pile head.
- (2) The total earth pressure in the liquefaction tests tends to be in phase with the superstructure inertia, making the bending moment at the pile head large. The proposed method gives a reasonable explanation of the difference in earth pressure between the different tests.
- (3) The total earth pressure in the liquefaction tests tends to increase, when the excess pore water pressure in the liquefied soil decreases.

Acknowledgements:

The non-liquefaction shaking table tests were made under Special Project for Earthquake Disaster Mitigation in Urban Areas, supported by Ministry of Education, Culture, Sports, Science and Technology (MEXT). The liquefaction tests were jointly conducted by NIED, Tokyo Institute of Technology, Kajima Corp., Taisei Corp., Takenaka Corp., Nippon Steel Corp. and Tokyo Soil Research Corp. The contribution and support of the above organizations are appreciated.

References:

- Fujii, S., Iseimoto, N., Satou, Y., Kaneko, O., Funahara, H., Arai, T. and Tokimatsu, K. (1998). "Investigation and analysis of a pile foundation damaged by liquefaction during the 1995 Hyogoken-Nambu earthquake", *Soils and Foundations, Special Issue on Geotechnical Aspects of the 1995 Hyogoken Nambu Earthquake*, No. 2, pp. 179-192.
- Horikoshi, K., Tateishi, A., and Fujiwara, T. (1998). "Centrifuge Modeling of a Single Pile Subjected to Liquefaction-induced Lateral Spreading", *Soils and Foundations, Special Issue on Geotechnical Aspects of the 1995 Hyogoken Nambu Earthquake*, No. 2, pp. 193-208.
- Miyamoto, Y., Sako Y, Koyamada K. and Miura K. (1997). "Response of pile foundation in liquefied soil deposit during the Hyogo-ken Nambu Earthquake of 1995", *Journal of Struct. Constr. Engng. AIJ*, No.493, pp.23-30. (in Japanese)
- Murono, Y. and Nishimura, A. (2000), "Evaluation of Seismic Force of Pile Foundation Induced by Inertial and Kinematic Interaction", *Proc. of 12th World Conf. on Earthq. Engrg.*, Reference No. 1496.
- Oh-Oka, H., Fukui, M., Hatanaka, M., Ohara, J. and Honda, S. (1998). "Permanent deformation of steel pipe piles penetrating compacted fill at wharf on port Island", *Soils and Foundations, Special Issue on Geotechnical Aspects of the 1995 Hyogoken Nambu Earthquake*, No. 2, pp. 147-162.
- Sato, M., Shamoto, Y. and Zhang, J. -M. (1995). "Soil Pile-structure during Liquefaction on Centrifuge", *Proc., 3rd International Conference on Recent Advances in Geotechnical Earthquake Engineering and Soil Dynamics*, 1, pp. 135-142.
- Tamura, S., Tsuchiya, T., Suzuki, Y., Fujii, S., Saeki, E. and Tokimatsu, K. (2000). "Shaking Table Tests of Pile Foundation on Liquefied Soil Using Large-scale Laminar Box (Part 1: Outline of Test)", *35th Japan National Con-*

- ference on Geotechnical Engineering, pp.1907-1908. (in Japanese)
- Tamura, S., Tokimatsu, K., Miyazaki, M., Yahata, K. and Tsuchiya, T. (2002a), "Seismic earth pressure acting on embedded footing based on liquefaction test using large scale shear ", Journal of Struct. Constr. Engng., No.554, pp.95-100. (in Japanese)
- Tamura, S., Tokimatsu, K., Uchida, A., Funahara, H. and Abe, A.(2002b). "Relation between Seismic Earth Pressure Acting on Embedded Footing and Inertial Force Based on Liquefaction Test Using Large Scale Shear Box", Journal of Struct. Constr. Engng., No.559, pp.129-134. (in Japanese)
- Tokimatsu, K. and Asaka, Y. (1998). "Effects of liquefaction-induced ground displacements on pile performance in the 1995 Hyogoken-Nambu Earthquake", Soils and Foundations, Special Issue of Geotechnical Aspects on the 1995 Hyogoken Nambu Earthquake, No. 2, pp. 163-177.
- Tokimatsu, K., Suzuki, H., Suzuki, Y. and Fujii, S.(2002). "Evaluation of Lateral Subgrade Reaction of Pile during Soil Liquefaction Based on Large Shaking Table Tests", Journal of Struct. Constr. Engng. , No.553 , pp.57-64. (in Japanese)
- Tokimatsu, K., Suzuki, H. and Sato, M.(2004). "Influence of inertial and kinematic components on pile response during earthquake", Proc. of 11th International Conference on Soil Dynamics and Earthquake Engineering & 3rd International Conference on Earthquake Geotechnical Engineering, Berkeley, Vol.1, pp. 768-775.
- Wilson, D. W., Boulanger, R. W. and Kutter, B. L.(2000). "Observed seismic lateral resistance of liquefying sand", J. Geotechnical and Geoenvironmental Engineering, ASCE, 12(10), pp.898-906.

DETECTION OF SUBSURFACE V_s RECOVERY PROCESS USING MICROTREMOR AND WEAK GROUND MOTION RECORDS IN OJIYA, JAPAN

H. Arai¹⁾

1) Deputy Team Leader, Earthquake Disaster Mitigation Research Center, National Research Institute for Earth Science and Disaster Prevention, Japan
arai@edm.bosai.go.jp

Abstract: Recovery process of S-wave velocity (V_s) of subsurface soils at two strong ground motion stations in Ojiya, Japan, are estimated after the 2004 Niigata-ken Chuetsu earthquake, based on conventional microtremor measurements and available ground motion records at the stations. The inverse analysis of the observed microtremor horizontal-to-vertical (H/V) spectra and weak-motion spectral ratios between the stations has resulted in the following: Before the main shock, the V_s values of top soil layers with about 3 m thick at the two stations are about 45-50 and 75-85 m/s. Just after the main shock, the subsurface V_s values have got smaller by a factor of about 0.8. The reduced V_s values, however, increase gradually with passing time, and they have regained in about 8-13 months after the main shock.

1. INTRODUCTION

The Niigata-ken Chuetsu earthquake of October 23, 2004 destroyed over 2,700 houses and buildings in the mid-area of Niigata prefecture, Japan. During the main shock, strong ground motions with high peak accelerations and velocities over about 800 cm/s^2 and 80 cm/s , respectively, were observed at several sites in the near-fault area (e.g., Midorikawa and Miura 2005). The building damage ratios and ground motion characteristics observed within the area, however, varied from place to place, for example, in the Ojiya city (Horie *et al.* 2005, Yamanaka *et al.* 2005). During the main shock, in fact, the values of peak ground accelerations and velocities (PGA and PGV, respectively) recorded at the strong motion station of the K-NET/NIED in the city were about 1.5 times those at the station of the Japan Meteorological Agency (JMA), where is only 800 m apart from the K-NET station (Figure 1). It has also been indicated that the local site conditions with nonlinear dynamic properties of subsurface soils had significant effects on the strong ground motion characteristics at both stations (Tokimatsu *et al.* 2006). This suggests that evaluating local site effects in the damaged area is fundamental to study the mechanisms and causes of the large earthquake disaster.

To evaluate local site effects, S-wave velocity (V_s) structure of subsurface soils at the site should be properly determined. In particular, the initial V_s value under the minute shear-strain condition, V_{s0} , is a key parameter for evaluating site effects. After strong ground shaking caused by a large earthquake, however, the V_{s0} values of

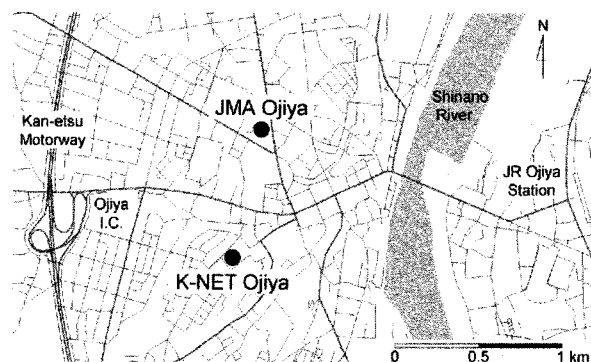


Figure 1 Map showing locations of K-NET and JMA strong ground motion stations in Ojiya, Japan

subsurface soils could have got smaller because of the large shear-strain hysteresis generated in the soils during the earthquake (Tokimatsu and Hosaka 1986). Similar possibility has been suggested for the subsurface soils at the K-NET and JMA stations in Ojiya (Tokimatsu *et al.* 2006). Based on the knowledge of geotechnical engineering, it is supposed that the reduced V_{s0} values of subsurface soils might increase gradually after the earthquake. Investigating unknown recovery process of subsurface V_{s0} values is, therefore, interesting and important to evaluate the local site effects in the damaged area.

The objective of this article is to detect the recovery process of subsurface V_{s0} values at the K-NET and JMA stations in Ojiya after the main shock, based on conventional microtremor measurements and weak ground motion records which are available at both stations.

2. ESTIMATION OF V_{s0} STRUCTURES FROM MICROTREMOR H/V SPECTRA

2.1 Background and Methodology

The V_{s0} values of subsurface soils can be determined by the conventional geotechnical or geophysical method using boreholes. It is, however, difficult to employ the conventional methods for detecting V_{s0} recovery process because of their cost and the time required. As an economical and practical substitute, microtremor measurements, which can be readily performed on the ground surface without drilling any borehole, have therefore been used.

Nakamura (1989) indicated that the horizontal-to-vertical (H/V) spectral ratio of microtremors, which can be determined conveniently with only one three-component sensor, may approximate the amplification factor of the site for vertically incident S-wave. After a number of studies on the microtremor H/V spectra, it has been widely confirmed that the peak period of microtremor H/V spectrum at a site corresponds nearly to the natural site period for S-wave when V_{s0} structure of the site has uniquely a high-contrast layer boundary. However, it has been revealed that the H/V spectrum of microtremors corresponds to that of surface (Rayleigh- and Love-) waves and thus reflects V_{s0} structure at a site (Tokimatsu and Miyadera 1992, Tokimatsu 1997, Arai and Tokimatsu 2004). The inverse analysis of microtremor H/V spectra, therefore, results appropriately in a V_{s0} profile of the site (Arai and Tokimatsu 2004). Details of the methodologies and conditions of the microtremor H/V inversion can be found in the recent article by Arai and Tokimatsu (2004).

2.2 Microtremor Measurements

The measurement system used consists of amplifiers, low-pass filters, 24-bit A/D converters, a GPS receiver, and a notebook computer, all built in a portable case. The acquisition system is connected to the three-component (one vertical and two orthogonal horizontal) moving-coil typed velocity sensor with a natural period of 2 s.

When about 115-117 hours had passed since the main shock, on October 28, 2004, conventional microtremor measurements using one three-component sensor were performed at the K-NET and JMA stations in Ojiya. Again the same measurement was conducted at each station on October 10, 2005. At any measurement, three-components of microtremors were observed simultaneously for about 10 minutes and digitized at a sampling frequency of 200 Hz. About 10-16 sets of data segments with 4096 points (i.e., 20.48 s length) each were selected from the digitized motions, and used for the following spectral analysis.

2.3 H/V Spectra of Microtremors

The H/V spectral ratio of microtremors at a frequency f , $(H/V)_m$, used in this study is defined as

$$(H/V)_m = \sqrt{\frac{P_{NS}(f) + P_{EW}(f)}{P_{UD}(f)}} \quad (1)$$

where $P_{UD}(f)$ is the Fourier power spectrum of vertical motion, and $P_{NS}(f)$ and $P_{EW}(f)$ are those of two orthogonal horizontal motions. The power spectra are determined by using the direct segment method (Capon 1969) without any smoothing window.

The H/V spectra of microtremors derived from the twice measurements at the K-NET and JMA stations are shown in Figures 2(a) and (b), respectively. In each figure, the microtremor H/V spectrum of October 10, 2005 is compared with that of October 28, 2004.

At the K-NET station, the peak period of the H/V spectrum on October 10, 2005 seems to be slightly shorter than that on October 28, 2004, but their difference is not so significant. At the JMA station, however, the H/V spectrum on October 10, 2005 is obviously shifted to the left-hand side of that on October 28, 2004. Based on the results of the recent microtremor H/V studies reviewed previously, this suggests that the V_{S0} values of subsurface soils at the JMA station could vary larger while the twice microtremor measurements. It is also suggested that a similar possibility might exist at the K-NET station.

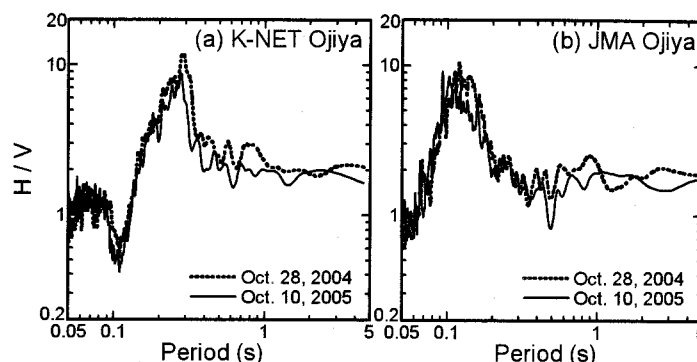


Figure 2 Comparison of microtremor H/V spectra of October 10, 2005 with those of October 28, 2004 at the stations of (a) K-NET and (b) JMA in Ojiya

2.4 Inversion of Microtremor H/V Spectra for V_{S0} Profiling

To determine the V_{S0} structure at each station on each observation date, an inverse analysis is conducted using the observed H/V data shown in Figure 2. In the inversion, the following assumptions are made: (1) the soil profile down to seismic bedrock with V_{S0} over 3 km/s at each station consists of an eight flat-layered half-space, and (2) the deep soil layers below engineering bedrock with V_{S0} over 500 m/s are those estimated from the large-array measurements of microtremors near the K-NET station (Yamanaka *et al.* 2005). This leaves unknown thicknesses and S-wave velocities of top two layers above the engineering bedrock to be sought in the inversion. For the subsurface two layers, furthermore, it is inferred that their thicknesses are stable in the twice microtremor measurements.

Tables 1(a) and (b) show the S-wave velocity profiles of subsurface soils estimated from the inversion at the K-NET and JMA stations, respectively. In each table, the V_{S0} profile estimated for the H/V data of October 10, 2005 is compared with that of October 28, 2004. It is confirmed that the V_{S0} values of the top layer with a thickness of about 3 m at both stations have got larger about 11% and 16%, respectively, while the twice microtremor measurements.

The standard error ratios of the parameters evaluated in the inversion (e.g., Arai and Tokimatsu 2004), shown as the percentage with brackets in Table 1, are sufficiently small in any estimation. Solid lines in Figures 3 and 4 are the H/V spectra of surface waves computed for the inverted soil profiles at the stations, compared with those of microtremors observed. In the figures, the computed values show fairly good agreement with the observed ones at both stations on any measurement date. The inverted profiles for the H/V data of October 28, 2004 are, furthermore, consistent with the subsurface V_S profiles derived from the velocity-logging tests at the stations, which were conducted after the main shock (Tokimatsu *et al.* 2006). These indicate that the inverse analysis has been performed with a reasonable degree of accuracy and that the estimated profiles are adequate for the stations.

With the estimated results from the microtremor H/V data of October 28, 2004, the natural site periods for S-wave computed at the K-NET and JMA stations are 0.25 and 0.12 s, respectively, and which are consistent with the H/V peak periods of microtremors at the stations (0.28 and 0.12 s, Figure 3). Similar relationship exists for the data of October 10, 2005. Based on the results of the recent microtremor H/V studies, it is indicated that these predominant periods are due mainly to the high-contrast layer boundary at a depth of about 3 m in both stations (Table 1).

Table 1 Subsurface S-wave velocity profiles estimated by inversion of microtremor H/V spectra

(a) K-NET Ojiya					(b) JMA Ojiya				
Layer No.	Thickness (m)	V _{s0} (m/s)		Soil Type	Layer No.	Thickness (m)	V _{s0} (m/s)		Soil Type
		Oct. 28, 2004	Oct. 10, 2005				Oct. 28, 2004	Oct. 10, 2005	
1	3.0 [1%]	47 [1%]	52 [1%]	Silty Clay, Peat	1	2.4 [2%]	74 [1%]	86 [2%]	Sandy Silt
2	26 [14%]	360 [8%]	360 [7%]	Gravel	2	17 [19%]	430 [11%]	430 [9%]	Gravel
3	*	500		Rock	3	*	500		Rock

* This layer connects to the top of deep soil layers with V_s = 650 m/s estimated by Yamanaka *et al.* (2005) at a depth of 90 m.

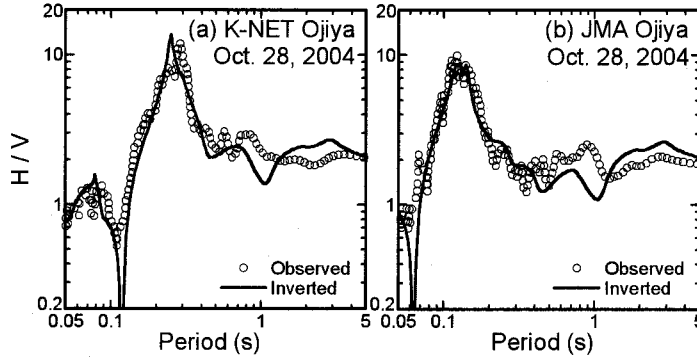


Figure 3 H/V spectra of microtremors on October 28, 2004 compared with those of surface waves for soil profiles estimated by inversion at the stations of (a) K-NET and (b) JMA in Ojiya

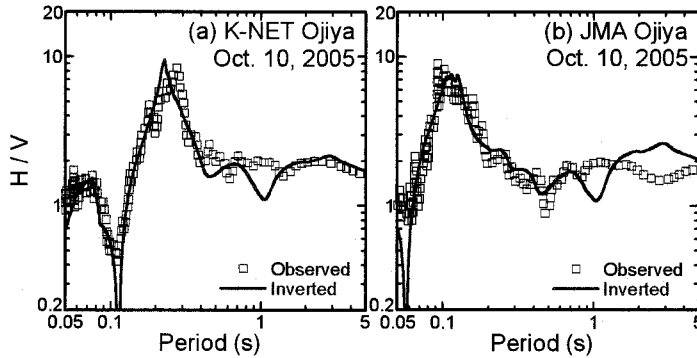


Figure 4 H/V spectra of microtremors on October 10, 2005 compared with those of surface waves for soil profiles estimated by inversion at the stations of (a) K-NET and (b) JMA in Ojiya

3. ESTIMATION OF SUBSURFACE V_{s0} VALUES USING WEAK GROUND MOTIONS

3.1 Background and Methodology

During 81 earthquakes occurred around the Niigata region in 1998-2005, strong and weak ground motions were observed at both K-NET and JMA stations in Ojiya, and their records are available as of early in March, 2006 (NIED, JMA). The 77 of the 81 earthquakes occurred after the 2004 Niigata-ken Chuetsu earthquake, and they were almost the aftershocks. Using the available earthquake records at the stations, therefore, the recovery process of subsurface V_{s0} values at the stations will be investigated in detail, and also might be detected the subsurface V_{s0} reduction caused by the main shock.

When P- and S-waves vertically propagating in sediments dominate the earthquake ground motions at the K-NET and JMA stations, the K-NET/JMA spectral ratio of the horizontal ground motions at a frequency f , R_O , can be approximately expressed as

$$R_O \equiv \frac{A_K(f)}{A_J(f)} \approx \frac{S_K(f)}{S_J(f)} \equiv R_C \quad (2)$$

where $A(f)$ is the Fourier spectrum of horizontal ground motion observed at a station, $S(f)$ is the site amplification factor for vertically propagating S-wave between seismic bedrock and ground surface at

a station, and subscripts K and J represent the K-NET and JMA stations, respectively. The site amplification factors, $S_K(f)$ and $S_J(f)$, can be evaluated by the one-dimensional response analysis of sediments for vertically incident S-wave using the equivalent-linear technique, i.e., SHAKE, using weak ground motions recorded at the K-NET and JMA stations, respectively.

In the SHAKE analysis, the V_{S0} structure and nonlinear dynamic properties of sediments at a site are required. Based on the results of the laboratory tests performed by Tokimatsu and Sekiguchi (2005), the nonlinear dynamic properties of subsurface soils at the K-NET and JMA stations may be mathematically modeled as shown in Figure 5. Thus, the V_{S0} values of subsurface soils at the stations can be estimated by solving the following generalized least-squares problem:

$$F = \int_{f_{\min}}^{f_{\max}} \left(\frac{R_o(f) - R_c(f)}{R_o(f)} \right)^2 df \bigg/ \int_{f_{\min}}^{f_{\max}} df \rightarrow \min. \quad (3)$$

in which f_{\min} and f_{\max} are the minimum and maximum frequencies considered. This problem can be interpreted as the identification analysis of the K-NET/JMA spectral ratios for horizontal ground motions. In the equation, the parameters to be identified are only the two V_{S0} values of the top layers with about 3 m thick at the K-NET and JMA stations. The V_{S0} values of the other layers down to seismic bedrock are inferred from Table 1 and the studies of Yamanaka *et al.* (2005). To solve the equation (3), a grid-search method is used in this study. The search area of V_{S0} values at the K-NET and JMA stations, i.e., the solution plane, are inferred in 10-100 and 50-140 m/s, respectively, and the grid-spacing on the solution plane is set as 1m.

3.2 Weak Ground Motion Data

From the 81 sets of earthquake ground motion records observed at both K-NET and JMA stations, the weak ground motion records to be used in the V_{S0} identification analysis are selected because the identification includes the equivalent-linear SHAKE analysis. In this study, the following criteria are introduced for the selection: (1) the signal-to-noise (S/N) ratios of ground motion records are larger than 10 in a frequency range of 0.2-15 Hz, (2) the JMA magnitude of earthquake, M_J , is about 3-5, (3) the focal depth of earthquake is greater than 6 km, and (4) for the aftershocks of the 2004 Niigata-ken Chuetsu earthquake, the epicentral distance to the K-NET station is less than about 30 km.

The selected earthquakes and weak ground motion records are summarized in Table 2. The PGA value shown in the table is the larger one of either the east-west (E-W) or the north-south (N-S) horizontal component. In the table, the earthquakes Nos. 1-3 occurred before the main shock, and the remaining Nos. 4-44 did after that. Solid line in Figure 6 shows the K-NET/JMA spectral ratio of the E-W ground motions observed during the earthquake No. 6. In the figure, the peak and trough periods of the spectral ratio, 0.35 and 0.13 s, are slightly longer than and close to the natural site periods at the K-NET and JMA stations, respectively.

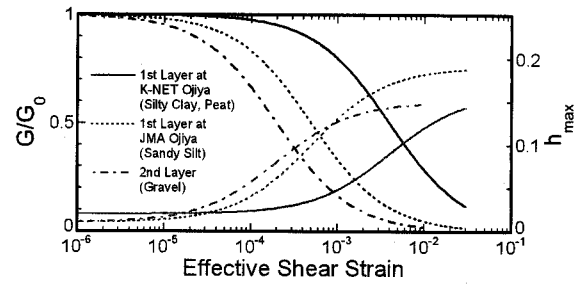


Figure 5 Dynamic properties of subsurface soils at K-NET and JMA stations in Ojiya, inferred from results of laboratory tests by Tokimatsu and Sekiguchi (2005)

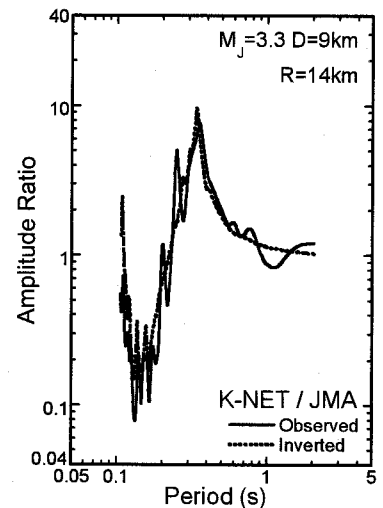


Figure 6 An example of observed and computed K-NET/JMA spectral ratios for horizontal ground motions (earthquake No. 6 in Table 2)

Table 2 List of earthquakes and weak motion records used for identification analysis of K-NET/JMA spectral ratios

No.	Date	Origin Time	Longitude (deg.)	Latitude (deg.)	M_I	Focal Depth (km)	Epicentral Distance (km)	P.G.A. (cm/s ²)	
								K-NET	JMA
1	2001/01/04	13:18:30	138.762 E	36.958 N	5.1	14	38	114.2	73.5
2	2004/01/09	22:05:00	138.725 E	37.293 N	4.0	16	6	49.4	207.0
3	2004/03/15	07:38:14	138.395 E	37.650 N	4.7	24	52	17.9	51.0
4	2004/10/24	04:31:30	138.848 E	37.283 N	3.1	17	5	18.3	126.4
5	2004/10/24	17:21:43	138.915 E	37.283 N	3.9	11	11	42.4	73.0
6	2004/10/24	21:10:40	138.917 E	37.232 N	3.3	9	14	21.0	50.4
7	2004/10/24	22:04:50	138.917 E	37.233 N	3.6	9	14	20.2	33.6
8	2004/10/25	00:53:39	138.892 E	37.205 N	3.7	9	13	25.3	58.8
9	2004/10/25	02:01:13	138.767 E	37.167 N	3.7	7	15	26.1	32.7
10	2004/10/25	02:33:03	138.878 E	37.295 N	3.2	15	7	18.9	57.5
11	2004/10/25	03:40:05	138.917 E	37.287 N	3.5	12	11	13.7	31.2
12	2004/10/25	14:46:45	138.885 E	37.317 N	3.7	15	8	31.9	57.4
13	2004/10/26	03:32:29	138.832 E	37.398 N	4.2	13	11	34.3	25.5
14	2004/10/26	20:37:25	138.943 E	37.270 N	4.0	12	13	34.1	32.0
15	2004/10/27	00:56:45	138.872 E	37.267 N	4.3	13	8	41.3	101.2
16	2004/10/27	02:05:46	138.848 E	37.205 N	3.8	11	11	48.7	60.7
17	2004/10/27	03:35:47	138.922 E	37.220 N	3.7	8	14	17.0	36.3
18	2004/10/27	10:35:28	138.853 E	37.395 N	3.9	14	11	25.9	38.7
19	2004/10/28	02:03:59	138.862 E	37.223 N	4.2	16	10	34.6	84.8
20	2004/10/29	10:27:39	138.847 E	37.402 N	3.6	9	12	13.9	13.6
21	2004/10/29	14:13:58	138.907 E	37.275 N	3.1	9	10	33.9	117.6
22	2004/11/03	03:58:04	138.903 E	37.240 N	3.8	9	11	17.4	29.0
23	2004/11/03	18:02:48	138.892 E	37.310 N	3.2	9	8	22.0	47.3
24	2004/11/05	14:56:49	138.828 E	37.173 N	4.2	7	14	44.2	70.1
25	2004/11/06	22:05:15	138.895 E	37.347 N	4.4	13	10	54.5	47.9
26	2004/11/08	01:56:05	138.910 E	37.248 N	3.3	6	12	19.1	11.6
27	2004/11/08	11:32:27	139.050 E	37.388 N	5.1	6	24	24.6	32.9
28	2004/11/11	18:04:46	138.905 E	37.238 N	3.9	7	12	43.2	68.7
29	2004/11/12	02:24:04	138.933 E	37.235 N	4.3	10	14	48.1	46.4
30	2004/11/13	10:01:53	138.802 E	37.162 N	4.1	9	15	38.5	31.7
31	2004/11/19	06:03:47	138.842 E	37.225 N	3.2	10	9	22.8	39.0
32	2004/11/28	14:03:48	138.860 E	37.290 N	3.8	13	6	15.6	35.6
33	2004/12/10	16:22:59	138.800 E	37.300 N	3.5	12	1	45.9	61.3
34	2004/12/21	03:44:59	138.900 E	37.400 N	3.5	10	14	20.3	20.8
35	2004/12/23	21:03:48	139.000 E	37.400 N	4.5	11	21	23.3	24.1
36	2004/12/28	18:30:43	139.000 E	37.300 N	5.0	8	18	36.8	27.7
37	2005/01/09	20:15:52	138.943 E	37.265 N	4.2	10	19	23.0	38.2
38	2005/01/18	21:50:41	138.997 E	37.370 N	4.7	8	19	37.9	32.6
39	2005/02/20	15:19:16	138.798 E	37.224 N	4.1	7	8	33.7	20.2
40	2005/05/02	08:08:32	138.831 E	37.187 N	3.5	9	13	54.2	54.0
41	2005/06/20	13:03:19	138.593 E	37.225 N	5.0	15	19	61.0	47.8
42	2005/06/20	13:15:37	138.596 E	37.219 N	4.4	13	19	14.8	10.1
43	2005/08/21	16:43:06	138.715 E	37.282 N	3.4	16	7	19.7	27.6
44	2005/11/04	01:02:03	138.480 E	37.434 N	4.8	28	31	21.9	36.6

The spectral ratio shapes for the other ground motions selected are similar to that shown in Figure 6. This indicates that the peak and trough of the observed spectral ratios between the K-NET and JMA stations are due mainly to the local site effects with nonlinear soil dynamics caused by the high-contrast layer boundary at a depth of about 3 m in both stations. Based on Figure 6 and the discussions above, also considering the frequency range set for the S/N ratio check, the values of f_{\min} and f_{\max} in the equation (3) are inferred as 0.5 and 12.5 Hz, respectively.

3.3 Identified Subsurface V_{s0} Values and Their Variation with Time

For each of the 44 sets of weak ground motion records listed in Table 2, the identification analysis of K-NET/JMA spectral ratios is performed. Figure 7 shows the projection of the misfit values, \sqrt{F} , on the solution plane in the identification analysis using the observed data shown in Figure 6. From the

figure, it is confirmed that a set of V_{S0} values for the K-NET and JMA stations can be uniquely determined to minimize the equation (3). Broken line in Figure 6 is the theoretical spectral ratio, R_C , which is defined in the equation (2), computed for the soil profiles with the identified V_{S0} values. In the figure, the computed theoretical values show fairly good agreement with the observed ones. Similar agreement exists in any other identification analysis. This indicates that the V_{S0} identification analyses for the selected earthquakes have been completed with a reasonable degree of accuracy and the estimated V_{S0} values are reliable.

Figure 8(a) shows the PGV values of all the weak ground motion data selected at the K-NET and JMA stations. Figures 8(b)-(d) summarize the results of the V_{S0} identification analyses: (b) the shear modulus ratios, (c) the effective shear strains, and (d) the identified V_{S0} values of the top layers with about 3 m thick at the stations. In the figures, the horizontal axis indicates the time passed since the main shock. For the three earthquakes before the main shock, the PGV values and the analysis results are separately presented on the left-hand sides of the figures.

The PGV values of the selected weak motions vary widely in a range of 0.1-10 cm/s. The values of the evaluated effective shear strains of subsurface soils also vary from 10^{-5} to 10^{-3} , in which the equivalent-linear SHAKE analysis can work out a reliable solution. The values of the shear modulus ratios resulted are greater than 0.6-0.8, indicating that the nonlinear behavior of soils at the stations during the earthquakes used could not be very significant.

Despite the dispersive trends of the PGV values and shear strains with the earthquakes, the identified V_{S0} values of subsurface soils are concentrative for each station and show a distinguishable trend: Before the main shock, the subsurface V_{S0} values estimated at the K-NET and JMA stations are about 45-50 and 75-85 m/s, respectively. Just after the main shock, the V_{S0} values at the stations have got smaller by a factor of about 0.8. The cause of the V_{S0} reduction might be due to the large shear-strain hysteresis generated in the subsurface soils at the stations during the main shock (Tokimatsu *et al.* 2006). The reduced V_{S0} values, however, increase gradually with passing time, and they have regained in about 6000-9000 hours (about 8-13 months) after the main shock.

Also shown in Figure 8(d) are the V_{S0} values estimated from microtremor H/V spectra at the K-NET and JMA stations (Table 1), which are consistent with

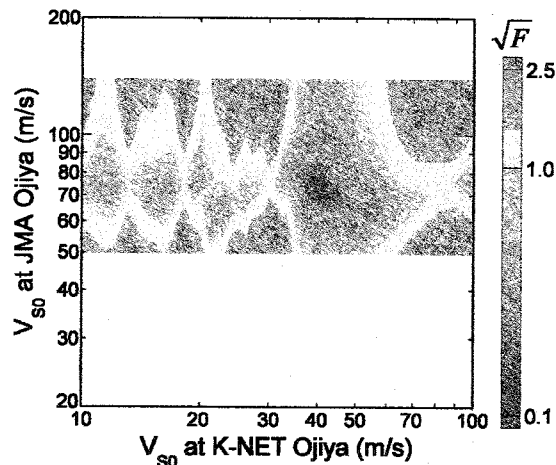


Figure 7 Projection of misfit values on solution plane in identification analysis of K-NET/JMA spectral ratio shown in Figure 6

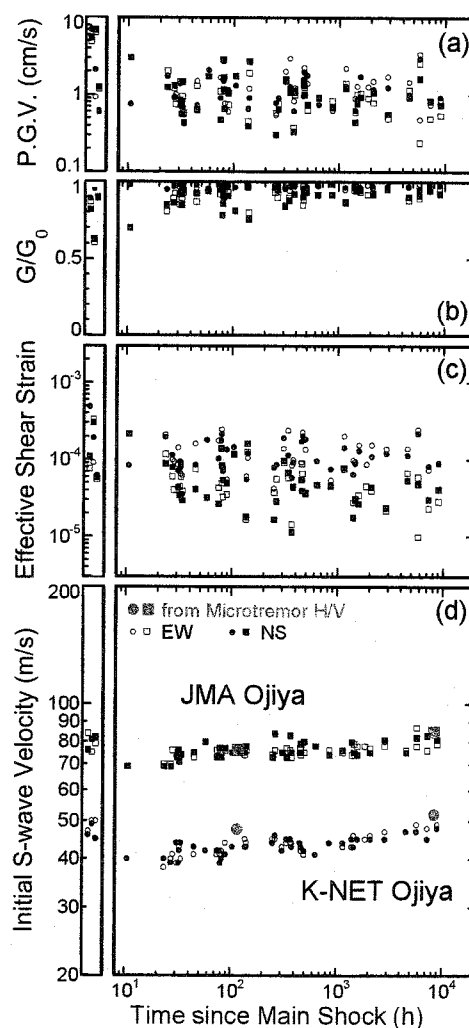


Figure 8 Results of identification analysis of K-NET/JMA spectral ratios: (a) peak ground velocities of weak motion data used, (b) shear modulus ratios, (c) effective shear strains, and (d) initial S-wave velocities of subsurface soils estimated at K-NET and JMA stations in Ojiya

those from the earthquake records. This again confirms that the estimated V_{S0} values of subsurface soils at the stations and their recovery process could be reasonably reliable.

4. CONCLUSIONS

Recovery process of initial S-wave velocity (V_{S0}) of subsurface soils at the K-NET/NIED and JMA strong ground motion stations in Ojiya are estimated after the 2004 Niigata-ken Chuetsu earthquake, based on conventional microtremor measurements and available ground motion records in 2001-2005 at the stations. The inverse analysis of the observed microtremor H/V spectra and weak-motion spectral ratios between the stations has resulted in the following:

- 1) Before the main shock, the V_{S0} values of the top soil layers with about 3 m thick at the K-NET and JMA stations are about 45-50 and 75-85 m/s, respectively.
- 2) Just after the main shock, the subsurface V_{S0} values have got smaller by a factor of about 0.8.
- 3) The reduced V_{S0} values, however, increase gradually with passing time, and they have regained in about 8-13 months after the main shock.

Acknowledgements:

The earthquake ground motion records used in this study were provided by the National Research Institute for Earth Science and Disaster Prevention, Japan (NIED) and the Japan Meteorological Agency (JMA). The author would like to express his sincere thanks and appreciation to these organizations. His gratitude and appreciation would extend to Profs. Kohji Tokimatsu and Hiroaki Yamanaka, Tokyo Institute of Technology, Japan, for their valuable information about the nonlinear dynamic properties of subsurface soils and the deep S-wave velocity structure in Ojiya, respectively.

References:

- Arai, H. and Tokimatsu, K. (2004), "S-wave velocity profiling by inversion of microtremor H/V spectrum," *Bulletin of the Seismological Society of America*, **94**(1), 53-63.
- Capon, J. (1969), "High-Resolution Frequency-Wave Number Spectrum Analysis," *Geophysics*, **34**(1), 21-38.
- Horie, K., Hayashi, H., Maki, N., Yoshitomi, N., Shigekawa, K., Tanaka, S., Okimura, T., and Torii, N. (2005), "A Study on Spatial Distribution of Building Damage in Ojiya City During the 2004 Niigata-ken Chuetsu Earthquake," *Proceedings of the 24 th Annual Meeting*, Japan Society for Natural Disaster Science, 7-8 (in Japanese).
- Japan Meteorological Agency (JMA), <http://www.jma.go.jp/>.
- Midorikawa, S. and Miura, H. (2005), "Strong Motion Records Observed in The 2004 Niigata-Ken-Chuetsu Earthquake," *Proceedings of the Second International Conference on Urban Earthquake Engineering*, Tokyo Institute of Technology, Tokyo, Japan, 21-26.
- Nakamura, Y. (1989), "A Method for Dynamic Characteristics Estimation of Subsurface Using Microtremor on the Ground Surface," *Quarterly Report of the Railway Technical Research Institute*, **30**(1), 25-33.
- National Research Institute for Earth Science and Disaster Prevention (NIED), <http://www.bosai.go.jp/>.
- Tokimatsu, K. (1997), "Geotechnical Site Characterization Using Surface Waves," *Proceedings of the IS-Tokyo '95 / the 1st International Conference on Earthquake Geotechnical Engineering*, Tokyo, Japan, **3**, 1333-1368.
- Tokimatsu, K. and Hosaka, Y. (1986), "Effects of Sample Disturbance on Dynamic Properties of Sand," *Soils and Foundations*, **26**(1), 53-64.
- Tokimatsu, K. and Miyadera, Y. (1992), "Characteristics of Rayleigh Waves in Microtremors and Their Relation to Underground Structures," *Journal of Structural and Construction Engineering*, Architectural Institute of Japan, **439**, 81-87 (in Japanese with English abstract).
- Tokimatsu, K. and Sekiguchi, T. (2005), "Relationship between Dynamic Properties Obtained from Laboratory Test and Those Observed in Strong Motion Accelerograms at K-NET and JMA Stations in Ojiya," *Proceedings of the 40 th Annual Meeting*, The Japanese Geotechnical Society, Hakodate, 2113-2114 (in Japanese).
- Tokimatsu, K., Sekiguchi, T., Miura, H., and Midorikawa, S. (2006), "Nonlinear Dynamic Properties of Surface Soils Estimated from Strong Motion Accelerograms at K-NET and JMA Stations in Ojiya," *Journal of Structural and Construction Engineering*, Architectural Institute of Japan, **600**, 43-49 (in Japanese with English abstract).
- Yamanaka, H., Motoki, K., Fukumoto, S., Takahashi, T., Yamada, N., and Asano, K. (2005), "Estimation of Local Site Effects in Ojiya City Using Aftershock Records of the 2004 Mid Niigata Prefecture Earthquake and Microtremors," *Earth Planets and Space*, **57**(6), 539-544.

ACTIVE TYPE SHEAR BOX AND ITS APPLICATION ON A STABILITY OF SHALLOW TUNNEL IN A CENTRIFUGE

J. Takemura¹⁾, J. Izawa²⁾, S. Shibayama³⁾ and O. Kusakabe⁴⁾

1) Associate Professor, Department of Civil Engineering, Tokyo Institute of Technology, Japan

2) Research Associate, Department of Civil Engineering, Tokyo Institute of Technology, Japan

3) Student, Department of Civil Engineering, Tokyo Institute of Technology, Japan

4) Professor, Department of Civil Engineering, Tokyo Institute of Technology, Japan

jtakemur@cv.titech.ac.jp, jizawa@cv.titech.ac.jp, sh4880@cv.titech.ac.jp, kusakabe@cv.titech.ac.jp

Abstract: In order to investigate complicated interaction between relatively shallow tunnel and soil subjected to shear deformation during earthquake, an active type shear box has been developed for the centrifuge facility in Tokyo Institute of Technology. This shear box had been originally designed and made focusing on deformation of a pile due to lateral movement of soil during earthquake under quasi-static condition. To cover the required tunnel depth the shear box was revised especially of its depth from 325mm to 500mm. This paper describes the revised apparatus and its performance observed in the preliminary tests on a semi-circular shape tunnel in dry sand.

1. INTRODUCTION

Underground structures were considered to have high seismic stability because of relatively low seismic motion in the ground. However, having serious damages of tunnel structures in 1995 Hyogoken-Nanbu Earthquake (Iida et al., 1996; Asakura and Sato, 1996), the design codes of tunnel have been revised especially for cut-and-cover tunnels and shield tunnels (JSCE, 1996). The revised specification recommends taking consideration on the soil-structure interactions by proper methods, such as seismic deformation methods and dynamic response analyses. The seismic deformation method is a kind of quasi-static approach in which seismically induced ground motion is applied to the tunnel through soil springs. As the reaction from the soil to the tunnel is affected many factors, e.g., stress conditions of soil, deformation, condition of tunnel surface, lining structures, there are many uncertainties in the application of seismic deformation method.

NATM tunnels have been commonly used for many mountain tunnels since 1980's in Japan and they have extended its application to urban tunnels in non-consolidated geological formation, like Pleistocene deposits consisted of sand and gravel or mad rock at relatively shallow depth. Because of unlined construction process in NATM, the stresses in the tunnel surrounding are released, which might create loosening area above tunnel. The lining sectional forces and deformation are affected by this complicated soil condition, which might be changed by the ground deformation due to earthquake. As the effects of these factors on the tunnel behavior are not easy to investigate from the performance of real tunnels, physical models can be employed for this purpose.

To satisfy the crucial similitude in the models and obtain reliable results from them, large scale model tests or centrifuge model test are conducted using shaking table tests. However, the soil structure interaction during shaking is so complicated, which makes the control or evaluation of displacements of ground and tunnel difficult. In order to avoid the complication and control a

important condition in the design, that is, ground deformation, an active type shear box can be used, although it is operated in a quasi-static condition, neglecting the inertial effects of the soil and tunnel. The active type shear box were first developed for investigating behavior of pile under controlled ground deformation in a large scaled model (Tsuchiya et al., 1997) and in a centrifuge model (Takahashi et al., 2001).

In this study, an active type shear box has been developed for the Tokyo Tech Mark III Centrifuge. This shear box had been originally designed and made focusing on deformation of a pile due to lateral movement of soil during earthquake under quasi-static condition. This paper describes the revised active type shear box and its performance observed in the preliminary tests on a semi-circular shape tunnel in dry sand.

2. ACTIVE TYPE SHEAR BOX IN THE TOKYO TECH MARK III CENTRIFUGE

2.1 Original active type shear box

Figure 1 shows the schematic diagram of the active type shear box developed for the test on piles subjected to lateral ground movement. In this system, shear box was consisted of 12 stacked laminae with the roller bearing support and one fixed laminar at the base. The shear deformation of the box was produced by three hydraulic actuators connected to three laminae at specific elevation. Lateral displacements of the other laminae were created by transmitting forces from the actuators to them through four linked sets of thin plate springs. Horizontal force can be applied to the pile head by a small actuator independently from the ground deformation. This shear box was designed to fit 0.9m by 0.9m swing platform of the Tokyo Tech Mark III centrifuge. Preliminary consideration in the design and description of the system were reported by Takahashi et al. (2001).

2.2 Revised active type shear box for tunnel tests

In the model test of urban tunnel, tunnel cover-diameter or width ratio (C/D) is very important parameter, as the depth controls the stress condition of tunnel surrounding, including formation of arching part above the tunnel. Using the original shear box, tests of shield tunnels were conducted (e.g., Yamada et al. 2002). However, due to the limitation of the box depth of 325mm, a small diameter model tunnel (e.g., 60mm) was used to have tunnel cover width ratio (C/D) of two. Although the depth of urban tunnel is relatively shallow, it normally has the depth a several times the tunnel width. In order to simulate the variable tunnel depth using a model tunnel of reasonable size (e.g., $D=100\text{mm}$) with various instrumentations, the active type shear box has been revised especially in the depth.

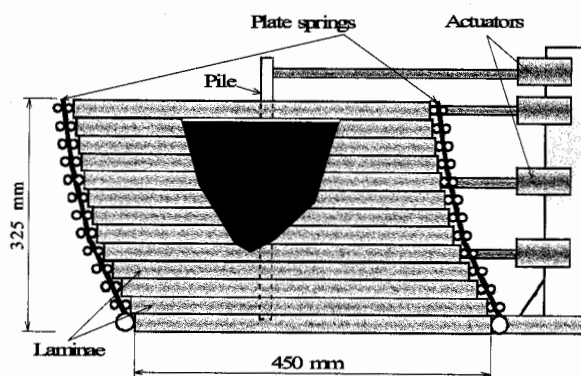


Figure 1 Schematic diagram of the active type shear box designed for tests on piles

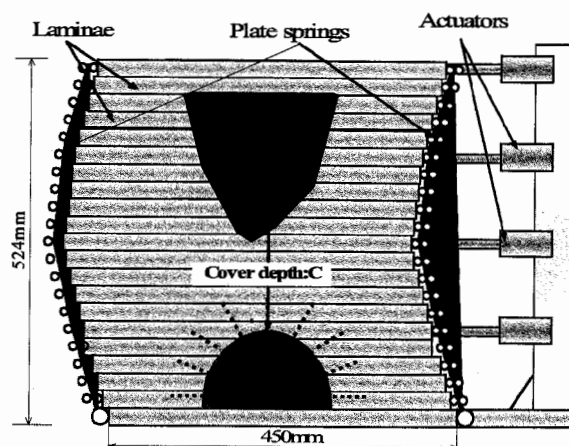


Figure 2 Schematic diagram of the active type shear box revised for tests on tunnels

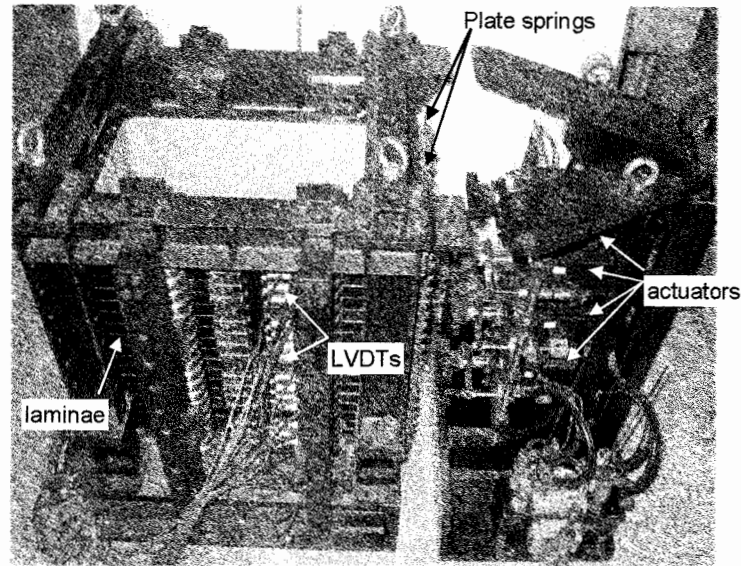


Figure 3 Active type shear box developed for the test on tunnels

Table 1 Specifications of the revised active type shear box

Maximum operational centrifugal acceleration		100g
Mass of whole apparatus		475kg (383kg)
Size of whole apparatus		W900 x B583 x H 700
Actuator	Number	4 (3)*
	Stroke	± 20 mm
	Force capacity at 20.5 MPa oil pressure	25.8kN for outward, 18.0kN for inward
	Peak velocity	133mm/sec
Laminar box	Dimensions of laminar	Outer: W512 x B262 x H24 mm Inner: W452 x B 202 x H24 mm round corner with radius of 20 mm
	Number of stacks	20(12) + fixed one at the bottom
	Inner size	W450 x B200 x H325 (H524) mm
	Flexural rigidity of plate spring: EI	0.56N.m ²
	Thickness of rubber sleeve	1mm

*Parenthesis: value before revision

Figures 2 and 3 show the schematic diagram and photo of the revised active type shear box. Major revisions of the new box are the height of the box and number of the actuator. Number of laminae was increased from 13 to 21 and the height of the box from 325mm to 524mm. The increment of the height is equivalent to C/D ratio of two for the model tunnel with 100mm width. Removing the small actuator for the pile head loading, one hydraulic actuator for displacing laminae was added to produce the continuous displacement of the laminae. Rubber sleeve is placed on the inner wall of the box to prevent the soil particles from getting into the gaps of the laminae. Thin stainless vertical sheets and a horizontal sheet of 0.2mm thickness with rough surface were fixed to the both end wall and the base respectively. These sheets are for developing the shear stresses on the inner boundary when the box sheared. Specifications of the active type shear box revised for the tunnel test are given in Table 1.

3. RESULTS OF PRELIMINARY TESTS ON PERFORMACE OF TUNNEL IN SAND

3.1 Deformation of sand in the shear box without tunnel

To verify the performance of the shear box, deformation of the sand without tunnel created by the

displacement of laminae was investigated to the sand of maximum height, 500mm, under 50g centrifugal acceleration using the test setup shown in Figure 4. Sand used in the verification test is dry silica sand with relative density of 80% and dry unit weight of 15.8kN/m^3 . Having prepared the model ground by poring, cyclic triangular shape horizontal displacements were applied to the laminar box under 50g. Maximum displacement amplitude ($\pm 20\text{mm}$) was input to the upper most actuator 1, which is equivalent of shear strain amplitude of the laminar box $\gamma_{LM}=4\%$. Four sinusoidal motions are applied in 100 seconds each cycle. The horizontal and vertical displacements at the sand surface were measured by laser displacement transducers and potentiometers at three location shown in the figure.

The horizontal displacements measured at the sand surface are shown in Figure 5 together with the displacement of the laminar box at the elevation of the sand surface. The observed horizontal motions at the sand surface are sinusoidal shape similar to the input one but their amplitudes are about 90% of the input one regardless of the location. This implies that horizontal compression and extension took place near the end wall and relatively uniform deformation could be created at the central part in the box. Vertical settlements of the sand surface observed during the tests are shown in Figure 6. Gradual increase of the settlement indicates the densification of sand due to cyclic shear. However, local upward heaving and settlement are also observed near the end wall when the walls move forward and backward to the soil respectively. At the center part, small heaving took place when the soil sheared to the both direction.

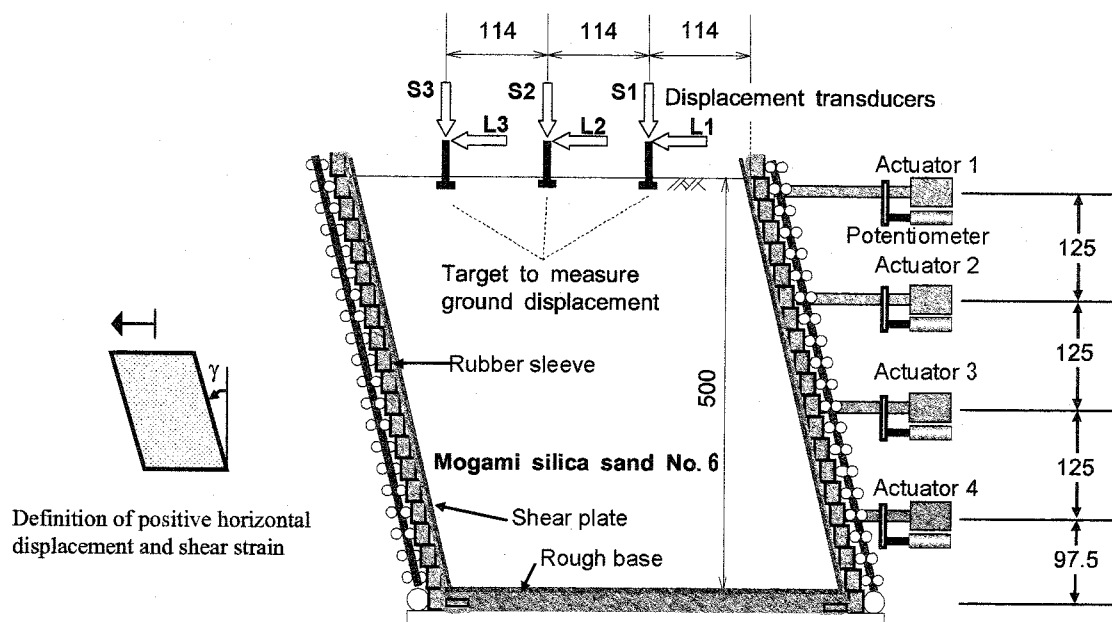


Figure 4 Test setup on the performance of active type shear box with sand

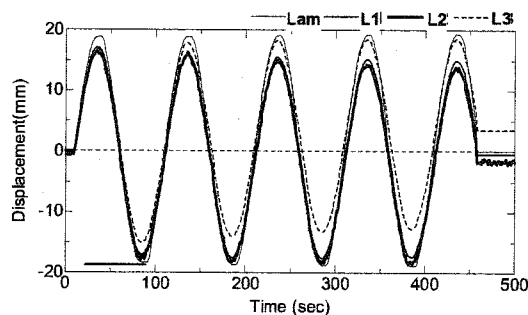


Figure 5 Observed displacements at sand surface caused by shear deformation of the box.

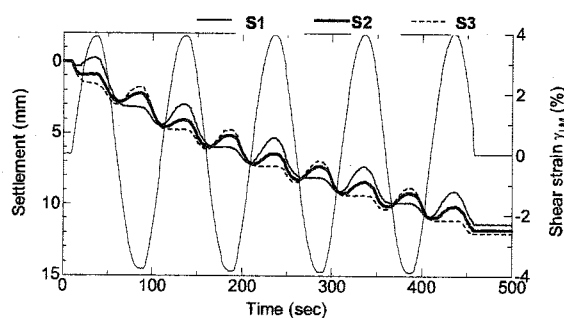


Figure 6 Observed settlements at sand surface during shearing

3.2 A test on tunnel in sand

As a first preliminary test using the new active type shear box, a test on semicircular tunnel was conducted using the same dry silica sand in the verification test explained above. Setup of the test is shown in Figure 7. Figures 8 and 9 shows the model tunnel used. 75mm height semi-circular tunnel model was made of 100mm diameter aluminum circular tube of 2mm thickness, which was rigidly fixed to the base plate by welding as shown in Figure 8. On both outer and inner side of the tunnel, the outer surface of the tunnel at the tunnel crown, springlines and the midparts between the crown and springlines. The tunnel cover depths in the test are 300mm and 100mm, which are 3D and 1D respectively. Sinusoidal input motions with variable shear strain amplitude of the laminar box γ_{LM} were applied to the models as shown in Figures 10 and 11.

Figures 12 show variations of earth pressure measured at the tunnel crown, left springline and the midpart between them in the case of $C=3D$ with $\gamma_{LM}=4\%$. Variation of bending moments near the three parts are also shown in Figures 13. In the cycle of M4-in, the model first sheared and the cycle of M4 were applied after several shear including M4-in. Earth pressures in the first cycle show gradual increase during shearing, but no marked increment due to shear cycles after having shearing history. Cyclic variation of the earth pressure and bending moment at the crown is smaller than those at the

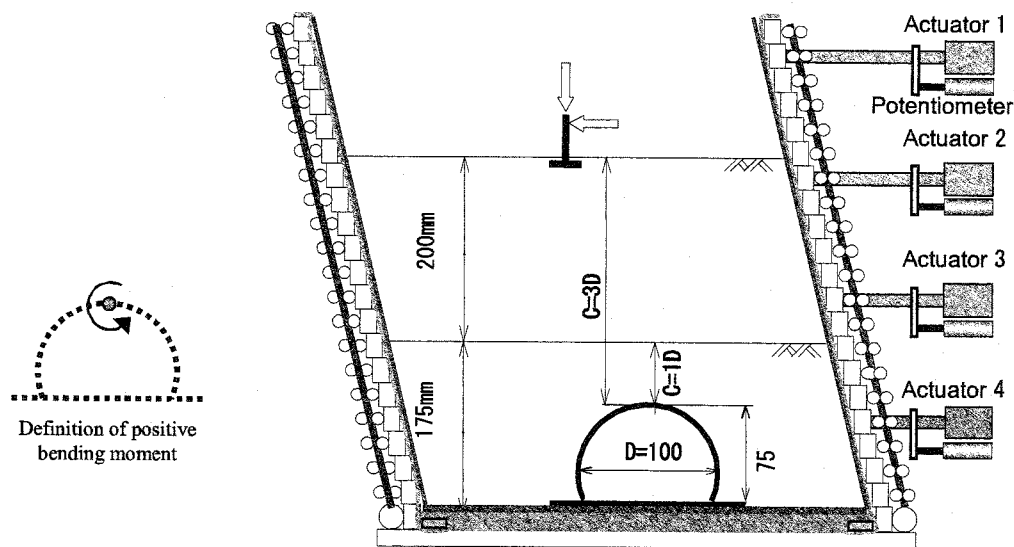


Figure 7 Test setup on sand with tunnel

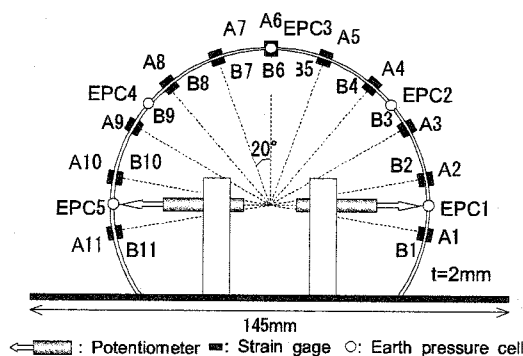


Figure 8 Instrumentation of the model tunnel

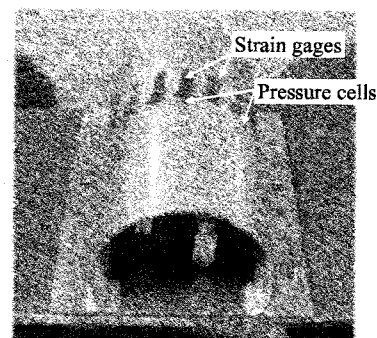


Figure 9 Model tunnel

tow parts. It is interesting to note that at the mid-part the earth pressure variation is very irregular, while the bending moment varies in the same phase of the input sinusoidal motion of the shear strain. The earth pressure at springline shows peak values when the input shear strain becomes maximum in both positive and negative side.

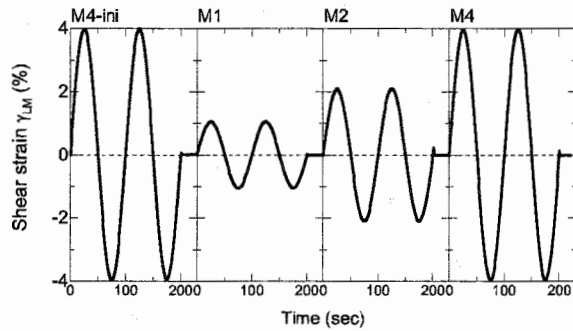


Figure 10 Input shear strain to the model of C=3D

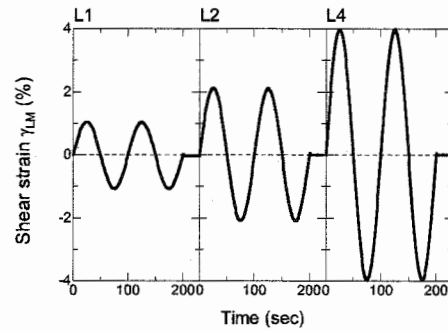


Figure 11 Input shear strain to the model of C=1D

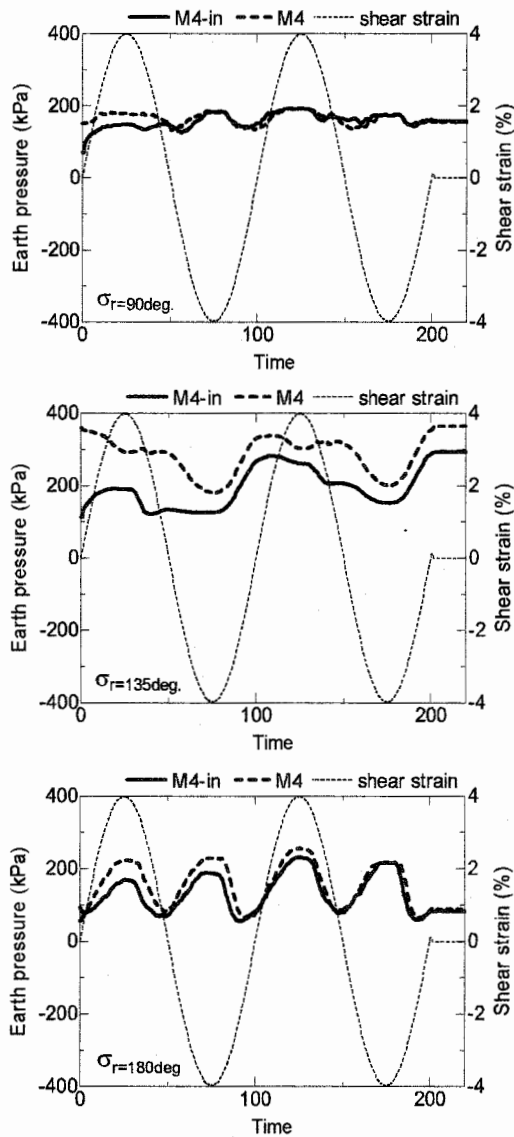


Figure 12 Measured earth pressures at crown, 45° and springline: C=3D & $\gamma_{LM}=4\%$

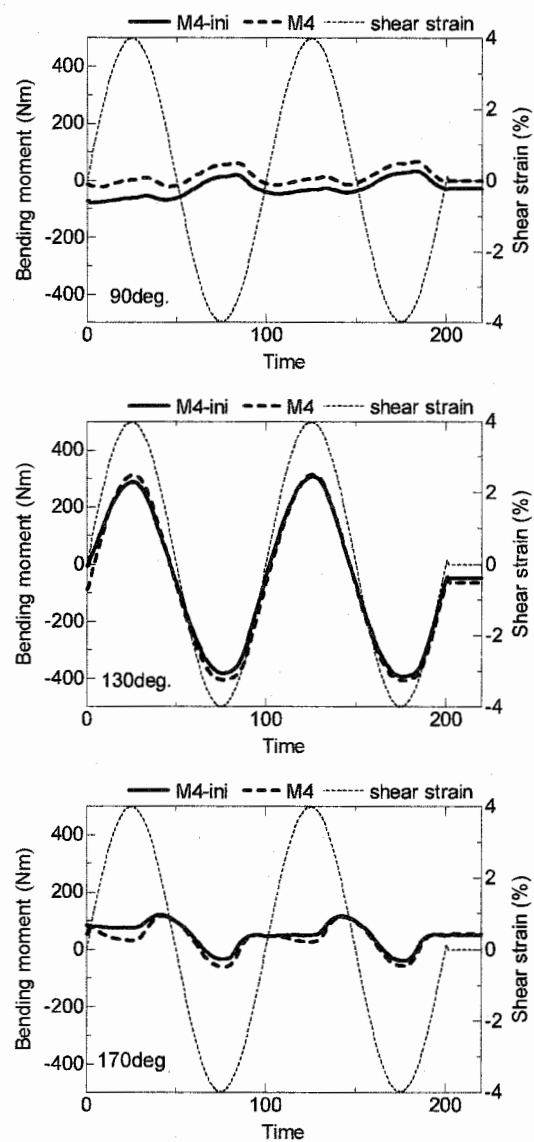


Figure 13 Measured bending moment: C=3D & $\gamma_{LM}=4\%$

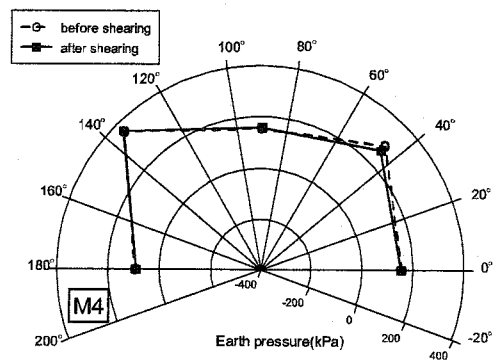
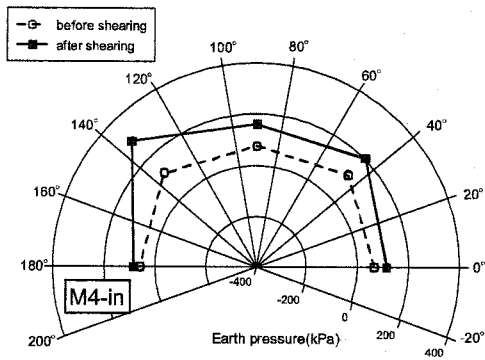


Figure 14 Earth pressure measured before and after shearing : $C=3D$ & $\gamma_{LM}=4\%$

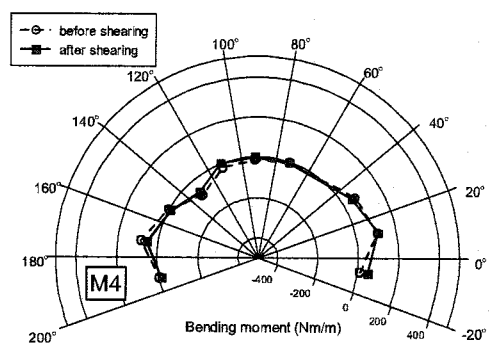
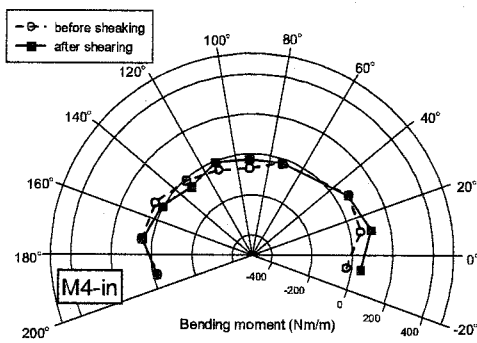


Figure 15 Bending moment measured before and after shearing : $C=3D$ & $\gamma_{LM}=4\%$

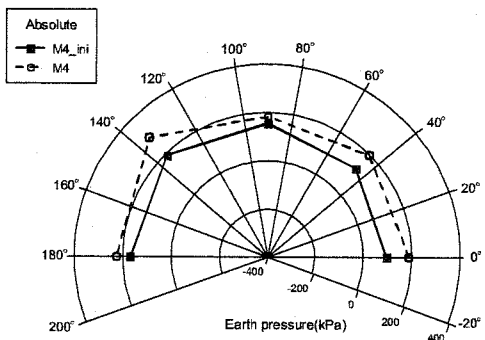


Figure 16 Earth pressures at maximum $\gamma_{LM}=4\%$

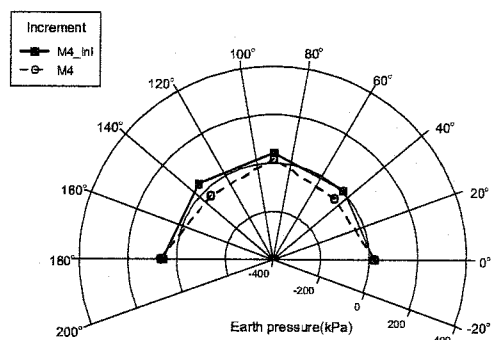


Figure 18 Increment of Earth pressures at maximum $\gamma_{LM}=4\%$

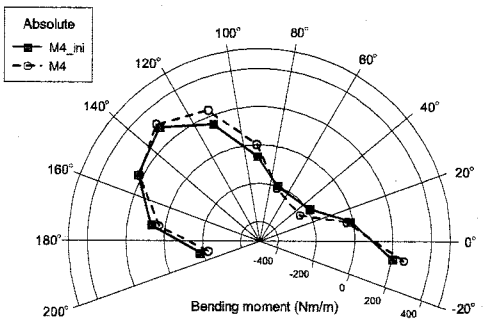


Figure 17 Bending moment at maximum $\gamma_{LM}=4\%$

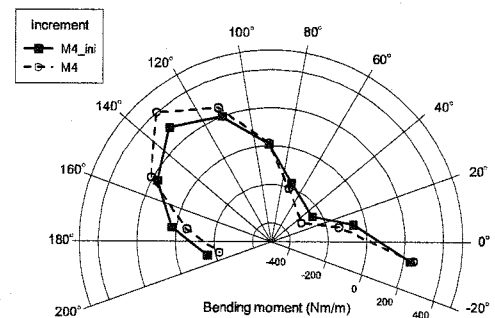


Figure 19 Increment of bending moment at maximum $\gamma_{LM}=4\%$

Figures 14 and 15 show the earth pressures and bending moments measured before and after cyclic shearing in M4-in and M4. Figures 16 and 17 show the earth pressures and moments measured when the positive maximum strain first applied in the M4-in and M4. The earth pressures before first shearing is smaller than those after shearing. This can be explained by arch action of the sand above the tunnel. Due to the overburden stress of the soil, the tunnel is deform vertically causing the loosening portion above the tunnel. But this arch action was diminished by shearing. After the first shearing, the soil-tunnel interaction showed elastic behavior with no change of pressure and bending moment before and after shearing. From the moment distribution at the maximum shear strain shown in Figure 17, it can be confirmed that the bending moment due to shear deformation of the ground becomes maximum at about 45° from the tunnel crown, which were also found by Yamada et al. (2002) from the circular shield tunnel model in a sand.

Figures 18 and 19 shows the increment of earth pressure and bending moment from the beginning to the first maximum positive shear strain point in M4-in and M4. The increment of the earth pressures are very small compared to the initial pressure shown in Figures 14. On the other hand large change of bending moment occurred due to shear deformation. This large bending moment might be attributed to the shear stress generated on the tunnel surface due to shear deformation.

4. CONCLUDING REMARKS

Using the newly revised active type shear box in the Tokyo Mark III centrifuge, the preliminary tests on a tunnel subjected to shear deformation of sand were conducted. Test results indicated applicability of the active type shear box to the study on soil-tunnel interaction in quasi-static condition. To verify the further applicability of the apparatus and have quantitative results, which can be utilized for validating numerical models and design approaches, measurement of deformation and stresses in the soil are crucial. Comparisons between the shear box tests and the shaking table tests are also recommended as a future work.

Acknowledgements:

The authors gratefully acknowledge the funding for this research from Japan Society for the Promotion of Science (JSPS) as Grant-in-Aid program.

References:

- Asakura, T. and Sato, Y. (1996), "Damage to Mountain Tunnels in Hazard Area", Soils and Foundation Special Issue on Geotechnical Aspects of the January 17 1995 Hyogoken-Nambu Earthquake, pp.301-310.
- Iida, H., Hirota, T., Yoshida, N. and Iwafuji, M. (1996), "Damage to Daikai Subway Station", Soils and Foundation Special Issue on Geotechnical Aspects of the January 17 1995 Hyogoken-Nambu Earthquake, pp.283-300.
- Japan Society of Civil Engineers (1996): Specification of cut-and cover tunnels.
- Takahashi, A. Takemura, J. Suzuki, A. and Kusakabe, O. (2001), "Development and Performance of an Active Type Shear Box in a Centrifuge", International Journal of Physical Modelling in Geotechnics, Vol.1, No.2, pp. 1-17.
- Tsuchiya, T. Kikuchi, D. Yamada, T. Kakurai, M. and Yamashita, K. (1997), "Lateral Loading Tests on the Model Pile in the large Scale Shearing pit Considering Deformation of Pile Top and Ground", Proc. 32nd Japan National Conference on Geotechnical Engineering, pp.1545-1548 (in Japanese).
- Yamada, T. Nagatani, H., Igarashi, H. and Takahashi, A. (2002), "Centrifuge Model Tests on Circular and Rectangular Tunnels Subjected to Large Earthquake-induced Deformation", Proc. Intn. Geotechnical Aspects of Underground Construction in Soft Ground, pp.673-678, Lyon, Balkema.

ESTIMATION OF SEISMIC BEHAVIOR OF PILE GROUP IN NON-LIQUEFIED AND LIQUEFIED GROUND THROUGH CENTRIFUGE MODEL TESTS

H. Suzuki¹⁾, K. Tokimatsu²⁾, and G. Ozawa³⁾

1) Research Associate, Dept. Architecture and Building Engineering, Tokyo Institute of Technology, Japan

2) Professor, Dept. Architecture and Building Engineering, Tokyo Institute of Technology, Japan

3) Graduate Student, Dept. Architecture and Building Engineering, Tokyo Institute of Technology, Japan
hsuzuki@arch.titech.ac.jp, kohji@o.cc.titech.ac.jp, gozawa4@mail.arch.titech.ac.jp

Abstract: Seismic behavior of pile groups in both dry and liquefiable saturated sands is investigated based on centrifuge tests on soil-pile-structure models constructed in a laminar shear box. Two pile models, a 2x2 pile group at 7.5 diameter spacing and a 4x4 pile group at 2.5 diameter spacing, were used for both dry and liquefiable saturated sand deposits. The test results show that, as the pile spacing decreases, the trailing piles tend to bear smaller shear force than the leading piles in the dry sand but the inside piles tend to bear smaller force than the outside piles in the liquefied sand. The difference in observed trends between non-liquefied and liquefied sands in closely spaced pile group is probably induced by the difference in mechanism of subgrade reaction development. In the non-liquefied sand, the subgrade reaction is induced by an increase in normal stress on the compression side of the pile and the increase in normal stress on the compression side of any trailing pile becomes smaller than that of the preceding pile as some of the normal stress is canceled out by the extension stress induced by the preceding pile. In the liquefied sand, the subgrade reaction is induced by the difference in pore water pressure changes on the compression and extension sides of the pile and the difference in pore water pressure changes on both sides of any inside pile becomes smaller than that of the outside pile due to the adverse effects of extension stress induced by the preceding pile and compression stress induced by the following pile.

1. INTRODUCTION

Toward establishing reasonable seismic design of pile foundations, it is important to estimate effects of soil-pile-structure interaction on pile behavior during earthquakes. In particular, if piles are closely spaced within a pile group, pile-soil-pile interaction effects, in which the stress zones induced by piles overlap with those of other piles, might have affected pile behavior. Previous studies on a pile group in non-liquefied sand (e.g., Rollins et al., 1998, Suzuki & Adachi, 2003) have indicated that load capacity of piles depends on its location within the pile group. In the case of a pile group in liquefied sand, Uchida et al. (2003) have indicated that pile stresses depend on its location within the pile group as is the case of non-liquefied ground, while Rollins et al. (2005) have shown that pile stresses become almost the same regardless of pile location. Lateral load capacity in most of the previous studies was based on lateral loading tests but has seldom been discussed based on shaking table tests on pile groups in both liquefied and non-liquefied ground.

The objective of this paper is to investigate horizontal load capacity of pile groups based on centrifuge model shaking table tests that were conducted on pile-structure systems having different pile number and spacing in both non-liquefied and liquefiable soils.

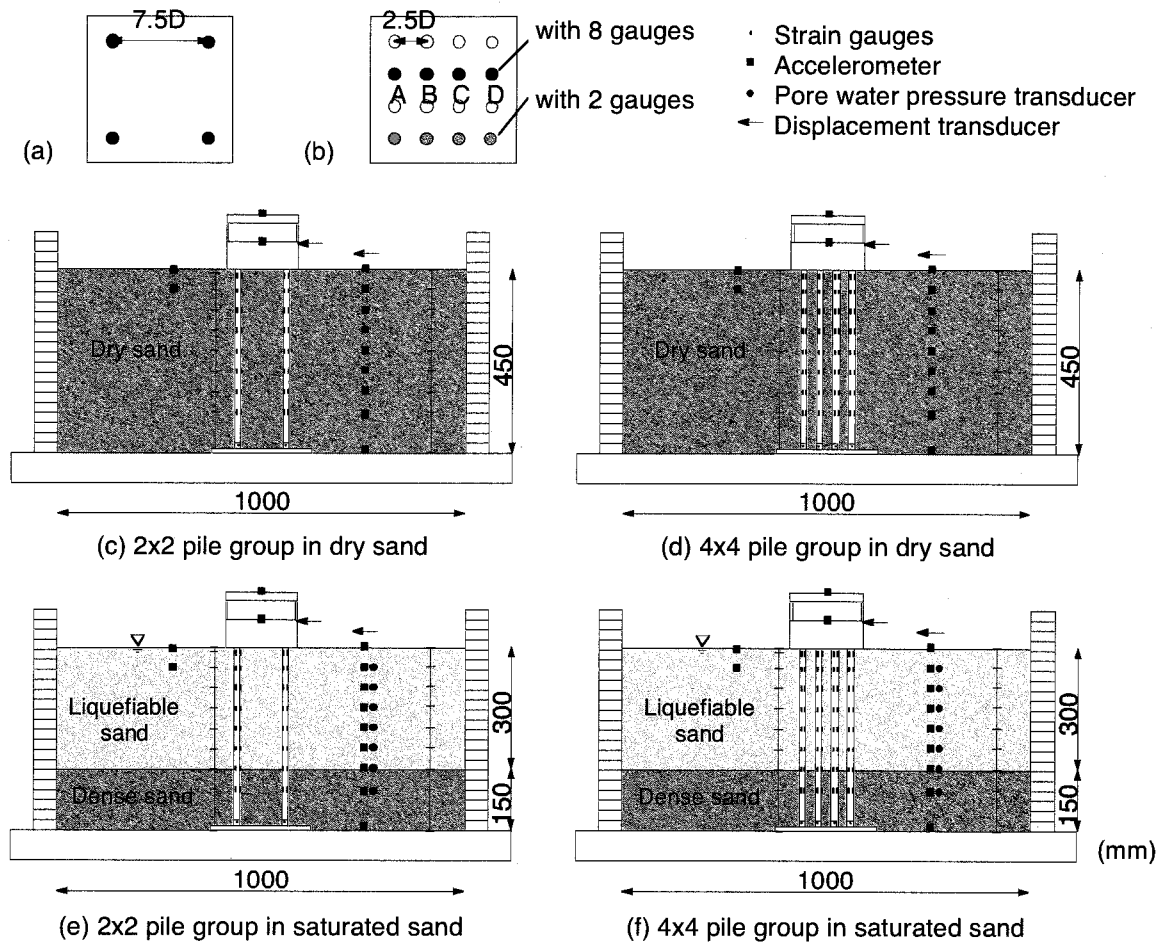


Figure 1 Test models

2. CENTRIFUGE MODEL TESTS ON SOIL-PILE-STRUCTURE SYSTEMS

To investigate seismic behavior of pile groups in both non-liquefied and liquefied ground, centrifuge model tests were conducted on four soil-pile-structure systems. Fig. 1 shows the four soil-pile-structure systems, constructed in a laminar shear box with dimensions of 560 mm x 1000 mm x 310 mm. All tests were performed on a 6.5 m radius centrifuge system at a centrifugal acceleration of 30 g. So, the test models were on a scale of 1:30 in length.

After placing a group of pile in the laminar shear box, sand was air-pluviated to a height of 450 mm, corresponding to a 13.5 m thick prototype soil layer. Toyoura Sand ($e_{\max} = 0.982$, $e_{\min} = 0.604$) was used to prepare sand deposits. The dry sand deposit prepared in the laminar shear box consisted of a homogeneous layer with a relative density of about 70%, while the saturated sand deposit consisted of both liquefiable layer with a relative density of about 70% and underlying non-liquefiable dense layer with a relative density of about 90%. The soil profile for liquefiable sand deposit was saturated under a vacuum with silicon oil, having a viscosity of thirty times that of water.

Two pile groups consisting of four (2x2) and sixteen (4x4) piles were used for both dry and saturated sand deposits. The 2x2 pile group was set up with a horizontal space of 7.5-diameter spacing center to center and the 4x4 pile group 2.5-diameter spacing (Fig. 1). Each pile consisted of a stainless steel pipe having a diameter of 15.9 mm with a 0.3 mm wall thickness and a length of 450 mm, corresponding to a 477 mm diameter, a 9 mm wall thickness and a 13.5 m length in prototype unit. The tips of piles were connected to the base of the laminar shear box with pin joints and their

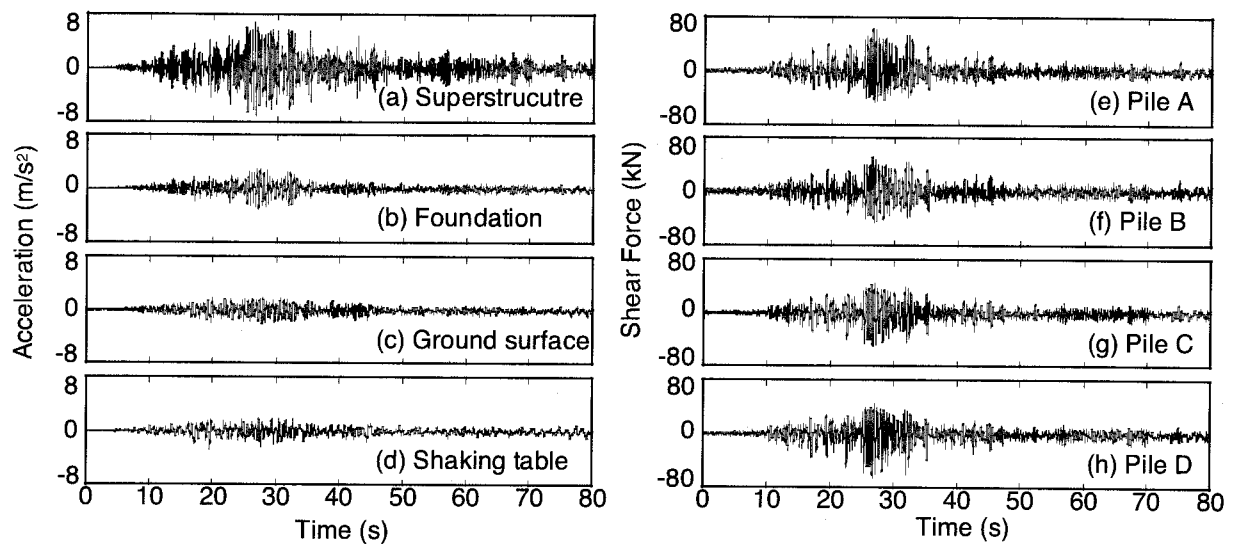


Figure 2 Time histories of accelerations and shear forces in test with 4x4 pile group in dry sand

heads were fixed to a foundation with a superstructure.

The soil-pile-structure system was instrumented with accelerometers, displacement transducers, strain gauges and, if saturated, pore pressure transducers, as shown in Fig. 1. Bending strains were measured all of the four piles in the 2x2 pile group or eight out of sixteen piles in the 4x4 pile group. Each of these piles had strain gauges at either two near the pile head or eight along the total length of the pile. The black piles in the plan view shown in Fig. 1(a)(b) indicate those with eight gauges, while the gray piles those with two gauges. In the shaking table tests, an artificial ground motion called Rinkai having a maximum acceleration scaled to 2.0 m/s^2 in prototype unit was used as an input motion to the shaking table. The shear forces at the pile head are calculated by differentiation of bending moment estimated from the observed strain gauge data and the inertial force by accelerations of the foundation and superstructure. The observed test results discussed hereafter are those in prototype unit with a scaling factor corresponding to 30 g.

3. ESTIMATION OF PILE GROUP EFFECTS

Fig. 2 shows time histories of accelerations of superstructure, foundation, ground surface and shaking table as well as those of shear forces observed at the four pile heads in the test conducted on the 4x4 pile group in dry sand. The location of the four piles (Piles A to D) is presented in Fig. 1 (a). The acceleration of the superstructure is amplified significantly, compared with those of shaking table, ground surface and foundation. The shear forces increase with increasing superstructure acceleration, confirming that the inertial force induces shear force in piles. It is interesting to note that the shear forces observed at the four piles show slightly different trends with each other. Namely, the shear force at Pile A becomes larger in the positive direction of inertial force than in the negative direction, while that at Pile D becomes larger in the negative direction than in the positive direction (Fig. 2(e)(h)). In contrast, the shear forces at Piles B and C are almost the same in both positive and negative directions (Fig. 2(f)(g)).

To investigate the difference in shear forces within the 4x4 pile in dry sand, Fig. 3 shows the relations between the inertial force and shear forces for the test within the 4x4 pile group in dry sand. With increasing inertial force in the positive direction, the shear force at Pile D becomes much larger than others. With increasing inertial force in the negative direction, on the contrary, the shear force at

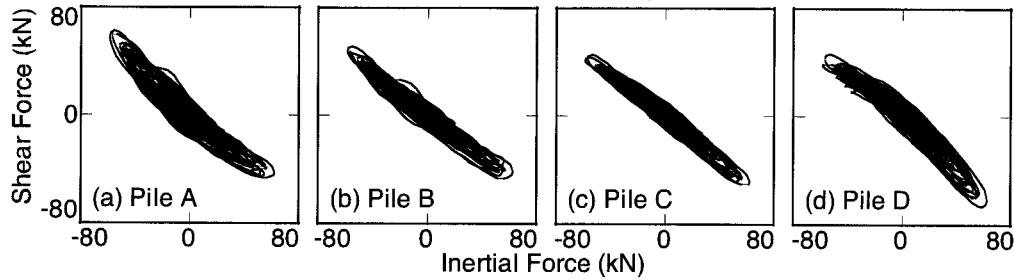


Figure 3 Relation between inertial force and shear forces within 4x4 pile group in dry sand

pile A becomes much larger than others. This indicates that shear force, depending on the direction of inertial force, becomes largest at the leading pile.

To compare shear forces within the pile groups tested with dry sand deposit, Fig. 4 shows the distributions of bearing shear force ratio within the two pile groups. The shear force ratio in the figure is given by dividing shear force at each pile by the total shear force of the pile group. The shear force at each pile is the average of those at ten instants when the inertial force takes its peak. The shear force ratio within the 4x4 pile group becomes larger in the leading row than in the trailing rows (Fig. 4(b)), corresponding to the trend shown in Fig. 3. The difference in shear forces within the 4x4 pile group is induced by shadowing effects of subgrade reaction, in which stress zones in soil induced by the following piles overlap with those by the preceding piles. The shear force ratios in the four piles of the 2x2 pile group are almost the same, the trend of which is different from those in the case of the 4x4 pile group. This indicates that the closer the pile spacing, the more significant the shadowing effects. The above findings relate to the previous studies (Rollins et al., 1998, Suzuki & Adachi, 2003), in which static horizontal loading tests were conducted on pile groups in non-liquefied sand.

To compare the shear forces within the 2x2 and 4x4 pile groups in saturated sand with those in dry sand, Fig. 5 shows the distributions of bearing shear force ratio of each pile within the pile groups in about 20 s after soil liquefaction. In the case of the 2x2 pile group, there exists no definite trend in which the shear force ratio in any of the piles becomes significantly larger than others (Fig. 5(a)). In the case of the 4x4 pile group, the shear force ratios of the exterior corner piles tend to become larger than others (Fig. 5(b)). This is different from the trend in dry sand, in which the shear force ratios become larger at the leading piles when pile spacing becomes small.

The difference in shear force ratio between liquefied and non-liquefied ground observed in a closely spaced pile group as shown in Figs. 4 and 5 could be induced by the difference in the mechanism of subgrade reaction development. Fig. 6 schematically shows why the shear force distribution in pile groups is different between non-liquefied and liquefied sands. With increasing relative displacement between a pile and ground, extension stress state occurs on one side of the pile and compression stress state on the other side, accompanied by an increase in shear stress on both sides as shown in Fig. 6. The subgrade reaction in non-liquefied ground is therefore induced by an increase in normal stress on the compression side.

If the piles are closely spaced within a pile group, the increase in normal stress induced by the following piles is canceled out by the extension stress caused by preceding piles (Fig. 6(a)), leading to small subgrade reactions of the trailing piles. As a result, the trailing piles bear smaller force than the leading piles. The subgrade reaction in liquefied sand, in contrast, is induced by the difference in pore water pressure changes between extension and compression sides. If the piles are closely spaced within a pile group, extension (otherwise compression) stress induced by one pile and compression (otherwise extension) stress induced by the other pile may cancel out with each other in the soil within the pile group (Fig. 6(b)), resulting in an insignificant difference in pore water pressures in the soil within the pile group. This might have led to small subgrade reaction of the inside piles.

As a result, the inside pile bears smaller shear force than the outside pile. The above findings suggest that pile spacing does have significant effects on horizontal load capacity distribution within a pile group in both non-liquefied and liquefied ground but in a different manner.

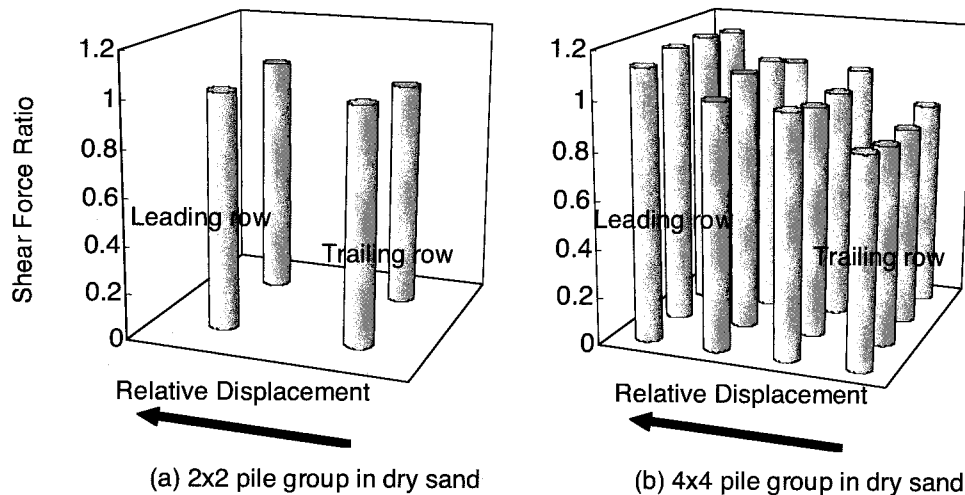


Figure 4 Bearing shear force rate within pile groups in non-liquefied dry sand

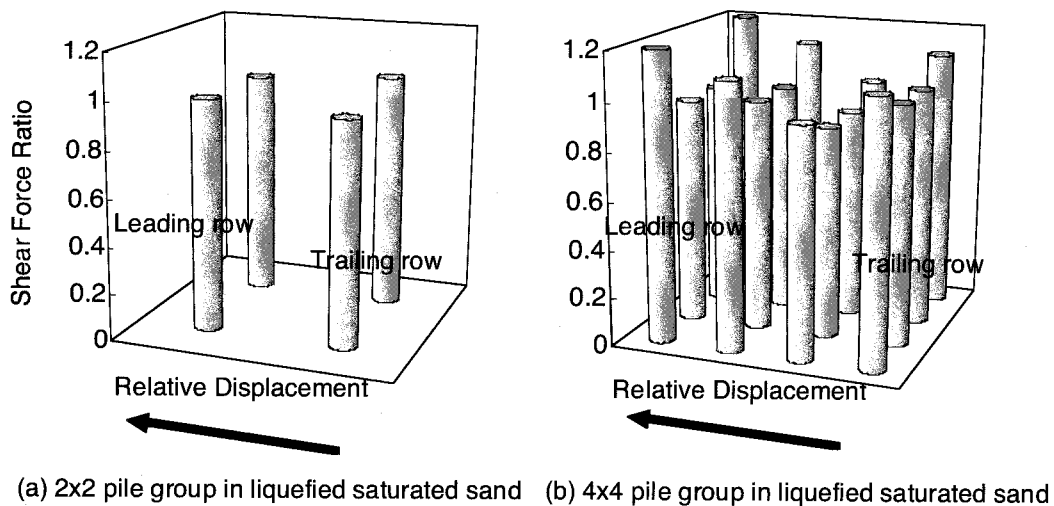


Figure 5 Bearing shear force rate within pile groups in liquefied saturated sand

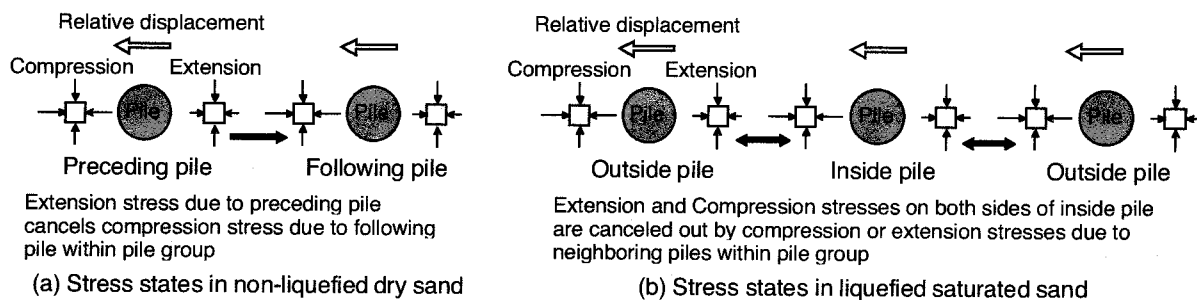


Figure 6 Stress state in soil around piles

4. CONCLUSIONS

To investigate seismic behavior of pile group, distributions of horizontal shear forces within pile groups as well as influential factors affecting them have been studied through the centrifuge model tests. The test results lead to the following:

1) In non-liquefied ground, the trailing piles tend to bear smaller force than the leading piles, as the pile spacing decreases. This is because the subgrade reaction is induced by an increase in normal stress on the compression side of the pile and the increase in normal stress on the compression side of any trailing pile becomes smaller than that of the preceding pile as some of the normal stress is canceled out by the extension stress induced by the preceding pile. As a result, the subgrade reaction becomes smaller in the trailing piles but larger in the leading piles, which induces smaller shear forces at the trailing piles but larger shear forces at the leading piles.

2) In liquefied ground, the inside piles tend to bear smaller force than the outside piles as the pile spacing decreases. This is probably because, in liquefied ground, the subgrade reaction is induced by the difference in pore water pressure changes on the compression and extension sides of the pile and the difference in pore water pressure changes on both sides of any inside pile becomes smaller than that of the outside pile due to the adverse effects of compression stress induced by the preceding pile and extension stress induced by the following pile. As a result, the subgrade reaction becomes smaller in the inside piles but larger in the outside piles, which induces smaller shear forces in the inside piles but larger shear forces in the outside piles.

Acknowledgements:

The centrifuge model tests described in this paper were conducted at the centrifuge system at Takenaka Research & Development Institute. The authors express their sincere thanks to the above organization.

References:

- Rollins, K. M., Kris, T. P. and Thomas, J. W. (1998), "Lateral load behavior of full-scale pile group in clay", *Journal of Geotechnical and Geoenvironmental Engineering*, American Society of Civil Engineers, **124**(6), 468-478.
- Suzuki, Y. and Adachi, N. (2003), "Relation between subgrade reaction and displacement of model pile group based on horizontal loading tests", *Journal of Structural and Construction Engineering*, Architectural Institute of Japan, **570**, 115-122 (in Japanese).
- Uchida, A., Hamada, J., Tsuchiya, T., Yamashita, K. and Kakurai, M. (2003), "Lateral loading tests on a model pile group in liquefied soil using large-scale laminar shear box", *Journal of Structural and Construction Engineering*, Architectural Institute of Japan, **572**, 117-122 (in Japanese).
- Rollins, K. M., Gerber, T. M., Lane, J. D. (2005), "Lateral resistance of full-scale pile group in liquefied sand", *Journal of Geotechnical and Geoenvironmental Engineering*, American Society of Civil Engineers, **131**(1), 115-125.
- Tokimatsu, K. and Suzuki, H. (2004), "Pore water pressure response around pile and its effects on p-y behavior during soil liquefaction", *Soils & Foundations*, Japanese Geotechnical Society, **44**(6), 101-110.

ANALYTICAL STUDY FOR DAMAGE TO CAST-IN-PLACE CONCRETE PILE IN LATERALLY SPREADING GROUND DURING THE 1995 HYOGOKEN-NAMBU EARTHQUAKE

K. Koyamada¹⁾, K. Tokimatsu²⁾, and Y. Miyamoto³⁾

1) Senior Research Engineer, Kobori Research Complex, Kajima Corp., Japan

2) Professor, Dept. of Architecture and Building Engineering, Tokyo Institute of Technology, Japan

3) General Manager, Kobori Research Complex, Kajima Corp., Japan

koyamada@kajima.com, kohji@o.cc.titech.ac.jp, y-miyamoto@kajima.com

Abstract: Pile foundations near the shoreline in Kobe city were severely damaged due to liquefaction induced lateral spreading during the Hyogo-ken Nambu Earthquake, January 17, 1995. Kuwabara and Yoneda (1998) presented a unique case history of damage to a cast-in-place concrete pile foundation of a building that was under construction during the earthquake and thus experienced lateral spreading without significant inertial effects. The objective of this study is to clarify the failure process of the pile foundation based on an effective stress response analysis of a soil-pile foundation system. The strong motion recorded at the bottom of the downhole array at Higashi-Kobe Bridge is employed as an input motion to the soil-pile foundation system. It is found that the pile foundations near the shoreline are greatly affected by liquefaction induced lateral spreading and that the failure process of pile foundations varies greatly with distance from the shoreline.

1. INTRODUCTION

Pile foundations near the shoreline of the reclaimed area were severely damaged during the Hyogo-ken Nambu Earthquake, January 17, 1995. Damage investigations have shown that not only PC piles and PHC piles but also RC piles and steel pipe piles were damaged due to liquefaction-induced lateral ground spreading (e.g. Kansai Branch of Architectural Institute of Japan, 1996). Many subsequent reports have suggested that the pile damage is closely related to large soil deformation due to lateral spreading (e.g. The Japanese Geotechnical Society, 1998).

Kuwabara and Yoneda (1998) presented a unique case history of a cast-in-place concrete pile foundation that was under construction during the 1995 Hyogo-ken Nambu Earthquake and thus experienced lateral spreading without significant inertial effects. Tokimatsu et. al. (1998) pointed out that the failure and deformation modes of the piles vary depending on the location due to spatial variation of lateral spreading. Koyamada et. al. (1999) conducted an earthquake response analysis for a pile-supported building model and indicated that pile damage occurred before or during soil liquefaction and got worse due to liquefaction-induced lateral spreading.

In this study, simulation analyses for the aforementioned field case history are conducted using the observed strong motion in order to verify the failure process of pile foundation in the laterally spreading ground. The analysis results clarify that pile foundation was damaged by soil deformation during the earthquake before the lateral spreading occurred, and the failure process of the pile foundations vary with distance from the shoreline due to the difference of the residual soil displacement induced by the lateral spreading.

2. OUTLINES OF PILE DAMAGE

Fig. 1 shows the location of the damaged building. The building was situated on a reclaimed land in Osaka Bay and located about 25m and 90m inland from the eastern and the southern coastlines, respectively. The quay walls had moved seawards by about 2.5-3.0m and ground surface around the building was also displaced about 0.5-1.0m due to soil liquefaction-induced lateral spreading. Fig. 2 shows a plot plan of the building. The building was a 7 by 2 spanned steel frame structure, 41.8m long in the east-west direction and 16.1m wide in the north-south direction. The pile foundations of the building were cast-in-place concrete piles 47-49m long with diameters of 1.2-1.7m. The building, six stories at its completion, experienced the earthquake when the steel frames of the third floor were constructed as shown in Fig. 3 and thus the piles carried only 2% of the long-term design load. This indicates that the piles might have been damaged by soil deformation during the earthquake and lateral spreading without an inertial force from a superstructure.

Vertical coring of the piles and excavation survey around the pile heads were conducted in order to investigate the damage of the pile foundation (Kuwabara and Yoneda, 1998). The vector slope angles of the pile heads are shown in Fig. 2. The features of pile damage are summarized as follows;

1. Concrete cracking concentrated at the depths smaller than 8m and at the depths below 14m and the maximum width of the crack was about 1cm.
2. The piles on the seaside of the building inclined landwards, while the piles on the landside inclined seawards in the longitudinal direction and the maximum pile slope angles were about 0.05 rad.

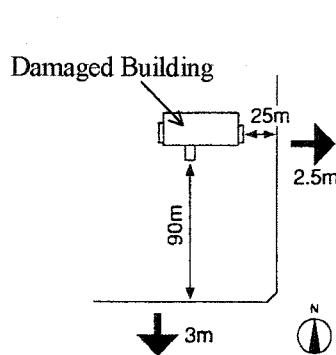


Figure 1 Map showing Damaged Building and Quay Wall Displacement

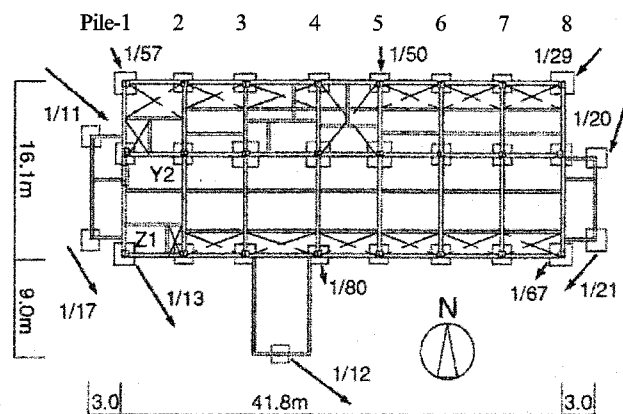


Figure 2 Vector Slope Angles of Pile Heads observed after Earthquake (Kuwabara and Yoneda, 1998)

3. ANALYSIS METHOD AND MODEL

In order to clarify the failure process of pile foundation due to lateral spreading, the analyses are conducted in the following two stages. Firstly, soil responses are calculated by a 2D-FEM effective stress analysis taking into account the lateral spreading. Then, the pile responses are calculated by the numerical model taking into account the nonlinear cross interaction between soil and pile foundation. Analysis method and model are shown as follows.

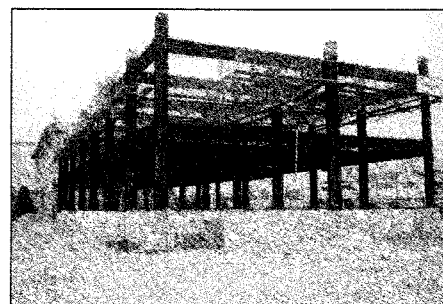


Figure 3 Full View of Damaged Building

3.1 Soil Response Analysis

The soil response analysis is conducted by a 2D-FEM effective stress analysis method using the computer program "FLIP" (Iai et. al., 1992). The computer program is a time history response analysis program and employs a multiple shear mechanism model for the strain dependency of soil stiffness and Iai-Towhata model for evaluating the generation of excess pore water pressure. Fig. 4 shows the analysis model and Table 1 shows the soil constants of the site. The depth of a quay wall is set at 8m and the influence of seawater is ignored. The quay wall is a box caisson type and is modeled as a linear solid element. The backfill sand and rubble mound are modeled as linear solid elements with shear wave velocities of 150m/s and 200m/s, respectively. The boundary condition of the bottom is set as fixed and that of the side is set as a viscous damper. The observed strong motion in the borehole array at Higashi-Kobe Bridge, near the damaged building, is employed as the input motion for the analysis. The soil constants are based on the geological survey made by Public Works Research Institute (1995). Fig. 5 shows a liquefaction resistance curve which is based on laboratory test on the reclaimed layer (Kobe City Development Bureau, 1995; Suzuki et. al., 1997).

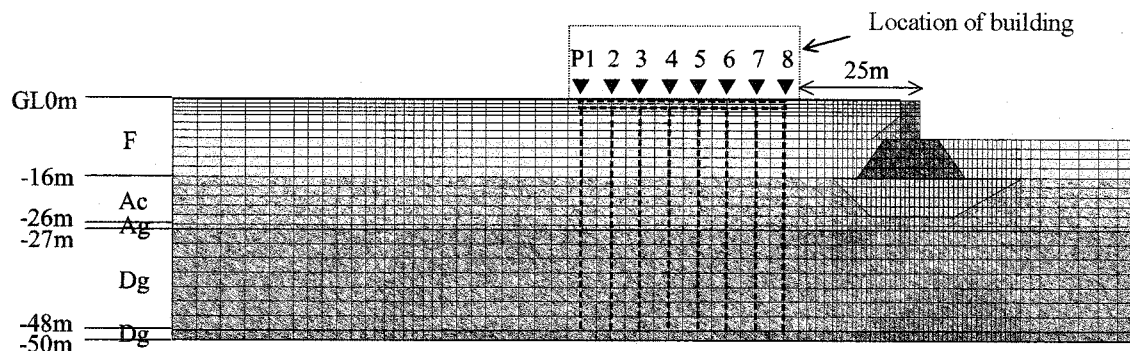


Figure 4 Analysis model for 2-D FEM effective stress analysis (EW-Direction)

Table 1 Soil Constants and
Location of Strong Motion Observation

N-Value	Soil Type	γ (g/cm ³)	V_s (m/s)	ϕ (deg.)	c (kPa)	Observed Motion
0	F*	1.8	170	32	-	0m
10	Ac	1.7	200	-	180	
20	Ag	1.9	250	36	-	
30	Dg	1.9	350	40	-	33m
40	Dg	1.9	450	-	-	Input Motion
50	Dg	1.9	450	-	-	

γ : unit weight, V_s : S-wave velocity
 ϕ : internal friction angle, c : cohesion
 * Parameters for Iai Model
 $W1=3.0, P1=0.5, P2=0.6, C1=1.0, S1=0.005$

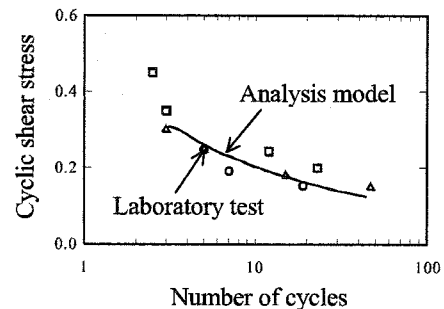


Figure 5 Liquefaction Resistance Curve on the Reclaimed Layer

3.2 Pile Response Analysis

The pile response analysis is conducted using a beam-interaction spring model, as shown in Fig. 6 (Miyamoto et. al., 1995; Sako and Miyamoto, 1999). The pile foundations are idealized by an 8-stick model with lumped masses and beam elements. The symbols ▼ P1-P8 show the positions of the piles. The lumped masses of the piles are connected to the free field soil through lateral and shear interaction springs. The initial values of the lateral and shear interaction soil springs of pile groups are obtained using Green's functions by ring loads in a layered stratum (Kausel and Peek, 1982) and they

are equalized to eight piles. The soil springs are modified in accordance with the relative displacements between soils and piles and with the generation of excess pore water pressures. The nonlinear properties of the piles are incorporated into the relationship between the bending moment M and the curvature ϕ , which is evaluated by a static push-over analysis with Fiber-Model and is modeled as a tri-linear relationship as shown in Fig. 7.

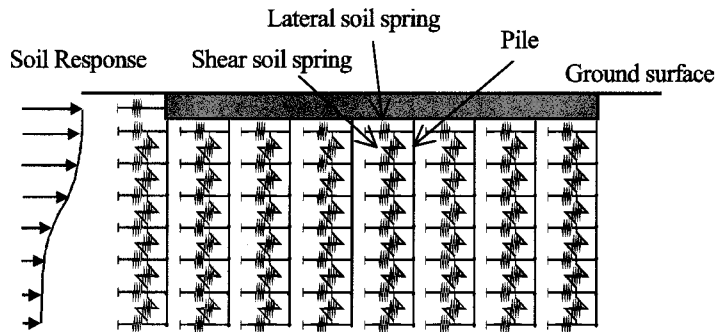


Figure 6 Numerical Model of Pile Foundation for Response Analysis

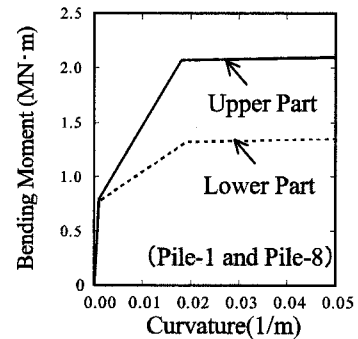


Figure 7 Tri-linear Model for Pile Nonlinearity

4. SOIL RESPONSE DUE TO LATERAL SPREADING

4.1 Simulation Analysis for Observed Motion

Fig. 8 shows time histories of simulation analysis results including acceleration and relative displacement at the ground surface and excess pore water pressure ratio (EPWPR) at a depth of 4m together with the observed motion. The EPWPR is the ratio of excess pore water pressure to the initial effective stress and it reached to about 1.0 at about 10s. The computed results indicate that liquefaction occurred in the reclaimed layer within 10s after the start of shaking. The maximum acceleration and relative displacement at the ground surface occurred at almost the same time. After the occurrence of soil liquefaction at 10s, the amplitudes of the ground surface acceleration became smaller, while the relative ground displacement became larger. The computed ground surface acceleration and displacement time histories are in good agreement with the observed ones.

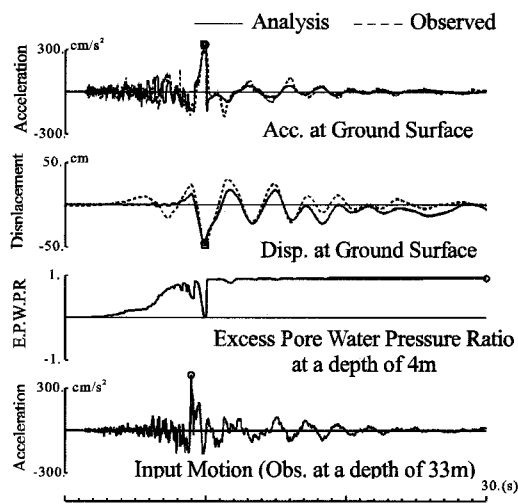


Figure 8 Simulation Results for Observed Motion

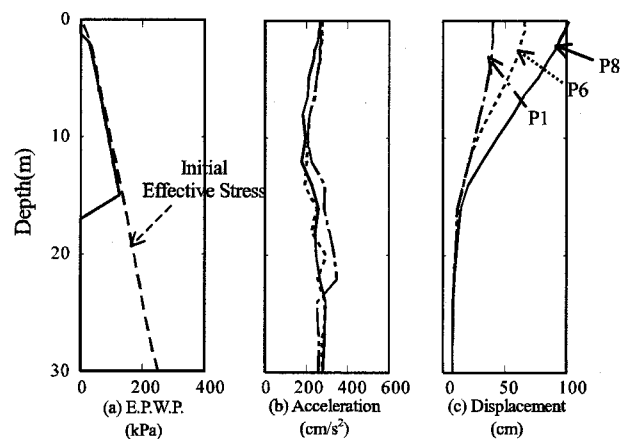


Figure 9 Maximum Soil Responses at Distances 28m (P8), 40m (P6) and 70m (P1) from Shoreline

4.2 Soil Deformation in Laterally Spreading Ground

Fig. 9 shows the distributions of maximum excess pore water pressure, ground acceleration and displacement at distances 28m (P8), 40m (P6) and 70m (P1) from the shoreline. The excess pore water pressures reached to the initial effective stress in the reclaimed layer above GL-16m. The maximum accelerations do not seem to amplify in the liquefied layer, the tendency of which is almost the same, regardless of the distance from the shoreline. The maximum relative displacement, in contrast, increases with decreasing distance from the shoreline, being equal to 102cm, 66cm and 40cm, at distances of 28m, 40m, and 70m, respectively.

Fig. 10 compares the observed and computed soil deformations near the eastern shoreline in the west-east section after the earthquake. The computed result indicates that the reclaimed fill near the shoreline deformed seawards due to the lateral spreading, accompanied by maximum quay wall displacements of 2.2m and 1.3m in horizontal and vertical direction, which are in good agreement with those observed in the field. The computed deformation mode including the seaward inclination of the quay wall also shows good agreement with the field observation.

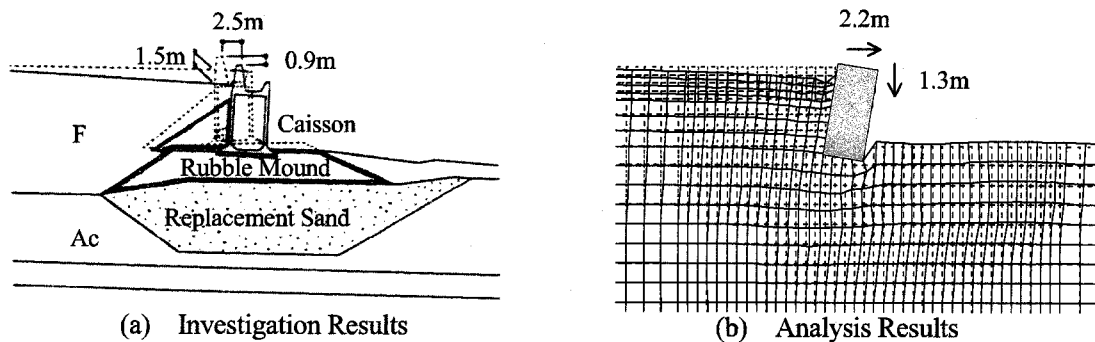


Figure 10 Soil Deformation near the Eastern Shoreline after the Earthquake

5. PILE DAMAGE DUE TO LATERAL SPREADING

5.1 Damage Mechanism of Pile Foundation

Fig. 11 shows the distributions of pile bending moments for Pile-1, 2, 4, 6 and 8 at two different times, 10s and 30s after the start of shaking. At 10s when the ground surface displacement became large before the lateral spreading occurred as shown Fig. 8, the bending moments of all piles became large and reach the ultimate strength (M_u) of the cast-in-place concrete pile not only at the pile head but also at a depth of 16m, the lower boundary of the reclaimed layer. At 30s when the soil deformations vary with the distance from the shoreline due to the lateral spreading as shown in Fig. 9, in contrast, the bending moments near the pile head of Pile-1, 2 and 4 (i.e. landside) are reverse to those of Pile-6 and 8 (i.e. seaside) and those at 8m in depth exceed the yield strength (M_y). Thus, the damage mechanism considerably varies with time and distance from the shoreline in the laterally spreading ground.

5.2 Failure Process of Pile Foundation

In order to verify the difference in damage mechanism between the landside and seaside piles, analyses are conducted using the two models (Cases N and C) as shown in Fig. 12. In Case-N, the pile heads of the eight piles are not connected with a foundation beam, but only the rotational deformations of the pile heads are fixed. In Case-C, the pile heads of the eight piles are connected with a foundation beam.

Fig. 13 shows the maximum displacements, slope angles and ductility ratios of Pile-1 (landside)

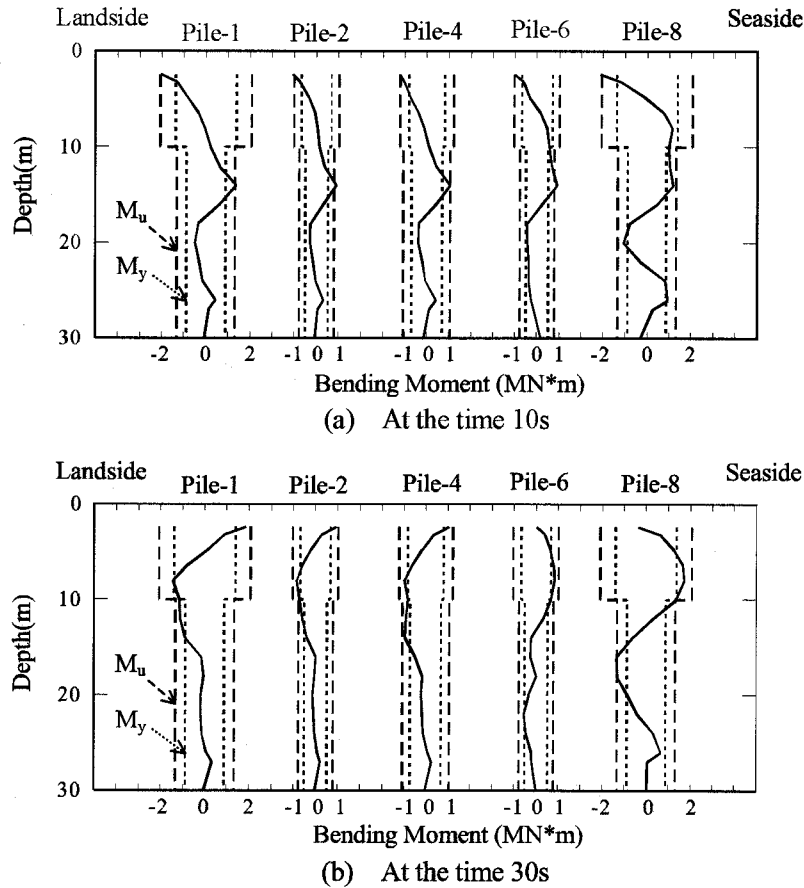


Figure 11 Distributions of Pile Bending Moments for Pile-1, 2, 4, 6 and 8 at 10s and 30s

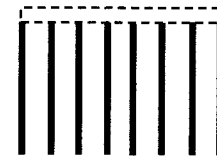
and Pile-8 (seaside) in Case-N. The ductility ratio is defined as the ratio of the maximum curvature to the ultimate point of the tri-linear type hysteresis loop. The pile displacements are amplified corresponding to the soil displacements in the reclaimed layer, being equal to 34 cm and 74 cm at the pile head of Pile-1 and Pile-8, respectively. The pile head of both the Pile-1 and Pile-8 inclined seawards and this tendency doesn't coincide with the field observation. The slope angles of Pile-8 (0.07rad) are much larger than those of Pile-1 (0.03rad). The ductility ratios take maxima at the pile head and at a depth of 16m, the lower boundary of the reclaimed layer. The maximum ductility ratios of Pile-8 are much larger than those of Pile-1.

Fig. 14 shows the maximum pile displacements, pile slope angles and pile ductility ratios of Pile-1 and Pile-8 in Case-C. The maximum pile displacement at pile head is 42cm. The pile displacement distributions of Pile-1 change almost linearly in the reclaimed layer, while those of Pile-8 swell at a depth of 8m, the bottom of the quay wall. The inclination near the pile head of the Pile-1 is reverse to that of Pile-8, and both of the maximum slope angles of Pile-1 and 8 are about 0.04rad. These results are almost the same as the field observation (0.05rad). The ductility ratio of Pile-8 at the depth of 16m in Case-C gets smaller than that in Case-N; however, it will still be much larger than that of Pile-1 in Cases-C and -N.

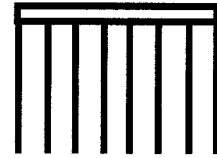
Fig. 15 shows time histories of pile curvatures at the pile head and at a depth of 16m for Pile-1 and Pile-8. The curvatures at the pile head and the depth of 16m for both Pile-1 and Pile-8 become large at 10s and all the ductility ratios exceed 1.0 in both Case-C and Case-N. This indicates that the damage to pile foundations was initiated before the lateral spreading occurred. After 10s, the curvatures at pile head of Pile-1 in Case-C increase and get larger than those in Case-N. Those of Pile-8 in Case-C,

on the contrary, inversely decrease and finally get smaller than those in Case-N. In the meanwhile, the curvatures at the depth of 16m of both Pile-1 and Pile-8 increase and those of Pile-1 in Case-C are almost the same as those in Case-N; however, those of Pile-8 in Case-C get smaller than those in Case-N.

The above computed results indicate that the failure process of the pile foundation varies greatly with distance from the shoreline. The seaside piles are pushed out seawards due to the large soil displacement induced by the lateral spreading; however, they are pulled back landwards by the landside piles. The landside piles are pulled seawards more by the foundation beam that is connected to the seaside piles subjected to much larger ground displacement.



(a) Case-N



(b) Case-C

Figure 12 Schema of Analyses Model

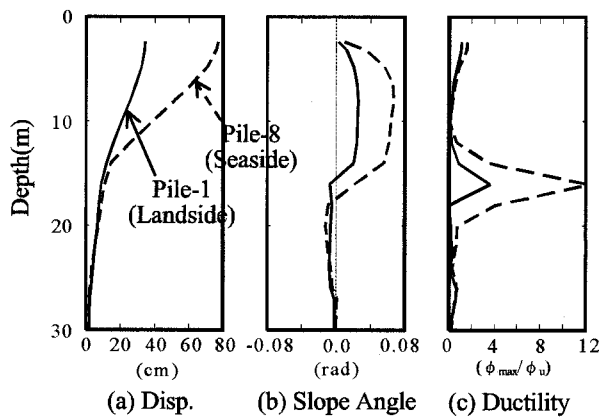


Figure 13 Maximum Pile Response for Pile-1 (Landside) and Pile-8 (Seaside) in Case-N

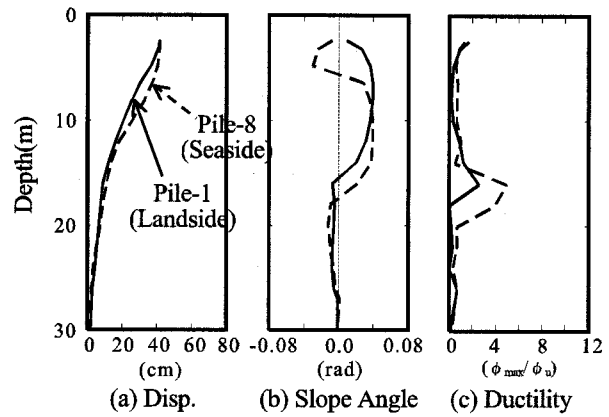
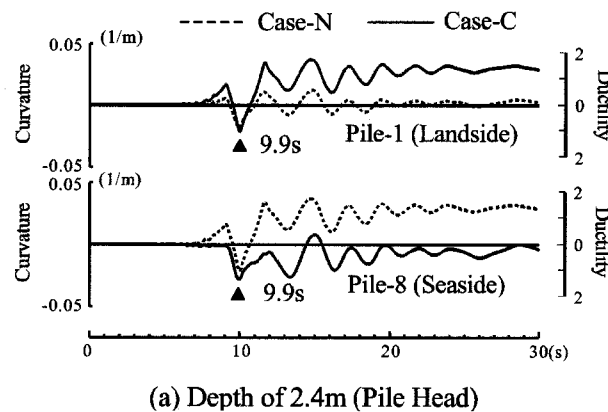
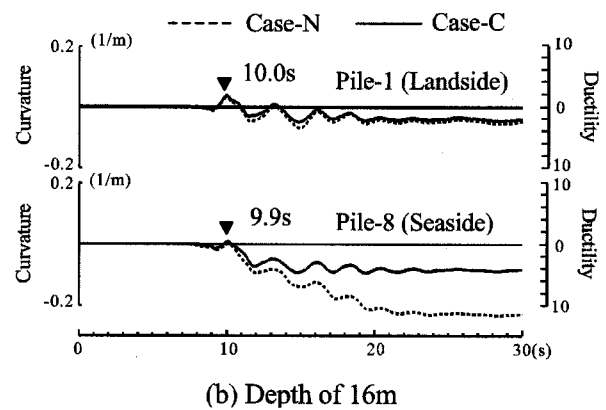


Figure 14 Maximum Pile Response for Pile-1 (Landside) and Pile-8 (Seaside) in Case-C



(a) Depth of 2.4m (Pile Head)



(b) Depth of 16m

Figure 15 Time Histories of Pile Curvatures at the Pile Head and at depth of 16m for Pile-1 and Pile-8 in Case-C and Case-N

6. CONCLUSIONS

In order to verify the failure process of the pile foundation due to the lateral spreading, simulation analyses were conducted for the case history of the cast-in-place concrete pile damaged using the observed ground motion during the 1995 Hyogo-ken Nambu earthquake. Concluding remarks are as follows.

1. The distributions of pile bending moments considerably varied with time and distance from the shoreline in the laterally spreading ground. After 10s of shaking when the ground surface displacement became large, the bending moments of all piles reached to the ultimate strength of the cast-in-place concrete pile at the pile head and at the lower boundary of the reclaimed layer. At 30s when the soil deformations vary with the distance from the shoreline due to lateral ground spreading, the bending moments near the pile head of the landside pile are reverse to those of the seaside pile.
2. The damage to the pile foundations was initiated before the lateral spreading occurred. The curvatures at the pile head and at the depth of 16m for both the landside pile and the seaside pile increased before the lateral spreading occurred, with all the ductility ratios exceeding 1.0.
3. The failure process of the pile foundation greatly varied due to lateral spreading. The seaside piles are pushed out seawards by large residual soil deformation near the shoreline. They are pulled back landwards when they are firmly connected with foundation beam. On the contrary, landside piles are pulled seawards by the seaside piles.
4. There were good agreements between simulation analyses results and field investigation data for the residual displacements of the quay wall, the pile slope angles and the pile head inclinations due to the lateral spreading. It indicates that the analysis model is very effective for evaluating a seismic performance of pile foundations during strong earthquakes.

Acknowledgements:

The authors would like to express their deep appreciation to Dr. Kuwabara, Professor of Nippon Institute of Technology, for providing information of the well-documented field investigation.

References:

- Iai, S., Matsunaga, Y. and Kameoka, T. (1992) : Strain Space Plasticity Model for Cyclic Mobility, Soils and Foundation, Vol.32, No.2, pp.1-15
- Kansai Branch of Architectural Institute of Japan (1996) : Report on Case Histories of Damage to Building Foundations in Hyogoken-Nambu Earthquake", Report presented by Committee on Damage to Building Foundations, (in Japanese)
- Kausel E. and Peek R. (1982) : Dynamic Loads in the Interior of a Layered Stratum- An Explicit Solution", Bulletin of the Seismological Society of America, Vol. 72, pp. 1459-1481
- Kobe City Development Bureau (1995). Report of Investigation for Liquefaction-induced Large Ground Displacement at Reclaimed Land (Port Island and Rokko Island) (in Japanese).
- Koyamada, K., Miyamoto, Y., Sako, Y. and Furue, M. (1999) : Pile Foundation Response due to Soil Liquefaction-Induced Lateral Spreading during the Hyogo-ken Nambu Earthquake of 1995, Journal of Structural and Construction. Engineering, Architectural Institute of Japan, No. 521, pp.49-56 (in Japanese)
- Miyamoto, Y., Sako, Y., Kitamura, E. and Miura, K. (1995) : Earthquake Response of Pile Foundation in Nonlinear Liquefiable Sand Deposit, Journal of Structural and Construction. Engineering, Architectural Institute of Japan, No. 471, pp.41-50 (in Japanese)
- Sako, Y. and Miyamoto, Y. (1999) : Earthquake Response of Pile Foundation Considering Contribution of Axial-force Fluctuation in Piles, Journal of Structural and Construction. Engineering, Architectural Institute of Japan, No. 523, pp.79-86 (in Japanese)
- Suzuki, Y., Hatanaka, M. and Uchida, A. : Drained and Undrained Shear Strengths of a Gravelly Fill of Weathered Granite from Kobe Port Island, Journal of Struct. Constr. Eng., AIJ, No.498, pp. 67-73, (in Japanese)
- The Japanese Geotechnical Society (1998) : Proceeding of the Symposium on Lateral Flow and Permanent Deformation of Soil during Earthquake, p.444, (in Japanese)
- Tokimatsu, K., Niwano, A. and Kuwabara, F. (1998) : Analysis of Deformation Modes of Cast-in-Place Concrete Piles Subjected to Lateral Spreading in the 1995 Hyogoken-Nambu Earthquake, Summaries of Technical Papers of Annual Meeting, AIJ, Vol.B-1, 569-570, (in Japanese)

THE CONSTRUCTION OF BEAM-ON-SPRING MODEL CONSIDERED LIQUEFACTION BETWEEN THE PILES

H. Yoshida¹⁾, A. Imamura²⁾, and F. Yagishita³⁾

1) Research Engineer, Arch. & Struc. Engineering Operation Center, Tokyo Electric Power Services Co., Ltd, Japan

2) Building Researcher, Seismic Design Group R&D Center, Tokyo Electric Power Company, Japan

*3) Seismic Group Manager, Arch. & Struct. Engineering Operation Center, Tokyo Electric Power Services Co., Ltd, Japan
yoshida@tepsc.co.jp, imamura.akira@tepsc.co.jp, yagishita@tepsc.co.jp*

Abstract: The method of calculating the state of liquefaction of the ground between piles was designed by requesting accumulated damage parameter by using the simple liquefaction evaluation technique from the stress caused in the shearing ground spring of the beam on spring model. In addition, the simulation analysis of the Centrifuge experiment of 25 group piles was done, and it was confirmed that the excess pore water pressure ratio of the ground between piles was able to be calculated by the proposed method.

1. INTRODUCTION

When we understand seismic behavior of the pile foundation, we often use the Penzien Model because appreciable immediately of the stress of the piling, and analysis are comparatively easy. On the other hand, it is thought that the influence of liquefaction is also large in the soft ground for which the pile foundation is used. Therefore, Miyamoto et al. (1995) proposed the beam on spring model that considers the liquefaction of the ground. However, it is not necessarily easy to deem that the state of liquefaction in free ground is equal to the state of liquefaction in the ground between piles, because the effect of the restraint of the pile is large in the ground between piles. Then, we propose the beam on spring model that considers the liquefaction of the ground between piles in this report, and report on the result of examining the influence.

2. NUMERICAL METHOD

2.1 Method of considering liquefaction of the ground between piles

According to Nukui et al. (2003), it is possible to calculate the excess pore water pressure p of the ground by the accumulated damage parameter D derived from the shearing stress τ and the liquefaction strength curve $r_u - N$ of the ground. Because the accumulated damage parameter is evaluated constantly in a half wave in the law so far, the decrease in the ground stiffness by liquefaction is discontinuous. However, continuously evaluating it of accumulated damage parameter became possible in the method in consideration of the shearing stress at each time. Applying the simple liquefaction technique became the seismic response analysis on structure-pile-ground system that one by one analyzed it nonlinearly with possible by using this method.

Then, to think that the shear spring of free ground is the one that free ground was modeled as a shearing soil column, it is thought that the shear spring of the beam on spring model is the one that the ground between piles was modeled as a shearing soil column. We can handily calculate the excess pore water pressure ratio of the ground between piles by using the idea similar to free ground as shown in Figure 1 even when the beam on

spring model is used.

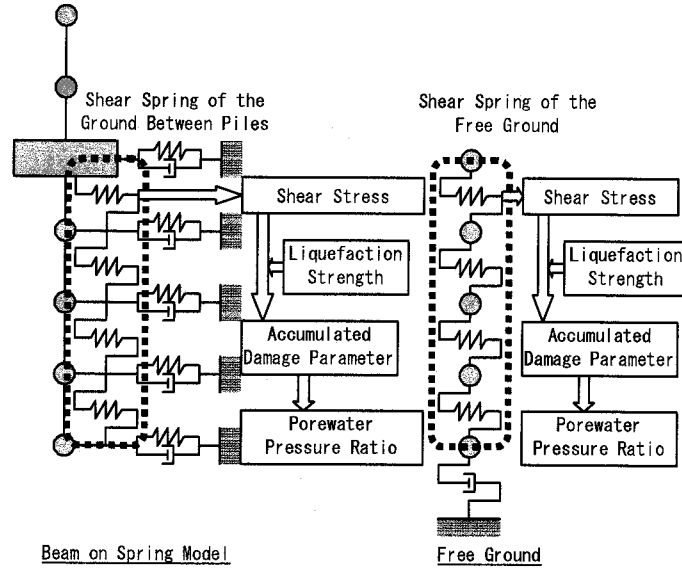


Figure 1 Method of Considering Liquefaction of the Ground between Piles

2.2 Stress that acts on pile

In the method so far at the time of assumed that the state of liquefaction of free ground and the state of liquefaction of the ground between piles are the same, that is, $G_p \approx G_f$. Then the shearing stress τ that acted on the pile is expressed as follows:

$$\tau = G_p \cdot \gamma_p - G_f \cdot \gamma_f \approx G_f(\gamma_p - \gamma_f) \quad (1)$$

by using difference between shear strain γ_f in free ground and shear strain γ_p in the ground between piles, that is, relative shear strain $\gamma_p - \gamma_f$, in which G_p = shearing modulus of the ground between the piles; G_f = shearing modulus of free ground.

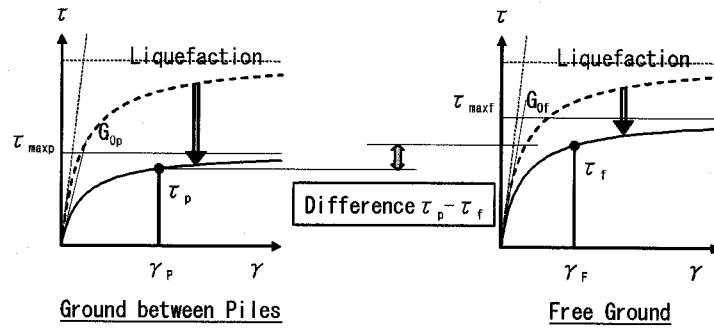


Figure 2 Stress That Acts on Pile

However, as shown in Figure 2, each stress strain relationship is expressed as follows:

$$G_{0f} = G_0 \cdot (\sigma'_{mf} / \sigma'_{m0})^{0.5} \quad (2)$$

$$\tau_{\max f} = \tau_{\max} \cdot (\sigma'_{mf} / \sigma'_{m0}) \quad (3)$$

$$G_{0p} = G_0 \cdot (\sigma'_{mp} / \sigma'_{m0})^{0.5} \quad (4)$$

$$\tau_{\max p} = \tau_{\max} \cdot (\sigma'_{mp} / \sigma'_{m0}) \quad (5)$$

in the method of considering the difference between the state of liquefaction of free ground and the state of

liquefaction of the ground between piles by the use of the hyperbolic model, in which G_{0f} = initial shearing modulus of free ground; G_{0p} = initial shearing modulus of the ground between the piles; τ_{maxf} = Shear strength of free ground; τ_{maxp} = Shear strength of the ground between the piles; σ'_{m0} = initial effective stress; σ'_{mf} = initial effective stress of free ground; σ'_{mp} = initial effective stress of the ground between the piles.

3. SIMULATION

3.1 Centrifuge Test

To verify the beam on spring model that considered liquefaction, the Centrifuge test of the multi number pile model was executed. The model made to 1/50 of the prototypes, and executed the experiment in a centrifugal place of 50G. As for the numerical value, the value of the prototype conversion is used for the following descriptions. The outline of the model used for the actual experiment is shown in Figure 3 and experimental conditions are shown in Table 1 respectively. To examine the influence that the liquefaction of the ground gives to the behavior of structure-pile-ground system, two cases (the case to assume relative density D_r of the ground to be 50% and the case assumed to be 90%) were executed for the Toyoura sand in the upper layer. The silicon oil of 50cs is used for the fluid.

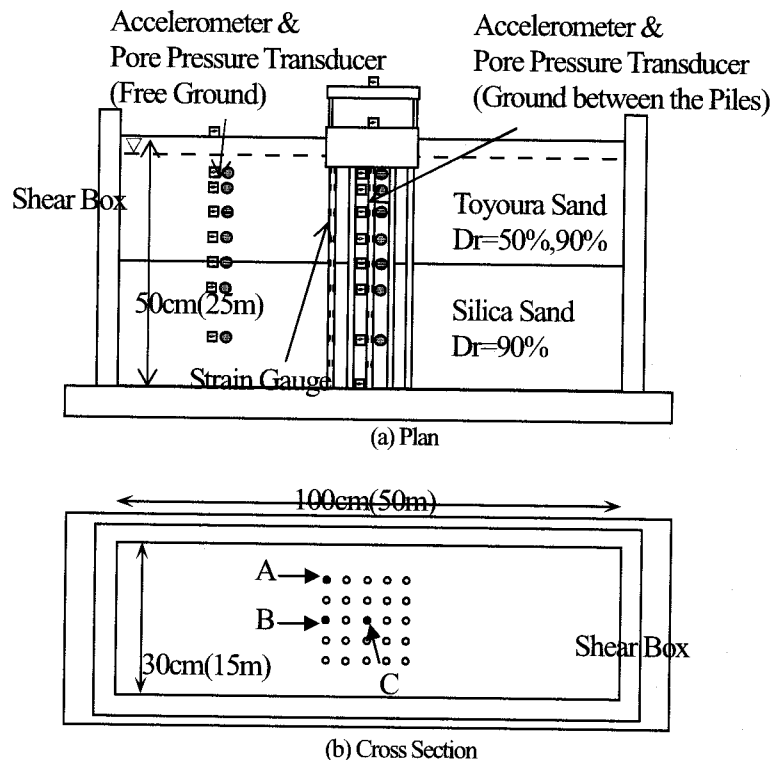


Figure 3 Outline of the Model Used for Centrifuge Test

Table 1 Experimental Conditions

		Model Specification	Prototype
Pile	Diameter	1.2cm	60cm
	Thickness	0.02cm	1.0cm
Base	Weight	9.4kg	1260ton
Structure	Weight	1.6kg	213ton
	Natural Period	39Hz	0.78Hz

The maximum value distribution of excess pore water pressure ratio in the ground of the model of

$D_r=50\%$ and $D_r=90\%$ is shown in Figure 4 . The excess pore water pressure ratio of the ground between piles is larger than that of both cases and the free ground. Thus, it is understood that the pile behavior influences the excess pore water pressure of the ground between piles. In this report, the excess pore water pressure ratio of the ground between piles is expressible by the beam on spring model is examined for the example of Toyoura sand $D_r=50\%$.

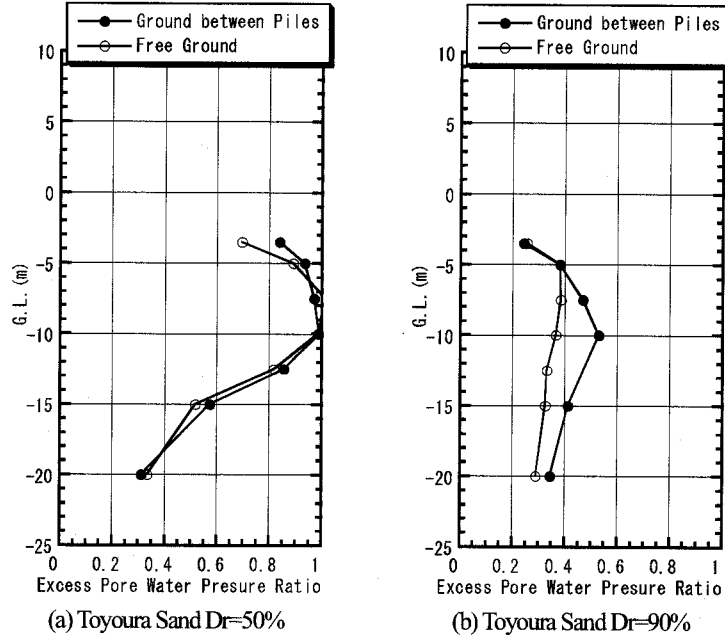


Figure 4 Maximum Value Distribution of Excess Pore Water Pressure Ratio in the Ground

3.2 Computational Model

The beam on spring model is set as follows. The interaction ground spring added to the pile is calculated by the methods of Hijikata (1997). That is, horizontal ground spring K_a and the limit ground reaction force P_{\max} are calculated to the spring of Francis (1964) and the limit ground reaction force of Broms (1965) in consideration of effect $\alpha^{4/3}$ of group piles. Here α is a coefficient stands for the effect of group piles in the pile head impedance, is expressed as follows:

$$\alpha = N^{-a} \quad (6)$$

$$a = 0.9f_x + \frac{1}{5 + \left(\frac{65B}{H}\right)^{1.5}} \quad (7)$$

$$f_x = \left[0.3 + \left\{ 0.16 - 4\left(\frac{B}{H}\right)^2 \right\} \text{Log}\left(\frac{E_p}{E_s}\right) \right] \cdot \left(\frac{B}{S}\right)^{0.75} \quad (8)$$

in which N = number of piles; B = diameter of pile; H = Thickness of layer from support layer + B ; E_p = Young's modulus of pile; E_s = Young's modulus of soil. And dashpot C_a is calculated by the method of Gazetas (1984). In addition, shearing ground spring K_b is calculated as stiffness of the shearing soil column. Lateral spring K_H added to the embedded base and the limit ground reaction force are calculated with the spring of Novak and passive earth pressure. The rotational spring K_R is added to a basic bottom.

Here, it is difficult to say for the model of the structure to have the ground of an enough size by can consider the examination object to be the free ground. Then, it was assumed that the free ground was connected with the shear box as shown in Figure 5, and it moved on earth. In this case, the weight of the shear box was consolidated in the weight of the free ground. Moreover, a structure and the free ground were connected through the

horizontal ground spring, and the interaction was considered.

The nonlinearity of the free ground is calculated by the simple liquefaction analysis technique for considering the accumulated damage parameter of Nukui (2001) et al. Moreover, the shearing ground spring decreases the spring value in consideration of the state of liquefaction of the ground between piles. In addition, the stress that acted on the pile was calculated from the difference between the shearing stress of the ground between piles and the shearing stress in the free ground.

The liquefaction strength curve is shown in Figure 6 and the parameter of the structure and the ground is shown in Table 2 and Table 3.

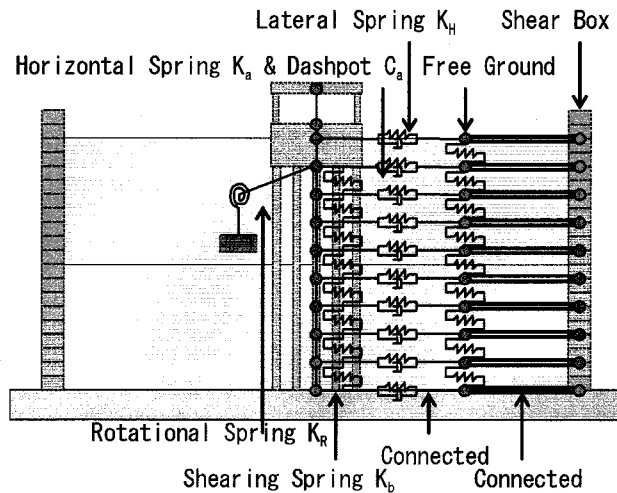


Figure 5 Computed Model

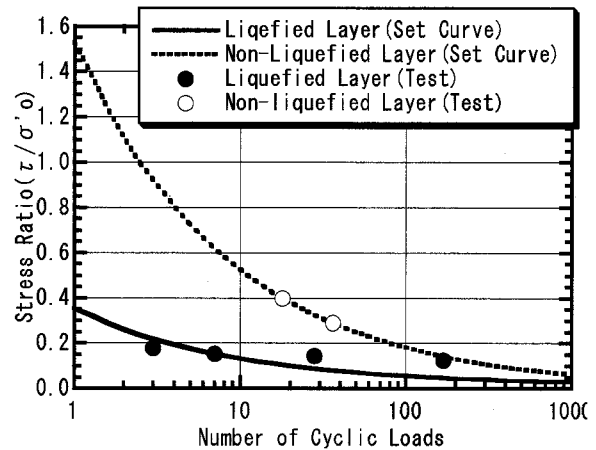


Figure 6 Liquefaction Strength Curve

Table 2 The Model of Structure

Node	Wright (kN)	Member	Spring (kN/m)
1	2130	2-1	5.22E+03
2	12600		

Table 3 The Model of Soil

	Material	Thickness H(m)	Density γ (t/m ³)	Shear Velocity V_s (m/s)	内部摩擦角 Φ (°)
Upper Layer Liquefaction	Toyoura Sand (Dr=50%)	12.5	1.888	170.7	27.3
Lower Layer Non-Liquefaction	Silica Soil (Dr=90%)	12.5	2.031	199.7	21.0

3.3 Computational Result

Figure 7 shows the simulation analysis result by the beam on spring model. In the excess pore water pressure ratio distribution of Toyoura sand Dr=50% shown in Figure 3, especially, the excess pore water pressure ratio of the ground between piles is larger than that of the free ground in vicinity (GL.-3.0m) of the pile head. Excess pore water pressure ratio of both and the differences can be simulated well in analytical results by the beam on spring model.

Moreover, the experiment result can be simulated well for the maximum response acceleration distribution. Therefore, it can be confirmed that the method of evaluating the excess pore water pressure ratio of the ground between piles proposed by this report is appropriate. However, it is undervaluation in the lower layer (non-liquefaction layer). It is confirmed that the reason for this phenomenon is that the influence of water permeability is not considered in another report.

Moreover, for the time history of the acceleration, the amplitude and the phase can be simulated well by both tops of the base and the layer boundaries. In addition, it is possible to simulate well including remaining moment for the time history of pile moment. Therefore, it was able to be confirmed that it was appropriate for the beam on spring model.

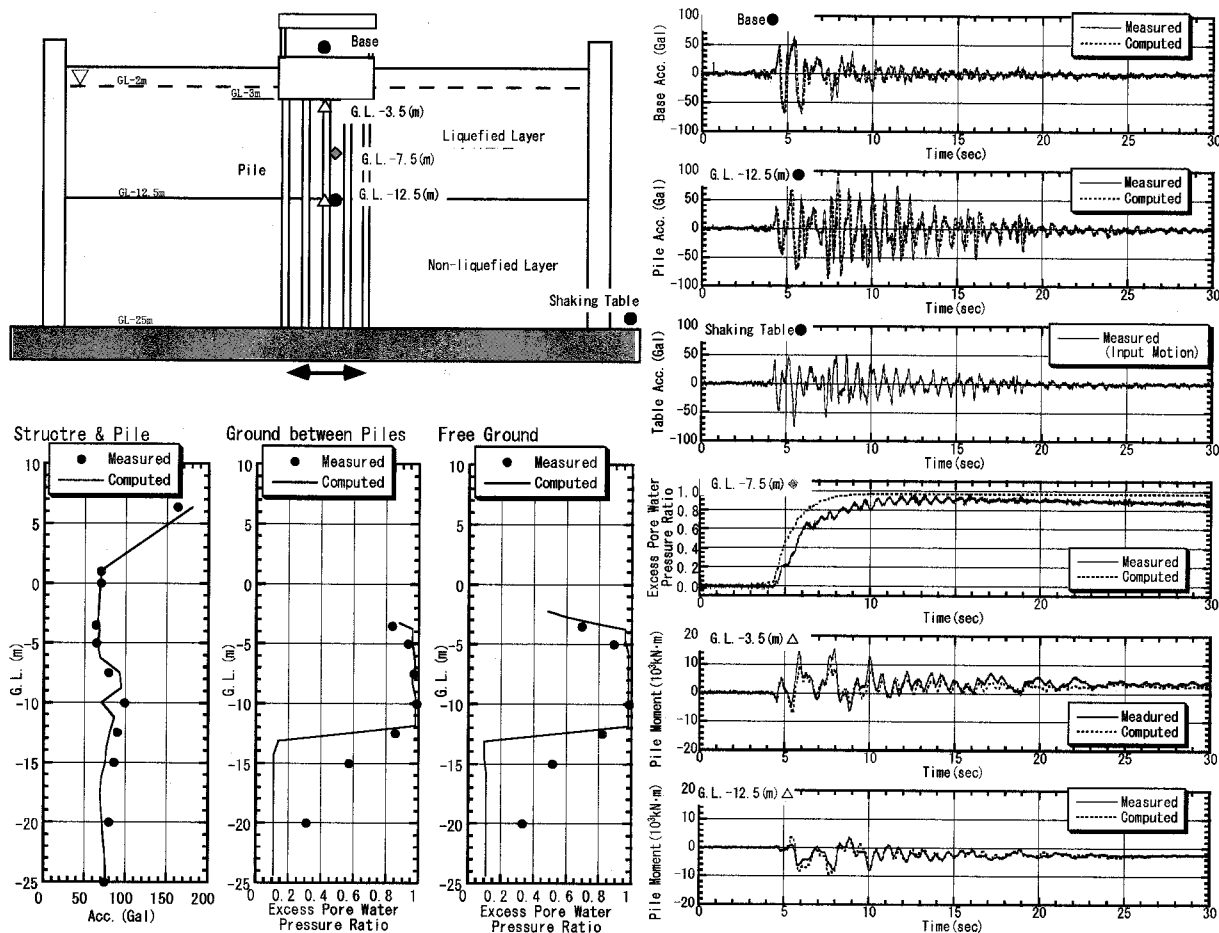


Figure 7 Computed Results

4. CONCLUSIONS

The method of calculating the state of liquefaction of the ground between piles was designed by requesting accumulated damage parameter by using the simple liquefaction evaluation technique from the stress caused in the shearing ground spring of the beam on spring model. In addition, the simulation analysis of the Centrifuge experiment of 25 group piles was done, and it was confirmed that the excess pore water pressure ratio of the ground between piles was able to be calculated by the proposed method. Moreover, it was able to be confirmed seismic behavior was expressible of structure-pile-ground system in consideration of the state of liquefaction of the ground between piles. It is hoped to use and to examine this proposed method because it is expected that the responses in the free ground and the ground between the pile is greatly different when there are a lot of numbers of the pile and the pile stiffness are high.

References:

- Miyamoto, Y. Sako, Y., Kitamura, E. and Miura, K. (1995), "Earthquake Response of Pile Foundation in Nonlinear Liquefiable Soil Deposit," *J. Struct. Constr. Eng., AIJ*, No439, 41-50.
- Nukui, Y. Yoshida, H. and Shiomi, T., et al (2003), "An Easy Effective Stress Analytical Method Using Accumulated Damage Parameter," *Proc. 38th National Conf. JGS*, 1869-1870.
- Hijikata, K. Narikawa, M. Imamura A. and Yagishita, F., et al. (1997), "Methods to Estimated Dynamic Interaction System for a Building of Thermal Power Plant Supported on Piles," *J. Struct. Constr. Eng., AIJ*, No502, 39-46.
- Francis A.J. (1964), "Analysis of Pile Groups with Flexural Resistance, Journal of the Soil Mechanics and Foundations Division", *ASCE*, Vol.90, pp.1-32
- Gazetas G, Dobry R. (1984), "Horizontal Response of Piles in Layered Soils, Journal of Geotechnical Engineering Division", *ASCE*, Vol.110, pp.20-40
- Broms B.B. (1965), "Design of Laterally Loaded Piles, Journal of the Soil Mechanics and Foundations Division", *ASCE*, Vol.91, pp.79-99

1-G SHAKING TABLE TESTS ON THE LATERAL RESISTANCE OF IN-LINE DOUBLE PILES SUBJECTED TO LATERAL SPREADING

J.R. Dungca¹⁾, J. Kuwano²⁾ and S. Nishio³⁾

1) Professor, Geosphere Research Institute, Saitama University, Japan

2) Graduate Student, Dept. of Civil Engineering, Tokyo Institute of Technology, Japan

3) Graduate Student, Department of Civil Engineering, Tokyo Institute of Technology, Japan
jrdungca@cv.titech.ac.jp, jkuwano@post.saitama-u.ac.jp, nishio@cv.titech.ac.jp

Abstract: This paper presents the results of 1G shaking table test series conducted on the lateral resistance of in-line double piles subjected to liquefaction-induced lateral flow. The main objective of this analysis is to check the behavior of the trailing and leading pile subjected to lateral spreading, to determine the maximum spacing of double piles where each individual pile can be treated as a single pile and to check the effects of loading rate and pile displacement on the lateral resistance of double piles. Results show that the lateral resistance of the leading pile has a lesser spacing dependency than the trailing pile. It is presumed that for the double piles with smaller spacing, the force on the compression side of the trailing pile can not be mobilized effectively due to the presence of the leading pile as the deformation of the soil in between them is limited. An efficiency factor for computing the lateral resistance of trailing pile as a function of the lateral resistance of the single pile is introduced.

1. INTRODUCTION

When a sloping ground liquefies, it behaves like fluid and moves downward like flowing water. Lateral flow sometimes causes serious damage to underground structures such as piles, waterworks, and so on. Many experiments have been conducted to estimate the lateral resistance of piles in liquefied ground using geotechnical centrifuges by many researchers (Abdoun & Dobry, 1998; Horikoshi et al., 1998, Takahashi et al. 1998). However, the mechanism of pile resistance against lateral flow of liquefied ground is not yet fully understood. Lateral resistance induced by the flow is governed by many factors such as seismic motions of the ground, excess pore pressure around the pile, velocity of ground flow, relative density of the ground and so on.

In this study, to measure the lateral resistance, the pile was modeled as a buried cylinder that correspond to a sectional model of the pile at a certain depth in the subsoil by applying vertical pressure on the model ground, as schematically illustrated in Figure1. The measurement of the drag force on the buried cylinder embedded in sand was based on almost the same concept as the one carried out by Towhata et al. (1999) but with a surcharge on the model ground. In this study, the pile was actuated in immovable ground, which is the opposite frame of reference on the real ground condition wherein the pile almost stands still in the flowing soil. Lateral loading tests on model piles in 1G field were conducted to evaluate the effects of pile spacing, ground vibration, excess pore pressure ratio, and loading rate of the pile on lateral resistance acting on pile.

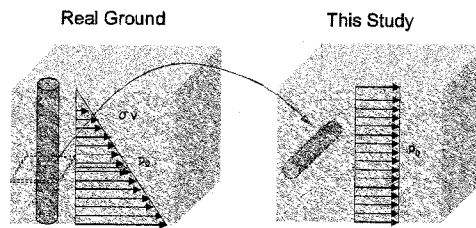


Figure 1. Modeling of pile in this study

If the piles are spaced widely apart, the lateral resistance for single piles may be used without any modification. As the piles are installed close to each other, their efficiency will decrease and the lateral resistance from the soil will decrease. The most effective way to reflect the loss of efficiency for such piles is to develop procedures for reducing the value of lateral resistance to reflect the close spacing.

The piles considered in this study are in line with each other. The center to center distances between the piles were varied. The different spacing of piles considered will be discussed in the succeeding section. If a pair of piles is moving in the rightward direction, as shown in Figure 2, the pile in the front will be referred in this study as the “leading pile”, while the pile at the back side will be referred as the “trailing pile”. The spacing of the piles will be referred as “ s ” throughout the course of this study.

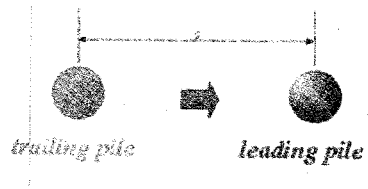


Figure 2. Leading and trailing piles

2. TEST PROCEDURE

2.1 Test Setup

Lateral loading tests were conducted in 1G field. The model container used in this study is shown in Figure 3. The front face of the container was made transparent to observe the deformation of the model ground. Schematic drawing of the experimental apparatus and the positions of sensors are shown in Figure 4. A pressure bag made of rubber was attached underneath the top lid of the container to apply overburden pressure by compressed air on the surface of the soil. Aluminum-made model piles equipped with pore pressure and earth pressure transducers, (schematic diagram is shown in Figure 5) were installed parallel to the bottom of the container through the rods which are connected to the actuator. Piles were actuated back and forth through the rods by an electro-hydraulic actuator. Ground was prepared by the air pluviation method using Toyoura sand ($D_{50}=0.19\text{mm}$) and saturated using methylcellulose solution. The viscosity of this fluid is 50 times higher than that of de-aired water. After the preparation of the model, the container was set on the mechanical shaker (Takemura et al., 1989). In almost all cases, the horizontal shaking of the container started one second prior to the pile loading. This duration was enough to liquefy the model ground.

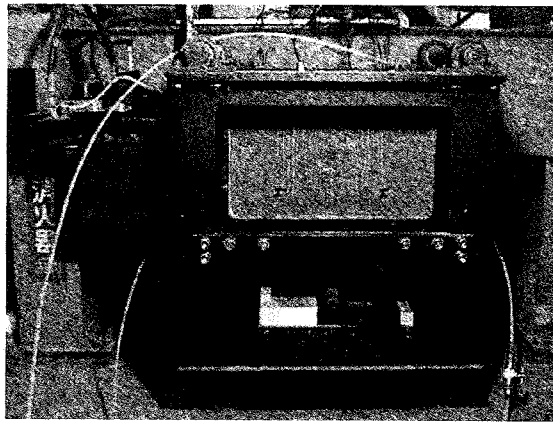


Figure 3. Photo of the container and the shaker

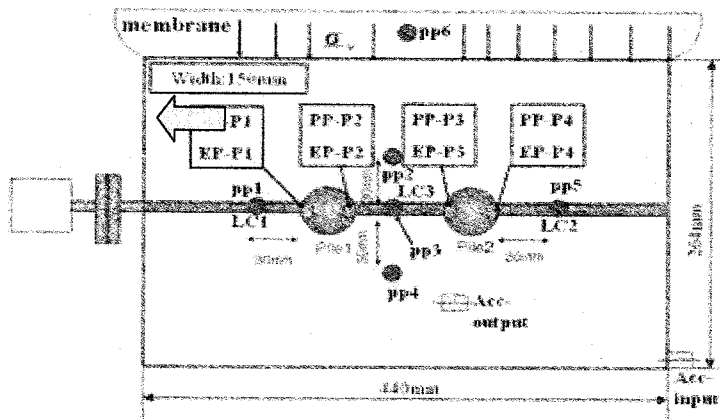


Figure 4. Position of sensors

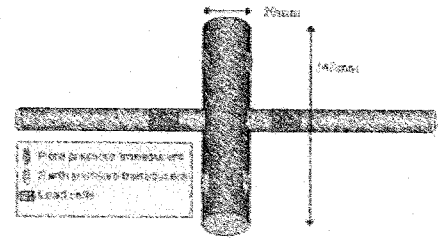


Figure 5. Model pile

2.2 Test Conditions

There were 24 test cases carried out in this study, as shown in Table 1. The first 21 cases are for double piles and the last 3 test cases are for single piles. There were five center to center distances of the piles considered; 55mm, 60mm, 65mm, 70mm and 75mm. The center to center distance of the piles of 55mm correspond to 2.75D which means that the distance between the two piles is 2.75 times the pile diameter (pile diameter used in this study was 20 millimeters). Thus, 3D, 3.25D, 3.5D and 3.75D for 60mm, 65mm, 70mm, 75mm center to center distances, respectively. A maximum spacing of 3.75D was used due to some limitations with the size of the model box used. The relative densities were in the range of 60% to 85%. The loading rates of the pile used were 10mm/s, 20mm/s and 200mm/s. Cyclic loading tests with symmetrical triangular waves were applied in order to achieve a constant loading rate. In all the cases, the applied effective overburden pressure, σ'_{vo} , used was also 49kPa.

3. TEST RESULTS

3.1 Change in the pore water pressure around the pile

The time histories of the pore water pressure, lateral resistance of the pile, pile displacements and input and output accelerations for Case D65-20 are presented in Figure 6. The pore water pressures for pp-p1, pp-p2, pp-p3, and pp-p4 were normalized by the effective overburden pressure of 49 kPa. The lateral resistance at Pile1 was computed as the difference between LC3 and LC1 while the difference

Table 1. Test conditions for double piles

Case	Dr	C to C Distance of piles		Pile Loading Rate	Overburden Pressure (kPa)	Frequency of Vibration (Hz)
	(%)	(mm)	(s/D)	(mm/s)	49	50
D55-10	66.9	55	2.75D	10		
D60-10	68.0	60	3D			
D65-10	64.1	65	3.25D			
D70-10	72.1	70	3.5D			
D75-10	67.1	75	3.75D			
D55-20	74.3	55	2.75D	20		
D60-20	74.6	60	3D			
D65-20	72.8	65	3.25D			
D70-20	79.2	70	3.5D			
D75-20	75.2	75	3.75D			
D55-200	81.5	55	2.75D	200		
D60-200	79.9	60	3D			
D65-200	79.7	65	3.25D			
D70-200	85.5	70	3.5D			
D75-200	81.9	75	3.75D			
D70-200 <i>l</i>	65.0	70	3.5D	200		
D70-200 <i>m</i>	75.2	70	3.5D	200		
D70-10 <i>d</i>	83.0	70	3.5D	10		
D65-200 <i>l</i>	67.7	65	3.25D	200		
D65-200 <i>m</i>	76.6	65	3.25D	200		
D65-10 <i>d</i>	83.9	65	3.25D	10		
S-10	71.1	-	-	10		
S-20	74.3	-	-	20		
S-200	83.2	-	-	100		

between LC2 and LC3 is the lateral resistance for pile 2.

The change in pore water pressure of pp-p1~pp-p4 at the peak displacement of 10mm is shown in Figure 7. We could observe in this figure that the reduction in pore water pressure at the back of the piles, both for the trailing and the leading pile, are smaller than that of the front. The smaller decrease in pore water pressure at the back of the leading pile can be attributed to the “shadowing effect” mentioned by Reese and Van Impe, 2001 in the analysis of closely spaced piles under lateral loading. The trailing pile shadows the leading pile, thus, giving smaller decrease in the pore water pressure. We could also observe in the later that this shadowing effect affects the lateral resistance of the leading and trailing piles. However, the smaller decrease of the pore water pressure at the back of the trailing pile was unexpected. It was presumed that there were some effects of boundary condition on the trailing pile since there was a small space between the trailing pile and the side wall of the model container. A further research might be necessary on this matter.

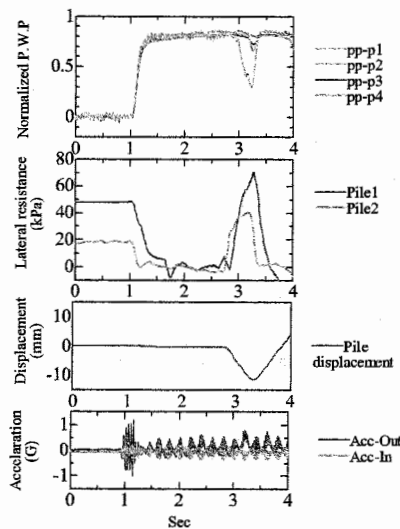


Figure 6. Time histories (Case D65-20)

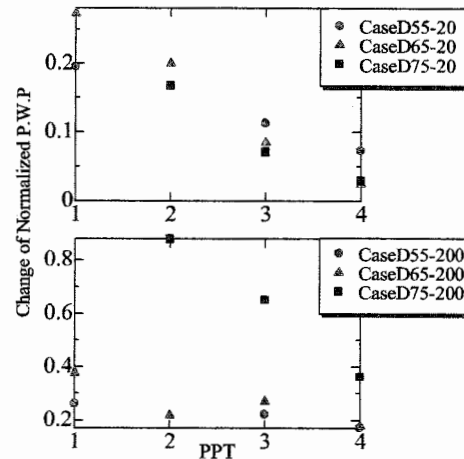


Figure 7. Change of pore water pressure

3.2 Deformation of the ground

Figure 8 shows the piles and the ground before the experiment and the corresponding deformations of the ground after the experiment for 3.5D and 2.75D cases, respectively. Looking closely at the 2.75D case, by observing the deformations of the Japanese noodles placed on the transparent wall of the box, we could observe a noticeable deformation of the ground in between the piles. However, in the 3.5D case, although the ground has also deformed, there were not much deformations that was observed as compared to the 2.75D case. We could say that the deformation of the ground is more pronounced for closely spaced piles than for the widely spaced piles. It is believed that trailing pile and surrounding ground were strongly affected by the presence of the leading pile when the piles are very close with each other, and the effect was small when the piles are spaced far apart.

3.3 Effects of Loading Rate on the Lateral Resistance of the Piles

We could also observe from Figs. 9 and 10 the effect of loading rate on the lateral resistance of the pile for both the leading pile and the trailing pile. The lateral resistances, for both the leading and trailing piles, increase with the increase in the loading rate. The higher strain rate brought by the higher loading rate during shaking makes the soil more rigid, thus, giving higher resistance as the loading rate becomes larger.

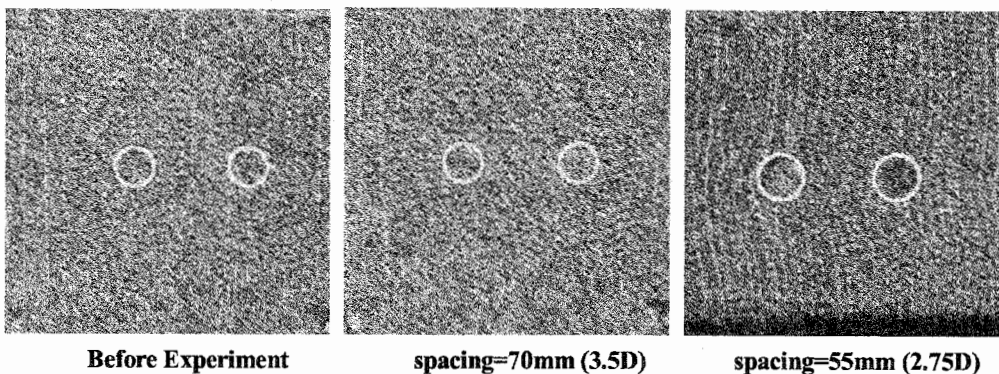
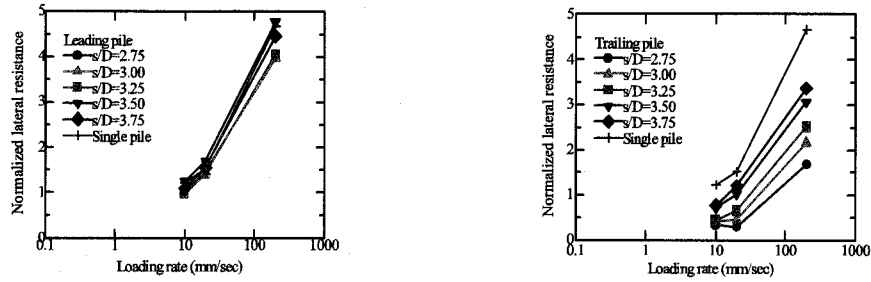


Figure 8. Ground before the experiment and ground deformations after the experiment



Figs. 9 and 10. Effects of loading rate on the lateral resistance of leading

3.4 Lateral resistances of the leading pile and trailing pile

As the piles move, the lateral resistance on each of the pile increases with the increase in pile displacement. The maximum lateral resistances for most of the cases are found to be at the maximum displacement of the pile (maximum displacement of the pile, δ , in this test series is 10 millimeters). In this study, the first cycle of the pile displacement was considered to correspond to the actual lateral flow of the ground.

Figs. 11 and 12 shows the relationship of the lateral resistance of the pile with the pile spacing for the leading pile and trailing pile, respectively. We could observe that the slope of the trend line in the leading pile is much smaller than that of the trailing pile. This means that the trailing pile has a more spacing dependency than the leading pile.

The lateral resistance of a pile subjected to laterally spreading liquefied ground is the sum of the forces at the front (compression) side of the pile and the rear (extension) side of the pile induced by the combined effects of (negative) pore water pressure and the increased stiffness of soil induced by the increase in effective stress (decrease in the pore pressure). The force on the compression side plays a more affecting role in the lateral resistance of a pile. In the case of trailing pile, with smaller spacing, the force on the compression side can not be mobilized effectively due to the presence of the leading pile as the deformation of the soil in between the two piles is limited, as observed in the tests. The deformation of the soil is the source of the decrease in the pore pressure, thereby, an increase in the stiffness of the soil. When the pile spacing is much bigger, the soil between the piles can deform more freely.

4. EMPIRICAL EQUATIONS FOR DOUBLE PILES

The effect of group pile is evident in a very close spacing, say two times the pile diameter, but as the spacing of the pile becomes higher the group effect is diminishing and approaching unity. Unity means that the lateral resistance of the pile is the same as that of a single pile. The spacing that will give a unity was investigated in this study. However, since the lateral resistances of the leading and trailing piles are different, the spacings that will give unity are also different. With this, leading and trailing piles were analyzed separately.

4.1 Efficiency factors for computing the lateral resistance of leading and trailing piles

Reese and Van Impe (2001) defined *efficiency* as the load on individual piles in the group divided by the load on a single pile at the same deflections. Derivations of the lateral resistance in the leading pile as well as the trailing pile will be the product of the lateral resistance of the single pile and this efficiency factor. To compute for the efficiency factors for the leading and trailing piles, an equation in the form shown below was used;

$$e = a \left(\frac{s}{D} \right)^b \quad (1)$$

where;

e – efficiency factor;
 a , and b – coefficients for the efficiency factor;
 s – spacing of piles;
 D – diameter of the pile.

The above equation was found to fit with the measured data for leading and trailing piles, as shown in Figs. 11 and 12, respectively. Applying the computed coefficients of a and b based on equation (1), an equation of efficiency factor for the leading pile, e_l , was derived as shown in equation (2). Similarly, an efficiency factor for trailing pile, e_t , was also derived and shown in equation (3).

Leading Pile:

$$e_l = 0.695 \left(\frac{s}{D} \right)^{0.26}, \text{ for } \frac{s}{D} \leq 4.0, e_l = 1.0 \quad (2)$$

Trailing Pile:

$$e_t = 0.0757 \left(\frac{s}{D} \right)^{1.6}, \text{ for } \frac{s}{D} \leq 5.0, e_t = 1.0 \quad (3)$$

where:

e_l = efficiency factor for leading pile;
 e_t = efficiency factor for trailing pile;
 s = center to center spacing between the piles;
 D = pile diameter.

We could also observe from Figs. 11 and 12 that the efficiency factor for the leading pile, e_l , has an efficiency of unity at a spacing of about four diameters (4D) while for trailing pile, e_t , has an efficiency of unity at a spacing of about five diameters (5D). Therefore, Equation (2) can be used for leading piles to a maximum spacing of 4D, equations for single piles will be used for pile spacing greater than 4D. Similarly, Equation (3) can be used for trailing piles to a maximum spacing of 5D, equations for single piles will be used for pile spacing greater than 5D.

4.2 Lateral resistance of leading and trailing piles

With the efficiency factors derived above, the lateral resistance on the leading pile and the trailing pile of an in-line double pile group subjected to laterally spreading liquefied ground can be computed as a function of single pile as shown in equation (4) and (5), respectively.

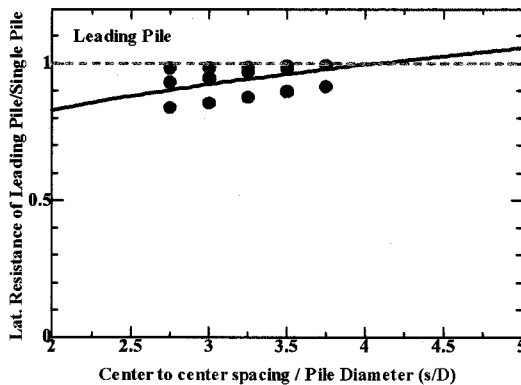


Figure 11. Data fit for leading pile

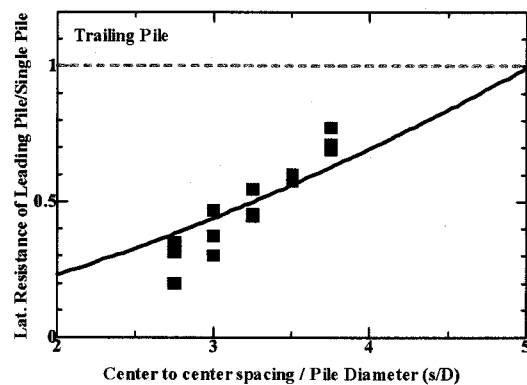


Figure 12. Data fit for trailing pile

$$\left(\frac{\sigma_d}{\sigma'_{vo}} \right)_l = e_l \left(\frac{\sigma_d}{\sigma'_{vo}} \right)_s \quad (4)$$

$$\left(\frac{\sigma_d}{\sigma'_{vo}} \right)_t = e_t \left(\frac{\sigma_d}{\sigma'_{vo}} \right)_s \quad (5)$$

where:

$\left(\frac{\sigma_d}{\sigma'_{vo}} \right)_l$ = lateral resistance of the leading pile in an in-line double pile arrangement;

$\left(\frac{\sigma_d}{\sigma'_{vo}} \right)_t$ = lateral resistance of the trailing pile in an in-line double pile arrangement;

$\left(\frac{\sigma_d}{\sigma'_{vo}} \right)_s$ = lateral resistance of a single pile.

5 CONCLUSIONS

This study discussed the 1-G shaking table test series on the lateral resistance of an in-line double pile group subjected to laterally spreading liquefied ground.

The deformation of the ground in between the piles is found to be more pronounced at close spacing. The trailing pile and the surrounding ground were strongly affected by the presence of the leading pile when the piles are very close with each other, and the effect was small when the piles are spaced far apart.

The lateral resistance of the leading pile was observed to be less dependent on pile spacing than the trailing pile. In the case of the trailing pile, with smaller spacing, the force on the compression side can not be mobilized effectively due to the presence of the leading pile as the deformation of the soil in between the two piles is limited. The deformation of the soil is believed to be the source of the decrease in the pore pressure, thereby, an increase in the stiffness of the soil. When the pile spacing is much bigger, the soil between the piles can deform more freely.

Efficiency factors were derived to compute for the lateral resistance of the leading and trailing piles as a function of the lateral resistance of the single pile. Using the derived equations for the efficiency factors of the leading pile and trailing pile, spacing at unity with the single piles were computed at about 4D and 5D, respectively.

References:

- Abdoun, A. & Dobry, R. (1998), "Seismically Induced Lateral Spreading of Two-Layer Sand Deposit and its Effect on Pile Foundations," *Proc. of the Int'l Conf. Centrifuge 98*, Vol.1, 321-328.
- Horikoshi, K., Tateishi, A. & Fujiwara, T. (1998), "Centrifuge Modeling of a Single Pile Subjected to Liquefaction-Induced Lateral Spreading," *Soils and Foundations, Special Issue on Geotechnical Aspects of the Jan. 17 1995 Hyogoken-Nambu Earthquake*, No.2, 193-208.
- Takahashi, A., Takemura, J., Kawaguchi, Y., Kusakabe, O. & Kawabata, N. (1998), "Stability of Piled Pier Subjected to Lateral Flow of Soils during Earthquake," *Proc. of the Int'l Conf. Centrifuge 98*, Vol.1, 365-370.
- Takemura, J., Kimura, T. & Suemasa, N. (1989), "Development of Earthquake Simulators at Tokyo Institute of Technology," *Technical Report of Dept. of Civil Eng., Tokyo Inst. of Tech.*, No.40, 41-68.
- Towhata, I., Vargas-Monge W., Orense, R.P. & Yao, M. 1999, "Shaking Table Tests on Subgrade Reaction of Pipe Embedded in Sandy Liquefied Subsoil," *Soil Dynamics and Earthquake Engineering*, Vol.18, No.5, 347-361.
- Reese, L.C. and Van Impe, W. (2001), "Single Piles and Pile Groups Under Lateral Loading," A.A.Balkema, Rotterdam, Netherlands..

EVALUATION OF NONLINEAR SOIL AMPLIFICATION AT OJIYA K-NET AND JMA STATIONS DURING THE 2004 MID NIIGATA PREFECTURE EARTHQUAKE

K. Tokimatsu¹⁾, T. Sekiguchi²⁾ and M. Yamataka²⁾

1) Professor, Dept. of Architecture and Building Engineering, Tokyo Institute of Technology, Japan

2) Graduate Student, Dept. of Architecture and Building Engineering, Tokyo Institute of Technology, Japan

Kohji@o.cc.titech.ac.jp, tsekiguc@mail.arch.titech.ac.jp, myama3@mail.arch.titech.ac.jp

Abstract: The peak ground acceleration of 1.33 G recorded at K-NET station in Ojiya city during the 2004 Mid Niigata prefecture Earthquake was 1.5 times greater than that at JMA station as well as that at the other rock outcrop station (SSI) in the same city. In order to examine the effects of local site conditions on the strong motion records, not only geological and geophysical logs but also non-linear properties of the surface soils at K-NET and JMA are determined by boring, sampling, and spectral analysis of surface wave methods, as well as laboratory tests on samples obtained from the sites. Dynamic analysis is then conducted using the soil profiles with the recorded rock outcrop motions at SSI to simulate the ground motions at the two stations. It is shown that near surface soil conditions including nonlinear soil properties might have played an important role on the ground motions at K-NET and JMA during the earthquake.

1. INTRODUCTION

The Mid Niigata prefecture Earthquake on October 23 2004 caused many landslides and severe damage to many buildings, resulting in more than 50 fatalities and 4,800 wounded. At the same time this earthquake provided a large number of strong ground motion records. Particularly interesting is the difference in recorded strong motion between three stations in Ojiya city that is located about 7 km west of the epicenter of the earthquake. These include K-NET (Kyoshin NET) and JMA (Japan Meteorological Agency) stations on soft soils, and SSI (Suisen House) on outcrop rock (Fig. 1). The peak ground acceleration of 1.33 G at K-NET station was 1.5 times greater than not only that at the rock outcrop station (SSI) but also that at JMA on soft soils. The difference in ground motion characteristics between K-NET and JMA on soft soils is probably due to the difference in site geological conditions. There exist, however, few geological and geophysical data available for examining such local site effects.

The objective of this study is to evaluate the effects of local site conditions on the ground motion characteristics during the 2004 Mid Niigata prefecture Earthquake. Field investigation including boring, sampling, and spectral analysis of surface wave methods as

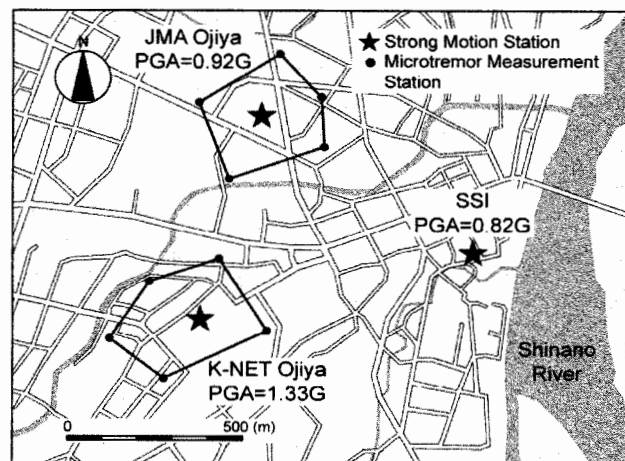


Figure 1 Map showing strong motion stations in Ojiya city

well as laboratory tests is conducted to evaluate near-surface soil profiles and their dynamic soil properties at K-NET and JMA. Dynamic analysis is then conducted using the soil profiles and properties determined for the two sites with the strong motions recorded at SSI as outcrop base motions.

2. GROUND MOTION CHARACTERISTICS OF STRONG MOTION STATIONS

A large number of strong ground motions but with less intensity were also recorded at the three stations during aftershocks. Fig. 2 shows the velocity response spectra with a damping ratio of 5% for the stronger EW component of the ground motions at the three stations during the main shock and one of the aftershocks (11/10/2004 03:43). The spectral shape including its amplitude and peak period is found to vary from station to station. Each of the spectra at K-NET and JMA during the main shock and aftershock has amplitude larger than that at SSI in most of the period range from 0.05 to 5 s with a prominent peak that does not appear in the spectra at SSI. In addition, the spectral peak periods of the two sites during the main shock are much larger than those during the aftershock. This suggests that the ground motions at K-NET and JMA could reflect nonlinear local site effects but those at SSI are associated with those observed at a rock outcrop site.

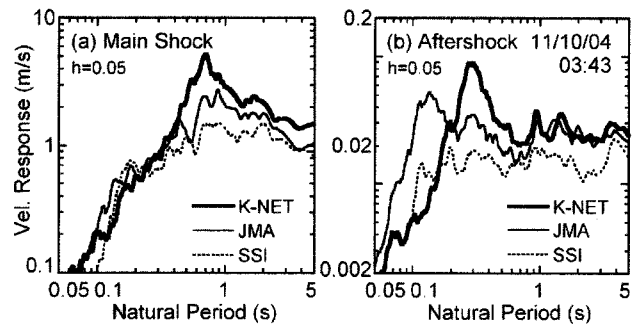


Figure 2 Velocity response spectra of EW components at three stations

3. FIELD INVESTIGATION

Geological and PS logs are available for K-NET and SSI stations (Tamari et al. 2004) but unavailable for JMA station. In addition, nonlinear soil properties of soft surface soil, which might have had significant effects on the ground motions at K-NET and JMA, were unknown. Field investigation including boring, sampling as well as spectral analysis of surface wave methods was, therefore, conducted to examine the surface soil profiles at K-NET and JMA.

3.1 Shear Wave Velocity Profiles from Spectral Analysis of Surface Wave Methods

Active and passive techniques of spectral analysis of surface wave methods were performed to estimate shear wave velocity profiles to a depth of about 200 m at K-NET and JMA. Linear arrays of several vertical sensors distributed at an equal distance of 0.5-2.0 m were used to observe waves from an artificial point

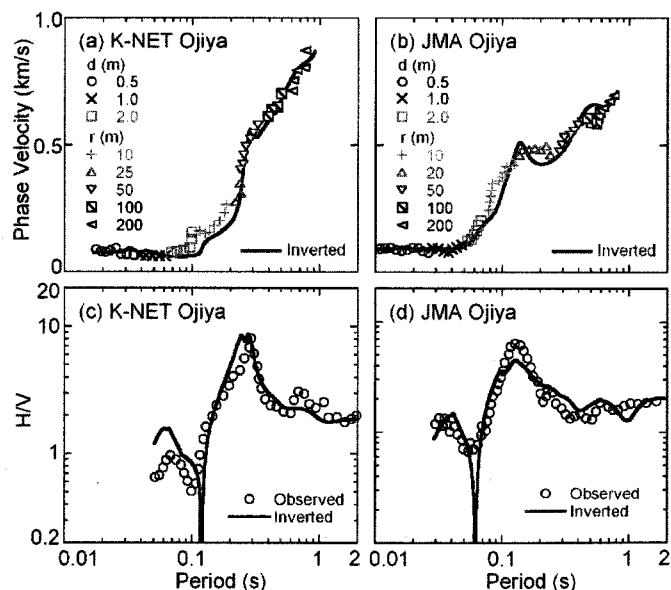


Figure 3 Surface wave dispersion curves and H/V spectra

source in a line of the sensors in the active method, while circular arrays of different array radius (10-200m) were used to observe microtremors in the passive method. The largest arrays used at the two stations are shown in Fig. 1.

Based on the F-k spectral analysis of observed vertical motions, dispersion characteristics at the two stations were computed and are shown in Figs. 3 (a), (b) in which the computed phase velocities are plotted against periods with symbols corresponding to the sensor distances used. The phase velocities at K-NET in periods less than 0.1 s are about 70 m/s and increase to more than 400 m/s at periods greater than 0.3 s. The phase velocities at JMA in periods less than 0.05 s are about 100 m/s and increase to more than 400 m/s at periods greater than 0.1 s.

The H/V spectra were calculated from the three component motions of microtremors at the two stations and are shown with open circles in Fig. 3 (c), (d). A sharp prominent peak occurs in each H/V spectrum at a period roughly corresponding to that of the velocity response spectrum of the aftershock as shown in Fig. 2 (b).

Shear wave velocity profiles down to a depth of 200 m for the two stations were estimated based on an inverse analysis (Arai and Tokimatsu, 2005) using both dispersion curves and H/V spectra. The solid lines in Fig. 3 show the theoretical dispersion curves and H/V spectra for the inverted shear wave velocity profiles. The computed values are in fairly good agreement with the observed ones, suggesting that the inverted structures could be reasonably reliable. The estimated shear wave velocity profiles to a depth of 200 m at the two stations are shown in Fig. 4 and close-ups of the near-surface values are shown in Fig. 5.

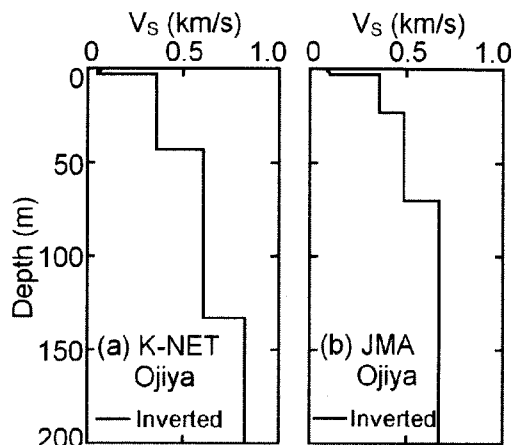


Figure 4 Shear wave velocity profiles estimated from surface wave methods

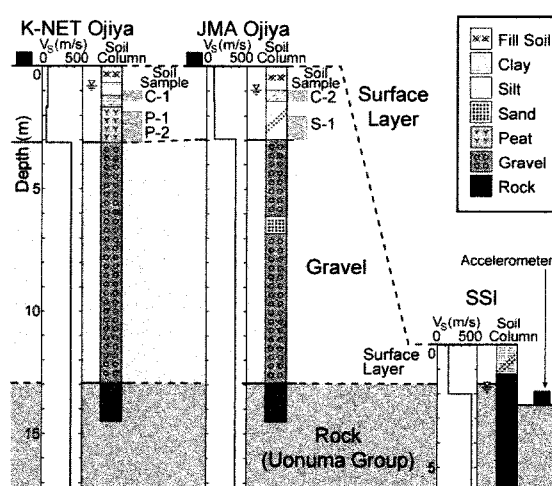


Figure 5 Geological and geophysical logs at three stations in Ojiya

3.2 Geological Logs from Current and Previous Studies

Boring was conducted to a depth of 7 m at both stations. Fig. 5 shows the geological logs and the shear wave velocity logs at both stations together with those at SSI (Tamari et al. 2004). The geological logs deeper than 7 m are based on previous investigation made by other institutions (K-NET and Ojiya Regional Fire Department).

The surface soil to a depth of 3 m at K-NET station is extremely soft, consisting of silty clay and peat with V_s as low as 50 m/s. The surface soil to a depth of 3 m at JMA station, in contrast, consists of silty clay and sandy silt with V_s about 100 m/s. Underlying below the 3-m thick surface layer at each station is a gravel layer with V_s of about 400 m/s, which is underlain by Pleistocene rock (Uonuma Group) occurring at a depth of about 13 m. Thus, the impedance ratios between the 3-m thick surface soil and the gravel layer at both stations are relatively high. The surface soil to a depth of 2 m at SSI site consists of sandy silt, which is underlain by Pleistocene rock with V_s of 430 m/s.

The strong motion seismometers at K-NET and JMA have been installed on the ground surface, while that at SSI station near the base of an isolator of a building founded on the Pleistocene rock

occurring at about 4 m below the ground surface. Thus the strong motions recorded at SSI are considered to be rock outcrop motions.

4. NONLINEAR DYNAMIC PROPERTIES OF SURFACE SOILS FROM LABORATORY TEST

To examine nonlinear dynamic soil properties of the surface soils at K-NET and JMA, cyclic torsion shear tests were conducted under undrained conditions on hollow specimens, 100 mm high having 70 mm outer and 30 mm inner diameters, that were trimmed from the samples obtained at the sites. The samples tested include silty clay (C-1) and peat (P-1, P-2) at K-NET and silty clay (C-2) and sandy silt (S-1) at JMA, the depths of which are shown in Fig. 5.

Fig. 6 shows the relations of shear modulus ratio and damping factor with shear strain for the specimens tested. Despite its very low shear wave velocity of about 50 m/s, the peat at K-NET (P-1, P-2) shows weaker nonlinearity than any other soils. Namely, the shear modulus ratio and damping factor of the peat at K-NET at a shear strain of 1 % are about 0.5 and 10%, the values of which are equivalent to those of the other soils at a shear strain of 0.1 %, which is about one order of magnitude smaller than 1 %. The shear modulus ratio and damping factor of the soils except the peat are as low as 0.1 and as high as 15-20 % at a shear strain of 1 %. Similar weak nonlinear dynamic characteristics of peat have been presented elsewhere (Boulanger et al. 1996, Wehling et al. 2003).

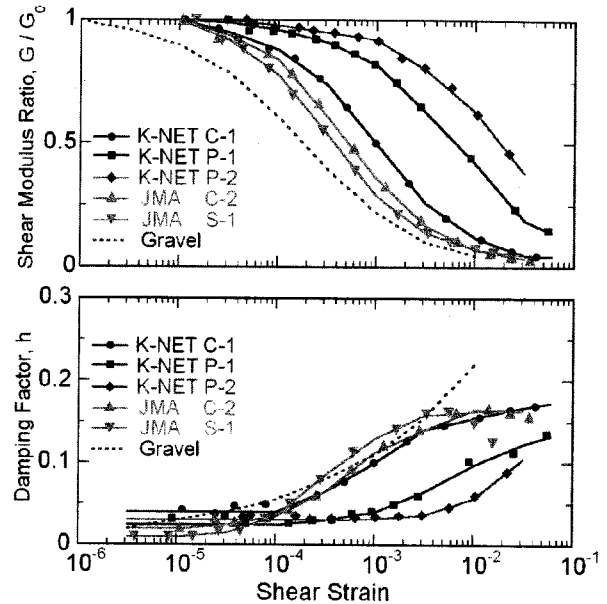


Figure 6 Strain-dependent shear modulus ratio and damping factor

5. EQUIVALENT LINEAR DYNAMIC RESPONSE ANALYSIS

To simulate the observed strong motions at K-NET and JMA during the Mid Niigata prefecture Earthquakes, one-dimensional equivalent linear dynamic response analysis originally presented by Schnabel et al. (1972) and later modified by Sugito et al. (1993) was conducted using the soil profiles shown in Fig. 5 and the representative nonlinear dynamic soil properties shown in Fig. 6 in solid lines. The ground motions recorded at SSI were used as input outcrop motions to the base rock layers at a depth of 13 m.

Fig. 7 compares the computed and observed ground surface acceleration time histories at K-NET and JMA for the main shock together with the input base motion that was recorded at SSI. The computed time histories for both stations agree reasonably well

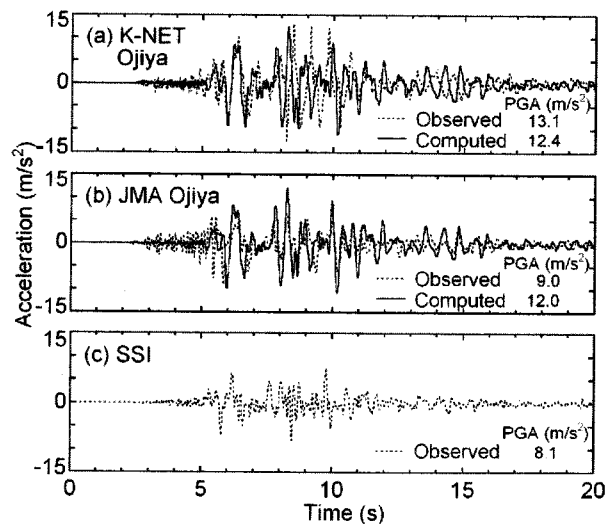


Figure 7 Comparison of computed and observed acceleration time histories

with the observed ones.

Fig. 8 compares the velocity response spectra with a damping ratio of 5% of the observed and computed motions at the two stations for the main shock as well as the aftershock. The velocity response spectra of the computed motions at both stations agree reasonably well with those of the observed motions.

To examine the effects of near-surface soft soils to a depth of 3 m on the observed ground motions, dynamic response analysis was also conducted, assuming that the gravel occurring at a depth of 3 m is the outcrop layer for the input motions.

Fig. 9 compares the velocity response spectra of the ground motions computed for the outcrop base motions input at depths of 3m and 13 m. There exists insignificant difference between the two velocity spectra, suggesting that the ground motions are significantly governed by the dynamic soil properties at depths smaller than 3 m.

The above finding and discussions indicate that the near-surface soils to a depth of 3 m including their nonlinear soil properties significantly affected the strong ground motions at K-NET and JMA during the 2004 Mid Niigata prefecture Earthquake.

6. CONCLUSIONS

The effects of local site conditions on the strong ground motions during the 2004 Mid Niigata prefecture Earthquake were examined based on the field investigations and subsequent analyses. Based on the results and discussions, the following conclusions may be made:

- (1) A 3-m thick soft layer of silty clay and peat with a shear wave velocity of about 50 m/s overlies a stiff gravel layer at K-NET, while a 3-m thick soft layer of sandy silt with a shear wave velocity of about 100 m/s overlies a gravel layer at JMA.
- (2) Despite its very low shear wave velocity, the near-surface peat at K-NET show weaker nonlinearity than the near-surface sandy silt at JMA.
- (3) The near-surface soil to a depth of 3 m including their nonlinear soil properties might have had a significant effect on the difference in ground motion in Ojiya city during the 2004 Mid Niigata prefecture Earthquake.

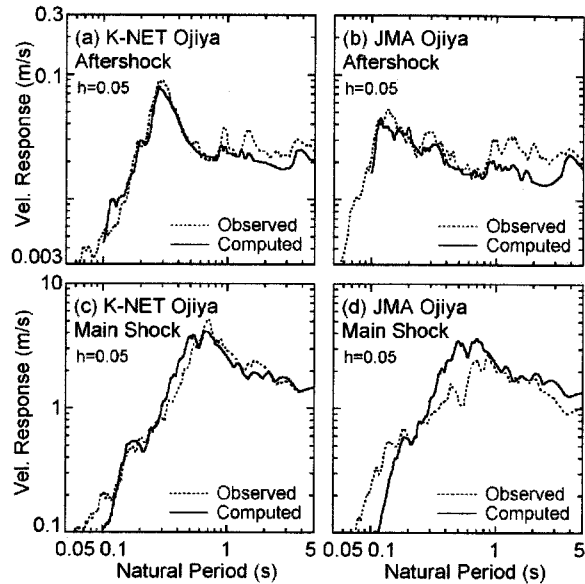


Figure 8 Comparison of velocity response spectra of observed and computed ground motions

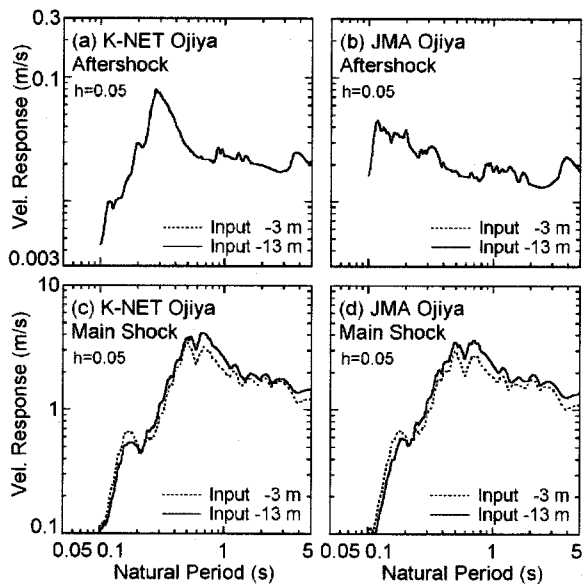


Figure 9 Comparison of velocity response spectra of ground motions computed for base motions input at a depth of 3m and 13 m

Acknowledgements:

The strong motion records at K-NET and JMA used in this study were provided by K-NET (NIED) and Japan Meteorological Agency. The geological logs at JMA were provided by Ojiya Regional Fire Department. The field investigation at K-NET and JMA was made by permission of Ojiya City Office and Ojiya Regional Fire Department. The strong motion records as well as the geological and PS logs at SSI were provided by Ojiya Polyclinic, Mitsubishi Jisho Sekkei and Taisei Corporation.

References:

- Arai, H. and Tokimatsu, K. (2005) "S-Wave Velocity Profiling by Joint Inversion of Microtremor Dispersion Curve and Horizontal-to-Vertical (H/V) Spectrum," *Bulletin of the Seismological Society of America*, 95(5), 1766-1778.
- Boulanger, R.W., Arulnathan, R., Harder Jr., L.F., Torres, R.A. and Driller, M.W. (1998) "Dynamic properties of Sherman Island peat," *Journal of Geotechnical and Geoenvironmental Engineering*, 124(1), 12-20.
- Kyoshin Network K-NET, National Research Institute for Earth Science and Disaster Prevention, available from : <http://www.kyoshin.bosai.go.jp/k-net/>
- Japan Meteorological Agency, available from : http://www.jma.go.jp/JMA_HP/jma/index.html
- P.B. Schnabel, J. Lysmer and H.B. Seed (1972), "SHAKE-A Computer Program for Earthquake Response Analysis of Horizontally Layered Sites," *EERC Report*, No.72-12
- Sugito, M., Goda, H., Masuda, T. and Etsunada, K. (1993), "Equi-linearized method with frequency-dependent shear modulus and damping," *Proceedings of the 28th Japan National Conference on Soil Mechanics and Foundation Engineering*, 1129-1132 (in Japanese).
- Tamari, T., and Tokida, T. (2004), "Earthquake motion records and vibration analysis results of a base isolated building," *Report on Damage Caused by the Mid Niigata Prefecture earthquake in 2004*, Japan Association of Earthquake (in Japanese).
- Wehling, T. M., Boulanger, R.W., Arulnathan, R., Harder Jr., L.F. and Driller, M.W., (2003) "Nonlinear dynamic properties of a fibrous organic soil", *Journal of Geotechnical and Geoenvironmental Engineering*, 129(10), 929-939.

MICRO-TREMOR MEASUREMENTS AT A FILL DAM DAMAGED BY THE 2004 NIIGATA-CHUETSU EARTHQUAKE

T. Ohmachi¹⁾ and S. Inoue²⁾

1) Professor, Center for Urban Earthquake Engineering, Tokyo Institute of Technology, Japan

2) Research Associate, ditto

ohmachi@envng.titech.ac.jp, shusaku@envng.titech.ac.jp

Abstract: The Niigata-ken Chuetsu earthquake (Mj6.8), Japan, which occurred on October 23, 2004 caused more or less damage to several fill dams located in and around the near field. Among them is 42.4m-high Shin-yamamoto dam, completed in 1990. It suffered large settlement of the crest exceeding 80cm and sand liquefaction. Thick sedimentation in front of the drain layer was presumably responsible for the liquefaction. After close inspection of the damage, repair work was conducted from April through November 2005, removing the liquefied or softened zones of surface layers followed by re-banking and compaction. Before and after the repair work, micro-tremor measurements were conducted along the crest of the dam. The measurement showed a considerable shortening of the vibration period of the dam, especially around the seriously damaged portion, implying remarkable effects of compaction work.

1. INTRODUCTION

The Niigata-ken Chuetsu earthquake (MJ6.8), Japan, occurred at 17:56 (local time) on October 23, 2004 (Fig. 1). Forty people were killed, and numerous landslides of various types took place on natural slopes and man-made banks. The highest seismic intensity of 7 on the JMA scale was registered at Kawaguchi town. Strong motion accelerometers of K-net registered peak acceleration of 1501gal at Ojiya, and 1750gal at Tokamachi during the main shock. The main shock was followed by many strong aftershocks for weeks. As detailed description about the earthquake and strong motion in near field is available elsewhere (Midorikawa et al 2005), it is omitted in the present paper.

Several fill dams built for hydroelectric power generation or agricultural irrigation were damaged by the earthquake. Due to the end of a harvest season, those dams for irrigation were empty of reservoir water at the time of the main shock, which served to avoid secondary damage to the downstream. While three dams for power generation were impounded with water from the Shinano river, the longest river in Japan. The three dams are Yamamoto Dam and Shin-yamamoto Dam located in Ojiya, 6 and 5km from the epicenter respectively, and Asagawara Dam in Tokamachi, 22km from the epicenter (see Location Map in Appendix). The electric power generated with the water from these dam is used to drive JR trains in the Tokyo metropolitan area. Since much of the electric power is used during morning and evening rush hours, these dams are always subjected to rapid draw down of the water level twice a day. Although these three dams suffered earthquake damage, there was no secondary damage to the downstream because the storage water was safely released from each reservoir after the damage to the dams was discovered. The owner of the dams (JR East) established a committee to investigate causes and effects of the damage. Although the author has been one of the committee members and given much information to be described in this paper, he is solely responsible

for any errors and misunderstanding.

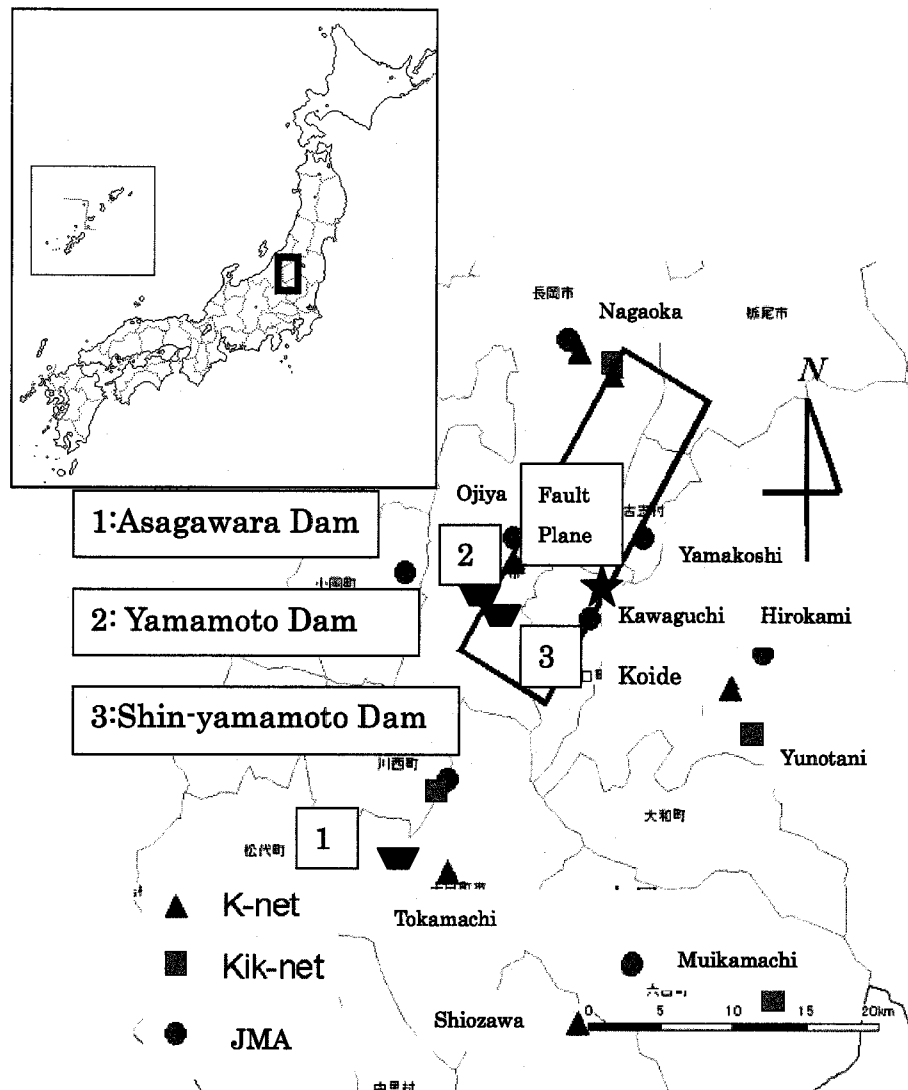


Figure 1 Location Map

2. DAMAGE TO SHIN-YAMAMOTO DAM

Shin-yamamoto dam was built in 1990. The dam is 42.4m high, and has a crest length of 1,392m with a standard cross section shown in Figure 2. This is a zoned fill dam with a dam axis of a semi-circular shape as shown in Figure 3, where red circles indicate observation points for micro-tremor measurements as described later. Both right and left ends of the dam are plunged into natural slopes. To facilitate the rapid draw down of the water level, there is a horizontal drain layer on the upstream side at the elevation of EL.143.8m~147.3m, which is just above the low water level of EL. 143.8m.

The strong shaking of the main shock and aftershocks caused some considerable damage to the dam. Settlement of the crest was about 10~40cm on the right half side of the dam where both core and shell zones are founded on rock, while it was about 50~90cm on the left half side where the

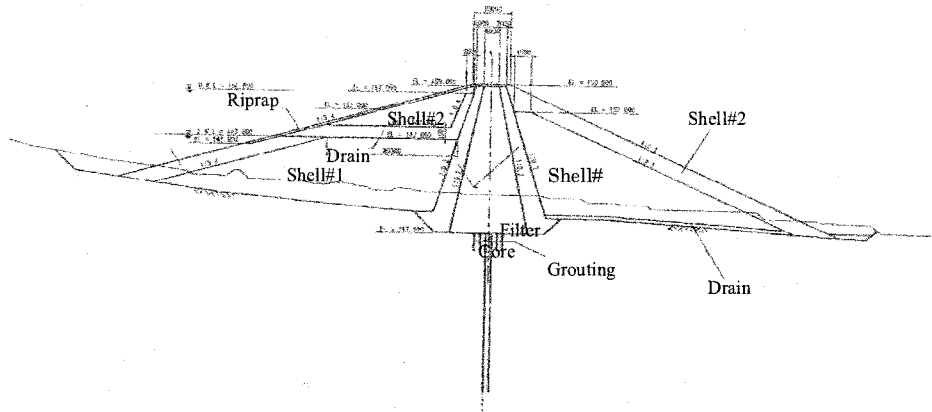


Figure 2 Vibration Modes of Space Frame with Dampers: (a) 1st Mode, and (b) 6th Mode

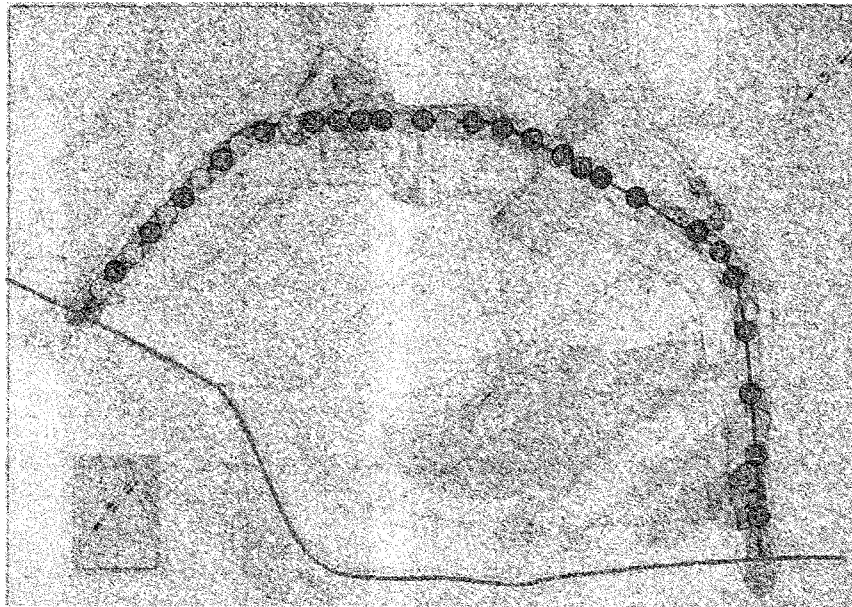
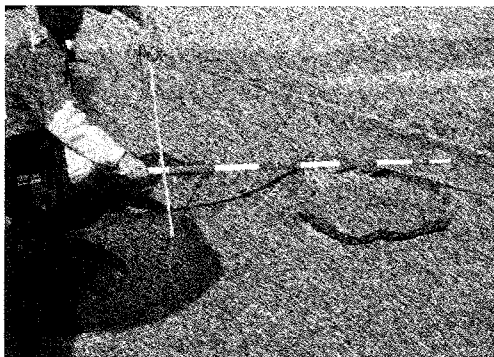


Figure 3 Standard Cross Section of Shin-yamamoto Dam



(a) H-beam's Top indicating Settlement



(b) Boiled Sand indicating Liquefaction

Figure 4 Settlement and Liquefaction Observed at Shin-yamamoto Dam

shelter zone is founded on terrace deposits. The crest was also displaced upstream about 20~40cm on the left half side, while downstream about 3~10cm on the right half side. Due to the large settlement, a top of an H-shaped steel beam which was embedded to protect monitoring cables from

bottom to crest in the filter zone was observed protruding about 30cm from the asphalt pavement as shown in Figure 4 (a).

On the upstream side near the left end, boiled sand was found at several places on the riprap surface at EL. 145~150m and nearby sedimentation as shown in Figure 4 (b). Trenches were excavated to investigate origin of the boiled sand and soil properties such as permeability and grain size distribution in and around the liquefied areas. The origin of the boiled sand was mostly concentrated in and around the drain layer whose sand content was higher than that at the construction stage. In addition, near the left end of the dam, it was noted that fine sedimentation was thick enough to cover the mouth of the drain layer. It seemed reasonable to think that the thick sedimentation in front of the drain layer caused pore water pressure buildup under the strong shaking followed by the liquefaction.

3. VIBRATION CHARACTERISTICS DETECTED BY MICROTREMOR MEASUREMENTS

3.1 Micro-tremor Measurements and Data Processing

Various kinds of investigation were conducted such as excavation of trenches and boreholes in and around the liquefied or settled areas, and removal of asphalt concrete and base course material of the crest for visual inspection of the clay-core. As a result, the clay-core was found to be free from the damage.

For restoration of the dam, in principle, damaged portions of the dam body such as upper ripraps and outer drain-layer were removed and banked with new materials to the original design. Special care was paid to compaction during the banking to obtain higher density of the dam material. The restoration work took more than seven months.

Micro-tremor measurements at the dam were conducted two times. One was in November, 2004, immediately after the earthquake damage; and the other was in November, 2005, almost at the end of the restoration work. In both cases, measurement points were set at the same 32 points along the crest, as shown with red circles in Figure 3.

Figure 5 shows an example of three-component micro-tremor observed simultaneously at Point No.32 in November, 2005. The upper two time histories in Fig.5 are those in the horizontal directions of normal and parallel to the dam axis, and the bottom in the vertical direction, respectively. Horizontal and vertical axes of the figure indicate time in seconds at a sampling rate of 1/100 s, and velocity in 10-5m/s. After selecting several 10.24sec-samples with high S/N ratios, Fourier spectra were calculated and averaged among the samples, as shown in Fig. 6.

Using the Fourier spectra shown in Fig. 6, the H/V spectral ratios were calculated to find vibration characteristics of the dam, as shown in Fig.7. Apparently, the H/V spectral ratios indicate some peaks and troughs, but it is difficult to find vibration modes of the dam associated from the peaks in H/V spectral ratios at one observation point alone. To cope with the difficulty, the H/V spectral ratios at all the observation points were arranged in numeric order from No.1 through No.32, as shown in Fig.8 in which three dotted lines (I)-(III) were drawn by connecting eminent peaks observable in adjacent H/V spectral ratios. The data processing similar to the above was applied to the micro-tremor data observed in November 2004, with a result shown in Fig. 9 in which five dotted lines (A)-(E) were drawn.

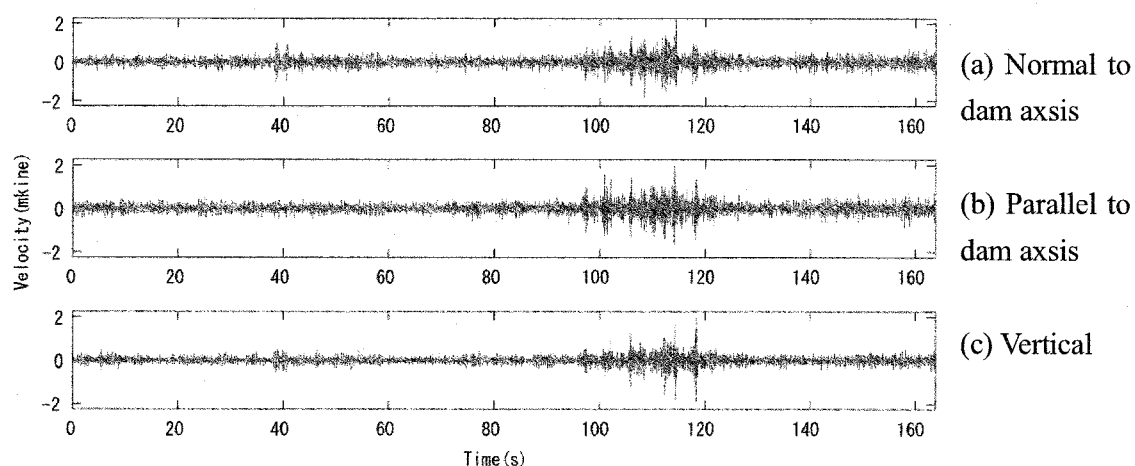


Figure 5 Time Histories of Microtremor observed on the dam.

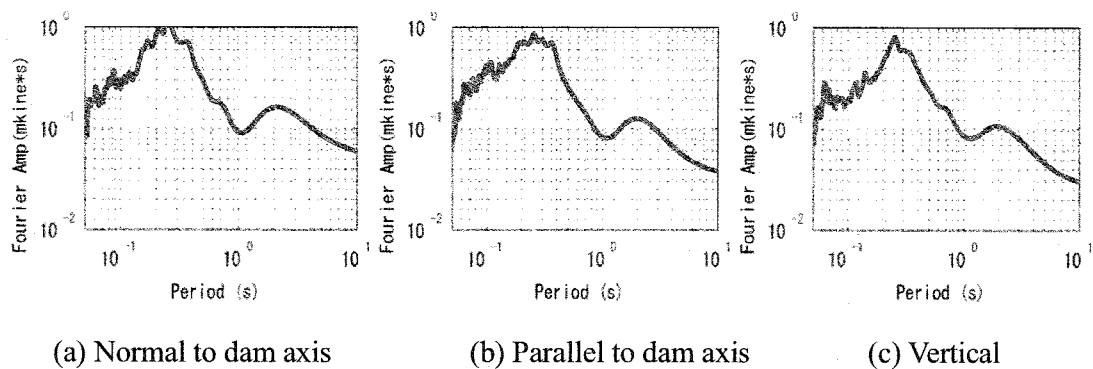


Figure 6 Fourier Spectra of Time Histories shown in Fig. 5.

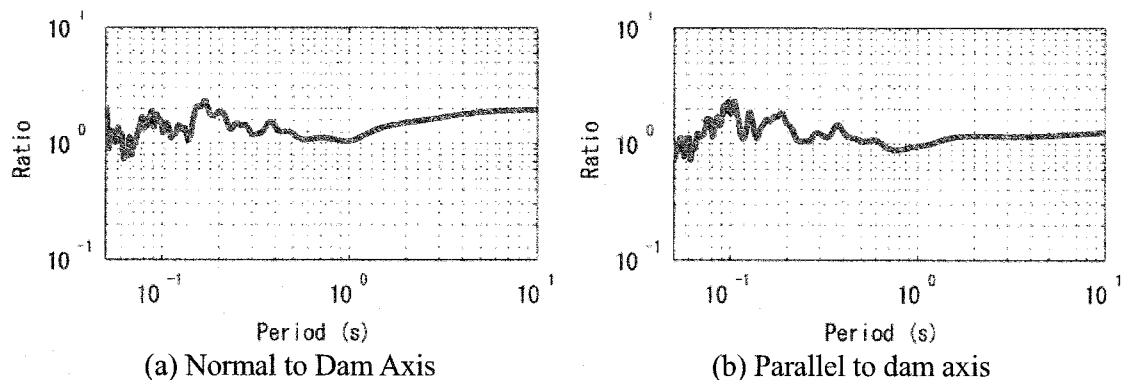


Figure 7 H/V spectral ratios from Fourier spectra shown in Fig. 6

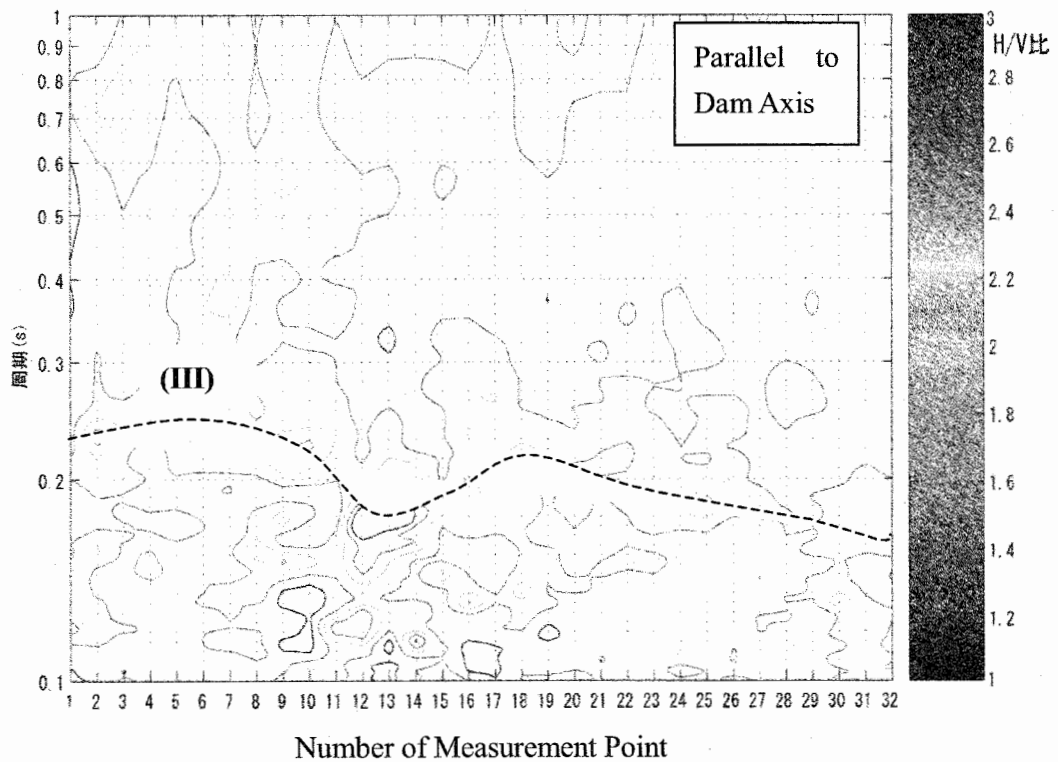
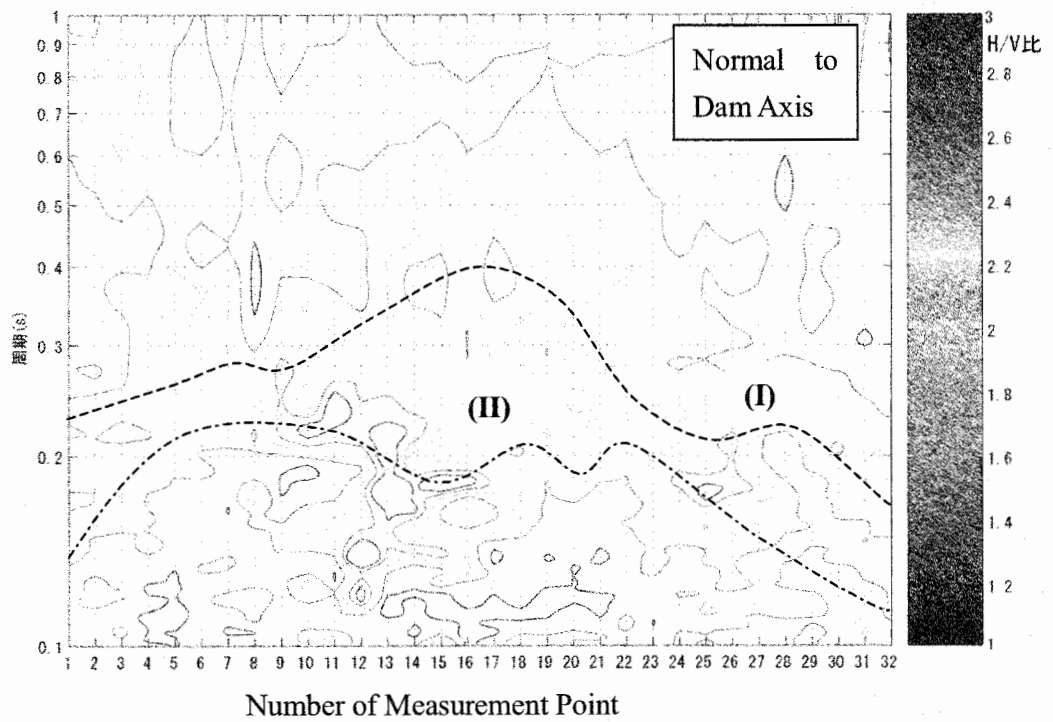


Figure 8 H/V Spectral Map from the Measurement in Nov. 2005

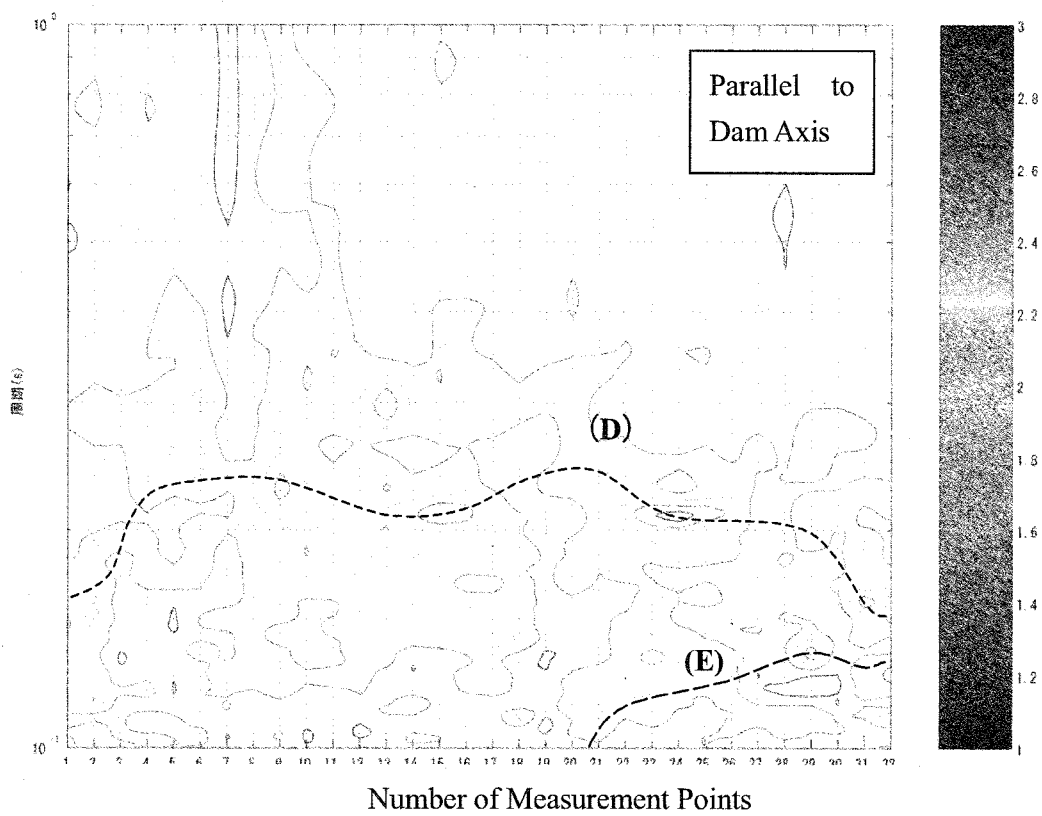
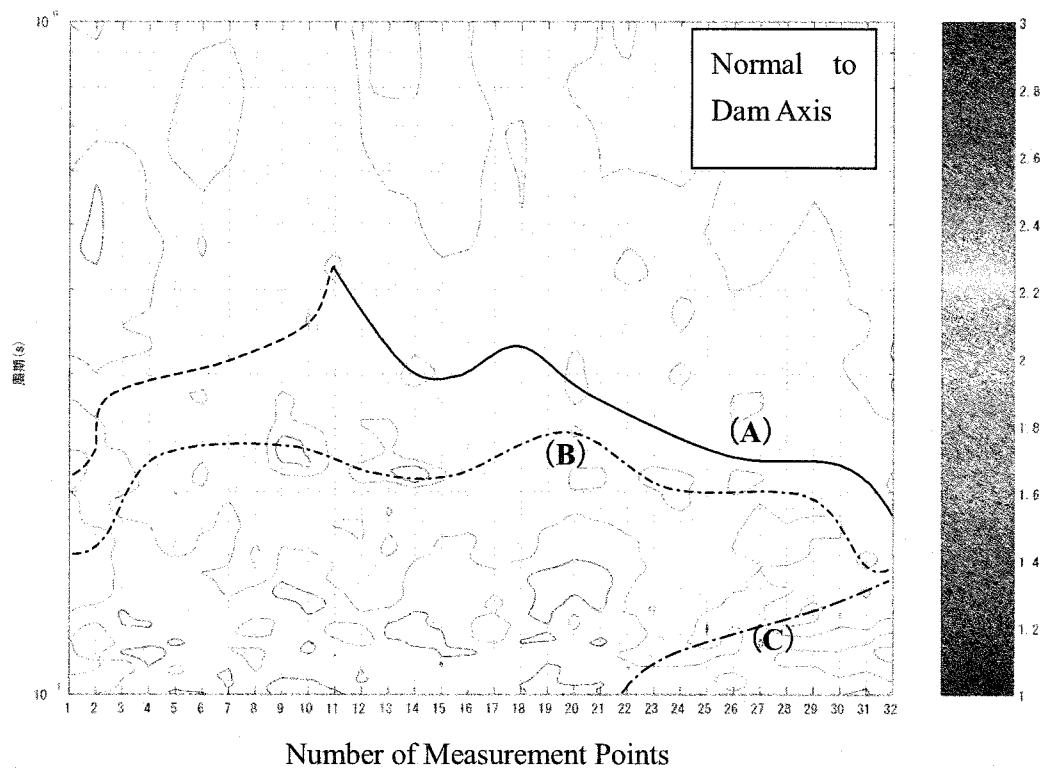


Figure 9 H/V Spectral Map from the Measurement in Nov. 2004

3.2 Vibration Characteristics of the Dam

As a rule of thumb, a fundamental period of rockfill dams is empirically given by $T=H/200$, where T and H are period in second and dam height in m, respectively. When $H=42.4\text{m}$ is substituted in this equation, an estimate of the period of the dam is $T=0.21\text{s}$. In addition, the dashed lines (II) and (III) in Fig. 8, and those (B) and (D) in Fig. 9 show similar periods and variation with each other. Accordingly, it seems reasonable to think that the lines (II) and (B) represent the fundamental mode of the dam in the normal direction, while the lines (III) and (D) the one in the parallel direction. Note that there is a considerable difference or change in the periods in Figs. 8 and 9. In the normal direction, for example, the change is as a whole from 0.24s in Fig. 8 to 0.20s in Fig. 9. The shortening in the period has probably resulted from adequate compaction during the reconstruction.

Moreover, it is also noteworthy that counterparts of the dashed lines (C) and (E) in Fig. 9 are not visible in Fig. 8. This is maybe because that those lines reflected some effects of the thick sedimentation near the left end of the dam as shown in Fig. 4(b), and that the sedimentation was thoroughly removed during the reconstruction.

For the time being, implication of the dashed lines (I) in Fig. 8 and (A) in Fig. 9 has not been clearly understood. Further study is needed to find causes and effects of filling of water in the reservoir.

4. CONCLUSIONS

The strong shaking in the near field of the 2004 Niigata-ken Chuetsu earthquake caused considerable damage to Shin-yamamoto dam. Special attention was paid to the large settlement and boiled sand observed on right half side of the dam. Since most of the sand was originated from the drain layer covered with fine sedimentation, the thick sedimentation in front of the drain layer was presumably responsible for the liquefaction of the sand.

The micro-tremor measurements along the dam crest showed a considerable decrease in the vibration period of the dam after the reconstruction work, implying that rigidity of the dam was significantly increased by the adequate compaction during the banking process. The thick sedimentation in the vicinity of the left bank was detected as a special peak line in the H/V spectral map shortly after the earthquake disaster, and it disappeared in the map after the sedimentation was removed during the reconstruction.

As shown here, the micro-tremor measurement has demonstrated to be useful as a handy tool to diagnose the state of dams, when it is properly applied.

Acknowledgements:

The authors acknowledge technical information and support given from JR East in the post earthquake investigation followed by active discussion on the causes and effects of the damage to the dam described in this paper.

References:

- Tatsuo Ohmachi (2005), "Safety of Fill Dams under Level 2 Earthquake Motions: Lessons from the 2004 Niigata-chuetsu Earthquake", pp.45-52, Proceedings of the 2nd International Conference on Urban Earthquake Engineering.
- Midorikawa, S. and Miura, H. (2005), "Strong Motion Records Observed in the 2004 Niigata-ken-chuetsu Earthquake," pp. 21-35, Proceedings of the 2nd International Conference on Urban Earthquake Engineering.

CONSIDERATION ABOUT INFLUENCE OF FLOOR CHARACTERISTICS ON FURNITURE BEHAVIOR DURING EARTHQUAKE

FUNDAMENTAL STUDY ON ESTABLISHMENT OF EVALUATION METHOD FOR SEISMIC RESISTANCE OF FLOOR FINISHING SYSTEM Part 2

Y. Yokoyama¹⁾, T. Yokoi²⁾, and R. Iida³⁾

1) Assoc. Prof., Dep. of Architecture and Building Eng., Tokyo Institute of Technology, Japan

2) 21st Century COE Postdoctoral Fellowship, Tokyo Institute of Technology, Dr. Eng.

3) Graduate School, Tokyo Institute of Technology

tyokoi@mail.arch.titech.ac.jp

Abstract: Tumble and movement of furniture are one of the most dangerous accident under a seismic disaster. They are influenced by floor's slipperiness, hardness, flatness, etc. So, the relations between easiness of tumbling, moving and characteristics of floors are considered in this thesis. At first, the behavior of furniture on various floors was observed by using the simple vibration table. As the result, it was found that slipperiness between furniture bottom and floor, easiness to be in rocking of furniture, and decrement of rocking greatly influence to tumble and movement of furniture. Then measurement methods of characteristics were established and characteristics of sample floors were measured. Finally, a substance of a relative evaluation method of a floor concerned with a behavior of furniture during earthquake was provided.

1. INTRODUCTION

Tumble and movement of furniture are one of the causes of human suffering under seismic disaster. Furniture's shape, weight, position of gravitational center, etc. greatly influence the behavior, but an influence of floor's slipperiness, hardness, flatness, etc. cannot be disregarded, too. There are a lot of report on furniture behavior, and most of them uses analytical method. But all of them take floor factor only from a view point of coefficient of floor friction, complex characteristic of floor including hardness, flatness, etc. is not considered.

The final purpose of this research is to establish the evaluation method of floor corresponding to the behavior of furniture. As a fundamental stage, an experiment to set furniture on various floors and observe the behavior during shaking floors was carried. Then characteristic of floor was measured by simple method, and relation between result of experiment and measurement was examined. This thesis describes passage and results of these experiments and considerations.

2. EXPERIMENT TO OBSERVE BEHAVIOR OF FURNITURE BY USING SIMPLE VIBRATION TABLE

2.1. Outline of Experiment

A behavior of furniture was observed by using the simple vibration table. **Figure 1** shows an outline of the simple vibration table developed at previous research¹⁾. This vibration table can

generate an input wave shown in **Figure 2**. The main part of this input wave is sign wave. And there are pre-position part and post-position part those accelerations change linearly. An acceleration amplitude (" a "), number of waves (" n "), frequency (" f ") of sign part and time (" t ") of pre-position and post-position part can be controlled. In this research, 3 kinds of input waves of $f=1, 2, 3$ Hz, $n=3$ and $t=1.5$ s were used. It depends on the following reasons those were found by the research¹⁾ targeted on random-access floor.

- A main range of frequency in real earthquake waves is 1-3 Hz.
- Few waves before and behind the largest part in real earthquake waves influence a furniture behavior mostly.

Table 1 shows an outline of 12 kinds of sample floors used to experiment. At a selection of these sample floors, it is noticed that slipperiness, hardness, flatness, etc. of sample floors vary in each floor.

Figure 3 shows an outline of a mock furniture used to experiment. This is imitating of a bookshelf. The ratio of thickness and height was 0.2 that is considered to be in dangerous side within actual range. A position of gravitational center is set on a center of the mock furniture. And weights (" W ") of the mock furniture are set at 3 degrees, 38.5 kgf as no books is put, 236.5 kgf as bookshelf is full of books, and 148.5 kgf as medium, those are adjusted by changing steel board put evenly on the mock furniture. The mock furniture touches a floor by four points (30×30 mm), that was

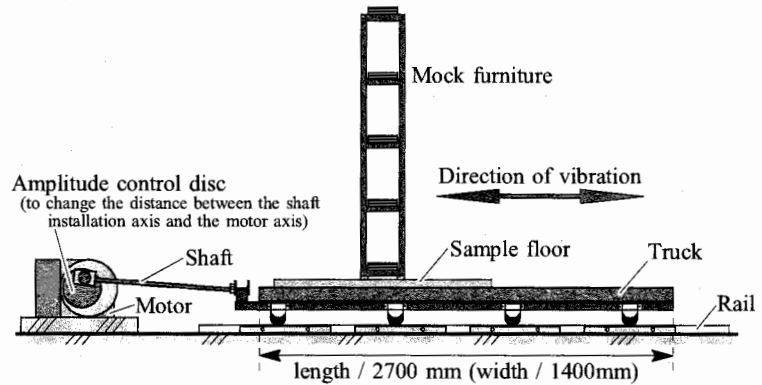


Figure 1 Outline of Simple Vibration Table

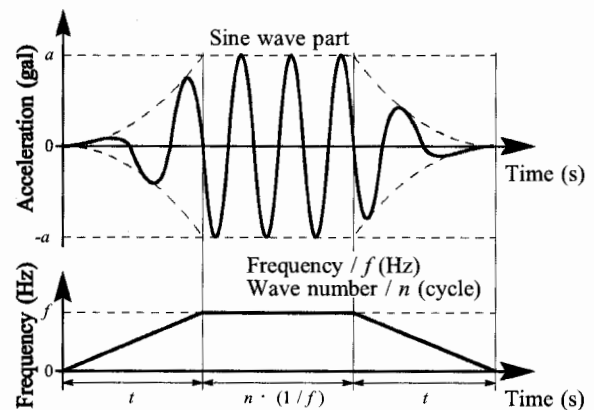


Figure 2 Outline of Simple Input Wave

Table 1 Outline of Sample Floor

No.	Outline of Sample Floor
1	Plywood flooring(thickness : 12 mm)
2	Carpet (Cutting pile, length of pile : 15 mm)
3	Vinyl seat (thickness: 2 mm, bumped (hight : 0.5mm, interval 3.5 mm))
4	Vinyl seat (thickness: 2 mm)
5	Vinyl seat (No. 4) + Foamed urethane (thickness: 30 mm)
6	Rubber tile (thickness: 2.8 mm, bumped (hight : 1 mm, interval 7 mm))
7	Rubber seat (thickness: 7 mm)
8	Teflon seat (thickness: 0.3 mm)
9	Carpet tile (Loop pile, length of pile : 3 mm)
10	Vinyl seat (No. 4) + Foamed urethane (thickness: 10 mm)
11	Vinyl seat (No. 3) + Foamed urethane (thickness: 5 mm)
12	Vinyl seat (No. 4) + Foamed urethane (thickness: 10 mm)

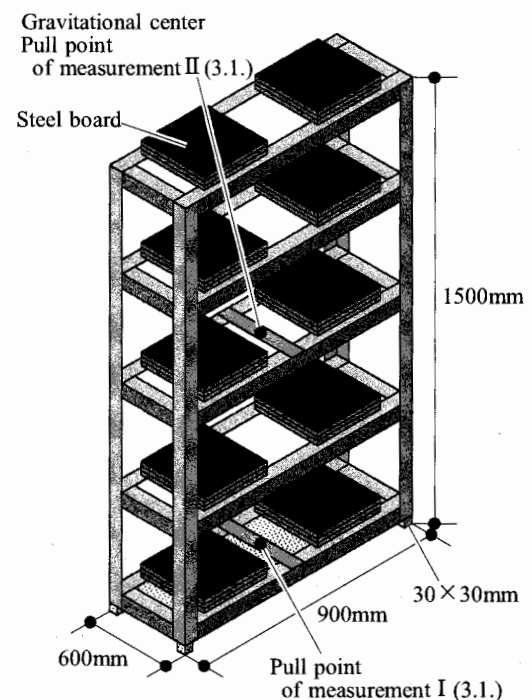


Figure 3 Outline of Mock Furniture

decided by a stability of preliminary experiment result.

At the experiment, the mock furniture was set on the sample floor, and shaken by nine combinations of frequency and wight (3 kinds of " f " and 3 kinds of " W "). Acceleration " a " is gradually increased. A magnitude and a shape of the input wave were confirmed with an accelerometer installed in the vibration table. Moreover, a behavior of the mock furniture during shaking is recorded by a video camera. Then tumble of mock furniture and the amount of movement in a shaking direction were visually observed by 2 observers. And judged as following.

- : Not tumbled, moved less than 30 mm.
- : Not tumbled, moved more than 30 mm, less than 100 mm.
- △ : Not tumbled, moved more than 100 mm.
- × : Tumbled.

Here, the reasons to set boundary amount at 30, 100 mm are as following.

- It is reported that about 30 mm movement cause unrest, by the research about amount of furniture movement that cause unrest at seismic disaster²⁾.
- It is judged that about 100 mm movement cause danger of hit to the person etc. .

Experiment was carried until the mock furniture tumble, of the acceleration became to be the limit of the ability of the vibration table.

2.2. Result and Consideration

Figure 4 shows an example of the result carried under $f=3$ Hz and $W=236.5$ kgf.

From this figure, it is seen that the mock furniture tumbles and amount of the movement grows as a increases in each sample floors. Then, in each W , the smallest a that the mock furniture tumbles (" a_T ") is found from these figures. Figure 5 shows them.

In the same way, the smallest a that the mock furniture moved 30 mm or 100 mm (" a_{30} " and " a_{100} ") are found. Figures 6 and 7 show them.

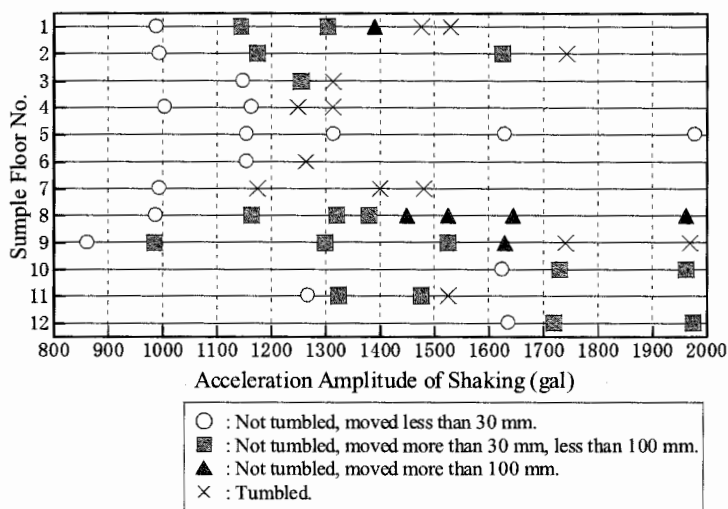


Figure 4 Example of Result
(Carried under $f=3$ Hz and $W=236.5$ kgf)

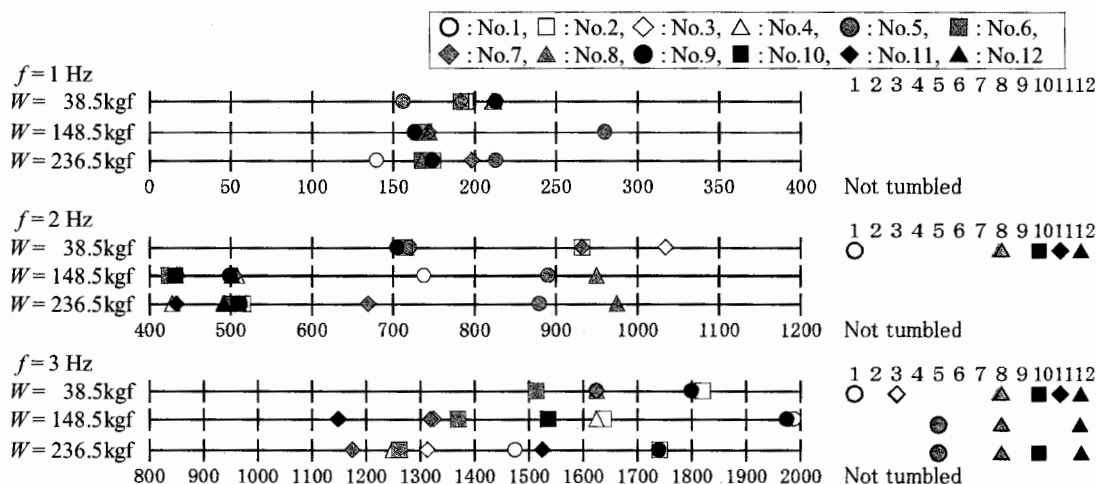


Figure 5 Tumbling Acceleration

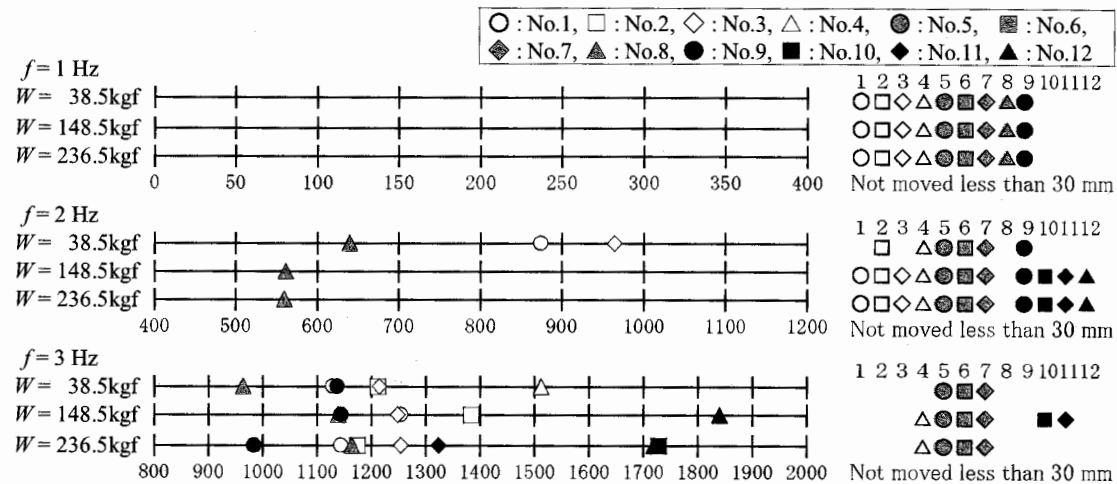


Figure 6 Moving Acceleration (30 mm)

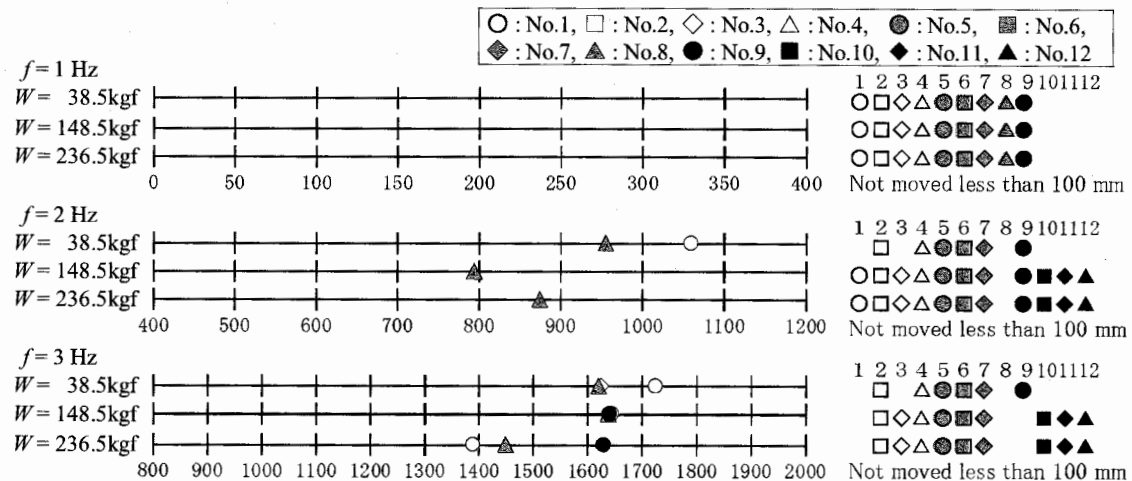


Figure 7 Moving Acceleration (100 mm)

The following matters can be considered from Figure 5-7.

- There is a large difference of a_T among sample floors in higher f . In $f=1$ Hz, a difference among sample floors is hardly seen.
- A number of sample floor that the mock furniture moves 30 mm or 100 mm before it tumbles increases in higher f . That is, furniture becomes slippery.

Additionally, it was considered that the result carried under $W=38.5$ kgf was comparatively not steady.

3. EXAMINATION OF QUANTITATIVE VALUE CORRESPONDING TO BEHAVIOR OF FURNITURE

3.1. Measurement of Characteristic of Floor Influence Behavior of Furniture

It is expected easily that a behavior of furniture is influenced by slipperiness between a bottom of furniture and a floor. Moreover, the following are appeared by a detailed review of the video described 2.. When a is large, mock furniture tumbles in an instant without rocking. On the other hand, when a is gradually increased from a very small range, rocking is caused at an early stage of shaking. And a is more increased, a phase of rocking and a phase of shaking are

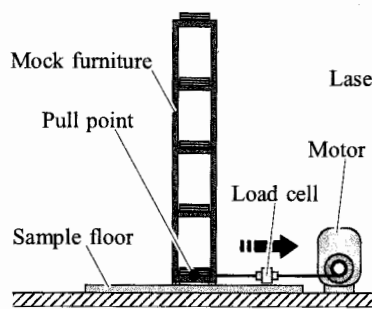


Figure 8 Measurement I

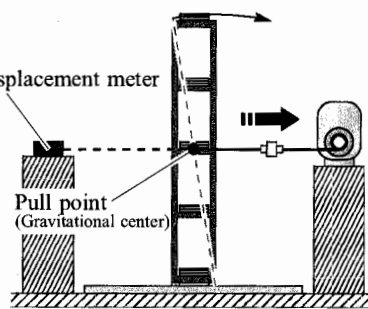


Figure 9 Measurement II

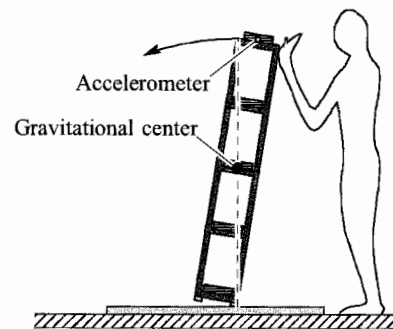


Figure 10 Measurement III

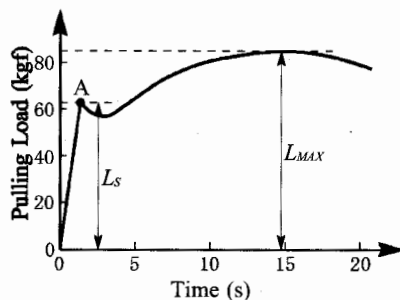


Figure 11 Result of I

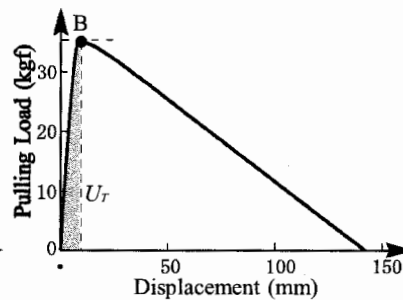


Figure 12 Result of II

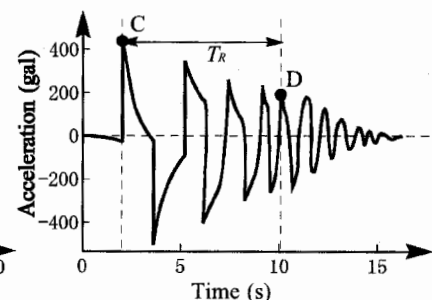


Figure 13 Result of III

synchronized in a middle of shaking, then mock furniture tumbles when a bad conditions comes in succession. Thus, at is influenced complicatedly by a slant of rocking generated in an early stage of a shaking, and by a relation between f and a cycle of rocking in a middle of shaking. And generally, a possibility that a bad condition comes in succession tend to be lower when a slant of rocking is small, and when a decrement of rocking is large.

From the above consideration, 3 kinds of characteristic of sample floors shown as following were to be measured.

- I Slipperiness between Furniture Bottom and Floor : A time change of a load during pulling the bottom of mock furniture is measured as shown in **Figure 8**. The bottom is pulled horizontally at constant speed (1 cm/sec).
- II Easiness to be in Rocking of Furniture : A load and a moved displacement during pulling the gravitational center of the mock furniture is measured as shown in **Figure 9**. The gravitational center is pulled horizontally at constant speed (1 cm/sec).
- III Decrement of Rocking of Furniture : Rocking is generated naturally after furniture is slanted immediately before tumble as shown in **Figure 10**, and a time change of an acceleration is measured with the accelerometer installed in the upper part of furniture.

3.2. Examination of Quantity Value Corresponding to Tumble of Furniture

Measurement I - III described by 3.1. were carried under 12 kinds of sample floors and 3 kinds of furniture.

Figure 11 shows an example of the load-time curve of measurement I. A shape of the load-time curve was able to be classified into some groups by each sample floor. The figure shows a case of sample floor No. 3 (carpet). The load in A point where furniture began to move (" L_s ") and the maximum value of the load (" L_{MAX} ") etc. were examined in detail. And finally the ratio to W of L_s (" L_s/W ") was set as an index of slipperiness between a furniture bottom and floor.

Figure 12 shows an example of the load-displacement curve of measurement II. According

to the slant of the mock furniture, the sample floor is transformed until B point. And when the slant become larger, 1 side of furniture bottom leaves from the floor (similar to in rocking). Examined in detail, the ratio to W of the energy that the floor absorbs to the B point (" U_T/W ") was set as an index of easiness to be in rocking of furniture.

Figure 13 shows an example of the acceleration-time curve of measurement III. As shown in the figure, the time (" T_R ") from C point (the point that the bottom contact the floor 1st) till D point (the point that the bottom become not to leave from the floor) was set as an index of decrement of rocking of furniture.

Figure 14 shows an example of the relation between U_T/W and T_R obtained by the above method. Both correspond comparatively well as shown in the figure. After all, the decrement of rocking of furniture, that is to be in rocking easily, is also large. Therefore, either of them is used for quantitative value corresponding to a behavior of furniture. In this research, U_T/W is used.

Then, relations between L_s/W , U_T/W and a_T , a_{30} , a_{100} were investigated. At this time, as described at 2., because a difference among sample floors was hardly seen in $f=1$ Hz and the result carried under $W=38.5$ kgf was comparatively not steady, the result carried under $f=2, 3$ Hz, and $W=148.5, 236.5$ kgf were investigated.

Figure 15 shows the relation between a_T and L_s/W . In the figure, the result carried under $W=148.5$ kgf is shown by \bullet or \blacktriangle , and the result carried under $W=236.5$ kgf is shown by \circ or \triangle . As the figure, excluding the point shown by \blacktriangle and \triangle , a_T and L_s/W of each f correspond comparatively well. In other words, when $f=2$ Hz, mock furniture rapidly comes not to tumble when L_s/W becomes about less than 0.2 regardless W at least in the range of $W=148.5$ -236.5 kgf. And when $f=3$ Hz, it comes not to tumble gradually by becoming small of L_s/W . On the other hand, the point shown by \blacktriangle , \triangle tends to come off from correspondence. In these sample floors, U_T/W are more than about 2.6 (for $f=2$ Hz) or 2.4 (for $f=3$ Hz). That is, when the floor becomes soft to some degree, furniture become not to be in rocking easily. And even if rocking is generated, decrement is large enough, and furniture become difficult to tumble for L_s/W .

3.3. Examination of Quantity Value Corresponding to Displacement of Furniture

Figure 16, 17 shows relations between a_{30} , a_{100} and L_s/W . As shown in these figures, L_s/W is less than about 0.2 (for $f=2$ Hz) or 0.4 (for $f=3$ Hz), the mock furniture moves more than 30

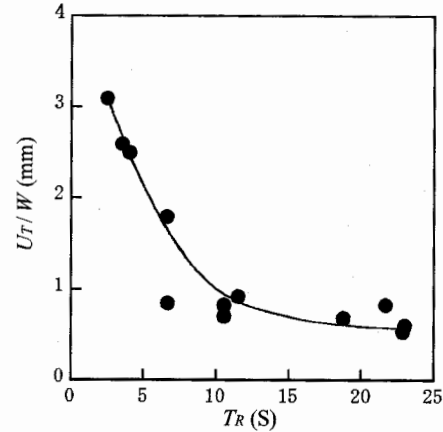


Figure 14 Relation between U_T/W and T_R

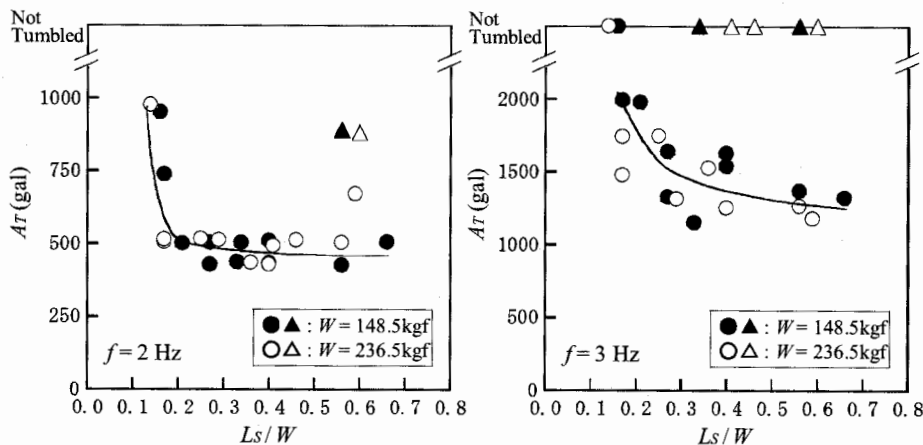


Figure 15 Relation between a_T and L_s/W

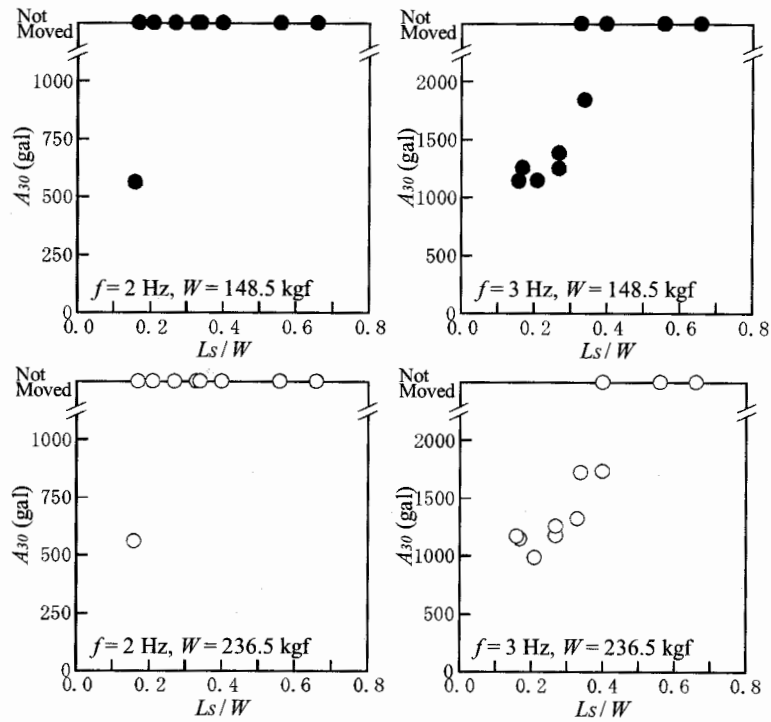


Figure 16 Relation between A_{30} and L_s/W

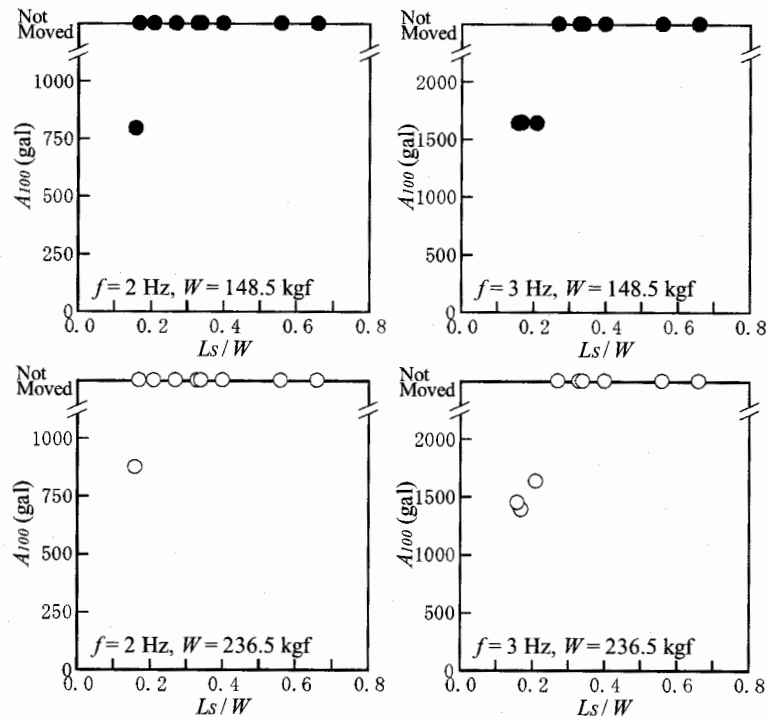


Figure 17 Relation between A_{100} and L_s/W

mm. And L_s/W is less than about 0.15 (for $f=2$ Hz) or 0.2 (for $f=3$ Hz), the mock furniture moves more than 100 mm. By referring L_s/W of a combination of a evaluation objective floor and furniture to these figure and **Figure 15**, it can be possible to predict whether the concerned furniture will tumble, or whether the furniture will move before it tumbles.

4. PROVIDING OF SUBSTANCE OF EVALUATION METHOD OF FLOOR CONCERNED WITH BEHAVIOR OF FURNITURE DURING EARTHQUAKE

From the result of investigation done till 3., the substance of a relative evaluation method of a floor concerned with a behavior of furniture during earthquake is provided as follows.

- ① Under the objective combination of furniture and floor, L_s/W is measured by the method shown in **Figure 8**. And, U_T/W is measured by the method shown in **Figure 9**.
- ② If U_T/W is more than a certain value, it is considered that a possibility of tumbling the concerned furniture on the concerned floor is low.
- ③ If U_T/W is less than a certain value, easiness of tumbling or moving of concerned furniture on the concerned floor are evaluated by referring L_s/W to figure that shows relation to acceleration of tumbling or moving.

At this point, it should be attended that boundary value of U_T/W using at ②, and absolute relation between L_s/W and acceleration of tumbling, moving are varied by various factors. And items shown in above are for a relative evaluation.

5. CONCLUSION

The result of this thesis is following.

- A behavior of the mock furniture on various sample floors during shaking was observed by using simple vibration tables.
- Characteristics of the sample floor were measured by simple method.
- The substance of a relative evaluation method of floor concerned with a behavior of furniture during earthquake is provided.

However, these are the results in a limited condition. Hereafter, the evaluation method based on the presented substance will be examined with taking systematically various factors, shape of input wave, characteristics of frequency, furniture's shape, weight, position of gravitational center and setting situation, etc.

References;

- Yokoyama, Y., Katagi, U., Yokoi, T. and Ono, H. (2005.9), "Configuration of Input Wave for Evaluating Seismic Resistance on Free access Floor", *Journal of Structural and Construction Engineering*, A.I.J., No. 586, 37-44
- Committee of Promoting Countermeasure Prevention for Tumble and Fall of Furniture (2004), "Investigation Result of Committee of Promoting Countermeasure Prevention for Tumble and Fall of Furniture", Tokyo Fire Department

TRUST, SECURITY, AND PEACE OF MIND

S. Fujii¹⁾, T. Kikkawa²⁾ and K. Takemura³⁾

1) Associate Professor, Tokyo Institute of Technology

2) Associate Professor, Keio University

3) Professor, Waseda University

fujii@plan.cv.titech.ac.jp, kazupsy@waseda.jp, geg01510@nifty.com

Abstract: This study sought to understand the determinants of risk acceptance. Thus, we implemented a survey (n = 200) to ask participants which policy measures would make approve each of the following risks: nuclear power plants, traffic accidents, food safety, electrical appliances, and medical mishaps. These results indicate that risk acceptance cannot be fully explained only by objectively achieved security, but other factors, such as scientific understanding and trust in workers and organizations, were also found to be important for increasing risk acceptance.

1. INTRODUCTION

Daily life incurs many risks. For example, a large earthquake may strike Japan in the next twenty to thirty years, traffic accidents occur daily, and human error has led to nuclear power plant disasters, such as at TMI or Chernobyl; furthermore, no one knows when the next infectious disease, such as SARS, will emerge. Unfortunately, few Japanese have the option of living in a place without earthquakes; we cannot drive a car without traffic accident risks, and our energy-consuming lifestyles lead us to rely on nuclear power plants. Even eating the food we need to survive incurs the slight risk of food poisoning. We can never truly free ourselves from risk.

There is a growing concern with risk and safety in Japan. This concern has been attributed to an increase in technological accidents that have occurred in recent years, as well as to scientific uncertainty over the probability of risks. While we must assiduously work to reduce technological risks, we still have to accept these risks, to some extent, because it is impossible to eliminate such risks completely.

Therefore, the practical problem with which this research was concerned was to understand how people accept risks, given the impossibility of achieving zero-risk status. To examine determinants of risk acceptance for several risk events, we surveyed 200 Tokyo residents to find their response to a variety of risks.

2. RISK ACCEPTANCE

When do people accept risks? Researchers have investigated this question for decades (e.g., Slovic et al., 1976). The simplest answer is that people do not accept risks and, instead, work to eliminate risk. If all risks are eliminated, security is guaranteed and a zero-risk state is achieved. Although risk-reduction efforts are necessary, society will always face some risks. Achieving zero-risk status might not be a realistic aim to strive for.

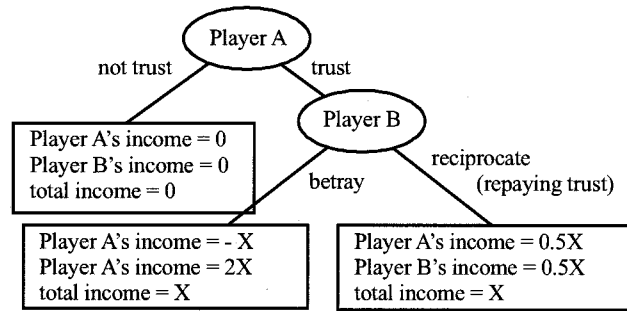


Figure 1 An example of the Trust Game

Another answer is that people rationally accept risks if they expect the benefit of an activity to exceed the cost (Fischhoff et al., 1978). For example, people may drive a car, knowing the risk of a traffic accident, if they believe that car use is beneficial. People may also accept nuclear plants, as long as the energy produced improves the quality of their lives.

However, many empirical studies (c.f. Dawes, 1998; Kahneman, Knetsch, & Thaler, 1991; Payne, Bettman & Johanson, 1993; Slovic, 1995) have contradicted the above claims. These studies have found that personal decision making frequently deviates from theories such as the “expected utility theory,” (Von Neumann & Morgenstern, 1947) or the “subjective expected utility theory,” (Savage, 1954), which assume rational, cost-benefit decision making. Cost and benefit expectations can be important determinants of risk acceptance, but they do not fully explain the process. No one yet knows the probabilistic distribution of some risks, such as endocrine-disrupting chemicals. Other risks, such as risks from electromagnetic fields, remain controversial. We cannot evaluate these risks by science, or by costs and benefits, alone.

We compared the relative weight of two components of risk: the possibility of risk and the damage from risk. These two possible determinants are closely related to cost expectation, which is assumed to determine decision making in rational choice models, such as the expected utility theory. We also investigated the effects of compensation after risk events have occurred. Compensation is expected to reduce or to eliminate the cost of risks. Additionally, we examined how understanding the scientific causes of a risk affected risk acceptance. Scientific understanding may reduce the extent of unknown risks (Fischhoff et al., 1978) and may lead to risk acceptance.

3. TRUST AND RISK ACCEPTANCE

We presumed that trust in workers and regulatory agencies constitutes another important determinant of risk acceptance. Instead of controlling risks by themselves, individuals may trust in, and delegate power to, organizations or institutions. This situation can be represented through the “Trust Game” (Kreps, 1990).

The Trust Game has two players: Player A (the truster) and Player B (the trusted). Player A can “trust” Player B by sending a monetary endowment X (see Fig. 1). Player B then receives double what player A has sent (i.e., $2X$). Player B must choose between “reciprocating” (returning X and taking X for himself) and “betrayal” (taking all he has received— $2X$). In this game, if Player A trusts Player B, the total monetary amount that Player A and Player B have increases by X . However, if Player A does not trust Player B, there is no collective increase. In this situation, trusting behavior is collectively beneficial. However, if Player B betrays Player A, Player A loses X . If Player A fears this risk, he does not trust Player B, which results in no collective benefit.

The basic structure underlying risk problems in our society may be seen as resembling that of the Trust Game, assuming that lay people represent Player A and risk experts represent Player B. Social

benefits may increase if lay people “trust” risk experts by asking them to administer risks. Risk experts may “reciprocate” by successfully managing the risk, or “betray” by failing to effectively manage risks. If people expect experts to reciprocate, trust and social benefits may increase. However, if people expect betrayal by the experts, trust and social benefits may not increase. For example, social benefits could increase if electricity companies repay the trust of the public by managing nuclear plants successfully. Social benefits would not increase if nuclear plants ceased operations due to a lack of public trust. If electricity companies fail in repaying public trust due to a serious nuclear plant problem, social benefits will decrease.

4. METHOD

4.1. Sample

Tokyo residents living within 50 km of the city center were randomly selected as participants for the August 2002 survey. A surveyor first visited the residents to ask them if they would participate in the survey. If the resident agreed to participate, a questionnaire was left at the home. After a few days, the surveyor again visited the home and collected the questionnaire.

4.2 Measures

As discussed above, we assumed that risk acceptance is determined by factors beyond subjective expectations of costs and benefits. We assumed that trust in persons and regulatory agencies in charge of risk would be another important determinant. Thus, we asked respondents to evaluate political policies or decisions implemented by administrators and the government. In the questionnaire, we asked respondents to consider six risk management measures and to choose three out of the six measures that would increase their risk acceptance for each of the following risks: nuclear power plants, traffic accidents, food safety, electrical appliances, and medical mishaps. The six choices were:

- (1) Decrease the probability that the risk occurs.
- (2) Minimize the damage when the risk occurs.
- (3) Compensate for damages when the risk occurs.
- (4) Know that the government adequately manages the risk.
- (5) Know that workers and regulatory agencies are trustworthy.
- (6) Know that scientific mechanisms of accidents and mishaps are well understood.

These six measures correspond to determinants of risk acceptance, as discussed in the first section. In the questionnaire, the following phrasing framed the question related to each risk:

With respect to (type of risk inserted here), how do you achieve a feeling of “an-shin”? Of the following six statements, which do you consider the first-, second-, and third-most important factors in creating a sense of “an-shin”?

An-shin in Japanese corresponds to “security” in English, but connotes, additionally, peace of mind. People may lack an-shin even when they are guaranteed security. People may have peace of mind, even when they are not guaranteed security from risks.

To ask participants directly whether they would be willing to accept certain risk events might not be appropriate, as almost all risks in our society exist as if they have already been accepted. Therefore, we measured an-shin instead of directly asking about risk acceptance. Note, that in the next section, we use the term “risk approval” for this measure of an-shin.

Table 1 Distributions and means of ranks of the six policy actions according to perceived effectiveness to increase risk approval.

		medical mishaps		food		electric appliance		nuclear plants		traffic accidents	
		freq.	%	freq.	%	freq.	%	freq.	%	freq.	%
decrease the probability that the risk occurs.	1st	46	23.0	55	27.5	51	25.5	49	24.5	103	51.5
	2nd	49	24.5	43	21.5	55	27.5	24	12.0	45	22.5
	3rd	44	22.0	39	19.5	43	21.5	48	24.0	29	14.5
	>=4th	61	30.5	63	31.5	51	25.5	79	39.5	23	11.5
	mean rank	2.91**		2.87**		2.73***		3.18**		1.98***	
minimize the damage when the risk occurs.	1st	23	11.5	19	9.5	36	18.0	42	21.0	31	15.5
	2nd	37	18.5	45	22.5	49	24.5	57	28.5	79	39.5
	3rd	48	24.0	31	15.5	47	23.5	40	20.0	30	15.0
	>=4th	92	46.0	105	52.5	68	34.0	61	30.5	60	30.0
	mean rank	3.51*		3.64		3.08*		2.91***		2.90**	
compensate for the damages when the risk occurs.	1st	6	3.0	3	1.5	8	4.0	1	0.5	15	7.5
	2nd	18	9.0	10	5.0	28	14.0	10	5.0	26	13.0
	3rd	37	18.5	39	19.5	40	20.0	24	12.0	66	33.0
	>=4th	139	69.5	148	74.0	124	62.0	165	82.5	93	46.5
	mean rank	4.24		4.40		4.02		4.59		3.65*	
know that the government adequately manage the risk.	1st	7	3.5	38	19.0	11	5.5	40	20.0	18	9.0
	2nd	17	8.5	28	14.0	8	4.0	21	10.5	13	6.5
	3rd	18	9.0	23	11.5	8	4.0	28	14.0	21	10.5
	>=4th	158	79.0	111	55.5	173	86.5	111	55.5	148	74.0
	mean rank	4.43		3.59*		4.58		3.61		4.24	
know that workers and regulatory agencies are trustworthy.	1st	99	49.5	74	37.0	30	15.0	38	19.0	20	10.0
	2nd	45	22.5	47	23.5	30	15.0	34	17.0	19	9.5
	3rd	23	11.5	30	15.0	26	13.0	20	10.0	26	13.0
	>=4th	33	16.5	49	24.5	114	57.0	108	54.0	135	67.5
	mean rank	2.12***		2.52***		3.69		3.53		4.06	
know that scientific mechanisms of accidents and mishaps are well understood.	1st	19	9.5	11	5.5	64	32.0	30	15.0	13	6.5
	2nd	34	17.0	27	13.5	30	15.0	54	27.0	18	9.0
	3rd	30	15.0	38	19.0	36	18.0	40	20.0	28	14.0
	>=4th	117	58.5	124	62.0	70	35.0	76	38.0	141	70.5
	mean rank	3.81		4.00		2.91**		3.19*		4.19	

Note: For calculating mean ranks, ranks for options that were not selected as top three options were assumed as "5.5" that is mean ranks between 4th and 7th.

*** the highest-ranked policy, ** the second-highest-ranked policy, * the third-highest-ranked policy

5. RESULTS

Table 1 shows the distributions and mean ranks of the six risk management measures, according to perceived effectiveness with regard to increased risk approval. The table shows that measures to decrease the probability of risk occurrence and measures to minimize damages from risk were evaluated as effective in increasing risk approval for the risks listed in the questionnaire. The former was the most effective in increasing risk approval for electrical appliance and traffic accidents, while the latter was the most effective in increasing risk approval for nuclear plants.

Respondents indicated that measures that decrease the expected cost of the risks (that is, measures minimizing the damage and probability of the risks) were also effective for medical mishaps and food risks. However, increasing trust in workers and regulatory agencies was evaluated as more effective than decreasing expected costs. Thus, increasing trust is the most effective risk management measure with regard to food risks and medical mishaps. Regarding electrical appliance and nuclear power plant

risks, respondents chose scientific understanding and explanation of accident mechanisms. These two risks differ from the other risks, such as traffic accidents, food, and medical mishaps, in that they are caused by more advanced technologies, which are less likely to be understood, even by risk experts.

Compensation for risk damages was not chosen as effective in increasing risk approval, except for the traffic accident risk. Respondents indicated that risk approval for traffic accidents may increase with the compensation measure. This may be because damage from traffic accidents is generally less than damage from the other risks presented in the questionnaire. Additionally, it is likely that many people will actually face traffic accidents in their lives.

6. DISCUSSION

This study sought to understand the determinants of risk acceptance. Thus, survey participants were asked which policy measures would make them feel “an-shin”, as an indicator of risk approval. The results showed that the risk management measures that would increase risk approval depended on the respective risks. The following three findings emerged from the survey.

- 1) For traffic accidents, nuclear power plants, and electrical appliance risks, the most effective measure for risk approval was that of minimizing the damage or the probability of accidents.
- 2) For food and medical mishap risks, the most effective policy was that of increasing trust in workers and regulatory agencies, rather than that of minimizing the damage or the probability of accidents.
- 3) Risk approval for electrical appliances and nuclear power plants could increase if people knew that the scientific mechanisms of accidents and mishaps were well understood.

A possible reason why trust in workers and organizations is so important for food and medical mishap risks is that medical and food workers, and their organizations, are assumed to have relatively more control over these risks, unlike the other risks presented here. Electrical appliance and nuclear accidents, on the other hand, are assumed to stem more from mechanical error than from human error. This explanation also agrees with the finding that better understanding of scientific mechanisms is important for electrical appliance and nuclear plants risks. Conversely, the mechanisms of food and medical mishaps may be simpler than problems associated with nuclear power and electrical appliances. Thus, people may believe that increasing accident prevention among workers and organizations is most effective in this case. Traffic accidents were assumed to be less under the control of workers and organizations (such as the police in charge of traffic) than accidents from medical mishaps and foods. We believe this is why trust was not considered as an important determinant for traffic accident risk approval.

These results indicate that risk acceptance cannot be fully understood by adopting a rational choice theory, which assumes that people maximize the expected benefits and/or minimize the expected costs. Minimizing damage and the probability of accidents were assumed to be just two examples of effective risk management measures for increasing risk approval or, in more commonly used words, risk acceptance. In other words, the feeling of an-shin, or risk approval, cannot be explained only by objectively achieved security. Other factors, such as scientific understanding and trust in workers and organizations, were also found to be important for increasing risk acceptance.

This indicates that those who wish to increase the public's risk acceptance should appear trustworthy and try to understand the scientific mechanisms of accidents; they should also try to minimize risk damage and probability. Trust is important, especially for risks where accidents can be prevented relatively easily by workers and/or organizations. These risks include those associated with food and medical mishaps. Scientific understanding of risk mechanisms is also important for risk acceptance, especially for risks involving mechanisms that are relatively complex, such as nuclear

power and electrical appliance risks.

Acknowledgements:

This paper was also presented at *the First International Symposium on Systems & Human Science: For Safety, Security, and Dependability*, Osaka, Japan, 2003 and was included in its proceedings (pp. 81-85).

References:

- Dawes, R. M., Behavioral decision making and judgment. In D. T. Gilbert, S. T. Fiske, & G. Lindzey (Eds.), *Handbook of Social Psychology* (4th ed.), McGraw-Hill, Boston, MA, pp. 497-548, 1998.
- Fischhoff, B., Slovic, P., Lichtenstein, S., Read, S., & Combs, B., How safe is safe enough? A psychometric study of attitudes toward technological risks and benefits, *Policy Sciences*, 9, pp. 127-152, 1978.
- Payne, J. W., Bettman, J. R. and Johnson, E. J., *The Adaptive Decision Maker*, Cambridge University Press, New York, 1993.
- Kahneman, D., Knetsch, J.L., and Thaler, R.H., Anomalies: The endowment effect, loss aversion and status quo bias, *Journal of Economic Perspectives*, 5, pp. 193-206, 1991.
- Kreps, D., Corporate culture and economic theory. In J. Alt and K. Shepsle (Eds.), *Perspectives on Positive Political Economy*, Boston: Harvard Business School Press, 1990.
- Slovic, P., The construction of preferences. *American Psychologist*, 50, pp. 364-371, 1995.
- Slovic, P., Fischhoff, B., and Lichtenstein, S. Cognitive Processes and Societal Risk Taking. In J.S. Carroll, & J.W. Payne (Eds.), *Cognition and Social Behavior*, Potomac, MD: Lawrence Earlbaum, 1976.
- Von Neumann, J., and Morgenstern, O., *Theory of Games and Economic Behavior*, 2nd ed., Princeton University Press, Princeton, 1947.
- Savage, I.R., *The Foundations of Statistics*, Wiley, New York, 1954.

USE OF DIGITAL CITY FOR SEISMIC HAZARD REPRESENTATION

S. Midorikawa¹⁾, H. Miura²⁾, and S. Inoue³⁾

1) Professor, Dept. of Built Environment, Tokyo Institute of Technology, Japan

2) Post-doctoral Research Fellow, Center for Urban Earthquake Engineering, Tokyo Institute of Technology, Japan

3) Engineer, Aero Asahi Corporation, Japan

smidorik@enveng.titech.ac.jp, hmiura@enveng.titech.ac.jp, satoshi-inoue@aeroasahi.co.jp

Abstract: This paper describes an attempt on representation of regional seismic hazard by using the digital city to improve disaster consciousness of citizens. The digital city of Yokohama city is constructed on the 3D-GIS system, and the seismic hazard information is represented in the digital city. The user will find delight in learning the regional seismic hazard by flying over the digital city.

1. INTRODUCTION

After the 1995 Kobe earthquake, various earthquake disaster mitigation programs have been planned and carried out. In the mitigation programs, the role of citizens and communities as well as the governments is important. Therefore, the Japanese government plans to promote the comprehensive disaster mitigation programs as the national movement (Central Disaster Prevention Council, 2005). Many of citizens, however, show no strong concern about the disaster mitigation activities. In order to deepen their concern, one of the key issues is to provide information on regional seismic hazard to them. The seismic hazard maps have been developed mainly for engineers and government officers, and are not necessarily attractive for citizens. The visualization technique will be a useful tool for getting their interest in the seismic hazard map. In this paper, we show an attempt on representation of regional seismic hazard by using the digital city to improve disaster consciousness of citizens.

2. EFFECTS OF SEISMIC HAZARD MAP ON DISASTER CONSCIOUSNESS OF CITIZENS

The seismic hazard maps will provide basic information for 1) improvement of earthquake awareness of citizens, 2) seismic design of structures, 3) strategies of disaster mitigation planning, and 4) seismic risk evaluation of facilities. When a citizen look the seismic hazard map, he thinks that "Is my house in the red zone?" and "If my house is in the red zone, what should I do?" (Olshansky, 2000). To reply his questions, the map should be the micro-scale one. The conventional seismic hazard maps are too large in scale to catch citizen's strong interest. As an advanced map for citizens, the detailed hazard map will be necessary for each region.

For this purpose, the city of Yokohama published "Yokohama City Shake Map" on June, 2001 (Midorikawa, 2005). More than 15,000 borehole data in the city were compiled. The soil profile sections are drawn from the borehole data and the geomorphological information, and 268 types of the soil profile models are constructed. For the mapping, the 50m mesh system is adopted because of

strong spatial variation of the geomorphological conditions in the city.

Using the detailed soil data, the deterministic ground shaking maps are computed for several scenario earthquakes. About 100,000 copies were printed and distributed to citizens. As the results, the numbers of applicants for seismic performance appraisal of wooden house and for seismic retrofiting subsidies by the city increased significantly. This is an evidence of improvement of earthquake awareness of citizens by the map. Central and local governments are stimulated by the experience of Yokohama and decided to start the detailed mapping study.

Although such detailed maps get more interest of citizens, the number of citizens who have interest in the maps seems to be still limited. For example, in a class of earthquake education at a junior high school, more than half of students show interest in the Yokohama map, but some of them show no interest (Morioka and Midorikawa, 2004). This means that more attractive representation of regional seismic hazard is necessary for the spread of knowledge on earthquake disaster.

3. CONSTRUCTION OF DIGITAL CITY

For more attractive representation of regional seismic hazard, we constructed the digital city of the city of Yokohama. The following data are compiled;

1) Natural environment data:

- 1-a) line data of rivers and coastlines
- 1-b) digital elevation model with 1m mesh
- 1-c) soil profile model with 50m mesh
- 1-d) geomorphological land classification data with 250m mesh
- 1-e) digital aerial photograph

2) Built environment data:

- 2-a) line data of administration boundaries, roads and railways
- 2-b) building GIS data with the attribute such as story number, structure and use
- 2-c) pattern texture of building surface
- 2-d) census data with 250m mesh
- 2-e) land use data with 100m mesh

In the surrounding area such as Tokyo and other cities, the similar data with the lower resolution are compiled as well as the LANDSAT images. Figure 1 shows the view of the digital city on the 3D-GIS system. In the figure, the digital aerial photograph is pasted on the ground surface with elevation. The buildings with pattern texture are located on the ground. The realistic texture is used for some landmark buildings. The user can fly over the digital city by the operation buttons on the lower right side of the screen.

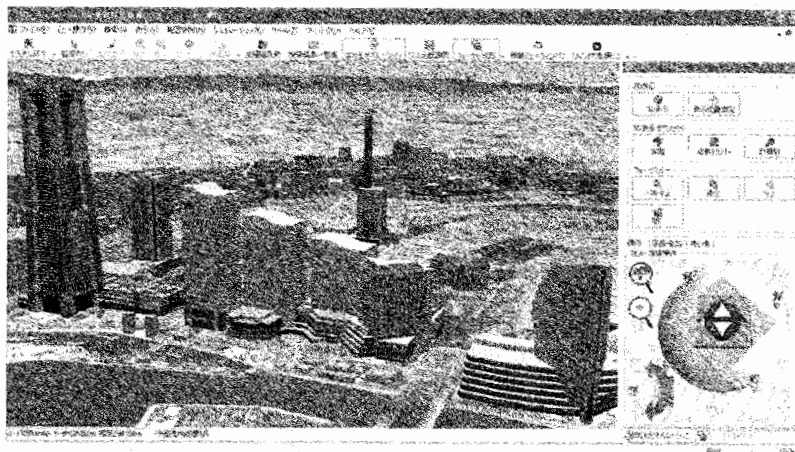


Figure 1 View of Digital City at the Central Part of Yokohama

4. EVALUATION AND REPRESENTATION OF SEISMIC HAZARD

In the system, the data on earthquakes and active faults is compiled as the basis for supposition of a scenario earthquake for seismic hazard evaluation. For a scenario earthquake, the seismic intensity is computed by the empirical attenuation relationship considering the local soil condition (Matsuoka and Midorikawa, 1995). For the Yokohama city area and the surrounding area, the intensities are given for each 50m mesh and 250m mesh, respectively. The liquefaction potential is also computed for each mesh considering the seismic intensity and soil condition (Matsuoka and Midorikawa, 1995). The slope failure susceptible area is extracted from the high-resolution digital elevation model (Miura et al., 2005). The slope failure potential for the susceptible area is roughly evaluated based on the height and slope angle of the area together with the seismic intensity of the corresponding mesh.

Figure 2 shows the seismic intensity map of the hypothetical Yokohama earthquake (M6.5). This type of the map has been published as the hazard map and is useful to understand the gross outline of the effects of the earthquake. For citizens, however, it is difficult to imagine the effects of the earthquake to their live from the map.

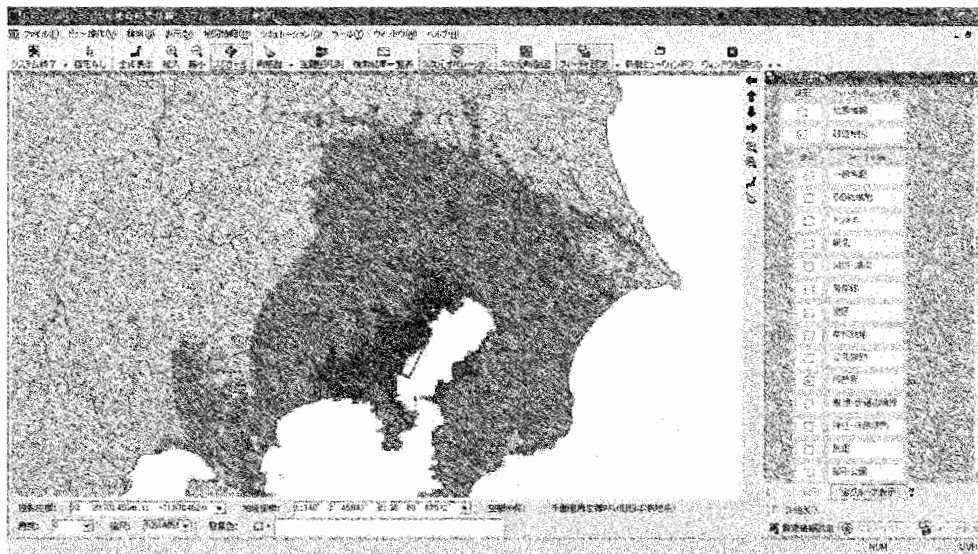


Figure 2 Conventional Seismic Hazard Map

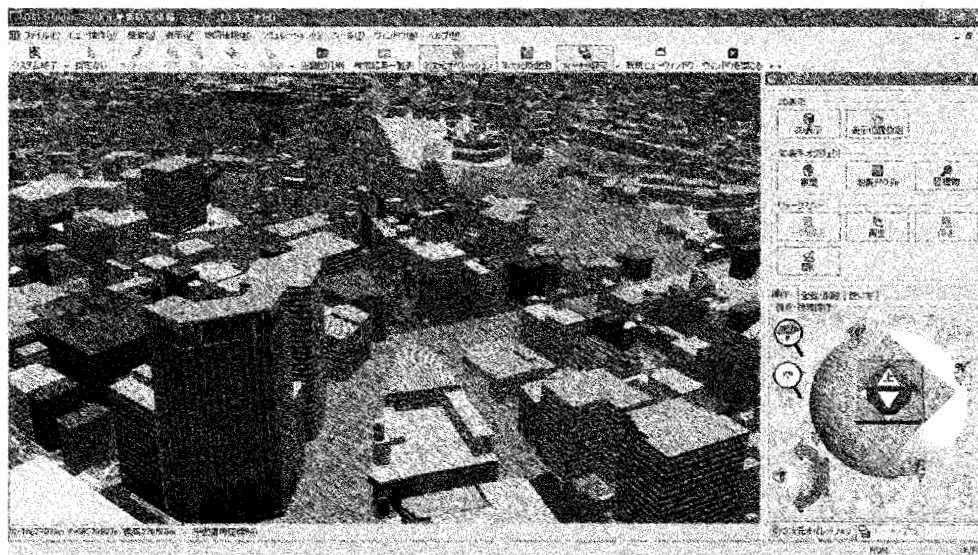


Figure 3 Seismic Hazard Map in Digital City

For more attractive and friendly representation of the seismic hazard, the information on the seismic hazard is incorporated into the digital city. Figure 3 is an example of the seismic hazard representation in the digital city. In the figure, the color on the surface shows the seismic intensity estimated. The dotted and hatched areas show the high liquefaction and slope-failure potential areas, respectively. The user will find delight in learning the regional seismic hazard by flying over the digital city.

5. CONCLUDING REMARKS

In this paper, we show a prototype of the digital city for attractive representation of regional seismic hazard. The seismic risk such as building damage, road blockade, and earthquake fire should be included in the digital city in order to catch the image of the urban earthquake disaster more realistically. Also earthquake education programs using the digital city system should be developed for improving disaster consciousness of citizens.

Acknowledgements:

The building GIS data and soil profile model are provided by the city of Yokohama. This study is financially supported by the 21st Century COE program "Evolution of Urban Earthquake Engineering" and the Grant-In-Aid for Scientific Research (Scientific Research B) "Construction of Digital City for Disaster Consciousness of Citizens".

References:

- Central Disaster Prevention Council (2005), <http://www.bousai.go.jp/kokuun/index.html> (in Japanese).
- Matsuoka, M. and Midorikawa, S. (1995), "GIS-Based Integrated Seismic Hazard Mapping for a Large Metropolitan Area", *Proceedings of the Fifth International Conference on Seismic Zonation*, 2, 1334-1341.
- Midorikawa, S. (2005), "Dense Strong-Motion Array in Yokohama, Japan, and Its Use for Disaster Management", *Directions in Strong Motion Instrumentation, NATO Science Series*, 58, 197-208.
- Miura, H., Midorikawa, S. and Inoue, S. (2005), "Extraction of Slope Failure Susceptible Areas in Urban Area Using High-Resolution Digital Elevation Model", *Journal of Social Safety Science*, 7, 299-306 (in Japanese with English abstract).
- Morioka, H. and Midorikawa, S. (2004), "Education to Improve Earthquake Emergency Preparedness in the Community – Education Software for Junior High School Students–", *Summaries of Technical Papers of Annual Meeting, Architectural Institute of Japan*, F1, 319-320 (in Japanese).
- Olshansky, R.B. (2000), "Is My House in the Red Zone? Local Communities and Seismic Hazard Mapping," *Proceedings of the Sixth International Conference on Seismic Zonation (CD-ROM)*.

RESEARCH ON WEIGHT REDUCTION OF COMPOSITE PC BEAMS USING PRESTRESSED UFC TRUSS

H. Murata¹⁾, J. Niwa²⁾, E. Chigira³⁾ and T. Miki⁴⁾

1) Ph.D. Candidate, Department of Civil Engineering, Tokyo Institute of Technology, Japan

2) Professor, Department of Civil Engineering, Tokyo Institute of Technology, Japan

3) Master Student, Department of Civil Engineering, Tokyo Institute of Technology, Japan

4) Assistant Professor, Department of Civil Engineering, Tokyo Institute of Technology, Japan

hmurata@cv.titech.ac.jp, jniwa@cv.titech.ac.jp, e-chigi@cv.titech.ac.jp, mikitomo@cv.titech.ac.jp

Abstract: In the improvement of seismic performance of a bridge structure, the weight reduction of a girder is one of the significant factors. To reduce the self-weight of girder, composite prestressed concrete (PC) girders, which web is made of steel truss, have been recently developed. However, due to a problem of durability in steel truss, composite PC girders using Ultra High Strength Fiber Reinforced Concrete (UFC) truss as web have been introduced in this study. UFC provides highly advanced mechanical properties, such as high compressive strength as 200N/mm^2 , high durability and high ductility. Therefore, UFC can be applied, instead of using steel, for solving the problem of durability. By taking the advantages of compressive strength in UFC, high prestress can be applied to UFC. The self-weight of girders using UFC can be reduced as well as the steel truss girder. The aim of this research is to investigate the mechanical properties of composite PC members using prestressed UFC truss and evaluate the effect of weight reduction. Then, composite PC beams are designed and experiments are carried out. In addition, the level of weight reduction of a web member is examined.

1. INTRODUCTION

For the improvement of seismic performance of bridge structures, the weight reduction of girders is one of the effective factors. Composite prestressed concrete (PC) girders, of which web member is made of steel truss, have been recently developed. Because of high strength of the web member, its cross sectional area can be reduced. As a result of volume reduction, the total weight of a bridge girder is also reduced.

Ultra High Strength Fiber Reinforced Concrete (UFC) (Rechard et al. 1994) has been developed since 1994. This material provides high compressive strength around 200N/mm^2 with high ductility because of the existence of steel fiber reinforcement. Moreover, due to high workability, variously shaped member can be made.

In this study, a composite PC girder utilizing UFC truss as web members is focused as shown in Figure 1. In case that UFC is used for web members, advantages are as follows: the complexity in the construction can be solved because web members are precast; the total cost of construction can be reduced; the self-weight of girders can be extremely reduced compared with normal PC girders. Then, in order to clarify the mechanical properties of this composite PC structural member with UFC truss web members, composite PC beams utilizing UFC truss as precast web members were constructed, and the loading test was carried out. The parameter considering in this study was whether prestress is needed to provide in UFC truss or not.

Finally, in point of weight of web members, the composite PC beams were compared with normal PC beams, which provide the same load carrying capacity, in order to discuss the reduction in weight.

2. EXPERIMENTS

2.1 Experimental Procedures

In this study, 2 specimens of composite PC beams using UFC as web members were prepared: named as HT and PHT as listed in Table 1. The parameter which was considered in this study was prestress in UFC truss. The thickness of web members is 40mm in both cases. Figure 2 illustrates joint methods of each specimen, which are the reinforcing bars with horizontal and vertical keys joint as shown in the work of Kawaguchi et al. (2003) and Sivaleepunth et al. (2004).

The test of simply supported composite PC beams under two points load was performed to compare the mechanical properties depending on prestress in UFC truss. The vertical force, P , was applied monotonically to the specimen through two loading points. In order to reduce the friction at the supports, friction-reducing pads, i.e., two Teflon sheets sandwiching the grease, were inserted between the specimen and the support plates.

In web members of composite PC beams, UFC was introduced because of its superior strength (compressive strength=200N/mm²). It results in the significant weight reduction and provides nearly limitless freedom of structural member shape as truss form. The mix proportion of UFC is shown in Table 2. The mixing time of UFC is about 12-14 minutes. There was no segregation and sinking of steel fiber from the matrix due to its high viscosity. After casting, the formwork was covered by plastic sheet and put into the chamber, in which the temperature was controlled at 20°C for 48 hours. After the formwork was removed, the specimens were cured again in air with 100% humidity at 90°C for 48 hours.

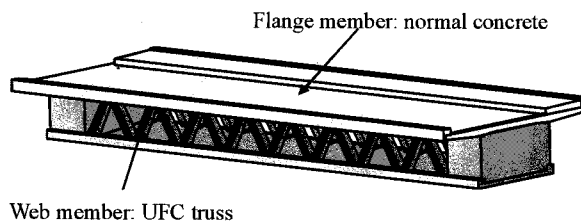


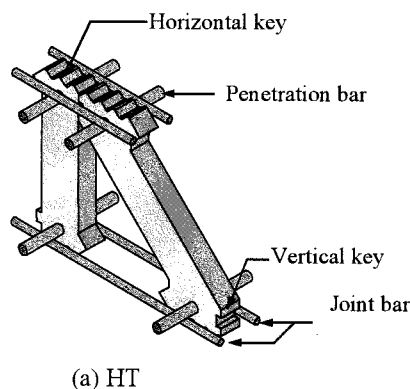
Figure 1 Composite PC Girder Using UFC Truss

Table 1 Specimen Names

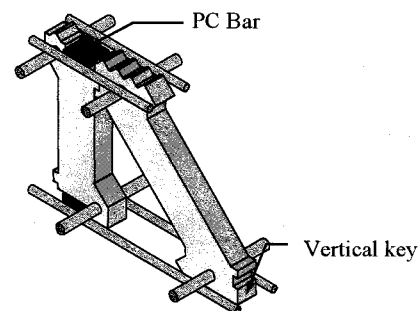
Specimen name	Prestress in UFC truss	Thickness of web members
HT	0N/mm ²	40mm
PHT	10N/mm ²	

Table 2 Mix Proportion of UFC [kg/m³]

Water	Premix	Steel fiber	Superplasticizer
180	2254	157	22

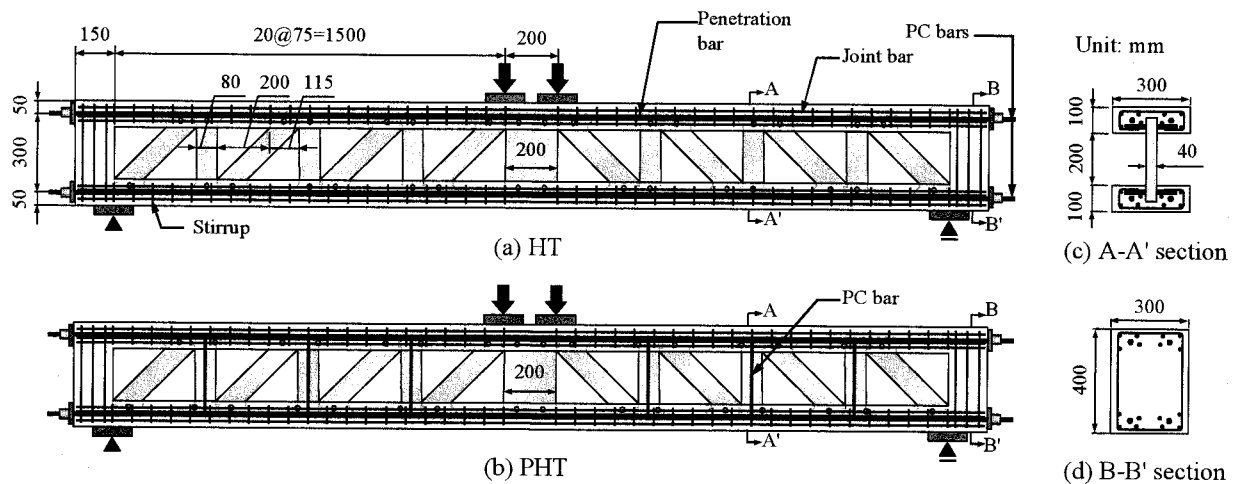


(a) HT



(b) PHT

Figure 2 Details of UFC Trusses



PC bars in flange: $A_p=132.7\text{mm}^2$ $f_y=1249\text{N/mm}^2$	PC bars in UFC trusses: $A_p=66.5\text{mm}^2$ $f_y=1251\text{N/mm}^2$
Stirrups: $A_s=71.3\text{mm}^2$ $f_y=349\text{N/mm}^2$	Penetration bars: $A_s=286.5\text{mm}^2$ $f_y=345\text{N/mm}^2$ Joint bars: $A_s=126.7\text{mm}^2$ $f_y=347\text{N/mm}^2$

Figure 3 Outlines of Specimens

Table 3 Mix proportion of Concrete

G_{\max} [mm]	W/C [%]	s/a [%]	Unit weight [kg/m ³]					
			Water	Cement	Fine aggregate	Coarse aggregate	Super-plasticizer	Defoaming agent
15	30.0	53.2	170	567	857	766	7.93	5.67

Note G_{\max} : maximum size of coarse aggregate, W/C: water-cement ratio in weight, s/a: sand aggregate ratio in volume

The outlines of experiments and properties of specimens were summarized in Figure 3. For all specimens, the shear span was set to be 1500mm, effective depth was 350mm and shear span to effective depth ratio was 4.29. In all specimens, four PC bars (cross sectional area $A_p=132.7\text{mm}^2$, yield strength $f_y=1249\text{N/mm}^2$) were arranged to both upper and lower flanges (two bars per each flange). In PHT, six PC bars ($A_p=66.5\text{mm}^2$, $f_y=1251\text{N/mm}^2$) were arranged and 10N/mm^2 prestress in compression was applied to each vertical members (see Figure 3(b)). The longitudinal reinforcement ratio was set to be 1.86%. For all the specimens, the stirrup (cross sectional area $A_s=71.3\text{mm}^2$, $f_y=349\text{N/mm}^2$) was used as the shear reinforcement in both upper and lower flanges. The shear reinforcement ratio for flanges was 0.63%.

Table 3 tabulates the mix proportion of concrete used in the flange. Before casting of concrete into the flange, precast UFC web members were arranged and connected with each other by using epoxy glue. After casting the flange part, the specimens were cured for 7 days. Then, the prestressing force was introduced to both upper and lower flanges in order to generate 3N/mm^2 and 5N/mm^2 in compression as the upper and lower fiber stresses, respectively. For all the specimens, grouting of cement paste was performed. After that, specimens were cured for another 7 days, thus curing period of concrete in the flange was totally 14 days before loading test.

2.2 Results and Discussions

Table 4 tabulates the results of experiments. From the experimental results of HT and PHT, the loading capacity were 132kN and 193kN, respectively. Figure 4 illustrates the load-deflection curves of composite PC beams. In HT, from the beginning, the curves rose up to the first peak load. After that the loads dropped until it reached the stable condition, and then the loads gradually increased again. On the other hand, in PHT, the load kept on rising until a vertical truss pulled out from lower

Table 4 Loading Capacity of Composite PC Beams and Material Strength

Specimen	Loading capacity [kN]	Concrete in Flange			UFC in Web		
		Compressive strength [MPa]	Tensile strength [MPa]	Young's modulus [GPa]	Compressive strength [MPa]	Tensile strength [MPa]	Young's Modulus [GPa]
HT	132	82.5	4.4	34.1	204	9.7	53.1
PHT	193	76.7	4.3	33.0	202	9.5	52.3

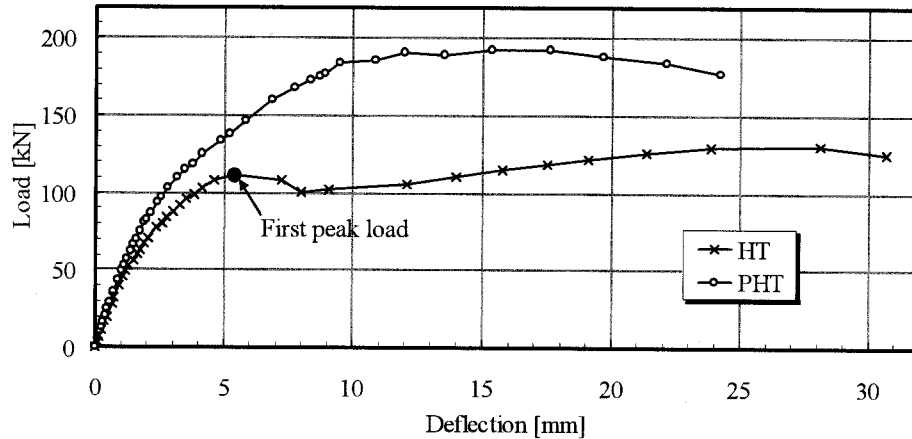


Figure 4 Load-Deflection Curves

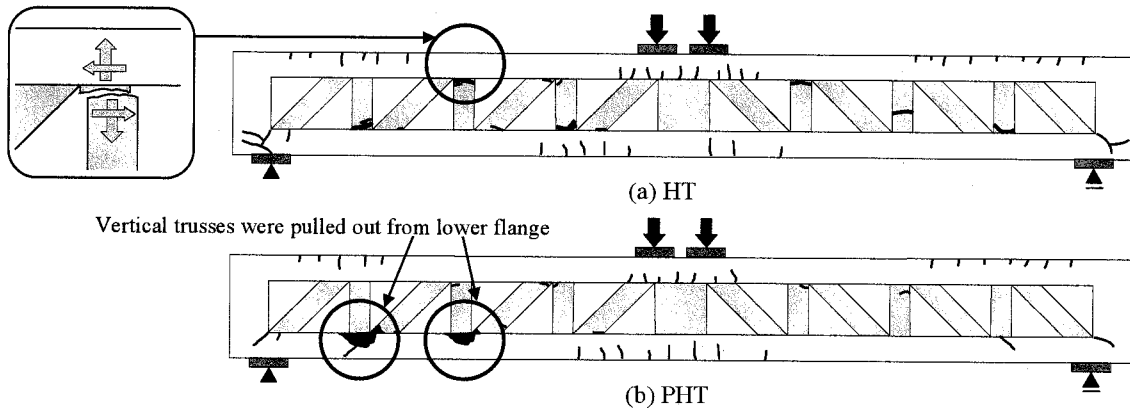


Figure 5 Crack Patterns

flange without the decrease in load. It can be noted that PHT has higher stiffness and higher load carrying capacity. In both cases, it should be noted that composite PC beams using UFC web members have very high ductility.

Figure 5 illustrates the crack patterns of specimens. First cracking loads of HT and PHT were 80.3kN and 88.2kN, respectively. In HT, first crack occurred in a UFC vertical truss. However, in PHT, the first crack arose in the lower flange.

In HT, crack was propagated in the vertical truss. When the crack width increased about 5mm, the sliding between the upper flange and UFC truss occurred as shown in Figure 5(a). It can be explained that this sliding caused the decrease in first peak load in Figure 4. After that, cracks occurred in the upper fibre of upper flange member in both side and the inner angle in the lower corner of concrete frame.

In PHT, crack was propagated in the lower flange. Then, 2 joints between vertical members and diagonal members in lower flange and vertical members were pulled out from the lower flange (see

Figure 5(b)). After that, cracks occurred in the upper fibre of upper flange member in both side and the inner angle in the lower corner of concrete frame as in the case of HT.

Thus, it can be understood that the prestress in vertical members significantly influence the failure mode of composite PC beams. Applying prestress to vertical truss is highly effective for improvement of load carrying capacity of composite PC beam.

3. COMPARISON WITH NORMAL PC BEAMS

3.1 Design of Normal PC Beams

I-shaped PC beams which have the same load carrying capacity as all composite PC beams were designed in order to examine the level of weight reduction of a web member. The characteristics of I-shaped PC beams are the same as in the composite PC beams as tabulated in Table 5 and the outlines of I-shaped PC beams are shown in Figure 7. The shear reinforcement ratio of I-shaped PC beams was set to be 0.30%. Prestressing force was 150kN just the same as composite PC beams.

The shear carrying capacity, V_u , of I-shaped PC beams can be obtained from the following Eqs. (1), (2) and (3) (JSCE code 2002).

$$V_u = V_c + V_s \quad (1)$$

$$V_s = \frac{A_w f_{wy} j d (\sin \alpha + \cos \alpha)}{s} \quad (2)$$

$$V_c = 0.2(f_c')^{1/3} \left(\frac{1000}{d} \right)^{1/4} (100 p_w)^{1/3} b_w d \left(1 + \frac{2M_o}{M_u} \right) \quad (3)$$

where, A_w : cross sectional area of stirrup [mm^2], f_{wy} : yield strength of stirrup [MPa], j : 1/1.15, d : effective depth [mm], α : inclined angle of stirrup to axis of beam ($= 90^\circ$), s : spacing of stirrup [mm], f_c' : compressive strength of concrete [MPa], p_w : longitudinal reinforcement ratio ($= A_s / (b_w d)$), b_w : web thickness of RC beam [mm], M_o : decompression moment [N·m] and M_u : ultimate moment [N·m].

Table 5 Characteristics of I-shaped PC beam and its Materials

Compressive strength	f_c' [N/mm ²]	60
Shear span	a [mm]	1500
Effective depth	d [mm]	350
Cross sectional area of longitudinal reinforcement ^{*1}	A_s [mm ²]	1058
Cross sectional area of stirrup	A_w [mm ²]	142.6
Yield strength of stirrup	f_{wy} [N/mm ²]	295

*1 Including PC bars (cross sectional area = 265.4mm²)

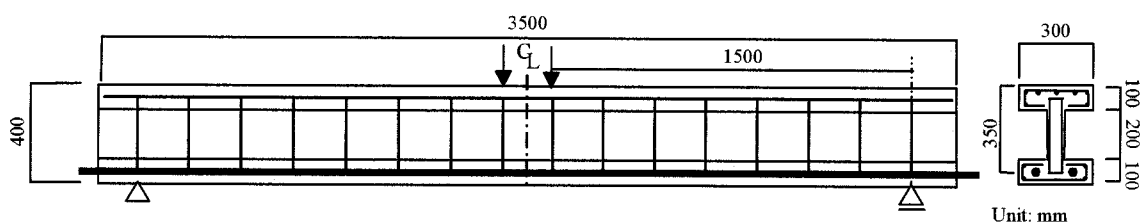


Figure 6 Outline of I-shaped PC beam

Table 6 Comparison of Results

Specimen	Maximum Load [kN]	Web thickness of I-shaped PC beams b_w [mm]	Web weight of I-shaped PC beams A [kg]	Web weight of composite PC beams B [kg]	Rate of weight reduction (A-B)/A [%]
HT	132	56.8	90.9	32.0	64.8
PHT	193	95.3	152.5	32.0	79.0

By setting the value of $2V_u$ to be corresponding to the maximum loads of composite PC beams, b_w (web thickness of I-shaped PC beams) was determined. From the densities of PC and UFC of 2.5t/m^3 , the weights of a web member of I-shaped PC beams and composite PC beams were compared.

3.2 Comparison of Weight

Table 6 shows the results of I-shaped beams with the same load capacity as composite PC beams. It was found that the weight of a web member can be reduced to about 65-79%. Especially, PHT can extremely reduce the weight of a web member. It means that the composite PC girder using prestressed UFC truss can make the large contribution to the weight reduction of a web member.

This implies that the self weight of a web member of the composite PC girder using prestressed UFC members is significantly reduced compared with normal PC girders. So, the seismic performance of composite PC bridge structures using prestressed UFC truss can be enormously improved.

4. CONCLUSIONS

The study of mechanical properties of composite PC beams using UFC truss and that using prestressed UFC truss was carried out. In addition, by the experiment, the level of weight reduction of a web member by using UFC truss was investigated in comparison with normal PC beams.

The conclusions of this study are as follows:

- 1) From the experimental results, it is turned out that the prestress in UFC truss significantly influence the failure mode of composite PC beams.
- 2) By comparing composite PC beams with I-shaped PC beams having the same resistance, the weight of a web member can be reduced 65-79% when using the UFC. Especially, composite PC beam using prestressed UFC truss can extremely reduced the weight of a web member.
- 3) The seismic performance of composite PC bridge structures using prestressed UFC truss can be enormously improved.

Acknowledgments:

Sincere gratitude is expressed to Taiheiyo Cement Corporation and Oriental Construction Co., Ltd. for their cooperation. The authors also would like to express their gratitude to the COE program for providing financial support to accomplish this research.

References:

- Richard, P. and Cheyrezy, M. H. (1994), "Reactive Powder Concretes with High Ductility and 200-800 MPa Compressive Strength.", *ACI Spring Convention*, SP144-24, 507-517.
- Kawaguchi, T., Kakei, T., Katagiri, M. and Niwa, J. (2003), "Experimental Research on Mechanical Properties of Composite PC Members Using UHSFRCC.", *Proceedings of the JCI*, **25**(2), 1987-1992. (in Japanese)
- Sivaleepunth, S., Murata, H., Niwa, J. and, Kawaguchi, T. (2004), "Experimental Study on Composite PC Beams by Applying UFC Truss as Web Member.", *Proceeding of the JCI*, **26**(2), 1801-1806.
- JSCE (JSCE CODE) (2002), "Structural Performance Verification, Standard Specification for Concrete Structures."

APPLICABILITY OF DESIGN CODE AND SIMPLIFIED TRUSS MODEL FOR SHEAR CARRYING CAPACITY OF EXTERNALLY PRESTRESSED CONCRETE BEAMS

C. Sivaleepunth¹⁾, J. Niwa²⁾ and T. Miki³⁾

1) *PhD. Candidate, Graduate School of Civil Engineering, Tokyo Institute of Technology, Japan*

2) *Professor, Department of Civil Engineering, Tokyo Institute of Technology, Japan*

3) *Assistant Professor, Department of Civil Engineering, Tokyo Institute of Technology, Japan*
chunyakom@cv.titech.ac.jp, jniwa@cv.titech.ac.jp, mikitomo@cv.titech.ac.jp

Abstract: Four externally prestressed concrete T-beams were tested to failure in order to determine the influence of compressive stress in concrete due to prestress and amount of transverse reinforcements on shear type of failure. The test results have shown that the beams having higher compressive stress provide higher shear carrying capacity and flatter inclination angle of diagonal crack. However, if the transverse reinforcements are introduced, the diagonal crack inclination becomes steeper. In this study, JSCE specification design code and simplified truss model are applied for examining its applicability on the prediction of the shear carrying capacity of externally prestressed concrete beams. It is found that there is a requirement to modify those prediction equations in order to obtain higher accuracy.

1. INTRODUCTION

By taking the advantages of prestressing force, the prestressed concrete members can be perfectly utilized to respond the requirements of high shear resistance and reduction of dead load to the substructures. When the earthquake occurred, it is necessary to confirm that the shear failure of prestressed concrete superstructures does not take place before the development of hinge in the columns as illustrated in Figure 1. Recently, externally prestressed concrete beams, in which the prestressing tendons are placed outside the concrete section and transfer the load to the concrete through end anchorages and deviators, have been recognized as an effective method for the modern construction of segmental box girder bridges and in the strengthening of existing structures. Their many advantages include the simplicity in constructions, aesthetic appeal and rapid construction. With the widely use of this type of structure, an examination of the design and analysis of such structures with high accuracy in prediction of shear carrying capacity is needed.

In conventional prestressed concrete slender beams (i.e. beams prestressed with bonded tendons), where the shear span to effective depth ratio, a/d , is greater than or equal to 2.5, most of them are found to fail in shear compressive mode of failure, and their shear carrying capacity can be examined as mentioned by JSCE (JSCE 2002) design code based on the empirical equation without the clarification of effect of significant factors. Later, Lertsamattiyakul (Lertsamattiyakul et al. 2005) conducted the parametric study by using the finite element method (FEM) and proposed the simplified truss model in order to evaluate the shear carrying capacity of prestressed concrete slender beams without transverse reinforcement. The influential parameters, such as lower fiber stress, upper fiber stress, etc., were found to have a significant effect on the change of the inclination of concentrated stress flow, which is a key to solve the problem of shear compression failure mode. The model was found to be able to predict the several experimental results of beams prestressed with bonded tendons very well. However, this model does not extend to solve the problem of externally prestressed

concrete beams with and without transverse reinforcement.

This study was therefore carried out to investigate the deficiency in the prediction of shear capacity and the inclination of diagonal cracks with emphasis on the influences of compressive stress in upper and lower extreme fibers of concrete due to the prestress, and the amount of transverse reinforcements. The objectives of this study are to investigate the influence of compressive stress in concrete due to prestress and the amount of transverse reinforcements in externally prestressed concrete beams on the shear carrying capacity and the inclination of diagonal cracks, to examine the failure mechanisms of externally prestressed concrete beams from the experimental study with the simplified truss model (Lertsamattiyakul et al. 2005), and to check the capability of JSCE design code (JSCE 2002), and the simplified truss model for externally prestressed concrete beams. This paper compared the shear carrying capacity from the test with JSCE design code (JSCE 2002) and the simplified truss model (Lertsamattiyakul et al. 2005).

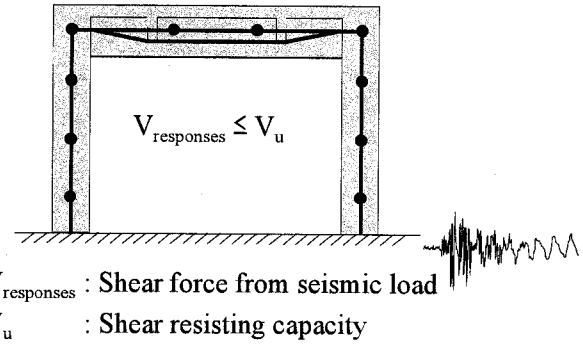


Figure 1 Seismic performance of externally prestressed concrete girder

2. LITERATURE REVIEWS

In JSCE design code, the shear carrying capacity, V_u , is separated into two components as

$$V_u = V_{pc} + V_s \quad (1)$$

where V_{pc} is the shear carrying capacity for the contribution of concrete and prestressing force; V_s is the shear carrying capacity for the contribution of vertical stirrups.

Decompression moment method (M_0 method), which is recommended as the standard specification in JSCE Design Code (JSCE 2002), mainly considers the influence of prestressing in term of lower extreme fiber stress, σ_l . The decompression moment is adopted to calculate the factor expressing the effect of axial force, β_n , and this factor is assessed from the empirical equation as expressed in Eq. (2). The expression for shear carrying capacity from the contribution of concrete and prestressing force due to the diagonal tension failure, V_{pc} , can be expressed as in Eq. (3):

$$\beta_n = 1 + 2 \frac{M_0}{M_u} \leq 2.0 \quad (2)$$

$$V_{pc} = \beta_n \cdot V_c \quad (3)$$

in which,

$$V_c = 0.2(f'_c)^{\frac{1}{3}}(100\rho_w)^{\frac{1}{3}}\left(\frac{1000}{d}\right)^{\frac{1}{4}}b_wd \quad (4)$$

where, M_0 is decompression moment, which required to make the lower fiber stress of the member become zero; M_u is ultimate moment. V_c is the shear carrying capacity for contribution of concrete; b_w is the width of web; d is the effective depth; f'_c is the compressive strength of concrete; ρ_w is the longitudinal reinforcement ratio.

$$V_s = \frac{A_v f_{yv} d}{s} \quad (5)$$

where A_v is the cross sectional area of two legs of a closed stirrup; f_{yv} is the yield strength of stirrups; s is the spacing of stirrups.

The schematic diagram of the simplified truss model (Lertsamattiyakul et al. 2005) for analyzing the shear carrying capacity of prestressed concrete beams without transverse reinforcement is illustrated in Figure 2. The model consists of 7 nodes and 11 elements for flexural compression members, transverse tension members, diagonal compression members and flexural tension members. The model is fixed in X-direction at both nodes along the center line and in Y-direction at the support. The parameter m is used in the model to represent the inverse of concentration of stress flow slope, where $m = \cot\theta$ and θ is an angle of the concentration stress flow. From the parametric study of the prestressed concrete beams without transverse reinforcement, the equation for estimating the value of m can be expressed as the following:

$$m = 2.55 \left(\left(1 + 0.2 \frac{\sigma_u}{\sigma_u + \sigma_l} \right) \sigma_l \right)^{-\frac{3}{5} \left(\frac{b_f}{b_w} \right)^{-1}} \left(\frac{a}{d} \right)^{\frac{1}{5} \left(\frac{b_f}{b_w} \right)^{-1}} \left(\frac{b_f}{b_w} \right)^{-\frac{3}{5}} \left(\frac{f'_c}{100} \right)^{\frac{3}{5}} \quad (6)$$

where σ_u is the upper extreme fiber stress; σ_l is the lower extreme fiber stress; b_f is the width of flange; a is the shear span length.

By considering the effects of bearing plates and effective depth, the values of the horizontal thickness in the vicinity area of a loading point, t_l , and support, t_s , are expressed in Eqs. (7) and (8). For the cross sectional area of each compression member, A_i , i.e. {1}-{4}, it can be obtained as the value of t_s for {1} and {2} and the value of t_l for {3} and {4} multiplied with the width of web and its inclination.

$$t_l = 2(r_l + 0.1d) \left(\frac{b_f}{b_w} \right)^{\frac{1}{5}} \quad (7)$$

$$t_s = 2(r_s + 0.1d) \left(\frac{b_f}{b_w} \right)^{\frac{1}{5}} \quad (8)$$

where r_l is the width of loading plate and r_s is the width of support plate.

The value of compression softening parameter, η , affected by the existence of cracks is also considered in order to compute the resisting capacity of each member, and can be simply expressed as in Eq. (9).

$$\eta = -0.3 \left(\frac{f'_c}{100} \right) + 0.7 \quad (9)$$

The resistance capacity of each diagonal compression member, R_i , can be obtained from following expression.

$$R_i = \eta f'_c A_i \sin \theta_i \quad (10)$$

The member force of each member due to the external shear force can be determined based on

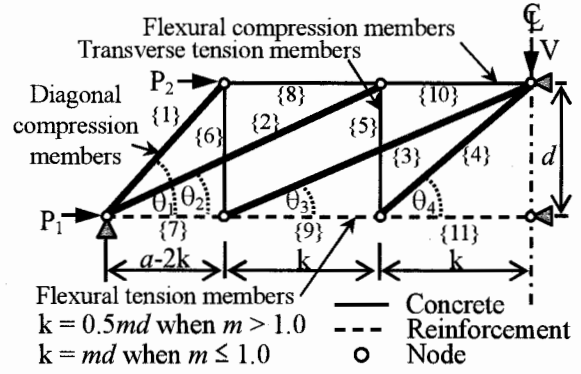


Figure 2 Schematic diagram of the simplified truss model

Castigliano's second theorem. The redundant member force, X_i , can be obtained when the strain energy, U is minimized as summarized in Eqs. (11) and (12). The critical diagonal compression member can be determined when the ratio of F_i and R_i becomes the maximum and equal to 1.0.

$$\frac{\partial U}{\partial X_i} = 0 \quad (11)$$

$$\sum_{i=1}^{11} \left[F_i \frac{\partial F_i}{\partial X_i} \frac{L_i}{E_i A_i} \right] = 0 \quad (12)$$

where $\frac{\partial F_i}{\partial X_i}$ is the unit force, L_i and E_i are the length and stiffness of each member, respectively.

Although the simplified truss model is proven to provide simplicity and high accuracy (mean = 1.0; coefficient of variation = 0.13) in the prediction on shear carrying capacity of concrete beams prestressed with bonded prestressing bars without transverse reinforcement (Lertsamattiyakul et al. 2005), it is not checked to extend this model to the externally prestressed concrete beams with and without transverse reinforcement, since the prestressing tendons in externally prestressed concrete beams are unbonded to the concrete, and when the beams are subjected to an externally applied load, the external tendons are free to move relative to the axis of the beams, defined as second order effects. This may cause the change of inclination of concentrated stress flow, θ .

3. TEST PROGRAMS

3.1 Detail of test specimens

The test specimens consisted of four concrete beams prestressed with external tendons, with the same total length at 3.5 m, cross section dimensions and reinforcement details as shown in Figure 3. The specimens were named as ns7, ns14, s7 and s14 as tabulated in Table 1. The main parameters in this experimental study were the compressive stress in concrete due to the prestress, and amount of transverse reinforcements. The effective prestress was set as 500 N/mm² for specimens ns7 and s7 in order to generate the compressive stress in concrete at the upper extreme fiber, σ_u , and the lower extreme fiber, σ_l , as -1.5 N/mm² and 7.4 N/mm², respectively. For specimens ns14 and s14, 1000 N/mm² of effective prestress was introduced in order to obtain the compressive stress in concrete at the upper extreme fiber, σ_u , as -3.0 N/mm² and the lower extreme fiber, σ_l , as 14.9 N/mm². Vertical transverse reinforcements were used as shear reinforcement for specimens s7 and s14; however, for specimens ns7 and ns14, the transverse reinforcement was not provided in the test span. In all specimens, the internal longitudinal tensile reinforcement consisted of four deformed steel bars with nominal diameter of 25 mm, and eight deformed steel bars are for longitudinal compressive reinforcement with nominal diameter of 6 mm. Their average yield strength, f_y , is 378 N/mm² and 355 N/mm², and average tensile strength, f_u , is 526 N/mm² and 523 N/mm², respectively. For specimens s7 and s14, transverse reinforcement with a nominal diameter of 6 mm and with yield strength, f_{yv} , of 355 N/mm² was provided in a web with the spacing, s , of 200 mm. The shear reinforcement ratio ($A_v/b_w s$) was 0.21 %. Two straight 19-wire prestressing tendons with a nominal diameter of 17.8 mm ($A_{ps} = 208.4 \text{ mm}^2$) were prepared for each specimen as external tendons. The yield strength, f_{py} , the tensile strength, f_{pu} , and the elastic modulus of external tendons, E_{ps} , were 1694 N/mm², 1934 N/mm² and 191.9 kN/mm², respectively. The concrete has a mix proportion as summarized in Table 2. The design cylindrical compressive strength of concrete, f'_c , was 50 N/mm² at 7 days. The actual strength of concrete was measured on the day of testing as tabulated in Table 3.

3.2 Experimental Procedure

Before testing, the beam specimens were prestressed using symmetrically arranged external

tendons on both sides of the section of externally prestressed concrete beams deviated at 916.7 mm from the supports by two deviators and anchored at the ends of beams. Teflon sheets were inserted between a specimen and supports and between tendons and deviators for reducing the friction. Three electrical strain gauges were placed on each tendon at the same section at the midspan of the beam. The strain of the prestressing tendon was taken as the average value of three measured locations.

All beams had straight tendon profiles, with a depth of 400 mm at the midspan section. The tendons were stressed to about $0.25f_{pu}$ for ns7 and s7, and $0.5f_{pu}$ for ns14 and s14 as illustrated as the effective prestress, f_{pe} , in Table 1. Each beam was instrumented to measure and monitor deflections at the midspan and deviators, crack width, prestressing force in external tendons, and strains of concrete, steel and tendon. The beams were simply supported over a span of 3.2 m and four-point symmetrical loading with a distance between loading points of 400 mm was provided. The shear span was set as 1.4 m, and the effective depth was 400 mm (i.e. shear span to effective depth ratio, a/d , was 3.5). The 150 mm width of loading and support plates were used in the test.

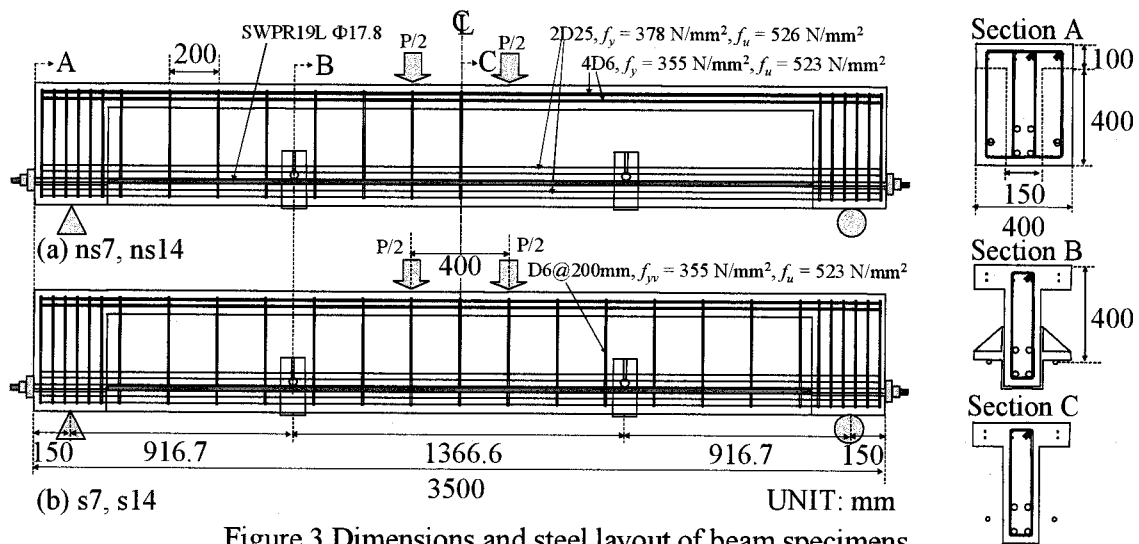


Figure 3 Dimensions and steel layout of beam specimens

Table 1 Detail of test beams

Beams	Effective span length, L [mm]	Loading distance, L_d [mm]	Deviator spacing, S_d [mm]	Depth of tendon, d_{ps} [mm]	Area of internal steel bars, A_s [mm ²]	Area of external tendon, A_{ps} [mm ²]	Effective prestress, f_{pe} [N/mm ²]	Shear reinforcement ratio in web [%]
ns7	3200	400	1366.6	400	2026.8	416.8	487.2	0
ns14							962.4	0
s7							487.2	0.21
s14							932.3	0.21

Table 2 Mix proportion of concrete

W/C	s/a	W ^{*1}	C ^{*2}	S ^{*3}	G ^{*4}	SP ^{*5}	AE ^{*6}
[%]	[%]	[kg/m ³]	[kg/m ³]	[kg/m ³]	[kg/m ³]	[kg/m ³]	[kg/m ³]
35.5	38.5	143	403	690	1114	0.75	1.21

*1 Water

*2 Early High-strength Portland Cement, specific gravity = 3.14

*3 Fine aggregate, specific gravity = 2.60, F.M. = 2.73

*4 Coarse aggregate, specific gravity = 2.63, F.M. = 6.68, G_{max} = 20mm

*5 Superplasticizer, specific gravity = 1.05

*6 Air-entraining agent, specific gravity = 1.02, 100 time dilute solution

Table 3 Mechanical properties of concrete from experiment

Beams	Compressive strength, f_c' [N/mm ²]	Tensile strength, f_t [N/mm ²]	Elastic modulus, E_c [kN/mm ²]
ns7	53.6	4.1	32.5
ns14	55.8	4.2	31.1
s7	57.4	3.7	31.8
s14	58.6	4.0	32.2

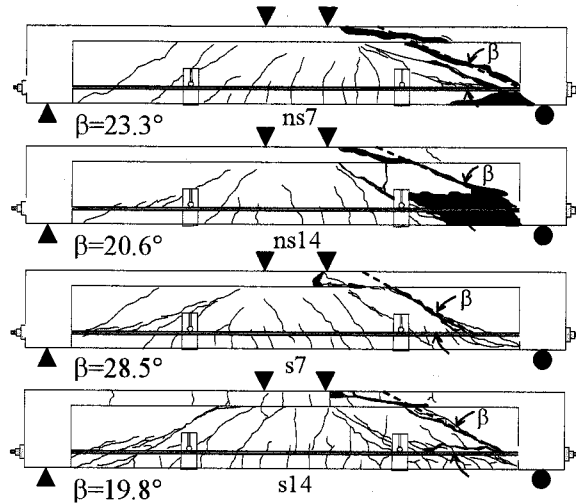


Figure 4 Crack patterns

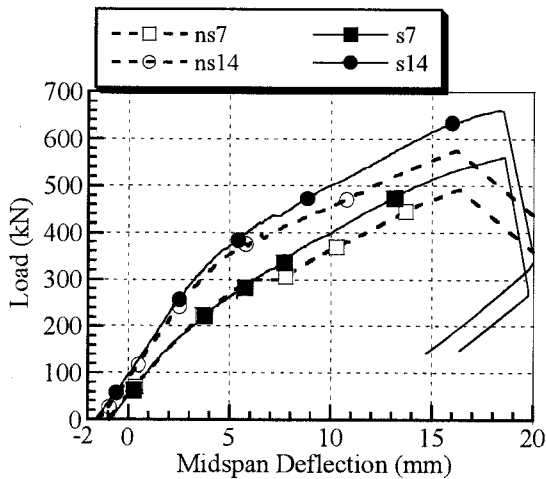


Figure 5 Load-deflection responses

Table 4 Summary of experimental results

Beams	ϵ_u^{*1}	f_{ps}^{*2}	P_{crack}^{*3}	P_{dia}^{*4}	$P_{u,EXP}^{*5}$	δ_u^{*6}	d_{pu}^{*7}
ns7	1437	658.2	193.5	303.4	491.2	16.4	396.9
ns14	1701	1144.1	295.5	373.1	574.8	16.2	397.5
s7	1457	698.2	192.6	379.2	560.6	18.6	396.8
s14	1920	1122.5	296.4	436.4	660.6	18.3	396.8

*1 Concrete strain of peak resistance at the top flange [$\times 10^{-6}$]

*2 Stress in tendon of peak resistance [N/mm^2]

*3 Load of first flexural crack [kN]

*4 Load of first diagonal crack [kN]

*5 Load of peak resistance [kN], $P_{u,EXP} = 2V_{u,EXP}$

*6 Midspan deflection at peak resistance [mm]

*7 Tendon depth of peak resistance [mm]

4. RESULTS AND DISCUSSION

4.1 Cracking Behavior

The crack patterns of all specimens were demonstrated in Figure 4. Flexural cracks were firstly observed in the flexural span between loading points, where the maximum moment region is. As the load increased, several new flexural cracks were developed in both shear spans, and these flexural cracks started to incline forming diagonal cracks. These diagonal cracks increased significantly in width and propagated upward to the compression zone of beams. These cracks were generally defined as flexural shear cracks. Although the diagonal crack formed, the beams could resist more loads. The loading was continued until the peak load of beams. For the specimens ns7 and ns14, which did not have any transverse reinforcement in the test span, a new diagonal crack penetrating from the loading point to the support was suddenly observed at the peak load, and the load suddenly decreased. However, in the specimens s7 and s14, which had transverse reinforcements, the primary diagonal crack gradually increased in width and failed at the peak load. The stress flow inside the beams exhibited as the compression arch to resist the shear force and failed in the shear compressive mode of failure, even though the concrete strain at the top flange was small as shown in Table 4. The inclination of diagonal crack, β , was measured by taking average values of crack angles measured from several locations of primary diagonal crack and illustrated in Figure 4. It is found that the inclinations of diagonal cracks become flatter in the beams with higher value of compressive extreme fiber stress, and become slightly steeper by introducing vertical shear reinforcements.

4.2 Load-deflection Characteristics

The responses of applied load versus deflection are illustrated in Figure 5. The summary of measured resistances of specimens from the cracking to the peak load together with the midspan deformation, stress in tendon at the peak and tendon depth at the peak are tabulated in Table 4. In the beginning, the beams behaved as the linear elastic body until the first flexural crack between loading points occurred that reduced the beam stiffness. It should be noted that by increasing the lower extreme fiber stress, σ_l , from $7.4 N/mm^2$ to $14.9 N/mm^2$, it makes the load at the first flexural crack increase for 50.7%. The loading was continued until the diagonal crack appeared, which caused the

loads slightly dropped and changed the beam stiffness for specimens ns7 and ns14, which did not have any transverse reinforcement in the test span. On the other hand, for specimens s7 and s14, which had transverse reinforcements, the loading was smoothly continued, and only the change in the beam stiffness could be observed when the diagonal crack was appeared. It is interesting to notice that the loading resistances at the first diagonal crack of ns14 (without transverse reinforcement, $\sigma_l = 14.9 \text{ N/mm}^2$) and s7 (with transverse reinforcement, $\sigma_l = 7.4 \text{ N/mm}^2$) are almost the same, even though there was no transverse reinforcement in the specimen ns14, which means that the lower extreme fiber stress in concrete, σ_l , has a significant impact to resist the shear force. And then the loads gradually increased again until the peak resistance. From the experiment, the shear contribution of vertical transverse reinforcement, $V_s (= V_u - V_{pc})$, can be obtained as 34.7 kN and 42.9 kN for s7 and s14, respectively. However, the shear contribution of vertical transverse reinforcement from computation ($V_s = A_v f_{yv} z/s$) can be obtained as 30.1 kN. Therefore, it can be concluded that the lower extreme fiber stress, σ_l , also affects the shear contribution of vertical transverse reinforcement due to the change of inclination of diagonal crack angle. The second order effects can be neglected in the case of shear failure mode, since from the experimental results, the tendon depth at the peak changed only about 0.75% from the initial tendon depth. The stress increment in tendons, $\Delta f_{ps} (= f_{ps} - f_{pe})$, did not increase as much as in the case of flexural problem, because the deflection of such beams, which failed in shear, is not as much as in the case of flexural problem (Sivaleepunth et al. 2005).

5. COMPARISON WITH JSCE DESIGN CODE AND THE SIMPLIFIED TRUSS MODEL

Table 5 describes the calculated results of V_{pc} , V_s and P_u evaluated from JSCE design code, Eqs. (1)-(5). It can be observed that the predicting results are underestimated the shear carrying capacity of externally prestressed concrete beams about 50% of its capacity. This is due to the fact that JSCE specification design code pay less attention on the influence of compressive stress in lower extreme fiber of concrete due to prestress, which is a significant parameter controlling the inclination angle of diagonal crack, and the inclination of concentrated stress flow. However, if the design code can predict the load resistance of the superstructure correctly, the dead weight of this superstructure can be reduced, which lead to resist more seismic load.

The applicability of the simplified truss model, Eqs. (6)-(12), on the externally prestressed concrete beams without transverse reinforcement was inspected with the experimental results by focusing on the comparison of failed members of the predicted results and the crack patterns in Figure 4 as illustrated in Figure 6. The analytical results in each member according to simplified truss

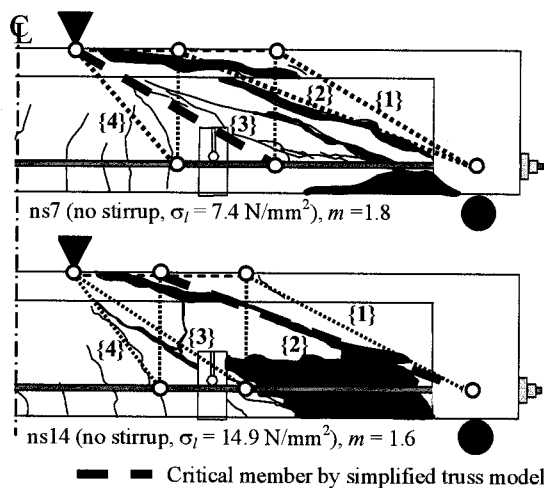


Figure 6 Critical members and crack patterns

Table 5 Comparison of prediction equations

Beams	JSCE				Lertsamattiyakul	
	V_{pc} [kN]	V_s [kN]	P_u [kN]	$P_{u,CAL}/P_{u,EXP}$	P_u [kN]	$P_{u,CAL}/P_{u,EXP}$
ns7	118.7	0.0	237.3	0.48	409.2	0.83
ns14	142.1	0.0	284.2	0.49	417.2	0.73
s7	121.0	30.1	302.2	0.54	N.A.	N.A.
s14	143.0	30.1	346.3	0.52	N.A.	N.A.

Table 6 Analytical results in each member

Member No.	ns7			ns14		
	F_i (kN)	R_i (kN)	F_i/R_i	F_i (kN)	R_i (kN)	F_i/R_i
1	-232.2	-508.5	0.46	-270.4	-432.9	0.62
2	-244.8	-257.0	0.95	-245.4	-245.5	1.00
3	-239.3	-239.4	1.00	-229.7	-300.0	0.77
4	-117.5	-557.8	0.21	-107.4	-640.5	0.17

model (Lertsamattiyakul et al. 2005) is shown in Table 6. It is apparent that the calculated results provide the well-predicted results compared with the test results and calculated results from JSCE design code for specimen ns7 as tabulated in Table 5, but the failed member obtained from the prediction is not the same as obtained from the test. From the test, the member {2} was a critical member, but in the simplified truss model, instead of member {2}, member {3} is a critical member as shown in Figure 6. However, from Table 6, it can be observed that the member {2} almost concurrently failed with the member {3}. On the other hand, in specimen ns14, the prediction of shear carrying capacity is quite conservative comparing to the test result; however, the predicted result from simplified truss model can still provide higher accuracy than the calculated result from JSCE design code. The prediction of failed member from simplified truss model, member {2}, is well predicted. This may be due to the fact that the prestressing tendons in externally prestressed concrete beams were unbonded to the concrete; therefore, the inverse of slope of concentrated stress flow, m , Eq. (6), may not be able to be estimated the model correctly. The modification of parameter m is required in order to predict the shear carrying capacity of externally prestressed concrete beams.

For the specimens s7 and s14, in which transverse reinforcements were provided, the inclination of diagonal crack becomes steeper, and the shear carrying capacity was also higher according to the experimental results in Figure 4 and Table 4. Therefore, from these results, it can be concluded that the inclination of concentrated stress flow, θ , needs to be modified in order to obtain a reliable inclination for beams with transverse reinforcements.

6. CONCLUSIONS

The experimental program was conducted to study the influence of compressive stress in concrete due to prestress in external tendons and amount of transverse reinforcements on shear carrying capacity and the inclination angle of diagonal crack of externally prestressed concrete beams. From the experimental results, the following conclusions were drawn:

- (1) By increasing the lower fiber stress in concrete, the shear carrying capacity also increases, and the diagonal crack inclination becomes flatter. However, if the transverse reinforcements are provided, the diagonal crack inclination becomes steeper.
- (2) From both experimental and calculated results of externally prestressed concrete beams, the shear compression failure is determined to cause the crushing of web concrete.
- (3) The modification of JSCE specification design code and the simplified truss model is required in order to obtain higher accuracy.

Acknowledgements:

Sincere gratitude is expressed to Mr. Satoshi Tamura and Dr. Yuzuru Hamada, research engineers, Research and Development Center, DPS Bridge Works Co., Ltd., and Dr. Khac Diep Bui, postdoctoral researcher, Department of Civil Engineering, Tokyo Institute of Technology for their assistance in conducting the experiment. The authors also would like to express their gratitude to the COE program for providing financial support to accomplish this research.

References:

- Japan Society of Civil Engineers (JSCE) (2002), "Standard Specification for Concrete Structures," *Structural Performance Verification*.
- Lertsamattiyakul, M., Niwa, J., Tamura, S., and Hamada, Y. (2005), "Simplified Truss Model for Shear Carrying Capacity Analysis of Non-rectangular Cross Sectional PC Slender Beams," *Proceeding of Second International Conference on Urban Earthquake Engineering (CUEE)*, 381-388.
- Sivaleepunth, C., Niwa, J., Tamura, S., and Hamada, Y. (2005), "Flexural Behavior of Externally Prestressed Concrete Beams by Considering Loading Application," *Proceeding of Japan Concrete Institute*, 27(2), 553-558.

PROPOSED TORSIONAL HYSTERETIC MODEL FOR RC COLUMNS UNDER COMBINED CYCLIC BENDING AND TORSION

P. Tirasit¹⁾ and K. Kawashima²⁾

1) Graduate Student, Department of Civil Engineering, Tokyo Institute of Technology, Japan

2) Professor, Department of Civil Engineering, Tokyo Institute of Technology, Japan

paiboon@cv.titech.ac.jp, kawasima@cv.titech.ac.jp

Abstract: Development of an empirical torsional hysteretic model for RC bridge columns under combined cyclic bending and torsion based on the experimental result is reported in this paper. The formulae of model parameters are formulated by applying the regression analysis. A tri-linear torsional hysteretic envelope is proposed to control the extent of the torsional restoring force of columns. The main concepts of proposed unloading and reloading rules are explained. The effect of the rotation-drift ratio r which is defined the level of combined bending and torsion and the number of loading cycles is taken into account in this model.

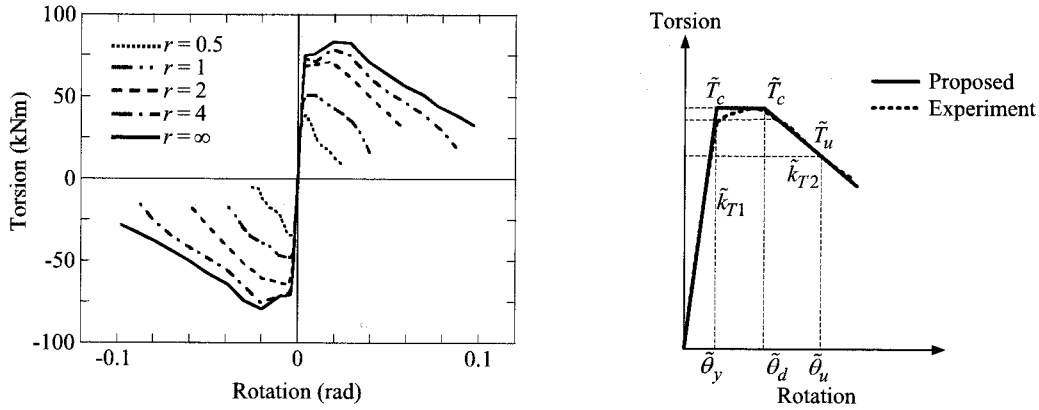
1. INTRODUCTION

Seismic torsion possibly takes place coupled with other internal forces in the piers of bridges with irregular structural placement, such as bridges supported by C-bent columns and skewed bridges (Nagata et al. 2005, Tirasit and Kawashima 2005(a)). The existence of seismic torsion can decrease the flexural capacity and ductility of the RC columns due to their interaction and alter the column seismic performance. Although frequently used hysteretic model like Takeda model (Takeda et al. 1970) can successfully idealize the cyclic flexural behavior of concrete member in the seismic analysis, it is failed to simulate the torsional characteristic because of the existing of high pinching effect. Moreover, even though there have been available hysteretic models taking account of the pinching phenomenon (Ozcebe and Saatcioglu (1987) and Kunnath et al. (1990)), none of them was formulated based on the torsion test results. The reliable nonlinear torsional hysteretic model which is necessary for the seismic analysis has not been available yet. This paper proposed an empirical torsional hysteretic model for RC columns taking account of the effect of combined bending and torsion based on the experimental study of the authors (Tirasit and Kawashima 2005(b)).

2. PROPOSED TORSIONAL HYSTERETIC ENVELOPE

2.1 Idealization of envelope

According to the torsional hysteretic envelopes of RC columns under different rotation-drift ratio r , which is the ratio between the rotation (radian) and the lateral drift at the column effective height, shown in Figure 1a, a tri-linear torsional hysteretic envelope is proposed to be the backbone of the hysteresis as shown in Figure 1b. The column is assumed to behave linearly with an initial torsional stiffness \tilde{k}_{T1} until it reaches the torsional strength \tilde{T}_c at the assumed yield rotation $\tilde{\theta}_y$. Since the initial torsional stiffness is virtually constant as shown in Figure 1a, \tilde{k}_{T1} is obtained from the first



(a) Torsional hysteretic envelopes from experiment (b) Idealization of torsional hysteretic envelope
Figure 1 Torsional hysteretic envelopes from experimental result and the proposed model

loading cycle of the first loading step of the experiment. The torsion is assumed to be constant until the column rotation reaches $\tilde{\theta}_d$. Subsequently, the torsion deteriorates significantly over $\tilde{\theta}_d$ with a negative torsional stiffness \tilde{k}_{T2} and it is assumed that the column reaches the ultimate stage when the torsion deteriorates to 80% of the torsional strength \tilde{T}_u . $\tilde{\theta}_u$ is the column rotation at ultimate.

The torsional stiffnesses \tilde{k}_{T1} and \tilde{k}_{T2} are therefore defined as

$$\tilde{k}_{T1} = \tilde{T}_c / \tilde{\theta}_y \quad (1)$$

$$\tilde{k}_{T2} = (\tilde{T}_u - \tilde{T}_c) / (\tilde{\theta}_u - \tilde{\theta}_d) \quad (2)$$

It is worth noting that all parameters defining the envelope are determined based on the averages of the test results in the positive and negative loadings.

2.2 Effect of the rotation-drift ratio

Based on the test result shown in Figure 1a, it is obvious that the performance of the columns depends on the rotation-drift ratio r . Empirical relationships are proposed based on the regression analysis to clarify the dependency of the torsional restoring force and the rotation of a column on r . The torsional strength of column under combined cyclic bending and torsion \tilde{T}_c increases and approaches to the torsional strength of column under cyclic torsion T_c as r increases as shown in Figure 2. Therefore, \tilde{T}_c which is normalized by T_c may be approximated as

$$\tilde{T}_c / T_c = \exp(-0.42/r) \quad (3)$$

Consequently, the ultimate torsion \tilde{T}_u can be determined from Eq. (4) as

$$\tilde{T}_u = 0.8\tilde{T}_c \quad (4)$$

The yield rotation $\tilde{\theta}_y$, the rotation when the torsion starts to deteriorate $\tilde{\theta}_d$ and the ultimate rotation $\tilde{\theta}_u$ increase and converge to the values of column under cyclic torsion as r increases as shown in Figure 2. $\tilde{\theta}_y$, $\tilde{\theta}_d$ and $\tilde{\theta}_u$ which are normalized by the yield rotation of column under cyclic torsion θ_y may be approximated as

$$\tilde{\theta}_y / \theta_y = \exp(-0.37/r) \quad (5)$$

$$\tilde{\theta}_d / \theta_y = 6.29(1 - \exp(-r/1.79)) \quad (6)$$

$$\tilde{\theta}_u / \theta_y = 12 \exp(-0.8/r) \quad (7)$$

Eq. (3) and Eqs. (5) to (7) provide a good approximation with the test result as shown in Figure 2.

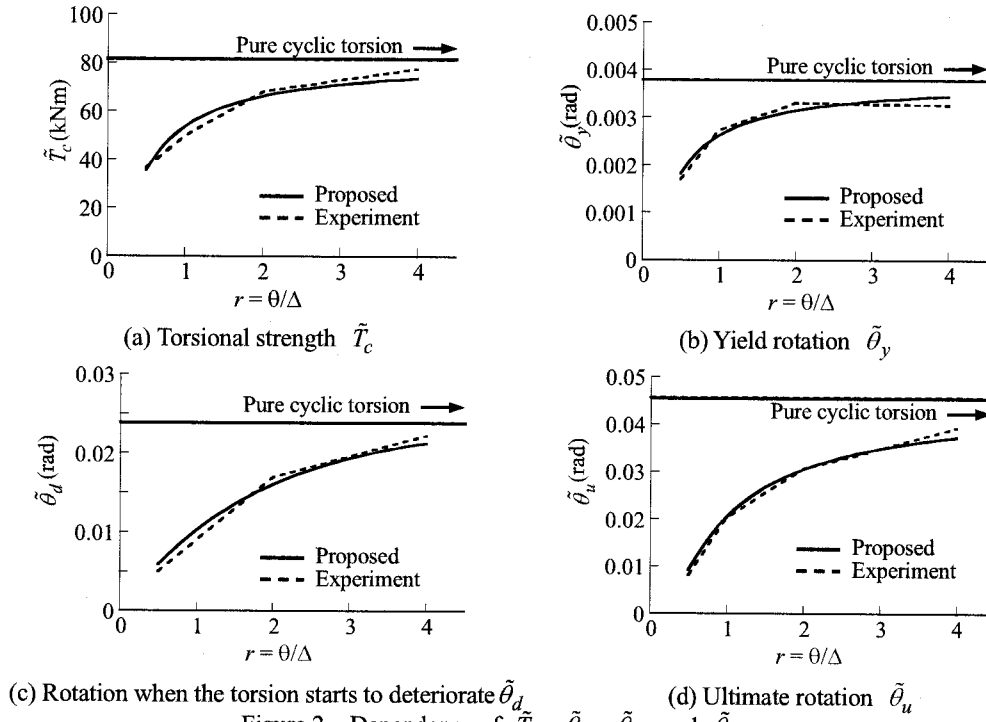


Figure 2 Dependence of \tilde{T}_c , $\tilde{\theta}_y$, $\tilde{\theta}_d$ and $\tilde{\theta}_u$ on r

3. PROPOSED UNLOADING AND LOADING/RELOADING RULES

The main concepts for tracing unloading and loading/reloading branches in the hysteretic model are proposed here. Figure 3 shows the definitions of the model parameters and how the column behaves along the torsional hysteretic paths. Column is assumed to be linear elastic along the initial stiffness of envelope (path 0, 1, 2, 0). If the rotation on one side of hysteresis exceeds $\tilde{\theta}_y$, the column hysteresis will follow the unloading and reloading rules below:

3.1 Unloading rules

1. The column is unloaded from the envelope at the point of unloaded rotation $\tilde{\theta}_m$ and unloaded torsion \tilde{T}_m . The unloading path orients towards $(\tilde{\theta}_{ucr,1}, \tilde{T}_{ucr,1})$, which is the point of changing stiffness, with the unloading stiffness $\tilde{k}_{Tul1,1}$ (path 5, 6 and path 10, 11). $\tilde{T}_{ucr,n}$ is defined to be the proportion of \tilde{T}_m and may be approximated as

$$\tilde{T}_{ucr,n}/\tilde{T}_m = A + B \exp(-C/D) \quad (8)$$

where

$$A = 0.399 \exp(-n/6.45) \quad (9)$$

$$B = -0.321 + 2.24(1 - \exp(-n/0.655)) \quad (10)$$

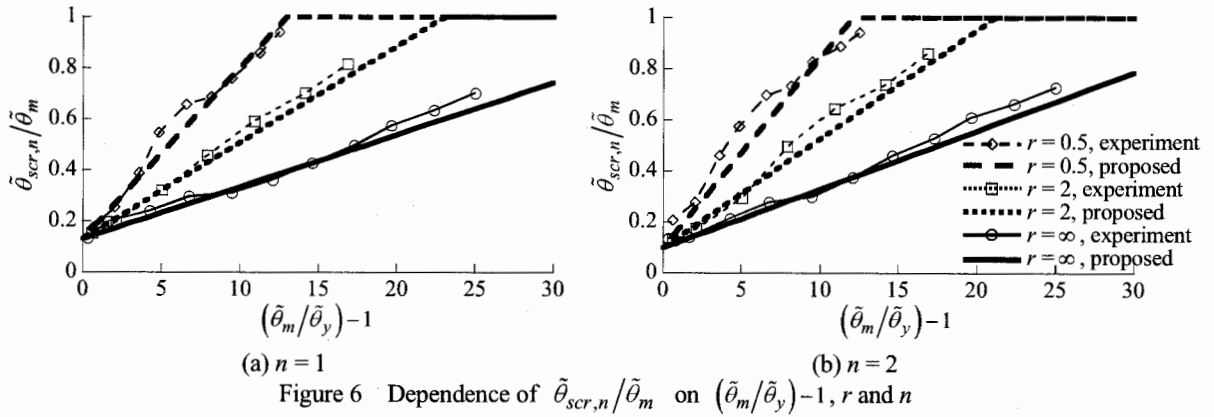
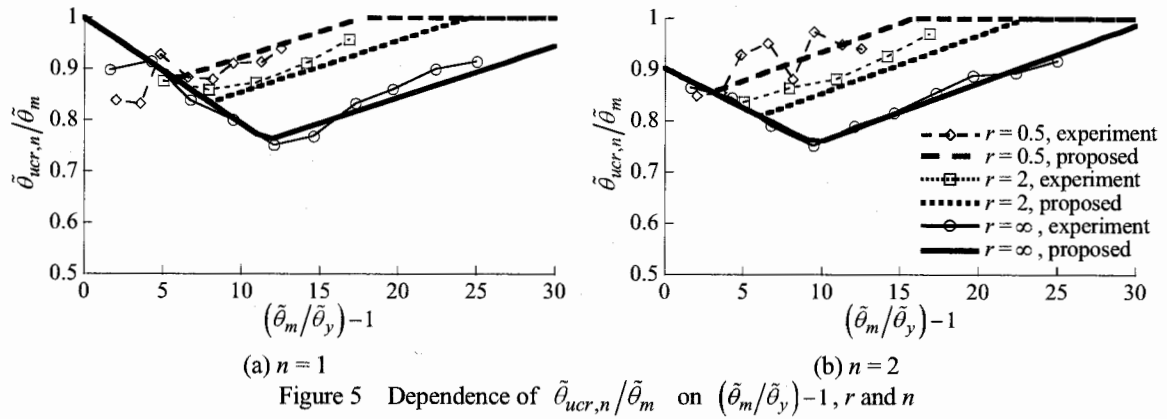
$$C = \tilde{\theta}_m/\tilde{\theta}_y \quad (11)$$

$$D = (3.13 + 5.88 \exp(-n/0.687)) \exp(-0.393/r) \quad (12)$$

and n is the index for counting number of loading cycles.

$\tilde{\theta}_{ucr,n}$ may be estimated as

$$\tilde{\theta}_{ucr,n}/\tilde{\theta}_m = \max \left\{ \frac{-E(C-1)+F}{G(C-1)+\{H+I(1-\exp(-1/M))\}} \leq 1 \right\} \quad (13)$$



Subsequently, the unloading path aims towards the zero torsion axis at $\tilde{\theta}_{scr,1}$, which is the reloading rotation of another loading side of column, with the unloading stiffness $\tilde{k}_{Tul2,1}$ (path 6, 7 and path 11, 12). $\tilde{\theta}_{scr,n}$ may be calculated as

$$\tilde{\theta}_{scr,n}/\tilde{\theta}_m = \{N + O(1 - \exp(-1/P))\}(C-1) + Q \leq 1 \quad (20)$$

in which

$$N = 0.0025n + 0.0179 \quad (21)$$

$$O = 0.0518 + 0.0209(1 - \exp(-n/0.856)) \quad (22)$$

$$P = r(-0.120n + 1.77) \geq 0 \quad (23)$$

$$Q = 0.0619 + 0.129 \exp(-n/1.56) \quad (24)$$

Figure 6 shows that $\tilde{\theta}_{scr,n}/\tilde{\theta}_m$ from the test result has a tendency to increase as the applied rotation increases. Eqs. (20) to (24) give a good correlation as shown in Figure 6.

2. If the column hysteresis on the unloading side has not experienced $\tilde{\theta}_y$, the unloading path follows the envelope until reaching the origin. Then it obeys the reloading rules which will be further explained (path 8, 9, 0).
3. When the column is unloaded from the pinching branch, the unloading path aims towards the zero torsion axis with the unloading stiffness $\tilde{k}_{Tul2,n}$ (path 23, 24 and path 26, 27). However, if the torsion at unloading point is larger than $\tilde{T}_{ucr,n}$, the unloading path points towards $\tilde{T}_{ucr,n}$ level with the unloading stiffness $\tilde{k}_{Tul1,n}$ and then directs towards the zero torsion axis with the unloading stiffness $\tilde{k}_{Tul2,n}$ (path 28, 29, 30).

3.2 Loading/reloading rules

1. If the column hysteresis in the reloading direction has exceeded $\tilde{\theta}_y$, the reloading path directs towards the point of the maximum rotation of preceding cycle $\tilde{\theta}_p$ and \tilde{T}_p , which is the torsion used to defined the pinching behavior, with the reloading stiffness \tilde{k}_{Tr11} . \tilde{T}_p may be evaluated to be the proportion of the preceding peak torsion \tilde{T}_p as

$$\tilde{T}_p' / \tilde{T}_p = R + S \exp(-U/T) \leq 1 \quad (25)$$

where

$$R = (-0.113/r) + 0.228 \geq 0 \quad (26)$$

$$S = (-1.5/r) + 4.74 \geq 0 \quad (27)$$

$$T = 2.68 + 1.27 \exp(-1/(0.105r)) \quad (28)$$

$$U = \tilde{\theta}_p / \tilde{\theta}_y \quad (29)$$

The reloading continues with \tilde{k}_{Tr11} until the column reaches $\tilde{\theta}_{cr,n}$ where the cracks are closed (path 12, 13 and path 22, 23, 26, 28, 31). $\tilde{\theta}_{cr,n}$ may be approximated as

$$\tilde{\theta}_{cr,n} / \tilde{\theta}_m = VC + W \leq 1 \quad (30)$$

where

$$V = 0.0106 + 0.00359 \exp(-n/1.01) \quad (31)$$

$$W = 0.0624 + 0.217(1 - \exp(-n/1.41)) \quad (32)$$

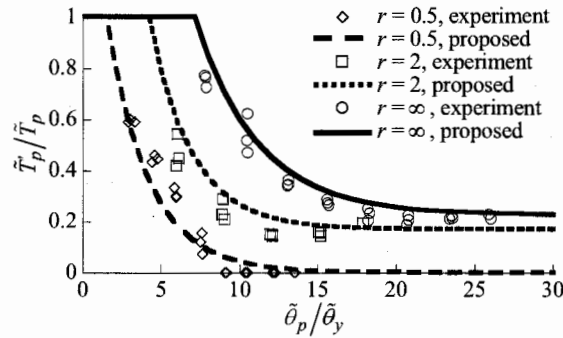


Figure 7 Dependence of $\tilde{T}_p' / \tilde{T}_p$ on $\tilde{\theta}_p / \tilde{\theta}_y$ and r

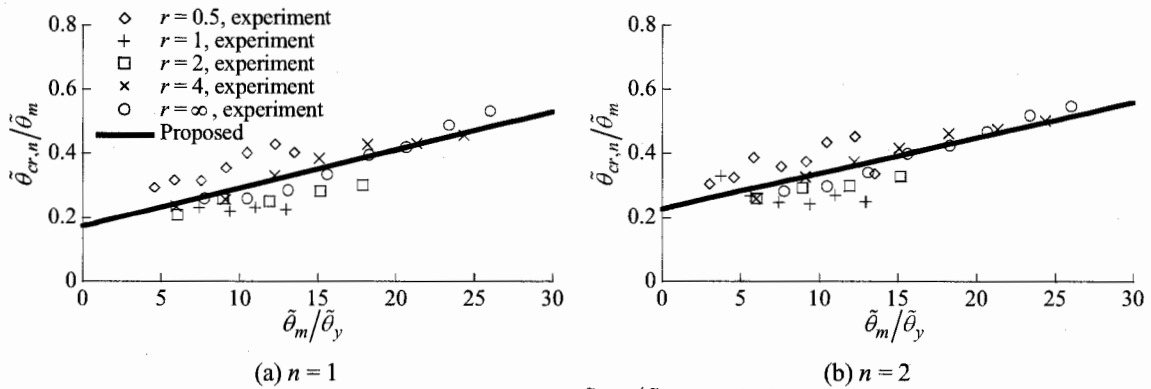


Figure 8 Dependence of $\tilde{\theta}_{cr,n} / \tilde{\theta}_m$ on $\tilde{\theta}_m / \tilde{\theta}_y$, r and n

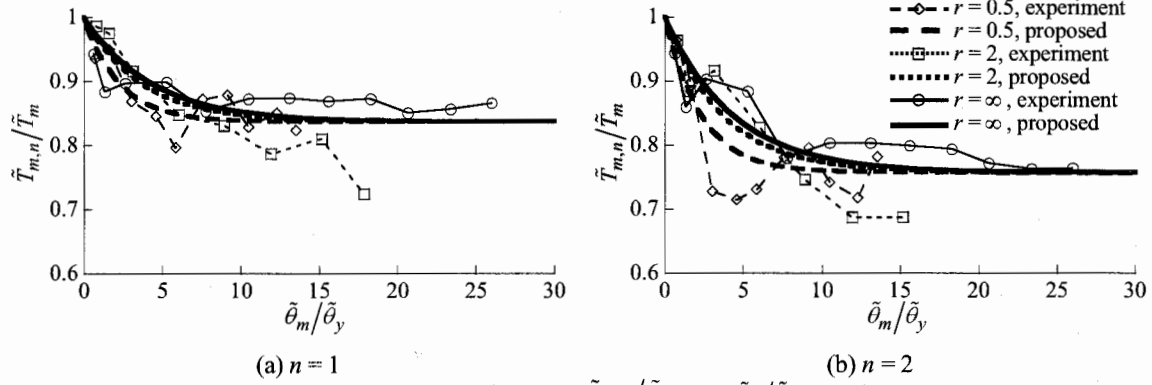


Figure 9 Dependence of $\tilde{T}_{m,n}/\tilde{T}_m$ on $\tilde{\theta}_m/\tilde{\theta}_y$, r and n

In accordance to the experimental result, \tilde{T}'_p/\tilde{T}_p tends to decreases while $\tilde{\theta}_{cr,n}/\tilde{\theta}_m$ is likely to increase as the applied rotation increases as shown in Figures 7 and 8, respectively. Eqs. (25) to (32) provide a good correlation to the test result.

Subsequently, the reloading path aims towards the envelope via the point of the maximum unloading rotation from the envelope $\tilde{\theta}_m$ and the deteriorated torsion $\tilde{T}_{m,n}$ with the reloading stiffness \tilde{k}_{Trl2} (path 13, 14, 16 and path 31, 32). $\tilde{T}_{m,n}$ may be estimated as

$$\tilde{T}_{m,n}/\tilde{T}_m = X + (1 - X) \exp(-C/Y) \quad (33)$$

in which

$$X = 0.925 \exp(-n/10.01) \quad (34)$$

$$Y = 4.29 \exp(-1/(3.11r)) \quad (35)$$

The experimental result indicates that $\tilde{T}_{m,n}/\tilde{T}_m$ decreases and converges to a certain value as the rotation increases and Eqs. (33) to (35) provide a good estimation as shown in Figure 9. Eqs. (33) to (35) is applied to the model when $\tilde{\theta}_m/\tilde{\theta}_y \geq 1$. For $\tilde{\theta}_m/\tilde{\theta}_y < 1$, $\tilde{T}_{m,n}/\tilde{T}_m$ is equal 1 because the column is assumed to be linear elastic.

2. If the column has not been loaded beyond $\tilde{\theta}_y$ in the reloading direction, the reloading branch points towards $\tilde{\theta}_{cr,n}$ on the envelope which is calculated by Eqs (30) to (32) based on $\tilde{\theta}_m/\tilde{\theta}_y = 1$ and $n = 1$. After that the column is reloaded along the envelope (path 7, 8, 9).
3. The column is reloaded on the same path as unloading with $\tilde{k}_{Tul1,1}$ towards the point of unloading on the envelope $(\tilde{\theta}_m, \tilde{T}_m)$ without the deterioration of torsion if reloading occurs before reaching $(\tilde{\theta}_{ucr,1}, \tilde{T}_{ucr,1})$ (path 3, 4, 3 and path 18, 19, 18).
4. The column is reloaded on the same path as unloading with $\tilde{k}_{Tul1,n}$ to the point of unloading on the reloading branch aiming towards $(\tilde{\theta}_m, \tilde{T}_{m,n})$ if the column was not unloaded to less than $\tilde{T}_{ucr,n}$ (path 14, 15, 14).
5. The reloading path directs towards the point of unloading on the envelope $(\tilde{\theta}_m, \tilde{T}_m)$ or on the reloading branch aiming towards $(\tilde{\theta}_m, \tilde{T}_{m,n})$ if the column was not unloaded over the zero torsion axis (path 20, 21, 22, 20).
6. If the column was unloaded over the zero torsion axis and reloading occurs on the same rotation side of hysteresis, the reloading path orients towards $(\tilde{\theta}_p, \tilde{T}'_p)$ until reaching $\tilde{\theta}_{cr,n}$ and then directs towards $(\tilde{\theta}_m, \tilde{T}_{m,n-1})$ (path 20, 21, 22, 24, 25, 20). However, if reloading begins at the rotation larger than $\tilde{\theta}_{cr,n}$, the reloading branch points towards $(\tilde{\theta}_m, \tilde{T}_{m,n-1})$ without changing of reloading stiffness..
7. In the pinching branch, the column is reloaded in the same path as unloading with $\tilde{k}_{Tul2,n}$ to the point of unloading if the column was not unloaded over the zero torsion axis (path 26, 27, 26). However, if the torsion at unloading point is larger than $\tilde{T}_{ucr,n}$, the reloading path points towards

to the point of unloading on the pinching slope (path 28, 29, 30, 28).

3.3 Counting of number of loading cycles

The index n for counting number of loading cycles are assigned 2 values simultaneously for positive and negative loadings. They have an initial value of 0 when the column hysteresis moves along the envelope. n becomes 1 as the column is unloaded from the envelope at the rotation larger than $\tilde{\theta}_y$. Currently, the value of n is assumed to increase every time the reloading starts from the opposite sign rotation and reverses at the rotation of at least 95% of maximum unloading rotation on the envelope $\tilde{\theta}_m$. n is kept constant even though the column is reloaded over $\tilde{\theta}_m$ and n becomes 0 again when the column reaches the hysteretic envelope. There is no change of n under small cycle below this deformation range.

4. CONCLUSIONS

An empirical torsional hysteretic model for RC bridge columns is proposed based on the test result. The model is governed by the proposed tri-linear envelope and the unloading and loading/reloading rules are stipulated to consider the hysteretic behavior. One unique characteristic of the torsional hysteresis is the pinching in the reloading path. However, this model is still under development to impose the model regulation into a computer program. Because the proposed formulae provide a good approximation to the experimental result, the authors believe that this proposed model is able to idealize the torsional hysteresis of RC columns within the consideration range of the experiment.

Acknowledgements:

The authors express their sincere gratitude to Messrs. Watanabe, G., Fukuda, T., Nagai, T., Wang, Y., Ogimoto, H., Kijima, K., Nagata, S., Maruyama, Y. and Ms. Sakellaraki, D. for their extensive support in constructing the column specimens and executing the experiment.

References:

- Kunnath, S. K., Reinhorn, A. M. and Park, Y. J. (1990), "Analytical Modeling of Inelastic Seismic Response of R/C Structures," *Journal of Structural Engineering*, American Society of Civil Engineers, **116**(4), 996-1017.
- Nagata, S., Kawashima, K. and Watanabe, G. (2005), "Seismic Performance of RC C-bent Columns based on a Hybrid Loading Test," *Proceedings of the 1st International Conference on Advance in Experimental Structural Engineering*, Nagoya, Japan, 227-234.
- Ozcebe, G. and Saatcioglu, M. (1989), "Hysteretic Shear Model for Reinforced Concrete Members," *Journal of Structural Engineering*, American Society of Civil Engineers, **115**(1), 132-148.
- Takeda, T., Sozen, M. A. and Nielsen, N. N. (1970), "Reinforced Concrete Response to Simulated Earthquakes," *Journal of Structural Engineering*, American Society of Civil Engineers, **96**(12), 2557-2573.
- Tirasit, P. and Kawashima, K. (2005a), "Seismic Torsion Response of Skewed Bridge Piers," *Journal of Earthquake Engineering*, Japan Society of Civil Engineers.
- Tirasit, P. and Kawashima, K. (2005b), "Combined Cyclic Bending-Torsional Loading Test of Reinforced Concrete Bridge Columns," *21st US-Japan Bridge Engineering Workshop*, PWRI, Tsukuba, Japan.

CARBON FIBER SHEET RETROFIT OF REINFORCED CONCRETE BRIDGE COLUMNS UNDER CYCLIC LOADING

R. M. Gallardo¹⁾ and K. Kawashima²⁾

1) Asst. Professor, Department of Civil Engineering, University of the Philippines at Los Baños, Philippines

2) Professor, Department of Civil Engineering, Tokyo Institute of Technology, Japan

richelle@cv.titech.ac.jp, kawasima@cv.titech.ac.jp

Abstract: This paper presents an analysis of the hysteretic behavior of CFS-retrofitted reinforced concrete circular columns. Fiber element analysis was conducted based on cyclic constitutive models of longitudinal reinforcement and concrete confined by both CFS and ties. The analysis was verified versus available cyclic test data of an earlier study on six columns under various combinations of CFS and tie reinforcement ratio. The analysis provides good agreement with the experimental results.

1. INTRODUCTION

Under strong seismic excitations, reinforced concrete bridge columns designed using earlier codes are commonly deficient in flexural ductility, shear strength and flexural strength. Various retrofitting techniques have been developed and the use of fiber-reinforced plastic/polymer (FRP) composite jackets has been widely applied to provide lateral confinement for enhanced strength and ductility. Among the FRP used for the retrofit of reinforced concrete columns, carbon fiber sheets (CFS) are widely used due to its high elastic modulus and tensile strength, the highest among the FRP composites.

Several constitutive models governing the behavior of CFS-confined concrete under monotonic loading have been developed (Samaan et al. 1998, Kawashima et al. 2000, Xiao and Wu 2000, Saiidi et al. 2005). On the other hand, very limited studies are available to assess its cyclic response. Kawashima et al. (2000) experimentally investigated the cyclic performance of circular-CFS retrofitted bridge columns with low amount of tie reinforcement and their results show that stable flexural capacity can be attained with CFS jacketing. Chang et al. (2004) conducted pseudo-dynamic testing of CFS-repaired rectangular concrete bridge columns. Their results show that the seismic performance of damaged concrete bridge columns can be effectively recovered after repair with CFS. Haroun and Elsanadedy (2005) reported tests on composite-jacketed scaled models of circular and square concrete bridge columns with insufficient lap-splice length under simulated seismic actions. Test results showed that the circular retrofitted columns had improved seismic behavior, with ductility factor larger than 6.0. However, tests conducted on square retrofitted columns showed limited improvement in clamping on the lap-splice region and for enhancing the ductility of column.

Although several experimental studies were conducted to investigate the cyclic performance of CFS-retrofitted columns, there is a need to develop analytical methods which can simulate its hysteretic response. In this study, a fiber element is used to model the CFS-retrofitted columns. The experimental data obtained by Kawashima et al. (2000) were used to validate the model.

2. EXPERIMENTAL TEST AND ANALYTICAL MODEL

2.1 Cyclic Loading Test

Six reinforced concrete column specimens 400mm in diameter and 1350mm in effective height, shown in Figure 1, were tested under constant axial load and reverse lateral load. Variables considered were the volumetric ratio of tie reinforcement and volumetric ratio of CFS.

As summarized in Table 1, the specimens were grouped into A and B series where each series consists of three specimens each; one was as-built while the second and third were wrapped laterally by CFS with single layer and two layers, respectively. CFS ratio was 0.111% and 0.222% when the columns were wrapped by single layer and two layers, respectively. CFS properties are shown in Table 2. The specimens were reinforced in the transverse direction by 6mm deformed bars having yield strength of 363MPa (SD295). The tie reinforcement ratio was 0.256% (150mm-spacing) for the A-series and 0.128% (300mm-spacing) for the B-series. All specimens were reinforced in the longitudinal direction by 16mm deformed bars having yield strength of 374MPa (SD295).

Under a constant compression of 185 KN, the piers were loaded in the lateral direction with a displacement increment of a half drift. At each increment, three cyclic loads were applied. The columns were designed such that they fail in flexure.

Table 1 Column Specimen Properties for Cyclic Loading Test

Specimens	Series A			Series B		
	A1	A2	A3	B1	B2	B3
Diameter (mm)	400					
Effective Height (mm)	1350					
Shear-Span Ratio	3.375					
Axial Reinforcement Ratio (%)	1.89					
Tie Spacing (mm)	D6@150			D6@300		
Tie Reinforcement Ratio, ρ_s (%)	0.256			0.128		
CFS Ratio, ρ_{CFS} (%)	0	0.111	0.222	0	0.111	0.222
Concrete Strength (MPa)	30.0	30.0	27.5	30.0	30.0	27.5

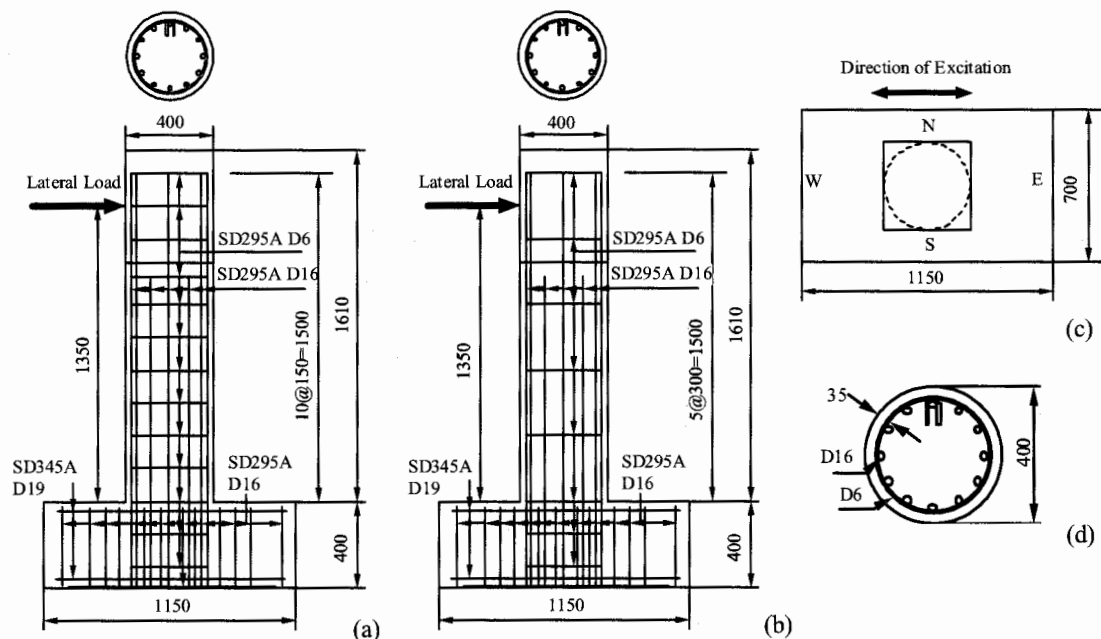


Figure 1 Column Specimens for Cyclic Loading Test: (a) A1~A3 Specimen, (b) B1~B3 Specimen, (c) Top View, and (d) Section

2.2 Analytical Model

To simulate the experimental behavior of the columns, they were modeled as illustrated in Figure 2. The analytical model consists of a beam element and a fiber element. The fiber element represents the plastic hinge region and its length was assumed to be half of the column diameter based on the seismic design requirements of the 2002 Japanese Specifications for Highway Bridges.

The stress vs. strain relation of concrete confined by ties was assumed based on a model by Hoshikuma et al. (1997). For concrete confined by CFS and ties, stress vs. strain relation was based on a model by Kawashima et al. (2000). Due to the unavailability of unloading and reloading model for concrete confined by CFS, Sakai and Kawashima (2006) unloading and reloading hysteresis model for concrete confined by transverse reinforcement was assumed as it includes the effect of repeated unloading/reloading cycles. The modified

Menegotto-Pinto model (Menegotto and Pinto 1973, Sakai and Kawashima 2003) was used to idealize the stress vs. strain relation of the longitudinal reinforcements.

The effect of local buckling and rupture of longitudinal reinforcement as well as slip of reinforcement at the plastic hinge length was not dealt with in the analysis.

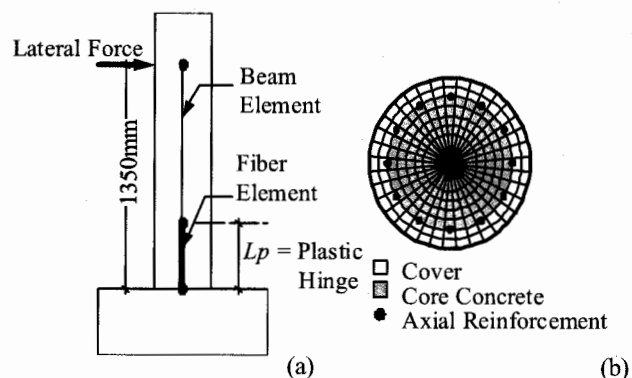


Figure 2 Analytical Model of CFS-Retrofitted Columns: (a) Column Model, and (b) Fiber Representation

Table 2 Properties of CFS used in the Experiment

Properties	Nominal	Measured
Amount of CF (g/m ²)	200	200
Thickness of sheet (mm)	0.111	0.111
Tensile Strength (MPa)	3400	4476
Elastic Modulus (GPa)	230	266
Rupture Strain (%)	1.50	1.63

3. MODEL VALIDATION

3.1 Experimental Behavior

Figure 3 illustrates the failure mode of columns A1 to B3. For the as-built columns A1 and B1, the cover concrete spalled-off 200mm and 300mm from the bottom, respectively, as shown in Figures 3(a) and 3(d). This induced buckling of the main bars which occurred at 3.5% drift for A1 and 3.0% drift for B1.

In contrast to the as-built columns, spalling-off of cover concrete for the retrofitted columns A2, A3, B2 and B3 was well prevented by the CFS. CFS did not rupture in all the retrofitted specimens, but cracks occurred along the lateral direction all around the specimens as shown in Figures 3(b), 3(c), 3(e) and 3(f). As the loading displacement increased, the crack widths also increased. Figure 4 shows the concrete surface after the CFS was removed. It can be observed that the cracks on the concrete correspond to the cracks on the CFS.

Figure 5 shows the lateral force vs. lateral displacement hysteresis of the columns under cyclic loading. For the as-built columns, it is noted that a sudden deterioration of the restoring force occurred in both A1 and B1 at 3.0% drift. This can be attributed to the spalling-off of cover concrete which induced the buckling of the main bars at these drift ratios. The restoring force decreased to less than 50% of the maximum at 3.5% drift in both A1 and B1.

Compared to the as-built columns, the retrofitted columns demonstrated a stable response in the entire loading displacement range tested as a result of CFS confinement. Deterioration of the

restoring force occurred at 5.5% drift for both A2 and B2 and 5% drift for both A3 and B3.

To determine the effect of the CFS for retrofit, CFS volumetric ratio was varied for different tie reinforcement ratios. It can be seen in Figures 6(a1) and 6(b1) that increased flexural strength and ductility is attained with increased volumetric ratio of CFS. However, the flexural strength and ductility of column confined by one layer of CFS ($\rho_{CF} = 0.111\%$) was larger compared to the column confined by two layers of CFS ($\rho_{CF} = 0.222\%$).

The effect of increasing tie reinforcement ratio on the hysteretic response of CFS-retrofitted columns is shown in Figures 7(a1) and 7(b1). Since low tie reinforcement ratios were considered, not much difference was observed on the response.

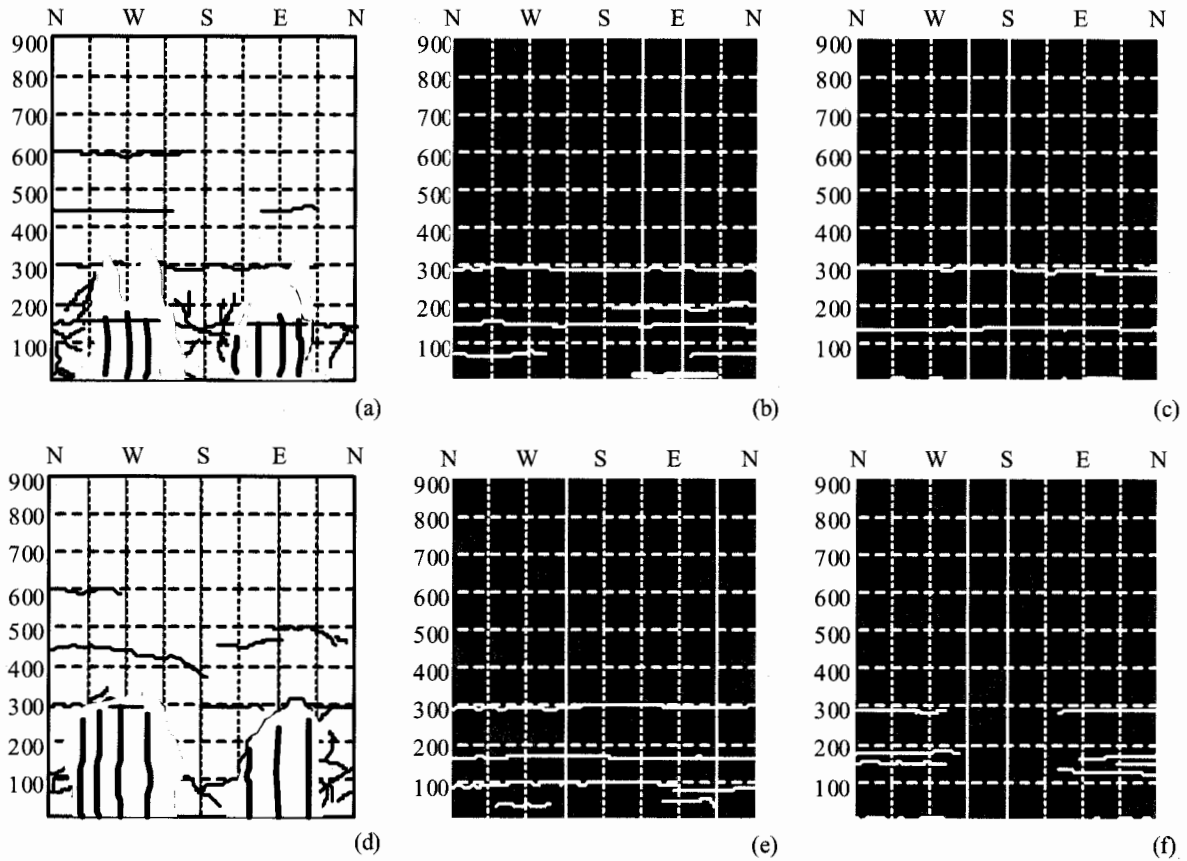


Figure 3 Failure Mode of Column Specimens:
(a) A1, (b) A2, (c) A3, (d) B1, (e) B2, and (f) B3

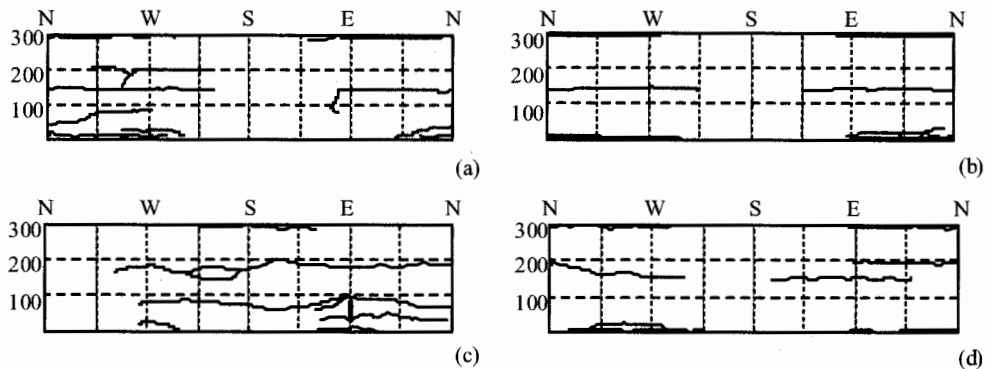


Figure 4 Concrete Surface After Removal of CFS:
(a) A2, (b) A3, (c) B2, and (d) B3

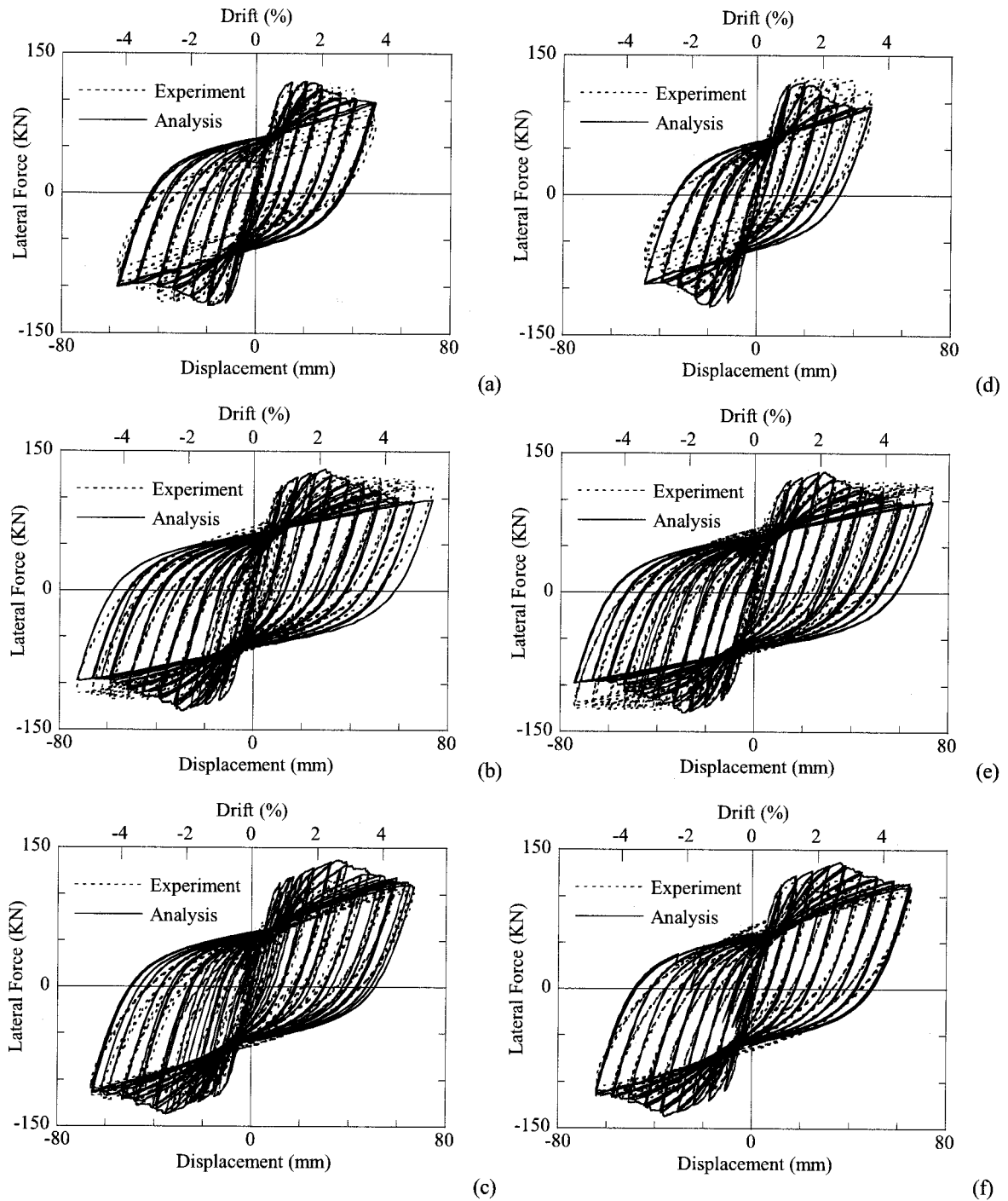


Figure 5 Comparison of Lateral Force vs. Lateral Displacement Hystereses between Experiment and Analysis:
(a) A1, (b) A2, (c) A3, (d) B1, (e) B2, and (f) B3

3.2 Analytical Correlation

Figure 5 shows the analytical hysteresis in comparison with the experimental hysteresis. In general, there is a very good agreement between the analytical and experimental results.

In the analysis, deterioration of the restoring force for all column specimens is much earlier compared to the experimental results. For the as-built columns A1 and B1, the restoring force decreased at 2.0% drift while for the retrofitted columns, deterioration occurred at 2.5% drift for

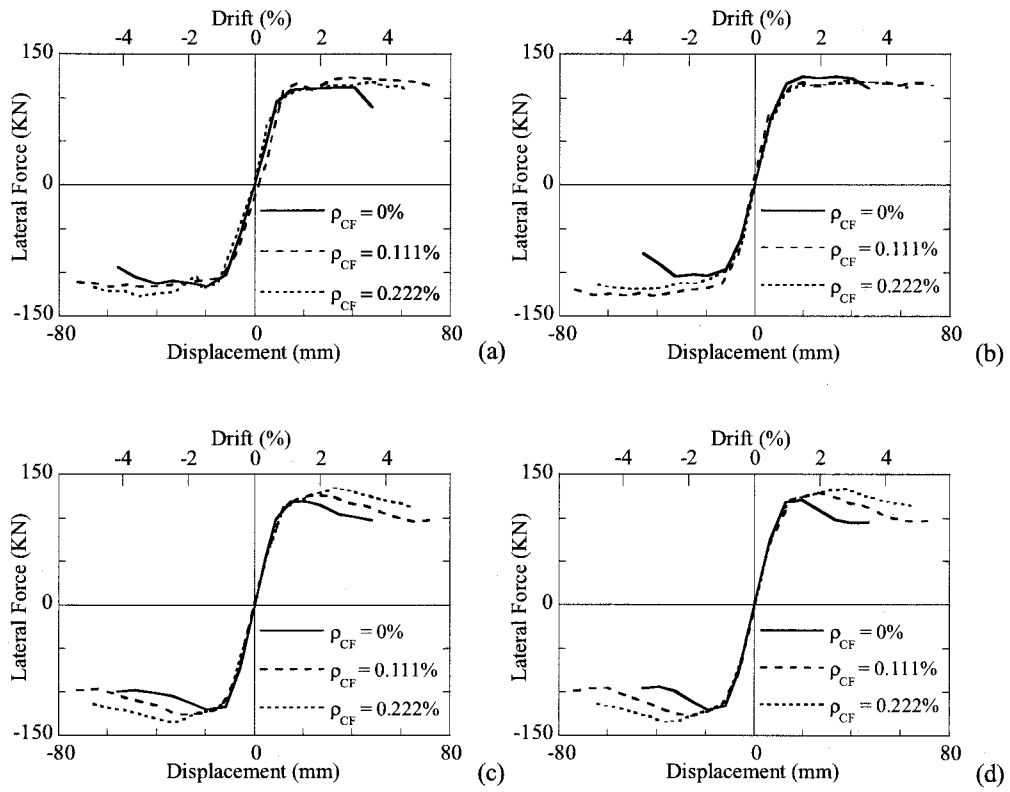


Figure 6 Effect of CFS Quantity: (a) Experiment ($\rho_s = 0.256\%$), (b) Experiment ($\rho_s = 0.128\%$)
(c) Analysis ($\rho_s = 0.256\%$) and (d) Analysis ($\rho_s = 0.128\%$)

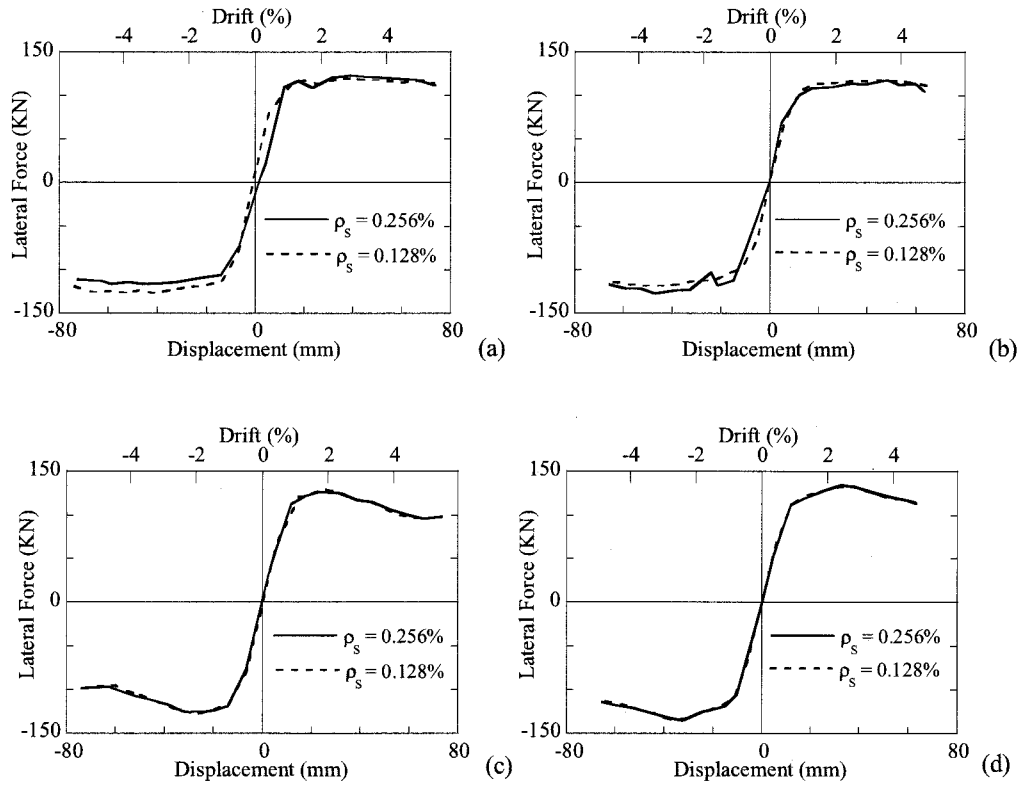


Figure 7 Effect of Tie Reinforcement Quantity: (a) Experiment ($\rho_{CF} = 0.111\%$), (b) Experiment ($\rho_{CF} = 0.222\%$),
(c) Analysis ($\rho_{CF} = 0.111\%$), (d) Analysis ($\rho_{CF} = 0.222\%$)

columns A2 and B2 and 3.0% drift for columns A3 and B3. It can be further observed from Figure 5 that unloading and reloading hysteresis of the experimental results is adequately simulated by the analysis.

Figure 8 shows the computed stress vs. strain hystereses of the cover concrete, core concrete and longitudinal reinforcement for columns A1 to A3. As shown in Figure 8(a1), for the as-built column A1 the cover concrete completely failed at 2.0% drift which led to a decrease in the restoring force. For the retrofitted columns A2 and A3, rupture of CFS occurred at 2.5% and 3% drift, respectively, as shown in Figures 8(a2) and 8(a3). With the rupture of CFS, cracking of concrete may occur causing a decline in the flexural strength.

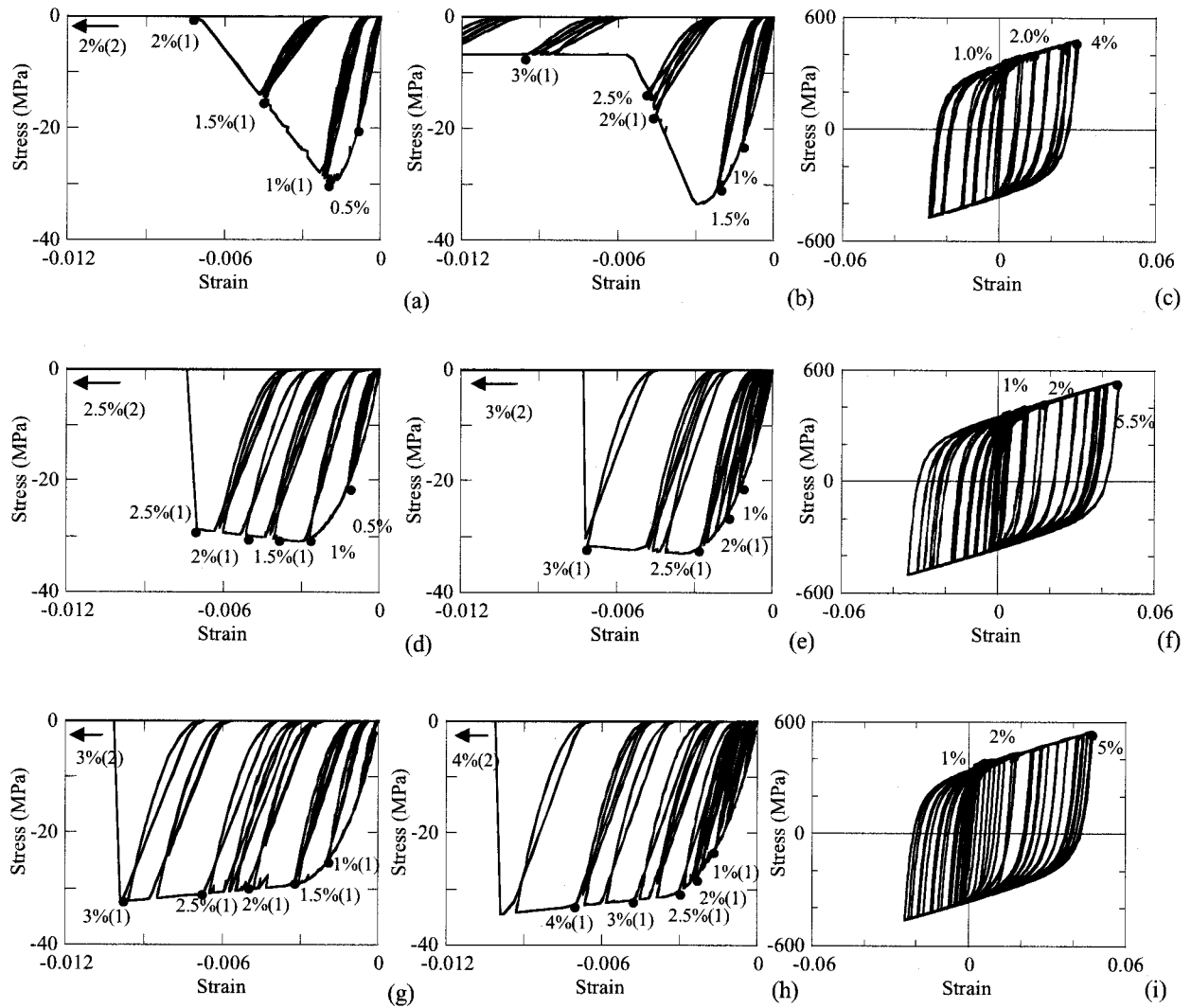


Figure 8 Stress vs. Strain Hystereses for Columns at Different Drift Ratios:
(a) A1 (Cover Concrete), (b) A1 (Core Concrete), (c) A1 (Longitudinal Reinforcement)
(d) A2 (Cover Concrete), (e) A2 (Core Concrete), (f) A2 (Longitudinal Reinforcement)
(g) A3 (Cover Concrete), (h) A3 (Core Concrete), (i) A3 (Longitudinal Reinforcement)
(Number in parenthesis represent the loading cycle)

It can be seen in Figure 8 that with CFS jacketing, the stress-strain envelope curve of the cover concrete and core concrete exhibits a bilinear behavior. With one layer of CFS for column A2, the envelope curve steadily decreases after the peak stress until rupture of CFS. However, with two

layers of CFS for column A3, the envelope curve steadily increases until failure occurs due to rupture of CFS. Figure 8 further shows that with CFS retrofit, the stress-strain hystereses of the cover concrete, core concrete and longitudinal reinforcement are more extensive compared to the as-built column demonstrating ductility enhancement of CFS-retrofitted columns.

Material stress-strain hystereses for column B1 was observed to be similar to column A1. Likewise, columns B2 and B3 exhibited similar material hystereses as columns A2 and A3.

Similar to the experiment, analysis shows that when CFS volumetric ratio increases, flexural strength and ductility also increases as shown in Figures 6(a2) and 6(b2). When tie reinforcement ratio is increased, not much difference is observed on the hysteretic response of CFS-retrofitted columns for low tie reinforcement ratios as shown in Figures 7(a2) and 7(b2).

3. CONCLUSIONS

To simulate the response of CFS-retrofitted circular columns under cyclic loading, a fiber element analysis was conducted. Based on the results of the analysis, the following conclusions can be made:

- (1) The fiber element analysis which is based on cyclic constitutive models of longitudinal reinforcement and concrete confined by both CFS and ties provides good numerical simulation of the experimental results.
- (2) The hysteretic response of as-built columns can be enhanced by CFS jacketing which is effective at increasing the lateral confinement, allowing an increase in strength and ductile behavior.

Acknowledgement:

The first author is grateful to the Japan Society for the Promotion of Science in support of this research at Tokyo Institute of Technology.

References:

- Chang, S., Li, Y. and Loh, C. (2004), "Experimental Study of Seismic Behaviors of As-Built and Carbon Fiber Reinforced Plastics Repaired Reinforced Concrete Bridge Columns," *Journal of Bridge Engineering*, American Society of Civil Engineers, **9**(4), 391-402.
- Haroun, M. and Elsanadedy, H. (2005), "Fiber-Reinforced Plastic Jackets for Ductility Enhancement of Reinforced Concrete Bridge Columns with Poor Lap-Splice Detailing," *Journal of Bridge Engineering*, American Society of Civil Engineers, **10**(6), 749-757.
- Hoshikuma, J., Kawashima, K., Nagaya, K. and Taylor, A. (1997), "Stress-Strain Model for Confined Reinforced Concrete in Bridge Piers," *Journal of Structural Engineering*, American Society of Civil Engineers, **123**(5), 624-633.
- Kawashima, K., Hosotani, M. and Yoneda, K. (2000), "Carbon Fiber Sheet Retrofit of Reinforced Concrete Bridge Piers," *Proceedings of the International Workshop on Annual Commemoration of Chi-Chi Earthquake*, Vol. II-Technical Aspect, National Center for Research on Earthquake Engineering, Taipei, Taiwan, ROC, 124-135.
- Menegotto, M. and Pinto, P. (1973), "Method of Analysis for Cyclically Loaded Reinforced Concrete Plane Frames Including Changes in Geometry and Non-Elastic Behavior of Elements under Combined Normal Force and Bending," *Proceedings of IABSE Symposium on Resistance and Ultimate Deformability of Structures Acted on by Well Defined Repeated Loads*, Lisbon, 15-22.
- Saiidi, M., Sureshkumar, K. and Pulido, C. (2005), "Simple Carbon-Fiber-Reinforced-Plastic-Confined Concrete Model for Moment-Curvature Analysis," *Journal of Composites for Construction*, American Society of Civil Engineers, **9**(1), 101-104.
- Sakai, J. and Kawashima, K. (2006), "Unloading and Reloading Stress-Strain Model for Confined Concrete," *Journal of Structural Engineering*, American Society of Civil Engineers, **132**(1), 112-122.
- Sakai, J. and Kawashima, K. (2003), "Modification of the Giuffre, Menegotto and Pint Model for Unloading and Reloading Paths with Small Strain Variations," *Journal of Structural Mechanics and Earthquake Engineering*, JSCE, No. 738/I-64, 159-169.
- Samaan, M., Mirmiran, A., and Shahawy, M. (1998), "Model of Concrete Confined by Fiber Composites," *Journal of Structural Engineering*, American Society of Civil Engineers, **124**(9), 1025-1031.
- Xiao, Y., and Wu, H. (2000), "Compressive Behavior of Concrete Confined by Carbon Fiber Composite Jackets," *Journal of Materials in Civil Engineering*, American Society of Civil Engineers, **12**(2), 139-146.

PROGRESS IN E-DEFENSE SHAKING TABLE EXPERIMENTS OF FULL-SCALE 5-STORY BUILDING WITH DAMPERS

K. Kasai¹⁾, Y. Ooki²⁾, S. Motoyui³⁾ and T. Takeuchi³⁾

¹⁾ Professor, Structural Engineering Research Center, Tokyo Institute of Technology, Japan

²⁾ Research Associate, Structural Engineering Research Center, Tokyo Institute of Technology, Japan

³⁾ Associate Professor, Department of Built Environment, Tokyo Institute of Technology, Japan

⁴⁾ Associate Professor, Department of Architecture and Building Eng., Tokyo Institute of Technology, Japan
kasai@serc.titech.ac.jp, ooki@serc.titech.ac.jp, motoyui@enveng.titech.ac.jp, totoru@arch.titech.ac.jp

Abstract: As a consequence of considerable economic losses realized in recent earthquakes, there is increased motivation to use passive control systems that can protect both the structure and its contents from earthquake damage. Current status of Japanese passive control technology implemented in Japan is overviewed, and in large the extensive research program that started in April 2005 is explained. The research focuses on performance evaluation of the new systems under realistic loading conditions. Three-dimensional (3-D) full-scale dynamic tests of a 5-story steel frame with 20 dampers will be conducted in 2008, by using the world's largest E-Defense shaking table. The test will be repeated by trying at least 5 different types of dampers. On-going preliminary design and analysis of the full-scale building are summarized.

1. INTRODUCTION

Passive control scheme has established its status as a viable means to enhance seismic performance of buildings (JSSI 2003, 2005). In this scheme, the damper connected to the structural frame dissipates the seismic input energy, thereby reducing the kinetic energy and vibration of the building.

Japanese desire for adopting this scheme has increased considerably, especially after the recent earthquakes caused serious socio-economical problems in the metropolitan areas of the United States (Northridge) and Japan (Kobe). Due to these earthquakes, many modern buildings ceased functioning and required costly structural and nonstructural repairs, although they successfully protected the lives of the occupants. Because of these, a number of Japanese major buildings constructed after the earthquakes and even small residential buildings utilize the passive control scheme to better protect buildings and their contents (JSCA 2000). The number of such buildings has increased to at least seven hundred in the year of 2005.

Considering the above circumstances, the writer has been conducting research into various issues for producing passively controlled buildings of high reliability and performance (Kasai et al. 1998a-2005f). The writer is also involved in development of design and construction manual of such buildings, leading the Response Control Committee, Japan Society of Seismic Isolation (JSSI). The first edition of this so-called "JSSI manual" was published in 2003, and the second edition in September 2005 (JSSI 2003, 2005). The manual refers to mechanism, design, fabrication, testing, quality control, analytical modeling of dampers, as well as design, construction, and analysis of passively controlled buildings. It was developed by more than 50 members who are university

researchers, structural designers, and engineers from about twenty damper manufacturing companies.

Although the manual has provided a common standard for design, construction, and quality for the technology, a great caution is required since the history of implementing passive control devices into a building is short. This new system has experienced neither a major earthquake nor frequent minor earthquakes, and database for actual performance is poor. Moreover, analysis and performance prediction are based on the extrapolation of limited experimental data that are typically created from testing of reduced-scale devices and systems, under highly idealized load and boundary conditions.

Based on these views, the writer is given an opportunity to lead an extensive research program that started in April 2005 to evaluate the seismic performance of the passive control systems under realistic loading conditions. Three-dimensional (3-D) full-scale dynamic tests of five-story steel frames with at least five different dampers will be conducted in the year of 2008 by using the world's largest E-Defense shaking table. This paper will inform on-going preliminary work of designing and analyzing the five-story building specimen.

2. E-DEFENSE SHAKING TABLE

The National Research Institute for Earth Science and Disaster Prevention (NIED) established the Hyogo Earthquake Engineering Research Center. This center was planned on the occasion of the Hanshin Awaji Great Earthquake in 1995 to undertake unprecedented experiments that observe damaging process, scale and causes of collapse of actual buildings under severe earthquakes. The center will use the E-Defense shaking table (Table 1), a full size three-dimensional vibration destruction facility that has is almost in full operation starting 2005. World-wide research on earthquake engineering, for example, the international joint research with the U.S. on earthquake durability of steel-reinforced buildings and bridges, will use this center as a core facility.

Specifications of Shaking System		
Payload	12MN (1,200tonf)	
Size	20m x 15m	
Driving Type	Accumulator Charge /Electro-Hydraulic Servo Control	
Shaking Direction	XY-Horizontal	Z-Vertical
Maximum Acceleration (at Maximum loading)	$>900\text{cm/s}^2$	$>1,500\text{cm/s}^2$
Maximum Velocity	200cm/s	70cm/s
Maximum Displacement	$\pm 100\text{cm}$	$\pm 50\text{cm}$
Maximum Allowable Moment	Overturning Moment	Yawing Moment
	150MN·m	40MN·m

Table 1. Specifications of E-Defense Shaking Table

E-Defense can precisely reproduce the 3-D ground motion recorded at the Kobe Earthquake in 1995 with a test model of 12,000 kN on the shaking table. The laboratory of an area 5,200 m² and height 43 m is equipped with the shaking table and two 4,000 kN overhead cranes for the handling of large-scale test models. As indicated in Table 1, the shaking table size is 20 m × 15 m, pay load capacity is 12,000 kN, and overturning moment capacity is 150,000 kN·m. Horizontal ground acceleration, velocity, and displacement of more than 900 cm/s², 200 cm/s, and ± 100 cm can be applied with the 12,000 kN payload. The shaking table is connected with 5 units of actuators for

horizontal x- and y-direction each, and 14 units for vertical z-direction, through 3-D links each.

Hydraulic pumps, accumulators, and gas engines are set in the separate building called the hydraulic unit building. The gas engines were selected as the power source of this facility, considering their eco-friendliness and economical efficiency. Fig. 1(a) shows a view of table validation study, in which a full-scale 5-story specimen with high stiffness and therefore very short vibration period of 0.2 to 0.3 sec. was set on the E-Defense table. The plan dimension of the frame was 9 m \times 12 m, and the height was 20 m. Total weight of the frame was 5,600 kN. Fig. 2(b) shows a full-scale specimen of a 6-story apartment building on the table. The plan dimension of the frame was 10 m \times 15 m, and the height was 16.2 m. Total weight of the frame was 10,000 kN.

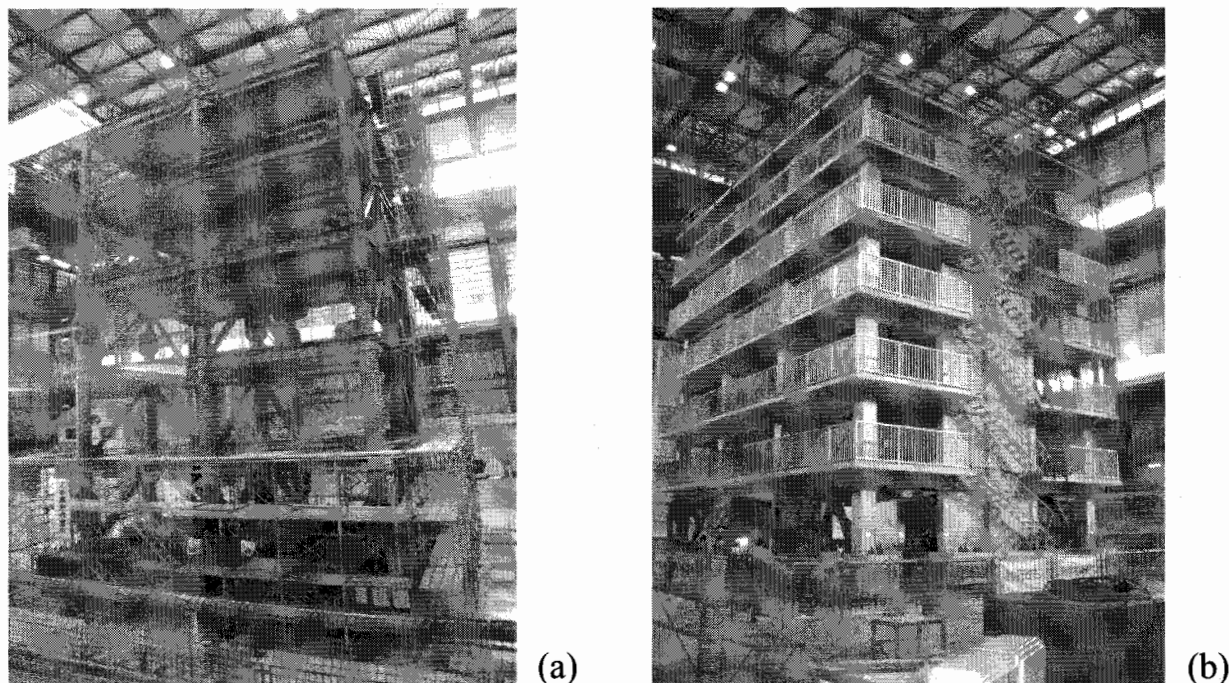


Figure 1 (a) Five-Story Steel Frame Used to Validate the Performance of the Shaking Table, and (b) Six-Story R.C. Concrete Frame Simulating Apartment Building.

3. FIVE DAMPER TYPES CONSIDERED FOR BUILDING SPECIMENS

Numerous dampers are being produced and developed in Japan, and they are categorized into five types; oil, viscous, viscoelastic, steel, and friction dampers, as shown in Fig. 2. A series of tests to be explained will use all these types, and they are briefly introduced below:

(1) *Viscous damper* produces the hysteresis loop of combined ellipse and rectangle. The material used is polymer liquid, and its resistance against flow produces the damper force. The damper possesses configurations of vertical panel, box, or cylinder (Furukawa et al. 2002, JSSI 2003, 2005). The viscous damper can be modeled as a series combination of elastic spring and nonlinear dashpot whose force is a fractional power of velocity (Kasai et al. 2003c). As suggested in Table 2, American dampers may be used in lieu of Japanese dampers.

(2) *Oil damper* produces the hysteresis loop of ellipse. The material used therein is oil, and its resistance against flow at orifice produces the damper force. The damper possesses the configurations of cylinder, and it is usually provided with a relief mechanism that prevents increase in force, making the hysteresis like a rectangle shape (Tsuyuki et al. 2002, JSSI 2003, 2005). The oil damper is modeled as a series combination of elastic spring and liner dashpot whose viscous coefficient, due to the relief mechanism, switches to a small value when subjected to a large velocity (Takahasi and Sekiguchi

2002, JSSI 2003, 2005).

(3) *Viscoelastic damper* produces the hysteresis loop of inclined ellipse. In some material, the hysteresis is close to bilinear especially under large deformation. The material used is polymer composite of acryl, butadiene, silicon, or others, and resistance against loading is produced from the molecular motion. Typical damper has configurations of vertical panel or tube, but it could be designed for many other configurations as well (Okuma et al. 2002, JSSI 2003, 2005). Viscoelastic damper of a linear type may be used for the tests. In order to simulate frequency and temperature sensitivities, temperature-rise due to energy dissipation, and consequent softening of the material, a sophisticated model using fractional time-derivatives of the force and deformation (Kasai et al. 2001a, 2002e, 2003a, JSSI 2003, 2005) will be used. Drastically simplified and practical model (Kasai and Okuma 2001b, 2002a) will be also used.

(4) *Steel damper* produces bi-linear hysteresis. Typical damper has configuration of vertical panel or tube, but it could be designed for many other configurations as well. This damper is the least expensive among the five types (Nakata .2002, JSSI 2003, 2005). The constitutive equations of steel material is readily known from the past research, but the analysis results must be cross-referenced to cumulative damage of the damper (e.g., Kasai et al. 2004a, Kasai and Ito 2005e), since the damper is typically designed to yield under the small and frequent seismic loads.

(5) *Friction damper* produces more ideal bi-linear hysteresis than the steel damper mentioned above. Typically the friction pad fastened by the bolts exhibits rigid-perfectly plastic behavior. The elastic stiffness is extremely high, and post-yield stiffness almost zero in this damper. Currently, this damper is least used in Japan, but is expected to be adopted increasingly in the near future.


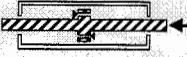


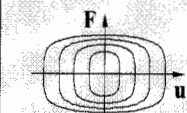
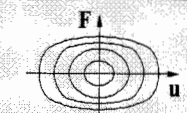

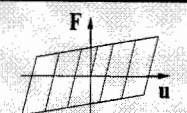
Viscous	Oil	Viscoelastic	Steel(&Friction)
			
Shear/Flow Resist. Panel, Box, Cylinder	Flow Resist Cylinder	Shear Resist. Cylinder, Panel, etc.	Axial/Shear Yielding Cylinder, Panel, etc.
$F = C \cdot \dot{u}$	$F = C_1 \cdot \dot{u}$ or $C_2 \cdot \dot{u}$	$F = K(\omega) \cdot u + C(\omega) \cdot \dot{u}$	$F = K \cdot f(u)$
			
1) US ($\alpha=0.4$) 2) Japan ($\alpha=0.1$)	1) Japan (bilinear)	1) US /Japan (linear) 2) Japan (nonlinear)	1) Japan / US

Table 2 Five Damper Types to Be Used for Full-Scale Building Tests

4. FULL- SCALE 5-STORY FRAME DESIGN

Fig. 2 shows the tentative elevation and plan of the 5-story building model. The plan dimension is 12 m \times 15 m, and total height from center line of the foundation beam is 18.1 m. Two bays are considered for each of x- and y-directions, respectively. The dampers are placed in a 6 m span bay of perimeter frames, and they are connected to braces, the effects of whose elastic stiffness will be considered in design/analysis. The seismic weight of each floor includes those of all structural and non-structural components, as well as a portion of live load following the Japanese standard.

The frame members consist of wide-flange beam sections of at most 60 cm deep, and square box column sections of at most 40 cm \times 40 cm. The yield strength of steel material for the beam and column shall be 360 N/mm². All the beam and column connections will be a fully-restrained type.

The steel deck with concrete on top will be considered for the floor slab, and fully composite beams will be created by using sufficient number of studs.

The exterior wall will be 12.5 cm thick light-weight concrete panel, and partitions provided inside the building. It is expected that mechanical, electrical, and plumbing systems as well as furniture will be placed in the building for limited number of tests.

Two dampers will be used in each of x- and y-directions per story. Thus, in total 20 dampers will be attached to the building. The method to determine the damper size will be briefly explained later.

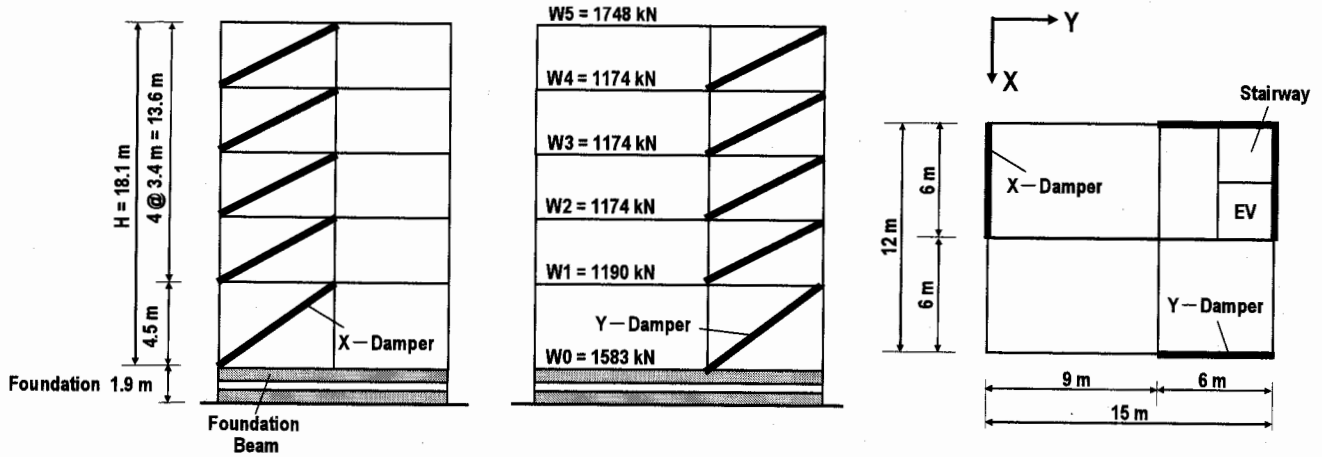


Figure 2 5-Story Building Specimen with 20 Dampers (Building Configurations are Tentative)

The target performance of the building is uniquely set against a major earthquake considered in Japan. For the so-called level 2 earthquake, the story drift angle shall be no more than $1/200$ ($=0.005$) radian at any story level, which is much more stringent requirement than considered for a traditional building. From this reason, the building specimen is considered to represent the “*high value-added*” building, in which not only the structural components but also non-structural components are protected from a major seismic attack.

Fig. 3 shows the pseudo-acceleration spectrum of the “major earthquake” considered by the Japanese code. The vibration periods of the building without dampers are 0.81 and 0.83 sec. in x-

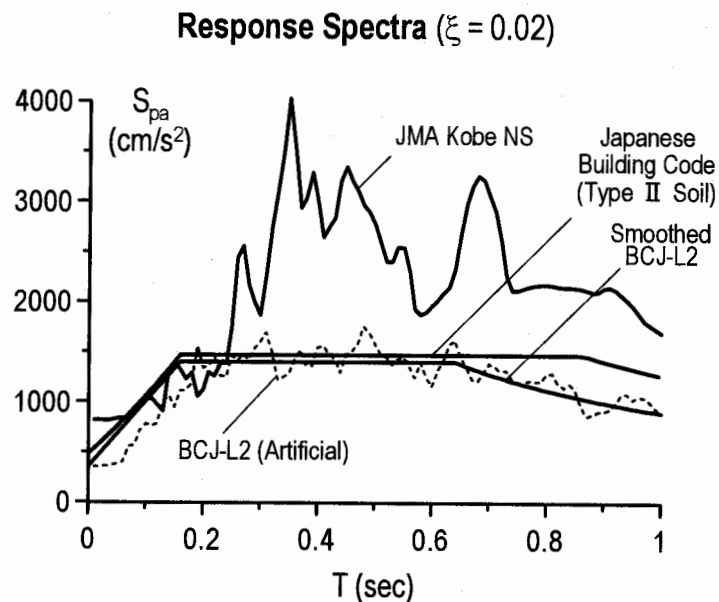


Figure 3 Pseudo-Acceleration Spectra

and y-directions, respectively. Those of the damped buildings, depending on the damper types, are in the range between 0.5 sec. and 0.7 sec. in both directions.

In order to meet the above requirement for the high value-added building design, the “performance curves” (Fig. 4) proposed by the writer (e.g., Kasai et al. 1998a, 1998b, 2005e, JSSI 2003, 2005) are being used effectively, and necessary sizes of damper and brace determined.

For instance, given an earthquake input of a smooth response spectrum, the peak displacement and base shear of the frame prior to damper installment can be predicted easily from the response spectrum. Then, the performance curve (Fig. 4) can estimate target reduction ratios of displacement and base shear based on the required performance. Considering the target reduction ratios and the performance curve, one can determine the necessary stiffness of the damper and brace. Optimum design solution to control both displacement and force can also be found from the performance curve. Fig. 4 shows example curves for a case of steel damper. Since the building period belongs to the region of constant acceleration spectrum (Fig. 3) as mentioned before, Fig. 4(a) is used.

Although the above procedure considers the building as a SDOF system, the design result can be equally applied to sizing of the dampers in the multistory case as well. That is, one could size the damper and brace such that the ratios of their stiffnesses to the frame story stiffness satisfy the ratios determined from the above SDOF approach. When modeling the MDOF frame by the SDOF system, one could use the first mode effective mass approximately equal to 0.8 times total mass for a regular building, and effective height based on the static deflected shape of the frame (e.g., Kasai et al. 1998a, 2005e, JSSI 2003, 2005).

Based on these, the required force capacity of each damper is estimated to be 300 kN to 1,200 kN from top story to bottom story of the building, and damper sizes are selected satisfying the required values. Installation of the dampers would require, depending on damper type, 1.5% to 4% increase in total construction cost of the building considered (Fig. 2).

Performance Curve: Normalized by Frame Response

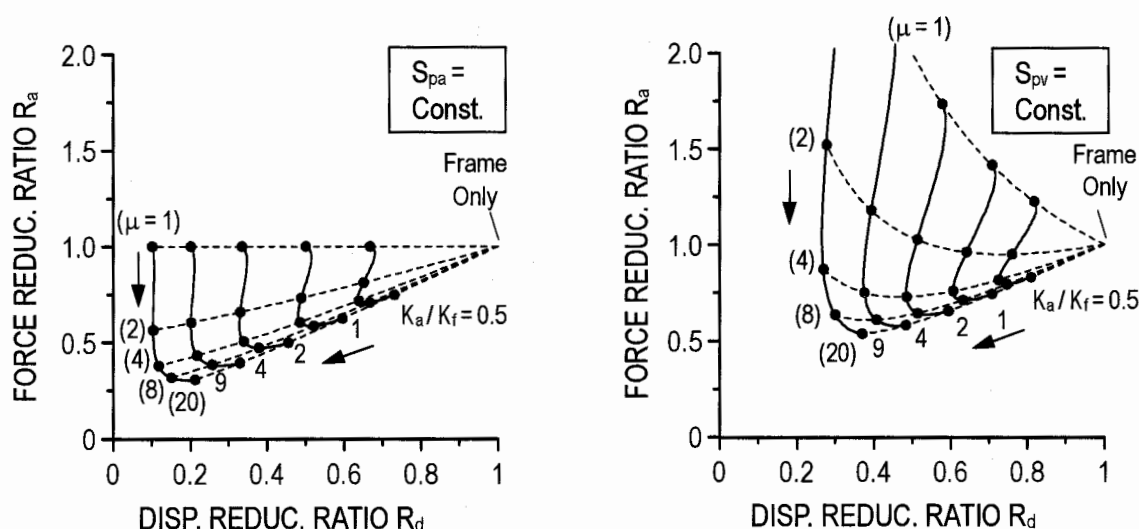


Figure 4 Examples of Steel Damper Case: Performance Curves under (a) Constant Spectral Acceleration, and (b) Constant Spectral Velocity

5. DYNAMIC ANALYSIS RESULTS

Fig. 5 shows results from time history analysis of the designed buildings having four different damper types as well as the building without dampers. The case of friction damper is not shown,

since the performance was similar to that of steel damper.

Against the artificial earthquake called BCJ-L2 whose spectrum characteristics are in conformity with the Japanese design code spectrum (Fig. 3), all buildings using different dampers satisfied the very stringent drift angle limit of 0.005 radian (Fig. 5 lower left). Displacements and story shears of all four buildings appear to be very similar, but some differences are noted for the floor accelerations (Fig. 5 upper right).

In order to examine the performance under the catastrophic earthquake, the 1995 JMA Kobe record is used and analysis results shown additionally in Fig. 5. Because the spectral acceleration of the JMA Kobe record is extremely high (Fig. 3), larger drift develops in all the four damped buildings. However, the story drift angles are less than 0.01 radian. This indicates frame members are mostly elastic, thereby avoiding any structural repair even after the catastrophic event.

Note also the damped buildings show about one-third times drift angles than the buildings without dampers, realizing high-value-added design.

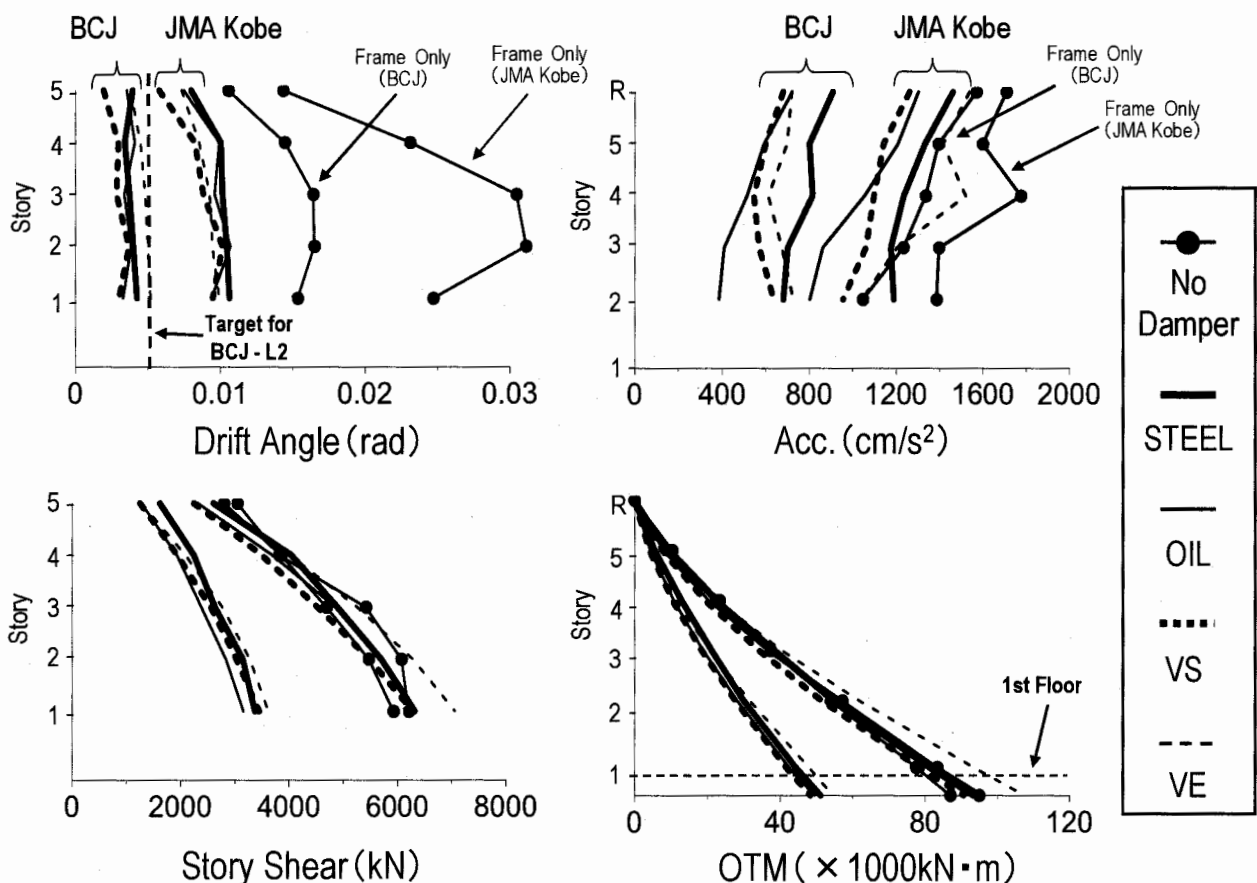


Figure 5 Dynamic Responses of the Full-Size Building Specimen Subjected to BCJ-Level 2 Earthquake and the 1995 Kobe Earthquake (BCJ = Building Center of Japan).

Fig. 6 shows story drift vs. story shear at the 2nd story level (between the 2nd and the 3rd floors) due to the BCJ-2 record, and Fig. 7 shows those due to the JMA-Kobe record. Against BCJ-L2 record, the hysteresis curves of the four different structures show almost the same peak story drift, peak story shear, and equivalent stiffness (Fig. 6). For much stronger JMA Kobe record, however, the curves show different trends: The structure with viscoelastic damper that is almost linear shows the largest equivalent stiffness and, consequently, larger story shear (Fig. 7(b)). The structure with oil damper

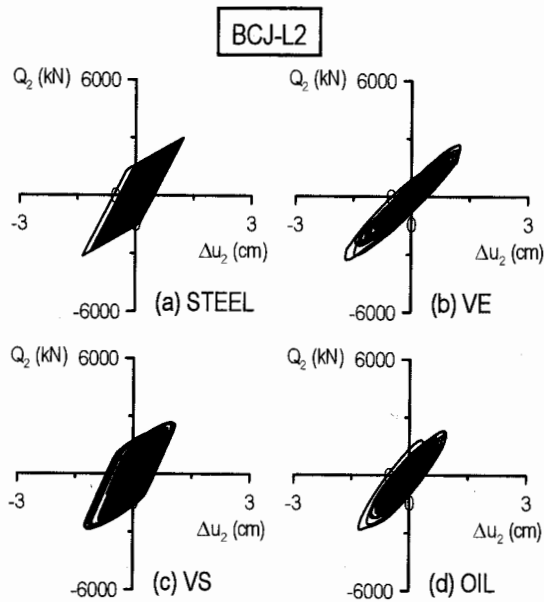


Figure 6 Story Drift and Shear at 2nd Story Level
(Due to BCJ-Level 2 Earthquake)

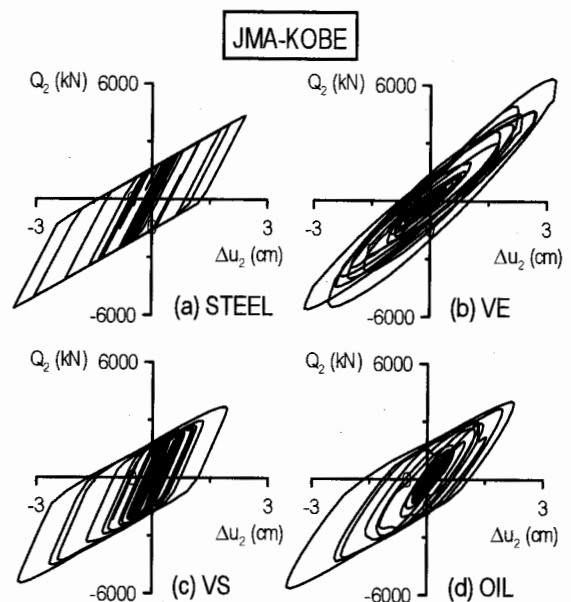


Figure 7 Story Drift and Shear at 2nd Story Level
(Due to JMA Kobe Earthquake)

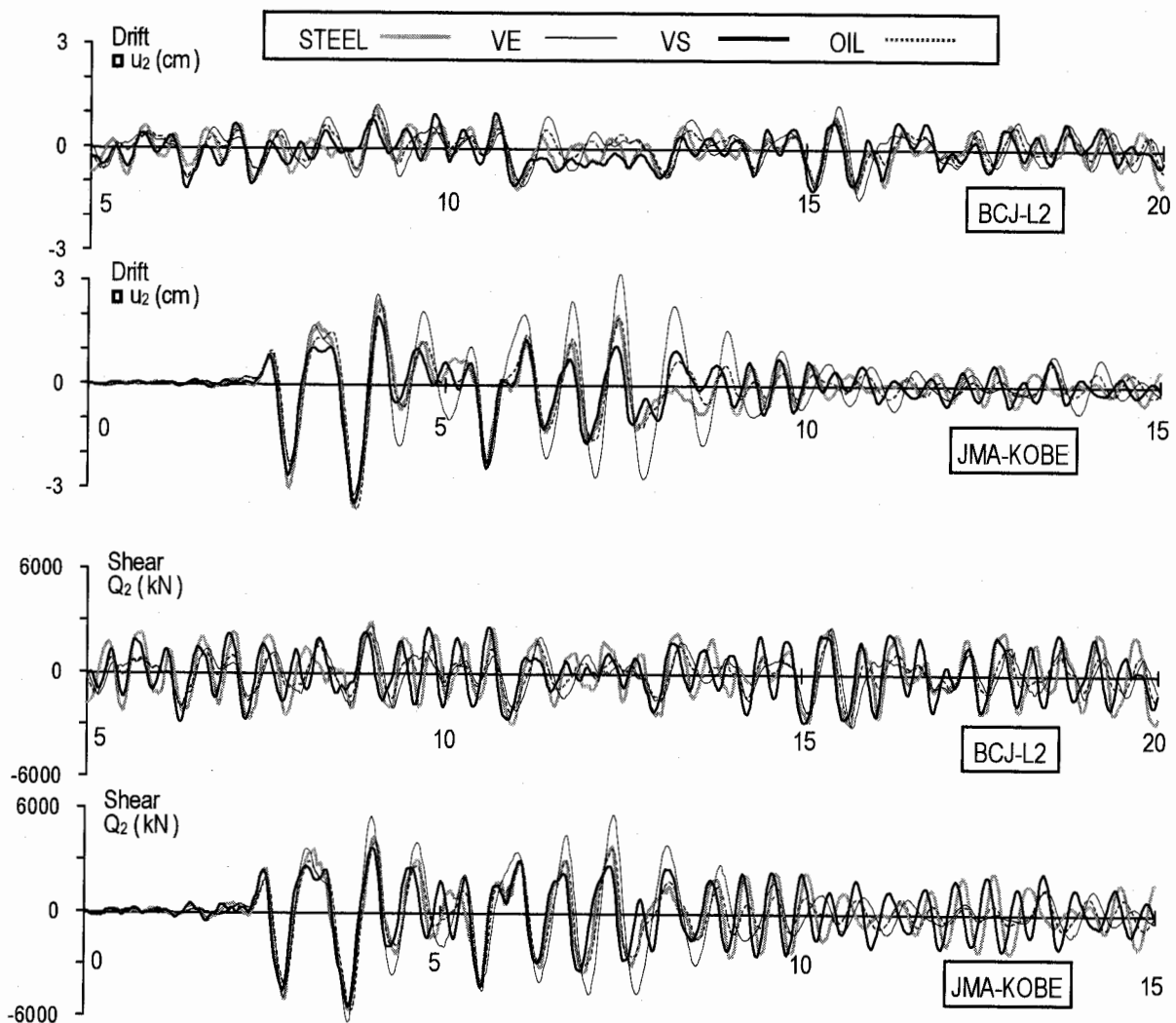


Figure 8 Time Histories of Story Drift and Story Shear at 2nd Story Level
(4 Different Dampers per Graph, BCJ-Level 2 Earthquake and JMA Kobe Earthquake)

showed the elliptical hysteresis due to the BCJ-L2 record (Fig. 6(d)), but it exhibits in contrast the bilinear hysteresis due to the JMA Kobe record (Fig. 7(d)). The bilinear behavior occurs due to the relief mechanism made active against the larger excitation.

Fig. 8 shows time histories of story drift and story shear at the 2nd story level, due to the BCJ-2 record, and JMA-Kobe record, respectively. Against BCJ-L2 record, the behaviors of four structures having different dampers behaved in a similar manner. However, their difference becomes prominent under the JMA Kobe record: four structures that are designed to show almost the same performance at a certain earthquake level will behave differently under different earthquake level.

6. CONCLUSIONS

Passive control scheme has established its status as a viable means to enhance seismic performance of buildings. Due to lack of information on its performance under actual major earthquake, and for the sake of further growth in this technology, it is necessary to verify the control performance by conducting realistic experiments.

Pursuant to this, the writers with other colleagues have been preparing for the three-dimensional full-scale dynamic tests of a five-story steel frame. The test will be repeated by trying at least 5 different types of dampers for the frame. It will be conducted in the year of 2008 by using the world's largest E-Defense shaking table. This paper has explained on-going preliminary work of design and analysis of the five-story building specimen.

Acknowledgements:

The writer acknowledges support from the National Research Institute for Earth Science and Disaster Prevention (NIED), as well as Japan Ministry of Education, Culture, Sport, Science, and Technology (MEXT) for his research described in this paper. The writer also thanks the students at Kasai Laboratory, Tokyo Institute of Technology for their dedications to this research. Special gratitude is given to Mr. Kibayashi, the Senior Manager of Building Structural Design Division, Takenaka Corporation, for his close collaboration with the writer during the entire period of formulating the 1st and 2nd editions of the JSSI manual.

References:

- JSSI Manual (2003), Design and Construction Manual for Passively Controlled Buildings, Japan Society of Seismic Isolation (JSSI), First Edition, Tokyo, JAPAN, October (in Japanese, 405 pages).
- JSSI Manual (2005), Design and Construction Manual for Passively Controlled Buildings, Japan Society of Seismic Isolation (JSSI), Second Edition, Tokyo, JAPAN, October (in Japanese, 515 pages).
- JSCA Specifications (2000), Design Methodologies for Response Controlled Structures, Japan Structural Consultants Association (JSCA), Tokyo, JAPAN, December, 2000 (in Japanese, 445 pages).
- Kasai, K., Fu, Y., and Watanabe, A. (1998a), "Passive Control Systems for Seismic Damage Mitigation," *Journal of Structural Engineering*, American Society of Civil Engineers, **124**(5), 501-512.
- Fu, Y. and Kasai, K., (1998b), "Comparative Study of Frames Using Viscoelastic and Viscous Dampers", *J. Struct. Eng.*, American Society of Civil Engineers, **122** [10], pp. 513-522.
- Kasai, K., Teramoto, M., Okuma, K., and Tokoro, K. (2001a), "Constitutive Rule for Viscoelastic Materials Considering Temperature, Frequency, and Strain Sensitivities (Part 1: Linear Model with Temperature and Frequency Sensitivities)", *Journal of Structural and Construction Engineering (Transactions of AIJ)*, No. 543, pp. 77-86, May. (in Japanese)
- Kasai, K. and Okuma, K. (2001b), "Kelvin-Type Formulation and Its Accuracy for Practical Modeling of Linear Viscoelastic Dampers (Part 1: One-Mass System Having Damper and Elastic / Inelastic Frame)", *Journal of Structural and Construction Engineering (Transactions of AIJ)*, No. 550, pp. 71-78, Dec. (in Japanese)
- Kasai, K. and Okuma, K. (2002a), "Accuracy Enhancement of Kelvin-Type Modeling for Linear Viscoelastic Dampers (A Refined Model Including Effect of Input Frequency on Material Property)", *Journal of Structural Engineering*, Architectural Institute of Japan (AIJ), **48B**, pp.545-553, March. (in Japanese)
- Kasai, K., Teramoto, M., and Watanabe, Y. (2002b), "Behavior of a Passive Control Damper Combining Visco-Elastic and Elasto-Plastic Devices in Series", *Journal of Structural and Construction Engineering (Transactions of AIJ)*, No. 556, pp. 51-58, June. (in Japanese)
- Kasai, K. and Jodai, A. (2002c), "Dynamic Property, Behavior, and Their Simplified Estimation Rules for a Passive Control System with Stud-Type Viscoelastic Damper", *Journal of Structural and Construction Engineering (Transactions of AIJ)*, No. 558, pp. 125-132, Aug. (in Japanese)
- Kasai, K., Motoyui, S., and Ooki, Y. (2002d), "Application of Viscoelastic Dampers to Space Frames and Response Prediction Methods for a Single-Directional Earthquake", *Journal of Structural and Construction Engineering (Transactions of AIJ)*, No. 561, pp. 125-135, Nov. (in Japanese)
- Kasai, K. and Tokoro, K. (2002e), "Constitutive Rule for Viscoelastic Materials Having Temperature, Frequency, and Strain Sensitivities (Part 2: Nonlinear Model Based on Temperature-Rise, Strain, and Strain-Rate)", *Journal of Structural and Construction Engineering (Transactions of AIJ)*, No. 561, pp. 55-63, Nov. (in Japanese)

- Kasai, K., Ooki, Y., Amemiya, K., and Kimura, K. (2003a), "A Constitutive Rule for Viscoelastic Materials Combining Iso-Butylene And Styrene Polymers (Part 1: Linear Model Considering Temperature And Frequency Sensitivities)", *Journal of Structural and Construction Engineering (Transactions of AIJ)*, No. 569, pp.47-54, July. (in Japanese)
- Kasai, K., Ito, H., and Watanabe, A. (2003b), "Peak Response Prediction Rule for a SDOF Elasto-Plastic System Based on Equivalent Linearization Technique", *Journal of Structural and Construction Engineering (Transactions of AIJ)*, No. 571, pp.53-62, Sep. (in Japanese)
- Kasai, K., Suzuki, A., and Oohara, K. (2003c), "Equivalent Linearization of a Passive Control System Having Viscous Dampers Dependent on Fractional Power of Velocity", *Journal of Structural and Construction Engineering (Transactions of AIJ)*, No. 574, pp.77-84, Dec. (in Japanese)
- Kasai, K. and Okuma, K. (2004a), "Evaluation Rule and Its Accuracy for Equivalent Period and Damping of Frequency-Dependent Passive Control Systems — Global Damping Model of One-Mass System Having Elastic Frame and Either Viscoelastic or Oil Damper —", *Journal of Structural and Construction Engineering (Transactions of AIJ)*, No. 580, pp.51-59, June (in Japanese)
- Ooki, Y., Kasai, K., and Takahashi, O. (2004b), "Performance of Velocity-Dependent Dampers under Extremely Small Excitations", *Journal of Structural Engineering*, Architectural Institute of Japan (AIJ), **50B**, pp. 601-609, March (in Japanese)
- Kasai, K., Sakata, H., Komehana, S., and Miyashita, Y. (2004c), "Experimental Study on Dynamic Behavior of Timber Frame with Viscoelastic Damper", *Journal of Structural Engineering*, Architectural Institute of Japan (AIJ), **50B**, pp. 349-360, March (in Japanese)
- Kasai, K. and Nishimura, T. (2004d), "Equivalent Linearization of Passive Control System Having Oil Damper Bi-Linearly Dependent on Velocity", *Journal of Structural and Construction Engineering (Transactions of AIJ)*, No.583, pp. 47-54, Sep. (in Japanese)
- Kasai, K., Ooki, Y., Suriyamongkol, P., and Xu, Y. (2004e), "Fundamental Study on Inelastic Behavior and Low-Cycle Fatigue of a Thick Shear Panel Fabricated Without Welding", *Journal of Structural and Construction Engineering (Transactions of AIJ)*, No.586, pp. 195-202, Dec. (in Japanese)
- Kasai, K., Watanabe, Y., and Minato, N. (2005a), "Study on Dynamic Behavior of a Passive Control System with Visco-Elasto-Plastic Damper", *Journal of Structural and Construction Engineering (Transactions of AIJ)*, No.588, pp. 87-94, Feb. (in Japanese)
- Kasai, K. and Kawanabe, Y. (2005b), "Equivalent Linearization to Predict Dynamic Properties and Seismic Peak Responses of a Structural System with High Viscous Damping and Hysteretic Damping", *Journal of Structural and Construction Engineering (Transactions of AIJ)*, No.591, pp. 43-52, May (in Japanese)
- Sakata, H., Kasai, K., Wada, A., and Miyashita, T. (2005c), "Experimental Study on Dynamic Behavior of a Wood Frame with Shear Link Passive Control Mechanism Involving Plywood Panel", *Journal of Structural and Construction Engineering (Transactions of AIJ)*, No.594, pp.65-73, Aug. (in Japanese)
- Kasai, K., Wada, A., Sakata, H., Midorikawa, M., Ooki, Y., and Nakagawa, T. (2005d), "Shaking Table Tests of Wood Frames with Deformation-Dependent Dampers", *Journal of Structural and Construction Engineering (Transactions of AIJ)*, No.594, pp.101-110, Aug. (in Japanese)
- Kasai, K. and Ito, H. (2005e), "Passive Control Design Method Based on Tuning of Stiffness, Yield Strength, and Ductility of Elasto-Plastic Damper", *Journal of Structural and Construction Engineering (Transactions of AIJ)*, No.595, pp.45-55, Sep. (in Japanese)
- Kasai, K., Sakata, H., Wada, A., and Miyashita, T. (2005f), "Dynamic Behavior of a Wood Frame with Shear Link Passive Control Mechanism involving K-Brace", *Journal of Structural and Construction Engineering (Transactions of AIJ)*, No.598, in Print, Dec. (in Japanese)
- Kasai, K., Sato, D., and Huang, Y. (2006a), "Analytical Methods for Viscoelastic Damper Considering Heat Generation, Conduction, and Transfer under Long Duration Cyclic Load", *Journal of Structural and Construction Engineering (Transactions of AIJ)*, No.599, in Print, Jan. (in Japanese)
- Kasai, K., Kibayashi M., Takeuchi T., Kimura Y., Saito Y., Nagashima I., Mori H., Uchikoshi M., Takahashi O., and Oohara K. (2002), "Principles and Current Status of Manual for Design and Construction of Passively-Controlled Buildings: Part-1: Background Scope, and Design Concept", *Proc. Structural Engineers World Congress (SEWC)*, Yokohama, JAPAN, CD-ROM, T2-2-a-1
- Kibayashi, M., Kasai, K., Tsuji, Y., Kato, S., Kikuchi, M., Kimura, Y., and Kobayashi, T. (2002), "Principles and Current Status of Manual for Design and Construction of Passively-Controlled Buildings: Part-2 JSSI Criteria for Implementation of Energy Dissipation Devices", *Proc. Structural Engineers World Congress (SEWC)*, Yokohama, JAPAN, CD-ROM, T3-3-1
- Takeuchi, T., Kasai, K., Ohara, K., Nakajima, H., and Kimura, Y. (2002), "Performance Evaluation and Design of Passively Controlled Buildings Using Equivalent Linearization", *Proc. Structural Engineers World Congress (SEWC)*, Yokohama, JAPAN, CD-ROM, T2-2-a-2
- Ichikawa, Y., Takeuchi, T., Morimoto, S., and Sugiyama, M. (2002), "Practical Design of High-Rise Structure Using Viscoelastic Dampers and Hysteretic Dampers", *Proc. Structural Engineers World Congress (SEWC)*, Yokohama, JAPAN, CD-ROM, T2-2-a-3
- Kanada, M., Kasai, K., and Okuma, K. (2002), "Innovative Passive Control Scheme: a Japanese 12-Story Building with Stepping Columns and Viscoelastic Dampers", *Proc. Structural Engineers World Congress (SEWC)*, Yokohama, JAPAN, CD-ROM, T2-2-a-5
- Ono, Y., Kaneko, H., and Kasai, K. (2002), "Time-History Analysis Models for Steel Dampers", *Proc. Structural Engineers World Congress (SEWC)*, Yokohama, JAPAN, CD-ROM, T2-2-b-1
- Ooki, Y., Kasai, K., and Tokoro, K. (2002), "Time-History Analysis Models for Linear and Nonlinear Viscoelastic Dampers", *Proc. Structural Engineers World Congress (SEWC)*, Yokohama, JAPAN, CD-ROM, T2-2-b-2
- Oohara, K., and Kasai, K. (2002), "Time-History Analysis Models for Nonlinear Viscous Dampers", *Proc. Structural Engineers World Congress (SEWC)*, Yokohama, JAPAN, CD-ROM, T2-2-b-3
- Sekiguchi, Y., and Takahashi, O. (2002), "Time-History Analysis Models for Nonlinear Viscous Damping Wall", *Proc. Structural Engineers World Congress (SEWC)*, Yokohama, JAPAN, CD-ROM, T2-2-b-4
- Takahashi, O. and Sekiguchi, Y. (2002), "Time-History Analysis Models for Nonlinear Oil Dampers", *Proc. Structural Engineers World Congress (SEWC)*, Yokohama, JAPAN, CD-ROM, T2-2-b-5
- Tsuyuki, Y., Kamei, T., Gofuku, Y., Iiyama, F., and Kotake, Y. (2002), "Performance and Quality Control of Oil-Damper", *Proc. Structural Engineers World Congress (SEWC)*, Yokohama, JAPAN, CD-ROM, T3-3-2
- Furukawa, Y., Kawaguchi, S., Sukagawa, M., Masaki, N., Sera, S., Kato, N., Washiyama, Y., and Mitsusaka, Y. (2002), "Performance and Quality Control of Viscous Dampers", *Proc. Structural Engineers World Congress (SEWC)*, Yokohama, JAPAN, CD-ROM, T3-3-3
- Okuma, K., Ishikawa, K., Oku, T., Sone, Y., Nakamura, H., and Masaki, N. (2002), "Performance and Quality Control of Viscoelastic Dampers", *Proc. Structural Engineers World Congress (SEWC)*, Yokohama, JAPAN, CD-ROM, T3-3-4
- Nakata, Y. (2002), "Performance and Quality Control of Steel Hysteretic Damper", *Proc. Structural Engineers World Congress (SEWC)*, Yokohama, JAPAN, CD-ROM, T3-3-5

EVALUATION OF EARTHQUAKE RESISTANCE OF STEEL BUILDING STRUCTURE BASED ON DEFORMATION CAPACITY OF MEMBERS

S. Yamada¹⁾

1) Associate Professor, Structural Engineering Research Center, Tokyo Institute of Technology, Japan

naniwa@serc.titech.ac.jp

Abstract: In this paper, evaluation method of earthquake resistance of weak beam type steel building structure is introduced. This method is based on the energy based earthquake resistant design which is developed by Prof. Hiroshi AKIYAMA.

In the former part of paper, outline of the evaluation method is introduced. In this method, the earthquake input is evaluated as input energy, and the earthquake resistance of the building structure is captured as energy absorption capacity. The input energy can be evaluated by the energy spectrum which is given in the design code. On the other hand, energy absorption capacity of building structure can be evaluated by plastic deformation capacity of members. Therefore, the most important index in the earthquake resistance evaluation is the plastic deformation capacity of members. The plastic deformation capacity of steel member under cyclic loading is evaluated based on the plastic deformation capacity in the skeleton curve which is clarified based on the experimental result.

In the latter part of paper, full scale cyclic loading test of composite beam is introduced. From this experiment, deformation capacity of composite beams determined by rupture is clarified. Using this result, earthquake resistance of weak beam type steel building structure can be evaluated.

1. INTRODUCTION

In Japan, energy based earthquake resistant design method came to be practically used. Generally, steel moment frames are designed as weak beam type frame. The evaluation of the earthquake resistance of weak beam type steel moment frame is an important problem. In this paper, energy based earthquake resistant design method which is developed by Prof. Hiroshi AKIYAMA (Akiyama, 1985) is enhanced as the evaluation method of earthquake resistance of weak beam type steel moment frame. In this method, the most important index is the plastic deformation capacity of members. Therefore, a series of cyclic loading test of composite beam was carried out. By reflecting experimental result, the earthquake resistance of weak beam type moment frame can be evaluated accurately.

2. ENERGY INPUT DUE TO EARTHQUAKE (Akiyama 1985)

The basis of the earthquake resistant design based on energy is shown by expression (1).

$$E = W_e + W_p + W_h \quad (1)$$

Where, E is the total input energy by earthquake, W_e is the elastic vibrational energy, W_p is the

cumulative plastic strain energy W_h is the energy consumed by the damping mechanism. The total energy input due to the earthquake E is a steady quantity obtained by the fundamental natural period T , the total mass M , and the energy spectrum of the earthquake. The energy spectrum show the relationship between equivalent velocity of the energy input of single degree of freedom elastic system with 10% damping $V_E = \sqrt{2E/M}$ and its natural period. The energy spectrum for response prediction is given as energy spectrum for the design. Therefore, the total energy input E is decided, if fundamental natural period and total mass of the building are decided. Denoting $W_e + W_p$ by E_D , and defining as the energy input attributable to damage. E_D is related to the total energy input by semi empirical formula (2) based on the response analysis result

$$E_D = \frac{1}{(1 + 1.2\sqrt{h} + 3h)^2} E \quad (2)$$

Where, h is damping factor.

3. EVALUATION OF EARTHQUAKE RESISTANCE OF WEAK BEAM TYPE STEEL BUILDING STRUCTURE (Akiyama 1985 and AIJ 1990)

The earthquake resistance evaluation based on energy is outlined referring to the steel moment resisting frame. In the earthquake resistance evaluation based on energy, the energy input attributable to damage E_D is compared with the energy absorption capacity of frame E_{Max} . Energy absorption capacity of frame E_{Max} is evaluated considering damage concentration to some story and deformation capacity of structural element.

The building is modeled as a equivalent single-degree-of-freedom system that fundamental natural period and total mass are equal. Restoring force characteristics of this system is elastic perfectly plastic type. E_{Max} is given in equation (3) as a sum of maximum value of the elastic strain energy $W_{e,max}$ and maximum value of the plastic strain energy $W_{p,max}$.

$$E_{max} = W_{e,max} + W_{p,max} = \left(1/2 + \eta_{eq}\right) \cdot Q_{y,eq} \cdot \delta_{y,eq} \quad (3)$$

Where η_{eq} is plastic deformation capacity of equivalent single-degree-of-freedom system which is expressed as cumulative plastic deformation ratio, $Q_{y,eq}$ is yield strength of equivalent single-degree-of-freedom system, $\delta_{y,eq}$ is yield deformation of equivalent single-degree-of-freedom system. Using the base shear ratio α , $Q_{y,eq}$ is expressed as αMg . Elastic stiffness of the equivalent single-degree-of-freedom system is $k_{eq} = 4\pi^2 m / T^2$. So the yield deformation is expressed as $\alpha g T^2 / 4\pi^3$. Therefore equation (3) becomes

$$E_{max} = \left(\frac{1}{2} + \eta_{eq}\right) \cdot \frac{\alpha^2 m g^2 T^2}{4\pi^2} \quad (4)$$

In case of the multistory frame, the first story is focused. The maximum value of the plastic strain energy $W_{p,max}$ is shown by the maximum value of plastic strain energy of the first story $W_{p,1,max}$ and damage distribution factor of the first story γ_1 .

$$W_{p,max} = \gamma_1 \cdot W_{p,1,max} = \frac{Mg^2 T^2}{4\pi^2} \cdot \frac{\gamma_1 \alpha_1^2 \eta_1}{\kappa_1} \quad (5)$$

$$\gamma_1 = \sum_{j=1}^N s_j \cdot p_j^{-n} / (s_1 \cdot p_1^{-n}) \quad (6)$$

Where $s_i = \sum_{j=i}^N (m_j / M)^2 \cdot k_i / k_1 \cdot \overline{\alpha_i}^2$, m_i is mass of i-th story, k_i is stiffness of i-th story, $\overline{\alpha_i}$ is optimum shear force coefficient distribution, (The shear force coefficient distribution in which cumulative plastic deformation ratio of each story becomes equal.) $p_i (= \alpha_i / (\alpha_1 \cdot \overline{\alpha_i}))$ shows the extent of deviation of shear force coefficient distribution from the optimum shear force coefficient distribution, n is damage concentration index (In case of the weak beam type frame, $n = 4$), α_i is shear force coefficient, η_1 is plastic deformation capacity of first story which is expressed as cumulative plastic deformation ratio, $\kappa_1 = k_1 / k_{eq}$.

On the other hand, the maximum value of the elastic strain energy is approximately shown by following equation.

$$W_{e,\max} = \frac{MgT^2}{4\pi^2} \cdot \frac{\alpha_1^2}{2} \quad (7)$$

From equations (5) and (7), equation (8) is obtained.

$$E_{\max} = \frac{MgT^2}{4\pi} \cdot \left(\frac{\alpha_1^2}{2} + \frac{\gamma_1 \alpha_1^2 \eta_1}{\kappa_1} \right) \quad (8)$$

Expressing it in equivalent velocity, equation (8) becomes equation (9)

$$V_{\max} = \sqrt{\frac{2E_{\max}}{M}} = \frac{gT\alpha_1}{2\pi} \sqrt{1 + \frac{2\gamma_1\eta_1}{\kappa_1}} \quad (9)$$

By substituting plastic deformation capacity of first story η_1 in equation (8) and (9), energy absorption capacity of the frame can be evaluated. Plastic deformation capacity of first story η_1 can be evaluated based on the plastic deformation capacity of member η in equation (10). The plastic deformation capacity of member η is the cumulative plastic deformation ratio ((dissipated strain energy)/($M_p \cdot \theta_p$)) in the skeleton curve (Fig.1). The cumulative plastic deformation ratio in the skeleton curve corresponds to the cumulative plastic deformation ratio under monotonic loading.

$$\eta_i = a_b \cdot \eta + a_{lb} \quad (10)$$

Where a_b is the coefficient according to the Bauschinger effect, a_{lb} is the constant considering the deteriorating range. In the weak beam type moment frame, $a_b = 2.0$. When the maximum strength of beam is decided in the rupture, $a_{lb} = 0$. When the maximum strength of beam is decided in local buckling, $a_{lb} = 1.0$.

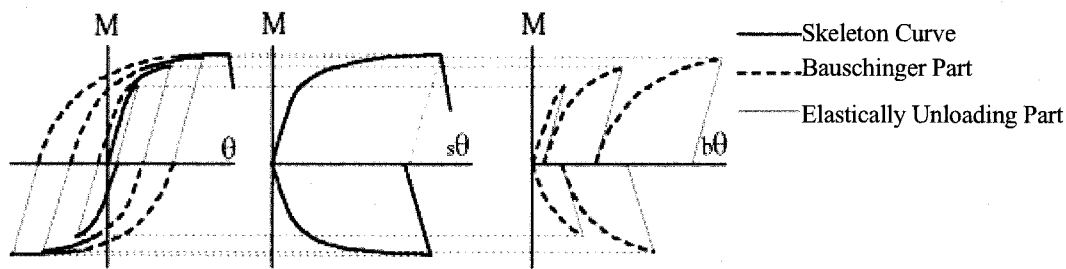


Fig.1 Skeleton Curve

4. Ultimate Deformation Capacity of Beams

In the Kobe Earthquake, damage of rupture in the beam-to-column connection was mainly observed in steel building structures. After the earthquake, a lot of experimental research works on the deformation capacity of steel beam, which is determined by rupture, were carried out. From those research works, the cause of the rupture, such as stress concentration at connection part and the lack of the quality of steel material, was pointed out. However, steel beams without slab were used in most of those research works. When the slab exists, large tensile strain is generated in bottom flange of beam under positive bending moment. So, it can be estimated that the existence of the slab greatly influences the deformation capacity of beam determined by rupture.

In order to evaluate the ultimate deformation capacity of composite beam determined by rupture, a series of full scale cyclic loading test was carried out. A list of the specimens is shown in Table 1 and the shape of specimen is shown in Fig. 2. The scale and the shape of the specimens were designed based on those of beam-to-column connections of medium-rise steel buildings. Testing setup is shown in Fig.3. During the tests, lateral deformation is restricted by frames positioned at the ends of the lateral beams and the free end of the main beam.

Moments versus rotation angle relationships are shown in Fig. 4, where ▼ shows the point where the flange ruptured. Full plastic moment calculations for composite beams and steel beams are shown by broken lines as cMp and sMp . The failure mode of all the specimens is flange rupture initiated by a ductile crack which generated at the tip of a weld access hole. Rupture of the composite beam specimens occurred in positive bending state. The cumulative plastic deformation ratio of each specimen were follows; No.1, $\eta = 2.3$, No.2, $\eta = 5.3$, No.3, $\eta = 1.9$, No.4, $\eta = 2.2$, No.5, $\eta = 1.8$. From this result, it was evaluated that plastic deformation capacity of composite beam is approximately 2.0 as the cumulative plastic deformation ratio.

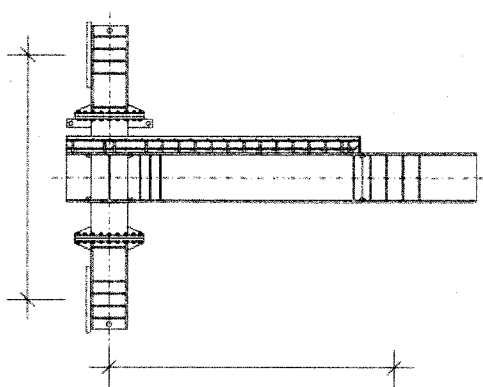


Fig.2.Specimen

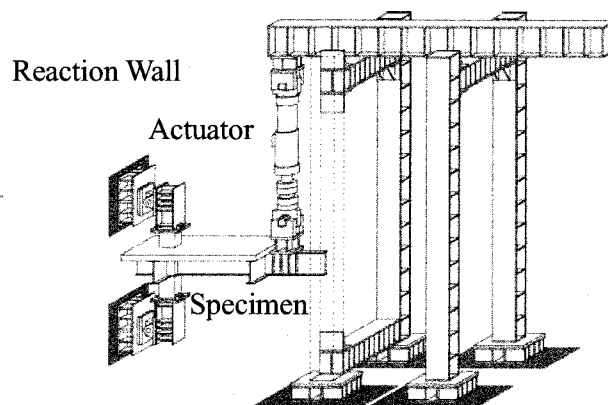


Fig.3 Set-up

Table 1 Specimen

No.	Parameter	Beam	cM_p [kN.m]	sM_p [kN.m]	$s\theta_p$ [rad.]	t_c [mm]	Weld Access Holes	Loading Pattern
1	Standard	R-H-612×202×13×23	2.24×10^3	1.41×10^3	0.0082	200	Conventional	1
2	(1) Existence of a slab without Slab	R-H-612×202×13×23	—	1.41×10^3	0.0082	0	Conventional	1
3	(2) Section properties Small Section Beam	R-H-596×199×10×15	1.69×10^3	0.99×10^3	0.0087	200	Conventional	1
4	(2) Section properties Thinner Slab	R-H-612×202×13×23	2.07×10^3	1.41×10^3	0.0082	140	Conventional	1
5	(3) Loading pattern Pattern 2	R-H-612×202×13×23	2.24×10^3	1.41×10^3	0.0082	200	Conventional	2

cM_p : full plastic moment calculation for composite beams [AIJ], sM_p : full plastic moment calculation for bare steel beams, $s\theta_p$: elastic rotation angle of bare steel beams subjected to sM_p , t_c : thickness of slabs

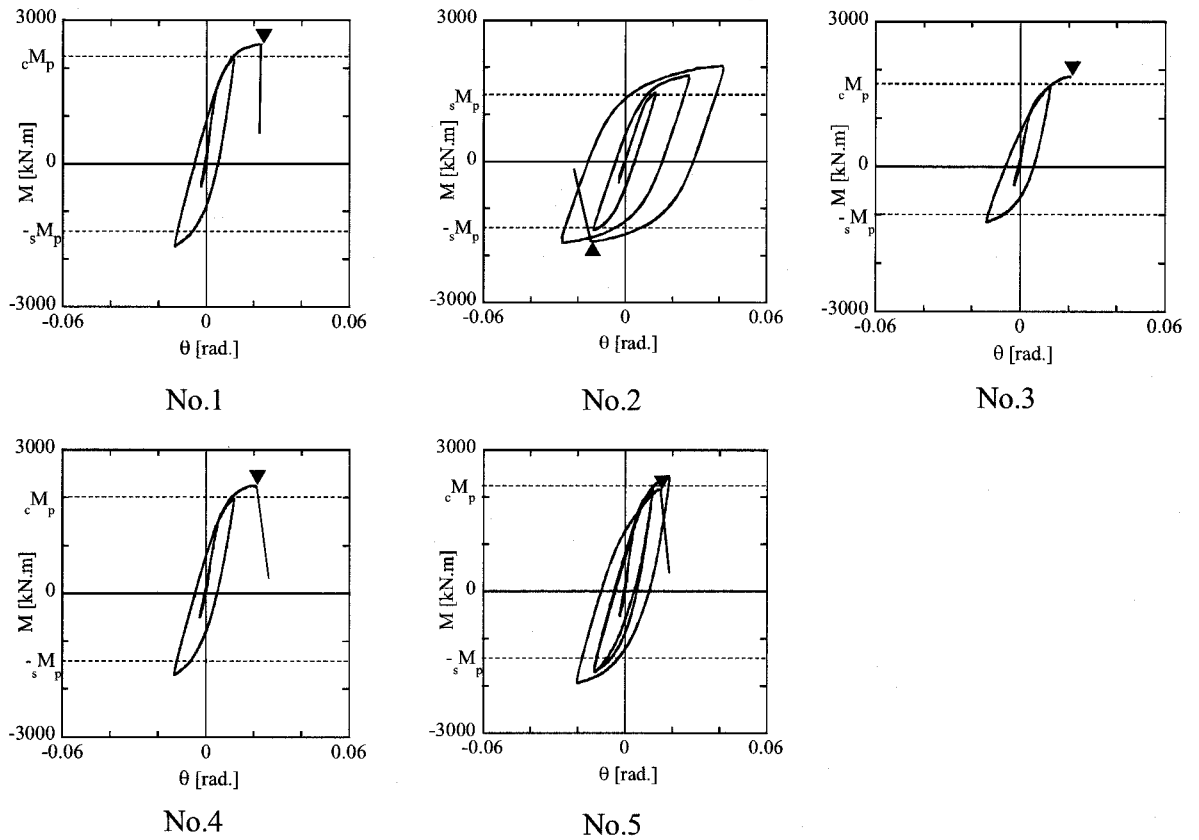


Fig.4 Moments versus rotation angle relationships

Equation (11) is got by substituting $a_b = 2.0$, $\eta = 2$ and $a_{lb} = 0$ in equation (10).
 $\eta_i = 4$

(11)

Equation (9) becomes

$$V_{\max} = \sqrt{\frac{2E_{\max}}{M}} = \frac{gT\alpha_1}{2\pi} \sqrt{1 + \frac{8\gamma_1}{\kappa_1}} \quad (12)$$

Equation (12) gives the evaluation of earthquake resistance of weak beam type steel building structure which is decided by the rupture.

5.Verification

Using response analytical result of multi-story frame (Yamada and Matsumoto, 2000), verification of equation (12) is carried out. Analytical models are 6-story, 9-story and 12 story moment resisting frames. Columns of analytical models have rectangular hollow section and beams have wide flange section. And the column bases of the models were exposed type column bases. In the analysis, hysteresis model by Akiyama and Takahashi (Akiyama and Takahashi, 1990) considering the Bauschinger effect was used. Input wave used in the analysis were NS component of the 1995 Kobe record (Japan; NTT Kobe record), NS component of the 1940 El Centro record (U.S.A) and EW component of the 1968 Hachinohe record (Japan).

In the evaluation of earthquake resistance, the beam in which the deformation in skeleton curve was most large was focused. It was called as the damage concentrated beam. Earthquake resistance of frames in analytical result is shown by equivalent velocity of absorbed energy V_p . Equivalent velocity of absorbed energy V_p is defined in equation (13).

$$V_p = \sqrt{2W_p / M} \quad (13)$$

Where W_p is the total absorbed energy in frame. In Fig.5, V_p is compared with V_{max} calculated in equation (12). In the calculation of V_{max} , following semi-empirical formula for weak beam type moment frame were used.

$$\kappa_1 = 0.48 + 0.52N \quad (14)$$

$$\gamma_1 = 1 + s_2 \left(\frac{1 + p_d}{2} \right)^{-4} + (\bar{s} - s_2) p_d^{-4} \quad (15)$$

Where N is number of story, $s_2 = \min(1.0, 0.05N + 0.55)$, $\bar{s} = 0.64(N - 1)$, $p_d = \text{Max}(1.1, 1.185 - 0.0014N)$

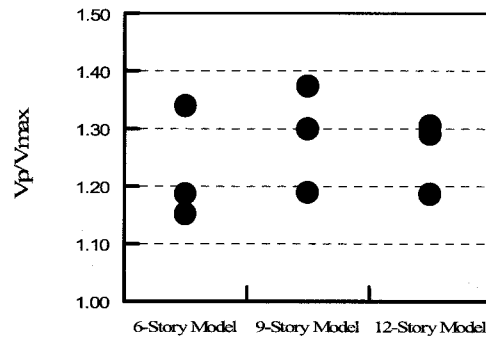


Fig.5 Verification of Equation (12)

In this comparison, equation (12) give a little conservative evaluation. It is considered that it is an appropriate evaluation, because the deformation capacity of beam which is decided by rupture disperses.

6. Conclusions

In this paper, evaluation method of earthquake resistance of weak beam type steel building structure based on the energy based earthquake resistant design method is introduced. In this method, most important index is the plastic deformation capacity of members. Therefore, deformation capacity of composite beams determined by rupture is clarified by full scale cyclic loading test of composite beam. Introduced estimation formula of earthquake resistance of weak beam type steel building structure is verified by response analytical result of multi-story moment frame. It is clarified that, the estimation formula give a little conservative evaluation. However, considering the dispersion of deformation capacity of beam which is decided by rupture, it can be said that it is a moderate evaluation.

References

- A.I.J. (Architectural Institute of Japan), 1998, Recommendation for Limit State Design of Steel Structures. (in Japanese).
- A.I.J. (Architectural Institute of Japan), 1990, Ultimate Strength and Deformation Capacity of Buildings in Seismic Design. (in Japanese).
- Akiyama, H., 1985. Earthquake-Resistant Limit-State Design for Buildings, University of Tokyo Press.
- Akiyama, H. and Takahashi, M., 1990, Influence of Bauschinger Effect on Seismic Resistance of Steel Structures. Trans. of A.I.J. No.418, pp.49-57. (in Japanese).
- Okada, K., Oh, S. H., Yamada, S., Imaeda, T., Yamaguchi, M., Chang, I. H. and Wada, A., 2001, Experimental Study on Deformation Capacity of the Composite Beams, Proc. of 6th PSSC, pp.233-238.
- Yamada, S., and Matsumoto, Y., 2000, Influence of the Ultimate Behavior of Beams on the Earthquake Resistance of Multi-Story Steel Frames, Journal of Struct. Constr. Eng., AIJ, No.535, pp.133-140.

**Center for Urban Earthquake Engineering (CUEE)
Tokyo Institute of Technology**

Suzukakedai Office ■

Department of Built Environment
Tokyo Institute of Technology
G3-11 4259 Nagatsuta-cho, Midori-ku, Yokohama, Japan 226-8502
Tel: +81-(0)45-924-5576 Fax: +81-(0)45-924-5199

O-okayama Office ■

Department of Architecture and Building Engineering
Tokyo Institute of Technology
M1-39 2-12-1 O-okayama, Meguro-ku, Tokyo, Japan 152-8552
Tel: +81-(0)3-5734-3200 Fax: +81-(0)3-5734-3200

Email:office@cuee.titech.ac.jp
URL:<http://www.cuee.titech.ac.jp>